Cardiac Mapping

THIRD EDITION

Edited by
Mohammad Shenasa MD
Gerhard Hindricks MD
Martin Borggrefe MD
Günter Breithardt MD

Foreword by
Douglas P. Zipes MD

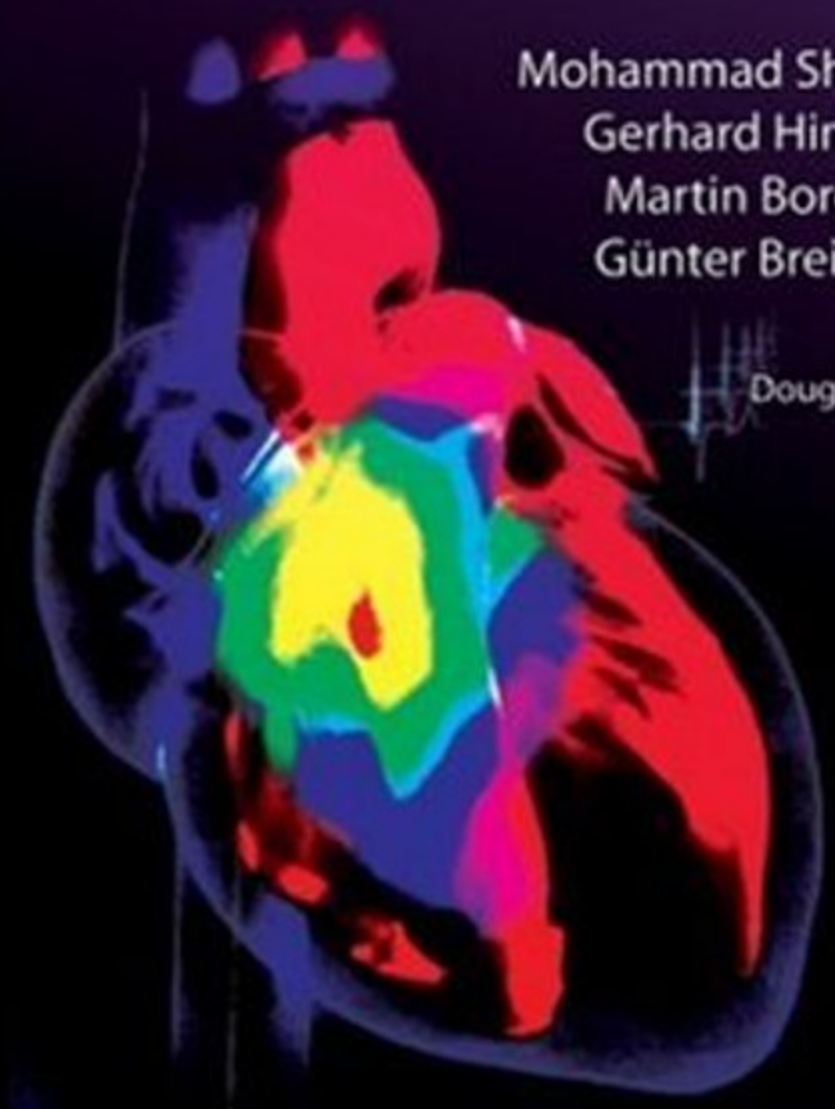

WILEY-BLACKWELL

Free CD-ROM

Cardiac Mapping

Cardiac Mapping, Third Edition Edited by Mohammad Shenasa, Gerhard Hindricks, Martin Borggrefe, and Günter Breithardt
 ISBN: 978-1-405-17572-2

Commissioning Editor: Oliver Walter
Development Editor: Laura Beaumont
Production Controller: Debbie Wyer

Cardiac Mapping

Third Edition

EDITED BY

Mohammad Shenasa, MD, FACC, FAHA, FESC, FHRS

Attending Physician
Department of Cardiovascular Services
O'Connor Hospital
San Jose, California, USA

Gerhard Hindricks, MD

Head, Department of Electrophysiology
University Leipzig, Heart Center
Leipzig, Germany

Martin Borggrefe, MD

Department of Medicine-Cardiology,
University Hospital of Mannheim,
Mannheim, Germany

Günter Breithardt, MD

Professor of Medicine (Cardiology)
Head, Department of Cardiology and Angiology
Hospital of the University of Münster
Münster, Germany

FOREWORD BY

Douglas P. Zipes, MD

Professor of Medicine, Indiana University, Indianapolis, Indiana, USA
Editor-in-Chief, *Heart Rhythm Journal*

WILEY-BLACKWELL

A John Wiley & Sons, Ltd., Publication

Blackwell Publishing was acquired by John Wiley & Sons in February 2007. Blackwell's publishing program has been merged with Wiley's global Scientific, Technical and Medical business to form Wiley-Blackwell.

Registered office: John Wiley & Sons Ltd, The Atrium, Southern Gate, Chichester, West Sussex, PO19 8SQ, UK

Editorial offices: 9600 Garsington Road, Oxford, OX4 2DQ, UK
The Atrium, Southern Gate, Chichester, West Sussex, PO19 8SQ, UK
111 River Street, Hoboken, NJ 07030-5774, USA

For details of our global editorial offices, for customer services and for information about how to apply for permission to reuse the copyright material in this book, please see our website at www.wiley.com/wiley-blackwell

Library of Congress Cataloging-in-Publication Data
Cardiac mapping / edited by Mohammad Shenasa . . . [et al.]. – 3rd ed.
p. ; cm.
Includes bibliographical references and index.
ISBN 978-1-4051-7572-2
1. Arrhythmia. 2. Electrocardiography. I. Shenasa, Mohammad.
[DNLM: 1. Electrocardiography. 2. Electrophysiology. 3. Heart Diseases – physiopathology. WG 140 C267 2009]
RC685.A65C287 2009
616.1′28–dc22

2008030334

ISBN: 9781405175722

A catalogue record for this book is available from the British Library.

Set in 9.5/12pt Minion by Aptara® Inc., New Delhi, India

Printed & bound in Singapore by Fabulous Printers Pte Ltd

1 2009

This book is dedicated to those who paved the “roads of cardiac mapping” and to all who taught us: our mentors, colleagues, students and patients.
We also dedicate this book to our wives, children, and parents for their continuous lifetime support and love

CD-ROM

A companion CD-ROM is included at the front of the book

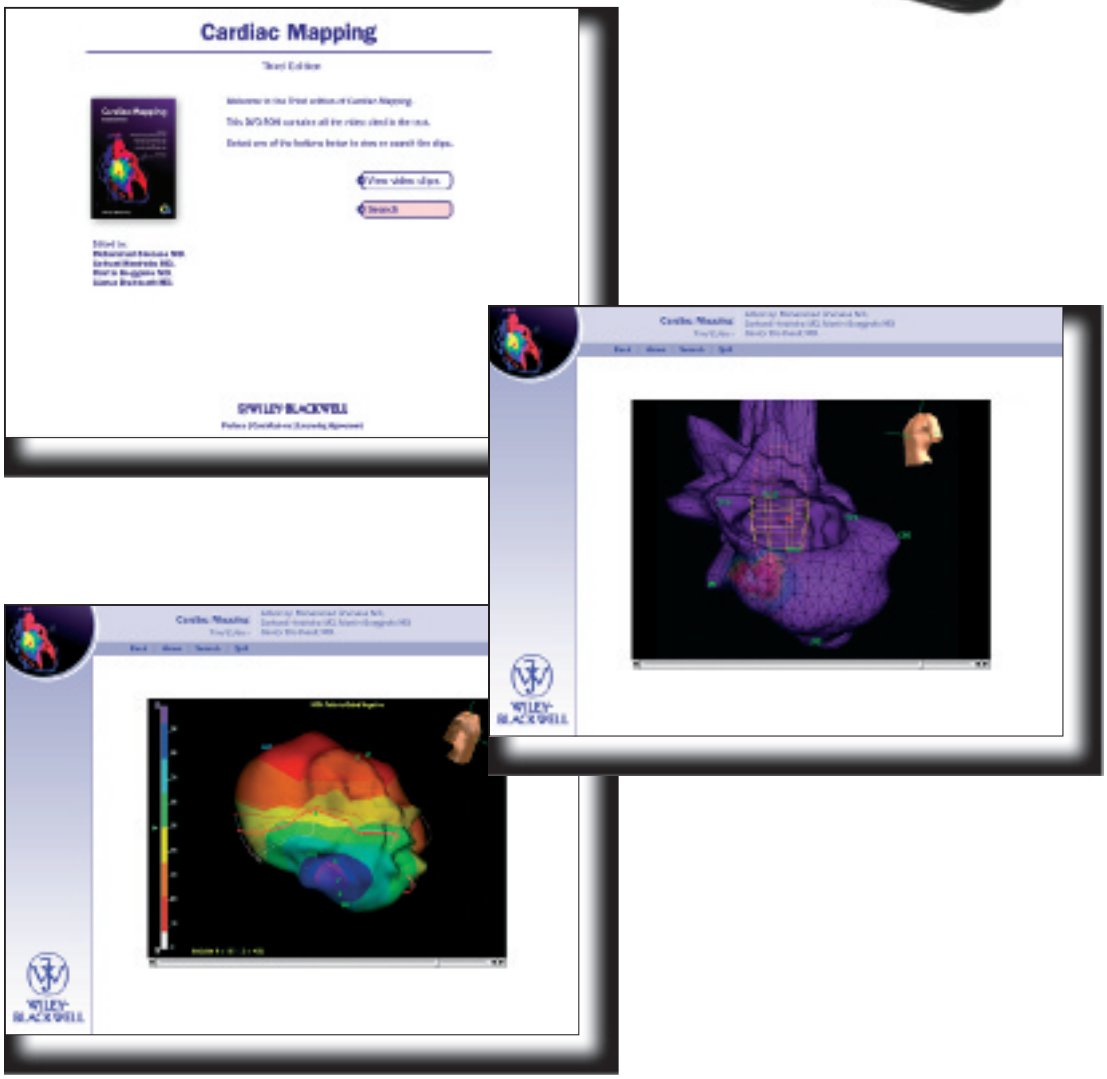

The CD includes:

A database of video clips

A search function

All video clips are referenced in the text where you see this icon.

Contents

A CR-ROM with the video clips referred to in the text is included with this book.

Acknowledgments

We wish to thank all the contributors for the substantial effort to deliver their state-of-the-art work in a very timely fashion. We thank Mona Soleimanieh for her assistance from the beginning to the end of this project.

We appreciate the superb job of Gina Almond, Beckie Brand, Laura Beaumont, Oliver Walter, and Blackwell Publishing who took on this project, and their continuous support toward the publication of this third edition of *Cardiac Mapping*, the only comprehensive text on the subject.

Finally, I would like to personally thank my brother, Dr. Hossein Shenasa, who freed me from my daily clinical routine so I could finish this project.

The Editors

Contributors

Amin Al-Ahmad, MD
Standford University, Palo Alto, CA, USA

Leonardo Arantes, MD
Hôpital Cardiologique Du Haut-Lévêque
Université Victor Segalen Bordeaux II
Bordeaux, France

Arash Arya, MD
Department of Electrophysiology
University of Leipzig Heart Center
Leipzig, Germany

André d'Avila, MD
Cardiac Arrhythmia Service
Massachusetts General Hospital
Harvard Medical School
Boston, MA, USA

Nitish Badhwar, MBBS
Cardiac Electrophysiology
Division of Cardiology
Department of Medicine
University of California – San Francisco
San Francisco, CA, USA

Shlomo A. Ben-Haim, MD, DSc
Caesarea, Israel

Omer Berenfeld, PhD
Center for Arrhythmia Research
University of Michigan
Ann Arbor, MI, USA

Deepak Bhakta, MD
Krannert Institute of Cardiology
Indiana University School of Medicine
Indianapolis, IN, USA

Frank Bogun, MD
Division of Cardiology
Department of Internal Medicine
University of Michigan Health System
Ann Arbor, MI, USA

Pierre Bordachar, MD
Hôpital Cardiologique Du Haut-Lévêque
Université Victor Segalen Bordeaux II
Bordeaux, France

Martin Borggrefe, MD
Department of Medicine-Cardiology
University Hospital of Mannheim
Mannheim, Germany

Günter Breithardt, MD, FESC, FACC, FHRS
Department of Cardiology and Angiology
Hospital of the Westfälische Wilhelms
University of Münster
Münster, Germany

Pedro Brugada, MD, PhD
Heart Rhythm Management Centre
Cardiovascular Centre
Free University of Brussels (UZ Brussel) VUB
Brussels, Belgium

Gil Bub, PhD
State University of New York
Downstate Medical Center
New York Harbor VA Healthcare System
Brooklyn, NY, USA

Matthew J. Budoff, MD FACC
Harbor-UCLA Medical Center
1000 West Carson Street
Torrance, CA, USA

J. David Burkhardt, MD, FACC
Staff Cardiovascular Medicine
Associate Program Director
Cardiac Electrophysiology and Pacing
Cleveland Clinic
Cleveland, OH, USA

José Angel Cabrera, MD, PhD
Hospital Quirón
Madrid, Spain

Hugh Calkins, MD
Division of Cardiology
The Johns Hopkins University School of Medicine
Baltimore, MD, USA

René Cardinal, PhD
Centre de Recherche
Hôpital du Sacré-Cœur de Montréal
Montréal, Canada

KR Julian Chun, MD
Department of Cardiology
Asklepios Klinik St. Georg
Hamburg, Germany

Jacques Clémenty, MD
Hôpital Cardiologique Du Haut-Lévêque
Université Victor Segalen Bordeaux II
Bordeaux, France

Nikolaos Dagres, MD
University of Athens
Second Cardiology Department
Attikon University Hospital
Athens, Greece

Mithilesh K. Das, MD
Krannert Institute of Cardiology
Indiana University School of Medicine
Indianapolis, IN, USA

Jacques MT de Bakker
Department of Experimental Cardiology
Academic Medical Center
Amsterdam, The Netherlands

Antoine Deplagne, MD
Hôpital Cardiologique Du Haut-Lévêque
Université Victor Segalen Bordeaux II
Bordeaux, France

Nicolas Derval, MD
Hôpital Cardiologique Du Haut-Lévêque
Université Victor Segalen Bordeaux II
Bordeaux, France

Derek J. Dosdall, PhD
Department of Medicine, Division of Cardiovascular Disease, Department of Physiology, and Department of Biomedical Engineering
University of Alabama at Birmingham
Birmingham, AL, USA

Imke Drewitz, MD
University Heart Center Hamburg
Department of Cardiology
Hamburg, Germany

Lars Eckardt, MD
Department of Cardiology and Angiology
Hospital of the Westfälische Wilhelms
University of Münster
Münster, Germany

Jeffery Edwards, RN
University of Oklahoma Medical Center
Oklahoma City, OK, USA

Nabil El-Sherif, MD
State University of New York
Downstate Medical Center
New York Harbor VA Healthcare System
Brooklyn, NY, USA

Zahra Emkanjoo, MD
Department of Pacemaker and Electrophysiology
Rajaie Cardiovascular Medical and Research Center
Iran University of Medical Sciences
Tehran, Iran

Sabine Ernst, MD
Royal Brompton and Harefield Hospital
National Heart and Lung Institute
London, UK

Tamer S. Fahmy, MD, PhD
Associate Professor, Critical Care Medicine Department
Cardiac Electrophysiology Division
Co-director of Experimental Research Lab
Cairo University Hospitals, Cairo, Egypt

Gregory K. Feld, MD
Division of Cardiology
Clinical Cardiac Electrophysiology Program
University of California, San Diego
San Diego, CA, USA

Muhammad Ghias, MD
University of Oklahoma Medical Center
Oklahoma City, OK, USA

Daniel Goodwin, MD, FACC
Keck School of Medicine
Division of Cardiovascular Medicine
University of Southern California Keck School of Medicine
Los Angeles, CA, USA

Majid Haghjoo, MD
Department of Pacemaker and Electrophysiology
Rajaie Cardiovascular Medical and Research Center
Iran University of Medical Sciences
Tehran, Iran

Michel Haïssaguerre, MD
Hôpital Cardiologique Du Haut-Lévêque
Université Victor Segalen Bordeaux II
Bordeaux, France

Henry R. Halperin, MD, MA, FAHA
Johns Hopkins University
Division of Cardiology
Baltimore, MD, USA

Gerhard Hindricks, MD, PhD
Department of Electrophysiology
University of Leipzig Heart Center
Leipzig, Germany

Siew Yen Ho, PhD
Professor of Cardiac Morphology
Imperial College London
Royal Brompton and Harefield NHS Trust
London, UK

Mélèze Hocini, MD
Hôpital Cardiologique Du Haut-Lévêque
Université Victor Segalen Bordeaux II
Bordeaux, France

Henry H. Hsia, MD
Stanford University
Stanford, CA, USA

Jeff M. Hsing, MD
Stanford University
Stanford, CA, USA

Mathew D. Hutchinson, MD
University of Pennsylvania Health System
Philadelphia, PA, USA

Raymond E. Ideker, MD, PhD
Department of Medicine
Division of Cardiovascular Disease
Department of Physiology, and
Department of Biomedical Engineering
University of Alabama at Birmingham
Birmingham, AL, USA

Warren M. Jackman, MD
University of Oklahoma Medical Center
Oklahoma City, OK, USA

Pierre Jaïs, MD
Hôpital Cardiologique Du Haut-Lévêque
Université Victor Segalen Bordeaux II
Bordeaux, France

Mohammad-Reza Jazayeri, MD, FACC, FAHA
Bellin Health Hospital Center
Green Bay, WI, USA

Ping Jia, PhD
Cardiac Bioelectricity Research and Training Center
Case Western Reserve University
Cleveland, OH, USA

Mark E. Josephson, MD
Harvard-Thorndike Electrophysiology Institute
Cardiovascular Division
Beth Israel Deaconess Medical Center
Harvard Medical School
Boston, MA, USA

Jérôme GM Jungschleger
Department of Cardiothoracic Surgery
Maastricht University
Maastricht, The Netherlands

Jérôme Kalifa, MD, PhD
Center for Arrhythmia Research
University of Michigan
Ann Arbor, MI, USA

Sébastien Knecht, MD
Hôpital Cardiologique Du Haut-Lévêque
Université Victor Segalen Bordeaux II
Bordeaux, France

Aravindan Kolandaivelu, MD
Johns Hopkins University
Division of Cardiology
Baltimore, MD, USA

Hans Kottkamp, MD, PhD
Department of Electrophysiology
Clinic Hirslanden Heart Center
Zurich, Switzerland

Karl-Heinz Kuck, MD
Department of Cardiology
Asklepios Klinik St. Georg
Hamburg, Germany

Vikram Lakireddy, MD
State University of New York
Downstate Medical Center
New York Harbor VA Healthcare System
Brooklyn, NY, USA

Albert C. Lardo, PhD, FAHA, FACC
Johns Hopkins University
Division of Cardiology
Baltimore, MD, USA

Ralph Lazzara, MD
University of Oklahoma Medical Center
Oklahoma City, OK, USA

Byron K. Lee, MD
Cardiac Electrophysiology
Division of Cardiology
Department of Medicine
University of California – San Francisco
San Francisco, CA, USA

Kang-Teng Lim, MD
Hôpital Cardiologique Du Haut-Lévêque
Université Victor Segalen Bordeaux II
Bordeaux, France

John C. Lopshire, MD
Krannert Institute of Cardiology
Indiana University School of Medicine
Indianapolis, IN, USA

Zhibing Lu, MD
University of Oklahoma Medical Center
Oklahoma City, OK, USA

Boris Lutomsky, MD
University Heart Center Hamburg
Department of Cardiology
Hamburg, Germany

Francis E. Marchlinski, MD
University of Pennsylvania Health System
Philadelphia, PA, USA

Seiichiro Matsuo, MD
Hôpital Cardiologique Du Haut-Lévêque
Université Victor Segalen Bordeaux II
Bordeaux, France

Thomas Meinertz
University Heart Center Hamburg
Department of Cardiology
Hamburg, Germany

John M. Miller, MD
Krannert Institute of Cardiology
Indiana University School of Medicine
Indianapolis, IN, USA

Annerie Moers, MD
University of Oklahoma Medical Center
Oklahoma City, OK, USA

Fred Morady, MD
Division of Cardiology
Department of Internal Medicine
University of Michigan Health System
Ann Arbor, MI, USA

Andrea Natale, MD, FACC, FHRS
Executive Medical Director of the Texas Cardiac Arrhythmia Institute
St. David's Medical Center, Austin, TX;
Consulting Professor, Division of Cardiology
Stanford University, Palo Alto, CA;
Clinical Associate Professor of Medicine
Case Western Reserve University
Cleveland, OH, USA

Guo-Dong Niu, MD
Cardiovascular Institute & Fuwai Hospital
Beijing, China

Jeffrey E. Olgin, MD
Cardiac Electrophysiology
Division of Cardiology
Department of Medicine
University of California – San Francisco
San Francisco, CA, USA

Mark D. O'Neill, MBBCh, DPhil
Hôpital Cardiologique Du Haut-Lévêque
Université Victor Segalen Bordeaux II
Bordeaux, France

Feifan Ouyang, MD
Department of Cardiology
Asklepios Klinik St. Georg
Hamburg, Germany

Pierre Pagé, MD
Centre de Recherche
Hôpital du Sacré-Cœur de Montréal
Montréal, Canada

Eugene Patterson, PhD
University of Oklahoma Medical Center
Oklahoma City, OK, USA

Sunny S. Po, MD, PhD
University of Oklahoma Medical Center
Oklahoma City, OK, USA

Christopher Piorkowski, MD
Department of Electrophysiology
University of Leipzig Heart Center
Leipzig, Germany

Javad Rahimian, PhD
Southern California Permanente Medical Group
Department of Radiation Oncology
Los Angeles, CA;
Lecturer

University of California-Los Angeles
Department of Radiation Oncology
Los Angeles, CA, USA

Kim Rajappan, MD, MRCP
The Department of Cardiology
St Bartholomew's Hospital and Queen Mary College
University of London
London, UK

Sergio Richter, MD
Heart Rhythm Management Centre
Cardiovascular Centre
Free University of Brussels (UZ Brussel) VUB
Brussels, Belgium

Thomas Rostock
University Heart Center Hamburg
Department of Cardiology
Hamburg, Germany

Yoram Rudy, PhD
Cardiac Bioelectricity and Arrhythmia Center
Washington University in St. Louis
St. Louis, MO, USA

Molly Sachdev, MD, MPH
Division of Cardiology
The Johns Hopkins University School of Medicine
Baltimore, MD, USA

Frederic Sacher, MD
Hôpital Cardiologique Du Haut-Lévêque
Université Victor Segalen Bordeaux II
Bordeaux, France

Mohammad Ali Sadr-Ameli, MD
Department of Pacemaker and Electrophysiology
Rajaie Cardiovascular Medical and Research Center
Iran University of Medical Sciences
Tehran, Iran

Damian Sánchez-Quintana, MD, PhD
Universidad de Extremadura
Badajoz, Spain

Navinder S. Sawhney, MD
Division of Cardiology
Clinical Cardiac Electrophysiology Program
University of California – San Diego
San Diego, CA, USA

Leslie A. Saxon, MD FACC
Keck School of Medicine
Division of Cardiovascular Medicine
University of Southern California Keck School of Medicine
Los Angeles, CA, USA

Mauricio Scanavacca, MD
Arrhythmia Service
Heart Institute (InCor)
University of Sao Paulo Medical School
Sao Paulo, Brazil

Michael Schäfers, MD
European Institute of Molecular Imaging–EIMI
University of Münster
Münster, Germany

Benjamin J. Scherlag, PhD
University of Oklahoma Medical Center
Oklahoma City, OK, USA

Richard J. Schilling, MD, FRCP
The Department of Cardiology
St. Bartholomew's Hospital and Queen Mary College
University of London
London, UK

Otmar Schober, MD, PhD, FESC
Department of Nuclear Medicine
University of Münster
Münster, Germany

Yitzhack Schwartz, MD
Structural Heart Disease
Pediatric Cardiology, and GUCH
Rambam Healthcare Campus
Meyer Children's Hospital
Haifa, Israel

Helge Servatius
University Heart Center Hamburg
Department of Cardiology
Hamburg, Germany

Hossein Shenasa, MD, MSc, FACC
Department of Cardiovascular Services
O'Connor Hospital
San Jose, CA, USA

Jafar Shenasa, MSc
Heart and Rhythm Medical Group
San Jose, CA, USA

Mohammad Shenasa, MD, FACC, FAHA, FESC, FHRS
Department of Cardiovascular Services
O'Connor Hospital
San Jose, CA, USA

Jerold S. Shinbane, MD, FACC
Keck School of Medicine
Division of Cardiovascular Medicine
University of Southern California Keck School of Medicine
Los Angeles, CA, USA

Timothy W. Smith, DPhil, MD
Cardiovascular Division
Washington University School of Medicine
St. Louis, MO, USA

Eduardo Sosa, MD
Arrhythmia Service
Heart Institute (In Cor)
University of Sao Paulo Medical School
Sao Paulo, Brazil

Daniel Steven, MD
University Heart Center Hamburg
Department of Cardiology
Hamburg, Germany

William G. Stevenson, MD
Clinical Cardiac Electrophysiology Program
Brigham and Women's Hospital
Boston, MA, USA

Rajesh Subbiah, Bsc (Med) MBBS, PhD
Hôpital Cardiologique Du Haut-Lévêque
Université Victor Segalen Bordeaux II
Bordeaux, France

Paul B. Tabereaux, MD, MPH
Department of Medicine
Division of Cardiovascular Disease
Department of Physiology, and
Department of Biomedical Engineering
University of Alabama at Birmingham
Birmingham, AL, USA

Usha B. Tedrow, MD, MSc
Clinical Cardiac Electrophysiology Program
Brigham and Women's Hospital
Boston, MA, USA

Christian Vahlhaus, MD
Department of Cardiology and Angiology
University Hospital Münster
Münster, Germany

Niraj Varma, MD, FRCP
Cardiac Electrophysiology
Heart and Vascular Institute
Cleveland Clinic
Cleveland, OH, USA

Marc A. Vos
Department of Medical Physiology and the Heart Lung Center
University Medical Center Utrecht
Center of Heart Failure Research,
Amsterdam, The Netherlands

Edward P Walsh, MD
Chief, Division of Cardiac Electrophysiology
Department of Cardiology
Children's Hospital Boston
Boston, MA, USA

Paul J. Wang, MD
Stanford University
Stanford, CA, USA

Hein J. Wellens
Cardiovascular Research Institute Maastricht
Maastricht, The Netherlands

Stephan Willems, MD
University Heart Center Hamburg
Department of Cardiology
Hamburg, Germany

John V. Wylie, Jr., MD
Harvard-Thorndike Electrophysiology Institute
Cardiovascular Division
Beth Israel Deaconess Medical Center
Harvard Medical School
Boston, MA, USA

Anil V. Yadav, MD
Krannert Institute of Cardiology
Indiana University School of Medicine
Indianapolis, IN, USA

Paul Zei, MD, PhD
Stanford University
Stanford, CA, USA

Shu Zhang
Cardiovascular Institute & Fuwai Hospital
Beijing, China

Preface to the Third Edition

Since the publication of the second edition of *Cardiac Mapping*, which stood as the only comprehensive textbook in the field, substantial achievements and breakthroughs have been made in the fields of interventional electrophysiology and imaging technologies. Today, mapping technology is no longer an investigational research tool; rather, it is an essential part of the clinical electrophysiology laboratory. The mapping of complex arrhythmias such as atrial and ventricular fibrillation introduces a new era in the management of these arrhythmias.

We are privileged that leading experts have accepted our invitation and provided a contemporary state-of-the-art reference work in the field. The third edition is somewhat different from its preceding editions in that it is focused on new developments in fields such as mapping of complex arrhythmias, stereotaxis, image integration, and future directions in cardiac mapping and imaging.

We hope that this new edition will remain a useful source for basic scientists and clinical electrophysiologists to understand mechanisms and improve patient outcomes by more accurate and safer mapping. In the introduction to the first edition we stated that cardiac mapping is an integral part of cardiac electrophysiology, which remains true; however, at this point, cardiac mapping and imaging are integrated, and we focus on the impact of new imaging technology and mapping.

The last chapter of this edition discusses new developments and future trends in cardiac mapping. A special chapter is also devoted to the limitations of each mapping technology. Paradoxically, in the recent AHA/ACC/ESC updated guidelines on clinical cardiac electrophysiology and ablation, very little was mentioned about mapping procedures: In view of the impressive progress in mapping techniques, a comprehensive review of the latest results is warranted.

As the field of interventional electrophysiology continues to evolve, cardiac mapping will remain an integral part of the science and practice of complex rhythm management.

Mohammad Shenasa, MD
Gerhard Hindricks, MD
Martin Borggrefe, MD
Günter Breithardt, MD

Preface to the Second Edition

The first edition of *Cardiac Mapping* stood out as the only textbook in the field with outstanding contributions from world-renowned authors. The book was well received and indeed sold out. Since the release of the first edition, there have been areas of significant progress and even major breakthroughs in the field of cardiac mapping and catheter ablation of arrhythmias. In particular, the technical advancements in noncontact and nonfluoroscopic mapping improved our understanding of the mechanism and thus the appropriate treatment of many arrhythmias, particularly atrial and ventricular fibrillation. The second edition offers a unique source for the latest developments in cardiac mapping of arrhythmias.

This new edition of *Cardiac Mapping* provides an important resource of the interventional electrophysiologist, rhythmologist, and those who are interested in understanding the mechanism of cardiac arrhythmias.

As the field of interventional electrophysiology continues to evolve, cardiac mapping will remain an integral part of the science and practice of electrophysiology.

The Editors
San Jose, CA, USA;
Mannheim and Münster, Germany

Preface to the First Edition

Cardiac mapping has always been an integral part of both experimental and clinical electrophysiology. Indeed, Sir Thomas Lewis systematically investigated the activation of the dog ventricle as early as 1915. The detailed activation map from that experiment is shown in Figure 1. Since then, cardiac mapping has evolved from single sequential probe mapping to very sophisticated computerized three-dimensional mapping. By the time cardiac mapping began being used in the surgical management of ventricular as well as supraventricular tachycardias, a large body of literature had already been collected.

Despite this significant progress, a collective textbook that attempted to discuss all aspects of cardiac mapping did not exist. When we first considered working on such a project, we were not sure if our friends and colleagues who have paved the road to this point would think it necessary to join us in this effort, especially in the era of implantable devices. We were surprised and encouraged by their unanimous positive support to go ahead with this text. (Many of the contributors have already asked about the second revised edition!) The contributors unanimously agreed to prepare manuscripts that discussed their latest work and that would subsequently be published in this, the only comprehensive book to present the state of the art on all aspects of cardiac mapping from computer simulation to online clinical application. Thus, we would like to thank all the contributors for presenting their best work here. Without them, this book would not have been possible.

A unique feature of this book is that the chapters are followed by critical editorial comments by the pioneer of that specific area, so that the state of the art is discussed. We hope this book will serve as an impetus to stimulate new ideas for cardiac mapping in the future.

The Editors

Foreword

The Merriam-Webster online dictionary defines a map as "a representation . . . of the whole or a part of an area." Indeed, reading maps is the fundamental process by which one navigates uncharted or unknown regions. The goal of such navigation may be simply to get from one point to another using the location of major structures such as mountains and rivers. For example, Lewis and Clark in 1803-4 explored the uncharted western United States, which allowed subsequent settlers to travel the same geography more easily, safely, and quickly. Maps can also be used to understand the composition of the underlying terrain, such as geologic maps of the earth's crust. Finally, maps can be employed to comprehend functional changes superimposed on the various fixed structures, such as weather and geothermal maps. To be used effectively, the functional map must be interpreted in light of the topography and composition.

Fundamental to all maps is the ability to create an image. Lewis and Clark imaged the Missouri River through the Rocky Mountains to the Pacific Ocean. Later maps represented the composition of the soil, while still later maps, the functional terrain. And this is the general development of maps and their corresponding images, from noting fixed structures, to drilling down (literally and figuratively) into the fixed structures, to understanding functional events unfolding on top of, and within, the structures.

Mapping in medicine has followed the same general concepts. Initially, anatomists such as Virchow and Rokitansky noted the gross anatomy, while Purkinje, His, Tawara, and Watson and Crick, explored the cellular and subcellular composition. Starling, Harvey, and Einthoven composed functional maps of muscle contraction, blood flow, and electrical activation.

In fact, mapping and image generation have reached unprecedented importance in modern medicine. Molecular and autonomic imaging, cardiac CT, MRI, echo, electrocardiographic and electrophysiologic imaging, PET, along with image integration to superimpose functional images on stationery ones, have revolutionized our tools and capabilities to diagnose and treat in unparalleled ways. While satellite mapping confers precise images of the earth's terrain, its composition, and functional events, so, too, the advances in medical imaging explore the body's every nook and cranny. Joe Louis (world heavyweight boxing champion, 1937–49) said, when facing a title bout against Billy Conn in 1941, "He can run, but he can't hide." There is no longer any hiding in medicine.

The present book admirably captures the latest electrophysiologic advances in cardiac mapping and imaging, transporting the reader from the structure (e.g., left ventricular anatomy), to composition (e.g., areas of scar), to functional interplay on and within its surface (e.g., activation sequence of ventricular tachycardia). In today's world, such knowledge is fundamental to delivering the latest diagnostic and therapeutic advances to our patients and makes reading this book mandatory.

Douglas P. Zipes, MD
Distinguished Professor
Krannert Institute of Cardiology
Indiana University School of Medicine
Editor-in-chief, Heart Rhythm

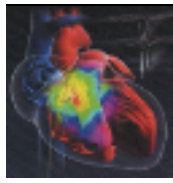

PART I

Historical Perspectives

Cardiac Mapping, Third Edition Edited by Mohammad Shenasa, Gerhard Hindricks, Martin Borggrefe, and Günter Breithardt
 ISBN: 978-1-405-17572-2

1

CHAPTER 1

Cardiac Activation Mapping: The Amsterdam Years

Hein J. Wellens, MD

University of Maastricht, Maastricht, The Netherlands

Summary

Starting in the late fifties of the last century professor Durrer and his cardiology group in Amsterdam developed a very strong base to expand our knowledge of electrocardiography and electrophysiology. It resulted in major accomplishments such as the unraveling of the complete excitation of the isolated perfused human heart and the introduction of programmed stimulation of the heart to induce and study clinically occurring cardiac arrhythmias.

Deciding factors in these advances were the presence of a brilliant leader, an interested and motivated group of coworkers, and the constant support from the department of medical physics.

Introduction

Essential for our understanding of cardiac function in health and disease is knowledge about the way, and in what sequence, the muscle cells of the different parts of the heart are activated. We require insight into the time course and instantaneous distribution of the excitatory process of the heart, and how this is represented in the electrocardiogram (ECG), which is a global representation of the activation process.

Already in 1918, Boden and Neukirch understood that in order to obtain data about total excitation of the heart the beating isolated heart should be studied [1]. It would take 50 more years, however, before epicardial and transmural activation of the isolated intact human heart would be accomplished by Dirk Durrer and colleagues in Amsterdam.

In the 1950s, Durrer, a cardiologist, started to study the cardiac activation process in the mammalian heart. He recognized from the beginning the necessity, especially in the ventricle, to study not only the activation process on the epicardium but also intramurally, in order to clearly delineate cardiac excitation and to correlate this excitation with the ECG.

Together with the physicist Henk van der Tweel, head of the department of medical physics at the University of Amsterdam, instrumentation was developed to study the activation in the ventricular wall. Needles were constructed allowing accurate measurements of transmural activation (Figure 1.1). Essential in this process was demonstration of the physico-mechanical basis of the intrinsic deflection of the electrogram indicating the timing of myocardial activation at the recording electrode. The outcomes of these 2D and 3D studies were published in four articles in the *American Heart Journal* in 1953–1955 [2–4]

Cardiac Mapping, Third Edition Edited by Mohammad Shenasa, Gerhard Hindricks, Martin Borggrefe, and Günter Breithardt
 ISBN: 978-1-405-17572-2

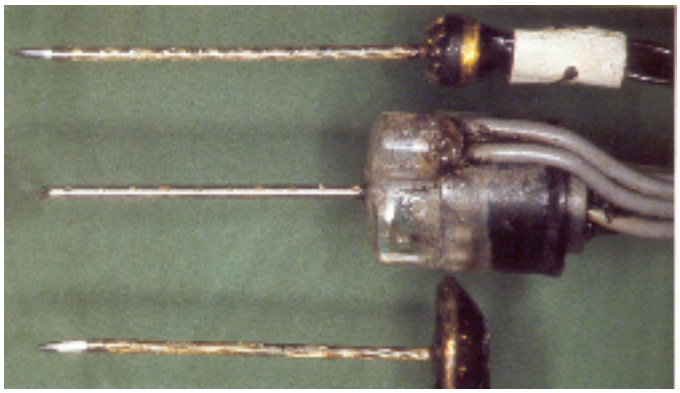

Figure 1.1 The so-called Durrer needle with 10 or 20 electrodes, allowing accurate transmural activation mapping.

Total Excitation of the Isolated Human Heart

The observations discussed above were made in the dog heart. But Durrer wanted to know how global electrical activation takes place in the intact human heart to help us understand its relation to the ECG. He assembled a group of investigators experienced in keeping the heart beating after being removed from the body, recording from multiple intramural terminals, and careful offline measurements of the recorded signals. Apart from Durrer, the group consisted of Rudolf van Dam, Gerrit Freud, Michiel Janse, Frits Meijler, and an American engineer, Robert Arzbaecher.

After control experiments in canine hearts had shown that isolation and perfusion of the heart outside the body did not affect mode and speed of excitation as measured in situ, human hearts were studied. With informed consent of family members, hearts were obtained from individuals who had died from various cerebral conditions without a previous history of heart disease. This was at a time before cardiac transplantation! ECGs taken several hours before death showed no evidence of cardiac disease. The hearts were removed within 30 min after death, the criterion being cessation of cardiac activity.

The aorta was cannulated and attached to a Langendorff perfusion apparatus. The hearts were perfused with an oxygenated, heparinized, modified Tyrode solution, with washed bovine erythrocytes. Most hearts resumed beating spontaneously within the first 5 min of perfusion; in a few cases electrical defibrillation was needed because of ventricular fibrillation. The hearts continued beating in a spontaneous sinus rhythm for periods ranging from 4 to 6 hr.

The electrical activity of the heart was recorded from epicardial (hand-held) and intramural (needle) electrodes. Unipolar and bipolar leads were recorded on a 14-channel Ampex tape recorder. Data quality was controlled online using a 14-channel Elema inkwriter. For measuring activation times the tapes were played on the Elema inkwriter at a paper speed of 960 mm/sec, giving a time resolution of better than 1 msec.

All activation times were expressed in milliseconds following the onset of left ventricular depolarization. Measurements were made from as many as 870 intramural terminals. Figures 1.2 and 1.3 are from the publication in *Circulation* [6] showing both a 2D and 3D isochronic representation of ventricular activation of an isolated human heart using epicardial and intramural activation times. The figures beautifully illustrate early activation at the exits of the bundle branches and the spread of activation thereafter.

The Wolff–Parkinson–White syndrome

Starting in the 1930s, Holzman and Scherf [7] and Wolferth and Wood [8] postulated that in patients with the Wolff–Parkinson–White (WPW) syndrome, two connections between atrium and ventricle were present, and that they could be incorporated in a tachycardia circuit with the impulse going from atrium to ventricle over one connection and from ventricle to atrium over the other.

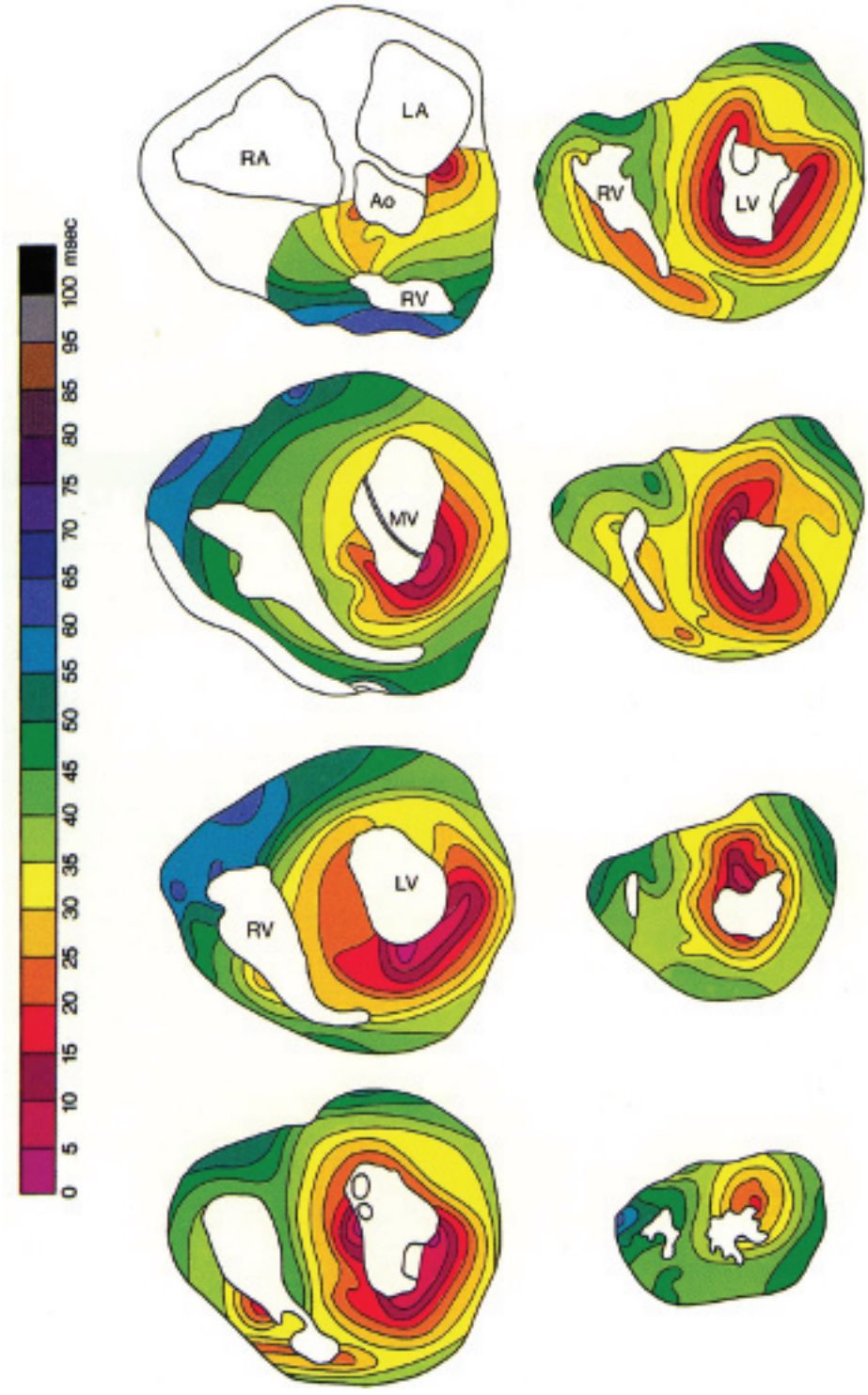

Figure 1.2 Isochronic representation of ventricular activation of an isolated human heart, using measurements at 870 intramural electrode terminals. Each color represents a 5-msec interval.

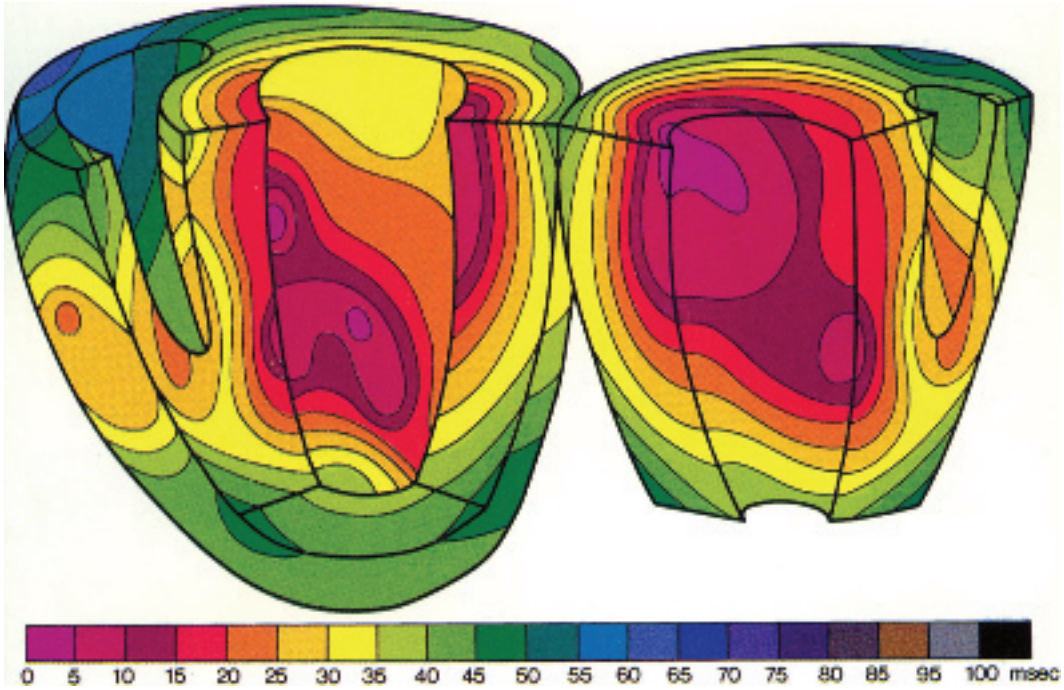

Figure 1.3 Three-dimensional isochronic representation of the activation of the same heart as in Figure 1.2. Color scheme identical to the one in Figure 1.2.

The author remembers discussions in Amsterdam in the early 1960s about this possibility, especially during visits from Howard Burchell of the United States. Around that time, a unique opportunity presented itself to obtain more information. In 1966, at Leiden University Hospital, A. G. Brom was scheduled to operate on a 21-year-old woman with an atrial septal defect of the secundum type. But the patient also had ECG changes that met the criteria for a diagnosis of WPW syndrome, and Brom consented to an epicardial map in the patient during sinus rhythm. So, Durrer and Jan Roos travelled to Leiden to map the epicardium of the heart prior to surgery

Figure 1.4 shows the 12-lead ECG of the patient before the operation. Figure 1.5 shows the ventricular epicardial map during sinus rhythm. It is clear that in this patient, in contrast to epicardial, ventricular activation in a person with a normal ECG did not start in the area pretrabecularis, close to the descending left coronary artery. The earliest epicardial activation was found in the anterolateral part of the right ventricle very close to the tricuspid annulus [9].

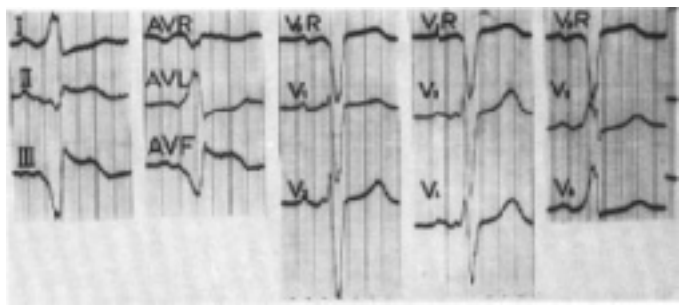

Figure 1.4 The electrocardiogram of the patient whose epicardial activation map is shown in Figure 1.5. At that time it was called WPW type B. Now we would say that the patient has a right free wall accessory AV pathway located anterolaterally.

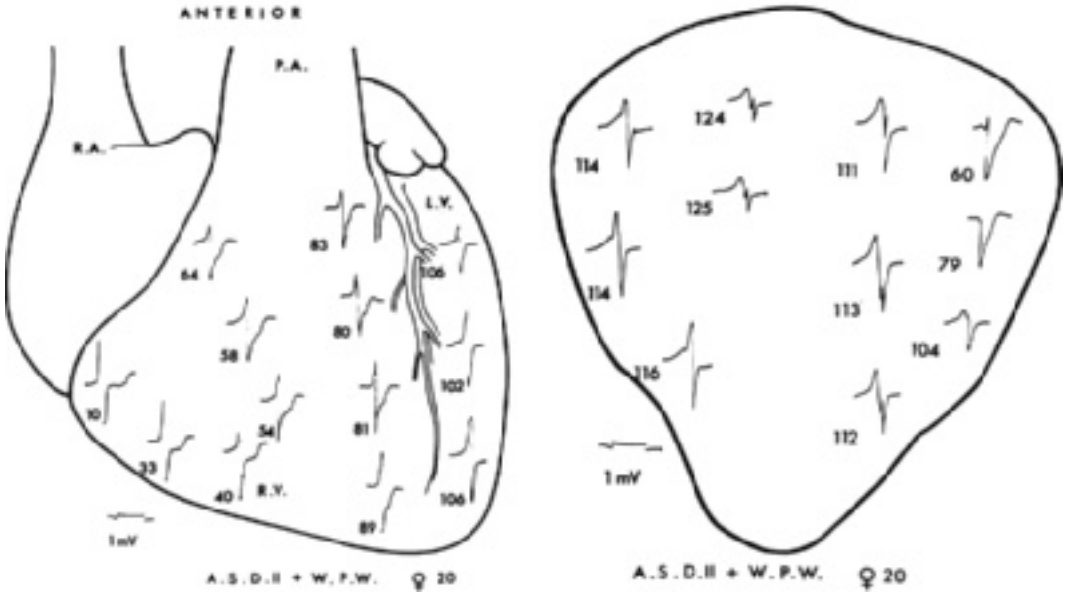

Figure 1.5 The epicardial excitation map of the patient whose ECG is shown in Figure 1.4. Note early right ventricular activation anterolaterally close to the tricuspid annulus.

That observation clearly demonstrated an abnormal ventricular activation pattern that was very suggestive of a connection between the right atrium and the right ventricle. Then the question arose of how to prove that such a connection could play a role in the tachycardias that are so often present in the WPW patient. Again, an important contribution came from the department of medical physics.

Already in the early 1950s, experiments had been performed to study cardiac excitability in dogs. This required a special stimulator. This stimulator, and several more versatile ones thereafter, was developed in close collaboration with van der Tweel and his group. To study WPW patients, however, a stimulator was required not only able to synchronize to the patient's rhythm and to give timed premature beats, but also able to perform basic pacing and induce premature stimuli at selected intervals.

Such a device was built by a young engineer, Leo Schoo, after long discussions between the medical physicists van der Tweel and Strackee, and the cardiologists Durrer and Reinier Schuilenburg. With this stimulator, stimuli with a regular rhythm could be produced by two basic pulse generators. The cycle length of these pulses could be varied with an accuracy of 1 msec from 9999 to 100 msec. Instantaneous changes in driving rate could be achieved by switching from one stimulator to the other. Two (in a later version, three) independent test pulses could be delivered during the spontaneous rhythm or during regular driving, with a selected interval accurate to 1 msec. The basic pulses and the two (or three) test pulses could be applied to one pair of stimulating electrodes or to separate pairs in any desired combination (Figure 1.6).

In the fall of 1966, this versatile stimulator was used in a patient with WPW syndrome. With catheters in the right atrium and right ventricle it was shown for the first time that by giving accurately timed stimuli, the properties of the two connections between atrium and ventricle differed, resulting in the initiation of a circus movement tachycardia using one connection for atrioventricular and the other one for ventriculo-atrial conduction. It was also demonstrated that these tachycardias could be terminated from atrium and ventricle by giving appropriately timed stimuli [10]. A registration from such a study is shown in Figure 1.7.

These observations, also the one by Coumel et al. [11], rapidly led on both sides of the Atlantic to the use of programmed electrical stimulation of the heart to study patients suffering from supraventricular tachycardias [12]. By placing catheters at

Figure 1.6 Photo of the sophisticated stimulation and registration equipment used in Amsterdam during the early studies in patients with tachycardias.

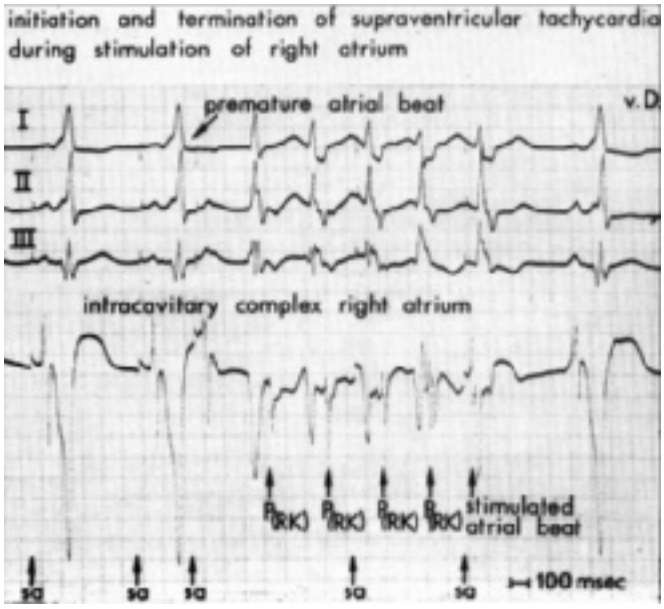

Figure 1.7 Example of the initiation and termination of a circus movement tachycardia by high right atrial stimuli. The intracardiac catheter is located in the coronary sinus. RK = retrograde Kent; sa = stimulus artefact.

different sites in the atrium, the ventricle, and the coronary sinus it soon became possible to map the site of origin or pathway of the tachycardia. This opened the door to new therapies for supraventricular tachycardias. The reproducible initiation and termination of ventricular tachycardia by programmed stimulation followed rapidly thereafter [13]. It took a while, however, before Mark Josephson and colleagues showed the importance of cardiac mapping in those patients [14]

In retrospect the advances made in Amsterdam were based on the presence of a brilliant, inspiring leader, a hard-working, motivated, interested group of coworkers, and the constant support from the department of medical physics. The Amsterdam years will always be remembered as an exciting journey into a new discovered land!

References

1 Boden E, Neukirch P. Electrokardiographische Studien am isolierten Saugetier- und Menschenherzen bei direkter und indirekter Ableitung. *Pflueger Arch Ges Physiol* 1918; **171**: 146–58.

2 Durrer D, van der Tweel LH. Spread of activation in the left ventricular wall of the dog. I. *Amer Heart J* 1953; **46**: 683–91.

3 Durrer D, van der Tweel LH. Spread of activation in the left ventricular wall of the dog. II. *Amer Heart J* 1954; **47**: 192–203.

4 Durrer D, van der Tweel LH, Blickman JR. Spread of activation in the left ventricular wall of the dog. III. *Amer Heart J* 1954; **48**: 13–35.

5 Durrer D, van der Tweel LH, Berreklouw S, van der Wey LP. Spread of activation in the left ventricular wall of the dog. IV. *Amer Heart J* 1955; **50**: 860–82.

6 Durrer D, van Dam R Th, Freud GE, Janse MJ, Meijler FL, Arzbaecher RC. Total excitation of the isolated human heart. *Circulation* 1970; **41**: 899–912.

7 Holzmann M, Scherf D, Ueber Elektrogramme und verkuerzter Vorhof–Kammer Distanz und positiven P-Zacken. *Z Klin Med* 1932; **404**: 1932–41.

8 Wolferth CC, Wood FC. The mechanism of production of short PR intervals and prolonged QRS complexes in patients with presumably undamaged hearts: Hypothesis of an accessory pathway of auriculo-ventricular conduction (bundle of Kent). *Amer Heart J* 1933; **8**: 297–308.

9 Durrer D, Roos JP. Epicardial excitation of the ventricles in a patient with WPW syndrome. *Circulation* 1967; **35**: 15–21.

10 Durrer D, Schoo LM, Schuilenburg RM, Wellens HJJ. The role of premature beats in the initiation and the termination of supraventricular tachycardia in the Wolff–Parkinson–White syndrome. *Circulation* 1967; **36**: 644–62.

11 Coumel Ph, Cabrol C, Fabiato A, Gourgon R, Slama R. Tachycardie permanente par rythme reciproque. *Arch Mal Coeur* 1967; **60**: 1830–47.

12 Wellens HJ. *Electrical Stimulation of the Heart in the Study and Treatment of Tachycardias.* Baltimore: Park Press 1971.

13 Wellens HJ, Schuilenburg RM, Durrer D. Electrical stimulation of the heart in patients with ventricular tachycardia. *Circulation* 1972; **46** :216–26.

14 Josephson ME, Horowitz LN, Farshidi A, Spear JF, Kastor JA, Moore EN. Recurrent sustained ventricular tachycardia. 2: Endocardial mapping. *Circulation* 1978; **57**: 440–51.

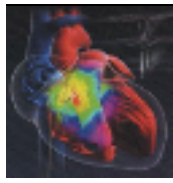

PART II

Methodological and Technical Considerations

Cardiac Mapping, Third Edition Edited by Mohammad Shenasa, Gerhard Hindricks, Martin Borggrefe, and Günter Breithardt
 ISBN: 978-1-405-17572-2

2

CHAPTER 2

Construction and Interpretation of Endocardial Maps: From Basic Electrophysiology to 3D Mapping

Lars Eckardt, MD, *& Günter Breithardt,* MD, FECS, FACC, FHRS

Hospital of the Westfälische Wilhelms–University of Münster, Münster, Germany

Summary

Cardiac mapping aims at characterizing and localizing the substrate of arrhythmias. It involves recording of electrical signals at multiple sites in the heart. This can be achieved by a variety of different techniques, which differ in their complexity, and usually mirror the complexity of the target arrhythmia. In recent years, advances in mapping technology and signal interpretation have significantly contributed to the understanding of cardiac electrophysiology. While conventional endocardial mapping remains the gold standard for the majority of supraventricular reentrant tachycardias 3D mapping techniques are increasingly used for understanding and guiding catheter ablation of complex arrhythmias.

Introduction

Mapping implies the recording of electrical activity from numerous electrodes positioned on or within the heart, or on or within the thorax, in order to characterize the substrate and the propagation of arrhythmias. Detailed mapping of electrical events is crucial for successful catheter ablation. Endocardial mapping involves recording of electrical signals at multiple sites in the heart. This is achieved by a variety of different methods, which differ in their complexity. With the increase in complexity of catheter technology and the recent appearance of very sophisticated "modern" or "novel" computerized mapping techniques, the classical endocardial electrogram recording via a relatively small number of strategically positioned catheters now appears almost old-fashioned. The "novel" mapping tools have been developed to target arrhythmias that seemed out of reach years ago. The aim of this chapter is to review the potential of the available classical and "modern" mapping technologies.

Conventional Contact Catheter Mapping

Contact catheter mapping is the most widely applied mapping technique because it predominately employs information obtained from catheter electrodes that are placed under fluoroscopic control for the diagnostic portion of an electrophysiology study. Nowadays, mapping and ablation of tachycardias are usually performed in a single procedure.

Cardiac Mapping, Third Edition Edited by Mohammad Shenasa, Gerhard Hindricks, Martin Borggrefe, and Günter Breithardt
 ISBN: 978-1-405-17572-2

We routinely place bipolar or quadripolar catheters in the high right atrium, right ventricular apex, and His bundle area. In addition, we often insert a multipolar catheter into the coronary sinus. This catheter marks the position of the coronary sinus ostium as well as the mitral annulus. To convert data obtained from mapping catheters into an understanding of an arrhythmia requires some experience and coordination with imaging for localization. This approach is adequate for arrhythmias in normal hearts when the substrate tends to be simple.

Using X-ray, the frontal projection is particularly useful for advancing catheters from the femoral or jugular/subclavian access site to the heart. It allows good visualization of the right ventricular outflow tract. In the right anterior oblique (RAO) view, the mitral, tricuspid, and aortic valves are seen side-on and can thus be easily crossed. The RAO view can also be used for positioning the His bundle catheter, which is located at the superior margin of the tricuspid ring. In the left anterior oblique projection, the mitral and tricuspid valve rings are seen face on-next to each other, with the septum between. The lateral tricuspid annulus anteriorly forms the right heart border, whereas the lateral mitral valve annulus posteriorly forms the left heart border.

Unipolar and Bipolar Electrograms

Potentials generated by current sources in the heart are always recorded with respect to a potential at a fixed reference site. Most electrophysiologists use a combination of multipolar recording catheters with the ablation catheter. We routinely use closely spaced (2 mm) recording bipoles separated by 6–10 mm in bi-, quadra-, deca-, or duodecapolar catheters for classical recording sites such as high right atrium, His bundle area, right ventricular apex or outflow tract, coronary sinus, or tricuspid annulus (the so-called "Halo" catheter). Steerability of a catheter is not required for standard positions although it brings comfort and allows relatively easy systematic coronary sinus catheterization via a femoral approach as well as recordings from virtually anywhere used by an experienced investigator. If the coronary sinus catheter is positioned via a jugular/subclavian access, steerability is almost never required.

One may choose to display unipolar or bipolar signals from a contact catheter. Bipolar recording is still far more popular than unipolar recording, as it allows clear identification of endocardial potentials separated by a flat baseline. In the case of unipolar signals, the recording is taken between the relevant pole of the catheter as the positive input and an extracardiac reference as the negative one. An intravascular rather than an extracardiac reference reduces sensing of electrical noise. Simultaneous recordings of intra- and extracellular electrograms have shown that the downstroke of a unipolar electrogram, the intrinsic deflection, coincides with the upstroke of the action potential beneath the exploring electrode [1, 2].

Sites at which an activation wave arises reveal themselves by an initially negative deflection in the unipolar recording. The use of bipolar and unipolar recording during catheter mapping in a patient with WPW syndrome is shown in Figure 2.1. The bipolar electrogram shows early activation before the onset of the delta wave in the surface ECG. However, this electrogram provides no information concerning the presence or absence of other sites with earlier activation. The synchronous unipolar signal shows the absence of an initial positivity of the ventricular signal at the mitral annulus indicating the spread of ventricular activation away from the recording site. This means that the recording electrode is precisely at the site of the pathway.

Unipolar recordings are also useful for catheter ablation procedures in patients with atrial tachycardias. Although the intrinsic deflection is a reliable marker of local activation, its detection may be hampered by large, remote components. Because the timing of signals at various sites is important, many clinical electrophysiologists prefer the bipolar recording mode, which reduces far-field effects. In the case of bipolar signals, the recording is made between two closely spaced poles of a multipolar catheter, both of which are either in contact with, or close to the endocardium. Because far-field effects will induce the same potential at both poles, remote effects will be cancelled.

In summary, unfiltered unipolar recording is superior to the usual bipolar recording mode in activation mapping procedures. Unipolar signals provide exact localization of target sites for ablation and a characteristic morphology at specific sites.

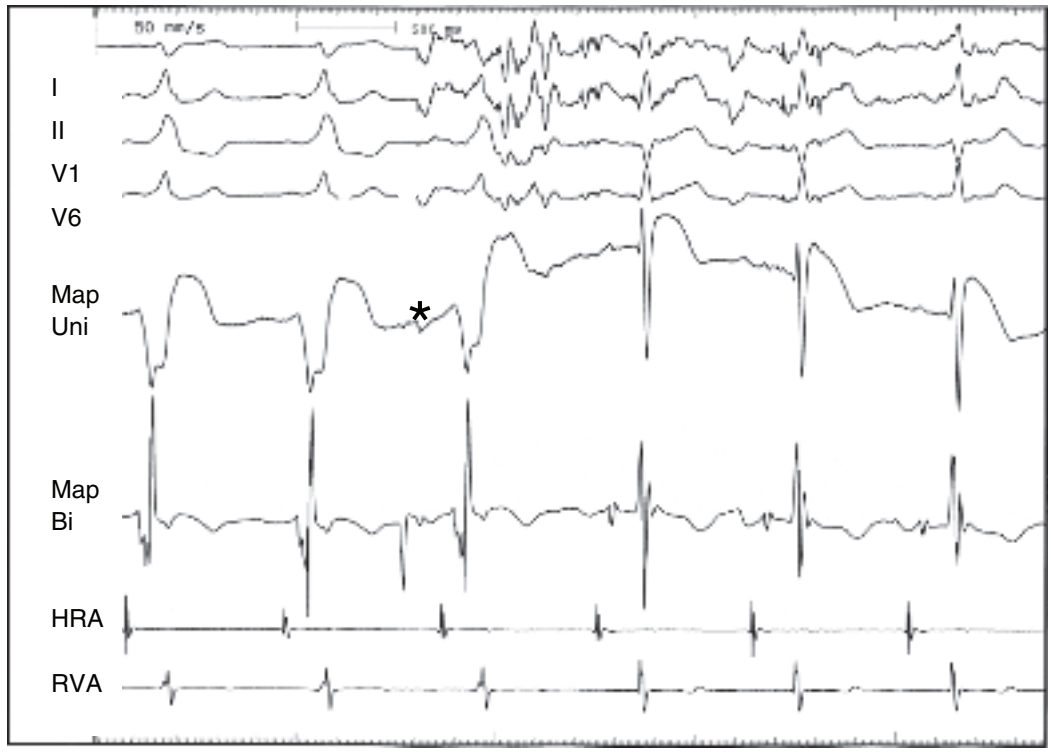

Figure 2.1 ECG recordings from a patient with Wolff–ParkisonWhite syndrome and a posterior pathway. Leads I, II, V1, and V6, as well as intracardiac signals from the right ventricular apex (RVA), the high right atrium (HRA), and the ablation catheter at the successful ablation site at the posterior mitral annulus are displayed. The unipolar (MAP uni) and the bipolar (MAP bi) mapping signals reveal the exact ablation site. A few milliseconds after starting the RF ablation (*), the block in the pathway occurs.

However, low-amplitude local signals may be buried in remote components in the unipolar mode so that bipolar recording may be favourable in such situations.

Classical Methods of Contact Catheter Mapping

Activation Sequence Mapping

Activation sequence mapping compares the timing of electrograms recorded from the roving catheter during tachycardia with the timing of a reference signal in order to either identify the earliest possible signal or a progression of activation around a macro-reentrant circuit. This technique is ideal for focal arrhythmias arising in structurally normal hearts such as focal atrial tachycardia or right ventricular outflow tract tachycardia.

Pace Mapping

Pace mapping is especially helpful in identifying the source of a focal tachycardia. The principle of the technique is that the cardiac activation sequence generated by a particular arrhythmia can be reproduced by pacing at its origin at a similar cycle length. In the case of VT arising in structurally normal hearts such as idiopathic outflow VT or fascicular VT, comparison of surface QRS morphologies at pacing sites can be seen to exactly match the QRS morphology generated by the tachycardia. However, the area with excellent pace map criteria may be relatively large, so that additional criteria for a successful ablation site are often required.

Entrainment Mapping

This technique may be used to map macro-reentrant circuits that have an excitable gap. The

ability to entrain a tachycardia by pacing confirms a reentrant mechanism. Because an excitable gap is a prerequisite for reentry, it is possible to induce stimuli from sites within or outside the reentrant circuit that capture myocardium. If pacing is performed within the reentrant circuit, two wave fronts are produced: one travels antidromically and collides with the returning orthodromic wavefront, while the other travels orthodromically within the circuit resetting the tachycardia.

If pacing is successfully performed outside the circuit, the wavefront propagates through the intervening myocardium, reaches the circuit, and propagates in both orthodromic and antidromic directions again resetting the tachycardia. If a train of stimuli is applied at a cycle length just below the tachycardia rate, it is possible to continuously reset, or entrain, the tachycardia [3] . To confirm that pacing has occurred within the tachycardia circuit, the result is examined for the following criteria:

1 The activation sequence of the chambers paced should be identical to that seen during tachycardia (concealed entrainment).

2 The interval between the pacing stimulus and a fixed reference point should be identical to the interval present during tachycardia between the electrogram recorded at the pacing site and the same reference point.

3 The return cycle at the pacing site should be equal to or less than 30 msec to the tachycardia cycle length.

"New" Mapping Technologies

Classical catheter mapping methods rely on electrical information from a relatively small number of electrodes of catheters and from anatomic information gathered from fluoroscopic images, in which the endocardial contours cannot actually be visualized. Activation sequence mapping with the classical catheter technology is time-consuming, technically difficult, not perfectly reproducible, and not suitable for hemodynamically unstable patients or spontaneous arrhythmias of short duration. The limitations of catheter ablation have been reduced by the development of complex computerized mapping systems, which have also increased our understanding and successful treatment of complex arrhythmias.

A new method for nonfluoroscopic catheter-based endocardial mapping that enables the generation of 3D electro-anatomical maps of the heart chambers was first introduced in 1997 [4]. Novel mapping technologies generally provide electrical information from a large number of sources, thus markedly increasing mapping resolution. Most systems can localize catheters or electrodes in 3D space. They are capable of reconstructing 3D endocardial activation maps as well as accurately localizing and guiding mapping catheters to sites that are suitable for ablation. The accuracy of the systems has recently been enhanced by the computerized incorporation of previously acquired computed tomography (CT) or magnetic resonance (MR) images of cardiac structures acquired prior to the mapping session to guide catheter navigation with further precision. The combination of precise 3D/CT or MRI guidance based on actual pulmonary vein anatomy has a tremendous potential in optimizing efficacy and safety of ablation.

Although the "new" systems may be better at confirming that a chosen target is, indeed, an appropriate site for ablation with reduced fluoroscopy and often but not always reduced procedure time, use of these systems is cost-intensive, relies on a stable position of the reference catheter, may be time-consuming, and requires a lot of operator experience.

The "new" mapping technologies can be subdivided into methods that combine electrophysiological data with anatomic information, which include CARTO (Biosence-Webster, Baldwin Park, CA) and more recently CARTOMerge (Biosence-Webster, Baldwin Park, CA), Realtime Position Management (RPM) (Cardiac Pathways–Boston Scientific EP MedSystems, Sunnyvale, CA), and NavX (St. Jude Medical, Inc., St. Paul, MN) and methods that provide continuous and complete data of all electrophysiological events within a cardiac chamber, including basket maps (Cardiac Pathways, EP Technologies, Sunnyvale, CA) and noncontact mapping (Ensite 3000, St. Jude Medical, Inc., St. Paul, MN). Noncontact mapping also combines anatomic and electrophysiologic information.

The first group of techniques localizes catheter position in space by sensing changes in its position within a magnetic field (CARTO; see below), assessing the relative position of catheters with ultrasonic

transducers (RPM), or by sensing impedance changes between the catheter and reference points (NavX; see below). In the cases of CARTO and RMP, this information is allied to the electrograms at each catheter site. In the case of RMP, the electrogram recorded at every catheter position can be recalled for later analysis and comparison. In addition, these systems require specific catheters, whereas NavX data can be obtained with any catheter and the data applied to any rhythm. With all these systems, a picture of the rhythm is built up from sequentially acquired points. In contrast, the second group of methods acquires global data so that a rhythm can be characterized from only one single beat. The accuracy of the maps created by a basket system depends on the number of splines on the basket, the number of electrodes on each spline, and the percentage of both that achieve endocardial contact.

The noncontact system (see below) is based around a midcavity sensor [a special multielectrode array (MEA)] that detects far-field endocardial activity. This far-field information is transformed via inverse-solution mathematical coronary sinus into computed equivalents of over 3300 contact "near-field" points on a "virtual" endocardium. The definition of the map is thus influenced by the size of the chamber and the distance between the MEA and the endocardium. All of the various mapping methods have successfully created maps of all four cardiac chambers, guiding successful ablation in each.

The CARTO system serves as an endocardial mapping system that allows the creation of 3D electroanatomic maps of cardiac chambers and can help navigate the roving catheter, reducing the need for fluoroscopy, and guiding it to target sites suitable for ablation. This method is based on using a special catheter connected to an endocardial mapping and navigation system. The system comprises a miniature passive magnetic field sensor located at the tip of the catheter, an external ultralow magnetic field, and a processing unit. The system uses the magnetic technology to accurately determine the location and orientation of the catheter in space. It simultaneously records intracardiac local electrograms from the catheter tip.

The 3D geometry of the chamber is reconstructed in real time with the electrophysiological information, which is color-coded with red representing the earliest and purple the latest points of activation and superimposed on the reconstructed 3D geometry of the chamber. Besides activation maps, the voltage of the electrograms can be displayed in a color-coded fashion, which enables the 3D visualization of areas with high amplitude signals (i.e., normal myocardium) and of those with reduced or loss of amplitude (i.e., fibrosis, scarring) [5].

The resolution of the map depends on the number of contact points. For activation mapping, at each endocardial point, the local activation time is calculated as the interval between a reference point (e.g., fixed point on a surface ECG or intracardiac electrogram) and the unipolar electrogram recorded from the mapping catheter. For atrial or ventricular arrhythmias, we routinely use an atrial reference of a coronary sinus recording or a right ventricular apex catheter, respectively.

The system has become a useful tool for mapping VT or areas of scarring and guiding the formation of linear lesions in all chambers. Facilitation of mapping and ablation of focal atrial tachycardias, as well as atrial reentrant circuits related to scarring late after repair of congenital heart disease, have also been reported [6]. In patients with atrial fibrillation, the system is used not only to guide linear lesions in the left atrium, but also to create circumferential lesions around pulmonary vein ostia and thus, electrically disconnect the pulmonary veins from the left atrium. Electroanatomic mapping has also been shown to be effective in reducing fluoroscopy times and facilitating ablation of typical atrial flutter [7]. More recently, fusion of 3D CT or MR images with an electroanatomic map has been developed (CARTOMerge) [8]. This technique seems particularly valuable in complex anatomic structures such as the left atrium where we use it for visualization of left atrila and PV anatomy.

The NavX (former LocaLisa) system is also a nonfluoroscopic catheter-positioning system that allows localization of a catheter in 3D space. The system has the significant advantage that no special catheters or arrays need to be used. It measures the voltage drop that occurs between electrodes placed on opposite sites of the chest wall and the catheter in three orthogonal planes. Three low-current (1 mA) fields, each with a characteristic frequency of approximately 30 kHz, are applied at right angles to each other through pairs of skin electrodes. Electrode position is determined by dividing each of

the three amplitudes by the corresponding electrical field strength and is averaged over 1–2 sec. The resulting voltage is recorded via standard catheter electrodes and is used to determine electrode position [9]. Additionally, the system has been shown to be helpful in reducing patient and operator exposure to radiation during mapping [10].

The real-time position management system measures the time required for conduction of ultrasound from reference points to a mapping catheter. With the conduction velocity in blood as a constant, the system calculates the distance as time multiplied by velocity. Special reference catheters are equipped with four ultrasound transducers, whereas a deflectable catheter used for mapping and ablation has three transducers. Ablation sites and other landmarks can be marked on the display, helping mapping, targeting ablation sites, and the creation of linear lesions. The system has been successfully used, for example, to aid mapping and ablation of atrial flutter, VT, and accessory pathways [11].

The nonsustained character and the poor hemodynamic tolerability of VT significantly reduces the number of patients with structural heart disease and reentrant VT suitable for catheter ablation by use of conventional techniques. In such a situation, the noncontact mapping system may be of particular value. It uses a multielectrode array, which is positioned in the chamber being mapped. This array consists of a 9F catheter with a 7.5 ml ellipsoid balloon. The balloon is surrounded by 64 electrically insulated wires, each with one small laser-etched break in insulation, allowing them to function as unipolar electrodes.

Far-field electrocardiographic data from the array are fed into an amplifier system. A ring electrode on the proximal shaft of the array catheter is used as a reference for unipolar electrogram recordings. Because the far-field electrogram recordings detected by the array are of low amplitude and frequency, the potentials are enhanced and resolved mathematically [11]. A low-current locator signal is used to locate the mapping catheter in space. By moving a catheter the system records the position in 3D space by recording a number of points on the endocardial surface. These points are used to reconstruct the endocardium of any chamber. The geometry matrix defines the relationship between the location of the 64 electrodes on the array and more than 3000 points on the endocardium where the reconstruction is computed, thus allowing the reconstruction of high-resolution endocardial isopotential and isochronal maps.

Using the same locator signal the system can also guide the mapping catheter without the need for X-ray. In contrast to the CARTO system, NavX, and RPM, the noncontact system can analyze the pattern of endocardial activation from a single beat of tachycardia [12]. Information can be displayed as reconstructed virtual electrograms, series of isopotential maps, or isochronal maps. Validation of the accuracy of the reconstructed electrogram has been published for all heart chambers [13–15]. The system has been used to map macro-reentrant VT complicating ischemic heart disease, where it has proven valuable in identifying and guiding ablation to the region of the diastolic pathway [16], as well as other VTs [17]. With the array deployed in the left atrium, the noncontact system can identify not only the arrhythmogenic pulmonary vein but also other origins of focally initiated atrial fibrillation. Noncontact mapping has also been used to guide mapping and ablation of tachyarrhythmias due to intra-atrial reentry, for example, after Fontan surgery [18]. Difficult arrhythmia sites for ablation may be more precisely localized allowing for new procedural strategies. In right ventricular outflow tract VT, noncontact mapping may assist in differentiating pericardial and endocardial sites as well as ablation of single extra beats [12] (Figure 2.2).

The need to simultaneously map a high number of endocardial sites in 3D space has prompted introduction of the *basket catheters.* They are constituted of flexible, elliptic, basket-shaped recording catheters incorporating 5–8 splines, on which up to 10 electrodes are arranged as bipolar pairs. The most commonly used catheter (Cardiac Pathways, EP Technologies, Sunnyvale, CA) has 64 electrodes on eight highly flexible splines and is capable of acquiring electrophysiological data from multiple sites simultaneously. Electrograms and color-coded activation maps are reconstructed online and are displayed on a monitor. Thus, tachycardia mapping is improved although with relatively limited resolution. The system has been successfully used to aid mapping of human VT [19], atrial tachycardias, and atrial flutter [20], and even inside pulmonary veins

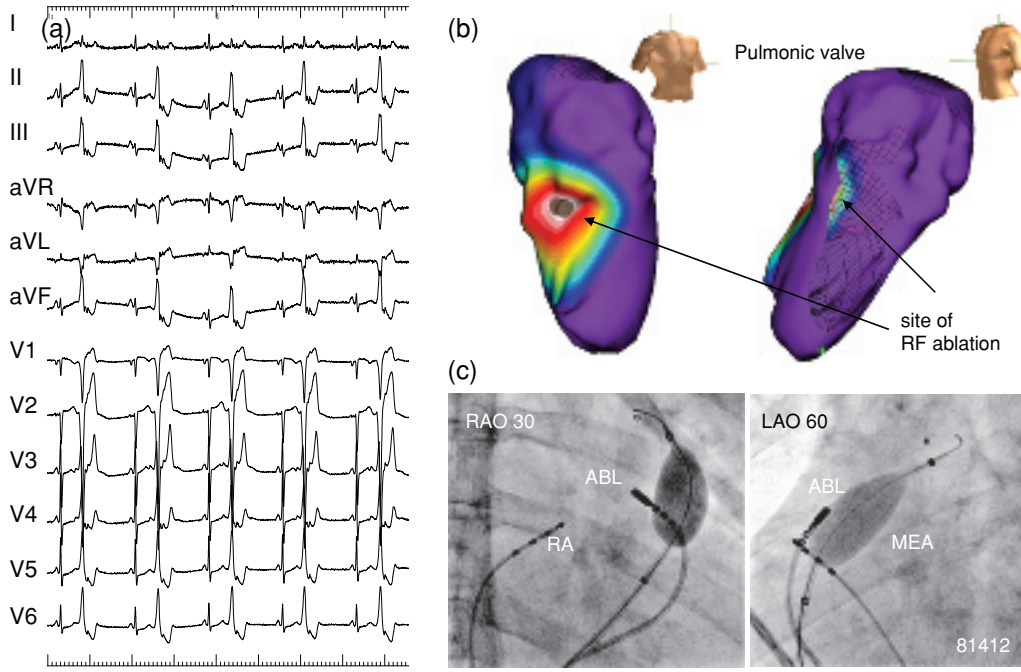

Figure 2.2 Noncontact mapping of a ventricular bigeminus with left-bundle branch block inferior axis morphology originating from the right ventricular outflow tract in a highly symptomatic patient (a). The multielectrode array catheter (MEA) is part of the noncontact mapping system (EnSite 3000; Endocardial Solutions, Inc.). The system permits mapping of a single QRS complex. The MEA, which is filled with a contrast–saline medium, is positioned in the right ventricular outflow tract (RAO/LAO: right/left anterior oblique views). The system calculates electrograms from 3000 endocardial points simultaneously by reconstructing far-field signals. Nondepolarized myocardium is shown in purple in this three-dimensional isopotential map (b). The map also shows the site of earliest depolarization (white circle). At this site the extrasystoles were successfully ablated using radiofrequency ablation. The ablation catheter (ABL) is located at the successful ablation site. RA: diagnostic catheter in the right atrium (c).

to map and ablate foci that initiate atrial fibrillation [21].

Which Technique for Which Tachycardia?

AV Nodal Reentrant Tachycardia

When typical AVNRT is induced, there is synchronous atrial and ventricular activation with long A-H and short H-A intervals. This reflects anterograde conduction via the slow and retrograde conduction occurring via the fast pathway as well as simultaneously with anterograde His–Purkinje conduction causing ventricular activation. In many centers, including our own, catheter modification of the slow pathway is performed by a combination of local electrograms and fluoroscopic position. The mapping catheter is positioned in the inferoposterior part of Koch's triangle on the tricuspid annulus, such that atrial electrograms are small in amplitude (about one-third to one-fourth of the ventricular electrogram) and long in duration. If there is no response to ablation in this region, the more superior midseptal tricuspid annulus is mapped and treated in a similar fashion.

Junctional rhythm during energy delivery is associated with successful ablation. More recently, catheter cryo-mapping and ablation have been proposed to overcome the small yet real risk of radiofrequency ablation–induced AV block. Unlike radiofrequency ablation, cryo-thermal ablation creates a lesion that is initially reversible and may obviate the occurrence of severe and definite complications in sensitive areas such as the slow pathway but also in anteroseptal/parahisian pathways and the pulmonary veins. Therefore, cryo-ablation seems

promising in unusual cases of AV nodal reentrant tachycardia.

Atrioventricular Reentrant Tachycardia

Catheter ablation of accessory pathways usually implies the introduction of several mapping catheters into the heart. In the case of left-sided accessory pathways, a coronary sinus catheter is helpful even in patients with antegrade conduction over the pathway. The coronary sinus catheter may have to be advanced during the procedure so that electrode poles lie on both medial and lateral sides of the pathway, thus enabling identification of the earliest atrial or ventricular activation. In some patients, this can only be achieved by placing the coronary sinus catheter via the jugular or subclavian vein. Nevertheless, a single catheter approach to ablation of overt left-sided free wall accessory pathways has been introduced by Kuck et al. as early as 1991 [22]

Despite its apparent benefits, this technique has not gained widespread acceptance because it requires enormous physician experience and does not allow a clear identification of the actually occurring clinical arrhythmia. In patients with accessory pathways, we perform programmed stimulation sequentially from the right ventricle and atrium to assess retrograde and antegrade conduction, localize an accessory pathway, and induce tachycardia.

In patients with preexcitation, mapping of the tricuspid or mitral annulus with a deflectable catheter may be performed during sinus rhythm, atrial pacing, orthodromic or antidromic tachycardia, or ventricular pacing. Because of the electrophysiological properties of concealed accessory pathways, mapping of such accessory pathways may be performed only during orthodromic tachycardia or ventricular pacing. The site showing the shortest atrioventricular conduction time or earliest ventricular activation is sought with the mapping catheter (Figure 2.1).

In the case of left free wall pathways, the coronary sinus bipole showing earliest ventricular activation can be used to guide the mapping catheter. It is important to note that because left-sided accessory pathways may have multiple atrial and ventricular attachments, the ablation site may need to be on a different radial point adjacent to the AV ring depending on whether the atrial or ventricular attachments of the accessory pathways are mapped and targeted. In the case of a right-sided accessory pathways, the procedure may be more difficult due to a number of factors including the lack of a coronary sinus equivalent that provides anatomic and electrophysiological guidance and difficulties in obtaining a stable position at the tricuspid annulus. Moreover, right-sided accessory pathways are more often multiple and are occasionally associated with structural abnormalities such as Ebstein's anomaly, in which AV nodal reentrant tachycardia are only rarely seen [23].

The retrograde atrial activation sequence during ventricular pacing can be helpful in distinguishing between anteroseptal and midseptal pathways. Retrograde atrial activation is often recorded simultaneously in the His bundle catheter and a bipole at the coronary sinus ostium in the case of midseptal accessory pathways, whereas it is earlier in the His bundle catheter signals in the case of anteroseptal accessory pathways [24].

Accessory atrioventricular connections may be found within the coronary sinus system, either within normal structures such as the coronary sinus or middle cardiac vein, or in abnormal structures, such as a coronary sinus diverticulum [25]. The earliest atrial activation during tachycardia may be at the coronary sinus OS either during atrioventricular reentrant tachycardia due to an inferoseptal accessory pathway, or during atypical AV nodal reentrant tachycardia. Introduction of ventricular extrastimuli synchronous with, or slightly earlier than the His spike during tachycardia, when the His bundle is refractory, may be useful in differentiating between the two. In the case of atrioventricular reentrant tachycardia, atrial activation is significantly advanced by the extrastimulus.

Atrial Flutter

Typical atrial flutter is defined as a macro reentrant tachycardia that depends on the cavotricuspid isthmus. In our opinion, the classical multiple catheter technique appears to be the most reliable to assess the presence of a complete bidirectional isthmus block [26]. Thus, we perform mapping of atrial flutter with deflectable multielectrode catheters positioned circumferentially around the tricuspid annulus, an ablation catheter, and a catheter positioned in the coronary sinus. In typical atrial flutter, the activation pattern demonstrates counterclockwise

or clockwise activation around the tricuspid annulus.

Concealed entrainment during pacing at the cavo-tricuspid isthmus confirms it as a critical area in the circuit that can be targeted for ablation. Ablation can be performed during atrial flutter or during pacing from the coronary sinus OS or low lateral right atrium. After a conduction block across the isthmus has been created, while pacing from the coronary sinus, the pattern of activation around the tricuspid annulus shows exclusively counterclockwise activation, with the distal pole of the circumferential mapping catheter showing the latest activation.

If the block is not complete, the ablation line may be mapped for double potentials [27]. An electrode close to the gap will record a relatively short interval between the two components of the double potential. This interval increases as the distance from the break in the line increases. Ablation to the site recording the double potential with the closest spacing (or even continuous activity between the two components) may complete the line of the conduction block.

In atypical atrial flutter, reentry occurs around other anatomic obstacles created in the right or left atrium by previous cardiac surgery. These include atriotomy scars and patches. Although the techniques of atrial flutter mapping including activation, entrainment, and linear mapping principles may provide useful information that helps define the reentrant circuit, it is usually helpful to use one of the "new" mapping systems.

Atrial Tachycardia

Atrial tachycardias may be of focal or reentrant origin. In some cases of atrial tachycardia, a classical technique using two catheters approaching a focus, one serving as a reference while the ablation one is sequentially moved, provides a reasonably effective approach. In complex cases, a sophisticated combination of entrainment mapping and activation mapping using the CARTO, NavX, or Ensite system leads to successful ablation

Atrial Fibrillation

The pulmonary veins are known to be the predominant source of left-sided atrial tachycardia, and focally initiated atrial fibrillation [28]. Linear left atrial ablation to isolate the septal and lateral pulmonary veins is performed on the assumption that isolated focal activity can no longer initiate atrial fibrillation [29]. During sinus rhythm, electrogram recordings taken inside pulmonary veins show a low-frequency potential reflecting adjacent atrial activation, followed by a high-frequency component reflecting local activation of PV muscular sleeves.

Many left-sided pulmonary veins require pacing from the distal coronary sinus to reveal the PV potential [30]. During ectopy, an endocardial activation time 75 msec earlier than the HRA signal has a sensitivity and specificity for identifying arrhythmogenic pulmonary veins of approximately 80% [31].

Lack of sufficient ectopic activity to allow the accurate identification of the arrhythmogenic pulmonary veins is the most common and important difficulty encountered during mapping of focally initiated atrial fibrillation. A number of manoeuvres can be performed in order to provoke ectopy. These include carotid sinus massage, the Valsalva manoeuvre, slow- and high-rate pacing, DC cardioversion, and drug administration. In patients with no or infrequent ectopy during the mapping procedure, use of 3D mapping can greatly facilitate the ablation procedure for electrical isolation of all pulmonary veins.

To aid in this goal, we place a circumferential pulmonary venous mapping catheter sequentially at the ostium of the pulmonary veins. This greatly facilitate the identification of the muscular sleeves electrically connecting the foci to the left atrium [32]. The more ostial PV ablation is performed, the lower is the risk of PV stenosis. Elimination of PV potentials, or their electrical disconnection from the left atrium, can then be used as endpoints for successful ablation, irrespective of the presence or absence of AF [30].

Mapping of Ventricular Tachycardia

Monomorphic ventricular tachycardia is the most common form of sustained VT and usually occurs after myocardial infarction. Reentry accounts for the majority of these VT. Endocardial catheter mapping and intraoperative mapping have shown that these arrhythmias originate within or at the border zone of the diseased myocardium. The size of the

reentrant circuit may be large, especially in patients with a left ventricular aneurysm, or may be confined to a small area. Briefly, the conditions necessary for reentry to occur may be summarized as follows: (i) a zone of unidirectional block must be present, and (ii) the impulse must travel around the zone of unidirectional block, activate the tissue distal to it with delay, invade the zone of the block retrogradely, and reexcite the tissue where the impulse originated. For reentry to occur, the impulse that is conducting around the reentrant circuit must always find excitable tissue in the direction it is propagating. Initiation and termination of VT by pacing stimuli, the demonstration of electrical activity bridging diastole (Figure 2.3), and a variety of other clinically used techniques are consistent with reentry.

Mapping of the reentrant circuit with conventional techniques in human infarct-related VT is often difficult because it is usually not possible to identify complete VT circuits. The areas of slow conduction have been shown to be desirable targets of ablation. Slowly conducting tissue may be identified during endocardial catheter mapping by fractionated and/or mid-diastolic electrograms (Figure 2.3), continuous electrical activity, or a long delay between a stimulus and the resulting QRS complex. Pacing from within the diastolic pathway during VT will generate QRS complexes of identical morphology to those seen in VT, and the interval between the pacing stimulus and QRS will be identical to that between the diastolic potential during VT and the onset of the VT QRS. Moreover, pacing at sites within the reentrant circuit or near its exit site can entrain the tachycardia, which appears to be accelerated to the pacing rate, without a change in QRS morphology [33].

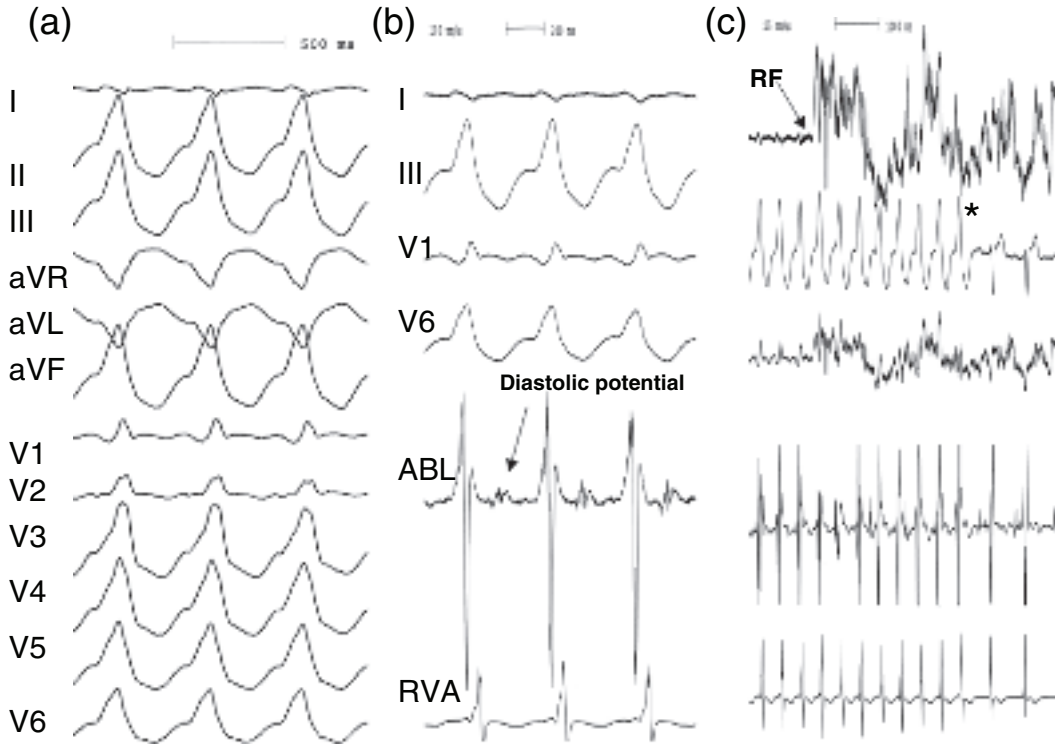

Figure 2.3 ECG where the VT terminated a few seconds after starting radiofrequency (RF) ablation recorded during VT in a patient with previous anterior myocardial infarction and recurrent sustained ventricular tachycardia (a). Catheter mapping and subsequent catheter ablation were performed. (b) Leads I, III, V1, and V6, as well as intracardiac signals from the right ventricular apex (RVA), and the ablation catheter at the successful ablation site (ABL) anteroseptal at the left ventricular base are displayed. Note the fragmented diastolic potential (c) at the successful ablation site (for further details, see text).

The post-pacing interval is within 30 msec of the VT cycle length when pacing is performed within the circuit, but it increases progressively with increasing distance between the pacing site and the circuit [34]. The described pacing results can be particularly helpful when used in combination. A combination of three criteria such as an exact QRS match during tachycardia, a return cycle within 30 msec of the VT cycle length, and the presence of diastolic potentials has been reported to terminate a VT with a single radiofrequency lesion [35].

In many patients, mapping of ventricular tachycardia (VT) remains challenging because of a combination of factors that include the frequent presence of multiple VT morphologies, the hemodynamic instability of the VT, especially in patients with impaired ventricular function, and, in the case of ischemic heart disease–related VT, the frequent existence of functional as well as anatomic areas of block that make mapping during sinus rhythm unreliable—although regions of low-amplitude potentials and fractionated electrograms indicate sites more likely to be critical to generating VT.

Because of the complexity of the reentrant circuit of VT in ischemic heart disease and the lack of reliable diagnostic mapping criteria for identifying the circuit, multiple mapping techniques are often required to identify critical parts of the macro reentry, which can subsequently be targeted for ablation. Moreover, full delineation of the reentrant circuit may not be possible during endocardial mapping because parts of, or occasionally the complete circuit, may have an intramural or epicardial location.

A technique that allows access to the pericardial space for mapping of epicardial VT circuits has been described for patients with Chagas' disease [36] but also for patients with VT related to previous myocardial infarction [37]. Epicardial identification of the circuit is based on techniques described above for endocardial mapping. Epicardial mapping can also be performed through the coronary sinus tributaries. Using standard mapping techniques, including activation sequence mapping, and pace mapping techniques, the location of pericardial electrodes can help guide roving endocardial catheters to sites of successful ablation [38].

For hemodynamically unstable VT, a predominately anatomical approach for conventional mapping in patients with coronary heart disease has been reported. The procedure involves defining areas of scarring by means of left ventricular angiography and the presence of low-frequency, low-amplitude, and fragmented electrograms. Linear lesions are then created with serial energy applications, which aim to connect the presumed exit regions to scars or anatomic structures, such as the mitral annulus [39] (Figure 2.4). In a report of post-ischemic VT in 20 patients, the noncontact mapping system has proven usefulness in showing exit sites in 99% of the studied VTs with complete VT circuits traced in about 20% of cases. Successful ablation was achieved by 77% of RF applications to relevant diastolic activity identified by the system, and was significantly more likely than at the VT exit or remote from diastolic activation [16].

The term idiopathic VT refers to tachycardias that arise from ventricles without apparent structural abnormalities. The group consists of several distinct entities, including the most common form originating from the right ventricular outflow tract (RVOT), which accounts for up to 80% of cases of idiopathic VT. Other idiopathic VT include idiopathic left VT, which often arises from the region of the left posterior fascicle, and an autonomic form that may originate from either ventricle. Activation sequence and pace mapping during tachycardia are used to identify the origin of the tachycardia. However, if these VT are only poorly inducible, the use of 3D mapping systems such as the noncontact system is extremely valuable (Figure 2). Basket catheters have also been used in a small series [19].

Noteworthy, in the presence of heart failure due to idiopathic dilated cardiomyopathy, reentry in the His–Purkinje system (bundle branch reentry; Figure 2.5) accounts for a substantial number of monomorphic VT. The reentry wavefront precedes down one bundle branch (mostly the right bundle branch), and up the contralateral bundle. This creates a QRS complex that has a LBBB contour and a normal or leftward frontal plane axis. Its significance lies in the fact that it can be easily cured by catheter ablation of the right bundle branch.

Conclusion

During recent years numerous advances in cardiac mapping have been obtained due to the introduction of complex recording techniques and

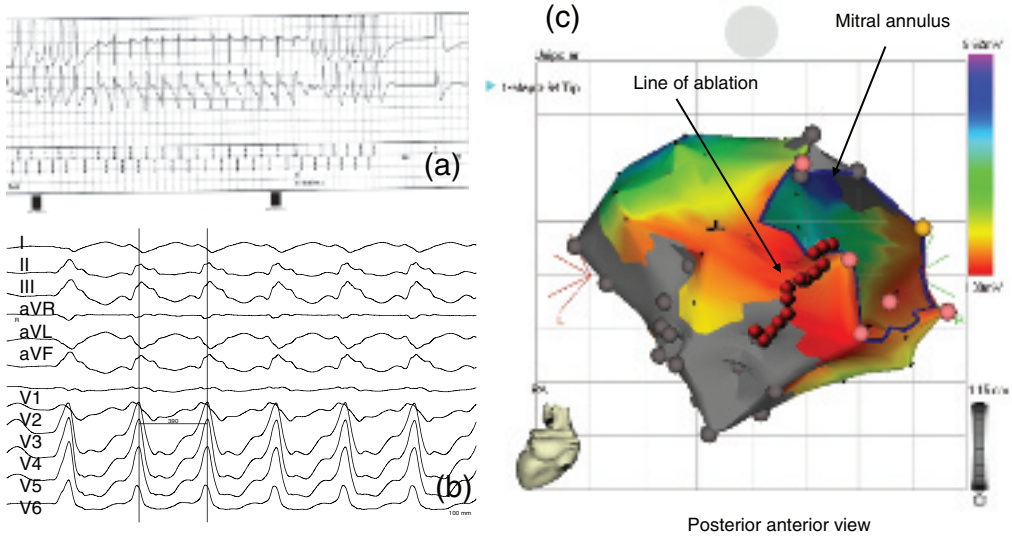

Figure 2.4 (a) Episode or ventricular tachycardia (cycle length ~400 msec) detected and terminated by an implanted cardioverter–defibrillator in a patient with a remote inferior myocardial infarction who experienced recurrent VT episodes. (b) Twelve-lead ECG of the VT in the same patient. (c) Posterior view of an electroanatomic voltage map (CARTO) of the left ventricle. Electroanatomic mapping can be used to define isthmus boundaries and thus guide successful ablation. The color range represents the voltage amplitude. Gray denotes dense scar tissue. A linear ablation lesion was placed from the mitral annulus to the edge of the scar tissue to prevent mitral "isthmus" reentrant tachycardias around the mitral valva and/or around the posterior scar.

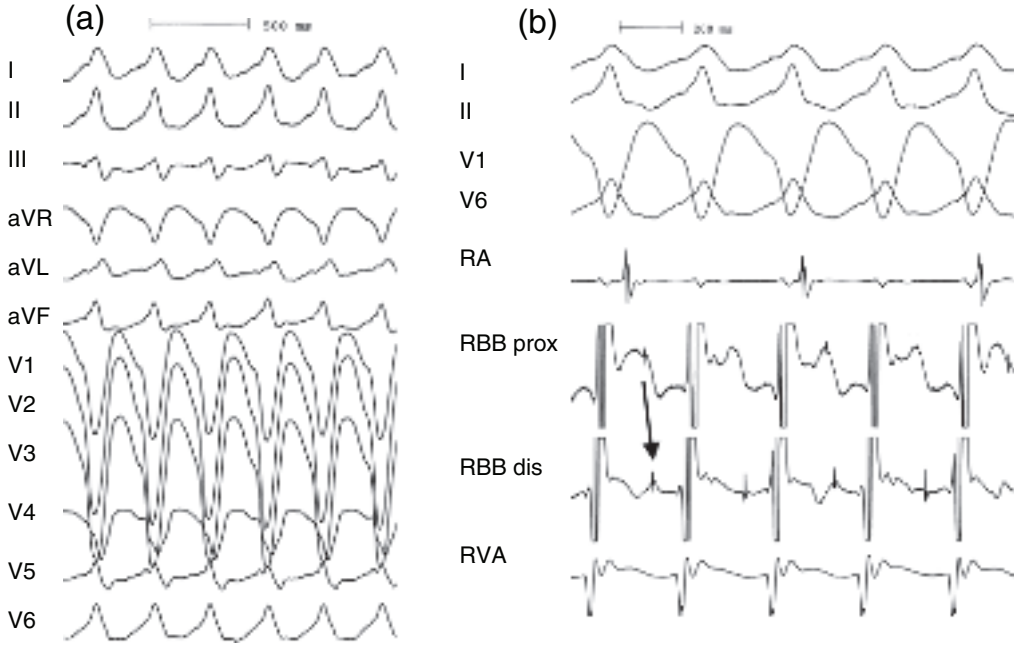

Figure 2.5 ECG recording in a patient with dilated cardiomyopathy and recurrent sustained ventricular tachycardia (a). A sustained bundle branch reentry tachycardia with a left bundle branch block morphology is displayed. Intracardiac signals (b) reveal ventriculo-atrial dissociation (RA: right atrial catheter; RVA: right ventricular apex) and activation of the right bundle branch (RBB) from proximal (RBB prox) to distal (RBB dis). The tachycardia was successfully ablated at the distal right bundle branch using radiofrequency current.

algorithms for presentation and evaluation of the multitude of signals. All these advances have contributed to a more and more complete understanding of cardiac electrophysiology and high success rates of catheter ablation.

References

1 Steinhaus BM. Estimating cardiac transmembrane activation and recovery times from unipolar and bipolar extracellular electrograms: a simulation study. *Circ Res* 1989; **64**: 449–62.

2 Spach MS, Miller WT, III, Miller-Jones E, Warren RB, Barr RC. Extracellular potentials related to intracellular action potentials during impulse conduction in anisotropic canine cardiac muscle. *Circ Res* 1979; **45**: 188–204.

3 Waldo AL, Henthorn RW, Plumb VJ, MacLean WA. Demonstration of the mechanism of transient entrainment and interruption of ventricular tachycardia with rapid atrial pacing. *J Am Coll Cardiol* 1984: **3**: 422–30.

4 Gepstein L, Hayam G, Ben HS. A novel method for nonfluoroscopic catheter-based electroanatomical mapping of the heart: in vitro and in vivo accuracy results. *Circulation* 1997; **95**: 1611–22.

5 Marchlinski FE, Callans DJ, Gottlieb CD, Zado E. Linear ablation lesions for control of unmappable ventricular tachycardia in patients with ischemic and nonischemic cardiomyopathy. *Circulation* 2000; **101**: 1288–96.

6 Sokoloski MC, Pennington JC, III, Winton GJ, Marchlinski FE. Use of multisite electroanatomic mapping to facilitate ablation of intra-atrial reentry following the Mustard procedure. *J Cardiovasc Electrophysiol* 2000; **11**: 927–30.

7 Kottkamp H, Hugl B, Krauss B, et al. Electromagnetic versus fluoroscopic mapping of the inferior isthmus for ablation of typical atrial flutter: a prospective randomized study. *Circulation* 2000; **102**: 2082–86.

8 Kistler PM, Rajappan K, Jahngir M, et al. The impact of CT image integration into an electroanatomic mapping system on clinical outcomes of catheter ablation of atrial fibrillation. *J Cardiovasc Electrophysiol* 2006; **17**: 1093–101.

9 Wittkampf FH, Wever EF, Derksen R, et al. LocaLisa: new technique for real-time 3-dimensional localization of regular intracardiac electrodes. *Circulation* 1999; **99**: 1312–17.

10 Wittkampf FH, Wever EF, Vos K, et al. Reduction of radiation exposure in the cardiac electrophysiology laboratory. *Pacing Clin Electrophysiol* 2000; **23**: 1638–44.

11 Khoury DS, Taccardi B, Lux RL, Ershler PR, Rudy Y. Reconstruction of endocardial potentials and activation sequences from intracavitary probe measurements: localization of pacing sites and effects of myocardial structure. *Circulation* 1995; **91**: 845–63.

12 Ribbing M, Wasmer K, Mönnig G, et al. Endocardial mapping of right ventricular outflow tract tachycardia using noncontact activation mapping. *J Cardiovasc Electrophysiol* 2003; **14**: 602–8.

13 Peters NS, Jackman WM, Schilling RJ, Beatty G, Davies DW. Human left ventricular endocardial activation mapping using a novel noncontact catheter. *Circulation* 1997; **95**: 1658–60.

14 Gornick CC, Adler SW, Pederson B, Hauck J, Budd J, Schweitzer J. Validation of a new noncontact catheter system for electroanatomic mapping of left ventricular endocardium. *Circulation* 1999; **99**: 829–35.

15 Kadish A, Hauck J, Pederson B, Beatty G, Gornick C. Mapping of atrial activation with a noncontact, multielectrode catheter in dogs. *Circulation* 1999; **99**: 1906–13.

16 Schilling RJ, Peters NS, Davies DW. Feasibility of a noncontact catheter for endocardial mapping of human ventricular tachycardia. *Circulation* 1999; **99**: 2543–52.

17 Schneider MA, Ndrepepa G, Zrenner B, Karch MR, Schreieck J, Deisenhofer I, Schmitt C. Noncontact mapping-guided catheter ablation of atrial fibrillation associated with left atrial ectopy. *J Cardiovasc Electrophysiol* 2000; **11**: 475–79.

18 Betts TR, Roberts PR, Allen SA, Salmon AP, Keeton BR, Haw MP, Morgan JM.Electrophysiological mapping and ablation of intra-atrial reentry tachycardia after Fontan surgery with the use of a noncontact mapping system. *Circulation* 2000; **102**: 419–25.

19 Schalij MJ, van Rugge FP, Siezenga M, van der Velde ET. Endocardial activation mapping of ventricular tachycardia in patients: first application of a 32-site bipolar mapping electrode catheter. Circulation 1998; **98**: 2168–79.

20 Zrenner B, Ndrepepa G, Schneider M, et al. Computer-assisted animation of atrial tachyarrhythmias recorded with a 64-electrode basket catheter. *J Am Coll Cardiol* 1999; **34**: 2051–60.

21 Michael MJ, Haines DE, Dimarco JP, Paul MJ. Elimination of focal atrial fibrillation with a single radiofrequency ablation: use of a basket catheter in a pulmonary vein for computerized activation sequence mapping. *J Cardiovasc Electrophysiol* 2000; **11**: 1159–64.

22 Kuck KH, Schluter M. Single-catheter approach to radiofrequency current ablation of left-sided accessory pathways in patients with Wolff–Parkinson–White syndrome. *Circulation* 1991; **84**: 2366–75.

23 Mönnig G, Wasmer K, Eckardt L. Atrioventricular nodal reentrant tachycardia in a patient with Ebstein anomaly. *Heart* 2004; **90**: e58.

24 Miles WM, Yee R, Klein GJ, Zipes DP, Prystowsky EN. The preexcitation index: an aid in determining the mechanism of supraventricular tachycardia and localizing accessory pathways. *Circulation* 1986; **74**: 493–500.

25 Eckardt L, Mönnig G, Wasmer K, Breithardt G. A NavX guided cryoablation of an accessory pathway in a large coronary sinus diverticulum. *J Cardiovasc Electrophysiol* 2005; **16**: 233–34.

26 Saoudi N, Nair M, Abdelazziz A, et al. Electrocardiographic patterns and results of radiofrequency catheter ablation of clockwise type I atrial flutter. *J Cardiovasc Electrophysiol* 1996; **7**: 931–42.

27 Tai CT, Haque A, Lin YK, et al. Double potential interval and trans-isthmus conduction time for prediction of cavotricuspid isthmus block after ablation of typical atrial flutter. *J Interv Card Electrophysiol* 2002: **7**: 77–82.

28 Haissaguerre M, Jais P, Shah DC, et al. Spontaneous initiation of atrial fibrillation by ectopic beats originating in the pulmonary veins. *N Engl J Med* 1998; **339**: 659–66.

29 Jais P, Shah DC, Haissaguerre M, Hocini M, Peng JT, Clementy J. Catheter ablation for atrial fibrillation. *Annu Rev Med* 2000; **51**: 431–41.

30 Haissaguerre M, Jais P, Shah DC, et al. Electrophysiological end point for catheter ablation of atrial fibrillation initiated from multiple pulmonary venous foci. *Circulation* 2000; **101**: 1409–17.

31 Tse HF, Lau CP, Kou W, et al. Comparison of endocardial activation times at effective and ineffective ablation sites within the pulmonary veins. *J Cardiovasc Electrophysiol* 2000; **11**: 155–59.

32 Haissaguerre M, Shah DC, Jais P, et al. Electrophysiological breakthroughs from the left atrium to the pulmonary veins. *Circulation* 2000;**102**: 2463–65.

33 Morady F, Kadish A, Rosenheck S, et al. Concealed entrainment as a guide for catheter ablation of ventricular tachycardia in patients with prior myocardial infarction. *J Am Coll Cardiol* 1991; **17**: 678–89.

34 Stevenson WG, Khan H, Sager P, et al. Identification of reentry circuit sites during catheter mapping and radiofrequency ablation of ventricular tachycardia late after myocardial infarction. *Circulation* 1993; **88**: 1647–70.

35 El-Shalakany A, Hadjis T, Papageorgiou P, Monahan K, Epstein L, Josephson ME. Entrainment/mapping criteria for the prediction of termination of ventricular tachycardia by single radiofrequency lesion in patients with coronary artery disease. *Circulation* 1999; **99**: 2283–89.

36 Sosa E, Scanavacca M, d'Avila A, et al. Endocardial and epicardial ablation guided by nonsurgical transthoracic epicardial mapping to treat recurrent ventricular tachycardia. J *Cardiovasc Electrophysiol* 1998; **9**: 229–39.

37 Sosa E, Scanavacca M, d'Avila A, Antonio J, Ramires F. Nonsurgical transthoracic epicardial approach in patients with ventricular tachycardia and previous cardiac surgery. *J Interv Card Electrophysiol* 2004; **10**: 281–88.

38 de Paola AA, Melo WD, Tavora MZ, Martinez EE. Angiographic and electrophysiological substrates for ventricular tachycardia mapping through the coronary veins. *Heart* 1998; **79**: 59–63.

39 Furniss S, nil-Kumar R, Bourke JP, Behulova R, Simeonidou E. Radiofrequency ablation of haemodynamically unstable ventricular tachycardia after myocardial infarction. *Heart* 2000; **84**: 648–52.

3

CHAPTER 3

Cardiac Anatomy for Interventional Electrophysiology and Mapping

Siew Yen Ho, PhD,[1] *José Angel Cabrera,* MD, PhD,[2] & *Damian Sánchez-Quintana,* MD, PhD[3]

[1]Imperial College London, London, UK
[2]Hospital Quirón, Madrid, Spain
[3]Universidad de Extremadura, Badajoz, Spain

Summary

Understanding of cardiac anatomy in 3D perspectives underscores interventional electrophysiology and mapping. This chapter provides an overview of the location and spatial relationships of cardiac chambers and neighbouring structures such as the phrenic nerves and esophagus. Consideration is given to the internal aspects of the atrial chambers and ventricular chambers, highlighting significant and salient anatomical landmarks so as to reduce risks of damage to important structures during interventions.

Introduction

Although the anatomy of the heart has remained more or less static since its earliest descriptions, our understanding of its anatomy as applied to various clinical fields has evolved. In recent decades, cardiac anatomy has become an integral part of interventional cardiac electrophysiology and mapping, especially with regard to developments in imaging of real anatomy for clinical procedures. Nevertheless, even with highly sophisticated imaging, there is still a need to understand some of the more subtle features of cardiac anatomy. Of paramount importance is understanding cardiac structures in attitudinal orientation [1, 2]. In this chapter, we will highlight the aspects that are of practical relevance when interrogating or intervening in the normally structured heart.

General Overview: Location and Spatial Relationships of Chambers

In his outstanding monograph, McAlpine [1] stressed the importance of the attitudinal approach that underscores understanding of cardiac anatomy in the clinical setting. Surrounded by the four cardiac chambers, the aortic root forms the centerpiece of the heart. Furthermore, the right ventricular outflow tract overlaps the left ventricular outflow tract,

Cardiac Mapping, Third Edition Edited by Mohammad Shenasa, Gerhard Hindricks, Martin Borggrefe, and Günter Breithardt
 ISBN: 978-1-405-17572-2

reflecting the ventricular arrangement, but this will be discussed later.

Lying between the lungs, the heart is nearer to the front of the thorax than to the back. The base of the heart lies anterior to the spine from the fifth to eighth thoracic vertebrae. Anteriorly, the heart is separated from the thoracic wall by the pleura and the thin anterior parts of the lungs. It is enclosed by the fibrous pericardium that separates it from neighboring structures. One-third of the heart lies to the right of the midline of the chest and two-thirds lie to the left. The phrenic nerves accompanied by phrenic vessels descend bilaterally onto the pericardium (Figure 3.1). The right phrenic nerve descends almost vertically, first along the right brachiocephalic vein, then along the right anterolateral surface of the superior caval vein and continues its descent immediately in front of the right pulmonary veins in the lung hilum before reaching the diaphragm [3]. Its upper course along the superior cavoatrial junction and proximity to the right superior pulmonary vein makes it vulnerable to damage when ablations are carried out for inappropriate or reentrant sinus tachycardia or during pulmonary vein isolation in atrial fibrillation [4, 5]. It may also be put at risk if a lateral right atrial isthmus is ablated for typical atrial flutter because the inferior course of the nerve is adjacent to the lateral border of the entrance of the inferior caval vein to the right atrium [3].

On the other side, the left phrenic nerve descends behind the left brachiocephalic vein, continues over the aortic arch and pulmonary trunk onto the pericardium overlying the left atrial appendage, and then descends either anteriorly or anterolaterally over the area of the left ventricle to insert in the diaphragm behind the cardiac apex. The course of the left phrenic nerve on the fibrous pericardium brings it into the vicinity of the left atrial appendage, which may be relevant in terms of ablating ectopic foci in the appendage or in device closure of the appendage OS (Figure 3.1). Its inferior course may overlie the great cardiac vein or obtuse marginal vein, a feature worth noting when implanting pacing leads in these veins.

The fibrous pericardium enclosing the heart is lined on the inside by the serous pericardium (the parietal layer), which also covers the surfaces of the heart as the epicardium (the visceral layer) and partly ensheaths the great vessels so as to form a closed sac containing a small amount of pericardial fluid. The aorta and pulmonary trunk are ensheathed together, whereas the veins are enclosed in another sheath. This arrangement leaves a reflection of the serous pericardium in between—the transverse sinus—which passes behind the great arteries and in front of the atriums. Another sinus, the oblique sinus, is bordered by the reflections at the veins. Its superior border at the transverse reflection lies at the level of the right pulmonary artery.

The pericardial space can be accessed via a subxiphoid puncture and it allows relatively free manipulation of catheters around the epicardial surface of the heart except in cases with pericardial adhesions. This portal is particularly useful for the ventricles. At the atrial level, pericardial reflections at the veins, particularly the pulmonary veins, are varied and they can restrict maneuvers, precluding complete encirclement for drawing ablation lines around the veins, for example [6, 7].

Following removal of the pericardium and viewing the patient from the front, it is apparent that the right margin of the heart is formed by the right atrium. Viewed from the front, the cavity of the right atrium is right and anterior, while the left atrium is situated to the left and mainly posteriorly. The front of the left atrium lies just behind the transverse pericardial sinus, while its posterior wall is just in front of the tracheal bifurcation and is therefore related to the course of the esophagus. Related posteriorly and inferiorly to the left atrium is the coronary sinus, which is the continuation of the great cardiac vein. The oblique vein, or ligament (of Marshall) passes between the left atrial appendage and the left superior pulmonary vein, along the postero-lateral atrial wall, to join the coronary sinus.

Traced from the inferior cardiac border, the right ventricular cavity can be seen to curve from inferiorly to pass cephalad over the left ventricular cavity. This results in the right ventricular outflow tract overlapping and crossing that from the left ventricle when the heart is viewed from the front [8], which is an important feature to note when ablating in the ventricular outlets (Figure 3.2). The pulmonary trunk passes to the left of the ascending aorta and branches into the right and left pulmonary arteries. The right pulmonary artery courses rightward over the antero-superior wall of the left atrium to

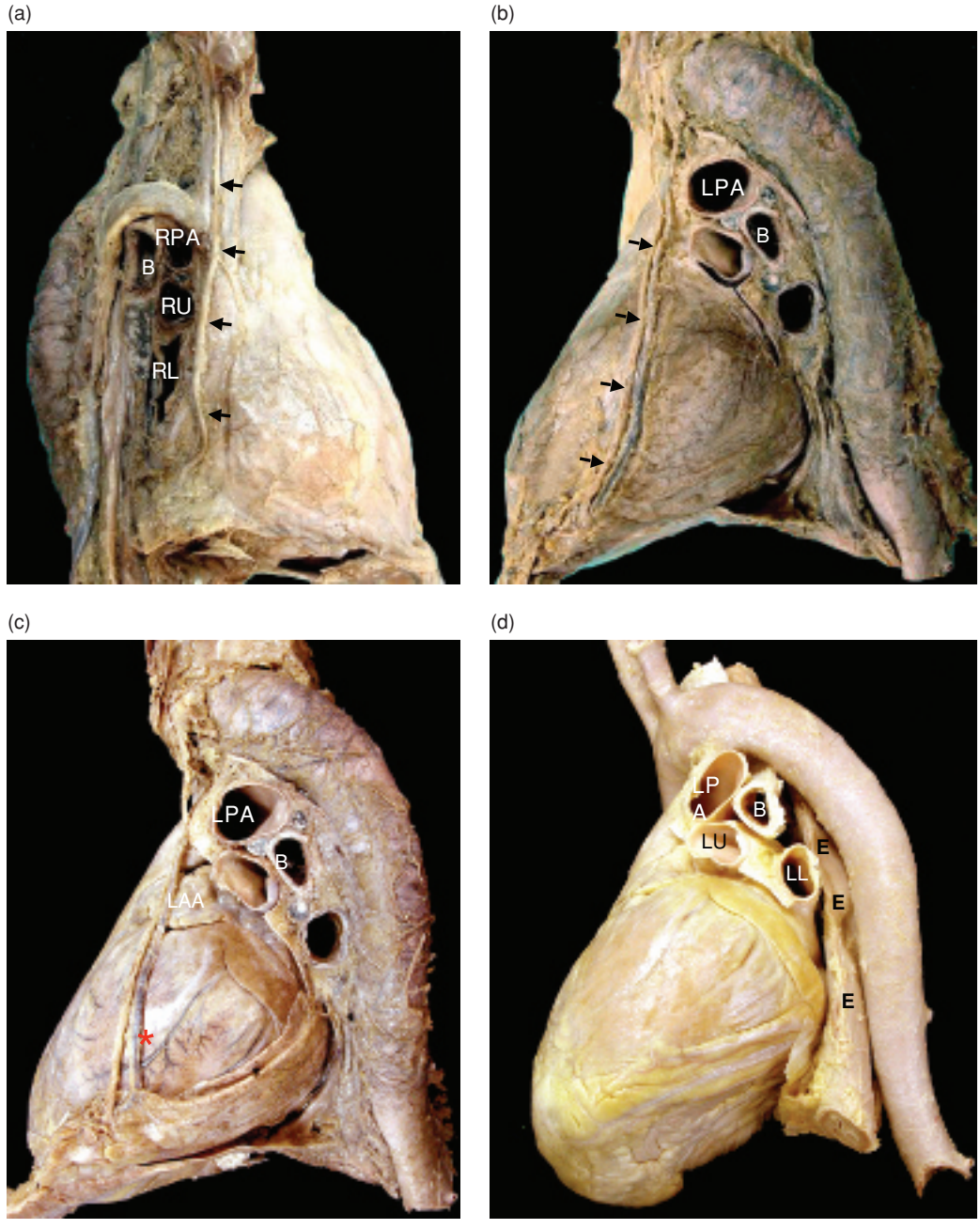

Figure 3.1 Parts (a) and (b) show views of a specimen from the right and from the left, respectively. The heart is enclosed by the fibrous pericardium. The arrows indicate the right and left phrenic nerves accompanied by arteries. Part (c) shows a window made in the fibrous pericardium of the specimen to reveal the relationship of the left phrenic nerve to the left atrial appendage (LAA) and the obtuse marginal artery and vein (asterisk). Part (d) shows the heart exposed following removal of the entire fibrous pericardium. The esophagus (E) is visible between the left atrium and the descending thoracic aorta. KEY: B = bronchus; LL = left lower pulmonary vein; LPA = left pulmonary artery; LU = left upper pulmonary vein; RL = right lower pulmonary vein; RPA = right pulmonary artery; RU = right upper pulmonary vein.

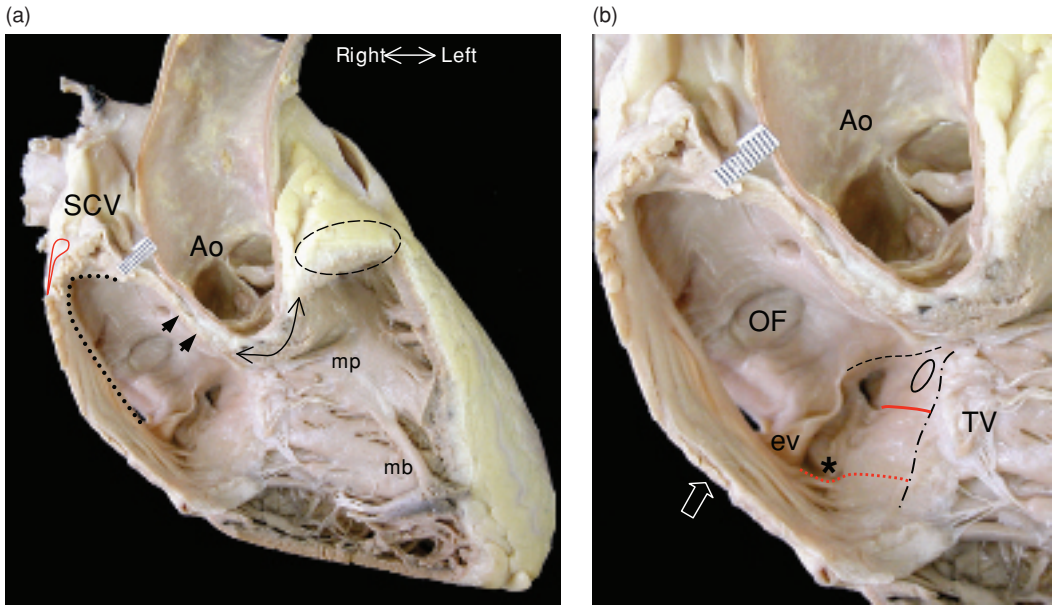

Figure 3.2 Part (a) is a dissection viewed from the front to show the location of the aortic valve between the right atrium and the right ventricular outflow tract. The curved arrow is the inner heart curvature or supraventricular crest separating tricuspid from pulmonary valves (pulmonary valve represented by oval). The small arrows point to the wall of the right atrium that lies behind the aorta but may be mistaken for being septal. The dotted line marks the course of the terminal crest, and the area of the sinus node is depicted by the red shape. Part (b) is a magnification with the borders of the triangle of Koch marked. The broken line represents the tendon of Todaro and the dot-and-dash line is the hingeline of the tricuspid valve. The atrioventricular node (oval) is at the apex. The solid red line marks the paraseptal isthmus and the dotted red line marks the cavotricuspid isthmus. The latter often passes through a pouch (asterisk). KEY: Ao = aorta; ev = Eustachian valve; mb = moderator band; mp = medial papillary muscle; OF = oval fossa; SCV = superior caval vein; TV = tricuspid valve. Open arrow indicates entrance of inferior caval vein.

pass behind the ascending aorta (Videoclip 1 ). The pulmonary valve is the most superiorly sited of the four cardiac valves. It lies almost horizontally behind the second and third costal cartilages. The plane of the aortic valve is tilted inferiorly at an angle posterior and to the right of the pulmonary valve (Figure 3.2).

The Chambers of the Heart

The Right Atrium

Anatomically, an atrial chamber is considered as having four components: the appendage, the venous part, the vestibule and the septum. The latter is shared by the two atriums. The right atrium is dominated by its large, triangular-shaped appendage which is located anterior and laterally. Characteristically the appendage is lined by an array of pectinate muscles on its endocardial aspect. In between the frond-like branches of the pectinate muscles, the wall of the appendage is exceptionally thin, with very little myocardial thickness. The branching and overlapping arrangement of the pectinate muscles may play a role in initiating intra-atrial reentry [9]. The pectinate muscles arise from the terminal crest ("crista terminalis"), which is a smooth muscle band that runs from the medial aspect anterior to the entrance of the superior caval vein, then sweeps rightward and posteriorly to descend toward the entrance of the inferior caval vein before branching into multiple small muscles bundles and branches (Figure 3.2) [10].

The crest may be a source of atrial tachycardias [11]. The pectinate muscles and the ramifications from the terminal crest stop short of reaching the tricuspid valve. They are separated from the valve by a circumferential region of smooth atrial wall that is the vestibule to the valve. The portion of the vestibule between the orifice of the

inferior caval vein and the tricuspid is the anterior part of the cavo-tricuspid isthmus (inferior isthmus), which is ablated in patients with common atrial flutter. It has a variable morphology but is usually composed of a fibrous posterior part, a fibromuscular middle part, and a smooth anterior part that is the vestibule [12, 13]. It is common to find a pouch-like formation in the middle part (Figure 3.2).

The vestibule between the orifice of the coronary sinus and the tricuspid valve is known as the "septal" isthmus that is used in slow-pathway ablation (Figure 3.2). Owing to the deep incursion of epicardial fat in the atrioventricular groove, this isthmus actually overlies the inferior pyramidal space and is paraseptal in location rather than "septal" [14]. The inferior extensions of the atrioventricular node have been implicated in atrioventricular nodal reentrant tachycardia [15]. The landmark for the compact atrioventricular node is the apex of a triangle bordered anteriorly by the hingeline of the septal leaflet of the tricuspid valve, posteriorly by the tendon of Todaro that is buried within the musculature of the Eustachian ridge (also known as the sinus septum), and inferiorly by the paraseptal isthmus (Figure 3.2).

In RAO projection the node and His bundle are superior and the coronary sinus is inferior. The sizes of the nodal triangle vary, and it has been suggested that hearts with small nodal triangles may have a more inferiorly located atrioventricular node that reaches toward the coronary sinus [16, 17]. The rightward margin of the compact node lies approximately 1 mm or so from the endocardial surface of the right atrium. The central fibrous body (including the membranous septum) abuts the apex of the nodal triangle and carries within it the penetrating bundle of His that extends from the compact node and normally is the only bridge of muscular continuity between atrial and ventricular myocardium [18].

Importantly for modifications of the sinus node for "inappropriate" sinus tachycardia [19], the anatomic landmark for the sinus node is the terminal groove close to the superior cavo-atrial junction (Figure 3.2). In most individuals the node is located anterolaterally in a comma shape with the head nearest the junction and the tail penetrating into the musculature of the terminal crest [20]. In approximately 10% of cases, the node is horse-shoe shaped and located medially as well as laterally in the terminal groove [21]. Prongs of nodal tissues often interdigitate with musculature of the terminal crest and may even extend into the muscular sleeves that surround the superior caval vein [20]. Between the sinus and atrioventricular nodes, the internodal myocardium does not show histologically specialized characteristics but is composed of atrial musculature arranged around the venous and valvar orifices [22].

The venous component of the right atrium lies between the entrances of the superior and inferior caval veins. It is characterized by its smooth wall. The Eustachian valve guarding the entrance of the inferior caval vein is variably developed (Figure 3.2). Usually it is a triangular flap of fibrous or fibromuscular tissue, but in some cases the valve is particular large and muscular, posing an obstacle to passage of catheters from the inferior caval vein to the inferior part of the right atrium. Occasionally, the valve is perforated, or is an extensive filigree sometimes described as a Chiari network.

The valve guarding the coronary sinus is usually a small crescentic flap that, frequently, is fenestrated. An imperforate valve or a band completely covering the orifice is very rare.

The Atrial Septum and Interatrial Connections

Accessing the left atrium from the right requires an appreciation of the extent of the true atrial septum. From the right atrial aspect, the true septum is marked by the valve of the oval fossa (Figure 3.2). This is the true septal structure that can be perforated without risk of exiting the heart or damaging the arterial supply to the sinus node [23]. Surrounding the valve of the fossa on the right atrial side is a raised muscle rim ("limbus") that is an infolding of the atrial wall. Importantly, the antero-medial wall of the right atrium appears to be "septal" but transgressing it leads to the back of the aorta (Figure 3.2). On the left atrial side, the septum lacks the crater-like feature of the right side. The valve itself is usually thin, approximately 1–3 mm thick, and in some cases it can be anuerysmal, herniating into the atrial chambers. Probe patency of the oval fossa is found in about 25% of the normal population (Figure 3.3).

Muscular continuity between atriums peripheral to the septum is frequently found as bridges in the

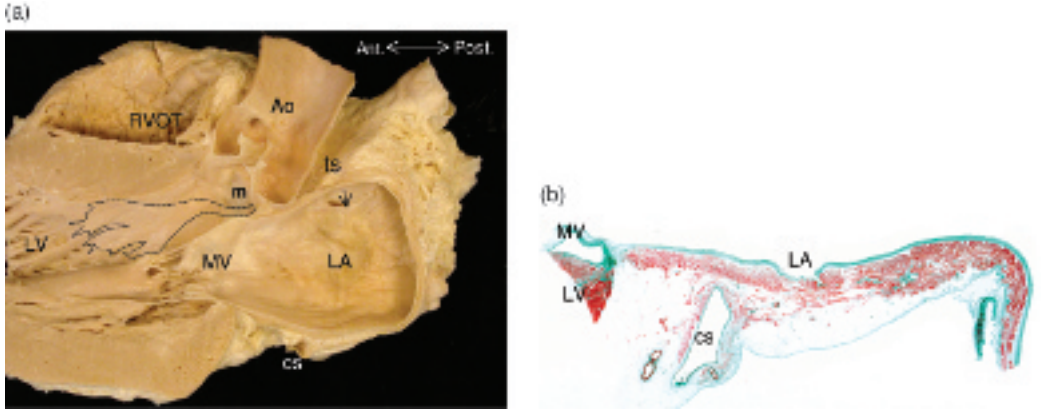

Figure 3.3 Part (a) is a longitudinal cut through the left atrium and left ventricle viewed from the left side. The aortic valve is behind the right ventricular outflow tract (RVOT) but in front of the left atrium (LA). The dotted lines represent the location of the atrioventricular conduction bundle together with the left bundle branch. The small arrow indicates the opening of the patent foramen ovale and proximity to location of the transverse pericardial sinus (ts). Part (b) is a histological section through the inferior wall of the left atrium in similar orientation to part (a) with the myocardium stained red and fibrous tissue stained green. It shows muscle bridges between the wall of the coronary sinus (cs) and the left atrium. KEY: Ao = aorta; LV = left ventricle; MV = mitral valve; m = membranous septum.

subepicardium [23, 24]. The most prominent interatrial bridge is Bachmann's bundle. This is a broad muscular band that runs in the subepicardium from the anterior wall of the superior caval vein into the anterior walls of both atriums. The muscular fibers in Bachmann's bundle, as in the terminal crest, are well aligned, allowing for preferential conduction. Smaller bridges are often present, giving the potential for macro reentry. Further bridges are often found posteriorly and inferiorly [23, 24].

The Left Atrium

The atrial appendage is characteristically a small finger-like cul-de-sac in human hearts. Owing to its tubular shape, its junction with the left atrium is narrow and well defined. In contrast to the right atrium, virtually all the pectinate muscles in the left atrium are confined within the appendage, and they form a complicated network of muscular ridges lining the endocardial aspect.

The major part of the atrium, including the septal component, is smooth-walled. The smoothest parts are the superior and posterior walls that make up the large pulmonary venous component and the vestibule. Externally, the posterior wall is related to the esophagus and its nerves (vagal nerves) and the thoracic aorta (Figure 3.1). The coronary sinus tracks along the postero-inferior part (Figure 3.3).

The anterior wall just behind the aorta ranges from 1.5 to 4.8 mm thick, but there is usually a small area inferior to Bachmann's bundle that is exceptionally thin. In close proximity to the right pulmonary artery, the superior wall, or dome, ranges from 3.5 to 6.5 mm in thickness, but it tends to be thinner near to the left pulmonary veins. The thickness of the lateral wall is between 2.5 and 4.9 mm [25]. Postero-laterally, between the os of the left atrial appendage and the left pulmonary veins, the atrial wall folds upon itself and appears like a ridge when viewed from within the chamber. The remnant of the vein of Marshall lies in this fold. This so-called ridge has variable widths; the narrower ridges can make it tricky to achieve a complete ablation line for encircling the left pulmonary veins [26].

Clinical imaging studies using magnetic resonance and multislice computed tomography have demonstrated the complex anatomy of the pulmonary veins with significant variability in dimensions, shape and branching patterns [27–30]. The orifices of the right pulmonary veins are directly adjacent to the plane of the atrial septum. The transition between atrium and vein is smooth. Inside the atrial chamber, it is often difficult to define entrances, or ostia, of the veins. Not infrequently, the ipsilateral veins coalesce into a short antrum (or vestibule) before entering the atrial chamber

proper (Videoclip 2). Musculature of the atrial wall extends into the veins to varying lengths, with the longest sleeves along the upper veins [31–33]. Close to the venous insertions, the sleeves are thicker and tend to surround the entire epicardial aspect of the vein. The distal margins of the sleeves, however, are usually thinner and irregular as the musculature fades out [31, 32].

The Right Ventricle

The inflow and outflow tracts of the right ventricle make an obtuse angle with the supraventricular crest marking the inner "bend" of the angle. The crest is a muscular fold that separates the tricuspid valve orifice from the pulmonary valve. It is not septal but continues into the subpulmonary muscular infundibulum cephalad and it also extends parietally (Figure 3.2). When mapping the right ventricular outflow tract, for example, in some cases of idiopathic right ventricular tachycardia, some forms of arrhythmogenic right ventricular cardiomyopathy, or some scar-related ventricular tachycardias, the operator should be aware that the area usually termed septal or high septal is not septal at all but is part of the muscular subpulmonary infundibulum that supports the pulmonary valve and also elevates the valve away from the septum [34]. More appropriately termed the paraseptal area, this part of the infundibulum lies anterior to the aortic root (Figure 3.3) and is related to the right and the left coronary aortic sinuses and, therefore, is close to the courses of the main coronary arteries [35, 36]. The semilunar hingelines of the pulmonary leaflets cross the ventriculo-arterial junction, thereby enclosing in the nadirs of the hingelines, small areas of ventricular myocardium that form the inferior portions of the pulmonary sinuses.

The atrioventricular junction provides the insulating tissue plane between atrial and ventricular myocardium. Breaches of this plane by accessory atrioventricular connections allow the cardiac impulse to bypass the normal atrioventricular conduction system. When mapping and ablating these pathways, it can be very difficult to distinguish between those that are so-called septal in location and those that are paraseptal according to the nomenclature proposed by Cosio and colleagues [2]. The "septal pathways" (also known as mid-septal) [37] are located in the area of the triangle of Koch and are inferior to the His bundle but may be close to the atrioventricular node. The inferior paraseptal pathways are related to the inferior pyramidal space, but because the pyramidal space can extend to the epicardial aspect of the triangle of Koch, "septal" may encroach upon inferior paraseptal. Pathways that have ventricular insertions into the supraventricular crest are in the superior paraseptal region (previously known as anteroseptal) (Figure 3.4). Being away from the septum, theoretically they are less risky to ablate than peri-Hisian pathways.

The His bundle is encased by the central fibrous body as it passes from right to left to emerge as the atrioventricular conduction bundle that is sandwiched between the membranous septum and the muscular septum. The bundle tends to remain on the left side of the septal crest for a short distance before separating into the left and right bundle branches that remain ensheathed in fibrous tissue in their proximal courses [18]. From the left of the septum, the right bundle branch passes through septal musculature to emerge at the base of the medial papillary that arises from the septal aspect of the right ventricle (Figure 3.2). Occasionally, the right bundle branch is visible in heart specimens as a thin white line that descends along the septal surface toward the insertion of the moderator band.

The Left Ventricle

Apart from its thicker muscular wall, the left ventricle has a different configuration from the right ventricle. The aortic and mitral valves are hardly ever separated by muscle (Figures 3.3 and 3.4). The inflow and outflow tracts form an acute angle, and they overlap each other when the heart is viewed from the front. Owing to the central location of the aortic valve in the heart, the left ventricular outflow tract lies between the ventricular septum and the aortic (or anterior) leaflet of the mitral valve (Figure 3.3). Because there is no supraventricular crest, it is exceedingly rare to find accessory pathways coursing through the area of fibrous continuity between aortic and mitral valves at this quadrant of the left atrioventricular junction. The hingeline of the mitral valve to the septum is considerably less compared to the tricuspid valve and it is located further from the cardiac apex. Owing to the "offset" between tricuspid and mitral insertions at the

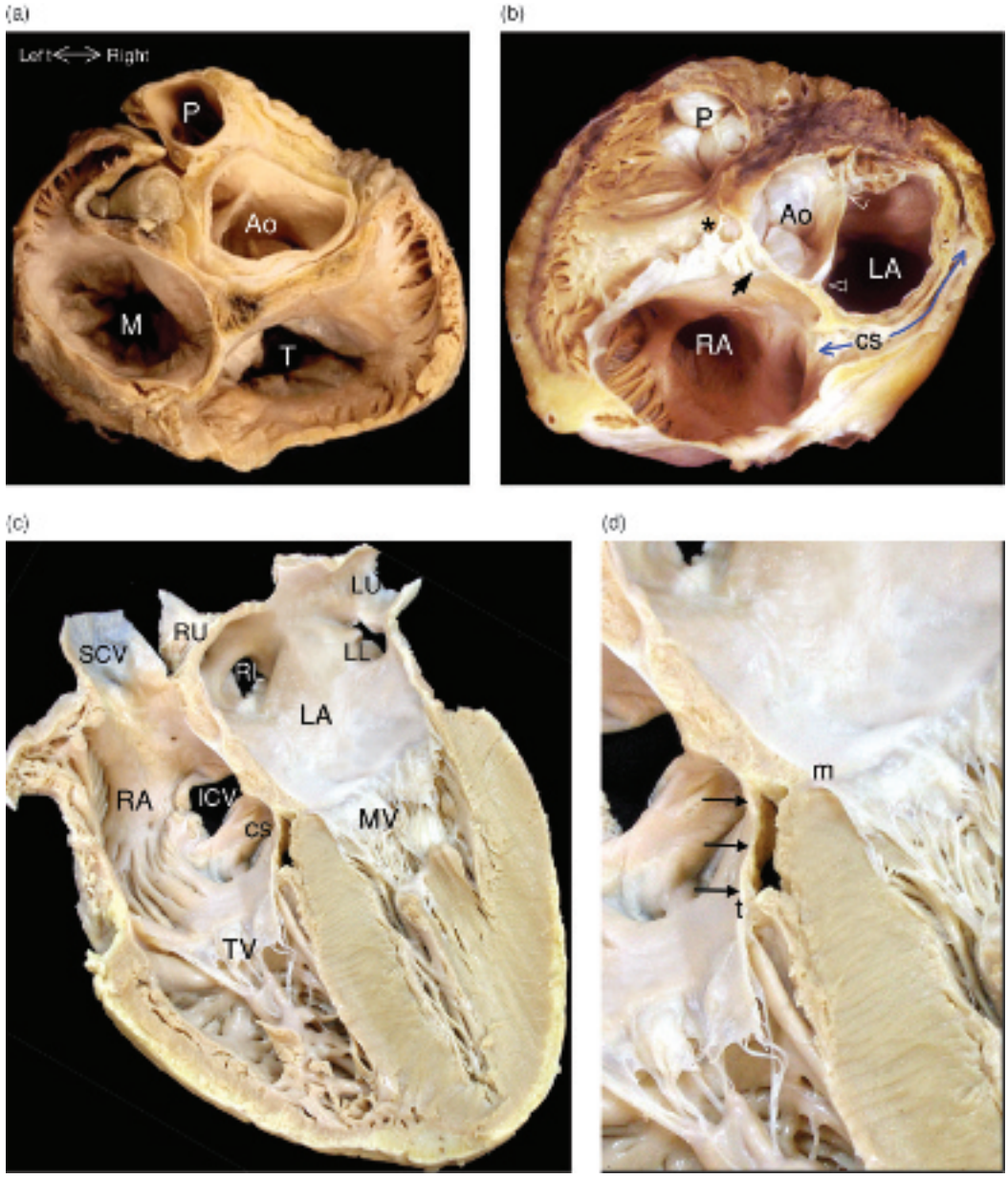

Figure 3.4 Parts (a) and (b) are basal and apical views, respectively, of a heart displaying the locations of the cardiac valves and the atrioventricular junctions. Part (a) shows the oblique orientation of the atrial septum, extensive pectinate muscles in the right atrium and the narrow left atrial appendage. Part (b) simulates an LAO view. The septal component of the atrioventricular junction is limited. Musculature is lacking between aortic and mitral valves (between triangles). The small arrow indicates the location of the atrioventricular conduction bundle and the membranous septum. Part (c) displays a heart cut through its four chambers revealing the parietal atrioventricular junctions and the inferior paraseptal junction. Part (d) is a magnified view showing the offset levels of attachments of the mitral (m) and tricuspid (t) valves. Part of the right atrial wall (arrows) overlies the inferior pyramidal space (dark area). KEY: Ao = aorta; cs = coronary sinus; ICV = inferior caval vein; LA = left atrium; LL = left lower pulmonary vein; LU = left upper pulmonary vein; M = mitral valve; P = pulmonary valve; RA = right atrium; RL = right lower pulmonary vein; RU = right upper pulmonary vein; SCV = superior caval vein; T = tricuspid valve; * = supraventricular crest.

septum, the right atrial wall bearing the triangle of Koch overlies the submitral portion of the ventricular septum (Figure 3.4).

The atrioventricular conduction bundle emerges from the central fibrous body to appear in between the membranous septum and the muscular ventricular septum [18]. From here, the left bundle branch cascades down the subendocardium toward the apical portion. The membranous septum adjoins the interleaflet area between the right and noncoronary leaflets (Figure 3.3).

While half of the aortic valve is in fibrous continuity with the mitral valve, the other half consisting of the right coronary sinus and the medial part of the left coronary sinus contains ventricular myocardium that can be important in some cases of ventricular ctachycardia [38, 39]. Significantly, these are also the sinuses that abut the subpulmonary muscular infundibulum externally. Mapping and intervention of ventricular tachycardia in the outlets require distinguishing the so-called high septal right ventricular outflow tract types from those arising from the aortic sinuses [34].

Because of the lack of musculature between the left cardiac valves, the potential for accessory atrioventricular connections are primarily in the inferior paraseptal and the parietal portions of the left atrioventricular junction. The course of the coronary sinus and its continuation into the great cardiac vein can be a guide, but it is worth noting that the veins seldom course adjacent to the mitral annulus. Frequently, they run a centimeter or so proximally (Figure 3.3) [40].

Conclusion

The convoluted arrangement between the right and left sides of the heart makes it challenging to understand and interpret spatial relationships of the various cardiac chambers and their valves. Imaging tools with the facility to reconstruct the heart and its surrounding structures in three dimensions can be helpful, especially for the beginner. Owing to constraints on the length of the chapter, we are not able to discuss all the cardiac structures or to provide a detailed account, but we have aimed at covering the most salient points relevant to intervention and mapping.

References

1 McAlpine WA. *Heart and Coronary Arteries*. Springer-Verlag, Berlin, 1975: 1.

2 Cosio FG, Anderson RH, Kuck K, et al. Living anatomy of the atrioventricular junctions. A guide to electrophysiological mapping. A consensus statement from the Cardiac Nomenclature Group of Arrhythmias, European Society of Cardiology, and the Task Force on Cardiac Nomenclature from NASPE. *Circulation* 1999; **100**: e31–e37.

3 Sanchez-Quintana, Cabrera JA, Climent V, et al. How close are the phrenic nerves to cardiac structures? Implications for cardiac interventionalists. *J Cardiovasc Electrophysiol* 2005; **16**: 309–13.

4 Durante-Mangoni E, Vecchio DD, Ruggiero G. Right diaphragm paralysis following cardiac radiofrequency catheter ablation for inappropriate sinus tachycardia. *Pacing Clin Electrophysiol* 2003; **26**: 783–4.

5 Lee BK, Choi KJ, Kim J, Rhee KS, Nam GB, Kim YH. Right phrenic nerve injury following electrical disconnection of the right superior pulmonary vein. *Pacing Clin Electrophysiol* 2004; **27**: 1444–46.

6 Chaffanjon P, Brichon PY, Faure C, et al. Pericardial reflection around the venous aspect of the heart. *Surg Radiol Anat* 1977; **19**: 17–21.

7 d'Avila A, Scanavacca M, Sosa E, et al. Pericardial anatomy for the interventional electrophysiologist. *J Cardiovasc Electrophysiol* 2003; **14**: 422–30.

8 Ho SY, McCarthy KP, Josen M, Rigby ML. Anatomic-echocardiographic correlates: an introduction to normal and congenitally malformed hearts. *Heart*. 2001; **86**: II3–II11.

9 Wu TJ, Yashima M, Xie F, et al. Role of pectinate muscle bundles in the generation and maintenance of intra-atrial reentry: potential implications for the mechanism of conversion between atrial fibrillation and atrial flutter. *Cir Res* 1998; **83**; 448–62.

10 Sanchez-Quintana D, Anderson RH, Cabrera JA, et al. The terminal crest: morphological features relevant to electrophysiology. *Heart* 2002; **88**: 406–11.

11 Kalman JM, Olgin JE, Karch MR, Hamdan M, Lee RJ, Lesh MD. "Cristal tachycardias": Origin of right atrial tachycardias from the crista terminalis identified by intracardiac echocardiography. *J Am Coll Cardiol* 1998; **31**: 451–59.

12 Cabrera JA, Sanchez-Quintana D, Ho SY, et al. Angiographic anatomy of the inferior right atrial isthmus in patients with and without history of common atrial flutter. *Circulation* 1999; **99**: 3017–23.

13 Cabrera JA, Sanchez-Quintana D, Farre J, et al. The inferior right atrial isthmus: Further architectural insights for current and coming ablation technologies. *J Cardiovasc Electrophysiol* 2005; **16**: 402–8.

14 Sanchez-Quintana D, Ho SY, Cabrera JA, et al. Topographic anatomy of the inferior pyramidal space: relevance to radiofrequency ablation. *J Cardiovasc Electrophysiol* 2001; **12**: 210–17.

15 Inoue S, Becker AE. Posterior extensions of the human compact atrioventricular node: a neglected anatomic feature of potential clinical significance. *Circulation* 1998; **87**: 188–93.

16 Ueng KC, Chen SA, Chiang CE, et al. Dimensions and related anatomical distance of Koch's triangle in patients with atrioventricular nodal reentrant tachycardia.*J Cardiovasc Electrophysiol* 1996; **7**: 1017–23.

17 Inoue S, Becker AE. Koch's triangle sized up: anatomical landmarks in perspective of catheter ablation procedures. *PACE* 1998; **21**: 1553–58.

18 Ho SY, McCarthy KP, Ansari A, et al. Anatomy of the atrioventricular node and atrioventricular conduction system. *J Bifurcation & Chaos* 2003; **12**: 3665–74.

19 Lee RJ, Kalman JM, Fitzpatrick AP, et al. Radiofrequency catheter modification of the sinus node for "inappropriate" sinus tachycardia. *Circulation* 1995; **92**: 2919–28.

20 Sanchez-Quintana D, Cabrera C, Farre J, et al. Sinus node revisited in the era of electroanatomical mapping and catheter ablation. *Heart* 2005; **91**: 189–94.

21 Anderson K R, Ho S Y, Anderson R H. The location and vascular supply of the sinus node in the human heart. *Br Heart J* 1979; **41**: 28–32.

22 Anderson RH, Ho SY, Smith A, Becker AE. The internodal atrial myocardium. *Anat Rec* 1981; **201**: 75–82.

23 Ho SY, Sanchez-Quintana D, Cabrera JA, et al. Anatomy of the left atrium: implications for radiofrequency ablation of atrial fibrillation. *J Cardiovasc Electrophysiol* 1999; **10**: 1525–33.

24 Ho SY, Anderson RH, Sanchez-Quintana D. Atrial structure and fibres: morphologic bases of atrial conduction. *Cardiovasc Res* 2002; **54**: 325–36

25 Cabrera JA, Farré J, Ho SY, Sánchez-Quintana D. Anatomy of the left atrium relevant to atrial fibrillation ablation. In: *Catheter Ablation of Atrial Fibrillation.* E Aliot, M Haissaguerre, W Jackman (eds.). London, Blackwell Futura, 2008: 3–31.

26 Kistler PM, Ho SY, Rajappan K, Morpher M, et al. Electrophysiologic and anatomic characterisation of sites resistant to electrical isolation during circumferential pulmonary vein ablation for atrial fibrillation: a prospective study. *J Cardiovasc Electrophysiol* 2007; **18**: 1282–87.

27 Wittkampf FH, Vonken EJ, Derksen R, et al. Pulmonary vein ostium geometry: analysis by magnetic resonance angiography. *Circulation* 2003; **107**: 21–23.

28 Kato R, Lickfett L, Meininger G, et al. Pulmonary vein anatomy in patients undergoing catheter ablation of atrial fibrillation: lessons learned by use of magnetic resonante imaging. *Circulation* 2003; **107**: 2004–10.

29 Tsao HM, Yu WC, Cheng HC, et al. Pulmonary vein dilation in patients with atrial fibrillation: detection by magnetic resonance imaging. *J Cardiovasc Electrophysiol* 2001; **12**: 809-13

30 Mansour M, Refaat M, Heist EK, et al. Three-dimensional anatomy of the left atrium by magnetic resonance angiography: implications for catheter ablation for atrial fibrillation. *J Cardiovasc Electrophysiol.* 2006; **17**: 719–23.

31 Saito T, Waki K, Becker AE. Left atrial myocardial extension onto pulmonary veins in humans: anatomic observations relevant for atrial arrhythmias. *J Cardiovasc Electrophysiol* 2000; **11**: 888–94.

32 Ho SY, Cabrera JA, Tran VH, et al. Architecture of the pulmonary veins: relevance to radiofrequency ablation. *Heart* 2001; **86**: 265–70.

33 Tagawa M, Higuchi K, Chinushi M, et al. Myocardium extending from the left atrium onto the pulmonary veins: a comparison between subjects with and without atrial fibrillation. *Pacing Clin Electrophysiol* 2001; **24**: 1459–63.

34 Ouyang F, Fotuhi P, Ho SY, et al. Repetitive monomorphic ventricular tachycardia originating from the aortic sinus cusp: electrocardiographic characterization for guiding catheter ablation. *J Am Coll Cardiol* 2002; **39**: 500–8.

35 Vaseghi M, Cesario DA, Mahajan A, et al. Catheter ablation of right ventricular outflow tract tachycardia: value of defining coronary anatomy. *J Cardiovasc Electrophysiol.* 2006; **17**: 632–37.

36 Ho SY. Letter to editor re Catheter ablation of right ventricular outflow tract. *J Cardiovasc Electrophysiol* 2006; **17**: E7.

37 Scheinman MM, Wang YS, Van Hare GF, Lesh MD. Electrocardiographic and electrophysiologic characteristics of anterior, midseptal and right anterior free wall accessory pathways. *J Am Coll Cardiol.* 1992; **20**: 1220–29.

38 Shimoike E, Ohnishi Y, Ueda N, et al. Radiofrequency catheter ablation of left ventricular outflow tract tachycardia from the coronary cusp: a new approach to the tachycardia focus. *J Cardiovasc Electrophysiol.* 1999; **10**: 1005–9.

39 Hachiya H, Aonuma K, Yamauchi Y, et al. How to diagnose, locate, and ablate coronary cusp ventricular tachycardia. *J Cardiovasc Electrophysiol.* 2002; **13**: 551–6.

40 Tops LF, Van de Veire NR, Schuijf JD, et al.. Noninvasive evaluation of coronary sinus anatomy and its relation to the mitral valve annulus: implications for percutaneous mitral annuloplasty. *Circulation.* 2007; **115**: 1426–32.

4

CHAPTER 4

Principles of Noncontact Endocardial Cardiac Mapping

Kim Rajappan, MD, MRCP, *& Richard J. Schilling,* MD, FRCP

St Bartholomew's Hospital and Queen Mary College, London, UK

Summary

Identification and treatment of hemodynamically unstable or nonsustained arrhythmias remains a challenge to electrophysiologists. Noncontact mapping has been used and validated in a number of such settings, including hemodynamically unstable or nonsustained ventricular tachycardia (VT), atypical atrial flutters, and other nonsustained atrial arrhythmias. Although electrogram reconstruction with noncontact mapping is accurate, this accuracy decreases as the distance between the multielectrode array and the endocardium increases (becoming significant when this distance is greater than 34 mm). Despite this limitation, success has been demonstrated not only in identification of the mechanism of these arrhythmias, but also in ablation of their critical components. Thus, noncontact mapping is a useful tool in the management of a significant number of patients.

Introduction

Accurate mapping is the cornerstone to successful ablative therapy of cardiac arrhythmias because it provides insight into the arrhythmia mechanism and identifies the location of a suitable target for ablation. Reentry is the mechanism responsible for the majority of sustained arrhythmias in humans [1–9]. Ablation of these arrhythmias is critically dependent on locating the narrowest part of the reentry circuit, which is usually the diastolic pathway [10, 11].

Using conventional mapping techniques, it has been possible to treat a wide range of arrhythmias with high success and low complication rates. There remain some arrhythmias that are difficult to treat with catheter ablation because of a number of factors that include the small lesion sizes produced by radiofrequency energy and difficulties with precise localization of the arrhythmia substrate. For this reason, developments in mapping techniques are fundamental to the success of catheter ablation of complex cardiac arrhythmias such as ventricular tachycardia (VT) in structural heart disease, as well as complex atrial arrhythmias.

Systems for 3D electroanatomical reconstruction of sequentially acquired contact catheter data are limited by the time available to acquire data points, and they are less useful in cases of nonsustained or hemodynamically unstable arrhythmias. Noncontact mapping techniques now allow collection of data *simultaneously* from the entire cardiac chamber. High-resolution maps can be produced, on

Cardiac Mapping, Third Edition Edited by Mohammad Shenasa, Gerhard Hindricks, Martin Borggrefe, and Günter Breithardt
 ISBN: 978-1-405-17572-2

which the position of mapping catheters can be shown, and the catheters can be guided to sites of interest. This facilitates mapping of nonsustained and hemodynamically unstable arrhythmias such as VT.

Background Theory

Body Surface Mapping

Body surface mapping is a method for improving the resolution and sensitivity of recordings of surface electrograms. It involves the recording of two or more electrograms from the subject's body surface and using these data to interpret the underlying cardiac activation patterns. The data acquired from each electrode is related to the distance of a point from the electrode and the nature of the tissue interposed between the two [12]. If this geometry and the nature of the thoracic tissues are known, it is theoretically possible to determine myocardial potentials from the body surface potentials. In electrocardiography this process is known as solution of the inverse problem.

The clinical application of body surface mapping has been limited by the resolution of the data provided. Solutions developed mathematically describing the "forward" relationship between a defined experimental model of cardiac activation and the resulting body surface potentials were constructed so that they produced body surface maps similar to those seen in clinical practice [13–16]. The resulting solutions, however, were not unique. A variety of electrical generators (i.e., myocardial potential fields) could have produced identical body surface maps.

Using animal hearts suspended in electrolytic tanks the complex potential field generated by the heart is equivalent to that in vivo, and the geometry between the heart and the body surface (i.e., the surface of the electrolytic tank) can be measured accurately [17]. However this model does not account for the nature of structures between the cardiac surface and the body surface such as lung or bone, and correction for this is highly complex and thus increases the time taken to construct body surface maps.

Endocardial Noncontact Mapping

An alternative "noncontact" concept was introduced by Taccardi [18] in which intracavitary potentials were measured from electrodes on an "olive"-shaped probe introduced through the LV apex of animal hearts. Taccardi noted that the pattern of endocardial activation was not precisely reflected in the raw cavity potentials recorded by the probe, which exhibit spatially averaged, lower-amplitude distributions.

This phenomenon closely resembled the noncontact recordings made during body surface maps. It was therefore a logical progression to conceive a mathematical inverse-solution to these noncontact endocardial potentials in a manner similar to that applied to body surface maps. This approach has several advantages over inverse solution of body surface potentials. Firstly, the noncontact probe is in closer proximity to the source than is achieved by body surface electrodes, thus reducing distance-related blurring of the endocardial potentials. Secondly, the space between the intracavitary probe and the endocardium is filled with a medium that may be treated as uniform and electrically inert (e.g. blood). This also means that development and validation of solutions to the inverse problem is easier because in vitro studies may be performed in a tank without having to account for the complexities of extracardiac thoracic tissues. Furthermore, validation of such techniques is feasible both in vitro and in vivo because it is possible to percutaneously access the endocardium in order to make recordings of contact endocardial electrograms with which to compare the reconstructed electrograms.

Noncontact Mapping System

The noncontact mapping system used clinically (EnSite Array, St. Jude Medical, St. Paul, MN) consists of a catheter-mounted multielectrode array (MEA), a custom-built amplifier system, and a workstation to run specially designed system software. The MEA (a woven braid of 64 0.003-in.-diam wires) is mounted on a 7.6-mL balloon on a 9F catheter (Figure 4.1).

Each wire has a 0.025-in. break in insulation, producing a noncontact unipolar electrode. The raw far-field electrographic data from the MEA are acquired and fed into a multichannel recorder and amplifier system, sampled at 1.2 kHz, and filtered with a bandwidth of 0.1–300 Hz. The amplifier also has 16 channels for contact catheters and

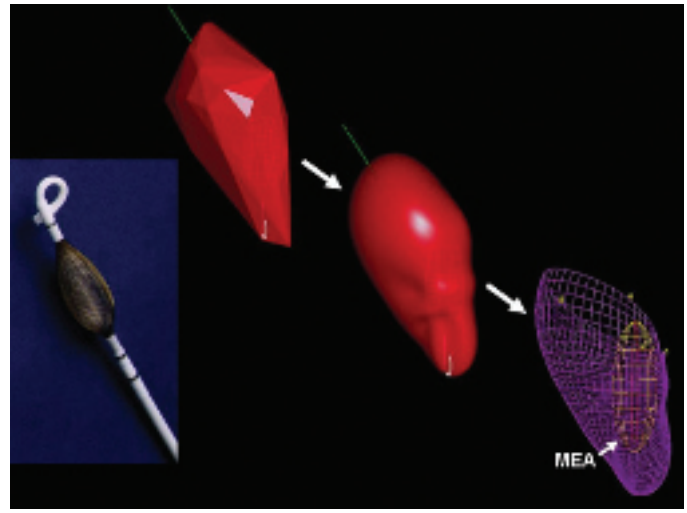

Figure 4.1 The noncontact mapping catheter is shown with its braided microelectrode array and 7.5-ml balloon deployed on the left of the panel. Generation of a virtual endocardium is also shown. The virtual endocardium is created by tracing the endocardial surface with a conventional catheter while the system tracks its position. The geometry has been partially defined at the top left; then completed and smoothed in the middle; and finally converted into an anatomically contoured, wire-frame 3D model at the bottom right. The multielectrode array is displayed by the system as a yellow wire-frame ellipsoid (MEA) in relation to the geometry created.

12 channels for the surface ECG. A ring electrode located on the proximal shaft of the MEA catheter in the descending aorta is used as a reference for both noncontact and contact unipolar electrogram recordings. The electrical activity detected by the MEA is generated primarily by the electrograms on the endocardial surface and is of lower amplitude and frequency than the source on the endocardium.

A technique to enhance and resolve these far-field potentials has been devised based on an inverse solution to Laplace's equation by use of a boundary element method. The potential field at any one electrode is influenced to a degree by the potentials from the entire endocardium, the degree of influence being inversely proportional to the distance between the electrode and each endocardial point. This finding makes it is possible to reconstruct >3300 unipolar endocardial electrograms simultaneously. The system is also able to locate any conventional catheter in space with respect to the MEA by passing a 5.68-kHz, low-current "locator" signal between the catheter being located and alternately between ring electrodes proximal and distal to the MEA on the noncontact catheter.

The MEA detects and determines the locator signal angles and thus positions the source. This locator signal serves two purposes. Firstly, it is used to provide measured samples for the geometry matrix of the inverse solution by constructing a 3D computer model of the endocardium (a so-called "virtual endocardium") which is required for the reconstruction of endocardial electrograms and isopotential maps (Figure 4.1). This model is acquired by moving a conventional catheter around the cardiac chamber, building up a series of coordinates for the endocardium, and generating a patient-specific, anatomically contoured model of its geometry.

To accomplish this, the system automatically stores only the most extreme points visited by the roving catheter in order to ignore those detected when the catheter is not in contact with the endocardial wall. The total time required to define the contoured geometry is typically between 5 and 10 min. Secondly, the locator signal can then be used to display and log the position of any catheter on the endocardial model. During catheter ablation procedures, the locator system is used to guide the catheter to sites of interest identified from the isopotential color maps and to log the position of radiofrequency energy applications on the virtual endocardium. Because the geometry of the cardiac chamber is taken with reference to the MEA, and is used to produce the inverse solution, it is critical that once geometry is established the MEA should not move. If the MEA is moved, then cardiac geometry has to be re-established.

The stiffness of the MEA catheter shaft and weight of the balloon means that after it has been sited, its position usually remains stable unless sited in a

very dynamic chamber such as the apex of a normal ventricle. Validation of the MEA in the human LV was first performed in patients in sinus rhythm [19]. This demonstrated that the system can accurately reconstruct electrograms at distances of at least 50 mm from the center of the MEA, but accuracy decreases with distance, and significantly so >34 mm from the MEA center. There was no significant difference in timing of maximum $-dV/dt$ between contact catheter and reconstructed electrograms 34 mm from the MEA center, but the timing of reconstructed electrogram maximum $-dV/dt$ becomes earlier than that of contact electrograms >34 mm from the MEA center.

Clinical Use

Ventricular Arrhythmias: Ischemic or Scar Related

Patients are studied in the postabsorptive state under local anaesthesia. A standard quadripolar catheter at the right ventricular apex is used for programmed stimulation. For mapping the LV, two mapping and ablation catheters (trans-septal and retrograde approach) may be used. This has the advantage of allowing access to areas of the endocardium that may be restricted by the MEA from either approach. In general, the LV septum may be reached more easily from the trans-aortic approach, while the trans-septal route provides better access to the lateral wall.

Continuous systemic (and sometimes pulmonary artery) pressures are monitored throughout the study. Before deployment of the MEA, patients are given 10,000 IU heparin with later boluses to maintain activated clotting time at 300–400 sec. The MEA catheter is deployed via the retrograde transaortic route over a 0.032-in. J-tipped guidewire advanced to the LV apex (Figure 4.2). With the pigtail of the MEA in the LV apex, the guidewire is withdrawn and the balloon is inflated.

It is important to carefully position the MEA in dilated LVs, because an eccentric position may result in poor reconstruction of electrograms on cardiac walls >34 mm from the MEA center [19]. With the aid of the locator signal the mapping/ablation catheter is dragged around the endocardial surface to collect a large series of points and construct a geometric model representative of the LV. Trabeculations may limit catheter manipulation, and it can be helpful to use a catheter inversion technique to access some parts of the LV to complete the reconstruction (Figure 4.2).

The electrograms derived from the reconstruction process are then superimposed onto the endocardial model to produce dynamic high-resolution

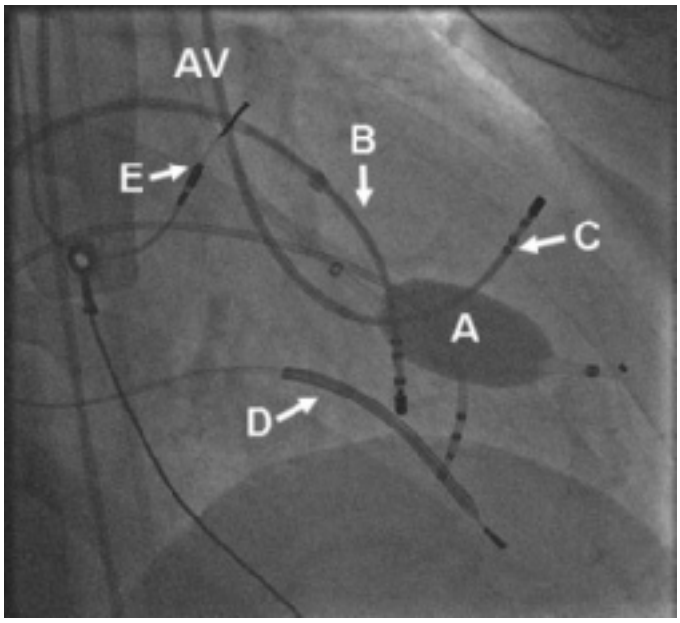

Figure 4.2 Fluoroscopic image demonstrating the noncontact multielectrode array filled with contrast medium/saline (A). This has been deployed in a retrograde fashion across the aortic valve (AV) in the left ventricle. A trans-septal mapping catheter (B) and a retrograde transaortic mapping catheter (C) are also shown. Note that this patient also has a dual chamber implantable cardioverter defibrillator with a lead (D) in the right ventricle and (E) in the right atrial appendage. The mapping catheter (in this case the transaortic mapping catheter) can be inverted to reach the basal parts of the left ventricle.

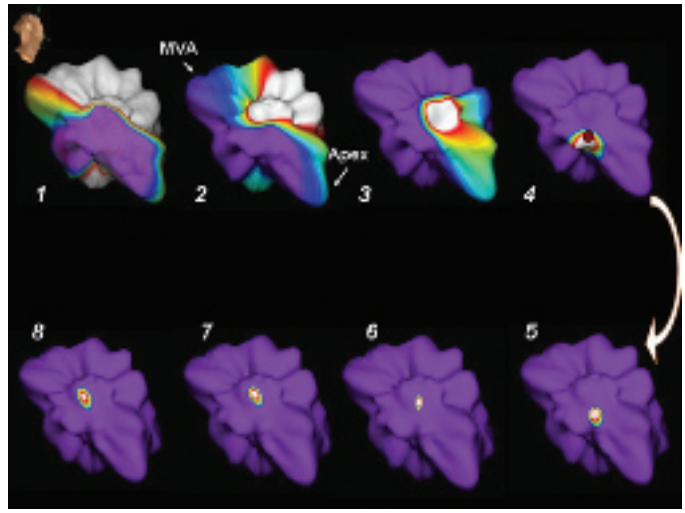

Figure 4.3 Isopotential maps recorded during mapping of a ventricular tachycardia (VT) circuit. The virtual endocardium may be rotated and the orientation in 3D space is depicted by the torso in the top left corner of the image. In this case the ventricle is orientated in a steep RAO view. The sequence of panels is shown as isopotential maps for a VT with cycle length 380 msec, in reverse order, as one would do if mapping this VT. Therefore, panel 1 shows the end of the systole and panel 8 the beginning of diatole. In panel 1 the virtual endocardium is translucent and the multielectrode array position can be seen. The translucency has been removed in the rest of the panels. Systolic activation is shown during VT in panels 1 and 2. The VT is then mapped backwards in time. Panels 3 and 4 show the probable exit site of the VT. Panels 4–8 show slow conduction (inferred from the small distance covered by the activation on the isopotential maps during a time period of 150 msec). This presumably represents part of the diastolic pathway for the VT circuit. Ablation at the exit site (marked by a red dot on panel 4) terminated VT and rendered it noninducible. KEY: MVA = mitral valve annulus.

isopotential maps (Figure 4.3). Isopotential maps are color-coded to represent changes in potential difference on the endocardium. Maximum $-dV/dt$ with endocardial activation is seen as a spectral change from resting purple to white color on the isopotential map.

After the basic geometry has been configured, VT is induced and mapping is undertaken as follows:

(i) Identification of diastolic pathways (Figure 4.3) is started by identification of the VT exit site which is defined as a rapidly spreading focus of activity coincident with onset of the QRS complex on the surface ECG, leading to systolic activation of the ventricle. Diastolic activity during VT is then defined as activity progressing in a continuous fashion to the VT exit site. In practice the exit site can be seen as a white spot of activation when an isopotential map is displayed at the onset of surface ECG QRS complex. Diastolic activity is then identified by moving the isopotential map display back in time. When a discrete spot of diastolic activity can no longer be seen on the map, then the limit of the diastolic pathway identified by the system has been reached and all diastolic activity identified before this is ignored.

(ii) Ablation catheters are navigated to the targets of interest identified by noncontact mapping.

(iii) Complimentary conventional mapping techniques are then used to assess and reconfirm target sites before ablation.

(iv) Ablation is performed during VT if possible. If VT is terminated then attempts are made to re-induce tachycardia. The clinical endpoint used to determine success of ablation is defined as rendering inducible VT noninducible.

Results with noncontact mapping techniques in patients with postmyocardial infarction VT have been reported by a number of groups. Initial experience in noncontact mapping and guiding ablation of sustained monomorphic VT was described in 24 patients [20], most of whom had poor LV function (mean ejection fraction 39%). Twenty-one of these patients had structural heart disease, of whom 19 had infarct-related VT.

In this study, repeat cross-correlation during VT between reconstructed and contact electrograms recorded from the same endocardial location, confirmed that almost all comparisons gave a correlation coefficient of greater than 0.8. Most patients had multiple VT morphologies with a total of 81 different VTs mapped, of which 24 were identified as clinical morphologies. A further 15 VTs were recorded prior to deployment of the MEA. Based on noncontact data, 80 (99%) exit sites were mapped and diastolic activity continuous to the point of endocardial breakout was identified in 54 (67%) VTs. Complete VT circuits were mapped in 17 (22%) VT morphologies, and partial diastolic pathways were seen in 37 VTs that constituted 36% ± 30% of the diastolic pathway.

Using a total of 154 radiofrequency energy applications (mean of four per VT), 38 target VTs were successfully ablated, 15 of which were clinical. Four VTs that shared complete diastolic pathways in contrarotation were ablated with only two radiofrequency energy applications. The importance of identifying diastolic activity for ablation is reflected in the highest success rate (80%) achieved at target sites where at least part of the diastolic activity was identified. This compares favorably to the poor results that were achieved at exit sites (21%) and regions remote from the diastolic pathway (9%).

Long-term follow-up has since been reported in 40 patients, all with infarct-related VT refractory to drug therapy [21]. The mean ejection fraction was 36%. Twelve patients had anterior infarction, eight inferior, three posterior, one lateral, and sixteen had multiple sites of infarction.

Patients took a variety of drugs including amiodarone, beta-blockers, mexiletine, and flecainide. Thirteen patients had ICDs (32.5%) in situ. Ablation was performed in 12 of these patients to reduce unacceptable frequency of device therapy and in one to enable discontinuation of amiodarone therapy. One-hundred and forty morphologies of VT were mapped (CL 400.75 ± 89.8 msec, mean 3.5 VTs per patient, range 0–13). Thirty-six of the mapped tachycardias (25.7%) were clinical VT morphologies (CL 415.4 ± 93.0 msec). One-hundred and four morphologies were either previously not documented or only induced at previous EP studies.

Noncontact mapping identified endocardial activation that preceded or was synchronous with QRS onset in all patients. Endocardial diastolic activation was seen in 55% of VT morphologies, with a complete reentrant circuit identified in 17% of cases. Diastolic activity could not be identified in 45% of tachycardias. An acute success rate of 82.7% was achieved, which is comparable to results of previous series using this technology [22], with studies of substrate mapping to guide linear ablation lines at infarct border zones [23–26] and with series using conventional mapping techniques alone [27–31].

The overall success rate might have been higher if irrigated-tip ablation catheters had been used routinely. Ablation was successfully completed in 33 patients. No patient suffered a cardiac complication as a result of MEA deployment. A total of 26 patients subsequently had ICDs in situ, with therapy histories available in 24 patients. Recurrence of an ablated VT occurred within the first week in four patients, of whom two required intracoronary ethanol injection at repeat procedures. Importantly, only 7.5% of patients following successful ablation had a documented recurrence of an *ablated* VT over a total mean 3-yr follow- up.

Despite the initial and long-term success rates for ablated VTs, however, both new nontargeted VTs and VF were seen in 45% of patients during follow-up. The estimated survival probabilities for all patients at 1, 2, 3, and 5 years were 0.85, 0.82, 0.72, and 0.60, respectively. Inducibility of VT immediately following the procedure did not predict probability of survival. The group with ICD histories prior to and following ablation provide a unique and more complete account of ablation success with this technique. Although ICD therapies were reduced in all patients, only 64% of patients in this group were completely free of device therapies after an average of 2 years; 27% received shocks, although only one patient had a recurrence of an ablated VT.

Similarly, despite a complete absence of recurrence of an ablated VT, 77% of patients who underwent ICD placement after ablation received therapies, including 62% who received shocks. New VTs seen after ablation may reflect the evolving nature of the underlying substrate in patients with ischemic heart disease and settles the question of whether all patients with infarct-related VT should be considered for an ICD prognostically as a matter of safety, irrespective of VT inducibility, because of the

long-term risk of developing malignant ventricular arrhythmias.

Ventricular Arrhythmias: Nonischemic

The use of noncontact mapping for ventricular arrhythmias is not limited solely to postinfarct VT. Several reports have been published on the use of the MEA in patients with right ventricular outflow tract (RVOT) ectopy and tachyarrhythmia [32] including children [33].

Ablation of the arrhythmia, which usually arises from abnormally triggered activity in the RVOT with characteristic left bundle inferior axis VT and a structurally normal heart, can be problematic. Although RF ablation can eliminate tachycardia in 83–100% of patients with frequent ectopy or VT [34], the absence of VT or clinical ectopy despite adrenergic and electrical stimulation in the electrophysiology laboratory limits localization of the arrhythmogenic substrate.

The noncontact mapping system permits generation of a potential map from a single premature ventricular complex, which can be valuable in patients with infrequent VT. In these cases the MEA is advanced through the vasculature in low profile to the RVOT over a 0.035-in. guidewire. A standard deflectable ablation catheter may be placed in the pulmonary artery and slowly withdrawn until sharp bipolar electrograms are recorded on the distal electrodes, signifying the pulmonary valve–RVOT junction. Using this position as a fluoroscopic landmark, the MEA is then deployed at least 1 cm below the valve (Figure 4.4). A geometry of the RV can then be created by sweeping a mapping catheter along the RV endocardium. Upon geometry completion, isopotential maps are generated and virtual electrograms are reconstructed to identify the earliest site of activation when the morphology of the recorded complexes matches the clinical arrhythmia.

After the earliest activation has been identified, the site may be ablated either during tachycardia or during normal sinus rhythm when nonsustained (Figure 4.4; Videoclip 3). In one series [32] noncontact mapping was used in a particularly difficult group of ten patients with RVOT VT. Of these, 70% had failed previous ablation, 30% had received ICD

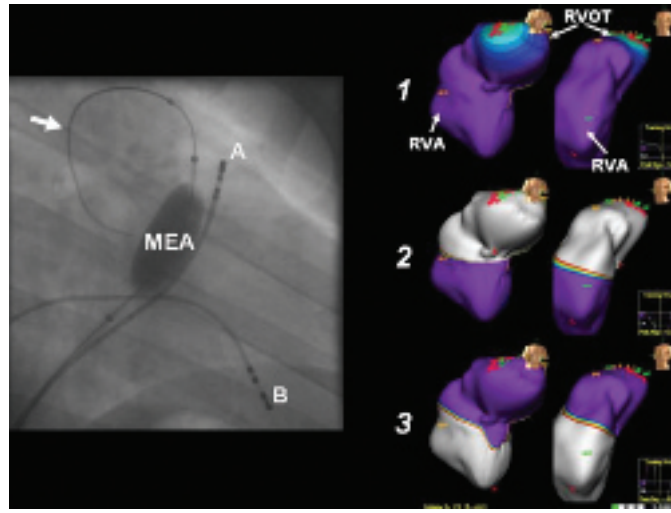

Figure 4.4 The fluoroscopic image on the left shows the noncontact multielectrode array (MEA) deployed in the right ventricular outflow tract (RVOT). The guidewire (arrow) is extended out of the MEA catheter and into the pulmonary artery to give stability. A mapping catheter (A) in the RVOT, and a diagnostic catheter (B) in the right ventricular apex (RVA) are also shown. Panels 1–3 on the right show the activation maps during a single beat of RVOT tachycardia, in two different views (torso denotes orientation). Panel 1 shows activation as a colored patch originating from the RVOT, and spreading to the rest of the right ventricle in panels 2 and 3. These maps could also have been generated from a single ventricular ectopic with a morphology matching that of the clinical tachycardia, and then used to guide ablation. In this particular case a cluster of ablation lesions in the RVOT (shown as red markers) rendered the arrhythmia noninducible with disappearance of any RVOT ectopy.

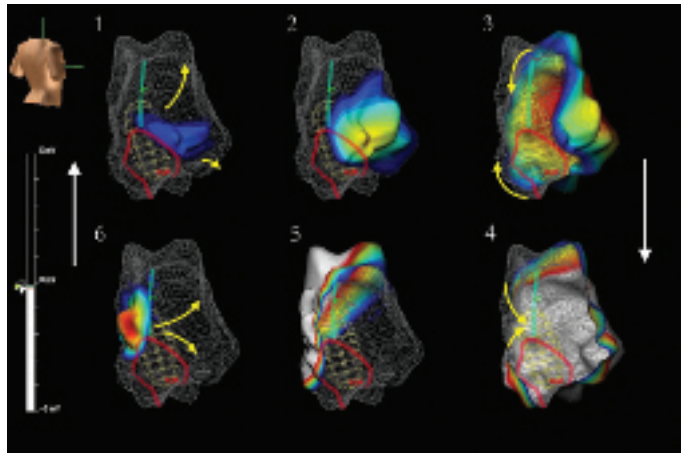

Figure 4.5 Isopotential maps depicting a macro-reentrant right atrial tachycardia following atriopulmonary Fontan. The right atrium (RA) is seen from the right posterior oblique view (torso denotes orientation). At the inferior aspect of the posterolateral wall an area of dense scar defined by simultaneous contact mapping (CARTO, Biosense Webster, Diamond Bar, CA) has been annotated to the noncontact reconstruction (red diamond outline). The possible position of the crista terminalis (CT) running from the scar to the superior aspect of the posterolateral wall has similarly been annotated (green line). During sinus rhythm activation was seen to proceed across the crista terminalis from the upper lateral to posterior wall. Amplitude of the local noncontact electrograms (EGM) are denoted by colors (see color bar on left of image); white denotes areas with lowest amplitude; clear areas are nondepolarized tissue and the spectrum of colors indicate EGM in between. During tachycardia conduction block as defined by double potentials separated by >50 msec were noted along the length of the CT. Activation is seen to break out from a gap in the line of block between the inferior scar (fixed block) and superior CT (functional block) and progress onto the lateral atrial wall (panels 1–2). The wave front rotates around the RA in an equatorial fashion (panels 3–5), ultimately returning to the crista gap which allows the circuit to perpetuate (panel 6). (Image kindly provided by Dominic J. Abrams.)

therapy before referral, and 50% had no sustained VT to guide mapping. Despite this, noncontact-guided ablation was acutely successful in 90% of this population, with no recurrence in 78% of acutely successful patients during a mean follow-up of 11 months.

Other nonischemic ventricular arrhythmias where the MEA has been used successfully include patients with arrhythmogenic right ventricular cardiomyopathy, idiopathic dilated cardiomyopathy [35], and idiopathic ventricular fibrillation [36].

Atrial Arrhythmias

The noncontact mapping system may be used to map any form of atrial arrhythmia, although its use is particularly suited to those forms that are nonsustained. When used in the right atrium the MEA is deployed over a 0.035-in. guidewire, which is usually advanced to the superior vena cava with the wire left in situ to support the balloon, and the rest of its use is similar to that in the ventricle with generation of a virtual endocardium onto which the isopotential maps are superimposed (Figure 4.5; Videoclip 4 ).

Patients are anticoagulated with 10,000 IU heparin and later boluses to maintain activated clotting time at 300–400 sec. The use of noncontact mapping in identification and treatment of focal atrial tachycardias (ATs) has been validated [37]. In 13 patients with 14 focal ATs, the noncontact mapping system was used to map and guide ablation of AT. AT origins were in the crista terminalis ($n = 8$), right atrial (RA) free wall ($n = 3$), Koch triangle ($n = 1$), anterior portion of RA–inferior vena cava junction ($n = 1$), and superior portion of tricuspid annulus ($n = 1$). Breakout sites were in the crista terminalis ($n = 5$), RA free wall ($n = 5$), middle cavotricuspid isthmus ($n = 2$), and RA–superior vena cava junction ($n = 2$). After applications of RF energy on the earliest activation site or the proximal portion of preferential conduction from the AT origin, 13 ATs were eliminated without complication. During a

follow-up period of 8 ± 5 months), 11 (91.7%) of the 12 patients with successful ablation were free of focal ATs.

Radiofrequency ablation of the cavotricuspid isthmus (CTI) is highly effective in eliminating typical right atrial (RA) flutter, but in contrast, the mechanisms of nonincisional atypical RA flutters is limited. Noncontact mapping has been used to demonstrate that atypical RA flutters can arise from single-loop or double-loop figure-of-eight reentry. During single-loop reentry, the activation wave front circulates around a central obstacle composed of a functional block area and the RA appendage. During figure-of-eight reentry, simultaneous upper and lower loop reentry through a crista terminalis gap, or simultaneous upper loop and free-wall reentry through the common channel between the crista terminalis and a central obstacle was found. Radiofrequency ablation of the free-wall channel and/or the crista terminalis gap is effective in eliminating these atrial flutters [38].

Use is not limited to the RA with respect to atrial arrhythmias. Left atrial tachycardias may also be successfully mapped and ablated using the MEA via a trans-septal route [39]. Use in patients with atrial fibrillation may be limited by proximity of the MEA to all of the left atrium [40], but arrhythmogenic pulmonary veins can still be identified successfully [41] and as a research tool the noncontact system may help to elucidate mechanisms of atrial fibrillation initiation and maintenance [42].

Arrhythmias in Patients with Congenital Heart Disease

The properties of noncontact mapping described may make it attractive for use in patients with congenital heart disease who often have complex arrhythmia substrates and multiple nonsustained arrhythmias. In one early series it was possible to identify and successfully ablate both macro reentrant and micro reentrant arrhythmias in patients after surgical correction of congenital heart disease in over 90% of cases [43]. Also, although it has been possible to demonstrate success in certain congenital heart disease patients, such as those after the Fontan procedure [44], limitations in this group of patients have recently been demonstrated, due to the size of the chambers being studied and hence inaccuracy at the limits of the MEA capabilities [45].

Potential Nonarrhythmic Applications of Noncontact Mapping

Cardiac resynchronization therapy (CRT) can help to improve left ventricular function in patients with heart failure, but only if those regions of myocardium that are mostly compromised by electromechanical desynchronization can be identified and effectively stimulated. Failure of CRT to produce clinical benefits may reflect left ventricular lead placement in regions of slow conduction that can be overcome by pacing in more normally activating regions. Noncontact mapping can be used to identify regions of slow conduction and hence guide the site of left ventricular pacing [46].

Similarly, for heart failure patients with right bundle branch block (RBBB), noncontact mapping has demonstrated significant LV activation delay in addition to that of the right ventricle, forming the electrophysiologic basis for recommending CRT in heart failure patients with RBBB [47]. It is even possible to use noncontact mapping in complex congenital heart disease patients to help define sites of late activation [48], although all of these applications require proper prospective evaluation.

Special Features and Limitations of Noncontact Mapping

Dynamic Substrate Mapping

It may be possible to address some of the limitations of mapping VT itself by using dynamic substrate mapping [49]. This technique allows identification of low voltage areas that may be the substrate for the arrhythmia and can be performed in sinus rhythm. As with isopotential mapping, the array may be used to acquire surface voltage characteristics during a single cardiac cycle. It is then possible to identify potential voltage barriers, such as scar tissue, and the threshold for low-voltage detection may be manually adjusted. The same limitations as for isopotential mapping are seen with this technique, that is, reduced accuracy with increasing distance from the MEA and alterations of the voltage map according to the filter settings. Ultimately, the technique has yet to be validated in ischemic VT, but may give additional guidance when diastolic potentials cannot be identified.

Difficulties in Demonstrating the Diastolic Pathway/Diastolic Potentials

Although the ability to map the entire tachycardia cycle length within a single cycle is clearly an inherent advantage when mapping unstable VT, it is not always possible to accurately demonstrate the diastolic pathway. Several factors contribute to this. Previous studies have demonstrated that although the exit point may be identified in almost all post-MI VT, and diastolic pathways may be identified in up to 80% of cases, an average of only 40% of the diastolic interval itself can be traced [20, 35, 50].

The entire reentry circuit can be mapped in up to 20% of post-MI VT using this technique [20]. It is possible that the reentry circuit is not entirely confined to the endocardial surface, with intramural or subepicardial areas of slow conduction. This has been previously demonstrated by surgical mapping [22]. Also, the volume of the tissue forming the diastolic component of the circuit may be insufficient to produce electrograms that can be identified by the noncontact mapping system. Identification is further hampered by saturation of the isopotential maps occurring with repolarization of the LV, as this may lead to similarities between the lower-frequency and amplitude diastolic potential electrograms detected by the system, and those of repolarization [51].

Filter Settings

Changing the filter settings used to display virtual electrograms can have a profound effect on the morphology of the electrogram (as it also can for contact electrograms). Although the focus shift with high-pass filter changes has little impact on the electrograms [52], when trying to identify and display the low-amplitude unipolar signals associated with diastolic potentials, adjustment of filtering may be necessary to differentiate true electrical activity from noise. Although definitions vary slightly, it is widely accepted that the maximum $-dV/dt$ defines local activation on a unipolar electrogram.

The effect on the inverse solution and noncontact reconstruction of electrograms appears to somewhat lower the frequency of low-amplitude potentials. It can therefore be difficult to distinguish the deflections of a unipolar virtual electrogram from baseline wander. Increasing the high-pass filter can help to distinguish such noise from true electrical activation on the ispotential maps, but it should be remembered that it may also filter out the virtual electrograms associated with true activation for this reason. A number of different filter settings may therefore need to be tried with the operator looking at the electrograms produced at the region of interest on the isopotential map, rather than relying on the isopotential map alone to guide ablation.

Conclusion

Noncontact mapping has been validated in a number of clinical settings including hemodynamically unstable or nonsustained ventricular tachycardia. The ventricular tachycardia and atrial flutter reentry circuits identified by the noncontact mapping system have also been validated by examining the outcome of application of RF energy on portions of the circuits critical to maintenance of the arrhythmias.

Electrogram reconstruction has been demonstrated to be accurate, but this accuracy decreases as the MEA–endocardial distance increases, and this becomes significant when this distance is greater than 34 mm. Noncontact mapping has also been able to provide new insights into the mechanisms of some arrhythmias, and may have potential for use in nonarrhythmic settings such as guiding cardiac resynchronization lead placement. Although there are limitations to the technique, noncontact mapping remains a useful tool in the management of a significant number of patients.

References

1 Allessie MA, Lammers WJEP, Smeets JRLM, Bonke FIM, Hollen J. Total mapping of atrial excitation during acetylcholine-induced atrial flutter and fibrillation in the isolated canine heart. In: Kulbertus HE, Olsson SB, Schlepper M, eds. *Atrial Fibrillation.* Lindgren and Soner, Mölndal, Sweden, 1982: 44–62.

2 Allessie MA, Lammers WJEP, Bonke FIM, Hollen J. Experimental evaluation of Moe's multiple wavelet hypothesis of atrial fibrillation. In: Zipes DP, Jalife J, eds. *Cardiac Arrhythmias.* Grune & Stratton, New York, 1985: 265–76.

3 Cauchemez B, Haissaguerre M, Fischer B, Thomas O, Clementy J, Coumel P. Electrophysiological effects of catheter ablation of inferior vena cava–tricuspid annulus isthmus in common atrial flutter. *Circulation* 1996; **93**: 284–94.

4 Cosio FG, Lopez-Gil M, Arribas F, Palacios J, Goicolea A, Nunez A. Mechanisms of entrainment of human common flutter studied with multiple endocardial recordings. *Circulation* 1994; **89**: 2117–25.
5 Josephson ME, Horowitz LN, Farshidi A, Kastor JA. Recurrent sustained ventricular tachycardia. I. Mechanisms. *Circulation* 1978; **57**: 431–39.
6 Karagueuzian HS, Fenoglio JJ, Weiss MB, Wit AL. Protracted ventricular tachycardia induced by premature stimulation in the canine heart after coronary artery occlusion and reperfusion. *Circ Res* 1979; **44**: 833–46.
7 de Bakker JMT, Coronel R, Tasseron S, et al. Ventricular tachycardia in the infarcted, Langendorf-perfused human heart: role of the arrangement of surviving cardiac fibres. *J Am Coll Cardiol* 1990; **15**: 1594–1607.
8 Wellens HJJ, Schuilenberg RM, Durrer D. Electrical stimulation of the heart in patients with ventricular tachycardia. *Circulation* 1972; **46**: 216–26.
9 Stevenson WG, Friedman PL, Kocovic D, Sager PT, Saxon LA Pavri B. Radiofrequency catheter ablation of ventricular tachycardia after myocardial infarction. *Circulation* 1998; **98**: 308–14.
10 Stevenson WG, Khan H, Sager P, et al. Identification of reentry circuit sites during catheter mapping and radiofrequency ablation of ventricular tachycardia late after myocardial infarction. *Circulation* 1993; **88**: 1647–70.
11 El-Sherif N, Mehra R, Gough WB, Zeiler RH. Reentrant ventricular arrhythmias in the late myocardial infarction period: interruption of reentrant circuits by cryothermal techniques. *Circulation* 1983; **68**: 644–56.
12 Gulrajani R, Roberge F, Savard P. The inverse problem of electrocardiography. In: Macfarlane P, Veitch Lawrie T, eds. *Comprehensive Electrocardiology.* Pergamon Press, New York, 1989: 237–88.
13 Frank E. Absolute quantitative comparison of instantaneous QRS equipotentials on a normal subject with dipole potentials on a homogenous torso model. *Circ Res* 1955; **3**: 243–51.
14 Savard P, Roberge FA, Perry JB, Nadeau RA. Representation of cardiac electrical activity by a moving dipole for normal and ectopic beats in the intact dog. *Circ Res* 1980; **46**: 415–25.
15 Ideker RE, Brody DA, Cox JW, Keller FW. Examination of a multiple dipole inverse cardiac generator based on accurately determined model data. *J Electrocardiol* 1973; **6**: 197–209.
16 Arthur RM, Geselowitz DB, Briller SA, Trost RF. Quadrupole components of the human surface electrocardiogram. *Am Heart J* 1972; **83,** 663–77.
17 Oster HS, Taccardi B, Lux RL Ershler PR, Rudy Y. Noninvasive electrocardiographic imaging: reconstruction of epicardial potentials, electrograms, and isochrones, and localization of single and multiple electrocardiac events. *Circulation* 1997; **96**: 1012–24.
18 Taccardi B, Arisi G, Macchi E, Baruffi S, Spaggiari S. A new intracavitary probe for detecting the site of origin of ectopic ventricular beats during one cardiac cycle. *Circulation* 1987; **75**: 272–81.
19 Schilling RJ, Peters NS, Davies DW. A noncontact catheter for simultaneous endocardial mapping in the human left ventricle: comparison of contact and reconstructed electrograms during sinus rhythm. *Circulation* 1998; **98**: 887–98.
20 Schilling RJ, Peters NS, Davies DW. Feasibility of a noncontact catheter for endocardial mapping of human ventricular tachycardia. *Circulation* 1999; **99**:2543–52.
21 Segal OR, Chow AW, Markides V, Schilling RJ, Peters NS, Davies DW. Long-term results after ablation of infarct-related ventricular tachycardia. *Heart Rhythm* 2005; **2**: 474–82.
22 Kaltenbrunner W, Cardinal R, Dubruc M, et al. Epicardial and endocardial mapping of ventricular tachycardia in patients with myocardial infarction: is the origin of the tachycardia always subendocardially localized? *Circulation* 1991; **84**: 1058–71.
23 Varanasi S, Dhala A, Blanck Z, Deshpande S, Akhtar M, Sra J. Electroanatomic mapping for radiofrequency ablation of cardiac arrhythmias. *J Cardiovasc Electrophysiol* 1999; **10**: 538–44.
24 Kautzner J, Cihak R, Peichl P, Vancura V, Bytesnik J. Catheter ablation of ventricular tachycardia following myocardial infarction using three-dimensional electroanatomical mapping. *Pacing Clin Electrophysiol* 2003; **26**: 342–47.
25 Reddy VY, Neuzil P, Taborsky M, Ruskin JN. Short-term results of substrate mapping and radiofrequency ablation of ischemic ventricular tachycardia using a saline-irrigated catheter. *J Am Coll Cardiol* 2003; **41**: 2228–36.
26 Soejima K, Suzuki M, Maisel WH, et al. Catheter ablation in patients with multiple and unstable ventricular tachycardias after myocardial infarction: short ablation lines guided by reentry circuit isthmuses and sinus rhythm mapping. *Circulation* 2001; **104**: 664–69.
27 Morady F, Harvey M, Kalbfleisch SJ, el-Atassi R, Calkins H, Langberg JJ. Radiofrequency catheter ablation of ventricular tachycardia in patients with coronary artery disease. *Circulation* 1993; **87**: 363–72.
28 Gonska BD, Cao K, Schaumann A, Dorszewski A, von zur Muhlen F, Kreuzer H. Catheter ablation of ventricular tachycardia in 136 patients with coronary artery disease: results and long-term follow-up. *J Am Coll Cardiol* 1994: **24**: 1506–14.
29 Rothman SA, Hsia HH, Cossu SF, Chmielewski IL, Buxton AE, Miller JM. Radiofrequency catheter ablation

of postinfarction ventricular tachycardia: long-term success and the significance of inducible nonclinical arrhythmias. *Circulation* 1997; **96**: 3499–3508.

30 Strickberger SA, Man KC, Daoud EG, et al. A prospective evaluation of catheter ablation of ventricular tachycardia as adjuvant therapy in patients with coronary artery disease and an implantable cardioverter–defibrillator. *Circulation* 1997; **96**: 1525–31.

31 O'Donnell D, Bourke JP, Simeonidou E, Furniss SS. Radiofrequency ablation for postinfarction ventricular tachycardia. Report of a single center experience of 112 cases. *Eur Heart J* 2002; **23**: 1699–1705.

32 Friedman PA, Asirvatham SJ, Grice S, et al. Noncontact mapping to guide ablation of right ventricular outflow tract tachycardia. *J Am Coll Cardiol* 2002; **39**: 1808–12.

33 Paul T, Blaufox ATD, Saul JP. Noncontact mapping and ablation of tachycardia originating in the right ventricular outflow tract. *Cardiol Young* 2002; **12**: 294–97.

34 Flemming MA, Oral H, Kim MH, et al. Electrocardiographic predictors of successful ablation of tachycardia or begeminy arising in the right ventricular outflow tract. *Am J Cardiol* 1999; **84**: 1266–68.

35 Della Bella P, Pappalardo A, Riva S, Tondo C, Fassini G, Trevisi N. Noncontact mapping to guide catheter ablation of untolerated ventricular tachycardia. *Eur Heart J* 2002; **23**: 742–52.

36 Betts TR, Yue A, Roberts PR, Morgan JM. Radiofrequency ablation of idiopathic ventricular fibrillation guided by noncontact mapping. *J Cardiovasc Electrophysiol* 2004; **15**: 1–3.

37 Higa S, Tai C-T, Lin Y-J, et al. Focal atrial tachycardia: new insight from noncontact mapping and catheter ablation. *Circulation* 2004; **109**: 84–91.

38 Tai C-T, Liu T-Y, Lee P-C, Lin Y-J, Chang M-S, Chen S-A. Noncontact mapping to guide radiofrequency ablation of atypical right atrial flutter. *J Am Coll Cardiol* 2004; **44**: 1080–86.

39 Cohen TJ, Juang G, Daggubati R. Utility of noncontact three-dimensional mapping of the left atrium for ablation of left atrial tachycardia. *J Invasive Cardiol* 2004; **16**: 100–01.

40 Earley MJ, Abrams DJ, Sporton SC, Schilling RJ. Validation of the noncontact mapping system in the left atrium during permanent atrial fibrillation and sinus rhythm. *J Am Coll Cardiol* 2006; **48**: 485–91.

41 Hindricks G, Kottkamp H. Simultaneous noncontact mapping of left atrium in patients with paroxysmal atrial fibrillation. *Circulation* 2001; **104**: 297–303.

42 Earley MJ, Abrams D, Sporton SC, Schilling RJ. High-frequency reentry circuits driving permanent AF: evidence from global left atrial mapping in humans. *Heart Rhythm* 2005; **2**: S105.

43 Paul T, Windhagen-Mahnert B, Kriebel T, et al. Atrial reentrant tachycardia after surgery for congenital heart disease: endocardial mapping and radiofrequency catheter ablation using a novel, noncontact mapping system. *Circulation* 2001; **103**: 2266–71.

44 Betts TR, Roberts PR, Allen SA, et al. Electrophysiological mapping and ablation of intra-atrial reentry tachycardia after Fontan surgery with the use of a noncontact mapping system. *Circulation* 2000; **102**: 419–25.

45 Abrams DJ, Earley MJ, Sporton SC, et al. Comparison of noncontact and electroanatomic mapping to identify scar and arrhythmia late after the Fontan procedure. *Circulation* 2007; **115**: 1738–46.

46 Lambiase PD, Rinaldi A, Hauck J, et al. Noncontact left ventricular endocardial mapping in cardiac resynchronization therapy. *Heart* 2004; **90**: 44–51.

47 Fantoni C, Kawabata M, Massaro R, et al. Right and left ventricular activation sequence in patients with heart failure and right bundle branch block. *J Cardiovasc Electrophysiol* 2005; **16**: 112–19.

48 Michael KA, Veldtman GR, Paisey JR, et al. Noncontact-mapping-guided cardiac resynchronization therapy for a failing systemic right ventricle. *Europace* 2007; **9**: 880–83.

49 Jacobson JT, Afonso VX, Eisenman G, et al. Characterization of arrhythmogenic substrate and ventricular tachycardia circuits with noncontact unipolar mapping in a porcine model of myocardial infarction (abstr). *J Am Coll Cardiol* 2005; **45**: Suppl 106A.

50 Strickberger SA, Knight BP, Michaud GF, Pelosi F, Morady F. Mapping and ablation of ventricular tachycardia guided by virtual electrograms using a noncontact, computerized mapping system. *J Am Coll Cardiol* 2000; **35**, 414–21.

51 Schilling RJ, Peters NS, Davies DW. Mapping and ablation of ventricular tachycardia with the aid of a noncontact mapping system. *Heart* 1999; **81**: 570–75.

52 Schneider MAE, Ndrepepa G, Weber S, Deisenhofer I, Schömig A, Schmitt C. Influence of high-pass filtering on noncontact mapping and ablation of atrial tachycardias. *Pacing Clin Electrophysiol* 2004; **27**: 38–46.

5

CHAPTER 5

Principles of Nonfluoroscopic Electroanatomical and Electromechanical Cardiac Mapping

Yitzhack Schwartz, MD[1] *& Shlomo A. Ben-Haim,* MD, DSc[2]

[1]Rambam Healthcare Campus Haifa, Israel
[2]Caesarea, Israel

Summary

The novel CARTO and NOGA 3D cardiac mapping systems have revolutionized the fields of therapeutic electrophysiology and interventional cardiology. This chapter summarizes more than a decade of intensive research and substantial clinical experience. It provides updated essential information for basic scientists and active clinicians and suggests foreseeable future developments.

Introduction

Conventional cardiac mapping entails recording electrograms from a multiplicity of sites within the heart, the result of which are presented as an activation map. A typical cardiac map is usually made up of several data points, each having two values: (i) the local information (i.e., activation time in electrophysiological maps, local shortening in mechanical maps), and (ii) the location coordinates within the heart. In the earlier years of cardiac electrophysiological tracking, as the recording electrodes were hard fixed to a recording array (e.g., epicardial sock), the location error was relatively small and thus disregarded. Until 1997, localization of the mapping electrode within the patient's heart was rather inaccurate as it was based solely on 2D fluoroscopic images. Determination of location using 2D fluoroscopic images is extremely limited and impeded the development of new ablation therapies for treating certain arrhythmia.

The nonfluoroscopic mapping system, first described in 1996 [1], simultaneously recorded the exact location and local electrograms sensed with the mapping electrode and facilitated the rapid development of diagnostic and therapeutic intervention in which the knowledge of relative location within the heart is essential. This chapter describes the method for cardiac electroanatomical and electromechanical mapping using an intrabody, real-time, high-resolution, nonfluoroscopic location and navigation system. Several well-established applications of the technology in both

Cardiac Mapping, Third Edition Edited by Mohammad Shenasa, Gerhard Hindricks, Martin Borggrefe, and Günter Breithardt
 ISBN: 978-1-405-17572-2

electrophysiology and interventional cardiology are presented. We also review the impact of an integrated mapping approach and will suggest several paths for its development in the future.

Method

Concept

The nonfluoroscopic electroanatomical cardiac electrophysiology mapping system is composed of an electrophysiologic recording catheter with an incorporated location sensor at its tip. This new "locatable" catheter enables automatic and simultaneous acquisition of the local electrograms sensed at the tip electrode together with the 3D location coordinates. The mapping system acquires the location of the catheter tip electrode (a single location at a fixed time during the cardiac cycle), together with its local electrogram (throughout the cardiac cycle), and reconstructs the 3D electroanatomical maps of the heart in real-time without the use of X-rays. In this manner, 3D electroanatomical maps of the human heart disclose, for the first time, the complex relationship between cardiac chamber anatomy and electrophysiological properties.

The nonfluoroscopic, elctromechanical, cardiac mapping system is similar to the electroanatomical mapping system. However, in the electromechanical mapping system the catheter locations are sampled throughout the cardiac cycle.

System Components

The mapping and navigation system (CARTO® Biosense Webster, Diamond Bar, CA) comprises a miniature passive magnetic field sensor (location sensor), an external ultralow magnetic field emitter (location pad), and a processing unit (Figure 5.1a). The location sensor is integrated into a regular electrophysiological deflectable catheter. The location pad is located beneath the patient table and generates an ultralow magnetic field (0.05–0.5 G). The emitted field possesses well-known temporal and spatial distinguishing characteristics that "code" the mapping space around the patient's chest. The sensing of the magnetic field by the location sensor enables determination of the location and orientation of the sensor in 6 degrees of freedom (X, Y, Z, and roll, yaw, and pitch).

Mapping Procedure

Electroanatomical Mapping

A locatable mapping catheter is introduced under fluoroscopic guidance and positioned inside the heart to be mapped. The mapping system determines the location and orientation of the mapping catheter, gated to a fiducial point in the cardiac cycle. The tip electrograms are recorded throughout the entire cardiac cycle and automatically associated with the catheter tip location. The mapping procedure typically involves sequentially dragging the catheter tip over the endocardium and acquiring multiple tip locations, together with their respective electrograms. The set of gated catheter tip locations is used to reconstruct the 3D endocardial surface. The local activation times (LAT) at each site are determined and presented as a color-coded graphic and incorporated into the endocardial surface reconstruction.

To correct for patient movement, a second locatable catheter is also utilized and positioned either within the heart or on the patient's back. The mapping system subtracts the location of the mapping catheter from that of the reference probe, thus compensating for any motion of the patient. When sufficient anatomical data are acquired, the operator may navigate the catheter without using fluoroscopy. Data may be acquired during the mapping procedure to delineate anatomical structures, local electrophysiological properties, or a combination of both. The stability of the catheter–endocardial contact is verified before data are added to the map by comparing the distance between consecutive end-diastolic locations (location stability, mm) and the time difference between consecutive LATs (LAT stability, msec). The reconstruction is updated in real-time with the acquisition of each new site.

Several maps are generated from the data acquired at each site, and they are as follows:

1 *Activation map*: Describes the dispersion of activation times in the mapped region.

2 *Propagation map*: A dynamic graphic representation of the activation wavefront throughout the cardiac cycle.

3 *Voltage maps*: Graphic representation of the peak-to-peak voltage of the local electrograms recorded.

4 *Geometrical maps*: Present graphic representations of the mapped anatomy.

Furthermore, the operator can mark an anatomical site with a colored tag. These tags can be used in designing the trajectory of complex ablations or as markers for the specific electrophysiological information.

Electromechanical Mapping

The basic electromechanical mapping procedure (NOGA® Biosense Webster) is identical to that described for the CARTO® system. However, as catheter tip locations are continuously obtained, the complete endocardial location trajectory throughout the cardiac cycle is acquired along with the local electrogram.

At each location, before data are added to the map, the stability of the catheter–endocardial surface contact throughout the cardiac cycle is tested by comparing the distance between consecutive location trajectories (loop stability, mm), and the time difference between consecutive LATs (LAT stability, msec). The reconstruction is updated in real-time with the acquisition of each new site.

Several maps are generated that from the data acquired at each site, and they are as follows:

1 *Voltage map*: Depiction of the peak-to-peak voltage of the local electrograms as recorded. In the normal heart, the maximal voltage map indicates a rather homogeneous dispersion of endocardial voltages (usually above 1 mV); however, the basal area of the mitral and aortic annuli has a typical low voltage signature in all maps.

2 *Local shortening maps*: The distance between adjacent endocardial sites throughout the cardiac cycle usually increases during diastole and decreases during systole. The local shortening index calculates the weighted average of endocardial distances around each site. Paradoxical shortening (i.e., increased distances during systole and decreased distances during diastole) are colored red, while highly contractile sites are colored purple. Local shortening mechanical maps in normal LVs demonstrate a typical homogenous endocardial shortening.

Accuracy and Reproducibility

The location capabilities were extensively tested in both in vitro and in vivo studies [2–8].

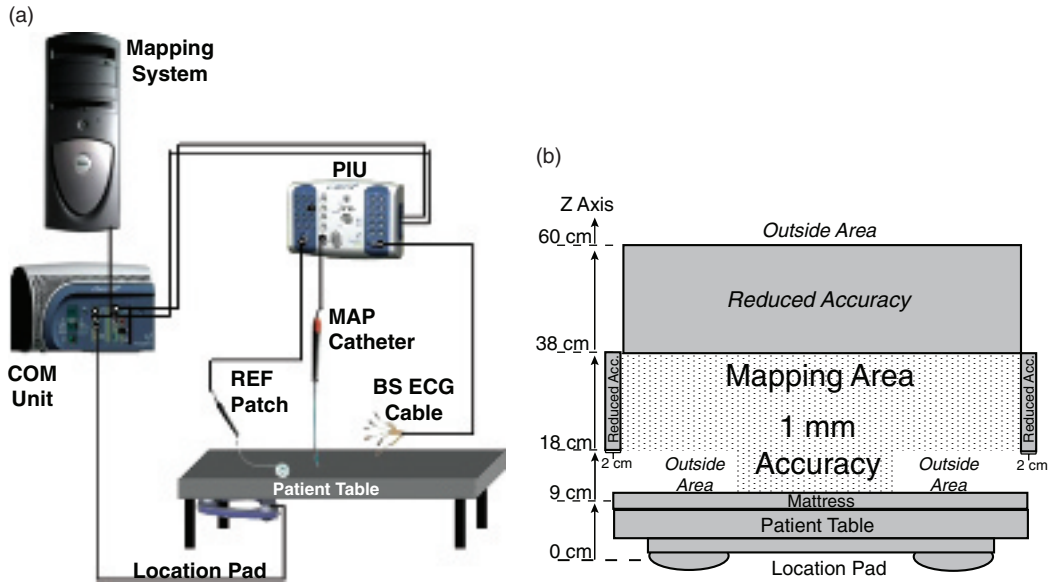

Figure 5.1 Main components of the mapping system and its mapping volume: (a) The CARTO is connected to the patient interface unit (PIU) through which the locatable catheter and the reference patch are connected. CARTO is also connected to the ultralow magnetic field generator (location pad). The communication unit (COM unit) is a processing unit for determining all location and ECG calculations and connection to the CARTO workstation. (b) The effective mapping zone where maximal accuracy is guaranteed is depicted in green (side view).

Electroanatomical Mapping

In Vitro Testing

The reproducibility of repeated-location in vitro measurements of the tip of the catheter, using different orientations at various sizes, was 0.16 ± 0.02 mm (mean $\pm$ SEM), and the maximal range of the standard deviation of the location error was 0.05 ± 0.07 mm [2]. Similarly, relative distances measured by the system between alternative sites with known locations were highly accurate (mean error 0.42 ± 0.05 mm) [2].

In Vivo Testing

The location error of repeated in vivo location determination of the catheter while in contact with a single site on a porcine left ventricular endocardium was 0.54 ± 0.05 mm, with a maximal range of 1.26 ± 0.08 mm [2, 3]. The relative distances measured by the system while sequentially withdrawing the mapping catheter inside a long sheath at 10-mm intervals inside the heart were also determined. The average location error for this was 0.73 ± 0.03 mm [3].

Repeated electroanatomical activation and propagation maps during sinus rhythm and pacing were similar and enabled accurate identification of the pacing site for all animal studies [4]. Accuracy was also tested by repeatedly applying radiofrequency (RF) energy to a site on the endocardium that was tagged on the electroanatomical map [2–4]. These studies indicated that the location accuracy could guide delivery of RF energy to create single and multiple lesions [5–7]. Furthermore, this navigation and tagging method can be used to direct repetitive applications of RF energy to adjoining sites in order to create a long and continuous lesion. A high correlation between the computer record of the length, location, and shape of linear atrial longitudinal lesions and the actual acute histopathological findings has been demonstrated [7].

Recently, a rare case was published of a patient who had ablation for VT storm and who died remotely from nonarrhythmic causes. The tagged ablation line in the electroanatomical CARTO® map highly correlated with the PM findings [8]. Maximal accuracy is guaranteed within an ample volume for practical unlimited cardiac mapping (Figure 5.1b).

Electromechanical Mapping

The capability of the system to reconstruct chamber morphology and then to calculate its volume was tested in both in vitro and in vivo studies.

In Vitro Testing

The average deviation in calculating the volume of an ellipsoid phantom was 2.23% [3, 9]. The volumetric measurement of 6 LV casts correlated well with their actual volume ($r = 0.94$) [3].

A dynamic jig was used to test the system capability to acquire multiple locations throughout the cardiac cycle. Comparison of the measured data to that of the calculated data indicated that the system had an average error of 1.43%, 0.69%, and 0.29% when calculating the end-diastolic volume, end-systolic volume, and ejection fraction, respectively.

In Vivo Testing

The mapping procedure was evaluated in vivo by measuring the inter-observer variability in determining the LV volumes, as well as by testing the correlation between the calculated stroke volumes to cardiac output measured with thermodilution [3]. The interobserver error of determining end-diastolic volume, end-systolic volume, and ejection fraction were 5.9%, 7.5%, and 11.3%, respectively.

The capability to measure myocardial viability was tested in animal models with infarcted LVs by comparing the calculated infarct locations and size to the actual pathology [10–12]. Results indicated a high correlation between the measured and calculated variables.

Continuous catheter tip stability during the cardiac cycle is essential and was confirmed by comparing its trajectory to that of a catheter fixed in place by an extended needle [13].

Multielectrode Mapping

One limitation of the classic electroanatomical and electromechanical mapping approaches described above was that maps were acquired on a point-by-point basis. To overcome this limitation a multielectrode catheter was introduced to enable simultaneous mapping in multiple sites. This catheter has a total of 26 electrodes, a single 4-mm tip, ring electrode, and six rows of four orthogonal electrodes. Two location sensors, one near the tip electrode and

the other proximal to the sixth set of orthogonal electrodes, enable the on-screen display of the shaft of the catheter. This reconstruction combines the accurate contact mapping with collected near-field electrical information via multiple electrodes.

The resolution of the image is continuously refined and updated as new points are acquired. After acquiring four tip locations, a true representation of the chamber's shape appears. A reconstruction of only 8–10 tip points is equivalent to a standard 50 contact points map [14]. Mapping of typical atrial flutter using this technique required 22 min compared to 45 min with contact mapping [14]. Integrated tip and shaft point mapping requires less catheter manipulation and results in much faster LA and PVs mapping and geometrical rendering [15]. Furthermore, the greater number of points obtained allows for a more precise geometric rendering of LA and PVs with clearer demarcation of PV ostia. This technique can generate a scout map that, in patients with structural heart disease and large macroreentrant or focal arrhythmias, accurately guides complete electroanatomic mapping using fewer point-by-point acquisitions than the bipolar catheter [16, 17]. It is also useful in epicardial mapping [18].

Inherent Limitations

Catheter mapping using a roving catheter is essentially a sequential, beat-by-beat mapping approach. This imposes two requirements on the mapping process: a stable rhythm and a fixed reference point. Furthermore, because the localization methodology is based on recording low-level magnetic fields, large ferromagnetic materials can affect the magnetic field scanned by the sensor in the catheter (usually when large objects are in the range of 1 cm from the tip).

Minimizing Radiation Exposure

Cardiac catheterization laboratories remain mostly X-ray suites. All cardiac interventions, even with modern digital X-ray equipment, are thus associated with a significant exposure to X-ray radiation. Increased concern over potential ionizing radiation effects has especially been raised regarding lengthy electrophysiology studies, usually followed by catheter ablation [19–25]. The risk for patients, especially children and young adults, cannot be underestimated. Even though radiation risk from the cardiac ablation procedure is moderate in comparison to other complications, it may highly exceed radiation risk from other common radiological procedures. For medical personnel with a heavy workload, especially in high-volume centers with dedicated therapeutic EP suites, the total exposure may lead to a significant cumulative radiation dose [26].

Nonfluoroscopic mapping has dramatically minimized patient and personnel radiation risk by reducing both overall procedure and fluoroscopy times as well as by decreasing the number of necessary repeated ablations [27, 28].

Clinical Utilization

Electroanatomical Mapping

Since the introduction of electroanatomical mapping to the clinical arena more than a decade ago, diverse modes of clinical use have been reported. The reported clinical applications include:

1 Activation mapping to identify the insertion of an accessory pathway [29–35].

2 Activation mapping for detection of foci of atrial tachycardia [36–48].

3 Identifying the location of the slow pathway during the treatment of atrioventricular nodal reentry [49–51].

4 Local cardiac anatomy mapping for guiding anatomically based atrial flutter ablation procedures [52–63].

5 Treatment of ventricular tachycardia [64–81].

6 Atrial fibrillation mapping and ablation [82–103].

7 Mapping and ablation of post surgical arrhythmia especially in structural heart disease [16, 17, 104–117].

Electromechanical Mapping

Electromechanical maps are highly correlated with echocardiography [118–122], LV angiography [123–126], dobutamine stress echocardiography [127, 128], SPECT [129–136], PET [122, 137, 138], and delayed enhanced MRI [139].

Electromechanical mapping is evidently a valuable online viability-testing tool [122, 126–136]. In patients with ischemic heart disease it is highly correlated with radionuclide perfusion and metabolism studies. Specifically, there was correlation between the location and size of areas with reduced electrical and mechanical function, indicating infarcted tissue, with fixed perfusion defects on radionuclide images. Furthermore, a high correlation was also demonstrated between the location and size of areas with preserved electrical but reduced mechanical activity, indicating electromechanical uncoupling of hibernating viable tissue, with areas of reversible defects and preserved metabolism on radionuclide images. Impedance mapping has indicated the transmurality of the infarct [141,142]. Electromechanical mapping can thus facilitate clinical decision making in the cath lab.

Epicardial and Hybrid Endocardial and Epicardial Mapping

In selected clinical scenarios, transthoracic epicardial mapping [143–146] and even concomitant hybrid endocardial and epicardial mapping [18, 147, 148], are valid valuable options.

Guidance of Interventional Procedures

Direct Myocardial Revascularization

Direct myocardial revascularization (DMR) has been examined as an attractive alternative treatment for patients with chronic refractory myocardial ischemic syndromes who are not candidates for conventional coronary revascularization. Although the exact mechanism was poorly understood it was hypothesized that the laser injury will induce a favorable angiogenic response.

The combination of a fiber optic carrying Ho:YAG laser radiation into the locatable catheter has enabled safe and accurate lasing of the endocardium. The accuracy and safety of the system were proved in both animal and human studies [149, 150]. The encouraging nonrandomized results have paved the way to a large-scale blind, randomized, placebo-controlled trial, the direct myocardial revascularization (DMR) in regeneration of endomyocardial channels (DIRECT) [151]. Some 298 patients from 14 centers were randomized to receive either the DMR procedure in which they received a low- or high-dose treatment (10–15 and 20–25 channels per zone, respectively) or a mock procedure in a blinded fashion.

DIRECT has showed unequivocally that treatment with percutaneous myocardial laser revascularization provides no benefit beyond that of a similar sham procedure. An improvement across all study groups clearly suggested a possible significant placebo effect. This observation has settled a long and fierce controversy, and percutaneous DMR has consequently been abandoned.

Direct Guided Myocardial Injection

Ischemic Heart Disease

Better understanding of the natural complex healing processes of cardiac regeneration, growth of endothelium-lined vessels (angiogenesis), and expansion of preexisting collaterals (arteriogenesis), have raised hopes that gene- and cell-based therapies are finally a viable option. Various novel therapeutic applications have accordingly been suggested for patients with ischemic heart disease. Many questions regarding these evolving therapies remain unanswered, including the fundamental issue of whether the myocardial scar boundaries or ischemic regions should be targeted. These new directions call for the ability to directly and accurately deliver drugs, factors, or genes into the myocardium. Although many routes of delivery exist, transendocardial intramyocardial injection seems an attractive choice because specific myocardial regions can be targeted, and higher local concentrations of an agent can be achieved.

A locatable injection catheter coupled with nonfluoroscopic electromechanical mapping system has thus been developed as the platform of choice for local intramyocardial delivery (Figure 5.2a). NOGA® -guidance enables online characterization of the myocardium, equally spacing the planned injections, and refraining from injecting twice in the same location or into strategic regions (Figure 5.2b). The accuracy and safety of the system were tested in animals [152, 153]. There was no significant loss or adverse effects to the cells when delivered through the injection catheter [154]. Unlike incomplete

(a)

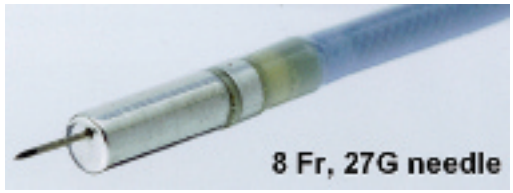

(b)

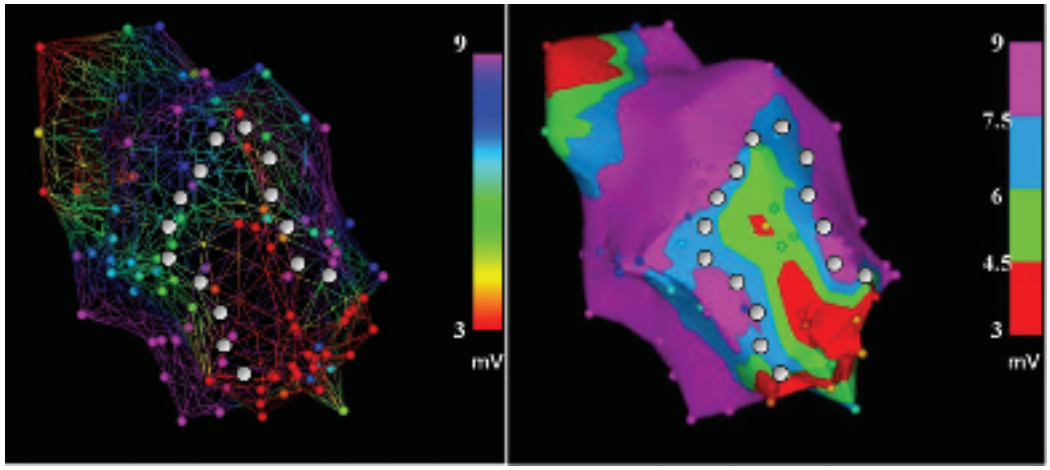

Figure 5.2 Guided intramyocardial injection: (a) MyoStar® locatable injection catheter with extendable 27G needle. (b) Preplanning of intramyocardial injection therapy can be facilitated by NOGA viability mapping. In this unipolar voltage map (anteroseptal view with a slight craniocaudal angle) the red zone with voltage values <4.5 mV indicates truly nonviable myocardium, as demonstrated by PET, whereas the green zone (4.5–6.0 mV) indicates viable myocardium that may benefit from cell- or gene-based therapy. The evenly spaced injection points are thus planned on the grid mesh on the boundaries of the green zone. Each point can then be reached accurately with MyoStar and the therapy executed as planned.

retention encountered with other injection catheters [155], delivery of FGF2 to the target myocardium is comparable to transepicardial delivery, both providing markedly higher myocardial deposition and retention and lower systemic recirculation of FGF2 than intracoronary, intrapericardial, or intravenous delivery [156].

The largest experience with preclinical and clinical intramyocardial gene delivery, including Euroinject ONE study, has consequently been gained by NOGA®-guidance [157–163].

Other published and ongoing cell transplantation studies, including endothelial progenitor cells, skeletal muscle cells, and bone marrow–derived cells, involve NOGA®-guidance [164–173]. Furthermore, electromechanical mapping was used to assess the cardioprotection effect of injected Erythropoietin [174] and the effect of a tissue-engineered patch [175].

Due to its inherent advantages electromechanical mapping will continue to play an integral part in fully developing these therapies.

Gene- and Cell-Based Therapies for Arrhythmia and Conduction Block Management

Innovative methods for focally modifying the electrical conduction in the heart via site-specific gene transfer (e.g., delivering adenovirus encoding Gαi2 subunit mimicking beta-adrenergic antagonists into AV nodal branch of the right coronary artery) [176], transplanting transfected fibroblasts expressing potassium channel Kv1.3 [177], calcium channel blocking by targeted Gem gene transfer [178] and

gene transfer of connexin43 mutants [179], have all been proposed lately.

Catheter-based modification of the AV node was successfully accomplished via CARTO-guided local injection of autologous fibroblasts with transforming growth factor-ß1 [180].

Furthermore, developing a biological pacemaker is currently being actively pursued. Several groups have reported encouraging results with Kir2.1AAA gene transfer [181], HCN2 overexpression [182, 183], expressing a synthetic pacemaker channel [184], gene transfer via transplanted human mesenchymal stem cells (MSC) [185, 186], and transplantation of cells derived from human embryonic stem cells (h-ES) [187].

CARTO-guidance is best suited for testing the feasibility and applicability of these solutions and would readily serve as a platform for performing these therapies in human patients.

Image Integration

Fusing multimodality imaging technologies into a single coherent display has long been advocated in order to facilitate intracardiac guidance especially in complex arrhythmia. The dramatic recent improvement in cardiac imaging technologies has coincided with the realization of the dependence of arrhythmias on their underlying anatomy and the limitations of contemporary mapping systems to reflect that anatomy. The last 5 years have thus witnessed the rapid development of image-integrated, anatomy-based mapping and ablation.

Integration of preacquired imaging with nonfluoroscopic cardiac mapping is already commonly used, whereas integration with real-time imaging is yet to be fully realized (Figure 5.3).

Preacquired Imaging

Attempts at PV identification and ostia location in the absence of previous PV imaging are subject to a broad error margin [188]. Only preacquired imaging can provide relevant data regarding PV anatomical variability and dynamic changes throughout the cardiac cycle [189–191] as well as the variable proximity of the esophagus to different areas of the posterior LA [192] and other data critical for successful atrial fibrillation ablation. Accordingly, the utilization of merged CT/MR electroanatomical mapping (CARTOMERGE) has a favorable impact on clinical outcome especially in atrial fibrillation ablation [193–200]. The merging process requires segmenting out of the chamber of interest from the entire CT/MR axial image set either on a radiology workstation or directly on the mapping system in the EP lab. A variety of landmark and surface registration techniques allow the processed image to be merged with the electroanatomical data. Clinical validation during the procedure with a visual representation of the distance between the map and the preacquired image shows high accuracy. However, further minimization of errors in integration and optimization of registration strategy are still required [201, 202].

Real-Time Imaging

Intracardiac echocardiography (ICE) has emerged as the mainstay of real-time imaging in the EP lab [203]. It provides highly focused real-time images of the endocardial surfaces critical for catheter positioning, establishment of catheter/tip tissue contact, and for monitoring energy delivery by depicting changing tissue echogenicity and microbubbles formation [204–206]. ICE capabilities have been accordingly successfully harnessed mainly for step-by-step guidance of atrial fibrillation ablation procedures [207–210]. ICE can even accurately localize the esophagus during LA ablation and decrease the risk of atrioesophageal fistula [211].

Integrating ICE imaging with electroanatomical mapping would open up new useful ways of using ICE. A recently launched novel SOUNDSTAR® catheter (Biosense Webster), combining an ACUNAV® (Siemens Medical Solutions, Malvern, PA) ICE catheter with a location sensor, enables acquiring real-time ultrasound images that are fully registered with the electroanatomical map and are thus displayed on the mapping system (Figure 5.3a) or on the ICE workstation.

In addition to the established ICE advantages, anatomical landmarks can be marked and contours of the desired anatomy can be drawn on frozen gated ultrasound frames. This information can be added to a 3D reconstruction. Typically the ICE catheter is positioned in the RA and the chamber of interest, LA or LV, is swiftly reconstructed from far. As traditional mapping with a probing catheter ensues the reconstruction is updated further. Preacquired

(a)

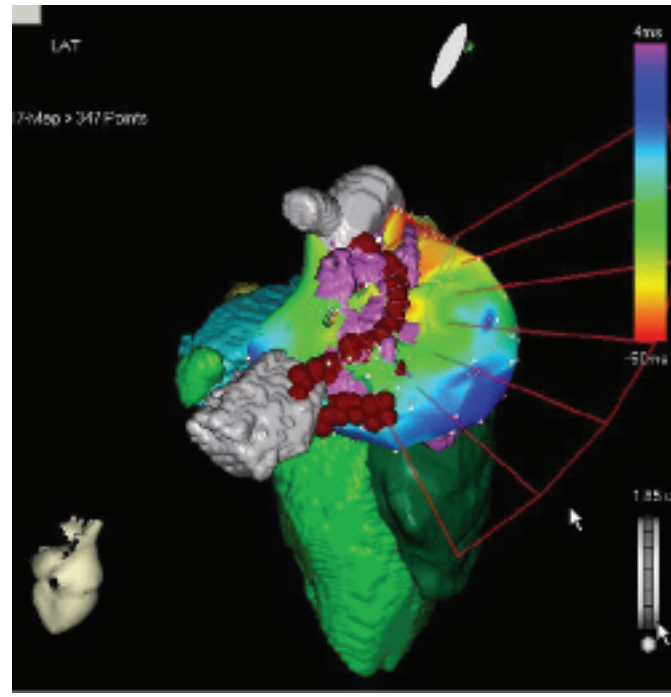

(b)

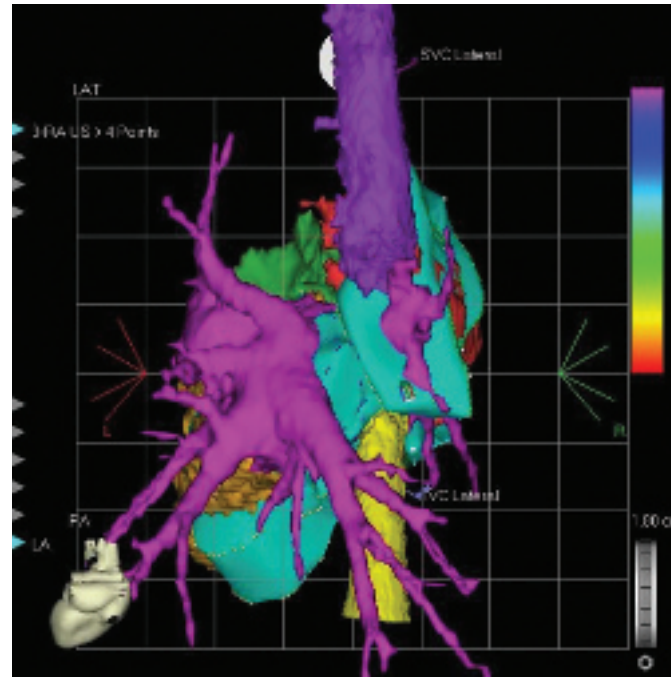

Figure 5.3 Enabling multimodality fusion: (a) An ultrasound-based cardiac reconstruction of a canine heart. All four chambers were reconstructed from real-time locatable ICE catheter (CartoSound) images. The fan depicts the orientation of the real-time ultrasound beam. The RA was then electrically mapped (LAT shown) and an ablation line was carried out. (b) An imported preacquired image (CartoMerge), segmented LA with the pulmonary veins, was fused on to a registered real-time ultrasound-based reconstruction.

CT/MR can optionally be imported (Figure 5.3b). Very early limited clinical experience is promising.

The feasibility and superior potential of 3D ICE has already been reported using two distinct approaches [212, 213]. Further development of this would eventually enable accurate 3D/4D integrated intracardiac echocardiographic and electrophysiologic imaging. This would theoretically benefit not only guided EP procedures but also optimization of cardiac resynchronization therapy (CRT) via measurement of area of left ventricular regional conduction delay, preserved myocardium, and regional wall motion [214], as well as facilitate monitoring of guided injection therapy or percutaneous valve repair procedures.

Remote Magnetic Navigation

As long as fluoroscopy remains the primary tool in the catheterization laboratory, the interventional cardiologists and electrophysiologists are not only exposed to radiation but are also at increased risk of spinal injury due to the use of lead aprons [215–217]. This, as well as the ability to access difficult locations regardless of the user's manual skills, was the major incentive for developing remote navigation systems.

As an example, the Stereotaxis Niobe® Magnetic Navigation System (Stereotaxis Inc., St. Louis, MO) utilizes a magnetic field of specified direction and magnitude, positioned externally to the patient, and multiple minuscule magnets in the tip and on the shaft of the interventional catheter. Integration of the Niobe® with the CARTO® RMT system (Figure 5.4a) has enabled closed-loop navigation from the control room of magnetically steered catheters. High accuracy and reproducibility [218] have resulted in satisfactory clinical performance [219–221], particularly in atrial fibrillation [222–223] and in scar-related ventricular tachycardia [224, 225]. The soft flexible NaviStar® RMT catheter, with available 4-mm tip and imminent 8-mm tip (Figure 5.4a), further contributes to the reduced complication rate. Interestingly, automatic mapping using a preprogrammed algorithm can safely be carried out with 100+ point chamber map created usually under 10 min. Aside from the high cost of the system, the only inherent limitation is the

Figure 5.4 Remote magnetic navigation: (a) Soft and steerable NaviStar RMT catheter. (b) A typical electroanatomical map (bipolar voltage) of the LA (AP view) during AF therapy. Arrows indicate the Niobe magnet vectors; green arrow indicates the desired vector and the yellow arrow indicates the actual vector. (c) A characteristic CartoMerge-based remote magnetic navigation for AF therapy (PA view). Note the additional contact bar information provided by Navigant.

(b)

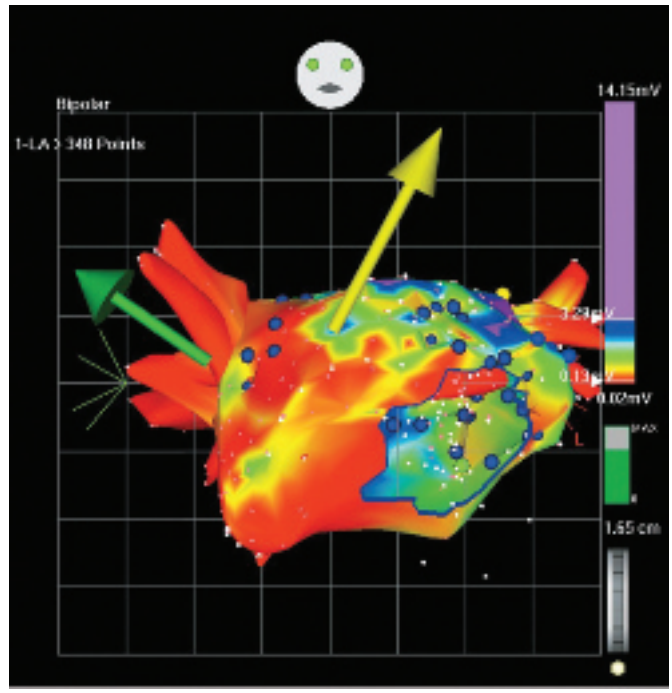

(c)

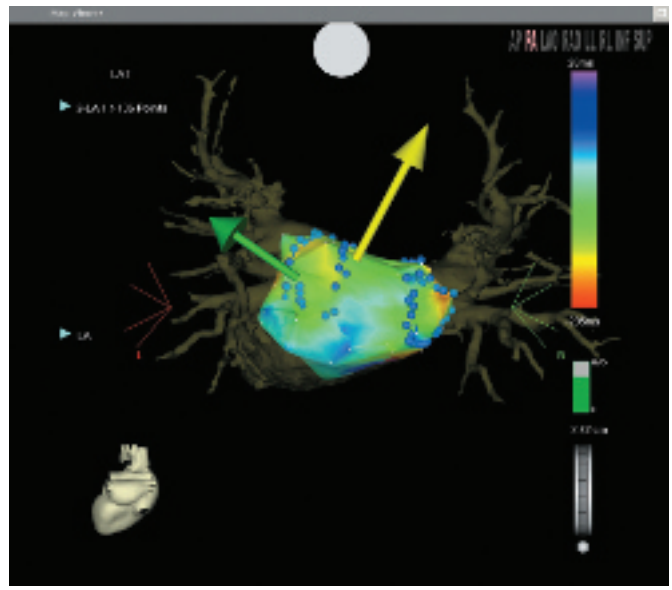

Figure 5.4 (*Continued*)

inability to simultaneously move more than one catheter.

The feasibility and early clinical experience with a different and much cheaper portable approach utilizing a robotic arm with tactile sensing technology, the Sensei™ Robotic Catheter System (Hansen Medical, Inc., Mountain View, CA), is also promising [226–228]. Similarly encouraging

are the preliminary results of yet another system, the CorPath® Robotic System (Corindus, Inc., Auburndale, MA) [229].

Electroanatomical Cardiac Mapping in the Next Decade

Therapeutic EP is the fastest growing field in cardiology mainly because of the large pool of patients and the recent development of ablative therapies. Certain developments will further expand our abilities to treat patients.

Future Image Integration

Automatic segmentation and registration will undoubtedly continue to evolve, and multimodality image fusion will improve. Integration with real-time 3D imaging, ICE, or CT-like fluoroscopy [230], will soon become available. Ultra rapid CT imaging, multiple image sets in a single cardiac cycle, will also be available for integration into the mapping system and will allow an even higher anatomic resolution down to the submillimeter level.

Advanced Parametric Analysis

Mapping capabilities demonstrating fractionation of electrograms are already being used successfully [231–234]. In the future many other measurable parameters will be displayed. For instance, mechanical assessment will be comprised of local endocardial area shortening, regional area shortening, radial and circumferential shortening, twist and torsion, and endocardial deformation.

Preplanning, Simulation, and Automatic Execution

With fully integrated capabilities it will be possible to perform preplanning and simulation by marking the exact locations of the desired intervention on the surface anatomy and predicting the clinical outcome [235–238].

Automatic execution of the desired therapeutic plan will be utilized; some may use robotic-steering systems. Therapeutic EP and guided interventional cardiology will hence become safer, more predictable, and less user-dependent.

Summary

For the first time, nonfluoroscopic 3D cardiac mapping enabled a new integrated look into cardiac electrophysiology and electromechanics, and opened a novel dimension for diagnosis and treatment of various disease states. Electroanatomical and electromechanical mapping have currently gained wide acceptance.

As predicted [239–242], within a single decade the use of a location system during interventional electrophysiologic procedures has indeed become common practice. The easily understood coherent color-coded maps and nomenclature have been fully adopted by the global EP community and have become the standard in other mapping systems as well. Reading 3D cardiac maps is already an integral part of professional EP training. Our understanding of normal conduction and arrhythmia has benefited enormously from the diagnostic capabilities of electroanatomical maps, which enabled viewing the interrelationship between cardiac anatomy and electrical activity. Effectively treating complex arrhythmias such as atrial fibrillation and ventricular tachycardia would not have been possible without the knowledge gained by electroanatomical maps and the ability to plan and accurately execute the complex ablative procedures.

In electromechanical mapping the interventional cardiologist, as never before, is afforded a clinically validated online method for determining the electromechanical coupling of the myocardium. Furthermore, it is a platform for guiding novel minimally invasive evolving gene- and cell-based therapies.

References

1 Ben-Haim SA, Osadchy D, Schuster I, et al. Nonfluoroscopic in vivo navigation and mapping technology. *Nat Med* 1996; **2**: 1393–95.

2 Hayam G, Gepstein L, Ben-Haim SA. Accuracy of the in vivo determination of location using a new nonfluoroscopic electroanatomical mapping system. *Pacing Clin Electrophysiol* 1996; **19**: 712.

3 Gepstein L, Hayam G, Shpun S, et al. Hemodynamic evaluation of the heart with a nonfluoroscopic electromechanical mapping technique. *Circulation* 1997; **96**: 3672–80.

4 Gepstein L, Hayam G, Josephson ME, et al. Cardiac volumetric measurement based on a novel method for nonfluoroscopic electroanatomical mapping of the heart. *Eur Heart J* 1996; **17**: 283.

5 Gepstein L, Hayam G, Ben-Haim SA. A novel method for nonfluoroscopic catheter-based electroanatomical mapping of the heart: in vitro and in vivo accuracy results. *Circulation* 1997; **95** 1611–22.

6 Gepstein L, Shpun S, Hayam G, et al. Accurate linear radiofrequency lesions guided by a nonfluoroscopic mapping method during atrial fibrillation. *Eur Heart J* 1997; **18**: 207.

7 Shpun S, Gepstein L, Hayam G, et al. Guidance of radiofrequency endocardial ablation with real-time three-dimensional magnetic navigation system. *Circulation* 1997; **96** 2016–21.

8 Koa-Wing M, Ho SY, Kojodjojo P, et al. Radiofrequency ablation of infarct scar-related ventricular tachycardia: correlation of electroanatomical data with postmortem histology. *J Cardiovasc Electrophysiol.* 2007; **18**: 1330–3.

9 Ben-Haim SA, Osadchy D, Hayam G, et al. Accuracy of volumetric measurements of a phantom with a new nonfluoroscopic cardiac mapping system. *J Am Coll Cardiol* 1996; **27**: 347A.

10 Kornowski R, Hong MK, Gepstein L, et al. Preliminary animal and clinical experiences using an electromechanical endocardial mapping procedure to distinguish infarcted from healthy myocardium. *Circulation* 1998; **98**: 1116–24.

11 Gepstein L, Goldin A, Lessick J, et al. Electromechanical characterization of chronic myocardial infarction in the canine coronary occlusion model. *Circulation* 1998; **98**, 2055–64.

12 Gepstein L, Hayam G, Shpun S, et al. Atrial linear ablations in pigs: chronic effects on atrial electrophysiology and pathology. *Circulation* 1999; **100**: 419–26.

13 Lessick J, Kornowski R, Fuchs S, et al. Assessment of NOGA catheter stability during the entire cardiac cycle by means of a special needle-tipped catheter. *Catheter Cardiovasc Interv* 1001; **52**: 400–6.

14 Chauhan VS, Downer E, Shah P. Rapid magnetic electroanatomic mapping of typical atrial flutter using a novel multielectrode catheter. *J Cardiovasc Electrophysiol* 2003; **14**: 673.

15 Lowe MD, Peterson LA, Packer DL. Expedited geometric rendering of left atrium and pulmonary veins using multipoint electroanatomical mapping. *J Am Coll Cardiol* 2004; **43**: A117

16 Chauhan VS, Nair GM, Sevaptisidis E, et al. Magneto-electroanatomic mapping of arrhythmias in structural heart disease using a novel multielectrode catheter. *Pacing Clin Electrophysiol* 2004; **27**: 1077–84.

17 Drago F, Brancaccio G, Grutter G, et al. Successful radiofrequency ablation of left atrial tachycardias in surgically repaired Ebstein's anomaly using the CARTO XP and the QwikStar catheter. *J Cardiovasc Med* 2007; **8**: 459–62.

18 Lemery R, Birnie D, Tang ASL, et al. Normal atrial activation and voltage during sinus rhythm in the human heart: an endocardial and epicardial mapping study in patients with a history of atrial fibrillation. *J Cardiovasc Electrophysiol* 2007; **18**: 402–8.

19 Kovoor P, Ricciardello M, Collins L, et al. Risk to patients from radiation associated with radiofrequency ablation for supraventricular tachycardia. *Circulation* 1998; **98**: 1534–40.

20 Rosenthal LS, Mahesh M, Beck TJ, et al. Predictors of fluoroscopy time and estimated radiation exposure during radiofrequency catheter ablation procedures. *Am J Cardiol* 1998; **82**: 451–58.

21 Perisinakis K, Damilakis J, Theocharopoulos N, et al. Accurate assessment of patient effective radiation dose and associated detriment risk from radiofrequency catheter ablation procedures. *Circulation* 2001; **104**: 58–62.

22 Kadish AH, Mayuga KA, Yablon Z, et al. Effectiveness of shielding for patients during cardiac catheterization or electrophysiologic testing. *Am J Cardiol* 2001; **88**: 1320–3.

23 McFadden SL, Mooney RB, Shepherd PH. X-ray dose and associated risks from radiofrequency catheter ablation procedures. *Br J Radiol* 2002; **75**: 253–65.

24 Macle L, Weerasooriya R, Jais P, et al. Radiation exposure during radiofrequency catheter ablation for atrial fibrillation. *Pacing Clin Electrophysiol* 2003; **26**: 288–91.

25 Lickfett L, Mahesh M, Vasamreddy C, et al. Radiation exposure during catheter ablation of atrial fibrillation. *Circulation* 2004; **110**: 3003–10.

26 Efstathopoulos EP, Katritsis DG, Kottou S, et al. Patient and staff radiation dosimetry during cardiac electrophysiology studies and catheter ablation procedures: a comprehensive analysis. *Europace* 2006; **8**: 443–48.

27 Kottkamp H, Burkhardt H, Beate K, et al. Electromagnetic versus fluoroscopic mapping of the inferior isthmus for ablation of typical atrial flutter: a prospective randomized study. *Circulation* 2000; **102**: 2082–86.

28 Sporton SC, Earley MJ, Nathan AW, et al. Electroanatomic versus fluoroscopic mapping for catheter ablation procedures: a prospective randomized study. *J Cardiovasc Electrophysiol* 2004; **15**: 310–15.

29 Hindrucks G, Kottkamp H, Brun J, et al. A new three-dimensional electromagnetic mapping technology for nonfluoroscopic catheter ablation of left-sided accessory pathways. *Eur Heart J* 1997; **18**: 205.

30 Hoffmann E, Reithmann C, Nimmermann P, et al. Electromechanical mapping of atrial tachycardia. *Eur Heart J* 1997; **18**: 207.

31 Miles WM, Engelstein ED, Krebs ME, et al. Nonfluoroscopic mapping and ablation of human atrial flutter. *Circulation* 1996; **94**: SI676.

32 Smeets JLRM, Ben-Haim S, Bern-David J, et al. Nonfluoroscopic endocardial catheter mapping: first experiences in patients. *Pacing Clin Electrophysiol* 1996; **19**: 627, Abstract.

33 Worley SJ. Use of a real-time three-dimensional magnetic navigation system for radiofrequency ablation of accessory pathways. *Pacing Clin Electrophysiol* 1998; **21**: 1636–45.

34 Smeets JLRM, Ben-Haim SA, Rodriguez L-M, et al. New method for nonfluoroscopic endocardial mapping in humans: accuracy assessment and first clinical results. *Circulation* 1998; **97**: 2426–32.

35 Morita N, Kobayashi Y, Katoh T, et al. Anatomic and electrophysiologic evaluation of a right lateral atrioventricular Mahaim fiber. *Pacing Clin Electrophysiol* 2005;**28**: 1138–41.

36 Kottkamp H, Hindricks G, Breithardt G, et al. Three-dimensional electromagnetic catheter technology: electroanatomical mapping of the right atrium and ablation of ectopic atrial tachycardia. *J Cardiovasc Electrophysiol* 1997; **18**: 1332–37.

37 Marchlinski F, Callans D, Gottlieb C, et al. Magnetic electroanatomical mapping for ablation of focal atrial tachycardias. *Pacing Clin Electrophysiol* 1998; **21**: 1621–35.

38 Miles WM, Engelstein ED, Krebs ME, et al. Nonfluoroscopic mapping and ablation of atrial tachycardias. *Circulation* 1996; **94**: SI380.

39 Miles WM, Engelstein ED, Krebs ME, et al. Nonfluoroscopic mapping of atrial tachyarrhythmias: early clinical results. *Eur J Cardiac Pacing Electrophysiol* 1996; **6**: 255.

40 Hoffmann E, Nimmermann P, Reithmann C, et al. New mapping technology for atrial tachycardias. *J Interv Card Electrophysiol 4 Suppl* 2000; **1**: 117–20.

41 Weiss C, Willems S, Rueppel R, et al. Electroanatomical mapping (CARTO) of ectopic atrial tachycardia: impact of bipolar and unipolar local electrogram annotation for localization the focal origin. *J Interv Card Electrophysiol* 2001; **5**: 101–7.

42 Volkmer M, Antz M, Hebe J, et al. Focal atrial tachycardia originating from the musculature of the coronary sinus. *J Cardiovasc Electrophysiol* 2002; **13**: 68–71.

43 Hoffmann E, Reithmann C, Nimmermann P, et al. Clinical experience with electroanatomic mapping of ectopic atrial tachycardia. *Pacing Clin Electrophysiol* 2002; **25**: 49–56.

44 Cavaco D, Adragao P, Morgado F, et al. Electroanatomical mapping and ablation of atrial tachycardias with the CARTO system. *Rev Port Cardiol* 2002; **21**: 407–18.

45 Nabar A, Timmermans C, Medeiros A, et al. Radiofrequency ablation of atrial arrhythmias after previous open-heart surgery. *Europace* 2005; **7**: 40–9.

46 Kantharia BK, Wilbur SL, Kutalek SP, et al. Electroanatomical mapping and radiofrequency catheter ablation of atrial tachycardia originating from the recipient heart with recipient-to-donor atrio-atrial conduction after orthotropic heart transplantation. *J Interv Card Electrophysiol* 2005; **12**: 61–7.

47 Arya A, Kottkamp H, Piorkowski C, et al. Low right atrial tachycardia with positive P waves in the inferior leads: explanation by electroanatomical mapping. *J Interv Card Electrophysiol* 2006; **15**: 201–2.

48 Kottkamp H, Hindricks G, Fetsch T, et al. Electromagnetic high-density catheter mapping within the triangle of Koch in AV node reentrant tachycardia: pathophysiology and implications for catheter ablation. *Eur Heart J* 1997; **18**: 206.

49 Miles WM, Engelstein ED, Olgin JE, et al. Slow pathway ablation using nonfluoroscopic guidance for the His bundle localization during energy delivery. *Circulation* 1996; **94**: 452.

50 Cooke PA, Wilber DJ. Radiofrequency catheter ablation of atrioventricular nodal reentry tachycardia utilizing nonfluoroscopic electroanatomical mapping. *Pacing Clin Electrophysiol* 1998; **21**: 1802–9.

51 Kopelman HA, Prater SP, Tondato F, et al. Slow pathway catheter ablation of atrioventricular nodal reentrant tachycardia guided by electroanatomical mapping: a randomized comparison to the conventional approach. *Europace* 2003; **5**: 171–74.

52 Shah DC, Jais P, Haissaguerre M, et al. Three-dimensional mapping of the common atrial flutter circuit in the right atrium. *Circulation* 1997; **96**: 3904–12.

53 Nakagawa H, Jackman WM. Use of a three-dimensional, nonfluoroscopic mapping system for catheter ablation of typical atrial flutter. *Pacing Clin Electrophysiol* 1998; 21: 1279–86.

54 Shah DC, Jais P, Coste P, et al. Propagation in the right atrium during common atrial flutter as determined by three-dimensional mapping. *Eur Heart J* 1996; **17**: 587.

55 Wilber D, Rubenstein D, Burke M, et al. Tricuspid annular activation during atrial flutter: insights from electroanatomical mapping. *Eur J Cardiac Pacing Electrophysiol* 1996; **6**: 257.

56 Sra J, Bhatia A, Dhala A, et al. Electroanatomic mapping to identify breakthrough sites in recurrent typical human flutter. *Pacing Clin Electrophysiol* 2000; **23**: 1479–92.

57 Willems S, Weiss C, Ventura R, et al. Catheter ablation of atrial flutter guided by electroanatomic mapping (CARTO): a randomized comparison to the conventional approach. *J Cardiovasc Electrophysiol* 2000; **11**: 1223–30.

58 Schumacher B, Wolpert C, Lewalter T, et al. Predictors of success in radiofrequency catheter ablation of atrial flutter. *J Interv Card Electrophysiol* 2000; **4**: 121–25.

59 Hassankhani A, Yao B, Feld GK. Conduction velocity around the tricuspid valve annulus during type 1 atrial flutter: defining the location of areas of slow conduction by three-dimensional electroanatomical mapping. *J Interv Card Electrophysiol* 2003; **8**: 121–27.

60 Ernst S, Ouyang F, Clausen C, et al. A model for in vivo validation of linear lesions in the right atrium. *J Interv Card Electrophysiol* 2003; **9**: 259–68.

61 Marrouche NF, Natale A, Wazni OM, et al. Left septal atrial flutter: electrophysiology, anatomy, and results of ablation. *Circulation* 2004; **109**: 2440–47.

62 Kubo R, Shoda M, Fuda Y, et al. Anatomical structure of the isthmus between the inferior vena cava and tricuspid annulus investigated with a three-dimensional electroanatomical mapping system. *Heart Vessels* 2004; **20**: 50–5.

63 Otomo K, Noda T, Nakagawa E, et al. Assessment of ability of activation mapping by duodecapolar catheter to diagnose complete isthmus block utilizing electroanatomical mapping system. *J Interv Card Electrophysiol* 2005; **14**: 183–92.

64 Miles WM, Engelstein ED, Krebs MA, et al. Nonfluoroscopic mapping and human ventricular tachycardia: implications of simultaneous earliest ventricular activation at more than one site. *Circulation* 1996; **94**: SI22.

65 Nademanee K, Kosar EM. A nonfluoroscopic catheter-based mapping technique to ablate focal ventricular tachycardia. *Pacing Clin Electrophysiol* 1998; **21**: 1442–47.

66 Stevenson WG, Delacretaz E, Freidman PL, et al. Identification and ablation of macroreentrant ventricular tachycardia with the CARTO electroanatomical mapping system. *Pacing Clin Electrophysiol* 1998; **21**: 1448–56.

67 Callans DJ, Ren JF, Michele J, et al. Electroanatomic left ventricular mapping in the porcine model of healed anterior myocardial infarction: correlation with intracardiac echocardiography and pathological analysis. *Circulation* 1999; **100**: 1744–50.

68 Marchlinski FE, Callans DJ, Gottlieb CD, et al. Linear ablation lesions for control of unmappable ventricular tachycardia inpatients with ischemic and nonischemic cardiomyopathy. *Circulation* 2000; **101**: 1288–96.

69 Yano K, Keida T, Suzuki K, et al. Catheter ablation of idiopathic left ventricular tachycardia with multiple breakthrough sites guided by an electroanatomical mapping system. *J Interv Card Electrophysiol* 2001; **5**: 211–14.

70 Sra J, Bhatia A, Dhala A, et al. Electroanatomically guided catheter ablation of ventricular tachycardias causing multiple defibrillator shocks. *Pacing Clin Electrophysiol* 2001; **24**: 1645–52.

71 Boulus M, Lashevsky I, Reisner S, et al. Electroanatomic mapping of arrhythmogenic right ventricular dysplasia. *J Am Coll Cardiol* 2001; **38**: 2020–27.

72 Marrouche NF, Verma A, Wazni O, et al. Mode of initiation and ablation of ventricular fibrillation storms in patients with ischemic cardiomyopathy. *J Am Coll Cardiol* 2004; **43**: 1715–20.

73 Brunckhorst CB, Delacretaz E, Soejima K,et al. Identification of the ventricular tachycardia isthmus after infarction by pace mapping. *Circulation* 2004; **110**: 652–59.

74 Brunckhorst CB, Delacretaz E, Soejima K, et al. Ventricular mapping during atrial and right ventricular pacing: relation of electrogram parameters to ventricular tachycardia reentry circuits after myocardial infarction. *J Interv Card Electrophysiol* 2004; **11**: 183–91.

75 Xia Y, Kongstad O, Hertervig E, et al. Activation recovery time measurements in evaluation of global sequence and dispersion of ventricular repolarization. *J Electrocardiol* 2005; **38**: 28–35.

76 Saleem MA, Burkett S, Passman R, et al. New simplified technique for 3D mapping and ablation of right ventricular outflow tract tachycardia. *Pacing Clin Electrophysiol* 2005; **28**: 397–403.

77 Verma A, Marrouche NF, Schweikert RA, et al. Relationship between successful ablation sites and the scar border zone defined by substrate mapping for ventricular tachycardia post-myocardial infarction. *J Cardiovasc Electrophysiol* 2005; **16**: 465–71.

78 Verma A, Kilicaslan F, Schweikert RA, et al. Short- and long-term success of substrate-based mapping and ablation of ventricular tachycardia in arrhythmogenic right ventricular dysplasia. *Circulation* 2005; **111**: 3209–16.

79 Braun MU, Knaut M, Rauwolf T, et al. Microwave ablation of an ischemic sustained ventricular tachycardia during aortocoronary bypass, mitral valve, and tricuspid valve surgery guided by a three-dimensional nonfluoroscopic mapping system (CARTO). *J Interv Card Electrophysiol* 2005; **13**: 243–47.

80 Satomi K, Kurita T, Suyama K, et al. Catheter ablation of stable and unstable ventricular tachycardias in patients with arrhythmogenic right ventricular dysplasia. *J Cardiovasc Electrophysiol* 2006; **17**: 469–76.

81 Volkmer M, Ouyang F, Deger F, et al. Substrate mapping vs. tachycardia mapping using CARTO in patients with coronary artery disease and ventricular tachycardia: impact on outcome of catheter ablation. *Europace* 2006; **8**: 968–76.

82 Schwartzman D, Kuck KH. Anatomy-guided linear atrial lesions for radiofrequency catheter ablation of atrial fibrillation. *Pacing Clin Electrophysiol* 1998; **21**: 1959–78.

83 Pappone C, Oreto G, Rosanio S, et al. Atrial electroanatomic remodeling after circumferential radiofrequency pulmonary vein ablation: efficacy of an anatomic

approach in a large cohort of patients with atrial fibrillation. *Circulation* 2001; **104**: 2539–44.

84 Schweikert RA, Perez Lugones A, Kanagaratnam L, et al. A simple method of mapping atrial premature depolarizations triggering atrial fibrillation. *Pacing Clin Electrophysiol* 2001; **24**: 22–7.

85 Weiss C, Willems S, Risius T, et al. Functional disconnection of arrhythmogenic pulmonary veins in patients with paroxysmal atrial fibrillation guided by combined electroanatomical (CARTO) and conventional mapping. *J Interv Card Electrophysiol* 2002; **6**: 267–75.

86 Pappone C, Rosanio S, Augello G, et al. Mortality, morbidity, and quality of life after circumferential pulmonary vein ablation for atrial fibrillation: outcomes from a controlled nonrandomized long-term study. *J Am Coll Cardiol* 2003; **42**: 185–97.

87 Ernst S, Antz M, Ouyang F, et al. Ostial PV isolation: is there a role for three-dimensional mapping? *Pacing Clin Electrophysiol* 2003; **26**: 1624–30.

88 Luo J, Yuan S, Hertervig E, et al. Electroanatomic mapping of right atrial activation in patients with and without paroxysmal atrial fibrillation. *J Electrocardiol* 2003; **36**: 237–42.

89 Ernst S, Ouyang F, Lober F, et al. Catheter-induced linear lesions in the left atrium in patients with atrial fibrillation: an electroanatomic study. *J Am Coll Cardiol* 2003; **42**: 1271–82.

90 Schwartzman D, Bazaz R, Nosbisch J. Catheter ablation to suppress atrial fibrillation: evolution of technique at a single center. *J Interv Card Electrophysiol* 2003; **9**: 295–300.

91 Pappone C, Vincenzo Santinelli V, Manguso F, et al. Pulmonary vein denervation enhances long-term benefit after circumferential ablation for paroxysmal atrial fibrillation. *Circulation* 2004; **109**: r7–r14.

92 Xia Y, Hertervig E, Kongstad O, et al. Deterioration of interatrial conduction in patients with paroxysmal atrial fibrillation: electroanatomic mapping of the right atrium and coronary sinus. *Heart Rhythm* 2004; **1**: 548–53.

93 Pappone C, Manguso F, Vicedomini G, et al. Prevention of iatrogenic atrial tachycardia after ablation of atrial fibrillation: a prospective randomized study comparing circumferential pulmonary vein ablation with a modified approach. *Circulation* 2004; **110**: 3036–42.

94 Beukema WP, Elvan A, Sie HT, et al. Successful radiofrequency ablation in patients with previous atrial fibrillation results in a significant decrease in left atrial size. *Circulation* 2005; **112**: 2089–95.

95 Hocini M, Sanders P, Jais P, et al. Prevalence of pulmonary vein disconnection after anatomical ablation for atrial fibrillation: consequences of wide atrial encircling of the pulmonary veins. *Eur Heart J* 2005; **26**: 696–704.

96 Vasamreddy CR, Dalal D, Eldadah Z, et al. Safety and efficacy of circumferential pulmonary vein catheter ablation of atrial fibrillation. *Heart Rhythm* 2005; **2**: 42–8.

97 Hindricks G, Piorkowski C, Tanner H, et al. Perception of atrial fibrillation before and after radiofrequency catheter ablation: relevance of asymptomatic arrhythmia recurrence. *Circulation* 2005; **112**: 307–13.

98 Mantovan R, Verlato R, Calzolari V, et al. Comparison between anatomical and integrated approaches to atrial fibrillation ablation: adjunctive role of electrical pulmonary vein disconnection. *J Cardiovasc Electrophysiol* 2005; **16**: 1293–97.

99 Pappone C, Augello G, Sala S, et al. A randomized trial of circumferential pulmonary vein ablation versus antiarrhythmic drug therapy in paroxysmal atrial fibrillation: the APAF Study. *J Am Coll Cardiol* 2006; **48**: 2340–47.

100 Lang CC, Gugliotta F, Santinelli V, et al. Endocardial impedance mapping during circumferential pulmonary vein ablation of atrial fibrillation differentiates between atrial and venous tissue. *Heart Rhythm* 2006; **3**: 171–78.

101 Antz M, Chun KR, Ouyang F, et al. Ablation of atrial fibrillation in humans using a balloon-based ablation system: identification of the site of phrenic nerve damage using pacing maneuvers and CARTO. *J Cardiovasc Electrophysiol* 2006; **17**: 1242–45.

102 Kojodjojo P, Peters NS, Davies DW, et al. Characterization of the electroanatomical substrate in human atrial fibrillation: the relationship between changes in atrial volume, refractoriness, wavefront propagation velocities, and AF burden. *J Cardiovasc Electrophysiol* 2007; **18**: 269–75.

103 Chun KR, Bansch D, Ernst S, et al. Pulmonary vein conduction is the major finding in patients with atrial tachyarrhythmias after intraoperative maze ablation. *J Cardiovasc Electrophysiol* 2007; **18**: 358–63.

104 Dorodtkar PC, Cheng J, Scheinman MM. Electroanatomical mapping and ablation of the substrate supporting intra-atrial reentrant tachycardia after palliation for complex congenital heart disease. *Pacing Clin Electrophysiol* 1998; **21**: 1810–19.

105 Kloosterman EM, Yamamura K, Alba J, et al. An innovative application of anatomic electromagnetic voltage mapping in a patient with Ebstein's anomaly undergoing permanent pacemaker implantation. *J Cardiovasc Electrophysiol* 2000; **11**: 99–101.

106 Sokoloski MC, Pennington JC 3rd, Winton GJ, *et al.* Use of multisite electroanatomic mapping to facilitate ablation of intra-atrial reentry following the Mustard procedure. *J Cardiovasc Electrophysiol* 2000; **11**: 927–30.

107 Reithmann C, Hoffmann E, Dorwarth U, et al. Electroanatomical mapping for visualization of atrial activation in patients with incisional atrial tachycardias. *Eur Heart J* 2001; **22**: 237–46.

108 de Groot NM, Kuijper AF, Blom NA, et al. Three-dimensional distribution of bipolar atrial electrogram voltages in patients with congenital heart disease. *Pacing Clin Electrophysiol* 2001; **24**: 1334–42.

109 Satomi K, Shimizu W, Suyama K, et al. Macroreentrant atrial flutter around a common atrioventricular canal in an infant with complicated congenital heart anomaly. *Pacing Clin Electrophysiol* 2002; **25**: 1530–31.

110 Arenal A, Glez-Torrecilla E, Ortiz M, et al. Ablation of electrograms with an isolated, delayed component as treatment of unmappable monomorphic ventricular tachycardias in patients with structural heart disease. *J Am Coll Cardiol* 2003; **41**: 81–92.

111 de Groot NM, Schalij MJ, Zeppenfeld K, et al. Voltage and activation mapping: how the recording technique affects the outcome of catheter ablation procedures in patients with congenital heart disease. *Circulation* 2003; **108**: 2099–106.

112 Rostock T, Willems S, Ventura R, et al. Radiofrequency catheter ablation of a macroreentrant ventricular tachycardia late after surgical repair of tetralogy of Fallot using the electroanatomic mapping (CARTO). *Pacing Clin Electrophysiol* 2004; **27**: 801–4.

113 Tanner H, Lukac P, Schwick N, et al. Irrigated-tip catheter ablation of intra-atrial reentrant tachycardia in patients late after surgery of congenital heart disease. *Heart Rhythm* 2004; **1**: 268–75.

114 Lukac P, Pedersen AK, Mortensen PT, et al. Ablation of atrial tachycardia after surgery for congenital and acquired heart disease using an electroanatomic mapping system: which circuits to expect in which substrate? *Heart Rhythm* 2005; **2**: 64–72.

115 Magnin-Poull I, De Chillou C, Miljoen H, et al. Mechanisms of right atrial tachycardia occurring late after surgical closure of atrial septal defects. *J Cardiovasc Electrophysiol* 2005; **16**: 681–87.

116 Nakao M, Ricard P, Dor V, et al. Catheter ablation of recipient right ventricular tachycardia after heterotopic heart transplantation. *J Cardiovasc Electrophysiol.* 2005; **16**: 789–92.

117 Eisenberger M, Fox DJ, Earley MJ, et al. Atrioventricular node reentrant tachycardia ablation in a patient with congenitally corrected transposition of the great vessels using the CARTO mapping system. *J Interv Card Electrophysiol* 2007; **19**: 129–32.

118 Lessick J, Smeets JL, Reisner SA, et al. Electromechanical mapping of regional left ventricular function in humans: comparison with echocardiography. *Catheter Cardiovasc Interv* 2000; **50**: 10–18.

119 Langenhove GV, Hamburger JN, Roelandt JRTC, et al. Comparison of mechanical properties of the left ventricle in patients with severe coronary artery disease by nonfluoroscopic mapping versus two-dimensional echocardiograms. *Am J Cardiol* 2000; **86**: 1047–50.

120 Lessick J, Hayam G, Zaretsky A, et al. Evaluation of inotropic changes in ventricular function by NOGA mapping: comparison with echocardiography. *J Appl Physiol* 2002; **93**, 418–26.

121 Kornowski R, Fuchs S, Shiran A, et al. Catheter-based electromechanical mapping to assess regional myocardial function: a comparative analysis with transthoracic echocardiography. *Catheter Cardiovasc Interv* 2001; **52**, 342–47.

122 Keck A, Hertting K, Schwartz Y, et al. Electromechanical mapping for determination of myocardial contractility and viability: a comparison with echocardiography, myocardial single-photon emission computed tomography, and positron emission tomography. *J Am Coll Cardiol* 2002; **40**: 1067–74.

123 Langenhove GV, Hamburger JN, Smits PC, et al. Evaluation of left ventricular volumes and ejection fraction with a nonfluoroscopic endoventricular three-dimensional mapping technique. *Am Heart J* 2000; **140**: 596–602.

124 Langenhove GV, Hamburger JN, Diamantopoulos L, et al. Validation of the local shortening function as assessed by nonfluoroscopic electromechanical mapping: a comparison with computerized left ventricular angiography. *Int J Cardiol* 2001; **77**: 33–41.

125 Sarmento-Leite R, Silva GV, Dohmann HF, et al. Comparison of left ventricular electromechanical mapping and left ventricular angiography: defining practical standards for analysis of NOGA maps. *Tex Heart Inst* 2003; **J30**: 19–26.

126 Jørgensen E, Madsen T, Kastrup J. Comparison of the left ventricular electromechanical map before percutaneous coronary stent revascularization and at one-month follow-up in patients with a recent ST elevation infarction. *Catheter Cardiovasc Intervent* 2005; **64**: 153–59.

127 Sheehan FH, Bolson EL, McDonald JA, et al. Method for three-dimensional data registration from disparate imaging modalities in the NOGA myocardial viability trial. *IEEE Trans Med Imaging* 2002; **21**: 1264–70.

128 Poppas A, Sheehan FH, Reisman M, et al. Validation of viability assessment by electromechanical mapping by three-dimensional reconstruction with dobutamine stress echocardiography in patients with coronary artery disease. *Am J Cardiol* 2004; **93**: 1097–101.

129 Kornowski R, Hong MK, Leon MB. Comparison between left ventricular electromechanical mapping and radionuclide perfusion imaging for detection of myocardial viability. *Circulation.* 1998; **98**: 1837–41.

130 Kornowski R, Fuchs S, Leon MB. Detection of myocardial viability in the catheterization laboratory using the

Biosense-guided electromechanical mapping system. *Int J Cardiovasc Intervent* 1999; **2**: 125–28.

131 Fuchs S, Kornowski R, Shiran A, et al. Electromechanical characterization of myocardial hibernation in a pig model. *Coron Artery Dis.* 1999; **10**: 195–98.

132 Kornowski R, Leon MB. Left ventricular electromechanical mapping: current understanding and diagnostic potential. *Catheter Cardiovasc Interv* 1999; **48**: 421–29.

133 Kornowski R, Hong MK, Shiran A, et al. Electromechanical characterization of acute experimental myocardial infarction. *J Invasive Cardiol* 1999; **11**: 329–36.

134 Vale PR, Losordo DW, Tkebuchava T, et al. Catheter-based myocardial gene transfer utilizing nonfluoroscopic electromechanical left ventricular mapping. *J Am Coll Cardiol* 1999; **34**: 246–54.

135 Fuchs S, Hendel RC, Baim DS, et al. Comparison of endocardial electromechanical mapping with radionuclide perfusion imaging to assess myocardial viability and severity of myocardial ischemia in angina pectoris. *Am J Cardiol* 2001; **87**: 874–80.

136 Gyöngyösi M, Sochor H, Khosand A, et al. Online myocardial viability assessment in the catheterization laboratory via NOGA electroanatomic mapping: quantitative comparison with thallium-201 uptake. *Circulation* 2001; **104**: 1005–11.

137 Graf S, Gyöngyösi M, Khorsand A, et al. Electromechanical properties of perfusion/metabolism mismatch: comparison of nonfluoroscopic electroanatomic mapping with 18F-FDG PET. *J Nuc Med* 2004; **45**: 1611–18.

138 Gyöngyösi M, Khorsand A, Sochor H, et al. Characterization of hibernating myocardium with NOGA electroanatomic endocardial mapping. *Am J Cardiol* 2005; **95**: 722–28.

139 Perin EC, Silva GV, Sarmento-Leite R, et al. Assessing myocardial viability and infarct transmurality with left ventricular electromechanical mapping in patients with stable coronary artery disease: validation by delayed-enhancement magnetic resonance imaging. *Circulation* 2002; **106**: 957–61.

140 Samady H, Choi CJ, Ragosta M, et al. Electromechanical mapping identifies improvement in function and retention of contractile reserve after revascularization in ischemic cardiomyopathy. *Circulation* 2004; **110**: 241014.

141 Wolf T, Gepstein L, Hayam G, et al. Three-dimensional endocardial impedance mapping: a new approach for myocardial infarction assessment. *Am J Physiol Heart Circ Physiol* 2001; **280**: H179–88.

142 Wolf T, Gepstein L, Dror U, et al. Detailed endocardial mapping accurately predicts the transmural extent of myocardial infarction. *J Am Coll Cardiol* 2001; **37**: 1590–97.

143 Tomassoni G, Stanton M, Richey M, et al. Epicardial mapping and radiofrequency catheter ablation of ischemic ventricular tachycardia using a three-dimensional nonfluoroscopic mapping system. *J Cardiovasc Electrophysiol* 1999; **10**: 1643–48.

144 Swarup V, Morton J, Arruda M, et al. Ablation of epicardial macroreentrant ventricular tachycardia associated with idiopathic nonischemic dilated cardiomyopathy by a percutaneous transthoracic approach. *J Cardiovasc Electrophysiol* 2002; **13**: 1164–68.

145 d'Avila A, Houghtaling C, Gutierrez P, et al. Catheter ablation of ventricular epicardial tissue: a comparison of standard and cooled-tip radiofrequency energy. *Circulation* 2004; **109**: 2363–69.

146 Nehgme RA, Carbinu MP, Care J, et al. Transthoracic percutaneous access for electroanatomic mapping and catheter ablation of atrial tachycardia in patients with a lateral tunnel Fontan. *Heart Rhythm* 2006; **3**: 37–43.

147 Reddy VY, Wrobleski D, Houghtaling C, et al. Combined epicardial and endocardial electroanatomic mapping in a porcine model of healed myocardial Infarction. *Circulation* 2003; **107**: 3236–42.

148 Pak HN, Hwang C, Lim HE, et al. Hybrid epicardial and endocardial ablation of persistent or permanent atrial fibrillation: new approach for difficult cases. *J Cardiovasc Electrophysiol* 2007; **18**: 917–23.

149 Kornowski R, Hong MK, Haudenschild CC, et al. Feasibility and safety of percutaneous laser revascularization using the Biosense system in porcine hearts. *Coron Artery Dis* 1998; **9**: 535–40.

150 Kornowski R, Baim DS, Moses JW, et al. Short- and intermediate-term clinical outcomes from direct myocardial laser revascularization guided by Biosense left ventricular electromechanical mapping. *Circulation* 2000; **102**: 1120–25.

151 Leon MB, Kornowski R, Downey WE, et al. A blinded, randomized, placebo-controlled trial of percutaneous laser myocardial revascularization to improve angina symptoms in patients with severe coronary disease. *J Am Coll Cardiol* 2005; **46**: 1812–19.

152 Kornowski R, Fuchs S, Tio FO, et al. Evaluation of the acute and chronic safety of the Biosense injection catheter system in porcine hearts. *Catheter Cardiovasc Interv* 1999; **48**: 447–53.

153 Kornowski R, Leon MB, Fuchs S, et al. Electromagnetic guidance for catheter-based transendocardial injection: a platform for intramyocardial angiogenesis therapy. Results in normal and ischemic porcine models. *J Am Coll Cardiol* 2000; **35**: 1031–39.

154 Oron U, Halevy O, Yaakobi T, et al. Technical delivery of myogenic cells through an endocardial injection catheter for myocardial cell implantation. *Int J Cardiovasc Intervent* 2000; **3**: 227–30.

155 Grossman PM, Han Z, Palasis M, et al. Incomplete retention after direct myocardial injection. *Cathet Cardiovasc Intervent* 2002; **55**: 392–97.

156 Laham R, Post M, Rezaee M, et al. Transendocardial and transepicardial intramyocardial fibroblast growth factor-2 administration: myocardial and tissue distribution. *Drug Metab Dispos* 2005; **33**: 1101–7.

157 Vale PR, Losordo DW, Milliken CE, et al. Left ventricular electromechanical mapping to assess efficacy of phVEGF (165) gene transfer for therapeutic angiogenesis in chronic myocardial ischemia. *Circulation* 2000; **102**: 965–74.

158 Kornowski R, Fuchs S, Epstein SE, et al. Catheter-based plasmid-mediated transfer of genes into ischemic myocardium using the pCOR plasmid. *Coron Artery Dis* 2000; **11**: 615–19.

159 Vale PR, Losordo DW, Milliken CE, et al. Randomized, single-blind, placebo-controlled pilot study of catheter-based gene transfer for therapeutic angiogenesis using left ventricular electromechanical mapping in patients with chronic myocardial ischemia. *Circulation* 2001; **103**: 2138–43.

160 Losordo DW, Vale PR, Hendel RC, et al. Phase 1/2 placebo-controlled, double-blind, dose-escalating trial of myocardial vascular endothelial growth factor 2 gene transfer by catheter delivery in patients with chronic myocardial ischemia. *Circulation* 2002; **105**: 2012–18.

161 Rutanen J, Rissanen TT, Markkanen JE, et al. Adenoviral catheter mediated intramyocardial gene transfer using the mature form of vascular endothelial growth factor D induces transmural angiogenesis in porcine hearts. *Circulation* 2004; **109**: 1029–35.

162 Kastrup J, Jorgensen E, Ruck A, et al. Direct intramyocardial plasmid vascular endothelial growth factor A165 gene therapy in patients with stable severe angina pectoris: a randomized double-blind placebo-controlled study: the EUROINJECT ONE trial. *J Am Coll Cardiol* 2005; **45**: 982–88.

163 Gyöngyösi M, Khorsand A, Zamini S, et al. NOGA-guided analysis of regional myocardial perfusion abnormalities treated with intramyocardial injections of plasmid encoding vascular endothelial growth factor A-165 in patients with chronic myocardial ischemia: subanalysis of the EUROINJECT-ONE multicenter double-blind randomized study. *Circulation* 2005; **112**: I157–65.

164 Fuchs S, Dib N, Cohen BM, et al. A randomized, double-blind, placebo-controlled, multicenter, pilot study of the safety and feasibility of catheter-based intramyocardial injection of AdVEGF121 in patients with refractory advanced coronary artery disease. *Catheter Cardiovasc Interv* 2006; **68**: 372–78.

165 Kawamoto A, Tkebuchava T, Yamaguchi JI, et al. Intramyocardial transplantation of autologous endothelial progenitor cells for therapeutic neovascularization of myocardial ischemia. *Circulation* 2003; **107**: 461–68.

166 Smits PC, van Geuns RJM, Poldermans D, et al. Catheter-based intramyocardial injection of autologous skeletal myoblasts as a primary treatment of ischemic heart failure clinical experience with six-month follow-up. *J Am Coll Cardiol* 2003; **42**: 2063–69.

167 Fuchs S, Baffour R, Zhou YF, et al. Transendocardial delivery of autologous bone marrow enhances collateral perfusion and regional function in pigs with chronic experimental myocardial ischemia. *J Am Coll Cardiol* 2001; **37**: 1726–32.

168 Fuchs S, Satler LF, Kornowski R, et al. Catheter-based autologous bone marrow myocardial injection in no-option patients with advanced coronary artery disease: a feasibility study. *J Am Coll Cardiol* 2003; **41**: 1721–24.

169 Perin EC, Dohmann HF, Borojevic R, et al. Transendocardial autologous bone marrow cell transplantation for severe, chronic ischemic heart failure. *Circulation* 2003; **107**: 2294–302.

170 Perin EC, Dohmann HF, Borojevic R, et al. Improved exercise capacity and ischemia 6 and 12 months after transendocardial injection of autologous bone marrow mononuclear cells for ischemic cardiomyopathy. *Circulation* 2004; **110**: II213–18.

171 Dohmann HF, Perin EC, Takiya CM, et al. Transendocardial autologous bone marrow mononuclear cell injection in ischemic heart failure: postmortem anatomicopathologic and immunohistochemical findings. *Circulation* 2005; **112**: 521–26.

172 Fuchs S, Kornowski R, Weisz G, et al. Safety and feasibility of transendocardial autologous bone marrow cell transplantation in patients with advanced heart disease. *Am J Cardiol* 2006; **97**: 823–29.

173 Losordo DW, Schatz RA, White CJ, et al. Intramyocardial transplantation of autologous CD34+ stem cells for intractable angina: a phase I/IIa double-blind, randomized controlled trial. *Circulation* 2007; **115**: 3165–72.

174 Krause KT, Jaquet K, Geidel S, et al. Percutaneous endocardial injection of erythropoietin: assessment of cardioprotection by electromechanical mapping. *Eur J Heart Failure* 2006; **8**: 443–50.

175 Ota T, Gilbert TW, Badylak SF, et al. Electromechanical characterization of a tissue-engineered myocardial patch derived from extracellular matrix. *J Thorac Cardiovasc Surg* 2007; **133**: 979–85.

176 Donahue JK, Heldman AW, Fraser H, et al. Focal modification of electrical conduction in the heart by viral gene transfer. *Nat Med* 2000; **6**: 1395–98.

177 Feld Y, Melamed-Frank M, Kehat I, et al. Electrophysiological modulation of cardiomyocytic tissue by transfected fibroblasts expressing potassium channels: a novel

strategy to manipulate excitability. *Circulation* 2002; **105**: 522–29.

178 Murata M, Cingolani E, McDonald AD, et al. Creation of a genetic calcium channel blocker by targeted Gem gene transfer in the heart. *Circ Research* **2004;** 95: 398–405.

179 Kizana E, Chang CY, Cingolani E*, et al.* Gene transfer of connexin-43 mutants attenuates coupling in cardiomyocytes: novel basis for modulation of cardiac conduction by gene therapy. *Circ Res* 2007; **100**: 1597–604.

180 Bunch TJ, Mahapatra S, Bruce GK, et al. Impact of transforming growth factor-ß1 on atrioventricular node conduction modification by injected autologous fibroblasts in the canine heart. *Circulation* 2006; **113**: 2485–94.

181 Miake J, Marbán E, Nuss HB. Biological pacemaker created by gene transfer. *Nature* 2002; **419**: 132–3.

182 Qu J, Plotnikov AN, Danilo PJ, et al. Expression and function of a biological pacemaker in canine heart. *Circulation* 2003; **107**: 1106–9.

183 Plotnikov AN, Sosunov EA, Qu J, et al. Biological pacemaker implanted in canine left bundle branch provides ventricular escape rhythms that have physiologically acceptable rates. *Circulation* 2004; **109**: r31–r37.

184 Kashiwakura Y, Cho HC, Barth AS, et al. Gene transfer of a synthetic pacemaker channel into the heart: a novel strategy for biological pacing. *Circulation* 2006; **114**: 1682–86.

185 Potapova I, Plotnikov AN, Lu Z, et al. Human mesenchymal stem cells as a gene delivery system to create cardiac pacemakers. *Circ Res* 2004; **94**: 952–59.

186 Plotnikov AN, Shlapakova I, Szabolcs MJ, et al. Xenografted adult human mesenchymal stem cells provide a platform for sustained biological pacemaker function in canine heart. *Circulation* 2007; **116**: 1–8.

187 Kehat I, Khimovich L, Caspi O, et al. Electromechanical integration of cardiomyocytes derived from human embryonic stem cells. *Nat Biotechnol* 2004; **22**: 1282–89.

188 Perez-Castellano N, Villacastin J, Moreno J, et al. Errors in pulmonary vein identification and ostia location in the absence of pulmonary vein imaging. *Heart Rhythm* 1985; **2**: 1082–89.

189 Kato R, Lickfett L, Meininger G, Dickfeld T, et al. Pulmonary vein anatomy in patients undergoing catheter ablation of atrial fibrillation: lessons learned by use of magnetic resonance imaging. *Circulation* 2003; **107**: 2004–10.

190 Mansour M, Holmvang G, Sosnovik D, et al. Assessment of pulmonary vein anatomic variability by magnetic resonance imaging: implications for catheter ablation techniques for atrial fibrillation. *J Cardiovasc Electrophysiol* 2004;**15**: 387–93.

191 Lickfett L, Dickfeld T, Kato R, et al. Changes of pulmonary vein orifice size and location throughout the cardiac cycle: dynamic analysis using magnetic resonance cine imaging. *J Cardiovasc Electrophysiol* 2005; **16**: 582–88.

192 Kottkamp H, Piorkowski C, Tanner H, et al. Topographic variability of the esophageal left atrial relation influencing ablation lines in patients with atrial fibrillation. *J Cardiovasc Electrophysiol* 2005; **16**: 146–50.

193 Tops LF, Bax JJ, Zeppenfeld K, et al. Fusion of multislice computed tomography imaging with three-dimensional electroanatomic mapping to guide radiofrequency catheter ablation procedures. *Heart Rhythm* 2005; **2**: 1076–81.

194 Malchano ZJ, Neuzil P, Cury RC, et al. Integration of cardiac CT/MR imaging with three-dimensional electroanatomical mapping to guide catheter manipulation in the left atrium: implications for catheter ablation of atrial fibrillation. *J Cardiovasc Electrophysiol* 2006; **17**: 1221–29.

195 Dong J, Calkins H, Solomon SB, et al. Integrated electroanatomic mapping with three-dimensional computed tomographic images for real-time guided ablations. *Circulation* 2006; **113**: 186–94.

196 Dong J, Dickfeld T, Dalal D, et al. Initial experience in the use of integrated electroanatomic mapping with three-dimensional MR/CT images to guide catheter ablation of atrial fibrillation. *J Cardiovasc Electrophysiol* 2006; **17**: 459–66.

197 Kistler PM, Earley MJ, Harris S, et al. Validation of three-dimensional cardiac image integration: use of integrated CT Image into electroanatomic mapping system to perform catheter ablation of atrial fibrillation. *J Cardiovasc Electrophysiol* 2006; **17**: 341–8.

198 Kistler PM, Rajappan K, Jahngir M, et al. The impact of CT image integration into electroanatomic mapping system on clinical outcomes of catheter ablation of atrial fibrillation. *J Cardiovasc Electrophysiol* 2006; **17**: 1093–101.

199 Pflaumer A, Deisenhofer I, Hausleiter J, et al. Mapping and ablation of atypical flutter in congenital heart disease with a novel three-dimensional mapping system (Carto Merge). *Europace* 2006; **8**: 138–9.

200 Piorkowski C, Hindricks G, Schreiber D, et al. Electroanatomic reconstruction of the left atrium, pulmonary veins, and esophagus compared with the "true anatomy" on multislice computed tomography in patients undergoing catheter ablation of atrial fibrillation. *Heart Rhythm* 2006; **3**: 317–27.

201 Heist EK, Chevalier J, Holmvang G, et al. Factors affecting error in integration of electroanatomic mapping with CT and MR imaging during catheter ablation of atrial fibrillation. *J Interv Card Electrophysiol* 2006; **17**: 21–7.

202 Pahmy TS, Mlcochova H, Wazni Om, et al. Intracardiac echo-guided image integration: optimizing strategies for

registration. *J Cardiovasc Electrophysiol* 2007; **18**: 276–82.

203 Packer DL, Stevens CL, Curley MG, et al. Intracardiac phased-array imaging: methods and initial clinical experience with high resolution, under blood visualization: initial experience with intracardiac phased-array ultrasound. *J Am Coll Cardiol* 2002; **39**: 509–16.

204 Wood MA, Shaffer KM, Ellenbogen AL, et al. Microbubbles during radiofrequency catheter ablation: composition and formation. *Heart Rhythm* 2005; **2**: 397–403.

205 Oh S, Kilicaslan F, Zhang Y, et al. Avoiding microbubbles formation during radiofrequency left atrial ablation versus continuous microbubbles formation and standard radiofrequency ablation protocols: comparison of energy profiles and chronic lesion characteristics. *J Cardiovasc Electrophysiol* 2006; **17**: 72–7.

206 Alaeddini J, Wood MA, Lee BP, et al. Incidence, time course, and characteristics of microbubble formation during radiofrequency ablation of pulmonary veins with an 8-mm ablation catheter. *Pacing Clin Electrophysiol* 2006; **29**: 979–84.

207 Mangrum JM, Mounsey JP, Kok LC, et al. Intracardiac echocardiography-guided, anatomically based radiofrequency ablation of focal atrial fibrillation originating from pulmonary veins. *J Am Coll Cardiol* 2002; **39**: 1964–72.

208 Ren JF, Marchlinski FE, Callans DJ, et al. Intracardiac Doppler echocardiographic quantification of pulmonary vein flow velocity: an effective technique for monitoring pulmonary vein ostia narrowing during focal atrial fibrillation ablation. *J Cardiovasc Electrophysiol* 2002; **13**: 1076–81.

209 Marrouche NF, Martin DO, Wazni O, et al. Phased-array intracardiac echocardiography monitoring during pulmonary vein isolation in patients with atrial fibrillation: Impact on outcome and complications. *Circulation* 2003; **107**: 2710–16.

210 Herweg B, Sichrovsky T, Polosajian L, et al. Anatomic substrate, procedural results, and clinical outcome of ultrasound-guided left atrial–pulmonary vein disconnection for treatment of atrial fibrillation. *Am J Cardiol* 2005; **95**: 871–75.

211 Kenigsberg DN, Lee BP, Grizzard JD, et al. Accuracy of intracardiac echocardiography for assessing the esophageal course along the posterior left atrium: a comparison to magnetic resonance imaging. *J Cardiovasc Electrophysiol* 2006; **18**: 169–73.

212 Smith SW, Light ED, Idriss SF, et al. Feasibility study of real-time three-dimensional intracardiac echocardiography for guidance of interventional electrophysiology. *Pacing Clin Electrophysiol* 2002; **25**: 351–57.

213 Knackstedt C, Franke A, Mischke K, et al. Semi-automated 3-dimensional echocardiography: development and initial clinical experience of a new system to guide ablation procedures. *Heart Rhythm* 2006; **3**: 1453–59.

214 Tse HF, Lee KL, Wan SH, et al. Area of left ventricular regional conduction delay and preserved myocardium predict responses to cardiac resynchronization therapy. *J Cardiovasc Electrophysiol* 2005; **16**: 690–95.

215 James A. Goldstein JA, Balter S, Cowley M, et al. Occupational hazards of interventional cardiologists: prevalence of orthopedic health problems in contemporary practice. *Catheter Cardiovasc Interv* 2004; **63**: 407–11.

216 Fadl YZ, Ellenbogen KA, Grubb RL, et al. A review of spinal injuries in the invasive cardiologist. Part 1: biomechanics and pain generation. *PACE* 2007; **30**: 1012–19.

217 Fadl YZ, Ellenbogen KA, Grubb RL, et al. A review of spinal injuries in the invasive cardiologist. Part II: prevention and treatment. *PACE* 2007; **30**: 1149–57.

218 Armacost MP, Adair J, Munger T, et al. Accurate and reproducible target navigation with the Stereotaxis Niobe magnetic navigation system. *J Cardiovasc Electrophysiol* 2006; **18**: S26–S31.

219 Ernst S, Ouyang F, Linder C, et al. Initial experience with remote catheter ablation using a novel magnetic navigation system: magnetic remote catheter ablation. *Circulation* 2004; **109**: 1472–75.

220 Kerzner R, Sanchez JM, Osborn JL, et al. Radiofrequency ablation of atrioventricular tachycardia using a novel magnetic guidance system compared with a conventional approach. *Heart Rhythm* 2006; **3**: 261–67.

221 Pappone C, Vicedomini G, Manguso F, et al. Robotic magnetic navigation for atrial fibrillation ablation. *J Am Coll Cardiol* 2006; **47**: 1390–400.

222 Pappone C, Santinelli V. Remote navigation and ablation of atrial fibrillation. *J Cardiovasc Electrophysiol* 2007;**18**: S18–S20.

223 Di Biase L, Fahmy TF, Patel D, et al. Remote magnetic navigation: human experience in pulmonary vein ablation. *J Am Coll Cardiol* 2007; **50**: 868–74.

224 Ray IB, Dukkipati S, Houghtaling C, et al. Initial experience with a novel remote-guided magnetic catheter navigation system for left ventricular scar mapping and ablation in a porcine model of healed myocardial infarction. *J Cardiovasc Electrophysiol* 2007; **18**: 520–25.

225 Aryana A, d'Avila A, Heist EK, et al. Remote magnetic navigation to guide endocardial and epicardial catheter mapping of scar-related ventricular tachycardia. *Circulation* 2007; **115**: 1191–200.

226 Al-Ahmad A, Grossman JD, Wang PJ. Early experience with a computerized robotically controlled catheter system. *J Interv Card Electrophysiol* 2005; **12**: 199–202.

227 Saliba W, Cummings JE, Oh S, et al. Novel robotic catheter remote control system: feasibility and safety of transseptal puncture and endocardial catheter navigation. *J Cardiovasc Electrophysiol* 2006; **17**: 1102–5.

228 Reddy VY, Neuzil P, Malchano ZJ, et al. View-synchronized robotic image-guided therapy for atrial fibrillation ablation: experimental validation and clinical feasibility. *Circulation* 2007; **115**: 2705–14.

229 Beyar R, Gruberg L, Deleanu D, et al. Remote-control percutaneous coronary interventions: concept, validation, and first-in-humans pilot clinical trial. *J Am Coll Cardiol* 2006; **47**: 296–300.

230 Manzke R, Reddy VY, Dalal S, et al. Intra-operative volume imaging of the left atrium and pulmonary veins with rotational X-ray angiography. *Med Image Comput Assist Interv* 2006; **9**: 604–11.

231 Nademanee K, McKenzie J, Kosar E, et al. A mew approach for catheter ablation of atrial fibrillation: mapping of the electrophysiologic substrate. *J Am Coll Cardiol* 2005; **43**: 2044–53.

232 Oral H, Chugh A, Good E, et al. Radiofrequency catheter ablation of chronic atrial fibrillation guided by complex electrograms. *Circulation* 2006; **115**: 2606–12.

233 Scherr D, Dalal D, Cheema A, et al. Automated detection and characterization of complex fractionated atrial electrograms in human left atrium during atrial fibrillation. *Heart Rhythm* 2007; **4**: 1013–20.

234 Schmitt C, Estner H, Hecher B, et al. Radiofrequency ablation of complex fractionated atrial electrograms (CFAE): preferential sites of acute termination and regularization in paroxysmal and persistent atrial fibrillation. *J Cardiovasc Electrophysiol* 2007; **18**: 1039–46.

235 Luo CH, Rudy Y. A model of the ventricular cardiac action potential. Depolarization, repolarization, and their interaction. *Circ Res* 1991; **68**: 1501–26.

236 Gong Y, Xie F, Stein KM, et al. Mechanism underlying initiation of paroxysmal atrial flutter/atrial fibrillation by ectopic foci: a simulation study. *Circulation* 207; **115**: 2094–102.

237 Rotter M, Dang L, Jacquemet V, et al. Impact of varying ablation patterns in a simulation model of persistent atrial fibrillation. *Pacing Clin Electrophysiol* 2007; **30**: 314–21.

238 Ruchat P, Dang L, Virag N, et al. A biophysical model of atrial fibrillation to define the appropriate ablation pattern in modified maze. *Eur J Card Surg* 2007; **31**: 65–9.

239 Gepstein L, Evans SJ. Electroanatomical mapping of the heart: basic concepts and implications for the treatment of cardiac arrhythmias. *Pacing Clin Electrophysiol* 1998; **21**: 1268–78.

240 Ben-Haim SA. Catheter navigation in modern electrophysiology. *J Cardiovasc Electrophysiol* 2000; **11**: 1193–95.

241 Packer DL. Evolution of mapping and anatomic imaging of cardiac arrhythmias. *J Cardiovasc Electrophysiol* 2004; **15**: 839–54.

242 Packer DL. Three-dimensional mapping in interventional electrophysiology: techniques and technology. *J Cardiovasc Electrophysiol* 2005; **16**: 1110–16.

6

CHAPTER 6

Principles of NavX Mapping

Christopher Piorkowski, MD, *& Gerhard Hindricks,* MD, PhD

University of Leipzig, Heart Center, Leipzig, Germany

Summary

Modern catheter intervention treatment concepts require 3D navigation systems for catheter orientation, anatomy reconstruction, and 3D linkages between anatomical and electrical information in a variety of complex arrhythmias.

Next to the CARTO system the NavX technology has evolved into a second widely used representative of 3D nonfluoroscopic cardiac mapping systems. The system is built on the basic concept of transthoracic low-power electrical currents to enable localization of intracardiac electrodes. After initial validation of that basic principle, NavX has been designed to function as a 3D mapping system with the ability to reconstruct several chamber surface anatomies, to perform sequential activation mapping, to perform voltage mapping, to display color-coded electrical information projected to the chamber surface, and to import true anatomical images derived from CT or MRI scans. Most recently the fusion technology to superimpose a CT/MRI image and a NavX map has been introduced. As a unique feature the NavX technology enables nonfluoroscopic visualization of multiple intracardiac electrode catheters from different catheter producers in real time and with a respiratory compensation algorithm.

Clinical experience with the use of NavX mapping is broad ranging from the treatment of simple arrhythmias such as AV-nodal-reentrant tachycardia, tachycardia resulting from accessory pathways, and typical isthmus-dependent right atrial flutter, up to the treatment of complex arrhythmias such as atrial fibrillation or atrial macro-reentrant tachycardia other than typical right atrial flutter. Clinical data concordantly report efficacious treatment results at significantly reduced radiation exposure. Following that path, the first patient cohorts exist, where mapping and ablation were performed while using NavX technology without any fluoroscopy.

Introduction

During the last decade invasive electrophysiology has paced the development of 3D cardiac mapping systems. The need for that development resulted from the desire to obtain and combine accurate anatomical positions with local electrical information (e.g., local activation time, local electrogram amplitude, special electrogram characteristics, and local entrainment information) in a 3D fashion. Two-dimensional fluoroscopy was insufficient to provide such an accurate spatial anatomical and spatial electrical orientation, which in return limited the ability to treat arrhythmias with a complex 3D substrate (e.g., atrial fibrillation, atrial macroreentrant tachycardia other than typical right atrial flutter, or ventricular tachycardia of myocardial origin).

Cardiac Mapping, Third Edition Edited by Mohammad Shenasa, Gerhard Hindricks, Martin Borggrefe, and Günter Breithardt
 ISBN: 978-1-405-17572-2

In 1996, the CARTO system was introduced as the first nonfluoroscopic electroanatomical catheter–based 3D cardiac mapping system [1]. In subsequent years, other technologies for 3D nonfluoroscopic real-time localization of intracardiac catheters have been developed. The concept of using transthoracic low-power electrical currents to enable localization of intracardiac electrodes was first published in 1999 [2]. Based on that principal idea, the nonfluoroscopic mapping system NavX (Endocardial Solutions, Inc., St. Paul, MN) has been developed to support 3D intracardiac electroanatomical mapping. This chapter describes the method of the NavX technology in conjunction with its clinical applications under the perspective of current developments in the field of 3D mapping.

Method

Concept and Components

The methodology of NavX is based on the principle that when an electrical current is applied across two electrodes, a voltage gradient can be measured along the electrode axis. With a pair of electrodes placed on the thorax, NavX generates a low-power 5.7-kHz electrical potential across the body, to create a voltage gradient along the axis. Using any intracardiac electrode, NavX measures the local voltage on the electrode and calculates the electrode position along the axis. When three pairs of electrodes are placed on the body in orthogonal directions (neck-leg, front-back, left-right), NavX alternately creates and measures a voltage gradient on each axis, to create a 3D navigation field [3].

Up to 64 electrodes can be located simultaneously. All intracardiac electrodes connected to NavX are located 93 times per second and can be displayed in real time. Having entered known catheter parameters such as electrode length and interelectrode spacing, the catheter shaft between visualized electrodes is accurately extrapolated and added as an animation (Figure 6.1a). In catheters with multiple electrodes added to the shaft, direct visualization not only of the catheter tip but also of longer parts of the whole distal catheter is possible.

A respiration compensation algorithm, based on the identification of gradual changes in transthoracic impedance, can be applied to help to reduce artefacts caused by patient respiration. Hardware filters allow navigation to continue during radiofrequency ablation. Reconstruction of cardiac chamber anatomy can be performed by moving any chosen catheter (also multipolar catheters) along the endocardial surface and collecting the visited 3D locations manually or through an automatic point collection mode (Figures 6.1b and 6.1c). Anatomical positions can be marked as projections onto the reconstructed chamber surface or as independent 3D lesion spheres (Figure 6.1a). Apart from geometry reconstruction the system offers sequential point-by-point mapping with recording of the local activation time or recording of the local voltage amplitude. The system allows 3D CT or MRI images of cardiac chambers to be imported, automatically synchronizes map and image to an AP view, and rotates map and image synchronously (Figure 6.2). Most recently the software has been implemented to allow fusion of map and image (Figure 6.3).

The NavX methodology results in an open system, where all kinds of electrode catheters (e.g., steerable catheters, nonsteerable catheters, mapping catheters, ablation catheters, Lasso catheters, Halo catheters, even pacemaker leads) from many companies can be used and visualized nonfluoroscopically (Figure 6.1a). The NavX system in itself only comprises the three pairs of single-use skin patches placed in orthogonal planes, a breakout box. and a computer unit to process the delivered signals.

Evaluation and Validation

Evaluation and validation of the general principle of nonfluoroscopic intracardiac catheter visualization through low-power transthoracic electrical currents had been performed with the LocaLisa system [2]. During initial testing effects of the externally applied field, influences of cardiac and respiration cycle, localization stability, and localization accuracy were evaluated in 74 patients [2]. While mapping the major portion of the right atrium, right ventricle, and left ventricle, and covering distances of over 50 mm, nonfluoroscopic measurements of interelectrode distances highly correlated with the true distances for each of the chambers [2].

During a time interval of 128+/−82 min the electrode localization was stable with an average change in position of 0.2+/−1.7 mm for the X, 0.1+/−0.3 smm for the Y, and 0.2+/−0.6 mm for

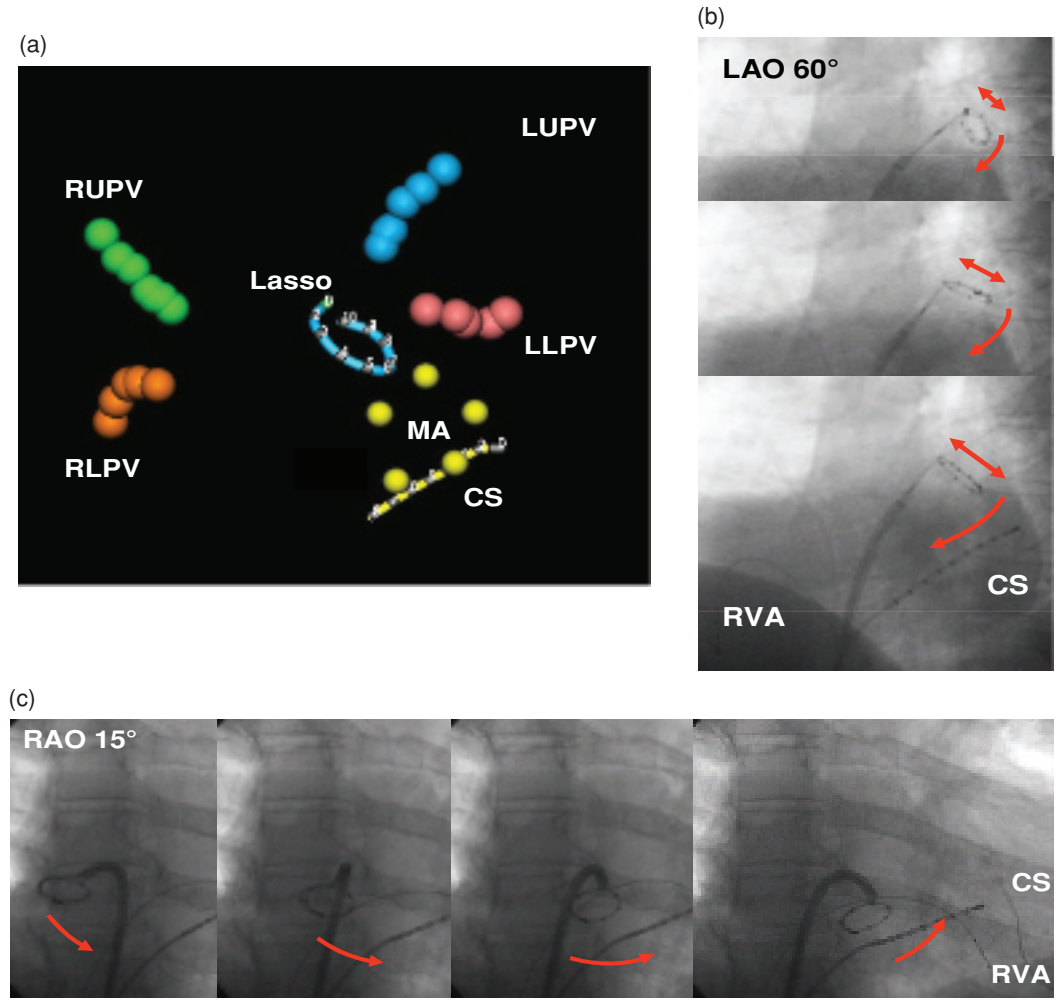

Figure 6.1 (a) Lasso and CS catheter visible in NavX. Pulmonary veins and mitral annulus have been tagged for general orientation. (b) Anatomical 3D reconstruction of the left upper pulmonary vein: Lasso is slowly withdrawn and opened to map the whole pulmonary vein funnel. (c) Anatomical 3D reconstruction of the left atrial septum: Lasso catheter is wiped over the septum from the right lower pulmonary vein to the mitral annulus.

the *Z* direction [2]. In the NavX system the field frequency of the external current is chosen near the geometric mean of biopotentials and radiofrequency ablation frequencies, which allows separation of the potentials, does not interfere with local electrogram quality, and enables catheter tracking during ablation [4]. The transthoracic current did not create any patient discomfort.

An early report on the clinical use of the NavX system for 3D reconstructions of cardiac chamber anatomy and for nonfluoroscopic visualization of intracardiac catheter positions was published in 2004. Among 16 patients, 20 arrhythmias were mapped and targeted for ablation, among them simple arrhythmias such as AVNRT or typical right atrial flutter, but also 11 cases of left atrial ablation for the treatment of atrial fibrillation already [4]. At that time the system still provided only anatomical information. Three-dimensional distribution of electrical information such as activation or voltage maps were implemented later, but are now routinely available (Figure 6.4).

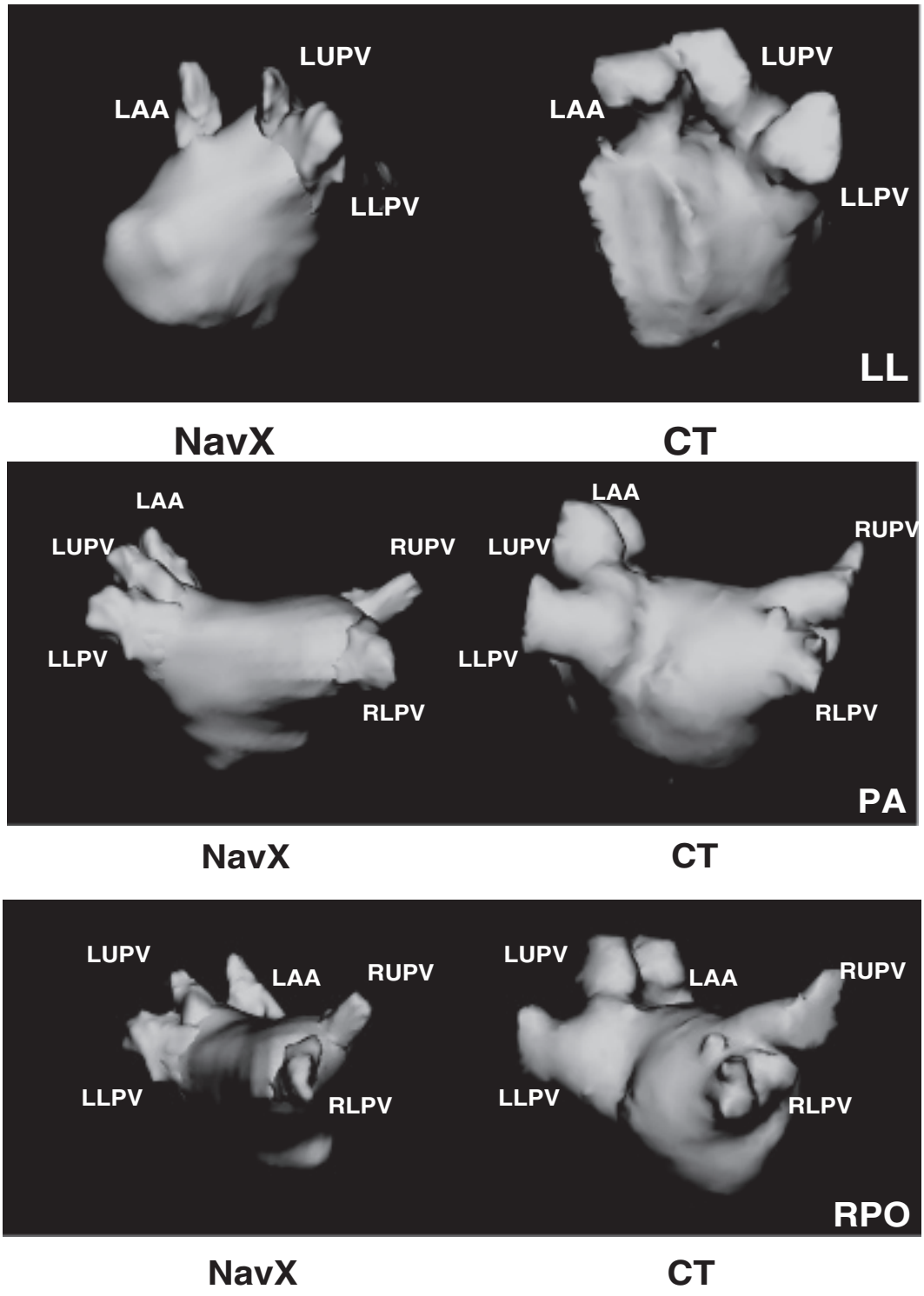

Figure 6.2 Left atrial 3D anatomy reconstructed on NavX using a multipolar (Lasso) catheter for automatic point acquisition, compared to the CT scan of the same patient from a LL, PA, and RPO view.

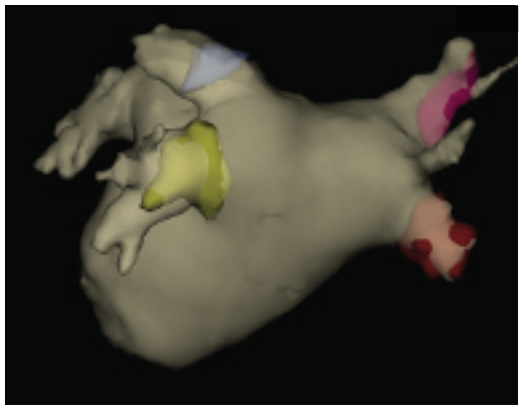

Figure 6.3 Complete integration of a preacquired 3D CT image (NavX fusion algorithm) of the left atrium. The surface of the four pulmonary veins has been reconstructed using a Lasso catheter for automatic acquisition of anatomical points. Each pulmonary vein was reconstructed in a separate anatomy (blue: left upper PV, yellow: left lower PV, red: right upper PV, brown: right lower PV). These reconstructed anatomies served as landmark surfaces for alignment and integrating of the CT image. The anatomy of the body of the left atrium was not reconstructed.

Three-Dimensional Mapping with NavX

Current electrophysiological catheter interventional treatment concepts require the availability of three distinct types of mapping procedures to be incorporated in a 3D mapping system that can be used in clinical routine. Depending on the type of arrhythmia, its inducibility, its stability, and the patient's hemodynamic response activation mapping, voltage mapping, or purely anatomical maps are needed.

Just like other 3D mapping systems NavX allows to acquire anatomical points with local activation time during sequential activation mapping. The activation time is calculated according to a fixed intracardiac reference signal. The points can be projected onto a pre-acquired 3D chamber anatomy, or the chamber anatomy can be reconstructed together with the point acquisition. Points of similar activation time are connected through color-coded isochronal lines, which are superimposed onto the anatomy and help to visualize the electrical information (e.g., earliest activation site, spread of activation) in a 3D fashion. Currently, sequential activation mapping is a preferred approach to study inducible, sustained, and hemodynamically tolerable arrhythmias.

For arrhythmias not meeting those criteria sequential activation mapping is of limited value. Simultaneous activation mapping offers the possibility to derive electrical information (e.g., exit point, earliest activation site, and spread of activation) from single beats of noninducible, nonsustained, or hemodynamically unstable arrhythmias. The EnSite balloon (Endocardial Solutions, Inc., St. Paul, MN) is the main representative for simultaneous non-contact activation mapping [5].

The 8-ml ellipsoid balloon is surrounded by 64 electrically insulated wires, each with a small laser-etched break in insulation, allowing them to function as unipolar electrodes. When the balloon is positioned in the target chamber, far-field electrographic data are fed into an amplifier system and a workstation. Based on mathematical models the spread of activation is calculated and projected onto the surrounding chamber surface. Inaccurate chamber anatomy with the lack of exact spatial orientation has been one of the limitations for a widespread use of the EnSite balloon. Today, with the EnSite technology being one of the components of the EnSite-NavX system, both technologies are integrated in one workstation and can be easily combined. The accurate anatomical reconstruction acquired through the NavX technology can be used as a surrounding chamber anatomy for the EnSite balloon. Larger clinical experiences with a simultaneous activation mapping approach through the combined use of EnSite and NavX are still awaited.

A different approach toward patients with noninducible, nonsustained, or hemodynamically unstable arrhythmias is to use information on the local electrogram amplitude to delineate diseased or even scarred myocardium and to plan an ablation strategy during sinus rhythm—so-called "voltage mapping." Using this concept, the NavX system allows us to describe larger areas of electrically diseased or even scarred myocardium serving as arrhythmia substrate in a 3D fashion.

The third type of mapping commonly required for ablation procedures is the pure reconstruction of a 3D chamber anatomy. This type of mapping procedure is needed for mainly anatomically based ablation concepts, such as the treatment of atrial

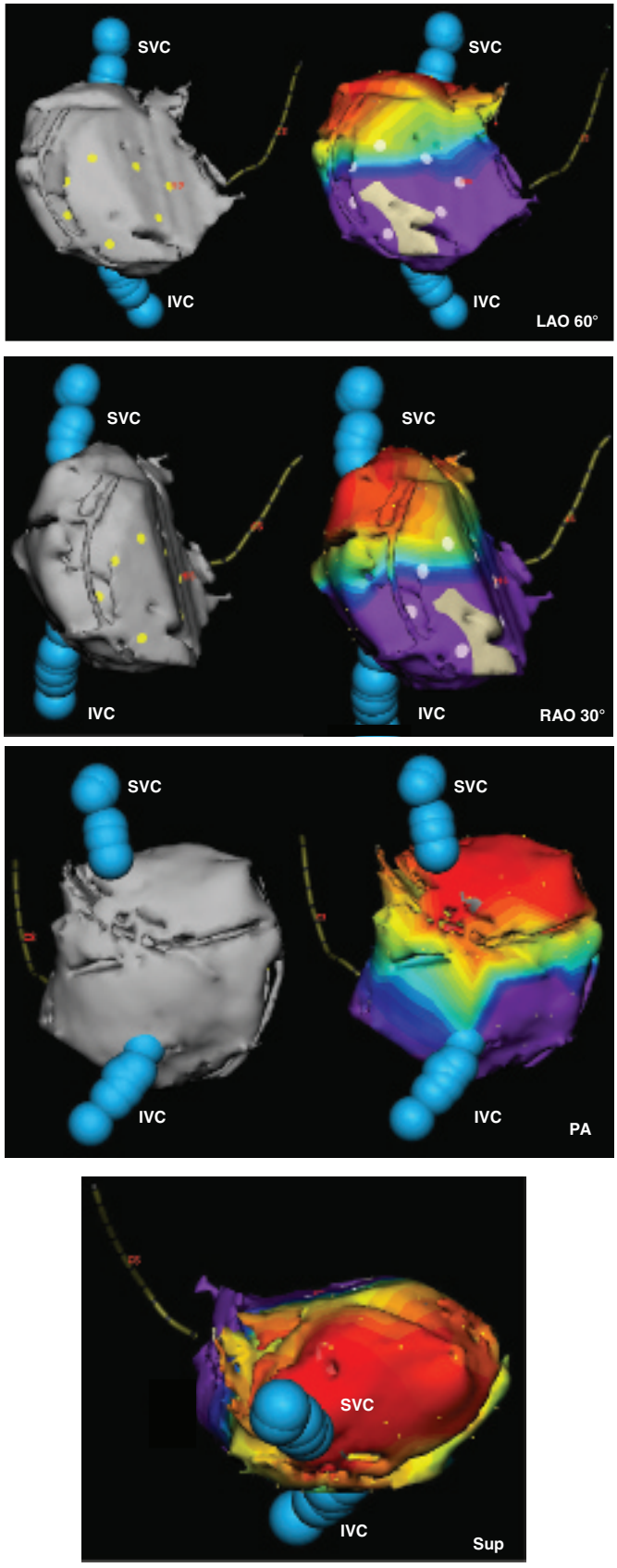

Figure 6.4 Patient presented for ablation with an atrial macroreentrant tachycardia. Complete integration of a pre-acquired 3D CT image (NavX fusion algorithm) of the right atrium was used for anatomical orientation. No anatomical surface reconstruction was performed. Registration, alignment, and integration of the CT scan was achieved solely through seven landmark points at the tricuspid annulus, one landmark point in the inferior isthmus, one landmark point in the fossa ovalis, and one landmark point in the right atrial appendage. Superior caval vein (SVC) and inferior caval vein (IVC) were marked through anatomical 3D points. The registered CT was the basis for 3D navigation and orientation. At different points within the right atrium, entrainment mapping was performed. The time difference between the post-pacing-interval and the tachycardia cycle length (= return cycle) was color-coded and projected onto the CT surface. Red areas indicate points with a short return cycle, therefore, being close to the reentrant circuit.
Three-dimensional distributions of the entrainment properties reveal a reentrant circuit around the superior caval vein (= upper loop reentry). Placement of an ablation line between the superior tricuspid annulus and the SVC terminated the tachycardia and left the patient noninducible. The incisions on the CT surface (especially in the PA projection) resulted from artefacts within the CT scan caused by the leads of a dual chamber ICD.

fibrillation or isthmus-dependent right atrial flutter. For 3D anatomical maps the focus lays on the accuracy and the resolution of the map to enable a realistic anatomical orientation, which is crucial to reach ablation target sites and to prevent collateral damage toward sensitive neighboring structures. In the NavX system reconstruction of cardiac chamber anatomy can be performed by moving any chosen catheter (also multipolar catheters) along the endocardial surface and collecting the visited 3D locations manually or through an automatic point collection mode (Figure 6.1). The latter algorithm in conjunction with a multipolar mapping catheter (e.g. a Lasso catheter, which can acquire anatomical points through all of its electrodes) offers a fast acquisition of a high density of anatomical locations resulting in a highly accurate 3D anatomy, especially in the region of the PV funnels and the LA–PV junction (Figures 6.1 and 6.2).

Special Features of 3D NavX Mapping

The need to three-dimensionally combine anatomical and electrical information to understand and successfully treat complex cardiac arrhythmias creates the need to use 3D nonfluoroscopic mapping systems. Accurate electrical and accurate anatomical information are mandatory for this purpose. The quality of the electrical signal is influenced by factors such as tissue contact, signal quality of the catheter electrode, and the presence of electrical noise.

Nowadays, most catheter companies and EP recording systems provide sufficient signal quality to allow for an accurate signal interpretation. The quality of the anatomical information is influenced by the accuracy and the resolution of the 3D reconstruction. The high density of anatomical points acquired during automatic NavX surface reconstruction algorithms provides the basis for the visualization of small details within the 3D chamber anatomies (Figure 6.2). Further improvement in anatomical orientation can be achieved through visualization of the patient's true anatomy obtained from 3D images. For this purpose NavX allows 3D CT or MRI images of cardiac chambers to be imported, automatically synchronizes a map and image to an AP view, and rotates the map and image synchronously (Figure 6.2).

Most recently, software has been released to allow complete fusion of map and image. In this way, catheter navigation, collection of electrical information, and ablation can be performed within the 3D CT/MRI image. Early experiences with the fusion technology are promising (Figure 6.3). The qualities of the registration and alignment process provide a highly accurate superimposition of the image over the map. It appears possible to limit the amount of anatomical chamber surface reconstruction and simply work within a highly accurate registered CT anatomy (Figure 6.4). For left atrial procedures, experience does exist to only reconstruct the pulmonary vein anatomy to be used as the landmark surface for the registration of the whole left atrium (Figure 6.3). Only using the 3D CT/MRI anatomy for the analysis and treatment of complex cardiac arrhythmias, such as atrial macroreentrant tachycardia, offers the charm that the electrical information obtained from the tip of the ablation catheter can be directly linked to its exact anatomical location of acquisition. NavX supports that approach by projecting electrical information such as activation or voltage maps onto the surface of the registered CT/MRI image (Figure 6.4).

Common catheter interventional treatment approaches require the placement of linear ablation lines within the target areas. Line continuity and transmurality appear to be critical points influencing the long-term success after the ablation procedure. Differential pacing is an electrophysiologically based approach to find and close gaps within the ablation line and to eventually verify line continuity. This approach requires at least two intracardiac electrodes to be positioned near to the ablation line in order to document bidirectional block. Fluoroscopically, this appears difficult given the 3D fashion of ablation line placement. As initially described, NavX allows us to nonfluoroscopically visualize multiple intracardiac electrode catheters. This enables accurate electrode positioning on both sides close to the ablation lesion and, therefore, represents a simple approach for differential pacing and testing of line continuity. In the same context the advantages of nonfluoroscopic 3D Lasso catheter visualization for achieving and assessment of complete pulmonary vein isolation have to be seen.

Clinical Experience with NavX Mapping

In 2004 and 2005, reports were published to use NavX for nonfluoroscopic anatomical orientation for ablation of simple arrhythmias such as AV-nodal-reentrant tachycardia, accessory pathways, or isthmus-dependent right atrial flutter [4, 6]. Because activation mapping was not yet available, the utility of the NavX system was limited to 3D nonfluoroscopic catheter orientations. Due to the known pathophysiology, the clearly defined treatment approach and procedural endpoint, and the excellent cure rates with conventional fluoroscopically guided catheter ablation for the treatment of these simple arrhythmias, NavX could not improve the clinical outcome; however, concordantly through all publications it significantly reduced radiation exposure.

In a study comparing CARTO and NavX against a conventional fluoroscope-guided ablation of AV-nodal-reentrant tachycardia, accessory pathway, and isthmus-dependent right atrial flutter, both nonfluoroscopic mapping systems significantly reduced fluoroscopy time at similar procedure durations but at the expense of higher procedural costs. The effect on radiation reduction exerted by NavX was significantly higher when compared to CARTO (median fluoroscopy time: 13 min conventionally, 6 min with CARTO, 4 min with NavX) [7]. The ability to dramatically reduce radiation exposure during electrophysiological procedures by using NavX technology has been further supported by two studies describing complete mapping and ablation of supraventricular arrhythmias without any fluoroscopy in an infant population [8, 9].

Soon after the initial clinical reports on the NavX system case series had been published, the technology was applied for ablation of complex left atrial arrhythmias such as atrial fibrillation as well. In a study using Lasso-guided PV isolation for AF treatment the system helped to reduce procedure and fluoroscopy time at similar success rates [10]. From today's perspective NavX technology represents an established nonfluoroscopic cardiac mapping system that is able to guide complex left atrial ablation procedures.

Other areas of possible clinical use have been shown by case publications reporting on nonfluoroscopic pacemaker implantation using NavX [11]. However, more clinical data are necessary to be able to fully judge that approach.

Summary

The need for accurate location information is becoming more and more important for successful treatment of arrhythmias originating from a complex 3D substrate. Nonfluoroscopic cardiac mapping systems are designed to provide the required spatial anatomical information in combination with local electrical information, thereby creating a 3D understanding and visualization on the mechanism of the tachycardia. During recent years the NavX technology has evolved as one of the major representatives of those nonfluoroscopic cardiac mapping systems. The ability to nonfluoroscopically visualize multiple electrode catheters, together with accurate anatomy reconstructions and an advanced image/map fusion technology have made NavX a helpful tool to understand and successfully treat simple and complex cardiac arrhythmias at shorter procedure times and a significantly reduced rate of radiation exposure.

References

1 Ben-Haim SA, Osadchy D, Schuster I, et al. Nonfluoroscopic, in vivo navigation and mapping technology. *Nat Med* 1996; **2**: 1393–95.

2 Wittkampf F, Wever E, Derksen R et al. LocaLisa: new technique for real-time 3-dimensional localization of regular intracardiac electrodes. *Circulation* 1999; **99**: 1312–17.

3 Markides V, Davies WD. New mapping technologies: an overview with a clinical perspective. *J Interv Card Electrophysiol* 2005; **13**: 43–52.

4 Krum D, Goel A, Hauck J, et al. Catheter location, tracking, cardiac chamber geometry creation, and ablation using cutaneous patches. *J Interv Card Electrophysiol* 2004; **12**: 17–22.

5 Peters NS, Jackman W, Schilling RJ, et al. Human left ventricular endocardial activation mapping using a novel noncontact catheter. *Circulation* 1997; **95**: 1658–60.

6 Ventura R, Rostock T, Klemm HU, et al. Catheter ablation of common-type atrial flutter guided by three-dimensional right atrial geometry reconstruction and catheter tracking using cutaneous patches: a randomized prospective study. *J Cardiovasc Electrophysiol* 2004; **15**: 1157–61

7 Earley MJ, Showkathali R, Alzetani M, et al. Radiofrequency ablation of arrhythmias guided by nonfluoroscopic catheter location: a prospective randomized trial. *Eur Heart J* 2006; **27**: 1223–29.

8 Smith G, Clark JM. Elimination of fluoroscopy use in a pediatric electrophysiology laboratory utilizing three-dimensional mapping. *PACE* 2007; **30**: 510–18.

9 Tuzcu V. A nonfluoroscopic approach for electrophysiology and catheter ablation procedures using a three-dimensional navigation system. *PACE* 2007; **30**: 519–25.

10 Estner HL, Deisenhofer I, Luik A, et al. Electrical isolation of pulmonary veins in patients with atrial fibrillation: reduction of fluoroscopy exposure and procedure duration by the use of a non-fluoroscopic navigation system (NavX). *Europace* 2006; **8**: 583–87.

11 Ruiz-Granell R, Morell-Cabedo S, Ferrero-De-Loma A, et al. Atrioventricular node ablation and permanent ventricular pacemaker implantation without fluoroscopy: use of an electroanatomic navigation system. *J Cardiovasc Electrophysiol* 2005; **16**: 793–95.

7

CHAPTER 7

Magnetic Navigation: Catheter Ablation

Sabine Ernst, MD, FESC

Royal Brompton and Harefield Hospital, London, UK

Summary

More than four years after the introduction of the remote-controlled navigation system Niobe (Stereotaxis, Inc.), this new platform has established its role in electrophysiologic (EP) laboratories worldwide. While most of the experience has been in SVT ablation procedures, recent reports have featured successful application of this technology to more complex arrhythmias such as ventricular tachycardia and atrial fibrillation. However, awaiting the availability of an irrigated magnetic catheter to perform more complex ablation procedures, electroanatomical 3D mapping has been successfully integrated into the system already.

Introdution

For more than four years. magnetic navigation has been available as a novel tool for catheter ablation procedures [1–2]. Small magnets are integrated into the tip of a very soft ablation catheter which can be moved by using a well-defined outer magnetic field (0.08 Tesla) [1, 2]. By changing the orientation of the outer magnets, the small magnets in the catheter tip arrange parallel to the outer magnetic field lines. The combination with a mechanical motor drive allows operating the magnetic mapping and ablation catheter fully remote-controlled [3].

Available Ablation Catheters

The first-generation ablation catheter equipped with a single magnet (1M) consisted of a 4-mm tip and a single-ring electrode (2 mm) allowing single bipolar recordings only. It was mostly used in supraventricular tachycardia (SVT) ablations [3–7]. The second-generation catheter had a total of three magnets embedded (3M) in the distal shaft, but still only two electrodes. Because all embedded magnets will parallel out in the outer magnetic field, the ability of this catheter to respond to more acute vectors was much improved. Further development led to the implementation of two additional ring electrodes to allow two bipolar recordings (3M quad). Subsequently, the catheter tip was extended to a total length of 8 mm (3M 8 mm) to achieve larger lesion formation. And, finally, an irrigated tip is supposed to become available shortly.

Compatibility with 3D Mapping Systems

Initially, only the LocaLisa system (Medtronic, Minneapolis, MN) and the NAVx mapping system

Cardiac Mapping, Third Edition Edited by Mohammad Shenasa, Gerhard Hindricks, Martin Borggrefe, and Günter Breithardt
 ISBN: 978-1-405-17572-2

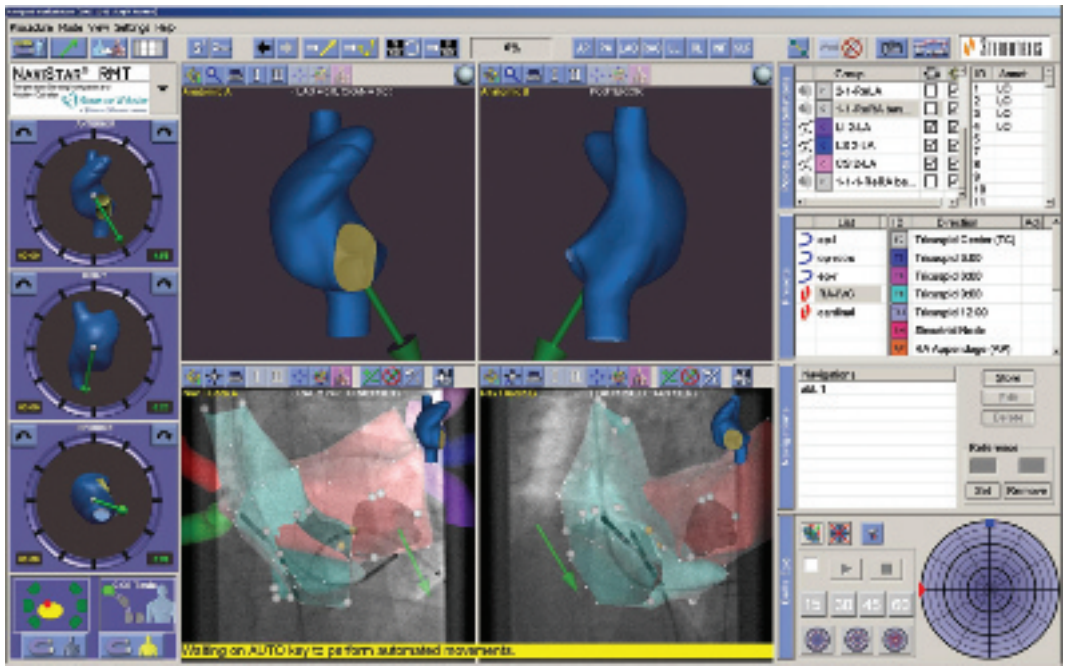

Figure 7.1 Example of the Navigant workstation with CARTO maps of both right (RA) and left atrium (LA) displayed in the corresponding fluoroscopy reference pictures.

(St. Jude Medical, St. Paul, MN) were compatible with the magnetic navigation system. Both work on the same principle which enables us to locate all catheters positioned in the thorax between the condensator-like patches.

Recently, a fully integrated 3D electroanatomical CARTO system (CARTO RMT, Biosense Webster, Bruessels, Belgium) was introduced that works with its ultralow electromagnetic field (10^{-12} T) with the permanent magnetic field of the navigation system (0.08 T). In addition, cross-talk between the fluoroscopy system, the magnetic navigation system, and the CARTO RMT system is enabled, such that the information is displayed superimposed on the fluoroscopic reference pictures (Figure 7.1). Figure 7.2 depicts an example of a fully remote-controlled reconstruction of the right and left atrium during sustained ectopic atrial tachycardia.

Tachycardia Substrates

After the first report on remote-controlled catheter ablation of AV nodal reentrant tachycardia, most of the reports have dealt with supraventricular tachycardia substrates [3–8]. However, several reports have focused on focal ventricular outflow tract arrythmias with excellent success rates [9–11]. Using the CARTO RMT system, an idiopathic left ventricular tachycardia has been successfully treated [12]. Theoretically, the soft catheter shaft should reducd the risk of mechanical block during mapping of the left ventricular septum.

Recently, remote-controlled mapping and subsequent ablation of scar-related left ventricular tachycardia has been reported [13]. Despite the need to switch to irrigated tip conventional ablation in several cases, mapping of the LV was mostly done remote-controlled. Accuracy of the acquired map was reported to be sufficient to identify the scar areas and to guide the potential reentrant circuits. Interestingly, the authors solved the problem of exposure of the mostly ICD wearing patients to the permanent magnetic field. Apparently, this did not cause any permanent losses or damages of the devices, but the authors did not go into details about this effect.

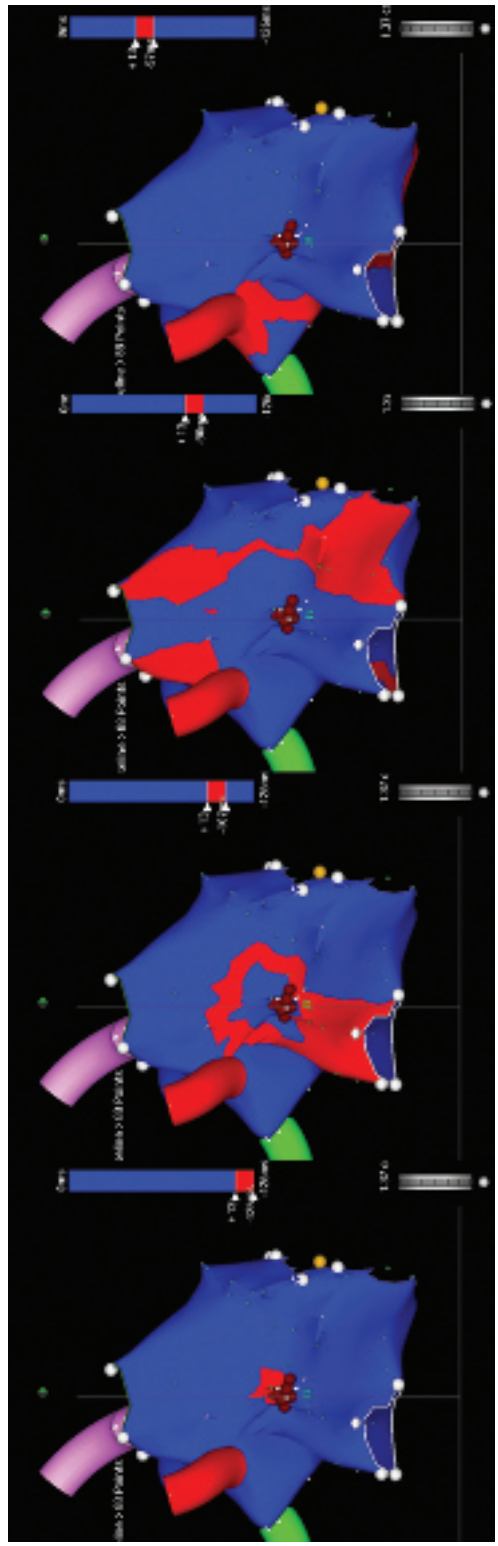

Figure 7.2 Propagation map of a RA ectopic atrial tachycardia (EAT) in right lateral projection. Note the radial spread of the activation wavefront in red on the blue shell of the reconstructed geometry of both RA and LA (origin of EAT at crista terminalis).

Transseptal Versus Antegrade Approach for Left-Sided Substrates

Several groups have meanwhile reported on their experiences addressing left-sided substrates [7, 14–15]. Some disagreement seems to exist on the most practical approach to achieve stable and effective catheter positioning (e.g., for a left lateral pathway. Surely, a remote-controlled retrograde passage of the aortic valve is doable; however. due to the papillary muscles and mitral valve tendons, in addition to the LV contraction pushing the soft catheter shaft, mapping along the mitral annulus is somewhat challenging [14–15]. Using the transseptal route, mapping along the smooth left atrial aspect of the mitral annulus is easily enabled using the target navigation mode of the system [7]. In the largest series published so far, success rates were dramatically improved when the investigators chose the transseptal access as the primary strategy. As an additional side effect, the total fluoroscopy exposure was significantly reduced in comparison to the retrograde approach.

Reduced Catheter Approach to SVT

In a recent report, a further strategy to use the magnetic navigation system was proposed. In contrast to the conventional diagnostic approach in electrophysiology (EP) studies, with several catheters displaying the electrical information simultaneously, a sequential diagnostic approach has been introduced into clinical practice [16]. Using the feature of preset vectors for specific sites such a the His recording site or coronary sinus ostium, the magnetic catheter is sequentially steered to multiple sites to record local activation in relation to a single diagnostic catheter positioned in the right ventricular apex (but with additional proximal electrodes).

Success rates in simple SVT substrates are excellent with a need to introduce additional catheters in only ∼15% of cases. However, facing more than a single SVT substrate or unusual cardiac anatomy, this strategy should be abandoned, but allows easy addition of additional conventional diagnostic catheters. In comparison to the conventional 5-catheter approach (but still using magnetic navigation for ablation), all procedural parameters were significantly reduced with a large emphasis on total radiation exposure [17].

Further Advantages of Remote Magnetic Navigation

One of the most obvious advantages of a remote-controlled catheter navigation system is the reduced fluoroscopy exposure for the investigator. After all catheters are inserted and positioned in the specific locations, mapping and subsequent ablation will be performed from the control room without further exposure to scattered radiation [18]. However, if this comes at the expense of increased radiation exposure for the patients, this remote position of the investigator would not be very beneficial because it would demonstrate the poor orientation of the investigator.

The outer magnetic field is permanent because it is formed by magnetic metals called "rare earthers," which have magnetic properties, so the position of the magnetic catheter is only changed when the field vector is altered. Therefore, the catheter position is stable, and good contact is ascertained by little beat-to-beat variation of the distal bipolar signal. When accustomed to being "remote," reduction of the overall fluoroscopy exposure can be demonstrated (Figure 7.3). This might potentially be of even greater interest in arrhythmias that require increased levels of fluoroscopy exposure, such as atrial fibrillation (AF) ablation.

Remote-Controlled Ablation of Atrial Fibrillation (AF)

Despite initial reports of a single center in their experience using the solid 4-mm tip, the majority of groups have not yet touched on this most interesting, but also most challenging, substrate [19]. Lately, a second group has published their experience using the 8-mm tip catheter in conjunction to the CARTO RMT system, and they have reported good success during short-term follow-up [20]. The urgently awaited irrigated-tip catheter will certain encourage more centers to apply their AF ablation strategy via remote control. So far, mostly mapping and ablation in re-procedures have been published. However, switching to a handheld irrigated catheter

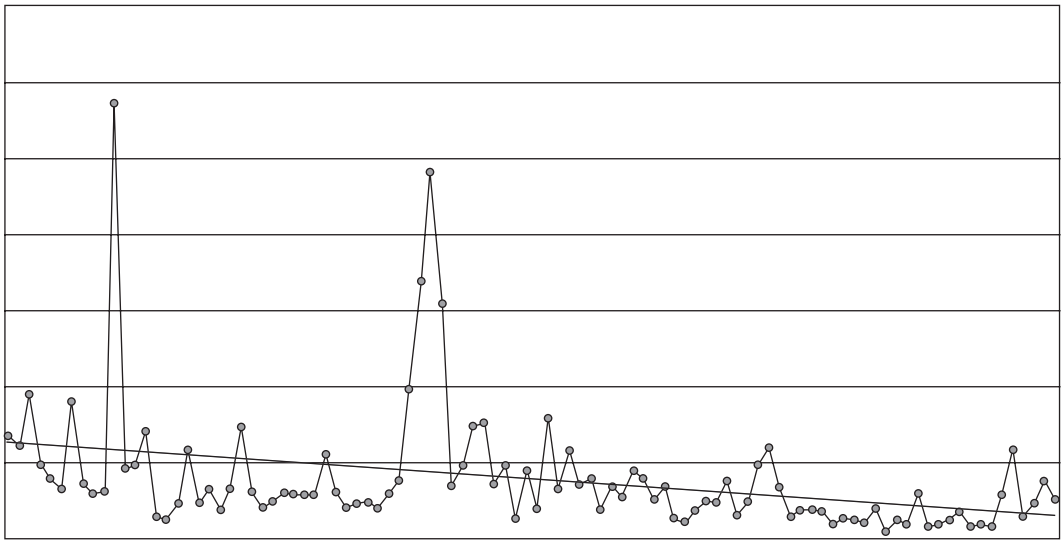

Figure 7.3 Effect of the learning curve based on the total fluoroscopy exposure in first 100 pts undergoing remote-controlled magnetic catheter ablation of AV nodal reentrant tachycardia (including a calculated linear trendline).

certainly reduces the effect on radiation exposure for the investigator.

Conclusion

The magnetic navigation system is, more than 5 years after its introduction into clinical practice, able to successfully perform all varieties of tachycardia substrates including ventricular tachycardia and even AF ablation. However, the irrigated tip catheter, expected to be available shortly, will further broaden the spectrum of addressable arrhythmias and will allow entering the arena of complex arrhythmias with fewer risks of potential side effects. A significant reduction of radiation exposure can be demonstrated for the investigator, in particular, but also for the patient, using the remote-controlled navigation system after fulfilment of a learning curve.

References

1 Faddis MN, Blume W, Finney J, et al. Novel, magnetically guided catheter for endocardial mapping and radiofrequency catheter ablation. *Circulation* 2002; **106**: 2980–85.

2 Faddis MN, Chen J, Osborn J, Talcott M, Cain ME, Lindsay BD. Magnetic guidance system for cardiac electrophysiology: a prospective trial of safety and efficacy in humans. *J Am Coll Cardiol* 2003; **42**: 1952–58.

3 Ernst S, Ouyang F, Linder C, et al. Initial experience with remote catheter ablation using a novel magnetic navigation system. *Circulation* 2004; **109**: 1472–75.

4 Ernst S, Ouyang F, Under C, et al. Modulation of the slow pathway in the presence of a persistent left superior caval vein using the novel magnetic navigation system *Niobe. Europace* 2004; **6**: 10–14.

5 Ernst S, Hachiya H, Chun JK, Ouyang F. Remote catheter ablation of parahisian accessory pathways using a novel magnetic navigation system-a report of two cases. *J Cardiovasc Electrophysiol* 2005;**16**: 659–62.

6 Kerzner R, Sanchez JM, Osborn JL, et al. Radiofrequency ablation of atrioventricular nodal reentrant tachycardia using a novel magnetic guidance system compared with a conventional approach. *Heart Rhythm* 2006; **3**: 261–67.

7 Chun JK, Ernst S, Matthews S, et al. Remote-controlled catheter ablation of accessory pathways: results from the magnetic laboratory. *Eur Heart J* 2007; **28**: 190–95.

8 Chun JKR, Ernst S, Schmidt B, Ujeyl A, Kuck KH. Remote-control magnetic ablation of a right anterolateral accessory pathway: the superior vena caval approach. *J Intervent Cardiovasc Electrophysiol* 2006, **16**: 65–8.

9 Thornton AS, Jordaens LJ. Remote magnetic navigation for mapping and ablating right ventricular outflow tract tachycardia. *Heart Rhythm* 2006; **3**: 691–96.

10 Burkhardt JD, Saliba WI, Schweikert RA, Cummings J, Natale A. Remote magnetic navigation to map and ablate left coronary cusp ventricular tachycardia. *J Cardiovasc Electrophysiol* 2006; **17**: 1142–44.

11 Thornton AS, Jordaens LJ. Remote magnetic navigation for mapping and ablating right ventricular outflow tract tachycardia. *Heart Rhythm* 2006; **3**: 691–96.

12 Thornton AS, Res J, Mekel JM, Jordaens LJ. Use of advanced mapping and remote magnetic navigation to ablate left ventricular fascicular tachycardia. *Pacing Clin Electrophysiol* 2006; **29**: 685–88.

13 Aryana A, d'Avila A, Heist EK, Mela T, Singh JP, Ruskin JN, Reddy VY. Remote magnetic navigation to guide endocardial and epicardial catheter mapping of scar-related ventricular tachycardia. *Circulation.* 2007; **115**: 1191–200.

14 Thornton AS, Jordaens L. A left-sided accessory pathway revisited with remote retrograde magnetic navigation. *Pacing Clin Electrophysiol.* 2007; **30**: 573–76.

15 Thornton AS, Rivero-Ayerza M, Knops P, Jordaens LJ. Magnetic navigation in left-sided AV reentrant tachycardias: preliminary results of a retrograde approach. *J Cardiovasc Electrophysiol* 2007; **18**: 467–72.

16 Ernst S, Chun JK, Ujeyl A, Ouyang F, Kuck KH. "Sequential" mapping mimicking "simultaneous" mapping using magnetic navigation during catheter ablation of supraventricular tachycardia: results of the Single DX Study. *J Cardiovascular Electrophysiol* 2007; **1**: S11–17.

17 Ernst S, Chun KRJ, Matthews S, et al. Catheter ablation of supraventricular tachycardia using the magnetic navigation system: a comparison of two different diagnostic strategies. *Heart Rhythm* 2006; **3**: S237 (Suppl).

18 Ernst S, Chun KRJ, Schmidt B, et al. The impact of remote catheter navigation on the radiation exposure during catheter ablation of supraventricular tachycardia: results of a prospective study in SVTablation. *Circulation* 2006; A2714.

19 Pappone C, Vicedomini G, Manguso F, et al. Robotic magnetic navigation for atrial fibrillation ablation. *J Am Coll Cardiol* 2006; **47**: 1390–400

20 Di Biase L, Fahmy TS, Patel D, et al. Remote magnetic navigation: human experience in pulmonary vein ablation. *J Am Coll Cardiol.* 2007; **50**: 868–74

8

CHAPTER 8

CT Angiography: Cardiac Anatomy for Mapping and Ablation of Arrhythmias

Jerold S. Shinbane, MD, FACC,[1] *Daniel Goodwin,* MD,[1]
Leslie A. Saxon, MD, FACC,[1] *Matthew J. Budoff,* MD, FACC[2]

[1]University of Southern California, Los Angeles, CA, USA
[2]Harbor-UCLA Medical Center, Torrance, CA, USA

Summary

Advanced imaging techniques have revolutionized approaches to mapping and ablation of arrhythmias in the electrophysiology laboratory. Technological advancements in cardiovascular computed tomographic angiography (CCT) have produced a level of temporal and spatial resolution that enables an accurate and detailed evaluation of cardiac anatomy and function. The ability to image and reconstruct the heart and thoracic structures allows for mapping and ablation referenced to an individual patient's 3D anatomy, with reconstructed images depicting coronary vasculature, cardiac chambers, and thoracic anatomy. The optimal use of CCT for electrophysiologic applications requires an understanding of the actual imaging techniques, as well as the strengths and limitations relevant to electrophysiologic procedures. This chapter will highlight the use of CCT for identification of cardiac substrates associated with arrhythmias, visualization of specific structures relevant to mapping and ablation, facilitation of mapping and ablation procedures, and post-procedural follow-up.

CCT Techniques: Special Considerations in Patients with Electrophysiological Issues

The indication for CCT is extremely important to decisions relating to the techniques used in the performance of a CCT scan. Most patients have undergone previous imaging as part of a cardiovascular work-up, usually with echocardiography, with an advanced imaging study such as CCT or cardiovascular magnetic resonance imaging (CMR) performed to answer questions not answered by other studies or specifically for use with electroanatomic image integration as part of an electrophysiologic procedure.

Although a noninvasive imaging technique, CCT requires intravenous iodinated contrast; therefore renal function and contrast allergy can contraindicate study. As radiation is used for imaging, the age of the patient as well as the need for other procedures that require radiation must be taken into account

Cardiac Mapping, Third Edition Edited by Mohammad Shenasa, Gerhard Hindricks, Martin Borggrefe, and Günter Breithardt
 ISBN: 978-1-405-17572-2

to minimize the cumulative dose over time. A typical radiation exposure is in the range of 10 mSv [1, 2]. Techniques are present to lower the exposure from an individual study such as dose modulation techniques at certain points in the cardiac cycle and prospective gating, but these techniques are challenging to use in the setting of atrial and ventricular ectopy as well as atrial fibrillation.

Most MDCT scanning necessitates heart rates of 50–60 beats per minute to decrease motion artifact. Beta-blocker therapy is the method of choice for achieving this goal, with both oral and intravenous protocols used, although effective control of the heart rate can still be challenging [3]. In contrast to CMR, patients with pacemakers and defibrillators can be routinely studied [4]. CT has been shown to potentially cause pacing oversensing although this is a transient phenomenon [5]. Programming of pacing features to regularize ventricular rates may be useful. These devices and leads can lead to blooming artifacts that may obscure anatomic structures. The use of appropriate filters during analysis can minimize these artifacts.

The patient should have abstained from solid food, but kept well-hydrated prior to the procedure. Image acquisition time is less than 10–12 sec, and an equally short breath hold is needed. The optimal time in the respiratory cycle for breath hold has not been clarified, although avoidance of extremes of the respiratory cycle is thought to be helpful when the images are to be used for registration with other mapping techniques in the electrophysiology laboratory. Effective imaging techniques require a 60–100 cc iodinated contrast bolus, which can be given via peripheral intravenous access. An initial timing run must be performed to estimate the circulation time, the transit time required for the contrast to reach the critical structures.

In order to image the beating heart while minimizing a motion artifact, the images are gated to the specific segments of the cardiac cycle. With retrospective gating, data are acquired throughout the cardiac cycle and specific reconstructions performed based on the percentage of the RR interval. Optimal images are usually obtained during the phase of the diastole when the heart is most quiescent. Often, 3D reconstructions are performed at 70–80% of the RR interval, although this may vary by patient and underlying heart rhythm and rate, with some studies demonstrating different optimal images during atrial fibrillation [6]. The most accurate images of the coronary vessels are obtained when the patient has a regular rhythm due to the motion of the coronary arteries, but this issue is not as significant when evaluating the left atrial and pulmonary venous anatomy. Sublingual nitroglycerin at the time of scanning is also recommended to optimize coronary artery visualization.

The specific goals of the study are important to making decisions relating to the field of view and contrast administration. The field of view must extend cranially enough to visualize the entirety of the left atrial appendage and left upper pulmonary vein and should additionally include thoracic arterial and venous vasculature when this is important for diagnosis or procedural facilitation.

For studies focusing on the left-sided structures, the timing of contrast administration and imaging is similar to that for coronary artery studies. When right-sided structures and/or thoracic vascular structures need to be well visualized, this may require greater amounts of contrast and contrast injection protocols to ensure adequate timing for arterial and venous visualization. The visualization of right atrial and right ventricular structure is further complicated by the fact that venous return from the contralateral arm, superior vena cava, and inferior vena cava provide noncontrast blood, which admixes with contrast, making use of virtual endocardial imaging more limited. These issues highlight the importance of communication with the cardiac imager to ensure that the patient parameters have been optimized and that the structures of importance are visualized given the individual clinical scenario and procedural plans.

Substrate Characterization: Specific Structural Analysis Relevant to Mapping and Ablation

Underlying structural abnormalities of the cardiovascular anatomy that predispose to arrhythmia and sudden death can be identified and characterized with CCT. As opposed to other imaging technologies requiring multiple imaging views, the serial axial slices of a CCT are reconstructed into a single 3D data cube that is available for analysis within minutes of the time of scanning.

For use in electroanatomic mapping with image integration, the actual DICOM files are imported into the mapping system with reconstruction, segmentation, and editing performed on this system at the time of study (Figures 8.1 and 8.2, discussed later in this chapter). The specific characterization of cardiovascular structures and their relation to thoracic structures is described below.

Left Atrium and Pulmonary Veins

CCT provides an accurate volumetric method of assessing the size of the left atrium [7]. Assessment of posterior left atrium and pulmonary veins is comparable to CMR [8]. Detailed analysis of the pulmonary venous anatomy has significant implications for the mapping and ablation of many supraventricular arrhythmias, including atrial fibrillation, atrial flutter, and focal atrial tachycardia. Because pulmonary vein isolation techniques are essential to atrial fibrillation ablation, detailed characterization of the pulmonary venous anatomy prior to the procedure is required through creation of anatomic roadmaps (Figure 8.3).

CCT is an established and accurate means of performing this evaluation. Comprehensive analysis of the pulmonary veins requires analysis of 2D and 3D views as well as virtual endocardial assessment of the pulmonary veins. The number, size, shape, and location of the pulmonary venous ostia are easily visualized on CCT and reconstructed accurately in a 3D rendering [9].

Quantification of veins with measurement of vein os maximum and minimum diameter, as well as eccentricity, can be performed. In order to accurately measure these parameters, the interface of the pulmonary vein os and the left atrium must be determined using multiple planes to define the long axis of the vein at the os and the true interface of the pulmonary vein os with the left atrium. The 3D spatial relationships of the pulmonary veins to the left atrium and other thoracic structures can also be characterized.

In addition to the pulmonary venous anatomy, data on other atrial characteristics are available in the 3D data cube provided by CCT and should be assessed for these findings. The atrial septum can be analyzed for evidence of a patent foramen ovale, assessment of the morphology of the atrial septum, the presence, size, and location of atrial septal defects, and assessment for atrial masses [10–13]. Evaluation of the atrial appendage for thrombus is important prior to atrial flutter and atrial fibrillation ablation procedures. The left atrial appendage is a complex structure due to the morphology and trabeculations of the appendage. CCT can provide detailed assessment of the left atrial appendage and can identify thrombi [14, 15].

Given the complexity of the appendage, though, contrast flow can mimic thrombus, and false positive studies can occur. Until further data are available, transesophageal echocardiography, and in some labs intracardiac echocardiography, remain the modalities of choice to rule out thrombus [16]. The preprocedure CCT should still be thoroughly assessed for possible evidence of left atrial thrombus.

Imaging studies can assess for evidence of fibrosis associated with atrial myopathy as well as fibrosis caused by radiofrequency catheter ablation lesions. CMR-delayed gadolinium images have been able to visualize fibrosis with radiofrequency catheter ablation for atrial fibrillation [17]. Delayed contrast enhancement should theoretically be able to visualize fibrosis associated with atrial myopathy or radiofrequency ablation, but is currently limited by technological issues including strategies to decrease radiation exposure which would allow delayed enhancement imaging.

Coronary Vasculature: Relationships to the Left Atrium and Other Cardiac Chambers

One of the main strengths of CCT is the ability to visualize the coronary arterial system. CCT has been useful for its value in ruling out coronary artery disease, and with newer techniques has demonstrated additional value in assessing the degree of coronary artery disease [18–22]. Additionally, coronary artery anomalies, some of which can be associated with sudden cardiac death, can be identified [23]. The assessment for significant coronary artery disease is extremely important to procedures that require ventricular stimulation protocols leading potentially to ventricular tachycardia or ventricular fibrillation.

(a)

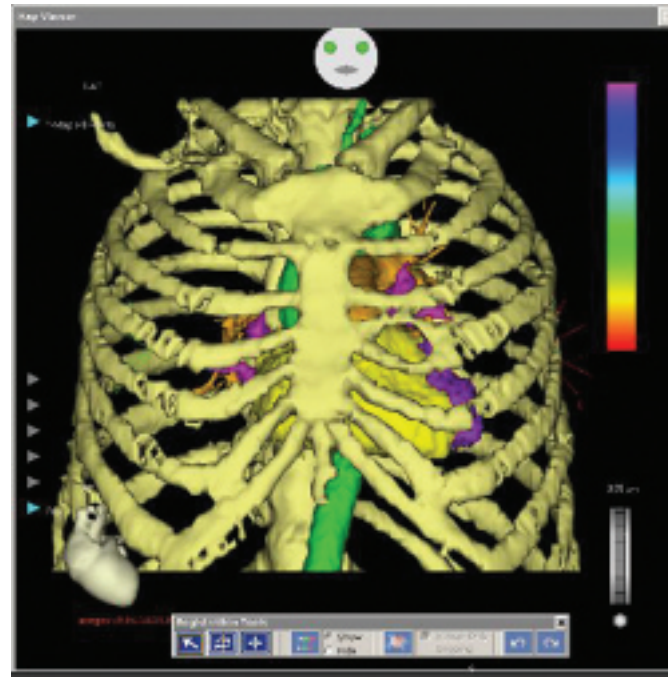

(b)

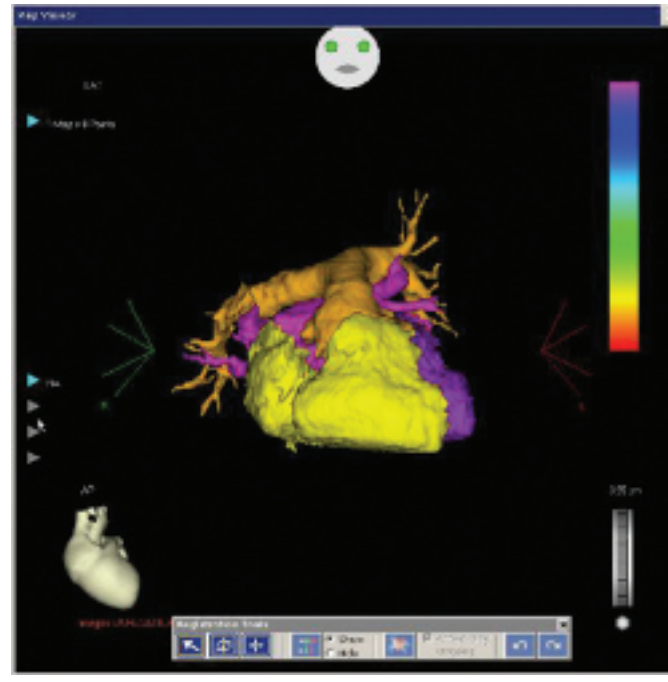

Figure 8.1 Three-dimensional reconstruction of a cardiovascular CT for electroanatomic mapping with image integration. (a) Three-dimensional image demonstrating all vascular and skeletal structures. (b) Editing of skeletal structures and aorta (green) with anterior view of pulmonary arteries (orange), right atrium and right ventricle (yellow), with the left atrium (purple). (c) Editing of pulmonary arteries. (d) Editing of right atrium and right ventricle. (e) Left atrium (posterior view).

(c)

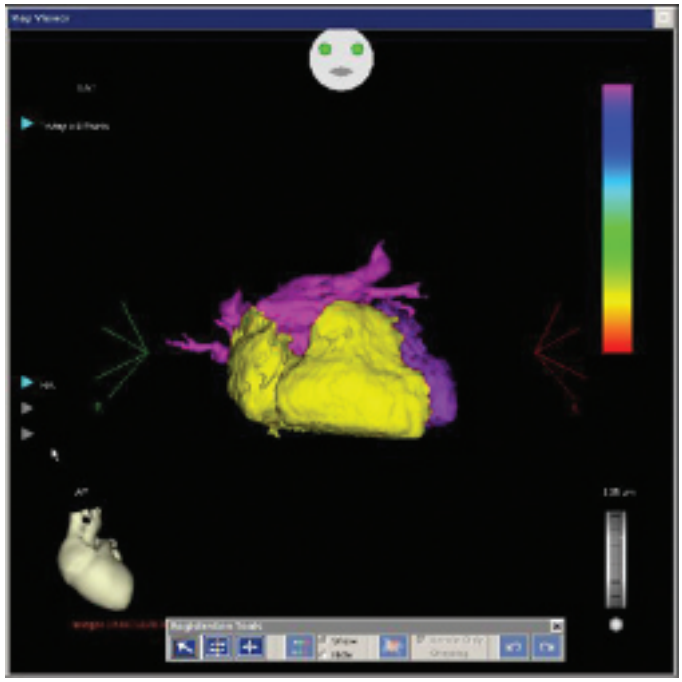

(d)

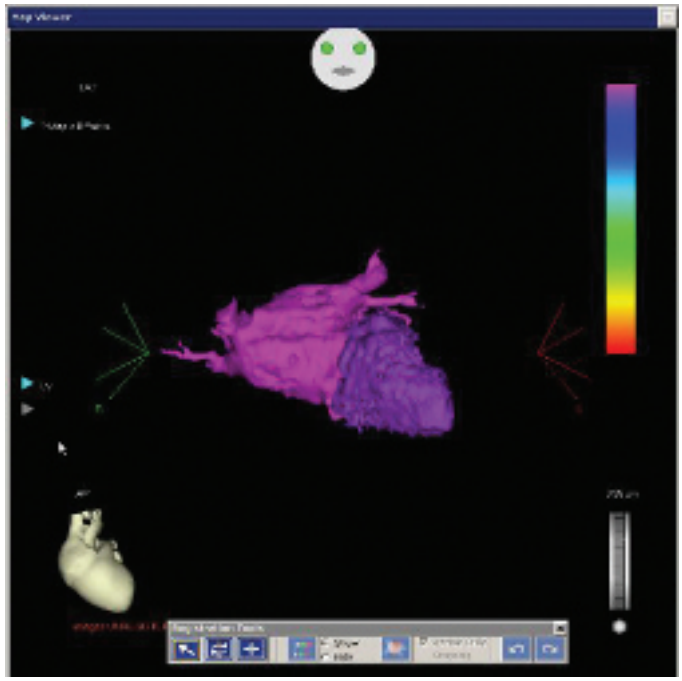

Figure 8.1 (Cont.)

(e)

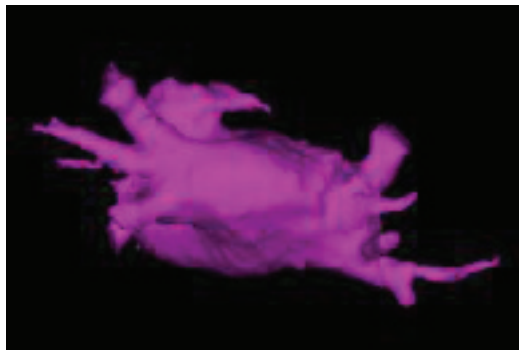

Figure 8.1 (Cont.)

The techniques used to visualize the coronary arteries also visualize the coronary venous system including identification and quantification of the coronary sinus os, coronary sinus, great cardiac vein, and branch veins [24–27]. Evaluation of the cardiac venous anatomy has become increasingly important because it provides venous access routes to map ablate or pace the left ventricle, left atrium, and posterior septum. Given the ability to visualize the coronary vasculature, the 3D relationships between the coronary arteries, coronary veins, mitral annulus, left atrium, and left ventricle can be visualized three-dimensionally.

Although coronary sinus catheters are used to approximate mapping of the left atrium, the distance between the coronary sinus/great cardiac vein and annulus is variable, often with a course along the atrium rather than along the true AV groove [28]. CCT provides 3D assessment of this relationship, which is important to the interpretation of electrograms for left-sided accessory pathways, left atrial tachycardia, atypical atrial flutter, and atrial fibrillation mapping and ablation procedures. Additionally, abnormalities of the coronary venous anatomy such as diverticula and Thebesian valves obstructing access to cannulation with catheters or leads can be identified [29].

The position of the coronary arteries relative to potential ablation positions in the left atrium can be identified. The relationship between the coronary arteries and coronary veins in relation to the atrium and ventricles are variable in overlapping areas of these structures with the vein more lateral to the artery in many cases (Figure 8.4) [24]. Understanding of a patient's individual anatomy in this regard is important to avoid coronary artery complications with the application of radiofrequency or other energy source applications.

Extracardiac Thoracic Structures: Relationships to the Left Atrium

An understanding of the 3D relationships of extracardiac thoracic structures is essential to the performance of electrophysiology procedures. The importance of the relationship of the esophagus to the thin posterior wall of the left atrium was made apparent by the reporting of fatal atrial esophageal fistulas associated with atrial fibrillation ablation [30, 31]. CCT can define the course of the esophagus in relation to the left atrium as well as the location and presence and characteristics of the tissues between the left atrium and the esophagus, such as a layer of adipose tissue that may provide some protection from thermal injury [32–34].

In addition to the variable course of the esophagus in relation to the left atrium, identification of location is made more complex by factors such as the timing of the CCT to the ablation procedure, patient position, peristalsis, and potential movement by catheters placed in the esophagus such as NG tubes and temperature probes. Measures to provide greater characterization of this relationship have included swallowing barium at the time of CCT with additional tagging of the esophagus during an electroanatomic map [35]. Given these limitations, additional modalities of monitoring have included temperature probes in the esophagus as well as the use of intracardiac echocardiography to identify the real-time relationship between the ablation catheter and esophagus prior to the application of radiofrequency energy [36].

The same concerns related to the esophagus have now become apparent with other structures posterior to the left atrium, including bronchi and the aorta [37]. Fatal broncho-atrial fistulas have been reported and therefore special attention needs to be given to the relationship between these structures when ablation in the posterior left atrium is considered [38]. Filtering techniques now allow the neurovascular sheath housing the phrenic nerve to be visualized, which may have great importance for

(a)

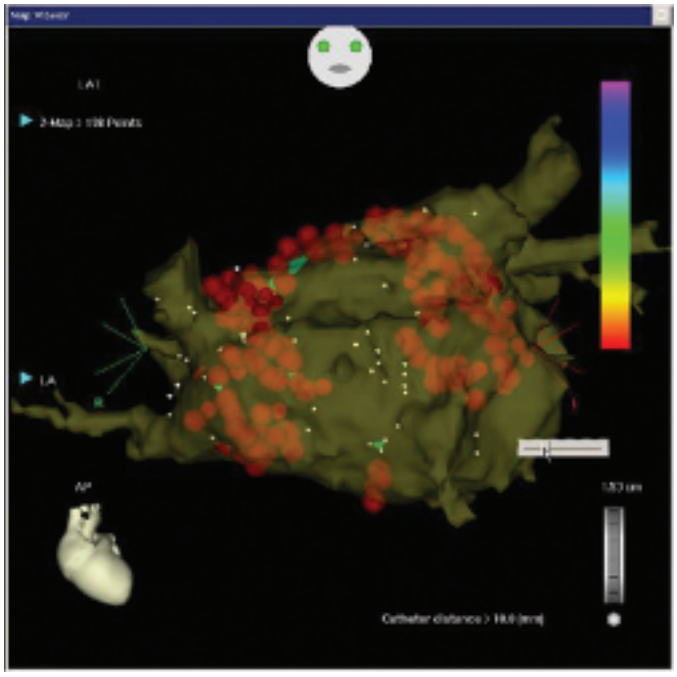

(b)

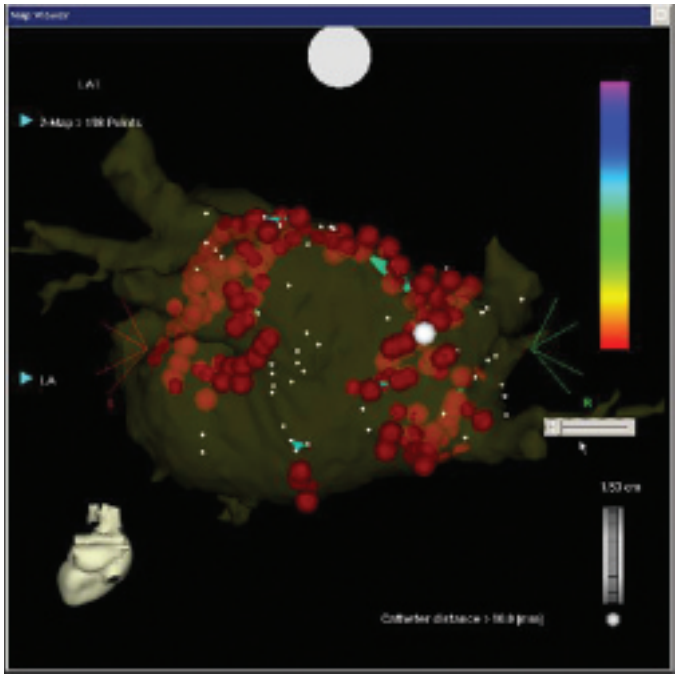

Figure 8.2 Electroanatomic mapping with image integration during atrial fibrillation ablation. (a) Anterior view demonstrating radiofrequency energy applications (red spheres). (b) Posterior left atrial view. (c) Endocardial view demonstrating circumferential radiofrequency energy applications around the left upper pulmonary vein. (d) Linear lesions along the "roof" of the left atrium.

(c)

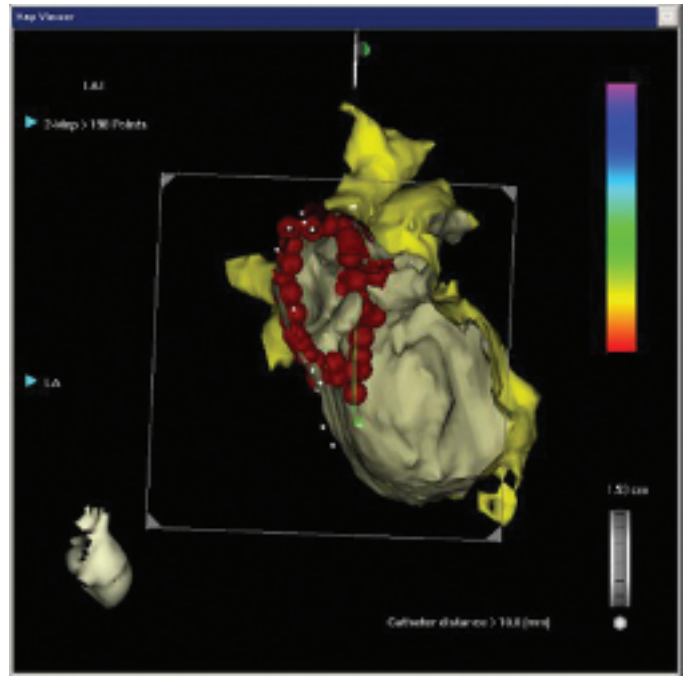

(d)

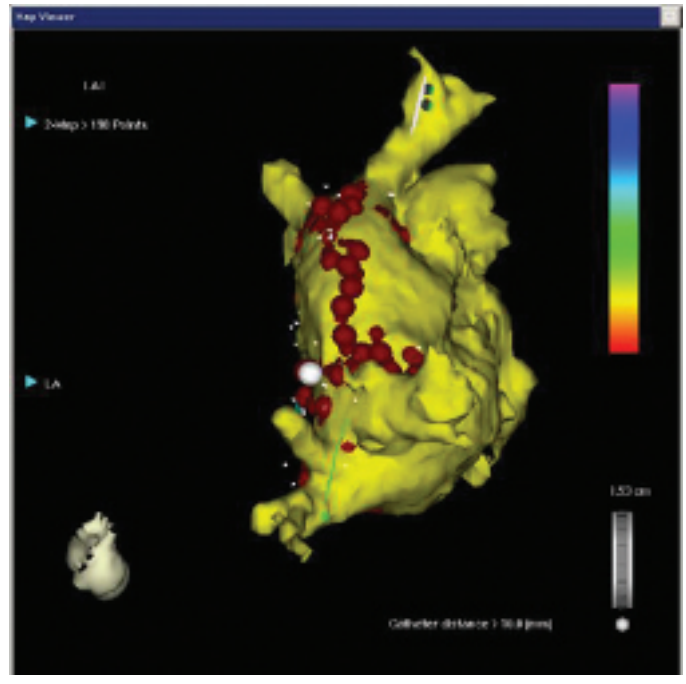

Figure 8.2 (Cont.)

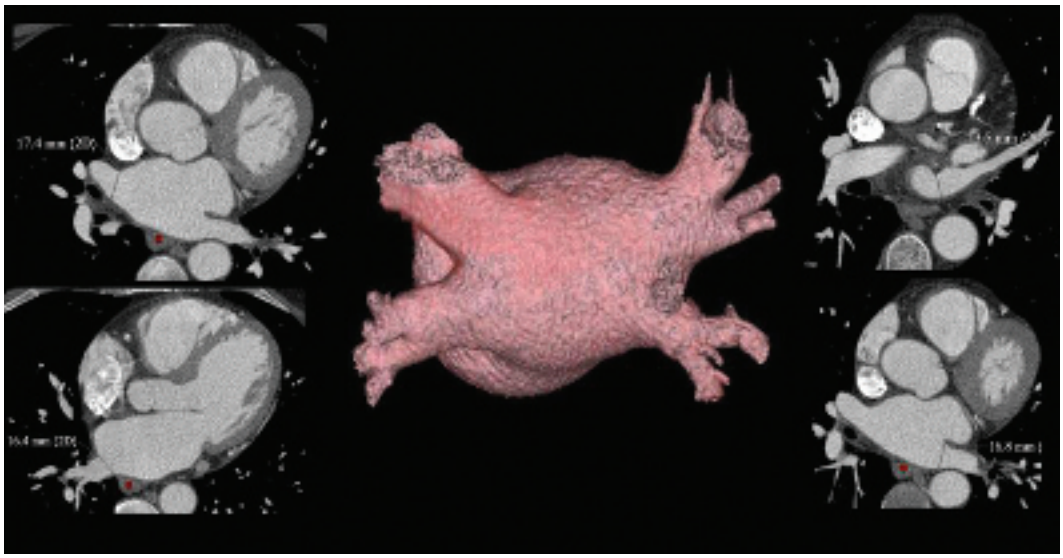

Figure 8.3 Three-dimensional posterior view of the left atrium (center) and axial images of the pulmonary veins. The relationship of the posterior left atrium and esophagus (red circle) is noted.

ablation or placement of chronic coronary venous pacing leads [39]. In addition to these thoracic structures mentioned above, thoracic veins and arteries can be assessed for anomalies such as persistent left superior vena cava to coronary sinus connections and significant aortic pathology which may limit or contraindicate catheter approached used for mapping and ablation of arrhythmias [40, 41].

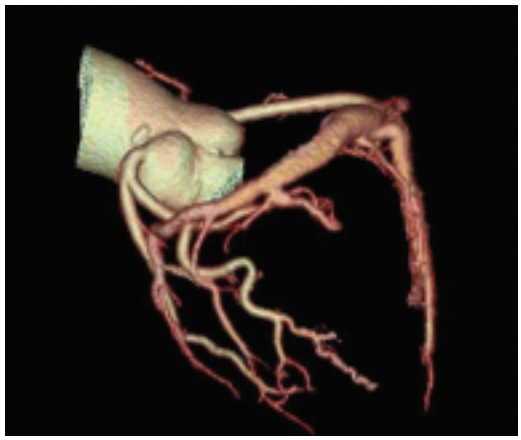

Figure 8.4 The relationship between the coronary arteries and coronary veins in overlapping areas of these structures with the great cardiac vein lateral to and overlapping the circumflex coronary artery.

Left Ventricle

Both CCT and CMR provide reproducible volumetric assessment of ejection fraction and can assess wall thickness, as well as regional wall motion, and are therefore useful in the characterization of cardiomyopathies including ischemic and nonischemic dilated cardiomyopathy and hypertrophic cardiomyopathy [42–45]. The ability to visualize coronary arteries with CCT is useful to the differentiation of ischemic versus nonischemic cardiomyopathy [44].

The use of delayed enhancement imaging with CMR has revolutionized imaging of areas of myocardial fibrosis. This technique allows defining borders between viable myocardium and areas of fibrosis important to risk stratification for ventricular arrhythmias, with studies demonstrating increased sudden death risk in dilated and hypertrophic cardiomyopathy associated with degree and pattern of delayed gadolinium enhancement [46, 47]. With CCT, characteristics such as myocardial hypoattenuation may be useful in defining areas of infarction [48]. Delayed enhancement imaging can be performed to identify areas of fibrosis with CCT, but technical issues and additional radiation associated with the need to rescan currently limit its practical application [49, 50].

Right Ventricle

The right ventricle can be quantified with CCT, with assessment of volumes, ejection fraction, wall motion, and wall thickness. Although CMR has historically been the gold standard for assessment of structural and functional changes with arrhythmogenic right ventricular cardiomyopathy, CCT can image for right ventricular structural and functional abnormalities [51]. CCT is particularly helpful in patients with preexisting devices who have not been given a diagnosis or are being followed for functional changes with a known diagnosis, although some artifact due to the device may be present. CCT can be useful in defining the relationship of the right coronary artery to the right ventricular outflow tract important to ablation of right ventricular outflow tract tachycardias [52].

Right Atrium

CCT can be used to image the right atrium and can characterize venous return to the right atrium including anomalous connection to right atrium, atrial septal defects, and right atrial masses [11, 53–55]. CCT can visualize the cavotricuspid isthmus, including the length of potential ablation lines to span the isthmus, the size of the isthmus, and the distance between the tricuspid valve and inferior vena cava important to atrial flutter ablation [56]. As opposed to visualization of the left atrium, the visualization of the right atrium is complicated by the fact that venous return to the right atrium includes contrast administration through an upper extremity vein admixed with other noncontrast venous return to the right atrium.

Image Integration for Procedural Facilitation

In addition to preprocedure assessment of vascular roadmap and detailed assessment of cardiac substrate, CCT and CMR allow for the use of the unprocessed DICOM images for import into mapping systems for intraprocedure electroanatomic mapping with image integration [57–61]. The process involves:

1 Importation of the unprocessed DICOM images into the mapping system.

2 Use of edge detection software to delineate and segment cardiac vascular structures (Figure 8.1), and the esophagus in cases where it has been imaged with barium.

3 Editing of structures relevant to the specific ablation type. In atrial fibrillation ablation this includes the left atrium and in some laboratories the aorta and esophagus.

4 Creation of a separate catheter-based anatomic map, using landmark points. These points include points with minimal motion and vary according to electrophysiology laboratory. One example would be the most cranial aspect of the interface of the pulmonary veins and left atrium.

5 Registration of endocardial surface points delineating the chamber to be studied. This catheter-based map is integrated with the CCT edited 3D reconstruction with assessment of markers of successful integration defined by an acceptable best surface to surface fit to the electroanatomic map [59].

For registrations, catheter-based points that do not define the endocardial border are deleted and new points are registered to ensure that the atrial endocardial surface has been adequately mapped. Registration issues may occur and depend on a variety of factors. Although heart rhythm was initially thought to affect issues related to registration, some studies have shown this not to be a significant factor [59, 62, 63]. The number of days between imaging and ablation in one study did not affect registration. Left atrial size was a factor affecting registration with atrial sizes greater than or equal to 110 cc causing greater integration error [63]. With regard to respiratory cycle issues, an expiratory breath hold during imaging is most consistent with maps obtained with electroanatomic mapping [64, 65].

Electroanatomic mapping with image integration utilizes a system in which mapping and ablation can be performed on a 3D map of the chamber analyzed, with current use predominantly for left atrial applications. Catheter position can be tracked in real time on this map with the ability to assess electrical activation and propagation, define electrically silent areas, assess catheter contact with endocardium, document radiofrequency energy application location, and repeat this process postablation.

With regard to atrial fibrillation ablation, the relation of the catheter tip to the pulmonary vein os can be visualized to avoid radiofrequency applications within the pulmonary veins or os. Assessment of contact and relation to the pulmonary vein os can be additionally enhanced with use of intracardiac echocardiography. The systems allow for tracking of the placement of contiguous ablative lesions around anatomic structures such as the ostia of the pulmonary veins. They can facilitate placement and documentation of catheter-based energy applications for segmental complete circumferential electrical isolation of the pulmonary veins, ablation of other ectopic atrial foci or abnormal signals in the atrium, and long linear ablation lesions (Figure 8.2).

The use of these techniques has been reported to decrease procedural fluoroscopy time, decrease recurrence of atrial fibrillation, and increase restoration of sinus rhythm compared to electroanatomic mapping alone [58]. Additional techniques using segmented CCT images to integrate with fluoroscopy systems are being investigated and have been shown to be feasible [6]. Initial studies demonstrate decreased procedure and fluoroscopy times compared to electroanatomic mapping alone, and will require further development.

Although the use of electroanatomic mapping with image integration has been primarily used for atrial fibrillation ablation, other arrhythmias are being mapped and ablated using this technology. These techniques are being used for facilitation of atrial flutter ablation in scenarios with complex anatomy and complex circuits [66–68]. The mapping and ablation of ventricular tachycardia is in evolution, as electroanatomic mapping with image integration may facilitate epicardial ablation approaches to ventricular tachycardia with regard to identification of anatomy and scar [69, 70]. Quantification epicardial fat—which may inhibit adequate ablation with epicardial approaches to ventricular tachycardia ablation—can also be performed [71].

Postablation Assessment

Pulmonary vein stenosis is a potential complication of atrial fibrillation ablation [72, 73]. The incidence of stenosis depends on ablation technique, the criteria used to define a "significant" stenosis, degree of follow-up surveillance for evidence of stenosis, and operator experience. The preprocedure CCT is a useful template to assess for postprocedural pulmonary vein stenosis and can identify preexisting pulmonary vein stenoses. It is often difficult to identify the precise boundary separating the ostia of the pulmonary veins and the posterior atrial wall, especially without the use of imaging in addition to fluoroscopy. Using current techniques, severe stenosis is rare; however, some level of change to the atrial and pulmonary venous anatomy is often found following ablation [74].

Symptoms are usually pulmonary and can mimic a host of common illnesses. They are generally of mild severity, unless multiple veins are in involved [73]. Postprocedure CCT evaluation is a reliable means of making this otherwise difficult diagnosis. Given that there is radiation exposure related to preprocedure study and procedural fluoroscopy, techniques such as dose modulation or use of another technology such as CMR should be considered to limit overall radiation exposure. CCT can also provide comprehensive postprocedure assessment of chest pain or shortness of breath, including pulmonary embolus, aortic dissection, pericardial effusion, and coronary artery complications.

Future Directions

The use of advanced imaging techniques has enhanced the understanding of anatomic factors relevant to the assessment and treatment of patients with electrophysiologically related issues. CCT provides patient-specific 3D characterization of cardiac anatomy, which has transformed approaches to arrhythmia mapping and ablation in the electrophysiology laboratory. The imaging techniques and applications in the electrophysiology laboratory will continue to evolve through multidisciplinary efforts.

References

1 Hausleiter J, Meyer T, Hadamitzky M, et al. Radiation dose estimates from cardiac multislice computed tomography in daily practice: impact of different scanning protocols on effective dose estimates. *Circulation* 2006; **113**: 1305–10.

2 Coles DR, Smail MA, Negus IS, et al. Comparison of radiation doses from multislice computed tomography coronary angiography and conventional diagnostic angiography. *J Am Coll Cardiol* 2006; **47**: 1840–45.
3 Shapiro MD, Pena AJ, Nichols JH, et al. Efficacy of prescan beta-blockade and impact of heart rate on image quality in patients undergoing coronary multidetector computed tomography angiography. *Eur J Radiol* 2008; **66**: 37–41.
4 Shinbane JS, Colletti PM, Shellock FG. MR in patients with pacemakers and ICDs: Defining the issues. *J Cardiovasc Magn Reson* 2007; **9**: 5–13.
5 McCollough CH, Zhang J, Primak AN, Clement WJ, Buysman JR. Effects of CT irradiation on implantable cardiac rhythm management devices. *Radiology* 2007; **243**: 766–74.
6 Sra J, Narayan G, Krum D, et al. Computed tomography–fluoroscopy image integration-guided catheter ablation of atrial fibrillation. *J Cardiovasc Electrophysiol* 2007; **18**: 409–14.
7 Yamanaka K, Fujita M, Doi K, et al. Multislice computed tomography accurately quantifies left atrial size and function after the MAZE procedure. *Circulation* 2006; **114**: I5–9.
8 Lacomis JM, Pealer K, Fuhrman CR, Barley D, Wigginton W, Schwartzman D. Direct comparison of computed tomography and magnetic resonance imaging for characterization of posterior left atrial morphology. *J Interv Card Electrophysiol* 2006; **16**: 7–13.
9 Kim YH, Marom EM, Herndon JE, 2nd, McAdams HP. Pulmonary vein diameter, cross-sectional area, and shape: CT analysis. *Radiology* 2005; **235**: 43–9; discussion 49–50.
10 Saremi F, Attai SF, Narula J. 64-multidetector CT in patent foramen ovale. *Heart* 2007; **93**: 505.
11 AboulHosn J, French WJ, Buljubasic N, Matthews RV, Budoff MJ, Shavelle DM. Electron beam angiography for the evaluation of percutaneous atrial septal defect closure. *Catheter Cardiovasc Interv* 2005; **65**: 565–68.
12 Otsuka M, Itoh A, Haze K. Sinus venosus type of atrial septal defect with partial anomalous pulmonary venous return evaluated by multislice CT. *Heart* 2004; **90**: 901.
13 Mandegar MH, Rayatzadeh H, Roshanali F. Left atrial myxoma: the role of multisclice computed tomography. *J Thorac Cardiovasc Surg* 2007; **134**: 795.
14 Jaber WA, White RD, Kuzmiak SA, et al. Comparison of ability to identify left atrial thrombus by three-dimensional tomography versus transesophageal echocardiography in patients with atrial fibrillation. *Am J Cardiol* 2004; **93**: 486–98.
15 Achenbach S, Sacher D, Ropers D, et al. Electron beam computed tomography for the detection of left atrial thrombi in patients with atrial fibrillation. *Heart* 2004; **90**: 1477–78.
16 Ren JF, Marchlinski FE, Callans DJ. Left atrial thrombus associated with ablation for atrial fibrillation: identification with intracardiac echocardiography. *J Am Coll Cardiol* 2004; **43**: 1861–67.
17 Peters DC, Wylie JV, Hauser TH, et al. Detection of pulmonary vein and left atrial scar after catheter ablation with three-dimensional navigator-gated delayed enhancement MR imaging: initial experience. *Radiology* 2007; **24**: 690–95.
18 Shabestari AA, Abdi S, Akhlaghpoor S, et al. Diagnostic performance of 64-channel multislice computed tomography in assessment of significant coronary artery disease in symptomatic subjects. *Am J Cardiol* 2007; **99**: 1656–61.
19 Cademartiri F, Schuijf JD, Pugliese F, et al.Usefulness of 64-slice multislice computed tomography coronary angiography to assess in-stent restenosis. *J Am Coll Cardiol* 2007; **49**: 2204–10.
20 Ropers D, Pohle FK, Kuettner A, et al. Diagnostic accuracy of noninvasive coronary angiography in patients after bypass surgery using 64-slice spiral computed tomography with 330-ms gantry rotation. *Circulation* 2006; **114**: 2334–41; quiz 2334.
21 Schuijf JD, Pundziute G, Jukema JW, et al. Diagnostic accuracy of 64-slice multislice computed tomography in the noninvasive evaluation of significant coronary artery disease. *Am J Cardiol* 2006; **98**: 145–48.
22 Ehara M, Surmely JF, Kawai M, et al. Diagnostic accuracy of 64-slice computed tomography for detecting angiographically significant coronary artery stenosis in an unselected consecutive patient population: comparison with conventional invasive angiography. *Circ J* 2006; **70**:564–71.
23 Berbarie RF, Dockery WD, Johnson KB, Rosenthal RL, Stoler RC, Schussler JM. Use of multislice computed tomographic coronary angiography for the diagnosis of anomalous coronary arteries. *Am J Cardiol* 2006; **9**: 402–6.
24 Mao S, Shinbane JS, Girsky MJ, et al. Coronary venous imaging with electron beam computed tomographic angiography: three-dimensional mapping and relationship with coronary arteries. *Am Heart J* 2005; **150**: 315–22.
25 Tada H, Kurosaki K, Naito S, Koyama K, Itoi K, Ito S, et al. Three-dimensional visualization of the coronary venous system using multidetector row computed tomography. *Circ J* 2005; **69**: 165–70.
26 Van de Veire NR, Schuijf JD, De Sutter J, et al. Noninvasive visualization of the cardiac venous system in coronary artery disease patients using 64-slice computed tomography.*J Am Coll Cardiol* 2006; **48**:1832–38.

27 Chen JJ, Lee WJ, Wang YC, et al. Morphologic and topologic characteristics of coronary venous system delineated by noninvasive multidetector computed tomography in chronic systolic heart failure patients. *J Card Fail* 2007; **13**: 482–88.

28 Shinbane JS, Lesh MD, Stevenson WG, et al. Anatomic and electrophysiologic relation between the coronary sinus and mitral annulus: implications for ablation of left-sided accessory pathways. *Am Heart J* 1998; **135**: 93–8.

29 Shinbane JS, Girsky MJ, Mao S, Budoff MJ. Thebesian valve imaging with electron beam CT angiography: implications for resynchronization therapy. *Pacing Clin Electrophysiol* 2004; **27**:1566–67.

30 Scanavacca MI, D'Avila A, Parga J, Sosa E. Left atrial-esophageal fistula following radiofrequency catheter ablation of atrial fibrillation. *J Cardiovasc Electrophysiol* 2004; **15**: 960–62.

31 Pappone C, Oral H, Santinelli V, et al. Atrio-esophageal fistula as a complication of percutaneous transcatheter ablation of atrial fibrillation. *Circulation* 2004.

32 Lemola K, Sneider M, Desjardins B, et al. Computed tomographic analysis of the anatomy of the left atrium and the esophagus. implications for left atrial catheter ablation. *Circulation* 2004; **110**: 3655–60.

33 Tsao HM, Wu MH, Higa S, Anatomic relationship of the esophagus and left atrium: implication for catheter ablation of atrial fibrillation. *Chest* 2005; **128**: 2581–87.

34 Wang SL, Ooi CG, Siu CW, et al. Endocardial visualization of esophageal-left atrial anatomic relationship by three-dimensional multidetector computed tomography "navigator imaging." *Pacing Clin Electrophysiol* 2006; **29**: 502–8.

35 Piorkowski C, Hindricks G, Schreiber D, et al. Electroanatomic reconstruction of the left atrium, pulmonary veins, and esophagus compared with the "true anatomy" on multislice computed tomography in patients undergoing catheter ablation of atrial fibrillation. *Heart Rhythm* 2006; **3**: 317–27.

36 Cummings JE, Schweikert RA, Saliba WI, et al. Assessment of temperature, proximity, and course of the esophagus during radiofrequency ablation within the left atrium. *Circulation* 2005; **112**:459–64.

37 Hoffmeister PS, Chaudhry GM, Mendel J, et al. Evaluation of left atrial and posterior mediastinal anatomy by multidetector helical computed tomography imaging: relevance to ablation. *J Interv Card Electrophysiol* 2007; **18**: 217–23.

38 Wu MH, Wongcharoen W, Tsao HM, et al. Close relationship between the bronchi and pulmonary veins: implications for the prevention of atriobronchial fistula after atrial fibrillation ablation. *J Cardiovasc Electrophysiol* 2007; **18**: 1056–59.

39 Matsumoto Y, Krishnan S, Fowler SJ, et al. Detection of phrenic nerves and their relation to cardiac anatomy using 64-slice multidetector computed tomography. *Am J Cardiol* 2007; **100**: 133–37.

40 Gerber TC, Kuzo RS. Images in cardiovascular medicine. Persistent left superior vena cava demonstrated with multislice spiral computed tomography. *Circulation* 2002; **105**: e79.

41 Shiga T, Wajima Z, Apfel CC, Inoue T, Ohe Y. Diagnostic accuracy of transesophageal echocardiography, helical computed tomography, and magnetic resonance imaging for suspected thoracic aortic dissection: systematic review and meta-analysis. *Arch Intern Med* 2006; **166**: 1350–56.

42 Dewey M, Muller M, Eddicks S, et al. Evaluation of global and regional left ventricular function with 16-slice computed tomography, biplane cineventriculography, and two-dimensional transthoracic echocardiography: comparison with magnetic resonance imaging. *J Am Coll Cardiol* 2006; **48**: 2034–44.

43 Sugeng L, Mor-Avi V, Weinert L, et al. Quantitative assessment of left ventricular size and function: side-by-side comparison of real-time three-dimensional echocardiography and computed tomography with magnetic resonance reference. *Circulation* 2006; **114**: 654–61.

44 Andreini D, Pontone G, Pepi M, et al. Diagnostic accuracy of multidetector computed tomography coronary angiography in patients with dilated cardiomyopathy.*J Am Coll Cardiol* 2007; **49**: 2044–50.

45 Rickers C, Wilke NM, Jerosch-Herold M, et al. Utility of cardiac magnetic resonance imaging in the diagnosis of hypertrophic cardiomyopathy. *Circulation* 2005; **112**: 855–61.

46 Assomull RG, Prasad SK, Lyne J, et al. Cardiovascular magnetic resonance, fibrosis, and prognosis in dilated cardiomyopathy. *J Am Coll Cardiol* 2006; **48**: 1977–85.

47 Moon JC, McKenna WJ, McCrohon JA, Elliott PM, Smith GC, Pennell DJ. Toward clinical risk assessment in hypertrophic cardiomyopathy with gadolinium cardiovascular magnetic resonance.*J Am Coll Cardiol* 2003; **41**: 1561–67.

48 Sanz J, Weeks D, Nikolaou K, et al. Detection of healed myocardial infarction with multidetector-row computed tomography and comparison with cardiac magnetic resonance delayed hyperenhancement. *Am J Cardiol* 2006; **98**: 149–55.

49 Baks T, Cademartiri F, Moelker AD, et al. Multislice computed tomography and magnetic resonance imaging for the assessment of reperfused acute myocardial infarction. *J Am Coll Cardiol* 2006; **48**: 144–52.

50 Shiozaki AA, Santos TS, Artega E, Rochitte CE. Images in cardiovascular medicine: myocardial delayed

enhancement by computed tomography in hypertrophic cardiomyopathy. *Circulation* 2007; **115**: e430–31.

51 Bomma C, Dalal D, Tandri H, et al. Evolving role of multidetector computed tomography in evaluation of arrhythmogenic right ventricular dysplasia/cardiomyopathy. *Am J Cardiol* 2007; **100**: 99–105.

52 Vaseghi M, Cesario DA, Mahajan A, et al. Catheter ablation of right ventricular outflow tract tachycardia: value of defining coronary anatomy. *J Cardiovasc Electrophysiol* 2006; **17**: 632–37.

53 Solomon SB, Dickfeld T, Calkins H. Real-time cardiac catheter navigation on three-dimensional CT images. *J Interv Card Electrophysiol* 2003; **8**: 27–36.

54 Haramati LB, Moche IE, Rivera VT, et al. Computed tomography of partial anomalous pulmonary venous connection in adults. *J Comput Assist Tomogr* 2003; **27**: 743–49.

55 Burri H, Bloch A, Hauser H. Characterization of an unusual right atrial mass by echocardiography, magnetic resonance imaging, computed tomography, and angiography. *Echocardiography* 1999; **16**: 393–96.

56 Komatsu S, Okuyama Y, Omori Y, et al. Evaluation of the cavotricuspid isthmus and right atrium by multidetector-row computed tomography in patients with common atrial flutter. *Heart Vessels* 2005; **20**: 264–70.

57 Reddy VY, Malchano ZJ, Holmvang G, et al. Integration of cardiac magnetic resonance imaging with three-dimensional electroanatomic mapping to guide left ventricular catheter manipulation: feasibility in a porcine model of healed myocardial infarction. *J Am Coll Cardiol* 2004; **44**: 2202–13.

58 Kistler PM, Rajappan K, Jahngir M, et al. The impact of CT image integration into an electroanatomic mapping system on clinical outcomes of catheter ablation of atrial fibrillation. *J Cardiovasc Electrophysiol* 2006; **17**: 1093–101.

59 Kistler PM, Earley MJ, Harris S, et al. Validation of three-dimensional cardiac image integration: use of integrated CT image into electroanatomic mapping system to perform catheter ablation of atrial fibrillation.*J Cardiovasc Electrophysiol* 2006; **17**: 341–48.

60 Tops LF, Bax JJ, Zeppenfeld K, et al. Fusion of multislice computed tomography imaging with three-dimensional electroanatomic mapping to guide radiofrequency catheter ablation procedures. *Heart Rhythm* 2005; **2**: 1076–81.

61 Kistler PM, Ho SY, Rajappan K, et al. Electrophysiologic and anatomic characterization of sites resistant to electrical isolation during circumferential pulmonary vein ablation for atrial fibrillation: a prospective study. *J Cardiovasc Electrophysiol* 2007; **18**: 1282–88.

62 Martinek M, Nesser HJ, Aichinger J, Boehm G, Purerfellner H. Accuracy of integration of multislice computed tomography imaging into three-dimensional electroanatomic mapping for real-time guided radiofrequency ablation of left atrial fibrillation: influence of heart rhythm and radiofrequency lesions. *J Interv Card Electrophysiol* 2006; **17**: 85–92.

63 Heist EK, Chevalier J, Holmvang G, et al. Factors affecting error in integration of electroanatomic mapping with CT and MR imaging during catheter ablation of atrial fibrillation. *J Interv Card Electrophysiol* 2006; **17**: 21–7.

64 Noseworthy PA, Malchano ZJ, Ahmed J, Holmvang G, Ruskin JN, Reddy VY. The impact of respiration on left atrial and pulmonary venous anatomy: implications for image-guided intervention. *Heart Rhythm* 2005; **2**: 1173–78.

65 Malchano ZJ, Neuzil P, Cury RC, et al. Integration of cardiac CT/MR imaging with three-dimensional electroanatomical mapping to guide catheter manipulation in the left atrium: implications for catheter ablation of atrial fibrillation. *J Cardiovasc Electrophysiol* 2006; **17**: 1221–29.

66 Dukkipati S, Holmvang G, Ruskin J, Mansour M. Ablation of mitral isthmus-dependent atrial flutter using integration of real-time electroanatomic mapping with three-dimensional computed tomography. *Heart Rhythm* 2006; **3**: 124.

67 Aryana A, Ellinor PT, Aleong RG, et al. Ablation of atrial flutter in a patient with situs inversus totalis using integration of real-time three-dimensional electroanatomical mapping. *J Cardiovasc Electrophysiol* 2007; **19**: 221–22.

68 Aryana A, Liberthson RR, Heist EK, et al. Images in cardiovascular medicine.: ablation of atrial flutter in a patient with mustard procedure using integration of real-time electroanatomical mapping with 3-dimensional computed tomographic imaging. *Circulation* 2007; **116**: e315–16.

69 Bello D, Kipper S, Valderrabano M, Shivkumar K. Catheter ablation of ventricular tachycardia guided by contrast-enhanced cardiac computed tomography. *Heart Rhythm* 2004; **1**: 490–92.

70 Zeppenfeld K, Tops LF, Bax JJ, Schalij MJ. Images in cardiovascular medicine. Epicardial radiofrequency catheter ablation of ventricular tachycardia in the vicinity of coronary arteries is facilitated by fusion of 3-dimensional electroanatomical mapping with multislice computed tomography. *Circulation* 2006; **114**: e51–2.

71 Abbara S, Desai JC, Cury RC, Butler J, Nieman K, Reddy V. Mapping epicardial fat with multidetector computed tomography to facilitate percutaneous transepicardial arrhythmia ablation.*Eur J Radiol* 2006; **57**: 417–22.

72 Saad EB, Marrouche NF, Saad CP, et al. Pulmonary vein stenosis after catheter ablation of atrial fibrillation:

emergence of a new clinical syndrome. *Ann Intern Med* 2003; **138**: 634–38.

73 Packer DL, Keelan P, Munger TM, et al. Clinical presentation, investigation, and management of pulmonary vein stenosis complicating ablation for atrial fibrillation. *Circulation* 2005; **111**: 546–54.

74 Dong J, Vasamreddy CR, Jayam V, et al. Incidence and predictors of pulmonary vein stenosis following catheter ablation of atrial fibrillation using the anatomic pulmonary vein ablation approach: results from paired magnetic resonance imaging. *J Cardiovasc Electrophysiol* 2005; **16**: 845–52.

9

CHAPTER 9

MRI Anatomy for Cardiac Mapping and Ablation

Aravindan Kolandaivelu, MD, *Henry R. Halperin,* MD, MA, FAHA, *Albert C. Lardo,* PhD, FAHA, FACC

Johns Hopkins University, Baltimore, MD, USA

Summary

Cardiac MRI has emerged as a useful imaging technique for peri and intra operative anatomical delineation and effectiveness of complex ablation procedures particularly atrial fibrillation and ventricular tachycardia. MRI's were initially used as pre procedure imaging with image integration to the electroanatomical mapping systems. However, recent system are capable of using MRI during ablation procedures to visualize and monitor ablation lesion. Future application and direction of MRI in interventional electrophysiology is discussed.

Introduction

Since its initial description in 1978, catheter-based radiofrequency ablation has evolved from an experimental procedure to the first-line therapy for a number of cardiac arrhythmias including atrioventricular nodal reentrant tachycardia, accessory pathway associated tachycardias, and typical atrial flutter [1, 2]. Conventional cardiac mapping directs ablation based on the timing of intracardiac electrograms and response to pacing maneuvers from contact electrode catheters positioned on standardized fluoroscopic views.

The anatomic variation of some cardiac arrhythmias, such as focal atrial tachycardia, and the complex arrhythmogenic substrate underlying atrial fibrillation and scar-based monomorphic ventricular tachycardia have led to more sophisticated and time-consuming mapping and ablation strategies. Fluoroscopy, however, is poor at delineating details of the underlying cardiovascular anatomy and carries the risk of ionizing radiation and radio-opaque contrast agents. These limitations have accelerated the adoption of more sophisticated electrospatial mapping techniques. These techniques track the 3D position of mapping and ablation catheters to create surface maps of intracardiac electrograms and ablation attempts. Three-dimensional mapping has extended the potential of ablative cure to most cardiac tachyarrhythmias while reducing the need for x-ray exposure.

With the application of more sophisticated ablation procedures to a broader patient population, electrophysiologists remain faced with suboptimal cure rates and prolonged procedure times for some arrhythmias, a risk of serious complications, and an increased awareness of normal and pathologic

Cardiac Mapping, Third Edition Edited by Mohammad Shenasa, Gerhard Hindricks, Martin Borggrefe, and Günter Breithardt
 ISBN: 978-1-405-17572-2

anatomic variants that influence procedure difficulty. Modern imaging techniques such as MRI, intracardiac ultrasound, and CT are increasingly used to approach the shortcomings of current mapping and ablation systems. Cardiac MRI is a particularly flexible imaging modality offering excellent soft tissue contrast, 3D imaging of complex cardiovascular anatomy, real-time 2D imaging along arbitrary imaging planes, and the ability to quantify cardiac motion and blood flow. This chapter will discuss the current and future applications of MRI for improved pre-procedural understanding of the arrhythmia substrate as well as the interventional use of MRI for procedure guidance and ablation lesion assessment.

Applications of MRI to Preprocedural Planning

MRI has been applied in a number of ways to understand the anatomic substrate and plan catheter ablation of atrial and ventricular arrhythmias. MR angiography (MRA), with and without the administration of gadolinium contrast, can provide detailed 3D atrial and venous anatomy. Delayed contrast-enhanced MRI has been used extensively to delineate regions of myocardial "scar" in ischemic and nonischemic cardiomyopathies that form part of the arrhythmogenic substrate in these conditions.

Myocardial tagging and phase-based motion tracking techniques permit the creation of 3D myocardial strain maps over the cardiac cycle that may be related to regional myocardial electrical activity through the process of electromechanical coupling. While MRI may assist procedure planning for arrhythmias such as typical atrial flutter and accessory pathway-mediated tachycardia [3–5], atrial fibrillation and monomorphic ventricular tachycardia have been the focus of MRI research and applications because they remain challenging to manage with current mapping and ablation techniques

Atrial Fibrillation

Atrial fibrillation (AF) is the most common clinically relevant arrhythmia, occurring in 0.4% of the general population [6]. Recognition that triggering foci for AF frequently arise from the pulmonary veins has led to catheter ablation strategies to isolate these triggers from atrial tissue.

In segmental pulmonary vein (PV) isolation, a mapping catheter is used to locate electrical activity originating from muscle strands within the PVs, and RF energy is applied to eliminate all detected PV potentials. Generally, 20–60% of the PV circumference is ablated in this process, introducing the risk of pulmonary vein injury and stenosis. Meta-analysis of studies using this technique demonstrate freedom from symptomatic AF in around 70% of patients with paroxysmal atrial fibrillation, but only 30% for persistent or permanent atrial fibrillation. A 6% major complication rate including significant PV stenosis in 3.6%, stroke in 0.8%, and tamponade in 1.7% has also been noted [7].

Circumferential PV ablation is an alternative approach in which RF energy is delivered around the entire circumference of each PV or pairs of PVs until local atrial electrogram voltage is reduced by 80% or to <40.1 mV. Pooling results from different centers, success rates of around 70% for paroxysmal AF and 50% for persistent AF have been achieved [7]. With this technique the risk of significant PV stenosis was reduced to around 1%; however, the rare but potentially lethal complication of atrioesophageal fistula has been reported. Hybrid techniques that combine focal ablation of PV triggers with circumferential PV ablation and linear ablation of the mitral isthmus and posterior LA have evolved with reports of improved outcomes. However, such procedures currently have similar efficacy when considering pooled results from available studies 7.

MRI for Preprocedure Planning of Atrial Fibrillation Ablation

Pulmonary vein anatomy is complex and poorly assessed by fluoroscopy alone. With the effort to improve the success and reduce complications of AF ablation, the use of 3D imaging to delineate left atrial (LA) and PV anatomy has become more widespread. MRA has been used to assess the size, shape, and anatomy of PVs in paroxysmal AF patients and normal subjects. One study identified LA anatomic variants in 38% of people including a common trunk to the left PVs, additional right middle and right upper PVs, and early branching of the PVs [8] (Figure 9.1). Some of these anatomic

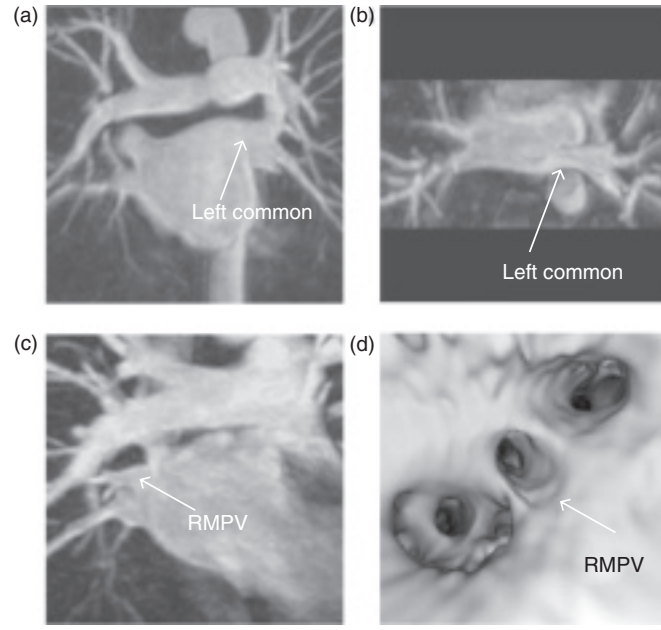

Figure 9.1 Examples of variant pulmonary vein anatomy depicted by MR angiography. (a) AP view of a long left common trunk; (b) axial view of a long left common trunk; (c) AP view of a right middle pulmonary vein; and (d) cardiocentric 3D surface view of the right middle pulmonary vein ostium. Figure reprinted with permission from *Circulation* [8].

variants have implications for procedure planning. Tsao et al. described the potential for right middle PVs to be a focus for AF initiation [9]. The common presence of an extra right middle pulmonary vein in 18–29% of patients referred for atrial fibrillation ablation has been confirmed in a number of 3D imaging studies [6].

Knowledge of LA and PV anatomy can also affect technical aspects of the ablation procedure. A right middle PV can make stable ablation device positioning at the PV ostia difficult because of the narrow tissue ridges separating it from the adjacent right PVs. Such atrial ridge anatomy has been assessed by MRA [10]. Other variants such as PVs with large funnel-shaped ostia or small ostia may make mapping catheter selection and positioning difficult for the segmental isolation approach, and ablation within small or early branching PVs increases the risk of stenosis in that vessel [10]. Recognition of such variants may favor the use of circumferential ablation and can help determine the applicability of non-RF based ablation modalities such as cryothermy, ultrasound, and laser, which may have particular PV geometry considerations.

One atrial region that poses technical difficulty for stable ablation catheter positioning during circumferential ablation is the tissue ridge separating the left PA from the left atrial appendage. Mansour et al. used MRA to show that this ridge was 5 mm or less in 92% of 50 patients undergoing circumferential PV ablation, clarifying the difficulty of stable catheter positioning in this area [10]. Merging 3D atrial anatomy from CT or MRA with catheter position determined by electrospatial mapping is being investigated and may assist in completing lines of ablation in such technically challenging areas [11]. The topic of using MRI to guide procedures will be discussed further below.

MRI for Improving Safety of Atrial Fibrillation Ablation

Three-dimensional imaging also has implications for improved safety of AF ablation procedures by delineating the relationship of the LA to the esophagus and adjacent vascular structures.

The potentially lethal complication of atrioesophageal fistula has motivated assessment of the relationship of the esophagus to the posterior LA and PVs. Two studies using CT demonstrated the ubiquitous contact of the esophagus with the posterior LA [12, 13]. Both studies found that the esophagus tends to course closer to the left inferior

pulmonary vein, but can have significant individual variation of positioning, suggesting another potential value of preprocedural 3D imaging. MRA has also been used to define the position of the esophagus and can similarly be used to guide reduction of ablation power around the esophagus and direct ablation away from this area when possible [14]. Variation of esophageal position due to peristalsis has been noted, but its impact on the reliability of using preprocedural imaging to define esophageal position requires further evaluation.

The proximity of adjacent vessels to the LA and PVs may be useful to consider particularly when using ablation technologies that are capable of creating deeper lesions such as irrigation-cooled RF ablation, ultrasound, cryothermy, and laser. In addition to directing ablation away from the PV ostia, 3D imaging can identify the position of the descending aorta which was noted to contact the posterior LA wall or left PVs in 77% of 65 subjects in one study [13]. Imaging can also delineate the right pulmonary artery course along the LA roof and the left circumflex coronary artery position adjacent to the anterior base of the LA appendage orifice [6]. Acute occlusion of the left circumflex coronary artery has been reported in an AF ablation procedure during completion of a mitral isthmus ablation line from the coronary sinus [15].

Scar-Based Monomorphic Ventricular Tachycardia

Ventricular tachycardias with repetitive uniform morphology arise from an anatomically fixed arrhythmia substrate that can be targeted for ablative modification and cure [16]. Some of these rhythms, including right ventricular outflow tract (RVOT), ventricular tachycardia (VT), left ventricular (LV) outflow tract VT, and LV reentrant VT, occur in structurally normal hearts and typically respond well to current ablative treatment techniques. Bundle branch reentry monomorphic VT is relatively common among nonischemic cardiomyopathy-associated VTs and responds well to ablation of the right bundle branch. However, myocardial scarring due to infarction, cardiomyopathy, sarcoidosis, ARVD, or cardiac surgery are common causes of monomophic VT that are difficult to treat medically or with ablation [16].

Scar-related VT is typically a reentrant arrhythmia that depends on critical isthmuses of conductive tissue bounded by nonexcitable scar or a valve annulus [17]. In contrast to the anatomic substrate for other monomorphic VTs, scar morphology and associated arrhythmia circuits are highly variable between patients. Such arrhythmias are often poorly tolerated hemodynamically limiting the use of traditional mapping techniques during the tachycardia. Substrate-based approaches utilizing electrospatial mapping of scar regions, pace mapping to reproduce VT morphology, and assessment of local electrogram characteristics such as isolated diastolic potentials have been used to identify possible isthmus and exit site regions of the arrhythmia circuit to target ablation [16, 18]. Still, the time-consuming nature of these procedures, the dependence of certain VT on epicardial pathways that require additional epicardial mapping or intramural pathways that are inaccessible to mapping, and suboptimal cure rates on the order of 70% or less even in experienced hands, make better targeted and alternative strategies for ablation attractive.

MRI for Ventricular Tachycardia Substrate Imaging and Risk Prediction

Using MRI to assess the arrhythmia substrate in scar-based VT is still in the investigational stages, but shows promise. Delayed gadolinium-enhanced MRI (DEMRI) has been used extensively to identify regions of myocardial scar in ischemic and a number of nonischemic cardiomyopathies [19, 20]. More recently, MRI scar characteristics have been correlated with the risk and electrical morphology of inducible monomorphic ventricular tachycardia.

The relationship of monomorphic VT to myocardial scar depicted by MRI has been most extensively established for myocardial infarction. Bello et al. used DEMRI to study the relationship of LV scar size to inducible VT in 48 coronary artery disease patients referred for electrophysiologic study (EPS). In this population, sustained monomorphic VT was induced in 18 patients. Infarct surface area and

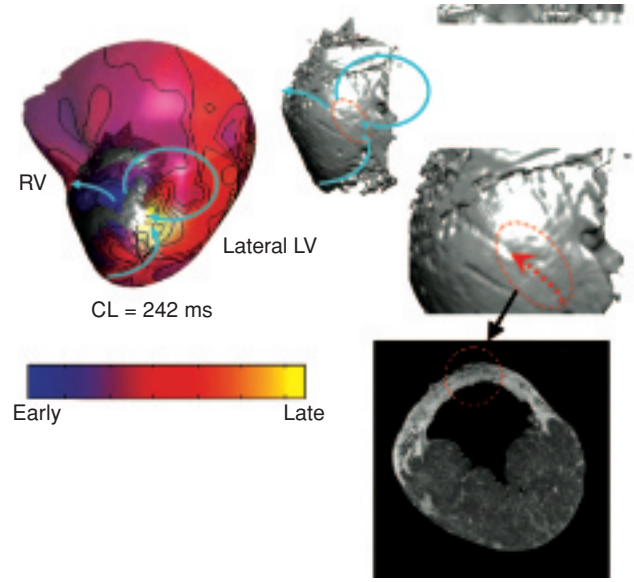

Figure 9.2 Example of the correlation between the isthmus of an induced VT circuit detected by epicardial activation mapping to an anatomic channel of viable myocardium depicted by very high resolution delayed enhancement MRI. (Left upper figure) High-resolution activation map obtained during induced VT. (Right lower figure) once slice through a 3D high resolution MRI image of myocardial scar. (Right upper figures) Visual correlation of the VT circuit isthmus with a channel of viable myocardium on a 3D surface reconstruction of the infarct scar. Figure reprinted with permission from *Circulation Research* [26].

infarct mass were found to be significant predictors of inducible VT while LV ejection fraction was not [21].

Schmidt and colleagues recently reported on the value of more detailed scar morphology assessment for ischemic VT prediction. They used an image intensity threshold method to quantify regions of dense scar and "scar border zone" (SBZ) hypothesizing that the SBZ regions correspond to potential regions of slow conduction, which could lead to reentrant VT [22]. In 47 patients with ischemic cardiomyopathy referred for primary prevention ICD placement, they found the amount of tissue classified as SBZ was significantly associated with VT inducibility [22]. Interestingly, the amount of dense scar, identified as a VT predictor in the previous study, and the transmural extent of scar, which has been identified as a risk factor for VT in nonischemic cardiomyopathy (CM), were not significantly associated with VT in this population [21, 23]. This points to the limitation of extrapolating findings of gross scar morphology association studies to different study populations and different CMs. However, there may be a more direct connection between scar morphology and specific reentrant VT circuits in individual patients. Several early reports suggest a relationship of DEMRI scar location to VT location based on surface EKG morphology for a number of cardiomyopathies including dilated CM, ARVD, and sarcoid [23–25].

Experimental Use of MRI for Ventricular Tachycardia Circuit Prediction

The potential for DEMRI to more directly assist in VT ablation planning has been assessed in recent animal studies. Ashikaga et al. used an epicardial sock with 300– 380 simultaneous recording sites to obtain high-resolution activation maps of inducible monomorphic VT in a pig infarct/reperfusion model [26] (Figure 9.2). The activation maps were then registered to very high-resolution ex vivo 3D DEMRI images (0.39 mm × 0.39 mm × 0.39 mm resolution) to assess the relationship of electrical propagation to scar morphology. Detailed scar imaging revealed numerous previously unseen features including 3D tracts of viable myocardium within scar and scar within viable myocardium that visually correlated with epicardial exit sites and isthmus pathways identified on epicardial activation mapping. The study also confirmed the limitations of assessing 3D VT circuits with 2D mapping on one surface of the myocardium and pointed to the

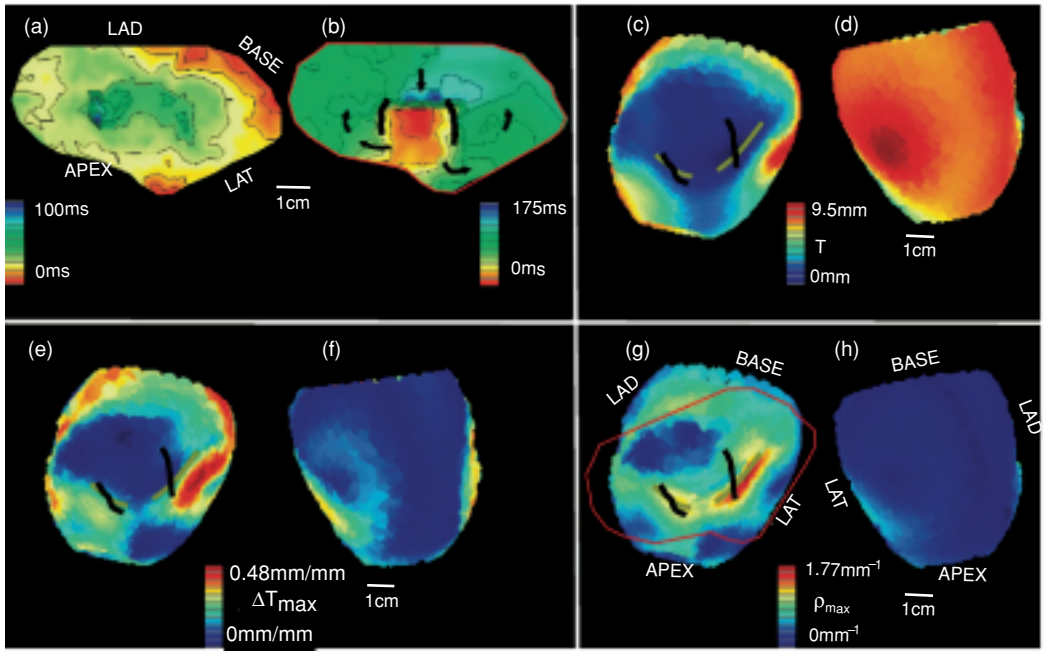

Figure 9.3 Example of VT isthmus site prediction using a model of wave front geometry based on regional scar thickness determined from high-resolution delayed enhancement MRI. The black lines represent the isthmus detected from activation mapping of an induced VT; the green lines represent the isthmus predicted from the model. (Left upper figure) Activation maps during sinus rhythm and VT. (Right upper figure) Regional scar thickness determined from 3D MR images. (Right lower figure) Model prediction of wave front geometry and resulting isthmus site prediction. Figure reprinted from permission from *Heart Rhythm* [27].

adjunctive potential of MRI for identifying intramural correlates of VT propagation [26].

Ciaccio recently reported use of high-resolution SBZ geometry determined by DEMRI to predict VT isthmus ablation sites in a canine transmural infarct model [27]. (Figure 9.3). Their analytic model used 2D scar thickness maps measured from histology sections and 0.4 mm × 0.4 mm × 0.4 mm pixel resolution ex vivo DEMRI to predict VT excitation wavefront propagation. Observed lines of block from epicardial activation maps during inducible VT were compared with model predicted block lines. Though the results were not divided into those from histology ($n = 4$) and those from DEMRI ($n = 3$) the results were qualitatively similar between techniques. The overall mean distance between the actual and estimated block lines was 6.5 ± 3.7 mm, and the estimated ablation target line through the center of the predicted isthmus overlapped the actual isthmus width by 91.8% ± 4.6% [27]. Techniques that use more detailed biodomain models incorporating ion channel physiology and structural characteristics obtained from 3D MRI are also being investigated.

Though these experimental studies use significantly higher resolution DEMRI maps than the typical 1.5 mm × 2.5 mm × 8 mm pixel resolution used clinically, methods to obtain higher-resolution scar maps in patients are being developed [28]. Together with studies to identify safe MR imaging procedures for patients with implanted defibrillators [23] and clinical correlation of DEMRI scar morphology to successful VT ablation sites, the role of MRI for clinical VT ablation will be better defined.

Applications of MRI for Ablation Procedure Guidance and Lesion Assessment

Using the detailed anatomic and functional information provided by MRI for preprocedural planning has been a preliminary step toward using the

information for intraprocedure guidance. The basic requirement for MR guidance of procedures is for the ablation device position to be accurately depicted relative to MR imaged anatomy. This would provide an ability to target arrhythmogenic anatomic regions while avoiding areas such as near the PV ostia and esophagus that could lead to complications. The initial step bringing this goal to clinical practice has been to register position data from electrospatial mapping to image based landmarks on pre-acquired 3D MRI or CT so that subsequent electrospatial mapping locations can be translated to corresponding 3D image locations. The development and applications of this technique will be discussed first.

Other potential benefits of MRI require updated imaging during the procedure. The orientation and stability of ablation device contact with the myocardium is known to be an important factor in lesion formation and could be directly visualized during catheter manipulation [29]. Additionally, direct visualization of ablation location and extent during the procedure would be helpful to confirm desirable positioning and to avoid complications. Finally, recovery of conduction through transient postprocedure regions of block appears to be a factor in arrhythmia recurrence [30, 31]. Imaging of ablation lesion continuity would provide a quantifiable measure for gauging outcomes and could be an important procedural endpoint if found to be useful for predicting arrhythmia cure. The past and current preclinical work toward bringing intraprocedure and "real-time" MRI to clinical practice will also be discussed.

Registration of Electrospatial Position Data with Preacquired 3D MRI for Procedure Guidance

Dickfeld et al. first reported the feasibility of using 3D MR angiogram images registered to a magnetic field–based catheter position tracking system to target and create cardiovascular RF ablation lesions without the use of fluoroscopy [32, 33]. Using multiple MR visible skin makers for registration with the electrospatial mapping system, they were able to ablate the center of the fossa ovalis with an accuracy of 3.9 $\pm$ 2.1 mm, and repeatedly ablate a right ventricular (RV) and inferior vena cavae (IVC) site with a precision of 3.9 $\pm$ 0.5 mm 4.4 $\pm$ 2.4 mm, respectively. They were also able to consistently manipulate a catheter from an internal jugular sheath to ablate within the left atrial appendage using only electrospatial mapping position and the preacquired MRA for guidance.

Imageguided electrospatial mapping has since been applied clinically for pulmonary vein isolation procedures [11, 34]. One group reported their technique for registering CARTO electrospatial mapping position to preacquired 3D MR and CT images in 16 patients undergoing circumferential PV ablation combined with segmental PV isolation [11]. After adequate registration was achieved, LA and PV anatomy depicted by 3D imaging was felt to be helpful for guiding the procedure. Of the patients studied, 47% exhibited variant PV anatomy, and the placement of circumferential lesions around pairs of left and right PVs could be tailored to the imaged anatomy [11] (Figure 9.4) Also, difficulty in stable catheter positioning at the LAA/PV junction corresponded to narrow ridge anatomy on 3D imaging. and lesion placement could be guided to the anterior portion of the left PV ostia. In line with previous results, freedom from AF recurrence at 6 months was noted in 80% in patients with paroxysmal AF, two of four patients with persistent AF, and zero of two patients with permanent AF [11]. As use of such image-guided electrospatial mapping becomes more widespread, the effect of this technology on AF ablation outcomes, safety, and ease will become more apparent.

Reddy and colleges have extended similar techniques to evaluate the feasibility of VT substrate ablation in a pig mid-LAD infarct model [35]. With a registration scheme using manual segmentation of the aorta from 3D imaging and minimizing the distance of this surface to nonspecific electrospatial mapping points placed within the aorta they were able to reduce the dependence of registration on time consuming high-density LV mapping. Using this system, they report targeting of sites in the LV with an accuracy of 1.8 $\pm$ 0.5 mm and confirmed that ablation lesions guided to the infarct edge on preacquired DEMRI were situated at the scar border zone area on gross pathology [35]. Use of this technique to guide clinical VT ablation has been slowed by the safety concerns of MR imaging in patients with ICDs and the lack of equivalent scar imaging

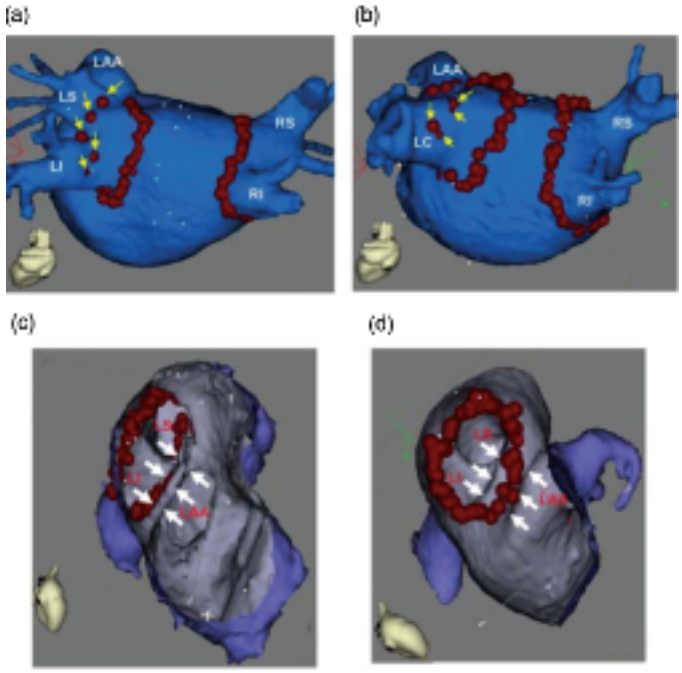

Figure 9.4 Example of tailored circumferential RF ablation around pulmonary vein ostia guided by electrospatial mapping registered to 3D surface anatomy obtained by MR angiography. Circumferential ablation (a) around a normal pattern of pulmonary veins, (b) around a left common trunk, (c) navigating a narrow ridge separating left-sided pulmonary veins from the left atrial appendage, and (d) placing lesions along a wide ridge separating left side pulmonary veins from the left atrial appendage. Figure reprinted with permission from *The Journal of Cardiovascular Electrophysiology* [11].

by CT. The possibility of MR scanning in this group of patients will be addressed below in the discussion of future directions.

While registering real-time device position from electrospatial mapping to preacquired 3D imaging is an improvement over the simple surface geometry constructed by electrospatial mapping alone, it suffers from the potential for registration error and it still does not depict the actual results of ablation. Even with careful attempts at coordinating the cardiac and respiratory phase of imaging with electrospatial mapping position through cardiac gating and reference catheter-based motion correction, the anatomy depicted by preacquired images routinely deviates from the intraprocedural anatomy. This is due in part to changes in chamber size associated with variations in heart rate, rhythm, and volume status [35].

In clinical practice additional errors can result from variations in patient positioning between the preacquired scan and procedure, and inadvertent subject motion during the procedure. From their initial 3D image registration experience, Dong et al. reported a PV isolation rate of only 32% after anatomic circumferential ablation [11]. They resorted to additional segmental mapping and ablation to achieve full PV isolation. Using irrigation catheters to produce more extensive ablation lesions, other groups still report only a 50–60% PV isolation rate after circumferential ablation [36, 37]. These results may reflect inherent limitations of electrospatial mapping for assessing the completeness of ablation lines.

Intraprocedure MRI for Guidance and Lesion Assessment

Real-time imaging during electrophysiology procedures has the potential to visualize device contact with moving local anatomy and evaluate the tissue response to ablation therapy [38, 39]. Intracardiac echocardiography (ICE) has brought some of the benefits of real-time imaging to current clinical practice [40]. However, ICE currently requires manipulation of a separate imaging catheter and physical limitations on image plane orientation and a restricted field of view limit the ability of ICE to evaluate lesion extent and characterize extended regions of ablation.

Intraprocedure high-resolution MRI together with real-time MRI can combine the detailed anatomic information useful for procedure planning with direct visualization of device position in relation to complex moving anatomy and

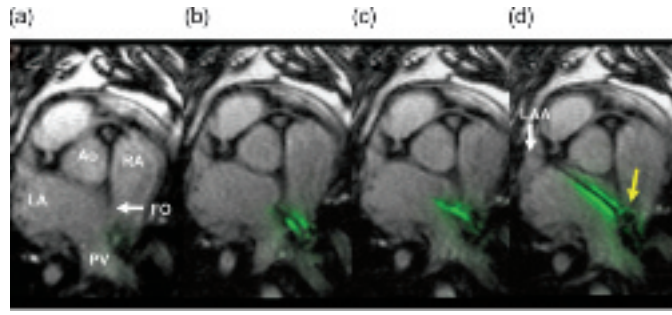

Figure 9.5 Real-time MRI visualization of atrial septal puncture. Stepwise images include (a) visualization of the fossa ovalis, (b) placement of an automatically highlighted needle at the fossa with observed tenting of the atrial septum, (c) controlled puncture of the atrial septum, and (d) passage of a floppy wire into the left atrial appendage through the puncture needle. The floppy wire appears highlighted due to electrical coupling with the needle. The yellow arrow points to the dilator sheath tip intentionally designed to create image distortion for improved visualization. Figure reprinted with permission from *Catheterization and Cardiovascular Interventions* [43].

flexible imaging of the response to ablation therapy including lesion extent and ablation line continuity. The high static magnetic field environment, strong oscillating electromagnetic fields generated during MR scanning, physical limitations to patient access within the scanner bore, and prior requirement for ECG gating and breath holding have made interventional MRI guidance of cardiac procedures challenging. However, technical advances over the last 20 years including the development of MR safe device construction techniques, short-bore high-field MRI scanners, and faster imaging capabilities are bringing the potential benefits of performing electrophysiology procedures under real-time MRI guidance closer to reality.

Lardo et al. reported the use of real-time MRI for performing all the basic steps involved in an EP procedure [41]. MR imaging with interactive image plane manipulation was used to guide a catheter constructed from nonferromagnetic materials from an internal jugular sheath to points in the right atrium and right ventricle in six dogs. The catheter was directed to the inferior lateral wall of the right atrium (RA) with visualization of catheter contact against the atrial wall and visual confirmation of various surrounding anatomic references including the vena cavae, coronary sinus, Eustachian ridge, fossa ovalis, and tricuspid valve. The catheter could also be advanced to the RV apex and RV lateral wall and RF power was applied to these sites while artifact free real-time imaging was performed.

Low-pass filtering was required to suppress ablation generator noise that would otherwise interfere with MR image acquisition. The lesions could be seen for 2 min after ablation using T2-weighted imaging without contrast as well as for 60 sec after the administration of contrast. The ablation lesion length, width, and depth derived from MR imaging correlated well with gross pathology examination [41]. Intracardiac electrograms were recorded during imaging using a shielded band-pass filter and confirmed a roughly 9-fold decrease of local IEGM magnitude after ablation. We have since extended these results to record simultaneous RA, His bundle, and RV electrograms from catheters maneuvered to the high right atrium, AV junction, and RV apex under real-time MR guidance.

Other techniques relevant to EP procedures have also been performed using real-time MRI guidance. Transseptal catheterization is the standard method for left atrial access during AF ablation. However, the procedure can be challenging to perform under fluoroscopy, particularly in the setting of distorted atrial anatomy, and carries the risk of serious complications including cardiac perforation. Real-time MRI has successfully been used to guide transeptal punctures in animal models under direct visualization of the needle, atria, fossa ovalis, and surrounding vasculature [42, 43] (Figure 9.5) Retrograde catheterization of the left ventricle from the femoral artery has also been performed under real-time MRI guidance [44].

Translation of real-time MR-guided EP studies to human subjects has been appropriately cautious due to concerns about the potential for catheter tip heating from current induction during MR

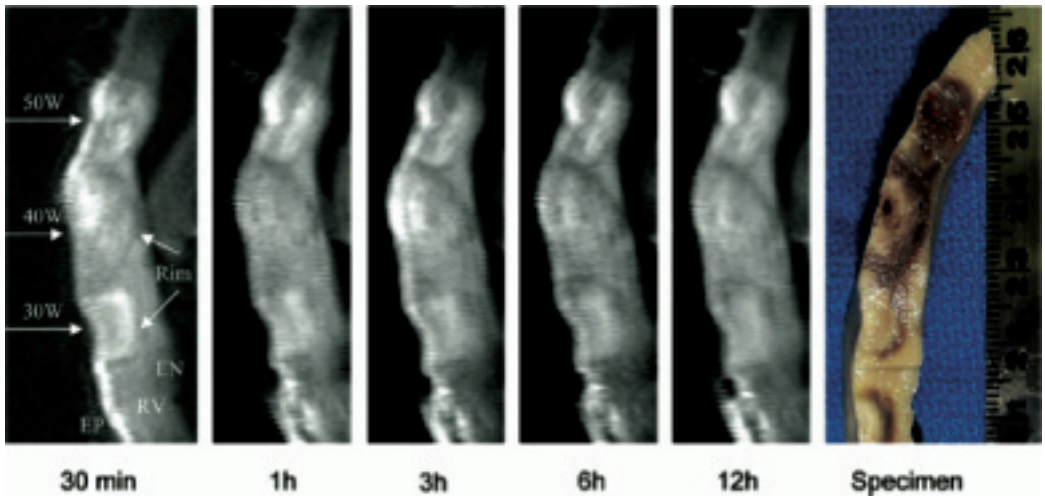

Figure 9.6 Example of noncontrast T2-weighted MR imaging of right ventricular epicardial RF ablation lesions with pathologic correlation. Stability of the imaged lesion size is demonstrated from 30 min to 12 hr after ablation. Figure reprinted with permission from *Heart Rhythm* [46].

imaging. Safe application of this technique to more general EP procedures in patients will require reliable induction current suppression techniques which will be further described below in the discussion of future directions.

Perhaps the most valuable advantage of MRI-guided ablation therapy is the unique ability to visualize and monitor ablation lesion formation with high temporal and spatial resolution. RF ablation lesions can be visualized because MRI is able to detect specific changes to proton precession and relaxation properties resulting from heating and heat-induced biophysical changes in cardiac tissue including interstitial edema, hyperemia, protein conformational changes, cellular shrinkage, and tissue coagulation [41].

Acute interstitial edema is most likely responsible for the hyperintense regions representing the area of damage observed by T2-weighted FSE imaging [41]. Changes in protein structure and temperature sensitivity of the T1 parameter allow lesions to be visualized by imaging protocols like SPGR [41, 45]. T1- and T2-weighted imaging of ablation lesions have been carefully evaluated in canine open-chest epicardial ablation studies [46]. Though the quality of T1-weighted lesion imaging was felt to be less consistent than T2-imaging, lesion size depicted by both T1- and T2-weighted imaging correlated well with gross pathology. Gaps between ablation lesions could also be visualized using both T1- and T2-weighted imaging. The imaged lesion characteristics were stable over the 30-min to 12-hr follow-up period, making MRI a tool to evaluate lesions over the course of an ablation procedure (Figure 9.6).

Gadolinium contrast DEMRI has also been used to visualize ablation lesions. The time to achieve full enhancement of RF ablation lesions, 1–2 hr, is longer than for myocardial infarct scar. However, good correlation with pathologic lesion size was noted for intermediate enhancement patterns from 1 min to 2 hr after contrast injection, allowing lesion extent to be assessed before full enhancement [39]. The 1–2 hr interval required for renal clearance between repeated dosing of gadolinium and the ceiling on total allowable gadolinium dose limits the use of this technique for serial lesion assessment during a procedure [45]. However, because it provides superior lesion visualization compared to noncontrast imaging, this technique may be useful for evaluating gaps in ablation lines after completion of a procedure. DEMRI of ablation lesions may also have a role in outpatient follow-up after catheter ablation procedures. DEMRI has recently been applied to noninvasively characterize lesions around the PVs after AF ablation.

Peters et al. described their initial patient experience with a technique permitting high-resolution DEMRI images of the LA to be obtained over 10 min

using image-based respiratory gating to avoid the need for repeated breath holds [47]. While currently in the proof-of-concept stage, this technique shows promise for being able to relate AF ablation procedure outcomes to postablation characteristics such as lesion continuity. The ability to noninvasively detect ablation lesions in the thin-walled atrium also supports the possibility of imaging atrial lesions noninvasively during MR-guided electrophysiology procedures. Transesophageal coils and intravascular coils may also be used to enhance visualization of lesions in the atria.

Though T1-weighted imaging is sensitive to temperature, proton resonance shift thermography is a more quantifiable temperature-sensitive imaging technique that has been used to follow tumor ablation in the uterus, liver, prostate, and brain using diverse energy sources including RF, high-frequency ultrasound, laser, and microwave [48–53]. Its use for following RF ablation in the beating heart is currently being investigated. More exotic techniques such as RF current–vector mapping are also being studied for monitoring the extent of tissue power deposition during RF ablation [54].

Future Directions

Taking real-time MRI guidance of electrophysiology procedures from the investigational stage to clinical use is within reach, but depends largely on the development of clinical-grade interventional devices that are designed to be safe in the MR imaging environment. Additional technologies such as device tracking with closed-loop scan plane control, 3D visualization software, parallel imaging techniques to improve imaging speed, and high-resolution free breathing imaging techniques for imaging patients without a need for breath hold cooperation are currently under development. Current progress in these areas will be surveyed.

Interventional MRI Device Safety

The most important consideration for any new diagnostic or therapeutic approach is safety. While a number of studies have been performed to determine the safety of conventional MRI with regard to electromagnetic energy exposure and internal heating [55, 56], interventional procedures present additional parameters and raise new safety concerns [57–60].

The most straightforward aspect to MRI device safety is the avoidance of ferromagnetic materials that could experience significant translation and torsion forces when brought close to the scanner. The strength of this force can become significant at the 5 Gauss line and increases exponentially closer to the scanner. A plan for methodical tracking and removal of ferromagnetic objects before approaching the scanner and clear marking of high magnetic field areas is mandatory [61].

Defibrillation is associated with an electric current that can also lead to strong displacement forces in high magnetic fields and should be performed with the defibrillator pads maintained outside the scanner bore [62]. Similar attention and safety measures are needed to address the ferromagnetic properties and electromagnetic compatibility of other equipment associated with electrophysiology procedures including physiology monitoring equipment, ablation and pacing sources, and anesthesia apparatus.

In addition, long conductive objects such as guidewires, wired electrodes, and metal braided catheters are subject to inductive heating, particularly when portions of the device are located close to the high-power radiofrequency transmit coil housed within the edge of the scanner bore [58, 59]. The safest way to avoid this problem is to construct devices from nonmetallic components such as Dacron for catheter braiding and glass fiber reinforced plastics for guidewires [41, 63]. Several approaches have also been developed to reduce current induction in signal-carrying structures such as electrode wires and intravascular imaging coils. These techniques include incorporation of RF chokes, transmission line transformers, decoupling circuits, and fiber optics into conductive catheter components [23, 64–72]. Now that several academic and industry research centers are focusing on heating safe device development, more rapid progress in this area is expected.

The compatibility of MRI with implanted devices such as pacemakers and ICDs is an important consideration for performing interventional MRI studies in the electrophysiology patient population. Specific concerns include static magnetic field induced movement of the device and scanning-induced

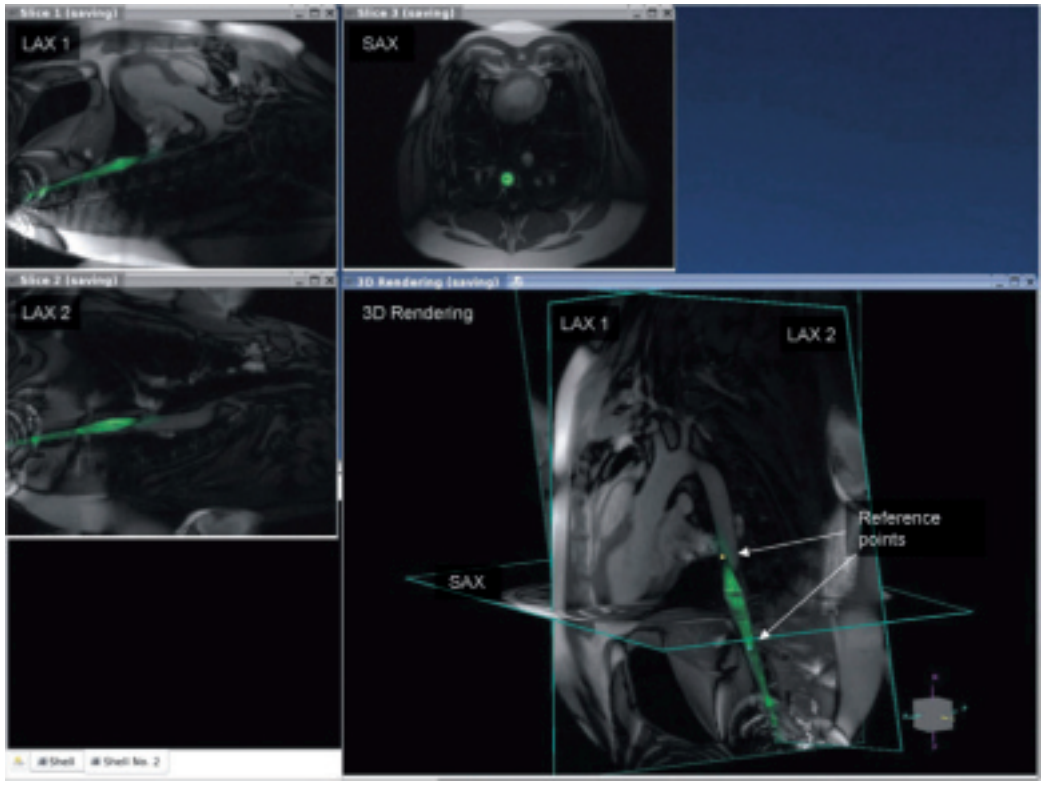

Figure 9.7 Example of using automatic catheter highlighting and reference image planes to navigate complex 3D anatomy using real-time MRI. The anatomic location of the catheter position on the image labeled LAX2 is better appreciated when overlaid with long- and short-axis images of the heart. Figure reprinted with permission from *The Journal of Magnetic Resonance Imaging* [79].

programming changes, device inhibition, activation of tachyarrhythmia therapies, and lead currents leading to heating or cardiac stimulation [73–76]. Modern devices address some of these concerns with the use of less ferromagnetic material and improved resistance to electromagnetic interference [77]. Experience is now growing for safe cardiac MRI scanning in patients with selected devices under controlled scanning conditions [23, 77, 78]. This experience includes use of sequences relevant to modern cardiac MR, including DEMRI, opening the possibility of substrate imaging in patients with VT who have ICDs. Still, the number of patients and devices studied thus far is limited and further work is needed to develop manufacturer protocols for establishing conditional MRI safety of pacemakers and ICDs. Carefully designed protocols for patient selection, monitoring, and scanning also need to be developed before imaging of patients with devices can be more routinely performed.

Other Directions for Research

Real-time MRI differs from fluoroscopy in that MRI typically generates an image from a 5–10 mm thick slice through the body as opposed to a typical X-ray projection containing the entire body thickness. While this allows for high-resolution depiction of structures in the imaging plane, it poses some difficulties for visualizing curved devices such as catheters which may not fall entirely within a single imaging plane. Several techniques have been developed to approach this problem including thick slab MR imaging that simulates fluoroscopy and active device tracking to detect the device tip position and automatically move the scan plane to the device position [79–81] Active device position tracking can

also be used to tag local IEGM data to the device position for constructing electroanatomic maps. Another difficulty posed by MR thin slice imaging is the ability to intersect anatomy in unfamiliar ways leading to user disorientation. Three-dimensional visualization tools are being developed that plot real-time thin slice images oriented relative to reference 2D and 3D images [32, 79] (Figure 9.7).

Finally, recent advances in scanning techniques are making their way to commercial MRI systems extending the potential of interventional MRI beyond specialized research centers. Fast scanning using coherent steady-state imaging sequences, parallel image reconstruction, and more efficient data sampling are pushing "real-time" MRI frame rates from the one frame per second reported in the initial MR guided EP study to 3–8 frames per second on many currently available scanners to 20 frames per second and the potential for real-time 3D imaging using speed optimized techniques on specialized hardware [41, 79, 82, 83]. The more general availability of parallel image reconstruction and image-based respiratory gating sequences is also opening the way for higher resolution 3D imaging in patients who cannot cooperate with breath holds during an interventional study [28].

Conclusion

MRI has demonstrated a number of uses for preablation planning, particularly for treatment of atrial fibrillation. The use of DEMRI for planning VT ablation procedures shows promise but requires further investigation of the safety of MRI in patients with ICDs. While in its infancy for guiding electrophysiology procedures, interventional MRI has been used to guide clinical procedures in other fields cost-effectively and with reductions in X-ray exposure [61, 84]. Available solutions for the remaining clinical safety barriers offer the possibility for more robust intraprocedure visualization of the moving arrhythmia substrate, interventional device placement, and adequacy of ablation in the near future. The ability to accurately guide devices and establish completeness of ablation lines without concern for radiation exposure could improve the way current ablation procedures are performed and open the way to ablative cure of arrhythmias such as permanent atrial fibrillation that currently respond poorly to minimally invasive approaches [85].

References

1 Calkins H, Yong P, Miller JM, et al. Catheter ablation of accessory pathways, atrioventricular nodal reentrant tachycardia, and the atrioventricular junction: final results of a prospective, multicenter clinical trial: The Atakr Multicenter Investigators Group. *Circulation* 1999; **99**: 262–70.

2 Mitsui T, Ijima H, Okamura K, Hori M. Transvenous electrocautery of the atrioventricular connection guided by the His electrogram. *Jpn Circ J* 1978; **42**: 313–18.

3 Lim KT, Murray C, Liu H, Weerasooriya R. Preablation magnetic resonance imaging of the cavotricuspid isthmus. *Europace* 2007; **9**: 149–53.

4 Da Costa A, Faure E, Thevenin J, et al. Effect of isthmus anatomy and ablation catheter on radiofrequency catheter ablation of the cavotricuspid isthmus. *Circulation* 2004; **110**: 1030–35.

5 Sanchez-Ortiz GI, Sermesant M, Rhode KS, et al. Localization of abnormal conduction pathways for tachyarrhythmia treatment using tagged MRI. *Med Image Comput Comput Assist Interv Int Conf Med Image Comput Comput Assist Interv* 2005; **8**: 425–33.

6 Wazni OM, Tsao HM, Chen SA, et al. Cardiovascular imaging in the management of atrial fibrillation. *J Am Coll Cardiol* 2006; **48**: 2077–84.

7 Dong J, Calkins H. Technology insight: catheter ablation of the pulmonary veins in the treatment of atrial fibrillation. *Nat Clin Pract Cardiovasc Med* 2005; **2**: 159–66.

8 Kato R, Lickfett L, Meininger G, et al. Pulmonary vein anatomy in patients undergoing catheter ablation of atrial fibrillation: lessons learned by use of magnetic resonance imaging. *Circulation* 2003; **107**: 2004–10.

9 Tsao HM, Wu MH, Yu WC, et al. Role of right middle pulmonary vein in patients with paroxysmal atrial fibrillation. *J Cardiovasc Electrophysiol* 2001; **12**: 1353–57.

10 Mansour M, Refaat M, Heist EK, et al. Three-dimensional anatomy of the left atrium by magnetic resonance angiography: implications for catheter ablation for atrial fibrillation. *J Cardiovasc Electrophysiol* 2006; **17**: 719–23.

11 Dong J, Dickfeld T, Dalal D, et al. Initial experience in the use of integrated electroanatomic mapping with three-dimensional MR/CT images to guide catheter ablation of atrial fibrillation. *J Cardiovasc Electrophysiol* 2006; **17**: 459–66.

12 Tsao HM, Wu MH, Higa S, et al. Anatomic relationship of the esophagus and left atrium: implication for catheter ablation of atrial fibrillation. *Chest* 2005; **128**: 2581–87.

13 Cury RC, Abbara S, Schmidt S, et al. Relationship of the esophagus and aorta to the left atrium and pulmonary

veins: implications for catheter ablation of atrial fibrillation. *Heart Rhythm* 2005; **2**: 1317–23.

14 Kenigsberg DN, Lee BP, Grizzard JD, Ellenbogen KA, Wood MA. Accuracy of intracardiac echocardiography for assessing the esophageal course along the posterior left atrium: a comparison to magnetic resonance imaging. *J Cardiovasc Electrophysiol* 2007; **18**: 169–73.

15 Takahashi Y, Jais P, Hocini M, et al. Acute occlusion of the left circumflex coronary artery during mitral isthmus linear ablation. *J Cardiovasc Electrophysiol* 2005; **16**: 1104–7.

16 Stevenson WG. Catheter ablation of monomorphic ventricular tachycardia. *Curr Opin Cardiol.* 2005; **20**: 42–47.

17 de Chillou C, Lacroix D, Klug D, et al. Isthmus characteristics of reentrant ventricular tachycardia after myocardial infarction. *Circulation* 2002; **105**: 726–31.

18 Marchlinski FE, Callans DJ, Gottlieb CD, Zado E. Linear ablation lesions for control of unmappable ventricular tachycardia in patients with ischemic and nonischemic cardiomyopathy. *Circulation* 2000; **101**: 1288–96.

19 Judd RM, Wagner A, Rehwald WG, Albert T, Kim RJ. Technology insight: assessment of myocardial viability by delayed-enhancement magnetic resonance imaging. *Nat Clin Pract Cardiovasc Med* 2005; **2**: 150–58.

20 Mahrholdt H, Wagner A, Judd RM, Sechtem U, Kim RJ. Delayed enhancement cardiovascular magnetic resonance assessment of nonischaemic cardiomyopathies. *Eur Heart J* 2005; **26**: 1461–74.

21 Bello D, Fieno DS, Kim RJ, et al. Infarct morphology identifies patients with substrate for sustained ventricular tachycardia. *J Am Coll Cardiol* 2005; **45**: 1104–8.

22 Schmidt A, Azevedo CF, Cheng A, et al. Infarct tissue heterogeneity by magnetic resonance imaging identifies enhanced cardiac arrhythmia susceptibility in patients with left ventricular dysfunction. *Circulation* 2007; **115**: 2006–14.

23 Nazarian S, Roguin A, Zviman MM, et al. Clinical utility and safety of a protocol for noncardiac and cardiac magnetic resonance imaging of patients with permanent pacemakers and implantable-cardioverter defibrillators at 1.5 tesla. *Circulation* 2006; **114**: 1277–84.

24 Tandri H, Saranathan M, Rodriguez ER, et al. Noninvasive detection of myocardial fibrosis in arrhythmogenic right ventricular cardiomyopathy using delayed-enhancement magnetic resonance imaging. *J Am Coll Cardiol* 2005; **45**: 98–103.

25 Redheuil AB, Paziaud O, Mousseaux E. Ventricular tachycardia and cardiac sarcoidosis: correspondence between MRI and electrophysiology. *Eur Heart J* 2006; **27**: 1430.

26 Ashikaga H, Sasano T, Dong J, et al. Magnetic resonance-based anatomical analysis of scar-related ventricular tachycardia: implications for catheter ablation. *Circ Res* 2007; **101**: 939–47.

27 Ciaccio EJ, Ashikaga H, Kaba RA, et al. Model of reentrant ventricular tachycardia based on infarct border zone geometry predicts reentrant circuit features as determined by activation mapping. *Heart Rhythm* 2007; **4**: 1034–45.

28 Ledesma-Carbayo MJ, Kellman P, Arai AE, McVeigh ER. Motion corrected free-breathing delayed-enhancement imaging of myocardial infarction using nonrigid registration. *J Magn Reson Imaging* 2007; **26**: 184–90.

29 Wittkampf FH, Nakagawa H. RF catheter ablation: lessons on lesions. *Pacing Clin Electrophysiol* 2006; **29**: 1285–97.

30 Ouyang F, Antz M, Ernst S, et al. Recovered pulmonary vein conduction as a dominant factor for recurrent atrial tachyarrhythmias after complete circular isolation of the pulmonary veins: lessons from double Lasso technique. *Circulation* 2005; **111**: 127–35.

31 Verma A, Kilicaslan F, Pisano E, et al. Response of atrial fibrillation to pulmonary vein antrum isolation is directly related to resumption and delay of pulmonary vein conduction. *Circulation* 2005; **112**: 627–35.

32 Dickfeld T, Calkins H, Zviman M, et al. Anatomic stereotactic catheter ablation on three-dimensional magnetic resonance images in real time. *Circulation* 2003; **108**: 2407–13.

33 Dickfeld T, Calkins H, Zviman M, et al. Stereotactic magnetic resonance guidance for anatomically targeted ablations of the fossa ovalis and the left atrium. *J Interv Card Electrophysiol* 2004; **11**: 105–15.

34 Malchano ZJ, Neuzil P, Cury RC, et al. Integration of cardiac CT/MR imaging with three-dimensional electroanatomical mapping to guide catheter manipulation in the left atrium: implications for catheter ablation of atrial fibrillation. *J Cardiovasc Electrophysiol* 2006; **17**: 1221–29.

35 Reddy VY, Malchano ZJ, Holmvang G, et al. Integration of cardiac magnetic resonance imaging with three-dimensional electroanatomic mapping to guide left ventricular catheter manipulation: feasibility in a porcine model of healed myocardial infarction. *J Am Coll Cardiol* 2004; **44**: 2202–13.

36 Hocini M, Sanders P, Jais P, et al. Prevalence of pulmonary vein disconnection after anatomical ablation for atrial fibrillation: consequences of wide atrial encircling of the pulmonary veins. *Eur Heart J* 2005; **26**: 696–704.

37 Mantovan R, Verlato R, Calzolari V, et al. Comparison between anatomical and integrated approaches to atrial fibrillation ablation: adjunctive role of electrical pulmonary vein disconnection. *J Cardiovasc Electrophysiol* 2005; **16**: 1293–97.

38 Lickfett L, Dickfeld T, Kato R, et al. Changes of pulmonary vein orifice size and location throughout the cardiac cycle: dynamic analysis using magnetic resonance cine imaging. *J Cardiovasc Electrophysiol* 2005; **16**: 582–88.

39 Dickfeld T, Kato R, Zviman M, et al. Characterization of radiofrequency ablation lesions with gadolinium-enhanced cardiovascular magnetic resonance imaging. *J Am Coll Cardiol* 2006; **47**: 370–78.

40 Asirvatham SJ, Bruce CJ, Friedman PA. Advances in imaging for cardiac electrophysiology. *Coron Artery Dis* 2003; **14**: 3–13.

41 Lardo AC, McVeigh ER, Jumrussirikul P, et al. Visualization and temporal/spatial characterization of cardiac radiofrequency ablation lesions using magnetic resonance imaging. *Circulation* 2000; **102**: 698–705.

42 Arepally A, Karmarkar PV, Weiss C, Rodriguez ER, Lederman RJ, Atalar E. Magnetic resonance image–guided trans-septal puncture in a swine heart. *J Magn Reson Imaging* 2005; **21**: 463–67.

43 Raval AN, Karmarkar PV, Guttman MA, et al. Real-time MRI-guided atrial septal puncture and balloon septostomy in swine. *Catheter Cardiovasc Interv* 2006; **67**: 637–43.

44 Lederman RJ, Guttman MA, Peters DC, et al. Catheter-based endomyocardial injection with real-time magnetic resonance imaging. *Circulation* 2002; **105**: 1282–84.

45 Schmidt EJ, Reddy VK, Ruskin JN. Nonenhanced magnetic resonance imaging for characterization of acute and subacute radiofrequency ablation lesions. *Heart Rhythm* 2007; **4**: 215–17.

46 Dickfeld T, Kato R, Zviman M, et al. Characterization of acute and subacute radiofrequency ablation lesions with nonenhanced magnetic resonance imaging. *Heart Rhythm* 2007; **4**: 208–14.

47 Peters DC, Wylie JV, Hauser TH, et al. Detection of pulmonary vein and left atrial scar after catheter ablation with three-dimensional navigator-gated delayed enhancement MR imaging: initial experience. *Radiology* 2007; **243**: 690–95.

48 Ishihara Y, Calderon A, Watanabe H, Okamoto K, Suzuki Y, Kuroda K. A precise and fast temperature mapping using water proton chemical shift. *Magn Reson Med* 1995; **34**: 814–23.

49 McDannold N, Tempany CM, Fennessy FM, et al. Uterine leiomyomas: MR imaging-based thermometry and thermal dosimetry during focused ultrasound thermal ablation. *Radiology* 2006; **240**: 263–72.

50 Vigen KK, Jarrard J, Rieke V, et al. In vivo porcine liver radiofrequency ablation with simultaneous MR temperature imaging. *J Magn Reson Imaging* 2006; **23**: 578–84.

51 Rieke V, Kinsey AM, Ross AB, et al. Referenceless MR thermometry for monitoring thermal ablation in the prostate. *IEEE Trans Med Imaging* 2007; **26**: 813–21.

52 Demura K, Morikawa S, Murakami K, et al. An easy-to-use microwave hyperthermia system combined with spatially resolved MR temperature maps: phantom and animal studies. *J Surg Res* 2006; **135**: 179–86.

53 Kahn T, Harth T, Kiwit JC, Schwarzmaier HJ, Wald C, Modder U. In vivo MRI thermometry using a phase-sensitive sequence: preliminary experience during MRI-guided laser-induced interstitial thermotherapy of brain tumors. *J Magn Reson Imaging* 1998; **8**: 160–64.

54 Shultz K, Pauly J, Scott G. Feasibility of full RF current–vector mapping for MR-guided RF ablations. Paper presented at: Proceeding of the Joint Annual Meeting ISMRM-ESMRMB, Berlin, 2007.

55 International Commission on Nonionizing Radiation Protection. Guidelines for limiting exposure to time-varying electric, magnetic, and electromagnetic fields (up to 300 GHz). *Health Phys* 1998; **74**: 494–522.

56 Shellock FG. Radiofrequency energy-induced heating during MR procedures: a review. *J Magn Reson Imaging* 2000; **12**: 30–6.

57 Knopp MV, Essig M, Debus J, Zabel HJ, van Kaick G. Unusual burns of the lower extremities caused by a closed conducting loop in a patient at MR imaging. *Radiology* 1996; **200**: 572–75.

58 Nitz WR, Oppelt A, Renz W, Manke C, Lenhart M, Link J. On the heating of linear conductive structures as guide wires and catheters in interventional MRI. *J Magn Reson Imaging* 2001; **13**: 105–14.

59 Konings MK, Bartels LW, Smits HF, Bakker CJ. Heating around intravascular guidewires by resonating RF waves. *J Magn Reson Imaging* 2000; **12**: 79–85.

60 Atalar E. Radiofrequency safety for interventional MRI procedures. *Acad Radiol.* 2005; **12**: 1149–57.

61 Razavi R, Hill DL, Keevil SF, et al. Cardiac catheterisation guided by MRI in children and adults with congenital heart disease. *Lancet.* 2003; **362**: 1877–82.

62 Raman VK, Lederman RJ. Interventional cardiovascular magnetic resonance imaging. *Trends Cardiovasc Med* 2007; **17**: 196–202.

63 Kreuger S, Schmitz S, Ruhl KM, et al. Evaluation of an MR-compatible guidewire made in a novel micro-pultrusion process. Paper presented at: Proceeding of the Joint Annual Meeting ISMRM-ESMRMB, 2007; Berlin.

64 Wirtz D, Lips O, David B, Krueger S, Wiess S. Diagnostic MR-electrophysiology catheter with highly reisistive wires for reduction of RF-heating. Paper presented at: Joint Annual Meeting ISMRM-ESMRMB, 2007; Berlin.

65 Ladd ME, Quick HH. Reduction of resonant RF heating in intravascular catheters using coaxial chokes. *Magn Reson Med* 2000; **43**: 615–19.

66 Atalar E. Safe coaxial cables. Paper presented at: 7th Annual Meeting ISMRM, 1999; Philadelphia.

67 Vernickel P, Schulz V, Weiss S, Gleich B. A safe transmission line for MRI. *IEEE Trans Biomed Eng* 2005; **52**: 1094–1102.

68 Weiss S, Vernickel P, Schaeffter T, Schulz V, Gleich B. Transmission line for improved RF safety of interventional devices. *Magn Reson Med* 2005; **54**: 182–89.

69 Ocali O, Atalar E. Intravascular magnetic resonance imaging using a loopless catheter antenna. *Magn Reson Med* 1997; **37**: 112–18.

70 Wong EY, Zhang Q, Duerk JL, Lewin JS, Wendt M. An optical system for wireless detuning of parallel resonant circuits. *J Magn Reson Imaging* 2000; **12**: 632–38.

71 Fandrey S, Weiss S, Muller J. Miniature optical signal transmission system for an active intravascular device. Paper presented at: Joint Annual Meeting ISMRM-ESMRMB, 2007; Berlin.

72 Quick HH, Ladd ME, Nanz D, Mikolajczyk KP, Debatin JF. Vascular stents as RF antennas for intravascular MR guidance and imaging. *Magn Reson Med* 1999; **42**: 738–45.

73 Hayes DL, Holmes DR, Jr., Gray JE. Effect of 1.5 tesla nuclear magnetic resonance imaging scanner on implanted permanent pacemakers. *J Am Coll Cardiol* 1987; **10**: 782–86.

74 Loewy J, Loewy A, Kendall EJ. Reconsideration of pacemakers and MR imaging. *Radiographics* 2004; **24**: 1257–67; discussion 1267–68.

75 Shellock FG, Crues JV. MR procedures: biologic effects, safety, and patient care. *Radiology* 2004; **232**: 635–52.

76 Kalin R, Stanton MS. Current clinical issues for MRI scanning of pacemaker and defibrillator patients. *Pacing Clin Electrophysiol* 2005; **28**: 326–28.

77 Shellock FG, Fischer L, Fieno DS. Cardiac pacemakers and implantable cardioverter defibrillators: in vitro magnetic resonance imaging evaluation at 1.5-tesla. *J Cardiovasc Magn Reson* 2007; **9**: 21–31.

78 Roguin A, Zviman MM, Meininger GR, et al. Modern pacemaker and implantable cardioverter/defibrillator systems can be magnetic resonance imaging safe: in vitro and in vivo assessment of safety and function at 1.5 T. *Circulation* 2004; **110**: 475–82.

79 Guttman MA, Ozturk C, Raval AN, et al. Interventional cardiovascular procedures guided by real-time MR imaging: an interactive interface using multiple slices, adaptive projection modes and live 3D renderings. *J Magn Reson Imaging* 2007; **26**: 1429–35.

80 Dumoulin CL, Souza SP, Darrow RD. Real-time position monitoring of invasive devices using magnetic resonance. *Magn Reson Med* 1993; **29**: 411–15.

81 Bock M, Muller S, Zuehlsdorff S, et al. Active catheter tracking using parallel MRI and real-time image reconstruction. *Magn Reson Med* 2006; **55**: 1454–59.

82 McVeigh ER, Guttman MA, Kellman P, Raval AN, Lederman RJ. Real-time, interactive MRI for cardiovascular interventions. *Acad Radiol* 2005; **12**: 1121–27.

83 Elgort DR, Duerk JL. A review of technical advances in interventional magnetic resonance imaging. *Acad Radiol* 2005; **12**: 1089–99.

84 Kucharczyk J, Hall WA, Broaddus WC, Gillies GT, Truwit CL. Cost-efficacy of MR-guided neurointerventions. *Neuroimaging Clin N Am* 2001; **11**: 767–72, xii.

85 Cox JL, Boineau JP, Schuessler RB, et al. Successful surgical treatment of atrial fibrillation. Review and clinical update. *JAMA* 1991; **266**: 1976–80.

10 CHAPTER 10

Challenges and Limitations of Electroanatomical Mapping Technologies

Jeff M. Hsing, MD, *Paul Zei,* MD, PhD, *Henry H. Hsia,* MD, *Paul J. Wang,* MD, and *Amin Al-Ahmad,* MD

Stanford University, Palo Alto, CA, USA

Summary

The use of electroanatomical mapping for the ablation of cardiac arrhythmias has increased greatly over the last decade. These technologies have aided in expanding our understanding of cardiac arrhythmias. Despite the great utility of these technologies, electroanatomical mapping systems have limitations that can impact the success of mapping and ablation procedures. A better understanding of these limitations can aid the clinician in avoiding pitfalls and understanding how best to utilize and interpret the maps created by these systems. This chapter highlights the limitations of both contact and noncontact mapping systems and illustrates how these limitations can impact the accuracy of mapping cardiac arrhythmias.

Introduction

Over the past decade, mapping technologies have made significant enhancements moving from fluoroscopy-guided catheter positioning to non-fluoroscopic 3D mapping. Prior to the advent of advanced mapping systems, fluoroscopy in multiple views was used to assess catheter position and to help determine tissue contact. The use of fluoroscopy alone has significant limitations and may be more time consuming and less accurate when mapping complex arrhythmias or coping with difficult cardiac anatomy. Detailed anatomical characteristics are often not well appreciated using standard fluoroscopy since the 3D structure is displayed as a 2D image. In addition, there is increased radiation exposure from prolonged fluoroscopy.

The ability to generate electroanatomical maps that couple voltage or activation information with the underlying anatomy has become an invaluable tool for the ablation of complex arrhythmias. However, electroanatomical mapping technologies should not substitute for traditional mapping approaches such as activation mapping, pace mapping, entrainment, and substrate mapping. While electroanatomical mapping systems can be used with conventional mapping methods, their utmost utility resides in defining the spatial relationships between electrophysiologic information and the

Cardiac Mapping, Third Edition Edited by Mohammad Shenasa, Gerhard Hindricks, Martin Borggrefe, and Günter Breithardt
 ISBN: 978-1-405-17572-2

underlying anatomy, as well as data registration in spatial and temporal domains. Electroanatomical mapping systems can tabulate and pinpoint locations of best pacemap, or areas with promising presystolic activities. Complex reentrant circuits with isthmus, entrance, and exit sites can be delineated using entrainment and sites depicted over a 3D anatomical construct created by the system. Additionally, underlying substrate voltage can be evaluated and putative arrhythmia circuits may be characterized based on this information.

Recently, cardiac mapping has become a multiimaging modality with the integration of computer tomography (CT), magnetic resonance imaging (MRI), and ultrasound (US). Despite the advancements achieved by the new mapping technologies, there are limitations to the current mapping systems. In this chapter we will examine the challenges and limitations of contact and noncontact mapping systems.

Challenges and Limitations of Contact Mapping Systems

For a contact mapping system, the mapping catheter must make direct contact with the tissue. Incorporated into such mapping system is a mechanism to locate the catheter in 3D space and the ability to simultaneously acquire electrogram data. The system acquires and keeps track of the 3D spatial coordinate of the catheter tip while it makes contact with the cardiac tissue and creates a 3D anatomic construct.

A 3D electroanatomical map can be constructed in real time without significant fluoroscopic exposure. Electrophysiologic information from the underlying cardiac tissue is recorded and overlaid on the anatomical surface. There are currently three main systems in use: Biosense Webster (CARTO^{TM}), St. Jude Medical (EnSite NavX^{TM}), and Boston Scientific Realtime Position Management (RPM^{TM}) (no longer being manufactured). Each of these systems utilizes a different technology and may have limitations that are unique to their technology in addition to limitations that are shared by all contact mapping systems. For example, the electromagnetic CARTO mapping system utilizes an ultra-low magnetic field (between 5×10^{-6} and 5×10^{-5} Tesla) generated by a three-coil external magnetic field emitter located under the patient's torso. A magnetic field sensor incorporated in the tip of the deflectable quadripolar mapping catheter (NAVI-STAR^{TM}) detects and codes both temporal and spatial information around the patient's chest [1]. Spatial information is encoded in the decaying magnetic field as a distance from the coil. Magnetic field sensors measure the strength of the field from each coil which is used to calculate the distance from each coil. The exact catheter location (pitch, roll, yaw) is based on a known decaying magnetic field from the source located beneath the patient.

While unlikely, in theory, any disturbance to the magnetic field strength may lead to inaccurate distance and position measurements. This limits the ability of using devices in the procedure room that may affect the magnetic field around the patient in an unpredictable way (such as the magnetic programming wand for implantable devices). While the CARTO system can currently work in a magnetic environment with the Stereotaxis system by taking the magnetic field generated by the fixed magnets into account, an unpredictable field may cause inaccuracies in the positioning of the electroanatomical map. It is, however, not likely given the fact that the majority of electrophysiology laboratories are well shielded to prevent disturbance of the magnetic field.

Another issue related to the magnetic field is related to the finite range of the magnetic field. As the catheter moves further away from the magnetic field source, the accuracy of the system can decrease. If the catheter moves out of range of the magnetic field, the catheter itself will disappear from the CARTO mapping screen. This may become an issue during epicardial mapping or endocardial mapping in a large left ventricle, in particular if the reference patch was placed too far from the chamber of interest.

Another example is the Realtime Position Management (RPM) system that was first described by de Groot et al. in 2000 [2]. This mapping system uses ultrasound to measure the distance between the ultrasound transducers located on the reference and ablation catheters. Assuming the speed of sound in blood is 1550 m/sec, the time delay between the ultrasound transmitter and the receiver is used to calculate the distance between any two reference points. When a 3D reference frame is created using two reference catheters, triangulation can be

Table 10.1 Summary of Limitations of Electroanatomical Mapping

Limitations and Challenges of Electroanatomical Mapping	*Solutions to Overcome the Limitations and Challenges*
Contact Mapping	
Alterations to the magnetic field or ultrasound	Eliminate the source of interference or change to a system that does not utilize a magnetic field or ultrasound.
Poor tissue contact	Ensure tissue contact; change catheter size.
Nonmappable arrhythmias	Substrate mapping in sinus rhythm; consider noncontact mapping system.
Fractionated electrogram	Manual adjustment of electrogram timing.
Reference catheter motion	Position reference catheter in stable position that is unlikely to move. Monitor catheter for movement during procedure.
Cardiac motion	Use proximal coronary sinus as reference.
Respiratory motion	Use end-expiration dataset for image registration.
Image registration	Use surface registration and end-expiration dataset.
Noncontact Mapping	
Distance	Know that accuracy is reduced for distances >34 mm; reposition array catheter or change to a contact mapping system.
Signal-to-noise ratio	Reposition array to minimize; may need to change to a contact mapping system.
Chamber size	May need multiple array repositioning.

used to track the position of additional transducers. Because the system utilizes ultrasound as the localization method, interference from other ultrasound devices can occur if the wavelength used is similar. This limits the utility of this mapping system in procedures where intracardiac ultrasound is used routinely such as atrial fibrillation ablation.

Additionally, because contact mapping systems require direct contact with the endocardium, there are challenges in talking multiple points at the same time. In the CARTO system, only a single point can be taken simultaneously with the mapping catheter. With the NavX system, mapping can be done with any catheter, not just the ablation catheter as with CARTO. A multipolar catheter can be used to take simultaneous points from locations that are in contact with the poles of the catheter. While this may allow faster mapping, care should be taken to ensure adequate contact (as will be discussed later) with the endocardial tissue when utilizing these simultaneous points to generate a map.

Lastly, although not a limitation per se; with the exception of the EnSite NavX system, proprietary catheter designs are often required for electroanatomical mapping. This limits the available catheter selection to the operator while using the mapping system. Limitations of contact mapping systems are summarized in Table 10.1.

Nonmappable Arrhythmias

In order to create an electroanatomical activation map during an arrhythmia, it is optimal that the arrhythmia be inducible, sustainable, and hemodynamically stable. However, a significant subset of atrial or ventricular arrhythmias is considered "unmappable," either due to arrhythmia noninducibility, inconsistent response to catheter manipulation/stimulation, nonsustained episodes, or hemodynamic intolerance.

While it may be difficult to obtain activation maps of these arrhythmias, the electroanatomical mapping system may still be helpful in keeping track of pacemap sites or determining the underlying substrate of the arrhythmia. In fact, a paradigm shift that focuses on the detailed characterization of the underlying electroanatomical substrate may overcome these limitation for the majority of "unmappable" arrhythmias [3]. Creating an underlying voltage map in a stable baseline rhythm, either sinus rhythm or ventricular paced rhythm may provide clues to scar tissue locations that are prone to develop arrhythmia circuits.

Applying radiofrequency (RF) energy lesions along the dense scar to the normal myocardium or anatomic boundary have been shown to control unmappable ventricular tachycardia [4]. In a study of sixteen patients with cardiomyopathy (nine ischemic and seven nonischemic) with drug refractory unmappable VT, an electroanatomical map was generated during the baseline rhythm. Radiofrequency lesions were made to extend from "dense scar," as defined by a voltage amplitude <0.5 mV, to anatomic boundaries or normal myocardium. A mean of 55 RF lesions producing a mean of four linear lesions averaging 3.9 cm in length were created. Follow-up showed that 75% (12/16) of the patients were free of VT and 25% (4/16) still had VT. Only one patient had frequent VT.

By mapping scar tissue and performing pace mapping along the low voltage border, one may be able to locate the reentry circuit isthmus. During pace map, the site that the QRS morphology most closely matched to the VT and had conduction delay from stimulus to QRS >40 msec was considered to be the site of reentry circuit isthmus and was ablated [5]. Thus, while noncontact mapping systems may be able to map a single beat, the contact mapping systems can still be very useful in these scenarios.

Tissue Contact

Contact mapping is based on a sequential point-by-point and beat-by-beat acquisition of electrograms. In order to create an accurate electroanatomical voltage and activation map, stable contact must be maintained between the catheter tip and the tissue when a point is recorded. Although electrogram timing is less affected by poor catheter–tissue contact during activation mapping, poor contact may result in low electrogram voltage measurements or false positional information, leading to a false-identification of low-voltage scar areas and a misrepresentation of the chamber size and geometry.

This may be of particular concern in areas with poor catheter stability, such as the valve planes, ventricular apex, and aneurysms. Catheter contact is dependent on the operator's skill, catheter design, as well as the sampling density. For example, large chambers may be difficult to map in cases when too small of a curve catheter is selected. The operator should interpret the electroanatomical maps with caution if adequate catheter contact can not be ascertained (Figure 10.1).

Electrogram Interpretation

Activation maps are created by tabulating the timing of a recorded local electrogram as compared to a stable electrogram reference (either endocardial or surface) during a stable rhythm. The local activation time is displayed as a color gradient over the anatomical construct to create an activation map. The mapping software can automatically select and label the timing of the electrograms either at the onset, signal peak/nadir, or the maximum/minimum slope. Such software may not be reliable when fractionated, multicomponent, or low-amplitude electrograms are encountered and the timing of the electrograms may be incorrectly labeled (Figure 10.2). This is particularly critical when mapping a reentrant arrhythmia, when "early" versus "late" electrogram signals must be accurately measured. In these situations, the timing of the electrograms may need to be manually adjusted in order to create an accurate representation of the overall activation pattern of the cardiac chamber. Relying too heavily on the automated timing detection of the electrogram may introduce a significant amount of error in the map, and lead to a failure to localize the earliest activation for effective treatment of a focal arrhythmia with ablation.

Movement of the Patient or Reference Electrode

For activation mapping, the timing of the individual local electrogram recording is compared to a fixed electrical reference in order to determine the "relative" activation pattern of the cardiac chamber during a stable rhythm. The selection of an appropriate, stable timing reference is therefore of the utmost importance. Positioning a reference electrode with a stable spatial location within the mapping chamber of interest is essential. Movement of the reference electrode results in a change in its timing of reference electrogram during the arrhythmia, and introduces timing errors in all other electrogram recordings relative to the reference. This will lead to shifts in the map and introduce inaccuracies that may confuse and delay the procedure. Therefore, problems with inappropriate selections of timing reference electrograms can have a significant impact

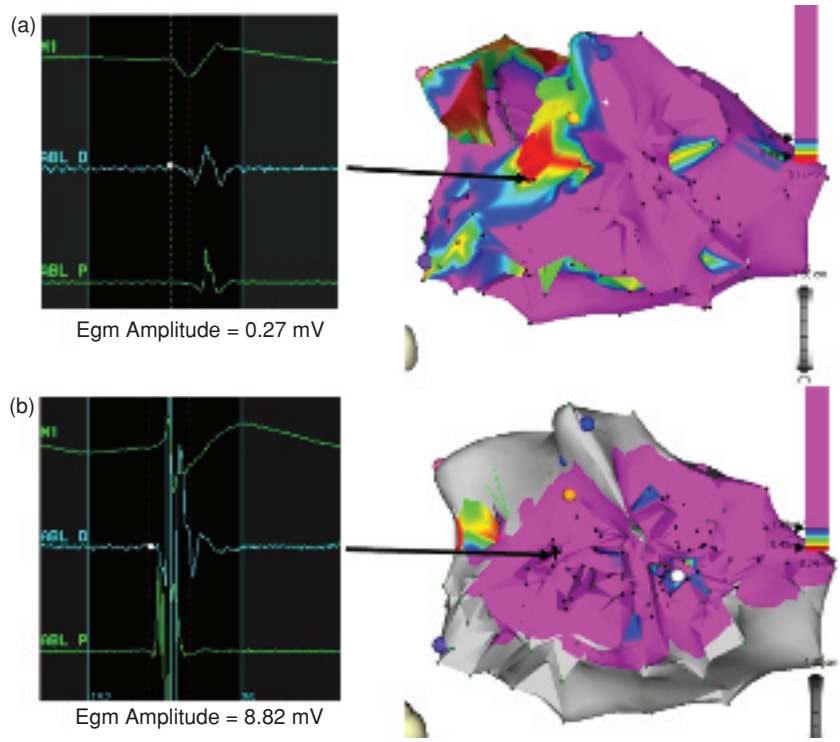

Figure 10.1 The effect of poor catheter tissue contact. An area of low voltage that can be misidentified as scar is seen in (a). Although the voltage is low on the EGM, it appears to be somewhat far-field. Improved contact in the same area (b) shows normal voltage, a sharp deflection, and appropriate color on the voltage map. (Reprinted with permission from *Electroanatomical Mapping: An Atlas for Clinicians.* Al-Ahmad A, Callans DJ, Hsia HH, Natale A, eds. Blackwell, London, 2008.)

on the accuracy of the electroanatomical map. Additionally, if the amplitude and waveform of the selected reference vary significantly, either on a beat-to-beat basis or during respiration, the map may be similarly affected and inaccurate (Figure 10.2).

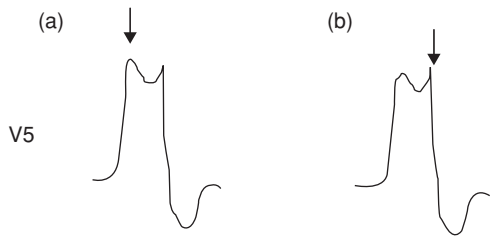

Figure 10.2 Selection of a surface reference for ablation of a RVOT VT. The selected reference causes the autodetection of the peak (selected in this case) to select the first peak in some beats (a) and the second peak in other beats (b). This leads to a significant error in the map. An electrogram with a single discrete peak would have been a better choice.

In addition to the instability of the timing reference catheter, accuracy may also be limited by cardiac motion due to movements of the position reference electrode. In one study of the NavX system, investigators calculated the relative motion of cardiac structures during the beating heart to assess positional errors and guide the choice of an optimized spatial reference during atrial fibrillation ablation [6]. For all left atrial structures, reference to the proximal coronary sinus resulted in the least mean displacement of 4.0 ± 1.1 mm, compared to an external static reference on body surface (4.9 ± 0.7 mm). Furthermore, the authors found no benefit in choosing distal coronary sinus or right atrial appendage as reference positions.

For the cavotricuspid isthmus, the best location for the reference catheter in decreasing order is proximal coronary sinus (3.8 ± 2.2 mm), azygos vein (4.6 ± 2.0 mm), right atrial appendage (5.0 ± 2.3 mm), and finally an external static reference

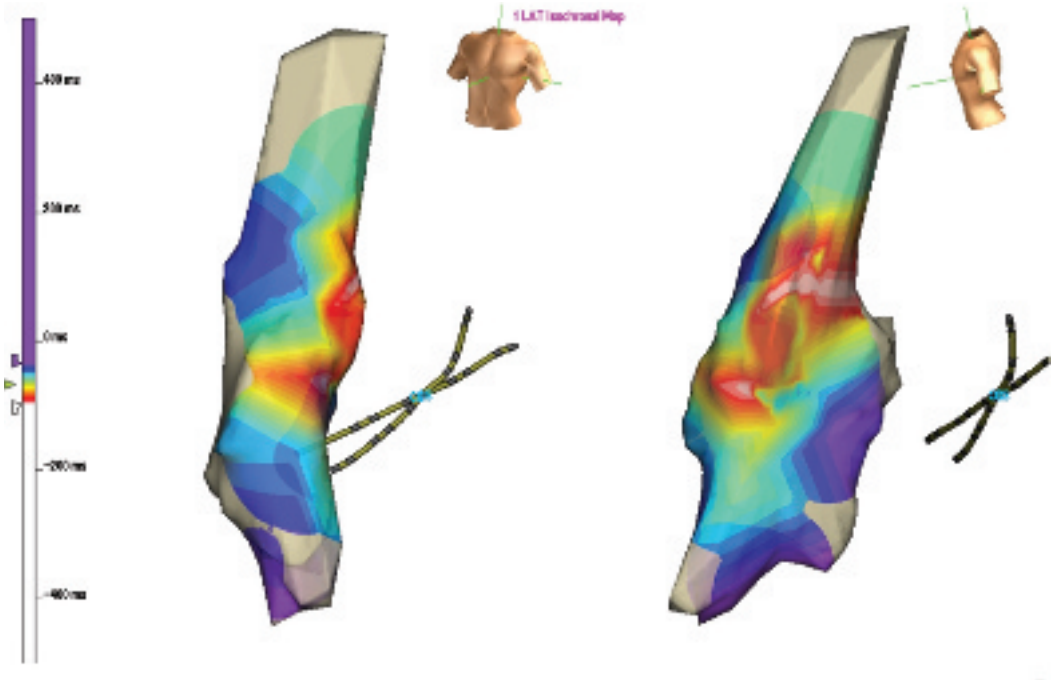

Figure 10.3 In this case of RVOT VT ablation, movement of the position reference catheter (timing reference was based on the surface QRS) led to an activation map that had two areas of early activation. A remap with the catheter stable led to appropriate ablation of the focus.

(5.5 ± 3.4 mm). The authors concluded that for left atrial procedures, the proximal coronary sinus provided the best electrogram reference in reducing location error. The right atrial appendage and azygos vein were also reasonable alternatives, although the risk of dislodgement was higher in the appendage.

This study highlighted the importance of selecting an appropriate reference catheter in minimizing error created by cardiac motion. Therefore, for activation mapping of atrial arrhythmias, it is common to select an electrogram in the coronary sinus catheter as the timing and/or position reference as this catheter tends to be more stable compared to other catheters located in the atrium. It is crucial to ensure stability of the reference electrode and monitor for movement during the procedure. With the CARTO system, the position reference is placed on the patient's back; therefore, patient movement will also result in reference patch movement with respect to the magnetic field. For this reason, the CARTO system is more sensitive to patient movement in terms of anatomical accuracy, whereas the NavX system is more sensitive to movement of the internal position reference catheter. If there is significant reference catheter/electrode movement or patient movement in the case of CARTO, the map may be inaccurate and a remap may be warranted (Figure 10.3).

Another type of motion that can affect spatial accuracy and referencing of the electroanatomical map is respiratory motion. Respiratory effects were assessed during atrial fibrillation ablation by the shift of the motion curve during inspiration and expiration. A study by Klemm et al. found that the pulmonary veins shifted on average 5.0 ± 0.5 mm as a result of expansion and contraction of the left atrium during respiration [6]. The study concluded that respiratory variations were less for left-sided pulmonary veins (4.7 ± 0.4 mm) compared to right-sided pulmonary veins (5.4 ± 0.1 mm). The inferior pulmonary veins (4.9 ± 0.6 mm) also moved less with respiration compared to the superior pulmonary veins (5.3 ± 0.4 mm) (Figure 10.4).

In another study, MRI angiography of the left atrium and pulmonary veins was acquired at both end-inspiration and end-expiration. After aligning

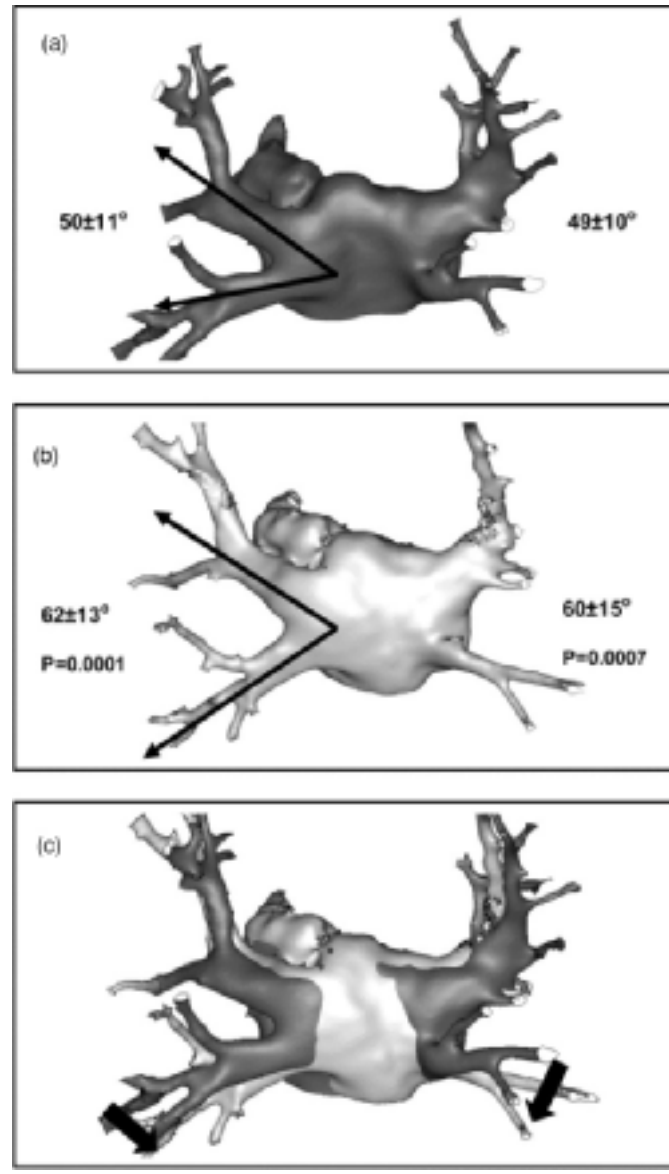

Figure 10.4 A shift in cardiac geometry, in particular the pulmonary veins, is demonstrated by the change in angle of the pulmonary veins during inspiration (a) and expiration (b). Reprinted with permission from Ref. 7.

the two surface datasets, the respiration variations were able to be calculated. The measured surface-to-surface distance between pulmonary veins ranged from 1.99 mm to 3.79 mm, and inferior pulmonary veins varied more than the superior pulmonary vein [7]. Registration of the electroanatomical model with the MRI models was better for the end-expiration dataset (2.30 ± 0.73 mm) compared to the end-inspiration dataset (3.03 ± 0.57 mm). Therefore, for ideal spatial accuracy, respiratory variations must be taken into consideration.

Image Registration

With the recent introduction of CARTO-Merge software, the integration of real-time catheter-based electroanatomic mapping with a previously acquired MRI and CT image set is now possible. The integration of these images has been used to assist catheter ablation where anatomical variations may be important to the ablation strategy such as in atrial fibrillation. The integration allows increased anatomic detail provided by MRI and CT to be superimposed on real-time mapping and

visualization of the ablation catheter in relation to relevant cardiac structures. However, there are limitations to the accuracy of the merged maps. A recent study evaluated 61 patients for atrial fibrillation ablation who underwent either MRI ($n = 50$) or CT ($n = 11$) scans prior to ablation.

Factors that influenced the overall accuracy of integrating electroanatomic points with CT and MRI reconstruction were evaluated using CARTO-Merge software [8]. The investigators found the only significant positive correlation for integration error was left atrial size, with a larger left atrial size having a less accurate registration. In this study, no significant differences in integration error were found between MRI and CT images, left ventricular ejection fraction, or paroxysmal versus persistent atrial fibrillation. Another recent study examined 30 patients undergoing atrial fibrillation ablation using the CARTO-Merge system and registered CT scan data. When pulmonary veins were selected as the cardiac landmark structures for registration, a positional error of 6.4 ± 2.8 mm was achieved with repeat registration required in some patients. When the CT data was registered by best fit to the electroanatomic surface geometry, an error of 2.3 ± 0.4 mm was achieved with the anterior wall most prone to error. It is hypothesized that this region of the left atrium has the greatest mobility resulting in error during CT segmentation. Cardiac rhythm at the time of the CT imaging, atrial fibrillation or normal sinus rhythm, did not show a significant difference in registration error (2.5 ± 0.3 mm for AF vs. 2.3 ± 0.5 mm in SR) [9]. The authors concluded that surface registration was more reliable than pulmonary vein registration and that the cardiac rhythm at the time of CT did not alter registration accuracy.

As mentioned previously, respiration variations can affect image registration accuracy with the end-expiration dataset resulting in less error than the end-inspiration dataset [7]. Although automatic image registration and integration sounds promising, the user must be aware of the limitations in terms of its accuracy, selection of registration points and respiratory phase of MRI/CT image to register against. Ideally, 3D images should be obtained at the time of the procedure and in the same rhythm and hemodynamic loading conditions to minimize registration error.

Limitations of Noncontact Mapping Systems

The concept of noncontact mapping eliminates the need for sequential point-by-point acquisition of a local electrogram using a mapping catheter. It was first described by Schilling et al. in 1998 [10]. This allows rapid generation of a complete map on a single beat without endocardial contact. While there is an advantage in terms of speed of mapping and the ability to map nonsustained or nontolerated rhythms, the mapping system utilizes "virtual" electrograms rather than recorded electrograms from direct contact with the endocardial surface. At the current time there is only one system that is a noncontact mapping system, the St. Jude EnSite Array™). The mapping system consists of a 7.6 ml (18×40 mm) ellipsoid balloon surrounded by 64 multielectrode array (MEA), which allows for simultaneous recordings from multiple sites within a single cardiac chamber. The MEA records far-field unipolar electrograms generated by the activation of the endocardial surface. By solving the reverse Laplace equation on the far-field electrograms, 3360 "virtual" endocardial electrograms of a single beat can be generated for activation mapping. In addition, the location of the roving electrode can also be determined by emitting an electrical signal from the roving catheter. Table 10.1 summarizes the limitations of a noncontact mapping system.

Distance

Limitations of the noncontact mapping system include the loss of accuracy of virtual electrograms as the endocardial surface moves further away from the recording electrodes on the balloon surface. This was first evaluated in vitro in an ellipsoid chamber that had good accuracy when the surface is less than 50 mm away from the center of the balloon. Within a range of 50 mm, the EnSite Array was able to locate a roving electrode to 0.33 ± 0.45 mm, whereas if the range was greater than 50 mm, the Array's precision was reduced to 0.75 ± 1.13 mm [11]. This was confirmed in humans by examining the cross-correlation morphology and timing of maximum $-dV/dt$ between contact and reconstructed electrogram of the left ventricle.

Cross-correlation of contact and noncontact virtual electrograms was 0.87 ± 0.12 for a center of

multielectrode balloon array to endocardial surface (M-E) distance of <34 mm and 0.76 ± 0.18 for distances >34 mm. The timing difference of maximum $-dV/dt$ was −1.94 ± 7.12 msec for M-E < 34 mm and significantly worse at −14.16 ± 19.29 msec for M-E >34 mm [10]. Thus, as the endocardial surface is further away from the center of the balloon Array, the less accurate the virtual electrogram is compared to the contact electrogram (both in accuracy of spatial localization and activation timing). The authors concluded that although the Array can reconstruct electrograms >50 mm, accuracy significantly decreases at distances >34 mm.

In another study, left atrial mapping was examined for patients undergoing atrial fibrillation ablation which showed significant decrease in accuracy when the endocardial surface was >40 mm away from the balloon Array [12]. For endocardial sites <40 mm the correlation was 0.87 compared to 0.73 for sites >40 mm away. So when using the Array, the chamber size must be taken into consideration because as the distance between the endocardial surface and the MEA increases, the less accurate the generated "virtual" electrograms will be.

Signal-to-Noise Ratio

Factors that reduce the signal-to-noise ratio will also reduce the accuracy of the virtual electrograms. During noncontact mapping, if the signal amplitude is low or when the level of noise is increased, the accuracy of the generated virtual electrograms needs to be scrutinized. This was shown in a study examined mapping of the left atrium for atrial fibrillation. When comparing the morphology and timing by cross-correlation of the direct contact electrograms to the virtual electrograms, the far-field ventricular electrograms correlated much better than the atrial electrograms, 0.96 vs. 0.87 [12]. This held true even at distances >40 mm. This was attributed to larger signal amplitudes of ventricular compared to atrial electrogram recordings.

One factor that affects the signal-to-noise ratio is slow conduction within scar tissue, which can generate very low voltage signals that may not be detected by the MEA [13]. Another factor is that because the MEA is composed of unipolar electrodes, it is susceptible to far-field signals that may interfere with the near-field signals of interest [14]. An example would be mapping 1:1 atrial arrhythmias that originated from areas close to the tricuspid or mitral annulus because the atrial amplitude may be lower than that of the ventricular amplitude. This may make the electrogram timing difficult to discern.

Chamber Size

Chamber size, both large and small, may limit noncontact mapping. As discussed earlier, for distant endocardial borders within a large chamber volume, it may require multiple MEA repositioning to collect adequate virtual electrogram data. In addition, because spatial resolution is decreased with distance away from the MEA balloon, the accuracy of the anatomical construct may be less reliable for larger chamber of interest. This makes mapping of ventricular tachycardia in a large left ventricle potentially difficult. In addition, the EnSite Array has a volume of about 8–10 mL, and positioning of the MEA in small areas may limit the movement of the ablation catheter [15].

Conclusion

Electroanatomical mapping systems have become an indispensable tool in the mapping and ablation of cardiac arrhythmias. These systems have provided insights into the mechanisms of arrhythmias as well as enhanced our understanding of the relationship between cardiac electrophysiology and substrate anatomy. While there are still challenges and limitations about which the practicing electrophysiologist should be aware, a better understanding of these limitations and where the accuracy of the electroanatomical map diminishes will help with procedural success and the selection of appropriate mapping technology for each specific case. The electrophysiologist must still be a master of all the traditional tools to map and ablate arrhythmias so as not to be limited by any technical inaccuracies encountered.

References

1 Gepstein L, Hayam G, Ben-Haim SA. A novel method for nonfluoroscopic catheter-based electroanatomical mapping of the heart: in vitro and in vivo accuracy results. *Circulation* 1997; **95**: 1611–22.

2 de Groot NM, Bootsma M, van der Velde ET, Schalij MJ. Three-dimensional catheter positioning during radiofrequency ablation in patients: first application of a real-time

position management system. *J Cardiovasc Electrophysiol* 2000: **11**: 1183–92.
3 Hsia HH. Substrate mapping: the historical perspective and current status. *J Cardiovasc Electrophysiol* 2003; **14**: 530–32.
4 Marchlinski FE, Callans DJ, Gottlieb CD, Zado E, Linear ablation lesions for control of unmappable ventricular tachycardia in patients with ischemic and nonischemic cardiomyopathy. *Circulation* 2000; **101**: 1288–96.
5 Soejima K, Suzuki M, Maisel WH, et al. Catheter ablation in patients with multiple and unstable ventricular tachycardias after myocardial infarction: short ablation lines guided by reentry circuit isthmuses and sinus rhythm mapping. *Circulation* 2001; **104**: 664–69.
6 Klemm HU, Steven D, Johnsen C, et al. Catheter motion during atrial ablation due to the beating heart and respiration: impact on accuracy and spatial referencing in three-dimensional mapping. *Heart Rhythm* 2007; **4**: 587–92.
7 Noseworthy PA, Malchano ZJ, Ahmed J, et al. The impact of respiration on left atrial and pulmonary venous anatomy: implications for image-guided intervention. *Heart Rhythm* 2005; **2**: 1173–78.
8 Heist EK, Chevalier J, Holmvang G, et al. Factors affecting error in integration of electroanatomic mapping with CT and MR imaging during catheter ablation of atrial fibrillation. *J Interv Card Electrophysiol* 2006; **17**: 21–7.
9 Kistler PM, Earley MJ, Harris S, et al. Validation of three-dimensional cardiac image integration: use of integrated CT image into electroanatomic mapping system to perform catheter ablation of atrial fibrillation. *J Cardiovasc Electrophysiol* 2006: **17**: 341–48.
10 Schilling RJ, Peters NS, Davies DW. Simultaneous endocardial mapping in the human left ventricle using a noncontact catheter: comparison of contact and reconstructed electrograms during sinus rhythm. *Circulation* 1998; **98**: 887–98.
11 Gornick CC, Adler SW, Pederson B, et al. Validation of a new noncontact catheter system for electroanatomic mapping of left ventricular endocardium. *Circulation* 1999; **99**: 829–35.
12 Earley MJ, Abrams DJ, Sporton SC, Schilling RJ. Validation of the noncontact mapping system in the left atrium during permanent atrial fibrillation and sinus rhythm. *J Am Coll Cardiol* 2006; **48**: 485–91.
13 Klemm HU, Ventura R, Steven D, et al. Catheter ablation of multiple ventricular tachycardias after myocardial infarction guided by combined contact and noncontact mapping. *Circulation* 2007; **115**: 2697–704.
14 Delacretaz E, Soejima K, Gottipaty VK, et al. Single catheter determination of local electrogram prematurity using simultaneous unipolar and bipolar recordings to replace the surface ECG as a timing reference. *Pacing Clin Electrophysiol* 2001; **24**: 441–49.
15 Packer DL. Three-dimensional mapping in interventional electrophysiology: techniques and technology. *J Cardiovasc Electrophysiol* 2005; **16**: 1110–16.

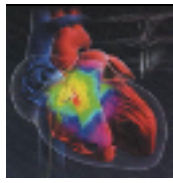

PART III

Mapping in Experimental Models of Cardiac Arrhythmias

Cardiac Mapping, Third Edition Edited by Mohammad Shenasa, Gerhard Hindricks, Martin Borggrefe, and Günter Breithardt
 ISBN: 978-1-405-17572-2

11 CHAPTER 11

Mapping of Atrial Neural Stimulation and Implications in Atrial Fibrillation

Pierre Pagé, MD, *René Cardinal,* PhD

Hôpital du Sacré-Cœur de Montréal, Montréal, Canada

Summary

To investigate the influence of the thoracic autonomic nerve hierarchy on arrhythmia formation, we compared, in canine preparations, the characteristics of atrial tachyarrhythmias induced by electrical stimulation of (i) the right vagosympathetic nerve complex at the cervical level and (ii) the more caudal juxta-cardiac mediastinal nerves located on the anterior surface of the superior vena cava. The effects of chemical activation of the right atrial ganglionated plexus on ventricular events were also investigated by ventricular repolarization mapping.

The sites of origin of atrial tachyarrhythmias were investigated by analyzing atrial activation maps of the early beats at the onset of arrhythmias. Neural effects on repolarization were determined by computing the integral surface subtended by unipolar recordings under basal conditions and at maximum neurally induced bradycardia, The mean area affected by nerve stimulation in all animals was significantly greater in response to vagosympathetic rather than to mediastinal nerve stimulation. Atrial cycle length prolongation prior to tachyarrhythmia onset was more pronounced in response to vagosympathetic than mediastinal nerve stimulation. The earliest epicardial activation in early tachyarrhythmia beats were localized in the right atrial free wall and the Bachmann bundle region in both cases, but with a higher incidence of double breakthroughs from septal sites of origin in response to vagosympathetic than mediastinal nerve stimulation.

Sites of early activation were identified in association with areas of neurally induced repolarization changes. Ventricular events induced by juxta-atrial ganglia were found in overlapping regions. Thus, differential contributions are made to the electrophysiologic substrate of neurally induced atrial tachyarrhythmias depending on the pattern of engagement of the intrathoracic autonomic neuronal hierarchy. Neurons located at multiple intrathoracic levels as well as in several cardiac ganglionated plexuses will have to be considered for therapeutic strategies. In fact, the concept of ablating cardiac ganglia for the treatment of atrial arrhythmias must be considered as one possible modality among a wide range of neuromodulatory approaches.

Cardiac Mapping, Third Edition Edited by Mohammad Shenasa, Gerhard Hindricks, Martin Borggrefe, and Günter Breithardt
 ISBN: 978-1-405-17572-2

Introduction

Recent developments in ablative procedures for the treatment of atrial fibrillation, which include neural targets [1–6], have fostered renewed interest for the role of the intrinsic cardiac nervous system in the pathophysiology of atrial arrhythmias [7–10]. It has been known for many years that atrial tachyarrhythmias can be induced in anaesthetized canines by electrical stimulation of the cervical vagosympathetic nerve complex [11–13] or by localized electrical stimuli delivered to small mediastinal nerve branches of the thoracic vagosympathetic nerve comple [14–16].

Recently, we have reported that atrial tachyarrhythmia/fibrillation can be induced by delivery of electrical stimuli during the atrial refractory period to discrete mediastinal nerves that course over the extra- or intrapericardial portions on the ventral aspect of the superior vena cava [16]. This consistently induced a sequence of events consisting of bradycardia followed by spontaneous atrial premature depolarization, atrial tachycardia, and atrial fibrillation.

An analogous sequence of events has been previously reported for arrhythmias that are induced, albeit less readily, when the cervical vagosympathetic nerve complex is subjected to continuous, intense electrical stimulation [17]. Dispersion of atrial refractory periods is of fundamental importance in the mechanism of atrial fibrillation [18, 19]. Earlier experiments in our laboratory suggested that electrical activation of discrete intrinsic cardiac nerves induce more localized changes in atrial repolarization than the more widespread biatrial effects induced by stimulating the vagosympathetic nerve complex at the cervical level [20].

In this chapter, the differential influence of the peripheral autonomic neuronal hierarchy on atrial tachyarrhythmia formation is reviewed. For this purpose, the sites of origin of atrial tachyarrhythmias and spatial distribution of repolarization changes, both induced by neural stimulation, were compared when electrical stimulate was applied at the cervical versus the mediastinal level, specifically, to the cervical right vagosympathetic nerve complex (RVSC) or to mediastinal nerves coursing over the superior vena cava (SVCN). The latter were selected on the basis of the recent characterization of their arrhythmogenic potential by Armour et al. [16]. Moreover, the influence of local delivery of pharmacological agonists (e.g., nicotine) on the ventricular myocardium was explored in an attempt to document interaction between different nexuses of the intrinsic cardiac nervous system.

Mapping Methodologies

The mapping techniques in use in our laboratory have been described in details elsewhere

Figure 11.1 Multielectrode mapping grids (right upper panel). Atrial surfaces unfolded and viewed from a posterior projection. Dots indicate the location of 191 unipolar recording contacts. Projection of anatomic orifices is indicated by circles. KEY: CSO = coronary sinus orifice; FO = fossa ovalis; IVC = inferior vena cava; LAA = left atrial appendage; PVs = pulmonary veins; RAA = right atrial appendage; SVC = superior vena cava; TV = tricuspid valve.

(a) Typical arrhythmia response to electrical stimulation of the right vagosympathetic nerve complex (RVSC). The blue dotted line at the top indicates vagal stimulation. The upper tracing (unipolar electrogram) indicates a marked bradycardia induced by nerve stimulation (CL 3150 msec). The double slash indicates tracing interruption due to space limitation, vagal stimulation outlasting this mark. Dissociated ventricular depolarization complexes are identified (V). Color-coded maps (a–c) show isochronal activation patterns for selected beats (isochronal lines drawn at 10-msec intervals).The site of the earliest epicardial activation (asterisk) and region of earliest 10-msec activation (red) shifted from a superior right atrial location in basal ("sinus") beats (map a) towards inferior regions during bradycardia (map b). In the escape beat (ESC, map c) the region of earliest 10-msec activation was localized to the Bachmann bundle region and spread radially to both atria.

(b) Typical arrhythmia response to electrical stimulation of a mediastinal nerve coursing over the superior vena cava (SVCN). Upper tracing illustrates a slight bradycardic response (cycle length increased from 460 to 490 msec) followed by an atrial premature depolarization complex (P) giving rise to atrial tachyarrhythmia (AT). Electrical stimuli (blue bars) were applied intermittently to a right-sided, extrapericardial mediastinal nerve during the atrial refractory period. The region of earliest 10-msec activation (red) was localized in a superior right atrial location in basal ("sinus") beats (map a). The region of earliest 10-msec activation shifted to the right lateral free wall during AT beats. Map b illustrates the existence of a wave front circulating around an area of functional dissociation in the right atrial free wall (orange arrow). (Modified from Ref. 22.)

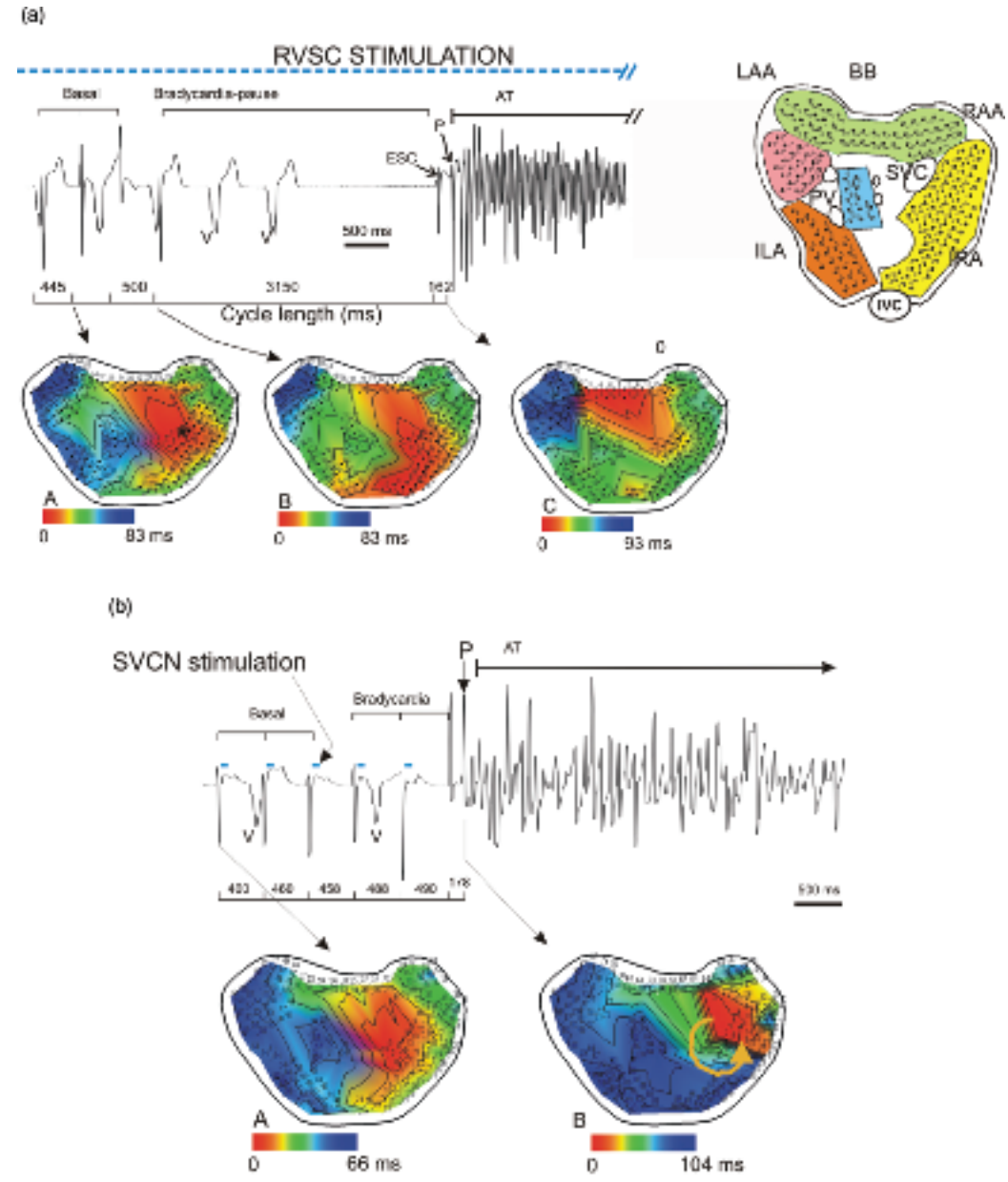

Figure 11.1

[16, 20–22]. In brief, silicone plaques carrying 191 unipolar recording contacts (4.6–5.9 mm spacing) are positioned epicardially over the right atrial free wall, the postero-inferior wall of the left atrium and coronary sinus, the posterior aspect of the left atrium between the pulmonary vein ostia, the lateral left atrial free wall and the interatrial band (Figure 11.1a, right upper panel). To map the distribution of neural effects on the ventricles, a sock electrode array (carrying 127 unipolar recording contacts with 5–10 mm spacing) was positioned over the entire biventricular surface [23].

The mapping electrodes and lead II ECG are connected to a multichannel recording system (EDI 12/256, Institut de Génie Biomédical, École Polytechnique de Montréal) controlled by custom-made

software (Cardiomap III: www.crhsc.umontreal.ca/cardiomap) using a PC computer. Activation times are identified as the moment at which the slope of the negative potential displacement ($-dV/dt$ max) in the activation complex of unipolar electrograms was maximal [24].

Isointegral Mapping of Repolarization Changes

The spatial distribution of neural effects on repolarization is assessed using isointegral difference maps [20–22]. Neurally mediated changes are caused, predominantly, via effects on the repolarization phase of unipolar electrograms. The net area subtended by the activation and repolarization complexes of each unipolar electrogram is computed by integration using a modified Simpson's technique and custom-made software [20, 25, 26]. The difference between prestimulation electrogram integral value and the one measured during nerve stimulation is calculated at each site and plotted on the atrial grid to generate isointegral distribution maps. The incidence, among preparations, of specific regional effects are assessed by counting the number of preparations that display integral changes beyond a threshold of $\pm$ 60 mV/msec corresponding to two standard deviations of changes obtained when measurements are repeated under basal conditions. Such results are displayed in cumulative incidence maps.

Atrial Arrhythmia Formation

Experiments were performed in 13 canine preparations by means of bilateral thoracotomy under anesthesia with Na thiopental and α-chloralose [22]. The right vagosympathetic nerve complex (RVSC) stimulation was maintained continuously, throughout the induction of bradycardia, until 10 sec after the initiation of atrial tachyarrhythmias.

In separate trials, electrical stimuli were delivered to individual right-sided mediastinal nerves coursing over the ventral and ventrolateral surfaces of the superior vena cava (SVCN) either within, or 1–2 cm craniad to the pericardial reflection. These small-diameter nerves can be identified by their accompanying vessels [16]. Five to seven active sites associated with these nerves can be identified such that, when stimulated electrically, atrial tachyarrhythmias occurs shortly thereafter. (Trains of 5 electrical stimuli, 1–2 mA, 1 msec duration, 5 msec pulse interval, delivered during the refractory period of the closest atrial regions.)

A total of 102 episodes were initiated in the 13 animals in response to intermittent (1–4 sec) stimulation of the multiple active sites identified in the SVCN. Only 20 episodes were induced in response to cervical RVSC stimulation as this required continuous ($\sim$10 sec), intense stimulation of the nerve (2.6 ± 1.1 mA, 17.9 ± 4.7 Hz). All atrial tachycardia episodes were preceded by a bradycardic phase, whether they were induced in response to RVSC or SVCN stimulation (upper tracings in Figures 11.1a and 11.b, respectively), indicating the presence of parasympathetic neuronal elements in both. The maximum cycle length prolongation was significantly greater in response to RVSC than SVCN stimulation, and the latency from the beginning of RVSC stimulation to atrial tachyarrhythmia initiation was significantly longer (Table 11.1).

Activation Patterns of Neurally Induced Atrial Arrhythmias

Epicardial maps determined in basal beats ("sinus" rhythm) displayed classical activation patterns consisting of a monofocal early breakthrough localized in the middle right atrial free wall adjacent to the superior vena cava ostium (map A, in Figure 11.1a). Bradycardic beats preceding tachycardia onset

Table 11.1 Induction Characteristics of Neurally Induced Atrial Tachyarrhythmias.

Protocol	*AT (N)*	*Basal CL (msec)*	*Longest pre AT CL (sec)*	*Latency (sec) (median)*	*Duration (sec) (median)*
RVSC stimulation	20	420 ± 67	$2923 \pm 2499^*$	$8.9 \pm 8.6^*$ (4.8)	196 ± 504§ (27.2)
SVCN stimulation	102	443 ± 60	$509 \pm 84^*$	$2.5 \pm 3.1^*$ (1.5)	42 ± 90§ (14.3)

KEY: AT = atrial tachyarrhythmias; RVSC = right vagosympathetic complex (cervical); SVCN = superior vena cava nerve (mediastinal). Mean $\pm$ SD. $^*p < 0.0001$, §< 0.004, RVSC vs. SVCN, ANOVA. (Reproduced with permission from Ref. 22.)

usually displayed a downward shift in pacemaker—75% (31 ± 16 mm) and 40% (18 ± 10 mm) of the maximal bradycardic beats obtained in response to RVSC and SVCN stimulation, respectively (Figure 11.1a, map B), in accordance with the previously reported cholinergically mediated displacements of the pacemaker site within the right atrial subsidiary pacemaker complex [27, 28].

All atrial tachyarrhythmia episodes degenerated after 3–4 cycles into atrial fibrillation, during which time it was no longer possible to define separate activation cycles. In episodes induced in response to SVCN stimulation, the early epicardial breakthrough pattern that was most frequently identified, that is, in 70% of the initial tachyarrhythmia beats, was one in which the earliest 10-msec activation was localized in the right atrial free wall, similarly to basal beats, suggesting an origin within the right atrial subsidiary pacemaker complex [28]. In the other beats (30%) epicardial maps displayed a Bachmann bundle breakthrough pattern, as previously reported for atrial tachyarrhythmias induced by mediastinal nerve stimulation [16].

Patterns of early epicardial breakthrough in the right atrium were also identified in the initial beats of atrial tachyarrhythmia episodes induced by RVSC stimulation but with a significantly lower incidence (35%) than in responses to SVCN stimulation (Table 11.2). Patterns of early epicardial breakthrough in the Bachmann bundle region were identified with a slightly higher incidence in RVSC trials (35% of early beats), but early epicardial breakthroughs were also identified in the left atrial free wall or left atrial appendage in 30% of early atrial tachycardia beats in RVSC trials.

Such early breakthrough locations were never observed in SVCN trials (Table 11.2). Another difference between atrial tachyarrhythmia episodes induced by SVCN and RVSC stimulation was the occurrence of a line of block and circulating wave front in the right atrial free wall 41/102 initial beats (40%) in SVCN trials (Figure 11.1, map B), whereas this type of activation pattern was never identified in any AT episode induced by RVSC stimulation. The lines of block were functionally determined, corresponding to dispersion of repolarization intervals during neural stimulation as shown below. Double potentials or fractionated electrograms were never detected in basal beats (sinus rhythm).

Dual epicardial breakthrough patterns (not shown) indicated a septal origin of the first tachycardia beat, as confirmed by mapping the endocardial surface of the right atrium. Such dual breakthrough patterns were identified in both series in the form of early activations arising within 10 msec of each other from both the Bachmann bundle region and lower RAFW, leading to impulse propagation in distinct directions. Such dual breakthrough patterns occurred more frequently in RVSC-induced than in SVCN-induced AT episodes (45% vs. 8%, respectively; $p < 0.001$).

Table 11.2 Spatial Distribution of Epicardial Breakthroughs During the First AT Complex.

Region	*SVCN stimulation*	*RVSC stimulation*
RAFW	71/102 (69.6%)	7/20* (35%)
BB	31/102 (30.4%)	7/20 (35%)
LAFW/LAA	0	6/ ** (30%)

SVCN vs. RVSC stimulation by Pearson Chi-square test: * $p = 0.013$, ** $p < 0.0001$. KEY: BB = Bachmann's bundle; BT = breakthrough; LAA = left atrial appendage; LAFW = left atrial free wall; RAA = right atrial appendage; RAFW = right atrial free wall. (Reproduced with permission from Ref. 22.)

Distribution of Neurally Induced Repolarization Changes

When the spatial distribution of neurally induced changes in the repolarization phase of atrial electrograms was mapped in bradycardia beats preceding atrial tachyarrhythmia induction, the changes were found to be predominantly localized in the right atrial free wall and Bachmann bundle region, whether they were induced in response to RVSC or to SVCN stimulation. In maps displaying cumulative incidences of significant changes in all animals, the changes were more widely distributed in response to RVSC than in response to SVCN stimulation (Figure 11.2). Accordingly, the mean area affected by nerve stimulation in all animals was significantly greater in response to RVSC than SVCN stimulation (2071 ± 550 mm^2 versus 574 ± 257 mm^2, $p < 0.001$), particularly in the RAFW region (1029 ± 225 mm^2 versus 290 ± 103 mm^2, $p < 0.0001$).

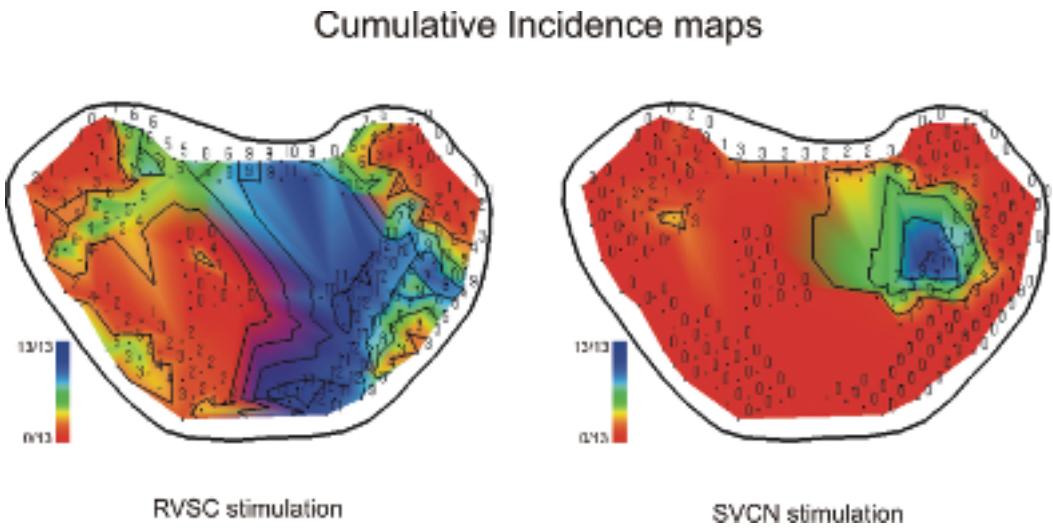

Figure 11.2 Cumulative regional incidence of atrial repolarization changes in response to RVSC (left-hand maps) vs. SVCN stimulation (right-hand maps). Maps show cumulative incidences, among preparations, of the ones showing significant neurally induced repolarization changes at each recording site. Data show the number of preparations that displayed, at each site, integral changes beyond the threshold for significance (2 × SD). Color code from 0 to 13. Note that the areas in which a high incidence of neurally mediated changes was noted are more extensive in response to RVSC than to SVCN stimulation. (Reproduced with permission from Ref. 22.)

Spatial Relationship Between Repolarization Changes and Arrhythmia Site of Origin

In all atrial tachycardia episodes induced by either form of neural stimulation, the sites of earliest activation identified in the early tachyarrhythmia beats were associated with areas of neurally induced repolarization changes (Figure 11.3, comparing panel a to panel b for each nerve stimulated). The tachycardia breakthroughs (white stars in those figures) were localized either next to the border line between affected and unaffected areas (RVSC: 44%, SVCN: 64%) or within 10 mm beyond this border line (RVSC: 38%, SVCN: 36%). In cases in which the origin of RVSC-tachyarrhythmia beats was localized to the septum by endocardial mapping (not shown), the earliest activity was identified at sites next to border lines determined by isointegral mapping of repolarization changes.

Ventricular Repolarization Changes

In addition to atrial changes, ventricular repolarization changes also occur in response to pharmacological activation of neurons within the right atrial ganglionated plexus (RAGP) by local nicotine injection. In the trial illustrated in Figure 11.4, increases in T-wave amplitude or changes in wave form polarity from negative to positive T-waves were identified, at ∼ 90 sec after nicotine injection, throughout the anterobasal wall of the left ventricule as illustrated with electrograms. Concomitantly, activation–recovery intervals shortened at similar locations. Such changes were reproducibly identified with repeat nicotine injection at the same RAGP locus (not shown). Interestingly, the data showed that, among preparations, repolarization changes occurred infrequently at the time of the negative atrial chronotropic responses (early: ∼ 20 sec after nicotine injection), but rather during positive atrial chronotropic responses (later phase: ∼ 90 sec after nicotine injection) and were identified in various ventricular regions in different preparations (most frequently in the posterior right ventricular wall).

Discussion

Our findings confirm previous reports that atrial tachyarrhythmias/fibrillation can be induced, in all animals, by localized electrical stimulation of small right-sided mediastinal nerves as well as by intense electrical stimulation of the cervical right vagosympathetic nerve complex [12–18]. In our studies, electrical stimulation was performed, in turn, at these two levels of the intrathoracic

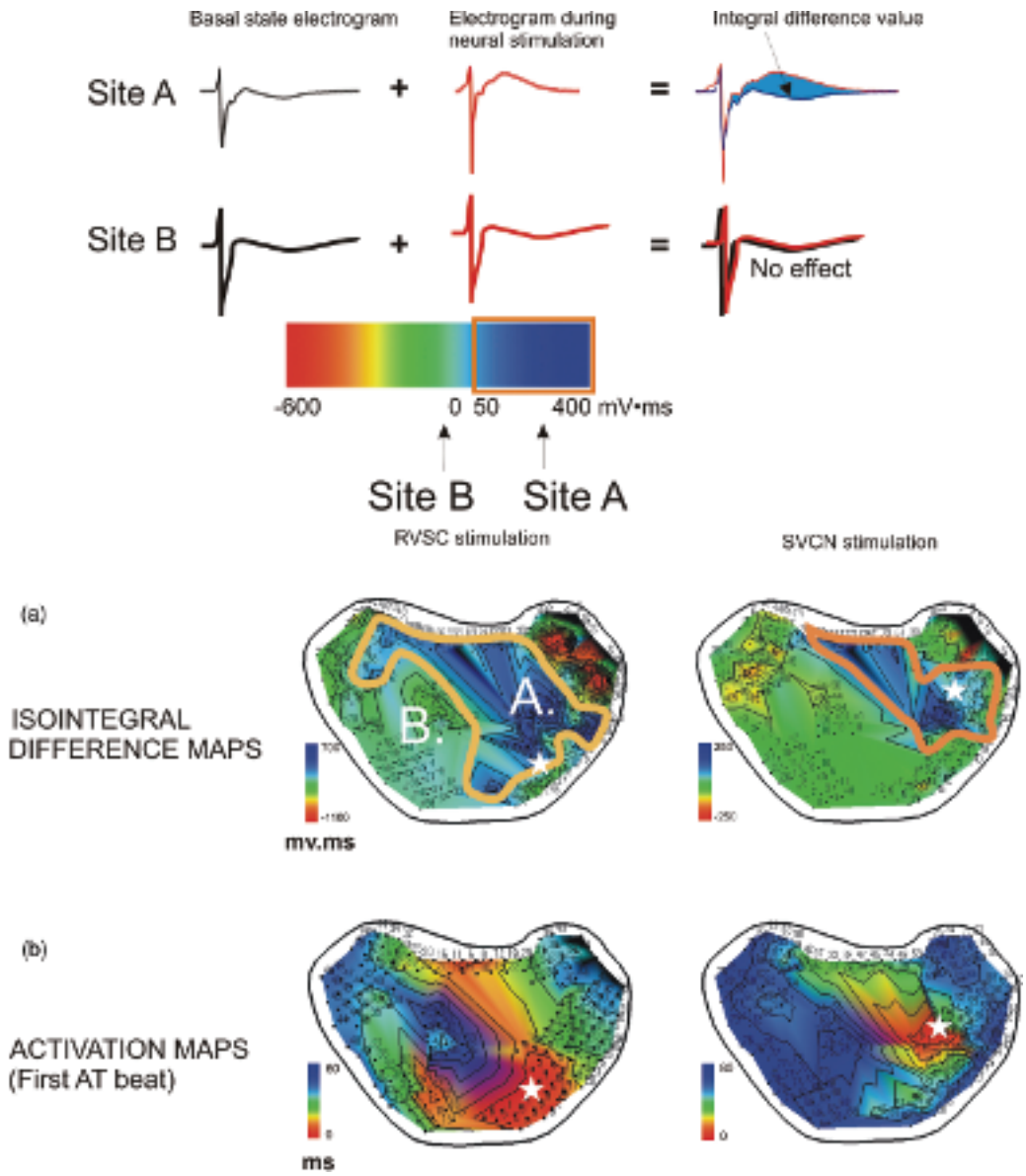

Figure 11.3 (Upper panel) Atrial unipolar electrograms recorded from selected sites (a and b) during basal state (black) and neural stimulation (red) are shown in upper and lower tracings. Right-hand diagrams illustrate the superimposed electrograms and the difference between the areas (integrals) subtended by the electrograms recorded under the two conditions. The area differences, which represent the magnitude of neurally induced changes, are plotted on the grid for each recording site to create an isointegral difference map as shown in the lower left-hand panels (differences of 60 mV · msec between lines; see also the color-coded scale of integral changes. (Lower panels) Differential distribution of atrial repolarization changes in response to RVSC (left-hand maps) vs. SVCN stimulation (right-hand maps). Isointegral difference maps (panel a, isocontour lines drawn at 100 mV · msec intervals) show that the regions of significant neurally induced changes (circumscribed within the orange line) were more extensive in response to RVSC than SVCN stimulation. Note the spatial proximity between the border of neurally induced repolarization changes (orange line) and the sites of origin of AT beats (white stars) identified by activation mapping (panel b, isochronal lines drawn at 10-msec intervals). The region of earliest 10-msec activation (red) was localized to a lower right atrial area in RVSC-induced AT (left-hand map) and to the mid right atrial free wall in SVCN induced AT (right-hand map). (Modified from Ref. 22.)

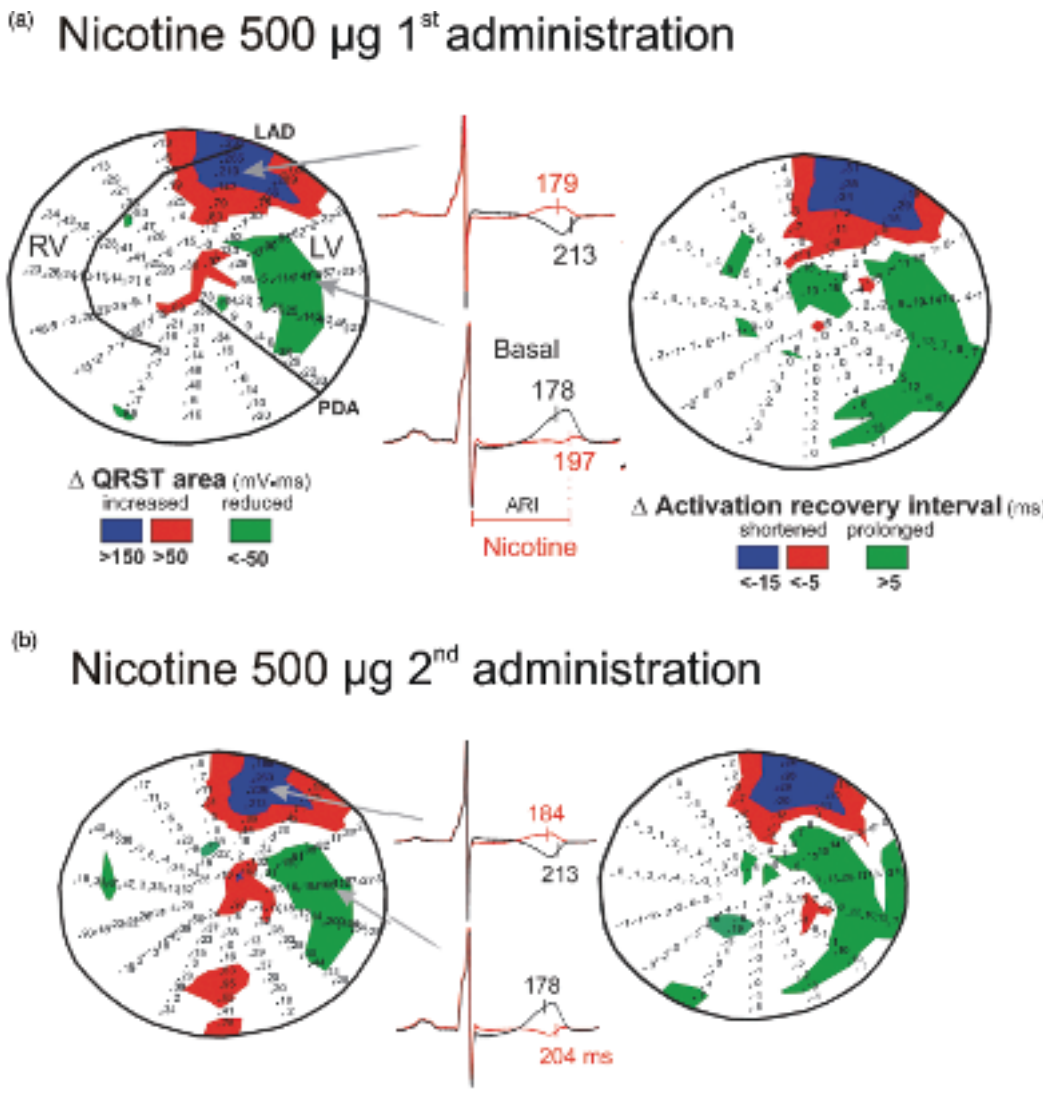

Figure 11.4 Ventricular repolarization changes induced in response to pharmacological activation of an atrial ganglionated plexus. Regional changes in QRST area (left-hand maps) or activation-recovery intervals (right-hand maps) are depicted on a polar representation of the ventricular surface in response to a first (a) and to a repeat (b) injection of nicotine (500 µg) into the RAGP (caudal component). In the polar representation, the base of the right and left ventricles (RV, LV) are along the circumference, and the LV apex at the center; the left anterior descending (LAD) and posterior descending (PDA) coronary arteries are indicated coursing from the basal to the apical regions. Ventricular repolarization changes were identified as regional increases in QRST area (red: >50 mV: msec, blue: >150 mV: msec) localized mainly to the anterior-basal RV and LV regions. Reciprocal changes were identified at most of these locations, shortening of the activation-recovery intervals were also identified (red: −5 ms, blue: −15 ms). Such changes were reproducibly identified at the base of the anterior LV wall and LV apex in response to both injections. Reciprocal changes consisting of QRST area reduction was identified in the posterolateral LV wall (green). The atrial cycle length remained stable at 445 msec in basal states and following the nicotine injections.

autonomic nerve hierarchy in each animal. In both cases, the general sequence of events leading to AT consisted of cycle length prolongation and a bradycardia beat or escape beat that is followed by a spontaneous atrial premature depolarization and subsequent tachyarrhythmia beats. Mild bradycardia that was rapidly followed by tachyarrhythmia was induced in response to brief periods of mediastinal nerve stimulation, whereas vagosympathetic nerve complex stimulation had to be delivered more persistently, thereby leading to marked bradycardia before inducing tachyarrhythmias.

The efferent axonal content within the cervical vagosympathetic trunk is mainly parasympathetic. But there is a smaller sympathetic efferent axonal population that has been functionally identified to represent about 10% of the total cardiac sympathetic efferent neural population [29]. In contrast, there is a relatively greater sympathetic efferent axonal content in the mediastinal nerves being stimulated. The different sympathetic efferent axonal content of these two structures might entail mechanistic differences with regard to the generation of the premature beat initiating the tachyarrhythmias considering that they might be associated with after-depolarizations. In response to stimulation of the RVSC (predominant parasympathetic efferent axons), the escape beat preceding the premature beat arose after a prolonged pause (median of 5 sec duration) which is consistent with early after-depolarization as the putative mechanism of the premature beat [30]. On the other hand, delayed after-depolarizations enhanced by β adrenoreceptor activation have been demonstrated in cardiomyocytes from various atrial location [18, 31]. Armour et al. reported in 2005 that atrial tachyarrhythmias induced by mediastinal nerve stimulation are modulated by β-adrenoreceptor blockade and are completely suppressed by atropine, suggesting mixed sympathetic and parasympathetic efferent neuronal influences in the SVCN paradigm [16].

It is important to note that the majority of early epicardial breakthroughs were localized in the right atrial free wall in tachyarrhythmia beats induced by SVCN stimulation, whereas the breakthrough patterns were equally distributed between the right atrial free wall and the Bachmann bundle region in tachyarrhythmia beats induced by RVSC. Moreover, dual breakthroughs in the inferior right atrial free wall and Bachmann bundle region, which have been shown by endocardial mapping to indicate a septal origin, occurred much more frequently in tachyarrhythmias induced by RVSC. Similar epicardial dual breakthrough patterns were also shown by Sharifov et al. to correspond to a septal origin [17]. In fact, early epicardial breakthrough patterns were localized to other areas in the left atrium in 25% of tachyarrhythmia beats induced by RVSC stimulation. Such findings are consistent with a more widespread distribution of neural effects in response to RVSC than SVCN stimulation.

Neurally Induced Repolarization Changes

In our studies, there was a relationship between the sites of origin of tachyarrhythmia beats and spatial distribution of effects on repolarization in response to activation of cervical vagosympathetic vs. mediastinal nerves. In SVCN stimulation trials, neurally induced repolarization changes, as detected by isointegral mapping, were spatially distributed to significantly smaller areas in the right atrial free wall than with RVSC stimulation.

In contrast, repolarization changes frequently extended to the Bachmann bundle region, the inferior right atrial wall, and the inferior left atrial wall in response to RVSC stimulation. No repolarization changes were identified in the pulmonary vein region with the present protocol (restricted to right-sided nerve stimulation) and no early breakthrough was localized to this region in tachyarrhythmia beats. This does not exclude the possible involvement of pulmonary veins in the mechanism of arrhythmias induced with other modalities (e.g., left-sided mediastinal nerves). In both SVCN and RVSC trials, there was a strong association between tachyarrhythmia sites of origin and the areas of repolarization changes. Sharper borders between affected and unaffected areas might explain the observation that, in the atrial tachyarrrhythmias induced by SVCN stimulation, lines of block and circulating wave fronts were identified in the right atrial free wall.

On the other hand, early activity foci with radial spread were mapped during RVSC-induced tachyarrhythmias. That repolarization changes were detected in a discrete portion of the atrium in response to SVCN activation might explain why this

nerve appeared to be more readily arrhythmogenic than the cranial cervical vagosympathetic nerve complex that produced more widespread atrial repolarization changes. This mechanism also appears to apply to tachyarrhythmias of septal origin, in which we have documented septal repolarization changes in response to RVSC stimulation [22].

It is commonly assumed that the severity and duration of the bradycardia phase preceding atrial tachyarrhythmia onset is a useful indication of the intensity of parasympathetic efferent neuronal tone leading to induction of atrial fibrillation [19, 32, 33]. However, the data reported herein are *not* consistent with a straightforward relationship between the susceptibility to atrial tachyarrhythmia/fibrillation and the severity of neurally induced bradycardia because the spatial distribution and extent of neurally mediated regional repolarization changes also contributed to the primary electrophysiologic substrate of atrial tachyarrhythmias in this study. Furthermore, differential contributions are made to the electrophysiologic substrate of neurally induced atrial tachyarrhythmias depending on the pattern of engagement of the intrathoracic autonomic neuronal hierarchy with, for instance, a varying degree of recruitment of sympathetic efferent neuronal elements.

Ventricular Effects of Atrial Ganglia

The most straightforward interpretation of distant effects between atrial ganglia and ventricular myocardium may be the result from activation of efferent autonomic neurons projecting from each atrial or ventricular ganglionated plexus to both atrial and ventricular muscle. Alternatively, local nicotine injection into individual ganglionated plexuses may activate local circuit neurons mediating interactions between atrial and ventricular ganglionated plexuses, similarly to interactions among the atrial ganglionated plexuses that have been postulated to explain redundant control of sinus node and AV nodal functions [10, 34]. That neurons in each major ganglionated plexus have the capacity of influencing widely dispersed cardiac regions is not surprising given recent anatomical [35] and functional data [36, 37] indicating that neurons in different intrinsic cardiac ganglionated plexuses are in constant communication with one another.

Conclusion

Data derived from this study indicate that the differential arrhythmogenic potential related to the intrathoracic autonomic nerve hierarchy represents an important consideration with respect to devising arrhythmia therapies. Neurons distributed throughout the intrathoracic autonomic nervous system as well as the entire intrinsic cardiac nervous system exert widely dispersed effects overlapping several cardiac regions. Intrinsic cardiac neurons, when excessively activated, can initiate ventricular [38] and atrial [16, 22] tachyarrhythmias as well as exacerbate ventricular ischemia [39].

That they exert redundant control over diverse cardiac regions suggests that it may be possible for ablation strategies to target neurons to attenuate their influence without, however, completely suppressing autonomic regulation. These data also indicate, however, that ablating or activating an anatomically discrete sector of the autonomic hierarchy will not necessarily result in definitive control of one specific type of cardiac event [40]. Neurons located at multiple intrathoracic levels or multiple cardiac ganglionated plexuses will have to be considered. In fact, the idea of ablating cardiac ganglia in the treatment of atrial arrhythmias must be considered as one possibility among a wide range of neuromodulatory approaches. These may include pharmacological as well as nonpharmacological therapies such as catheter ablation of juxtacardiac nerves [8] or even spinal cord stimulation [39, 41, 42].

Acknowledgements

The authors wish to thank Caroline Bouchard for expert technical assistance, Yalin Yin and Michel Velmeulen for data collection and analysis, and Suzan Senechal for secretarial assistance. This work was supported by an operating grant awarded by the Canadian Institutes of Health Research to Pierre Pagé.

References

1 Hsieh, MH, Chiou, CW, Wen, ZC, et al. Alterations of heart rate variability after radiofrequency catheter ablation of focal atrial fibrillation originating from pulmonary veins. *Circulation* 1999; **100**: 2237–43.

2 Pappone, C, Santinelli, V, Manguso, F, et al. Pulmonary vein denervation enhances long-term benefit after circumferential ablation for paroxysmal atrial fibrillation. *Circulation* 2004; **109**: 327–34.

3 Mehall JR, Kohut RM, Jr, Schneeberger EW, Taketani T, Merrill WH, Wolf RK. Intraoperative epicardial electrophysiologic mapping and isolation of autonomic ganglionic plexi. *Ann Thorac Surg* 2007; **83**: 538–41.

4 Scanavacca M, Pisani CF, Hachul D, et al. Selective atrial vagal denervation guided by evoked vagal reflex to treat patients with paroxysmal atrial fibrillation. *Circulation* 2006; **114**: 876–85.

5 Lemery R, Birnie D, Tang AS, Green M, Gollob M. Feasibility study of endocardial mapping of ganglionated plexuses during catheter ablation of atrial fibrillation. *Heart Rhythm* 2006; **3**: 387–96.

6 Scherlag BJ, Nakagawa H, Jackman WM, et al. Electrical stimulation to identify neural elements on the heart: their role in atrial fibrillation. *J Interv Card Electrophysiol* 2005; **13**: 37–42.

7 Olgin, JE, Sih, HJ, Hanish, S, et al. Heterogeneous atrial denervation creates substrate for sustained atrial fibrillation. *Circulation* 1998; **98**: 2608–14.

8 Schauerte, P, Scherlag, BJ, Patterson, E, et al. Focal atrial fibrillation: experimental evidence for a pathophysiologic role of the autonomic nervous system. *J Cardiovasc Electrophysiol* 2001; **12**: 592–99.

9 Lin J, Scherlag BJ, Zhou J, et al. Autonomic mechanism to explain complex fractionated atrial electrograms (CFAE). *J Cardiovasc Electrophysiol* 2007; **18**: 1197–205.

10 Hou Y, Scherlag BJ, Lin J, et al. Ganglionated plexi modulate extrinsic cardiac autonomic nerve input: effects on sinus rate, atrioventricular conduction, refractoriness, and inducibility of atrial fibrillation. *J Am Coll Cardiol* 2007; **50**: 61–8.

11 Lewis, T, Meakins, J, White, PD. The excitatory process in the dog's heart. I. The auricles. *Phil Trans B* 1914; **205**: 375–420.

12 Loomis, TA, Krop, S. Auricular fibrillation induced and maintained in animals by acetylcholine or vagal stimulation. *Circ Res* 1955; **3**: 390–96.

13 Wilber, DJ, Morton, JB. Vagal stimulation and atrial fibrillation: experimental models and clinical uncertainties. *J Cardiovasc Electrophysiol* 2002; **13**: 1280–82.

14 Armour, JA, Hageman, GR, Randall, WC. Arrhythmias induced by local cardiac nerve stimulation. *Am J Physiol* 1972; **223**: 1068–75.

15 Hageman, GR, Goldberg, JM, Armour, JA, Randall, WC. Cardiac dysrhythmias induced by autonomic nerve stimulation. *Am J Cardiol* 1973; **32**: 823–30.

16 Armour, JA, Richer, LP, Pagé, P, et al. Origin and pharmacological response of atrial tachyarrhythmias induced by activation of mediastinal nerves in canines. *Auton Neurosci* 2005; **118**: 68–78.

17 Sharifov, OF, Zaitsev, AV, Rosenshtraukh, LV, et al. Spatial distribution and frequency dependence of arrhythmogenic vagal effects in canine atria. *J Cardiovasc Electrophysiol* 2000; **11**: 1029–42.

18 Wang, J, Liu, L, Feng, J, Nattel, S. Regional and functional factors determining the induction and maintenance of atrial fibrillation in dogs. *Am J Physiol* 1996; **271**: H148–58.

19 Liu, L, Nattel, S. Differing sympathetic and vagal effects on atrial fibrillation in dogs: role of refractoriness heterogeneity. *Am J Physiol* 1997; **273**: H805–16.

20 Pagé, PL, Dandan, N, Savard, P, Nadeau, R, Armour, JA, Cardinal, R. Regional distribution of atrial electrical changes induced by stimulation of extracardiac and intracardiac neural elements. *J Thor Cardiovasc Surg* 1995; **109**: 377–88.

21 Pagé PL, Cardinal R: Efferent autonomic innervation of the atrium: assessment by isointegral mapping. In: Shenasa M, Borggrefe M, Breithardt G, eds. *Cardiac Mapping.* 2nd ed. Futura Publishing Co., Inc., Armonk, NY, 2003: Chapter 17, 363–71.

22 Pagé P, Armour JA, Yin Y, Vermeulen M, Nadeau R, Cardinal R: Differential effects of cervical vagosympathetic and mediastinal nerve activation on atrial arrhythmia formation in dogs. *Auton Neurosci* 2006; **128**: 9–18.

23 Derakchan K, Cardinal R, Brunet S, et al. Polymorphic ventricular tachycardias induced by d-sotalol and phenylephrine in canine preparations of atrioventricular block : initiation in the conduction system followed by spatially unstable reentry. *Cardiovasc Res* 1998; **38**: 617–30.

24 Hélie, F, Vinet, A, Cardinal, R. Cycle length dynamics at the onset of postinfarction ventricular tachycardias induced in canines: dependence on interval-dependent excitation properties of the reentrant substrate. *J Cardiovasc Electrophysiol* 2000; **11**: 531–44.

25 Savard, P, Cardinal, R, Nadeau, RA, Armour, JA. Epicardial distribution of ST segment and T-wave changes produced by stimulation of intrathoracic ganglia or cardiopulmonary nerves in dogs. *J Auton Nerv Syst* 1991; **34**: 47–58.

26 Cardinal, R, Pagé, PL. Neuronal modulation of atrial and ventricular electrical properties. In: Armour, JA, Ardell, JL, eds. *Basic and Clinical Neurocardiology*. Oxford University Press, New York, 2003: Chapter 11, 315–39.

27 Boineau, JP, Schuessler, RB, Roeske, WR, Miller, CB, Wylds, AC, Hill, DA. Autonomic organization of the atrial pacemaker complex. In: Zipes, DP, Jalife, J, eds. *Cardiac Electrophysiology and Arrhythmias*. Grune & Stratton, Orlando, FL, 1985: 151–58.

28 Schuessler, RB, Boineau, JP, Wylds, AC, Hill, DA, Miller, CB, Roeske, WR. Effect of canine cardiac nerves on heart rate, rhythm, and pacemaker location. *Am J Physiol* 1986; **250**: H630–44.

29 Hopkins DA, Armour JA. Localization of sympathetic postganglionic and parasympathetic preganglionic neurons which innervate different regions of the dog heart. *J Comp Neurol* 1984; **229**: 186–98.

30 Chen YJ, Chen SA, Chang, MS, Lin CI. Arrhythmogenic activity of cardiac muscle in pulmonary veins of the dog: implication for the genesis of atrial fibrillation. *Cardiovasc Res* 2000; **48**: 265–73.

31 Henning, B, Wit, AL. The time course of action potential repolarization affects delayed after depolarization amplitude in atrial fibers of the canine coronary sinus. *Circ Res* 1984; **55**: 110–15.

32 Coumel, P. Autonomic influences in atrial tachyarrhythmias. *J Cardiovasc Electrophysiol* 1996; **13**; 83–7.

33 Hill, LL, Kattapuram, M, Hogue, CW, Jr. Management of atrial fibrillation after cardiac surgery. I: Pathophysiology and risks. *J Cardiothorac Vasc Anesth* 2002; **16**; 483–94.

34 Hou Y, Scherlag BJ, Lin J, et al. Interactive atrial neural network: determining the connections between ganglionated plexi. *Heart Rhythm* 2007; **4**: 56–63.

35 Gray AL, Johnson TA, Ardell Jl, Massari VJ. Parasympathetic control of the heart. II. A novel interganglionic intrinsic cardiac circuit mediates neural control of heart rate. *J Appl Physiol* 2004; **96**: 2273–78.

36 Randall DC, Brown DR, McGuirt AS, Thompson GW, Armour JA, Ardell JL. Interactions within the intrinsic cardiac nervous system contribute to chronotropic regulation. *Am J Physiol Regul Integr Comp Physiol* 2003; **285**: R1066–75.

37 Waldmann M, Thompson GW, Kember GC, Ardell JL, Armour JA. Stochastic behavior of atrial and ventricular intrinsic cardiac neurons. *J Appl Physiol* 2006; **101**: 413–19.

38 Huang MH, Wolf SG, Armour JA. Ventricular arrhythmias induced by chemically modified intrinsic cardiac neurons. *Cardiovasc Res* 1994; **28**: 636–42.

39 Cardinal R, Ardell JL, Linderoth B, Vermeulen M, Foreman RD, Armour JA. Spinal cord stimulation differentially modulates ischaemic electrical responses to different stressors in canine ventricles. *Auton Neurosci* 2004; **111**: 37–47.

40 Oh S, Zhang Y, Bibevski S, Marrouche NF, Natale A, Mazgalev TN. Vagal denervation and atrial fibrillation inducibility: epicardial fat pad ablation does not have long-term effects. *Heart Rhythm* 2006; **3**: 701–8.

41 Foreman, RD, Linderoth, B, Ardell, JL, et al. Modulation of intrinsic cardiac neural activity by spinal cord stimulation: implications for its therapeutic use in angina pectoris. *Cardiovasc Res* 2000; **47**: 367–75.

42 Olgin, JE, Takahashi, T, Wilson, E, Verekei, A, Steinberg, H, Zipes, DP. Effects of thoracic spinal cord stimulation on cardiac autonomic regulation of the sinus and atrioventricular nodes. *J Cardiovasc Electrophysiol* 2002; **13**: 475–81.

12 CHAPTER 12

Mapping of Neurally Based Atrial Arrhythmias

Guo-Dong Niu, MD,[1] *Benjamin J. Scherlag,* PhD,[2]
Zhibing Lu, MD,[2] *Jeffery Edwards,* RN,[2]
Eugene Patterson, PhD,[2] *Muhammad Ghias,* MD,[2]
Annerie Moers, MD,[2] *Shu Zhang,*[1] *Ralph Lazzara,* MD,[2]
Warren M. Jackman, MD,[2] *Sunny S. Po,* MD, PhD[2]

[1]Cardiovascular Institute Fuwai Hospital, Beijing, China
[2]University of Oklahoma Medical Center, Oklahoma City, OK, USA

Summary

In the last half of the twentieth century, experimental studies by several groups of investigators described the anatomic and functional aspects of the intrinsic cardiac autonomic nervous system. This system, as distinct from the autonomic inputs to the heart from the brain and spinal cord (extrinsic autonomic nervous system), consists of clusters of ganglionated plexi (GP) localized in the vicinity of the pulmonary veins and on the great vessels adjacent to the heart. Extending from these GPs are axonal fields that not only project throughout the atria but also constitute an interconnected neural network. Together with the extrinsic autonomic inputs, they serve to modulate numerous cardiac functions.

Only in the past decade have basic and clinical studies revealed the critical role played by the GP in the initiation and maintenance of atrial fibrillation (AF), particularly, the focal form that is resistant to drugs and cardioversion. In the present study, we used a multielectrode balloon array to map the activation patterns associated with sudden occurrence of AF arising from the pulmonary veins (PVs) or from non-PV sites. These maps allowed the delineation of activation via nonmyocardial connections in the initiation of focal sources of AF. Both electrical and chemical methods were used acutely to induce sustained AF ($\geq$10 min) via putative neural pathways. Ordinarily the normal dog heart will not sustain AF in response to burst pacing at high rates; AF lasts but a few seconds.

We also mapped the onset of inappropriate sinus tachycardia induced by the injection of the adrenergic neurotransmitter, epinephrine, into the GP adjacent to the sinus node to induce prolonged periods ($\geq$30 min) of heart rates over 200/min. Mapping showed the origin of this tachycardia from a specific portion of the sinus node. Previous animal studies have shown that stimulation of autonomic nerves in the pulmonary artery can induce and closely simulate the clinical patterns seen in right ventricular outflow tract tachycardias. Future studies are contemplated for targeting other neural pathways suspected in the initiation of various atrial and ventricular arrhythmias.

Cardiac Mapping, Third Edition Edited by Mohammad Shenasa, Gerhard Hindricks, Martin Borggrefe, and Günter Breithardt
 ISBN: 978-1-405-17572-2

Historical Background

Amory and West in 1962 [1] and West and Toda in 1969 [2] demonstrated that direct stimulation of the sinus node and the A-V junction in the isolated rabbit heart induced slowing of the heart rate and AV conduction, respectively. These authors suggested that this low-level electrical stimulation, which did not excite the myocardium, involved stimulation of cholinergic and adrenergic nerves and ganglia. In 1973, Lazzara et al [3] described the ability to slow the heart rate and A-V conduction in the in situ dog heart by similar low-level electrical stimulation of a fat pad containing autonomic ganglia at the caudal end of the sinus node and another fat pad at the junction of the inferior vena cava and left atrium, respectively. Histological sections of these fat pads showed that they were populated with clusters of ganglia. These isolated reports were systematically investigated by Randall and his associates [4–7] over the next 30 years, culminating in a concept of the intrinsic autonomic cardiac nervous system as delineated by Ardell in the publication *Neurocardiology* in 1994 [8].

Two seemingly unrelated clinical reports appeared recently [9, 10] which revealed that patients with paroxysmal atrial fibrillation (AF) who were resistant to drugs and cardioversion showed ectopic firing from the pulmonary veins (PVs) that triggered the AF episodes. On the basis of these singular findings, the now widely accepted strategy of PV isolation, electrically disconnecting the PVs from the atria, was instituted in major clinical electrophysiological centers around the world to "cure" AF [9–12]. However, this empirical approach did not address the fundamental issue, that is, what mechanisms were responsible for the ectopic firing arising from the PVs and even non-PV sites [13–15] triggering AF. Several basic studies suggested that the PVs were particularly sensitive to autonomic neurotransmitters, both cholinergic and adrenergic [16].

More direct evidence for the relationship between PV ectopy and autonomic neurotransmitters released from the ganglionated plexi (GP) located at the entrances of the PVs was provided by recent experimental studies [17, 18]. Clinical studies have also been forthcoming implicating the critical role of the GP, in the initiation and maintenance of AF in patients resistant to drug and cardioversion therapy [19–21].

The Intrinsic Cardiac Autonomic Nervous System

The intrinsic cardiac autonomic nervous system consists of the ganglia and nerves found on the heart and large vessels adjacent to the heart (superior vena cava, inferior vena cava, pulmonary artery, and aorta) all within the confines of the pericardium. There are five major clusters of ganglia (GP) on the dog heart [22] and two located on vessels within the pericardial space. Those on the heart are found in fat pads at the PV–atrial junctions [7, 8, 23]. The noncardiac GP are located on the surface of the right pulmonary artery [24–27] or in the fibrofatty interface tissue located between the proximal portions of the aorta and the pulmonary artery [28].

A variety of terms have been applied to these cardiac GP. We have designated them as follows: The anterior right (ARGP) at the entrance of the right superior (RS) PV; the inferior right (IRGP) found at the junction of the inferior vena cava and the right and left atria; the superior left (SLGP) located at the juncture of the left pulmonary artery and left superior (LS) PV; and the inferior left (ILGP) at the entrance of the left inferior (LI) PV. A smaller number of GP can be found within the lower end of the ligament of Marshall (see Figure 12.1). As for the noncardiac GP (not shown in Figure 12.1) there is the right pulmonary artery fat pad which has been called the posterior atrial fat pad (PAFP) [25], the third fat pad [26], and the right pulmonary artery fat pad (RPAFP) [27]; and the GP in the fibrofatty tissue between the proximal pulmonary artery and aorta which has been referred to as the cranial medial ventricular GP [28] or the intertruncal plexus [29].

Mapping the Onset of Focal Atrial Fibrillation from a Pulmonary Vein (PV)

Jais and Haissaguerre [9, 10] provided a seminal observation that triggering beats arising in the PVs were the initiators of AF in those patients with drug and cardioversion-resistant AF. Our basic studies sought to establish experimental models that would closely simulate paroxysmal AF arising from PV and non-PV sites allowing insights into the mechanism(s) responsible for this form of AF.

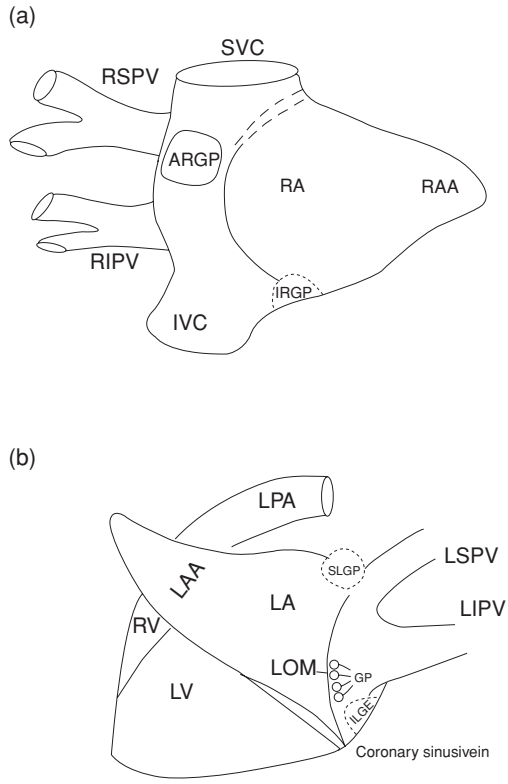

Figure 12.1 A schematic representation of the right atrium and portions of the left atrium seen via a right thoracotomy. The major clusters of ganglionated plexi are found in fat pads at the entrances of the pulmonary veins. The anterior right (ARGP) at the entrance of the right superior (RS) PV; the inferior right (IRGP) found at the junction of the inferior vena cava and the right and left atria; the superior left (SLGP) located at the juncture of the left pulmonary artery and left superior (LS) PV; and the inferior left (ILGP) at the entrance of the left inferior (LI) PV. A smaller number of GP are located in the inferior part of the ligament of Marshall (LOM). The noncardiac GP are not shown; see text.

In a series of studies in the pentobarbital anesthetized dog [18], the heart was exposed through a right thoracotomy. The mapping system consisted of a 9Fr catheter with a multielectrode array incorporated into a 7.5-mL balloon mounted toward its distal end (EnSite 3000, Endocardial Solutions, St. Paul, MN). Heparin (1000–2000 IU) was administered intravenously to prevent thrombus formation on the array. The array catheter was introduced via the right external jugular vein over a 0.035-in. guidewire and passed into the atrium (RA). The tip of the catheter was stabilized in the inferior vena cava. The balloon was inflated with 7.5 mL saline when it was situated subtending the mid-portion of the RA. The array uses 5.68-kHz signal to locate another electrode catheter, which was moved to different positions in RA, thereby allowing the EnSite system to construct a virtual geometry in three dimensions of the chamber, the venous inputs, and the RA appendage. With mathematical algorithms, the system can provide more than 3000 virtual unipolar electrograms. Both static and video images of local activation during dynamic processes such as AF can be displayed on the system's monitor as well as the virtual electrograms from selected sites on the constructed endocardium.

Octapolar electrode catheters were attached by sutures to the RSPV and RIPV. Another multielectrode catheter was sutured to the right atrium (RA). Acetylcholine (0.5 cc, 10 mM) was injected into the ARGP fat pad through a 26 gauge needle. Within 2–5 min, four of eleven animals manifested spontaneous and sustained AF ($\geq$10 min). Figure 12.2 shows the site of the onset of AF recorded by the EnSite mapping system (RAO view). AF was triggered by a spontaneous premature beat (arrow head) localized in the area of the RIPV by four virtual electrograms as indicated by the unipolar recordings displaying primary negativity, particularly, virtual electrodes showing the earliest site of activation. The EnSite mapping image reveals that the area at the RIPV is the earliest site of activation (white color) associated with the location of the virtual electrograms [8–11] shown in panel a. Color spectrum from white to blue represents a 0.5-mV voltage gradient.

Mapping the Onset of Focal AF from a Non-PV Site: Electrical Induction

Although most of the patients undergoing ablation manifest triggering beats arising from the PVs, some show focal firing arising at non-PV sites such as the superior vena cava [30], the ligament of Marshall [31, 32] as well as the free walls of the atria [33]. Figure 12.3 shows the EnSite maps resulting from a strong premature stimulus (12 ma) delivered at the RAA. The EnSite maps were made in the right lateral view.

The premature beat activated the RAA, and the myocardial wavefront started to traverse the atrium.

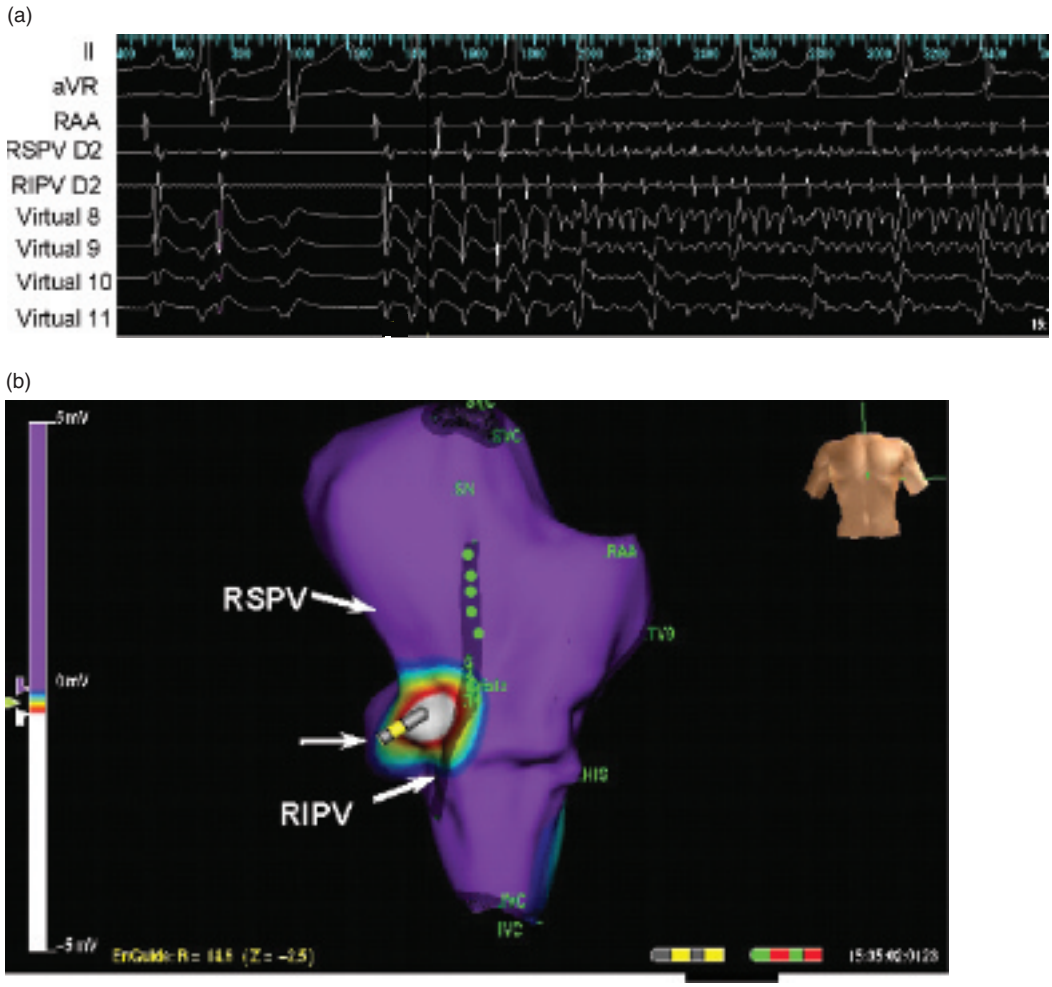

Figure 12.2 The onset of AF minutes after the injection of Ach into the fat pad, containing the ARGP, as recorded by the EnSite mapping system (RAO view). (Panel a) AF triggered by a spontaneous premature beat (arrow head) was localized by four virtual electrograms in the area of the RIPV, unipolar electrograms displaying primary negativity. (Panel b) EnSite mapping reveals that the distal electrode head at the RIPV is the earliest site of activation (white color) associated with the location of the virtual electrograms [8–11] shown in panel (a). Color spectrum from white to blue represents a 0.5–mV voltage gradient. KEY: SVC = superior vena cava; SN = head of the sinus node; RAA = right atrial appendage; TV = tricuspid annulus; His = His bundle area; Crista = area of the crista terminalis; IVC = inferior vena cava.

However, the endocardium at the ARGP was activated prior to the propagated wavefront reaching that area. In the lower panel another such incident is shown. The leading edge of the wavefront was outlined by the black dots. The white line indicates the distance (2 cm) between the leading edge of the depolarization and the edge of the ARGP. The right-sided image shows the actual activation (arrow) of the endocardium subtending the ARGP, 5 msec after the left map was recorded. The calculated conduction velocity across the myocardial activation gap was 4 mm/msec, much faster than the range of atrial conduction, 0.5–0.8 mm/msec but more consistent with neural conduction (>2 mm/msec).

The possibility that neural conduction from a peripheral (non-PV) site could play a role in the initiation of AF arising from the PV led us to investigate

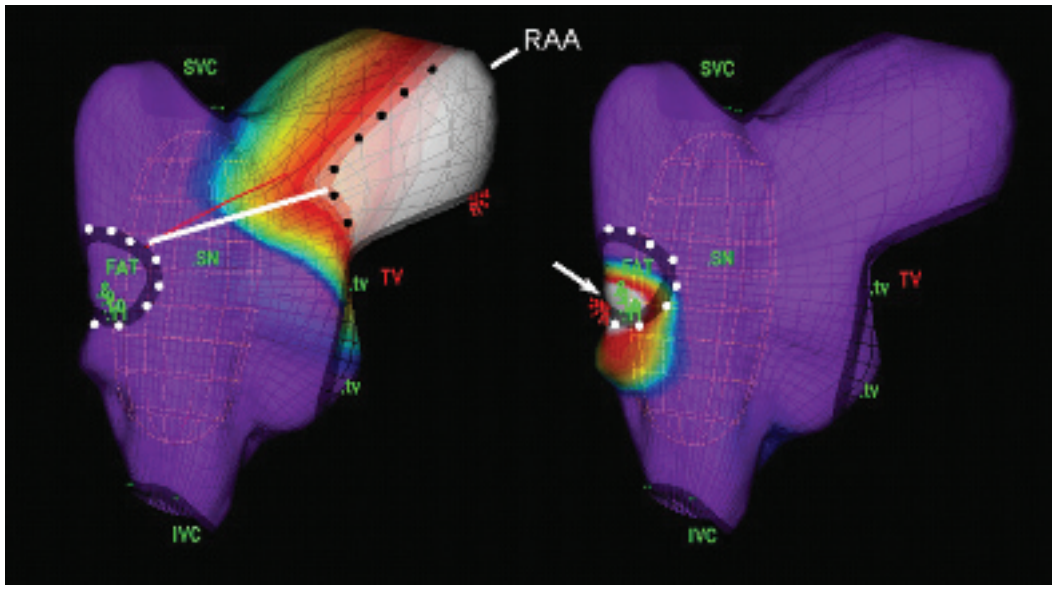

Figure 12.3 EnSite maps showing the initiation of AF by strong premature stimuli delivered to the right atrial appendage (RAA). (Upper panel) The endocardium, underlying the fat pad containing the ARGP, was activated while the propagating wavefront was just starting to traverse the RA. Abbreviations are the same as described in legend for Figure 12.2. See text for further details.

other experimental means to induce AF at non-PV sites.

Chemical Induction of AF from a Non-PV Site

In order to induce spontaneous, sustained AF from a non-PV site we used a modification of the technique described by Scherf et al. [34] who applied a high concentrations of acetylcholine (Ach) to the atria. Multipolar electrodes were attached to record electrograms at the superior and inferior PVs, the right atrial free wall (RA), and the right atrial appendage (RAA). In addition, a polyethylene tube sutured across the RAA and sealed on the appendage side with tissue glue provided a leak proof barrier when a gauze pad moistened with Ach (100 mM) was applied on the RAA.

Of the dogs studied, 15 of 19 showed spontaneous, sustained ($\geq$10 min) AF in response to the topically applied Ach at the RAA. Figure 12.4 illustrates an example of the onset of spontaneous AF, as depicted with the EnSite mapping technology. Note that the initial unipolar electrograms show a QS pattern, indicative of the earliest site of activation arising in the vicinity of the RIPV. This pattern persists for several beats at a cycle length of 50 msec prior to switching over to a QS pattern arising at the RAA (Figure 12.4) at a shorter cycle length of 30 msec. Thus, the application of a high concentration of Ach on the RAA provides a chemical counterpart to the previously described electrical initiation of AF by a strong stimulus applied at the RAA (see above). Neural mediation by the GP in the induction of AF arising from adjacent PV as well as from non-PV sites remains a viable explanation for these finding and awaits the results of ongoing investigations in our laboratory.

Neural Mechanisms Underlying Paroxysmal AF

In a previous study, we determined the extent to which ARGP stimulation would affect the atrial refractory period (ARP) and inducibility of AF at measured distances in the atria and adjacent PV [35]. For completeness, we also determined the inducibility for AF by delivery of premature beats to a peripheral site, the RAA, over a wide range of

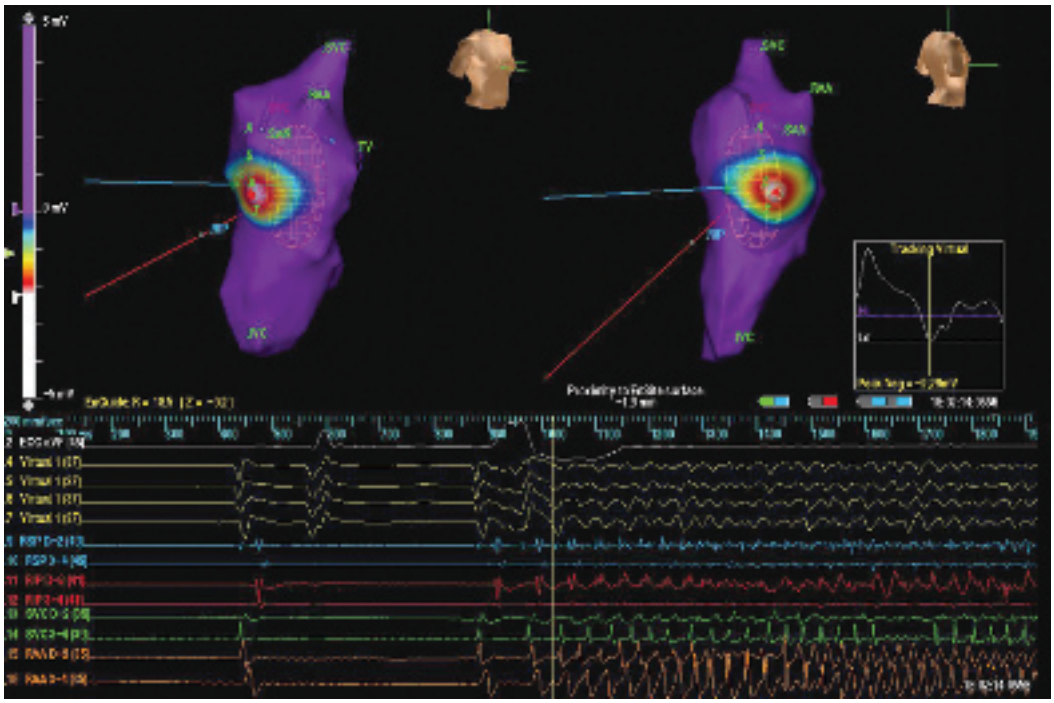

Figure 12.4 EnSite map and electrograms showing onset and continuation of sustained AF induced after application of Ach, 100 mM, on the right atrial appendage (RAA). (Panel a) The first 12–14 atrial electrograms (cycle length = 50 msec) show the initial onset of AF arising from the right inferior pulmonary vein RIPV. Note the QS pattern at the cursor and the late activation of RAA electrograms (RS pattern). (Panel b) After the initial atrial electrograms arising at the RIPV, the earliest activation switches to the RAA. Note the abrupt occurrence of the QS pattern as the RIPV site breaks down into fractionated electrograms. The cycle length has markedly shortened to 30 msec. The images show activation originating from the RAA, where the QS patterns were being recorded. See text for further details.

coupling intervals down to the ARP. The inducibility for AF was quantitated by determining the longest minus the shortest coupling interval that induced AF. The difference represented the window of vulnerability (WOV). At increasing voltage levels of stimulation of the ARGP, there was consistent gradient of ARP and WOV from close to the GP and moving away into the PV or towards the atrial appendage. Specifically, the ARPs were generally shortest close to the GP and lengthened at the more peripheral sites. On the other hand, there was a consistent decrease in the WOV along the same gradients at any voltage level. Furthermore, the WOVs were significantly increased as the voltage was increased. These studies suggested that GP activation and associated release of the cholinergic (ARP shortening) and adrenergic (triggering early after-depolarizations, EADS) neurotransmitters may play a critical role in the initiation of paroxysmal AF arising from PV as well as non-PV sites. Findings from other studies supported this hypothesis by showing that stimulation of local nerve ending in the PVs, studied in vitro, could induce both marked action potential duration shortening (ARP reduction) as well as EADs which triggered rapid PV firing. The same effects could be achieved by addition of acetylcholine or norepinephrine to the superfusing solution. These electrical and chemical actions could be completely inhibited by the addition of specific autonomic blocking agents [16].

Chemical Induction of Inappropriate Sinus Tachycardia

Inappropriate sinus tachycardia (IST) is considered a vexing clinical problem not effectively treated by either pharmacological agents or other means.

Table 12.1 The Effects of Electrical Stimulation of ARGP on Heart Rate (HR)

	Voltage applied to ARGP		
Study #	*Baseline*	*0.6 V*	*1.5 V*
1	164	137	127
2	150	128	94
3	131	130	106
4	176	143	148
5	158	140	88
6	142	86	81
7	126	121	89
8	130	103	62
9	143	132	77
Average	**147**	**126**	**97**
STD	**17**	**20**	**26**
***P* value**		**0.004***	**0.05***

* *P*-values calculated for the comparison of the average HRs during ARGP stimulation and the baseline.

Radiofrequency catheter ablation of the sinus node (SN) in patients has had variable success [36]. We hypothesized that IST is a dysautonomia affecting the intrinsic cardiac neurons innervating the SN and adjacent areas by releasing excessive amounts of neurotransmitters, specifically, catecholamines [37].

Nine dogs, each weighing 20–25 kg, were anesthetized with Na-pentobarbital prior to performing a right thoracotomy. A 26-gauge needle with a polyethylene tube attached was inserted into the fat pad (FP) containing the ARGP at the entrance of the right pulmonary veins (PVs). A plaque electrode was sutured over the FP for electrical stimulation of the ARGP at incremental voltages 0.6–4.0 volts (V). ECG leads, right atrial electrograms, blood pressure (BP), and core temperature were continuously monitored.

Table 12.1 shows that the baseline heart rate (HR) averaged 147 ± 17/min and consistently decreased with ARGP stimulation: 0.6 V, 126 ± 20/min*; 1.5 V, 97 ± 26/min* (* $p < 0.05$ compared to baseline). To induce IST, Epi 200 μg was injected into the FP causing a significant increase in HR (average: 211 ± 11/min, $p < 0.05$ compared to control) but little change in SBP, 151 ± 17 mmHg versus control 149 ± 10 mmHg, p = NS (Table 12.2). The tachycardia lasted >30 min. Ice mapping on the atrial surface in conjunction with *P*-wave morphology revealed that the tachycardia originated at the head of the sinus node in 7/9 and in the lower end of the sinus node-crista terminalis junction in 2/9. Injection of 0.4 cc of formaldehyde into the FP restored the heart rate toward the baseline (150 ± 10). These results in our experimental model are consistent with the dysautonomia hypothesis.

A recent case report by Taketani et al. [38] described a surgical approach, through a small thoracotomy, to expose the superior vena cava–sinus node area in a patient with IST. The application of radiofrequency energy to ablate the tissues in and around the sinus node including the fat adjacent to the node, the site of the ganglionated plexi at the pulmonary vein entrance. This patient had previously failed a catheter based procedure to reduce her resting (110–130 beats/min) and exercise (160–200 beats/min) heart rate. Six months following the surgical procedure, the patient's heart rate in sinus rhythm, with normal *P*-waves, was 70–80 beats/min. The authors ascribe these salutary effects to partial denervation of the sinus node. Further reports targeting the GP, particularly the ARGP adjacent to the sinus node, may determine the feasibility of a new approach, either surgical or by endocardial catheter ablation for treating IST.

Table 12.2 The Effect of Epinephrine (Epi) Injected Into the Fat Pad Containing the Anterior Right Ganglionated Plexi (ARGP) on Heart Rate (HR) and Systolic Blood Pressure (SBP)

Study #	*Control HR*	*Epi-HR*	*Control SBP*	*Epi-SBP*
1	166	203	148	153
2	158	232	134	140
3	150	212	141	137
4	148	208	155	158
5	141	202	141	161
6	176	206	179	154
7	173	223	173	148
8	122	199	138	144
Average	**154**	**211**	**151**	**149**
STD	**18**	**11**	**17**	**10**
***P* value**		**0.003***		**0.8***

* Indicates the *p*-values for the average HR and SBP caused by epinephrine injection compared to their control levels.

(a)

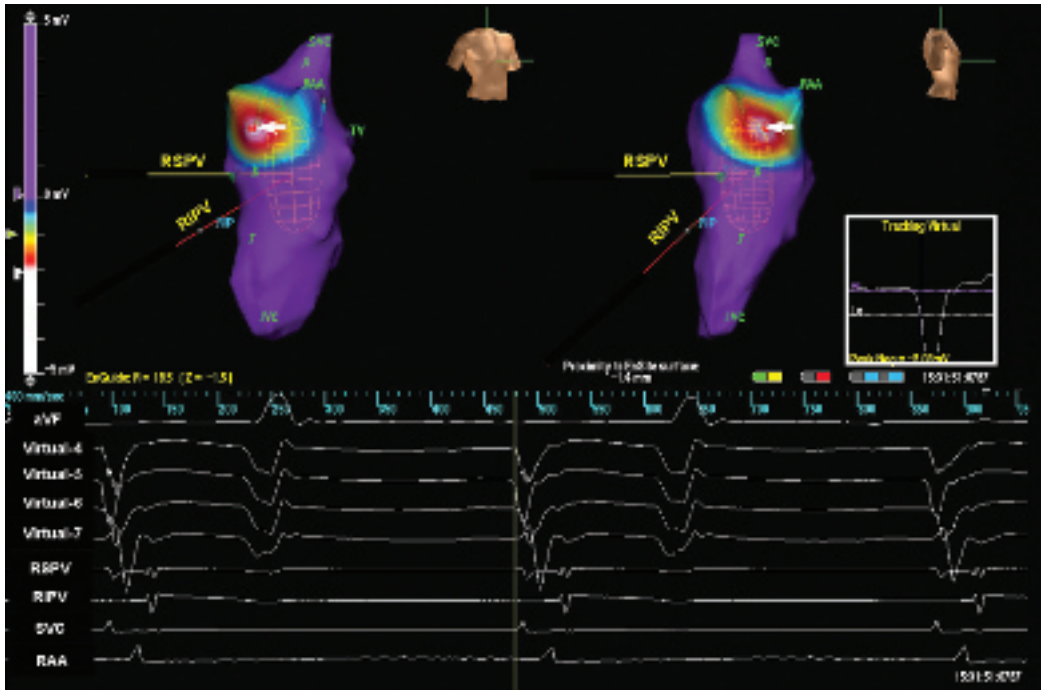

Figure 12.5 The effect of electrical stimulation of the interganglionic nerve (IGN) connecting the stellate ganglion and the ARGP, on heart rate acceleration. (Panel a) During sinus rhythm the EnSite map shows the onset of atrial activity at the head of the sinus node, at the confluence of the superior vena cava and the right atrial appendage. The heart rate was 150/min. (Panel b) IGN electrical stimulation (at 6 V) induced an acceleration of the heart rate to 186/min with little change in the earliest site of activation at the head of the sinus node. However, when the voltage was raised to 8 V, (panel C) the heart rate increase (211/min) was associated with a leftward and slightly inferior shift of the earliest site of activation. See text for further discussion.

Electrical Induction of Inappropriate Sinus Tachycardia

Previous investigators described a slender nerve bundle running from the stellate ganglion's ventral ansa to the ARGP located at the caudal end of the sinus node. Initially this nerve was designated as the right stellate cardiac nerve, but then was renamed the right interganglionic nerve (IGN) [39; p. 22]. Electrical stimulation of the IGN caused sinus, that is, heart rate, acceleration [39, p. 30]. In the pentobarbital anesthetized dog, we localized the IGN as it coursed along the innominate vein and down the vena cava toward the heart. High-frequency stimulation (20 Hz, each stimulus = 0.1 msec in duration, voltages from 4.5 to 9.3 V) applied to the IGN above the myocardial sleeve of the superior vena cava induced progressive acceleration of the heart rate with incremental changes in voltage. However, there were no significant changes in the A-H interval on the His bundle electrogram and no change in average blood pressure in a series of 19 studies.

Using the EnSite mapping system, we found that the sinus node pacemaker showed a slight shift leftward during IGN stimulation (Figure 12.5c) compared to the position of the earliest activation recorded during sinus rhythm (Figure 12.5a). Moderate increases in the heart rate with IGN stimulation caused little shift in the site of origin of the pacemaker at the sinus node (Figure 12.5b). Radiofrequency ablation of the ARGP markedly attenuated the ability of electrical stimulation to cause sinus acceleration, although the highest voltages were still able to cause a slight but significant increase in heart rate compared to control [40], indicative of postganglionic that bypass the IGN connection to the ARGP.

(b)

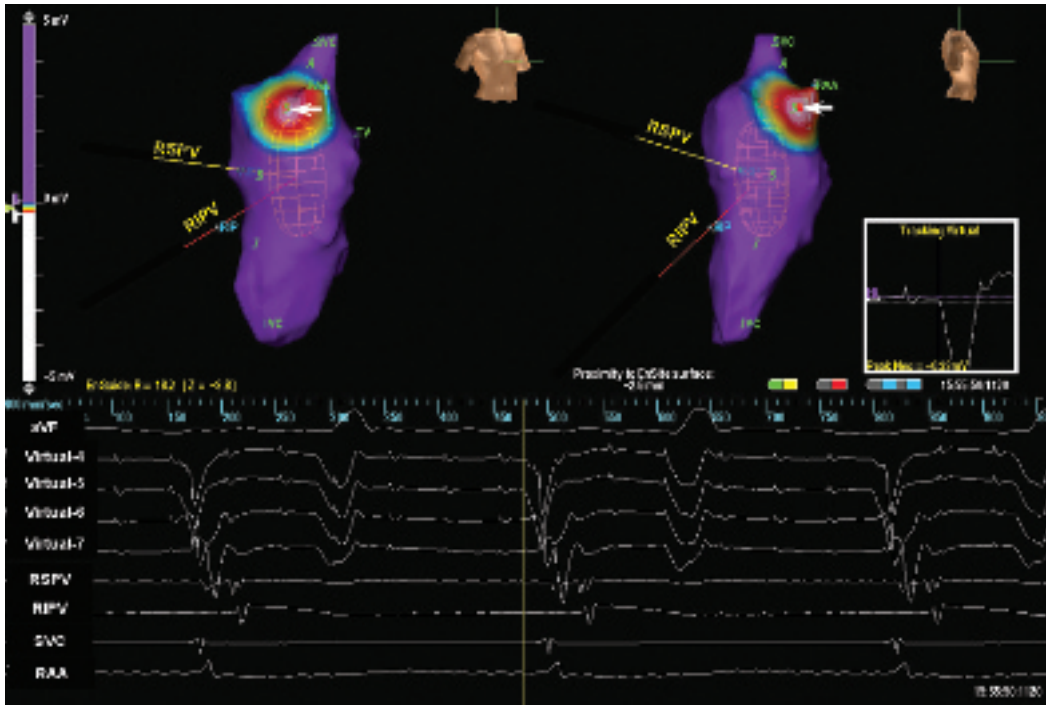

(c)

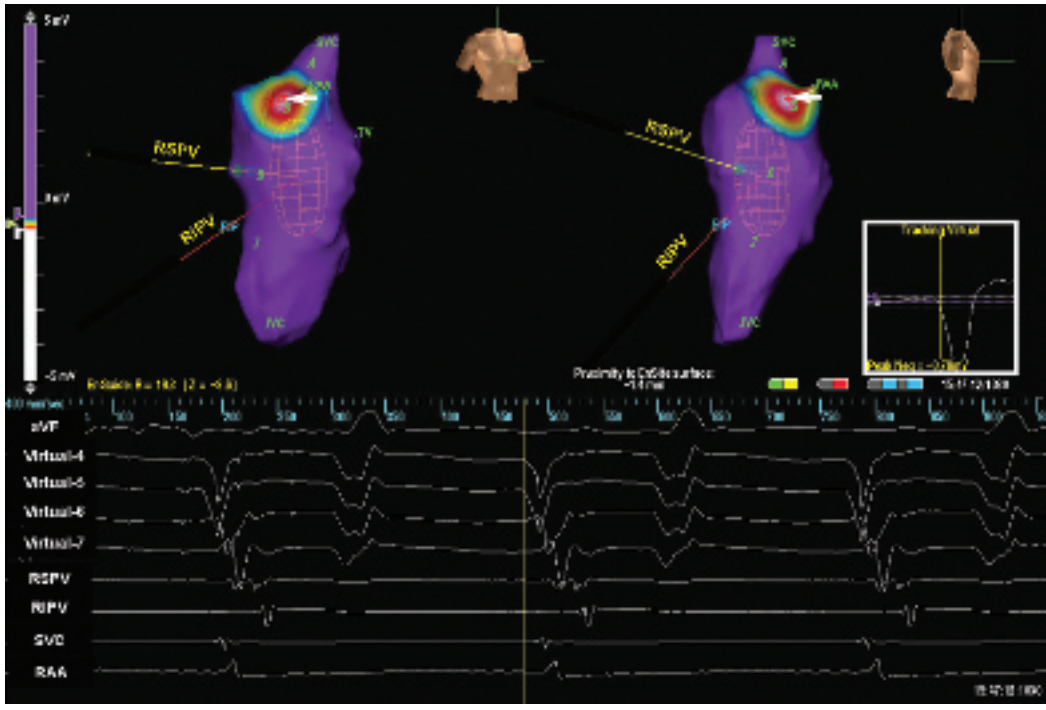

Figure 12.5 (*Continued*)

Other Experimental Models and Their Clinical Correlates

Studies from our laboratory have focused on other neurally based cardiac arrhythmias including focal atrial tachycardia (AT) [41] and right ventricular outflow tract tachycardia (RVOT-VT) [42]. In our experimental models, we used chemical and electrical means to activate GP or nerves of the intrinsic cardiac autonomic nervous system to induce the clinical characteristics of these arrhythmias. Specifically, the injection of atropine into the ARGP caused suppression of cholinergic activity, because electrical stimulation to the GP no longer slowed the heart rate or AV conduction; but higher voltages resulted in sustained AT ($\geq$5 min). Ice mapping allowed the localization of a focus mostly at the crista terminalis [41]. Clinically, the most likely right atrial sites for focal AT was shown to be the crista terminalis [43]. Similarly, we used electrical stimulation of sympathetic nerves at the proximal pulmonary artery to induce and beta blockade to suppress the characteristic ECG patterns of RVOT-VT [42]. Recent clinical reports [44, 45] have found the earliest ventricular activation in the proximal pulmonary artery, in patients with RVOT-VT. Furthermore, both in the experimental [42] and in the clinical studies [44, 45] an unusual electrical potential preceding the abnormal QRS complexes was reported.

Acknowledgments

This work was supported in part by Grant 0650077Z from the American Heart Association to Dr. Po; Grant K23HL069972 from the National Heart, Lung, and Blood Institute to Dr. Po; a grant from the Helen and Wil Webster Arrhythmia Research Fund of the University of Oklahoma Foundation to Dr. Scherlag; and support from St. Jude Medical, AF Division, Endocardial Solutions, Inc.

References

1 Amory DW, West TC. Chronotropic response following direct stimulation of the isolated sinoatrial node: a pharmacologic evaluation. *J Pharmacol Exp Therap* 1962; **137**: 14–23.

2 West TC, Toda N. Response of the A-V node of the rabbit to stimulation of intracardiac cholinergic nerves. *Circ Res* 1967; **20**: 18–31.

3 Lazzara R, Scherlag BJ, Robinson M J, Samet P. Selective in situ parasympathetic control of the canine sinoatrial and atrioventricular nodes. *Circ Res* 1973; **32**: 393–401.

4 Randall WC, Ardell JL, Wurster RD, et al. Vagal postganglionic innervation of the canine sinoatrial node. *J Auton Nerv System* 1987; **20**: 13–23.

5 Randall WC. *Neural Regulation of the Heart*. Oxford University Press, New York 1977: Chapter 2.

6 Randall WC. *Nervous Control of Cardiovascular Function*. Oxford University Press, New York, 1984: Chapter 3.

7 Armour JA, Murphy DA, Yuan B-X, et al. Gross and microscopic anatomy of the human intrinsic cardiac nervous system. *Anat Rec* 1997; **247**: 289–98.

8 Ardell JL. Structure and function of the mammalian intrinsic cardiac neurons, In: *Neurocardiology*. Armour JA, Ardell JL, eds. Oxford University Press, New York, 1944: Chapter 5.

9 Jais P, Haissaguerre M, Shah DC et al. A focal source of atrial fibrillation treated by discrete radiofrequency ablation. *Circulation* 1997; **95**: 572–76.

10 Haissaguerre M, Jais P, Shah DC et al. Spontaneous initiation of atrial fibrillation by ectopic beats originating in the pulmonary veins. *N Engl J Med* 1998; **339**: 659–66.

11 Pappone C, Oreto F, Rosario S et al. Atrial electroanatomical remodeling after circumferential radiofrequency pulmonary vein ablation: efficacy of an anatomic approach in a large cohort of patients with atrial fibrillation. *Circulation* 2001; **104**: 2539–44.

12 Verma A, Marrouche NF, Natale A. Pulmonary vein antrum isolation: intracardiac echocardiography-guided technique. *J Cardiovasc Electrophysiol* 2004; **15**: 1335–40.

13 Tsai CF, Tai CT, Hsieh MH, et al. Initiation of atrial fibrillation by ectopic beats originating from the superior vena cava: electrophysiological characteristics and results of radiofrequency ablation. *Circulation* 2000; **102**: 67–74.

14 Hwang C, Wu T-J, Doshi RN et al. Vein of Marshall cannulation for the analysis of electrical activity in patients with focal atrial fibrillation. *Circulation* 2000; **101**: 1503–5.

15 Chen SA, Tai CT, Yu WC et al. Right atrial focal atrial fibrillation: electrophysiologic characteristics and radiofrequency catheter ablation. *J Cardiovasc Electrophysiol* 1999; **10**: 328–35.

16 Patterson E, Po S, Scherlag BJ, Lazzara R. Triggered firing in pulmonary veins initiated by in vitro autonomic nerve stimulation. *Heart Rhythm* 2005; **2**: 624–31.

17 Scherlag BJ, Yamanashi WS, Patel U et al. Autonomically induced conversion of pulmonary vein focal firing into atrial fibrillation. *J Am Coll Cardiol* 2005; **45**: 1878–86.

18 Po SS, Scherlag BJ, Yamanashi WS, et al. Experimental model for paroxysmal atrial fibrillation arising at the

pulmonary vein–atrial junctions. *Heart Rhythm* 2006; **3**: 201–8.

19 Platt M, Mandapati R, Scherlag BJ, et al. Limiting the number and extent of radiofrequency applications to terminate atrial fibrillation and subsequently prevent its inducibility (abstract). *Heart Rhythm* 2004; **1**: S11.

20 Pappone C, Santinelli V, Manguso F, et al. Pulmonary vein denervation enhances long-term benefit after circumferential ablation for paroxysmal atrial fibrillation. *Circulation* 2004; **109**: 327–34.

21 Lemery R, Birnie D, Tang AS, Green M, Gollob M. Feasibility study of endocardial mapping of ganglionated plexuses during catheter ablation of atrial fibrillation. *Heart Rhythm* 2006; **3**: 387–96.

22 Yuan B-X, Ardell JL, Hopkins DA, et al. Gross and microscopic anatomy of the canine intrinsic cardiac neurons. *Anat Rec* 1994; **239**: 75–87.

23 Pauza DH, Skripka V, Pauziene N. Morphology of the intrinsic cardiac nervous system in the dog: a whole-mount study employing histochemical staining with acetyl cholinesterase. *Cells Tissues Organs* 2002; **1721**: 292–320.

24 Cooper TB, Hageman GR, James TN, Waldo AL. Neural effects on sinus rate and atrioventricular conduction produced by electrical stimulation from a transvenous electrode catheter in the canine right pulmonary artery. *Circ Res* 1980; **46**: 48–57.

25 Mick JD, Wurster RD, Duff M, Weber M, Randall WC, Randall DC. Epicardial sites for vagal mediation of sinoatrial function. *Am J Physiol* 1992; **262**: H1401–6.

26 Chiou CW, Eble JN, Zipes. Efferent vagal innervation of the canine atria and sinus and atrioventricular nodes. *Circulation* 1997; **95**: 2573–84.

27 Schauerte P, Scherlag BJ, Pitha J, et al. Catheter ablation of cardiac autonomic nerves for prevention of vagal atrial fibrillation. *Circulation* 200; **102**: 2774–80,

28 Ardell JL. Structure and function of the mammalian intrinsic cardiac neurons. In: *Neurocardiology*. Armour JA, Ardell JL, eds. Oxford University Press, New York, 1994: 96.

29 James TN. Combinatorial roles of the human intertruncal plexus in mediating both afferent and efferent autonomic neural traffic and in producing a cardiogenic hypertensive chemoreflex. *Prog Cardiovasc Dis* 2004; **46**: 539–72.

30 Tsai CF, Tai CT, Hsieh MH, et al. Initiation of atrial fibrillation by ectopic beats originating from the superior vena cava: electrophysiological characteristics and results of radiofrequency ablation. *Circulation* 2000; **102**: 67–74.

31 Hwang C, Wu TL, Doshi RN, et al. Vein of Marshall cannulation for the analysis of electrical activity in patients with focal atrial fibrillation. *Circulation* 2000; **101**: 1503–8.

32 Lin WS, Tai CT, Hsieh MH, et al. Catheter ablation of paroxysmal atrial fibrillation initiated by nonpulmonary vein ectopy. *Circulation* 2003; **125**: 3176–83.

33 Chen S-A, Tai CT, Yu WC, et al. Right atrial focal atrial fibrillation: electrophysiologic characteristics and radiofrequency catheter ablation. *J Cardiovasc Electrophysiol* 1999; **10**: 328–35.

34 Scherf D, Morgenbesser LJ, Nightingale EJ, Schaeffler KT. Further studies on the mechanisms of auricular fibrillation. *Proc Soc Exptl Biol NY* 1950; **73**: 650–54.

35 Zhou J, Scherlag BJ, Edwards J, Jackman WM, Lazzara R, Po SS. Gradients of atrial refractoriness and inducibility of atrial fibrillation due to stimulation of ganglionated plexi. *J Cardiovasc Electrophysiol* 2007; **18**: 83–90.

36 Shen WK, Low PA, Jahangir A, et al. Is sinus node modification appropriate for "inappropriate" sinus tachycardia with features of postural orthostatic syndrome? *PACE* 2001; **24**: 217–30.

37 Scherlag BJ, Yamanashi WS, Amin R, Lazzara R, Jackman WM. Experimental model of inappropriate sinus tachycardia: Initiation and ablation. *J Intervent Cardiac Electrophysiol* 2005; **13**: 21–9.

38 Taketani T, Wolf RK, Garrett JV. Partial cardiac denervation and sinus node modification for inappropriate sinus tachycardia. *Ann Thorac Surg* 2007; **84**: 652–54

39 Randall WC. *Neural Regulation of the Heart*. Oxford University Press, New York, 1977: Chapter 2, pp. 22 and 30.

40 Zhou J, Scherlag BJ, Yamanashi WS, Po SS, Jackman WM, Lazzara R. Anatomy and physiology of the right interganglionic nerve: implications for the treatment of inappropriate sinus tachycardia. *Circulation* 2006; **112**: II–189 (abstract).

41 Lin J, Scherlag BJ, Hou Y-L, Zhang Y, Lazzara R, Po SS. Focal atrial tachycardia mediated by activation of ganglionated plexi. *J Cardiovasc Electrophysiol* 2007; **18**: 129 (abstract).

42 Zhou J, Scherlag BJ, Yamanashi W, et al. Experimental model simulating right ventricular outflow tract tachycardia: a novel technique to initiate RVOT-VT. *J Cardiovasc Electrophysiol* 2006; **17**: 771–75.

43 Kistler PM, Roberts-Thomson KC, Haqqani HM, et al. P-wave morphology in focal atrial tachycardia: development of an algorithm to predict the anatomic site of origin. *J Am Coll Cardiol* 2006; **48**: 1010–17.

44 Timmermans C, Rodriguez L, Medeiros A, Crijns H, Wellens HJJ. Radiofrequency catheter ablation of idiopathic ventricular tachycardia originating in the main stem of the pulmonary artery. *J Cardiovasc Electrophysiol* 2002; **13**: 281–84.

45 Whitwam W, Rule S, Narayan SM. Noncontact mapping of small pulmonary artery potentials preceding ectopy from right ventricular outflow tract. *Heart Rhythm* 2007; **4**: 959–63.

13

CHAPTER 13

Electrophysiological Mapping of the Right and Left Ventricle in Animals

Jacques MT de Bakker, PhD,[1] *Jérôme GM Jungschleger*, MD,[2] *Marc A. Vos*, PhD[1]

[1]University Medical Center, Utrecht, The Netherlands
[2]Maastricht University, Maastricht, The Netherlands

Summary

Due to differences in structure and ion channel composition between the right (RV) and left (LV) ventricle, electrophysiological characteristics of the two ventricles differ. Still, conduction parameters are not that different, and repolarization appears equal for the two ventricles. Only under pathological circumstances, when conduction and repolarization are challenged to the limit, do the intrinsic differences become evident and possibly result in ventricular arrhythmias. Structural factors that influence these properties are: (i) fiber direction, (ii) wall thickness, and (iii) cell size. Transmural and apico-basal gradients for ion channel expression have been described for RV and LV. In addition, interventricular differences in ion channel expression exist.

I_{TO1} and I_{Kr} densities are significantly higher in cells isolated from RV than LV, resulting in shorter action potentials and more outspoken spike and dome characteristics of action potentials of RV myocytes. In addition, pathology may result in an asymmetric down-regulation of ion channels. In the chronic AV block dog down-regulation of I_{Kr} occurs in both ventricles, but I_{Kr} was only significantly reduced in RV. Several clinical and experimental studies suggest that RV has the weakest conduction reserve, whereas LV has a more sensitive repolarization reserve. Animal models with global alterations in only one electrophysiological parameter (decreased connexin or sodium channel expression) indeed show that the alteration affects conduction in RV more than in LV. Only under such limited pathological circumstances does it become possible to quantify these differences between RV and LV by mapping and, more importantly, relate them to arrhythmogenesis.

Cardiac Mapping, Third Edition Edited by Mohammad Shenasa, Gerhard Hindricks, Martin Borggrefe, and Günter Breithardt
 ISBN: 978-1-405-17572-2

Introduction

At first glance, conduction and repolarization parameters do not differ between RV and LV in

normal, nonremodeled, hearts. Still, RV and LV show considerable differences in structural and electrical characteristics. Functionally, these differences can lead to ventricular arrhythmias, but only under pathological circumstances do they become manifest. The epicardial activation pattern of the right (RV) and left (LV) ventricle shows an elliptical configuration in case the ventricle is paced from the center of an epicardial recording grid. This pattern is caused by the anisotropic nature of the ventricles and allows determination of conduction velocity parallel and perpendicular to the fiber direction. Although the elliptical axis differs between RV and LV, conduction velocity in longitudinal and transverse direction is similar in both ventricles. It suggests that the electrophysiological parameters that determine conduction velocity are comparable in LV and RV.

This is the case during normal propagation in the healthy heart, but differences may arise between both ventricles in case of cardiac disease or abnormal activation. An inherited cardiac disease such as Brugada syndrome, which is suggested to be caused by a sodium channel mutation, and arrhythmogenic right ventricular dysplasia (ARVD), which involves a desmosomal mutation, are expected to effect RV and LV in the same way. However, they appear to be predominantly a right ventricular disease and cardiac arrhythmias preferentially occur in the right ventricle.

In addition, it has been shown that LV and RV do differ in regard to ion channel properties that govern cardiac repolarization. In regard to repolarization reserve and arrhythmogenic susceptibility the LV seems more vulnerable to repolarization-related ventricular tachycardias, including drug-induced torsade de pointes. Also, with regard to ventricular fibrillation (VF), differences exist between RV and LV. This arrhythmia has been shown to be more complex in LV than in RV.

These observations suggest that there are electrophysiological differences between the two ventricles that are preferentially manifested when the heart is challenged. In this chapter the structural and electrical differences between RV and LV will be outlined as obtained from mapping studies and the electrophysiological and arrhythmogenic consequences will be discussed.

Structural Differences Between RV and LV

Fiber Orientation and Cell-to-Cell Coupling

Fiber orientation plays an important role in propagation of the electrical impulse and is responsible for the difference in conduction velocity parallel and perpendicular to the fiber direction. Anisotropy results from the spatial alignment of elongated cardiomyocytes and the preferential sites where cell-to-cell coupling arises. Isotropic myocardium results in circular activation patterns if stimulation is performed from the center of the recording area. This was nicely demonstrated by Bursac and co-workers, who used cardiomyocyte cultures with controlled anisotropy [1]. Control of anisotropy was obtained by growing cells on micro-abrading PVC cover slips. Activation patterns were circular if cells were cultured on untreated cover slips and myocytes were randomly oriented. Patterns became elliptical if the cell cultures were grown on micro-abraded cover slips. Coarser structures (wider and deeper abrasion grooves) increased the eccentricity of the ellipse. Conduction velocity in longitudinal direction increased with eccentricity, whereas transverse conduction decreased.

In the same study the investigators used the micro-abrasion technique to produce monolayers with sharp but continuous changes in fiber direction. Sites with a sudden change in fiber direction have been shown to favor conduction block [2]. Disruption of myocyte orientation giving rise to myocardial disarray occurs in hypertrophic cardiomyopathy (HCM) [3]. This disruption of the normal alignment of myocardial cells is only found sporadically in the other types of heart disease. In HCM, focal and widespread interstitial fibrosis are present as well, whereas the distribution pattern of gap junctions exhibiting connexin 43 are randomly distributed rather than being confined to intercalated discs. Lateralization of connexins occurs between adjacent myocytes. In addition, the gap junction surface area was reduced despite a normal number of intercellular contact points. HCM is the most common cause of sudden cardiac death (SCD) in healthy young individuals. Fiber disarray, disorientation of connexins, increased fibrosis, and reduced

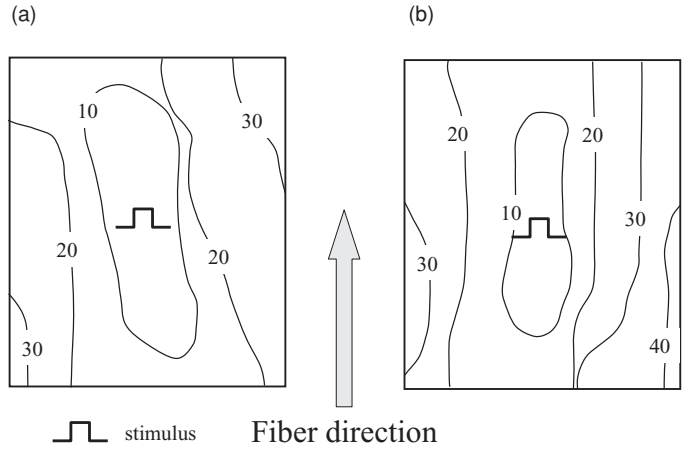

Figure 13.1 Epicardial activation pattern before (a) and after (b) freezing of the subendocardial and intramural layers of the left ventricular wall. Maps show an elliptical pattern with fast conduction parallel and slow conduction perpendicular to the fiber direction. Longitudinal conduction was similar before and after freezing. Transverse conduction times were, however, significantly prolonged after freezing. Lines are isochrones at intervals of 10 msec. Numbers indicate activation times in milliseconds. (Adapted from Schalij MJ, Anisotropic conduction and ventricular tachycardia, Thesis, Elinkwijk, Utrecht, page 52.)

excitability all favor conduction delay and form an electrically unstable myocardial substrate supporting the occurrence of arrhythmias.

In the heart, the effect of fiber direction is further complicated by rotation of fibers from epicardium to endocardium. A gradual counterclockwise rotation of fibers occurs and range from 120 degrees in the dog to 180 degrees in the pig [4, 5]. Using transmural electrodes, Frazier and co-workers determined activation patterns in planes of recording electrodes parallel to the epicardium and endocardium during stimulation from the epicardial center of the electrode grid [6]. Activation patterns were elliptical in each plane.

The ellipses rotated with respect to each other, but the twist of the long axis of the ellipses was less than that of the corresponding transmural rotation of the fibers. This was caused by the fact that in deeper layers activation will run faster in a direction that is transverse at the epicardium. This implies that rotation of fibers with depth affects the epicardial activation pattern and that thickness and degree of rotation can affect determination of conduction velocity from epicardial activation patterns. This was demonstrated in a study by Schalij and co-workers, who reduced the wall thickness of the left ventricle of a rabbit heart using a cryo procedure [7]. Langendorff-perfused rabbit hearts were immersed in a tissue bath containing perfusion fluid of 30°C. A cryo probe with liquid nitrogen was inserted into the left ventricular cavity, and coronary circulation was interrupted while the heart was frozen for 7 min. After this period, coronary circulation was restored. In this way the endocardial and intramural parts of the left ventricular free wall and the interventricular septum were destroyed. Only a thin left ventricular epicardial layer about 1 mm thick remained. The epicardium was stimulated from the center of the mapping electrode consisting of a 13 × 15 grid with an interelectrode distances of 1 mm.

Propagation along the epicardial fiber axis was not affected by the cryo procedure and activation times of electrograms in longitudinal direction were unaltered. In contrast, activation times in the transverse direction were significantly prolonged (Figure 13.1). The initial transverse epicardial wave front is interrupted after about 3–4 mm by epicardial breakthrough of deeper longitudinal running wave fronts. The "shortcut" effect of activation running in deeper layers was absent after freezing. Fiber rotation may therefore lead to an overestimation of the transverse conduction velocity if determined from epicardial activation maps. At distances greater than 3 mm local differences in transverse conduction

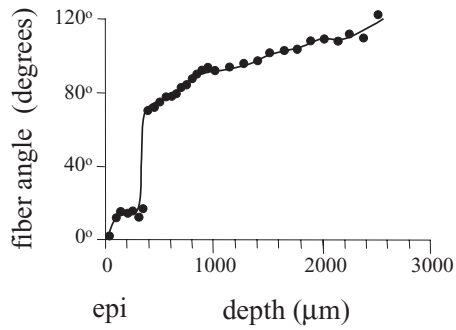

Figure 13.2 Rotation of the fiber direction with depth from epicardium (epi, zero degrees) in the right ventricle of a swine heart. (Adapted from Vetter et al., *Circ Res* 2005; 96: 244–51.)

times were significantly shorter in control hearts compared to frozen hearts. In the same study the authors showed that freezing and hence wall thickness did not affect the epicardial refractory period. The maximal pacing rate was also not affected by the freezing procedure.

Vetter and co-workers reported that in the subepicardium of the right ventricle of the swine, an abrupt [8] change of 64 degrees in fiber angle was observed at a mean depth of 500 μm underneath the epicardium (ranging from 110 to 928 μm) (Figure 13.2). The depth at which the abrupt change in fiber direction occurred had a profound effect on the epicardial activation pattern during epicardial stimulation. In preparations where the depth of transition was small (110 μm) and magnitude of transition large (72 degrees), the pattern was diamond-shaped. Rectangular activation patterns were associated with intermediate values of depth and magnitude, whereas the classical elliptical pattern occurred at largest depth and small magnitude of transition (900 μm and 50 degrees, respectively). Most often, the rectangular pattern was observed.

Observations made by Streeter and Bassett showed that qualitatively similar patterns with sudden fiber rotation were observed in LV of swine hearts [4]. Both ventricles have a subepicardial layer with virtually no fiber rotation followed by a region of rapid fiber rotation. Then a region with constant rotation per millimeter occurs. Close to the endocardium the value of rotation increases. Because of the larger wall thickness of LV the maximal rate of fiber rotation is significantly less in LV than in RV. As a consequence of this geometric scaling the diamond- and rectangular-shaped patterns on the epicardium of LV are less likely during epicardial stimulation. There are indications that also in other species a thin outer layer with significantly different fiber orientation exists [9, 10].

Ventricular Wall Thickness

Wall thickness is supposed to affect abnormal rhythms such as VF. Rogers and co-workers proposed that increased ventricular wall thickness destabilizes VF wave fronts and therefore is an important determinant of VF activation patterns [11]. They determined epicardial activation simultaneously from RV and LV in open chest pigs. Each electrode array contained 504 unipolar electrode terminals (arranged in a 21 × 24 grid) at interelectrode distances of 2 mm. Activation maps showed that VF was more organized in RV than LV and contained fewer and larger wave fronts. In RV activation fronts followed fewer distinct pathways and fragmented or collided less frequently with other wave fronts compared to LV. The size and cycle length of reentrant circuits were similar in the two ventricles, but RV reentry persisted for more cycles. These results could not be attributed to the differences in electrophysiologic properties between LV and RV. The authors concluded that the geometry of the ventricular wall, particularly wall thickness, is an important determinant of VF activation patterns.

However, other studies suggest that fiber direction is at least as important in determining complexity of VF activation patterns and continuation of VF. Ikeda et al. hypothesized that the structural complexity of septal tissue influences the maintenance of reentrant wavelets in the ventricle [12]. Endocardial activation patterns were determined during VF in isolated perfused canine RV free wall, the interventricular septum, and the LV free wall. Each tissue sample was cut progressively to reduce tissue mass until VF terminated. More wavelets were seen during VF in the septa than in the RV and LV free walls. Furthermore, VF cycle length was shorter in the septa than in the RV and LV free walls.

At reduced tissue mass, VF became successively more organized in all regions. Immobile solitary and "figure-of-eight" reentrant wavelets were often observed after tissue mass reduction in the RV free walls but rarely in LV free walls. In contrast, such fixed circuits were not observed in the septa. The

amount of tissue required to maintain VF in the septa was much less than in the RV and LV free walls. Anatomic and histologic examinations indicated that the tissue structure of the septa is more complex than that of the RV and LV free walls. Thus, the authors concluded that the structural complexity of tissue is important for the maintenance of VF.

Cell Size of RV and LV

Although cell-to-cell coupling and excitability are major parameters for determining conduction velocity, tissue architecture including cell size and morphology play an important role as well. During cardiac pathology these parameters for conduction are usually all remodeled. Therefore it is difficult to estimate the effect of cell size, gap junction expression/distribution, and excitability separately on conduction in an experimental setting.

Spach et al. have used computer models to address the role of cell size on transverse and longitudinal conduction [13]. These simulations suggested that cell size may be as important as gap junction expression and distribution. Because in pathology the effects of changed cell size and cell-to-cell coupling on conduction may strengthen or weaken each other, both an increase or decrease in conduction velocity may result. In animal studies unchanged as well as decreased and increased conduction velocities have been reported in the setting of heart failure [14–16]. In addition, time aspect of remodeling may play a role. For instance, in a guinea pig model of heart failure conduction velocity was decreased at day 50 after aortic banding, but was increased at day 150 [17]. Different types of remodeling for the various models and the dynamic behavior in time may explain the differences in remodelling-induced conduction velocity changes.

In rats and hamsters, myocytes from the RV had smaller cell volume and cross-sectional area values compared to any region of the LV [18]. A transmural gradient of cellular dimensions existed in the LV of the rat, but not in hamster, with cell size differences of endocardium being the largest and epicardium the smallest. Endocardial volume and the cross-sectional area of cells were larger than at all other regions in the hamster heart, but the difference was not significant compared to the epicardial cell volume. In the guinea pig, no significant differences in cell volume existed between RV and LV or between the three LV regions. No pattern of regional differences was seen between ventricular cross sectional area values in the guinea pig.

In the study by Shimada, cell length and width of RV were shorter than of LV, but the difference was not significant [19]. Only after aorta constriction did differences become statistically significant (cell length 139.2 ± 1.2 vs. 130.2 ± 1.2 μm, cell width 40.9 ± 0.6 vs. 31.4 ± 0.5 μm). In mouse hearts measurement of cell size showed that myocytes originating from the RV have a smaller cross-sectional area than those originating in the LV. Aging of mice resulted in a significant decrease in cell size in the aged ventricles compared to the young ones and this difference is also present between the aged right and left ventricle [20].

Volders and co-workers determined myocardial cell size in chronic AV block dog hearts and controls. They compared myocytes from RV free wall and LV mid-myocardium [21]. In control hearts, RV myocytes were of equal length and width compared to left mid-myocardial myocytes. In chronic AV block (AVB) hearts, myocytes from both RV and LV were significantly longer than in control hearts. Additionally, a significant difference in cell length of right versus left ventricle in chronic AVB hearts occurred. In contrast, the width of myocardial cells from chronic AVB dogs was not different from the control hearts.

Functional Differences Between RV and LV

Electrophysiological Composition of RV and LV in Normal Hearts

Heterogeneity in electrophysiological parameters plays an important role in arrhythmogenicity. Both dispersion in refractoriness and conduction have been shown to favor reentrant arrhythmias [22–24]. Differences in the refractory period between adjacent areas may block conduction of a premature impulse in the region with the longest refractory period, while continuing in regions with short refractory periods. Under normal conditions, the differences between longest and shortest refractory period and/or action potential duration in the ventricles is in the order of 40 msec. The intrinsic electrical heterogeneities in ventricular myocardium are responsible for the dispersion in repolarization.

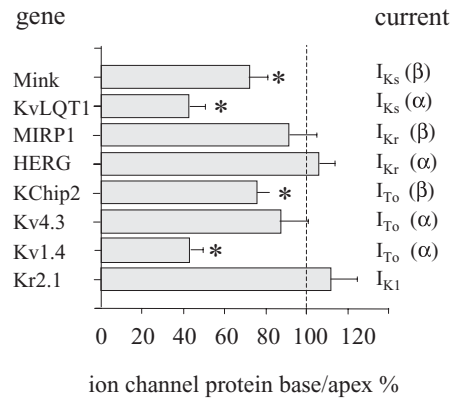

Figure 13.3 Basal-apical gradient of potassium channels in the dog heart. (Adapted from Szentadrassy et al., *Cardiovasc Res* 2005; 65: 851–60.)

Both transmural and apico-basal gradients have been observed in the heart. The transmural gradient arises because the different cell types involved—epicardial, mid-myocardial and endocardial myocytes—reveal differences in the expression of the various potassium currents. These differences have been described for LV by the group of Antzelevitch [25].

Although the transmural gradient has gained much attention, there is also an apico-basal gradient of ion channels in LV, which probably plays an equal or even more important role in arrhythmogenicity. Studies in the mouse, dog, and human hearts show that the action potential duration at the base is longer compared to the apex. Szentadrassy and co-workers showed that in basal cells of LV, Kv1.4 (encoding the α-subunit of the ion channel for I_{TO}), and KvLQT1 (encoding the α-subunit for the ion channel for I_{KS}) are expressed to only 40% of the amount expressed in apical cells (Figure 13.3) [26].

Double transgenic mice, lacking both the fast and slow component of the transient outward current have action potential prolongation and spontaneous ventricular arrhythmias [27]. Conduction velocity did not differ from control hearts, but action potential duration was prolonged and dispersion of refractoriness between apex and base of LV was enhanced compared to the control hearts. A single premature pulse elicited a reentrant ventricular tachycardia. In the I_{TO} knock out mice, reentrant arrhythmias were induced due to enhanced dispersion of repolarization.

Electrophysiological Heterogeneities

The role of APD heterogeneities as a substrate for unidirectional block and reentry has been supported by simulation studies from Viswanathan and Rudy [28]. In hypertrophied and failing myocardium the inherent differences may be enhanced by changes in density, distribution or properties of the potassium currents [29–30].

Other studies have shown that in the healthy heart heterogeneous expression of repolarizing voltage-gated potassium currents is not limited to the left ventricle, but that interventricular differences exist as well. Whole-cell voltage-clamp recordings showed that mean peak I_{TO1} densities are significantly higher in cells isolated from mouse RV than LV [31]. In contrast, the densities of $I_{K,slow}$ and I_{ss} in murine RV, LV apex, and LV base cells are not significantly different.

Myocardial cells isolated from RV and LV mid-myocardium of the canine heart revealed that I_{TO1} density was significantly larger in RV than LV, while steady-state inactivation and rate of recovery were similar [32]. I_{Ks} currents were considerable larger in RV, but I_{Kr} and I_{K1} were not different. The higher values of I_{TO1} and I_{Ks} may well explain the shorter action potentials in RV compared to LV. The differences in expression of I_{TO1} and I_{Ks} corresponded with the observed different expression levels in the right ventricle (RV) and left ventricular (LV) free wall of KChIP2 and KCNQ1, respectively [33].

Also sodium channels seem to be distributed heterogeneously throughout the heart. Cardiomyocytes isolated from subendocardial and subepicardial layers of the rat heart show that a transmural gradient of sodium current is present in the left ventricle [34]. Sodium current in the LV subendocardium was significantly larger than at the subepicardium (-49.7 ± 2.5 pA/pF vs. -32.9 ± 3.2 pA/pF). The sodium current in RV was similar to that of that at the left subendocardium of LV (-49.7 ± 3.7 pA/pF). Functional studies on the consequence of this difference have to be performed.

Different Repolarization Reserve Between RV and LV in the Pathological Conditioned Chronic AV Block Dog Heart

The dog with chronic AV block (AVB) is an animal model of acquired torsade de pointes (TdP).

Clinical and experimental studies suggest that action potential prolongation and/or increased regional dispersion of repolarization are underlying factors for the arrhythmia. Analysis of potassium currents in both RV and LV revealed that a significant down regulation of the delayed rectifier current I_{Ks} occurred in both ventricles. I_{Kr} was only significantly reduced in RV. I_{TO1} and I_{K1} were not different between chronic AVB and control [32].

Schreiner and co-workers studied the mechanism of polymorphic ventricular tachycardia in chronic AVB dog after exposure to almokalant [35]. Recordings were made with 240 needles each containing four electrode terminals at interelectrode distances of 2.5 mm. The needle electrodes were evenly distributed over the left and right ventricular wall. Mapping studies were carried out in vivo at day 5 (acute AVB) or day 62 (chronic AVB) following AV nodal ablation. Application of almokalant did not result in arrhythmias in acute AV block animals, but resulted in tachycardias in 9 out of 14 chronic AVB dogs.

Arrhythmias originated predominantly from an LV endocardial focus. Centrifugal spread of activation, suggestive for a focal origin, was also observed in consecutive beats of the arrhythmias. Reentry was observed in two episodes only. In the chronic AVB dog a significant increase in effective refractory period (280 $\pm$ 28 msec vs. 260 $\pm$ 37 msec) and QT interval (339 $\pm$ 16 vs. 288 $\pm$ 12 msec) occurred. Dispersion of an effective refractory period was similar for acute and chronic AV block. Thus, the authors concluded that the arrhythmias in this model were primarily linked to prolonged repolarization.

QT prolongation and a high incidence of spontaneous TdP were also observed in a rabbit heart with chronic AV block [36]. QT prolongation in AV block rabbits was caused by action potential duration increase. This was related to down regulation of both I_{Kr} and I_{Ks} in association with altered $I_{Ca,L}$ activation kinetics.

In a study carried out in our lab on chronic AV block dogs, characteristics of TdP arrhythmias were similar to those found in the study of Schreiner et al. [35]. During Ibutilide induced TdP, premature activation originated from an endocardial focus. Consecutive beats continued to reveal centrifugal activation patterns in the majority of the cases, but the origin shifted if morphology changed. Reentrant activation was found only sporadically.

An example of TdP is illustrated in Figure 13.4. Panel A shows surface electrograms of short runs of ectopic beats of which the one marked by the red rectangle reveals the characteristic ECG feature of TdP. The first ectopic complex, which has a negative deflection in lead II, arises from the subendocardium of the mid/apical free wall (panel B). Latest activation occurs 100 msec later at the antero-septal wall.

The sixth complex has turned to a positive deflection and arises from the septal region. More recently, similar results (LV predisposition) have been reported in a canine model of long-QT1, in which pharmacological block of I_{Kr} (HMR 1556) in combination with β-adrenergic stimulation (isoprenalin) led to EAD in LV but not in RV [37].

Results obtained from a mapping study carried out in an anthopleurin-A canine model of LQTS yielded another mechanism for TdP [38]. In this study by El-Sherif and co-workers, needle electrodes were used to record intramural electrograms to construct activation maps. In 26 episodes of nonsustained TdP, VT activation maps were constructed during QRS-axis transitions in the surface ECG leads. The first beat of all VTs arose at the subendocardium by focal activity. Subsequent beats, however, proved to be caused by reentrant excitation in the form of rotating scrolls and VT ended when reentrant excitation was terminated.

The common mechanism for initiation or termination of bifurcation was the development of functional conduction block between the anterior or posterior right ventricle free wall and the ventricular septum. Recently, we have introduced an electrical marker that may be indicative for repolarization reserve [39]. This arrhythmic parameter "beat-to-beat variability of repolarization" did increase in LV but not in RV prior to drug-induced TdP. This suggests that the LV subendocardium has the weakest repolarization reserve and is the location for EAD dependent TdP.

Different Conduction Reserve Between RV and LV in Mice Hearts with Reduced Connexin43 or SCN5A Expression

Clinical studies suggest that global alterations in electrophysiological parameters may affect RV more

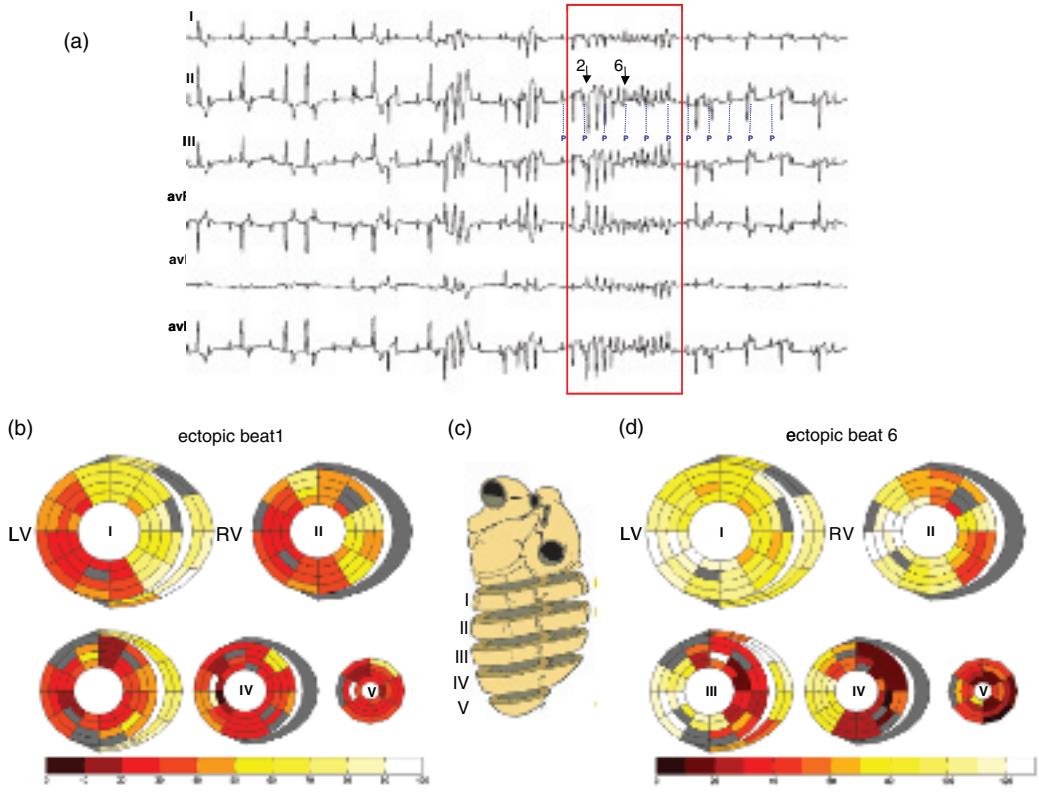

Figure 13.4 (Panel a) Surface ECG of Ibutilide-induced runs of ectopic beats in a chronic AV-block dog. The red rectangle marks a mapped short run of TdP. (Panel b) Activation patterns of the first beat of TdP at five different cross-sections of the heart (panel c). Earliest activation arises subendocardially in the IV slice. (Panel d) Activation patterns of the sixth beat of TdP at five different cross-sections of the heart. Earliest activation arises subendocardially in the septal area. Note that the electrograms of beats 2 and 6 have opposite deflection.

than LV. Brugada syndrome, which is supposed to be a sodium channel mutation, may give rise to cardiac arrhythmias that preferentially originate from RV [40]. Arrhythmogenic right ventricular dysplasia, which seems to be related to a desmosomal mutation and affects ventricular myocytes from both RV and LV, also induces arrhythmias that preferentially arise in RV [41].

We studied the effect of mutation on activation in RV and LV in conditional Cx43 knockout and heterozygous SCN5A mice [42, 43]. Activation maps and conduction parameters were compared between wild-type and mutated animals. Epicardial mapping of RV and LV of isolated, Langendorff-perfused murine hearts from wild-type animals showed similar, elliptical activation patterns. The long axis of the ellipse has a different direction for LV and RV because of the different fiber direction.

Conduction velocity determined from the activation maps was similar for LV and RV both, in both transverse and longitudinal directions. There was, however a difference in the refractory period, which was shorter in RV than in LV, albeit not significant (54.6 ± 1.9 vs. 71.4 ± 4.04. In the connexin 43 knockout (KO) mice differences between RV and LV activation maps were present (Figure 13.5).

Longitudinal (CV_{long}) and transversal (CV_{trans}) conduction velocity was significantly reduced in RV of the Cx43 knock out mice compared to control (38.0 ± 1.5 vs. 31.6 ± 1.7 and 24.4 ± 2.4 vs. 10.1 ± 1.1, respectively). In LV, however, CV_{long} was not different between KO mice and controls; only for CV_{trans} did the conduction velocity reduce from 16.8 ± 1.5 to 11.3 ± 1.4 cm/sec. In the heterozygous SCN5A mice the conduction velocity was only reduced in RV. In LV, both CV_{long} and CV_{trans}

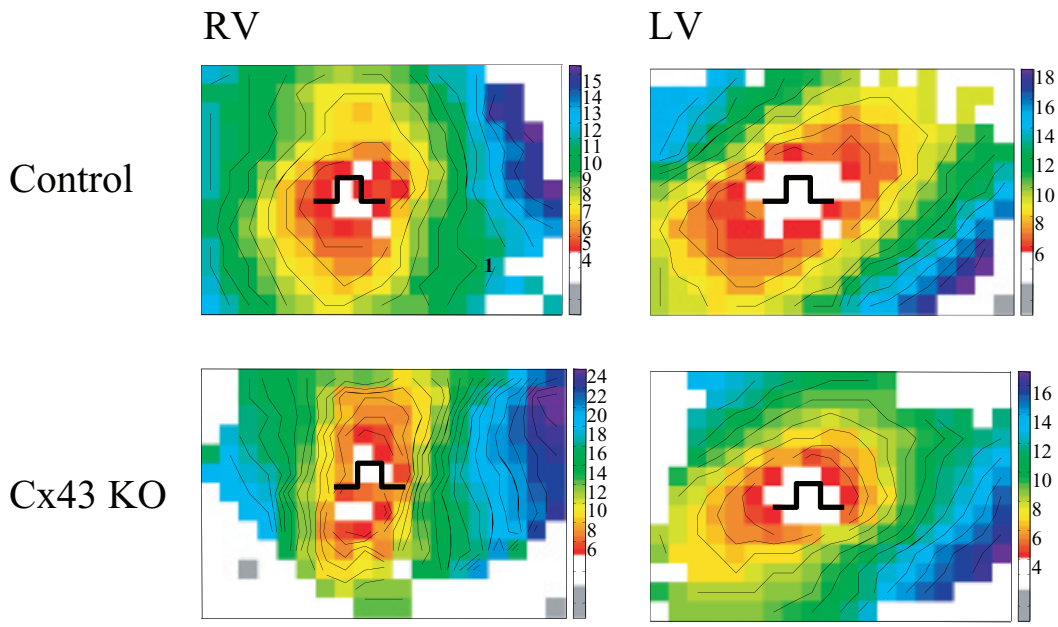

Figure 13.5 Epicardial activation maps of RV and LV of a wild-type (upper panels) and a Cx43 knock out (lower panels). The knock out mouse revealed 10% Cx43 expression compared to the wild-type mouse heart. Reduced Cx43 expression reveals crowding of isochrones in RV only, indicating reduced conduction velocity in RV.

were not changed in the SCN5A heterozygous mice. Similar results were obtained in an SCN5A mutant mouse carrying the equivalent mutation of human *SCN5A*-1795insD [44].

The experimental observations, outlined earlier, indicate that there are various differences between RV and LV, both structural and functional, which affect electrophysiological characteristics of the ventricles in a different way. Conduction reserve in RV appears to be less compared to LV, whereas LV has more sensitive repolarization reserve. Although the differences are small under normal conditions, they may be greatly enhanced if the heart is challenged by abnormal activation or cardiac disease.

References

1 Bursac N, Parker KK, Iravanian S, Tung L. Cardiomyocyte cultures with controlled macroscopic anisotropy: a model for functional electrophysiological studies of cardiac muscle. *Circ Res* 2002; **91**: e45–54.

2 Spach MS, Miller WT 3rd, Dolber PC, Kootsey JM, Sommer JR, Mosher CE Jr. The functional role of structural complexities in the propagation of depolarization in the atrium of the dog: cardiac conduction disturbances due to discontinuities of effective axial resistivity. *Circ Res* 1982; **50**: 175–91.

3 Varnava AM, Elliott PM, Sharma S, McKenna WJ, Davies MJ. Hypertrophic cardiomyopathy: the interrelation of disarray, fibrosis, and small vessel disease. *Heart* 2000; **84**: 476–82.

4 Streeter DD. Gross morphology and fiber geometry of the heart. In: Berne RM, ed. *Handbook of Physiology*, Section 2: The Cardiovascular System. American Physiological Society, Bethesda, MD, 1979.

5 Streeter DD Jr, Spotnitz HM, Patel DP, Ross J Jr, Sonnenblick EH. Fiber orientation in the canine left ventricle during diastole and systole. *Circ Res* 1969; **24** :339–47.

6 Frazier DW, Krassowska W, Chen PS, et al. Transmural activations and stimulus potentials in three-dimensional anisotropic canine myocardium. *Circ Res* 1988; **63**: 135–46.

7 Schalij MJ, Lammers WJ, Rensma PL, Allessie MA. Anisotropic conduction and reentry in perfused epicardium of rabbit left ventricle. *Am J Physiol* 1992; **263**: H1466–78.

8 Vetter FJ, Simons SB, Mironov S, Hyatt CJ, Pertsov AM. Epicardial fiber organization in swine right ventricle and its impact on propagation. *Circ Res* 2005; **96**: 244–51.

9 Thomas CE. The muscular architecture of the ventricles of hog and dog hearts. *Am J Anatomy* 1957; **101**: 17–57.

10 Drouin E, Charpentier F, Gauthier C, Laurent K, Le Marec H. Electrophysiologic characteristics of cells spanning the left ventricular wall of human heart: evidence for presence of M cells. *J Am Coll Cardiol* 1995; **26**: 185–92.
11 Rogers JM, Huang J, Pedoto RW, Walker RG, Smith WM, Ideker RE. Fibrillation is more complex in the left ventricle than in the right ventricle. *J Cardiovasc Electrophysiol* 2000; **11**: 1364–71.
12 Ikeda T, Kawase A, Nakazawa K, et al. Role of structural complexities of septal tissue in maintaining ventricular fibrillation in isolated, perfused canine ventricle. *J Cardiovasc Electrophysiol* 2001; **12**: 66–75.
13 Spach MS, Heidlage FJ, Barr, RC, Dolber PC. Cell size and communication: role in structural and electrical development and remodeling of the heart. *Heart Rhythm* 2004; **4**: 500–15.
14 Zhu WX, Johnson SB, Brandt R, Burnett J, Packer DL. Impact of volume loading and load reduction on ventricular refractoriness and conduction properties in canine congestive heart failure. *J Am Coll Cardiol* 1997; **30**: 825–33.
15 Laurita KR, Chuck ET, Yang T, et al. Optical mapping reveals conduction slowing and impulse block in iron-overload cardiomyopathy. *J Lab Clin Med* 2003; **142**: 83–9.
16 Wiegerinck RF, Verkerk AO, Belterman CN, et al. Larger cell size in rabbits with heart failure increases myocardial conduction velocity and QRS duration. *Circulation* 2006; **113**: 806–13.
17 Cooklin M, Wallis WR, Sheridan DJ, Fry CH. Conduction velocity and gap junction resistance in hypertrophied, hypoxic guinea-pig left ventricular myocardium. *Exp Physiol* 1998; **83**: 763–70.
18 Campbell SE, Gerdes AM, Smith TD. Comparison of regional differences in cardiac myocyte dimensions in rats, hamsters, and guinea pigs. *Anat. Rec* 1987; **219**: 53–9.
19 Shimada Y, Gunasegaram S, Yokoyama H, Avkiran M, Inhibition of angiotensin-converting enzyme reduces susceptibility of hypertrophied rat myocardium to ventricular fibrillation. *Circ J* 2002; **66**: 1045–53
20 Lim CC, Apstein CS, Colucci WS, Liao R.Impaired cell shortening and relengthening with increased pacing frequency are intrinsic to the senescent mouse cardiomyocyte. *J Mol Cell Cardiol* 2000; **32**: 2075–82.
21 Volders PG, Sipido KR, Vos MA, Kulcsar A, Verduyn SC, Wellens HJ. Cellular basis of biventricular hypertrophy and arrhythmogenesis in dogs with chronic complete atrioventricular block and acquired torsade de pointes. *Circulation* 1998; **98**: 1136–47.
22 Wolk R, Kane KA, Cobbe SM, Hicks MN. Apex-to-base dispersion of refractoriness underlies the proarrhythmic effect of hypokalaemia/hypomagnesaemia in the rabbit heart. *J Electrocardiol* 2002; **35**: 245–52.
23 Baker LC, London B, Choi BR, Koren G, Salama G. Enhanced dispersion of repolarization and refractoriness in transgenic mouse hearts promotes reentrant ventricular tachycardia. *Circ Res* 2000; **86**: 396–407.
24 Li D, Fareh S, Leung TK, Nattel S. Promotion of atrial fibrillation by heart failure in dogs: atrial remodeling of a different sort. *Circulation* 1999; **100**: 87–95.
25 Liu DW, Gintant GA, Antzelevitch C. Ionic bases for electrophysiological distinctions among epicardial, midmyocardial, and endocardial myocytes from the free wall of the canine left ventricle. *Circ Res* 1993; **72**: 671–87.
26 Szentadrassy N, Banyasz T, Biro T, et al. Apico-basal inhomogeneity in distribution of ion channels in canine and human ventricular myocardium. *Cardiovasc Res* 2005; **65**: 851–60.
27 London B, Baker LC, Petkova-Kirova P, Nerbonne JM, Choi BR, Salama G. Dispersion of repolarization and refractoriness are determinants of arrhythmia phenotype in transgenic mice with long QT. *J Physiol* 2007; **578**: 115–29.
28 Viswanathan PC, Rudy Y. Cellular arrhythmogenic effects of congenital and acquired long-QT syndrome in the heterogeneous myocardium. *Circulation* 2000; **101**: 1192–98.
29 Näbauer M, Käab S. Potassium channel down-regulation in heart failure. *Cardiovasc Res* 1998; **37**: 324–34.
30 Tomaselli GF, Marban E. Electrophysiological remodeling in hypertrophy and heart failure. *Cardiovasc Res* 1999; 42: 270–83.
31 Brunet S, Aimond F, Li H, et al. Heterogeneous expression of repolarizing, voltage-gated K+ currents in adult mouse ventricles. *J Physiol* 2004; **559**: 103–20.
32 Volders PG, Sipido KR, Carmeliet E, Spatjens RL, Wellens HJ, Vos MA. Repolarizing K+ currents ITO1 and IKs are larger in right than left canine ventricular midmyocardium. *Circulation* 1999; **99**: 206–10.
33 Ramakers C, Stengl M, Spatjens RL, Moorman AF, Vos MA. Molecular and electrical characterization of the canine cardiac ventricular septum. *J Mol Cell Cardiol* 2005; **38**: 153–61.
34 Ashamalla SM, Navarro D, Ward CA. Gradient of sodium current across the left ventricular wall of adult rat hearts. *J Physiol* 2001; **536**: 439–43.
35 Schreiner KD, Voss F, Senges JC, et al. Tridimensional activation patterns of acquired torsade de pointes tachycardias in dogs with chronic AV-block. *Basic Res Cardiol* 2004; **99**: 288–98.
36 Tsuji Y, Opthof T, Yasui K, et al. Ionic mechanisms of acquired QT prolongation and torsades de pointes in rabbits with chronic complete atrioventricular block. *Circulation* 2002; **106**: 2012–18.
37 Gallacher DJ, van de Water A, van der Linde H, et al. In vivo mechanisms precipitating torsades de pointes in a canine model of drug-induced long-QT1 syndrome. *Cardiovasc Res* 2007; **76**: 247–56.

38 El-Sherif N, Chinushi M, Caref EB, Restivo M. Electrophysiological mechanism of the characteristic electrocardiographic morphology of torsade de pointes tachyarrhythmias in the long-QT syndrome: detailed analysis of ventricular tridimensional activation patterns. *Circulation* 1997; **96**: 4392–99.

39 Thomsen MB, Verduyn SC, Stengl M, et al. Increased short-term variability of repolarization predicts *d*-sotalol-induced torsades de pointes in dogs. *Circulation* 2004; **110**: 2453–59.

40 Meregalli PG, Wilde AA, Tan HL. Pathophysiological mechanisms of Brugada syndrome: depolarization disorder, repolarization disorder, or more? *Cardiovasc Res* 2005; **67**: 367–78.

41 Corrado D, Fontaine G, Marcus FI, et al. Arrhythmogenic right ventricular dysplasia/cardiomyopathy: need for an international registry. European Society of Cardiology and the Scientific Council on Cardiomyopathies of the World Heart Federation. *J Cardiovasc Electrophysiol* 2000; 11: 827–32.

42 van Rijen HV, Eckardt D, Degen J, et al. Slow conduction and enhanced anisotropy increase the propensity for ventricular tachyarrhythmias in adult mice with induced deletion of connexin 43. *Circulation* 2004; **109**: 1048–55.

43 van Veen TA, Stein M, Royer A, et al. Impaired impulse propagation in Scn5a-knockout mice: combined contribution of excitability, connexin expression, and tissue architecture in relation to aging. *Circulation* 2005; **112**: 1927–35.

44 Remme CA, Verkerk AO, Nuyens D, et al. Overlap syndrome of cardiac sodium channel disease in mice carrying the equivalent mutation of human SCN5A-1795insD. *Circulation* 2006; **114**: 2584–94.

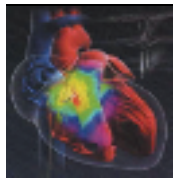

PART IV

Mapping of Supraventricular Tachyarrhythmias

Cardiac Mapping, Third Edition Edited by Mohammad Shenasa, Gerhard Hindricks, Martin Borggrefe, and Günter Breithardt
 ISBN: 978-1-405-17572-2

14 CHAPTER 14

Endocardial Catheter Mapping in Patients with Wolff–Parkinson–White Syndrome and Variants of Preexcitation

Nikolaos Dagres, MD,[1] *Hans Kottkamp*, MD, PhD[2]

[1]University of Athens, Second Cardiology Department, Attiken University Hospital, Athens, Greece
[2]Clinic Hirslanden—Heart Center, Zurich, Switzerland

Summary

Since the first description of radiofrequency (RF) catheter ablation of an atrioventricular accessory pathway (AP) in 1987 [1], RF ablation has become curative treatment of first choice in patients with APs with excellent success and low complication rates [2–4]. This chapter provides an overview of mapping techniques for the common APs as well as the variants of preexcitation.

Catheter Mapping in Patients with Wolff–Parkinson–White (WPW) Syndrome

Anatomical Findings

Anatomically, the common APs are muscular fibers that cross the atrioventricular grooves and create anomalous conduction pathways between the atria and the ventricles outside the specialized conduction tissue [5]. These pathways are remnants of the embryological continuity between the atrial and ventricular myocardium, are almost always composed of working myocardial fibers, and can be found anywhere within the atrioventricular junctions which surround the orifices of the mitral and tricuspid valve [6] with the exception of the aortomitral continuity. Apart from these common APs, there are special variants such as the Mahaim pathways which are discussed in the second part of the chapter.

For the description of the pathway location, a new, anatomically accurate nomenclature was introduced in 1999 [7]. The criterion used by the nomenclature is the AP position along the left and right atrioventricular junction, as assessed in the electrophysiological laboratory by the fluoroscopic images in the left anterior oblique (LAO) projection. APs are classified as left, right, and septal/paraseptal. Left-sided APs, that is, APs located at the parietal side of the left atrioventricular junction, are further subclassified into superior, superoposterior, posterior, inferoposterior, and inferior. Right-sided APs, located at the parietal side of the right

Cardiac Mapping, Third Edition Edited by Mohammad Shenasa, Gerhard Hindricks, Martin Borggrefe, and Günter Breithardt
 ISBN: 978-1-405-17572-2

atrioventricular junction, are subclassified into superior, superoanterior, anterior, inferoanterior, and inferior. Septal and paraseptal pathways are subclassified into superoparaseptal, inferoparaseptal, and septal.

Left-sided APs are the most frequent pathways, representing approximately 55% of all pathways followed by the paraseptal APs (~15–20%), the right-sided APs (~12%), and the septal ones (~10%) [8, 9]. Multiple APs are present in ~5% of the patients [8].

Principles of the Mapping Procedure

For successful ablation, a stable catheter position providing good tissue contact is crucial. The catheter approach depends on the location of the targeted AP.

For left-sided APs, the mapping catheter is usually introduced through the femoral artery and then advanced retrogradely across the aortic valve into the left ventricle to the ventricular aspect of the mitral annulus. Electrograms at these sites are characterized by a small atrial and a large ventricular potential. An alternative approach is to advance the catheter via the femoral vein into the right atrium and transseptally, either through a patent foramen ovale or most commonly with transseptal puncture, into the left atrium and the atrial aspect of the mitral annulus.

These sites are characterized by a larger atrial potential compared with the ventricular aspect of the annulus, which may reach or exceed the amplitude of the ventricular potential. Mapping at the atrial side of the atrioventricular groove is facilitated by the smooth atrial endocardium, which stands in contrast with the heavily trabeculated ventricular side. As the experience of electrophysiologists with the technique of transseptal puncture grows due to the rising number of atrial fibrillation ablation, the transseptal approach is increasingly used for AP ablation. Of note, advancing the retrogradely positioned catheter further over the mitral valve into the left atrium allows targeting of the atrial insertion site of the AP.

Clockwise rotation in the left ventricle brings the catheter to more posterior/superior positions; counterclockwise rotation to more inferior positions of the mitral annulus. For right-sided APs, the mapping catheter is introduced into the right atrium, almost always via the femoral veins. The ablation normally takes place at the atrial site of the tricuspid annulus. Catheter position at this site is in general less stable, and the contact area between the ablation electrode and the tissue surface smaller than at the ventricular site of the mitral annulus. Therefore, longer procedure and fluoroscopy times and more RF applications may be needed at these sites and the success rate is slightly lower compared with APs located at the mitral annulus [4, 9]. Although the femoral approach is the rule for right-sided APs, a jugular or subclavian approach is also reported to be preferred in some cases, especially for right superior or superoparaseptal pathways because of the poor catheter stability provided by the femoral approach in these positions [10]. Alternatively, a long preshaped venous sheath, which may be advanced via the femoral vein up to the inferior caval vein or the right atrium, may also provide significant assistance in these cases.

The mapping technique depends on the conduction properties of the AP: approximately 60–70% of all APs have both antegrade conduction properties leading to manifest preexcitation on the resting ECG and retrograde conduction, whereas the remaining 30–40% show only retrograde conduction and are termed concealed [8, 9]. Mapping can be performed focusing on the antegrade, if present, and/or the retrograde conduction over the AP. Of note, the term Wolff–Parkinson–White syndrome is correct only when used for patients with preexcitation, that is, with manifest APs.

Mapping of Antegradely Conducting APs

In the presence of preexcitation on the resting ECG, mapping can be performed during sinus rhythm or during fixed atrial stimulation. During atrial stimulation, preexcitation is usually enhanced due to the fact that the antegrade conduction of the great majority of APs is not decremental in contrast with the decremental conduction of the atrioventricular node. Thus, the balance between ventricular activation over the atrioventricular node and over the AP is shifted during atrial stimulation in favor of the AP.

Both the bipolar and the unipolar electrogram of the mapping catheter are evaluated. The bipolar electrogram is recorded between the two electrodes of the distal electrode pair of the catheter,

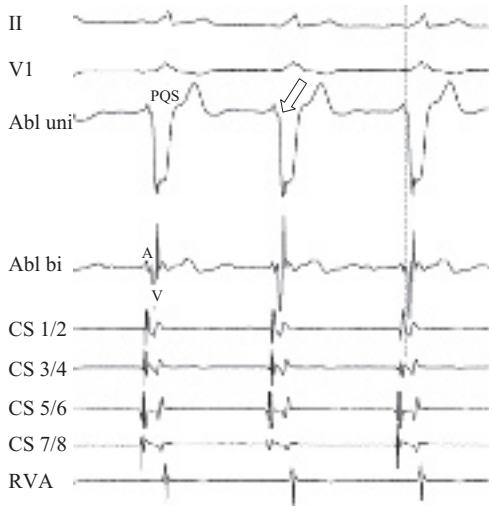

Figure 14.1 Surface ECG leads and intracardiac recordings during mapping of the antegrade conduction of a left-sided accessory pathway at an optimal ablation target site. The ablation catheter is placed at the parietal mitral annulus. The bipolar electrogram of the ablation catheter demonstrates an early onset of the local ventricular activation, which is simultaneous with the start of the delta wave on the surface ECG (dashed vertical line) as well as a very short local atrioventricular interval that gives the impression of an almost continuous electric activity with fusion of the local atrial (A) and local ventricular (V) potential. The unipolar electrogram shows a PQS pattern (arrow) with an atrial activation followed by a solely negative ventricular deflection without an isoelectric interval between atrial and ventricular activation. RF application at this site successfully abolished accessory pathway conduction. Note that the shortest local atrioventricular interval in the coronary sinus is recorded in the distal electrode pair (CS 1/2), which is consistent with a left-sided pathway. KEY: Abl uni = unipolar electrogram of the ablation catheter; Abl bi = bipolar electrogram of the ablation catheter; CS = coronary sinus; RVA = right ventricular apex.

whereas the unipolar electrogram is recorded between the single distal electrode of the catheter and the Wilson Central Terminal (Figure 14.1). Several characteristics of the bipolar and unipolar electrocardiograms have been found to predict successful RF applications and may be used for mapping purposes [11–17]. These are:

1. The earliest preexcited local ventricular activation. This is identified by measuring the time interval between the onset of the local ventricular activation on the mapping catheter and the onset of the delta wave on the ECG (V-delta interval) at different sites along the mitral or tricuspid annulus. The ECG lead with the earliest begin of the delta wave should be used for this purpose. Successful ablation sites are characterized by a local ventricular activation that precedes the onset of the delta wave by several milliseconds. The V-delta intervals that are reported for successful sites range mostly between −2 and −20 ms.

2. The recording of an AP activation potential. This is a sharp deflection recorded between the atrial and the ventricular activation on the mapping catheter.

3. The shortest local atrioventricular interval. This is the interval between the onset of the atrial and the onset of the ventricular activation on the mapping catheter. At successful ablation sites, this interval is minimized (∼40 ms) and the local electrogram often gives the impression of a continuous electric activity.

4. A unipolar electrogram with a PQS pattern. Three different patterns of unipolar electrograms can be recorded which are characterized as (i) P-rS: an atrial activation followed by an isoelectric interval and then a small positive and a larger negative ventricular deflection; (ii) P-QS: an atrial activation followed by a solely negative ventricular deflection, separated from the atrial deflection by an isoelectric interval; and (iii) PQS: an atrial activation followed by a solely negative ventricular deflection without the recording of an isoelectric interval between the atrial and ventricular activation. As shown previously, the success rate grows progressively as we move from sites with a P-rS pattern to P-QS and PQS. Hence, the PQS pattern is considered to be a significant independent predictor of successful RF application, whereas sites with a P-rS pattern have a very low success rate.

It should be noticed that none of these criteria alone allows an absolutely correct discrimination between successful and unsuccessful ablation sites. Thus, a positive V-delta interval, an AP potential, a short atrioventricular interval, or a PQS pattern may be found at several unsuccessful sites. For the evaluation of target sites during mapping, a combination of these criteria should be applied.

Apart from all these criteria, catheter stability is important and represents an independent predictor of successful ablation [12, 13]. Catheter stability can be judged by the stability of the amplitude of the

recorded potentials and by the lack of appearance or disappearance of new deflections. The catheter moves in the fluoroscopic image may also provide useful information in this regard.

In addition to these criteria which are used for mapping of the antegrade AP conduction, ablation of manifest APs may also be performed by mapping of the retrograde AP conduction, as described in the following for concealed pathways.

Mapping of Retrogradely Conducting APs

Mapping of retrograde activation can be performed during either orthodromic atrioventricular reentrant tachycardia or during ventricular stimulation. Atrial activation during ventricular stimulation results from a fusion of retrograde activation via the atrioventricular node and via the AP. In contrast, atrial activation during tachycardia occurs only via the AP and allows more accurate mapping, especially in the presence of an atrioventricular (AV) node with fast retrograde conduction or in a great distance of the AP from the septal area.

Mapping is performed by searching for the site with the earliest local atrial activation. This is identified by measuring the time between the onset of the ventricular activation on the ECG and the atrial activation on the mapping catheter (VA interval) at different sites along the mitral or tricuspid annulus. Only the bipolar mapping electrograms are evaluated for this purpose. An AP activation potential may also be recorded between the ventricular and the atrial activation on the mapping catheter.

Like mapping, RF application may occur either during tachycardia or during ventricular stimulation. It should be considered that successful AP ablation during tachycardia may lead to catheter dislodgement due to abrupt tachycardia termination.

Specific Mapping Considerations in Relation to the AP Location

In addition to the general mapping principles outlined above, particular points must be considered in relation to the location of the targeted AP.

Left-Sided APs

For mapping of left-sided APs, the placement of a multielectrode catheter in the coronary sinus (CS) is performed routinely and may offer significant help. The CS is located in the left atrioventricular groove. In most cases, it is situated closer to the atrial than to the ventricular myocardium, and therefore atrial potentials on the CS catheter have usually higher amplitudes than the ventricular ones.

The electrode pair that fulfils in best way the mapping criteria described above indicates the location of the AP along the parietal side of the mitral annulus and guides the ablation to this area. However, the successful ablation site is often slightly different from the optimal position as suspected from the electrograms of the CS catheter. This is due to the fact that the majority of the APs do not have a perpendicular course over the atrioventricular groove but an oblique one with the atrial insertion site located up to 30 mm more distal or more proximal than the ventricular insertion site [18, 19]. A direct alignment of atrial and ventricular insertion sites is present only in the minority of the cases.

Right-Sided APs

Due to the course of the right coronary artery in the right atrioventricular groove, the placement of a thin electrode catheter in the right coronary artery has been described for mapping of right-sided APs similar to the placement of a CS catheter for mapping of left-sided APs [20, 21]. This may be especially helpful in patients with Ebstein's anomaly. These patients have a high incidence of APs and ablation is hindered by the anomalous position of the right atrioventricular groove, by the frequent incidence of multiple APs and by the presence of fragmented local electrograms which may prevent the distinction between atrial and ventricular potentials or the identification of AP potentials. Overall, right coronary artery mapping is performed very rarely and only on special occasions.

Septal/Paraseptal APs

Mapping of the septal/paraseptal space deserves a separate description due to the complex anatomy of this region.

Septal APs

According to the new nomenclature, septal APs are the APs that were classified previously as "midseptal." These are located in the area between the His bundle recording and the CS ostium which is

the only truly septal region of the atrioventricular junctions. Septal APs can be in most cases successfully targeted from the right atrial side; in 15–20% of septal APs, ablation has to be performed from the mitral side approached either by the retrograde transaortic approach or by transseptal puncture [8, 9].

A small His bundle potential is frequently recorded on the mapping catheter at the optimal target site. Due to the close vicinity of this region to the AV node, ablation of these APs carries a significantly increased risk of induction of AV block and particular attention is required with a reduction of RF generator power and target temperature [4, 8, 9, 22, 23]. At the occurrence of junctional beats or an increase of the amplitude of the His bundle recording on the mapping catheter, the RF pulse should be interrupted in order to avoid AV block. After unsuccessful ablation attempts, pacing maneuvers should be performed for the evaluation of AV nodal conduction before proceeding with additional RF pulses. In view of the fact that the compact AV node has a close subendocardial location, whereas the His bundle is relatively protected within the central fibrous body, some authors suggest to begin ablation with RF application at the ventricular side of the tricuspid annulus [22].

Superoparaseptal APs

Superoparaseptal APs are the APs that were classified previously as "anteroseptal." These pathways are located anteriorly and superiorly to the His bundle recording and are characterized by the simultaneous recording of an AP activation potential and a His bundle potential on the His catheter [24]. Anatomically, this area lies anterosuperiorly in relation to the septum, does not belong to the septum itself, and is part of the parietal right atrioventricular junction [5].

The increased risk of AV block induction, which was described above for the ablation of septal pathways, also applies to the superoparaseptal pathways due to the close vicinity to the AV conduction system. Therefore, the same precautions must be taken. The APs are almost exclusively ablated from the right atrial side. As already indicated, a His bundle potential is often recorded on the ablation catheter at sites with otherwise good mapping electrograms. To reduce the risk of AV block, RF application should be performed at sites with either no or only very small His bundle recording. Although a jugular or subclavian approach is preferred by some investigators [10], most of these pathways can be successfully targeted with the femoral approach [22] with or without the use of long preshaped venous sheaths advanced up to the right atrium. Because of the close course of the right bundle, the induction of right bundle branch block is also observed as a complication [24].

Inferoparaseptal APs

Inferoparaseptal APs are the APs that were classified previously as "posteroseptal." This area does not belong anatomically to the true septum, is located inferiorly to it, and is actually the muscular floor that overlies the superior extension of the posterior atrioventricular groove [5]. It corresponds to the inferior pyramidal space, which is bounded by the central fibrous body, the ventricular mass, and the convergence of the right and left atrial walls [25]. The CS passes through the base of this area and has a myocardial coat extending along the middle cardiac vein and the posterior coronary vein. This myocardial coat has extensive connections to the left and right atria [26, 27]. Thus, APs in this region may directly connect the atrial and ventricular myocardium, or arise from this muscular connection between the CS sleeve and the ventricle.

Given this complex anatomical situation and the fact that the pathways may pass transversely, tangentially, or directly across the inferoseptal space, it is not surprising that the ablation of inferoparaseptal APs poses particular difficulties. These APs can be approached from the right side, the left side, from within the CS, or from within the middle cardiac vein and their ramifications [28]. The majority, approximately 60%, are successfully approached from the right atrial side, whereas the remaining portion are to an almost equal extent ablated from the mitral side, from within the CS and from within the middle cardiac vein [28]. A CS diverticulum is observed in a minority of the cases [27] and the diagnosis can be set by a CS venogram. In these cases, the AP is usually located in the neck of the diverticulum (Figure 14.2).

Although some features of the preexcited ECG, in particular, the polarity of the QRS complex

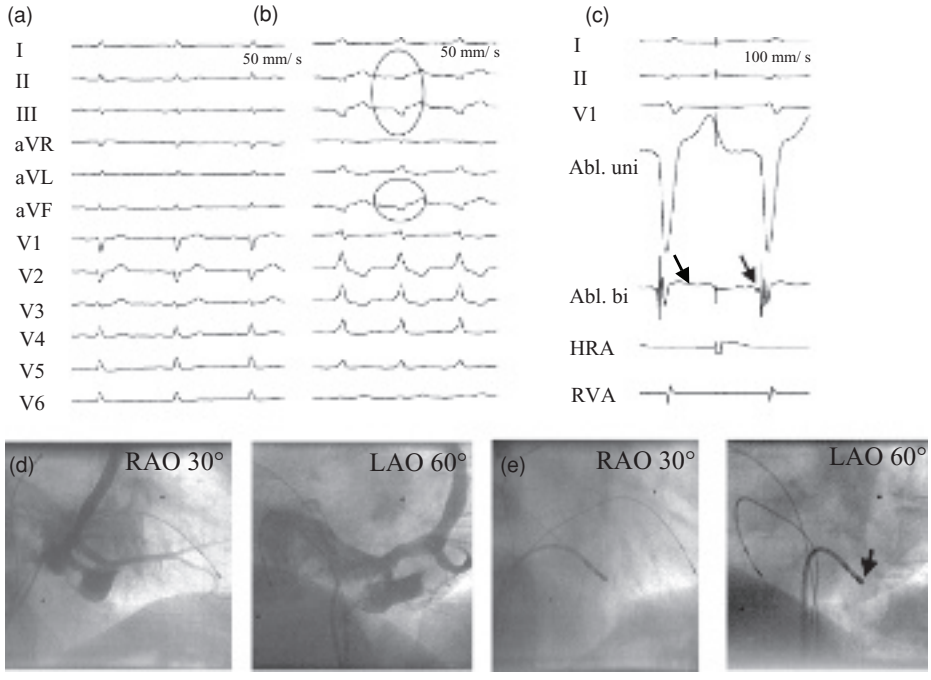

Figure 14.2 Findings in a patient with an accessory pathway located in a coronary sinus diverticulum. (a) The 12-lead ECG during sinus rhythm shows almost no preexcitation. (b) During atrial stimulation with constant rate, preexcitation becomes visible with an almost isoelectric delta wave in II and negative delta waves in III and aVF. (c) Surface ECG leads and intracardiac recordings at the successful ablation site. Mapping is performed during atrial stimulation. The unipolar electrogram of the ablation catheter shows a PQS pattern. An activation potential of the accessory pathway is recorded in the bipolar electrogram (arrow). (d) Coronary sinus angiography in the right and left anterior oblique views showing the diverticulum in the proximal part of the coronary sinus. (e) Fluoroscopic image of the successful ablation site in the right and left anterior oblique views. The arrow indicates the tip of the ablation catheter. The pathway is located in the neck of the diverticulum. KEY: Abl uni = unipolar electrogram of the ablation catheter; Abl bi = bipolar electrogram of the ablation catheter; HRA = high right atrium; RVA = right ventricular apex.

and the delta wave in leads II, aVR, and V1, have been described to offer assistance for the location prediction of inferoparaseptal APs [28], the diagnosis is set by mapping and successful ablation. Most investigators suggest to begin mapping on the right atrial side and to move then to the left side or to the CS, if ablation is not successful or if mapping results with application of the conventional criteria for evaluation of mapping electrograms as described above are not satisfactory. Due to the induction of deeper lesions, ablation catheters with irrigated tip may allow successful ablation from sites that would fail with conventional catheters. Naturally, the electrograms on the CS catheter are helpful for a first evaluation of AP location.

Permanent Junctional Reciprocating Tachycardia

The permanent junctional reciprocating tachycardia (PJRT) has distinct characteristics and deserves particular mentioning. It is an incessant or almost incessant tachycardia with long RP interval due to an AP that is usually located in the inferoparaseptal area [29–31]. These APs have a decremental, slow retrograde conduction and an absent or very slow antegrade conduction resulting in the absence of a delta wave or the presence of only minimal preexcitation in the ECG.

Characteristically, the RP interval is longer than the PR interval, the *P*-waves are negative in the inferior leads, and the conduction over the AP is

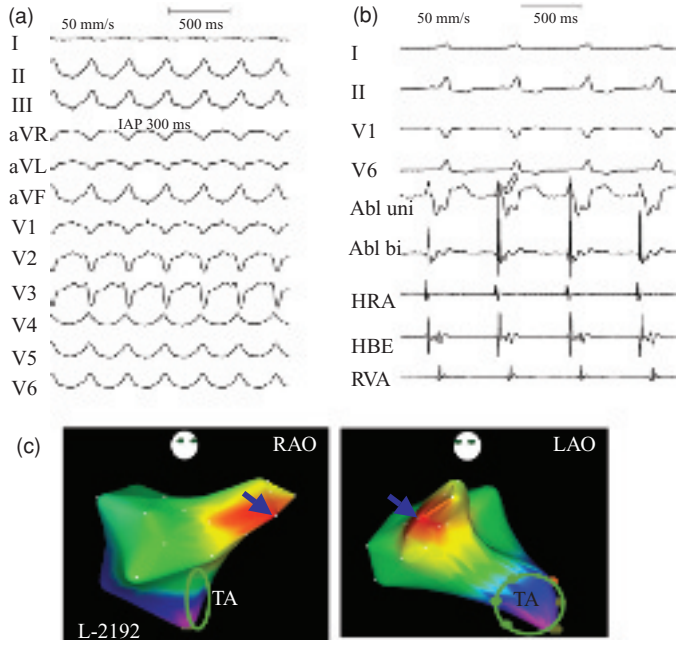

Figure 14.3 Findings in a patient with an accessory pathway with atrial insertion in the right atrial appendage. (a) The 12-lead ECG during atrial stimulation with constant rate shows preexcitation with left bundle-branch block morphology and negative QRS complexes up to lead V3. (b) Surface ECG leads and intracardiac recordings at the successful ablation site in the right atrial appendage. The unipolar electrogram of the ablation catheter shows a PQS pattern (arrow); the bipolar electrogram shows an almost continuous electric activity with fusion of the large local atrial potential and the small local ventricular potential. (c) Three-dimensional reconstruction with use of the CARTO electromagnetic mapping system in the right and left anterior oblique views. The successful ablation site in the right atrial appendage is indicated by the arrow. KEY: Abl uni = unipolar electrogram of the ablation catheter; Abl bi = bipolar electrogram of the ablation catheter; HBE = His bundle recording site; HRA = high right atrium; RVA = right ventricular apex. TA = tricuspid annulus.

adenosine-sensitive and also influenced by autonomic changes which can be evident as changes of the VA interval during the course of the mapping procedure. The differential diagnosis includes an atrial tachycardia from this region or an atypical AV nodal reentrant tachycardia. Although the PJRT usually does not cause significant symptoms, it is mostly refractory to antiarrhythmic therapy, may lead to tachycardia-induced cardiomyopathy and should therefore be treated with ablation.

As stated above, the great majority of these APs, approximately 75%, lie in the inferoparaseptal area and may be ablated either from the right atrial side or, in some cases, from within the CS [30, 31]. The remaining APs may be located in the septal area (commonly ablated from the right atrial side), or more seldom on the right or left free wall.

Atypical Atrioventricular Accessory Pathways

In very rare cases, accessory pathways may connect the right atrial appendage with the underlying right ventricular myocardium (Figure 14.3).

Outcome

Many studies have consistently shown the excellent outcome of RF ablation of APs. In recent reports, success rates exceeding 95% have been documented for left-sided APs, whereas ablation of right-sided, septal, and paraseptal APs is characterized by lower success rates of approximately 90% [4, 9, 32].

The greater difficulty posed by right-sided, septal and paraseptal APs is also reflected in a higher rate of patients requiring a second procedure for achieving success and in a higher recurrence rate for these APs

compared with the left-sided ones. Thus, in a recent large multicenter clinical trial, left-sided APs had a recurrence rate of 3% compared with 12–17% for right-sided, septal, and paraseptal APs [4]. Interestingly, recurrence may affect only the retrograde or the antegrade conduction leading to orthodromic tachycardia with retrograde conduction over the AP without evidence of a recurrent delta wave on the ECG or to the recurrence of the delta wave without evidence for retrograde conduction.

Major procedural complications are rare and include perforation of the atrial or ventricular myocardium leading to tamponade requiring emergency drainage, stroke, induction of high-grade atrioventricular block necessitating pacemaker implantation, pulmonary emboli, aortic dissection, or retroperitoneal haematoma. These complications occur with a frequency of approx. 1% [8]. Death caused by one of these is extremely rare [33].

As described above, atrioventricular block with pacemaker implantation is observed mainly during ablation of septal or paraseptal pathways, due to the close vicinity of the target area to the AV node [4, 8, 9]. Coronary artery lesions following RF ablation have also been reported but are extremely rare [32, 34]. Minor complications are more frequent and include vascular complications, such as pseudoaneurysm, arteriovenous fistula, haematoma at the puncture site, but also transient and spontaneously reversible AV conduction abnormalities when ablation is performed in the septal or paraseptal area. These minor complications normally resolve without need for treatment.

Obviously, specific invasive techniques such as transseptal puncture or puncture of the jugular veins may have their own well-known complications.

Heparin Administration During the Procedure

To avoid thrombus formation with possible embolic complications, heparin should be administered in all cases of mapping on the left side with the usual initial dosage being 5,000 IU. In cases of prolonged mapping, a second dose should be given, for example, an additional 2,500 IU. For procedures on the right side, most centers administer heparin only in cases of prolonged mapping time.

Alternative Energy Sources

Due to the high success rate and its wide availability, RF current is the generally preferred energy source for ablation of APs. The use of alternative energy sources such as cryoenergy is reported [35–37] but has not gained wide application in daily practice for AP ablation.

Catheter Mapping in Patients with Mahaim and Other Variants of Preexcitation

Introduction

At the end of the nineteenth century, Kent and His sought to find the normal conduction system between atria and ventricles [38, 39]. His discovered the penetrating AV bundle; Kent reported on muscular connections in the left and right lateral walls of mammalian hearts. Later, Tawara described the human specialized functional area including the AV node, the penetrating AV bundle, the bundle branches and their ramifications [40]. A specialized node-like structure in the lateral atrial aspect of the right AV sulcus was later described by Kent in a human heart [41–45].

In 1930, the WPW syndrome was described [46] and an accessory AV connection, such as the ones described by Kent, was considered to be the correlate for this syndrome [47, 48]. Later, an accessory AV connection was demonstrated histologically in a patient with WPW syndrome [49, 50]. However, the muscular connections identified histologically did not resemble the node-like structure reported by Kent. In contrast, the AV ring specialized tissue described by Anderson strongly resembled this node-like structure [51, 52].

In contrast to the AV connections in patients with WPW syndrome, functional–morphological correlations do not exist to the same extent for the variants of preexcitation, that is, for atriofascicular, nodofascicular, and fasciculoventricular connections. Mahaim described connections of the AV node to the myocardial septum and connections of the origin of the left bundle branch to the upper part of the interventricular septum [53–56]. Since then, the role of so-called "Mahaim pathways" in tachycardias with the typical left bundle branch block morphology as well as their characteristics has been controversial.

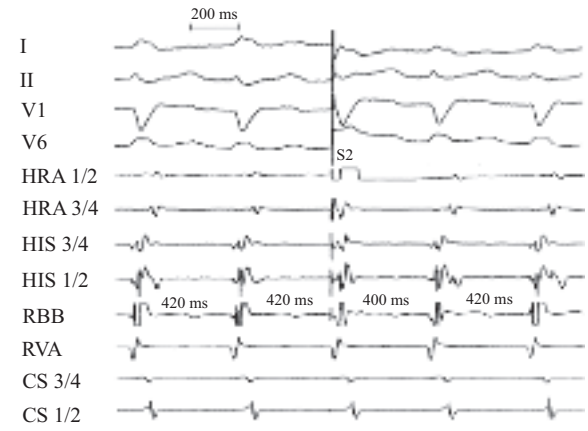

Figure 14.4 Surface ECG leads and intracardiac recordings during antidromic atrioventricular reentrant tachycardia (AVRT) involving an atriofascicular pathway as the antegrade limb and the AV node as the retrograde limb of the circuit. The AVRT is reset with a late atrial extrastimulus (S2) delivered from the high right atrium (HRA) without anterograde penetration into the normal AV node and without a change in the QRS morphology and the ventricular activation sequence indicating the "extranodal" origin of the atriofascicular pathway. KEY: His = His bundle; RBB = right bundle branch: RVA = right ventricular apex; CS = coronary sinus.

Originally, APs were designated as "Mahaim pathways" when they were thought to originate within the AV node and to insert into the distal right bundle branch ("nodofascicular" pathways) or into the right ventricular myocardium ("nodoventricular" pathways) [57–63]. This concept was challenged when Gillette reported surgical interruption at the right parietal tricuspid annulus of APs that had been believed to be nodoventricular because of their electrophysiological properties [64]. The atrial insertion of these APs was identified at a distance from the AV node at the lateral free wall of the tricuspid annulus [65–67]. Overall, the concept of nodofascicular and nodoventricular pathways as correlates of this preexcitation subset has been replaced by the concept of atriofascicular pathways. The existence of nodoventricular and fasciculoventricular pathways—or at least their functional role in preexcited tachycardias—remains controversial.

In the following, we describe the findings in patients with different variants of preexcitation and the results of catheter ablation.

Specialized Atriofascicular and AV Pathways

In 1981, Gallagher et al. observed that right atrial pacing resulted in greater degrees of preexcitation compared with coronary sinus pacing at comparable pacing cycle lengths, and suggested that the atrial insertion of these APs was functionally related to the right atrium. They suggested that an alternative explanation to the old concept of so-called nodoventricular pathways would be an accessory AV node [62]. Tchou et al. also demonstrated that late atrial extrastimuli delivered during antidromic AV reentrant tachycardia (AVRT) could advance the ventricular activation despite their inability to enter the AV node (Figure 14.4), suggesting that the atrial pathway insertion originated directly from the right atrium remote from the normal AV node [67].

McClelland et al. observed conduction time prolongation of atriofascicular pathways during atrial extrastimulation and adenosine, a Wenckebach periodicity proximal to the recording of the AP activation potential, and an intrinsic pathway automaticity (Figure 14.5) [73]. The earliest ventricular activation during maximal preexcitation was usually found remote from the tricuspid annulus at the apical third of the right ventricular free wall [73–75].

The relative late ventricular activation at sites close to the tricuspid annulus and the relative early ventricular activation at sites close to the right ventricular apex during preexcited QRS complexes suggested an insulated pathway course. The recording of a high-frequency potential at the ventricular insertion during antidromic AVRT and during sinus rhythm indicated the pathway insertion in the distal segments of the right bundle branch. Further evidence for the insulated connection of atriofascicular APs to the right bundle branch system came from arrhythmia surgery [80, 81]. The loss of AP conduction resulting from light catheter-exerted pressure suggests an endocardial course [73–75]. However, in some patients, the distal pathway insertion was found close to the tricuspid annulus indicating atrioventricular pathways [73, 80].

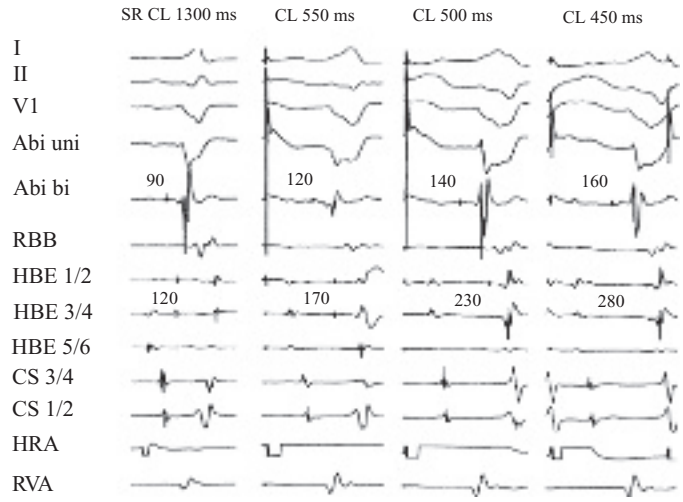

Figure 14.5 Surface ECG leads I, II, and V_1, and intracardiac recordings in a patient with an atriofascicular pathway during sinus rhythm (SR) and high right atrium pacing (HRA) at cycle lengths (CLs) of 550, 500, and 450 ms, respectively. During sinus rhythm, the interval from the atrial potential to the atriofascicular potential measured 90 ms. During HRA stimulation, this interval increased to 120, 140, and 160 ms, respectively. Note that the interval between the atriofascicular potential and the onset of the QRS complex remained constant at 50 ms. On the other hand, the atrium–His interval at the His bundle catheter (HBE) increased from 120 ms to 170, 230, and 280 ms, respectively. Note, that during stimulation at a cycle length of 450 ms, the His bundle is activated retrogradely (distal HBE 1/2 before proximal HBE 3/4). KEY: Abl uni = unipolar electrogram of the ablation catheter placed at the parietal tricuspid annulus; Abl bi = bipolar electrogram of the ablation catheter; RBB = right bundle branch; CS = coronary sinus; RVA = right ventricular apex.

In a report by Guiraudon et al., examination of the right atrial attachment of atriofascicular APs showed AV nodal cells within AV nodal tissue organization [82] confirming the hypothesis that atriofascicular pathways represent an accessory AV node and connecting AV conduction system. Thus, the correlate for these APs has nothing to do with Mahaim's descriptions [53–56] but rather with Kent's [41–45].

Later, Anderson et al. described a complete ring of specialized tissue around the tricuspid orifice and in the posterior margin of the mitral orifice in fetal specimens [52]. In infant hearts, specialized tissue was found at various points around the tricuspid valve attachment. In this stage, the specialized tissue was separated from the ventricular myocardium by the developed annulus fibrosus [52]. Contiguities of the specialized tissue with ventricular myocardium were often observed during the early stage of ontogenesis through gaps of the developing fibrous skeleton [52]. In a later series from the same group, the specialized ring tissue was confined to the right AV junction [84].

Anderson et al. described the arrangement of the atrial fibers around the specialized tissue areas as reminiscent of the transitional cells of the AV node [52]. The specialized ring tissue is also a remnant of the inlet–outlet ring, which, at the inner curve, has an AV location and, according to recent analysis, is true nodal tissue [85]. In adult hearts, remnants of AV ring specialized tissue were found in 15% of the cases [52]. These remnants were most frequently observed in the anterolateral area but also in the lateral to posterolateral region and, in a single case, on the left side of the heart posterior to the mitral orifice. The AV ring specialized tissue was confined to the atrial myocardium and separated from the ventricular myocardium by the fibrous skeleton. Anderson et al. suggested that in abnormal situations, the AV ring specialized tissue might form a specialized substrate for ventricular preexcitation besides the more often observed AV accessory connections in WPW syndrome composed of ordinary myocardium [52].

Thus, atriofascicular pathways seem to originate from remnants of the specialized ring tissue from

which a connecting AV conduction system might arise. The predilection of the atrial insertion of electrophysiologically defined atriofascicular fibers for the antero- to posterolateral aspect of the tricuspid annulus represents further evidence for this hypothesis. Becker et al. reported a patient who had, in addition to an accessory AV pathway composed of working myocardium, a second connection in a right anterolateral position arising from a node-like structure [88] and coursing caudally to become contiguous with the ventricular myocardium. It seems very likely that this accessory AV pathway represented a specialized atriofascicular or AV pathway. Definitive pathological assessment of a complete atriofascicular pathway including the ventricular course of the connecting conduction system to the distal ramifications of the normal right bundle branch, however, is still missing.

In an attempt to add to the commonly used nomenclature [85, 89], a descriptive name for these accessory AV nodes and AV bundles could be specialized atriofascicular and specialized AV pathways. The term "specialized" would clearly differentiate these pathways from the accessory AV connections composed of working myocardium in the WPW syndrome.

An atriofascicular pathway is now suggested if preexcitation is minimal or absent and the PR interval is within normal limits during sinus rhythm, and if incremental atrial stimulation or atrial extrastimuli reveal preexcitation with a left-bundle branch block-like morphology that is identical to the configuration during tachycardia. Atriofascicular fibers exhibit long conduction times, decremental conduction properties by atrial extrastimuli, or incremental atrial pacing, and conduction only in the anterograde direction. The earliest retrograde conduction during ventricular pacing or tachycardia is found at the fast or slow pathway of the AV node or via an accessory AV pathway remote from the atriofascicular pathway. Late extrastimuli that are delivered at the high or lateral right atrium reveal advancement of the tachycardia ("reset") without changing the QRS configuration and without anterograde penetration into the AV node indicating the extranodal atrial origin of the atriofascicular pathway and participation of the right atrium in the reentrant circuit.

Ablation of Specialized Atriofascicular and AV Pathways

Stimulus to delta wave mapping during constant-rate atrial pacing was performed in the initial ablation studies [71, 72, 75]. A shortcoming is the variability of the conduction time through the AV-node-like proximal portion of the specialized atriofascicular fibers. This might be avoided by applying atrial extrastimuli during antidromic AVRT when constant AV intervals usually are present.

Ablation of the retrograde route during antidromic AVRT, that is, ablation of the fast pathway of the AV node, has been described after failed ablation of the atriofascicular pathway [76]. However, this cannot be recommended. First, successful selective fast pathway ablation might not be distinguished from complete anterograde block in the normal AV node. Second, the retrograde route during antidromic AVRT must be carefully investigated because the slow pathway of the AV node as well as additional accessory AV pathways with retrograde conduction capabilities might serve as the retrograde limb. Third, even when the fast pathway is identified during catheter mapping as the retrograde limb, the slow pathway might also be capable of conducting retrogradely.

In contrast, catheter ablation guided by the recording of atriofascicular pathway activation potentials as target sites is highly successful [73–79]. RF energy may be applied at the proximal-node-like structure close to the tricuspid annulus. In these cases, accelerated "junctional" rhythms originating in the node-like structure of specialized atriofascicular pathways may be recorded closely resembling the junctional rhythms seen during AV nodal modification in patients with AV node reentrant tachycardia. Ablation is also effective when energy is applied to the subannular level of the tricuspid annulus and/or along the ventricular pathway course proximal to the merging point with the distal branching system of the normal right bundle branch. Atrial fibrillation occurring during mapping may complicate the recording of AP activation potentials at the subannular level. In these cases, successful ablation can be performed close to the ventricular insertion, where a high-frequency potential can be recorded separated from the local ventricular electrogram by a short isoelectric interval (Figure 14.6).

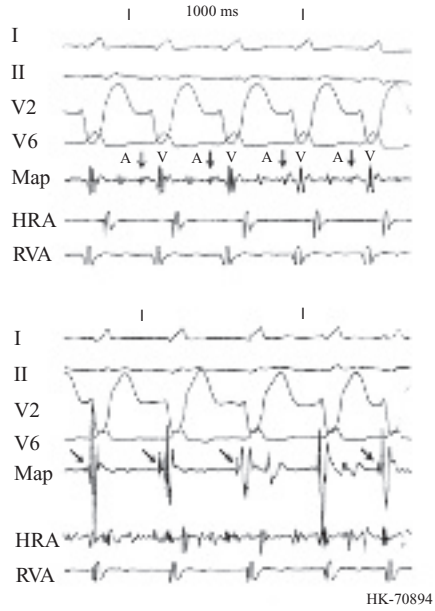

Figure 14.6 Surface ECG leads I, II, V_2, and V_6 and intracardiac electrograms from the mapping and ablation catheter (Map), high right atrium (HRA), and right ventricular apex (RVA) (patient with Ebstein's anomaly). (Top) During antidromic atrioventricular reentrant tachycardia (cycle length 400 ms), mapping at the subannular level of the tricuspid annulus revealed a relatively large atrial potential (A), a ventricular potential (V), and an activation potential of the atriofascicular pathway (arrow). The atrial-atriofascicular pathway potential interval measured 150 ms; the interval from the atriofascicular pathway potential to the onset of the QRS complex measured 50 ms. Note the basal ventricle close to the tricuspid annulus is activated late (45 ms after the onset of the QRS complex), whereas the right ventricular apical region is activated relatively early (10 ms after the onset of the QRS complex).

(Bottom) During the electrophysiological study, the antidromic atrioventricular reentrant tachycardia degenerated into atrial fibrillation with predominant conduction over the atriofascicular pathway (mean ventricular rate 125 beats per minute). The recording of irregular atrial potentials during atrial fibrillation did not allow the reliable recording of an atriofascicular activation potential at the subannular level of the tricuspid annulus. Mapping of the atriofascicular pathway was therefore performed close to the ventricular insertion at the apical part of the right lateral free wall. An atriofascicular pathway activation potential could be recorded (arrows), which was separated by the ventricular potential by a short isoelectric line and that preceded the onset of the QRS complex by 20 ms (successful ablation site). Reproduced with permission from Ref. 76.

Nodofascicular and Nodoventricular Pathways

The rare variants of preexcitation, that is, nodofascicular/ventricular pathways and fasciculoventricular connections, are even less well elucidated. Mahaim et al. described anatomical connections of the AV node to the myocardial septum and connections of the origin of the left bundle branch to the upper part of the interventricular septum [53–56]. However, these connections were rather delicate and their functional role was questioned [54].

The concept of nodofascicular and nodoventricular pathways has been replaced by the concept of specialized atriofascicular pathways, and presently the pure existence of nodofascicular or nodoventricular pathways, or at least their functional role in preexcited tachycardias with left bundle branch block morphology, is doubted.

Studies of the AV conduction system of the human fetal heart indicated that the fetal AV conduction system worked comparably to that of the adult heart [90]. However, this mature function without evidence for preexcitation was in contrast to the morphological immaturity because the fibrous annulus was incompletely developed and the AV node, the AV bundle, and right bundle branch were in histological contiguity with the ventricular myocardium [90].

Nodoventricular connections were also described additionally to accessory AV pathways in cases of WPW syndrome without evidence of clinical significance [91, 92]. A clinicopathological correlation of a presumed nodoventricular bypass was described by Gmeiner et al. [93]. The preexcited tachycardia showed a left bundle branch block morphology, pathological examination revealed a nodoventricular tract originating from the posterior extension of the compact AV node and inserting in the crest of the ventricular septum.

Electrophysiological Findings in Nodofascicular/Ventricular Pathways and Radiofrequency Catheter Ablation

The differential diagnosis for a nodofascicular or nodoventricular pathway includes a midseptal accessory pathway with decremental properties. However, the preexcitation pattern of nodofascicular pathways with left bundle branch block morphology elicited by atrial pacing with progressively

shorter cycle length cannot be distinguished from the typical preexcitation pattern of atriofascicular fibers and thereby indicates an *apical* insertion of the nodofascicular pathway at or close to the distal right bundle branch similar to specialized atriofascicular pathways.

However, no obvious anatomical route exists for a nodofascicular fiber from the under surface of the AV node to the right bundle branch, and this pathway type might therefore also insert into ventricular myocardium with subsequent early activation of the right bundle branch. Strong evidence for the potential participation of nodoventricular pathways in reentrant tachycardias came from Gallagher et al. [62] who described ventriculoatrial dissociation during tachycardia with 2:1 retrograde conduction.

Grogin et al. [74] reported one patient with a nodoventricular pathway and dual AV node physiology presenting with both AV node reentrant tachycardia and antidromic AVRT with the nodoventricular pathway as the anterograde limb of the reentrant circuit. RF application to the midseptal region successfully ablated the nodoventricular pathway and the slow AV node pathway [74].

In another series, a nodofascicular pathway served as a bystander in AV node reentrant tachycardia [76]. The preexcitation pattern during tachycardia resembled that seen in atriofascicular pathways. Fast pathway ablation was performed to eliminate the retrograde pathway during AV node reentrant tachycardia and the retrograde route of potential AVRTs incorporating the nodofascicular pathway. It resulted in an increment of the PR interval from 150 ms to 270 ms and in complete ventriculoatrial block. Interestingly, no preexcitation was visible during sinus rhythm after ablation despite the long PR interval. Instead, preexcitation occurred during incremental atrial pacing at cycle lengths of less than 400 ms that was identical to the preexcitation pattern before ablation, indicating that the proximal portion of the nodofascicular pathway was located distal to the delay-producing area of the normal AV node. After ablation, no AV node reentrant tachycardia or AVRT incorporating the nodofascicular pathway could be induced [76].

In a patient with an atypical nodofascicular pathway, the atrial insertion of the pathway was identified at the midseptal region using atrial-delta wave interval mapping [94]. Maximal preexcitation revealed a right bundle branch block pattern and left axis deviation suggestive of an insertion at or near the left posterior fascicle. RF application targeted at the low midseptal right atrium resulted in disappearance of preexcitation but also in complete block in the AV node [94].

Overall, in cases with nodofascicular pathways, no pathway potential can be recorded at the parietal tricuspid annulus. Instead, transient mechanically induced conduction block of the AP may be observed during mapping at the septal area. A nodoventricular or nodofascicular fiber is suggested if ventriculoatrial dissociation occurs during tachycardia or if atrial extrastimuli fail to reset the tachycardia without anterograde penetration into the AV node [62, 67]. An atriofascicular or nodoventricular pathway is considered a bystander in AV node reentrant tachycardia if fusion of the QRS complex is observed during tachycardia spontaneously or in response to programmed atrial or ventricular stimulation [76].

Fasciculoventricular Fibers

Fasciculoventricular connections are suggested if the proximal insertion of the accessory pathway is found to arise from the His bundle or bundle branches. The PR interval is expected within normal limits during sinus rhythm unless associated anomalies including enhanced conduction within the AV node or an additional accessory AV pathway are present. The QRS complex is expected to be slightly prolonged with a discrete R wave slurring suggesting a small delta wave [62].

No isolated His bundle potential can be recorded in the typical His bundle area. A potential may be recorded that cannot be distinguished between a His bundle potential or an AP potential following the local atrial potential after an isoelectric line. This potential is directly followed by a local ventricular potential, that is, the His bundle-ventricle interval is zero.

Atrial stimulation with extrastimuli and constant pacing with different cycle lengths reveals progressively increasing AV intervals and a constant degree of preexcitation that is identical to that during normal sinus rhythm. Therefore, the proximal insertion is suggested to arise distal to the AV node at the site of the penetrating AV bundle. The earliest ventricular activation at the His bundle recording site is earlier

than the ventricular activation at the right or left bundle branch indicating the ventricular insertion in the ventricular summit.

Fasciculoventricular connections may give rise to ventricular preexcitation but usually serve as innocent bystanders during orthodromic AVRT incorporating a muscular accessory AV pathway or AV node reentrant tachycardia [76]. In a series of 11 patients, the PR interval was mostly abbreviated because of enhanced AV node conduction, the QRS complex was slightly prolonged because of discrete preexcitation during sinus rhythm and the PR interval was prolonged during programmed atrial stimulation in association with a constant degree of preexcitation [95]. No arrhythmias causally related to the fasciculoventricular connections were observed [95]. A patient with fixed preexcitation in which the accessory pathway served as a bystander during AV node reentrant tachycardia was recently described [74]. Transiently effective fast AV node pathway ablation led to PR prolongation without change in the preexcitation pattern. RF application in the midseptal area finally abolished the slow AV node pathway and resulted in loss of preexcitation. This pathway was interpreted as nodofascicular originating from the final common pathway of the AV node reentrant circuit or the His bundle [74].

Overall, two different kinds of nodofascicular/ventricular and fasciculoventricular connections seem to exist: first, as described by Mahaim, the AV node and the AV bundle and/or bundle branches may be in direct histological contiguity with the ventricular septal myocardium, that is, connections as a result of insulation defects of poorly developed fibrous skeletons or fibrous tissue sheaths. These nodoventricular or fasciculoventricular connections therefore might be better called paraspecific connections than APs. In many cases, these incompletely differentiated AV conduction systems seem to be functionally mature not giving rise to preexcitation [90].

Second, there is rare but conclusive evidence that accessory nodofascicular/ventricular pathways indeed exist as a very rare variant of true APs with their ventricular insertion close to or at the distal right bundle branch. These pathways may give rise to ventricular preexcitation during AV node reentrant tachycardia or even serve as the anterograde limb in antidromic AVRT [74].

In addition, connections from atrial myocardium to the His bundle had been described and termed atriofascicular by the European Study Group for Preexcitation [89, 96]. These APs may result in a clinical entity with short PR interval and normal QRS complex. However, they seem to be extremely rare and their role in the initiation or perpetuation of atrial or AVRTs is unknown. The distinction from accelerated AV node conduction may be impossible. In the light of current concepts, these connections may now be termed atrio-Hisian [85]. Together with enhanced AV node conduction, atrio-Hisian tracts may thus form the anatomical substrate for the Lown–Ganong–Levine syndrome [97].

References

1 Borggrefe M, Budde T, Podczeck A, et al. High-frequency alternating current ablation of an accessory pathway in humans. *J Am Coll Cardiol* 1987; **10:** 576–82.

2 Jackman WM, Wang XZ, Friday KJ, et al. Catheter ablation of accessory atrioventricular pathways (Wolff–Parkinson–White syndrome) by radiofrequency current. *N Engl J Med* 1991; **324**: 1605–11.

3 Kuck KH, Schlüter M, Geiger M, et al. Radiofrequency current catheter ablation of accessory atrioventricular pathways. *Lancet* 1991; **337**: 1557–61.

4 Calkins H, Yong P, Miller JM, et al. Catheter ablation of accessory pathways, atrioventricular nodal reentrant tachycardia, and the atrioventricular junction: final results of a prospective, multicenter clinical trial. The Atakr Multicenter Investigators Group. *Circulation* 1999; **99**: 262–70.

5 Anderson RH, Ho SY. Anatomy of the atrioventricular junctions with regard to ventricular preexcitation. *Pacing Clin Electrophysiol* 1997; **20**: 2072–76.

6 Becker AE, Anderson RH. The Wolff–Parkinson–White syndrome and its anatomical substrates. *Anat Rec* 1981; **201**: 169–77.

7 Cosio FG, Anderson RH, Kuck KH, et al. Living anatomy of the atrioventricular junctions: a guide to electrophysiologic mapping. A Consensus Statement from the Cardiac Nomenclature Study Group, Working Group of Arrhythmias, European Society of Cardiology, and the Task Force on Cardiac Nomenclature from NASPE. *Circulation* 1999; **100**: e31–7.

8 Dagres N, Clague JR, Kottkamp H, et al. Radiofrequency catheter ablation of accessory pathways: outcome and use of antiarrhythmic drugs during follow-up. *Eur Heart J* 1999; **20**: 1826–32.

9 Kobza R, Kottkamp H, Piorkowski C, et al. Radiofrequency ablation of accessory pathways: contemporary

success rates and complications in 323 patients. *Z Kardiol* 2005; **94**: 193–99.

10 Schlüter M, Kuck KH. Catheter ablation of septal accessory conduction pathways with high-frequency electric current. *Z Kardiol* 1992; **81**: 249–57.

11 Haissaguerre M, Dartigues JF, Warin JF, et al. Electrogram patterns predictive of successful catheter ablation of accessory pathways: value of unipolar recording mode. *Circulation* 1991; **84**: 188–202.

12 Chen X, Borggrefe M, Shenasa M, et al. Characteristics of local electrogram predicting successful transcatheter radiofrequency ablation of left-sided accessory pathways. *J Am Coll Cardiol* 1992; **20**: 656–65.

13 Calkins H, Kim YN, Schmaltz S, et al. Electrogram criteria for identification of appropriate target sites for radiofrequency catheter ablation of accessory atrioventricular connections. *Circulation* 1992; **85**: 565–73.

14 Cappato R, Schlüter M, Mont L, et al. Anatomic, electrical, and mechanical factors affecting bipolar endocardial electrograms: impact on catheter ablation of manifest left free-wall accessory pathways. *Circulation* 1994; **90**: 884–94.

15 Hindricks G, Kottkamp H, Chen X, et al. Localization and radiofrequency catheter ablation of left-sided accessory pathways during atrial fibrillation: feasibility and electrogram criteria for identification of appropriate target sites. *J Am Coll Cardiol* 1995; **25**: 444–51.

16 Grimm W, Miller J, Josephson ME. Successful and unsuccessful sites of radiofrequency catheter ablation of accessory atrioventricular connections. *Am Heart J* 1994; **128**: 77–87.

17 Sousa J, Brandao L, Vagueiro MC. A comparison of unipolar versus bipolar mapping in the ablation of left-sided accessory atrioventricular conduction pathways. *Rev Port Cardiol* 1997; **16**: 449–55.

18 Jackman WM, Friday KJ, Yeung-Lai-Wah JA, et al. New catheter technique for recording left free-wall accessory atrioventricular pathway activation: identification of pathway fiber orientation. *Circulation* 1988; **78**: 598–611.

19 Tai CT, Chen SA, Chiang CE, et al. Identification of fiber orientation in left free-wall accessory pathways: implication for radiofrequency ablation. *J Interv Card Electrophysiol* 1997; **1**: 235–41.

20 Cappato R, Schlüter M, Weiss C, et al. Radiofrequency current catheter ablation of accessory atrioventricular pathways in Ebstein's anomaly. *Circulation* 1996; **94**: 376–83.

21 Shah MJ, Jones TK, Cecchin F. Improved localization of right-sided accessory pathways with microcatheter-assisted right coronary artery mapping in children. *J Cardiovasc Electrophysiol* 2004; **15**: 1238–43.

22 Brugada J, Puigfel M, Mont L, et al. Radiofrequency ablation of anteroseptal, para-Hisian, and mid-septal accessory pathways using a simplified femoral approach. *Pacing Clin Electrophysiol* 1998; **21**: 735–41.

23 Tai CT, Chen SA, Chiang CE, et al. Electrocardiographic and electrophysiologic characteristics of anteroseptal, midseptal, and para-Hisian accessory pathways: implication for radiofrequency catheter ablation. *Chest* 1996; **109**: 730–40.

24 Schlüter M, Kuck KH. Catheter ablation from right atrium of anteroseptal accessory pathways using radiofrequency current. *J Am Coll Cardiol* 1992; **19**: 663–70.

25 Sanchez-Quintana D, Ho SY, Cabrera JA, et al. Topographic anatomy of the inferior pyramidal space: relevance to radiofrequency catheter ablation. *J Cardiovasc Electrophysiol* 2001; **12**: 210–17.

26 Chauvin M, Shah DC, Haissaguerre M, et al. The anatomic basis of connections between the coronary sinus musculature and the left atrium in humans. *Circulation* 2000; **101**: 647–52.

27 Sun Y, Arruda M, Otomo K, et al. Coronary sinus–ventricular accessory connections producing posteroseptal and left posterior accessory pathways: incidence and electrophysiological identification. *Circulation* 2002; **106**: 1362–67.

28 Kobza R, Hindricks G, Tanner H, et al. Paraseptal accessory pathway in Wolff–Parkinson–White syndrome: ablation from the right, from the left, or within the coronary sinus/middle cardiac vein? *J Interv Card Electrophysiol* 2005; **12**: 55–60.

29 Chien WW, Cohen TJ, Lee MA, et al. Electrophysiological findings and long-term follow-up of patients with the permanent form of junctional reciprocating tachycardia treated by catheter ablation. *Circulation* 1992; **85**: 1329–36.

30 Gaita F, Haissaguerre M, Giustetto C, et al. Catheter ablation of permanent junctional reciprocating tachycardia with radiofrequency current. *J Am Coll Cardiol* 1995; **25**: 648–54.

31 Meiltz A, Weber R, Halimi F, et al. Permanent form of junctional reciprocating tachycardia in adults: peculiar features and results of radiofrequency catheter ablation. *Europace* 2006; **8**: 21–8.

32 Scheinman MM, Huang S. The 1998 NASPE prospective catheter ablation registry. *PACE* 2000; **23**: 1020–28.

33 Hindricks G. Complications of radiofrequency catheter ablation of arrhythmias. The Multicentre European Radiofrequency Survey (MERFS). *Eur Heart J* 1993; **14**: 1644–53.

34 Bertram H, Bökenkamp R, Peuster M, et al. Coronary artery stenosis after radiofrequency catheter ablation of accessory atrioventricular pathways in children with Ebstein's malformation. *Circulation* 2001; **103**: 538–43.

35 Friedman PL, Dubuc M, Green MS, et al. Catheter cryoablation of supraventricular tachycardia: results of the multicenter prospective "frosty" trial. *Heart Rhythm* 2004; **1**: 129–38.

36 Kirsh JA, Gross GJ, O'Connor S, et al. Transcatheter cryoablation of tachyarrhythmias in children: initial experience from an international registry. *J Am Coll Cardiol* 2005; **45**: 133–36.

37 Rodriguez LM, Geller JC, Tse HF, et al. Acute results of transvenous cryoablation of supraventricular tachycardia (atrial fibrillation, atrial flutter, Wolff–Parkinson–White syndrome, atrioventricular nodal reentry tachycardia). *J Cardiovasc Electrophysiol* 2002; **13**: 1082–89.

38 Kent AFS. Researches on the structure and function of the mammalian heart. *J Physiol* 1893; **14**: 233–54.

39 His W Jr. Die Tätigkeit des embryonalen Herzens und deren Bedeutung für die Lehre von Herzbewegungen beim Erwachsenen. *Arbeiten aus der Medizinischen Klinik zu Leipzig* 1893; **1**: 14–49.

40 Tawara S. *Das Reizleitungssystem des Säugetierherzens*. Gustav Fischer, Jena, Germany, 1906: 135–49.

41 Kent AFS. Observations on the auriculo-ventricular junction of the mammalian heart. *Q J Exp Physiol* 1913; **7**: 193–95.

42 Kent AFS. The structure of the cardiac tissues at the auriculo-ventricular junction. *J Physiol* 1913; **47**: xvii–xviii.

43 Kent AFS. The right lateral auriculoventricular junction of the heart. *J Physiol* 1914; **48**: xxii–xxiv.

44 Kent AFS. A conducting path between the right atrium and the external wall of the right ventricle in the heart of the mammal. *J Physiol* 1914; **48**: lvii.

45 Kent AFS. Illustrations of the right lateral auriculo-ventricular junction in the heart. *J Physiol* 1914; **48**: lxiii–lxiv.

46 Wolff L, Parkinson J, White PD. Bundle-branch block with short P-R interval in healthy young people prone to paroxysmal tachycardia. *Am Heart J* 1930; **5:** 685–704.

47 Holzmann M, Scherf D. Über Elektrokardiogramme mit verkürzter Vorhof–Kammer–Distanz und positiven P-Zacken. *Z Klin Med* 1932; **121**: 404–23.

48 Wolferth CC, Wood FC. The mechanism of production of short P-R intervals and prolonged QRS complexes in patients with presumably undamaged hearts: hypothesis of an accessory pathway of auriculo-ventricular conduction (bundle of Kent). *Am Heart J* 1933; **8**: 297–311.

49 Wood FC, Wolferth CC, Geckeler GD. Histologic demonstration of accessory muscular connections between auricle and ventricle in a case of short P-R interval and prolonged QRS complex. *Am Heart J* 1943; **25**: 454–62.

50 Öhnell RF. Preexcitation: a cardiac abnormality. *Acta Med Scand* 1944; **152** (Suppl CLII): 1–167.

51 Anderson RH, Taylor IM. Development of atrioventricular specialized tissue in human heart. *Br Heart J* 1972; **34**: 1205–14.

52 Anderson RH, Davies MJ, Becker AE. Atrioventricular ring specialized tissue in the normal heart. *Eur J Cardiol* 1974; **2**: 219–30.

53 Mahaim I. Le bloc bilatéral manqué, nouvelle forme anatomique de bloc du coer, à substituer au bloc dit "d'arborisations." *Ann de Méd* 1932; **32**: 347.

54 Mahaim I, Benatt A. Nouvelle recherches sur les connexions supérieures de la branche gauche du faisceau de His–Tawara avec cloison interventriculaire. *Cardiologia* 1938; **1**: 61–8.

55 Mahaim I, Winston MR. Recherches d'anatomie comparée et de pathologie expérimentale sur les connexions hautes de faisceau de His–Tawara. *Cardiologia* 1941; **5**: 189–260.

56 Mahaim I. Kent's fibers and the A-V paraspecific conduction through the upper connections of the bundle of His–Tawara. *Am Heart J* 1947; **33**: 651–53.

57 Wellens HJJ. Tachycardias related to the pre-excitation syndrome. In: Wellens HJJ, ed. *Electrical Stimulation of the Heart in the Study and Treatment of Tachycardias*. University Park Press, Baltimore 1971: 97–109.

58 Lev M, Fox SM, Bharati S, et al. Mahaim and James fibers as a basis for a unique variety of ventricular preexcitation. *Am J Cardiol* 1975; **36**: 880–87.

59 Tonkin AM, Dugan FA, Svenson RH, et al. Coexistence of functional Kent- and Mahaim-type tracts in the preexcitation syndrome: demonstration by catheter techniques and epicardial mapping. *Circulation* 1975; **52**: 193–202.

60 Touboul P, Vexler AM, Chatelain MT. Reentry via Mahaim fibers as a possible basis for tachycardia. *Br Heart J* 1978; **40**: 806–11.

61 Ward DE, Camm AJ, Spurell RAJ. Ventricular preexcitation due to anomalous nodo–ventricular pathways: report on 3 patients. *Eur J Cardiol* 1979; **9**: 111–27.

62 Gallagher JJ, Smith WM, Kasell JH, et al. Role of Mahaim fibers in cardiac arrhythmias in man. *Circulation* 1981; **64**: 176–89.

63 Bardy GH, German LD, Packer DL, et al. Mechanism of tachycardia using a nodofascicular Mahaim fiber. *Am J Cardiol* 1984; **54**: 1140–41.

64 Gillette PC, Garsoh A Jr, Cooley DA, et al. Prolonged and decremental antegrade conduction properties in right anterior accessory connections: wide QRS antidromic tachycardia of left bundle branch block pattern without Wolff– Parkinson–White–configuration during sinus rhythm. *Am Heart J* 1982; **103**: 66–74.

65 Klein GJ, Guiraudon GM, Kerr CR, et al. "Nodoventricular" accessory pathway: evidence for a distinct accessory atrioventricular pathway with atrioventricular node-like properties. *J Am Coll Cardiol* 1988; **11**: 1035–40.

66 Ross DL, Johnson DC, Koo CC, et al. Surgical treatment of supraventricular tachycardia without the WPW syndrome: current indications, techniques and results. In: Brugada P, Wellens HJJ, eds. *Cardiac Arrhythmias: Where to Go From Here?*: Futura Publishing Co., Mount Kisco, NY, 1987: 591–603.

67 Tchou P, Lehmann MH, Jazayeri M, et al. Atriofascicular connection or a nodoventricular Mahaim fiber? Electrophysiologic elucidation of the pathway and associated reentrant circuit. *Circulation* 1988; **77**: 837–48.

68 Bhandari A, Morady F, Shen EN, et al. Catheter-induced His bundle ablation in a patient with reentrant tachycardia associated with a nodoventricular tract. *J Am Coll Cardiol* 1984; **4**: 611–16.

69 Ellenbogen KA, O'Callaghan WG, Colavita PG, et al. Catheter atrioventricular junction ablation for recurrent supraventricular tachycardia with nodoventricular fibers. *Am J Cardiol* 1985; **55**: 1227–29.

70 Haissaguerre M, Warin JF, Metayer P, et al. Catheter ablation of Mahaim fibers with preservation of atrioventricular nodal conduction. *Circulation* 1990; **82**: 418–27.

71 Okishige K, Strickberger SA, Walsh EP, et al. Catheter ablation of the atrial origin of a detrimentally conducting atriofascicular accessory pathway by radiofrequency current. *J Cardiovasc Electrophysiol* 1991; **2**: 465–75.

72 Klein LS, Hackett FK, Zipes DP, et al. Radiofrequency catheter ablation of Mahaim fibers at the tricuspid annulus. *Circulation* 1993; **87**: 738–47.

73 McClelland JH, Wang X, Beckman KJ, et al. Radiofrequency catheter ablation of right atriofascicular (Mahaim) accessory pathways guided by accessory pathway activation potentials. *Circulation* 1994; **89**: 2655–66.

74 Grogin HR, Lee RJ, Kwasman M, et al. Radiofrequency catheter ablation of atriofascicular and nodoventricular Mahaim tracts. *Circulation* 1994; **90**: 272–81.

75 Cappato R, Schlüter M, Weiss C, et al. Catheter-induced mechanical conduction block of right-sided accessory fibers with Mahaim-type preexcitation to guide radiofrequency ablation. *Circulation* 1994; **90**: 282–90.

76 Kottkamp H, Hindricks G, Shenasa M, et al. Variants of preexcitation: specialized atriofascicular pathways, nodofascicular pathways, and fasciculoventricular pathways. *J Cardiovasc Electrophysiol* 1996; **7**: 916–30.

77 Hluchy J, Schlegelmilch P, Schickel S, et al. Radiofrequency ablation of a concealed nodoventricular Mahaim fiber guided by a discrete potential. *J Cardiovasc Electrophysiol* 1999; **10**: 603–10.

78 Hluchy J, Schickel S, Jörger U, et al. Electrophysiologic characteristics and radiofrequency ablation of concealed nodofascicular and left anterograde atriofascicular pathways. *J Cardiovasc Electrophysiol* 2000; **11**: 211–17.

79 Peinado R, Merino JL, Ramirez L, et al. Decremental atriofascicular accessory pathway with bidirectional conduction: delineation of atrial and ventricular insertion by radiofrequency current application. *J Cardiovasc Electrophysiol* 2001; **12**: 489–92.

80 Murdock CJ, Leitch JW, Klein GJ, et al. Epicardial mapping in patients with "nodoventricular" accessory pathways. *Am J Cardiol* 1991; **68**: 208–14.

81 Sealy WC, Kopelman HE, Murphy DA. Accessory atrioventricular node and bundle: A cause of antidromic reentry tachycardia. *Ann Thorac Surg* 1992; **54**: 306–10.

82 Guiraudon GM, Guiraudon CM, Klein GJ, et al. Atrio-fascicular (Mahaim) fibers—surgical anatomy and pathology—experience with 13 patients. *Eur Heart J* 1994; **15**(Suppl): 431, Abstract.

83 Keith A, Flack A. The form and nature of the muscular connections between the primary divisions of the vertebrate heart. *J Anat Physiol* 1907; **41**: 172–89.

84 Lamers WH, Wessels A, Verbeek FJ, et al. New findings concerning ventricular septation in the human heart: implications for maldevelopment. *Circulation* 1992; **86**: 1194–205.

85 Anderson RH, Ho SY, Gillette PC, et al. Mahaim, Kent, and abnormal atrioventricular conduction. *J Cardiovasc Res* 1996; **31**: 480–91.

86 Mönckeberg JG. Zur Entwicklungsgeschichte des Atrioventrikularsystems. *Verhandlung Dtsch Path Ges* 1913; **16**: 228.

87 Anderson RH, Arnold R, Wilkinson JL. The conducting system in congenitally corrected transposition. *Lancet* 1973; **1**: 1286–88.

88 Becker AE, Anderson RH, Durrer D, et al. The anatomical substrates of Wolff–Parkinson–White syndrome: A clinicopathologic correlation in seven patients. *Circulation* 1978; **57**: 870–79.

89 Anderson RH, Becker AE, Brechenmacher C, et al. Ventricular preexcitation: A proposed nomenclature for its substrates. *Eur J Cardiol* 1975; **3**: 27–36.

90 Janse MJ, Anderson RH, van Capelle FJL, et al. A combined electrophysiological and anatomical study of the human fetal heart. *Am Heart J* 1976; **91**: 556–62.

91 Lev M, Gibson S, Miller RA. Ebstein's disease with Wolff–Parkinson–White syndrome. *Am Heart J* 1955; **49**: 724–41.

92 Lev M, Fox SM, Bharati S, et al. Mahaim and James fibers as a basis for a unique variety of ventricular preexcitation. *Am J Cardiol* 1975; **36**: 880–88.

93 Gmeiner R, Ng CK, Hammer I, et al. Tachycardia caused by an accessory nodoventricular tract: A clinicopathologic correlation. *Eur Heart J* 1984; **5**: 233–42.

94 Okishige K, Friedman PL. New obserations on decremental atriofascicular and nodofascicular fibers: implications for catheter ablation. *Pacing Clin Electrophysiol* 1995; **18**: 986–98.

95 Gallagher JJ. Role of nodoventricular and fasciculoventricular connections in tachyarrhythmias. In: Benditt DG, Benson DW, eds. *Cardiac Preexcitation Syndromes*. Martin Nijhoff Publishing, Boston, 1986: 201–32.

96 Brechenmacher C. Atrio-His bundle tracts. *Br Heart J* 1975; **37**:853–55.

97 Lown B, Ganong WF, Levine SA. The syndrome of short P-R interval, normal QRS complex, and paroxysmal rapid heart action. *Circulation* 1952; **5**: 693–706.

15 CHAPTER 15

Cryomapping of the Perinodal Region: A Safe and Effective Technique for Ablation of the AV Nodal Reentrant Tachycardia

Mohammad-Reza Jazayeri, MD, FACC, FAHA

Bellin Health Hospital Center, Green Bay, WI, USA

Summary

Cryothermal technology made its first appearance in the medical field during the 1940's and 1950's as a tool for destroying undesirable tissues. Since its initial applications in the human heart in 1972, it has become increasingly popular in treating cardiac arrhythmias. However, it was not until eight years ago that it became available as a transcatheter technology. This chapter will focus on various aspects of cryoablation of atrioventricular nodal reentrant tachycardia as an alternative modality to its radiofrequency counterpart.

Historical Perspective

In 1942, for the first time, David Scherf demonstrated the effect of cooling on the ventricular arrhythmia. In his in vitro experiment, he could either completely abolish or slow the rate of the arrhythmia by cooling the cardiac tissue to 50–60°F [1]. Subsequently, permanent myocardial injury was produced in dogs by exposing the cardiac tissues to −60°F of hypothermia [2, 3]. The resulting lesions were transmural, homogeneous, and well demarcated. Furthermore, these lesions did not disrupt the integrity of the cardiac tissue, nor did they cause any intracardiac thrombosis.

The first surgical interruption of accessory AV pathways was successfully performed in a patient with supraventrticular tachycardia (SVT) [4], and the technique of a closed-chest ablation was tested in animals in the late 1960s [5, 6]. After both the safety and efficacy of cryothermia in creating myocardial lesions were established in experimental studies [2, 3, 7–11] this technology was introduced in the late 1970s as a useful tool for surgical intervention of cardiac arrhythmia [12–14]. Over the subsequent decades, further surgical cryoablation of both ventricular and supraventricular arrhythmias proved this modality as a useful, effective, and safe technique [15–19].

A case of persistent AV block produced by direct current (DC) electrical countershock inadvertently delivered to the region of the AV node/His bundle

Cardiac Mapping, Third Edition Edited by Mohammad Shenasa, Gerhard Hindricks, Martin Borggrefe, and Günter Breithardt
 ISBN: 978-1-405-17572-2

was reported in 1979 [20]. This observation paved the way for further clinical investigations testing the feasibility of producing AV node/His bundle block in patients by deliberately delivering DC countershock to the AV junction [21, 22]. These efforts commenced the new era of interventional electrophysiology (EP) with catheter-based technology for ablation of various cardiac arrhythmias.

In 1979, during a surgical attempt to produce AV block in a patient with AVNRT, the AV node reentry was fortuitously modified and AVNRT was rendered noninducible with the AV conduction integrity remaining intact [23]. Subsequently, after being tested in a canine model of AV nodal reentry [24], surgical cryotherapy was introduced as a modality for providing a permanent cure in patients with AVNRT [17]. Although the cryothermal energy has been available since the 1950s for ablation of various tissues including myocardium [25], there was a hiatus in keeping up with the transcatheter technology until the early 1990s, shortly after the RF emerged as the primary source of energy for ablating cardiac arrhythmias.

Initially, an 11 French (Fr) intravascular catheter was used in pigs to produce AV block by ablating the node/His bundle [26, 27]. This prototypical catheter only functioned as a nondeflectable conduit to freeze the tissue by passing pressurized liquid nitrogen to the catheter tip and was not capable of recording electrical signals or pacing the neighboring myocardial tissues. Further refinement of the catheter resulted in an 8 Fr steerable bipolar electrode catheter that was used successfully in animals to create AV block [28, 29]. Finally, in 2000, the first 9 Fr steerable quadripolar cryoablation catheter with a 4-mm-tip became available for clinical trials in patients with AVNRT [30].

Cryothermia-Induced Tissue Injuries

Early Changes

During cryoapplication, the tissue heat is removed, and the hypothermic changes begin as soon as the local temperature falls below the body temperature. At subfreezing temperatures, a cascade of events leads to cellular and vascular injuries [31–34] as outlined below.

Cellular Injury

The extent of tissue injury during cryoablation directly depends on the temperature and duration of each application. The hypothermia interferes with the normal cell metabolism resulting in alteration of myocardial electrophysiological properties such as conduction block and prolongation of refractoriness. These changes are usually appreciable within the first 30 sec of exposing the cardiac tissues to subfreezing (i.e., -20°C to -30°C) temperatures. When the temperature is quickly returned to its normal value, these transient electrophysiological changes are reversed in a similar manner. This reversible phenomenon, also known as "cryomapping," is unique to cryothermia and has been introduced as a useful feature in identifying the appropriate target sites for successful ablation.

As the temperature approaches the target range, the catheter tip adheres to the neighboring myocardium by forming an iceball, a feature known as "cryoadhesion." During cryoablation, areas closer to the catheter-tip lose heat rapidly (rapid freeze), whereas the areas more distant from the catheter-tip experience slower heat removal (slow freeze). With rapid freezing to temperatures $<-30^{\circ}$C, the ice crystals are mostly formed inside the cells, destroying the cell membrane and the intracellular structures. On the other hand, slower freezing predominantly results in the extracellular ice crystal formation, which in turn increases the osmotic pressure of the extracellular compartment. The resulting osmotic gradient across the cell membrane causes the cells to become dehydrated.

Given enough time in this dehydrated state, the resulting changes in the intracellular milieu are often detrimental to tissue integrity and function. If the dehydration is too severe, the toxic effect of the high electrolytes concentration can permanently injure the cells. Regardless of whether the ice crystal formation is predominantly extracellular or intracellular, the end-result is invariably water removal from the biologic milieu leading to tissue desiccation. It is important to note that fast freezing is more destructive than slow freezing.

Thawing by itself may further intensify the cellular damage and extend the tissue destruction. The existing ice crystals fuse to form larger crystals (recrystallization) as the tissue warms to temperatures above -40°C. These larger crystals may be

mechanically disruptive to the cell membrane. With warmer temperatures, the ice crystals gradually melt, increasing the extracellular water content. Subsequent flow of free water into the intracellular compartment may further damage the cells that were partially injured during the freezing phase. Slow thawing plays an important role in tissue destruction during the course of cryotherapy. The available data suggest that slow thawing is more crucial for cellular damage than rapid cooling. It has been shown that repetition of the freeze–thaw cycle enhances the cryothermal-induced lesion size, especially in the remote areas (i.e., at the periphery of lesion) where the local temperature is only in the range of −20°C to −30°C.

Vascular Injury

The initial vascular response to the freezing insult is a local vasoconstriction leading to diminished/ceased blood flow and also damage to the vascular endothelial layers. Subsequent thawing is usually associated with vasodilatation, tissue edema due to increased vascular permeability, and microthrombi secondary to platelet aggregation. Ultimately, these vascular injuries result in ischemic necrosis of surviving cells in the targeted tissue.

Late Changes

The initial tissue necrosis during the freeze/thaw phase is followed by hemorrhagic and inflammatory changes that may last for several weeks. The end-result is formation of a discrete, well-demarcated, and homogeneous scar tissue.

Unique Features of Cryothermal Technology

Cryoadhesion

When the catheter tip temperature is reduced below 0°C, progressive ice-ball formation adheres the catheter tip to the adjacent tissue. This feature by preventing dislodgment of the catheter alleviates the need for periodic fluoroscopic assessment of catheter-tip stability during cryoablation. Because of this feature, patients may be left on a continuous isoproterenol infusion during cryoablation if the AVNRT inducibility requires such pharmacological stimulation.

Cryomapping

With this unique feature, one is able to temporarily diminish or completely cease the electrophysiological activities of the targeted myocardial tissue as demonstrable by either conduction block (delay) or termination of arrhythmia. This reversible process, also known as "ice mapping," involves cooling the tissue at a temperature of −30°C for up to a maximum time of 80 sec. The use of cryomapping enables one to identify the critical site(s) for successful ablation. When cooling is terminated, the local electrophysiological activities are usually resumed within a few minutes without any residual permanent damage to the tissue undergoing cryomapping.

Transcatheter Equipment

Currently, CryoCath Technologies (Kirkland, Quebec, Canada) is the only manufacturer in North America that produces intravascular cryoablation equipment approved by the United States Food and Drug Administration. Their catheters (Freezor™) are quadripolar deflectable catheters available in three sizes: 7 Fr Freezor™ with a 4-mm tip, 7 Fr Freezor Xtra™ with a 6-mm tip, and Freezor Max™ with an 8-mm tip.

A temperature sensor (thermocouple) is embedded in the gold-plated copper distal tip. The central lumen of the catheter is a conduit for delivering pressurized liquid nitrous oxide (N_2O) refrigerant from the console to the distal tip. The N_2O undergoes a liquid-to-gas phase change at the catheter tip resulting in drop of temperature. Returning back to the console through an outer lumen, the vapor N_2O is then removed from the distal tip under a constant vacuum. The delivery system has two algorithms: (i) a cryomapping algorithm, which slowly decreases the temperature at the distal electrode to −30°C for up to 80 sec; (ii) a cryoablation algorithm, which adjusts the N_2O flow to freeze at temperatures down to anywhere between −70°C and −85°C for a maximum duration of 480 sec.

Cryoablation versus RF Ablation of Perinodal Tissue

There are several fundamental histological and practical differences between these two modalities that will be highlighted here. First, it has been shown

histologically [35] that compared to the lesions created by RF, cryolesions are more homogeneous and discrete with a smoother and sharper demarcation from the rest of the myocardium. Endothelial disruption is minimal with underlying tissue and extracellular matrix architecture remaining well preserved.

It has been noted (personal observation) that patients undergoing cryoablation have considerably less effusion than those undergoing RF ablation. This may be a reflection of the fact that the tissue integrity is preserved and therefore blood oozing from the ablated tissue is not a common phenomenon in cryoablation. Similarly, another advantage of cryoablation is its safety when being delivered within the terminal portion of the coronary sinus or adjacent to the coronary arteries [36, 37].

Secondly, the frequency and the extent of thrombus formation with cryoablation are significantly less than those encountered with RF [35]. In creating lesions of comparable size, the risk of thrombus formation is at least five times greater with RF than with cryoablation. Thirdly, catheter-tip movement is a common observation during RF ablation. This phenomenon, also known as the "brushing effect," involves a relatively large area that may be affected by the RF energy delivery.

On the other hand, in cryoablation the catheter-tip is adhered to the target site due to its inherent "cryoadhesion effect," which limits the cryolesion to a very discrete area. This issue may have important clinical implications when the area of interest is situated in the close proximity of the AV node/His bundle. Fourthly, cryolesions do not irritate the sensory nerve endings and, thus, they cause nearly no pain in awake and nonsedated patients [38]. Finally, accelerated junctional rhythm, the hallmark of successful RF ablation, does not occur during cryoablation, and therefore this phenomenon cannot be utilized as a marker for assessing successful outcomes in the latter procedure.

Cryomapping Technique

The principles of AV nodal modification using RF have been previously addressed and will not be detailed here [39–43]. Cryomapping and cryoablation share the same principles for the most part. The choice of catheter-tip size is primarily dependant uon the operator's preference and the patient's body size. A rule of thumb is that in most adults and older children, catheters with 6- or 8-mm distal tips (7 Fr or 9 Fr catheter size, respectively) can be used successfully without any problems, whereas a 7 Fr catheter with a 4-mm tip is preferable for younger children and newborns. The cryolesion dimensions seem directly proportional to the catheter-tip size [31, 35]. Although there is no published data to demonstrate the greater efficacy of an 8-mm catheter-tip compared to that of a 6-mm catheter-tip in AV nodal modification, such superiority has been suggested in ablation of atrial flutter [44].

Cryomapping of the perinodal area is done by using a combination of fluoroscopic and electrographic guidance. Under fluoroscopic surveillance, cryomapping is usually commenced in the most posterior aspect of the tricuspid septal annulus (site P1) and gradually moved up anteriorly (up to site A1) until the desired effect is accomplished [39, 41, 42]. The local atrial electrogram is preferably fractionated or multiphasic and has a juxta-annular characteristic (A/V ratio of less than 0.5). The efficacy of each application can be judged by at least one of the following methods: (i) termination of sustained AVNRT; (ii) prolongation of the AV nodal effective refractoriness; or (iii) elimination of the "PR $\geq$ RR" and reduction of the maximal achievable AH interval during shortest 1:1 AV conduction.

If the patient has reproducibly inducible AVNRT, the easiest and most reliable stimulation method is determined prior to any ablation attempt. This may sometimes require burst ventricular pacing if premature atrial stimulation or burst atrial pacing are not fruitful. Subsequently, cryomapping is applied to a site of interest during tachycardia. If AVNRT is terminated within 30 sec, the optimal target site has been identified (Figures 15.1 and 15.2). Further testing can be carried out with the predetermined method(s) of AVNRT induction while the cryothermal application is taking place. Otherwise, cryomapping is discontinued and a new site is sought during sinus rhythm by examining the A/V ratio in order to assure a juxta-annular position.

Seeking a new site must be done during sinus rhythm because A and V deflections are nearly simultaneous during AVNRT and thus the A/V ratio

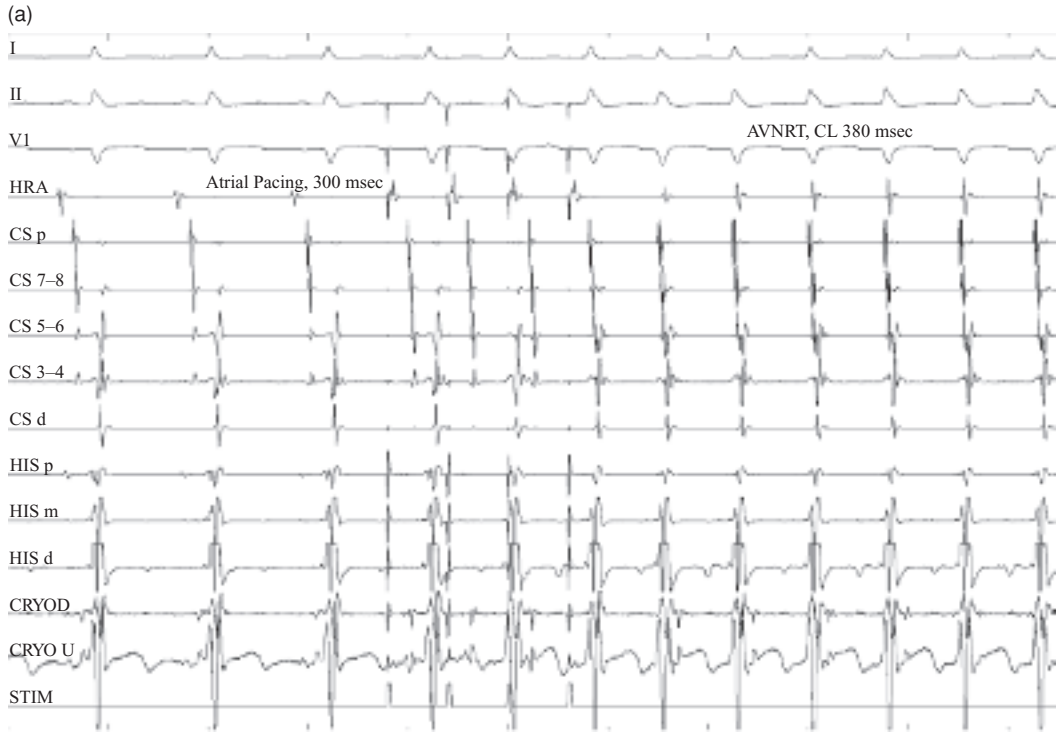

Figure 15.1 Cryomapping and cryoablation of typical AVNRT. Tracings from top to bottom are: Surface ECG leads I, II, and V1; high right atrium (HRA); coronary sinus (CS) from proximal (p) to distal (d); His bundle electrogram (His) from proximal to distal; electrograms obtained from the ablation catheter (CRYO), d and unipolar (U) recordings; and the stimulation marker (STIM). Panel A demonstrates AVNRT initiation by a short burst of rapid atrial pacing at 300 msec delivered during sinus rhythm. The cycle length (CL) of AVNRT is 380 msec. Also note that the "PR ≥ RR" feature is present during rapid atrial pacing. Panel B shows that AVNRT is terminated when the last atrial impulse blocks antegradely in the slow pathway approximately 11 sec after initiation of cryomapping. Panel C illustrates the loss or reversal of "PR ≥ RR" feature during atrial pacing at 300–310 msec while the cryothermal application is on, as evidenced by appearance of a high-frequency noise in CRYO. Also notice that AVNRT is no longer inducible.

cannot be readily estimated. Similarly, cryomapping can be applied while premature atrial stimulation (A1–A2) is performed at A1–A2 coupling intervals associated with A2 conduction exclusively via the AV nodal slow pathway. This is obviously applicable to those who demonstrate dual AV nodal pathway physiology with a sudden A2–H2 jump at a certain range of A1–A2 coupling intervals. This phenomenon is frequently associated with the initiation of AV nodal reentry as single reentrant echo beats or AVNRT.

If cryomapping at a site eliminates these sudden A2–H2 jumps and their accompanied echo beats/AVNRT, the site is considered suitable for ablation. Finally, another technique to elicit exclusive slow pathway conduction is to pace the atrium at the shortest cycle length, maintaining 1:1 AV conduction, while ensuring the "PR ≥ RR" feature is demonstrable [45].

In successful AV nodal modification by cryoablation of the AV nodal slow pathway, one should expect the elimination or reversal of the (PR ≥ RR) equation and marked reduction in the maximal AH interval achievable postoperatively [46]. When a suitable target site is identified by cryomapping during one or more of the aforementioned methods, a switch is made from cryomapping to cryoablation mode. Otherwise, cryomapping is continued at a new site. During cryomapping, the patient's ECG is monitored closely for any change in the PR interval (if performed during sinus rhythm) or QRS morphology. The application must be

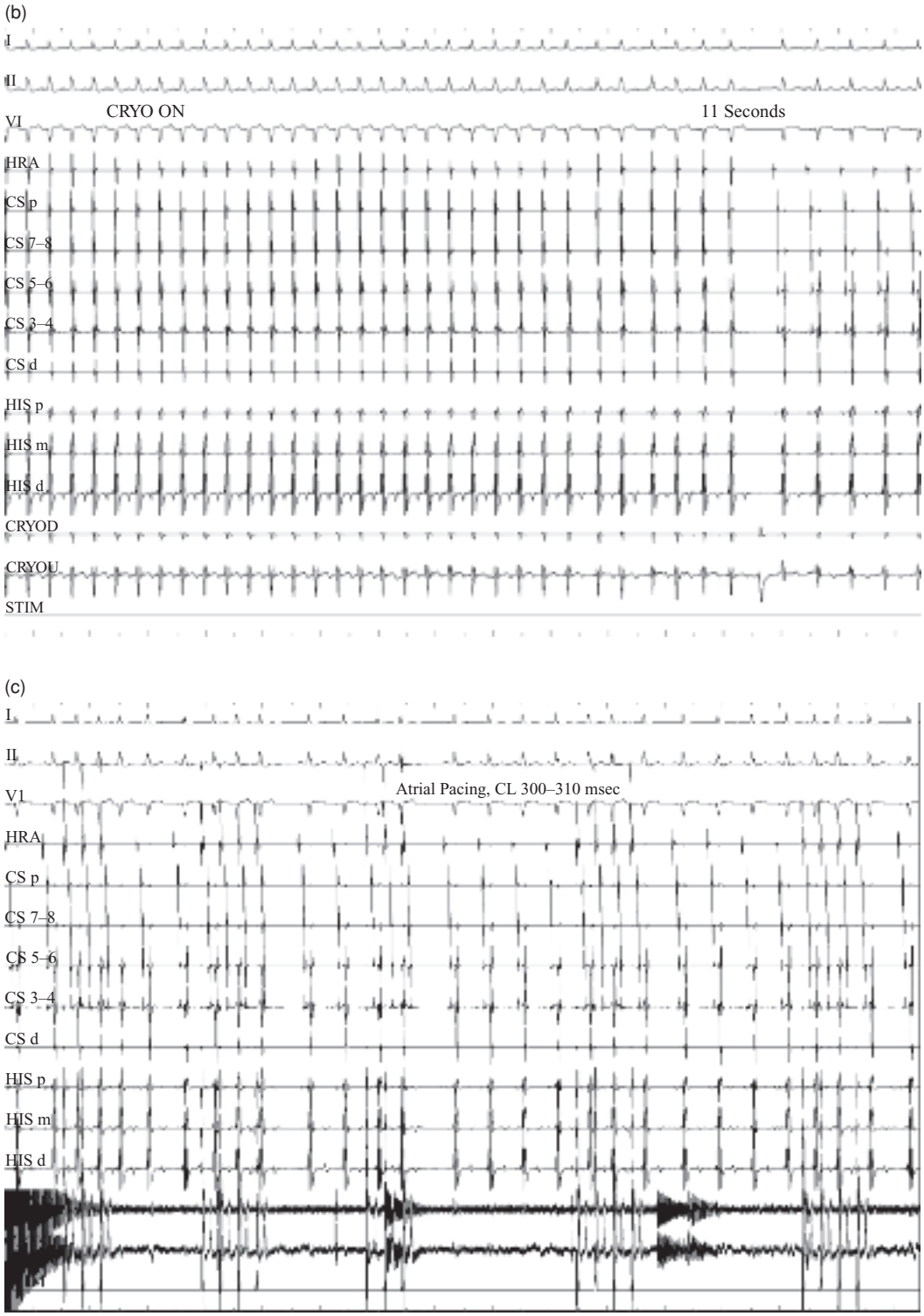

Figure 15.1 (*Continued*)

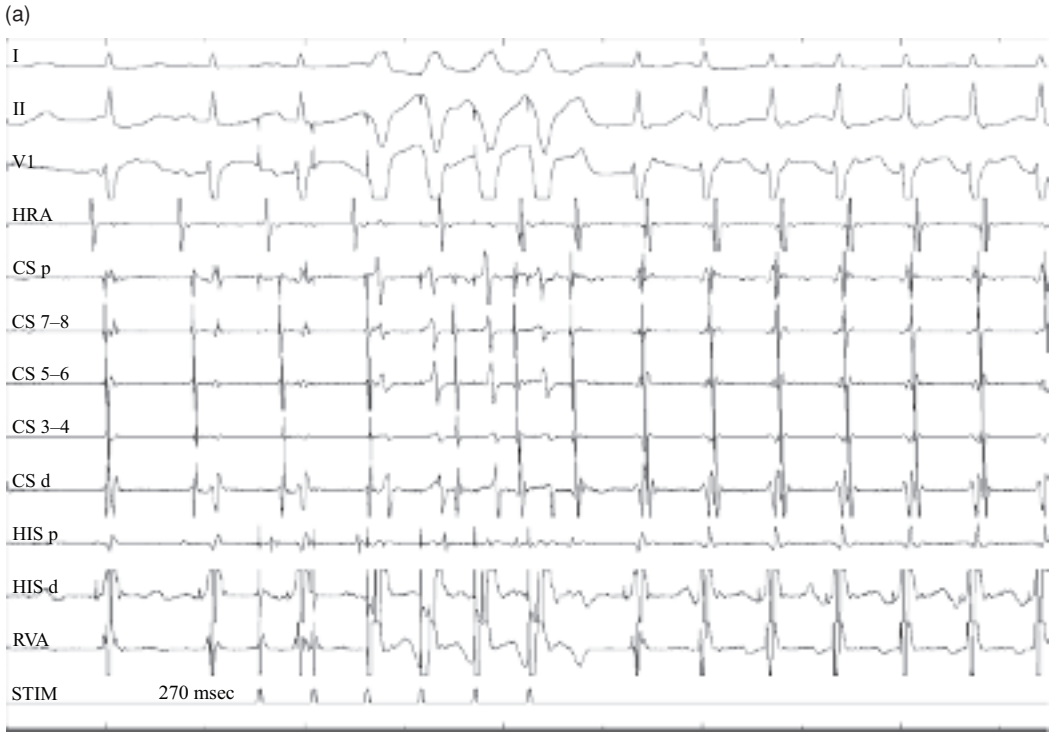

Figure 15.2 Cryoablation of AVNRT inducible only by ventricular pacing. Tracings are arranged in the same format as Figure 15.1. A short burst of ventricular pacing at 270 msec delivered during sinus rhythm induces typical AVNRT (panel a). This was the only reproducible way of AVNRT initiation. AVNRT is terminated shortly after cryomapping is turned on (panel b). Short bursts of ventricular pacing during cryoablation only induce a single AV nodal reentrant echo beat but no sustained AVNRT (panel c). KEY: ABLd = distal ablation catheter electrogram; RVA = right ventricular apical electrogram.

terminated immediately if there is any PR interval prolongation, AV block, or change in the QRS configuration.

Cryoablation

When the target site is identified by cryomapping, the catheter-tip is cooled to the lowest achievable temperature (usually $<-70^{\circ}C$) and kept at that temperature for 4 min. Similar to cryomapping, during each cryoablation application, the patient's ECG should be monitored closely for any PR interval prolongation or QRS morphology change in order to immediately terminate cryoablation if any change in these parameters occurs or if AV block develops. Because of the cryoadhesion feature, the inducibility of AVNRT or the status of the AV nodal dual pathway physiology can be assessed during each application without any concern for inadvertent movement or dislodgment of the ablation catheter-tip. Cryoablation should be considered ineffective at the site if AVNRT remains inducible, and a new site should be sought for cryomapping.

The above-described method of cryomapping and cryoablation is primarily for ablation of the typical (slow/fast) form of AVNRT. In the case of atypical (fast/slow or slow/slow) forms of AVNRT, the retrograde slow pathway conduction can also be utilized as a marker, in addition to AVNRT inducibility, to assess the efficacy of the procedure. The antegrade AV nodal dual pathway physiology is less prevalent and thus less helpful in successful ablation of patients with the atypical form of AVNRT. On the other hand, the presence of retrograde dual AV nodal pathway physiology during programmed ventricular stimulation (V1–V2) may be regarded as a more reliable marker for ablation in this type of patients.

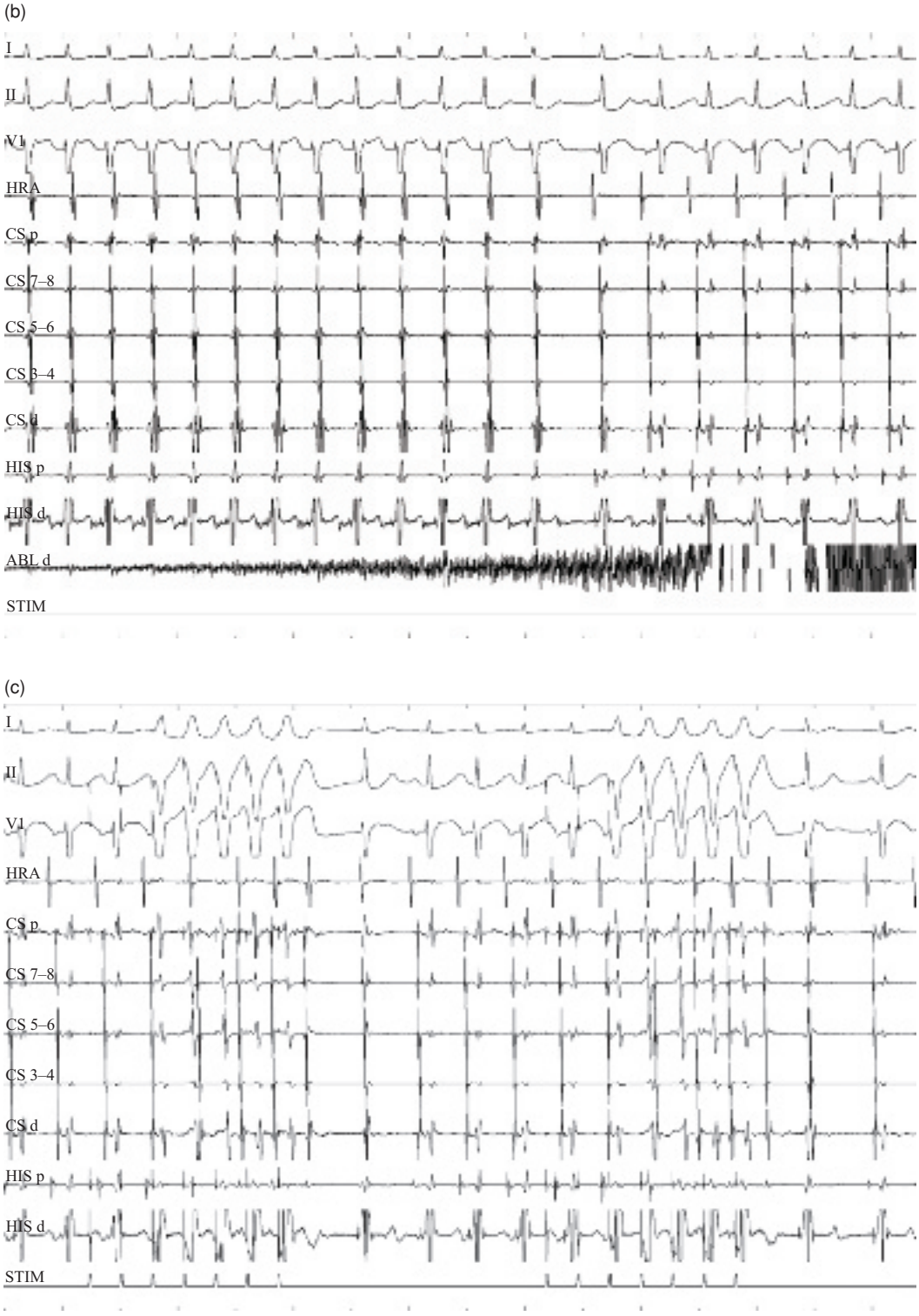

Figure 15.2 (*Continued*)

Helpful Tips for Effective and Safe Ablation

There are several points worthy of mention:

(i) The AV nodal dual pathway physiology is demonstrable in approximately 65% of patients with the typical form of AVNRT, and its disappearance occurs in almost half of these patients following successful ablation [40]. Thus, this phenomenon is not sufficiently reliable to be used in many patients as the sole marker for assessing the efficacy of cryoablation.

(ii) After termination of each application, the catheter-tip should be rewarmed and safely disengaged from the cardiac tissue by increasing the tip temperature to $>0^{\circ}$C before removal from its position. Otherwise, a premature attempt at removing the catheter-tip could potentially result in serious tissue damage, right atrial perforation, and cardiac tamponade.

(iii) Repeating the freeze/thaw sequence has been shown to be effective in augmenting the volume of the cryoablation lesion [8, 33] Therefore, it may be a good practice to deliver at least two successive applications (insurance lesions) at the successful site.

(iv) A delayed drop in the catheter-tip temperature, temperatures $>-70^{\circ}$C, or too much fluctuation in the refrigerant flow and/or the catheter-tip temperature, should alert one to either lack of optimal contact between the catheter-tip and the cardiac tissue or an obstruction/problem in the refrigerant delivery system. The application should be aborted and further attempts made after identifying and solving the problem.

(v) The closer the ablation site is to the critical AV nodal slow pathway, the faster AVNRT termination occurs. Ideally, AVNRT termination should take place within 15–20 sec after the catheter-tip temperature has reached -30°C. Ordinarily, it takes approximately 10 sec from the onset of cooling to the time that the catheter-tip temperature reaches -30°C. Thus, one should expect to see the effect within the first 30 sec after the cryothermal application is turned on. (See Videoclip 5.)

(vi) AVNRT termination is regarded as a sign of successful targeting only when it is caused by one of the following situations: (a) antegrade block in the slow pathway in the typical AVNRT, (b) retrograde slow pathway block in the fast/slow AVNRT, or (c) either antegrade or retrograde block in one of the critical slow pathways of the slow/slow form of AVNRT.

Therefore, AVNRT termination due to any other factors (e.g., antegrade fast pathway block in typical AVNRT) should not be considered as a successful endpoint if the AV nodal slow pathway is targeted. In such situations, successful cryoablation of the slow pathway may not be achievable in the same procedural session if AVNRT is no longer inducible and the AV nodal dual pathway physiology is no longer demonstrable. In the absence of such markers, it seems advisable to suspend any further immediate ablation attempts and to watch the patients clinically for any AVNRT recurrence. Alternatively, one could consider switching from cryoablation to RF ablation as will be discussed later.

Electroanatomic Mapping as a Useful Tool in Cryoablation

Two nonfluoroscopic three-dimensional (3D) mapping systems are commercially available for assisting catheter ablation of various cardiac arrhythmias. These systems have been shown to reduce the length of procedure and its corresponding radiation exposure [47–49]. Currently, the EnSite NavX^{TM} (St. Jude Medical, St. Paul, MN) is the only mapping system compatible with any EP catheter. During aquisition of the endocardial anatomy, a steerable EP catheter is used to trace the inner surface of the right atrium, as well as specific anatomical landmarks including the caval veins, the coronary sinus ostium, the His bundle recording site, and the tricuspid annulus. Each is identified and labeled respectively. The resultant real-time 3D geometry map enables catheter navigation without the use of fluoroscopy. (See Videoclip 6.)

Creation of such a detailed geometry takes approximately 10–15 min. Subsequent mapping of the perinodal area is performed as described earlier. When the target sites of the AV nodal slow pathway are identified for ablation, cryomapping and/or cryoablation is performed and each site is highlighted accordingly (Figure 15.3). This technique has several advantages over the conventional mapping and ablating method using fluoroscopic guidance. Firstly, it minimizes the extent to which the patients, operator and laboratory personnel are

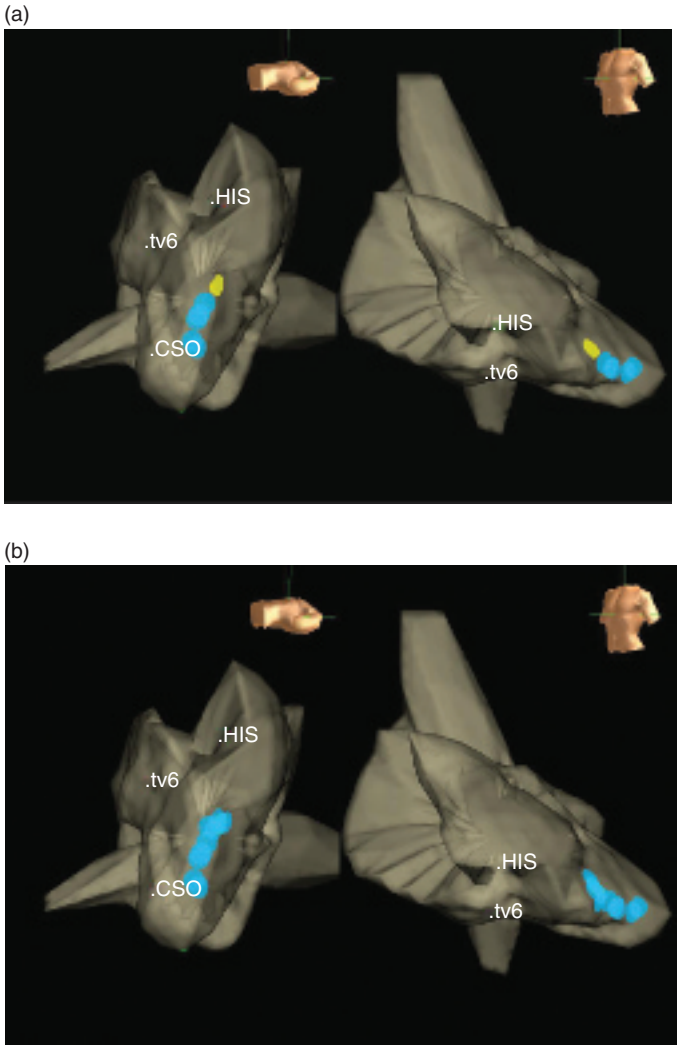

Figure 15.3 Electroanotomical mapping as a useful tool for successful cryoablation. Geometric maps of the right atrium are shown in the lateral caudal (left) and left anterior oblique views (right). In panel a, blue spots depict unsuccessful cryomaping sites and yellow spot represent the successful site terminating AVNRT. In panel b, further cryoablation was performed in multiple sites adjacent to the successful site, shown as a cluster of blue spots overlapping the yellow spot. KEY: CSO = coronary sinus ostium; His = His bundle recording site; tv6 = tricuspid valve annulus at 06:00 o'clock position.

exposed to radiation. Secondly, the AV junction can be delineated precisely and, therefore, cryomapping or cryoablation may be done while the patient is in AVNRT. Thirdly, one can designate sites that are ineffective or associated with transient AV block so those sites will not be targeted again. (See Videoclip 7. 👁) Fourthly, new areas for further attempts may only be a few millimeters away from ineffective sites. These sites are easily identifiable by the computerized mapping technique while conventional fluoroscopic imaging is incapable of such precision. Finally, it facilitates delivering insurance lesions adjacent to a successful site (Figure 15.3).

Immediate and Long-Term Outcomes

Over the past seven years, a wealth of data on the subject of technique, efficacy, and safety of cryoablation in AVNRT has been published by a number of centers worldwide (Table 15.1) [30, 50–58]. The reported immediate success rate ranged from 83% to 99% with most centers experiencing greater than a 90% success rate. Of these initial successful outcomes, 91–100% (average, 95%) enjoyed long-term success. It should be noted that these cases were ablated using either 4-mm or 6-mm tip cryoablation

Table 15.1 Published Studies in Cryoablation of AVNRT.

Study	*Year published*	*Number (patients)*	*Mean age (years)*	*Follow-up (months)*	*Catheter-tip size*	*Immediate success rate (%)*	*Long-term success rate (%)**	*Transient AV block (%)*	*Persistent AV block (%)*
Skanes et al. (Ref. 30)	2000	18	44 ± 14	5 ± 2	7 F 4 mm	94	100	5	0
Riccardi et al. (Ref. 50)	2003	32	43 ± 18	10 ± 4	7 F 4 mm	97	90	0	0
Friedman et al. (Ref. 51)	2004	103	50 ± 15	6	7 F 4 mm	91	94	10	0
Kirsh et al. (Ref. 52)	2004	30	<18	3	7 F 4 or 6 mm	83	92	?	0
Miyazaki et al. (Ref. 53)	2005	22	14 ± 3	8	7 F 4 or 6 mm	95	95	32	0
Kriebel et al. (Ref. 54)	2005	13	11 ± 3	9	7 F 4 or 6 mm	85	100	23	0
Drago et al. (Ref. 55)	2005	14	13 ± 4	12	7 F 4 mm	93	85	7	0
Jensen-Urstad et al. (Ref. 56)	2006	75	53 ± 16	9	7 F 6 mm	99	95	8	0
Khairy et al. (Ref. 57)	2007	185	43 ± 15	24	7 F 4 or 6 mm	92	91	4	0
De Sisti et al. (Ref. 58)	2007	69	37 ± 15	18 ± 9	7 F 4 or 6 mm	87	93	21	0
Total	–	561	33 ± 11§	>3	–	92	94	12	0

*Long-term success rate in patients with acute successful results.
§The mean values are averaged out.

catheters. In a recent preliminary report [59], 30 patients underwent AV nodal modification using an 8-mm tip Freezor Max™. Immediate success was achieved in 100% of patients with transient 2:1 AV block occurring only in one patient. In a median follow-up period of 66 days (range 0–206 days), no patients experienced clinical recurrence.

To date, four published studies have compared the outcome of cryoablation with that of RF ablation (Table 15.2) [60–63]. Three of these studies [two randomized prospective [60, 61] and one retrospective [63]] elicited comparable immediate success rates for both modalities, while the remaining (retrospective) study [62] showed a higher primary failure rate for cryoablation.

Concerning the long-term outcomes, three studies showed a higher recurrence rate for cryoablation [61–63]. The results of these single-center series should be interpreted in light of the following limitations. First, 4-mm tip cryothermal catheters were utilized in the vast majority of the subject patients. It has been shown that the lesions made by these catheters are smaller in volume than those created by RF catheters of the same size [15]. Secondly, RF technology has been utilized for ablation of cardiac arrhythmias since 1990, whereas transcatheter cryoablation became available just a few years ago. Therefore, it is possible that the ablation operators in these studies were more familiar with RF than cryoablation and their learning curves for the latter modality had not reached a plateau by the time the studies were conducted. Finally, only two of these studies were done in a randomized prospective fashion. For a more meaningful comparison between these two modalities, 6- or 8-mm tip catheters should also be included in larger, randomized prospective studies.

Potential Complications

Regardless of the ablation modality, the AV nodal slow pathway ablation is considered a safe procedure in which the incidence of complications is low. Aside from the general complications associated with the invasive EP studies, adverse outcomes specifically related to AV nodal modification are due to inadvertent block along the AV node-His bundle axis. These conduction disturbances may include first-degree AV bock (PR interval of longer than 220 msec), second-degree Mobitz I (Wenckebach periodicity), second-degree Mobitz II (2:1 AV block), third-degree AV block, and right bundle branch block.

Among several published studies in pediatric as well as adult populations, not one has reported permanent third-degree AV block in cryoablation of AV nodal slow pathways (Table 15.1). The conduction abnormalities occurring with cryoablation are usually transient with spontaneous recovery occurring in a matter of a few seconds to several minutes [30, 50–58]. This lack of complete AV block is clearly a major advantage of cryoablation over RF ablation, in which 1.3–2% incidence of complete AV block has been reported [64, 65].

When to Consider Switching to RF Ablation

In the following circumstances, one might consider RF ablation as the first modality or switching from cryoablation to RF ablation if the former has been proven unsuccessful: (i) Clinically documented SVT with no reproducibly inducible AVNRT, dual pathway physiology, or "PR $\geq$ RR" feature demonstrable. (ii) AVNRT recurrence after a seemingly successful cryoablation attempt. (iii) Incidental and persistent injury to the AV nodal fast pathway with no subsequent dual pathway physiology or "PR $\geq$ RR" feature demonstrable. (iv) A total procedure time in excess of two hours with AVNRT still remaining inducible.

Cryomapping of the Fast Pathway

Fast pathway ablation was introduced in the late 1980s as the first technique for AV nodal modification in treating patients with AVNRT. However, because of its unacceptably high incidence of permanent AV block [64] this technique became abandoned rather quickly and was superseded by the emergence of slow pathway ablation.

The fast pathway technique has not been revisited thoroughly, despite the availability of cryoablation. Therefore, the data on the safety and efficacy of fast pathway cryoablation is scarce [66]. Nonetheless, because the cryothermal mediated AV block is usually transient and reversible, cryomapping of the AV nodal fast pathway may be contemplated in rare circumstances of AVNRT where the slow pathway

Table 15.2 Cryoablation Versus Radiofrequency Ablation.

			Cryoablation				*Radiofrequency Ablation*			
Study	*Year published*	*Follow-up*	*Number (patients)*	*Catheter-tip size*	*Immediate/ long-term success (%)*	*AV block (%)*	*Number (patients)*	*Catheter-tip size*	*Immediate/ long-term success (%)*	*AV block (%)*
Kimman et al.[60]§	2004	13 ± 7 months	30	4 mm	94/90	0	33	4 mm	97/90	0
Zrenner et al.[61]§	2004	246 days	100	4 mm	97/91	0	100	4 mm	98/99	0
Gupta et al.[62]¶	2006	66 ± 12 days	71	4–6 mm	85/80	0	71	4 mm	97/94	1
Collins et al.[63]*¶	2006	6–12 months	57	4 mm	95/92	0	60	4 mm	100/98	0

*Pediatric population.
§Randomized prospective study.
¶Retrospective study.

ablation cannot be accomplished [66]. Furthermore, cryoablation of the fast pathway may be relevant in some forms of preexcited tachycardias in which the AV nodal fast pathway is used as the retrograde limb of the tachycardia.

A specific form of preexcited tachycardia is present in patients who have an atriofascicular pathway, with the AV nodal fast pathway functioning as a part of the retrograde limb of the reentrant circuit [43]. Ordinarily, the atriofascicular pathway itself is targeted for ablation. However, cryoablation of the fast pathway may be considered if ablation of the atriofascicular pathway cannot be accomplished due to a procedural failure or technical difficulty in demonstrating the antegrade conduction via the accessory pathway. The latter situation may arise when a transient but long lasting (i.e., several hours) trauma to the accessory pathway occurs during manipulation of the intracardiac catheters.

Technically, for cryothermal mapping and ablation of the fast pathway, the catheter is maintained with a clockwise torque at the anterior aspect of the tricuspid septal annulus where a large atrial electrogram along with a small (<0.1 mV) or no His bundle potential is recorded. Cryomapping of this area is switched to cryoablation mode if a gradual PR interval prolongation is observed during sinus rhythm with no dropped P wave. The subsequent cryoablation should also be carried out during sinus rhythm under close electrocardiographic surveillance to assure that the integrity of AV conduction remains intact. The procedure is considered successful if a complete loss of retrograde fast pathway conduction during ventricular pacing is accompanied by noninducibility of a tachycardia. Finally, a word of caution: Fast pathway cryoablation should be performed only during sinus rhythm with termination of the cryothermal application occurring immediately after a second- or third-degree AV block is noted.

Conclusion

Cryomapping is a unique way of identifying the critical limb(s) of the AVNRT circuit for successful cryoablation. Because the overall safety and efficacy of cryoablation are comparable to those of RF ablation, all electrophysiologists involved in ablation of cardiac arrhythmias should become familiarized with cryothermal mapping and cryoablation of AVNRT. This catheter-based technology may be used as the primary modality or in certain situations, as an alternative to RF ablation when the latter carries a higher risk of third degree AV block.

Acknowledgment

The author would like to express his gratitude and appreciation to Jean Woerner for her excellent technical assistance.

References

1 Scherf D. Response of focus of origin of experimental ventricular extrasystole to warming and cooling. *Proc Soc Exp Biol Med* 1942; **51**: 224–26.
2 Hass GM, Taylor CB. A quantitative hypothermal method for production of local injury to tissue. *Arch Pathol* 1948; **45**: 563–80.
3 Taylor CB, Davis CB, Vawter GF, Hass GM. Controlled myocardial injury produced by a hypothermal method. *Circulation* 1951; **3**: 239–53.
4 Cobb FR, Blumenschein SD, Sealy WC, et al. Surgical interruption of the bundle of Kent in a patient with Wolff–Parkinson–White syndromes. *Circulation* 1968; **38**: 1028–29.
5 Turina MI, Babotai I, Wegmann W. Production of chronic atrioventricular block in dogs without thoracotomy. *Cardiovasc Res* 1968; **2**: 389–93.
6 Steiner C, Kovalik ATW. A simple technique for production of chronic complete hear block in dogs. *J Appl Physiol* 1968; **25**: 6331–32.
7 Mazur M, Causes of injury in frozen and thawed cells. *Fed Proc* 1965; **24**: 5175–82.
8 Gill W, Fraser J, Carter DC. Repeated freeze–thaw cycles in cryosurgery. *Nature* 1968; **219**: 410–13.
9 Mazur P. Cryobiology: the freezing of biological systems. *Science* 1970; **168**: 939–49.
10 Cooper IS, Samra K, Wisniewska K. Effects of freezing on major arteries. *Stroke* 1971; **2**: 471–82.
11 Mikat EM, Hackel DB, Harrison L, et al. Reaction of the myocardium and coronary arteries to cryosurgery. *Lab Invest* 1977; **37**: 632–41.
12 Harrison L, Gallagher JJ, Kasell J, et al. Cryosurgical ablation of the A-V node–His bundle: a new method for producing A-V block. *Circulation* 1977; **55**: 463–70.
13 Gallagher JJ, Sealy WC, Anderson RW, et al. Cryosurgical ablation of accessory atrioventricular connections: a method for correction of the preexcitation syndrome. *Circulation* 1977; **55**: 471–79.
14 Gallagher JJ, Anderson RW, Kasell J, et al. Cryoablation of drug-resistant ventricular tachycardia in a patient with a variant of scleroderma. *Circulation* 1978; **57**: 190–97.

15 Klein GJ, Sealy WC Pritchett EL, et al. Cryosurgical ablation of the atrioventricular node His bundle: long-term follow-up and properties of the junctional pacemaker. *Circulation* 1980; **61**: 8–15.

16 Camm J, Ward DE, Spurrell RA, et al. Cryothermal mapping and cryoablation in the treatment of refractory cardiac arrhythmias. *Circulation* 1980; **62**: 67–74.

17 Cox J, Holman W, Cain W. Cryosurgical treatment of atrioventricular node reentrant tachycardia. *Circulation* 1987; **76**: 1329–36.

18 Caceres J, Werner P, Jazayeri M, et al. Efficacy of cryosurgery alone for refractory monomorphic sustained ventricular tachycardia due to inferior wall infarction. *J Am Coll Cardiol* 1988; **11**: 1254–59.

19 Doll N, Kiaii BB, Fabricius AM, et al. Intraoperative left atrial ablation (for atrial fibrillation) using a new argon cryocatheter: early clinical experience. *Ann Thorac Surg* 2003; **76**: 1711–15.

20 Vedel J, Frank R, Fontaine G, Grosgogeat Y. Bloc auriculoventriculaire intra-Hisien définitive induit au cours d'une exploration endo cavitaire droite. *Arch Mal Coeur* 1979; **72**: 107–111.

21 Gallagher JJ, Svenson RH, Kasell JH, et al. Catheter technique for closed chest ablation of the atrioventricular conduction system. *N Engl J Med* 1982; **306**: 194–200.

22 Scheinman MM, Morady F, Hess DS, Gonzalez R. Catheter induced ablation of the atrioventricular junction to control refractory supraventricular arrhythmias. *JAMA* 1982; **248**: 851–55.

23 Pritchett LC, Anderson RR, Benditt DG, et al. Reentry within the atrioventricular node: surgical cure with preservation of of atriventricular conduction. *Circulation* 1979; **60**: 440

24 Holman WL, Ikeshita M, Lease JG, Ferguson Jr TB, Lofland GK, Cox JL. Alteration of anterograde atrioventricular conduction by cryoablation of periatrioventricular nodal tissue: implication for the surgical treatment of atrioventricular nodal reentry tachycardia. *J Thorac Cardiovasc Surg* 1984; **88**: 67–75.

25 Theodorescu D. Cancer cryotherapy: evolution and biology. *Rev Urol* 2004; **6**: S9–19.

26 Gillette PC, Swindle MM, Thompson RP, et al. Transvenous cryoablation of the bundle of His. *PACE* 1991; **14**: 504–10.

27 Fujino H, Thompson RP, Germroth PG, et al. Histologic study of chronic catheter cryoablation ofatrioventricular conduction in swine. *Am Heart J* 1993; **125**: 1632–37.

28 Dubuc M, Talajic M, Roy D, et al. Catheter cryoablation: a novel technology for ablation of cardiac arrhythmias. *Circulation* 1996; **94**: I–557 Abstract.

29 Dubuc M, Talajic M, Roy D, et al. Feasibility of cardiac cryoablation using a transvenous steerable electrode catheter. *J Interven Cardiol Electrophysiol* 1998; **2**: 285–92.

30 Skanes AC, Dubuc M, Klein GJ et al. Cryothermal ablation of the slow pathway for the elimination of atrioventricular nodal reentrant tachycardia. *Circulation* 2000; **102**: 2856–60.

31 Mazur P. Kinetics of water loss from cells at subzero temperatures and the likelihood of intracellular freezing. *J Gen Physiol* 1963; **47**: 347–69

32 Mazur P. Freezing of living cells: mechanisms and implications. *Am J Physiol* 1984; **247**: C125–42.

33 Lustgarten DL, Keane D, Ruskin J. Cryothermal ablation: mechanism of tissue injury and current experience in the treatment of tachyarrhythmias. *Prog Cardiovasc Dis* 1999; **41**: 481–98.

34 Theodorescu D. Cancer cryotherapy: evolution and biology. *Rev Urol* 2004; **6**: S9–19.

35 Khairy P, Chauvt P, Lehmann J, et al. Lower incidence of thrombus formation with cryoenergy versus radiofrequency catheter ablation. *Circulation* 2003; **107**: 2045–50.

36 Skanes AC, Jones DL, Teefy P, Guiraudon C, Yee R, Khran AD, Klein GJ. Safety and feasibility of cryothermal ablation within the mid- and distal coronary sinus. *J Cardiovasc Electrophysiol* 2004; **15**: 1319–23.

37 Aoyama H, Nakagawa, Pitha JV, et al. Comparison of cryothermia and radiofrequency current in safety and efficacy of catheter ablation within the canine coronary sinus close to the left circumflex coronary artery. *J Cardiovasc Electrophysiol* 2005; **16**: 1218–26.

38 Timmermans C, Ayers GM, Crijns HJ, Rodriguez LM. Randomized study comparing radiofrequency ablation with cryoablation for the treatment of atrial flutter with emphasis on pain perception *Circulation* 2003; **107**: 1250–52.

39 Jazayeri M, Hempe SL, Sra JS, et al. Selective transcatheter ablation of the fast and slow pathways using radiofrequency energy in patients with atrioventricular nodal reentrant tachycardia. *Circulation* 1992; **85**: 1318–28.

40 Jazayeri MR, Sra JS, Deshpande SS, et al. Electrophysiological spectrum of atrioventricular nodal behavior in patients with atrioventricular nodal reentrant tachycardia undergoing selective fast or slow pathway ablation. *J Cardiovasc Electrophysiol* 1993; **4**: 99–111.

41 Jazayeri MR. Atrioventricular nodal reentrant tachycardia: characterization of the reentrant circuit before and after selective fast and slow pathway ablation. In: Shenasa M, Borggrefe M, Breithardt G, eds. *Cardiac Mapping*. Futura Publishing Co, Inc., Mount Kisco, NY, 1993: 411–34.

42 Jazayeri MR, Sra JS, Akhtar M. Atrioventricular nodal reentrant tachycardia: electrophysiologic characteristics, therapeutic interventions, and specific reference to anatomic boundary of the reentrant circuit. *Cardiol Clin* 1993; **11**: 151–81.

43 Jazayeri, MR, Deshpande S, Dhala A, Blanck Z, Sra J, Akhtar M. Transcatheter mapping and radiofrequency

ablation of cardiac arrhythmias. *Curr Problems Cardiol* 1994; **19**: 285–396.

44 Montenero A. Bruno N, Antonelli A et al. Comparison between a 7 French 6-mm tip cryothermal catheter and a 9 French 8-mm tip cryothermal catheter for cryoablation treatment of common atrial flutter. *J Interven Cardiac Electrophysiol* 2005; **13**: 59–69.

45 Barker JH 2nd, Plumb VJ, Epstein AE, Kay GN. PR/RR interval ratio during rapid atrial pacing: a simple method for confirming the presence of slow pathway conduction. *J Cardiovasc Electrophysiol* 1996; **7**: 287–94.

46 Collins KK, Dubin AM, Chiesa NA, McDaniel GM, Van Hare GF. Cryoablation in pediatric atrioventricular nodal reenter: electrophysiologic effects on atrioventricular nodal conduction. *Heart Rhythm* 2006; **3**: 557–63.

47 Papagiannis J, Tsoutsinos A, Kirvassilis G, et al. Nonfluoroscopic catheter navigation for radiofrequency catheter ablation of supraventricular tachycardia in children. *Pacing Clin Electrophysiol* 2006; **29**: 971–78.

48 Earley MJ, Showkathali R, Alzetani M, et al. Radiofrequency ablation of arrhythmias guided by nonfluoroscopic catheter location: a prospective randomized trial. *Eur Heart J* 2006; **27**: 1223–29.

49 Tuzcu V. A nonfluoroscopic approach for electrophysiology and catheter ablation procedures using a threedimentional navigation system. *Pacing Clin Electrophysiol* 2007; **30**: 519–25.

50 Riccardi R, Gaita F, Caponi D, et al. Percutaneous catheter cryothermal ablation of atrioventricular nodal reentrant tachycardia: efficacy and safety of a new ablation technique. *Ital Heart J* 2003; **4**: 35–43.

51 Friedman PL, Dubuc M, Green MS, et al. Catheter cryoablation of supraventricular tachycardia: results of the multicenter prospective "frosty" trial. *Heart Rhythm* 2004; **1**:129–38.

52 Kirsh JA, Gross GJ, O'Connor S, Hamilton RM. Transcatheter cryoablation of tachyarrhthmias in children: initial experience from an international registry. *J Am Coll Cardiol* 2005; **45**: 133–36.

53 Miyazaki A, Blaufox AD, Fairbrother DL, Saul JP. Cryoablation for septal tachycardia substrates in pediatric patients: mid-term results. *J Am Coll Cardiol* 2005; **45**: 581–88.

54 Kriebel T, Broistedt C, Kroll M, Jux C, Paul, T. Safety and efficacy of cryoablation in the therapy of supraventricular tachycardias in children and adolescents. *J Cardiovasc Electrophysiol* 2005; **16**: 960–66.

55 Drago F, De Santis A, Grutter G, Silvetti MS. Transvenous cryothermal catheter ablation of re-entry circuit located near the atrioventricular junction in pediatric patients: efficacy, safety, and mid-term follow-up. *J Am Coll Cardiol* 2005; **45**: 1096–103.

56 Jensen-Urstad M, Tabrizi F, Kennebäck G, Wredlert, C, Klang C, Insulander P. High success rate with cryomapping and cryoablation of atrioventricular nodal reentry tachycardia. *Pacing Clin Electrophysiol* 2006; **29**: 487–89.

57 Khairy P, Novak PG, Guerra PG, et al. Cryothermal slow pathway modification for atrioventricular nodal reentrant tachycardia. *Europace* 2007; **9**: 909–14.

58 De Sisti A, Tonet J, Barakett N, Lacotte J, Leclercq JF, Frank R. Transvenous cryo-ablation of the slow pathway for the treatment of atrioventricular nodal reentrant tachycardia: a single-centre initial experience study. *Europace* 2007; **9**: 401–6.

59 Dumont F, Khairy P, Guerra PG, et al. Initial experience with an 8-mm tip cryocatheter for slow pathway modification in AV nodal reentrant tachycardia (AVNRT). *Heart Rhythm* 2007; **4**: S113.

60 Kimman GP, Theuns DA, Szili-Torok T, Scholten MF, Res JC, Jordaens LJ. CRAVT: a prospective, randomized study comparing transvenous cryothermal and radiofrequency ablation in atrioventricular nodal reentrant tachycardia. *Eur Heart J* 2004; **25**: 2232–37.

61 Zrenner B, Dong J, Schreieck J, et al. Transvenous cryoablation versus radiofrequency ablation of the slow pathway for the treatment of atrioventricular nodal reentrant tachycardia: a prospective randomized pilot study. *Eur Heart J* 2004; **25**: 2226–31.

62 Gupta D, Al-Lamee RA, Earley MJ, et al. Cryoablation compared with radiofrequency ablation for atrioventricular nodal reentrant tachycardia: analysis of factors contributing to acute and follow-up outcome. *Eurpace* 2006; **8**: 1022–26.

63 Collins KK, Dubin AM, Chiesa NA, Avasarala K, Van Hare GF. Cryoablation versus radiofrequency ablation treatment of pediatric atrioventricular nodal reentrant tachycardia: initial experience with 4-mm cryocatheter. *Heart Rhythm* 2006; **3**: 564–70.

64 Hindricks G. Complications of radiofrequency of catheter ablation of arrhythmias. *Eur Heart J* 1993; **14**: 1644–53.

65 Calkins H, Yong P, Miller JM, et al. The Ataker Multicenter Investigators Group Catheter ablation of accessory pathways, atrioventricular nodal reentrant tachycardia, and the atrioventricular junction: final results of a prospective, multicenter clinical trial. *Circulation* 1999; **99**: 262–70.

66 De Ponti R, Tritto M, Lanzotti ME, et al. Successful selective ablation of fast atrioventricular node pathway by cryothermal energy application. *Pacing Clin Electrophysiolo* 2004; **27**: 1170–71.

16

CHAPTER 16

Mapping and Ablation of AVNRT and Its Subtypes

Stephan Willems, MD, *Daniel Steven*, MD, *Boris Lutomsky*, MD, *Imke Drewitz*, MD, *Helge Servatius*, MD, *Thomas Meinertz*, MD, *Thomas Rostock*, MD

University Heart Center, Hamburg, Germany

Summary

AV nodal reentrant tachycardia is even now one of the classic indications in interventional electrophysiology. However, questions regarding pathophysiology, classification and optimal treatment strategies remain despite the high success rates of catheter ablation. These issues will be discussed in the present chapter. Although, adopted according to novel experimental and clinical studies it is yet consensus, that at least two modalities of ("slow and "fast") conduction are prerequisites for the establishment of an AVNRT circuit. These components of AVNRT are currently assumed to be areas with distinct electrophysiological characteristics rather than traditionally called "pathways" typically located at the superior (anterior) and inferior (posterior) part of the right atrial septum. Recently the importance of a left atrial input into the AV node has been highlighted by clinical mapping studies. Contemporary classification of AVNRT subtypes includes activation sequence and timing intervals. Additionally the presumed presence of a lower common pathway should be considered. The most frequent slow-fast form ("common type AVNRT") is characterized by a long A-H interval (>200 msec) and retrograde activation via the fast pathway at the superior septum above the tendon of Todaro (H-A < 70 msec) typically without evidence for a lower common pathway. In the presence of the slow-slow variant retrograde activation is detectable at the inferior septum or proximal coronary sinus. Antegrade fast pathway conduction (A-H interval < 200 msec) and earliest retrograde activation occurring at the infero septal region is compatible with the "fast-slow" variant. Additionally, in the majority of slow-slow and fast-slow AVNRT variants criteria for a lower common pathway can be discovered. The presence of a lower common pathway is assumed, when the HA interval of the AVNRT is shorter than during ventricular pacing (delta HA > 15 msec). The discussion on the presence of an upper common pathway is still controversial since only occasional reports on the persistence of AVNRT despite VA conduction block exist. Criteria for selecting appropriate target sites for slow pathway (SP) modulation include anatomic aspects starting inferoseptally close to the ostium of the coronary sinus and electrogram

Cardiac Mapping, Third Edition Edited by Mohammad Shenasa, Gerhard Hindricks, Martin Borggrefe, and Günter Breithardt
 ISBN: 978-1-405-17572-2

characteristics (AV ratio, duration, SP potentials). When radiofrequency current delivery is applied in a controlled (eventually titrated) fashion and is monitored thoroughly AVNRT can be abolished without AV block (<1%) in almost all cases including the elderly with prolonged PR intervals at baseline. Thus, AVNRT is not only well amenable for interventional treatment with a very favourable risk-benefit ratio but can also be more precisely characterised due to recent mapping studies.

Introduction

Mapping and ablation of AV nodal reentrant tachycardia (AVNRT) was one of the first targets in the history of interventional electrophysiology, especially after introducing radiofrequency current as the preferred energy source for selective AV node modulation [1, 2]. Despite the growing number of ablation procedures aimed at treatment of atrial fibrillation, AV nodal modulation for AVNRT is still among the most frequent daily indications in the EP lab.

Interventional treatment of AVNRT has emerged as the established first-line therapy in symptomatic patients, supported by the current guidelines [3]. However, despite the widespread application of this treatment modality there is still an ongoing debate on the exact location of the reentrant circuit [4–6]. This discussion underscores the fact that we routinely perform a procedure—effectively modulating the AV node adhering to the physiological AV nodal conduction—without knowing exactly which pathophysiological basis constitutes this beneficial effect.

Thus, questions persist regarding this complex arrhythmia, which is amenable interventional treatment, particularly with regard to the pathophysiological basis and the optimal mapping strategies. Of note, precise knowledge of contemporary criteria for differential diagnosis, especially in variants of AVNRT, and of mapping criteria associated with an effective and safe treatment modality, are crucial in order to maintain a high standard of care, especially for electrophysiologists in training or working in institutions with relatively low numbers of interventions.

Anatomy and Pathophysiological Basis

Because the exact localization of the reentrant circuit in AVNRT is still a matter of controversy, it is important to recall the anatomic landmarks and the histological basis of AVNRT. The triangle of Koch (Figure 16.1) consists of the tendon of Todaro at the posterior superior aspect, the coronary sinus ostium at the base and inferior aspect, and the tricuspid annulus located anteriorly [7]. The compact AV node at the anterior superior area and its posterior extensions constitutes the crucial anatomic region for AVNRT [7, 8]. Additionally, the importance of a left-sided input mediated via the interatrial septum and the superior aspect of the proximal coronary sinus has been highlighted by the group of Jackman and co-workers [9]. This also suggests an involvement of a relatively large area of the atrium to the tachycardia circuit.

The classic model of function dissociation of the AV node still has practical implications ever since the first description of dual AV nodal pathways by Mines in 1913 [10] and AVNRT with slow and fast pathway conduction by Moe in 1956 [11]. Later, the functional importance of perinodal inputs participating in various forms of AVNRT was underscored by intraoperative cryo mapping [12].

It is still well accepted that the circuit of AVNRT requires two different conduction modalities (slow and fast pathway). At the present time these traditional "pathways" are assumed to be certain areas of different electrophysiological capabilities more than anatomically circumscribed connections. Although reentry involving slow and fast pathway conduction is the dominant mechanism of supraventricular tachycardias, simultaneous slow and fast pathway conduction can occur during sinus rhythm, mimicking atrial fibrillation.

Figure 16.2a shows the 12-lead ECG of a 59-year-old woman who was originally referred for pulmonary vein isolation in suspected drug refractory paroxysmal atrial fibrillation. However, analysis of the intracardiac electrogramms (Figure 16.2b) revealed a simultaneous conduction via the slow and fast "pathway" in terms of a "double-firing" AV

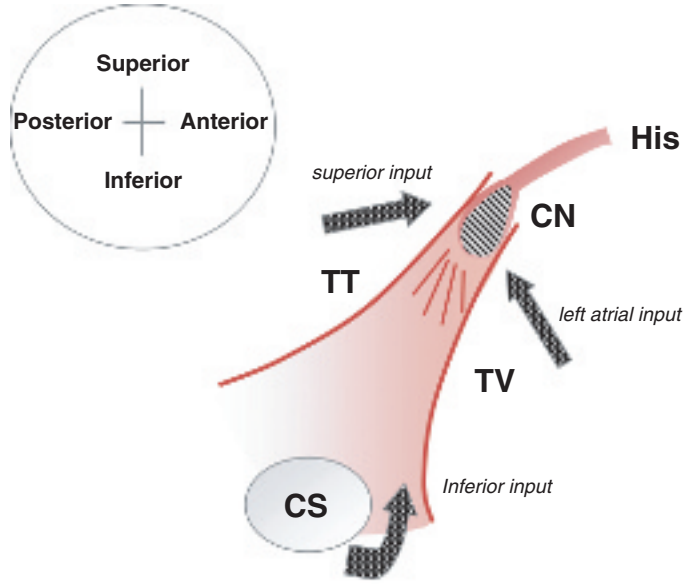

Figure 16.1 Simplified schematic illustration of the triangle of Koch and AV nodal inputs (arrows) in RAO projection. Landmarks are the tendon of Todaro (TT) at the posterior superior aspect, the coronary sinus ostium (CS) at the base, and the tricuspid annulus (TA) located anteriorly. The apex of the triangle is composed by the compact AV node (CN).

node, also underscoring the plausibility of the "dual pathway model."

Two different areas connecting the atrial myocardium to the His bundle have been identified by histological studies: The wide transitional cell area is divided into three zones located antero-superior to the AV node, as well as posterior inferior and into a deep layer coming from the left atrial septum. The other cell type constitutes the central part of the compact AV node. The AV nodal cells have been divided into different cells based on electrophysiologic characteristics with distinct action potential properties. Functionally identified AV nodal cells were classified as AN (atrionodal), N (nodal), and NH (nodal-His) in the experimental setting [13]. A gradual transmission from one cell area to the other with intermediated cells and intermediated action potentials with changes depending on the autonomic tone has been observed in isolated perfused preparations [8, 13].

However, in the clinical setting the AN cells are potentially correlated with transitional cells. These cells, although morphologically different from the working atrial fibers, are distributed within the nodal approaches as mentioned above [7]. The proximal atrial insertion of fast and slow pathways can be anatomically determined during retrograde conduction with an atrial exit of the fast pathway typically located at the superior (anterior) aspect of the atrial septum close to the site of recording a His bundle potential [9].

Retrograde fast pathway conduction can occur not only right supero septally with the tendon of Todaro constituting a line of block, but also mediated via a left atrial input based on left septal conduction and a myocardial coat located around the coronary sinus [9]. Recently, it has been also demonstrated that the left atrial input into the human AV node can be mediated via the mitral annulus by pacing maneuvers applied to the infero septal aspect. This study suggested that the mitral annulus can constitute a direct input into the AV nodal, not necessarily mediated via coronary sinus musculature [14].

Additionally, the earliest retrograde activation during fast pathway conduction can also be detected above the tendon of Todaro or in the right infero septal region close to the coronary sinus ostium [9, 12, 15, 16]. This variation of retrograde fast pathway conduction underscores the presence

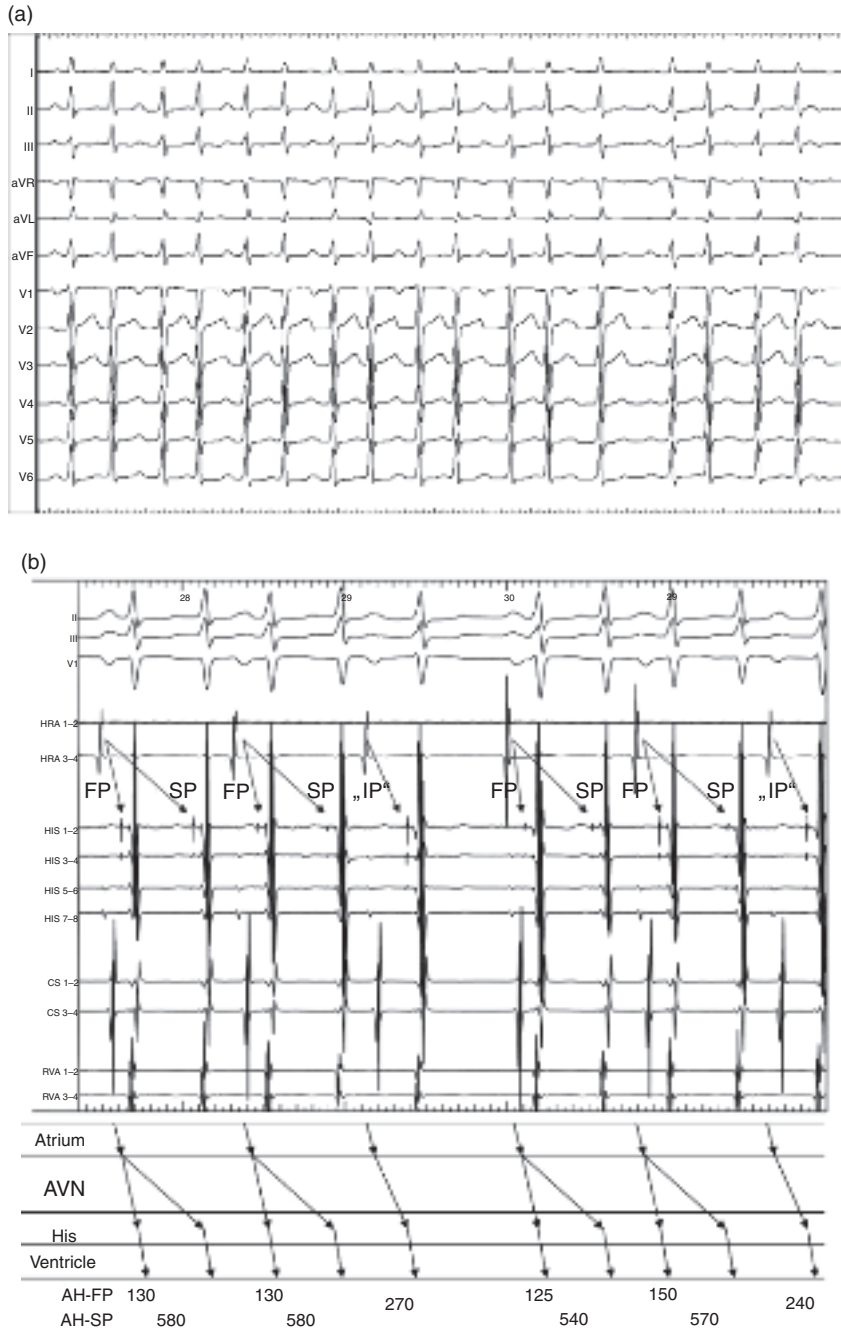

Figure 16.2 (a) A 59-years-old female patient with the suspected diagnosis of paroxysmal atrial fibrillation was referred for pulmonary vein isolation. The 12-lead surface ECG has been initially interpreted as paroxysms of atrial runs. However, careful examination revealed a fixed RR interval pattern in response to a positive P wave prior to every second QRS complex, indicating a "double firing" AV node during sinus rhythm. (b) Intracardiac electrograms reveal a 1:2 response to normal sinus rhythm via the AV node by a simultaneous conduction via fast und slow pathways. Of note, a double response only occurs at a time when the conduction first traverses to the ventricle via a fast pathway (FP) with a short AH interval (≤150 msec) and then via a slow pathway (SP) with a long HA interval (≥540 msec). On the other hand, a single AV node response to sinus rhythm only occurs when the conduction traverses through an "intermediate pathway" (IP) with an AH interval between 240 and 300 msec.

of areas with multiple conduction modalities resulting in various breakthrough sites, but not distinct pathways constituting nodal extensions. Retrograde slow pathway conduction typically occurs at the inferior (posterior) septum between the tricuspid annulus and coronary sinus ostium or infero septally inside the coronary sinus [9, 17].

Contemporary Classification of AVNRT Subtypes

Subforms of AVNRT are distinguishable on the basis of atrial activation sequence and timing intervals. Additionally, the presumed presence or absence of a lower common pathway can be a further criterion and will be discussed later [6]. In a recent publication of Heidbüchel and Jackman, 81% of 344 investigated patients observed antegrade slow and retrograde fast pathway conduction via the superior septum, initially suggesting the most frequently observed slow–fast form.

Using antegrade slow pathway conduction and earliest atrial activation at the inferior septum or proximal coronary sinus (slow–slow form), AVNRT was assumed in 14% of cases. An essential aspect for differentiation between slow–fast and slow–slow AVNRT is the importance of the earliest atrial activation and not only the H-A interval during tachycardia, which can be confusingly short despite retrograde conduction via a slow pathway. Additionally, the presence or absence of a lower common pathway was systematically assessed. Subsequently, the following criteria have been suggested and were applied by Heidbüchel and Jackman [6]

For the presence of slow–fast AVNRT: (i) Antegrade conduction via a slow pathway with an A-H interval during tachycardia of >200 msec. (ii) Retrograde conduction via the fast pathway documented by earliest H-A activation in the superior septum above the tendon of Todaro. (iii) An H-A interval during AVNRT <70 msec. Generally no evidence for a lower common pathway is present in these subtypes.

Slow–slow AVNRT is characterized by antegrade conduction via the slow pathway with an A-H interval >200 msec and earliest retrograde conduction via the slow pathway at the inferior septum or proximal coronary sinus. The H-A interval is usually >70 msec and there is evidence for a significant lower common pathway. However, the H-A intervals show a great overlap between slow–fast and slow–slow AVNRT, not reliably allowing an exact differentiation between both entities.

During fast–slow AVNRT the AH interval is <200 msec which is compatible with antegrade conduction via the fast pathway and the earliest atrial retrograde activation occurring in the infero septal region. Additionally, evidence for a lower common pathway is demonstrated in most of these cases. Interestingly, and important for the differential diagnosis in 94% of fast–slow AVNRT, one-to-one retrograde VA conduction during ventricular pacing at the tachycardia cycle length was absent, suggesting a lower common pathway during AVNRT entity [6].

These findings again stress that various ways of fast and slow conduction can be present in this setting and that the subtypes of AVNRT may also alternate using various pathways even in the same patient (Figures 16.2 and 16.3). Thus, the reentrant circuit in fast–slow AVNRT is not necessarily the reversal of the slow–fast AVNRT, which is underscored by the marked difference with regard to the evidence of a lower common pathway. Finally, 77% of all AVNRTs were categorized to be slow–fast, 12% the slow–slow, and 5% the fast–slow subtype using the above-mentioned criteria. However, 6.5% of the observed tachycardias demonstrated inconsistent findings not compatible with any of the classic AVNRT subtypes. Thus, a minor but substantial portion of patients with AVNRT cannot be classified by using the currently existing criteria [6].

Is There a Lower Common Pathway in AVNRT?

There is an ongoing debate on the presence or absence of an identifiable lower common pathway [6, 18, 19]. The functional length of the lower common pathway has been previously assessed by comparison of the H-A interval during tachycardia and ventricular pacing at the same cycle length. With this method the conduction path between the distal turnaround point of the antegrade and retrograde conduction pathway and the HIS bundle can be determined by comparing the retrograde atrial activation sequence during tachycardia and pacing [6].

(a)

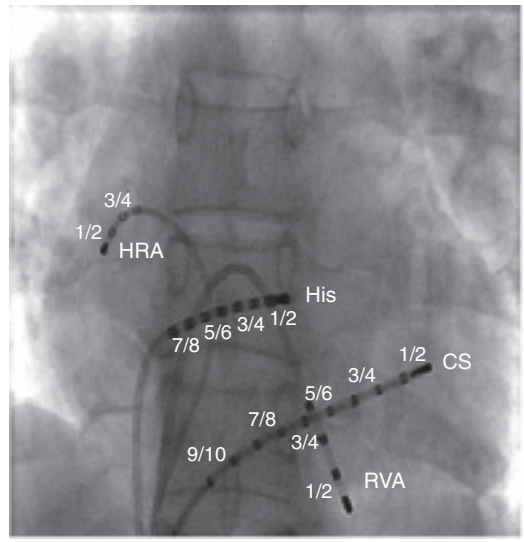
3/4
1/2
HRA
His
7/8
5/6
3/4
1/2
1/2
CS
3/4
5/6
7/8
3/4
9/10
1/2
RVA

(b)

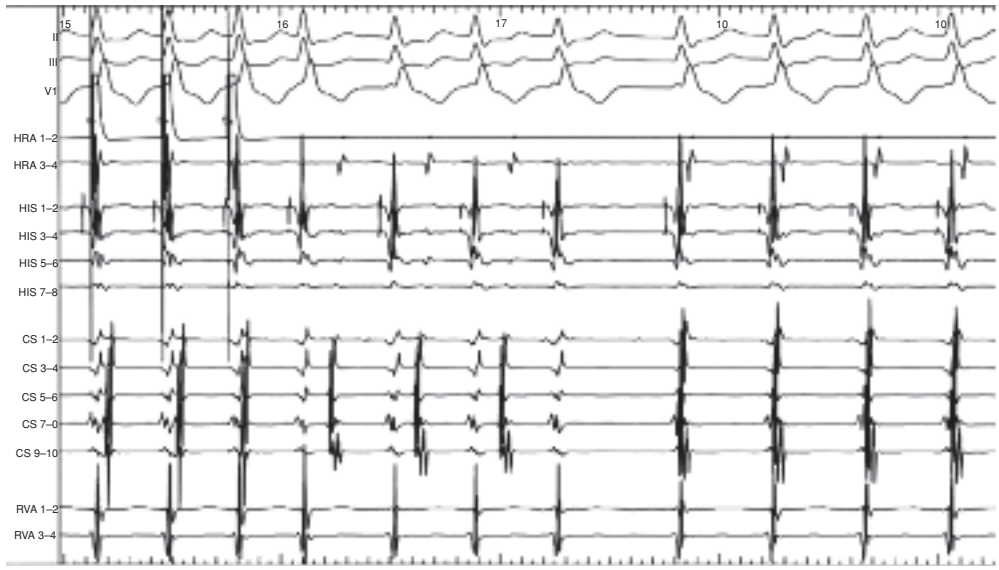
15
16
17
10
10
I
III
V1
HRA 1–2
HRA 3–4
HIS 1–2
HIS 3–4
HIS 5–6
HIS 7–8
CS 1–2
CS 3–4
CS 5–6
CS 7–0
CS 9–10
RVA 1–2
RVA 3–4

c)

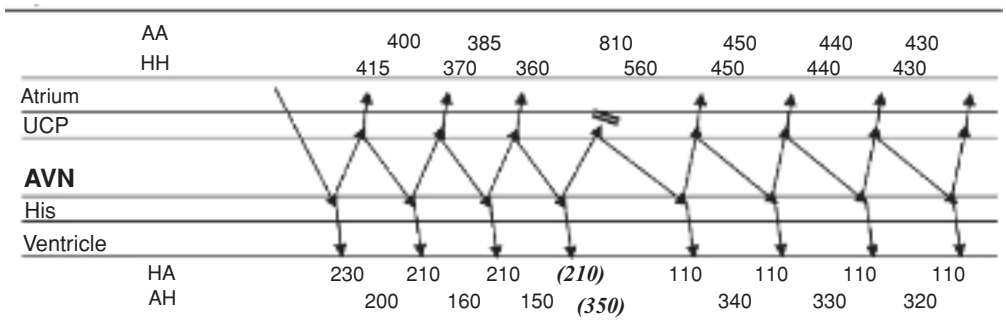
AA
HH
400
385
810
450
440
430
415
370
360
560
450
440
430
Atrium
UCP
AVN
His
Ventricle
HA
AH
230
210
210
(210)
110
110
110
110
200
160
150
(350)
340
330
320

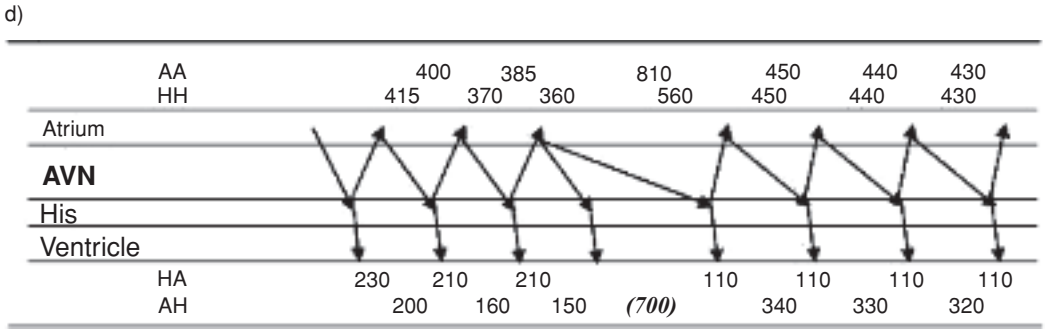

Figure 16.3 A 46-year-old female patient with a prolonged PR interval (225 msec) and a right bundle brunch block (QRS = 144 msec). The tracing illustrates the reproducible tachycardia induction with the above pattern. The proximal coronary sinus (CS) electrodes are intentionally placed in the CS ostium (CS 7/8) and in the right infero-paraseptal (CS 9/10) region (Figure 16.3a). Programmed atrial stimulation (S_1/S_2 – 330/300) induced a tachycardia with a long HA interval without an AH jump (Figure 16.3b). After the fourth retrograde rotation, an assumed pause occurred followed by a tachycardia sequence change. Of note, the pause has a HH interval of 560 msec, the sum of the HA interval (230 msec) during the first three consecutive beats prior to the "pause" and AH interval (330 msec) of the following sustained tachycardia. Thus, the induction mechanism indicates an uncommon type of AVNRT with different AH and HA conduction properties (e.g., slow–slow), which is blocked to atria after the fourth retrograde rotation (in an upper common pathway, UCP) and then changes to a common type AVNRT with a slow–fast sequence. An alternative explanation of the observed phenomenon might be an antegrade fast pathway and a retrograde "intermediate pathway" conduction for the first three consecutive beats. After the first three rotations, there then occurs retrograde block of the "intermediate pathway" due to the TCL acceleration, which allows the prior atrial electrogram to conduct down simultaneously both the fast (150 ms) and slow pathway (700 ms), resulting in a 1:2 AV node conduction ("double fire") that initiate typical slowfast AVNRT (16.3d).

In a current investigation, a delta HA interval of >15 msec was arbitrarily chosen as a cut-off point for the presence of an assumed lower common pathway [6]. In the presence of a lower common pathway during tachycardia there is simultaneous conduction from the lower turnaround of the circuit to the atrium and to the HIS bundle. During entrainment by parahisian pacing the impulse has to retrogradely depolarize the lower common pathway and the fast or slow pathway, respectively, leading to an H-A interval during tachycardia being shorter than during parahisian stimulation.

A lower common pathway has been previously suggested in the setting of most slow–fast AVNRT [18]. As addressed previously, Heidbüchel et al. recently demonstrated [6] that in most cases of slow–fast AVNRT no lower common pathway was detectable and that the presence of a lower common pathway is strongly associated with slow–slow and fast–slow subtypes of AVNRT. This finding primarily suggested that the evaluation of a lower common pathway could be used as an additional criterion for characterization of AVNRT sub forms.

Recently, the current concept of AVNRT characterization has been challenged by findings of Otomo and co-workers in patients with slow–fast AVNRT [4]. They hypothesized that in the one-third of slow–fast AVNRT resistant to adenosine triphosphate with regard to block of the retrograde fast pathway, a concealed atrio-hisian bypass tract may constitute the retrograde fast limb of the reentrant circuit. This assumption is based on the lack of a lower common pathway revealed by parahisian pacing in these cases [20]. Another finding suggesting that the lower turnaround of the reentrant circuit is located above the His bundle is the observation of a transient 2:1 block proximal to the His potential during the tachycardia (Figure 16.4) which can be observed occasionally [19].

Is There an Upper Common Pathway in AVNRT?

Discussion of this question is ongoing, and controversial, because only a few reports exist on the persistence of AVNRT despite the occurrence of different VA conduction block patterns indicating the

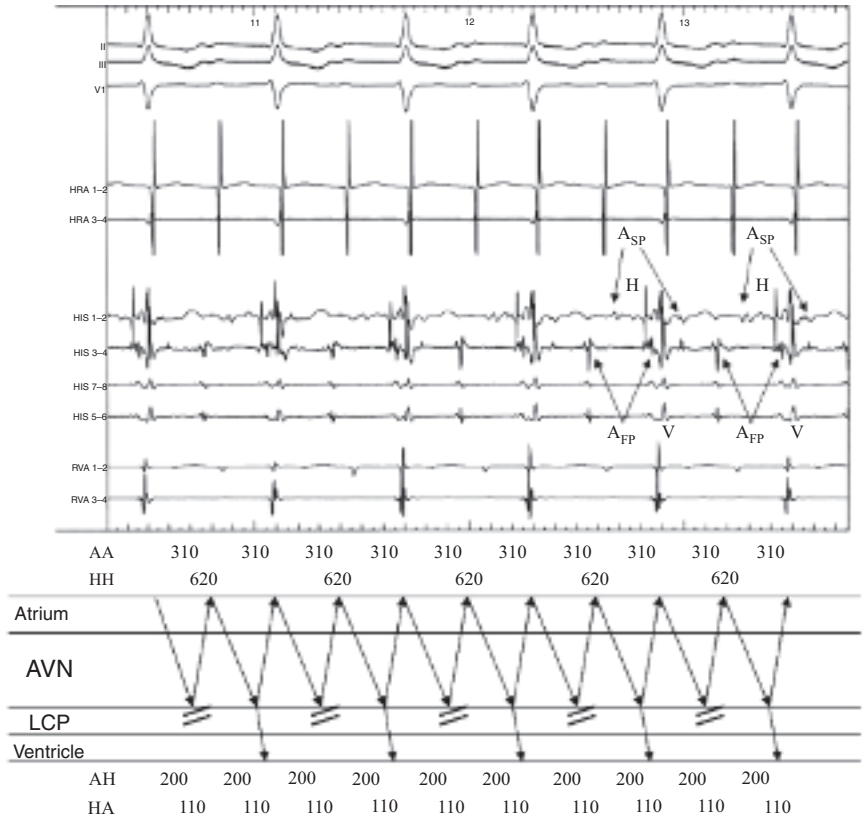

Figure 16.4 This patient presented with slow–fast AVNRT that changed spontaneously between a 1:1 and 2:1 conduction to the ventricles. In this tracing, a 2:1 AV response is visible with a His potential that only precedes the ventricular electrogram (so the level of the His is activated only in case of a ventricular activation) indicating a 2:1 supra-His block that which occurs due to a long refractory period of the lower common pathway (LCP), for example, in response to a short coupled ventricular premature beat during AVNRT with 1:1 conduction. Interestingly, in this tracing, the atrial far-field potentials of both the retrograde conducting fast pathway (FP) just prior to the atrial potential in the right atrium (HRA) and the antegrade conducting slow pathway (SP) immediately after the HRA potential are visible.

existence of an upper common pathway connecting a subatrial (intranodal) reentrant circuit to the atria [22].

Recently, Otomo and co-worker reported a unique series of six cases of AVNRT [4] demonstrating various VA conduction block patterns. Three different patterns were distinguished: Wenckebach type H-A block in four patients, 2:1 HA block in one patient, and variable H-A conduction time while the H-H interval remained constant in one patient (Figure 16.5). This led the authors to hypothesize that no substantial amount of atrial tissue is involved in the upper turnaround of the circuit, but that this area of the AVNRT circuit is composed of a functionally protected intranodal reentry with multiple atrial exits suggested by the observation of variable H-A intervals. Thus, it is possible that the reentrant circuit is located within a functionally protected region in the transitional zone between posterior AV nodal extension and atrial myocardium (Figure 16.5).

Mapping of AVNRT

For the purpose of catheter ablation, mapping is usually performed during sinus rhythm. However, in order to further characterize the reentrant circuit, for example, determination of the earliest retrograde, atrial excitation by activation mapping can be useful. Adding ventricular extrastimuli during

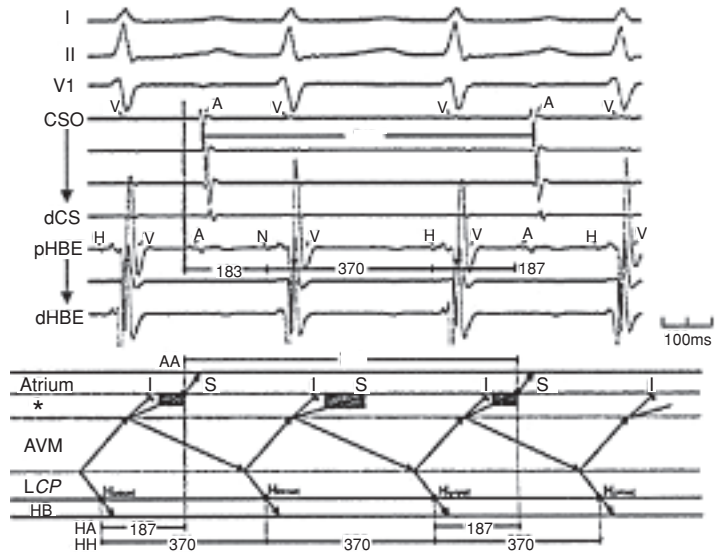

Figure 16.5 Surface and intracardiac electrograms during AVNRT with 2:1 HA conduction after radiofrequency current application. Perpetuation of AVNRT without depolarization of the perinodal atrium demonstrated that the atrium is not a necessary upper link between anterograde and retrograde limbs of the reentrant circuit. These findings are compatible with the concept of reentry within the functionally protected AV nodal area with two atrial exits and a lower common pathway. Ladder diagrams depict the activation sequences including gray areas highlight the postulated regions with functional delay or block. KEY: * = a zone of tissue responsible for 2:1 HA conduction; I = inferoparaseptal atrial exit; S = superoparaseptal exit. Reprinted with permission from Otomo et al., *Heart Rhythm* 3, May 2006.

the tachycardia cannot only help to exclude accessory pathway conduction, for example, in fast–slow AVNRT, but also unmasks the area of earliest retrograde activation.

Additionally special techniques for the identification of critical components of the reentrant circuit (i.e., subthreshold stimulation) have been introduced. Termination of the various AVNRT subtypes [23, 24] by subthreshold stimulation can be helpful to detect target sites for safe and effective slow pathway ablation. Selective termination by block of the anterograde (slow–fast form) or retrograde (fast–slow form) slow pathway is a prerequisite for the validity of this technique. Subthreshold stimulation can help to avoid the induction of inadvertent block of the fast pathway and thus potentially the complete antegrade AV conduction, especially in the setting of atypical fast pathway location as previously demonstrated [16].

Target sites for slow pathway ablation were initially described by the working groups of Haissaguerre [1] and Jackman [2] in 1992. Depending on the filtering technique the appearance of local electrograms recorded in the right infero-septal region varies markedly but is generally characterized by broad, fractionated atrial activity recorded before the appearance of a His potential. These characteristics are mediated by anisotropic conduction caused by heterogenic fiber orientation in this region around the coronary sinus ostium.

Jackman et al. described a distinct and sharp local electrogram resembling a His potential [2]. On the other hand, Haissaguerre et al. [1] attempted to map the area between the His bundle and the coronary sinus ostium in order to detect fractionated, late atrial electrograms in the area of the postero-inferior extension of the AV node (Figure 16.6). In general, the practical approach for slow pathway mapping is a combination of anatomic and electrogram guided strategy.

The electrophysiological landmarks such as the His bundle and coronary sinus ostium are delineated by temporary or continuous catheter placement throughout the procedure in the respective regions. Mapping is than started at the ventricular right infero-septal aspect. The catheter is withdrawn

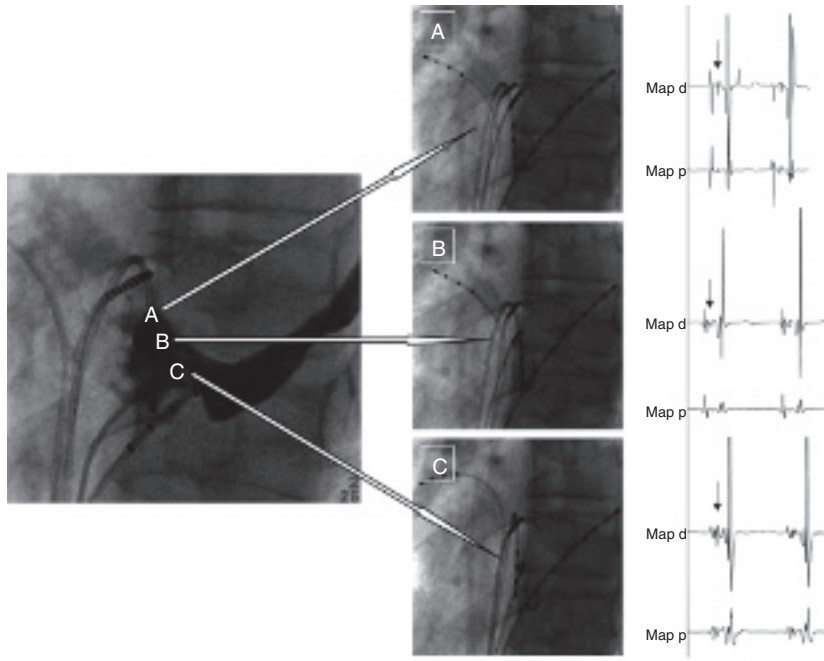

Figure 16.6 Sequential mapping of the triangle of Koch as described by Haissaguerre et al. [1]. The fluoroscopic images in a LAO 30° angulation demonstrates the classical recording sites of His and slow pathway potentials indicated by arrows. (a) An (early) atrial potential clearly separated from the sharp His potential is mapped in supero-septal (His) area. (b) By moving the catheter toward the mid-septal region a slow potential appears after the atrial potential which is earlier than the His potential. (c) In the infero-paraseptal region (the "classical" slow pathway area), the slow potential becomes more fractionated and earlier, while the atrial potential appears later than in the mid- and supero-septal region.

until an AV ratio of <0.5/0.7 with detectable atrial signal is reached. It is then attempted to record broad atrial electrograms with or without presumed "slow pathway potentials" reflecting not a specific pathway but typical conduction capabilities in the region around the coronary sinus ostium [1, 2, 23–26].

It is very important to assure that the terminal component of the fractionated atrial electrograms is not compatible with a His bundle potential. This can be verified by exactly analyzing the local electrograms obtained via the mapping catheter during premature atrial stimulation before energy delivery (Figure 16.6). When energy application around the coronary sinus ostium does not lead to the abolition of AVNRT, the steerable mapping catheter is maneuvered carefully to more mid-septal sites starting just above the level of the coronary sinus ostium by using the electrogram criteria mentioned previously.

Catheter Ablation

Temperature-controlled radiofrequency current (RFC) delivery [25, 26] is currently applied by using two strategies. Either RFC is applied with an initially chosen energy level of 40 W (even 50 W in some centers) or titration of the energy level starting at 20 W to 40 W before moving towards more mid-septal sites is performed. Although not investigated prospectively in a systematic fashion, the latter may lead to a more selective approach, avoiding very rapid junction ectopic rhythms and thus maybe also induction of AV block.

During energy application, accelerated junction and ectopic beats are predictors with high sensitivity but low specificity for effective energy application [1, 2]. Of cause, these rhythms have to be monitored carefully with regard to continuous 1:1 VA conduction. RFC has to be interrupted immediately in case of transient VA block. The endpoint of slow pathway

modification is as reliable as complete slow pathway ablation with regard to AVNRT recurrences as suggested by the follow-up of previous studies [1, 2, 26].

Another matter of debate is the question of whether a waiting period is required following achievement of the preselected endpoint (i.e., abolition of AVNRT induction with or without persistence of dual AV nodal physiology). In most EP laboratories, a waiting period of 20 to 30 min is the rule. Therefore, we conducted a study prospectively investigating this parameter. We included 130 patients with a recurrence rate of 4.6% in this ongoing trial, but we could not show any significant benefit regarding a postablational waiting period. Although the completion of the study has to be awaited, the preliminary results suggest that immediate procedure termination may be recommended in the future after achieving the acute endpoint.

The overall primary success rate of interventional treatment of AVNRT including its subtypes, is reported to be 97% and greater [1, 2, 23, 24, 26, 27] with a recurrence rate of <3% up to 6.9% [23–27]. The induction of inadvertent AV block still remains the most deleterious complication in the setting of interventional treatment of AVNRT. The overall rate is currently reported to be less than 1% [25–27]. However, catheter ablation of AVNRT was considered to be associated with an increased risk in the elderly with regard to AV block induction due to a preexisting attenuated conduction system [28].

Therefore, we recently summarized our data from 1998 to 2004 and divided patients into those with an age of <75 years and those with an age of >75 years. Despite significantly prolonged baseline values for PR interval and antegrade and retrograde Wenckebach cycle length in the elderly, no increased risk regarding AV block induction by RFC was observed [27]. In both groups the success rate was 100% and the rate of AV block (<1%) as well as the incidence of AVNRT recurrences (<3%) was not increased in the elderly. Nevertheless, overall procedure duration and fluoroscopy time was significantly longer in the elderly. This was probably due to the fact that underlying heart disease was more frequent in the elderly and that more time and care was taken to achieve a stable and accurate catheter position in patients with a preexisting prolonged PR interval. Thus, there is no reason to further withhold invasive therapy of AVNRT only because of advanced age in symptomatic patients.

In very rare cases, a left atrial, transseptal access may be required in order to selectively target the slow pathway [29]. However, this can also lead to ablation of the fast pathway [30] as it has been described for a right septal approach [16]. In general, only a few case reports have been published in this regard due to the effective conventional treatment in almost all patients. But it is important to bear in mind that this can be an alternative including ablation within the coronary sinus in selected cases resistant to conventional mapping and ablation.

Conclusion

Although, in most cases AVNRT and its subtypes are arrhythmias easily amenable for catheter ablation, the pathophysiological understanding still remains challenging. Nonetheless, clinical mapping studies recently helped to elucidate the exact confinement of the reentrant circuit by characterization of a lower and/or upper common pathway, adding pieces to a puzzle that is not yet completely a clear picture. Additionally, the subtypes of AVNRT are more clearly distinguishable not only on the basis of timing intervals, but also considering atrial activation sequence and the presence or absence of a lower common pathway. However, a small subset of AVNRT variants still remains to be undetermined or truly atypical [6]. The recent efforts to further characterize AVNRT should be a stimulus for future studies, because "easy to ablate, difficult to understand," should not be the final conclusion in this setting [5].

References

1 Haissaguerre M, Gaita F, Fischer B, et al. Elimination of atrioventricular nodal reentrant tachycardia using discrete slow potentials to guide applications of radiofrequency energy. *Circulation* 1992; **85**: 655–56.

2 Jackman WM, Beckman KJ, McClelland JH, et al. Treatment of supraventricular catheter ablation of slow pathway conduction. *N Engl J Med* 1992; **327**: 313–18.

3 Antman EM, Smith SC, Alpert JS, et al. ACC/AHA/ESC guidelines for the management of patients with supraventricular arrhythmias: executive summary, Task Force

Members. A Report of the American College of Cardiology/American Heart Association Task Force on Practice Guidelines and the European Society of Cardiology Committee for Practice Guidelines (Writing Committee to Develop Guidelines for the Management of Patients with Supraventricular Arrhythmias) Developed in collaboration with NASPE-Heart Rhythm Society. *Eur Heart J* 2003; **24**: 1857–97.

4 Otomo K, Okamura H, Noda T, et al. Unique electrophysiologic characteristics of atrioventricular nodal reentrant tachycardia with different ventriculoatrial block patterns: effects of slow pathway ablation and insights into the location of the reentrant circuit. *Heart Rhythm* 2006; **3**: 544–54.

5 Rostock T, Willems S. Atrioventricular nodal reentrant tachycardia: is there a "common pathway" to understanding the mechanism? *Heart Rhythm* 2006; **3**: 555–56.

6 Heidbüchel H, Jackman WM. Characterization of subforms of AV nodal reentrant tachycardia. *Europace* 2004; **6**: 316–29.

7 Mazgalev T, Ho SJ, Anderson RH. Anatomic-electrophysiologic correlations concerning the pathways for atrioventricular conduction.*Circulation* 2001; **103**: 2660–67.

8 Wu J, Wu J, Olgin J, et al. Mechanisms for atrioventricular nodal reentry and ventricular tachycardia determined form optical mapping of isolated perfused preparations. In: Zipes DP, Haissaguerre M, eds. *Catheter Ablation of Arrhythmias*, 2nd ed. Futura Publishing Co., Inc., Armonk, NY, 2002.

9 Otomo K, Wang Z, Lazarra R, et al. Atrioventricular nodal reentrant tachycardia: electrophysiological characteristics of four forms and implications for the reentrant circuit. In: Zipes DP, Jalife J, eds. *Cardiac Electrophysiology: From Cell to Bedside*, 3rd ed. W.B. Saunders Company, Philadelphia, 1999: 504–21.

10 Mines GR. On dynamic equilibrium of the heart. *J Physiol* 1913; **46**: 349–82.

11 Moe GK, Preston JB, Burlington H. Physiologic evidence for a dual A-V transmission system. *Circ Res* 1956; **4**: 357–75.

12 Keim S, Werner P, Jazayeri M, et al. Localization of the fast and slow pathways in atrioventricular nodal reentrant tachycardia by intraoperative ice mapping. *Circulation* 1992; **86**: 919–25.

13 Janse MJ, van Capelle FJL, Anderson RH, et al. Electrophysiology and structure of the atrioventricular node of the isolated rabbit heart. In: Wellens HJJ, Lie KI, Janse MJ, eds. *The Conduction System of the Heart*, Stenfert Kroese, Leiden, The Netherlands, 1976: 296–311.

14 Gonzalez MD, Cotreras LJ, Cardona F, et al. Demonstration of left atrial input to the atrioventricular node in humans. *Circulation* 2002; **106**: 2930–34.

15 McGuire MA, Bourke JP, Robotin MC, et al. High-resolution mapping of Koch's triangle using 60 electrodes in humans with atrioventricular junctional (AV nodal) reentrant tachcardia. *Circulation* 1993; **88**: 2315–28.

16 Engelstein ED, Stein KM, Markowitz SM, et al. Posterior fast atrioventricular node pathways: implications for radiofrequency catheter ablation of atrioventricular node re-entrant tachycardia. *J Am Coll Cardiol* 1996; **27**: 1098–105.

17 Sung RJ, Waxman HL, Saksena S, et al. Sequence of retrograde atrial activation in patients with dual atrioventricular nodal pathways. *Circulation* 1981; **64**: 1059–70.

18 Anselme F, Poty H, Cribier A, et al. Entrainment of typical AV nodal reentrant tachycardia using para-Hisian pacing: evidence for a lower common pathway within the AV node. *J Cardiovasc Electrophysiol* 1999; **10**: 655–61.

19 Li YG, Bender B, Bogun F, et al. Location of the lower turnaround point in typical AV nodal reentrant tachycardia: a quantitative model. *J Cardiovasc Electrophysiol* 2000; **11**: 34–40.

20 Otomo K, Suyama K, Okamura H, et al. Participation of a concealed atriohisian tract in the reentrant circuit of the slow–fast type atrioventricular nodal reentrant tachycardia. *Heart Rhythm* 2007; **4**: 703–10.

21 Schmitt C, Miller JM, Josephson ME. Atrioventricular nodal supraventricular tachycardia with 2:1 block above the bundle of His. *Pacing Clin Electrophysiol* 1988; **12**: 395–403.

22 Josephson ME, Miller JM. Atrioventricular nodal reentry: evidence supporting an intranodal location. *Pacing Clin Electrophysiol* 1993; **16**: 599–614.

23 Willems S, Rostock T, Shenasa M, et al. Subthreshold stimulation in variants of atrioventricular nodal reentrant tachycardia: electrophysiological effects and impact for guidance of slow pathway ablation. *Eur Heart J* 2004; **25**: 1249–56.

24 Willems S, Weiss C, Shenasa M, et al. Optimized mapping for slow pathway ablation guided by subthreshold stimulation: a randomized prospective study in patients with recurrent AV nodal reentrant tachycardia. *J Am Coll Cardiol* 2001; **37**: 1645–50.

25 Willems S, Shenasa H, Kottkamp H, et al. Temperature-controlled slow pathway ablation for treatment of atrioventricular nodal reentrant tachycardia using a combined anatomical and electrogram-guided strategy. *Eur Heart J* 1996; **17**: 1092–102.

26 Clague JR, Dagres N, Kottkamp H, et al. Targeting the slow pathway for atrioventricular nodal reentrant tachycardia: initial results and long-term follow-up in 379 consecutive patients. *Eur Heart J* 2001; **22**: 82–8.

27 Rostock R, Risius T, Ventura R, et al. Efficacy and safety of radiofrequency catheter ablation of atrioventricular nodal reentrant tachycardia in the elderly. *J Cardiovasc Electrophysiol* 2005; **16**: 608–10.

28 Boulos M, Hoch D, Schecter S, et al. Age dependence of complete heart block complicating radiofrequency ablation of the atrioventricular nodal slow pathway. *Am J of Cardiol* 1998; **82**: 390–91.

29 Jais P, Haissaguerre M, Shah DC, et al. Successful radiofrequency ablation of a slow atrioventricular nodal pathway on the left posterior atrial septum. *Pacing Clin Electrophysiol* 1999; **22**: 525–27.

30 Kobza R, Hindricks G, Tanner H, et al. Left-septal ablation of the fast pathway in AV nodal re-entrant tachycardia refractory to right septal ablation. *Europace* 2005; **7:** 149–53.

17 CHAPTER 17

New Observations on Mapping and Ablation of Atrial Flutter

Navinder S. Sawhney, MD, *Gregory K. Feld,* MD

University of California, San Diego, CA, USA

Summary

Type 1 atrial flutter (AFL) is a common atrial arrhythmia that is difficult to treat medically, and may cause severe symptoms or lead to serious complications, including embolic stroke, myocardial ischemia and infarction, and rarely a tachycardia induced cardiomyopathy due to rapid atrio-ventricular conduction. The electrophysiologic substrate underlying type 1 AFL is a combination of slow conduction velocity in the cavo-tricuspid isthmus (CTI), plus anatomical and/or functional conduction block along the crista terminalis and Eustachian ridge. This electrophysiologic substrate creates a reentrant path length that is long enough, relative to the average wavelength around the tricuspid valve annulus, to allow for sustained reentry.

As a result of the well-defined anatomical substrate and the pharmacological resistance of type 1 AFL, catheter ablation has emerged as a safe and effective first-line treatment. The most widely accepted, successful approach for curing type 1 AFL is an anatomically guided ablation of the CTI. Recent technological developments, including three-dimensional (3D) electro-anatomical contact and noncontact mapping, and the use of large-tip ablation electrode catheters with high-power generators, have produced nearly uniform efficacy without increased risk. This chapter will review the electrophysiology of human type 1 AFL, and the latest techniques for its diagnosis and ablation.

Atrial Flutter Terminology

Due to the variety of terms used to describe atrial flutter in humans, including type 1 AFL and type 2 AFL, typical and atypical atrial flutter, counterclockwise and clockwise atrial flutter, isthmus and nonisthmus dependent flutter, the Working Group of Arrhythmias of the European Society of Cardiology and the North American Society of Pacing and Electrophysiology published a consensus document in 2001 to standardize terminology for atrial flutter [1]. The terminology recommended by this working group to describe cavo-tricuspid isthmus-dependent, right atrial macroreentrant tachycardia, with either a counterclockwise or clockwise direction around the tricuspid valve annulus, was typical and reverse typical AFL, respectively [1]. The terms "typical" and "reverse typical AFL" will be used in this chapter, or "type 1 AFL" when referring to both.

Cardiac Mapping, Third Edition Edited by Mohammad Shenasa, Gerhard Hindricks, Martin Borggrefe, and Günter Breithardt
 ISBN: 978-1-405-17572-2

Pathophysiologic Mechanisms of Type 1 Atrial Flutter

The development of successful radiofrequency catheter ablation (RFCA) techniques for type 1 AFL was largely dependent on delineation of its electrophysiologic mechanism. Through the use of advanced electrophysiologic techniques, including intraoperative and transcatheter activation mapping [2–7], type 1 AFL was determined to be due to a macroreentrant circuit rotating in either a counterclockwise (typical) or clockwise (reverse typical) direction in the right atrium around the tricuspid valve annulus, with an area of relatively slow conduction velocity in the low posterior right atrium (Figure 17.1a,b).

The predominate area of slow conduction in the AFL reentry circuit has been shown to be in the CTI, through which conduction times may reach 80–100 msec, accounting for one-third to one-half of the AFL cycle length [9–11]. The CTI is anatomically bounded by the inferior vena cava and Eustachian ridge posteriorly and the tricuspid valve annulus anteriorly (Figure 17.1a,b), both of which form lines of conduction block or barriers delineating a protected zone of slow conduction in the reentry circuit [5, 12–14].

The presence of conduction block along the Eustachian ridge has been confirmed by demonstrating double potentials along its length during AFL (Figure 17.2a,b). Double potentials have also been recorded along the crista terminalis, suggesting that it too forms a line of block separating the smooth septal right atrium from the trabeculated right atrial free wall. Such lines of block, which may be either functional or anatomic, are necessary to create an adequate path length for reentry to be sustained and to prevent short-circuiting of the reentrant wavefront [13–16].

The medial CTI is contiguous with the interatrial septum near the coronary sinus ostium, and the lateral CTI is contiguous with the low lateral right atrium near the inferior vena cava (Figure 17.1a,b). These areas correspond electrophysiologically to the exit and entrance to the zone of slow conduction, depending on whether the direction of reentry is counterclockwise (CCW) or clockwise (CW) in the right atrium. The path of the reentrant circuit outside the confines of the CTI consists of a broad activation wavefront in the inter-atrial septum and right atrial free wall around the crista terminalis and the tricuspid valve annulus [12–16].

The slower conduction velocity in the CTI, relative to the interatrial septum and right atrial free wall, may be caused by anisotropic fiber orientation in the CTI [2, 9–11, 17, 18]. This may also predispose to development of unidirectional block in the CTI during rapid atrial pacing, and account for the observation that typical AFL is more likely to be induced when pacing is performed from the coronary sinus ostium, and conversely reverse typical AFL is more likely to be induced when pacing

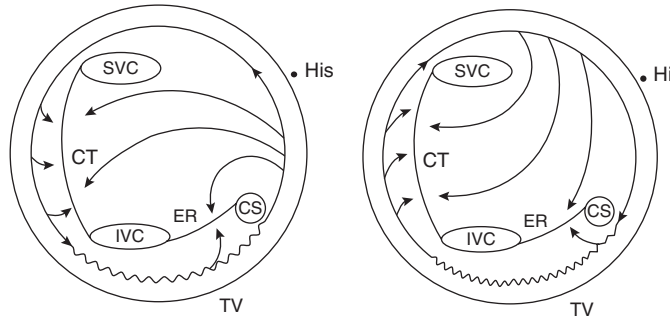

Figure 17.1 Schematic diagrams demonstrating the activation patterns in the typical (a) and reverse typical (b) forms of human type 1 AFL, as viewed from below the tricuspid valve annulus (TV) looking up into the right atrium. In the typical form of AFL, the reentrant wavefront rotates counterclockwise in the right atrium, whereas in the reverse typical form reentry is clockwise. Note that the Eustachian ridge (ER) and crista terminalis (CT) form lines of block, and that an area of slow conduction (wavy line) is present in the isthmus between the inferior vena cava (IVC) and Eustachian ridge and the tricuspid valve annulus. KEY: CS = coronary sinus ostium, His = His bundle, SVC = superior vena cava. Adapted from Ref [8].

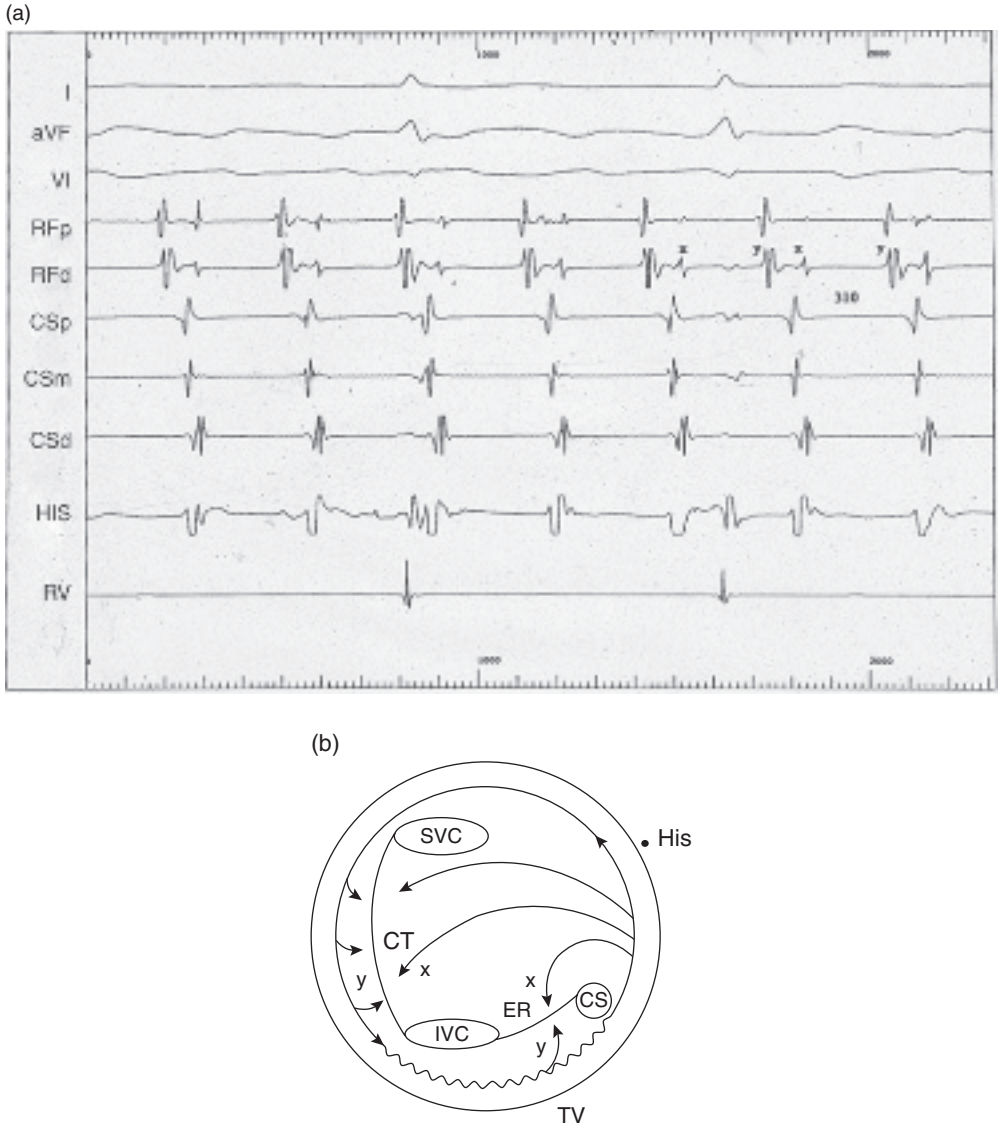

Figure 17.2 (a) Schematic diagram demonstrating the locations where double potentials (*x*, *y*) are typically recorded during typical AFL, along the Eustachian ridge and crista terminalis. (b) Double potential electrogram recordings from an ablation catheter (RFp&d) positioned at the Eustachian ridge during typical AFL. KEY: I, aVF,V1 = surface ECG leads; RFp&d = proximal and distal bipolar recordings from the ablation catheter; CSp-d = proximal to distal coronary sinus electrogram recordings; RV = right ventricular electrogram recording. Adapted from Ref [15].

from the low lateral right atrium [19–21]. The predominate clinical presentation is typical AFL, likely because the trigger(s) commonly arise from the left atrium in the form of premature atrial contractions or nonsustained atrial fibrillation [22], which conduct to the right atrium via the coronary sinus or interatrial septum and enter the CTI medially, resulting in clockwise unidirectional block in the CTI with resultant initiation of counterclockwise typical AFL.

ECG Diagnosis of Type 1 Atrial Flutter

The surface 12-lead ECG is helpful in establishing a diagnosis of type 1 AFL, particularly the typical form, with an inverted saw-tooth F wave pattern in the inferior ECG leads II, III, and aVF, low-amplitude biphasic *F*-waves in leads I and aVL, an upright *F*-wave in precordial lead V1, and an inverted *F*-wave in lead V6. In contrast, in reverse typical AFL, the *F*-wave pattern on the 12-lead ECG is less specific, often with a sine wave pattern in the inferior ECG leads (Figure 17.3a,b).

The determinants of *F*-wave pattern on ECG are largely dependent on the activation pattern of the left atrium, with inverted *F*-waves in the inferior ECG leads in typical AFL resulting from activation of the left atrium initially posterior near the coronary sinus, and upright *F*-waves inscribed in the inferior ECG leads in reverse typical AFL as resulting from activation of the left atrium initially anterior near Bachman's bundle [23–24]. Following extensive left atrial ablation, for example, after left atrial substrate modification for ablation of atrial fibrillation, the ECG presentation of typical atrial flutter may be significantly different from the characteristic saw-tooth pattern described above. Because the typical and reverse typical forms of type 1 AFL utilize the same reentry circuit, but in opposite directions, their rates are usually similar.

Standard Catheter Mapping of Type 1 Atrial Flutter

Despite the utility of the 12-lead ECG in making a presumptive diagnosis of typical AFL, an electrophysiologic study with mapping and entrainment must be performed to confirm the underlying mechanism if radiofrequency catheter ablation is to be successfully performed. This is particularly true in the case of reverse typical AFL, which is much more difficult to diagnose on 12-lead ECG. For standard multielectrode catheter mapping, catheters are positioned in the right atrium, His bundle region, and coronary sinus.

To determine the endocardial activation sequence, a Halo^{TM} 20-electrode mapping catheter (Cordis-Webster, Inc., Diamond Bar, CA) is most commonly used in the right atrium positioned around the tricuspid valve annulus (Figure 17.4). Recordings obtained during AFL from all electrodes are then analyzed to determine the right atrial activation sequence. In patients presenting to the laboratory in sinus rhythm it is necessary to induce AFL in order to confirm its mechanism. Induction of AFL is best accomplished by rapid atrial pacing from the coronary sinus ostium, or low lateral right atrium, at cycle lengths between 180 and 240 msec. Induction of atrial flutter typically occurs following the onset of unidirectional conduction block in the crista terminalis and CTI [19, 20].

A diagnosis of typical or reverse typical AFL is suggested by observing a counterclockwise or clockwise activation pattern in the right atrium and around the tricuspid valve annulus, as seen in Figure 17.5a in a patient with typical AFL, or in Figure 17.5b in a patient reverse typical AFL. Pacing during AFL from the CTI demonstrating concealed entrainment then confirms the isthmus dependence of the AFL.

Radiofrequency Catheter Ablation of Type 1 Atrial Flutter

Radiofrequency catheter ablation of type 1 AFL is performed with a steerable mapping/ablation catheter with a large distal ablation electrode positioned in the right atrium via a femoral vein [3, 5–7, 25–28]. Current RFCA radiofrequency catheter ablation systems utilize a thermistor or thermocouple embedded in the distal ablation electrode to monitor electrode–tissue interface temperature, which is programmable and controlled by automatically adjusting power output to achieve a stable temperature of 50–60°C, and occasionally 70°C. (Note: RFCA ablation seemed redundant, so the author took out the RFCA). Temperatures in excess of 70°C may cause tissue vaporization (steam pops), tissue charring, and formation of blood coagulum on the ablation electrode, resulting in a rise in impedance that limits energy delivery and lesion formation, and may lead to complications such as cardiac perforation or embolization.

A variety of ablation catheters with different shapes and curve lengths are currently available

(a)

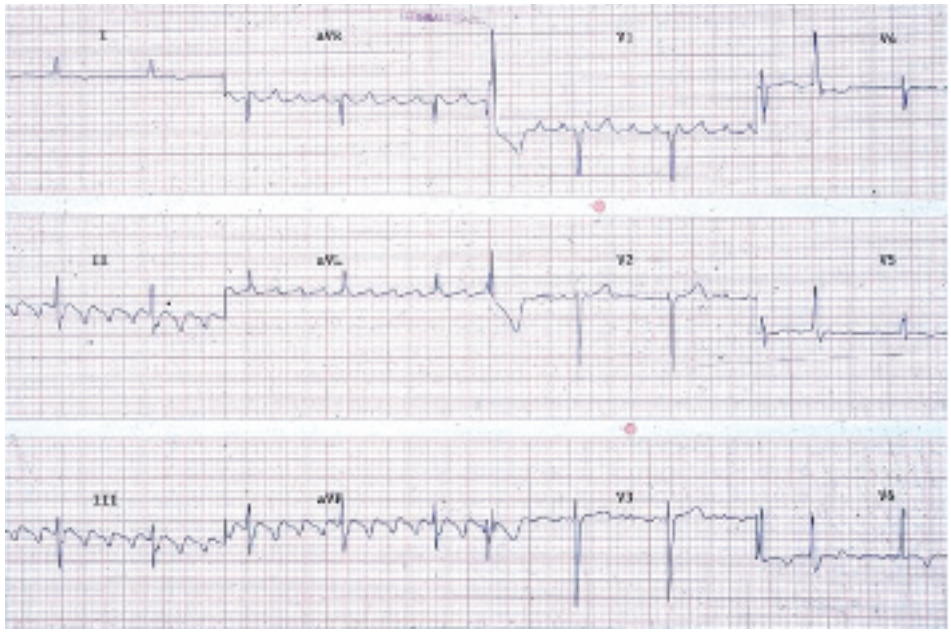

(b)

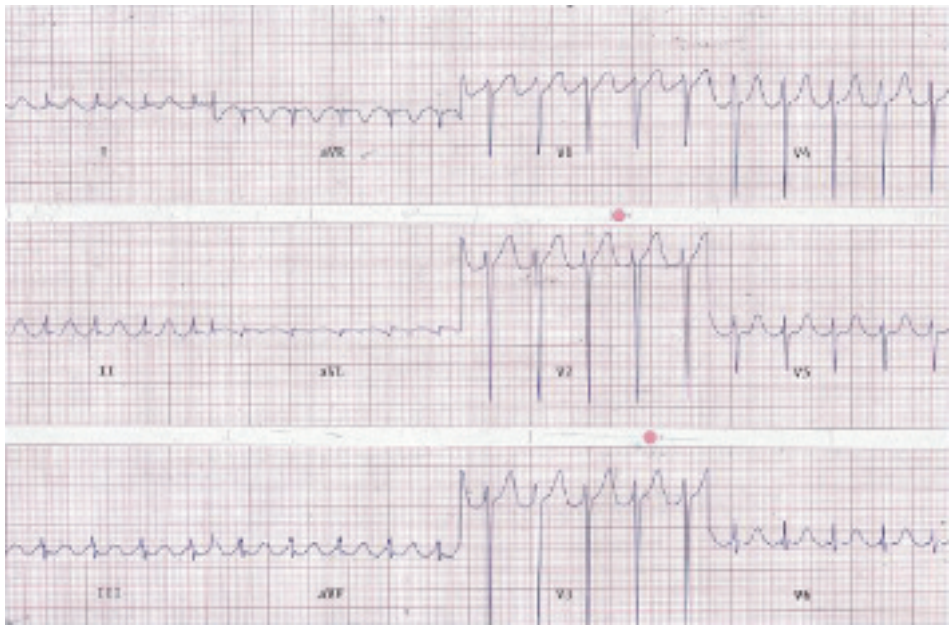

Figure 17.3 (a) Twelve-lead electrocardiogram recorded from a patient with typical AFL. Note the typical saw-toothed pattern of inverted F waves in the inferior leads II, III, aVF. Typical AFL is also characterized by flat-to-biphasic F waves in I and aVL, respectively, an upright F wave in V1, and an inverted F wave in V6. (b) 12-lead electrocardiogram recorded from a patient with the reverse typical AFL. The F wave in the reverse typical form of AFL has a less distinct sine wave pattern in the inferior leads. In this case the F waves are upright in the inferior leads II, III, aVF; biphasic in leads I, aVL, and V1; and upright in V6. Adapted from Ref [8].

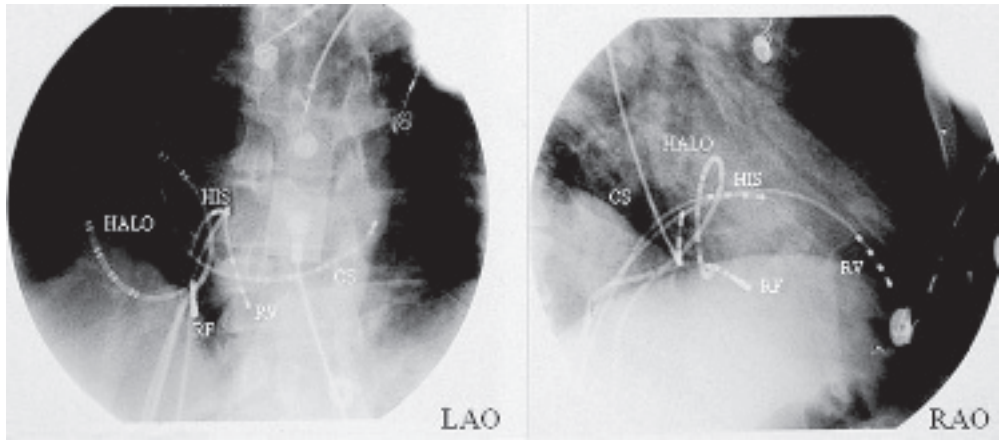

Figure 17.4 Left anterior oblique (LAO) and right anterior oblique (RAO) fluoroscopic projections showing the intracardiac positions of the right ventricular (RV), His bundle (HIS), coronary sinus (CS), Halo (HALO), and mapping/ablation catheter (RF). Note that the Halo catheter is positioned around the tricuspid valve annulus with the proximal electrode pair at 1 o'clock and the distal electrode pair at 7 o'clock in the LAO view. The mapping/ablation catheter is positioned in the sub-Eustachian isthmus, midway between the interatrial septum and low lateral right atrium, with the distal 8-mm ablation electrode near the tricuspid valve annulus. Adapted from Ref [8].

from several commercial manufacturers. We prefer to use a larger curve catheter, with or without a preshaped guiding sheath in order to ensure that the ablation electrode will reach the tricuspid valve annulus. For RFCA of AFL, catheters with either saline-cooled ablation electrodes or large distal ablation electrodes (i.e., 8–10 mm) are preferred.

During ablation with saline-cooled catheters, the use of lower power and temperature settings is recommended to avoid steam pops because the intramyocardial tissue temperatures are typically higher than those measured at the tissue–electrode interface due to the electrode cooling effect of saline perfusion [29–31]. A maximum power of 35–40 W and temperature of 43–45° C should be used initially to avoid complications such as steam pops [29–32]. In contrast, the large-tip (8–10 mm) ablation catheters require up to 100 W power to achieve target temperatures of 50–70° C due to the greater energy dispersive effects of the larger ablation electrode. This also requires the use of two grounding pads applied to the patient's skin to avoid skin burns [25, 31, 33–34].

The preferred target for type 1 AFL ablation is the CTI (Figure 17.6a), which when using standard electrode catheters is localized with a combined fluoroscopically and electrophysiologically guided approach [3, 5–7, 25, 26–32, 34]. Typically, the ablation catheter is positioned fluoroscopically (Figure 17.4) across the CTI with the distal ablation electrode near the TV annulus in the right anterior oblique view, and midway between the septum and low right atrial free wall (6 or 7 o'clock position) in the left anterior oblique (LAO) view. The distal ablation electrode is then positioned to record an atrial to ventricular electrogram amplitude ratio of 1:2 or 1:4, as seen in Figure 17.5a. The ablation catheter is then withdrawn slowly, a few millimeters at a time (usually the length of the distal ablation electrode) pausing for 30–60 sec at each location during a continuous or interrupted RF energy application.

Electrogram recordings may be employed, in addition to fluoroscopy, to ensure that the ablation electrode is in contact with viable tissue in the CTI throughout each energy application. Ablation of the entire CTI may require several sequential 30–60 sec energy applications during a stepwise catheter pullback, or a prolonged energy application of up to 120 sec or more during a continuous catheter pullback. The catheter should be gradually withdrawn until the distal ablation electrode records no atrial electrogram, indicating it has reached the inferior vena cava, or until the ablation electrode is

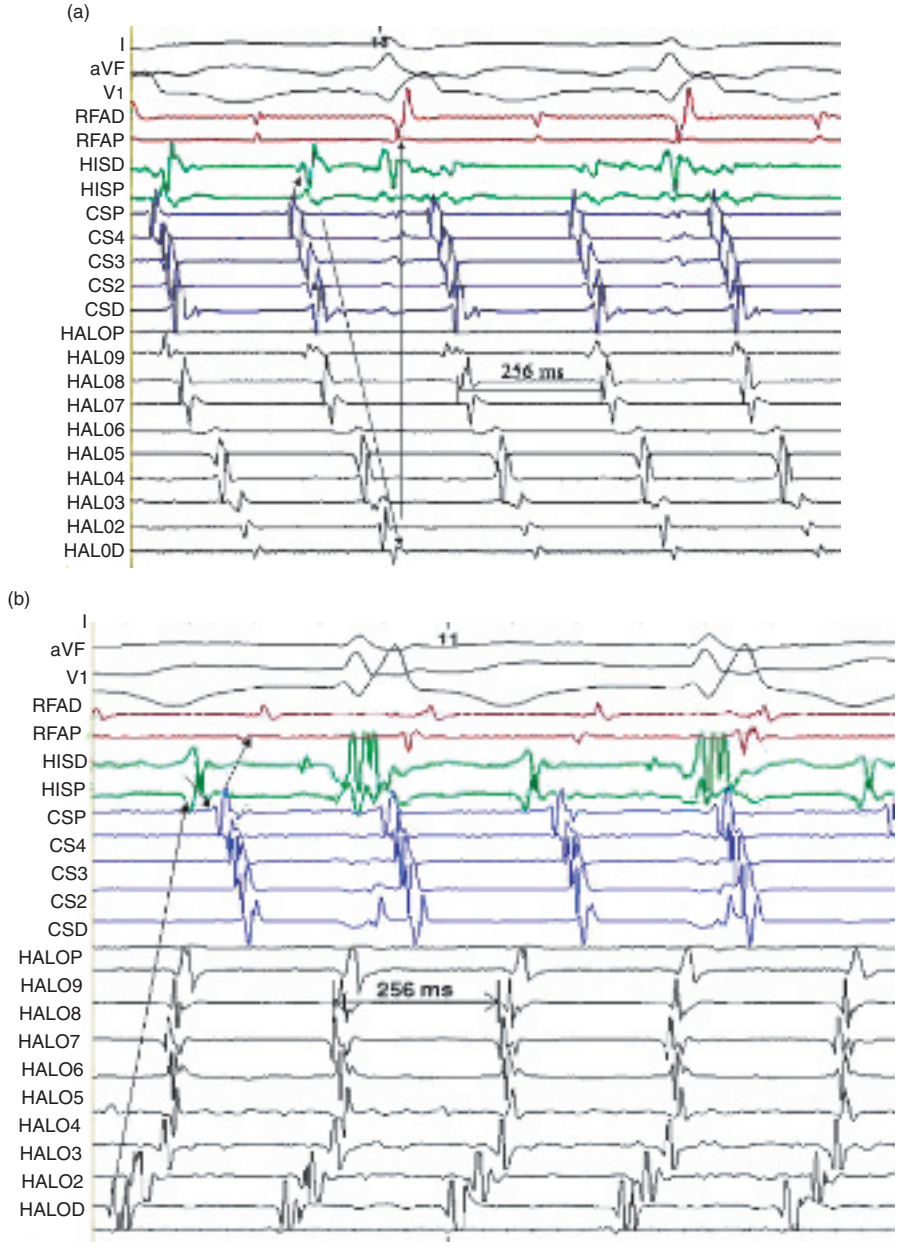

Figure 17.5 Endocardial electrograms from the mapping/ablation, Halo, CS, and His bundle catheters, and surface ECG leads I, aVF, demonstrating a counterclockwise (CCW) rotation of activation in the right atrium in a patient with typical AFL (a) and a clockwise (CW) rotation of activation in the right atrium in a patient with reverse typical AFL (b). The AFL cycle length was 256 msec for both CCW and CW forms. Arrows demonstrate activation sequence. Halo D–Halo P tracings are 10 bipolar electrograms recorded from the distal (low lateral right atrium) to proximal (high right atrium) poles of the 20 pole Halo catheter positioned around the tricuspid valve annulus with the proximal electrode pair at 1 o'clock and the distal electrode pair at 7 o'clock. KEY: CSP = electrograms recorded from the coronary sinus catheter proximal electrode pair positioned at the ostium of the coronary sinus; HISP = electrograms recorded from the proximal electrode pair of the His bundle catheter; RF = electrograms recorded from the mapping/ablation catheter positioned with the distal electrode pair in the cavo-tricuspid isthmus. Adapted from Ref [8].

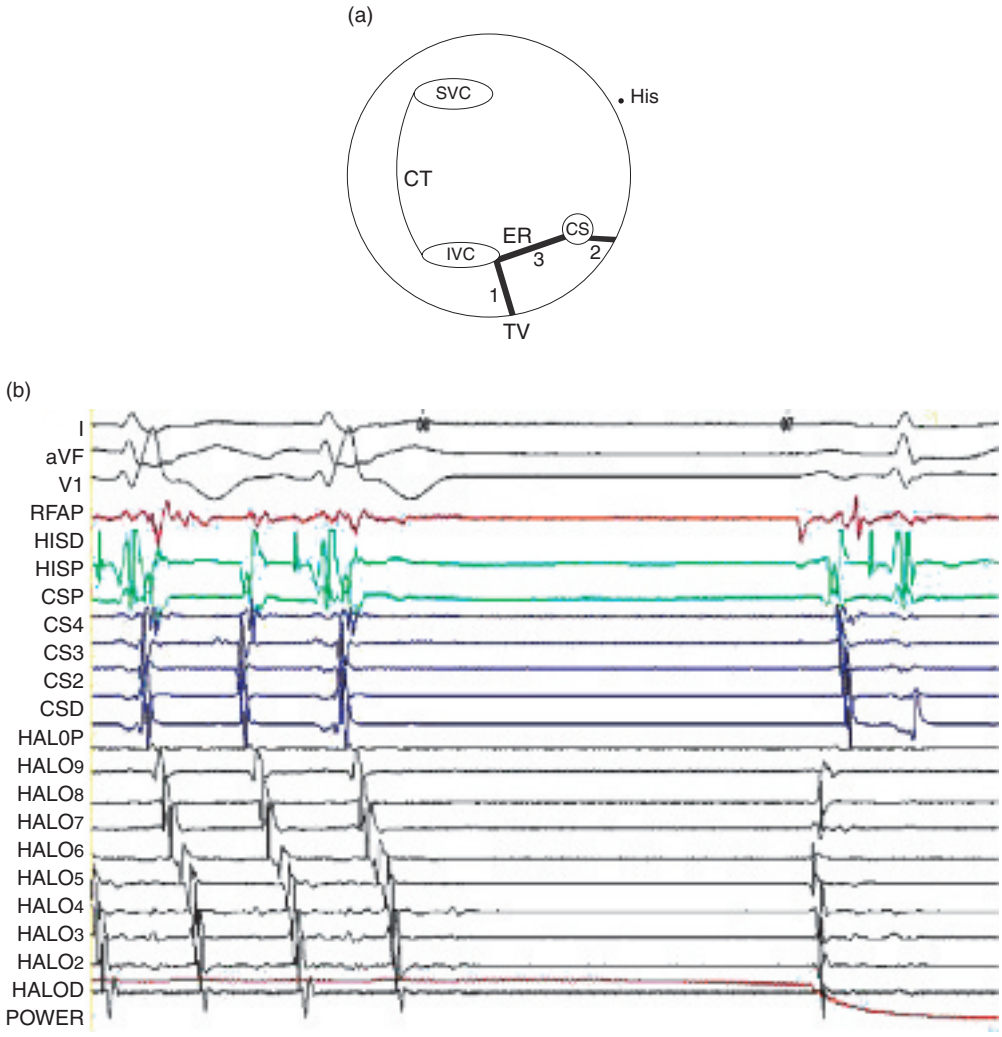

Figure 17.6 (a) A schematic diagram of the right atrium demonstrating the possible targets for ablation for cure of type 1 AFL, including the CTI (1), the tricuspid valve annulus–coronary sinus isthmus (2), the coronary sinus–Eustachian ridge isthmus (3). The preferred target for ablation is the CTI (1). (b) Surface ECG and endocardial electrogram recordings during ablation of the CTI at the time of termination of typical AFL. Note the abrupt termination of AFL, which occurred in this patient as the ablation catheter reached the Eustachian ridge, followed by restoration of normal sinus rhythm. KEY: I, aVF, V1 = surface ECG leads; RFAP = proximal ablation electrogram; Hisp&d = proximal and distal His bundle electrograms; CSd-p = distal to proximal coronary sinus electrograms; Halo d-p = distal to proximal Halo catheter electrograms; Imped = impedance; Temp = temperature. Adapted from Ref [15].

noted to abruptly slip off the Eustachian ridge on fluoroscopy. Radiofrequency energy application should be immediately interrupted when the catheter has reached the inferior vena cava, because ablation in the venous structures is known to cause significant pain.

Procedure Endpoints for Radiofrequency Catheter Ablation of Type 1 Atrial Flutter

Ablation may be performed during sustained AFL or during sinus rhythm. If performed during AFL,

the first endpoint is its termination during energy application (Figure 17.6b). Despite termination of AFL however, it is common to find that CTI conduction persists. After the CTI ablation is completed, electrophysiologic testing should be performed by pacing at a cycle length of 600 msec (or greater, depending on sinus cycle length) to determine if there is bidirectional CTI conduction block (Figures 17.7a,b and Figure 17.8a,b).

Bidirectional CTI conduction block is confirmed by demonstrating a strictly cranial-to-caudal activation sequence in the contralateral right atrium during pacing from the coronary sinus ostium, or low lateral right atrium respectively [35–37]. The presence of bidirectional CTI conduction block is further supported by recording widely spaced double potentials along the ablation line during pacing from the low lateral right atrium or coronary sinus ostium (Figure 17.9) [38–39]. The use of bidirectional CTI conduction block as an endpoint for type 1 AFL ablation is associated with a significantly lower recurrence rate of type 1 AFL during long-term follow-up [35–37, 39]. Programmed stimulation and burst pacing should be repeated over the course of at least 30 min to ensure that bidirectional CTI block has been achieved, and that neither typical nor reverse typical AFL can be reinduced [3, 5–7, 25–30, 32–34, 41].

If AFL is not terminated during the first attempt at CTI ablation, the activation sequence and isthmus dependence of the AFL should be reconfirmed and ablation should be repeated. Repeat ablation may then be necessary using a slightly higher power and/or ablation temperature, or by rotating the ablation catheter away from the initial ablation, either medially or laterally in the CTI, in order to create new or additional lines of block. In addition, if ablation is initially unsuccessful using a standard 5-mm tip electrode, repeat ablation with a larger-tip 8–10 mm electrode catheter or cooled-tip ablation catheter may be successful [25, 29–34].

Outcomes and Complications of Catheter Ablation of Type 1 Atrial Flutter

Although early reports [3–6] of RFCA for AFL revealed recurrence rates up to 20–45% (Table 17.1), both acute and chronic success rates (defined as termination of AFL and bidirectional isthmus block, and no recurrence of type 1 atrial flutter during follow-up, respectively) are currently in excess of 95%. Contributing in large degree to these improved results has been the introduction of bidirectional CTI conduction block as an endpoint for successful RFCA of AFL [25–34].

In the most recent studies using either large-tip (8–10 mm) electrode ablation catheters with high-power radiofrequency generators, or cooled-tip electrode ablation catheters with standard radiofrequency generators, acute success rates as high as 100% and chronic success rates as high as 98% have been reported [25, 30–34, 41]. Randomized comparisons of internally cooled, externally cooled, and large-tip ablation catheters, suggest a slightly better acute and chronic success rate with the externally cooled ablation catheters, compared to internally cooled ablation catheters, or large-tip ablation catheters [29–30, 32, 34, 41].

Radiofrequency catheter ablation for type 1 AFL is relatively safe, but serious complications can occur, including heart block, cardiac perforation and tamponade, and thromboembolic events including pulmonary embolism and stroke. In recent large-scale studies, including those using large-tip catheters and high power generators, major complications have been observed in only 2.5–3.0% of patients [25, 34, 41].

Computerized 3D Mapping in Diagnosis and Ablation of Type 1 Atrial Flutter

The 3D electroanatomical Carto™ (BioSense-Webster, Baldwin Park, CA) and noncontact Ensite™ (Endocardial Solutions, St. Paul, MN) activation mapping systems, while not required for successful ablation of type 1 AFL, have specific advantages that have made them a widely used and accepted technology. Although it is not within the scope of this article to describe the technological basis of these systems in detail, there are unique characteristics of each system that make them more or less suitable for mapping and ablation of atrial flutter.

The Carto system utilizes a magnetic sensor in the ablation catheter, a magnetic field generated by a grid placed under the patient, and a reference pad

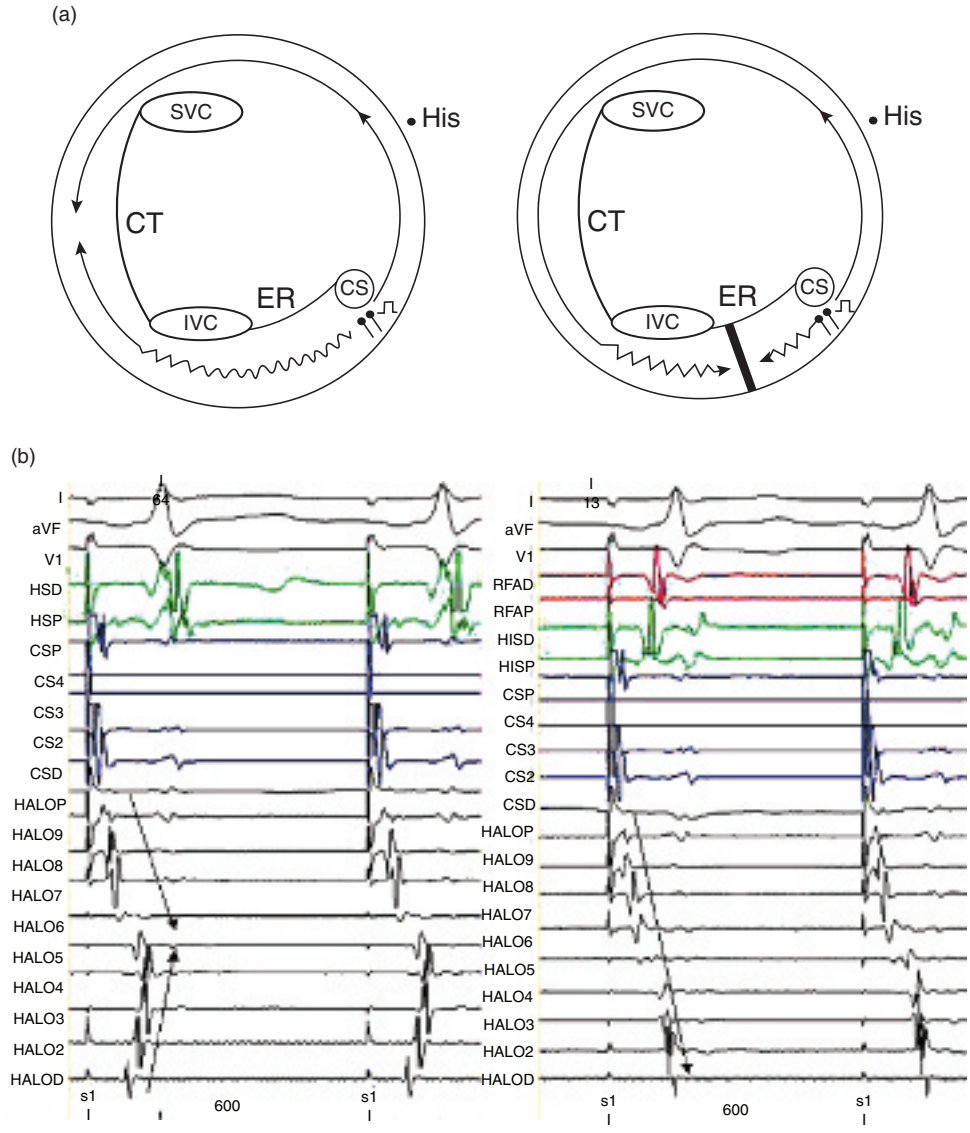

Figure 17.7 (a) A schematic diagram of the expected right atrial activation sequence during pacing in sinus rhythm from the coronary sinus (CS) ostium before (left panel) and after (right panel) ablation of the cavo-tricuspid isthmus (CTI). Prior to ablation the activation pattern during coronary sinus pacing is caudal to cranial in the interatrial septum and low right atrium, with collision of the septal and right atrial wavefronts in the mid-lateral right atrium. Following ablation the activation pattern during coronary sinus pacing is still caudal to cranial in the interatrial septum, but the lateral right atrium is now activated in a strictly cranial-to-caudal pattern (i.e., counterclockwise), indicating complete clockwise conduction block in the CTI. KEY: CT = crista terminalis; ER = Eustachian ridge; His = His bundle; IVC = inferior vena cava; SVC = superior vena cava. (b) Surface ECG and right atrial endocardial electrograms recorded during pacing in sinus rhythm from the coronary sinus (CS) ostium before (left panel) and after (right panel) ablation of the cavo-tricuspid isthmus (CTI). Tracings include surface ECG leads I, aVF, and V1, and endocardial electrograms from the proximal coronary sinus (CSP), His bundle (HIS), tricuspid valve annulus at 1 o'clock (HaloP) to 7 o'clock (HaloD), and high right atrium (HRA or RFA). Prior to ablation during coronary sinus pacing there is collision of the cranial and caudal right atrial wavefronts in the mid-lateral right atrium (HALO5). Following ablation the lateral right atrium is activated in a strictly cranial-to-caudal pattern (i.e., counterclockwise), indicating complete medial to lateral conduction block in the CTI. Adapted from Ref [8].

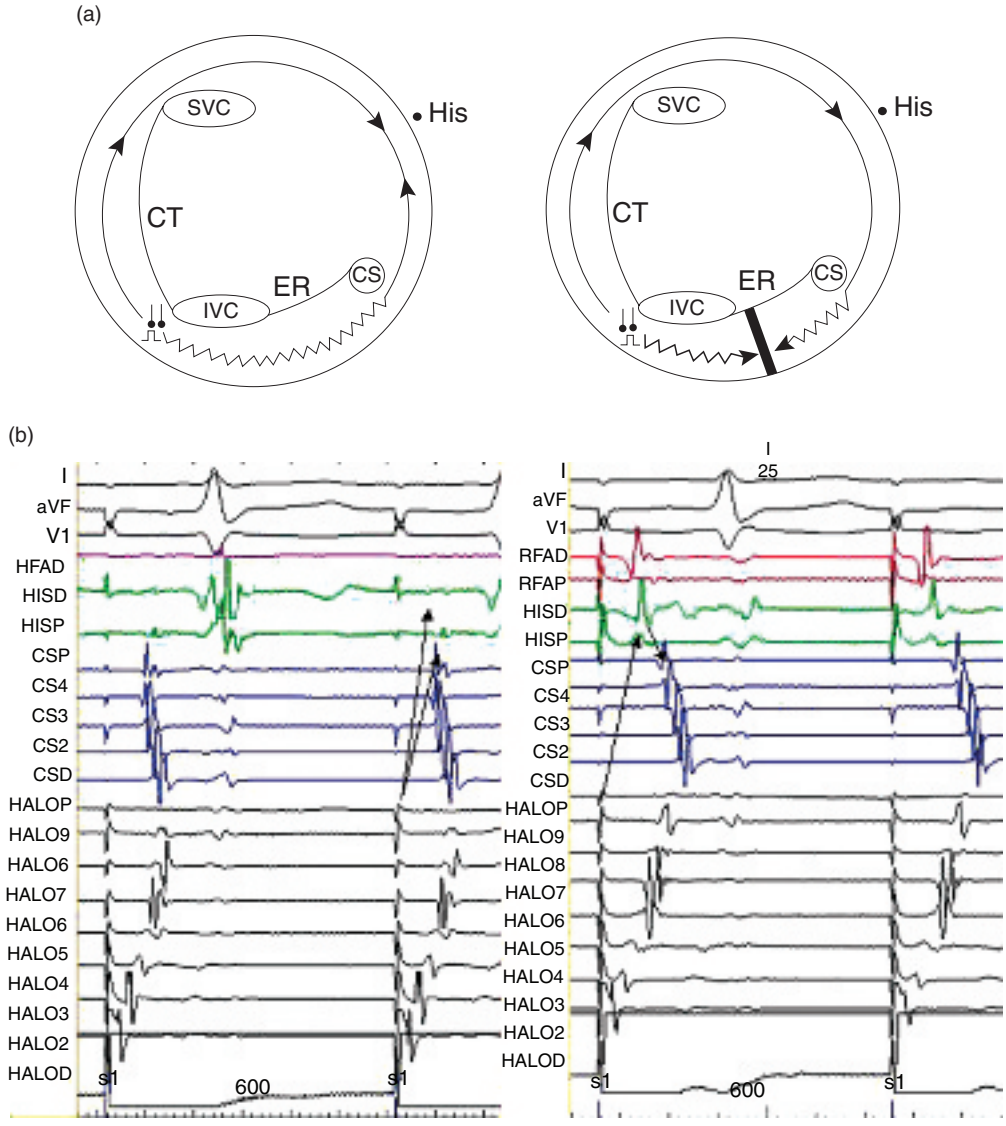

Figure 17.8 (a) Schematic diagrams of the expected right atrial activation sequence during pacing in sinus rhythm from the low lateral right atrium before (left panel) and after (right panel) ablation of the cavo-tricuspid isthmus (CTI). Prior to ablation the activation pattern during coronary sinus pacing is caudal-to-cranial in the right atrial free wall, with collision of the cranial and caudal wavefronts in the mid-septum, with simultaneous activation at the His bundle (HISP) and proximal coronary sinus (CSP). Following ablation the activation pattern during low lateral right atrial sinus pacing is still caudal-to-cranial in the right atrial free wall, but the septum is now activated in a strictly cranial-to-caudal pattern (i.e., clockwise), indicating complete lateral to medial conduction block in the CTI. KEY: CT = crista terminalis; ER = Eustachian ridge; His = His bundle; SVC = superior vena cava; IVC = inferior vena cava.

(b) Surface ECG and right atrial endocardial electrograms during pacing in sinus rhythm from the low lateral right atrium before (left panel) and after (right panel) ablation of the CTI. Tracings include surface ECG leads I, aVF, and V1, and endocardial electrograms from the proximal coronary sinus (CSP), His bundle (HIS), tricuspid valve annulus at 1 o'clock (HaloP) to 7 o'clock (HaloD), and high right atrium (HRA or RFA). Prior to ablation during low lateral right atrial pacing there is collision of the cranial and caudal right atrial wavefronts in the mid-septum (HIS and CSP). Following ablation the septum is activated in a strictly cranial-to-caudal pattern (i.e., clockwise), indicating complete lateral to medial conduction block in the CTI. Adapted from Ref [8].

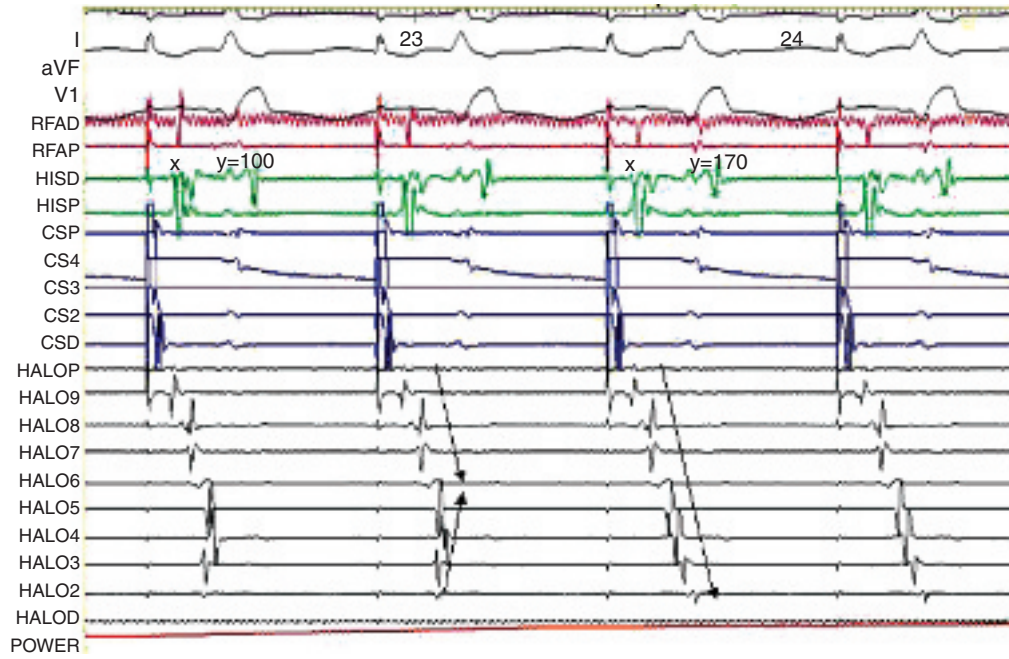

Figure 17.9 Surface ECG leads I, aVF, and V1, and endocardial electrograms from the coronary sinus, His bundle, Halo, mapping/ablation (RF), and right ventricular catheters during radiofrequency catheter ablation of the CTI during pacing from the coronary sinus ostium. Note the change in activation sequence in the lateral right atrium on the Halo catheter from bidirectional to unidirectional, indicating development of clockwise block in the CTI. This was associated with development of widely spaced (170 msec) double potentials (*x* and *y*) on the RF catheter along the ablation line, confirming medial-to-lateral conduction block. All abbreviations are the same as in previous figures. Adapted from Ref [15].

Table 17.1 Success Rates for Radiofrequency Catheter Ablation of Atrial Flutter

Author	*Year (Ref.)*	*N*	*Electrode length*	*% Acute success*	*Follow-up (months)*	*% Chronic success*
Feld	1992 (5)	16	4	100	4 ± 2	83
Cosio	1993 (6)	9	4	100	2–18	56
Kirkorian	1994 (25)	22	4	86	8 ± 13	84
Fischer	1995 (24)	80	4	73	20 ± 8	81
Poty	1995 (34)	12	6/8	100	9 ± 3	92
Schwartzman	1996 (35)	35	8	8	1–21	92
Chauchemez	1996 (38)	20	4	4	8 ± 2	80
Tsai	1999 (31)	50	8	92	10 ± 5	100
Atiga	2002 (30)	59	4 vs. cooled	88	13 ± 4	93
Scavee	2004 (28)	80	8 vs. cooled	80	15	98
Feld	2004 (23)	169	8 or 10	6	6	97
Calkins	2004 (39)	150	8	6	6	87
Venturs	2004 (32)	130	8 vs. cooled	100	14 ± 2	98

KEY: *N* = number of patients studied; % acute success = termination of atrial flutter during ablation and/or demonstration of isthmus block following ablation; % chronic success = % of patients in whom type 1 atrial flutter did not recur during follow-up. Acute and chronic success rates are reported as overall results in randomized or comparison studies.

on the skin to track the ablation catheter in 3D space. The computer system sequentially records anatomical location and electrograms for online analysis of activation time and computation of isochronal patterns which are then superimposed on the endocardial geometry (Figure 17.10a). A live propagation map can also be produced (see Videoclip 8 👁).

The advantages of the Carto systeminclude precise anatomical representation of the right atrium including the CTI and adjacent structures, precise localization of the ablation catheter within the right atrium, and static activation and propagation maps of endocardial activation can be constructed during atrial flutter and during pacing after ablation to assess for CTI conduction block (Figure 17.10b). The disadvantages of the Carto system include the need to use the proprietary catheters and ablation generator, and the inability to map the entire endocardial activation sequence in one beat.

The Ensite system utilizes a saline inflated balloon catheter on which is mounted a wire mesh containing electrodes that are capable of sensing the voltage potential of surrounding atrial endocardium, without actual electrode–tissue contact, from which the computerized mapping system can generate up to 3000 virtual endocardial electrograms and create a propagation map of the AFL. In addition, a low-amplitude high-frequency electrical current emitted from the ablation catheter can be sensed and tracked in 3D space by the mapping balloon.

A 3D anatomy is created by roving the mapping catheter around the right atrial endocardium, upon which the propagation map is superimposed (see Videoclips 9–11 👁). The appropriate ablation target can then be localized and the ablation catheter positioned appropriately and tracked while ablation is performed. Following ablation, the mapping system can then be used to assess for bidirectional CTI conduction block during pacing from the low lateral right atrium and coronary sinus ostium.

The advantages of the Ensite system include the ability to map the entire AFL activation sequence in one beat, precise anatomical representation of the right atrium including the CTI and adjacent structures, precise localization of the ablation catheter within the right atrium, and propagation maps of endocardial activation during atrial flutter and pacing after ablation to assess for CTI conduction block. In addition, any ablation catheter system can be used with the Ensite system. The major disadvantage of the Ensite system is the need to use the balloon mapping catheter with its large 10 Fr introducer sheath, and the need for full anticoagulation during the mapping procedure.

The 3D computerized mapping systems, while not required to map and ablate AFL, may be particularly useful in difficult cases such as those where prior ablation has failed (Figure 17.11), or in those where complex anatomy may be involved including idiopathic or post-operative scarring (Figure 17.12), or unoperated or surgically corrected congenital heart disease (Figure 17.13a). In such cases, activation sequence mapping may reveal that an atypical AFL on ECG is in fact an isthmus-dependent type 1 AFL that will respond to CTI ablation (Figures 17.11 and 17.12). In other cases, voltage mapping may also be helpful to identify areas of thinner muscle tissue in the CTI that may be more easily ablated (Figure 17.13b,c).

Simplified Approach to Ablation of Type 1 AFL

In our laboratory we have recently developed a simplified approach for CTI ablation in patients with type 1 AFL involving the use of only two catheters; a decapolar steerable coronary sinus catheter, and a large-tip (8- or 10-mm) RF ablation catheter.

Ablation of type 1 AFL can be completed rapidly and with minimal fluoroscopy time using this approach. Both catheters are inserted percutaneously from the right femoral vein. The decapolar catheter is positioned in the coronary sinus with the proximal pair at the ostium near the medial CTI, and the ablation catheter is placed in a flexed position in the low lateral right atrium with the distal pair near the lateral CTI (Figure 17.14a). Pacing from the proximal coronary sinus and the ablation catheter can then demonstrate bidirectional CTI conduction and AFL inducibility before CTI ablation and bidirectional CTI block (Figure 17.14b,c) and AFL noninducibility after CTI ablation.

Ablation is performed in a standard manner with the large-tip catheter using a high-power generator. Following CTI ablation using this simplified catheter approach, medial-to-lateral CTI conduction block is defined by both the presence of a high-to-low (i.e., proximal to distal) activation sequence

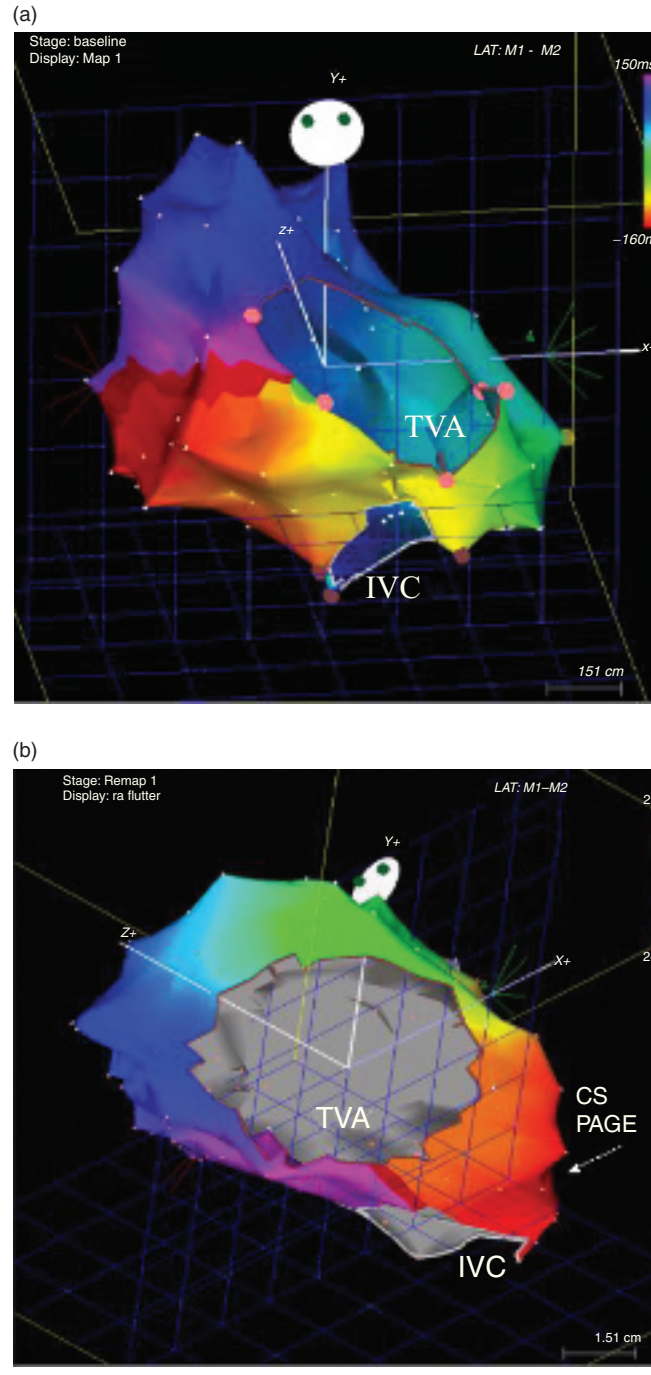

Figure 17.10 (a) A 3D electroanatomical map of the right atrium using the Carto system (Biosense-Webster, Inc.) in a patient with typical AFL, before (a) and after (b) CTI ablation. Note the counterclockwise activation pattern around the tricuspid valve during AFL (a), based on color scheme indicating activation time from early (orange) to late (purple). Following ablation of the CTI (b) during pacing from the coronary sinus ostium, there is evidence of medial-to-lateral isthmus block as indicated by juxtaposition of orange and purple color in the CTI, indicating early and late activation, respectively. KEY: IVC = inferior vena cava; TVA = tricuspid valve annulus. Adapted from Ref [8].

on the ablation catheter (when placed in the flexed position in the low lateral right atrium) during pacing from the proximal coronary sinus, and by equal conduction times (typically >130 msec) from medial-to-lateral, and from lateral-to-medial, during pacing from the proximal coronary sinus and low lateral right atrium, respectively. In addition, pacing from the proximal coronary sinus with the ablation catheter positioned on the ablation line can demonstrate widely spaced double potentials,

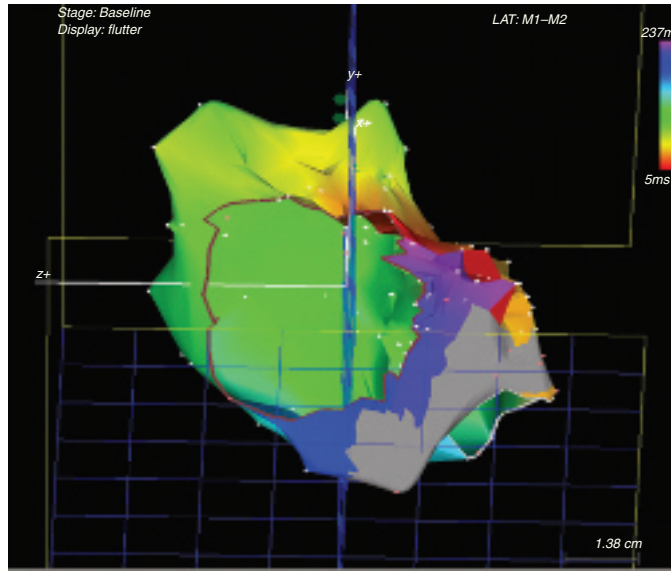

Figure 17.11 A Carto 3D activation sequence map is shown in a patient who had previously undergone attempted CTI ablation, but in whom AFL had recurred with an atypical ECG pattern. Note the typical AFL activation sequence map, with extensive scarring (gray area) of the CTI near the inferior vena cava, with only a narrow rim of viable tissue near the tricuspid valve annulus allowing conduction through the CTI, which was easily ablated resulting in elimination of further AFL. Adapted from Ref [15].

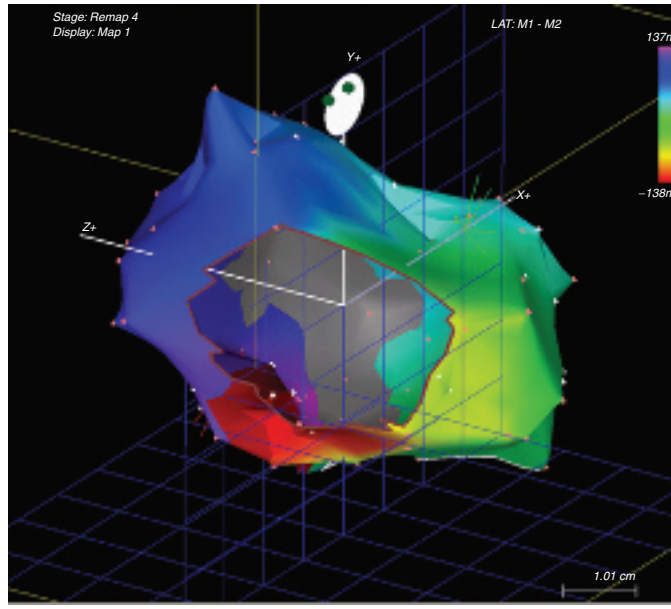

Figure 17.12 A Carto 3D activation sequence map is shown in a patient who had extensive idiopathic posterior right atrial wall scarring (gray area) and an atypical AFL pattern on ECG. Note the typical AFL activation sequence map, however. The CTI was ablated in this patient eliminating further AFL recurrence.

(a)

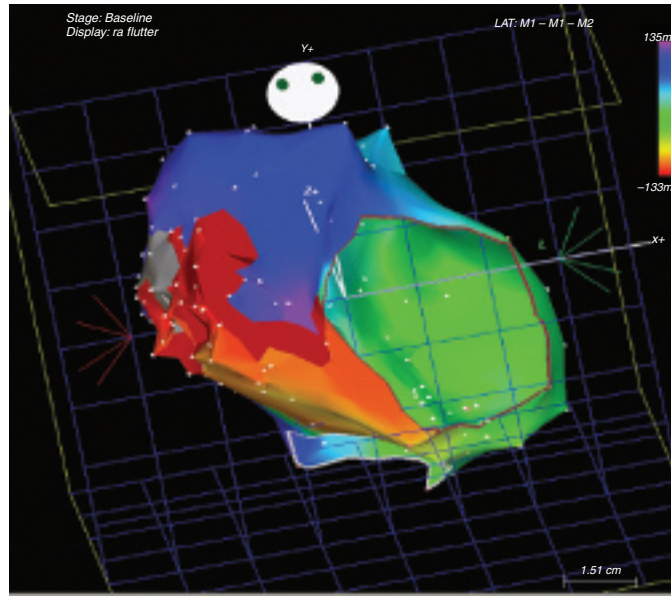

(b)

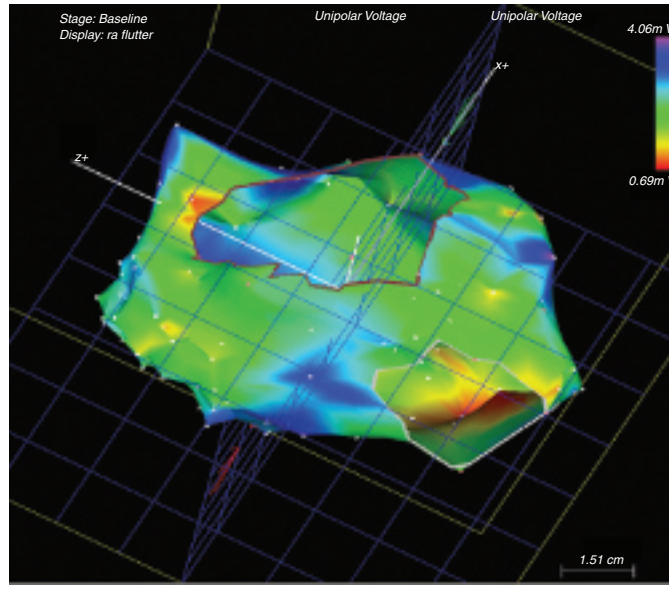

Figure 17.13 (a) A Carto 3D activation sequence map is shown in a patient who had previously undergone atrial septal defect repair. Note the typical AFL activation sequence map, despite the presence of a right atriotomy scar (gray area). Adapted from Ref [15].

(b) A Carto 3D voltage map of this atrium and CTI revealed a relatively high voltage area (green) in the middle CTI, and lower voltage area (blue) in the lateral CTI, suggesting that CTI ablation should be performed more laterally in this case.

(c) A Carto 3D activation sequence map is shown during pacing from the proximal coronary sinus after ablation of the lateral CTI as guided by the voltage map, demonstrating unidirectional medial-to-lateral conduction block. Pacing from the low lateral right atrium (not shown) confirmed the presence of bidirectional CTI conduction block.

(c)

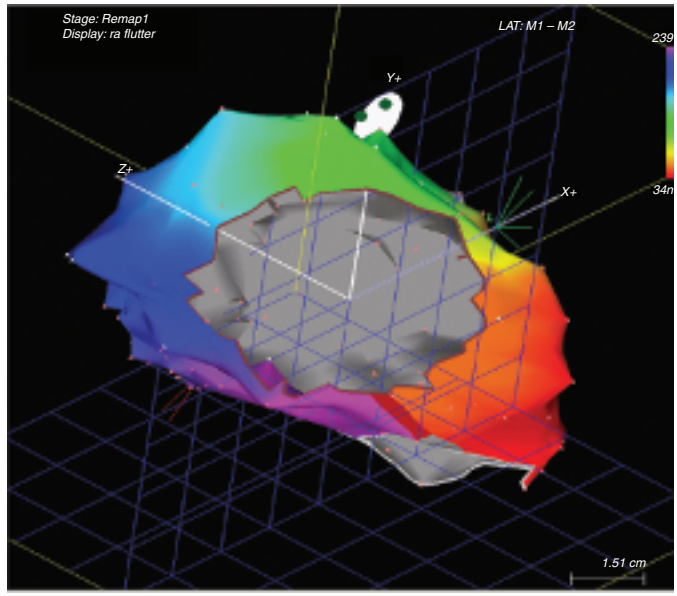

Figure 17.13 (*Continued*)

further confirming the presence of medial-to-lateral CTI conduction block. This approach has been validated in our laboratory in a large number of patients by showing a precise correlation between the findings using this simplified approach, and those using multiple electrode catheters including a coronary sinus, Halo, His bundle catheter, and ablation catheter.

Alternative Energy Sources for Ablation of Type 1 Atrial Flutter

The development of new energy sources for ablation of cardiac arrhythmias is an ongoing effort due to the disadvantages of radiofrequency energy for ablation, including the risk of coagulum formation, tissue charring, subendocardial steam pops, embolization, failure to achieve transmural ablation, and long procedure and fluoroscopy times required to ablate large areas of myocardium. Many of these disadvantages have been overcome in the case of ablation of type 1 AFL in the past decade. Nonetheless, several clinical and preclinical studies have recently been published on the use of catheter cryoablation and microwave ablation of AFL [42–48].

Recent studies have demonstrated that catheter cryoablation of type 1 AFL can be achieved with results similar to radiofrequency ablation [42–44]. The potential advantages of cryoablation include the lack of pain associated with ablation, the ability to produce a large transmural ablation lesion, and the lack of tissue charring or coagulum formation. Cryoablation for type 1 AFL using the CryoCor^{TM} ablation system has been approved by the FDA in the United States and is also approved in Europe (CryoCor, San Diego, CA). In addition, early work has begun on the use of a linear microwave ablation catheter system (Medwaves, San Diego, CA) with antenna lengths up to 4 cm [45–48]. These studies have shown the feasibility of linear microwave ablation, which may have the advantage of very rapid ablation of the CTI with a single energy application over the entire length of the ablation electrode.

Conclusion

Radiofrequency catheter ablation has become a first-line treatment for type 1 AFL with nearly

uniform acute and chronic success, and low complication rates. The most effective approach is a combined anatomically and electrophysiologically guided ablation of the CTI, with procedure endpoints of arrhythmia noninducibility and bidirectional CTI conduction block.

Currently the use of a large-tip 8–10 mm ablation catheter with a high-output radiofrequency generator (i.e., up to 100 W) or a cooled-tip ablation catheter is recommended for optimal success rates. Computerized 3D activation mapping is an adjunctive method, which while not mandatory to cure AFL, may have significant advantages in some cases, resulting in overall improved success rates. New alternate energy sources including cryoablation and microwave ablation are under investigation with the hope of further improving procedure times and success rates, and potentially reducing the risk of complications during AFL ablation.

(a)

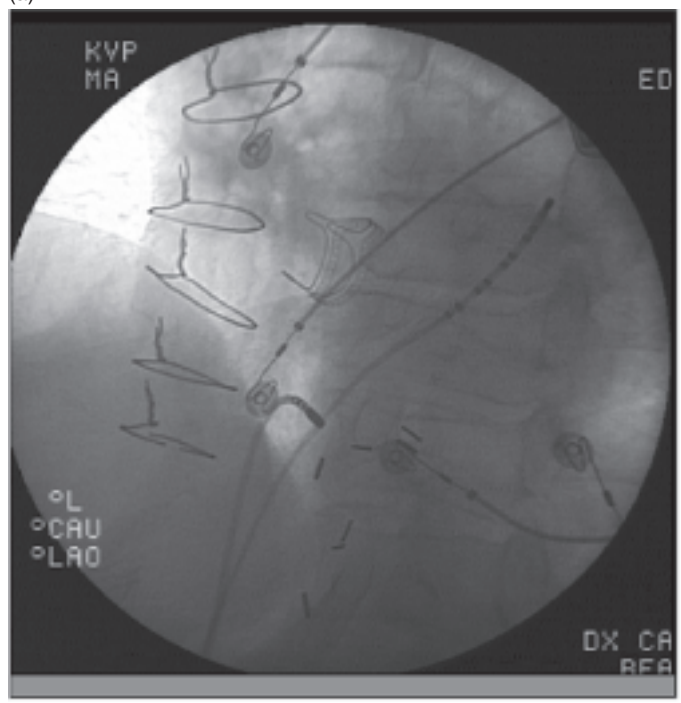

Figure 17.14 (a) Left anterior oblique fluoroscopic projection showing the positions of the decapolar coronary sinus catheter and the large-tip ablation catheter after CTI ablation to demonstrate conduction block. Note the proximal coronary sinus catheter electrode is positioned near the coronary sinus ostium, and the large-tip ablation catheter is positioned near the lateral CTI.

(b) Surface ECG and endocardial electrogram recordings during pacing from the proximal coronary sinus demonstrating a proximal-to-distal (high-to-low) activation sequence on the ablation catheter with a conduction time of 136 msec confirming medial-to-lateral CTI conduction block. KEY: I, aVF, V1 = surface ECG leads; RFd&p = distal and proximal ablation catheter electrograms; CSd-p = distal to proximal coronary sinus electrograms.

(c) Surface ECG and endocardial electrogram recordings during pacing from the ablation catheter located in the low lateral right atrium demonstrating a conduction time to the proximal coronary sinus electrode of 138 msec, similar to the medial-to-lateral conduction time, confirming lateral-to-medial CTI conduction block. See part (a) for key to abbreviations.

(d) Surface ECG and endocardial electrogram recordings during pacing from the proximal coronary sinus demonstrating widely spaced double potentials (*X* and *Y*) on the ablation catheter positioned on the ablation line, providing further evidence for medial-to-lateral CTI conduction block. See part (a) for key to abbreviations.

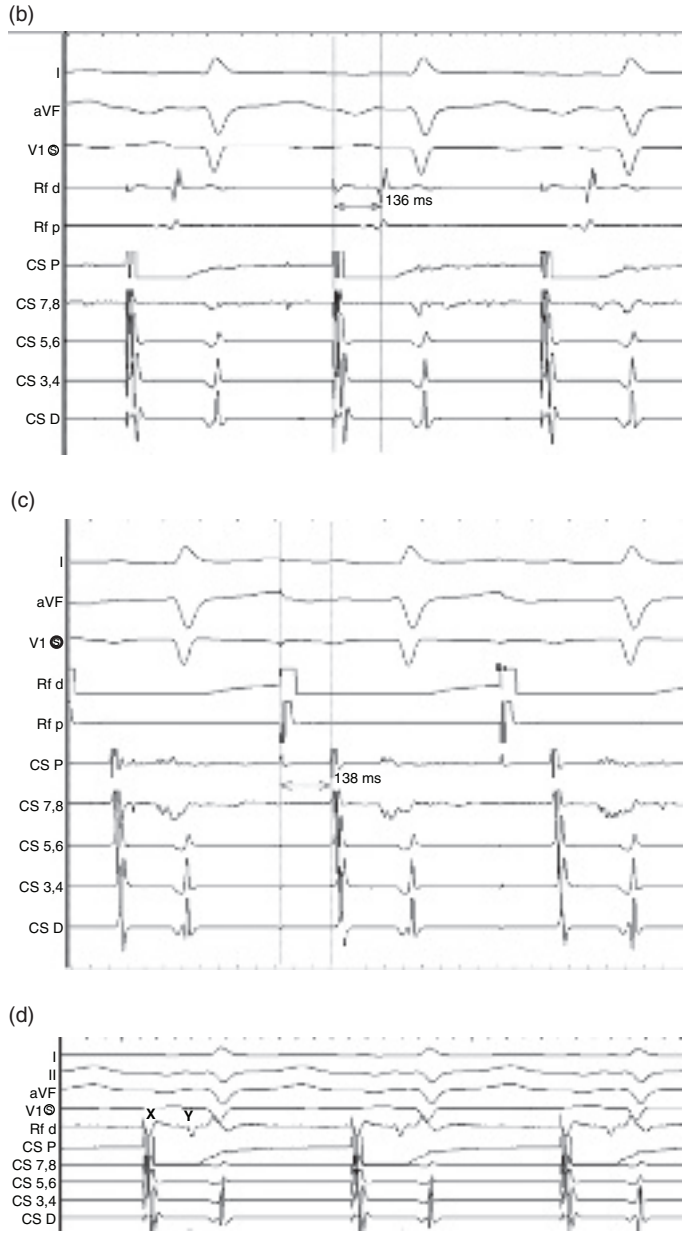

Figure 17.14 (*Continued*)

References

1 Saoudi N, Cosio F, Waldo A, et al. Classification of atrial flutter and regular atrial tachycardia according to electrophysiologic mechanism and anatomic bases: a statement from a joint expert group from the Working Group of Arrhythmias of the European Society of Cardiology and the North American Society of Pacing and Electrophysiology. *J Cardiovasc Electrophysiol* 2001; **12**: 852–66.

2 Olshansky B, Okumura K, Hess PG, Waldo AL. Demonstration of an area of slow conduction in human atrial flutter. *J Am Coll Cardiol* 1990; **16**: 1639–48.

3 Lesh MD, Van Hare GF, Epstein LM, et al. Radiofrequency catheter ablation of atrial arrhythmias: results and mechanisms. *Circulation* 1994; **89**: 1074–89.

4 Cosio FG, Goicolea A, Lopez-Gil M, Arribas F, Barroso JL, Chicote R. Atrial endocardial mapping in the rare form of atrial flutter. *Am J Cardiol* 1990; **66**: 715–20.

5 Feld GK, Fleck RP, Chen PS, et al. Radiofrequency catheter ablation for the treatment of human type 1 atrial flutter: identification of a critical zone in the reentrant circuit by endocardial mapping techniques. *Circulation* 1992; **86**: 1233–40.

6 Cosio FG, Lopez-Gil M, Goicolea A, Arribas F, Barroso JL. Radiofrequency ablation of the inferior vena cava–tricuspid valve isthmus in common atrial flutter. *Am J Cardiol* 1993; **71**: 705–9.

7 Tai CT, Chen SA, Chiang CE, et al. Electrophysiologic characteristics and radiofrequency catheter ablation in patients with clockwise atrial flutter. *J Cardiovasc Electrophysiol* 1997; **8**: 24–34.

8 Feld GK, Srivatsa U, Hoppe B. Ablation of isthmus-dependent atrial flutters. In: Huang SS, Wood MA, eds. *Catheter Ablation of Cardiac Arrhythmias.* Elsevier, Philadelphia, 2006: 95–218.

9 Feld GK, Mollerus M, Birgersdotter-Green U, et al. Conduction velocity in the tricuspid valve–inferior vena cava isthmus is slower in patients with type I atrial flutter compared to those without a history of atrial flutter. *J Cardiovasc Electrophysiol* 1997; **8**: 1338–48.

10 Kinder C, Kall J, Kopp D, Rubenstein D, Burke M, Wilber D. Conduction properties of the inferior vena cava–tricuspid annular isthmus in patients with typical atrial flutter. *J Cardiovasc Electrophysiol* 1997; **8**: 727–37.

11 Da Costa A, Mourot S, Romeyer-Bouchard C, et al. Anatomic and electrophysiological differences between chronic and paroxysmal forms of common atrial flutter and comparison with controls. *Pacing Clin Electrophysiol* 2004; **27**: 1202–11.

12 Kalman JM, Olgin JE, Saxon LA, Fisher WG, Lee RJ, Lesh MD. Activation and entrainment mapping defines the tricuspid annulus as the anterior barrier in typical atrial flutter. *Circulation* 1996; **94**: 398–406.

13 Olgin JE, Kalman JM, Lesh MD. Conduction barriers in human atrial flutter: correlation of electrophysiology and anatomy. *J Cardiovasc Electrophysiol* 1996; **7**: 1112–26.

14 Olgin JE, Kalman JM, Fitzpatrick AP, Lesh MD. Role of right atrial endocardial structures as barriers to conduction during human type I atrial flutter: activation and entrainment mapping guided by intracardiac echocardiography. *Circulation* 1995; **92**: 1839–48.

15 Feld GK, Birgersdotter-Green U, Narayan S. Diagnosis and ablation of typical and reverse typical (type 1) atrial flutter. In: *Catheter Ablation of Cardiac Arrhythmias: Basic Concepts and Clinical Applications*, 3rd ed. Wilber D, Packer D, Stevenson W, eds. Blackwell Publishing, Oxford, 2007.

16 Tai CT, Huang JL, Lee PC, Ding YA, Chang MS, Chen SA. High-resolution mapping around the crista terminalis during typical atrial flutter: new insights into mechanisms. *J Cardiovasc Electrophysiol* 2004; **15**: 406–14.

17 Spach MS, Dolber PC, Heidlage JF. Influence of the passive anisotropic properties on directional differences in propagation following modification of the sodium conductance in human atrial muscle: a model of reentry based on anisotropic discontinuous propagation. *Circ Res* 1988; **62**: 811–32.

18 Spach MS, Miller WT, 3rd, Dolber PC, Kootsey JM, Sommer JR, Mosher CE, Jr. The functional role of structural complexities in the propagation of depolarization in the atrium of the dog: cardiac conduction disturbances due to discontinuities of effective axial resistivity. *Circ Res* 1982; **50**: 175–91.

19 Olgin JE, Kalman JM, Saxon LA, Lee RJ, Lesh MD. Mechanism of initiation of atrial flutter in humans: site of unidirectional block and direction of rotation. *J Am Coll Cardiol* 1997; **29**: 376–84.

20 Suzuki F, Toshida N, Nawata H, et al. Coronary sinus pacing initiates counterclockwise atrial flutter while pacing from the low lateral right atrium initiates clockwise atrial flutter: analysis of episodes of direct initiation of atrial flutter. *J Electrocardiol* 1998; **31**: 345–61.

21 Feld GK, Shahandeh-Rad F. Activation patterns in experimental canine atrial flutter produced by right atrial crush injury. *J Am Coll Cardiol* 1992; **20**: 441–51.

22 Haissaguerre M, Sanders P, Hocini M, Jais P, Clementy J. Pulmonary veins in the substrate for atrial fibrillation: the "venous wave" hypothesis. *J Am Coll Cardiol* 2004; **43**: 2290–92.

23 Oshikawa N, Watanabe I, Masaki R, et al. Relationship between polarity of the flutter wave in the surface ECG and endocardial atrial activation sequence in patients with typical counterclockwise and clockwise atrial flutter. *J Interv Card Electrophysiol* 2002; **7**: 215–23.

24 Okumura K, Plumb VJ, Page PL, Waldo AL. Atrial activation sequence during atrial flutter in the canine pericarditis model and its effects on the polarity of the flutter wave in the electrocardiogram. *J Am Coll Cardiol* 1991; **17**: 509–18.

25 Feld G, Wharton M, Plumb V, Daoud E, Friehling T, Epstein L. Radiofrequency catheter ablation of type 1 atrial flutter using large-tip 8- or 10-mm electrode catheters and a high-output radiofrequency energy generator: results of a multicenter safety and efficacy study. *J Am Coll Cardiol* 2004; **43**: 1466–72.

26 Fischer B, Haissaguerre M, Garrigues S, et al. Radiofrequency catheter ablation of common atrial flutter in 80 patients. *J Am Coll Cardiol* 1995; **25**: 1365–72.

27 Kirkorian G, Moncada E, Chevalier P, et al. Radiofrequency ablation of atrial flutter: efficacy of an anatomically guided approach. *Circulation* 1994; **90**: 2804–14.
28 Calkins H, Leon AR, Deam AG, Kalbfleisch SJ, Langberg JJ, Morady F. Catheter ablation of atrial flutter using radiofrequency energy. *Am J Cardiol* 1994; **73**: 353–56.
29 Jais P, Haissaguerre M, Shah DC, et al. Successful irrigated-tip catheter ablation of atrial flutter resistant to conventional radiofrequency ablation. *Circulation* 1998; **98**: 835–38.
30 Scavee C, Jais P, Hsu LF, et al. Prospective randomized comparison of irrigated-tip and large-tip catheter ablation of cavotricuspid isthmus-dependent atrial flutter. *Eur Heart J* 2004; **25**: 963–69.
31 Calkins H. Catheter ablation of atrial flutter: do outcomes of catheter ablation with "large–tip" versus "cooled–tip" catheters really differ? *J Cardiovasc Electrophysiol* 2004; **15**: 1131–32.
32 Atiga WL, Worley SJ, Hummel J, et al. Prospective randomized comparison of cooled radiofrequency versus standard radiofrequency energy for ablation of typical atrial flutter. *Pacing Clin Electrophysiol* 2002; **25**: 1172–78.
33 Tsai CF, Tai CT, Yu WC, et al. Is 8-mm more effective than 4-mm tip electrode catheter for ablation of typical atrial flutter? *Circulation* 1999; **100**: 768–71.
34 Ventura R, Klemm H, Lutomsky B, et al. Pattern of isthmus conduction recovery using open cooled and solid large-tip catheters for radiofrequency ablation of typical atrial flutter. *J Cardiovasc Electrophysiol* 2004; **15**: 1126–30.
35 Mangat I, Tschopp DR, Jr., Yang Y, Cheng J, Keung EC, Scheinman MM. Optimizing the detection of bidirectional block across the flutter isthmus for patients with typical isthmus-dependent atrial flutter. *Am J Cardiol* 2003; **91**: 559–64.
36 Poty H, Saoudi N, Abdel Aziz A, Nair M, Letac B. Radiofrequency catheter ablation of type 1 atrial flutter: prediction of late success by electrophysiological criteria. *Circulation* 1995; **92**: 1389–92.
37 Schwartzman D, Callans DJ, Gottlieb CD, Dillon SM, Movsowitz C, Marchlinski FE. Conduction block in the inferior vena caval–tricuspid valve isthmus: association with outcome of radiofrequency ablation of type I atrial flutter. *J Am Coll Cardiol* 1996; **28**: 1519–31.
38 Tada H, Oral H, Sticherling C, et al. Double potentials along the ablation line as a guide to radiofrequency ablation of typical atrial flutter. *J Am Coll Cardiol* 2001; **38**: 750–55.
39 Tai CT, Haque A, Lin YK, et al. Double potential interval and trans-isthmus conduction time for prediction of cavotricuspid isthmus block after ablation of typical atrial flutter. *J Interv Card Electrophysiol* 2002; **7**: 77–82.
40 Cauchemez B, Haissaguerre M, Fischer B, Thomas O, Clementy J, Coumel P. Electrophysiological effects of catheter ablation of inferior vena cava–tricuspid annulus isthmus in common atrial flutter. *Circulation* 1996; **93**: 284–94.
41 Calkins H, Canby R, Weiss R, et al. Results of catheter ablation of typical atrial flutter. *Am J Cardiol* 2004; **94**: 437–42.
42 Manusama R, Timmermans C, Limon F, Philippens S, Crijns HJ, Rodriguez LM. Catheter-based cryoablation permanently cures patients with common atrial flutter. *Circulation* 2004; **109**: 1636–39.
43 Timmermans C, Ayers GM, Crijns HJ, Rodriguez LM. Randomized study comparing radiofrequency ablation with cryoablation for the treatment of atrial flutter with emphasis on pain perception. *Circulation* 2003; **107**: 1250–52.
44 Feld GK, Daubert JP, Weiss R, et al., for the CAFÉ trial investigators. Acute and chronic efficacy and safety of catheter cryoablation of the cavo-tricuspid isthmus for treatment of atrial flutter. *Heart Rhythm* 2005; **2**: S238.
45 Adragao P, Parreira L, Morgado F, Bonhorst D, Seabra-Gomes R. Microwave ablation of atrial flutter. *Pacing Clin Electrophysiol* 1999; **22**: 1692–95.
46 Liem LB, Mead RH. Microwave linear ablation of the isthmus between the inferior vena cava and tricuspid annulus. *Pacing Clin Electrophysiol* 1998; **21**: 2079–86.
47 Iwasa A, Storey J, Yao B, Liem LB, Feld GK. Efficacy of a microwave antenna for ablation of the tricuspid valve–inferior vena cava isthmus in dogs as a treatment for type 1 atrial flutter. *J Interv Card Electrophysiol* 2004; **10**: 191–98.
48 Chan JY, Fung JW, Yu CM, Feld GK. Preliminary results with percutaneous transcatheter microwave ablation of typical atrial flutter. *J Cardiovasc Electrophysiol* 2007; **18**: 286–89.

18 CHAPTER 18

Mapping of Macroreentrant Atrial Tachycardia

Mohammad Shenasa, MD, FACC, FAHA, FESC, FHRS,[1] *Hossein Shenasa,* MD, MSc, FACC,[1] *Christopher Piorkowski,* MD,[2] *Gerhard Hindricks,* MD,[2]

[1]O'Connor Hospital, San Jose, CA, USA
[2]University Leipzig Heart Center, Leipzig, Germany

Summary

Macroreentrant atrial tachycardia (AT) is rare among paroxysmal SVT and often involves complex reentry circuits and anatomical substrates. These tachycardias are commonly seen in patients with structural heart disease including postsurgical correction of congenital heart disease and, most importantly, following left atrial catheter ablation procedures. Reentrant pathways of right and left atrial macroreentrant tachycardia can be reliably assessed using conventional mapping strategies as well as using advanced 3D mapping systems. Both activation mapping and entrainment mapping are important to understand these complex and often multiple reentrant pathways. Ablation of critical isthmuses is curative for most patients with symptomatic macroreentrant tachycardia.

Introduction

The term "atrial tachycardia" encompasses several types of tachycardia that originate in the left or right atrium and do not require the participation of the atrioventricular node for maintenance of the arrhythmia. These tachycardias have different mechanisms including abnormal automaticity, triggered activity, and reentry. Traditionally, atrial tachycardia was classified according to the ECG pattern and was mainly grouped into typical atrial flutter, atypical atrial flutter, and ectopic atrial tachycardia.

In 2001, the Joint Expert Group from the Working Group on Arrhythmias of the European Society of Cardiology and the North American Society of Pacing and Electophysiology introduced a new classification for regular atrial tachycardia according to electrophysiological mechanisms and anatomical structures [1]. In this classification, a focal tachycardia is defined as atrial activation starting at a relatively small area and is characterized by radial spread of activation not covering the whole cycle. By contrast, macroreentrant tachycardias are characterized by circular patterns of activation that cover the whole cardiac cycle. Reentrant activation occurs around a large central obstacle as a fixed and/or functional barrier, usually several centimeters in diameter. However, recent observations indicate that

Cardiac Mapping, Third Edition Edited by Mohammad Shenasa, Gerhard Hindricks, Martin Borggrefe, and Günter Breithardt
 ISBN: 978-1-405-17572-2

micro-reentrant activation may also be operative as a mechanism of atrial reentrant tachycardia. Well-characterized macroreentrant atrial tachycardias include:

- typical atrial flutter,
- reverse typical atrial flutter,
- lesion macroreentrant tachycardia,
- lower loop reentry,
- right atrial free wall macro-reentry without atriotomy,
- left atrial macroreentrant tachycardias.

While various studies have investigated the mechanisms of right atrial macroreentrant tachycardia (RAMRT), mechanisms underlying left atrial macroreentrant tachycardia (LAMRT) have been investigated only recently by means of invasive electrophysiological studies and catheter ablation. This is particularly because the access to the left atrium is more complex compared to the right atrium, as transseptal puncture is required in most patients. However, today in the era of atrial fibrillation catheter ablation, access to the left atrium has become a safe routine procedure for the interventional electrophysiologist. This has dramatically increased knowledge and understanding of LAMRT. In this chapter, the electrocardiographic and electrophysiologic characteristics of RAMRT and LAMRT are presented separately.

Right Atrial Macroreentrant Tachycardia (RAMRT):

Tachycardias arising from right atrium include the following:

1 Inappropriate sinus tachycardia (chronic nonparoxysmal sinus tachycardia).
2 Sinus node reentry tachycardia.
3 Isthmus-dependent atrial flutter.
4 Non-isthmus-dependent atrial flutter.
5 Focal atrial tachycardia.
6 AT arising from right atrial septum or crista terminalis.
7 Postoperative AT.

Atrial flutter and focal AT are discussed in separate chapters. Electrocardiographically AT is defined as arrhythmias with a rate of 110–240 bpm (without antiarrhythmic drugs) in which atrial activity is separated by an isoelectric line. This definition, however, does not distinguish focal from reentrant mechanisms. AT is rare among other SVTs and is independent from the A-V node, and may have a 1:1, 2:1, or higher level of A-V conduction block. Macroreentrant AT may be induced, entrained, and terminated by programmed electrical stimulation [2]. These tachycardias usually arise around a functional, that is, normal structure such as crista terminalis or an anatomical obstacle such as post surgical scars or patches [3–5]. Tachycardias arising from crista terminalis are usually in the absence of structural heart disease and may be of focal or reentrant nature [5]. Many macro-reentry AT, particularly those arising from right lateral wall related to atriotomy scars, demonstrate large circuits, and are often complex and require detailed mapping.

Atrial macro-reentry involving coronary sinus has also been reported [6]. Table 18.1 summarizes the electrocardiographic and electrophysiologic characteristics of different types of AT. AT may present as (i) recurrent nonsustained; (ii) paroxysmal sustained; (iii) incessant; and (iv) paroxysmal with A-V block usually seen in digitalis toxicity. Paroxysmal AT are relatively rare and account for only about 10–15% of all SVTs [7]. Unlike AVNRT and AVRT, patients with AT usually have structural heart disease. Sino atrial nodal reentrant tachycardia (SNRT) and macroreentrant AT are the two major paroxysmal SVT that do not involve the AV node or an A-V pathway as an active part of the reentry circuit.

SNRT is rare and is often mistaken for sinus tachycardia. SNRT demonstrates a similar atrial activation and *P*-wave morphology to that of sinus rhythm. The PR interval in SNRT is usually longer than sinus tachycardia [8].

Electrocardiographic (ECG) Characteristics and Surface ECG Mapping of RAMRT

To identify the site of origin of AT, 12-lead ECG is useful. Difficulty arises when there is 1:1 A-V ratio during AT. Longer RP than PR during tachycardia suggests AT. Positive *P*-wave in lead I, II, II excludes junctional tachycardia; negative *P*-wave in lead I or AVL and positive *P*-wave in V1 suggests left atrial origin. Positive or biphase *P*-wave in AVL and negative *P*-wave in leave V1 suggests right atrial tachycardia. Negative *P*-wave in AVR suggests right atrial

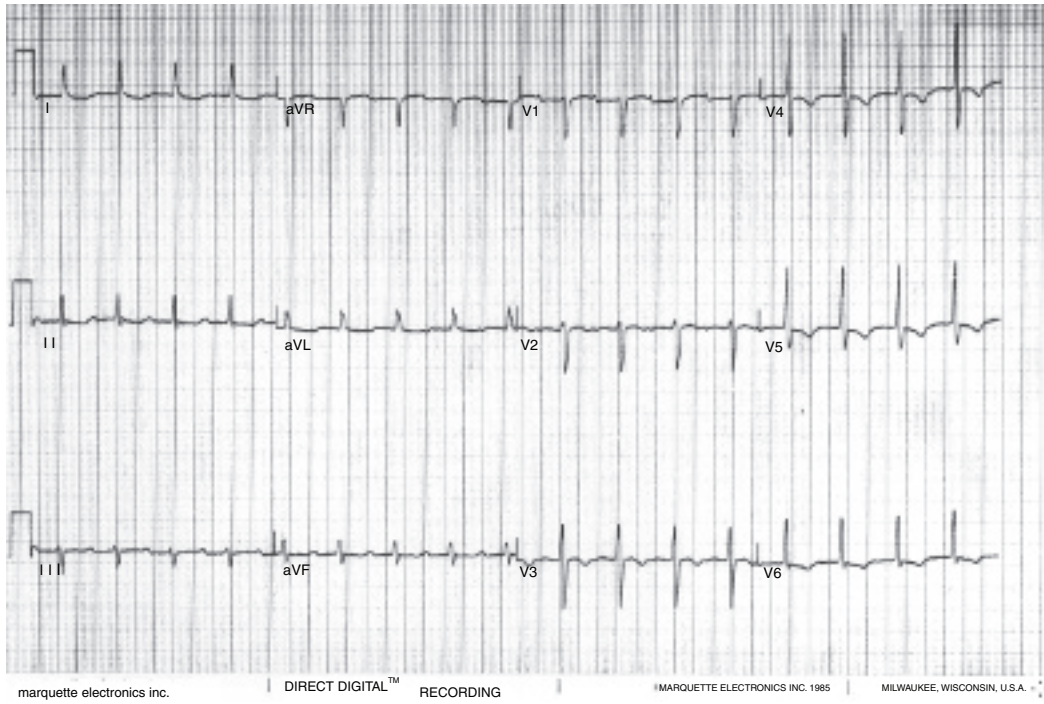

Figure 18.1 Twelve-lead electrocardiogram of a patient with macroreentrant atrial tachycardia. *P*-waves are of low amplitude and biphasic in V1, V2, III, and AVF, suggesting low right septal origin of the tachycardia.

tachycardia arising from crista terminalis. In SNRT, *P*-waves are identical to those with sinus rhythm, with the PR interval usually longer than SR, whereas in AT the *P*-wave morphology is different from in SR.

AT arising from the tricuspid annulus demonstrates a negative or biphasic *P*-wave in precordial and inferior leads (Figure 18.1), whereas AT arising from mitral annulus *P*-wave is negative in AVL and positive in V1**.** A more detailed relation of the *P*-wave morphology to the site of origin of AT is well described in [9, 10]. Because of the presence of multiple atrial reentrant circuits and other macroreentrant AT—that is, isthmus-dependent and non-isthmus-dependent tachycardia may mimic macroreentrant AT—surface *P*-wave mapping is often not adequate. A thorough ECG algorithm of *P*-wave morphology for localization of AT is well described in Chapter 20 of the book and does not need to be repeated here [11]. Vagal maneuvers or pharmacological agents that show A-V conduction may produce 2:1 or 3:1 A-V conduction and confirms AT.

Body Surface Potential Mapping (BSPM)

BSPM of *P*-waves during AT have been used for localization of the site of origin of AT and have provided more accurate localization of the arrhythmogenic site [10, 12, 13] than 12-lead electrocardiogram. This method, however, is time consuming and is not widely used.

Electrophysiological Characteristics and Diagnosis of Macroreentrant AT

1 Reproducible initiation and termination of AT by atrial extrastimuli and atrial pacing.
2 Initiation of tachycardia by critically timed atrial extrasystole demonstrates an inverse relationship between atrial coupling interval and first beat of tachycardia.
3 Demonstration of manifest and/or concealed entrainment during atrial pacing.

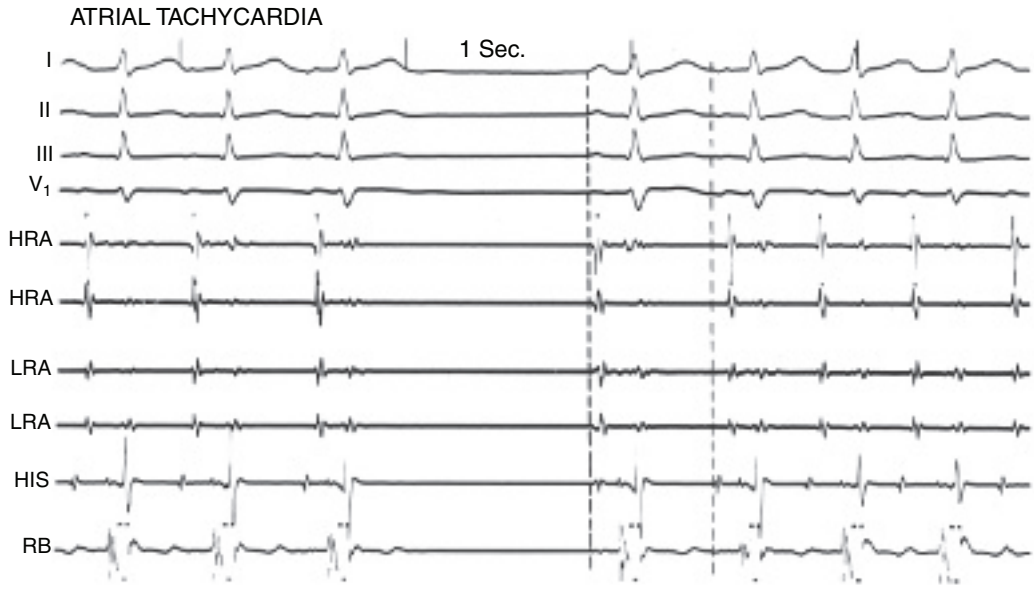

Figure 18.2 Illustrates spontaneous termination of atrial tachycardia, which reinitiates after one sinus beat. Note the change in *P*-wave morphology and change in intracardiac electrogram sequence. This tachycardia originates from the low right atrium near the His bundle.

4 *P*-wave morphology and atrial activation sequence during AT be different from sinus rhythm (Figure 18.2).

5 Demonstration of tachycardia to be independent from the sinus node and A-V node, that is, the presence of A-V block of variable degree without affecting the tachycardia (Figure 18.3).

6 Change in tachycardia cycle length (A-A interval), preceding the change in ventricular cycle length (V-V interval). Difficulty may arise when there is 1:1 conduction and differential diagnosis is from A-V nodal reentrant tachycardia or A-V reentrant tachycardia using a concealed septal tachycardia, particularly in the case when AT arises from septal aria.

7 Pacing maneuvers such as delivery of ventricular extrasystole that advances to the atria the time that His bundles is refractory or termination of tachycardia without conduction to the atria basically excludes AT. Continuation of atrial tachycardia during ventricular pacing, that is, A-V disassociation, favors the presence of AT and bypass tracts are excluded.

8 Double atrial response (A-A) upon cessation of ventricular pacing in patients with AT who demonstrate intact ventriculo atrial conduction is a highly sensitive and specific diagnostic tool [14] (Figure 18.4). Obviously this method is not applicable to those patients with ventriculo atrial block. However, in the latter group A-V dissociation is present, thus the diagnosis of AT is easier.

9 Pharmacological maneuvers such as the use of IV adenosine, calcium antagonist or beta blockers to slow A-V nodal conduction and demonstrate A-V block while AT continues maybe useful.

Some investigations have reported a mechanism-specific response to IV adenosine or Verapamil. Focal AT and rarely macroreentrant ATs arising from crista terminalis as well as some left AT terminate with IV adenosine. SNRT also terminate with IV adenosine. Automatic AT originating from crista terminalis are usually adenosine sensitive [15–17]. Iwai et al. reported in their series of eight patients with macroreentrant, AT failed to terminate with IV adenosine. The mechanism of tachycardias in this study was documented with electroanatomical mapping [15].

Markowitz et al. recently reported that a subset of adenosine-insensitive focal AT is due to microreentry [18]. Figure 18.5 shows an example of termination of macroreentrant atrial tachycardia

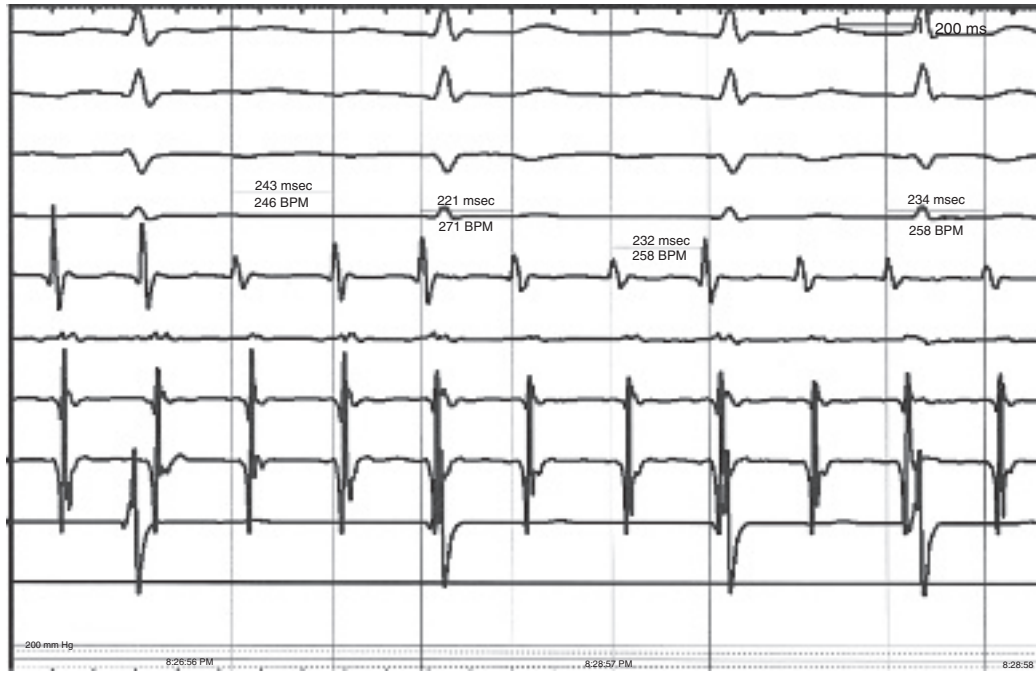

Figure 18.3 Surface EKG recording and intracardiac electrogram of a macroreentrant atrial tachycardia with some degree of tachycardia cycle length oscillation. This tachycardia did not terminate with IV adenosine and originated from the area near ostium of the coronary sinus.

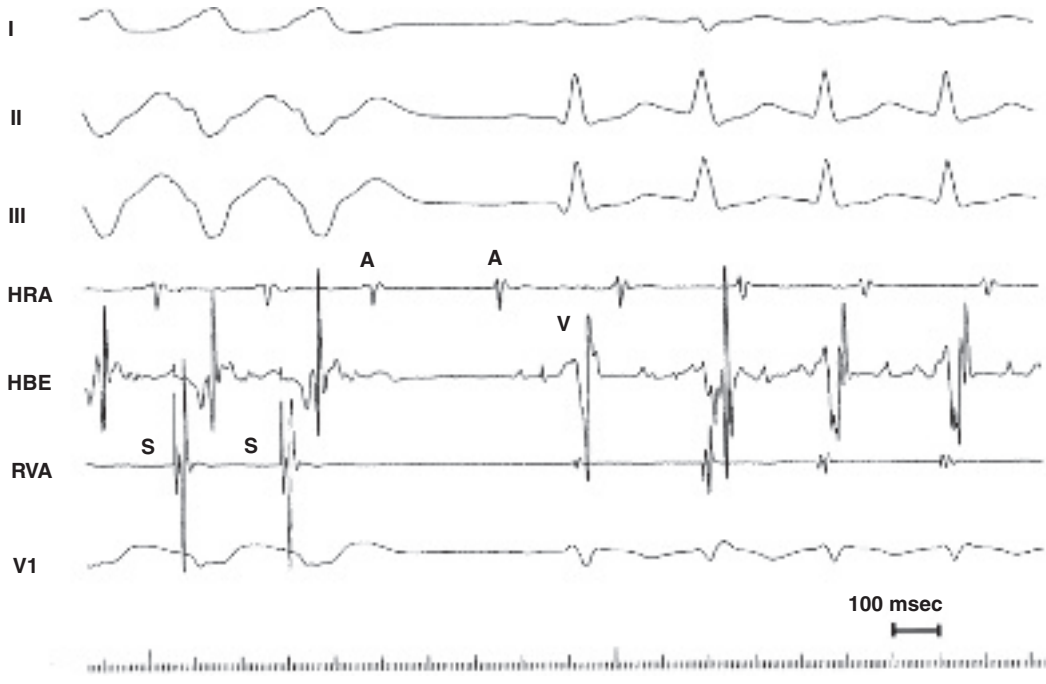

Figure 18.4 The response to ventricular pacing with 1:1 ventriculoatrial conduction during tachycardia in a patient with atrial tachycardia. Note a double atrial response (A:A) upon cessation of ventricular pacing. Reprinted with permission from Ref. 14.

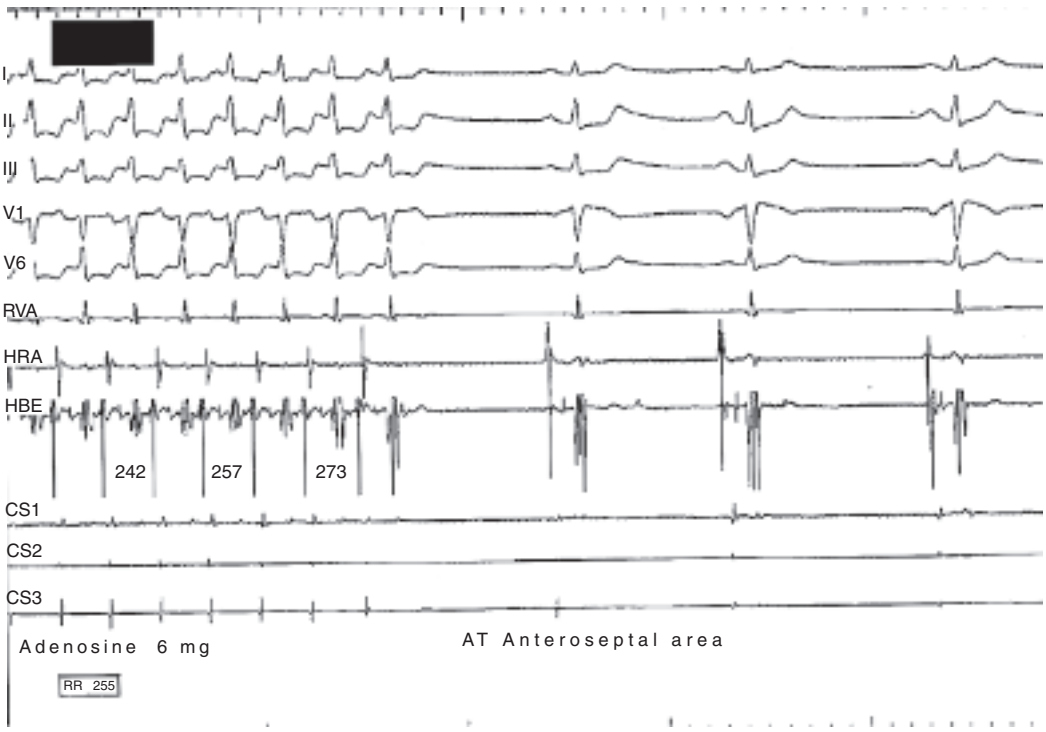

Figure 18.5 Illustrates an example of termination by IV adenosine of a macroreentrant atrial tachycardia arising from anteroseptal region of the right atrium.

arising from the anteroseptal area of the atrium by I.V. adenosine.

A subset of Lidocaine-sensitive low AT has also been reported [19]. Electrical stimulation maneuvers remain the gold standard to distinguish between tachycardia mechanisms that is, reentry, triggered activity, or automaticity. Termination of atrial tachycardia with Verapamil suggests the presence of slow calcium conduction which favors reentry [2].

Entrainment Mapping

Macroreentrant AT circuits demonstrate manifest or concealed entrainment. Concealed entrainment can identify the site of reentry circuit. Pacing is usually done at cycle lengths of 20–40 msec shorter than the AT cycle length.

A criterion for concealed entrainment has been described in detail [20–22]. Briefly, (i) *P*-wave morphology and an intracardiac electrogram during entrainment should be similar to those of tachycardia. (ii) The postpacing interval (defined as the conduction time from pacing site to the reentrant circuit) and (iii) stimulus to the *P*-wave interval during pacing should both be equal to the electrogram of a *P*-wave interval during tachycardia, and should be 10 msec or less for both measurements. A long stimulus-to-*P*-wave interval suggests that pacing is in the exit tail of the reentry circuit, where slow conduction is present. Radiofrequency ablation at this site is usually effective.

Manifest entrainment is defined as constant fusion at a constant pacing rate and progressive fusion with incremental pacing. Fusion occurs because of atrial activation that occurs in part from the stimulus site and in part from the previous paced wave front exiting the zone of slow conduction. When entrainment is manifest, the last captured *P*-wave is entrained at the pacing cycle length but does not demonstrate fusion [20, 21, 23]. Demonstration of manifest entrainment suggests that AT is not focal. Acceleration of AT and/or conversion to atrial flutter or fibrillation during pacing hampers the study.

Pace Mapping

Atrial pace mapping will allow precise localization of the site of origin of AT. Pacing is done during sinus rhythm at different sides to obtain locations that the paced *P*-wave matches the tachycardia *P*-wave in morphology, size, and configuration [10, 13, 21]. This can be done in unipolar or bipolar mode. Pace mapping is particularly useful when AT is noninducible or nonsustained. Pace mapping may become less accurate when the paced *P*-wave merge into the previous QRS/*T*-wave. Furthermore, the spatial resolution of unipolar atrial pace mapping is not as accurate as was assumed previously [24]. Therefore, AT due to reentry entrainment mapping is the key to localization of tachycardia circuits, and in patients with focal AT, pace mapping and identification of the earliest site of activity is more helpful.

Activation Mapping of Macroreentrant AT

AT may arise from any localization in the atria; thus accurate localization is often challenging. Multipolar catheter mapping in AT is quite feasible and accurate. Timing is usually referenced to the onset of a *P*-wave or to an arbitrarily chosen site in the atrium. If AT is not sustained, IV isoprotererol will enhance induction and sustenance of the tachycardia. Pre-*P*-wave electrical activity and fractionated electrograms are often observed at the site of origin of macroreentrant AT and those of SNRT. In the case of macroreentrant AT, the entire tachycardia cycle should be mapped; thus a multipolar electrode catheter such as Halo Catheter (Cordis Webster, Baldwin Park, CA) with 2-mm interelectrode spacing or a basket catheter provides further detail.

Mapping Criteria for Localization of AT Reported Previously in Details [25]

1 Local electrical activity preceding the onset of surface *P*-wave by 20–45 msec (Figure 18.6). Local electrogram are often fractionated, prolonged, and have low-amplitude features.

2 Concealed entrainment with a short stimulus-to-*P*-wave interval by 20–30 msec, suggesting that the pacing site is at the exit position of the tachycardia circuit.

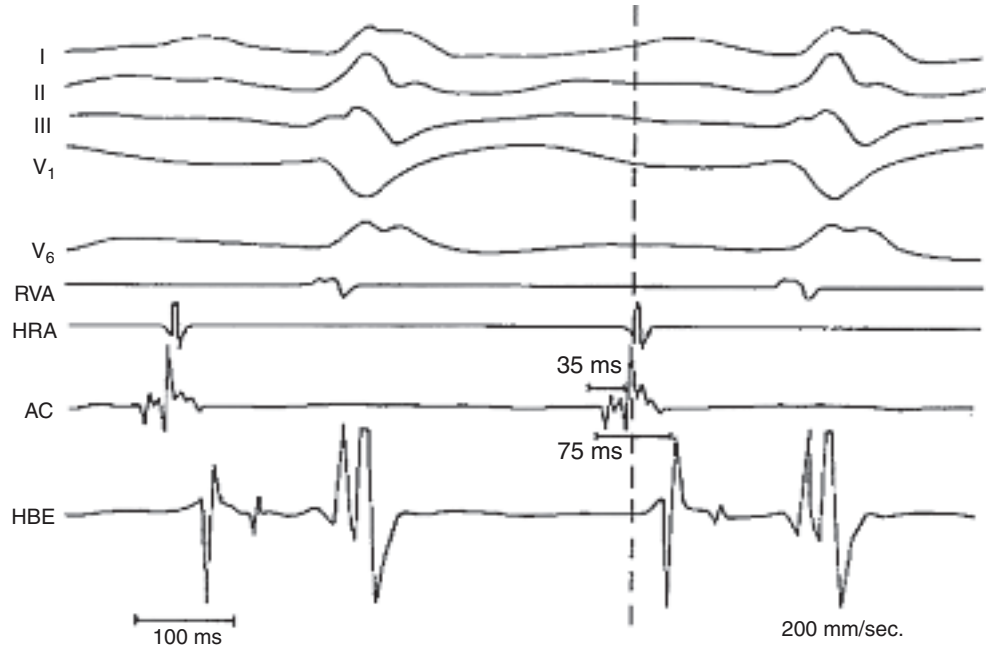

Figure 18.6 An atrial tachycardia arising in the sinus node area with the local electrical activity preceding the *P*-wave by 35 msec. KEY: AC = ablation catheter.

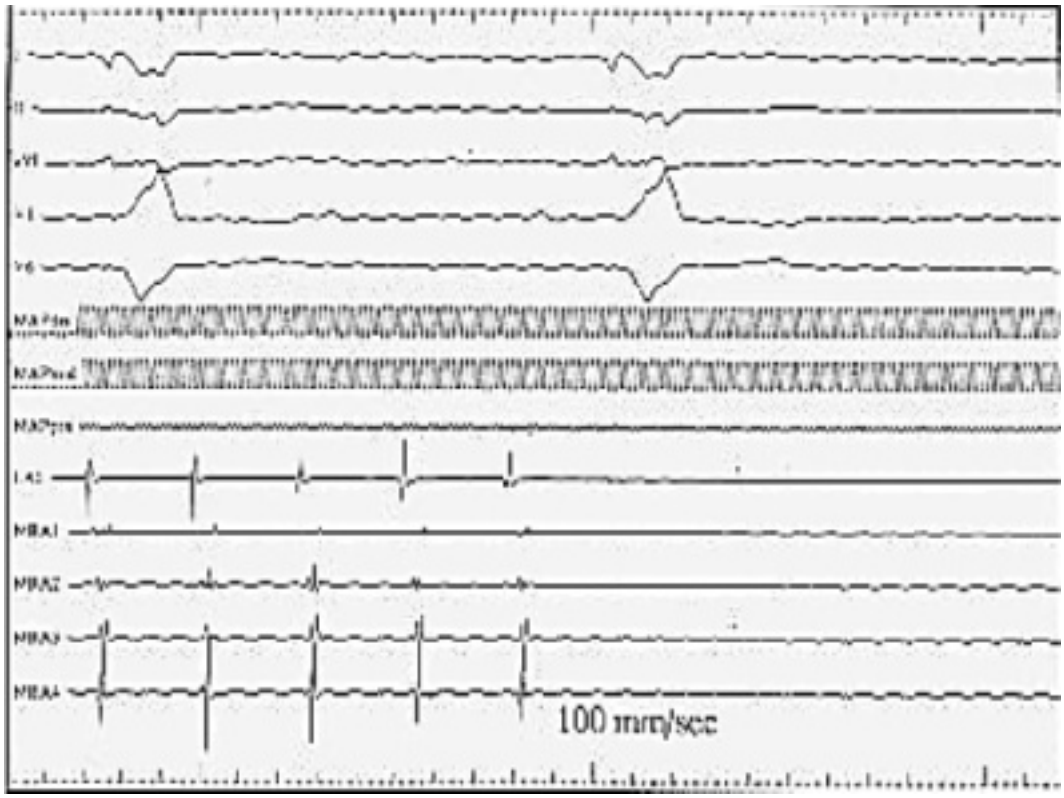

Figure 18.7 Rapid elimination of atrial tachycardia, a few seconds after radiofrequency ablation.

3 Rapid elimination of tachycardia with few seconds of radiofrequent current application to the target site (Figure 18.7).
4 Termination of AT by subthreshold stimulation suggest that pacing is adjacent to the critical zone of AT.
5 Diastole potential and gaps or so-called "isolated channels" have been reported in patients with large macroreentrant AT, particularly those postatrial fibrillation ablation and postsurgical repair of congenital heart disease [26].

Electrode Backet Mapping

Schmitt et al. reported use of a multielectrode basket catheter to map macroreentrant right AT [27]. This technique was used in 31 patients with AT, which were located in the right atrium in 21 patients (70%), while the remainder were in the left atrium (Figure 18.8).

Figure 18.9 illustrates electrograms from the basket electrode of a right atrial tachycardia originating from the midseptal region. Note the earliest activity recorded about 30 msec in advance of the *P*-wave [27]. Zenner et al. reported on the use of a basket electrode and computer-assisted animation of AT of either focal or reentrant mechanisms in 32 patients and atrial flutter in 38 patients (Figure 18.10) [28]. This computer-based animation system provided a 3D activation pattern of the tachycardia and a subsequently high success rate for the ablation procedure. Electrode basket mapping provides rapid simultaneous contact recording of the anatomical chamber and provides reasonable global density; however, its resolution is limited.

3D Mapping

Electroanatomical Mapping

With commercially available new and upgraded computerized mapping systems, electrode catheter mapping has become less frequently used. Electroanatomical mapping (Carto™; Biosense Webster, Inc., Baldwyn Park, CA) provides rapid

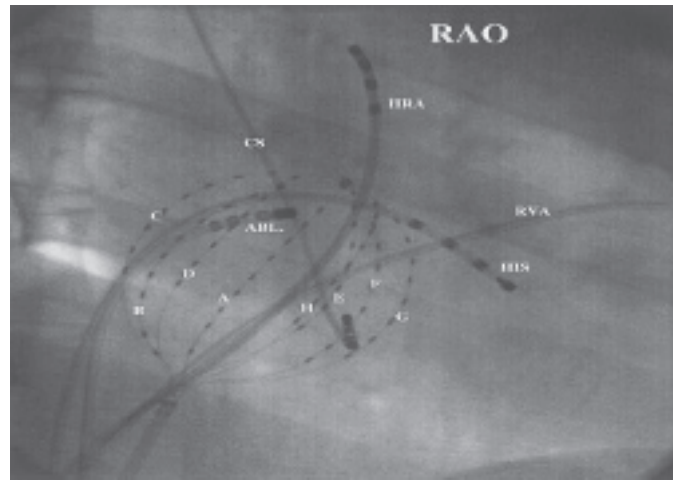

Figure 18.8 Fluoroscopic RAO view of the electrode basket catheter in the right atrium. Reprinted with permission from Ref. 27.

visualization of the entire AT circuit as well as the right atrium. The system has been described previously [29].

In order to construct the right atrial geometry, several anatomical landmarks such as high right atrium, right atrial appendage, antrum of superior and inferior vena cava, tricuspid annulus, ostium of the coronary sinus and His bundle region are tagged and registered. Isochronal maps (propagation maps) are then generated during sinus rhythm

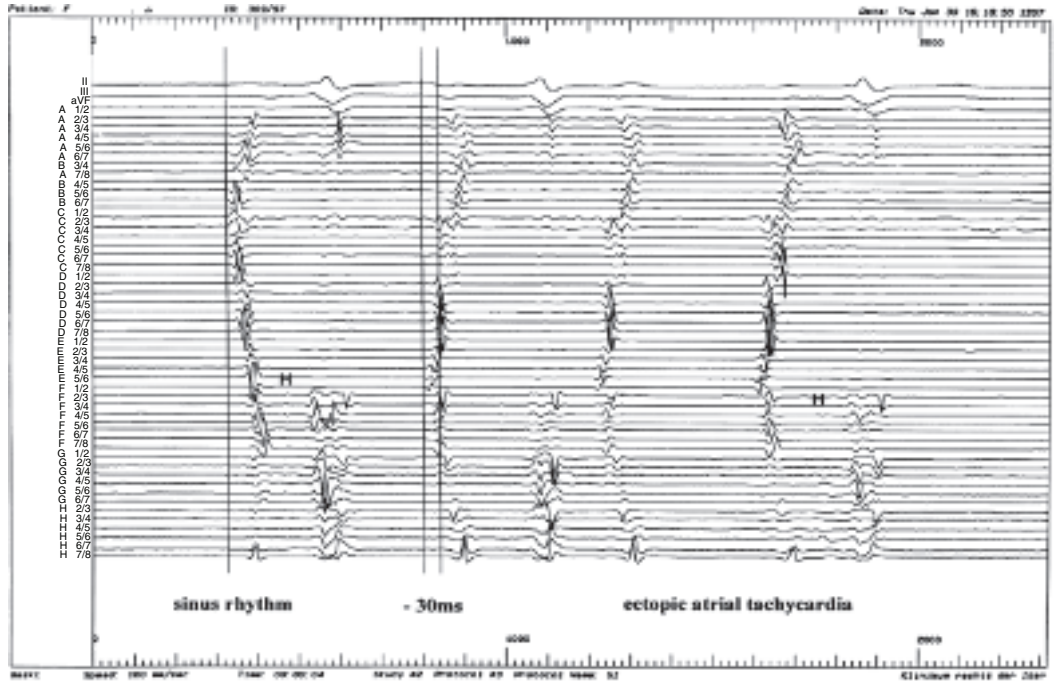

Figure 18.9 Initiation of short episode of RAT. Standard lead II, III, and aVF and MBC bipolar electrograms are displayed. First, sinus beat is sinus; three consecutive beats are ectopic originating from midseptal region. *P*-wave in inferior leads is predominantly negative with terminal positive forces. Activation sequence of RA is reversed. Earliest activity recorded from basket electrodes is 30 msec in advance of the beginning of the *P*-wave. Reprinted with permission from Ref. 27.

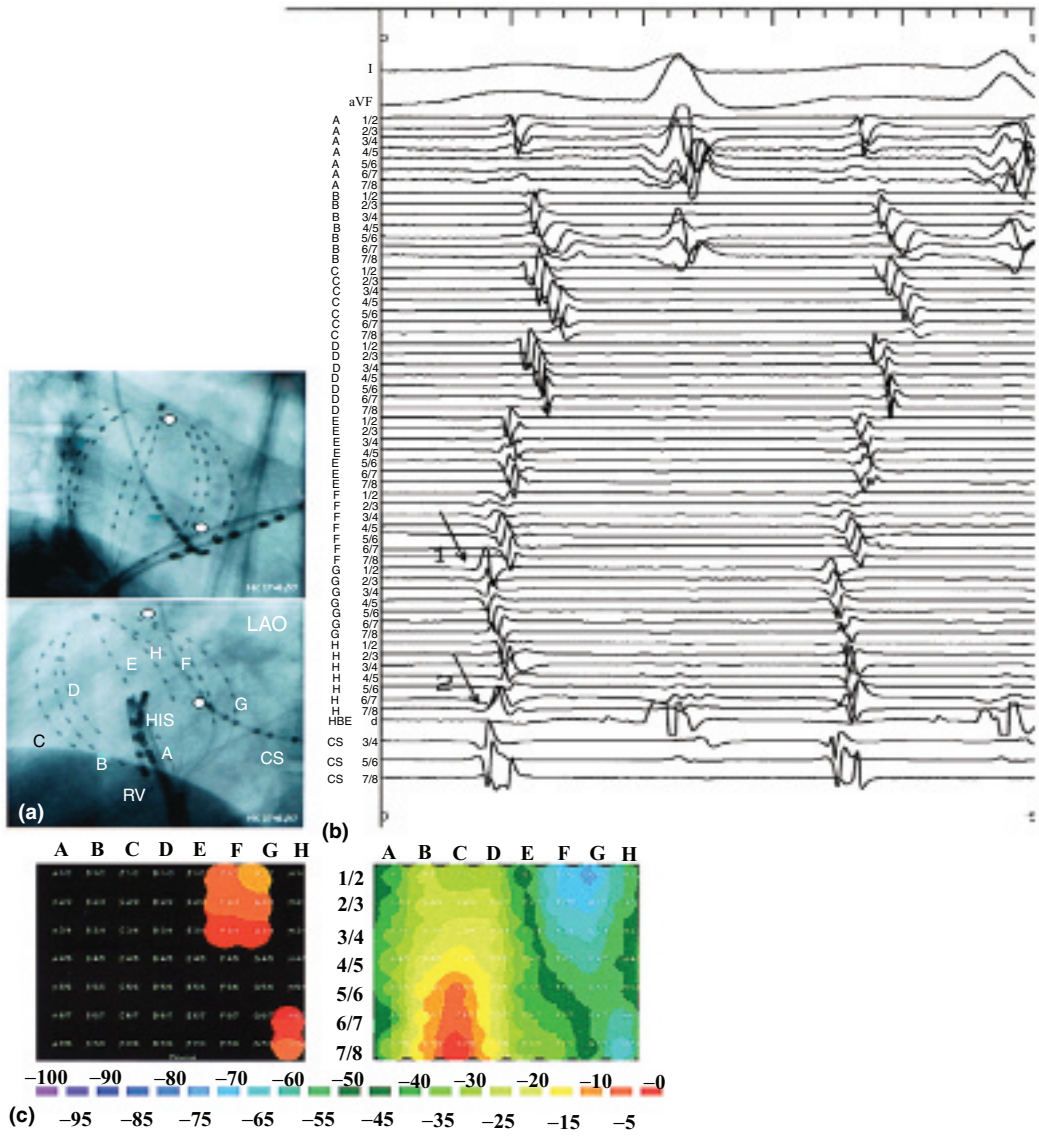

Figure 18.10 Left AT. (a) Fluoroscopic views of the BC. Small white circles mark the positions of electrode pairs G_{1-2} and H_{7-8} located in the high anteroseptal and low posteroseptal regions. Red letters mark splines located anteriorly. (b) Simultaneous recordings of the surface ECG, leads I and aVF, and bipolar electrograms from the BC and CS. Electrode pairs G_{1-2} and H_{7-8} (arrows) record the earliest activation in the RA. (c) Animated maps of the BC recordings. (Left panel) First 15 msec of activation in the RA. (Right panel) Complete activation of the RA. Reprinted with permission from Zenner B, et al. *Circulation* 1999; **99**: 2414–22.

and AT. An appropriate window of interest, usually adapted with a filter setting between 10 and 400 Hz high-density maps with electrogram analysis, allows rapid identification of the arrhythmogenic site and subsequently successful ablation.

An isochronal map demonstrates a progressive activation around the right atrium. This method uses multiple sequential recording of either unipolar or bipolar electrograms and displays them in 3D modes. Usually some editing is required by the

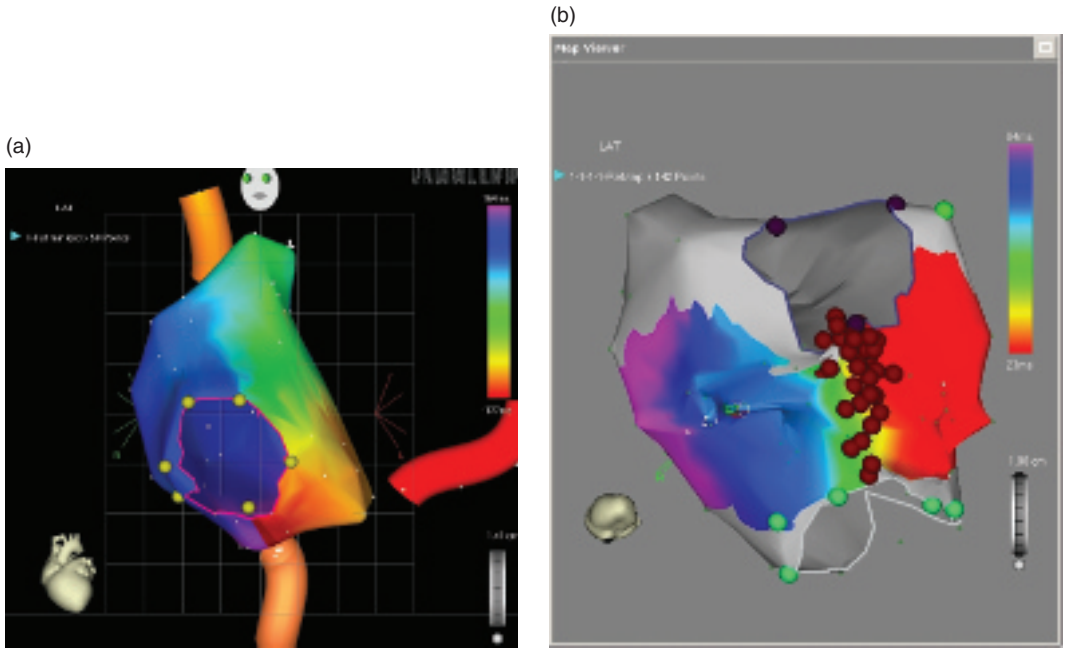

Figure 18.11 (a) An electroanatomical map of a patient with macroreentrant atrial tachycardia. (b) Shows the scar tissue and the dot represent radiofrequency current delivery.

operator. Points with poor quality signal or those that were inconsistent with anatomical geometry (i.e., tagged ones) were excluded. Areas of multiple breakthroughs were carefully examined for multiple reentry circuits or artifacts. (Figure 18.11a,b illustrates an example of scar-related macroreentrant AT.) The area of the earliest activation is then identified. The activation propagates around the scar tissue (gray color) in the superior posterior direction and turns around anteriorly (see Video Clip 12–18).

Mapping may be acquired during SR, tachycardia and entrainment maneuvers. Other forms of maps i.e. voltage maps can also be generated. Voltage maps can easily intensify scar tissues that can localize an obstacle of reentrant circuit. Electroanatomical mapping also allows substrate mapping and elucidation of scar related reentry circuit. In most cases of macroreentrant of AT up to 90% of the tachycardia cycle length can be mapped. Technical details of electroanatomical mapping systems have been described previously [30–32]. Mapping and successful ablation of multiple macro-reentry AT in adult patients with repaired congenital heart disease using electroanatomical mapping has also been reported [33].

Noncontact Mapping

This technique uses multielectrode array recording of a unipolar electrogram and provides a 3D view of the right atrium and reentry circuit (Ensite 3000^{TM}; Endocardial Solutions, St. Jude's, CA). Noncontact mapping uses simultaneous acquisition of many electrical signals from different sites of a single tachycardia beat and digitally transfers them to a computer workstation. The noncontact mapping system uses the inverse solution principle. The computer then generates a virtual 3D endocardial anatomy with activation or repolarization maps.

A unipolar local electrogram from any selected site can be displayed. The software recognizes the region of preferential conduction from the site of origin to the exit point (head-to-tail) of the reentry circuit [34]. Figure 18.12a,b illustrates a noncontact map of a sinus rhythm during macroreentrant atrial tachycardia with variable AV conduction evident from the surface ECG and virtual electrograms.

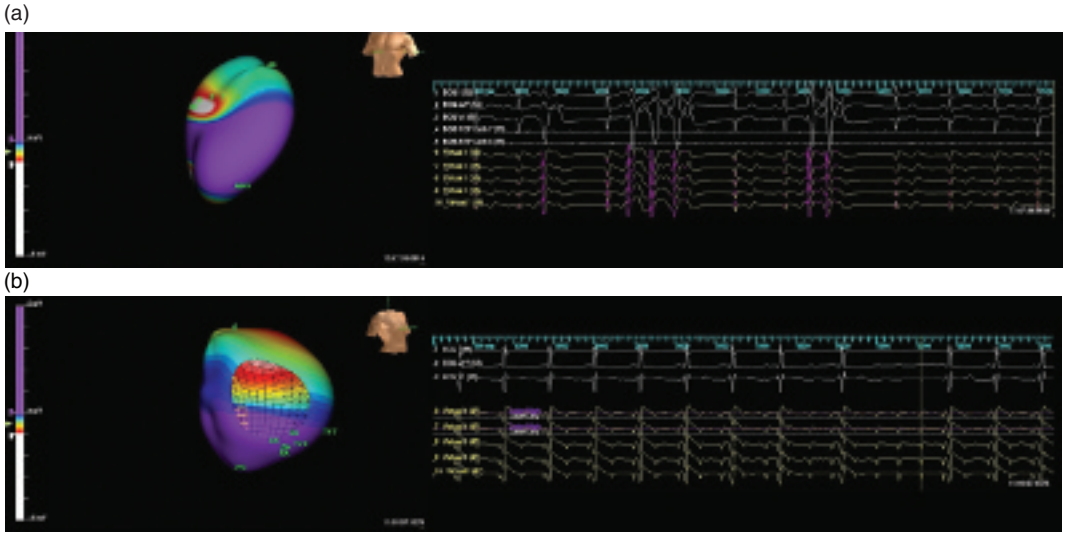

Figure 18.12 (a) Noncontact map during sinus rhythm. (b) Noncontact map of macroreentrant atrial tachycardia arising from the anterior part of the right atrium. Note variable AV conduction on surface ECG and virtual electrograms.

Note a different atrial activation from the sinus rhythm to the atrial tachycardia.

Lin et al. used noncontact mapping and acquired voltage maps in patients with AT, flutter, and fibrillation and compared them with patients with AVNRT. The peak negative voltage was significantly reduced in patients with AT, flutter, and fibrillation compared to those with AVNRT [34]. Voltage maps are quite useful in macroreentrant AT because they detect areas of slow and depressed conduction [35]. Tai et al. reported use of noncontact 3D mapping of the upper loop reentry originating at the crista terminalis. Radiofrequency current delivered at the crista terminalis eliminated the tachycardia [36].

High-density mapping using a high-density catheter (Pentary™; Biosense-Webster) had been used to evaluate focal atrial tachycardia [37]. This technique is not useful for reentrant atrial tachycardia.

Intracardiac Echocardiography (ICE)

ICE is quite useful for mapping and ablation of AT, particularly for identification of crista terminalis and other complex postcongenital surgery cases. Application of ICE reportedly increases the success rate of radiofrequency ablation of AT. Kalman et al. reported the value of ICE in identification of crista terminalis as a distribution of focal atrial tachycardias [5].

ICE is used for catheter positioning and evaluation of surgically corrected structure in relation to tachycardia mechanism. Olgin et al. reported the use of ICE in experimental studies of long linear atrial lesions in the right atrium and found out the technique was useful to guide anatomical placement of the catheters in catheter–tissues contact. Furthermore, ICE was accurate within 0.3 mm for the anatomical target to create ablation lesions [38].

Multimodality Image Integration

Recently, multimodality imaging and image integration has been used to provide a detailed chamber geometry construction to improve mapping and ablation of different types of atrial arrhythmias. These include integration of ICE, cardiac CT, and MRI of the right and left atrium and have been used for mapping and ablation atrial fibrillation and AT. These new modalities certainly improve our understanding of the anatomical relation to the arrhythmogenic substrate and increase efficacy of ablative therapies [39–43].

Ablation of RAMRT

Because antiarrhythmic therapy for AT is often ineffective and poorly tolerated, transcatheter ablation

of the arrhythmogenic substrate that provides curative therapy is now the first-line approach. After target sites were identified, radiofrequency ablation was performed using a 4-mm tip electrode catheter with simultaneous monitoring of intracardiac electrograms, blood pressure, and temperature (usually 50–60°C) and power (usually 20–40 W). Mapping and ablation catheters were positioned in right and left anterior oblique fluoroscopic views. The success rate of radiofrequency ablation of AT is about 90% with usually a 5–10% recurrence during long-term follow-up. However, some recurrences may not be the same as ablated tachycardia.

Left Atrial Macroreentrant Tachycardia (LAMRT)

In general, the same criteria as described above for right atrial tachycardia regarding the tachycardia mechanism also apply for left atrial tachycardia, that is, the differentiation between focal and reentrant mechanisms. This part of the chapter on atrial macroreentrant tachycardia will particularly focus on the specific electrophysiological features and catheter ablation strategies of LAMRT. Today, LAMRT is most frequently observed following left atrial surgical or catheter ablation of atrial fibrillation. Depending on the ablation strategy applied (i.e., pulmonary vein disconnection, pulmonary vein isolation, placement of linear lesion) the incidence of LAMRT following AF-ablation varies between approx. 5% and 15%. Thus, the recognition, correct diagnosis, and appropriate treatment strategy will be of increasing importance in many EP labs in the future. Most patients with LAMRT who have not undergone previous left atrial ablation procedures are suffering from cardiovascular disease. In the absence of any organic heart disease, LAMRT is a very rare arrhythmia.

Electrocardiographic and Electrophysiological Characteristics of LAMRT

As atrial fibrillation LAMRT may occur as a paroxysmal, persistent, or longstanding persistent arrhythmia. Long episodes are common. The cycle length of LAMRT usually varies between 180 and 350 msec. However, shorter as well as longer cycle length may occur, and the rate range is too wide to be reliably used for the determination of the arrhythmia mechanism and the differentiation from other types of atrial tachycardia. In response to antiarrhythmic drugs (especially class Ic drugs) cycle length lengthens; however, termination of LAMRT by antiarrhythmic drugs can only be achieved in less than 50% of cases. LAMRT does not usually terminate in response to adenosine injection.

The electrocardiographic pattern of most forms of RAMRT, that is, continuous electrical activation without visible isoelectric baseline, can not be applied per se for LAMRT. These tachycardias may result in an ECG pattern typical for focal atrial tachycardia with discrete *P*-waves and isoelectric baseline [44], but may also appear with a surface ECG presentation with continuous undulation without an isoelectric period. Thus, LAMRT has a highly variable ECG pattern (Figure 18.13).

The surface ECG of most LAMRT is characterized by prominent forces in lead V1 with flat deflections in other surface leads. In the case of left septal reentrant circuits, both positive and negative polarity of the flutter wave in lead V1 has been described, depending on the sequence of septal and left atrial activation [45]. If flutter waves are visible in the surface leads, the voltage is usually decreased in the inferior leads compared to typical atrial flutter [46]. The usefulness of the surface ECG to determine the location of reentrant circuits is very limited in patients with AMRT following extensive left atrial ablation to cure atrial fibrillation: typical atrial flutter may present with an atypical surface ECG pattern [47] and vice versa—although to a rarer extent LAMRT may mimic the surface ECG of typical atrial flutter.

Delineation of Reentrant Circuits and Catheter Ablation of LAMRT

Invasive electrophysiological study is required for a definite diagnosis of LAMRT. In our laboratory, multipolar electrode catheters are placed in the high right atrium or along the tricuspid annulus, at the His-bundle, and in the coronary sinus (Figure 18.14). The main differential diagnoses of LAMRT are: (i) RAMRT; (ii) focal right and left atrial tachycardia and micro-reentrant atrial tachycardia.

The electrophysiological criteria to differentiate focal atrial tachycardia from macro-reentrant tachycardia have been described above in detail.

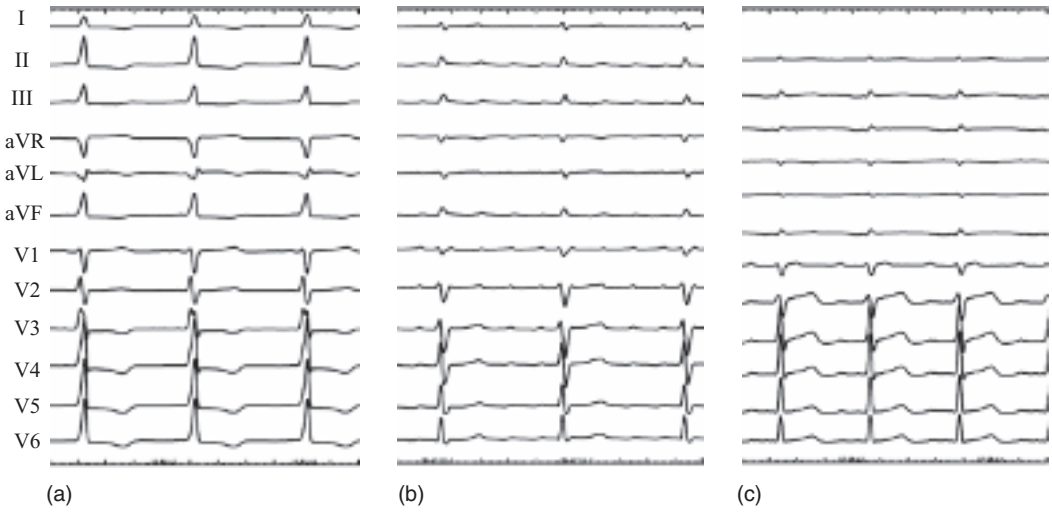

Figure 18.13 Twelve-lead surface ECG obtained from three different LAMRT. Panel A shows no visible flutter waves at all. Electrophysiological study demonstrated septal LAMRT. Panel B shows positive flutter waves in the inferior leads and in V1 (perimitral LAMRT), and panel C shows very slow LAMRT (380 msec) with flutter waves only visible in lead V1 (LAMRT travelling around the left atrial appendage).

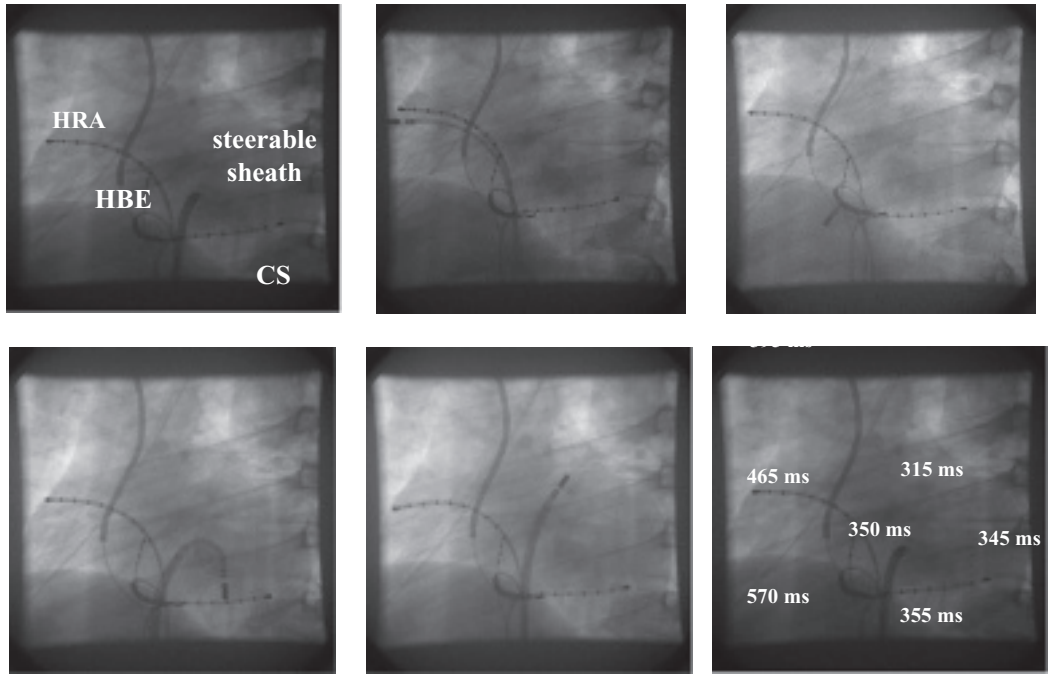

Figure 18.14 Positioning of conventional electrode catheters and the mapping and ablation catheter [panels (b)–(e)] for the diagnosis of left atrial macro-reeentrant tachycardia. Multipolar catheters are placed in the high right atrium (HRA), the His-bundle region (HBE), and the coronary sinus (CS). In addition, a steerable sheath is introduced transseptally to the left atrium. Panels (b)–(e) depict different positions of the mapping and ablation catheter for entrainment stimulation in the high right atrium (b), the right atrial isthmus (c), the inferior mitral annulus (e) and the left atrial roof (e). The postpacing interval (PPI) assessed at each entrainment site is measured and used to generate a PPI gradient. The shortest PPI of 335 msec (cycle length of the tachycardia 315 msec) is measured along the roof of the left atrium.

However, a simple but useful algorithm has been recently introduced to define the mechanism and the chamber of origin of atrial tachycardias [48]. This algorithm takes into account the bi-atrial activation time in relation to the tachycardia cycle length and the sequence of atrial activation. If the total bi-atrial activation time is less than 40% of the tachycardia cycle length, a focal mechanism is highly likely, while bi-atrial activation times of more than 40% of tachycardia cycle length indicate a reentrant mechanism. As a second step of the algorithm, entrainment stimulation using the standard catheters placed in the right atrium and the coronary sinus is applied. After the chamber of origin of the macroreentrant tachycardia is identified, the reentrant circuit is analyzed in detail using voltage mapping, activation mapping, and entrainment mapping.

Mapping and Identification of Reentrant Circuits

The essential point to understand arrhythmia and to plan a curative ablation approach is to comprehend the path of electrical activation within the true 3D anatomy and by that the anatomical location of the reentrant circuit. Therefore, 3D anatomical mapping systems such as CARTO or NavX are playing an increasingly important role for mapping and ablation of complex MRT, and thereby mainly LAMRT.

The electrophysiological analysis of LAMRT incorporates information on local activation time, local electrogram voltage, and entrainment analysis, which all represent different mapping approaches and all of which can be used in conjunction with 3D mapping systems.

Activation Mapping

Three-dimensional activation mapping of MRT is based on sequential acquisition of anatomical location points together with their local activation time. The activation time is calculated according to a fixed intracardiac reference signal. The points can be projected onto a preacquired 3D chamber anatomy, or the chamber anatomy can be reconstructed together with the point acquisition. Color-coded visualization of local activation time is superimposed onto the anatomy and helps to visualize the spread of electrical activation in a 3D fashion (Figure 18.15). Currently, sequential activation mapping is a preferred approach to study inducible, sustained, and hemodynamically tolerable MRTs.

Using activation mapping, the complex left atrial pathways can be reliably identified. Moreover, zones of conduction block or electrically silent areas due to scars are visualized. Anatomical obstacles, areas of scars, and zones of functional conduction block intersected by strands and channels of conducting atrial myocardium constitute isthmuses of low voltage and usually slow conduction critical for the maintenance of LAMRT.

Single as well as multiple reentrant pathways may be operative [49, 50]. However, detailed reconstruction of the reentrant pathways by activation mapping has to be done very systematically and requires some experience to correctly annotate the individual electrograms within the tachycardia cycle. Furthermore, stable reentrant activation is a prerequisite for the generation of correct and thereby useful maps.

Voltage Mapping

For tachycardias not meeting these requirements anatomical description of the arrhythmia substrate during sinus rhythm by use of voltage mapping may help to understand localization and mechanism of the arrhythmia (Figure 18.16). For that local electrogram, voltage is displayed three-dimensionally in a color-coded fashion. It clearly delineates scar areas and may even be used to detect channels of surviving myocytes within the scar serving as an area of slow conduction and critical isthmus of LAMRT. With that information strategic and potentially curative ablation lesions can be planned and placed to target the underlying arrhythmia mechanism. However, little information is currently available regarding the long-term success of linear lesion ablation based on voltage maps to cure LAMRT.

PPI Mapping

While 3D activation mapping and voltage mapping have been established as the standard approaches to map patients with LAMRT, both strategies carry significant limitations in patients with severely electrically diseased atria containing multiple scars and areas of slow conduction, giving rise to a diffuse and extended arrhythmia substrate. This is especially the case in patients following catheter ablation of atrial fibrillation, who currently represent the majority of

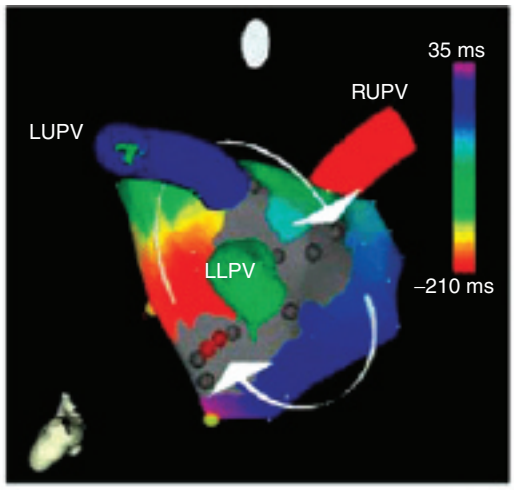

(a)

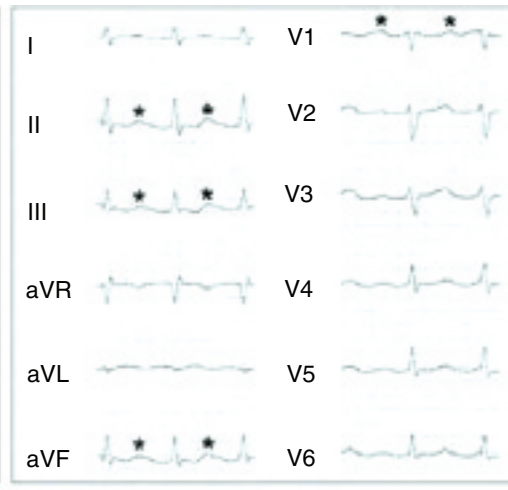

(b)

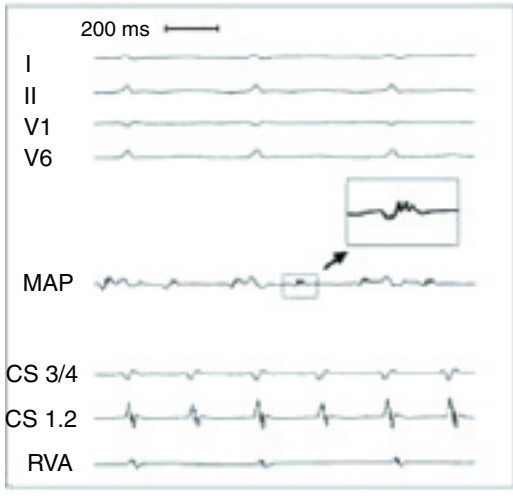

(c)

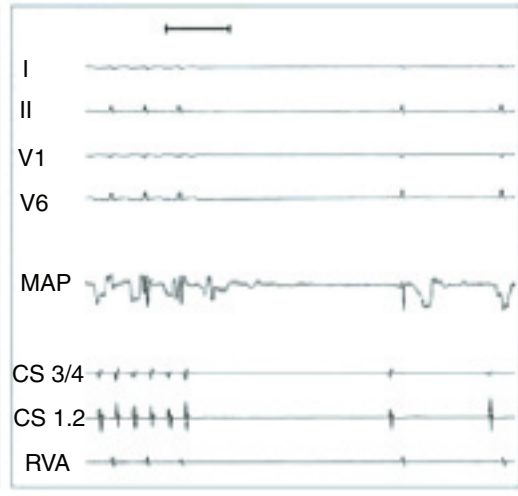

(d)

Figure 18.15 Electroanatomic activation map of the left atrium during left atrial macroreentrant tachacardia in a left posterior oblique view [panel (a)]. Color bars indicate the local activation time relative to the reference catheter. Gray color represents the scars caused by prior radiofrequency catheter ablation for atrial fibrillation. The arrhythmia revealed a circle (arrows) travelling around the left pulmonary veins, travelling through the left atrial isthmus in a caudo-cranial direction along the roof of the left atrium and in a cranio-caudal direction down along the posterior wall of the left atrium. The red points show a gap in the ablation line previously induced where application of radiofrequency energy terminated the LAMRT. The surface ECG with positive flutter waves in the inferior leads and lead V1 (stars) is depicted in panel (b). Panels (c) and (d) show the local fragmented electrogram recorded at the gap site and the successful tachycardia termination.

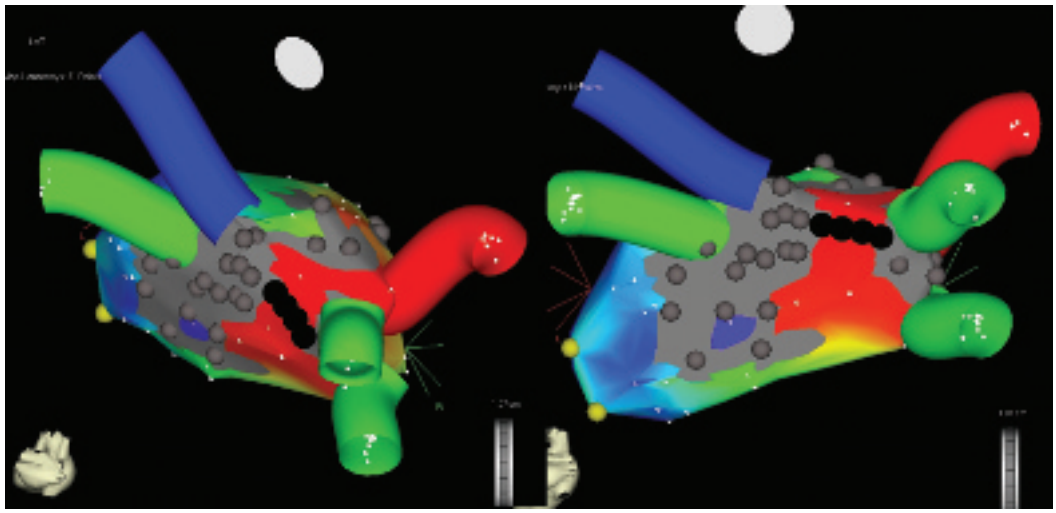

Figure 18.16 Voltage map of the left atrium in a patient with LAMRT. After transseptal puncture the tachycardia terminated during catheter manipulation and entrainment stimulation and was no longer inducible. Thus, voltage mapping of the left atrium was done and two scar areas extending from the pulmonary veins to the posterior free wall of the left atrium were detected. Between these scar areas a channel of approx. 1–1.5 cm with extremely low voltage was detected. A strategic lesion line was placed across the channel.

patients interventionally treated for LAMRT, and who on EP study present with a difficult picture showing a mixture of initially disease-related atrial scars together with multiple discontinuous ablation lines at the junction between pulmonary vein antrum and left atrium or even within the left atrial body itself.

In these patients, multiple regions with conduction delay create difficulties in allocating the appropriate local activation, often mislead the operators' understanding of the arrhythmia, and limit the success of the ablation procedure. Targeting these limitations, a third strategy of 3D mapping has been introduced: color-coded 3D entrainment mapping. This strategy is based on the concept that entrainment stimulation with measurement of the postpacing interval (PPI) is known to describe the distance of the local catheter tip position from the actual reentrant circuit, with equality of PPI and tachycardia cycle length (TCL) exactly within the reentrant circuit.

To achieve advanced understanding of the arrhythmia mechanism, sequential CARTO or NavX mapping of the suspected chamber of origin has to be performed together with entrainment stimulation at each mapping point. On the conventional EP recording system the postpacing interval (PPI), defined as the time interval from the last pacing artefact to the first local atrial electrogram, is measured from the tip of the ablation catheter. The time difference between PPI and TCL is calculated and stored together with the 3D anatomical position on the electroanatomic mapping system in a color-coded fashion (Figures 18.17 and 18.18).

Due to the lack of a specific mode for color coding of entrainment information on either electroanatomic mapping system (Carto or NavX), the algorithms for activation mapping can be utilized in both systems with manual input of the PPI-TCL time difference as obtained from the EP recording system. Sequential 3D PPI mapping quickly results in a color-coded visualization of the whole reentrant circuit in a 3D fashion and allows for strategic lesion line placement.

Ablation Strategies to Cure LAMRT

Ablation of the Critical Isthmus

Given the pathophysiological understanding of macroreentrant tachycardia, the area of slow conduction containing the critical isthmus of the arrhythmia has evolved as the main target for localized RF application in order to terminate the arrhythmia. On one hand the success of the ablation

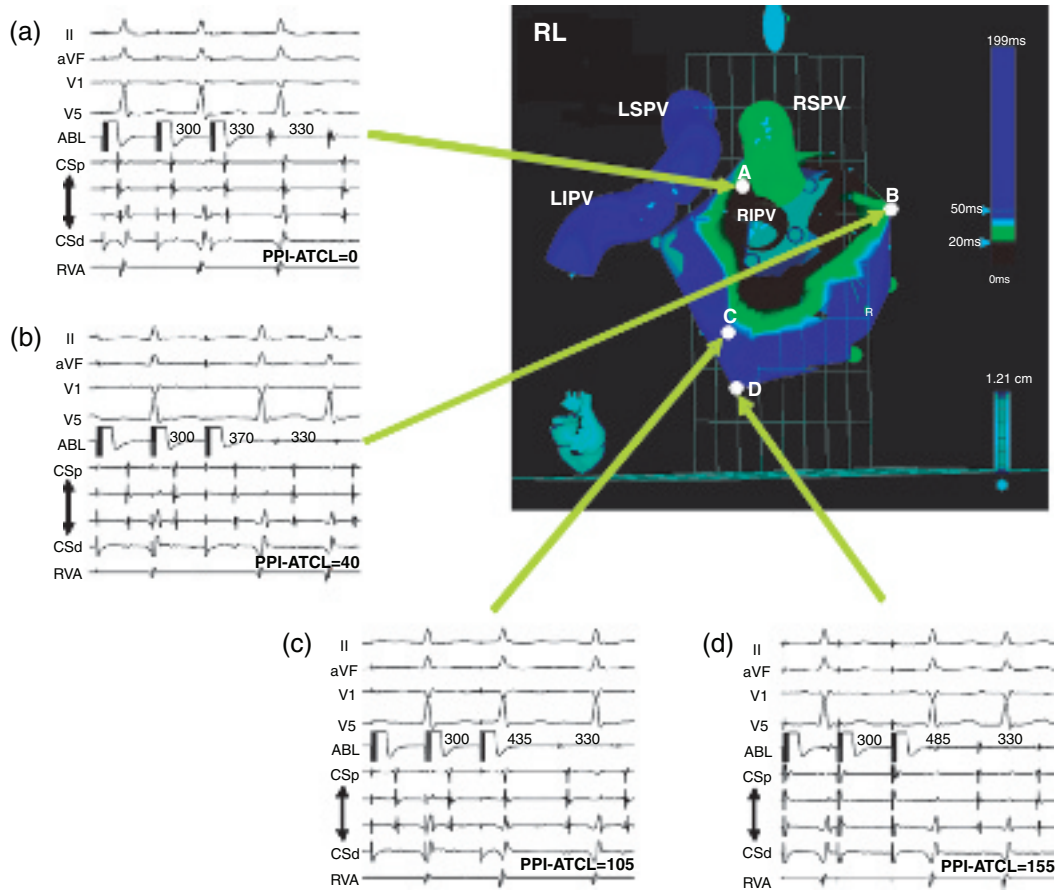

Figure 18.17 Principle of 3D-PPI mapping. Right posterior oblique view of an electroanatomical reconstruction of the left atrium in a patient with LAMRT. The left-sided (LSPV, LIPV) and right-sided (RSPV, RIPV) pulmonary veins are shown as well. Cycle length of the tachacardia is 330 msec. Panels (a)–(d) depict four different stimulation sites were entrainment stimulation at a cycle length of 300 msec was performed and the postpacing interval (PPI) as well. The PPI was annotated in the 3D-map: the red area indicates a PPI similar or close to spontaneous tachycardia cycle length, while green, blue, and purple colors are indicative for long PPI. In this particular case the LAMRT traveled around the right sides of the pulmonary veins.

depends on the accurate anatomical description of the critical isthmus, while on the other hand the nature of the isthmus may vary from patient to patient ranging from a small distinct isthmus based on only a few surviving myocyte channels within a scarred area, to patients with a broad arrhythmia isthmus. Those isthmus characteristics are likely to additionally influence the success of a localized RF application approach.

Strategic Lesion Line Placement

Recognizing the above-described difficulties of critical isthmus ablation related to the understanding of anatomical location of the isthmus, as well as the nature of the isthmus itself, strategic lesion line concepts of linear atrial ablation based on 3D entrainment mapping information are more and more used to dissect the MRT circuit at any suitable location and not necessarily the critical isthmus itself.

Following the concept of 3D entrainment mapping and subsequent strategic lesion line placement, patients with LAMRT can be categorized into six groups of patients presenting with similar tachycardia mechanisms and requiring similar ablation line concepts:

(i) Patients presenting with LAMRT involving the antrum of the pulmonary veins (PV) may be divided into patients containing the whole reentrant

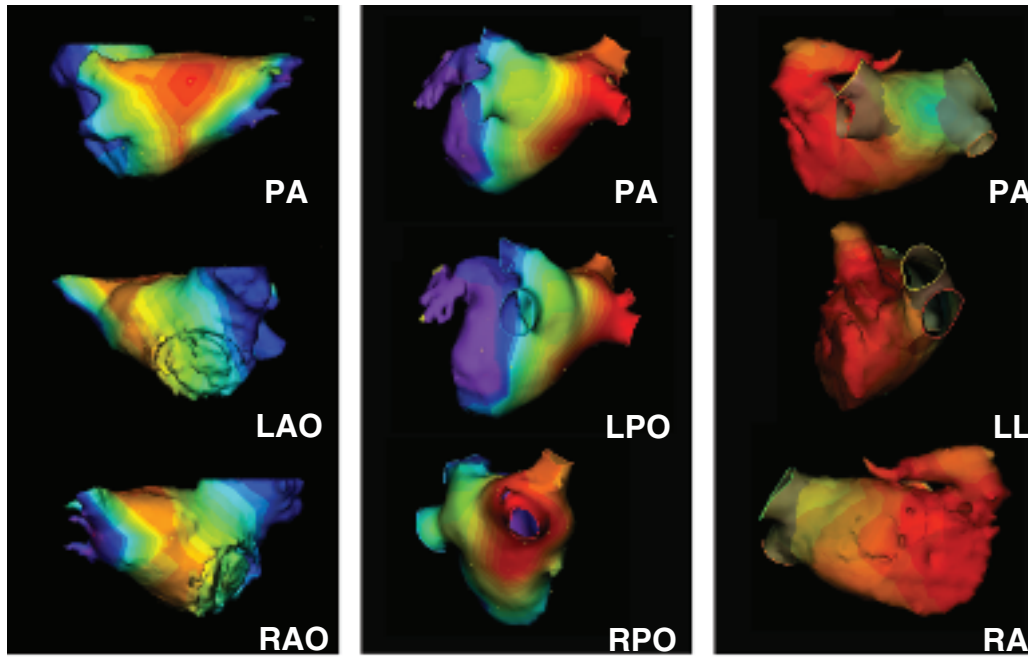

Figure 18.18 Case examples of NavX-guided color-coded PPI maps. Panel (a) shows LAMRT traveling along the roof of the left atrium and panel (b) around the right pulmonary veins. Panel (c) depicts a LAMRT traveling around the left atrial appendage. Each tachycardia pathway show represents a typical from of LAMRT occurring after catheter ablation of atrial fibrillation. For details and curative treatment strategies see text. KEY: PA = posterior view; LPO = left posterior oblique; RPO = right posterior oblique; LL = left lateral.

circuit within the PV antrum and patients showing entrance and exit gaps with part of the reentrant circuit being localized within the PV antrum and part of it outside in the left atrial body. The treatment of choice for all patients with PV antrum–related MRT is completion of electrical isolation of the whole PV antrum by closure of any gap within the circumferential ablation line.

(ii) Patients with MRT involving the left atrial roof almost exclusively have reentrant circuits that circumvent the whole left atrium. A roof line connecting the left upper PV with the right upper PV is the treatment of choice.

(iii) For patients presenting with perimitral MRT a left atrial mitral isthmus line should be attempted as a curative strategic lesion line concept. In the case of unsuccessful endocardial ablation, additional epicardial lesions placed from within the coronary sinus (CS) may be needed to terminate the tachycardia.

(iv) MRT originating from within and around the left atrial appendage can be targeted with circumferential ablation around the left atrial appendage. The question of whether or not complete electrical isolation of the atrial appendage should be attempted may be discussed controversially given the considerations on thromboembolic risk and need for anticoagulation during long-term follow-up.

(v) MRT originating from within the coronary sinus can be targeted by linear ablation within CS; however, especially in the case of an ostial location, quite often they are associated with septal reentrant circuits given the muscular connections within the paraseptal region.

(vi) Due to the difficulty in accessing all parts of the interatrial septum from within the left atrium and due to the anatomical vicinity to the AV node, interventional treatment of septal MRTs currently has the lowest success and the highest recurrence rate [51]. An alternative ablation approach toward these arrhythmias can be attempted by placement of a linear ablation line from the SVC to the IVC across the intraatrial septum from the right side of the

septum [7]. The last mechanism of LAMRT to be found represents scar-related MRT within the left atrial body. Though rather rare, ablation of these arrhythmias can be achieved by connecting the causative scar area with an anatomical obstacle such as an isolated PV antrum through a linear ablation line.

Catheter Ablation of LAMRT

In our laboratory catheter ablation of LAMRT is exclusively done using irrigated ablation technology. In addition, to facilitate the mapping procedure and to enhance lesion induction a steerable sheath is used in all cases. Power output is 40 W; irrigation rate is 30 mL/min. However, if necessary, power output at certain spots may be increased up to 50 W with an irrigation rate up to 50 mL/min. Radiofrequency application is continued until complete abandonment of local electrograms has occurred. Whenever possible, radiofrequency ablation is performed during ongoing LAMRT because termination is the best proof for the correctness of the treatment strategy. If ablation is performed during sinus rhythm or after termination of LAMRT, pacing is performed during radiofrequency application and current delivery is continued until loss of capture. This provides some functional feedback and correlates quite well with abandonment of bipolar electrograms. After completion of strategic lesion lines pacing maneuvers are applied to prove conduction block (Figure 18.19).

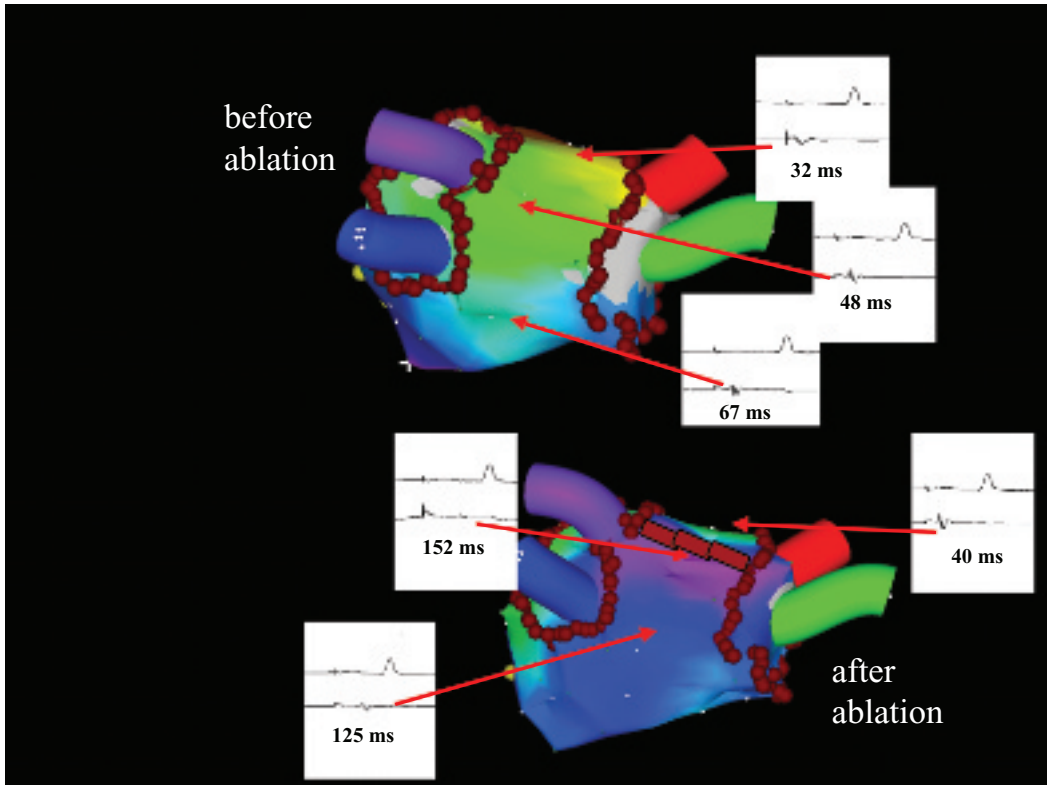

Figure 18.19 Confirmation for complete conduction block along a linear lesion line induced in a patient with LAMRT along the roof. During left atrial appendage stimulation before induction of the lesion line, conduction traveled along the left atrial roof. Conduction time anterior measured 32 msec, at the roof 48 mssec, and posterior 67 msec. Following linear ablation complete block along the lesion line occurred. Conduction time anterior to the lesion line remained unchanged (40 msec) while reversal of conduction could be demonstrated posterior to the lesion line: the impulse traveled from inferior posterior left atrium (125 msec) upward to the site of conduction block (152 msec).

Conclusion

Macroreentrant AT is complex and often involves complex anatomy and multiple arrhythmias; detailed mapping is often required. The size and location of reentry circuit is variable. Focal AT or micro-reentrant circuits, which may present with centrifugal pattern that may not propagate the entire atria, needs to be ruled out. Electroanatomical mapping is very useful to elucidate the AT reentry circuit and the success of radiofrequency ablation techniques depends on the accuracy of electrophysiology investigation and mapping systems. Ablation is highly effective with a low recurrence rate considered the first-line therapy for right and left atrial macroreentrant tachycardia.

References

1 Saoudi N, Cosio F, Waldo A, et al. Classification of atrial flutter and regular atrial tachycardia according to electrophysiologic mechanism and anatomic base: a statement from a joint expert group from the Working Group of Arrhythmias of the European Society of Cardiology and the North American Society of Pacing and Electrophysiology. *J Cardiovasc Electrophysiol* 2001; **12**: 852–66.

2 Chen S-A, Chiang C-E, Yang C-J, et al. Sustained atrial tachycardia in adult patients: electrophysiological characteristics pharmacological response, possible mechanisms, and effects of radiofrequency ablation. *Circulation* 1994; **90**: 1262–78.

3 Lesh MD, Van Hare GF, Epstein LM, et al. Radiofrequency catheter ablation of atrial arrthmyias: results and mechanisms. *Circulation* 1994; **89**: 1074–89.

4 Olgin JE, Kalman JM, Kalman JM, Fitzpatrick AP, Lesh MD. Role of right atrial endocardial structures as barriers to conduction during human type I atrial flutter: activation and entrainment mapping guided by intracardiac echocardiography. *Circulation* 1995; **92**: 1839–48.

5 Kalman JM, Olgin JE, Karch MR, et al. "Cristal tachycardias": origin of right atrial tachycardias from the crista terminalis identified by intracardiac echocardiography. *J Am Coll Cardiol* 1998; **31**: 451–59.

6 Olgin JE, Jayachandran JV, Engelstein E, et al. Atrial macroreentry involving the myocardium of the coronary sinus: a unique mechanism for atypical flutter. *J Cardiovasc Electrophysiol* 1998; **9**: 1094–99.

7 Ganz LI, Friedman PL. Supraventricular tachycardia. *N Engl J Med* 1995; **332**: 162–73.

8 Shenasa H, Curry P, Shenasa M. Atrial arrhythmias: clinical concepts and advances in mechanism and management. In: *Cardiac Arrhythmias*, 3rd ed. Mandel WJ, ed. J.B. Lippincott, Philadelphia, 1995.

9 Tang CW, Scheinman MM, Van Hare G, et al. Use of *P*-wave configuration during atrial tachycardia to predict site of origin. *J Am Coll Cardiol* 1995; **26**: 1315–24.

10 SippensGroenewegen A, Roithinger F, Lesh M. Mapping of atrial arrhythmias: role of *P*-wave morphology. In: *Cardiac Mapping*, 2nd ed. Shenasa M, Borggrefe M, Breithardt G, eds. Blackwell Publishing, Inc., London, 2003: 429–54.

11 Badhwar N, Lee B, Olgin N. Mapping of focal atrial tachycardias. In: *Cardiac Mapping*, 3rd ed. Shenasa M, Borggrefe M, Breithardt G, eds. Blackwell Publishing, London, 2003.

12 SippensGroenewegen A, Peeters H, Jessurun E, et al. Body surface mapping during pacing at multiple sites in the human atrium: *P*-wave morphology of ectopic right atrial activation. *Circulation* 1998; **97**: 369–80.

13 SippensGroenewegen A, Steiner PR, Karch MR, et al. Body surface mapping of atrial tachycardia: correlation of *P*-wave integral map pattern with site or origin assessed using activation sequence mapping. *J Am Coll Cardiol* 1997; **29**: 21A. Abstract

14 Knight BP, Zivin A, Souza J, et al. A technique for the rapid diagnosis of atrial tachycardia in the electrophysiology laboratory. *J Am Coll Cardiol* 1999; **33**: 775–81.

15 Iwai S, Markowitz SM, Stein KM, et al. Response to adenosine differentiates focal from macroreentrant atrial tachycardia: validation using three-dimensional electroanatomic mapping. *Circulation* 2002; **106**: 2793–99.

16 Iesaka Y, Takahashi A, Goya M, et al. Adenosine sensitive atrial reentrant tachycardia originating from the atrioventricular nodal transitional area. *J Cardiovasc Electrophysiol* 1997; **8**: 854–64.

17 Markowitz SM, Stein KM, Mittal S, et al. Differential effects of adenosine on focal and macroreentrant atrial tachycardia. *J Cardiovasc Electrophysiol* 1999; **10**: 489–502.

18 Markowitz SM, Nemirovsky D, Stein KM, et al. Adenosine-insensitive focal atrial tachycardia: evidence for de novo micro-reentry in the human atrium. *J Am Coll Cardiol* 2007: **49**; 1324–33

19 Chiale PA, Franco A, Selva HO, et al. Lidocaine-sensitive atrial tachycardia. *J Am Coll Cardiol* 2000; **36**: 1637–45.

20 Kalman JM, Van Hare GF, Olgin JE, et al. Ablation of "incisional" reentrant atrial tachycardia complicating surgery for congenital heart disease: use of entrainment to define a critical isthmus of conduction. *Circulation* 1996; **93**: 502–12.

21 Stevenson WG, Sager PT, Friedman PL. Entrainment techniques for mapping atrial and ventricular tachycardias. *J Cardiovasc Electrophysiol* 1995; **6**: 201–1622.

22 Tracy CM, Swartz JF, Fletcher RD, et al. Radiofrequency catheter ablation of ectopic atrial tachycardia using paced activation sequence mapping. *J Am Coll Cardiol* 1993; **21**: 910–17.

23 Morton J, Sanders P, Deen V, et al. Sensitivity and specificity and concealed entrainment for the identification of a critical isthmus in the atrium: relationship to rate, anatomic location, and antridromic penetration. *J Am Coll Cardiol* 2002; **39**: 896–906.

24 Man KC, Chan KK, Kovack P et al. Spatial resolution of atrial pace mapping as determined by unipolar atrial pacing at adjacent sites. *Circulation* 1996; **94**: 1357–63.

25 Chen SA. Chiang CE, Yang CJ, et al. Radiofrequency catheter ablation of sustained intraatrial reentrant tachycardia in adult patients: identification of electrophysiological characteristics and endocardial mapping techniques. *Circulation* 1993; **88**: 578–87.

26 Nakagawa H, Shah N, Matsudaira K, et al. Characterization of reentrant circuit in macroreentrant right atrial tachycardia after surgical repair of congenital heart disease: isolated channels between scars allow "focal" ablation. *Circulation* 2001; **103**: 699–709.

27 Schmitt C, Zrenner B, Schneider M, et al. Clinical experience with a novel multielectrode basket catheter in right atrial tachycardias. *Circulation* 1999; **99**: 2414–22.

28 Zrenner B, Ndrepepa G, Schneider M, et al. Computer-assisted animation of atrial tachyarrhythmias recorded with 64-electrode basket catheter. *J Am Coll Cardiol* 1999: **34**: 2051–60.

29 Ben-Haim SA, Osadchy D, Schuster I, et al. Nonfluoroscopic in vivo navigation and mapping technology. *Nat Med* 1996; **2**: 1393–95.

30 Marchlinski F, Callans D, Gottlieb C, et al. Magnetic electroanatomical mapping for ablation of focal atrial tachycardias. *PACE* 1998; **21**: 1621–35.

31 Wetzel U, Hindricks G, Schirdewahn P, et al. A stepwise mapping approach for localization and ablation of ectopic right, left, and septal atria foci using electroanatomic mapping. *Euro Heart J* 2002; **23**: 1387–93.

32 Higa S, Tai CT, Lin YJ, et al. Focal atrial tachycardia: new insight from noncontact mapping and catheter ablation. *Circulation* 2004; **109**: 84–91.

33 Delacretaz E, Ganz IL, Soejima K, et al. Multiple atrial macro-reentry circuits in adults with repaired congenital heart disease: entrainment mapping combined with three-dimensional electroanatomic mapping. *J Am Coll Cardiol* 2001; **37**: 166–76.

34 Lin YJ, Tai CT, Huang JL, et al. Characteristics of virtual unipolar electrograms for detecting isthmus block during radiofrequency ablation of typical atrial flutter. *J Am Coll Cardiol* 2004; **43**: 2300–4.

35 Kaltman J, Schultz J, Wieand T, et al. Mapping in critical diastolic pathway in intra-atrial reentrant tachycardia using an automated voltage mapping program. *J Cardiovasc Electrophysiol* 2006; **17**: 786–88.

36 Tai CT, Huang JL, Kin YK, et al. Noncontact three-dimensional mapping and ablation of upper loop reentry originating in the right atrium. *J Am Coll Cardiol* 2002; **40**: 746–53.

37 Sanders P, Hocini M, Jais P, et al. Characterization of focal atrial tachycardia using high-density mapping. *J Am Coll Cardiol* 2005; **46**: 2088–99.

38 Olgin J, Kalman J, Chin M, et al. Electrophysiological effects of long linear atrial lesions placed under intracardiac ultrasound guidance. *Circulation* 1997; **96**: 2715–21.

39 Tops FL, van der Wall EE, Schalij MJ, et al. Multimodality imaging to assess left atrial size, anatomy, and function. *Heart* 2007; **93**: 1461–70.

40 Dong J, Calkins H, Solomon SB, et al. Integrated electroanatomic mapping with three-dimensional computed tomographic images for real-time guided ablations. *Circulation* 2006; **113**: 186–94.

41 Tops LF, Bax JJ, Zeppenfeld K, et al. Fusion of multislice computed tomography imaging with three-dimensional electroanatomic mapping to guide radiofrequency catheter ablation procedures. *Heart Rhythm* 2005; **2**: 1076–81.

42 Kistler PM, Rajappan K, Jahngir M, et al. The impact of CT image integration into an electroanatomic mapping system on clinical outcomes of catheter ablation of atrial fibrillation. *J Cardiovasc Electrophysiol* 2006; **17**: 1093–101.

43 Dickfeld T, Lei P, Dilsizian V, et al. Integration of three-dimensional scar maps for ventricular tachycardiea ablation with positron emission tomography-computed tomography, *J Am Coll Cardiol Img* 2008; **1**: 73–82.

44 Saoudi N, Chairman, Cosio F, et al. Classification of atrial flutter and regular atrial tachycardiea according to electrophysiologic mechanism an anatomic bases: a statement from a joint expert group from the Working Group of Arrhythmias of the European Society of Cardiology and the North American Society of Pacing and Electrophysiology. *J Cardiovasc Electrophysiol* 2001; **12**: 852–66.

45 Marrouche NF, Natale A, Wazni OM, et al. Left septal atrial flutter electrophysiology, anatomy, and results of ablation. *Circulation* 2004; **109**: 2440–47.

46 Bochoeyer A, Yang Y, Cheng J, et al. Surface electrocardiographic characteristics of right and left atrial flutter. *Circulation* 2003; **108**: 60–66.

47 Chugh A., Latchamsetty R., Oral H., et al. Characteristics of cavotricuspid isthmus-dependent atrial flutter after left

atrial ablation of atrial fibrillation. *Circulation* 2006; **113**: 609–15.

48 Shalganov TN, Vatasescu R, Paprika D, et al. A simple algorithm for defining the machanism and the chamber of origin in atrial tachycardias. *J Electrocardiol* 2006; **39**: 369–76.

49 Jais P, Shah C, Haissaguerrre M, et al. Mapping and ablation of left atrial flutters: LA reentrant tachycardias are related to individually varying circuits and are amenable to mapping guided radiofrequency ablation. *Circulation* 2000; **101**: 2928–34.

50 Ouyang F, Ernst, S, Vogtmann, T, et al. Characterization of reentrant circuits in left atrial macroreentrant tachycardia. critical isthmus block can prevent atrial tachycardia recurrence. *Circulation* 2002; **105**: 1934–42.

51 Chae S, Oral H, Good E, et al. Atrial Tachycardia after Circumferential pulmonary vein ablation of atrial fibrillation. *J Am Coll Cardiol* 2007; **50**:1781–7.

19 CHAPTER 19

Mapping of Focal Atrial Tachycardias

Nitish Badhwar, MBBS, *Byron K. Lee,* MD, *Jeffrey E. Olgin,* MD

University of California, San Francisco, CA, USA

Summary

Focal atrial tachycardias (AT) usually arise from well-defined anatomical regions in the right and the left atrium. The mechanisms include automaticity, triggered activity, and microreentry. While the common presentation is paroxysmal supraventricular tachycardia (SVT), incessant tachycardia with cardiomyopathy has also been reported in some cases. Distinctive *P*-wave morphology on a 12-lead electrocardiogram (EKG) can help localize the site of origin of focal AT. Recent technological advances in 3D mapping and navigation systems have contributed significantly to the improved success of catheter ablation of these arrhythmias.

Introduction

Focal atrial tachycardia is defined as atrial activation starting rhythmically at a small area (focus) from where it spreads out centrifugally and without endocardial activation over significant portions of the cycle length [1]. By definition, they do not use the atrioventricular junction or an accessory pathway as an essential portion of their circuit and can continue indefinitely and independently of them [2]. This is in distinction from macroreentrant atrial tachycardias (or flutters), where electrical activation can be recorded throughout the entire atrial cycle length (these are discussed in Chapters 17 and 21).

Focal atrial tachycardias usually occur along the crista terminalis in the right atrium and the pulmonary veins in the left atrium [3–11]. Less frequently, they can arise from the coronary sinus musculature [12], the coronary sinus ostium [13], the parahisian region [14], the appendages [15, 16], or rarely along the tricuspid [17] or mitral annulus [18].

Pathophysiology

Chen et al. [19] showed that focal atrial tachycardia can occur in any age group with a greater incidence in the adult middle age population and no gender preference. It more commonly arises from the right atrium, and a second focus of atrial tachycardia may be found in up to 13% of the patients. Older patients have been noted to have a higher incidence of right-sided and multiple AT; women were noted to have a higher incidence of nonautomatic AT in one study [20]. Atrial tachycardia accounts for 5–15% of adults undergoing electrophysiological studies, with higher rates in children [21].

Cardiac Mapping, Third Edition Edited by Mohammad Shenasa, Gerhard Hindricks, Martin Borggrefe, and Günter Breithardt
 ISBN: 978-1-405-17572-2

Focal atrial tachycardias may have an automatic, triggered, or microreentrant mechanism. Although precisely defining the basic mechanism of a particular atrial tachycardia may be difficult, understanding their basic principles may help with certain therapeutic decisions [4, 22]. The arrhythmogenic mechanisms should not be used with stringency, and flexibility should be used in the judgment of apparent inconsistencies in a particular tachycardia mechanism.

Abnormal automaticity, likely caused by a positive ionic influx during phase 4 depolarization, is thought to be the most common underlying mechanism for focal atrial tachycardias. Clinically, automatic tachycardias are characterized by sudden onset with a warm-up period, facilitation by adrenergic surge or exogenous catecholamines. Vagal stimulation, beta-blockers, and calcium channel blockers may suppress these types of atrial tachycardias, and adenosine may provoke an ambiguous response [23]. In the electrophysiology laboratory, these tachycardias are not inducible by programmed stimulation and may be suppressed by overdrive pacing, but occur either spontaneously or with infusion of isoproterenol. The fact that these tachycardias can also be sensitive to sedation should be taken into account when planning an EP study and ablation.

Triggered activity is the mechanism by which the cardiac cell depolarizes due to afterpotentials. The role of afterdepolarizations in atrial tachycardias appears to be limited and is inferential from data in single-cell recordings; however, evidence suggests that this mechanism may play a role in atrial tachycardia during digitalis toxicity [24]. Triggered tachycardias usually are inducible by programmed stimulation—commonly, constant rate pacing. It may have a warm-up period and it is facilitated by catecholamines. It may also be accelerated by overdrive pacing. Vagal maneuvers, use of beta-blockers, calcium channel blockers, and adenosine may terminate this type of atrial tachycardia [23, 25].

Reentry is another mechanism of focal atrial tachycardias. In reentry, the arrhythmia is maintained by a self-perpetuating circuit that travels around an area of scar or slow conduction. When the reentry circuit is discrete (microreentrant), it is still classified as focal AT. In contrast, when the reentry circuit is larger, it is classified as a macroreentrant atrial tachycardia. Focal reentrant tachycardias can be ablated with a single ablation lesion, whereas macroreentrant atrial tachycardias typically require a series of ablation lesions. Focal reentrant atrial tachycardia is characterized by initiation and termination with programmed atrial stimulation. Because of the small circuit size relative to a mapping electrode, criteria for entrainment of these tachycardias can be difficult to demonstrate. This form of focal AT has been shown to be insensitive to adenosine [26]. Markowitz et al. have proposed an algorithm to differentiate the mechanism of focal AT based on the response to adenosine [26].

Clinically, patients with atrial tachycardia may present with varying degrees of symptoms from being only mildly symptomatic to having overt congestive heart failure from tachycardia-induced cardiomyopathy. The latter scenario warrants emphasis because patients with incessant atrial tachycardias and tachycardia-induced cardiomyopathy can be misdiagnosed as having a compensatory sinus tachycardia in the setting of an idiopathic dilated cardiomyopathy. Often this distinction can be difficult to make, but curing the atrial tachycardia with ablation can save the former patient from eventual cardiac transplantation.

Electrocardiographic Characteristics

Previous studies have used the surface *P*-wave morphology during AT to predict the site of origin [10]. Leads aVL and V_1 are the most useful to distinguish between left atrial (LA) and right atrial (RA) origin. A positive or biphasic *P*-wave in aVL predicts a right atrial origin of the tachycardia with a sensitivity of 88% and a specificity of 79%. In lead V_1, a negative or biphasic with negative terminal *P*-wave demonstrated a specificity of 100% for a RA focus, and a positive or biphasic with positive terminal *P*-wave demonstrated a sensitivity of 100% for a LA focus [27].

Focal AT arising from the crista terminalis (high or mid) can be associated with negative *P*-waves in aVL, while foci from the right superior pulmonary vein (RSPV) can have a positive *P*-wave in aVL. Tang et al. [10] made the important observation that RSPV foci showed a change in configuration in lead V_1 from biphasic in sinus rhythm to upright in AT, a

Table 19.1 *P*-Wave Morphology During Focal Atrial Tachycardias.

						ECG	Lead					
Site of origin	*I*	*II*	*III*	*aVR*	*aVL*	*aVF*	V_1	V_2	V_3	V_4	V_5	V_6
Superior CT	+	+	+	−	+	+	−	−	−	−	−	−
Inferior CT	+	−	−	−	+	−	−	−	−	−	−	−
Inf lateral TA	− / iso	−	−	−	++	−	−	−	−	−	+	+
Inf medial TA	iso	−	−	−	+	−	−	−	−	−	−	−
RAA	+	+	+	−	iso, −	+	−	−	−	−	−	iso, −, +
Parahisian	+	−	−	+	+	−	−/+, −,iso	−	−	−	−	−
CS ostium	iso,+	−	−	+	+	−	−/+, iso/+	−/+, −	−	−	−	−
CS body	−, iso	−	−	+	+/−, +/iso	−	+	+	+, −,iso	−	−	−
RSPV	+	+	+	−	+, −	+	+	+	+	+	+	+
LSPV	−, iso	+	+	−	−	+	+	+	+	+	+	+
LAA	−	+	+	iso, −	−	+	+	+	+	+	+	iso
Superior MA	−	iso	iso	−	−	iso	iso/+	iso/+	−/iso	−/iso	iso	iso

KEY: CS = coronary sinus; CT = crista terminalis; ECG = electrocardiographic; LAA = left atrial appendage; LSPV = left superior pulmonary vein; MA = mitral annulus; RAA = right atrial appendage; RSPV = right superior pulmonary vein; TA = tricuspid annulus; iso = isoelectric.

change not seen in RA foci. Table 19.1 summarizes the *P*-wave morphology in the most common focal ATs.

In addition, leads II, III, and aVF may help differentiate a superior (with positive *P*) from an inferior focus (with negative *P*-wave) [10]. In the RA, a negative *P*-wave in lead aVR suggests a right lateral location, specifically the crista terminalis with 100% sensitivity and 93% specificity, while negative *P*-waves in leads V5 and V6 suggest an inferomedial location [28]. AT arising from the nonseptal tricuspid annulus had a preference for the inferoanterior region with negative *P*-waves in precordial leads, positive in aVL and negative in lead III [17].

AT arising from the apex of the triangle of Koch (parahisan AT) usually demonstrates isoelectric *P*-waves in V_1 and shorter *P*-wave duration in the inferior leads during AT as compared to sinus rhythm [28]. Focal AT arising from the coronary sinus ostium is associated with deep negative *P*-waves in inferior leads, positive *P*-wave in aVL and −/+ or iso/+ in V_1 [13]. Focal AT arising from the right atrial appendage has *P*-wave morphology similar to sinus rhythm and can be misdiagnosed as inappropriate sinus tachycardia.

In the LA, focal AT commonly arises from the pulmonary veins (PV) and is associated with a characteristic *P*-wave morphology that is positive in precordial leads, negative in aVR and aVL (RSPV can give positive *P*-wave in aVL as discussed earlier) [29]. Left-sided PVs are associated with notched and wider *P*-waves with lead III/II ratio >0.8, while right-sided PVs are positive in lead I. Focal AT arising from the coronary sinus musculature gives positive *P*-waves in V_1 with transition to negative *P*-wave in V_3- V_4, negative *P*-waves in inferior leads and positive in aVR and biphasic (+/−, +/iso) in aVL [12]. AT arising from the mitral annulus tend to cluster at the superior aspect close to the aortomitral continuity with biphasic (−/+) *P*-waves in V_1, negative or isoelectric in I, aVL and low amplitude positive or isoelectric in the inferior leads [18]. AT arising from the LA appendage is associated with broad positive *P*-waves in precordial leads, deep negative *P*-wave in lead I and aVL and positive *P*-waves in inferior leads [16].

While these rules generally hold true, there are some limitations to using *P*-wave vectors for diagnosis. There is spatial limitation of the *P*-wave morphology, which is indistinguishable when they originate from paced sites 17 mm apart or less [30]. It has also been shown that the *P*-wave morphology is largely determined by the direction of septal and left atrial activation [31]; hence the morphology may vary amongst patients with the same AT depending on the dominant route of LA activation. The

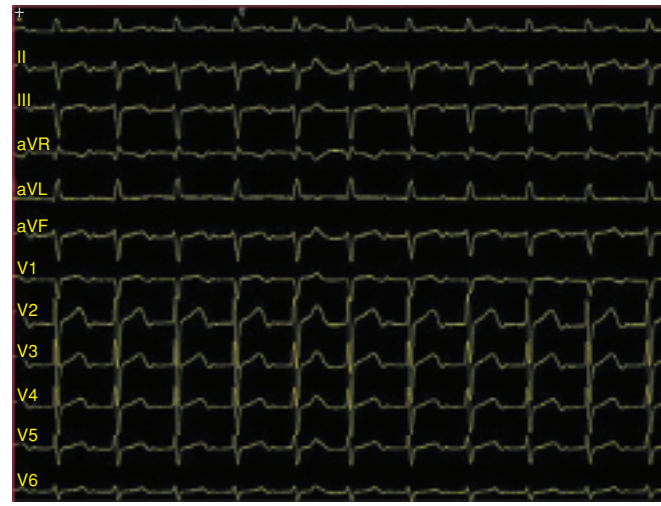

Figure 19.1 Twelve-lead electrocardiogram of a patient with atrial tachycardia arising from the parahisian region. It is a long RP tachycardia (more commonly associated with atrial tachycardia) with narrow *P*-waves that are negative in the inferior leads, biphasic in V_1, positive in aVR, aVL and I.

presence of 1:1 atrioventricular conduction may cause distortion of the *P*-waves by the QRS complex or *T*-wave.

Commonly used techniques in the electrophysiology laboratory to identify the *P*-wave include ventricular pacing and administration of adenosine. Focal AT in patients with structural heart disease, congenital heart disease, or prior extensive ablation procedures may produce markedly different *P*-wave morphologies than those outlined above.

Electrophysiological Characteristics

The R-P relationship during SVT can often be useful in the differential diagnosis [32]. Atrial tachycardia is typically a long R-P SVT (Figure 19.1), whereas atrioventricular nodal reentrant tachycardia (AVNRT) and atrioventricular reentrant tachycardia (AVRT) are usually short R-P SVTs. However, in rare circumstances these expected R-P relationships do not hold.

Distinguishing focal AT from AVNRT or AVRT requires analysis of conventional intracardiac electrogram recordings during tachycardia, and the response of the arrhythmia to stimulation maneuvers and pharmacological manipulation [33]. Spontaneous termination of the tachycardia with atrial depolarization makes AT unlikely. Variable AV conduction with more atrial than ventricular signals strongly suggests atrial tachycardia; rarely AV node reentry with block in the lower common pathway can also show this pattern [34].

In addition, for ATs originating distant from the AV valve annuli or coronary sinus ostium, atrial activation is usually inconsistent with AVRT using an accessory pathway or AVNRT. However, when there is 1:1 AV conduction and the atrial activation sequence is suggestive of an annular location, differentiation from AVNRT and AVRT can be more difficult and standard electrophysiological maneuvers to determine the necessity of the AV node for the arrhythmia are used.

Ventricular pacing maneuvers can be very helpful in differentiating AT from AVNRT and AVRT. If burst pacing in the right ventricle at a rate slightly faster than the tachycardia rate dissociates the ventricle from the tachycardia, AVRT is excluded. If burst pacing reproducibly terminates the tachycardia without conducting to the atrium, AT is excluded. If burst pacing in the ventricle captures the atrium and there is a V-A-A-V response following the last paced beat (Figure 19.2a), AT is most likely the diagnosis. In contrast, a V-A-V response (Figure 19.2b) is more consistent with AVNRT of AVRT [33].

Atrial pacing maneuvers can also be helpful. Pacing the high right atrium during sinus rhythm at the tachycardia cycle length can be used to differentiate AT from atypical AVNRT based on the

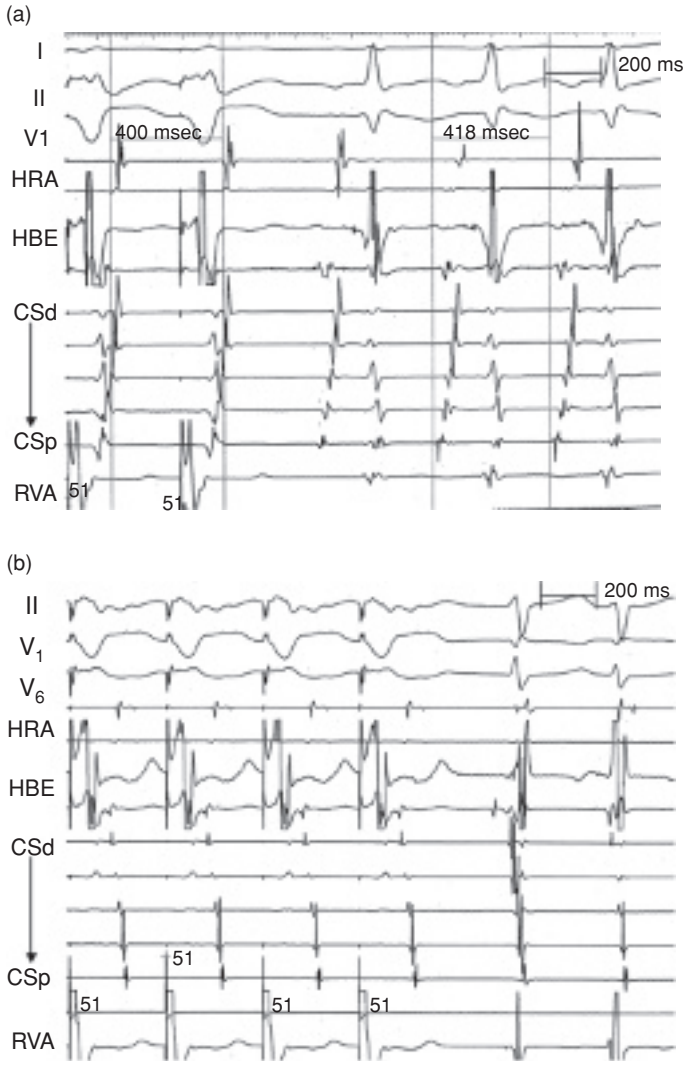

Figure 19.2 (a) Intracardiac electrogram recording during tachycardia after the cessation of ventricular overdrive pacing. V-A-A-V response following the last right ventricular paced beat suggests atrial tachycardia. (b) V-A-V response following the last right ventricular paced beat during tachycardia suggests AVNRT or AVRT.

differences in the AH interval during SVT and pacing ($AH_{pace} - AH_{svt} > 40$ msec with atypical AVNRT) [35]. One can also pace the atrium at a rate faster than the tachycardia rate during SVT. If the VA interval of the return cycle length is within 10 msec of the VA interval during the tachycardia, there is "VA linking" and AVNRT or AVRT is more likely. If the VA interval is variable, atrial tachycardia is most likely.

Finally, the response to pharmacological termination with adenosine also may be helpful. While adenosine can be useful to dissociate the tachycardia from the AV node and ventricle, some atrial tachycardias are adenosine-sensitive [36]. Nevertheless, termination of the tachycardia in the AV node (last electrogram seen is the A), if reproducible, makes the diagnosis of AT unlikely.

Electroanatomical Mapping

Successful ablation of a focal AT requires precise mapping of the tachycardia focus. As discussed in the EKG section, the *P*-wave morphology during AT can localize the site of origin for more detailed mapping. Activation mapping, where the earliest local activation is compared to the onset of the

(a)

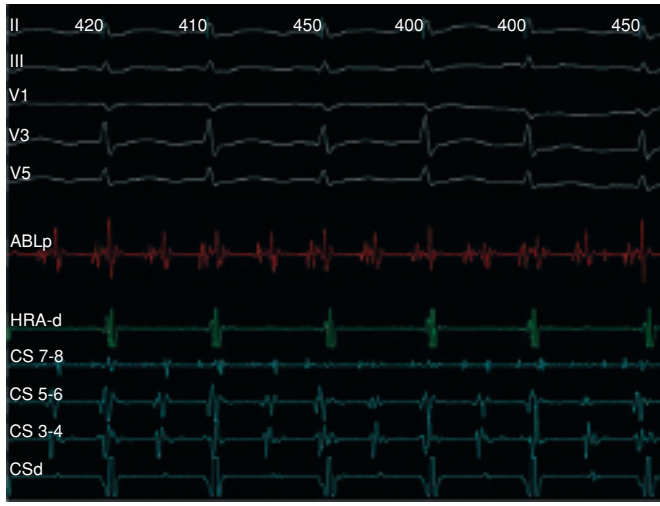

(b)

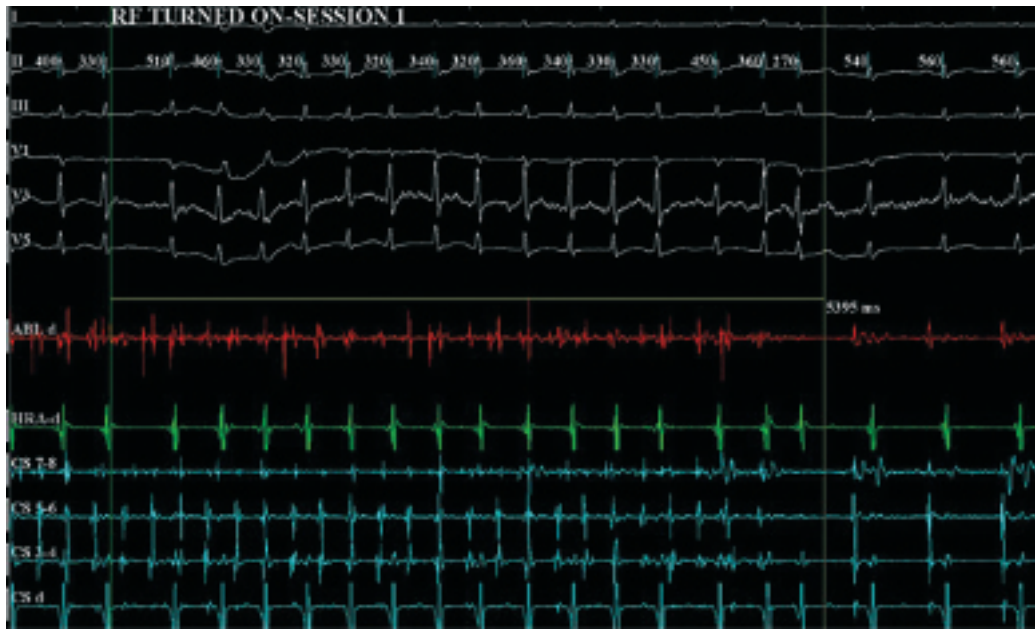

Figure 19.3 (a) Intracardiac electrogram recording from a patient with focal atrial tachycardia with 2:1 conduction to the ventricle. The ablator signal (recorded from the proximal coronary sinus) shows fractionated potentials that preceded the surface *P*-wave by 90 msec, suggesting that this is the site of origin of the tachycardia. (b) Catheter ablation performed at this site successfully terminates tachycardia in 5.4 sec.

tachycardia *P*-wave is the most common technique for mapping. With this technique, sites with local activation ranging from 20 msec to 60 msec prior the *P*-wave onset are targeted for ablation [8]. Often, the electrogram at the earliest site will be fractionated (Figure 19.3). Multielectrode catheters (such as a 20 pole catheter placed along the crista terminalis and a multipolar CS catheter) can be useful to guide initial mapping [3].

Activation mapping is most effective when there is sustained tachycardia to map. Occasionally, the use of high doses (up to 20 μg/min) of isoproterenol

is necessary to induce the tachycardia. Additionally, some atrial tachycardias are observed during the "washout" phase of isoproterenol. Other adrenergic stimuli such as norepinephrine or aminophylline are rarely useful. Minimizing or eliminating sedation may also be helpful. In women, scheduling a procedure at a different point in their menstrual cycle may also help.

For instance, when tachycardia is not sustained or difficult to induce, pace mapping can be useful. It is also useful as an adjunct to activation mapping. Pace mapping is performed by pacing at the lowest capture output; the paced *P*-wave morphology is then compared with the *P*-wave during tachycardia. This technique has the limitation of requiring a "pure" *P*-wave on the 12-lead EKG, undisturbed by the QRS or *T*-wave. However, utilizing surrogate markers such as multiple intracardiac recordings has been proposed [37].

Non-fluoroscopic 3D mapping systems offer many advantages in the ablation of focal ATs. In general, these systems allow construction of a 3D geometry of the heart chamber suspected to be the source of the tachycardia and show movement of the ablation catheter within this 3D image. By using this image to guide mapping and ablation, fluoroscopy exposure is significantly minimized [38, 39]. If mapping is done during sustained atrial tachycardia, the systems can produce an activation map that identifies the earliest site of atrial activation that is targeted for ablation (Figure 19.4 and Video Clip 19 ).

Finally, the 3D systems allow marking of interesting sites noted during mapping. Marking of the His cloud to show areas to avoid during ablation can be helpful, particularly in parahisian AT. When the ablation catheter is unstable during tachycardia, marking the earliest site during tachycardia facilitates returning to that same site for ablation during sinus rhythm.

The generated 3D activation map can also be very helpful in distinguishing a focal atrial tachycardia from a macroreentrant tachycardia. In macroreentrant atrial tachycardia, the activation map will span the entire tachycardia cycle length and the earliest site will meet the latest site. In focal atrial tachycardias, the activation map will typically not span the entire tachycardia cycle length and the latest site usually will not meet the earliest site (Figure 19.4 and Videoclip 19 ).

Some of the 3D mapping systems have unique features that make them particularly useful. The Carto™ (Biosense Webster, CA) uses magnetic field for sequential 3D mapping and can create voltage maps that accurately identify areas of scar with no electrical signal (useful for macroreentrant AT). The RPM™ system (Boston Scientific, MA,) uses ultrasound ranging techniques for 3D mapping and functions similarly to the Carto system [40].

The LocaLisa™ (Medtronic, MN) system uses standard catheter electrodes as sensors for a high-frequency transthoracic electrical field, which is applied via standard skin electrodes [41]. Unlike the Carto and RPM systems that require specialized expensive mapping catheters, LocaLisa utilizes all catheters and also multiple mapping catheters, allowing for a combination of sequential and simultaneous mapping. However, it does not create a 3D geometry or give voltage maps. Based on the same technology, Ensite NavX™ (St. Jude Medical, St. Paul, MN) has the same advantages as LocaLisa with the added ability to create 3D geometry and voltage maps.

A major limitation of these systems is the inability to map transient nonsustained tachycardias or sustained tachycardias that are hemodynamically unstable. The EnSite array 3D mapping system utilizes a 64 wire-array mounted to a 10-mL balloon-catheter. When the anatomy is obtained by tracing the chamber with a standard catheter, the system superimposes to it over 3,200 electrograms obtained by mathematical reconstruction simultaneously, and creates isopotential maps [42]. The biggest advantage of this system is its ability to map nonsustained tachycardias, and even single beats. The spatial resolution, however, is lost when the system is used in a very large atrium.

Ablation

When mapping identifies the optimal site, 25–50 W of radiofrequency energy is delivered for 30–60 sec. Standard ablation catheters with 4-mm tips are usually satisfactory. Larger tipped catheters or high-energy catheters are typically unnecessary. Acceleration of the tachycardia before termination and also termination within 10 sec suggests that the ablation will be successful (Figure 19.3). A successful ablation is verified by the inability to reinduce the

(a)

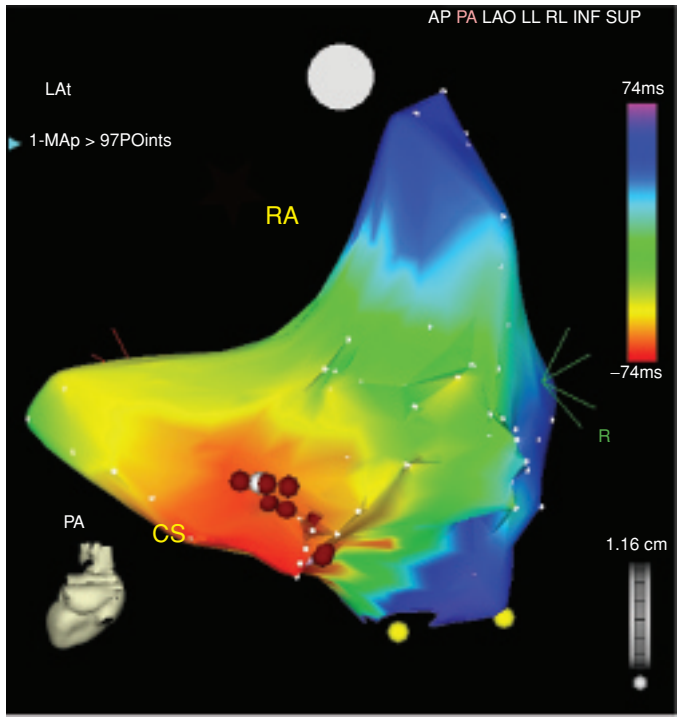

(b)

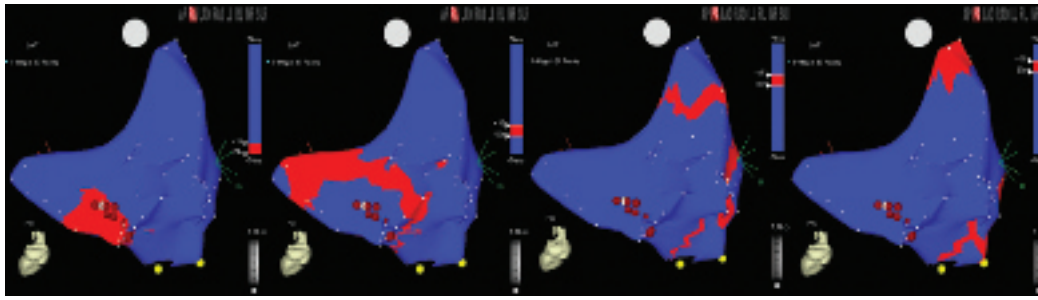

Figure 19.4 (a) Simultaneous CARTO map of the right atrium (RA) and coronary sinus (CS) during tachycardia demonstrates a focal activation pattern. The activation map does not span the entire tachycardia cycle length. (b) The propagation map (in a posteroanterior view) shows earliest activation in the proximal CS followed by activation of the rest of the CS and the RA. This suggests focal origin of the tachycardia from the proximal CS.

tachycardia following ablation. If isoproterenol was necessary for induction prior to ablation, it should be used again during attempts at reinduction to confirm success.

Some ATs originate from the coronary sinus and pulmonary veins. Lower energy and temperature settings may be required in these vascular structures to minimize the risk of perforation and thrombosis. Coronary angiography should be performed prior to ablation in the coronary sinus to avoid damage to the coronary arteries.

Ablation of parahisian AT is associated with a higher risk of complete heart block. Cryoablation, which uses cooling to ablate tissue, allows testing of potential ablation sites by adhering to the target tissue and chilling it to create a reversible electrical effect. If there is no heart block, the catheter tip can be cooled further to create a permanent

lesion. Cryoablation has been employed successfully to ablate parahisian ATs [43]. Successful ablation of parahisian ATs from the noncoronary aortic sinus has been described recently; this was not associated with the risk of AV block [44].

Intracardiac echocardiography can also help with ablation by localizing anatomic structures, aiding with catheter positioning and catheter tip contact, and confirming and identifying lesion size and location [3, 45–47]. It is particularly useful in helping to guide fine catheter movement between the upper crista terminalis and the right atrial posterior wall opposing the right upper pulmonary vein, which can quickly differentiate a crista terminalis atrial tachycardia from a right upper pulmonary vein atrial tachycardia prior to deciding whether to perform a transseptal puncture. Intracardiac echocardiography also can help with transseptal puncture in terms of recognition of early complications, such as perforations and clot formation, and with reducing fluoroscopy time.

Remote magnetic catheter navigation has been the latest innovation in the field of catheter ablation. The Niobe^{TM}system (Stereotaxis, Inc., St. Louis, MO) uses an externally applied magnetic field to direct the orientation of a catheter. It consists of two computer-controlled permanent magnets located on opposite sides of the patient, which create a steerable external magnetic field (0.08 T). A small magnet embedded in the catheter tip causes the catheter to align and to be steered by the external magnetic field. A motor drive advances or retracts the catheter, enabling complete remote navigation.

This system has been integrated with the CARTO 3D mapping system and can create a merge image with the imported CT scan of the chamber of interest [48]. Stereotaxis allows creation of a dense map in the region of interest by allowing precise catheter movement (1° deflections and 1-mm steps). By creating a stored magnet orientation for the site of earliest activation, one can return to the location of interest with remarkable precision. This has the potential to reduce fluoroscopy exposure and the risk of catheter perforation while achieving better efficacy due to stability of catheter position [49–52]. The potential disadvantage is the high initial cost of system and the cost of the specific ablation catheters that are used with it.

Catheter ablation for focal AT has been proven to be safe and effective [3, 5, 6, 9, 10, 19, 37, 53–55], with reported success rates between 77% and 100%. It also has been shown to improve patient quality-of-life scores [56]. Therefore, ablation is indicated for all symptomatic patients who have persistent symptoms despite medical therapy or intolerable side effects from medicines. Furthermore, patients who are unwilling to use medical therapy should also be considered.

Conclusion

Several advances have taken place in the past several years that have improved our ability to ablate focal atrial tachycardias. The 3D mapping systems now provide a straightforward approach that can identify the origin of the focal atrial tachycardias even when these arrhythmias are unstable or nonsustained. Intracardiac echocardiography can facilitate mapping and ablation. Finally, remote catheter navigation has significantly improved the safety and efficacy of the procedure, including a reduction in fluoroscopy exposure. Although the ablation of focal ATs can still be complex and challenging, these advances have allowed us to safely and successfully expand the use of curative catheter ablation for these arrhythmias.

References

1 Saoudi N, Cosio F, Waldo A, et al. A classification of atrial flutter and regular atrial tachycardia according to electrophysiological mechanisms and anatomical bases; a statement from a joint expert group from The Working Group of Arrhythmias of the European Society of Cardiology and the North American Society of Pacing and Electrophysiology. *Eur Heart J* 2001; **22**: 1162–82.

2 Scheinman MM, Basu D, Hollenberg M. Electrophysiologic studies in patients with persistent atrial tachycardia. *Circulation* 1974; **50**: 266–73.

3 Kalman JM, Olgin JE, Karch MR, Hamdan M, Lee RJ, Lesh MD. "Cristal tachycardias": origin of right atrial tachycardias from the crista terminalis identified by intracardiac echocardiography. *J Am Coll Cardiol* 1998; **31**: 451–59.

4 Callans DJ, Schwartzman D, Gottlieb CD, Marchlinski FE. Insights into the electrophysiology of atrial arrhythmias gained by the catheter ablation experience: "learning while burning, Part II." *J Cardiovasc Electrophysiol* 1995; **6**: 229–43.

5 Lesh MD, Van Hare GF, Epstein LM, et al. Radiofrequency catheter ablation of atrial arrhythmias: results and mechanisms. *Circulation* 1994; **89**: 1074–89.

6 Pappone C, Stabile G, De Simone A, et al. Role of catheter-induced mechanical trauma in localization of target sites of radiofrequency ablation in automatic atrial tachycardia. *J Am Coll Cardiol* 1996; **27**: 1090–97.

7 Chen SA, Chiang CE, Yang CJ, et al. Radiofrequency catheter ablation of sustained intra-atrial reentrant tachycardia in adult patients: identification of electrophysiological characteristics and endocardial mapping techniques. *Circulation* 1993; **88**: 578–87.

8 Walsh EP, Saul JP, Hulse JE, et al. Transcatheter ablation of ectopic atrial tachycardia in young patients using radiofrequency current [see comments]. *Circulation* 1992; **86**: 1138–46.

9 Kay GN, Chong F, Epstein AE, Dailey SM, Plumb VJ. Radiofrequency ablation for treatment of primary atrial tachycardias [see comments]. *J Am Coll Cardiol* 1993; **21**: 901–9.

10 Tang CW, Scheinman MM, Van Hare GF, et al. Use of *P*-wave configuration during atrial tachycardia to predict site of origin. *J Am Coll Cardiol* 1995; **26**: 1315–24.

11 Jais P, Shah DC, Haissaguerre M, Hocini M, Garrigue S, Clementy J. Atrial fibrillation: role of arrhythmogenic foci. *J Interv Card Electrophysiol* 2000; **4**: 29–37.

12 Badhwar N, Kalman JM, Sparks PB, et al. Atrial tachycardia arising from the coronary sinus musculature: electrophysiological characteristics and long-term outcomes of radiofrequency ablation. *J Am Coll Cardiol* 2005; **46**: 1921–30.

13 Kistler PM, Fynn SP, Haqqani H, et al. Focal atrial tachycardia from the ostium of the coronary sinus: electrocardiographic and electrophysiological characterization and radiofrequency ablation. *J Am Coll Cardiol* 2005; **45**: 1488–93.

14 Iesaka Y, Takahashi A, Goya M, et al. Adenosine-sensitive atrial reentrant tachycardia originating from the atrioventricular nodal transitional area. *J Cardiovasc Electrophysiol* 1997; **8**: 854–64.

15 Roberts-Thomson KC, Kistler PM, Haqqani HM, et al. Focal atrial tachycardias arising from the right atrial appendage: electrocardiographic and electrophysiologic characteristics and radiofrequency ablation. *J Cardiovasc Electrophysiol* 2007; **18**: 367–72.

16 Yamada T, Murakami Y, Yoshida Y, et al. Electrophysiologic and electrocardiographic characteristics and radiofrequency catheter ablation of focal atrial tachycardia originating from the left atrial appendage. *Heart Rhythm* 2007; **4**: 1284–91.

17 Morton JB, Sanders P, Das A, Vohra JK, Sparks PB, Kalman JM. Focal atrial tachycardia arising from the tricuspid annulus: electrophysiologic and electrocardiographic characteristics. *J Cardiovasc Electrophysiol.* 2001; **12**: 653–59.

18 Kistler PM, Sanders P, Hussin A, et al. Focal atrial tachycardia arising from the mitral annulus: electrocardiographic and electrophysiologic characterization. *J Am Coll Cardiol* 2003; **41**: 2212–19.

19 Chen SA, Tai CT, Chiang CE, Ding YA, Chang MS. Focal atrial tachycardia: reanalysis of the clinical and electrophysiologic characteristics and prediction of successful radiofrequency ablation. *J Cardiovasc Electrophysiol* 1998; **9**: 355–65.

20 Kammeraad JA, Balaji S, Oliver RP, et al. Nonautomatic focal atrial tachycardia: characterization and ablation of a poorly understood arrhythmia in 38 patients. *Pacing Clin Electrophysiol* 2003; **26**: 736–42.

21 Roberts-Thomson KC, Kistler PM, Kalman JM. Focal atrial tachycardia I: clinical features, diagnosis, mechanisms, and anatomic location. *Pacing Clin Electrophysiol* 2006; **29**: 643–52.

22 Steinbeck G, Hoffmann E. "True" atrial tachycardia. *Eur Heart J* 1998; **19**: E10-2, E48–9.

23 Engelstein ED, Lippman N, Stein KM, Lerman BB. Mechanism-specific effects of adenosine on atrial tachycardia. *Circulation* 1994; **89**: 2645–54.

24 Rosen MR. Cellular electrophysiology of digitalis toxicity. *J Am Coll Cardiol* 1985; **5**: 22A–34A.

25 Iwai S, Markowitz SM, Stein KM, et al. Response to adenosine differentiates focal from macroreentrant atrial tachycardia: validation using three-dimensional electroanatomic mapping. *Circulation* 2002; **106**: 2793–99.

26 Markowitz SM, Nemirovksy D, Stein KM, et al. Adenosine-insensitive focal atrial tachycardia: evidence for de novo micro-reentry in the human atrium. *J Am Coll Cardiol* 2007; **49**: 1324–33.

27 Kistler PM, Roberts-Thomson KC, Haqqani HM, et al. *P*-wave morphology in focal atrial tachycardia: development of an algorithm to predict the anatomic site of origin. *J Am Coll Cardiol* 2006; **48**: 1010–17.

28 Tada H, Nogami A, Naito S, et al. Simple electrocardiographic criteria for identifying the site of origin of focal right atrial tachycardia. *Pacing Clin Electrophysiol* 1998; **21**: 2431–39.

29 Kistler PM, Sanders P, Fynn SP, et al. Electrophysiological and electrocardiographic characteristics of focal atrial tachycardia originating from the pulmonary veins: acute and long-term outcomes of radiofrequency ablation. *Circulation* 2003; **108**: 1968–75.

30 Man KC, Chan KK, Kovack P, et al. Spatial resolution of atrial pace mapping as determined by unipolar atrial pacing at adjacent sites. *Circulation* 1996; **94**: 1357–63.

31 Okumura K, Plumb VJ, Page PL, Waldo AL. Atrial activation sequence during atrial flutter in the canine pericarditis model and its effects on the polarity of the flutter

wave in the electrocardiogram. *J Am Coll Cardiol* 1991; **17**: 509–18.

32 Kalbfleisch SJ, el-Atassi R, Calkins H, Langberg JJ, Morady F. Differentiation of paroxysmal narrow QRS complex tachycardias using the 12-lead electrocardiogram. *J Am Coll Cardiol* 1993; **21**: 85–9.

33 Knight BP, Ebinger M, Oral H, et al. Diagnostic value of tachycardia features and pacing maneuvers during paroxysmal supraventricular tachycardia. *J Am Coll Cardiol* 2000; **36**: 574–82.

34 Miller JM, Rosenthal ME, Vassallo JA, Josephson ME. Atrioventricular nodal reentrant tachycardia: studies on upper and lower "common pathways." *Circulation* 1987; **75**: 930–40.

35 Man KC, Niebauer M, Daoud E, et al. Comparison of atrial-His intervals during tachycardia and atrial pacing in patients with long RP tachycardia. *J Cardiovasc Electrophysiol* 1995; **6**: 700–10.

36 Glatter KA, Cheng J, Dorostkar P, et al. Electrophysiologic effects of adenosine in patients with supraventricular tachycardia. *Circulation.* 1999; **99**: 1034–40.

37 Tracy CM, Swartz JF, Fletcher RD, et al. Radiofrequency catheter ablation of ectopic atrial tachycardia using paced activation sequence mapping [see comments]. *J Am Coll Cardiol* 1993; **21**: 910–17.

38 Earley MJ, Showkathali R, Alzetani M, et al. Radiofrequency ablation of arrhythmias guided by nonfluoroscopic catheter location: a prospective randomized trial. *Eur Heart J*. 2006; **27**: 1223–29.

39 Marchlinski F, Callans D, Gottlieb C, Rodriguez E, Coyne R, Kleinman D. Magnetic electroanatomical mapping for ablation of focal atrial tachycardias. *Pacing Clin Electrophysiol* 1998; **21**: 1621–35.

40 Schreieck J, Ndrepepa G, Zrenner B, et al. Radiofrequency ablation of cardiac arrhythmias using a three-dimensional real-time position management and mapping system. *Pacing Clin Electrophysiol* 2002; **25**: 1699–707.

41 Wittkampf FH, Wever EF, Derksen R, Ramanna H, Hauer RN, Robles de Medina EO. Accuracy of the LocaLisa system in catheter ablation procedures. *J Electrocardiol* 1999; **32**: 7–12.

42 Kadish A, Hauck J, Pederson B, Beatty G, Gornick C. Mapping of atrial activation with a noncontact, multielectrode catheter in dogs. *Circulation* 1999; **99**: 1906–13.

43 Wong T, Markides V, Peters NS, Davies DW. Clinical usefulness of cryomapping for ablation of tachycardias involving perinodal tissue. *J Interv Card Electrophysiol* 2004; **10**: 153–58.

44 Ouyang F, Ma J, Ho SY, et al. Focal atrial tachycardia originating from the noncoronary aortic sinus: electrophysiological characteristics and catheter ablation. *J Am Coll Cardiol* 2006; **48**: 122–31.

45 Lesh MD, Kalman JM, Karch MR. Use of intracardiac echocardiography during electrophysiologic evaluation and therapy of atrial arrhythmias. *J Cardiovasc Electrophysiol* 1998; **9**: S40–7.

46 Kalman JM, Olgin JE, Karch MR, Lesh MD. Use of intracardiac echocardiography in interventional electrophysiology. *Pacing Clin Electrophysiol* 1997; **20**: 2248–62.

47 Chu E, Kalman JM, Kwasman MA, et al. Intracardiac echocardiography during radiofrequency catheter ablation of cardiac arrhythmias in humans. *J Am Coll Cardiol* 1994; **24**: 1351–57.

48 Di Biase L, Fahmy TS, Patel D, et al. Remote magnetic navigation: human experience in pulmonary vein ablation. *J Am Coll Cardiol* 2007; 50: 868–74.

49 Ernst S, Ouyang F, Linder C, et al. Initial experience with remote catheter ablation using a novel magnetic navigation system: magnetic remote catheter ablation. *Circulation* 2004; **109**: 1472–75.

50 Pflaumer A, Hessling G, Luik A, Wu J, Zrenner B. Remote magnetic catheter mapping and ablation of permanent junctional reciprocating tachycardia in a seven-year-old child. *J Cardiovasc Electrophysiol* 2007; **18**: 882–85.

51 Davis DR, Tang AS, Birnie DH, Gollob MH. Successful ablation of a concealed parahisian accessory pathway using a remote magnetic navigation system following failure by conventional methods. *J Interv Card Electrophysiol* 2006; **16**: 149–51.

52 Chun JK, Schmidt B, Kuck KH, Ernst S. Remote-controlled magnetic ablation of a right anterolateral accessory pathway: the superior caval vein approach. *J Interv Card Electrophysiol* 2006; **16**: 65–8.

53 Feld GK. Catheter ablation for the treatment of atrial tachycardia. *Prog Cardiovasc Dis* 1995; **37**: 205–24.

54 Poty H, Saoudi N, Haissaguerre M, Daou A, Clementy J, Letac B. Radiofrequency catheter ablation of atrial tachycardias. *Am Heart J* 1996; **131**: 481–89.

55 Roberts-Thomson KC, Kistler PM, Kalman JM. Focal atrial tachycardia II: management. *Pacing Clin Electrophysiol* 2006; **29**: 769–78.

56 Bubien RS, Knotts-Dolson SM, Plumb VJ, Kay GN. Effect of radiofrequency catheter ablation on health-related quality of life and activities of daily living in patients with recurrent arrhythmias [see comments]. *Circulation* 1996; **94**: 1585–91.

20

CHAPTER 20

Interpretation of Atrial Electrograms During Atrial Fibrillation

Sébastien Knecht, MD, *Rajesh Subbiah,* Bsc (Med), MBBS, Phd, *Mélèze Hocini,* MD, *Pierre Jaïs,* MD, *Kang-Teng Lim,* MD, *Seiichiro Matsuo,* MD, *Leonardo Arantes,* MD, *Mark D. O'Neill,* MBBCh, DPhil, *Nicolas Derval,* MD, *Frederic Sacher,* MD, *Antoine Deplagne,* MD, *Pierre Bordachar,* MD, *Jacques Clémenty,* MD, *Michel Haïssaguerre,* MD

Hôpital cardiololgique du Haut Lévêque–Université Victor Segalen Bordeaux II, Bordeaux, France

Summary

An understanding of electrogram analysis of pulmonary vein potentials and atrial electrograms is critical to the success of atrial fibrillation ablation. Foci triggering atrial fibrillation predominantly originate in the four pulmonary veins, but potential sources of triggers include left atrial tissue and other thoracic veins. In the context of persistent atrial fibrillation, after pulmonary vein isolation, ablation is first guided by complex electrograms when atrial activity is chaotic. Electrograms having the most impact on the atrial fibrillation process manifested as continuous electrical activity, while electrogram voltage or degree of fractionation have lesser impact.

Limited knowledge is available, however, to distinguish potentially active and passive areas. During organized atrial activity, sources maintaining atrial fibrillation can be mapped and targeted. By converging to the origin of atrial activation, the area displaying centrifugal activation may include either a discrete site, which allows tracking of the earliest activity, or more frequently a localized reentry, which gives local electrical activity spanning most of the cycle length and/or a temporal gradient between proximal and distal bipoles. Complexity of electrograms is strongly correlated with atrial fibrillation cycle length, which also allows monitoring of the impact of ablation at each region during electrogram-based ablation.

Cardiac Mapping, Third Edition Edited by Mohammad Shenasa, Gerhard Hindricks, Martin Borggrefe, and Günter Breithardt
 ISBN: 978-1-405-17572-2

Introduction

Various approaches targeting triggers and/or substrate have been validated for treating atrial fibrillation (AF) with catheter ablation [1–4]. Early attempts were inspired by the Maze surgical technique. Linear lesions in both atria were performed aimed at reducing the critical mass of atrial tissue necessary to sustain AF. These lesions were ineffective in the right atrium (RA) and successful in the left atrium (LA) at reducing AF, but they were associated with a high complication rate [5–7].

The crucial role of the LA in AF compared to the RA is counterintuitive in the context of the wavelet hypothesis, where one would expect a contributory role, proportionate to mass of both the RA and the LA. The demonstration of the pivotal role of pulmonary veins (PV) in triggering and perpetuating paroxysmal AF [1] led to PV isolation (PVI) as the standard approach for AF ablation. In addition to PVI, different strategies based on electrogram analysis have been attempted to determine the atrial areas critical for AF maintenance. These include frequency domain analysis [8–11], complex fractionated atrial electrogram (CFAE) analysis [2, 12], and activation mapping for identification of localized sources [13, 14] sometimes helped by 3D navigation systems [3, 15].

Even though each of these techniques has merit, none are effective alone in persistent AF. In contrast, a stepwise approach starting with PVI, followed by electrogram-based ablation, linear lesions, and finally ablation of residual atrial tachycardias (AT) [16], is associated with a high success rate [17]. Effective delivery of these steps required a comprehensive understanding of "conventional" electrogram analysis, which will be discussed in this chapter.

Triggering of AF

Foci that trigger AF predominantly originate in the four PVs, but other sources of triggers include LA tissue and thoracic veins [coronary sinus (CS), superior vena cava (SVC), vein of Marshall, or persistent left SVC)].

Pulmonary Veins

The identification of PV ectopy is facilitated by the "dead end" configuration of PV muscular fascicles, resulting in opposing sequences of activation in ectopy vs. sinus rhythm. During sinus rhythm, double potentials are recorded from the PVs. The first low-amplitude potential represents activation of the adjacent LA (or RA for the anterior part of the right PVs), and is usually synchronous with the first or second half of the *P*-wave for the right and left PVs, respectively. The second "sharp" potential (sometimes with multiple peaks) reflects activity from the PV striated musculature. As the mapping catheter is pulled closer to the PV ostium, the PV potentials (PVP) and LA potentials become fused.

When ectopy occurs in a PV, there is a reversal of the described activation sequence with the PVP preceding the LA potential (Figure 20.1). However, if the mapping catheter is located deep inside the vein, ectopy from the venous ostium can result in an unchanged sequence. Mapping of the earliest site of activity during ectopy allows identification of discrete sites inside the vein, while the atrial exit site is dependent on the width of muscular fascicles. Polarity reversal on adjacent bipoles can also facilitate localization of PV breakthroughs, particularly in the context of wide synchronous PVPs [18].

Ectopy originating from the PVs may have a short coupling interval to the previous sinus beat, resulting in nonconducted activity to the atrium. Present in 42–70% [19] of arrhythmogenic PVs, these "concealed ectopies" are usually synchronous to the local ventricular potential and require pacing maneuvers to confirm their origin.

Mapping of PVPs is facilitated by the use of a circumferential catheter, which allows an instantaneous assessment of the extent and activation of the PV musculature in sinus rhythm or during AF. In the more proximal part of the PV, synchronous potentials indicate wider fascicles, while sequentially activated potentials indicate tighter fascicles. Also, the potentials diminish in amplitude and in coverage when the catheter is advanced deeper into the PV, signifying a gradual decline in the muscular fascicles.

While pacing maneuvers during sinus rhythm can easily distinguish PVs from far-field potentials, other methods are required during AF. Firstly, the activation sequence of PV potentials is often variable during ablation, while that of far-field signals is relatively stable. Secondly, progressive or abrupt prolongation of electrogram cycle length during

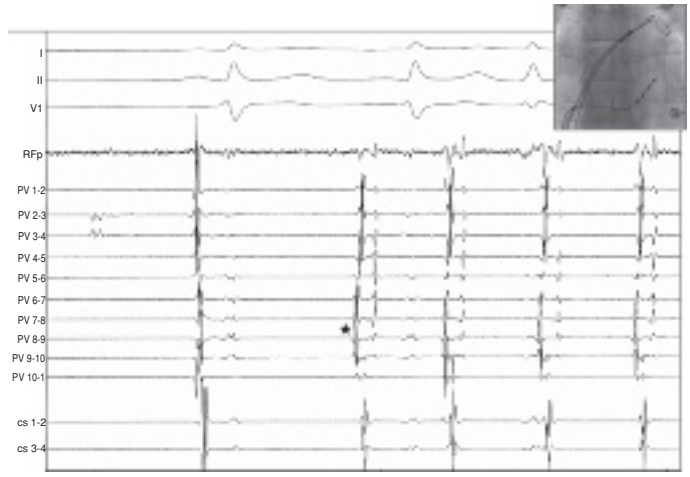

Figure 20.1 Recording of pulmonary veins potentials (PV) with a circumferential catheter placed within the vein and with the ablation catheter (RF) placed at the ostium of the vein. During sinus rhythm (first beat), there is a fusion between atrial and pulmonary vein potentials. When ectopy occurs in the pulmonary vein, there is a reversal of the activation sequence with the pulmonary vein potential preceding the left atrial potential. The earliest potential is confined to bipole 8–9 (solid star) with polarity the reverse of the adjacent 9–10 bipole.

ostial ablation usually indicates a PV origin rather than atrial potentials. Thirdly, PV potentials represent local myocardial activity and are therefore usually sharper and larger than far-field potentials. Lastly, if doubt remains, far-field potentials can be unmasked by placing a recording catheter in the incriminated structure. In general, far-field potentials can be recorded in the anterior part of the left PVs reflecting LAA activation. In the right superior PV, far-field signals can arise from the anterior part of SVC or RA. Other far-field potentials can also be recorded from posterior or inferior LA.

Nonpulmonary Veins Triggers

In a study by Shah et al. [20], non-PV foci triggering AF were located at the ostium of the PVs (46%) (highlighting the need for proximal ablation of the PVs), posterior LA (35%), other LA tissue (6%), RA (6%), as well as CS, SVC, persistent left SVC, or vein of Marshall (7%). Both vena cava [21, 22] have a muscular "dead end" configuration, allowing first-sight diagnosis by reversal of the activation pattern during ectopy.

CS [23–26], persistent left SVC [27], or vein of Marshall [28] have more than one connection to the atria requiring the tracking of earliest activity. Involvement of a persistent left SVC or vein of Marshall has to be considered particularly in the context of triple potentials in the vicinity of the left PVs. In addition, as for both atria, the earliest activity with a QS pattern on the unipolar lead during ectopy should be mapped.

Mapping of Atrial Electrograms During AF

Different strategies have been described to map atrial electrograms during AF: based on complex fractionated atrial electrograms (CFAE) [2], sites of dominant frequency (DF) [8], areas displaying characteristics of localized sources, and noncontact mapping [29–31].

Mapping During Chaotic Activity

In persistent AF, atrial activity is often chaotic and too complex to allow analysis of the local cycle length, morphology, or activation. Disorganized sites are ubiquitous in the LA and the first step of mapping is to determine the most *favorable* areas at which ablation will result in slowing and organization of global LA activity. Takahashi et al. [32] showed that electrogram patterns having the most impact on AF ablation were continuous electrical activity (>70% of the cycle length) with predictive positive and negative values of only 52% and 67%, respectively. Other variables such as fractionation index (representing the number of deflections

of fractionated activity), low-voltage electrograms, or local mean cycle length were not discriminating predictors of effective sites for AF ablation.

Complex Fractionated Atrial Electrograms

Cosio et al. first described fragmentation in zones of slow interatrial conduction produced by extrastimulation in patients with AF [33]. They concluded that patients with AF have a higher likelihood of developing fractionation than others. Jaïs et al. defined complex electrical activity as continuous electrical activity or electrograms with atrial potential intervals of less than 100 msec [34]. They proposed that this represents the ultimate degree of temporal asynchrony and demonstrated a heterogeneous distribution during paroxysmal AF, mostly in the posterior LA and septum.

CFAE were subsequently defined by Nademanee et al. as atrial electrograms with a cycle length shorter than 120 msec, displaying fractionated electrograms composed of three deflections or more, and/or have a perturbation of the baseline with continuous deflection of a prolonged activation complex [2]. In general, they exhibit multiple low-voltage signals (between 0.05 and 0.25 mV). Different underlying mechanisms may explain CFAE.

Konings et al. showed that fractionation may be caused by asynchronous activation of local muscle bundles [35] due to tissue anisotropy, and the presence of insulating collagenous septa between atrial muscle bundles. Fractionation may represent zones of colliding wavefronts or pivoting points between different wavelets participating in the AF process. These areas of slow conduction could shorten the wavelength of the wandering wavelets, thereby increasing the number that can coexist in the atria and the complexity of AF.

Rostock et al. reported that the occurrence of CFAE was associated with prior acceleration of the AFCL and that duration of CFAE was inversely correlated with the preceding AFCL [14] and Videoclip 20  . Consequently, a given region may harbor apparently normal potentials during slow AFCL episodes, while fractionation may be observed after acceleration of the AFCL.

Kalifa et al. analyzed in the posterior LA of the isolated sheep heart the relation between local frequency, AF wave propagation and electrogram fractionation during sustained AF [36]. They showed that sites where most fractionation occurs were located at the margin of the more rapid areas (Figure 20.2). Fractionation would arise from slow conduction at the outer limit of the region displaying the higher frequency and the most regular activity.

All the above studies reinforce that fractionation/CFAE is a manifestation of slow conduction with a tight functional relationship with CL. Therefore, location of CFAE may be a Consequence of anisotropic Conduction from a region with faster activity.

The autonomic nervous system is also thought to be implicated in the mechanism of fractionation, by release of acetylcholine from the ganglionated plexi, which results in a shortening of the action potential and effective refractory period [37, 38]. Acetylcholine administration has been shown to be capable of inducing AF [36], and a spatial correlation between ganglionated plexi and CFAE localization has been observed [37]. However, given the ubiquitous presence of CFAE in long-lasting AF patients, the main issue is to distinguish active from passive patterns [14] and Videoclip 23 , and criteria defining more optimal electrograms are certainly required to improve success of ablation.

Frequency Domain

Sites with high-frequency activity may correspond to drivers of AF, and spectral analysis can estimate atrial activation rates during AF [8, 38–46]. Dominant frequency (DF) has been used to detect areas of rapid activity, rate changes after ablation, and supposed differences in pathophysiology. Using Fourier transform (in general fast Fourier transform, or FFT), DF is the frequency of the sinusoidal waveform with the highest amplitude, which best approximates the signal and relates to the signal rate. The main benefit of DF analysis is that it can be easily applied to complex electrograms of AF, even in the case of high-amplitude variability [47]. Sanders et al. demonstrated that ablation of DF sites coincided with slowing and termination of AF in 87% of patients in whom arrhythmia terminated during ablation [8] and Videoclip 21 & 22 . Sites of high DF could identify sites of high organization, possibly representing

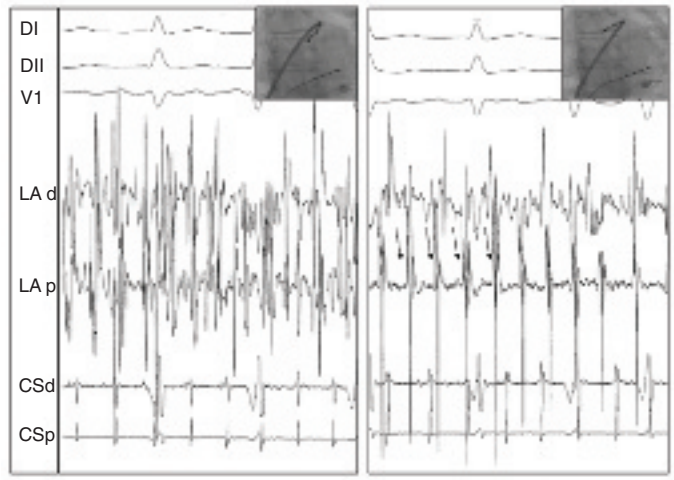

Figure 20.2 Highly complex fractionated atrial site recorded with the ablation catheter (LAd and LAp) on the posterior wall of the left atrium (left panel). Quadripolar catheter placed within the coronary sinus (CSd and CSp). By advancing the ablation catheter toward the roof (in an opposite direction from the coronary sinus) (right panel), recording of a more rapid and organized activity with a distal to proximal pattern (arrows). Thus, fractionated potentials were located at the margin of the more rapid areas. Ablation was performed at the earliest site of organized fast activity and resulted in restoration of sinus rhythm, suggesting the presence of a localized source.

sources maintaining AF. High-regularity activity emanating from PVs has been highlighted, suggesting that these structures may have a role in maintaining AF through localized short CL reentry or focal high-frequency activity [43, 44, 48]. This was confirmed by other studies showing short CL activities in the PVs [49, 50] associated with a progressive slowing and termination of the AF process during PV isolation of paroxysmal AF [51].

During persistent AF, DF sites did not demonstrate critical zones [8]. Lazar et al. showed that there is a frequency gradient between both atria during paroxysmal but not persistent AF [39]. They suggested that the importance of the posterior free wall during paroxysmal AF may reduce with time, and that a more global involvement of both atria could be observed. Nitta et al. also showed the existence of multiple areas of focal activation in the LA and RA in patients with permanent AF and mitral valve disease that may explain ablation failure [52].

High variability of activation electrogram as seen during complex fractionation or split double potentials does not allow easy characterization because of the lack of a sine wave corresponding to the frequency of activation [47]. It results in multiple peaks of frequencies with a very similar power as the dominant one. Small changes in the signal can cause shifts in DF, without discriminating real activation rate. Failure to terminate persistent AF using DF may thus partially be explained by more complex electrogram patterns displaying high variability of activation, resulting in multiple peaks close to the dominant one.

Linear Lesions

From experimental and simulation studies, AF has been shown to be maintained by wandering reentrant wavelets [53] or macroreentrant loops [54]. Linear lesions are still often used during disorganized AF despite the challenging achievement of complete linear block [55, 56]. The observed therapeutic efficacy of linear lesions may be related in part to an interruption of wavelet and macroreentries, but also alteration of autonomic innervation, atrial debulking. or the effect on local complex electrograms. As data suggest, a high risk of AT recurrence in the case of incomplete conduction block [57] and also based on the wavelet hypothesis, conduction block should be achieved (and verified during sinus rhythm) to prevent reentrant wavelet perpetuation.

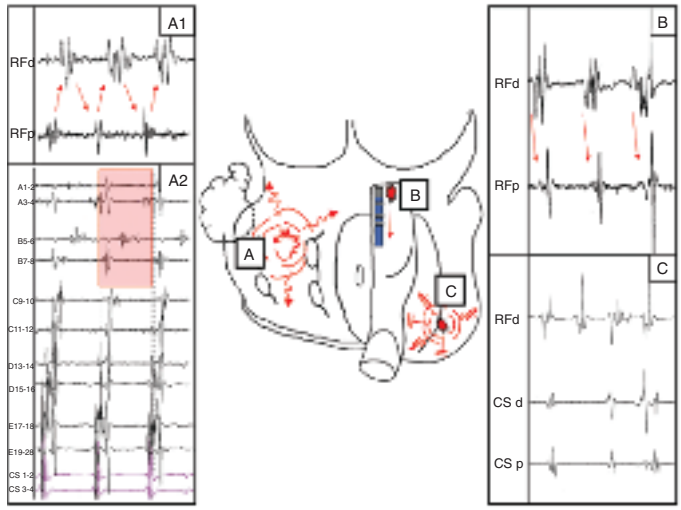

Figure 20.3 Schematic representation of both atria and thoracic veins as well as the different electrophysiological properties of localized sources. (a) Schematic illustration of localized reentry, recorded with the ablation catheter as a temporal gradient between distal (RFd) and proximal (RFp) bipoles (a1) and with 20 poles high-density mapping [from (a) to (e)] as local activity spanning all the cycle length specified by the CS cathehter (especially on arms a and b, pink rectangle) (a2). (b) Discrete activity originating from a "dead end" area (superior vena cava), with one-to-one conduction to the surrounding atria, recorded with the ablation catheter (RFd and RFp) as a distal to proximal pattern. (c) Discrete rapid source without one to one conduction to the surrounding atrium as seen on the coronary sinus (CS) which is slower.

Mapping During Organized Atrial Fibrillation

Organized AF is defined by endocardial mapping during AF displaying (i) irregular atrial cycle length (i.e., AF) with beat-to-beat variations of ≥20 msec; (ii) discrete atrial complexes with a consistent activation sequence for ≥75% of the time in both atria; and (iii) the stability of activation evaluated over a 10-min period of spontaneous or induced AF [13].

The evidence for localized sources perpetuating AF has been reported experimentally as either automatic foci or small rapid circuits during acetylcholine-induced AF [58–60], in chronic pacing-induced AF [61], and in computer simulation models of AF [62]. Such sources have also been evidenced in man by persistent fibrillatory activity confined within isolated LA areas surrounded by the atria in sinus rhythm [63].

These sources play an important role in AF maintenance, in addition to PV and reentrant loops [13]. After PVI and linear lesions, ablation at these sites remains the last step of substrate elimination and results in AT conversion or restoration of sinus rhythm. When organized AF allows converging to the origin of atrial activation, a small area displaying centrifugal activation and including the localized source can be mapped [13] (Figure 20.3). This area may include in 58% of cases a discrete point (harboring less than 75% of the CL), which allows tracking of the earliest activity (Figure 20.3b,c).

In this scenario, local electrograms display centrifugal activation with or without one-to-one conduction to the adjacent atrium (same or faster cycle length of the source compared to AFCL, respectively). In 42% of cases, the area of earliest activation displays electrical activity covering most of the cycle length, suggesting a localized circuit (Figure 20.3a). By mapping with a high-density 20-pole catheter, all the cycle can be visualized on the different spines. By mapping with a conventional quadripolar ablation catheter, continuous activity probably indicating a localized isthmus or temporal alternating potentials between distal and proximal bipoles (depending on the reentrant circuit size and properties) will be displayed. A sequential mapping of the source with the distal bipole of the ablation catheter can also be performed with the aim to map different parts of the CL (Figure 20.4).

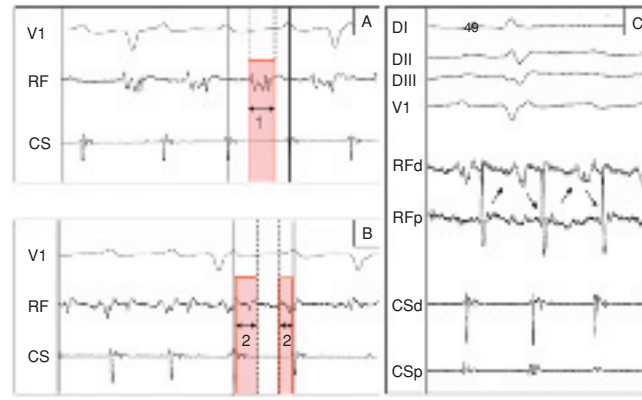

Figure 20.4 Sequential mapping of a source displaying properties of localized reentry. Relative stability of the cycle length (seen on the coronary sinus (CS) catheter) allowing to map the first (a) and the second half (b) of circuit covering all the cycle length. When the ablation catheter crosses the localized reentry, it will display temporal gradient of activity between distal (RFd) and proximal bipoles of the catheter.

Anatomic localizations of sources are predominantly distributed to the CS and inferior LA interface, as well as the ostium of the LAA, and the anterior LA. Such anatomical areas display heterogeneous fibers with properties favoring anatomic reentry or anchoring rotors [60, 61] and importantly were also incriminated in AT occurrence in the context of prior AF ablation [64].

Sanders et al. demonstrated ATs apparently focal, i.e,. displaying centrifugal activation but where the site of origin was actually an *area* harboring the entire tachycardia cycle length [64]. Half of these patients had arrhythmias induced by programmed stimulation, and a reentrant mechanism was confirmed by entrainment. These "localized reentrant ATs" display the same electrophysiological characteristics as localized fibrillatory sources and probably represent close electrophysiological mechanisms.

Noncontact Mapping

While point-to-point sequential mapping is required for electroanatomical mapping, limiting spatial and especially temporal resolution, noncontact mapping may provide a dynamic and simultaneous aspect of atrial beat-to-beat wavefront activation during AF. The electrode array should be in close proximity to the endocardial potentials, only separated from it by blood, which is uniform and electrically noncontributory. However, although it intuitively seemed a perfect mapping system for AF, accuracy of electrogram reconstruction has been disappointing due to ventricular far-field signals, and low voltage potentials especially if separated by more than 40 mm from the mapping system [31, 65].

Nevertheless, Schilling et al. demonstrated evidence of reentrant circuits in the RA, particularly at regions where orientation of atrial fibers might favor interatrial conduction [30]. Other studies in paroxysmal AF have confirmed the existence of both trigger zones and wavefronts potentially capable of maintaining AF [66], as well as evidence of focal triggers breaking up and forming reentrant circuits over a line of functional block in the LA [67].

Importance of Atrial Fibrillation Cycle Length

AFCL can be reliably monitored during the procedure by averaging 30 consecutive cycles at the left and right atrial appendages, which display unambiguous high-voltage and reproducible electrograms. Various early studies have shown that AFCL correlates with the local refractory period, that it shortens in parallel with the duration of AF and that drugs may affect it [68–70]. AFCL prolongation during ablation at remote sites raises evidence that it is not only due to the local refractory period. Based on computer simulation, AFCL represent the sum of all fibrillatory activities converging on one area. It can be reliably measured by positioning a mapping catheter in both appendages, which may thereby be considered as "sentinels." AFCL measurement has different implications:

1 Initial AFCL has been shown to be the strongest predictor of success for persistent AF ablation, along with the duration in years of persistent AF. Baseline

AFCL is longer in patients in whom AF terminates during ablation (156 ± 23 msec, $n = 52$ vs. 130 ± 14 msec, $n = 8$) [16]. AFCL of less than 140 ms is associated with AF termination in less than 69%, while a higher AFCL is associated with more than 89% of AF termination.

2 Impact of ablation of each region during electrogram-based ablation can be followed and estimated with AFCL monitoring. After each step of ablation, a gradual prolongation of AFCL is observed. Conversion to sinus rhythm or atrial tachycardia usually occurs when AFCL reaches 180 and 200 msec in patients off drugs. If AF persists during ablation of the LA despite a prolonged LAA CL, a lesser prolongation of the RAA CL suggests the RA is or has become the principal driver of AF.

Conclusion

An understanding of electrogram analysis of PV potentials and atrial electrograms is critical to the success of AF ablation, in particular in the context of persistent AF. Complexity of electrograms is strongly correlated with AFCL. During chaotic atrial activity, ablation is guided by complex atrial electrograms but limited knowledge is available to distinguish potentially active and passive areas. During organized atrial activity, sources maintaining AF can be mapped and targeted, with the most predominant mechanism being localized reentry.

References

1 Haissaguerre M, Jais P, Shah DC, et al. Spontaneous initiation of atrial fibrillation by ectopic beats originating in the pulmonary veins. *N Engl J Med* 1998; **339**: 659–66.

2 Nademanee K, McKenzie J, Kosar E, et al. A new approach for catheter ablation of atrial fibrillation: mapping of the electrophysiologic substrate. *J Amer Coll Cardiol* 2004; **43**: 2044–53.

3 Oral H, Pappone C, Chugh A, et al. Circumferential pulmonary-vein ablation for chronic atrial fibrillation. *N Engl J Med* 2006; **354**: 934–41.

4 Ouyang F, Bansch D, Ernst S, et al. Complete isolation of left atrium surrounding the pulmonary veins: new insights from the double-lasso technique in paroxysmal atrial fibrillation. *Circulation* 2004; **110**: 2090–96.

5 Haissaguerre M, Jais P, Shah D, et al. Right and left atrial radiofrequency catheter therapy of paroxysmal atrial fibrillation. *J Cardiovasc Electrophysiol* 1996; **7**: 1132–44.

6 Schwartz JF, Pellersels G, Silvers J. A catheter-based curative approach to atrial fibrillation in humans. *Circulation* 1993; **90**: I–335.

7 Jais P, Shah DC, Takahashi A, Hocini M, Haissaguerre M, Clementy J. Long-term follow-up after right atrial radiofrequency catheter treatment of paroxysmal atrial fibrillation. *Pacing Clini Electrophysiol* 1998; **21**: 2533–38.

8 Sanders P, Berenfeld O, Hocini M, et al. Spectral analysis identifies sites of high-frequency activity maintaining atrial fibrillation in humans. *Circulation* 2005; **112**: 789–97.

9 Sanders P, Nalliah CJ, Dubois R, et al. Frequency mapping of the pulmonary veins in paroxysmal versus permanent atrial fibrillation. *J Cardiovasc Electrophysiol* 2006; **17**: 965–72.

10 Takahashi Y, Sanders P, Jais P, et al. Organization of frequency spectra of atrial fibrillation: relevance to radiofrequency catheter ablation. *J Cardiovasc Electrophysiol* 2006; **17**: 382–88.

11 Takahashi Y, Hocini M, O'Neill MD, et al. Sites of focal atrial activity characterized by endocardial mapping during atrial fibrillation. *J Amer Coll Cardiol* 2006; **47**: 2005–12.

12 Oral H, Chugh A, Good E, et al. Radiofrequency catheter ablation of chronic atrial fibrillation guided by complex electrograms. *Circulation* 2007; **115**: 2606–12.

13 Haissaguerre M, Hocini M, Sanders P, et al. Localized fibrillatory sources maintaining atrial fibrillation. *Heart Rhythm* 2005; **2**: S20.

14 Rostock T, Rotter M, Sanders P, et al. High-density activation mapping of fractionated electrograms in the atria of patients with paroxysmal atrial fibrillation. *Heart Rhythm* 2006; **3**: 27–34.

15 Pappone C, Rosanio S, Oreto G, et al. Circumferential radiofrequency ablation of pulmonary vein ostia : a new anatomic approach for curing atrial fibrillation. *Circulation* 2000; **102**: 2619–28.

16 Haissaguerre M, Sanders P, Hocini M, et al. Catheter ablation of long-lasting persistent atrial fibrillation: critical structures for termination. *J Cardiovasc Electrophysiol* 2005; **16**: 1125–37.

17 Haissaguerre M, Hocini M, Sanders P, et al. Catheter ablation of long-lasting persistent atrial fibrillation: clinical outcome and mechanisms of subsequent arrhythmias. *J Cardiovasc Electrophysiol* 2005; **16**: 1138–47.

18 Yamane T, Shah DC, Jais P, et al. Electrogram polarity reversal as an additional indicator of breakthroughs from the left atrium to the pulmonary veins. *J Amer Coll Cardiol* 2002; **39**: 1337–44.

19 Haissaguerre M, Jais P, Shah D, et al. Catheter ablation of chronic atrial fibrillation targeting the reinitiating triggers. *J Cardiovasc Electrophysiol* 2000; **11**: 2–10.

20 Shah D, Haissaguerre M, Jais P, Hocini M. Nonpulmonary vein foci:. do they exist? *Pacing Clin Electrophysiol* 2003; **26**: 1631–35.
21 Tsai CF, Tai CT, Hsieh MH, et al. Initiation of atrial fibrillation by ectopic beats originating from the superior vena cava: electrophysiological characteristics and results of radiofrequency ablation. *Circulation* 2000; **102**: 67–74.
22 Scavee C, Jais P, Weerasooriya R, Haissaguerre M. The Inferior vena cava: an exceptional source of atrial fibrillation. *J Cardiovasc Electrophysiol* 2003; **14**: 659–62.
23 Hocini M, Takahashi Y, Sanders P, et al. P6-83 multifocal arrhythmogenicity of the coronary sinus in chronic atrial fibrillation. *Heart Rhythm* 2006; **3**: S329.
24 Rotter M, Sanders P, Takahashi Y, et al. Coronary sinus tachycardia driving atrial fibrillation. *Circulation* 2004; **110**: e59–e60.
25 Chauvin M, Shah DC, Haissaguerre M, Marcellin L, Brechenmacher C. The anatomic basis of connections between the coronary sinus musculature and the left atrium in humans. *Circulation* 2000; **101**: 647–52.
26 Oral H, Ozaydin M, Chugh A, et al. Role of the coronary sinus in maintenance of atrial fibrillation. *J Cardiovasc Electrophysiol* 2003; **14**: 1329–36.
27 Hsu LF, Jais P, Keane D, et al. Atrial fibrillation originating from persistent left superior vena cava. *Circulation* 2004; **109**: 828–32.
28 Kamunu S, Tan AY, Peter CT, Hwang C, Chen P. Vein of Marshall activity during sustained atrial fibrillation. *J Cardiovasc Electrophysiol* 2006; **17**: 839–46.
29 Schilling RJ, Peters NS, Goldberger J, Kadish AH, Davies DW. Characterization of the anatomy and conduction velocities of the human right atrial flutter circuit determined by noncontact mapping. *J Amer Coll Cardiol* 2001; **38**: 385–93.
30 Schilling RJ, Kadish AH, Peters NS, Goldberger J, Davies DW. Endocardial mapping of atrial fibrillation in the human right atrium using a noncontact catheter. *Eur Heart J* 2000; **21**: 550–64.
31 Earley MJ, Abrams DJR, Sporton SC, Schilling RJ. Validation of the noncontact mapping system in the left atrium during permanent atrial fibrillation and sinus rhythm. *J Amer Coll Cardiol* 2006; **48**: 485–91.
32 Takahashi Y, O'Neill MD, Hocini M, et al. Characterization of electrograms associated with termination of chronic atrial fibrillation by catheter ablation. *J Amer Coll Cardiolo* 2008; **51**:1003–10
33 Cosio FG, Palacios J, Vidal JM, Cocina EG, Gomez-Sanchez MA, Tamargo L. Electrophysiologic studies in atrial fibrillation: slow conduction of premature impulses: a possible manifestation of the background for reentry. *J Amer J Cardiol* 1983; **51**: 122–30.
34 Jais P, Haissaguerre M, Shah D, Chouairi S, Clementy J. Regional disparities of endocardial atrial activation in paroxysmal atrial fibrillation. *Pacing Clin Electrophysiol* 1996; **19**: 1998–2003.
35 Konings KTS, Smeets JLRM, Penn OC, Wellens HJJ, Allessie MA. Configuration of Unipolar atrial electrograms during electrically induced atrial fibrillation in humans. *Circulation* 1997; **95**: 1231–41.
36 Kalifa J, Tanaka K, Zaitsev AV, et al. Mechanisms of wave fractionation at boundaries of high-frequency excitation in the posterior left atrium of the isolated sheep heart during atrial fibrillation. *Circulation* 2006; **113**: 626–33.
37 Lemery R, Birnie D, TANG ASL, Green M, Gollob M. Feasibility study of endocardial mapping of ganglionated plexuses during catheter ablation of atrial fibrillation. *Heart Rhythm* 2006; 3: 387–96.
38 Scherlag BJ, Yamanashi W, Patel U, Lazzara R, Jackman WM. Autonomically induced conversion of pulmonary vein focal firing into atrial fibrillation. *J Amer Coll Cardiol* 2005; **45**: 1878–86.
39 Lazar S, Dixit S, Marchlinski FE, Callans DJ, Gerstenfeld EP. Presence of left-to-right atrial frequency gradient in paroxysmal but not persistent atrial fibrillation in humans. *Circulation* 2004; **110**: 3181–86.
40 Sahadevan J, Ryu K, Peltz L, et al. Epicardial mapping of chronic atrial fibrillation in patients: preliminary observations. *Circulation* 2004; **110**: 3293–99.
41 Lin YJ, Tai CT, Kao T, et al. Frequency analysis in different types of paroxysmal atrial fibrillation. *J Amer Coll Cardiol* 2006; **47**: 1401–7.
42 Huang JL, Tai CT, Lin YJ, et al. The mechanisms of an increased dominant frequency in the left atrial posterior wall during atrial fibrillation in acute atrial dilatation. *J Cardiovasc Electrophysiol* 2006; **17**: 178–88.
43 Skanes AC, Mandapati R, Berenfeld O, Davidenko JM, Jalife J. Spatiotemporal Periodicity during atrial fibrillation in the isolated sheep heart. *Circulation* 1998; **98**: 1236–48.
44 Mandapati R, Skanes A, Chen J, Berenfeld O, Jalife J. Stable Microreentrant sources as a mechanism of atrial fibrillation in the isolated sheep heart. *Circulation* 2000; **101**: 194–99.
45 Mansour M, Mandapati R, Berenfeld O, Chen J, Samie FH, Jalife J. Left-to-right gradient of atrial frequencies during acute atrial fibrillation in the isolated sheep heart. *Circulation* 2001; **103**: 2631–36.
46 Berenfeld O, Zaitsev AV, Mironov SF, Pertsov AM, Jalife J. Frequency-dependent breakdown of wave propagation into fibrillatory conduction across the pectinate muscle network in the isolated sheep right atrium. *Circ Res* 2002; **90**: 1173–80.
47 Ng J, Kadish AH, Goldberger JJ. Effect of electrogram characteristics on the relationship of dominant frequency to atrial activation rate in atrial fibrillation. *Heart Rhythm* 2006; **3**: 1295–305.

48 Wu TJ, Doshi RN, Huang HL, et al. Simultaneous biatrial computerized mapping during permanent atrial fibrillation in patients with organic heart disease. *J Cardiovasc Electrophysiol* 2002; **13**: 571–77.

49 O'Donnell D, Furniss SS, Bourke JP. Paroxysmal cycle length shortening in the pulmonary veins during atrial fibrillation correlates with arrhythmogenic triggering foci in sinus rhythm. *J Cardiovasc Electrophysiol* 2002; **13**: 124–28.

50 Oral H, Ozaydin M, Tada H, et al. Mechanistic significance of intermittent pulmonary vein tachycardia in patients with atrial fibrillation. *J Cardiovasc Electrophysiol* 2002; **13**: 645–50.

51 Haissaguerre M, Sanders P, Hocini M, et al. Changes in atrial fibrillation cycle length and inducibility during catheter ablation and their relation to outcome. *Circulation* 2004; **109**: 3007–13.

52 Nitta T, Ishii Y, Miyagi Y, Ohmori H, Sakamoto Si, Tanaka S. Concurrent multiple left atrial focal activations with fibrillatory conduction and right atrial focal or reentrant activation as the mechanism in atrial fibrillation. *J Thoracic Cardiovasc Surg* 2004; **127**: 770–78.

53 Moe GK, Abildskov JA. Atrial fibrillation as a self-sustaining arrhythmia independent of focal discharge. *Amer Heart J* 1959; **58**: 59–70.

54 Schuessler RB, Kawamoto T, Hand DE, et al. Simultaneous epicardial and endocardial activation sequence mapping in the isolated canine right atrium. *Circulation* 1993; **88**: 250–63.

55 Jais P, Hocini M, Hsu LF, et al. Technique and results of linear ablation at the mitral isthmus. *Circulation* 2004; **110**: 2996–3002.

56 Hocini M, Jais P, Sanders P, et al. Techniques, evaluation, and consequences of linear block at the left atrial roof in paroxysmal atrial fibrillation: a prospective randomized study. *Circulation* 2005; **112**: 3688–96.

57 Rostock T, O'Neill MD, Sanders P, et al. Characterization of conduction recovery across left atrial linear lesions in patients with paroxysmal and persistent atrial fibrillation. *J Cardiovasc Electrophysiol* 2006; **17**: 1106–11.

58 Schuessler RB, Grayson TM, Bromberg BI, Cox JL, Boineau JP. Cholinergically mediated tachyarrhythmias induced by a single extrastimulus in the isolated canine right atrium. *Circ Res* 1992; **71**: 1254–67.

59 Allessie MA, Bonke FI, Schopman FJ. Circus movement in rabbit atrial muscle as a mechanism of tachycardia. II. The role of nonuniform recovery of excitability in the occurrence of unidirectional block, as studied with multiple microelectrodes. *Circ Res* 1976; **39**: 168–77.

60 Jalife J, Berenfeld O, Mansour M. Mother rotors and fibrillatory conduction: a mechanism of atrial fibrillation. *Cardiovasc Res* 2002; **54**: 204–16.

61 Morillo CA, Klein GJ, Jones DL, Guiraudon CM. Chronic rapid atrial pacing: structural, functional, and electrophysiological characteristics of a new model of sustained atrial fibrillation. *Circulation* 1995; **91**: 1588–95.

62 Kneller J, Zou R, Vigmond EJ, Wang Z, Leon LJ, Nattel S. Cholinergic atrial fibrillation in a computer model of a two-dimensional sheet of canine atrial cells with realistic ionic properties. *Circ Res* 2002; **90**: 73e–87.

63 Rostock T, Rotter M, Sanders P, et al. Fibrillating areas isolated within the left atrium after radiofrequency linear catheter ablation. *J Cardiovasc Electrophysiol* 2006; **17**: 807–12.

64 Sanders P, Hocini M, Jais P, et al. Characterization of focal atrial tachycardia using high-density mapping. *J Amer Coll Cardiol* 2005; **46**: 2088–99.

65 Abrams DJ, Earley MJ, Sporton SC, et al. Comparison of noncontact and electroanatomic mapping to identify scar and arrhythmia late after the fontan procedure. *Circulation* 2007; **115**: 1738–46.

66 Weber S, Ndrepepa G, Schneider M, et al. Characterization of onset mechanism and waveform analysis in patients with atrial fibrillation using a high-resolution noncontact mapping system. *J Cardiovasc Electrophysiol* 2003; **14**: 176–81.

67 Markides V, Schilling RJ, Yen Ho S, Chow AWC, Davies DW, Peters NS. Characterization of left atrial activation in the intact human heart. *Circulation* 2003; **107**: 733–39.

68 Kim KB, Rodefeld MD, Schuessler RB, Cox JL, Boineau JP. Relationship between local atrial fibrillation interval and refractory period in the isolated canine atrium. *Circulation* 1996; **94**: 2961–67.

69 Wijffels MCEF, Kirchhof CJHJ, R, Allessie MA. Atrial fibrillation begets atrial fibrillation: a study in awake chronically instrumented goats. *Circulation* 1995; **92**: 1954–68.

70 Wang Z, Page P, Nattel S. Mechanism of flecainide's antiarrhythmic action in experimental atrial fibrillation. *Circ Res* 1992; **71**: 271–87.

21 CHAPTER 21

Different Mapping Approaches for Atrial Fibrillation Ablation

KR Julian Chun, MD, *Feifan Ouyang*, MD, *Karl-Heinz Kuck*, MD

Asklepios Klinik St. Georg, Hamburg, Germany

Summary

Recently, catheter ablation has evolved as a well-accepted therapeutic strategy in atrial fibrillation (1). However, various mapping and ablation strategies defining different procedural endpoints such as segmental pulmonary vein (PV) isolation, circumferential PV ablation, deployment of linear lesions, circumferential PV isolation, and ablation of complex fractionated potentials are currently performed. In the future, novel technical developments such as magnetic navigation or balloon-based catheter technologies may eventually facilitate mapping and AF ablation.

Introduction

Recent studies have demonstrated that myocardium around the pulmonary vein (PV) ostia plays an important role in the initiation and perpetuation of atrial fibrillation (AF) [2]. This important finding has led to the development of segmental PV ostial isolation [3, 4], circumferential ablation [5] or isolation around the PVs guided by 3D electroanatomic mapping [6]. Also, substrate modification with the use of limited linear ablation (such as roof line and left isthmus line) [7, 8] or ablation of areas associated with complex fractionated electrograms [9, 10] have proved to be of value in patients with AF.

The most commonly used method in the majority of the ablation centers is PV isolation either using segmental PV isolation or circumferential complete PV isolation guided by 3D mapping. In these procedures electrical information from the Lasso™ catheter (Biosense Webster, Diamond Bar, CA) sitting within the PV is important to identify sites of electrophysiological connections between the PV and the left atrium (LA). Also, 3D electroanatomical mapping provides more precise information on the individual atrial and PV anatomy and contributes to shorter fluoroscopy time.

In this chapter, we describe the currently performed different mapping and ablation approaches for AF with special emphasis on our recently introduced double Lasso guided circumferential ablation technique in conjunction with 3D electroanatomical LA mapping. Novel upcoming AF mapping and ablation tools such as the magnetic navigation system or balloon-based catheter technologies are also discussed.

Left Atrial Imaging

Catheter ablation procedures have been traditionally guided by electrophysiological mapping.

Cardiac Mapping, Third Edition Edited by Mohammad Shenasa, Gerhard Hindricks, Martin Borggrefe, and Günter Breithardt
 ISBN: 978-1-405-17572-2

However, novel ablation strategies such as PV isolation are mostly based on anatomic considerations. Therefore, understanding the complex morphological characteristics of LA anatomy is an essential prerequisite for safe, efficient, and successful AF ablation.

Correct understanding of LA anatomy is mandatory to prevent inadvertent radio-frequency ablation (RFC) ablation. Various techniques can be used to visualize each patient's individual LA anatomy. These include computer tomography (CT), magnetic resonance imaging (MRI), intracardiac echo (ICE), electro-anatomic mapping using either the Carto™ system (Biosense Webster, Diamond Bar, CA) or the creation of an LA model using the NavX™ system (St. Jude Medical, St. Paul, MN).

Multidetector CT (MDCT) scan is noninvasive and offers detailed 3D information of the LA. These characteristics make this modality ideal for assessing PV size and anatomic variations prior to ablation. However, MDCT scan is associated with a significant radiation exposure that is lacking when MRI is used. Both noninvasive imaging techniques can display the LA and PVs and provide valuable information prior to AF ablation [11, 12]. Ultimately, both techniques can be used for image integration with 3D mapping systems (Carto, NavX) allowing direct catheter manipulation and ablation within the LA anatomy. First reports indicate feasibility, safety, and sufficient accuracy for an anatomic-guided AF ablation using this technique [13–16].

AF Mapping and Ablation Strategies

Segmental PV Isolation

Segmental ostial isolation of the PV requires two catheters in the left atrium, one of which is usually a decapolar Lasso catheter placed at the PV–LA junction [3, 4]. The procedure is most frequently used in sinus rhythm (SR) or atrial pacing, but is also feasible during AF.

PV potentials are characterized as sharp bipolar signals on the Lasso catheter. Optimal ablation targets are identified by the earliest bipolar or sharpest and steepest unipolar electrogram in the mapping catheter. Because muscular fascicles often course circumferentially around the PVs, a single RFC application may eliminate PV potentials at several poles on the Lasso catheter. The endpoint is a complete entrance and exit block in and out of the PV. Obviously, this approach is associated with the potential risk of PV stenosis, especially if RFC energy is deployed at more distal PV portions [17]. Further on, there is growing evidence that the so-called "left atrial antrum" plays an important role in the genesis of AF and should not be excluded from the ablation process [18].

Circumferential PV Ablation

The circumferential PV ablation technique has been proposed by Pappone et al. [5]. Using a single transseptal puncture, a 3D electroantomical LA reconstruction (CARTO) is performed. Wide circular linear lesions around each ipsilateral PV ostium are deployed to modify the substrate for AF and to delay LA-PV conduction. PVs are marked as virtual "tubes" using a special Carto function despite the limitation that true PV anatomy may differ. RFC lesions (initially: solid 8-mm tip, power: up to 100 W, temperature: 65°C) are deployed to achieve the procedural endpoint of $\geq$80% local signal amplitude reduction or $\leq$1m V and a conduction delay over the ablation line. Recently, the additional deployment of linear lesions was suggested to reduce iatrogenic left atrial macroreentry tachycardias [19].

Complex Fractionated Atrial Electrograms (CFAE)

This AF mapping and ablation approach differs substantially from approaches aiming for PV isolation. This approach is based on the hypothesis that atrial regions showing very fractionated, low-voltage electrical activity during AF represent preferred areas of slow conduction and pivotal points of reentrant wavelets [9]. It is suggested that these areas represent critical regions for the persistence of microreentries, and therefore ablation should result in elimination of AF.

Another hypothesis is that rotors, drivers, or generators of AF, which are characterized by fractionated potentials, can be abolished by RFC ablation resulting in termination of AF. Interestingly, it was suggested that regions displaying complex fractionated potentials may be anatomically related to autonomic ganglionated plexi [20].

Nademanee et al. [9] used the 3D reconstruction system Carto for an anatomic LA reconstruction.

In our experience, most commonly regions of fractionated potentials can be identified at the base of the left atrial appendage, anterior mitral annulus, PV ostia, LA sites adjacent to the coronary sinus (CS), inside the CS, and the CS ostium. The endpoint of this ablation procedure is AF termination or noninduciblity of AF [9, 21, 22]. However, a recent analysis of CFAE ablation in chronic AF patients could not demonstrate a prognostic relevance in terms of AF recurrence if AF termination was achieved [23]. The ultimate role of CFAE mapping and ablation in AF needs to be determined.

Double Lasso Technique for Circumferential PV Isolation

This procedure has been recently established in our center [6] and is routinely performed under sedation with continuous infusion of propofol. Prior to the procedure a TEE is performed in all patients to rule out LA thrombi. Anticoagulation treatment with warfarin is stopped 3 days before admission and replaced by intravenous heparin to maintain a partial thromboplastin time at two to three times higher than the control value in all patients.

Transseptal Puncture

Three 8F SL1 sheaths (St. Jude Medical, Inc., Minnetonka, MN) are advanced to the LA by a modified Brockenbrough technique: two sheaths over one dilated puncture site and the third sheath via a second puncture site. For this sheath, the inferoposterior site of the foramen ovale is punctured to better reach the right inferior PV After transseptal catheterization, intravenous heparin is administered to maintain an activated clotting time of 250–300 sec. Additionally, continuous infusions of heparinized saline are connected to the transseptal sheaths (flow rate of 10 mL/hr) to avoid thrombus formation or air embolism.

LA Reconstruction

Left atrial 3D electroanatomical mapping is performed with a 3.5-mm-tip catheter (ThermoCool Navi-Star^{TM}, Biosense Webster, Diamond Bar, CA) during coronary sinus pacing, sinus rhythm (SR), or AF by using the Carto system. Most importantly, mapping is only performed in the LA. All mapping points deep within the PV are deleted to ensure that the posterior wall is flat in the right lateral and left lateral views, respectively.

Identification of PV Ostia Using Selective PV Venographies

After LA reconstruction, ipsilateral PV ostia are identified by selective venographies (RAO 30°, LAO 40° projections) (Figure 21.1) and carefully tagged on the electroanatomic map (Figure 21.2). This represents the crucial step then allowing the design of the circumferential ablation lines. Misunderstanding of PV ostia may lead to difficulties or even inability to achieve PV isolation and increases the potential risk for PV stenosis. For example, the isolation of the left-sided PVs in the setting of a narrow ridge [11] between the left atrial appendage and the left PVs can be very challenging if the anterior edge of the left PV ostium has been inappropriately marked in the left atrial appendage (Figure 21.3). On the other side, severe PV stenosis can be produced if the PV ostium is tagged inside the PVs [24].

Double Lasso Technique

Two decapolar Lasso catheters (Biosense-Webster, Diamond Bar, CA) are placed within the ipsilateral superior and inferior PVs or within the superior and inferior branches of a common PV before radiofrequency delivery in the majority of patients with AF (Figure 21.1).

Both Lasso catheters within the ipsilateral PVs should be in a stable position to ensure reliable signals during the procedure. If the Lasso catheter is placed too distally, the PV potential could be too small or unrecordable, especially in patients with fibrosed atria in long standing AF. The double Lasso technique markedly facilitates the whole mapping and ablation process twofold: (i) constant fluoroscopic PV marking and (ii) simultaneous electrical PV recordings displayed on both Lassos (Figure 21.2) contribute to shorter fluoroscopy and procedure times.

Electrical Isolation of Ipsilateral PVs

Irrigated RF energy is delivered with a target temperature of 43°C, a maximal power limit of 40 W, and an infusion rate of 17 mL/min. In all patients, maximal power of 30 W is allowed at the posterior wall to reduce the potential risk of LA-esophageal fistula. RF ablation sites are tagged on the

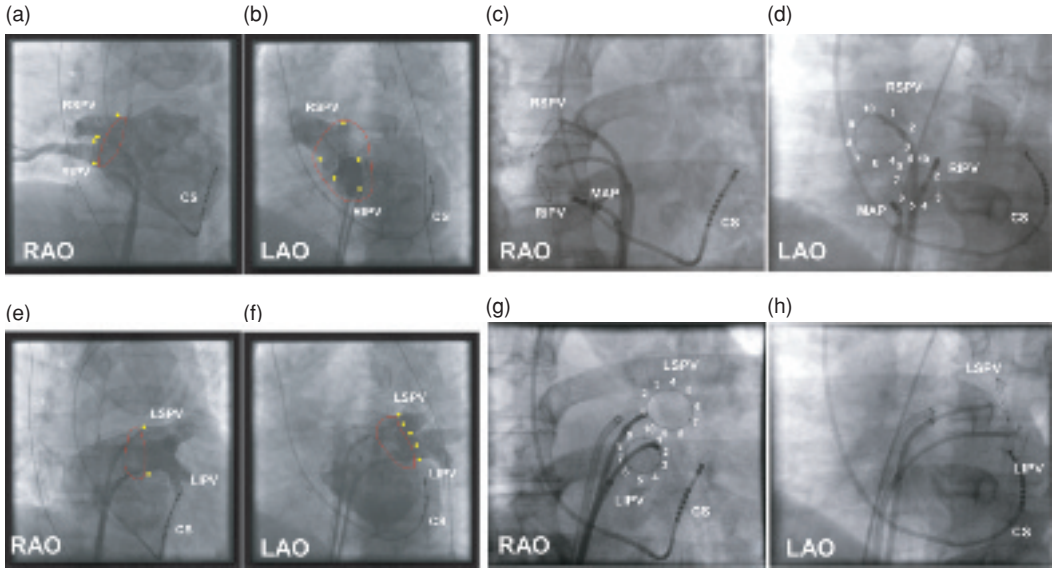

Figure 21.1 Parts (a)–(d): Fluoroscopic right and left anterior oblique views (RAO 30° and LAO 30° of the left atrium and the right-sided pulmonary veins (PV). PV ostia are marked by yellow points. The red line indicates the proposed ablation line around the right-sided PVs. Two Lasso catheters are positioned within the right-sided PVs, the mapping catheter (map) in left atrium and a catheter inside the coronary sinus (CS). Numbers indicate Lasso electrodes positions (d). KEY: RAO = right oblique view; LAO = left oblique view; CS = coronary sinus; RSPV = right superior pulmonary vein; RIPV = right inferior pulmonary vein.

Parts (e)–(h): Fluoroscopic right and left anterior oblique views (RAO 30 and LAO 30° of the left atrium and the left-sided pulmonary veins (PV). PV ostia are marked by yellow points. The red line indicates the proposed ablation line around the left sided PVs. Two Lasso catheters are positioned within the left-sided PVs, a catheter is inside the coronary sinus (CS). KEY: Numbers indicate Lasso electrodes positions (G). RAO = right oblique view; LAO = left oblique view; CS = coronary sinus; LSPV = left superior pulmonary vein; LIPV = left inferior pulmonary vein.

reconstructed 3D LA. RF energy is applied for up to 30 sec until the maximal local electrogram amplitude decreases to <70% or double potentials appear, and the sequence of PV activation recorded from the double Lasso catheters changes. RF ablation is performed in the posterior wall more than 1 cm and in the anterior wall ≈5 mm from the angiographically defined PV ostia.

Procedure Endpoint

The majority of the right PVs can be electrically isolated after anatomical completion of continuous circumferential lesions (CCLs) alone; however, a significant percentage of left PVs still conduct after the completion of CCLs even if performed by highly experienced operators. The remaining conduction gaps can then easily be identified using the 3D map and the activation sequence displayed on the two Lasso catheter within the ipsilateral PVs.

Additional RFC applications closing remaining conduction gaps between LA and PV are delivered according to the activation sequence of both Lasso catheters (Figure 21.2). In patients with paroxysmal or persistent AF, the ablation endpoint of CCLs is defined as the absence of all PV spikes during SR documented with both Lasso catheters within the ipsilateral PVs at least 30 min after PV isolation. Complete electrical PV isolation has been associated with high success rates [25, 26]. Termination of AF is not defined as an endpoint in our procedure. Electrical cardioversion is performed after complete isolation of the bilateral PVs in case of AF persistence.

Electrophysiological Findings of Double Lasso Catheters During CCLs

The double Lasso technique provides better information of LA-PV conduction and interesting

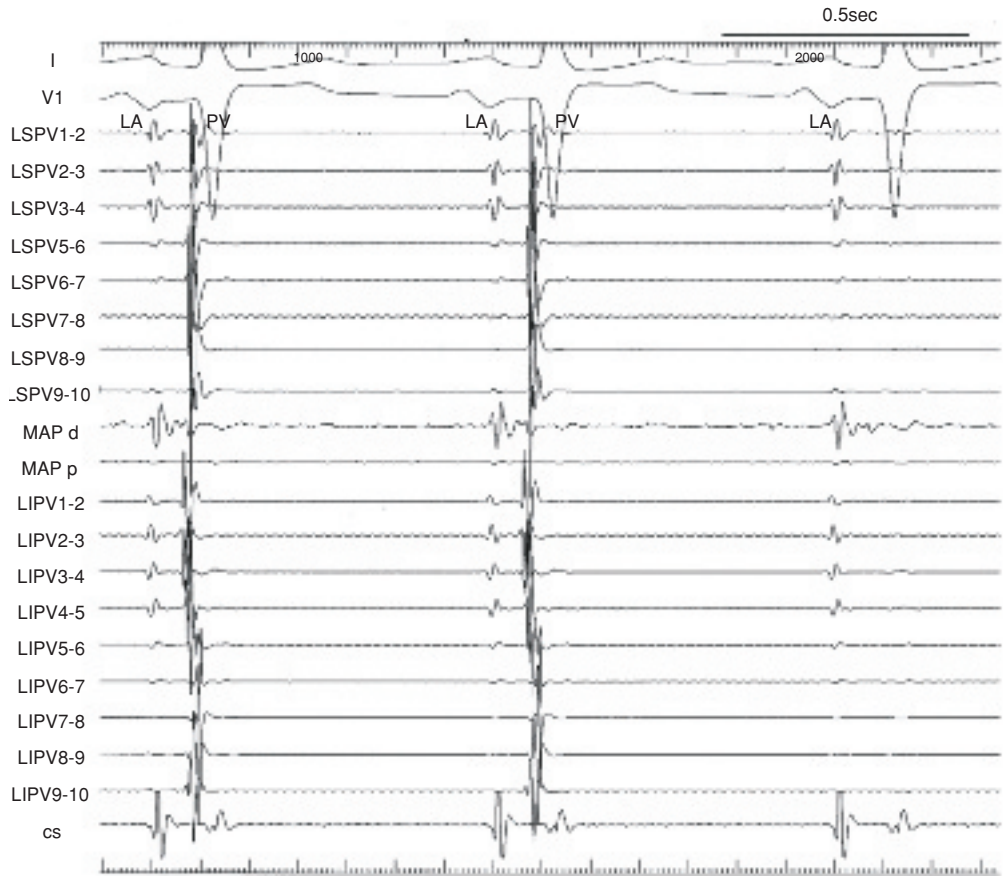

Figure 21.2 Tracings during sinus rhythm (ECG leads I, V1). Intracardiac electrograms recorded from two Lasso catheters within the left superior and inferior pulmonary veins (LSPV, LIPV), a mapping catheter (map), and a catheter inside the coronary sinus (CS) during RFC application in a patient with paroxysmal AF. Note a simultaneous isolation of both LSPV and LIPV when the right continuous circular lesions are complete. KEY: LA = left atrium; PV = pulmonary vein; RFC = radiofrequency current.

electrophysiological findings about PV activation. This technique is also helpful for the complete PV isolation by CCLs. The comprehension of the electrophysiological findings recorded by the Lasso catheter is critical for electrophysiological PV isolation.

Complete PV Isolation by CCLs

Our studies have demonstrated that CCLs can be performed during SR or CS pacing or during AF. During SR or CS pacing, CCLs resulted in progressive prolongation and sequence change of PV activation recorded from two Lasso catheters within ipsilateral PVs. Isolation of ipsilateral PVs is achieved without amplitude reduction of the PV spike (Figure 21.2). We immediately stop the RF application to avoid the potential risk of PV stenosis in case of catheter dislodgement into the PV. Moreover, according to our previous experiences before using the double Lasso technique, ablation at more distal PV sites may lead to the attenuation of PV signals or partial PV isolation which both complicate the analysis of PV activation sequence and gap identification.

During CCL deployment in AF, the initially disorganized PV activation within the PVs becomes progressively organized and shows cycle length prolongation until finally both ipsilateral PVs are simultaneously isolated. The fibrillatory cycle lengths recorded from the CS was also longer after ablation

(a)

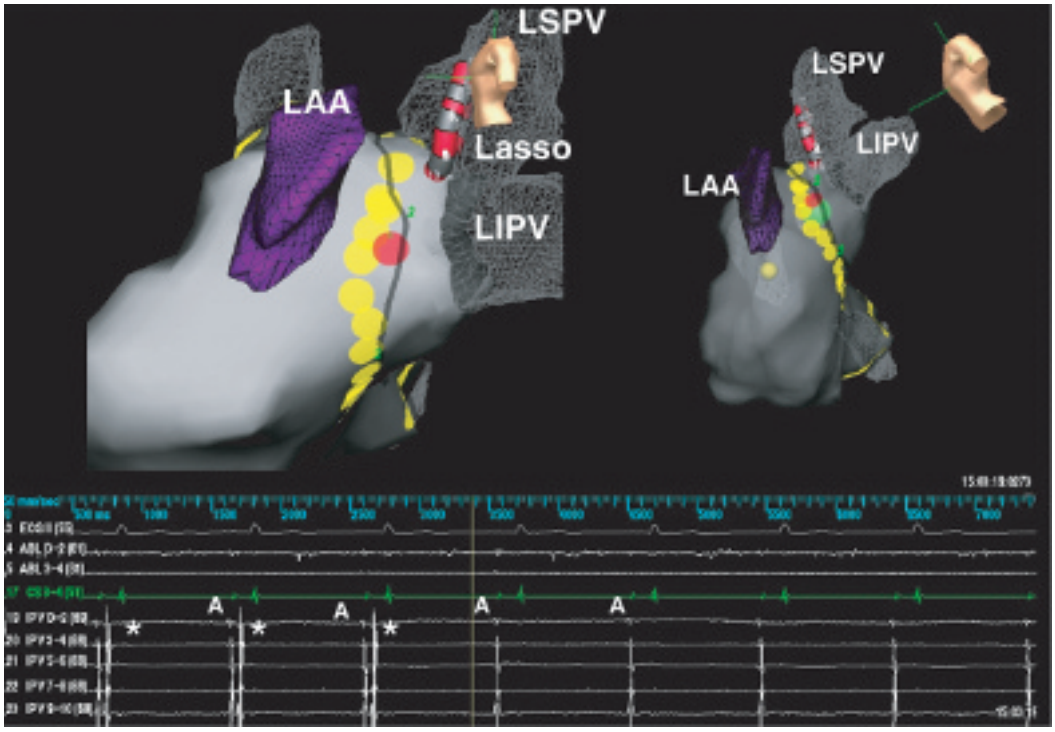
LSPV
LAA
Lasso
LIPV
LSPV
LIPV
LAA
A
A
A
A

(b)

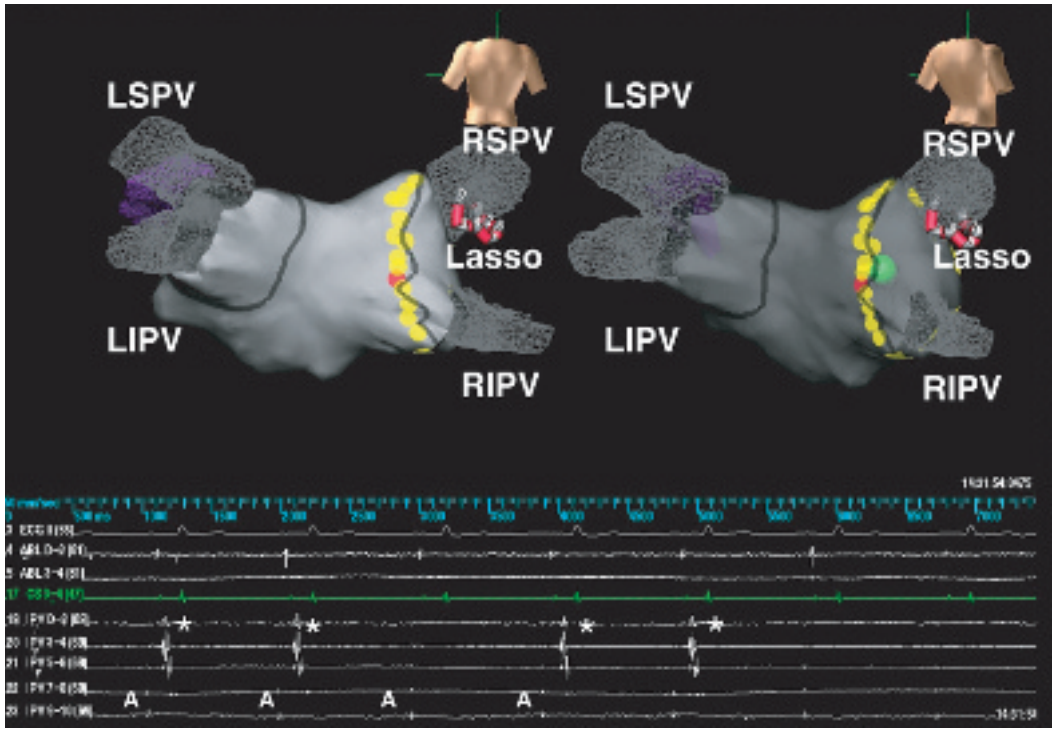
LSPV
RSPV
Lasso
LIPV
RIPV
LSPV
RSPV
Lasso
LIPV
RIPV
A
A
A
A

than that before ablation in patients without termination of AF. The ipsilateral PV spikes disappeared simultaneously in the majority of patients at completion of the respective CCL. This important finding provides the scientific evidence that complete PV isolation by CCL can be confirmed in the setting of clinical practice by using a single Lasso catheter in one of the ipsilateral PVs.

Automatic Activity and Tachycardia in PVs

After complete isolation of the PVs, regular or irregular automatic activity within the PVs dissociated from the atrial activity was observed in ≈95% patients. Also, induced or spontaneous sustained fast PV tachyarrhythmias were observed within the isolated PV after complete isolation of PV in ≈45% patients. The high incidence of automatic activity and fast PV tachyarrhythmias within the PVs may be due to a greater portion of myocardium within the isolated area compared to previous studies using segmental PV isolation.

AF Termination During CCLs

In a recent study [27], 51 patients with paroxysmal AF underwent complete PV isolation during AF. After complete PV isolation, external cardioversion (CV) was required to terminate AF only in 5 patients (9.8%); in the remaining 46 patients (90.2%), AF termination occurred before or immediate after complete PV isolation. Importantly, a single PV as AF origin was demonstrated in 5 patients (9.8%), in whom sustained PV fibrillation or tachycardia was always observed within the PV before isolation during AF and after isolation during SR.

However, in patients with persistent AF lasting more than 7 days and less than one year, AF termination only occurred in 30% of cases [28]. Also, in the majority of cases, AF termination occurred before isolation of the bilateral PVs. AF termination in patients with paroxysmal or persistent AF may be explained by the fact that CCLs eliminate a number of random reentries and consequently result in inability of AF perpetuation. Based on this observation, AF termination should not be the endpoint for catheter ablation, because AF terminated before complete isolation in most cases.

Electrical cardioversion is performed after complete isolation of the bilateral PVs in case of AF persistence. Interestingly, in some patients the PVs still conducted with marked conduction delay immediately during SR after cardioversion. Conduction through CCLs between LA and PV may be cycle length dependent, therefore complete PV isolation should be confirmed during SR.

Future Perspectives in AF Mapping and Ablation

Magnetic Navigation

The magnetic navigation system Niobe (Stereotaxis, St. Louis, MO) enables the operator to perform safe remote-controlled catheter ablation in supraventricular and ventricular tachycardias [29–32]. Two permanent magnets positioned next to the patient's table create a steerable permanent magnetic field. The soft mapping and ablation catheter has to align parallel to the resulting magnetic vector. In conjunction with a motor drive unit, true remote controlled catheter ablation from the control room can be performed, which obviously reduces the operator's radiation exposure significantly. In addition, the system can memorize all once-applied magnetic

Figure 21.3 (a) (Modified left lateral view) Successful PV isolation of lateral PVs. NavX reconstruction of left atrium showing the ridge between the left atrial appendage and the lateral pulmonary veins. Yellow dots indicate sites of RF lesions. Red dot indicates site of PV isolation at the anterior ridge. Please note elimination of PV spike from the Lasso recording. KEY: A = atrium; * = PV spike; LAA = left atrial appendage; LSPV = left superior pulmonary vein; LIPV = left inferior pulmonary vein; RF = radiofrequency.

(b) (Modified PA view): Successful PV isolation of septal PVs. NavX reconstruction of the left atrium showing circumferential RF lesions encircling the septal pulmonary veins. Yellow dots indicate sites of RF lesions. Red dot indicates site of PV isolation at the posterior roof. Please note elimination of PV spike from the Lasso recording. KEY: A = atrium; * PV = spike; LAA = left atrial appendage, RSPV = right superior pulmonary vein; RIPV = right inferior pulmonary vein.

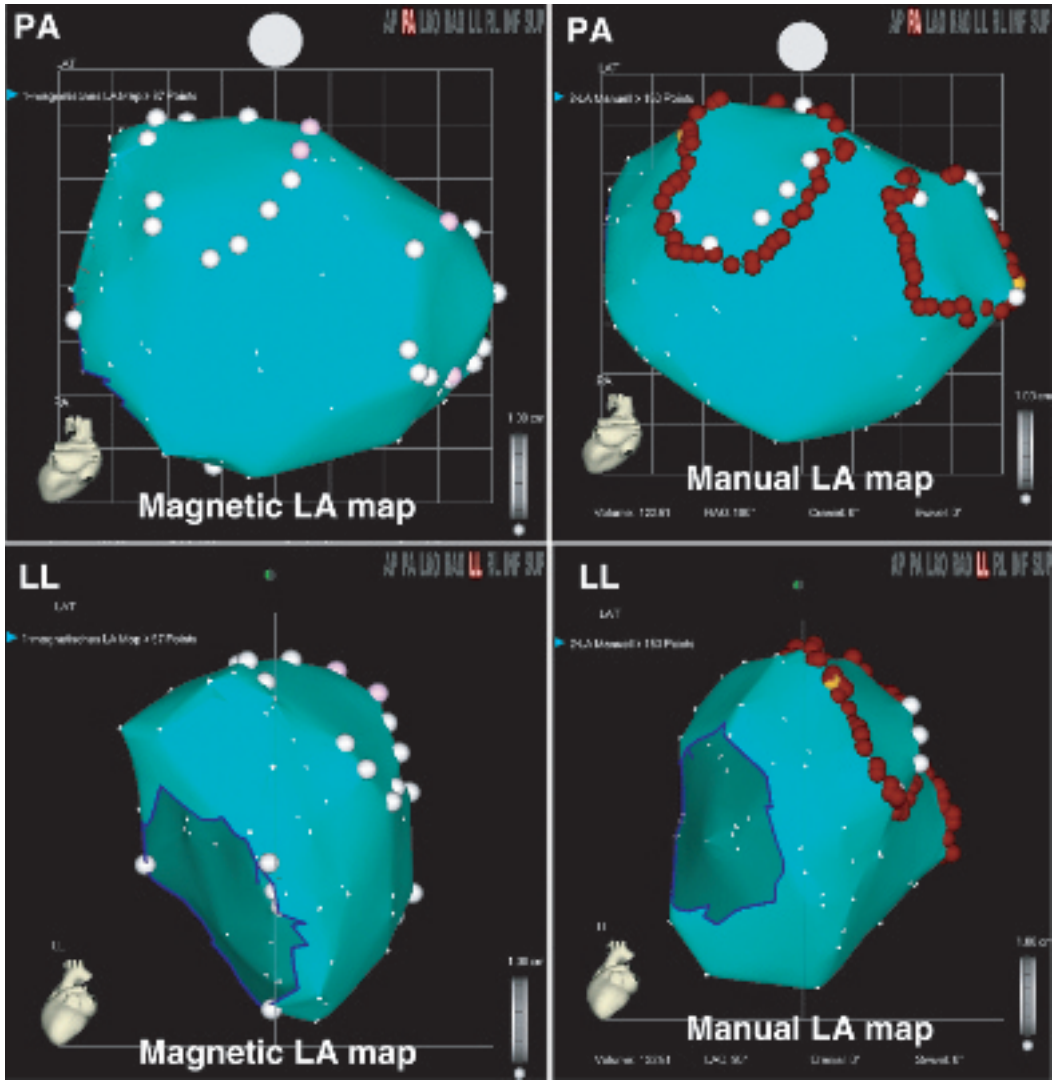

Figure 21.4 Left panel shows complete remote-controlled LA map using the magnetic navigation system Niobe II™ (Stereotaxis, St. Louis, MO) in conjunction with the Carto RMT system (Biosense Webster, Diamond Bar, CA). PV ostia have been identified and tagged in the LA map (white dots) shown in a PA and an LL view. Right panel shows subsequent manual re-LA map and tagged PV ostia (white dots) and deployment of circumferential linear lesions around each ipsilateral PVs (red dots) and sites of successful PV isolation (yellow dots) shown in a PA and LL view. Key: LA = left atrium; PV = pulmonary vein; PA = postero-anterior; LL = left lateral.

vectors facilitating the mapping and ablation process.

Recently, this technology has allowed the additional use of a 3D electroanatomic reconstruction system (Carto, Biosense Webster, Diamond Bar, CA) to perform LA reconstruction as a prerequisite for subsequent PV isolation (Figure 21.4). Interestingly, this platform technology allows the fusion and simultaneous visualization of fluoroscopic and electroanatomic information improving the operators anatomic orientation. However, only solid-tip catheters (4-mm, 8-mm) have been available so far, which excludes from our perspective extensive left atrial RF energy application. The release of the novel magnetic 3.5-mm open irrigated tip catheter may overcome this limitation.

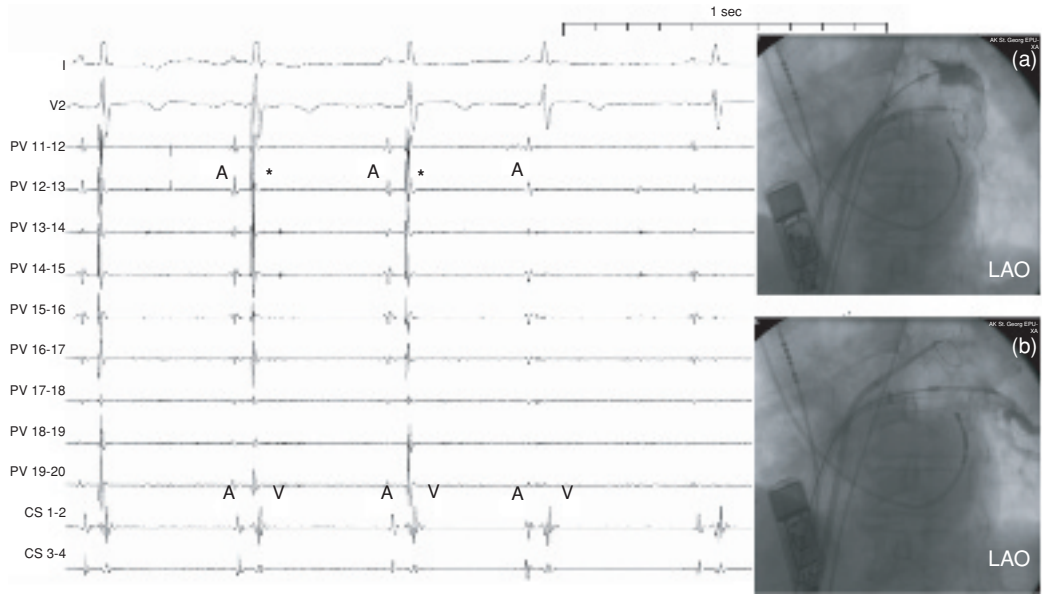

Figure 21.5 Cross-talk phenomenon: After freezing the LSPV with the 28-mm cryoballoon (a) switch of the cryoballoon position to the LIPV and the Lasso to the LSPV (b). Intracardial electrograms show successful LSPV isolation documented by loss of PV spike (*) displayed on the Lasso catheter placed inside the LSPV while freezing at the LIPV. Key: LSPV = left superior pulmonary vein; LIPV = left inferior pulmonary vein; A = atrium; * = PV spike.

Balloon-Based PV Isolation

Sequential point-to-point burning with radiofrequency current makes catheter ablation a technically complicated procedure. This results in long learning curves and time-consuming ablation procedures, increasing the discomfort and risk for complications for both the patient and the physician. This technical complexity is also one explanation of nonreproducibility of published clinical success rates in non-high volume centers.

In contrast, balloon-based catheters represent an emerging novel technology that may facilitate PV isolation. Different balloon-based energy sources are currently under investigation such as the endoscopic laser system (CardioFocus™, Marlborough, MA), the high-frequency-focused ultrasound system (ProRhythm™, Ronkonkoma, NY), or the cryothermal energy system (Cryocath™, Montreal, Canada). All balloon systems share right phrenic nerve palsy as the most common complication when applying energy at the right superior PV [33].

Recently, the so-called "single big balloon technique," using cryothermal energy, has been established for acute PV isolation [34]. This "single big balloon" technique uses only the largest available balloon (28 mm) and requires two transseptal punctures, one for the 12 Fr cryoballoon catheter, and one for the Lasso catheter to record PV potentials before and after each cryo application. The big balloon is utilized to obtain proximal antrum isolation and to avoid the right phrenic nerve. Notably, it is important to be proximal and not distal inside the PV to avoid phrenic nerve damage. Otherwise, cryothermal energy has been shown to be safe, and there are no significant complications, such as PV stenosis or damage to the esophagus. PV occlusion reflecting balloon-to-tissue contact is assessed by contrast venous angiograms via the lumen of the balloon catheter. If the contrast medium remained within the PV, electrical isolation can be achieved with a single freeze (Figure 21.5). However, long-term persistence of cryothermal induced lesions remain to be evaluated.

References

1 Fuster V, Ryden LE, Cannom DS, et al; American College of Cardiology/American Heart Association Task Force on Practice Guidelines; European Society of Cardiology Committee for Practice Guidelines; European

Heart Rhythm Association; Heart Rhythm Society. ACC/AHA/ESC 2006 Guidelines for the Management of Patients with Atrial Fibrillation: a report of the American College of Cardiology/American Heart Association Task Force on Practice Guidelines and the European Society of Cardiology Committee for Practice Guidelines (Writing Committee to Revise the 2001 Guidelines for the Management of Patients with Atrial Fibrillation): developed in collaboration with the European Heart Rhythm Association and the Heart Rhythm Society. *Circulation* 2006; **14**: 257–354.

2 Haïssaguerre M, Jaïs P, Shah DC, et al. Spontaneous initiation of atrial fibrillation by ectopic beats originating in the pulmonary veins. *N Engl J Med* 1998; **339**: 659–66.

3 Haïssaguerre M, Jaïs P, Shah DC, et al. Electrophysiological endpoint for catheter ablation of atrial fibrillation initiated from multiple pulmonary venous foci. *Circulation* 2000; **101**: 1409–17.

4 Oral H, Knight BP, Tada H, et al. Pulmonary vein isolation for paroxysmal and persistent atrial fibrillation. *Circulation* 2002; **105**: 1077–81.

5 Pappone C, Rosanio S, Oreto G, et al. Circumferential radiofrequency ablation of pulmonary vein ostia: a new anatomic approach for curing atrial fibrillation. *Circulation* 2000; **102**: 2619–28.

6 Ouyang F, Bänsch D, Ernst S, et al. Complete isolation of left atrium surrounding the pulmonary veins: new insights from the double Lasso technique in paroxysmal atrial fibrillation. *Circulation* 2004; **110**: 2090–96.

7 Haïssaguerre M, Sanders P, Hocini M, et al. Changes in atrial fibrillation cycle length and inducibility during catheter ablation and their relation to outcome. *Circulation* 2004; **109**: 3007–13.

8 Jaïs P, Hocini M, Sanders P, Hsu LF, et al. Long-term evaluation of atrial fibrillation ablation guided by noninducibility. *Heart Rhythm* 2006; **3**: 140–45.

9 Nademanee K, McKenzie J, Kosar E, et al. A new approach for catheter ablation of atrial fibrillation: mapping of the electrophysiologic substrate. *J Am Coll Cardiol* 2004; **43**: 2054–56.

10 Oral H, Chugh A, Good E, et al. A tailored approach to catheter ablation of paroxysmal atrial fibrillation. *Circulation* 2006; **113**: 1824–31.

11 Schmidt B, Ernst S, Ouyang F, et al. External and endoluminal analysis of left atrial anatomy and the pulmonary veins in three-dimensional reconstructions of magnetic resonance angiography: the full insight from inside. *J Cardiovasc Electrophysiol* 2006; **17**: 957–64.

12 Schwartzman D, Lacomis J, Wigginton WG. Characterization of left atrium and distal pulmonary vein morphology using multidimensional computed tomography. *J Am Coll Cardiol* 2003; **41**: 1349–57.

13 Tops LF, Bax JJ, Zeppenfeld K, Jongbloed MR, Lamb HJ, van der Wall EE, Schalij MJ. Fusion of multislice computed tomography imaging with three-dimensional electroanatomic mapping to guide radiofrequency catheter ablation procedures. *Heart Rhythm* 2005; **2**: 1076–81.

14 Dong J, Calkins H, Solomon SB, et al. Integrated electroanatomic mapping with three-dimensional computed tomographic images for real-time guided ablations. *Circulation* 2006; **113**: 186–94.

15 Malchano ZJ, Neuzil P, Cury RC, et al. Integration of cardiac CT/MR imaging with three-dimensional electroanatomical mapping to guide catheter manipulation in the left atrium: implications for catheter ablation of atrial fibrillation.J *Cardiovasc Electrophysiol* 2006; **17**: 1221–29.

16 Martinek M, Nesser HJ, Aichinger J, Boehm G, Purerfellner H. Impact of integration of multislice computed tomography imaging into three-dimensional electroanatomic mapping on clinical outcomes, safety, and efficacy using radiofrequency ablation for atrial fibrillation. *Pacing Clin Electrophysiol* 2007; **30**: 1215–23.

17 Yu WC, Hsu TL, Tai CT, et al. Acquired pulmonary vein stenosis after radiofrequency catheter ablation of paroxysmal atrial fibrillation. *J Cardiovasc Electrophysiol* 2001; **12**: 887–92.

18 Marrouche NF, Martin DO, Wazni et al. Phased-array intracardiac echocardiography monitoring during pulmonary vein isolation in patients with atrial fibrillation: impact on outcome and complications. *Circulation* 2003; **107**: 2710–16.

19 Pappone C, Manguso F, Vicedomini G, et al. Prevention of iatrogenic atrial tachycardia after ablation of atrial fibrillation: a prospective randomized study comparing circumferential pulmonary vein ablation with a modified approach. *Circulation* 2004; **110**: 3036–42.

20 Lemery R, Birnie D, Tang AS, Green M, Gollob M. Feasibility study of endocardial mapping of ganglionated plexuses during catheter ablation of atrial fibrillation. *Heart Rhythm* 2006; **3**: 387–96.

21 Haissaguerre M, Hocini M, Sanders P, et al. Catheter ablation of long-lasting persistent atrial fibrillation: clinical outcome and mechanisms of subsequent arrhythmias. *J Cardiovasc Electrophysiol* 2005; **16**: 1138–47.

22 Haissaguerre M, Sanders P, Hocini M, et al. Catheter ablation of long-lasting persistent atrial fibrillation: critical structures for termination. *J Cardiovasc Electrophysiol* 2005; **16**: 1125–37.

23 Oral H, Chugh A, Good E, et al. Radiofrequency catheter ablation of chronic atrial fibrillation guided by complex electrograms. *Circulation* 2007; **115**: 2606–12.

24 Ernst S, Ouyang F, Goya M, et al. Total pulmonary vein occlusion as a consequence of catheter ablation for atrial fibrillation mimicking primary lung disease. *J Cardiovasc Electrophysiol* 2003; **14**: 366–70.

25 Ouyang F, Antz M, Ernst S, et al. Recovered pulmonary vein conduction as a dominant factor for recurrent atrial tachyarrhythmias after complete circular isolation of the pulmonary veins: lessons from double Lasso technique. *Circulation* 2005; **111**: 127–35.

26 Chun KR, Bansch D, Ernst S, et al. Pulmonary vein conduction is the major finding in patients with atrial tachyarrhythmias after intraoperative maze ablation. *J Cardiovasc Electrophysiol* 2007; **18**: 358–63.

27 Huang H, Wang X, Chun J, et al. A single pulmonary vein as electrophysiological substrate of paroxysmal atrial fibrillation. *J Cardiovasc Electrophysiol* 2006; **17**: 1193–201.

28 Ouyang F, Ernst S, Chun J, et al. Electrophysiological findings during ablation of persistent atrial fibrillation with electroanatomic mapping and double Lasso catheter technique. *Circulation* 2005; **112**: 3038–48.

29 Ernst S, Ouyang F, Linder C, et al. Initial experience with remote catheter ablation using a novel magnetic navigation system: magnetic remote catheter ablation. *Circulation* 2004; **109**: 1472–75.

30 Chun JK, Ernst S, Matthews S, et al. Remote-controlled catheter ablation of accessory pathways: results from the magnetic laboratory. *Eur Heart J* 2007; **28**: 190–95.

31 Aryana A, d'Avila A, Heist EK, et al. Remote magnetic navigation to guide endocardial and epicardial catheter mapping of scar-related ventricular tachycardia. *Circulation*. 2007; **115**: 1191–200.

32 Pappone C, Vicedomini G, Manguso F, et al. Robotic magnetic navigation for atrial fibrillation ablation. *J Am Coll Cardiol* 2006; **47**: 1390–400.

33 Antz M, Chun KR, Ouyang F, Kuck KH. Ablation of atrial fibrillation in humans using a balloon-based ablation system: identification of the site of phrenic nerve damage using pacing maneuvers and CARTO. *J Cardiovasc Electrophysiol* 2006; **17**: 1242–45.

34 Chun J, Antz M, Ouyang F, et al. The "single-big-cryoballoon" technique for pulmonary vein isolation: a new ice age? *Circulation* 2007; **116**: II–726 Abstract.

22

CHAPTER 22

Integration of Nonelectrophysiological Imaging Technologies into the Mapping of Atrial Fibrillation

Tamer S. Fahmy, MD, PhD,[1] *J. David Burkhardt,* MD, FACC,[2] *Andrea Natale,* MD, FACC, FHRS[3]

[1]Cairo University Hospitals, Cairo, Egypt
[2]Cleveland Clinic, Cleveland, OH, USA
[3]Stanford University, Stanford, CA, USA

Summary

Precise visualization of the left atrial (LA) anatomy during ablation of atrial fibrillation (AF) is an important determinant of the success and safety of the procedure. Many efforts in this field have focused on properly visualizing and locating important structures as the pulmonary veins and the left atrial appendage. With advances in cardiac mapping, the currently available mapping systems have markedly improved the understanding of the cardiac structures in 3D. However, the constructed cardiac chamber is susceptible to human errors; many areas that are not visited by the mapping catheter may be missed in the reconstructed chamber. Moreover, the stiffness of the mapping catheter may inadvertently result in indentations of the chamber surface during point acquisition, which, with further point editing, may undoubtedly affect the geometry of the constructed surface.

Efforts have been made to add a true image to substitute or complement the constructed map. Different imaging modalities have been used, such as computerized tomography (CT) magnetic resonance (MRI), intracardiac echo, and fluoroscopy. These resulting different images have been integrated to the primary mapping tools, namely, the 3D mapping systems and fluoroscopy. Nevertheless, the accuracy of this integration process is dependent on many factors that may limit the advantages of integration. These factors include quality of the scanned image, the time from image acquisition to registration, the rhythm during which the image has been scanned as well as technical aspects of data acquisition, segmentation, and registration.

Cardiac Mapping, Third Edition Edited by Mohammad Shenasa, Gerhard Hindricks, Martin Borggrefe, and Günter Breithardt
 ISBN: 978-1-405-17572-2

Types of Image Integration

The integration process consists of fusing two images acquired via different modalities. Both images

would have a common 3D axis, such that a mapping/ablation catheter navigating on one image would correspond to the exact same location on the other. This can be achieved by one of three ways:

1 Registering a preacquired image into a 3D mapping system.

2 Using one/two catheters in a single system to reconstruct the chamber of interest via different modalities.

3 Registering two different systems, with auto registering of the produced image.

Registering a Preacquired Image into a Mapping System

With this technique, a real 3D shell of the left atrial chamber is registered with a recreation of the same chamber generated by the operator using a 3D mapping system. One image provides the precise anatomical details of the chamber to be mapped (CT or MRI), while the other serves as an aide in mapping or navigation (3D mapping systems or fluoroscopy) (Figure 22.1).

Integrating CT/MRI with 3D Mapping Systems

Integrating CT/MRI with 3D maps constitutes the initial attempts of image integration in AF ablation [1–9]. The process of image integration follows three phases:

Image Acquisition

Images are acquired using a contrast-enhanced multislice detector CT or MRI. ECG-gated images are acquired during breath-holding for retrospective 3D reconstruction of the axial images. Raw data are then uploaded to the mapping system and segmented to extract the left atrium and the pulmonary veins semiautomatically.

Segmentation

This is the process of extracting the structure of interest in 3D from the surrounding cardiac and thoracic structures. The segmentation process is performed in three steps: first, the boundaries of the pertinent structures are delineated by setting the threshold intensity range to allow for differentiation between the blood pool (high intensity) and the endocardium (low intensity). Different thoracic structures are annotated by specific markers. The software algorithm (Image Integration Module™, Biosense Webster, Inc., Diamond Bar, CA) can then be used to depict the structure of interest in a 3D volume rendered image. If further adjustments are required, manual slicing is performed. Finally, the outer most part of the contrast, the shell, is exported into the study to perform the integration process.

Registration

This can be performed in two ways:

(i) *Landmark registration*, which consists of selecting and acquiring a well-defined point on the

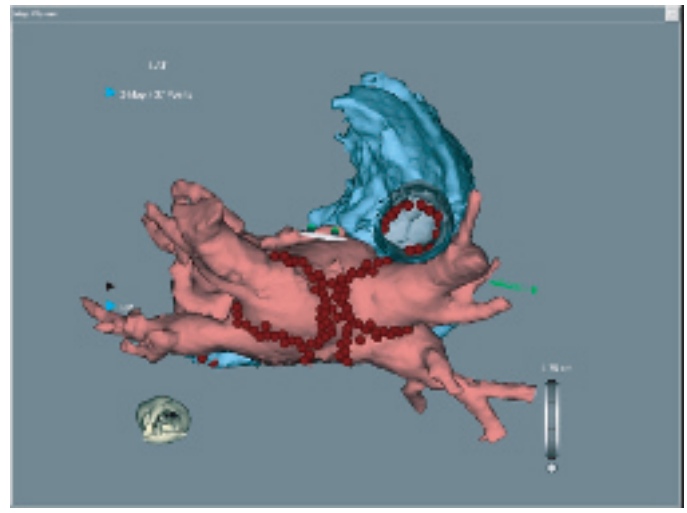

Figure 22.1 Image integration of CT with electroanatomical map in AF ablation.

electroanatomical map (EAM) and annotating its corresponding location on the CT/MR image. Three to four pairs of points (map and CT) are required to register the left atrium. A recent study has shown that the posterior points on the pulmonary vein–left atrial junction are the most appropriate landmark points to register the CT image to the EAM [10].

(ii) *Surface registration*, which consists of acquiring 30–40 surface points from different regions of the left atrial surfaces. Although points need to be well distributed, acquiring points on the anterior surface may lead to indentation and distortion of the left atrial map and may affect the registration accuracy [10].

Other methods of manual registration, including visual alignment or local registration of a certain area, have been used, but have not yet been compared in controlled studies. This also includes the rendering of an electroanatomic map on a remote magnetic navigation workstation.

Integrating CT/MR with Fluoroscopy

Similar to CT/MR integration with 3D maps, image acquisition and segmentation follow the same techniques, although segmentation is performed on a separate workstation [11, 12].

Registration

Registration follows a different approach where predetermined fluoroscopic projections are acquired, and the CT/MR image is automatically registered on a workstation platform using custom software. In a study performed to register 3D CT with fluoroscopy projections, the coronary sinus and the superior vena cava (with a catheter inserted via the superior approach) were taken as landmark locations for registration. Despite automated registration, manual readjustments were required in almost half of the cases [12]. This is expected when registering a 3D modality image with a projection images in 2D. In another study, MRI was successfully integrated with angiographic images [13]. However, in the latter study tracking the mapping catheter was not possible in real time.

Evaluation of Accuracy of the Integration Process

Studies have used different methods to evaluate the accuracy of image integration. Postmortem evaluation studies have always been the gold standard. Two previous studies reported that ablation points were located 2 mm away from targets they marked [5, 14]. On the other hand, the only real-time in vivo study using intracardiac echo has found that despite a registration error of 2.1 mm, surface registration misaligns the image with the pulmonary vein ostia with an error reaching up to 1.5 cm [10].

Importantly, the accuracy of alignment should not be evaluated numerically only. This is because when the surface registration "best fit for the maximum number of points" is applied, despite satisfactory map-to-shell distance (2.1 mm), the acquired points may not attach to their corresponding surface or their accurate location on the corresponding surface. Assessing the accuracy of integration with fluoroscopy is, on the other hand, only based on visual (qualitative) rather than quantitative assessment. This can be guided by angiography of one of the pulmonary veins or other structures, such as the coronary sinus, to check the alignment together with the primary registration landmark.

General Pitfalls for Static Image Integration

Registering two static images together may be affected by several factors that may influence the accuracy of the registration:

The image is usually acquired hours to days prior to the study. The patient volume status, cardiac rhythm, and rate may affect the left atrial size of both images.

When acquiring an image during AF, several studies have shown that 45–50% of the cycle length would be a good target to reconstruct the image while during sinus rhythm, the CT image is usually reconstructed at 70–80% of the cycle length [9, 11, 13]. However a recent study did not show a significant difference in the atrial size when images are acquired during sinus rhythm versus AF [9].

Respiration may have a significant effect on the matching of both images. Whereas the CT/MRI images are acquired during end-inspiratory breath-holding, the EAM points are acquired during end-expiration. This may have a significant effect on the left atrial size as it relates to venous return, as well as the pulmonary vein location which is subject to the splaying effect during respiration [15]. Perhaps

acquiring CT scans during the resting expiratory phase would eliminate this problem.

Pitfalls Related to Image Integration with Cardiac Maps

Both landmark and surface registration techniques have pitfalls that influence its accuracy. Whereas landmark points anchor the CT image at specific points, they may not align the whole left atrium accurately. On the other hand, because of the surface indentation during point acquisition and potentially missed areas during mapping, the constructed left atrium may not represent the exact anatomy of the left atrium. Hence, although the surface-to-surface alignment may be better with surface registration, due to the globular nature of the acquired left atrial map, surface fitting of the integrated image is not synonymous and does not guarantee the correct alignment of the pulmonary vein ostia [10] (Figure 22.2).

Pitfalls Related to Integration with Fluoroscopy

Unless the fluoroscopic projections are ECG-gated, acquiring the exact phase to fuse with the CT/MR will be subject to human error, even if the cine frames are reviewed and the frame showing maximum displacement of the coronary sinus is taken.

Using the coronary sinus as a landmark may not be optimal as the coronary sinus is a very dynamic structure and its location may vary significantly from mid- to end-diastole. This can be a potential source of misalignment. Moreover, in many cases, the coronary sinus may be difficult to segment from the CT due to incomplete contrast filling, and increasing the filling threshold may overfill the left atrium, and affect its size during segmentation.

Integration of Imaging into Mapping Systems to Facilitate Image Registration

Integrating ICE with Electroanatomical Mapping

Being an accurate real-time imaging modality, intracardiac echo (ICE) is an invaluable imaging tool during ablation procedures. The usefulness of ICE during procedures has been previously discussed, including facilitating trans-septal punctures, direct real-time visualization of the pulmonary ostia, and other important structures such as the appendage, ensuring accuracy of tissue contact, and direct visualization of complications during the procedure, such as pericardial effusion [16–24]. Moreover, two different forms of 3D ICE are currently under trial for use in electrophysiologic procedures; real-time volumetric echo, and 3D reconstructed images from 2D acquired images. Recently, 3D reconstruction of cardiac structures followed by integration with the 3D maps has been attempted.

This is achieved with an 8–10 Fr 64-phased-array 3D ultrasound catheter. The catheter has a location sensor (providing location information to the mapping system) and an ultrasound transducer (acquiring real-time ultrasound images) embedded in the tip. This 3D ultrasound catheter, when connected to the mapping system, provides real-time integration of ultrasound images with electroanatomically acquired maps.

Technique of 3D Data Acquisition

- The ICE catheter is introduced to the right atrium before the trans-septal puncture is performed.
- The wedge-shaped plane through the left atrium appears on the mapping system.
- The borders of the structure are marked according to the echo density. The edge delineation may be automatically or manually performed.
- In the usual manner, the ICE catheter is rotated in a clockwise direction to scan a different plane until the whole left atrium has been constructed. Slight posterior tilt would be required to visualize the right pulmonary veins. In each plane, the same procedure of border delineation is being performed, and is added to the previous set.
- Special structures as the pulmonary veins and the left atrial appendage can be marked out separately and added as separate structures to the original map.
- After completion of the whole left atrium, the electro-anatomical mapping/ablation catheter is introduced to the left atrium and further fine tuning of the map is performed.
- During the entire procedure, the mapping catheter tip appears "as an icon" on the cut plane as well as the reconstructed chamber (Figure 22.3).

(a)

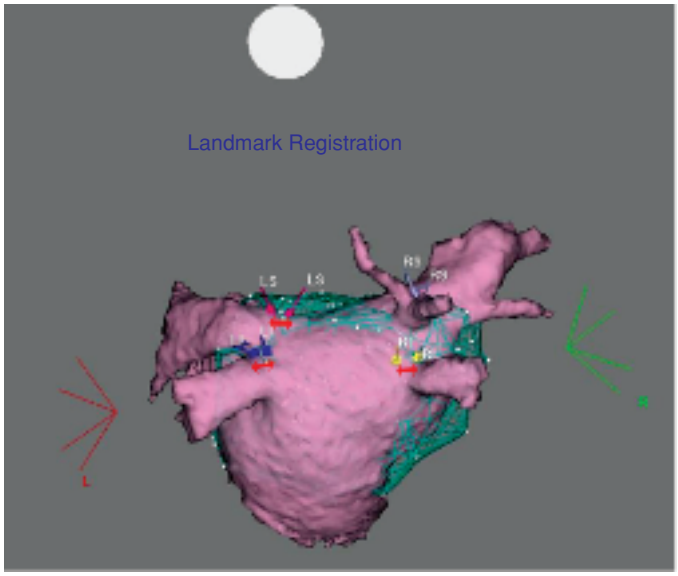

(b)

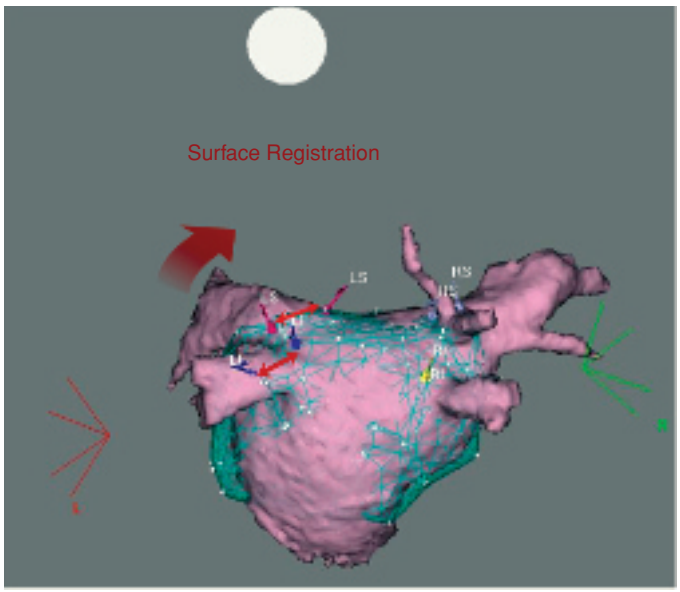

Figure 22.2 Errors of registration.

- Finally, other imaging modalities CT/MR can be integrated with the derived image in the usual manner for image registration.

Potential Advantages and Pitfalls

The major advantage of this technology is that ICE is the only real-time imaging tool that can be used during ablation procedure. Moreover, because the catheter is already equipped with a location sensor common to both, the EAM and the ICE data sets, there are no or minor errors of registration. A recent animal study has shown errors of registration using this technique to be only 1–2 mm, which was significantly better than that seen with CT image registration [25]. Even the distorted shape of the chamber created by the roving mapping catheter

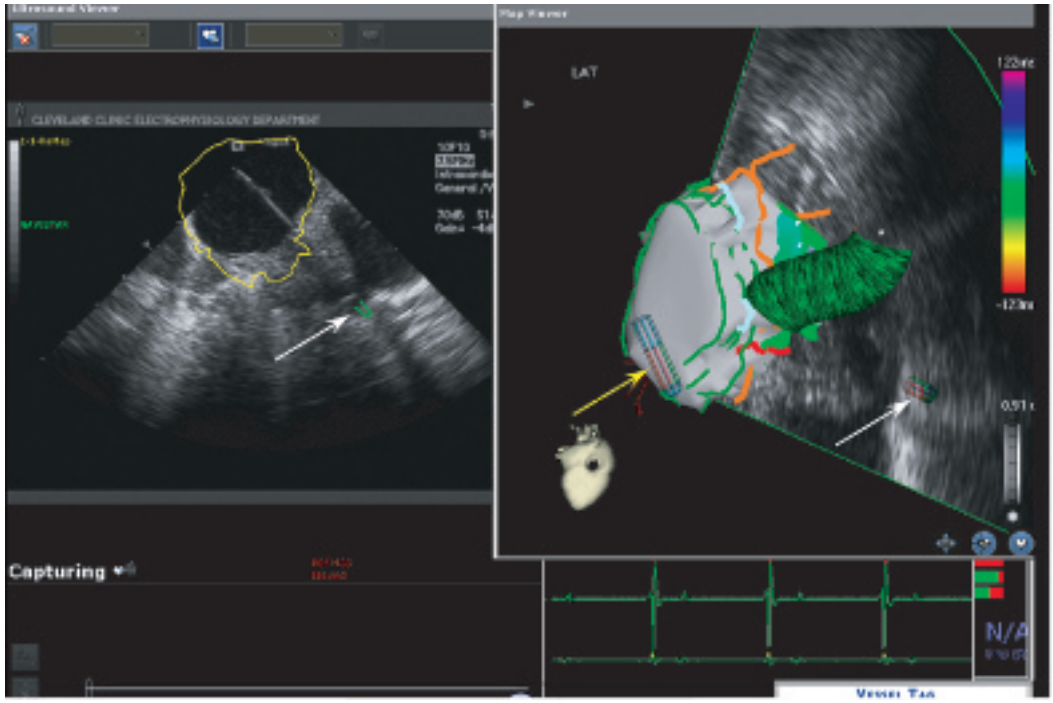

Figure 22.3 Vessel tagging technique using ICE-Carto integration.

can be obviated by using the echo volumetric shell to register the 3D CT/MRI (Figure 22.4).

However, the current technique is still tedious, time-consuming, and subject to human errors when outlining the border of the constructed chamber. Moreover, the chamber is generated by adding several thin wedge-shaped echo slices. This process may require a long time to accurately construct the left atrium. Perhaps with the continuous threshold detection and automated acquisition of data, the

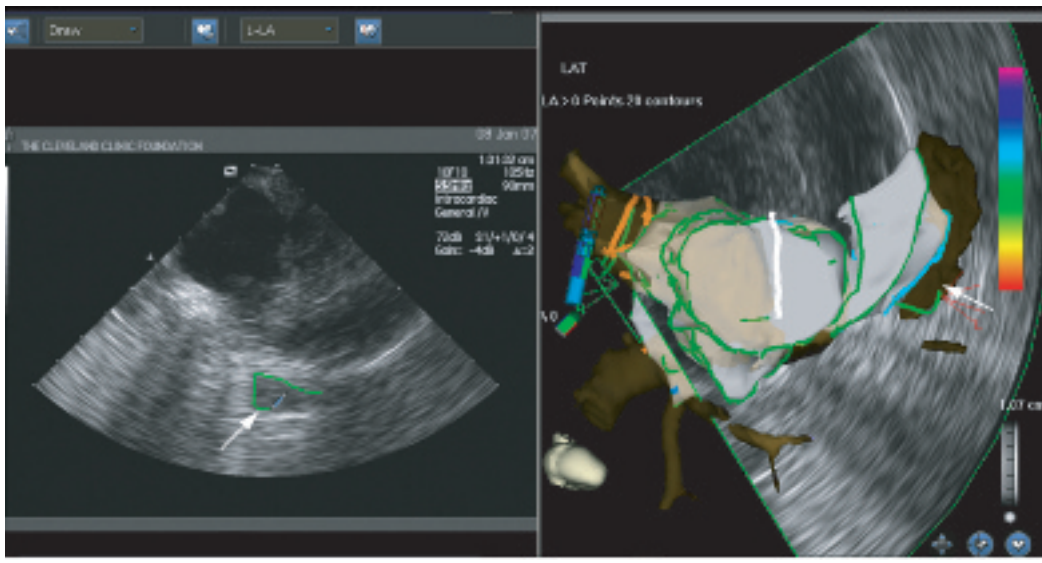

Figure 22.4 Reconstructing the LAA using ICE-Carto-CT integration.

time required for construction of the map can be abbreviated if the precision is not compromised. Finally, because there is no smoothing software, when the different slices are connected to each other by the custom software, gaps between acquired planes emerge, ending up in a "peaks and valleys" pattern.

Registering Two Different Systems Together

The idea of co-registering two different systems and synchronizing them together would probably obviate the need for further image registration. An image acquired or constructed by one system would automatically be registered on the other system. However, the degree of accuracy of the system registration, and the degree of freedom in manipulating the transferred images, are crucial determinants of the accuracy and benefits achieved with the integration process.

Image Integration on Remote Navigation Systems

Going one step further, the fluoroscopy projection and the EAMs were successfully integrated through this approach. At the outset, both systems are registered to each other via specific points on a common landmark location. Two different X-ray projections are acquired, preferably ECG-gated, and stored on the navigation system platform. The EAM that is later acquired is automatically transferred and viewed, yet not manipulated, on the magnetic navigation system. For this reason, it is actually synchronization and superimposition rather than true integration. Furthermore, CT/MRI image can also be integrated with the EAM/fluoro-integrated image. The latter process can be performed either directly through the system, in which case this image can be manipulated on the navigation system, or registered to the EAM on the mapping system and transferred to be viewed on the navigation system (Figure 22.5).

This technique allows points acquired and virtual lines drawn on the EAM to be sent to the fluoroscopy projections for automatic navigation of the catheter to the desired location, and vice versa.

Potential Advantage and Pitfalls

In prelaunching studies, the multiple-point registration technique for aligning the mapping system to the magnetic navigation system has shown a registration error of 0.5–1 mm, whereas image/image registration in different studies has shown a mean error ranging from 1.7 to 2.7 mm. This larger error

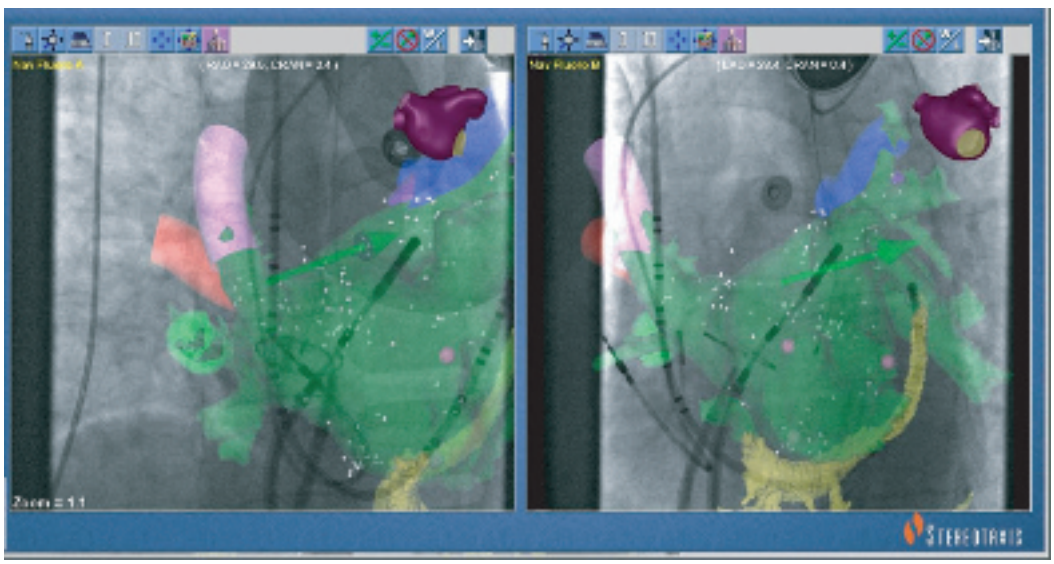

Figure 22.5 CT-CARTO integration with Fluoroscopy using Stereotaxis.

may be partially attributed to point acquisition on the EAM, which by itself may have an error of 0.8–1.2 mm. However, the bidirectional synchrony with manipulation of the EAM on the fluoroscopy is still not optimal.

Integration of 3D Fluoroscopy with EAM

Recently, fluoroangiography has been used to construct 3D images [26]. A rotational angiography of the left atrium is acquired using a monoplane fluoroscopy. This image is further reconstructed to create a 3D shell of the left atrium (Figure 22.6).

Technique of Acquisition

- A long sheath is inserted into the pulmonary trunk or the inferior vena cava.
- Around 80–100 mL of contrast is injected using an electronic injector.
- After a predetermined duration, during which the contrast circulates to reach the left atrium, the sweep maneuver starts.
- The C-arm is rotated 270° over the patient in 5 sec bidirectionally in two sweeps, during which around 200–250 projections are acquired. Images are ECG -gated and acquired during inspiratory the hold.

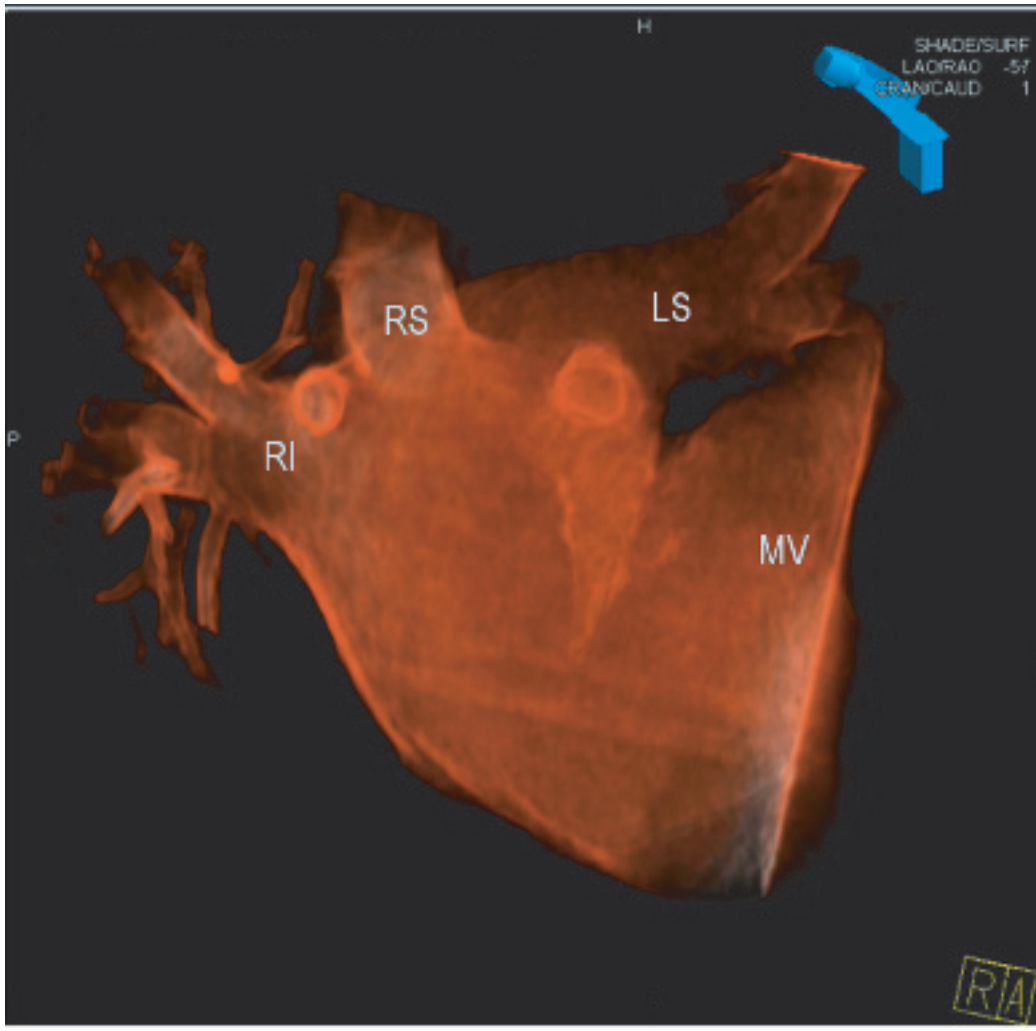

Figure 22.6 Rotational Angiography with 3D reconstruction of the LA.

- Image reconstruction is then performed on a separate workstation and a 3D image of the LA can be attained.

Potential Advantages and Pitfalls of the 3D Fluoroscopic Image

The 3D fluoroscopic image has been previously tried in operating theaters for orthopedic and vascular surgery and recently in the heart with an acceptable resolution compared to the 3D CT scans [26–29]. It is a simple and cost-effective procedure. The 3D image can be integrated with the real-time fluoroscopy, and its potential advantage may be greater if the navigating catheter can be tracked on the 3D image. The degree of transparency depends on the amount of dye injected, yet one disadvantage is that the injecting sheath artifact appears in the image.

Image Integration of 3D Fluoroscopy with EAM

Currently, trials are underway to integrate the fluoroscopy image to the EAM. Both systems can be coregistered together and after the image is acquired and reconstructed, it is automatically transferred to the 3D mapping system. Both images become superimposed with no further registration required.

Conclusion

Image integration for the ablation procedure may be a useful tool to enhance mapping and navigation, but this is highly dependent on accurate registration. Registering static images has many pitfalls that may outweigh its potential benefits. Using a single system that can display more than one real-time imaging modality is a promising technique if the time required for chamber construction is abbreviated. Finally registering two systems together does have good potentials, particularly if 3D fluoroscopy is used. In the future, the introduction of real-time interventional MRI may obviate the need for image integration.

References

1 Solomon SB, Dickfeld T, Calkins H. Real-time cardiac catheter navigation on three-dimensional CT images. *J Interv Card Electrophysiol* 2003; **8**: 27–36.

2 Dickfeld T, Calkins H, Zviman M, et al. Stereotactic magnetic resonance guidance for anatomically targeted ablations of the fossa ovalis and the left atrium. *J Interv Card Electrophysiol* 2004; **11**: 105–15.

3 Verma A, Marrouche N, Natale A. Novel method to integrate three-dimensional computed tomographic images of the left atrium with real-time electroanatomic mapping. *J Cardiovasc Electrophysiol* 2004; **15**: 968.

4 Dong J, Dickfeld T, Lamiy SZ, Calkins H. Catheter ablation of atrial fibrillation guided by registered computed tomographic image of the atrium. *Heart Rhythm* 2005; **2**: 1021–22.

5 Sra J, Krum D, Hare J, Okerlund D, et al. Feasibility and validation of registration of three-dimensional left atrial models derived from computed tomography with a noncontact cardiac mapping system. *Heart Rhythm* 2005; **2**: 55–63.

6 Tops LF, Bax JJ, Zeppenfeld K, et al. Fusion of multislice computed tomography imaging with three-dimensional electroanatomic mapping to guide radiofrequency catheter ablation procedures. *Heart Rhythm* 2005; **2**: 1076–81.

7 Dong J, Calkins H, Solomon SB, et al. Integrated electroanatomic mapping with three-dimensional computed tomographic images for real-time guided ablations. *Circulation.* 2006; **113**: 186–94.

8 Dong J, Dickfeld T, Dalal D, et al. Initial experience in the use of integrated electroanatomic mapping with three-dimensional MR/CT images to guide catheter ablation of atrial fibrillation. *J Cardiovasc Electrophysiol* 2006; **17**: 459–66.

9 Kistler PM, Earley MJ, Harris S, et al. Validation of three-dimensional cardiac image integration: use of integrated CT image into electroanatomic mapping system to perform catheter ablation of atrial fibrillation. *J Cardiovasc Electrophysiol* 2006; **17**: 341–48.

10 Fahmy TS, Mlcochova H, Wazni OM, et al. Intracardiac echo-guided image integration: optimizing strategies for registration.*J Cardiovasc Electrophysiol* 2007; **18**: 276–82.

11 Sra J, Krum D, Belanger B, Vaillant R. Registration of three-dimensional left atrial computed tomographic images with fluoroscopy. *Heart Rhythm* 2005; **2**: 1020.

12 Sra J, Krum D, Malloy A, Vass M, et al. Registration of three-dimensional left atrial computed tomographic images with projection images obtained using fluoroscopy. *Circulation.* 2005; **112**: 3763–68.

13 Ector J, De Buck S, Adams J, et al. Cardiac three-dimensional magnetic resonance imaging and fluoroscopy merging: a new approach for electroanatomic mapping to assist catheter ablation. *Circulation* 2005; **112**: 3769–76.

14 Dong J, Calkins H, Solomon SB, et al. Integrated electroanatomic mapping with three-dimensional computed

tomographic images for real-time guided ablations. *Circulation*. 2006; **113**: 186–94.

15 Noseworthy PA, Malchano ZJ, Ahmed J, Holmvang G, Ruskin JN, Reddy VY. The impact of respiration on left atrial and pulmonary venous anatomy: implications for image-guided intervention. *Heart Rhythm* 2005; **2**: 1173–78.

16 Verma A, Marrouche NF, Natale A. Pulmonary vein antrum isolation: intracardiac echocardiography-guided technique. *J Cardiovasc Electrophysiol* 2004; **15**: 1335–40.

17 Verma A, Marrouche NF, Yamada H, et al. Usefulness of intracardiac Doppler assessment of left atrial function immediately post-pulmonary vein antrum isolation to predict short-term recurrence of atrial fibrillation. *Am J Cardiol*. 2004; **94**: 951–54.

18 Szili-Torok T, Kimman GP, Theuns D, Res J, Roelandt JR, Jordaens LJ. Visualisation of intra-cardiac structures and radiofrequency lesions using intracardiac echocardiography. *Eur J Echocardiogr* 2003; **4**: 17–22.

19 Scaglione M, Caponi D, Di Donna P, et al. Typical atrial flutter ablation outcome: correlation with isthmus anatomy using intracardiac echo 3D reconstruction. *Europace* 2004; **6**: 407–17.

20 Szili-Torok T, McFadden EP, Jordaens LJ, Roelandt JR. Visualization of elusive structures using intracardiac echocardiography: insights from electrophysiology. *Cardiovasc Ultrasound* 2004; **2** :6.

21 Morton JB, Kalman JM. Intracardiac echocardiographic anatomy for the interventional electrophysiologist. *J Interv Card Electrophysiol* 2005; **13**: 11–16.

22 Rao HB, Saksena S, Mitruka R. Intra-cardiac echocardiography guided cardioversion to help interventional procedures (ICE-CHIP) study: study design and methods. *J Interv Card Electrophysiol* 2005; **13**: 31–36.

23 Shalganov TN, Paprika D, Borbas S, Temesvari A, Szili-Torok T. Preventing complicated transseptal puncture with intracardiac echocardiography: case report. *Cardiovasc Ultrasound* 2005; **3**: 5.

24 Zanchetta M, Rigatelli G, Pedon L, et al. Intracardiac echocardiography: gross anatomy and magnetic resonance correlations and validations. *Int J Cardiovasc Imaging*. 2005; **21**: 391–401.

25 Okumura Y, Johnson SB, Packer DL. Quantitative validation of real-time, three dimensional ultrasound image-based mapping and intervention. *Heart Rhythm* 2007; **4**: Abstract.

26 Al-Ahmad A, Sandner-Porkrisl D, Wigstrom, L, et al. Comparison of left atrial volume using gated cardiac fluoroscopy 3D image rendering vs. cardiac-computed tomography.*J Am Coll Cardiol* 2007; **49**: 9A Abstract.

27 Euler E, Wirth S, Linsenmaier U, Mutschler W, Pfeifer KJ, Hebecker A. [Comparative study of the quality of C-arm-based 3D imaging of the talus]. *Unfallchirurg* 2001; **104**: 839–46.

28 Deinsberger R, Regatschnig R, Ungersbock K. Intraoperative evaluation of bone decompression in anterior cervical spine surgery by three-dimensional fluoroscopy. *Eur Spine J* 2005; **14**: 671–76.

29 Gorges S, Kerrien E, Berger MO, et al. Model of a vascular C-arm for 3D augmented fluoroscopy in interventional radiology. *Med Image Comput Comput Assist Interv Int Conf Med Image Comput Comput Assist Interv* 2005; **8**: 214–22.

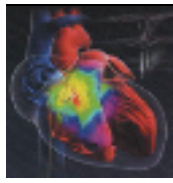

PART V

Mapping of Ventricular Tachyarrhythmias

Cardiac Mapping, Third Edition Edited by Mohammad Shenasa, Gerhard Hindricks, Martin Borggrefe, and Günter Breithardt
 ISBN: 978-1-405-17572-2

23 CHAPTER 23

Substrate Mapping for Ablation of Ventricular Tachycardia in Coronary Artery Disease

John V. Wylie, Jr., MD,[1] *Timothy W. Smith*, DPhil, MD,[2] *Mark E. Josephson*, MD[1]

[1]Harvard-Thorndike Electrophysiology Institute, Boston, MA, USA
[2]Washington University School of Medicine, St. Louis, MO, USA

Summary

Ventricular tachycardia occurs in patients with myocardial scar resulting from coronary artery disease. Endocardial catheter mapping and ablation has become an accepted therapy for patients with recurrent ventricular tachycardia. Traditional entrainment and pace-mapping techniques have limitations and may not be useful in some patients. Substrate mapping guided by intracardiac electrograms and 3-D electroanatomic mapping systems allows the identification of myocardial scar. Potential sites of reentrant circuits may be identified and targeted for linear ablation lesions. This technique has been shown to be effective in selected patients for preventing recurrent VT and ICD shocks.

Introduction

Ventricular tachycardia (VT) degenerating to ventricular fibrillation is a major cause of mortality in patients with coronary artery disease (CAD) and previous myocardial infarction (MI) [1]. Scar at the site of the healed infarction provides the substrate for reentry, the most common mechanism of VT in the setting of coronary disease.

The primary approach to patients with coronary disease thought to be at high risk for ventricular arrhythmia and sudden cardiac death has become implantable cardioverter–defibrillator (ICD) implantation. Antiarrhythmic agents are a second-line therapy, used in the management of patients with recurrent VT or who are unable to undergo ICD implantation. Neither of these approaches is curative, however. Antiarrhythmic agents may prevent or slow VT, making it more tolerable; but the efficacy is far less than 100% [2].

Side effects, including proarrhythmia and toxicity, also decrease the utility of currently available antiarrhythmic agents. ICDs can be life-saving, but programming limitations may prevent reliable identification of certain VTs, and repeated ICD shocks can be extremely traumatic for patients. Moreover, ICD implantation and therapy is not free

Cardiac Mapping, Third Edition Edited by Mohammad Shenasa, Gerhard Hindricks, Martin Borggrefe, and Günter Breithardt
 ISBN: 978-1-405-17572-2

of morbidity [3, 4]. In addition, ICDs may not prevent syncope and injury associated with ventricular arrhythmias. Many patients require additional therapy after ICD implantation to prevent multiple ICD shocks.

Surgical or catheter ablation of VT may be curative. Endocardial catheter mapping is established as the primary means of guiding ablation [5]. Conventional methods using activation and entrainment mapping require pacing and recording during relatively extended periods of VT. This requirement excludes those patients who have VT that causes hemodynamic collapse too rapidly to permit detailed mapping. This, in part, explains the relatively limited success rate of VT ablation [6, 7]. Indeed, the vast majority of patients at risk for life-threatening ventricular arrhythmias cannot undergo conventional mapping and ablation [8]. In addition, a significant number of patients are not able to have their clinical VT induced in the electrophysiology laboratory despite having a history of recurrent VT. For these patients, activation and entrainment mapping is also impossible.

The anatomical substrate of healed MI corresponds to a specific electrophysiologic substrate. This can be mapped and ablated in sinus rhythm guided by a substrate map. Three-dimensional electroanatomic systems for activation mapping and ablation provide guidance during catheter ablation therapy and are also extremely useful in substrate mapping. Application of substrate mapping and ablation during sinus rhythm allows curative therapy for many of the large proportion of VT patients who cannot undergo conventional VT mapping and ablation.

Methods of Mapping for VT

Mechanism of VT in CAD

Reentry is the most common mechanism of VT in the setting of coronary disease and healed MI [9]. Reentry requires a functional and/or anatomic circuit with a region of unidirectional block and a path of slow conduction through which the excitatory wavefront propagates, allowing the rest of the circuit to recover excitability and perpetuate reentry. Scar tissue in the region of a healed MI contains normal myocytes interspersed with connective tissue [10].

The heterogeneity of the tissue creates nonuniform anisotropy and slow conduction through the region of the scar [11, 12], The connective tissue itself and/or its production of functional block due to nonuniform anisotropy are thought to isolate an isthmus through which the wavefront passes. Most of these regions are in the subendocardium of the scar [13]. During VT, local electrical activity in this protected isthmus can be detected during diastole using a bipolar recording catheter; occasionally, electrical activity spanning all of diastole can be recorded. Curative surgical resection has been found to abolish these abnormal electrograms, strengthening the hypothesis that they are closely associated with substrate for VT [14].

Entrainment Mapping

The standard technique for mapping and ablating VT is based on localizing the protected isthmus and placing an ablation lesion to interrupt the isthmus. The method for localizing the critical site for maintenance of reentry is known as entrainment mapping [8, 15–17]. This method requires that VT must be induced by programmed electrical stimulation and be hemodynamically tolerated well enough to map the ventricle and examine of the interaction of the VT circuit with further programmed stimulation.

Candidate sites are selected on the basis of the ventricular anatomy, the VT morphology, and the presence of diastolic electrical activity. If the response to pacing at the candidate site is appropriate, the site likely represents a protected isthmus that is a necessary part of the reentrant circuit [17, 18], Creation of an ablation lesion that spans the isthmus and therefore causes conduction block in the reentrant circuit will terminate the tachycardia and render it noninducible.

Limitations of Entrainment Mapping

If a tachycardia rapidly leads to hemodynamic collapse and the need for immediate termination, entrainment mapping cannot be performed. Unfortunately, because of the hemodynamic instability of VT, the majority of patients at high risk for VT in CAD cannot readily undergo this method of mapping and ablation. Alternative methods may be used, but all have drawbacks.

One approach is administration of an antiarrhythmic agent such as procainamide to transform polymorphic VT into monomorphic VT so that it may be better tolerated [19]. Antiarrhythmic agents such as amiodarone or procainamide may also slow unstable rapid VT to a rate that is stable. Unfortunately, a drug may allow inducibility of a VT that is not inducible in the drug-free state, or it may occasionally render a VT noninducible in the EP laboratory. Another method is to induce a tachycardia repeatedly for short periods of mapping followed by termination. This technique is time-consuming and exposes the patient to multiple episodes of hemodynamically unstable VT and often multiple cardioversion shocks. An alternative is to use intraaortic balloon pump or cardiopulmonary bypass to support a patient during extended periods of VT. However, such procedures introduce additional risks and morbidity.

Pace Mapping

Pace mapping is the technique of pacing at potential ablation sites and comparing the 12-lead ECG to the ECG of the patient's clinical and/or induced VT [20, 21]. Pace mapping should not be confused with entrainment, which occurs during the tachycardia; pace mapping is performed entirely in sinus rhythm. The technique is effective for guiding ablation of idiopathic VT in normal hearts [22, 23], However, pace mapping has proven disappointing in the setting of CAD and MI. Because the scar surrounds the site of the protected isthmus that may have several dead-end pathways, pacing from many sites within the scar may produce an identical QRS morphology to the tachycardia if the wavefront's exit from the scar is the same as the tachycardia. Moreover, experience has shown that in VT associated with CAD, it is rare to find a pacing site that matches the VT identically in terms of the QRS morphology at a site of successful ablation in the isthmus [20, 24].

Noncontact Mapping

Newer noncontact mapping systems use a 64-pole multielectrode balloon catheter placed in the left ventricle to provide an activation map from a single beat of a tachycardia. The multielectrode array allows reconstruction of 3360 electrograms superimposed on a computer model of the ventricle. This system has been shown to be able to be used as a guide for mapping and ablation of VT [25, 26]. While this is technically activation mapping, only a single beat of a tachycardia is required, allowing effective mapping of a nontolerated VT. However, entrainment mapping is not able to be performed without sustained VT, and identification of critical isthmus sites may be difficult using this technology alone.

Substrate Mapping

Substrate mapping is a strategy that may be used to guide catheter ablation for VT based on findings during the baseline rhythm. Cassidy et al. found that electrograms in areas of healed MI had recognizable abnormalities that can be seen during sinus rhythm. These abnormalities were not seen in patients with normal hearts [27, 28]. They examined the abnormalities and categorized the abnormal electrograms as fractionated, late, and abnormally long (Figure 23.1). Normal left

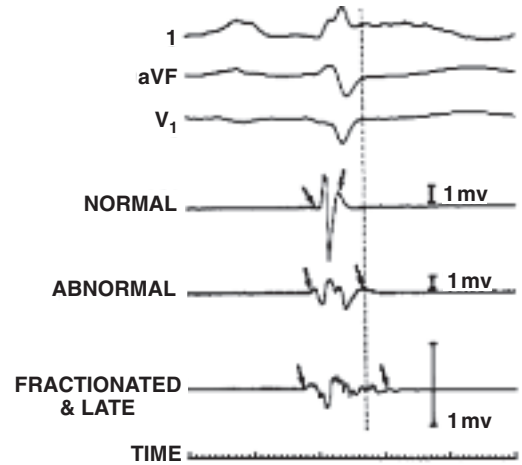

Figure 23.1 Normal and abnormal electrograms recorded in sinus rhythm. Three surface electrocardiographic recordings (leads I, aVF, and V1) and three local bipolar electrograms (normal, abnormal, and fractionated and late) recorded from different left ventricular endocardial sites are shown. The dotted vertical line denotes the end of the surface QRS activity. The arrows show the onset and offset of local electrical activity. 10 mV calibration bars are shown for each electrogram. Reproduced with permission from Ref. 27.

ventricular bipolar electrograms have amplitude greater than 3 mV, duration less than 70 msec, and amplitude/duration ratio greater than 0.045. Abnormal electrograms have been shown to be present in all patients with previous MI and VT. Most groups define areas of infarction as those with bipolar electrogram amplitude less than 1.5 mV [29, 30].

Further experience with conventional mapping has shown that the site of origin of VT is nearly always associated with an abnormal electrogram, and patients with VT have more marked abnormalities than patients with scar but no history of VT [31]. Furthermore, cardiac arrest patients with marked substrate abnormalities but not inducible VT were found to be at higher risk for clinical recurrence of ventricular arrhythmia than those who did not have abnormal substrate [32].

Finally, endocardial recordings made prior to and after subendocardial resection for the treatment of VT revealed diminution of the abnormality of the electrograms in the region of resection [14]. The authors of this study concluded that fractionated electrograms were generated by heterogeneous myocardium and connective tissue in the resected subendocardium. Work in animal models of MI has confirmed that the margin of an infarct-related scar can be identified by qualitative and quantitative differences in electrograms recorded from the scar and from surrounding normal myocardium [33]. Recent work has demonstrated that infarct heterogeneity at the border zones between dense scar and normal tissue can be seen using cardiovascular magnetic resonance imaging, and that the volume of this region is strongly correlated with inducibility of ventricular arrhythmias [34].

These data provide the basis for substrate mapping to guide ablation therapy for VT in coronary disease. Electrograms are recorded at multiple sites during sinus rhythm, and areas defined by abnormal electrograms are resected or ablated to remove the substrate. Such a procedure eliminates the need for prolonged periods of VT for mapping. Unfortunately, the specificity of substrate mapping is poor.

Cassidy et al. concluded that surgical resection based on substrate mapping was highly likely to result in an excessive amount of myocardial resection [27]. This low specificity is likely due to the fact that not all parts on a prior infarction are capable of sustaining reentry, despite the presence of abnormal electrograms. In contrast to the low specificity of substrate mapping for identifying specific sites critical to a reentrant tachycardia, the sensitivity of abnormal electrograms in substrate mapping of VT was found to be 86% by these investigators. This high sensitivity raises the possibility that catheter ablation techniques designed to isolate potential sites of origin of VT can be successful. The ablation targets are less focal than conventional mapping techniques, but rather encompass the border zone of prior infarcts. The goal of substrate ablation is creation of linear lesions to interrupt any isthmuses of myocardium that could support VT.

Practical Aspects of Substrate Mapping

Three-dimensional electroanatomic mapping systems are routinely used for substrate mapping of VT associated with CAD. The Carto™ (Biosense-Webster, Diamond Bar, CA) system uses ultralow magnetic fields to continuously localize the mapping catheter tip in 3D space. In combination with electrograms recorded by the catheter at multiple sites throughout the ventricle, the system can develop a map of the chamber using the timing, amplitude, and location of each recorded electrogram [35–37]. A resulting 3D map is produced in real time, and catheter movement within this map is tracked. The activation map is color coded to display the local activation time of the electrogram at each site relative to a consistent reference such as a surface electrocardiogram QRS complex. Activation mapping using this system has been very successful for a variety of tachyarrhythmias, but requires that a tachycardia be induced and sustained to allow mapping.

Substrate mapping can also be performed effectively using the Carto system. An electrogram amplitude map is first created in sinus rhythm in order to define areas of scar and potential isthmus sites. An electrogram map is shown in Figure 23.2a for a patient with a prior inferior MI. The electrograms of lowest amplitude (red) identify the site of infarction. The border zone of the infarction and the surrounding normal myocardium can be seen.

The Carto system is highly versatile and a large amount of information can be obtained from the maps. Figure 23.2b is an unusual map created from

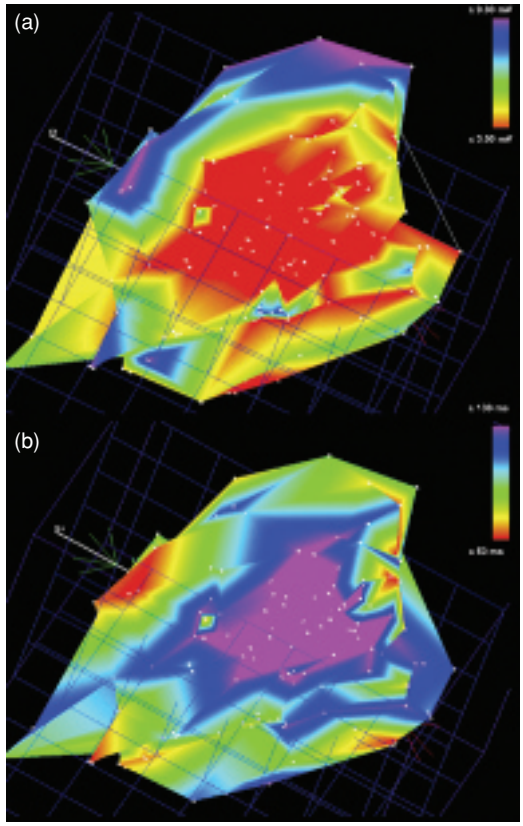

Figure 23.2 CARTO recorded in sinus rhythm from a patient with previous inferior myocardial infarction. The map is seen from the inferoposterior viewpoint. (a) Local electrogram amplitude map. Red regions represent the lowest amplitude electrograms (<3 mV) and correspond to the inferior myocardial infarction. (b) Map of duration of local electrograms in the same patient, also from the inferoposterior viewpoint. The longest electrograms were recorded in the blue and purple regions, which correspond to the area of infarction.

the same data as the map in Figure 23.2a. The map shows duration of the recorded electrograms, calculated from the local activation times of the beginning and end of the electrograms. The longer duration of the electrograms (blue and purple) correlate well to the known area of the infarct and to the low-amplitude electrograms seen in Figure 23.2a.

The definition of scar and the voltage scale of the display is an important consideration during voltage mapping. Some groups define scar as electrograms with voltage less than 0.5 mV, while others have found more accurate identification of scar and protected channels of slow conduction by defining scar as less than 0.2 mV [30, 38]. Other groups define scar as inexcitable tissue unable to be paced with the roving catheter at high output [39]. In practice, all of these methods may be used—a less-specific higher-voltage cutoff may be used to define the general area of infarcted myocardium, and then more specific lower cutoffs and high output pacing can be used to further examine this area of abnormal myocardium to define potential channels of viable tissue and isthmus locations.

When the areas of scar are defined, potential channels of viable myocardium through these regions are often readily identified (see Figure 23.3) as regions with an intermediate electrogram voltage. Pacing from these regions will often result in a long stimulus–QRS interval, reflecting the possible role of these regions as protected isthmuses during a reentrant tachycardia [38]. Pacing will not always reproduce the tachycardia morphology, as a protected isthmus site may have several pathways to normal myocardium when pacing in sinus rhythm. However, if pacing from these sites produces a surface ECG morphology identical to the clinical VT, then that site is likely to be connected to the VT reentrant circuit, either as part of the circuit or as a nearby "bystander" site [40].

Another guide to ablation during substrate mapping is identification of abnormal electrograms within the scar or in the border zones as described above. Isolated, delayed electrograms and fractionated electrograms identified during sinus rhythm or right ventricular apical pacing have been shown to correlate with isthmus sites critical to the VT circuit [41]. Mapping during right ventricular apical pacing may be more sensitive than mapping during sinus rhythm for identifying isolated delayed electrograms indicative of potential sites for ablation [42]. Areas of abnormal electrograms may mark sites critical in a reentrant circuit and are targets for substrate-based ablation.

Ablation Strategies

After voltage mapping, pace-mapping, and recording of abnormal electrograms have identified areas of scar, potential isthmus sites, and sites that may be part of a reentrant circuit, ablation is then performed. Linear ablation lesions are created through point-to-point catheter ablations. Strategies for placing these ablations vary somewhat, but

(a)

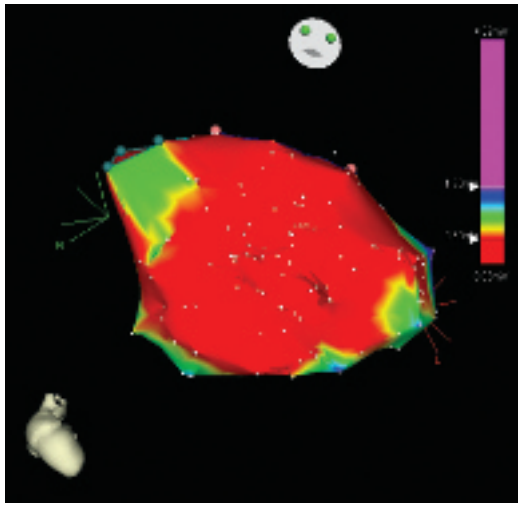

(b)

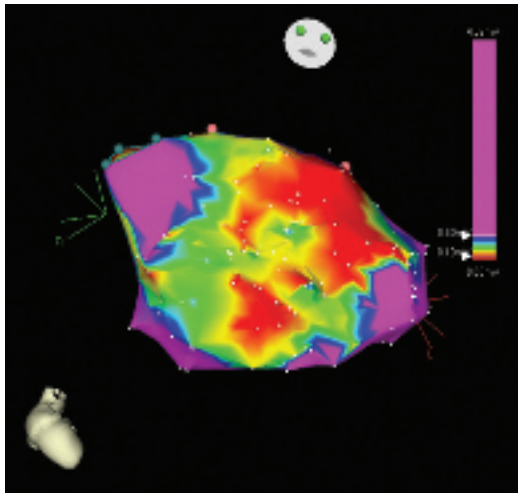

Figure 23.3 CARTO maps showing the importance of voltage mapping and definition of scar. Electroanatomic CARTO maps of the left ventricle with large septal and inferoseptal scar are shown. The image is shown in a modified RAO orientation, and voltage maps are shown at different color voltage scales. In part (a), the scale is 0.5–1.5 mV (see scale on the right), and a large area of scar is identified along the anterior wall, septum, and inferior wall. In part (b), the voltage scale has been changed to 0.1–0.5 mV. At this scale, regions of viable myocardium can be identified within the scar which may represent potential protected isthmus channels during reentrant VT.

the goal is to interrupt the VT circuit. Therefore, ablation lines should cross areas of putative critical isthmuses, encompass sites of abnormal electrograms in the "border zone" of scar, and connect areas of dense scar with either anatomic boundaries (such as the mitral annulus) or with areas of normal myocardium [30, 43] (see Figure 23.4). These lines may extend along the putative isthmus from deep within an area of scar extending across the border zone of fractionated electrograms into normal tissue. Another strategy is to place the lines along the border zones of fractionated electrograms perpendicular to the isthmus and extending across the exit site identified by pace mapping. Extending lines of ablation from areas of dense scar to anatomic boundaries or other areas of scar and creating complete linear ablation lines are important principles to ensure successful ablation. Effective lines of

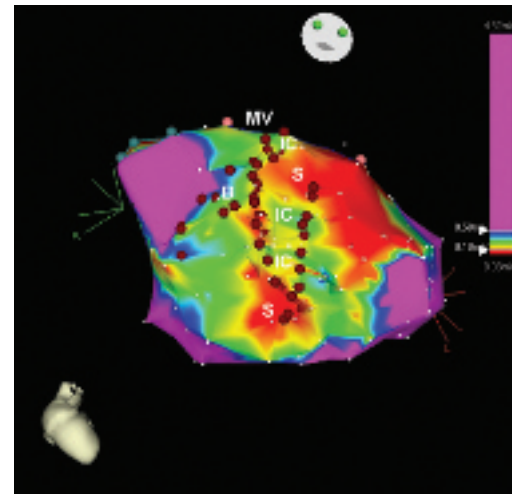

Figure 23.4 Linear ablation strategies in substrate ablation. The electroanatomic CARTO map of the left ventricle from Figure 23.3 is shown. The voltage scale is 0.1–0.5 mV, and a region of viable myocardium within the larger area of scar, as shown in Figure 23, is identified. The red dots represent sites of ablation. Note that two ablation lines extend from a region of dense scar (S) across putative isthmus channels (IC) extending to another area of dense scar (S). Additional ablation was performed from the upper region of scar across another potential isthmus channel (IC) to the anatomic boundary of the mitral valve (MV) annulus. An additional horizontal ablation line is shown perpendicular to the isthmus channel (IC) across the border zone (B) of the dense scar. This line was created in regions with abnormal fractionated electrograms and it also crosses the isthmus channel to join with the linear ablation.

conduction block without gaps are crucial in this procedure. When exit sites or a critical isthmus cannot be identified, empiric ablation of fractionated electrograms in the border zone of scar may be performed. Serial linear lesions can be made encircling the scar border in approximately 3- to 5-cm intervals in an attempt to interrupt all possible exit sites [30].

Other Mapping and Navigation Systems

The noncontact mapping system described above can also be used for dynamic substrate mapping. Areas of low voltage are able to be recorded by this system. Pacing is performed around the area of the infarct and regions of low voltage are recorded based on the direction of wavefront excitation. The results from pacing at different sites are combined to create a substrate map displaying endocardial electrograms for identification of VT exit sites to be used as a guide for ablation [44]. This technique remains under development currently.

Role for Substrate Mapping and Ablation

Substrate mapping can be used to guide ablation therapy for VT in coronary disease without prolonged periods of VT in the electrophysiology laboratory. This may provide the means for curative therapy for patients who cannot undergo conventional mapping procedures. Because only a small percentage of patients with VT have inducible hemodynamically tolerated VT in the laboratory, this method is commonly used for treatment of recurrent VT.

Substrate mapping and ablation are unlikely to guarantee prevention of arrhythmia, but it may prevent clinically observed VT and decrease ICD shocks. A recently reported study examined the role of substrate mapping and ablation in patients with ICDs at high risk for recurrent ventricular arrhythmias. The SMASH-VT study randomized patients with an ICD and a history of VT, ventricular fibrillation, syncope with inducible VT, or recent ICD shock to substrate-based ablation or observation. Patients in the group undergoing substrate-based ablation had significantly fewer ICD therapies (shocks or antitachycardia pacing) and fewer ICD shocks [45].

Conclusion

Substrate ablation may provide a method for potentially curative therapy in patients without hemodynamically tolerated VT. One randomized trial has demonstrated the efficacy of this technique, and further research is required to better define its indications. As ICD use becomes widespread, the number of patients who survive VT and experience repeated shocks is increasing. This further highlights the need for better catheter-based treatments of VT. Further development of substrate mapping and ablation techniques in sinus rhythm for the prevention of VT is necessary.

References

1 Kempf FC, Jr., Josephson ME. Cardiac arrest recorded on ambulatory electrocardiograms. *Am J Cardiol* 1984; **53**: 1577–82.

2 Buxton AE, Lee KL, Fisher JD, et al. A randomized study of the prevention of sudden death in patients with coronary artery disease. Multicenter Unsustained Tachycardia Trial Investigators. *N Engl J Med* 1999; **341**: 1882–90.

3 Rosenqvist M, Beyer T, Block M, et al. Adverse events with transvenous implantable cardioverter–defibrillators: a prospective multicenter study. European 7219 Jewel ICD investigators. *Circulation* 1998; **98**: 663–70.

4 Reynolds MR, Cohen DJ, Kugelmass AD, et al. The frequency and incremental cost of major complications among medicare beneficiaries receiving implantable cardioverter–defibrillators. *J Am Coll Cardiol* 2006; **47**: 2493–97.

5 Josephson ME, Horowitz LN, Spielman SR, et al. Comparison of endocardial catheter mapping with intraoperative mapping of ventricular tachycardia. *Circulation* 1980; **61**: 395–404.

6 Callans DJ, Zado E, Sarter BH, et al. Efficacy of radiofrequency catheter ablation for ventricular tachycardia in healed myocardial infarction. *Am J Cardiol* 1998; **82**: 429–32.

7 O'Callaghan PA, Poloniecki J, Sosa-Suarez G, et al. Long-term clinical outcome of patients with prior myocardial infarction after palliative radiofrequency catheter ablation for frequent ventricular tachycardia. *Am J Cardiol* 2001; **87**: 975–79, A4.

8 Morady F, Harvey M, Kalbfleisch SJ, et al. Radiofrequency catheter ablation of ventricular tachycardia in patients with coronary artery disease. *Circulation* 1993; **87**: 363–72.

9 Josephson ME, Horowitz LN, Farshidi A, et al. Recurrent sustained ventricular tachycardia. 1. Mechanisms. *Circulation* 1978; **57**: 431–40.

10 Fenoglio JJ, Jr., Pham TD, Harken AH, et al. Recurrent sustained ventricular tachycardia: structure and ultrastructure of subendocardial regions in which tachycardia originates. *Circulation* 1983; **68**: 518–33.
11 Spach MS, Dolber PC. Relating extracellular potentials and their derivatives to anisotropic propagation at a microscopic level in human cardiac muscle: evidence for electrical uncoupling of side-to-side fiber connections with increasing age. *Circ Res* 1986; **58**: 356–71.
12 de Bakker JM, van Capelle FJ, Janse MJ, et al. Reentry as a cause of ventricular tachycardia in patients with chronic ischemic heart disease: electrophysiologic and anatomic correlation. *Circulation* 1988; **77**: 589–606.
13 Josephson ME, Zimetbaum P, Huang D, et al. Pathophysiologic substrate for sustained ventricular tachycardia in coronary artery disease. *Jpn Circ J* 1997; **61**: 459–66.
14 Miller JM, Tyson GS, Hargrove WC, 3rd, et al. Effect of subendocardial resection on sinus rhythm endocardial electrogram abnormalities. *Circulation* 1995; **91**: 2385–91.
15 Josephson ME, Horowitz LN, Farshidi A, et al. Sustained ventricular tachycardia: evidence for protected localized reentry. *Am J Cardiol* 1978; **42**: 416–24.
16 Morady F, Frank R, Kou WH, et al. Identification and catheter ablation of a zone of slow conduction in the reentrant circuit of ventricular tachycardia in humans. *J Am Coll Cardiol* 1988; **11**: 775–82.
17 Stevenson WG, Khan H, Sager P, et al. Identification of reentry circuit sites during catheter mapping and radiofrequency ablation of ventricular tachycardia late after myocardial infarction. *Circulation* 1993; **88**: 1647–70.
18 El-Shalakany A, Hadjis T, Papageorgiou P, et al. Entrainment/mapping criteria for the prediction of termination of ventricular tachycardia by single radiofrequency lesion in patients with coronary artery disease. *Circulation* 1999; **99**: 2283–89.
19 Buxton AE, Josephson ME, Marchlinski FE, et al. Polymorphic ventricular tachycardia induced by programmed stimulation: response to procainamide. *J Am Coll Cardiol* 1993; **21**: 90–8.
20 Josephson ME, Waxman HL, Cain ME, et al. Ventricular activation during ventricular endocardial pacing. II. Role of pace-mapping to localize origin of ventricular tachycardia. *Am J Cardiol* 1982; **50**: 11–22.
21 Josephson ME, Simson MB, Harken AH, et al. The incidence and clinical significance of epicardial late potentials in patients with recurrent sustained ventricular tachycardia and coronary artery disease. *Circulation* 1982; **66**: 1199–204.
22 Morady F, Kadish AH, DiCarlo L, et al. Long-term results of catheter ablation of idiopathic right ventricular tachycardia. *Circulation* 1990; **82**: 2093–99.
23 Klein LS, Shih HT, Hackett FK, et al. Radiofrequency catheter ablation of ventricular tachycardia in patients without structural heart disease. *Circulation* 1992; **85**: 1666–74.
24 Waxman HL, Josephson ME. Ventricular activation during ventricular endocardial pacing: I. Electrocardiographic patterns related to the site of pacing. *Am J Cardiol* 1982; **50**: 1–10.
25 Schilling RJ, Peters NS, Davies DW. Feasibility of a noncontact catheter for endocardial mapping of human ventricular tachycardia. *Circulation* 1999; **99**: 2543–52.
26 Strickberger SA, Knight BP, Michaud GF, et al. Mapping and ablation of ventricular tachycardia guided by virtual electrograms using a noncontact, computerized mapping system. *J Am Coll Cardiol* 2000; **35**: 414–21.
27 Cassidy DM, Vassallo JA, Buxton AE, et al. The value of catheter mapping during sinus rhythm to localize site of origin of ventricular tachycardia. *Circulation* 1984; **69**: 1103–10.
28 Cassidy DM, Vassallo JA, Marchlinski FE, et al. Endocardial mapping in humans in sinus rhythm with normal left ventricles: activation patterns and characteristics of electrograms. *Circulation* 1984; **70**: 37–42.
29 Soejima K, Suzuki M, Maisel WH, et al. Catheter ablation in patients with multiple and unstable ventricular tachycardias after myocardial infarction: short ablation lines guided by reentry circuit isthmuses and sinus rhythm mapping. *Circulation* 2001; **104**: 664–69.
30 Marchlinski FE, Callans DJ, Gottlieb CD, et al. Linear ablation lesions for control of unmappable ventricular tachycardia in patients with ischemic and nonischemic cardiomyopathy. *Circulation* 2000; **101**: 1288–96.
31 Cassidy DM, Vassallo JA, Miller JM, et al. Endocardial catheter mapping in patients in sinus rhythm: relationship to underlying heart disease and ventricular arrhythmias. *Circulation* 1986; **73**: 645–52.
32 Kadish AH, Rosenthal ME, Vassallo JA, et al. Sinus mapping in patients with cardiac arrest and coronary disease: results and correlation with outcome. *Pacing Clin Electrophysiol* 1989; **12**: 301–10.
33 Callans DJ, Ren JF, Michele J, et al. Electroanatomic left ventricular mapping in the porcine model of healed anterior myocardial infarction: correlation with intracardiac echocardiography and pathological analysis. *Circulation* 1999; **100**: 1744–50.
34 Schmidt A, Azevedo CF, Cheng A, et al. Infarct tissue heterogeneity by magnetic resonance imaging identifies enhanced cardiac arrhythmia susceptibility in patients with left ventricular dysfunction. *Circulation* 2007; **115**: 2006–14.

35 Ben-Haim SA, Osadchy D, Schuster I, et al. Nonfluoroscopic, in vivo navigation and mapping technology. *Nat Med* 1996; **2**: 1393–95.

36 Gepstein L, Hayam G, Ben-Haim SA. A novel method for nonfluoroscopic catheter-based electroanatomical mapping of the heart: in vitro and in vivo accuracy results. *Circulation* 1997; **95**: 1611–22.

37 Gepstein L, Evans SJ. Electroanatomical mapping of the heart: basic concepts and implications for the treatment of cardiac arrhythmias. *Pacing Clin Electrophysiol* 1998; **21**: 1268–78.

38 Arenal A, del Castillo S, Gonzalez-Torrecilla E, et al. Tachycardia-related channel in the scar tissue in patients with sustained monomorphic ventricular tachycardias: influence of the voltage scar definition. *Circulation* 2004; **110**: 2568–74.

39 Stevenson WG, Sager PT, Natterson PD, et al. Relation of pace mapping QRS configuration and conduction delay to ventricular tachycardia reentry circuits in human infarct scars. *J Am Coll Cardiol* 1995; **26**: 481–88.

40 Brunckhorst CB, Delacretaz E, Soejima K, et al. Identification of the ventricular tachycardia isthmus after infarction by pace mapping. *Circulation* 2004; **110**: 652–59.

41 Bogun F, Good E, Reich S, et al. Isolated potentials during sinus rhythm and pace-mapping within scars as guides for ablation of post-infarction ventricular tachycardia. *J Am Coll Cardiol* 2006; **47**: 2013–19.

42 Arenal A, Glez-Torrecilla E, Ortiz M, et al. Ablation of electrograms with an isolated, delayed component as treatment of unmappable monomorphic ventricular tachycardias in patients with structural heart disease. *J Am Coll Cardiol* 2003; **41**: 81–92.

43 Kottkamp H, Wetzel U, Schirdewahn P, et al. Catheter ablation of ventricular tachycardia in remote myocardial infarction: substrate description guiding placement of individual linear lesions targeting noninducibility. *J Cardiovasc Electrophysiol* 2003; **14**: 675–81.

44 Jacobson JT, Afonso VX, Eisenman G, et al. Characterization of the infarct substrate and ventricular tachycardia circuits with noncontact unipolar mapping in a porcine model of myocardial infarction. *Heart Rhythm* 2006; **3**: 189–97.

45 Reddy VY, Reynolds MR, Neuzil P, et al. Prophylactic catheter ablation for the prevention of defibrillator therapy. *N Engl J Med.* 2007; **357**: 2657–65.

24 CHAPTER 24

Mapping of Unstable Ventricular Tachycardia

Usha B. Tedrow, MD, MSc, *William G. Stevenson,* MD

Brigham and Women's Hospital, Boston, MA, USA

Summary

Catheter ablation plays an important role in reducing VT episodes in ICD patients and in controlling incessant VT and electrical storms. Present techniques enable ablation for multiple and hemodynamically unstable VTs, formerly considered to be "unmappable." VT can be unstable for mapping due to hemodynamic intolerance, requiring immediate termination, inability to reliably induce VT, or frequent changes in QRS morphology indicating changing reentry circuits. Monomorphic VTs are most often due to repetitive ventricular activation from a structural substrate or focus that can be targeted for ablation. Catheter ablation techniques for stable VT rely on activation and entrainment mapping during sustained VT, which is typically only possible in a limited way when VT is unstable. Substrate mapping with adjuvant pace mapping during sinus rhythm is quite feasible for these unstable VTs. Polymorphic VT may not have a fixed substrate, but in some cases ablation targeting the initiating ventricular ectopic beats can be successful. Adjuvant methods of hemodynamic support can also be helpful to facilitate mapping during VT.

Introduction

Ventricular tachycardia (VT) is an important cause of morbidity and mortality in patients with structural heart disease. Implantable cardioverter defibrillators (ICDs) can be life-saving, but recurrent defibrillation can be painful and traumatic, and may contribute to exacerbation of heart failure in these patients [1–3]. Some patients suffer syncope despite appropriate VT detection and therapy from their ICD [4]. Catheter ablation for VT is an important adjunct to the management of these patients, reducing shocks and allaying the need for antiarrhythmic drugs, which have their own toxicities [1]. Catheter ablation can be life-saving when VT is incessant [5–7].

Catheter ablation requires mapping to locate the arrhythmogenic substrate. Of patients with ICDs who are considered for ablation after failing antiarrhythmic drug therapy, fewer than one-third have VT that is sufficiently stable to allow mapping during VT. The majority have a combination of stable and unstable VTs, or only unstable VT. VT can be unstable for mapping due to hemodynamic intolerance, requiring immediate termination, inability to reliably induce VT, or frequent and spontaneous shifts in morphology. Catheter ablation techniques for stable VT rely on activation and entrainment

Cardiac Mapping, Third Edition Edited by Mohammad Shenasa, Gerhard Hindricks, Martin Borggrefe, and Günter Breithardt
 ISBN: 978-1-405-17572-2

mapping during sustained VT, which is only possible in a limited way in patients with unstable VT. Substrate mapping techniques can be used to guide ablation for these unstable VTs during stable sinus or paced rhythm.

The type of VT and underlying heart disease direct the approach to mapping and ablation. Most VTs that are considered for ablation are monomorphic, a structural substrate or focus that can be targeted for ablation, and are due to reentry through regions of ventricular scar [8]. Recognition of other types of arrhythmia such as bundle branch reentry or interfascicular reentry is important. Ablation can also be used to control recurrent unstable polymorphic VT by targeting the initiating ventricular ectopic beats [6, 9–12].

Substrate Mapping : Scar-Related Sustained Monomorphic VT

Reentry related to ventricular scars from prior myocardial infarction, cardiomyopathies, or surgical incisions is the most common cause of sustained monomorphic VT associated with structural heart disease. Scars are comprised of variable regions of dense fibrosis that create conduction block with interposed surviving myocyte bundles and interstitial fibrosis. Diminished cellular coupling produces circuitous paths and zones of slow conduction that promote reentry [13]. These circuits can be modeled as having an isthmus or channel comprised of a small mass of tissue that does not contribute to the surface ECG.

The QRS complex begins when the excitation wave front emerges from an exit along the border of the scar and spreads across the ventricles. Scars related to VT often border a valve annulus that forms a border segment for part of the circuit [14–16]. Multiple VTs with different QRS morphologies can be due to multiple exits from the same region of scar, or changes in activation remote from the circuit due to functional regions of block [15, 17–19]. Ablation at one region often abolishes more than one VT [19, 20–22]. Multiple reentry circuits from widely separated areas also occur.

The delineation of the likely arrhythmogenic substrate during a stable sinus or paced rhythm is referred to as "substrate mapping." This method often allows identification of likely exits and channels without mapping during VT (Figure 24.1), facilitating ablation in patients with multiple and unstable VTs [15, 18, 23, 24].

Identification of Target Sites: Voltage Mapping and Pace Mapping

Areas of ventricular scar are characterized by low-amplitude bipolar electrograms (<1.55 mV). Plots of peak-to-peak electrogram amplitude displayed in electroanatomic mapping reconstructions are referred to as "voltage maps" (Figures 24.1 and 24.2) [18, 24]. The low-voltage region is likely to contain the reentry circuit, but is often extensive, exceeding 20 cm in circumference in many patients [15]. Ablation of the entire region is typically not possible. Additional analyses of electrograms, voltage, or pace-mapping are used to refine selection of target sites.

The border region typically extends along the scar margin defined by electrogram amplitude between 0.5 and 1.5 mV. Exit regions are located along the scar border. Pacing while in stable sinus or paced rhythm, or "pace mapping," in the exit region replicates the QRS morphology of VT (Figure 24.3b) [25, 26]. The interval between the stimulus and QRS onset is typically short, consistent with the exit location in the infarct border.

Several markers of potential channels within low-voltage regions have been identified. Delayed activation of a channel during sinus or paced rhythm can create isolated potentials inscribed after the end of the QRS [27, 31]. Pacing in a channel produces a QRS that emerges after a delay (S − QRS > 40 msec) due to slow conduction through the channel (Figure 24.3c). When the stimulated wavefront propagates through the channel to an exit region, the paced QRS morphology resembles VT, suggesting that the pacing site is in a reentry circuit isthmus [25, 30]. If the wavefront leaves the scar by another path, such as the entrance to a channel, the paced QRS morphology may differ from VT, or resemble a different VT. Potential channels can also be exposed by assessing the relative electrogram amplitudes in a low-voltage region [32, 33].

Electrically unexcitable areas of scar (EUS) that are regions of fixed conduction block can be identified from a high pacing threshold (>10 mA at

(a)

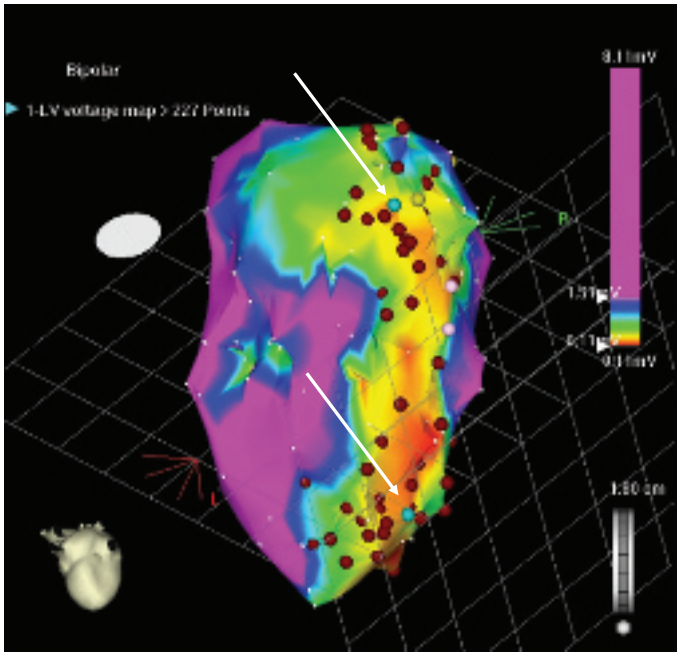

(b)

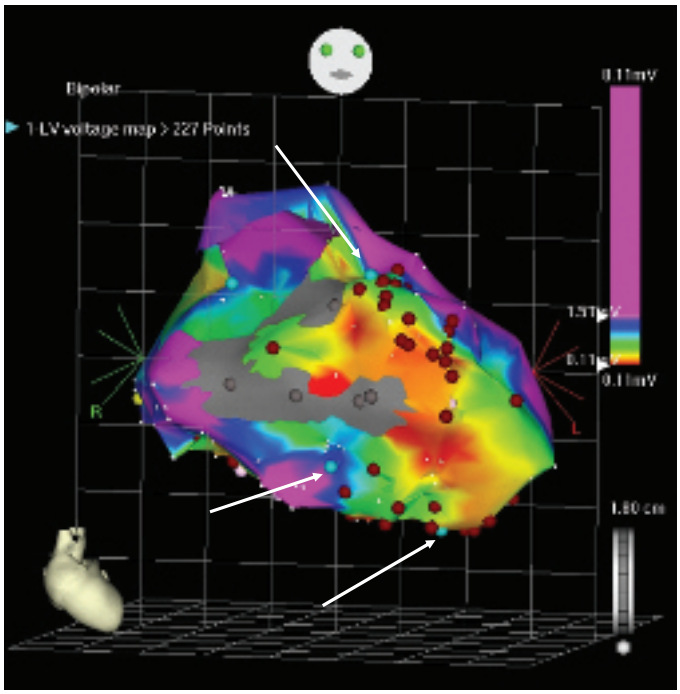

Figure 24.1 Electroanatomic endocardial voltage maps in a patient with ischemic cardiomyopathy and multiple unstable VTs. Panel (a) shows a voltage map of the left ventricle viewed from the inferior oblique position, and panel (b) depicts the same map from the right anterior oblique position. Purple indicates a bipolar electrogram amplitude of 1.5 mV or greater; amplitude diminishes from blue, to green, to yellow, to red. Gray indicates electrically unexcitable scar (EUS). A low-amplitude region of scar is present extending along the inferior and anterior walls. White arrows indicate the sites along the scar channel where pacing produced activation similar to the induced VT morphologies. Dark red spots indicate ablation lesion sites.

(a)

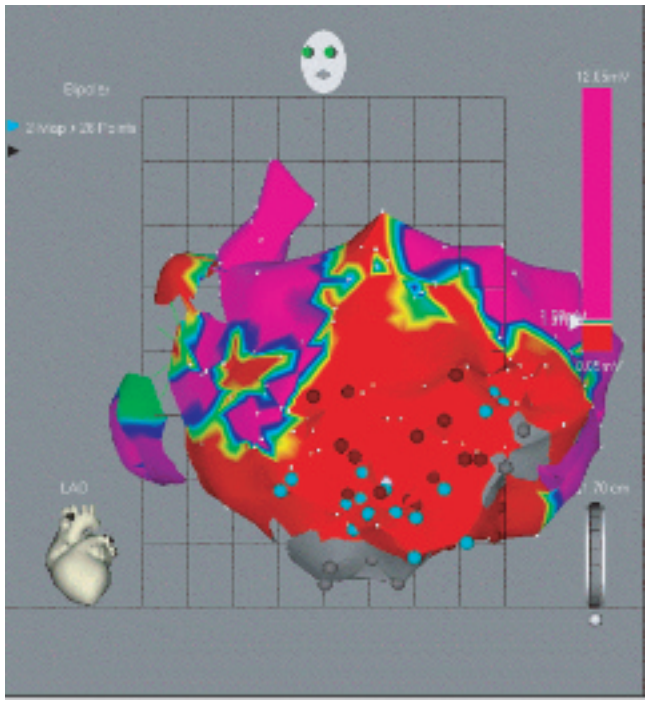

(b)

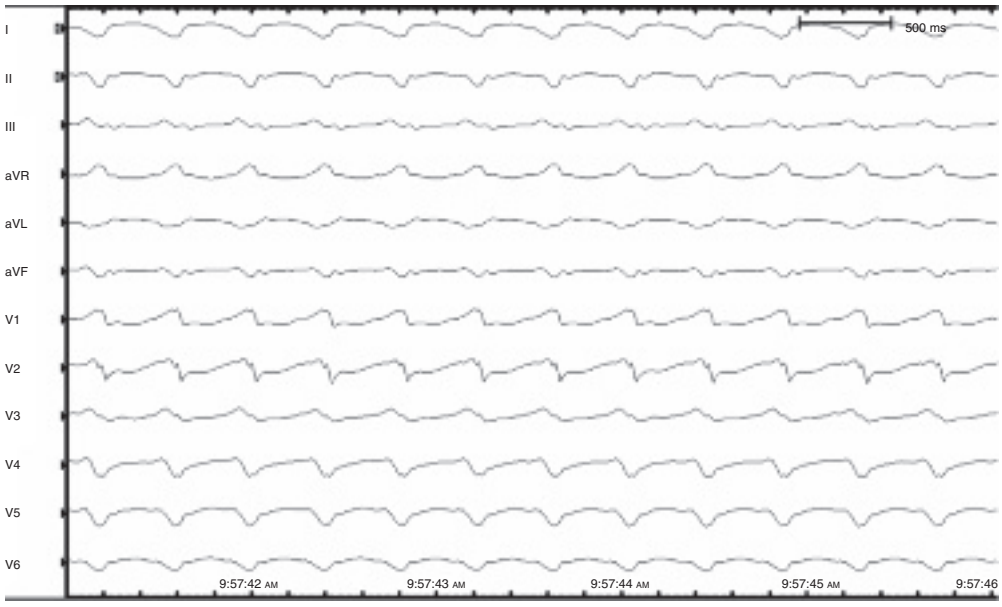

Figure 24.2 Findings from epicardial mapping during sinus rhythm for a patient with VT due to idiopathic cardiomyopathy. Panel (a) depicts an epicardial voltage map obtained by percutaneous subxyphoid access. The color scale is similar to that shown in Figure 24.1. There is a large zone of low voltage (red). Areas that paced with delay are indicated with blue dots. Dark red spots indicate ablation lesion sites. Panel (b) shows the 12-lead ECG of the epicardial VT morphology with slow QRS upstroke, producing a pseudo-delta waves, possibly related to delayed activation of the endocardial Purkinje system as compared to endocardial VTs.

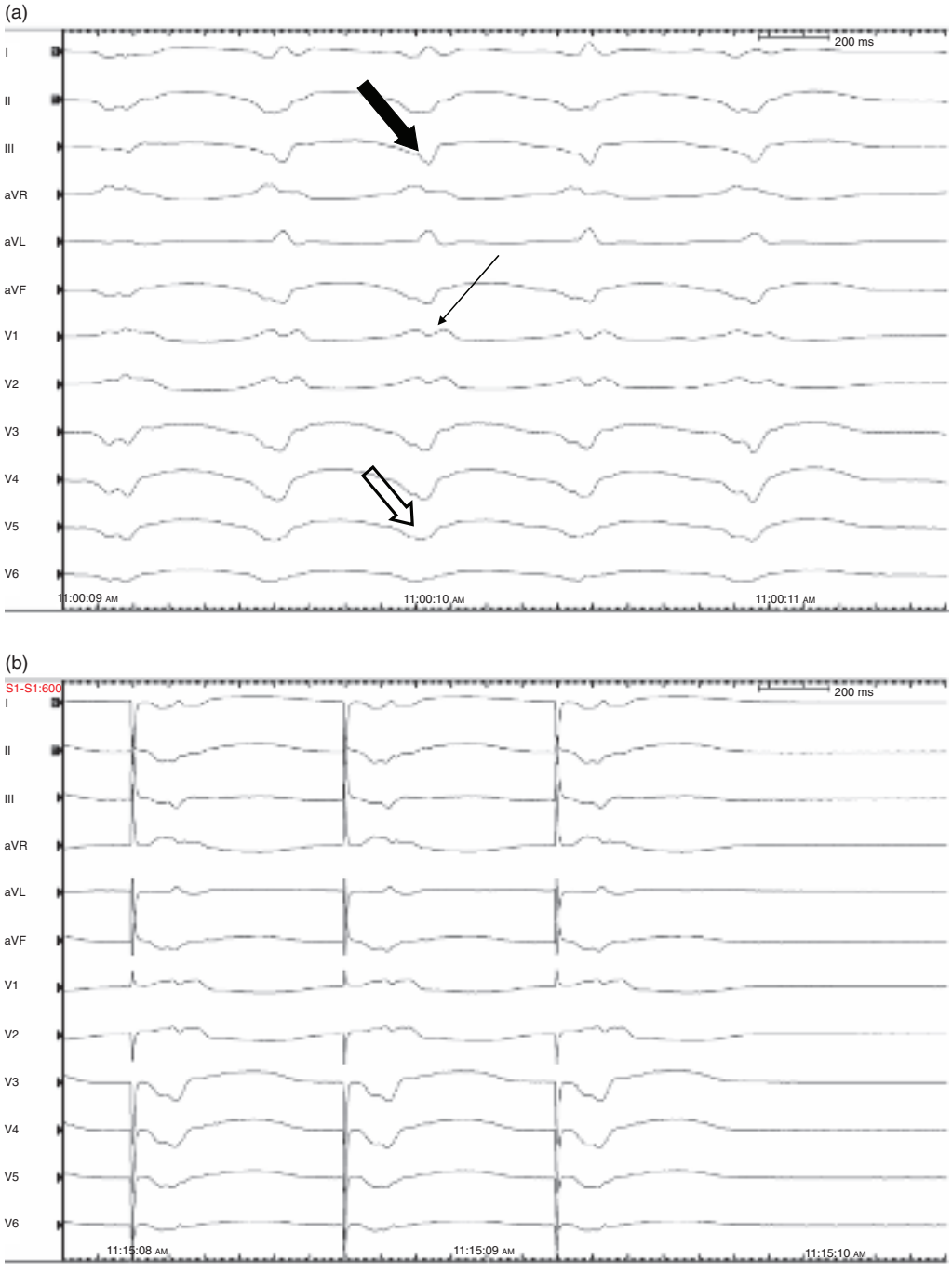

Figure 24.3 Twelve-lead ECG in VT and with pace-mapping in a patient with prior anterior infarction. Panel (a) shows the 12 leads of an induced VT. It has a right-bundle-like configuration in lead V1 (thin black arrow), superior axis (heavy black arrow), and negative deflections in V3 and V4 (white arrow), consistent with its origin in the inferoapical aspect of the LV. Panel (d) shows the endocardial voltage map for this patient, with color scale similar to Figure 24.1. An apical aneurysm with scar is demonstrated. Panel (b) shows pacing near the scar border, with morphology similar to the clinical VT but very short S-QRS [thin white arrow on panel (d)]. Panel (c) shows pacing deep in the scar area [heavy white arrow on panel (d)]. Ablation at the indicated dark red spots rendered VT noninducible.

(c)

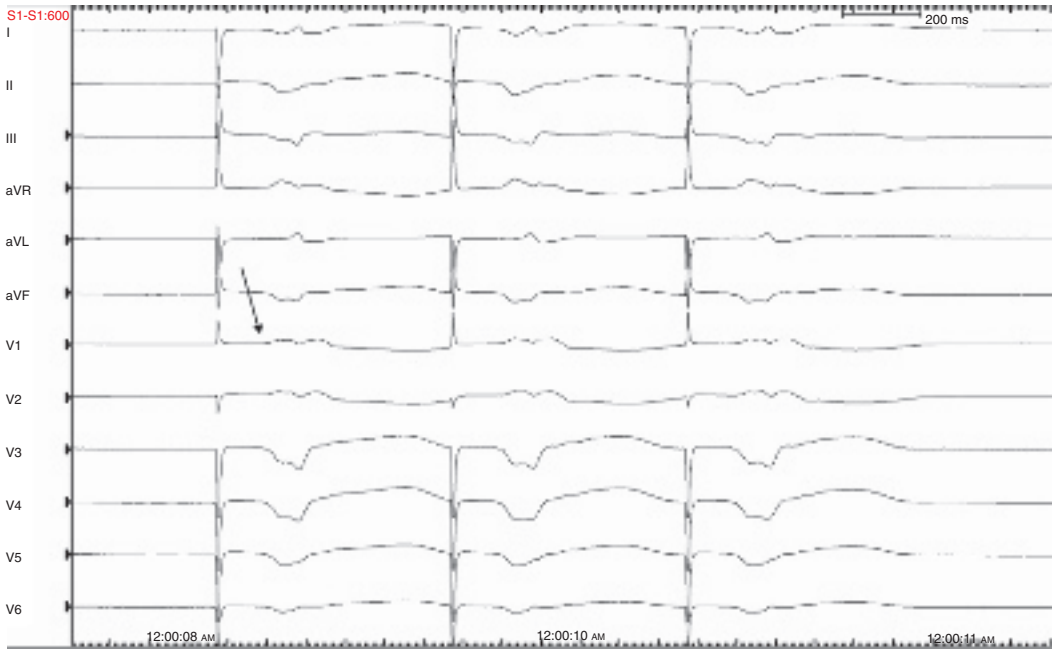

(d)

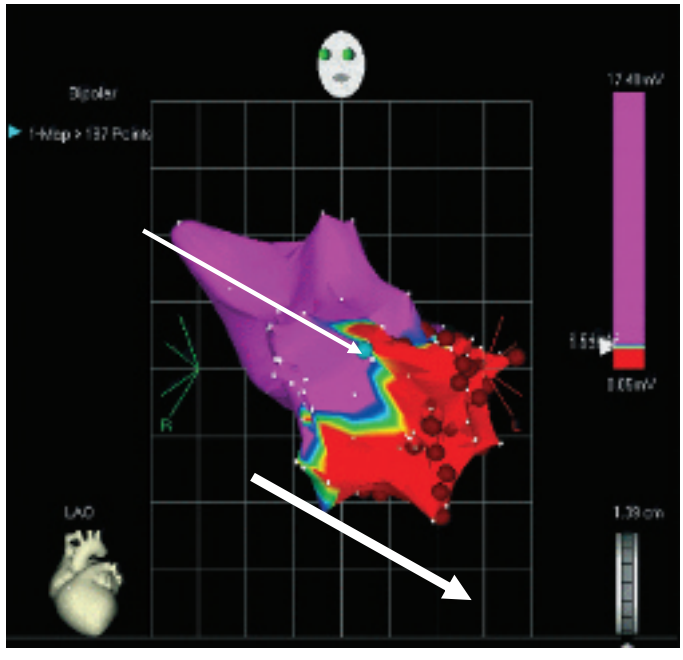

Figure 24.3 (*Continued*)

2-msec pulse width with unipolar pacing) [20]. In some low-voltage regions, marking EUS creates a visual map of potential channels. Narrow bands of fibrosis are likely to escape detection with this method. Inadequate electrode myocardial contact is also a potential source of error. EUS cannot be reliably detected based on electrogram amplitude alone. Pacing captures at the majority of sites with very low electrogram amplitude of <0.25 mV. In contrast, some EUS sites have electrogram amplitude >0.5 mV, due to the presence of large far field potentials. Thus, electrogram characteristics and pacing techniques provide complimentary information during substrate mapping.

The complexity of the reentry circuit configurations and areas of slow conduction and block in diseased ventricles are such that they are not always sufficient to define a reentry circuit location. Even in the case of unstable VT, limited activation mapping and potentially entrainment during VT can be helpful to confirm that an identified region is in a reentry circuit and to facilitate successful ablation with fewer ablation lesions [15]. Alternatively, RF lesions can be placed through presumptive exits and/or channels, followed by retesting for inducible VT [15, 18, 26].

QRS Morphology as a Guide to the VT Exit

After the substrate is established, though the induced VT may be unstable, briefly inducing VT to assess QRS morphology can be exceedingly helpful to help localize the exit. Brief entrainment and assessment of local activation times may be possible to better define a candidate channel or scar region (discussed below). Attention to options for promptly terminating the VT in the unstable patient either with overdrive pacing or cardioversion is warranted.

The QRS morphology of VT is an indication of the reentry circuit exit location (Figure 24.3a) [34]. A left bundle branch block-like configuration in lead V1 indicates an exit in the right ventricle or interventricular septum; dominant R waves in V1 indicate a left ventricular exit. The frontal plane axis points away from the exit. A superiorly directed axis indicates an inferior wall exit. An inferiorly directed axis indicates an anterior wall exit. The closer an exit is to a precordial lead, the more negative the *S*-wave in that lead, providing an indication of exit location between the base and apex. Apical exits generate dominant *S*-waves in leads V3 and V4. Basal exits generate dominant *R*-waves in these leads. Epicardial reentry circuits produce VTs that typically have a relatively long QRS duration, slow QRS upstroke, producing a pseudodelta waves (Figure 24.2b), possibly related to delayed activation of the endocardial Purkinje system as compared to endocardial VTs [35].

It is important to recognize that the QRS morphology only suggests a starting point for localization of the VT circuit. Areas of scars, conduction block, and abnormal ventricular anatomy can render the QRS morphology misleading. Pacemapping can suggest the relation between anatomic location and anticipated QRS morphology is as expected in an individual patient.

Limited Mapping During VT

When VT is stable for mapping, assessment of activation and electrograms and entrainment are useful for targeting the reentry circuit [15, 17, 36, 37]. When VT is unstable, these assessments may still be useful during brief episodes of tachycardia to confirm that a region identified during substrate mapping is involved in the tachycardia. Parsimonious use of VT induction can be exceedingly helpful to confirm that an identified substrate region is involved in the clinical VT, before terminating the VT with ablation, pacing or cardioversion.

Activation Mapping and Electrograms

During VT the circuit exit and isthmus have presystolic (prior to the QRS onset) and diastolic activation. Isolated diastolic potentials are often recorded at the isthmus. Their timing is presystolic near the exit and progressively earlier relative to the QRS onset at sites further from the reentry circuit isthmus. Sites that are proximal in the circuit can be activated at the end of the QRS complex, (end systolic rather than diastolic activity), but can be identified by entrainment [38].

Multielectrode and noncontact mapping systems acquire electrograms from multiple sites simultaneously to provide an assessment of activation over a broad area, which can be helpful if the time spent in VT is brief due to instability. Detection of low-amplitude signals in the VT isthmus is difficult, and often not clearly demonstrable. The larger amplitude signals in the border regions are more easily detected. The exit region along the border of the infarct is identifiable in over 90% of VTs as the region of presystolic endocardial activation with spread of activation away from that point [19, 39–41]. Some diastolic activity is identified in approximately two-thirds of patients, but complete reentry circuits are defined in fewer than 20% of patients, likely due to low signal amplitude, or locations that are remote from the balloon electrodes, or intramural or epicardial [39].

Electrogram timing alone, particularly at individual sites, is limited as an indication of a reentry circuit location. Presystolic and diastolic electrograms can also occur at bystander sites that are not in the circuit. Some portions of the reentry circuit are depolarized during the QRS complex [42]. Pacing maneuvers and entrainment are useful for further characterizing potential reentry circuit sites.

Entrainment

Confirmation that a site is involved in the reentry circuit can be obtained by entrainment mapping [15, 36, 42, 43]. During entrainment, pacing at a rate faster than the tachycardia continuously resets the reentry circuit. Entrainment is confirmed by the criteria developed by Waldo and coworkers, which includes evidence of constant fusion between paced orthodromic and antidromic wavefronts, and progressive fusion due to proportionately greater activation of the ventricles by paced antidromic wavefronts as the pacing rate is increased [44]. The demonstration of entrainment indicates that reentry with an excitable gap in the circuit is the tachycardia mechanism.

Determination of whether the pacing site is in a narrow isthmus in the circuit is made from assessment of QRS fusion during pacing. Entrainment with concealed fusion usually indicates that the pacing site is in a reentry circuit isthmus, in which case the S-QRS interval equals the prematurity of activation (electrogram to QRS interval) at the site and the postpacing interval (PPI) is similar to the tachycardia cycle length (Figure 24.4). At sites that are in broad portions of the reentry circuit, such as reentry loops along the border of the scar, entrainment occurs with QRS fusion due to propagation of stimulated wavefronts away from the pacing site, but the PPI still indicates that the pacing site is in the circuit [45]. Other findings that indicate that a site is in the reentry circuit include reproducible VT termination by catheter-induced mechanical pressure and termination of VT by ablation during VT [36, 46, 47]. It is not necessary to define the entire circuit, if an isthmus can be identified for ablation, which is a helpful strategy in patients with unstable VT.

Special Substrate Considerations

The Purkinje System and VT

Approximately 8% of patients with sustained monomorphic VT associated with structural heart disease have bundle branch reentry as the cause of one of their VTs, although scar related reentry is often also present [8]. Most, but not all, have a prolonged HV interval in sinus rhythm and interventricular conduction delay or bundle branch block, in which case, VT can resemble the sinus rhythm QRS morphology in sinus rhythm. Most commonly, the reentry circuit involves anterograde conduction over the right bundle branch and retrograde conduction over the left bundle branch, giving rise to VT with a left bundle branch block configuration. The PPI at the apical septum indicates that this region is in or near the circuit [48]. A right bundle potential and/or His bundle electrogram preceding and linked to the QRS helps establish the diagnosis. Ablation of the right bundle branch typically eliminates this VT. Occasionally interfascicular reentry requires ablation of left bundle fascicles.

Portions of the Purkinje system can also be involved in scar-related reentry circuits, particularly after myocardial infarction [49, 50]. These VTs can have a relatively narrow QRS duration of <145 msec with Purkinje potentials present in the exit region.

Rarely, automaticity in the Purkinje system is the cause of VT in patients with structural heart disease

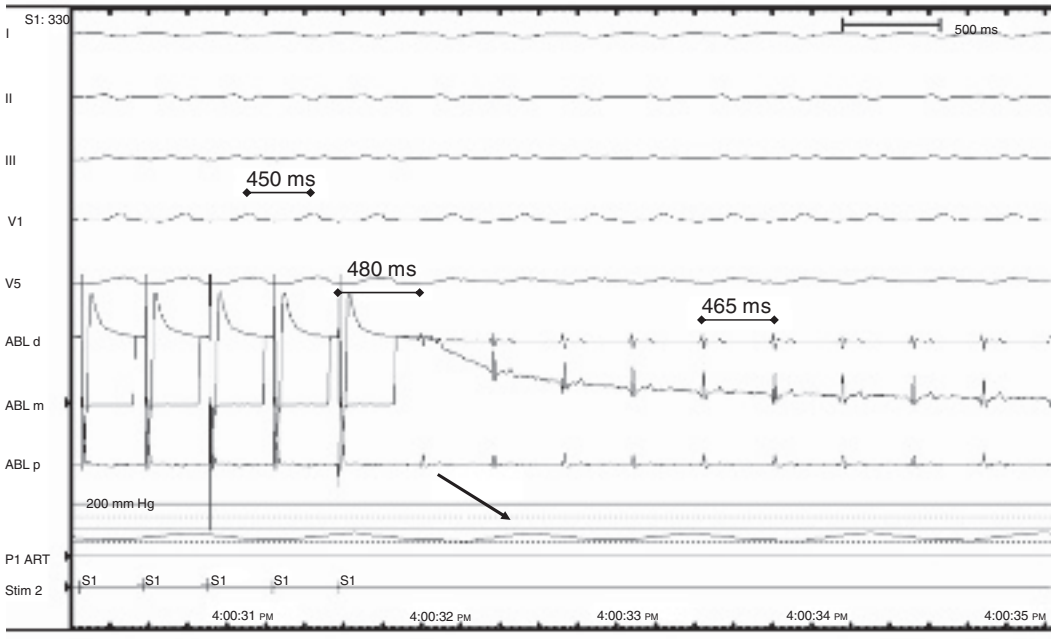

Figure 24.4 Entrainment of VT in a patient with a left ventricular assist device. The tracing shown is an incessant VT from a patient with ischemic cardiomyopathy and a left ventricular assist device (LVAD). Note that the arterial blood pressure tracing is dissociated from the electrical activation of the heart (indicated by the arrow). Depicted is entrainment at a candidate site for ablation. The postpacing interval is 480 msec with a tachycardia cycle length of 465 msec. The QRS morphology of the paced complexes resembles the VT, and the SQRS is prolonged, suggesting the pacing site is in the isthmus for this VT.

[8]. VT often requires isoproterenol administration for initiation. A Purkinje potential is often present at the successful ablation site.

Ablation for Polymorphic VT and Ventricular Fibrillation

Recurrent polymorphic VT causing an "electrical storm" that is not due to ongoing acute ischemia is rare, but occurs in idiopathic ventricular fibrillation, the long QT syndrome, Brugada syndrome, and early and late after myocardial infarction [6, 9, 11, 12]. VT is often initiated by premature beats from one or a few foci that can be targeted for ablation if they occur with sufficient frequency. Sharp potentials consistent with Purkinje activation are often recorded from foci in the left or right ventricles. Less frequently an RVOT focus is a trigger. Arrhythmias can wax and wane. Immediate patient transport to the laboratory when the arrhythmia is active is warranted if ablation is to be attempted. In selected patients, approximately 90% of patients are free from recurrences during follow-up [6, 9, 11, 12].

Optimization and Support for Mapping

Preprocedure Optimization

The pooled procedure-related mortality for all VT ablation patients is approximately 2%, with most deaths related to uncontrollable, incessant VT with hemodynamic deterioration in patients with severe disease [51]. These risks are likely concentrated among those with unstable VT. Preprocedure planning is essential to minimize risks. Underlying heart disease should be carefully defined. The potential for myocardial ischemia should be assessed. Although ischemia is not usually the cause of monomorphic VT, it may contribute to hemodynamic instability and increase the risk of the procedure. It is important to consider electrolyte abnormalities,

anemia, and metabolic abnormalities, such as hyperthyroidism, that may contribute to hemodynamic deterioration or development of uncontrollable arrhythmias during the procedure.

Fluid balance is an important consideration. Although elevated filling pressures are common in this patient population, relatively low filling pressures related to aggressive diuresis and periods without oral intake prior to procedures cause unexpected hypovolemia in some patients. Relative hypovolemia combined with sedation contributes to hemodyamic intolerance of some VTs. Assessment of intracardiac filling pressures with a pulmonary artery catheter can be helpful in adjusting volume status.

In patients with advanced disease, preprocedure consideration of patient candidacy for conventional ventricular assist devices and transplantation is important when assessing the balance of risk and benefit of catheter ablation.

Hemodynamic Support During Mapping

Intravenous administration of inotropic agents, dopamine, norepinephrine, or epinephrine have been used to improve hemodynamic tolerance during VT, increasing the time for mapping during the arrhythmia. Aggravation of ventricular arrhythmia with the risk of the arrhythmia becoming incessant is a concern. Vasoconstrictors such as phenylephrine or vasopressin can be useful, particularly if anesthesia-induced vasodilation is a contributor to hypotension. The afterload introduced by pure vasoconstriction can potentially contribute to pulmonary edema and ischemia in some vascular beds. Careful monitoring and titration is required.

Intraaortic balloon counterpulsation, can provide hemodyanamic stability in some patients, particularly those with relatively slow VTs for which balloon inflation can be appropriately timed. Mapping catheters can be easily passed by the balloon using the retrograde aortic route; we generally suspend balloon inflation briefly during transit of the catheter across the descending aorta. Inflation of the balloon against the catheter in the aorta can produce artifact, mimicking diastolic potentials. A transeptal approach for the LV mapping catheter avoids the need for a second arterial access and the balloon catheter interaction.

Peripheral ventricular assist devices have been used to provide hemodynamic support during VT [52, 53]. Attention to sites of access for VT in such patients is extremely important. Two types of pVADs exist. One is delivered via a large trans-septal and arterial cannulae providing left atrial to femoral bypass [54]. Approach to the LV for ablation is via retrograde aortic or epicardial access, but additional trans-septal access is not possible. Suggested low-dose heparinization (ACT 200–250 sec) may also limit access options.

A second type of pVAD device is placed via retrograde aortic approach and sits across the aortic valve [55]. VT ablation has not yet been reported with this second type of device, though theoretically trans-septal and epicardial approaches to the LV during ablation may be possible. VT ablation is feasible in patients with implanted standard left ventricular assist devices (Figure 24.4) as well [56]. Ablation is usually required in scenarios where right ventricular function, and consequently LVAD filling, is compromised by VT.

Antiarrhythmic Drug Therapy to Improve Hemodynamic Tolerance

Administration of an antiarrhythmic drug, such as intravenous procainamide to slow VT in the hope of improving hemodyanmic tolerance, or converting a polymorphic VT to a stable monomorphic VT, has also been reported [57]. However, the additional conduction slowing, vasodilatory and negative hemodynamic effects of some of these medications seems to offset the potential benefit of rate slowing in some patients. There is also concern that the arrhythmia characteristics and substrate would be modified, impairing detection of important arrhythmia substrates. Administration of an antiarrhythmic is occasionally unavoidable when VT becomes incessant and uncontrollable.

Conclusion

Catheter ablation of VT has an important role in reducing VT episodes in patients with ICDs and controlling incessant VT and electrical storms. Present techniques enable ablation for multiple and

hemodynamically unstable VTs. Monomorphic VTs are most often scar related and substrate mapping can guide ablation [8]. Unstable polymorphic VT can be addressed by targeting the initiating ventricular ectopic beats [6, 9–12]. Attention to preprocedure optimization is important to minimize risks. Adjuvant methods of hemodynamic support can be helpful. Ablation failure is often related to anatomic obstacles, such as intramural circuits that would potentially benefit from further technologic advances.

References

1 Connolly SJ, Dorian P, Roberts RS, et al. Comparison of beta-blockers, amiodarone plus beta-blockers, or sotalol for prevention of shocks from implantable cardioverter defibrillators: the OPTIC study: a randomized trial. *JAMA* 2006; **295**: 165–71.

2 Schron EB, Exner DV, Yao Q, et al. Quality of life in the antiarrhythmics versus implantable defibrillators trial: impact of therapy and influence of adverse symptoms and defibrillator shocks. *Circulation* 2002; **105**: 589–94.

3 Moss AJ, Greenberg H, Case RB, et al. Long-term clinical course of patients after termination of ventricular tachyarrhythmia by an implanted defibrillator. *Circulation* 2004; **110**: 3760–65.

4 Sweeney MO. Antitachycardia pacing for ventricular tachycardia using implantable cardioverter defibrillators. *Pacing Clin Electrophysiol* 2004; **27**: 1292–305.

5 Brugada J, Berruezo A, Cuesta A, et al. Nonsurgical transthoracic epicardial radiofrequency ablation: an alternative in incessant ventricular tachycardia. *J Am Coll Cardiol* 2003; **41**: 2036–43.

6 Bansch D, Oyang F, Antz M, et al. Successful catheter ablation of electrical storm after myocardial infarction. *Circulation* 2003; **108**: 3011–16.

7 Zipes DP, Camm AJ, Borggrefe M, et al. ACC/AHA/ESC 2006 guidelines for management of patients with ventricular arrhythmias and the prevention of sudden cardiac death: a report of the American College of Cardiology/American Heart Association Task Force and the European Society of Cardiology Committee for Practice Guidelines (Writing Committee to Develop Guidelines for Management of Patients with Ventricular Arrhythmias and the Prevention of Sudden Cardiac Death). *J Am Coll Cardiol* 2006; **48**: e247–e346.

8 Lopera G, Stevenson WG, Soejima K, et al. Identification and ablation of three types of ventricular tachycardia involving the His–Purkinje system in patients with heart disease. *J Cardiovasc Electrophysiol* 2004; **15**: 52–8.

9 Szumowski L, Sanders P, Walczak F, et al. Mapping and ablation of polymorphic ventricular tachycardia after myocardial infarction. *J Am Coll Cardiol* 2004; **44**: 1700–6.

10 Noda T, Shimizu W, Taguchi A, et al. Malignant entity of idiopathic ventricular fibrillation and polymorphic ventricular tachycardia initiated by premature extrasystoles originating from the right ventricular outflow tract. *J Am Coll Cardiol* 2005; **46**: 1288–94.

11 Haissaguerre M, Extramiana F, Hocini M, et al. Mapping and ablation of ventricular fibrillation associated with long-QT and Brugada syndromes. *Circulation* 2003; **108**: 925–28.

12 Marrouche NF, Verma A, Wazni O, et al. Mode of initiation and ablation of ventricular fibrillation storms in patients with ischemic cardiomyopathy. *J Am Coll Cardiol* 2004; **43**: 1715–20.

13 de Bakker JM, van Capelle FJ, Janse MJ, et al. Slow conduction in the infarcted human heart. "Zigzag" course of activation. *Circulation* 1993; **88**: 915–26.

14 Marchlinski FE, Zado E, Dixit S, et al. Electroanatomic substrate and outcome of catheter ablative therapy for ventricular tachycardia in setting of right ventricular cardiomyopathy. *Circulation* 2004; **110**: 2293–98.

15 Soejima K, Suzuki M, Maisel WH, et al. Catheter ablation in patients with multiple and unstable ventricular tachycardias after myocardial infarction: short ablation lines guided by reentry circuit isthmuses and sinus rhythm mapping. *Circulation* 2001; **104**: 664–69.

16 Soejima K, Stevenson WG, Sapp JL, et al. Endocardial and epicardial radiofrequency ablation of ventricular tachycardia associated with dilated cardiomyopathy: the importance of low-voltage scars. *J Am Coll Cardiol* 2004; **43**: 1834–42.

17 de Chillou C, Lacroix D, Klug D, et al. Isthmus characteristics of reentrant ventricular tachycardia after myocardial infarction. *Circulation* 2002; **105**: 726–31.

18 Marchlinski FE, Callans DJ, Gottlieb CD, et al. Linear ablation lesions for control of unmappable ventricular tachycardia in patients with ischemic and nonischemic cardiomyopathy. *Circulation* 2000; **101**: 1288–96.

19 Klemm HU, Ventura R, Steven D, et al. Catheter ablation of multiple ventricular tachycardias after myocardial infarction guided by combined contact and noncontact mapping. *Circulation* 2007; **115**: 2697–704.

20 Soejima K, Stevenson WG, Maisel WH, et al. Electrically unexcitable scar mapping based on pacing threshold for identification of the reentry circuit isthmus: feasibility for guiding ventricular tachycardia ablation. *Circulation* 2002; **106**: 1678–83.

21 Della Bella P, Riva S, Fassini G, et al. Incidence and significance of pleomorphism in patients with postmyocardial infarction ventricular tachycardia: acute and long-term

outcome of radiofrequency catheter ablation. *Eur Heart J* 2004; **25**: 1127–38.

22 Bogun F, Li YG, Groenefeld G, et al. Prevalence of a shared isthmus in postinfarction patients with pleiomorphic, hemodynamically tolerated ventricular tachycardias. *J Cardiovasc Electrophysiol* 2002; **13**: 237–41.

23 Cesario DA, Vaseghi M, Boyle NG, et al. Value of high-density endocardial and epicardial mapping for catheter ablation of hemodynamically unstable ventricular tachycardia. *Heart Rhythm* 2006; **3**: 1–10.

24 Reddy VY, Neuzil P, Taborsky M, et al. Short-term results of substrate mapping and radiofrequency ablation of ischemic ventricular tachycardia using a saline-irrigated catheter. *J Am Coll Cardiol* 2003; **41**: 2228–36.

25 Brunckhorst CB, Delacretaz E, Soejima K, et al. Identification of the ventricular tachycardia isthmus after infarction by pace mapping. *Circulation* 2004; **110**: 652–59.

26 Kottkamp H, Wetzel U, Schirdewahn P, et al. Catheter ablation of ventricular tachycardia in remote myocardial infarction: substrate description guiding placement of individual linear lesions targeting noninducibility. *J Cardiovasc Electrophysiol* 2003; **14**: 675–81.

27 Arenal A, Glez-Torrecilla E, Ortiz M, et al. Ablation of electrograms with an isolated, delayed component as treatment of unmappable monomorphic ventricular tachycardias in patients with structural heart disease. *J Am Coll Cardiol* 2003; **41**: 81–92.

28 Harada T, Stevenson WG, Kocovic DZ, et al. Catheter ablation of ventricular tachycardia after myocardial infarction: relation of endocardial sinus rhythm late potentials to the reentry circuit. *J Am Coll Cardiol* 1997; **30**: 1015–23.

29 Brunckhorst CB, Stevenson WG, Jackman WM, et al. Ventricular mapping during atrial and ventricular pacing: relationship of multipotential electrograms to ventricular tachycardia reentry circuits after myocardial infarction. *Eur Heart J* 2002; **23**: 1131–38.

30 Bogun F, Good E, Reich S, et al. Isolated potentials during sinus rhythm and pace-mapping within scars as guides for ablation of postinfarction ventricular tachycardia. *J Am Coll Cardiol* 2006; **47**: 2013–19.

31 Bogun F, Bender B, Li YG, et al. Analysis during sinus rhythm of critical sites in reentry circuits of postinfarction ventricular tachycardia. *J Interv Card Electrophysiol* 2002; **7**: 95–103.

32 Arenal A, del Castillo S, Gonzalez-Torrecilla E, et al. Tachycardia-related channel in the scar tissue in patients with sustained monomorphic ventricular tachycardias: influence of the voltage scar definition. *Circulation* 2004; **110**: 2568–74.

33 Hsia HH, Lin D, Sauer WH, et al. Anatomic characterization of endocardial substrate for hemodynamically stable reentrant ventricular tachycardia: identification of endocardial conducting channels. *Heart Rhythm* 2006; **3**: 503–12.

34 Josephson ME, Callans DJ. Using the twelve-lead electrocardiogram to localize the site of origin of ventricular tachycardia. *Heart Rhythm* 2005; **2**: 443–46.

35 Berruezo A, Mont L, Nava S, et al. Electrocardiographic recognition of the epicardial origin of ventricular tachycardias. *Circulation* 2004; **109**: 1842–47.

36 Bogun F, Kim HM, Han J, et al. Comparison of mapping criteria for hemodynamically tolerated, postinfarction ventricular tachycardia. *Heart Rhythm* 2006; **3**: 20–6.

37 Verma A, Marrouche NF, Schweikert RA, et al. Relationship between successful ablation sites and the scar border zone defined by substrate mapping for ventricular tachycardia postmyocardial infarction. *J Cardiovasc Electrophysiol* 2005; **16**: 465–71.

38 Bogun F, Knight B, Goyal R, et al. Discrete systolic potentials during ventricular tachycardia in patients with prior myocardial infarction. *J Cardiovasc Electrophysiol* 1999; **10**: 364–9.

39 Segal OR, Chow AW, Markides V, et al. Long-term results after ablation of infarct-related ventricular tachycardia. *Heart Rhythm* 2005; **2**: 474–82.

40 Della Bella P, Pappalardo A, Riva S, et al. Noncontact mapping to guide catheter ablation of untolerated ventricular tachycardia. *Eur Heart J* 2002; **23**: 742–52.

41 Strickberger SA, Knight BP, Michaud GF, et al. Mapping and ablation of ventricular tachycardia guided by virtual electrograms using a noncontact, computerized mapping system. *J Am Coll Cardiol* 2000; **35**: 414–21.

42 Delacretaz E, Stevenson WG. Catheter ablation of ventricular tachycardia in patients with coronary heart disease. Part I: Mapping. *Pacing Clin Electrophysiol* 2001; **24**: 1261–77.

43 El-Shalakany A, Hadjis T, Papageorgiou P, et al. Entrainment/mapping criteria for the prediction of termination of ventricular tachycardia by single radiofrequency lesion in patients with coronary artery disease. *Circulation* 1999; **99**: 2283–89.

44 Henthorn RW, Okumura K, Olshansky B, et al. A fourth criterion for transient entrainment: the electrogram equivalent of progressive fusion. *Circulation* 1988; **77**: 1003–12.

45 Stevenson WG, Friedman PL, Sager PT, et al. Exploring postinfarction reentrant ventricular tachycardia with entrainment mapping. *J Am Coll Cardiol* 1997; **29**: 1180–89.

46 Bogun F, Good E, Han J, et al. Mechanical interruption of postinfarction ventricular tachycardia as a guide for catheter ablation. *Heart Rhythm* 2005; **2**: 687–91.

47 Soejima K, Delacretaz E, Suzuki M, et al. Saline-cooled versus standard radiofrequency catheter ablation for

infarct-related ventricular tachycardias. *Circulation* 2001; **103**: 1858–62.

48 Merino JL, Peinado R, Fernandez-Lozano I, et al. Bundle-branch reentry and the postpacing interval after entrainment by right ventricular apex stimulation: a new approach to elucidate the mechanism of wide-QRS-complex tachycardia with atrioventricular dissociation. *Circulation* 2001; **103**: 1102–8.

49 Hayashi M, Kobayashi Y, Iwasaki YK, et al. Novel mechanism of postinfarction ventricular tachycardia originating in surviving left posterior Purkinje fibers. *Heart Rhythm* 2006; **3**: 908–18.

50 Bogun F, Good E, Reich S, et al. Role of Purkinje fibers in postinfarction ventricular tachycardia. *J Am Coll Cardiol* 2006; **48**: 2500–7.

51 Stevenson WG, Chaitman BR, Ellenbogen KA, et al. Clinical assessment and management of patients with implanted cardioverter–defibrillators presenting to nonelectrophysiologists. *Circulation* 2004; **110**: 3866–69.

52 Zanobini M, Rossi F, Bertera A, et al. Cardiopulmonary support during electrophysiological procedures for ventricular tachycardias not haemodynamically tolerated. *Perfusion* 2003; **18**: 79–82.

53 Friedman PA, Munger TM, Torres N, et al. Percutaneous endocardial and epicardial ablation of hypotensive ventricular tachycardia with percutaneous left ventricular assist in the electrophysiology laboratory. *J Cardiovasc Electrophysiol* 2007; **18**: 106–9.

54 Burkhoff D, Cohen H, Brunckhorst C, et al. A randomized multicenter clinical study to evaluate the safety and efficacy of the Tandem Heart percutaneous ventricular assist device versus conventional therapy with intraaortic balloon pumping for treatment of cardiogenic shock. *Am Heart J* 2006; **152**: 469e1–469e8.

55 Cohen RE, Domniez T, Elhadad S. High-risk left main coronary stenting supported by percutaneous impella recover LP 2.5 assist device. *J Invasive Cardiol* 2007; **19**: E294–E296.

56 Dandamudi G, Ghumman WS, Das MK, et al. Endocardial catheter ablation of ventricular tachycardia in patients with ventricular assist devices. *Heart Rhythm* 2007; **4**: 1165–69.

57 Buxton AE, Josephson ME, Marchlinski FE, et al. Polymorphic ventricular tachycardia induced by programmed stimulation: response to procainamide. *J Am Coll Cardiol* 1993; **21**: 90–8.

25

CHAPTER 25

Endocardial and Epicardial Mapping of Nonischemic Right and Left Ventricular Cardiomyopathy

Mathew D. Hutchinson, MD, *Francis E. Marchlinski,* MD

University of Pennsylvania Health System, Philadelphia, PA, USA

Summary

A minority of patients with left and right ventricular cardiomyopathies will present with sustained ventricular tachycardia. The vast majority of these patients are found to have perivalvular scarring noted with noninvasive imaging and electroanatomical mapping. The etiology of the scarring in these patients is likely multifactorial, and may represent a genetically predetermined adverse response to cardiac injury. The perivalvular fibrosis provides the substrate for tachycardias which are predominantly reentrant in mechanism, and are amenable to traditional activation and entrainment mapping. When entrainment mapping is not possible due to poorly tolerated tachycardias, then a substrate-based ablation strategy can be utilized in which detailed substrate characterization and pacemapping of tachycardia exit sites are performed to design an ablation strategy.

The presence of combined left and right ventricular cardiomyopathies is more common than previously recognized, and has important implications with respect to the management of ventricular tachycardias. Ventricular tachycardia after repaired tetralogy of Fallot is the most common form of incisional tachycardia. These patients typically present decades after their surgical correction with macroreentrant tachycardias that are bounded by incisional scars or graft materials; tachycardias in this setting are treated with a linear ablation strategy.

Introduction

Catheter-based ablative therapy for patients with ventricular tachycardia (VT) in the setting of right and/or left ventricular cardiomyopathy (ARVC, LVCM) represents a relative frontier in electrophysiology. Our understanding and characterization of the substrate in these disorders has evolved substantially over the past decade. Although we continue to use standard activation and entrainment mapping techniques for tolerated VT originating in proximity to the endocardium, we now recognize that both the substrate and origin for much of the VT in this setting is epicardial and the ECG can provide valuable clues related to its localization.

Cardiac Mapping, Third Edition Edited by Mohammad Shenasa, Gerhard Hindricks, Martin Borggrefe, and Günter Breithardt
 ISBN: 978-1-405-17572-2

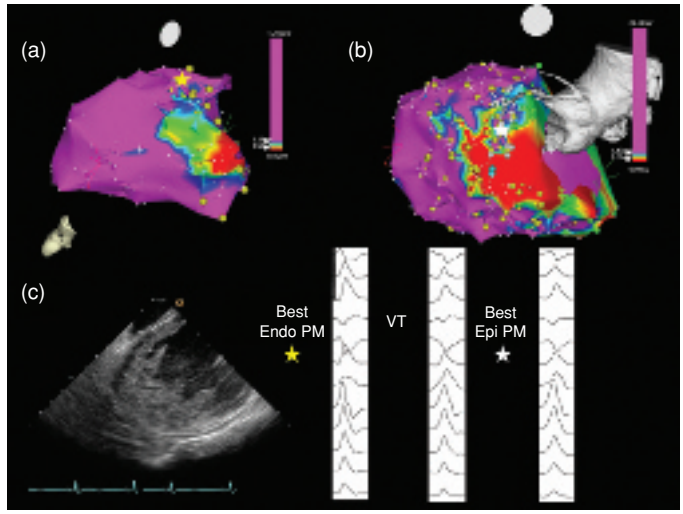

Figure 25.1 Images taken from a 52-year-old man with VT in the setting of idiopathic LV cardiomyopathy with epicardial scar defined by intracardiac echo (ICE). Endocardial bipolar voltage map (panel a) revealed a small, well-circumscribed region of low voltage at the lateral mitral annulus. The epicardial bipolar voltage map (panel b) revealed a larger region of low voltage extending from the lateral annular region. Panel c is an intracardiac echo image taken from the RV inflow tract, which reveals LV thinning and an epicardial echodensity noted at the more basal aspect of the lateral LV wall that corresponded to the epicardial low-voltage abnormality. The patient's clinical VT was induced with programmed stimulation; however, it was poorly tolerated hemodynamically. The presence of QS in V1 suggests an epicardial location. Pacemapping failed to produce a perfect VT match from the superior scar border on the epicardium (white star in panel b) or from the endocardium (yellow star in panel a). This case illustrates the limitations of pacemapping within scar to replicate the clinical VT morphology. Bidirectional activation from even those sites within the VT isthmus may produce QRS with pacing that does not mimic the activation with VT. Furthermore, the effect of increased virtual electrode size with the required high output pacing may further enhance the likelihood of QRS fusion that does not mimic VT QRS. Finally, mid-myocardial circuits may result in a ventricular activation pattern that is not replicable by pacing from the endocardial or epicardial surfaces.

Importantly, ablation strategies aggressively targeting the identified endocardial and epicardial VT substrate using imaging and bipolar voltage mapping techniques have resulted in control for unmappable VT [1]. This chapter addresses the approach to the mapping, localization, and ablation of VT in the setting of nonischemic left ventricular (LV) and right ventricular (RV) cardiomyopathies highlighting these recent developments

General Procedural Considerations

Given the inherent complexity and risk associated with VT ablation, the preoperative integration of the patient's previous historical and diagnostic information is critical in optimizing procedural planning. Primary data is gathered including: echocardiograms, computed tomography and magnetic resonance images, and coronary angiography. The assessment of LV systolic function, heart failure status, and significant valvular and/or occlusive coronary artery disease is routine prior to induction of VT in the electrophysiology laboratory. In patients with nonischemic cardiomyopathy, preablation imaging frequently provides clues with respect to the anticipated electrophysiologic substrate. When targeting VT in the setting of nonischemic cardiomyopathy, we perform detailed intracardiac echo assessment of the RV and LV anatomy. The thickness of the basal perivalvular RV and LV anatomy, the presence of ventricular noncompaction, and the presence of pericardial thickening or epicardial scar all provide valuable clues with respect to the likely origin of VT as well as the challenges that may be faced with a catheter based ablation. (Figure 25.1)

It is also important to obtain information about the patient's spontaneous arrhythmias prior to the procedure. This information is fundamental both in targeting the appropriate "clinical" arrhythmias and in determining the exit site of the VT circuit by analyzing the 12-lead ECG during VT. All available 12-lead electrocardiograms, intracardiac electrograms, and telemetry strips of the patient's clinical VTs are evaluated in detail. When 12-lead ECGs are not available, it is often possible to correlate online ICD electrogram recordings of arrhythmias induced in the EP lab with the intracardiac electrograms from the spontaneous arrhythmia episodes. Two lead telemetry strips can also give important information about the gross morphologic characteristics (i.e., bundle branch block pattern, frontal plane axis) and cycle lengths of the patient's arrhythmias. Sometimes one can infer the likely VT mechanism (reentrant versus focal) if the spontaneous initiation and/or termination of the tachycardia are available.

We have specifically found that the presence of unanticipated Q-waves on surface ECG recordings of sustained VT to be of particular value in identifying a likely epicardial origin for VT in patients with nonischemic cardiomyopathies. Unusual degrees of delay in the initial components of the QRS complex during VT also support an epicardial exit [2, 3].

Left Ventricular Cardiomyopathy

Epidemiology

Numerous studies have demonstrated a high incidence of premature ventricular contractions and nonsustained ventricular tachycardia in patients with left ventricular cardiomyopathy (LVCM) [4–6]. Patients with a history of sustained, monomorphic ventricular tachycardia have a higher incidence of inducible VT during programmed ventricular stimulation; however, VT induction can be demonstrated in a substantial minority of patients without previously documented arrhythmias [7, 8]. Noninvasive risk factors such as: abnormal signal-averaged ECG, extent of myocardial fibrosis, and the presence of myocyte hypertrophy and myofibrillar degeneration have been correlated with increased risk of spontaneous VT; however, they are not widely utilized for this purpose [9–13]. Despite these data, the ejection fraction is the primary factor considered in the assessment of mortality risk in LVCM [14].

Chagas' disease is a zoonotic infection caused by the protozoan *Trypanosoma cruzi*; it is the most common cause of cardiomyopathy in Latin America. Arrhythmias are seen most commonly in the chronic phase of the disease, which is often more than a decade after the initial infection. Up to two-thirds of Chagas'-related mortality is attributable to sudden cardiac death [15–17].

Substrate Characterization

Patients with VT in the setting of left ventricular cardiomyopathy (LVCM) have a variety of underlying disease processes; however, there is a striking similarity in the distribution of scar seen on imaging studies and electroanatomical mapping. The substrate distribution differs fundamentally from ischemic cardiomyopathy (ICM) in that the scar is not subtended by a discrete coronary arterial territory. The endocardial scar in LVCM most consistently originates in the basal aspect of the left ventricle, usually extending from the mitral and/or aortic valve annuli. In a series of 19 patients with LVCM from our institution, all had voltage abnormalities involving the basal LV while only 1/19 had apical scar [18].

Previous work by Cassidy and colleagues assessed the endocardial electrogram characteristics in patients with VT in the setting of structural heart disease [19]. Abnormal bipolar voltage was defined as $\leq$3.0 mV using a standard Josephson quadripolar electrode catheter. As in patients with ICM, abnormal electrograms are demonstrable within the scar boundary of LVCM. Fractionated potentials representing nonuniform conduction within scar and late potentials representing delayed activation of "protected" myocardial bundles are frequently seen with electroanatomical mapping in sinus rhythm. As with substrate distribution, there are important differences in the extent and distribution of abnormal electrograms in LVCM compared to ICM. When compared to patients with ICM, the patients with LVCM had less extensive endocardial voltage abnormalities (15% vs. 43%), as well as significantly fewer sites with fractionated (1% vs. 7%) and late (2% vs. 12%) electrograms. These differences are less profound if VT is present. In patients with unimorphic VT in NICM the endocardial abnormal

substrate is more similar to patients with ICM and VT with 37% of recorded electrograms abnormal [18].

We have also shown that patients with LVCM and sustained monomorphic VT showed a significant increase in the percentage of sites with abnormal electrograms recorded from both the endocardium (38%) and the epicardium (47%) when compared to those patients who presented with a cardiac arrest without inducible VT where the percentage of abnormal electrograms on both endocardium (18%) and epicardium (6%) was much less [18]. Interestingly, a minority of LVCM patients demonstrate scar on only the endocardium or the epicardium; this finding has important implications when considering catheter ablation in such patients.

The patients with Chagas'-related monomorphic VT often have demonstrable voltage and wall motion abnormalities in the basolateral LV, similar to that seen with in idiopathic LVCM. Less frequently, apical aneurysms are seen, but even when present are the typical source of VT. Histopathologic examination of the basolateral LV wall in these patients can demonstrate either focal or diffuse fibrosis that is more prominent on the subepicardial surface [20]. Given the subepicardial substrate distribution in Chagas' patients, a combined endo- and epicardial ablation approach is commonly utilized in this setting.

In light of the experience in ablation of Chagas' patients and the increasing evidence of defined epicardial voltage/substrate abnormalities, the utility of epicardial mapping in most patients with LVCM and VT regardless of the etiology has been confirmed.

Soejima and colleagues demonstrated the importance of epicardial mapping in patients failing endocardial VT ablation [21]. In their cohort of 22 patients with reentrant VT, they reported a 46% failure rate with an endocardial ablation strategy alone. In the five patients who underwent both endocardial and epicardial mapping, all had low-voltage regions that were more extensive on the epicardium. The basal and lateral epicardial regions of the LV are most frequently involved in this process. Although these sites typically compliment the regions of endocardial scar in terms of anatomic location, in some patients the abnormal area of low voltage can be confined to the epicardium.

VT Morphology

Patients with LVCM often have multiple VT morphologies inducible during EP study. Soejima et al. found an average of 2.9 morphologies per patient (range 1–7) [21]. Most VT in LVCM has a right bundle branch (RBB) morphology; the presence of VT with LBB morphologies suggests concomitant LV septal or RV involvement.

The 12-lead ECG morphology has been demonstrated to be of value in predicting epicardial sites of origin for VT. A variety of algorithms have been developed for predicting LV epicardial sites in patients without structural heart disease and in patients with primarily ischemic heart disease. It is also suspected that the ECG will be of value in identifying and epicardial origin in patients with NICM although this requires additional validation.

Berruezo and colleagues previously reported the following criteria for LV epicardial sites: pseudo-delta wave $\geq$34 msec, intrinsicoid deflection $\geq$85 msec, or precordial RS complex duration $\geq$121 msec [2]. We prospectively assessed the predictive value of these criteria using pacemapping and found that only an intrinsicoid deflection $\geq$85 msec consistently predicted an epicardial site of origin. Our group demonstrated that epicardial pacemaps from the inferior LV surface more frequently demonstrates *Q*-waves in leads II, III, and aVF than corresponding endocardial sites. Moreover, the presence of a *Q*-wave in lead I or a QS complex in lead V1 and V2 suggests an anterior or anterolateral LV epicardial origin [22]. This latter ECG clue is of particular value given the common location of the VT substrate in the perivalvular region in NICM.

Entrainment Mapping

The majority of VT in the setting of LVCM is reentrant. In a series of 26 patients with LVCM referred for VT ablation, Delacretaz and colleagues demonstrated scar-based reentry (using standard criteria) in 62% of patients [23]. From the same study, 19% of patients had bundle-branch or fascicular reentry. The prevalence of both reentrant and nonreentrant VT within the same patient appears to be uncommon.

As in ICM, reentrant VT is most commonly initiated with programmed electrical stimulation [21, 23]. The mechanism of reentry is established either by the resetting response or by entrainment

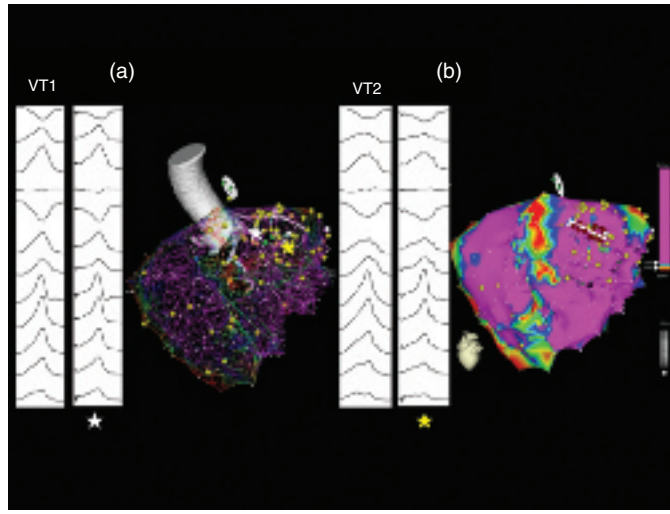

Figure 25.2 Images from a 52-year-old man with idiopathic LV cardiomyopathy and recurrent VT with epicardial focal triggers identified by pacemapping. He had a previous endocardial ablation procedure that was unsuccessful. He was referred to our institution for an epicardial ablation procedure, during which VT1 and VT2 were induced. The VT was poorly tolerated and thus not amenable to entrainment mapping. The ECG morphology of each VT reveals a characteristic QS pattern in lead I and delayed intrinsicoid deflection in the precordial leads characteristic of an epicardial site of origin. Although the epicardial bipolar voltage map (panel b) identified only low voltage in proximity to the coronaries. Identical pacemaps for VT1 and VT2 were obtained from the epicardium at sites represented by the white and yellow stars (panel a). A preacquired CT image of the aortic root and coronary arteries was segmented and merged with the electroanatomical map to demonstrate the proximity of the pacemap sites to the left coronary arteries. Ablation connecting the regions with good pacemaps for VT1 and VT2 rendered both VTs noninducible.

criteria. In patients with tolerated VT, conventional entrainment mapping is performed to elucidate critical components of the arrhythmia circuit. Sites with early diastolic activation during tachycardia are targeted as pacing sites to assess an appropriate entrainment response. A return cycle equal to the VT cycle length with evidence of concealed fusion and a 12 out of 12 lead ECG match of VT during pacing identifies appropriate ablation targets for mappable VT.

Pacemapping

Nonreentrant VT may occur in up to 20% of patients with LVCM [23]. Such arrhythmias often occur spontaneously or with isoproterenol infusion, and are inconsistently initiated and terminated with programmed stimulation. The sites of origin for focal VT may mimic those seen in idiopathic VT (e.g., LV septum) or may be found within scar. In tachycardias originating within preserved myocardium, electroanatomical mapping reveals a focal site of origin that spreads in all directions. The ablation strategy involves targeting the site with the earliest presystolic potential.

It may not be possible to induce a sustained VT in some patients due to excessive sedation, catheter trauma, or concomitant antiarrhythmic drug administration. Comparing the morphology of a paced complex to the 12-lead ECG morphology of the clinical arrhythmia can localize the arrhythmia site of origin to an anatomic region that will allow more detailed pacemapping and ablation (Figure 25.2).

Substrate Modification

If poorly tolerated arrhythmias are induced (so-called "unmappable" tachycardias), then a substrate-based ablation strategy is performed [24]. In such cases, the critical elements of the arrhythmia circuit cannot be determined with entrainment mapping. For scar-based VT, the approximate exit sites for induced arrhythmias are determined by pacemapping around the scar border zone in sinus rhythm. Linear lesion sets are constructed to

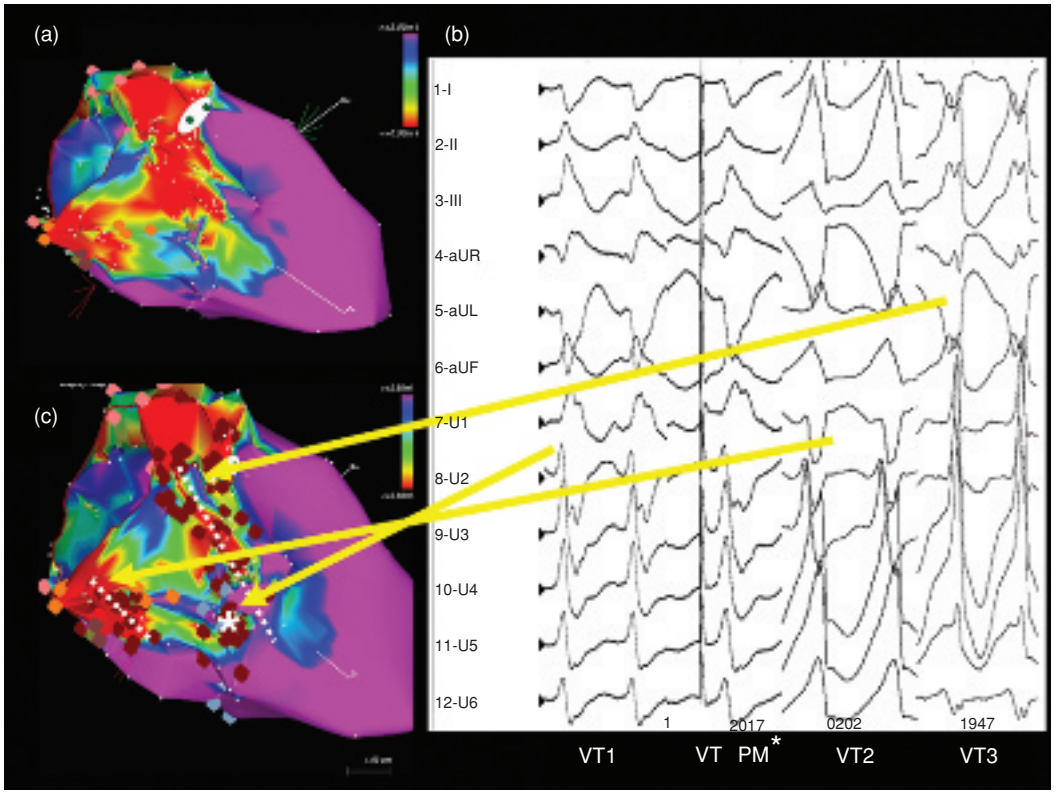

Figure 25.3 Endocardial sinus rhythm bipolar voltage map and location of linear lesions in a patient with LV cardiomyopathy and multiple poorly tolerated VT. Panel A shows a coronal view of the LV which identifies a large area of low voltage extending from the perivalvular mitral and aortic valves. In panel (b), the three VT morphologies and the location of the region of the best pacemap match for one of the VTs are shown. In panel (c), linear ablation lesions (red dots) crossing through sites of best pacemaps extending through the abnormal myocardium to the valve structures eliminated the three VTs.

incorporate the purported VT exit sites and extend into and transect the dense scar and frequently connect to the valve annuli (which typically serve as the anatomic border for part of the substrate) (Figure 25.3).

If the VT is still inducible, linear lesions can be created tangential to the scar border zone. These linear lesions assume some anatomic dimension of the VT circuit that is approximated using pacemapping information. In anticipation of a circuit exit not perfectly perpendicular to the scar border, most operators currently draw lines perpendicular to each other that cover a distance of 3–4 cm in an attempt to disturb the core of a larger purported circuit. Because some circuits may be microreentrant, a larger set around an area of the best pacemap is employed in some patients (Figure 25.2).

Finally, abnormal electrograms characterized by late or fractionated potentials may also be empirically targeted within the scar, thereby disconnecting surviving muscle bundles. Programmed stimulation is performed following the initial lesion sets to assess for additional inducible tachycardias. Additional lesions are given if necessary with the endpoint of noninducibility. Because some of the substrate appears to be intramural, irrigated ablation is the rule.

Right Ventricular Cardiomyopathy

Epidemiology

Right ventricular cardiomyopathy (ARVC) is characterized by a variable extent of fibrous and fatty infiltration of the right ventricle [25, 26]. It has a male

predominance, and can occur in either sporadic or inherited patterns [27]. In patients with ARVC, more than half of patients present with ventricular arrhythmias including up to 20% with sudden death [28]. Importantly, more than half of patients with ARVC who receive an ICD will receive appropriate therapies for ventricular arrhythmias [28]. A combined strategy of ICD implantation and ablative therapy has been demonstrated to achieve an excellent long-term outcome in patients with ARVC [1].

Another common cause of acquired ARVC occurs after surgical repair of congenital heart disease. The most common substrate for ventricular arrhythmias in this setting is the tetralogy of Fallot (TOF). In a 10-year follow-up of patients undergoing surgical repair of TOF, the incidence of sustained VT was 4% and sudden death was 2% [29]. Clinical predictors for sustained VT or sudden death in patients with repaired TOF include: age at repair; history of ventriculotomy; QRS duration >180 msec; presence of moderate pulmonic insufficiency; or male sex [29–37].

Substrate

Patients with ARVC presenting with VT invariably have perivalvular voltage abnormalities that extend apically in a cone-like distribution, usually involving the free wall of the RV and, to a lesser extent, the septum. There are three distinct patterns of perivalvular involvement [1]:

- Pattern 1 (25%): Low voltage involves the tricuspid valve only.
- Pattern 2 (25%): Low voltage involves the pulmonic valve only.
- Pattern 3 (50%): Low voltage involves both the tricuspid and the pulmonic valves.

The septal surface of the perivalvular regions are involved in 71% of cases, but the voltage abnormality is usually more pronounced on the free wall. The RV apex is often spared; however, the apical extension of the perivalvular scar can be prominent in many patients [1].

A significant minority of patients with ARVC will have epicardial voltage abnormalities that are out of proportion to the endocardial substrate. Tachycardia circuits with epicardial components may be more difficult to approach with an endocardial strategy, owing in part to the distance between the endocardial and epicardial surfaces around the perivalvular regions, which can exceed 2 cm in selected patients (Figure 25.4)

The surgical correction of TOF involves both patch closure of the ventricular septal defect (VSD) and resection of the stenotic portion of the right ventricular outflow tract (RVOT). A patch is placed along the ventriculotomy either in a subvalvular or transannular location. The arrhythmia substrate in repaired TOF results from fibrosis along the infundibular patch [38]. The extent of fibrosis is variable, and some patients exhibit a substantial voltage abnormality [39]. It is unclear whether this variability results from operative technique, patch size, or heterogeneity in the individual patient's response to injury.

Baseline ECG/VT Morphology

Although the baseline ECG can be normal some patients presenting with VT in the setting of ARVC, the most common abnormalities in affected patients include:

- *T*-wave inversion in the right precordial leads without RBBB (V1–V3) (85%).
- QRS widening in a right bundle delay pattern (50%).
- Epsilon waves.

Although epsilon waves are frequently confined to the anterior precordial leads, occasionally they can be identified in the inferior leads 2, 3, and aVF. The latter patients uniformly have perivalvular low-voltage areas with dramatic late potentials surrounding the inferior aspect of the tricuspid valve annulus. The Johns Hopkins group compared 50 ARVC patients with matched controls with VT from the RV outflow tract. They found that a delay in the terminal upstroke in V1–V3 (>55 msec) correlated with disease severity and VT inducibility at the time of EP testing [40].

In patients with ARVC referred for EP study at our institution, an average of 3.7 distinct VT morphologies per patient are induced. LBB morphologies predominate (93%) and are mapped within 3 cm of the tricuspid valve in 78% of cases. As stated previously, the induction of RBB morphologies may indicate concomitant perimitral scarring [1]. We have also demonstrated that epicardial pacemaps from the inferior RV more frequently have a *Q*-wave in leads II, III, and aVF than corresponding

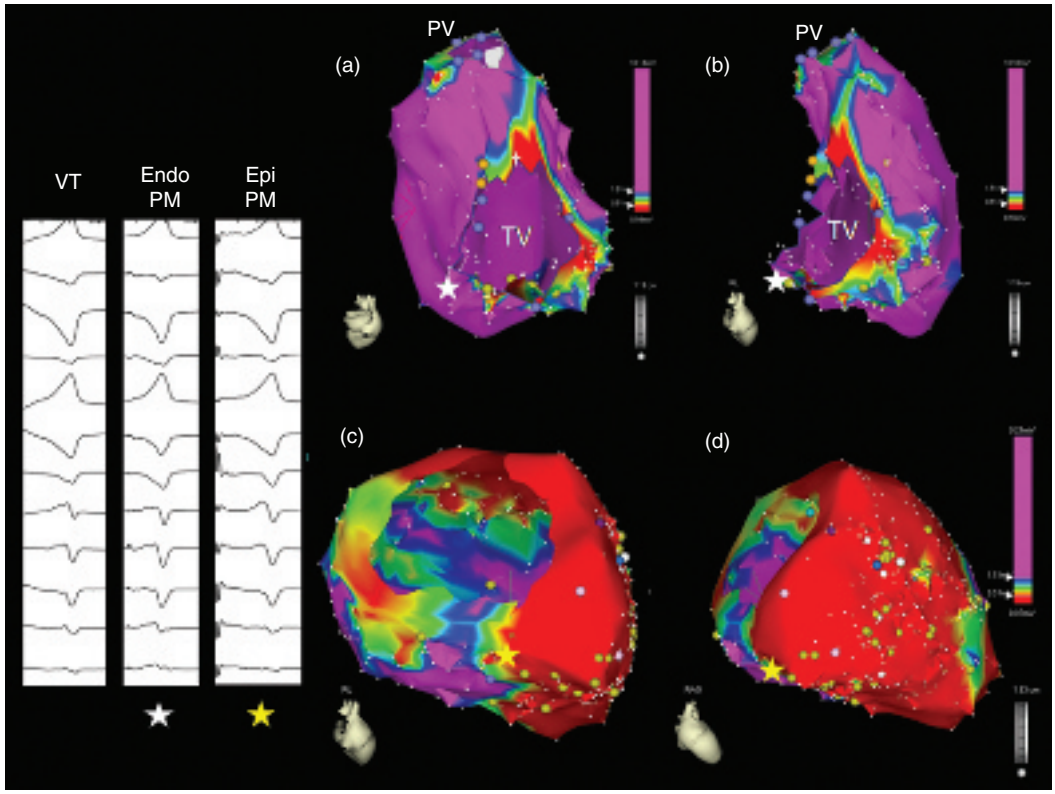

Figure 25.4 Images taken from a 47-year-old woman with right ventricular cardiomyopathy (RVCM) and recurrent VT. The endocardial bipolar voltage maps (panels a and b) reveal a small focal region of peri-tricuspid valve scarring. The epicardial map (panels c and d) revealed a more extensive, confluent region of low voltage that extended to the apical boundary of the RV. Low-voltage electrograms on the epicardium were frequently noted to also be fractionated with many late signals noted. In our experience, the more extensive epicardial voltage abnormality has been typical in patients with RVCM. Pacemapping along the epicardium (yellow star) more closely mimicked the spontaneous VT than the endocardial pacemap (white star). The VT was eliminated with ablation targeting the epicardium at the acute angle of the RV after endocardial ablation was unsuccessful.

endocardial sites. The presence of a *Q*-wave in lead I or a QS complex in lead V1 suggests an anterior RV epicardial origin for VT [3] (Figure 25.4).

In patients with TOF repair, the tachycardia usually propagates around the infundibular patch, and less frequently the VSD patch. The direction of propagation dictates the surface ECG morphology (Figure 25.5). Clockwise rotation around the patch demonstrates a left or right bundle, inferior axis tachycardia; right bundle tachycardias may reflect preferential LV septal activation. Counterclockwise rotation around the patch reveals a left bundle, superior axis tachycardia. Concomitant rotation around the septal VSD patch typically produces a right bundle morphology [41, 42]. A figure-of-eight reentry can also exit with circuits spinning simultaneously around the two fixed anatomic barriers.

Entrainment Mapping

As in LVCM, the majority of VT in the setting of RVCM is reentrant. In a series of 12 patients with ARVC referred for VT ablation, scar-based reentry was present in 67% of patients [43]. Traditional entrainment mapping is performed when possible, and is often limited in patients with rapid tachycardias or severely compromised right ventricular function (Figure 25.6).

In patients with TOF the critical zone of conduction differs among patients, and may result from

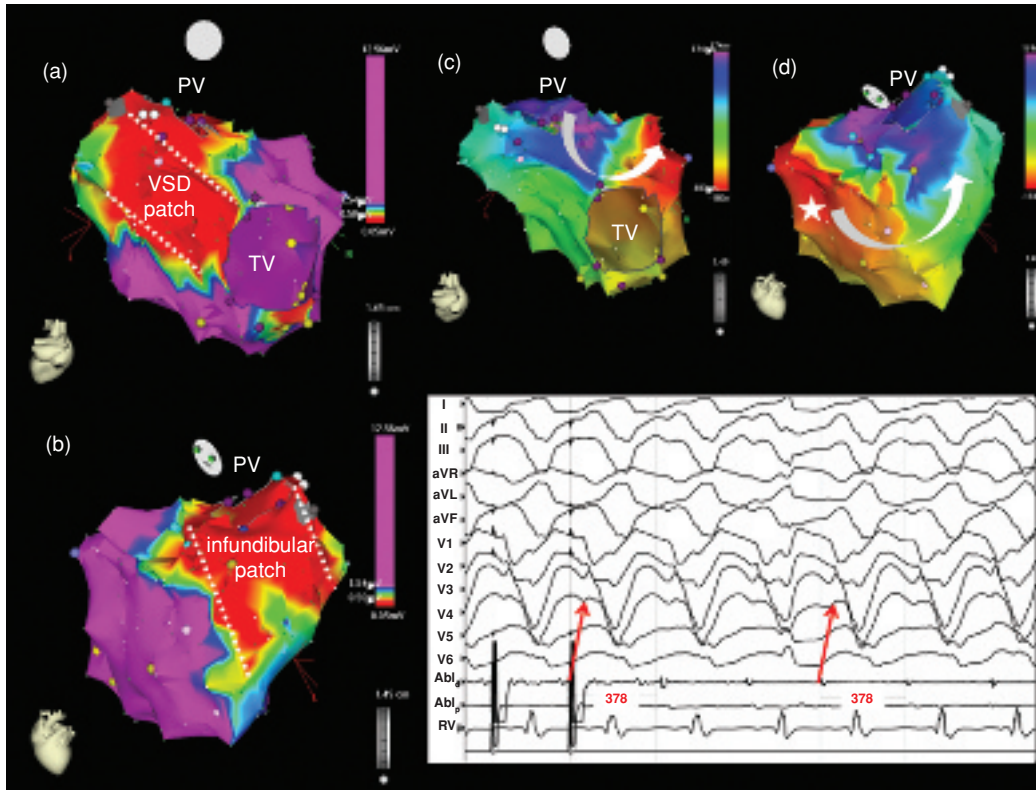

Figure 25.5 Images taken from a 56-year-old man with tetralogy of Fallot who had surgical correction 40 years previously consisting of an infundubular resection, pulmonic valve commisurotomy, and ventricular septal defect patch. He presented with recurrent VT with a left bundle, left superior axis morphology. Panels (a) and (b) demonstrate low-voltage regions corresponding to the infundibular scar (a) and the VSD patch (b). His clinical VT was induced with programmed stimulation; entrainment mapping was performed which revealed a broad, macroreentrant circuit that propagated around the infundibular scar (panels c and d). The intracardiac tracing was obtained from the region marked by the star in panel (d); it reveals entrainment with concealed fusion with a postpacing interval (PPI) equal to the tachycardia cycle length (TCL).

the surgical procedure performed. In patients with infundibular incisions originating below the pulmonic valve, the critical isthmus for the VT circuit often lies between the pulmonic valve and the top of the ventriculotomy scar [44]. Early surgical ablation experience involved targeting this region to complete the line of block to the pulmonic valve [39, 41, 42, 45].

The most common current ablation strategy for TOF VT involves creating a line of block through a critical tachycardia isthmus and connecting two inexcitable structures, most commonly the pulmonic valve or infundibular patch and the tricuspid annulus. In cases utilizing a transannular patch, there may be no residual conducting tissue between the patch and pulmonic valve. In these cases the patch may serve as a fixed conduction barrier and the tachycardia propagates around the patch inferiorly and passes between the tricuspid and pulmonic valves; interruption of conduction through this isthmus abolishes the tachycardia [46]. Bidirectional block across the linear lesion set is easily demonstrated by pacing on one side of the line and recording delayed and sequential activation on the opposite side of the line [46].

Pacemapping

Nonreentrant VT may occur in up to 30% of patients with RVCM [43]. As in LVCM, nonreentrant arrhythmias can be difficult to induce and often

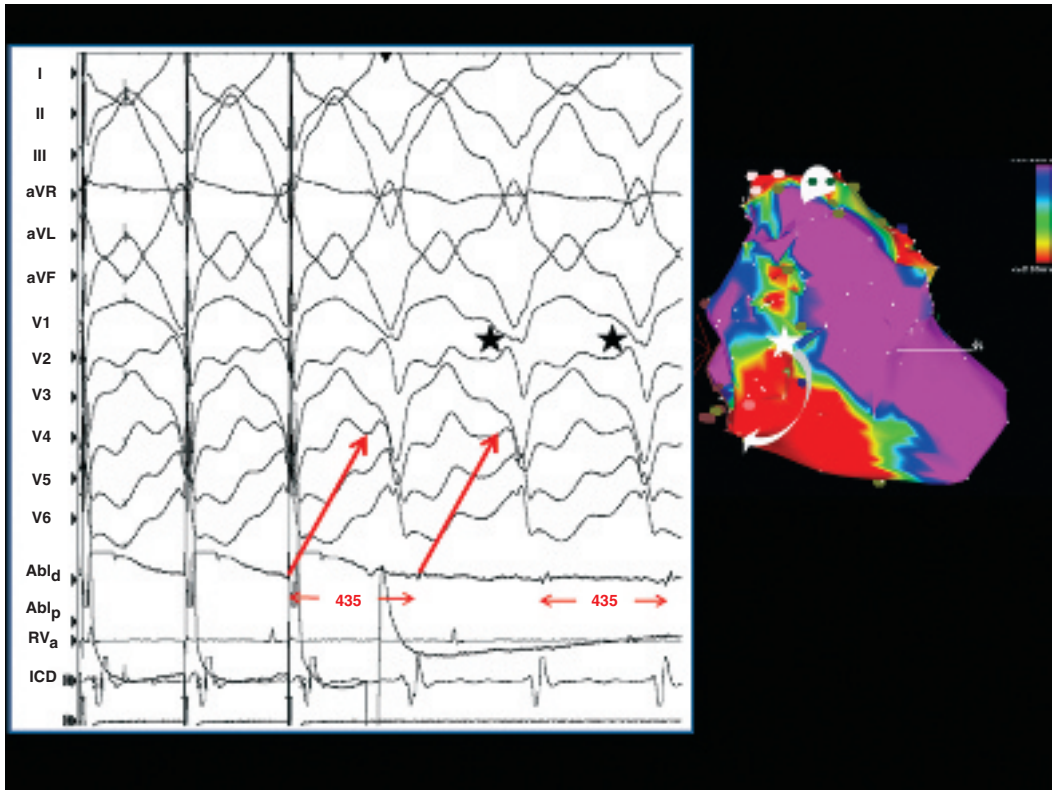

Figure 25.6 Images taken from a man with right ventricular cardiomyopathy who had recurrent left bundle branch morphology VT. His electroanatomical map is shown on the right panel and reveals a confluent area of scar involving the inferior aspect of the RV free wall with patchy extension superiorly toward the pulmonic valve. The patient's VT was well-tolerated and entrainment mapping was performed. The pacing site represented by the white star on the voltage map is shown on the left panel. Pacing during VT reveals a concealed fusion with a long stimulus-QRS interval (red arrows), consistent with an entrance site of the VT isthmus. The VT morphology demonstrates a characteristic pattern break with an initial R wave in V2 (black stars) which is typical for tachycardias exiting from the inferior septal aspect of the tricuspid annulus many centimeters from the entrance of the VT circuit. Most VT in the setting of RVCM is macroreentrant and can a large circuit can typically be identified.

require administration of agents such as isoproterenol. As stated above, patients with impaired RV function often demonstrate labile hemodynamics which can be exacerbated by beta agonists. In patients with poorly tolerated or noninducible arrhythmias, frequent isolated ventricular ectopy may help to identify preferential VT exit sites.

Early catheter-based experience also described successful ablation using sinus rhythm pacemapping and entrainment maneuvers in the RVOT in patients with prior TOF repair [47]. Given the breadth of the VT isthmus in some patients, focal ablation techniques are not appropriate when targeting macroreentrant circuits, and point lesion are usually extended to anatomic barriers to enhance circuit interruption.

Substrate Modification

If unmappable tachycardias are induced, then a substrate-based ablation strategy using linear lesions is performed [1]. As in LVCM, the approximate exit sites for induced arrhythmias are determined by pacemapping within and around the scar border zone in sinus rhythm. Linear lesion sets are constructed to incorporate the purported VT exit sites and extend into the dense scar. Abnormal electrograms characterized by late or fractionated

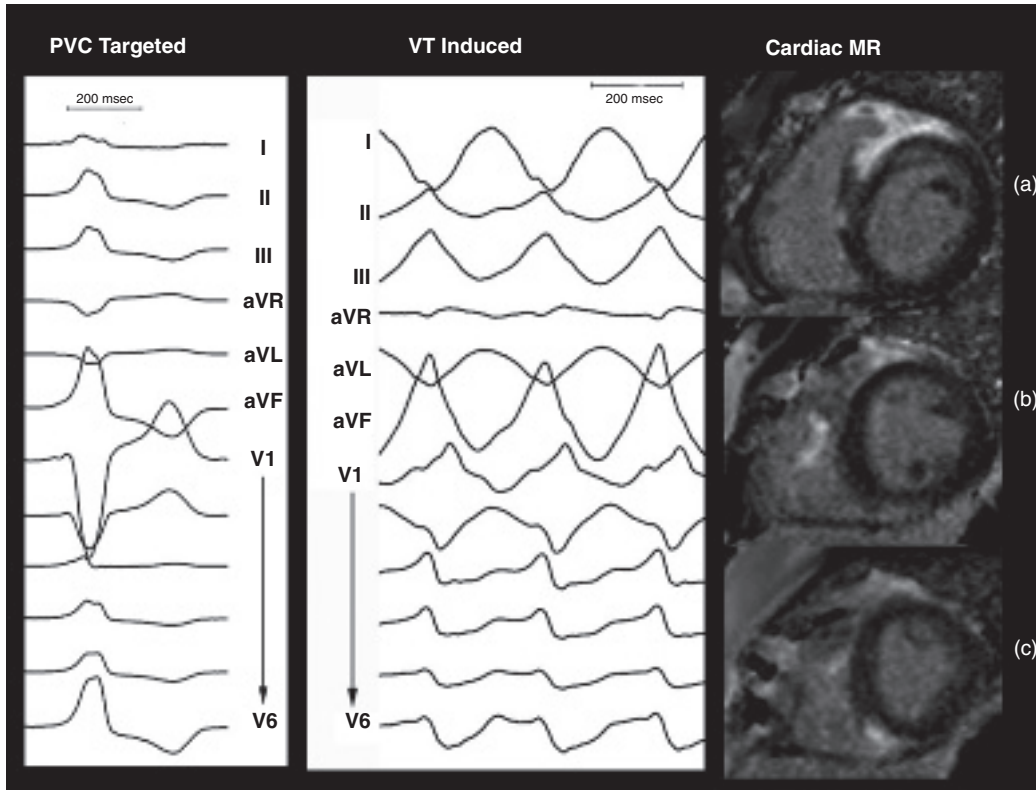

Figure 25.7 Images from a patient who presented with recurrent palpitations and mildly depressed LV function. Frequent, spontaneous ventricular ectopy (left panel) with a QRS morphology consistent with a site of origin from the right ventricular outflow tract. Initially the patient was thought to have a PVC-induced cardiomyopathy. However with programmed stimulation, a right bundle right inferior axis VT (middle panel) was consistently induced; the morphology of this tachycardia is most consistent with an epicardial LV exit (QS in lead I, "pattern break" in V1-V2-V3, and delayed intrinsicoid deflection). The patient's MR imaging (right panel) demonstrated a large region of delayed hyper-enhancement in the basal superior LV and interventricular septum. This case illustrates the importance of excluding the presence of a more diffuse myopathic process in many patients with nonischemic cardiomyopathy.

potentials are empirically targeted within the scar, thereby disconnecting surviving muscle bundles.

Combined Left and Right Ventricular Cardiomyopathy

The presence of combined LV and RV voltage abnormalities is important and under-recognized. In 19 patients with RV cardiomyopathy and VT who underwent biventricular mapping at our institution, five patients had significant LV voltage abnormalities involving the perimitral valve area. Four of the five patients with LV scar also had inducible VT, which was mapped and ablated from the LV [1]. Another series found that patients presenting with RV aneurysms or mural thrombosis were more likely to have concomitant LV involvement [48].

Careful assessment of preoperative assessment of biventricular function, as well as evaluation of the ECG morphology of tachycardias induced during EP study, may help identify these patients. For example, the induction of right bundle tachycardias in patients with right ventricular cardiomyopathy should raise suspicion about LV involvement (Figure 25.7).

Whether this more global disorder represents a sporadic or genetically predetermined response to injury remains unproven. We believe that these data suggest that triggers for initiation of a

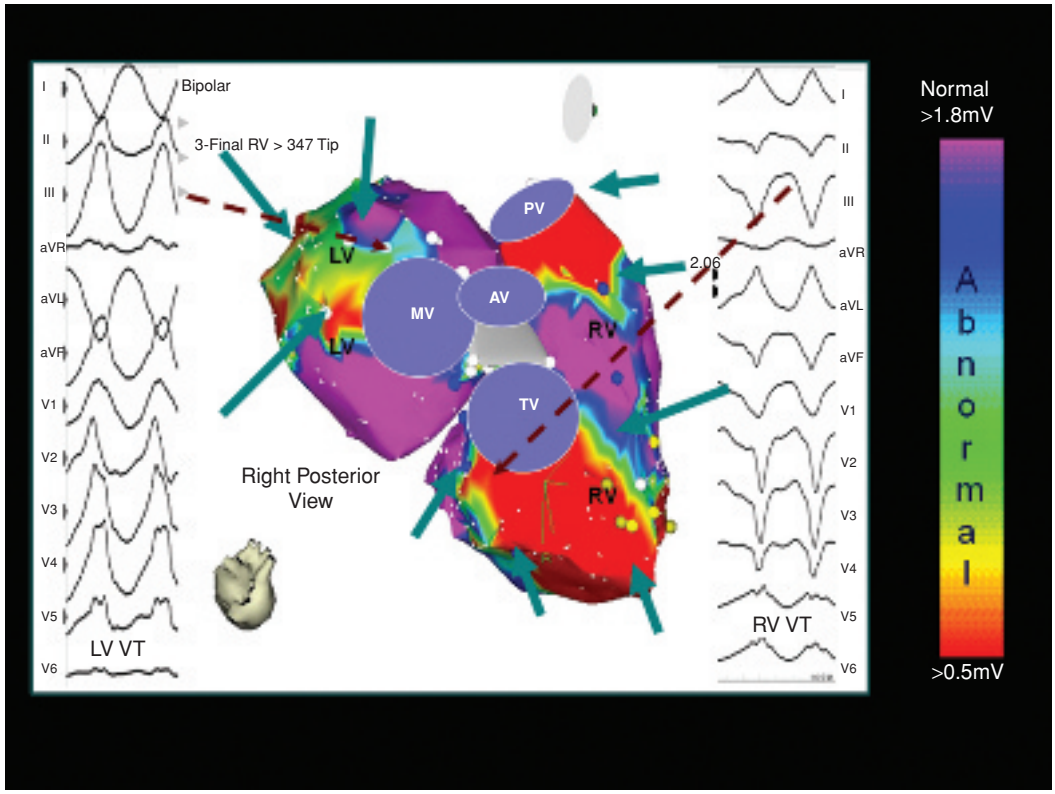

Figure 25.8 Images from patients with biventricular perivalvular low-voltage areas and RV and LV VT. Low-voltage region surrounds the peri-mitral, tricuspid and pulmonic valves. Left bundle branch block VT originated from the RV in the low-voltage region at the bottom of the tricuspid valve and right bundle branch block VT originates from the peri-mitral valve region. Biventricular involvement occurs more commonly than previously recognized and suggest a common pathogenesis in RV and LVCM.

cardiomyopathy may be common infections with subclinical pericarditis and myocarditis leading to more chronic fibrotic changes in susceptible individuals. These infectious triggers may act on a genotypic predisposition that prevents adequate healing and leads to postinflammatory fibrotic changes that frequently involve both the ventricular chamber and occasionally the right and left atrium. The thinner right ventricle may be more susceptible to mechanical stresses, thus explaining why those patients with desmosomal genetic abnormalities may manifest abnormalities in the right ventricle in response to a more generalized inflammatory response.

The diffuse nature of many cardiomyopathic processes should force the electrophysiologist involved with mapping and ablation procedures in nonischemic cardiomyopathy to be constantly vigilant for biventricular involvement (Figure 25.8). Detailed biventricular electroanatomic mapping, careful ECG analysis of spontaneous VT, and sophisticated imaging techniques should be the rule for many patients.

References

1 Marchlinski FE, Zado E, Dixit S, et al. Electroanatomic substrate and outcome of catheter ablative therapy for ventricular tachycardia in setting of right ventricular cardiomyopathy. *Circulation* 2004; **110**: 2293–98.

2 Berruezo A, Mont L, Nava S, Chueca E, Bartholomay E, Brugada J. Electrocardiographic recognition of the epicardial origin of ventricular tachycardias. *Circulation* 2004; **109**: 1842–47.

3 Bazan V, Bala R, Garcia FC, et al. Twelve-lead ECG features to identify ventricular tachycardia arising from the

epicardial right ventricle. *Heart Rhythm* 2006; **3**: 1132–39.

4 Meinertz T, Treese N, Kasper W, et al. Determinants of prognosis in idiopathic dilated cardiomyopathy as determined by programmed electrical stimulation. *Am J Cardiol* 1985; **56**: 337–41.

5 Meinertz T, Hofmann T, Kasper W, et al. Significance of ventricular arrhythmias in idiopathic dilated cardiomyopathy. *Am J Cardiol* 1984; **53**: 902–7.

6 Huang SK, Messer JV, Denes P. Significance of ventricular tachycardia in idiopathic dilated cardiomyopathy: observations in 35 patients. *Am J Cardiol* 1983; **51**: 507–12.

7 Das SK, Morady F, DiCarlo L, Jr, et al. Prognostic usefulness of programmed ventricular stimulation in idiopathic dilated cardiomyopathy without symptomatic ventricular arrhythmias. *Am J Cardiol* 1986; **58**: 998–1000.

8 Poll DS, Marchlinski FE, Buxton AE, Josephson ME. Usefulness of programmed stimulation in idiopathic dilated cardiomyopathy. *Am J Cardiol* 1986; **58**: 992–97.

9 Goedel-Meinen L, Hofmann M, Ryba S, Schomig A. Prognostic value of an abnormal signal-averaged electrocardiogram in patients with nonischemic dilated cardiomyopathy. *Am J Cardiol* 2001; **87**: 809–12, A9.

10 Mancini DM, Wong KL, Simson MB. Prognostic value of an abnormal signal-averaged electrocardiogram in patients with nonischemic congestive cardiomyopathy. *Circulation* 1993; **87**: 1083–92.

11 Pelliccia F, Critelli G, Cianfrocca C, et al. Interstitial fibrosis as a substrate of spontaneous nonsustained ventricular-tachycardia in idiopathic dilated cardiomyopathy. *J Am Coll Cardiol* 1994; **23**: 340A.

12 Lo YS, Billingham M, Rowan RA, Lee HC, Liem LB, Swerdlow CD. Histopathologic and electrophysiologic correlations in idiopathic dilated cardiomyopathy and sustained ventricular tachyarrhythmia. *Am J Cardiol* 1989; **64**: 1063–66.

13 Roberts WC, Siegel RJ, McManus BM. Idiopathic dilated cardiomyopathy: analysis of 152 necropsy patients. *Am J Cardiol* 1987; **60**: 1340–55.

14 Bardy GH, Lee KL, Mark DB, et al. Amiodarone or an implantable cardioverter–defibrillator for congestive heart failure. *N Engl J Med* 2005; **352**: 225–37.

15 Rassi A, Jr, Rassi A, Rassi SG. Predictors of mortality in chronic Chagas' disease: a systematic review of observational studies. *Circulation* 2007; **115**: 1101–8.

16 Sternick EB, Martinelli M, Sampaio R, et al. Sudden cardiac death in patients with Chagas' heart disease and preserved left ventricular function. *J Cardiovasc Electrophysiol* 2006; **17**: 113–16.

17 Rassi A, Jr, Rassi SG, Rassi A. Sudden death in Chagas' disease. *Arq Bras Cardiol* 2001; **76**: 75–96.

18 Hsia HH, Callans DJ, Marchlinski FE. Characterization of endocardial electrophysiological substrate in patients with nonischemic cardiomyopathy and monomorphic ventricular tachycardia. *Circulation* 2003; **108**: 704–10.

19 Cassidy DM, Vassallo JA, Marchlinski FE, Buxton AE, Untereker WJ, Josephson ME. Endocardial mapping in humans in sinus rhythm with normal left ventricles: activation patterns and characteristics of electrograms. *Circulation* 1984; **70**: 37–42.

20 Sosa E, Scanavacca M, D'Avila A, et al. Endocardial and epicardial ablation guided by nonsurgical transthoracic epicardial mapping to treat recurrent ventricular tachycardia. *J Cardiovasc Electrophysiol* 1998; **9**: 229–39.

21 Soejima K, Stevenson WG, Sapp JL, Selwyn AP, Couper G, Epstein LM. Endocardial and epicardial radiofrequency ablation of ventricular tachycardia associated with dilated cardiomyopathy: the importance of low-voltage scars. *J Am Coll Cardiol* 2004; **43**: 1834–42.

22 Bazan V, Gerstenfeld EP, Garcia FC, et al. Site-specific twelve-lead ECG features to identify an epicardial origin for left ventricular tachycardia in the absence of myocardial infarction. *Heart Rhythm* 2007; **4**: 1403–10.

23 Delacretaz E, Stevenson WG, Ellison KE, Maisel WH, Friedman PL. Mapping and radiofrequency catheter ablation of the three types of sustained monomorphic ventricular tachycardia in nonischemic heart disease. *J Cardiovasc Electrophysiol* 2000; **11**: 11–17.

24 Marchlinski FE, Callans DJ, Gottlieb CD, Zado E. Linear ablation lesions for control of unmappable ventricular tachycardia in patients with ischemic and nonischemic cardiomyopathy. *Circulation* 2000; **101**: 1288–96.

25 Marcus FI, Fontaine GH, Guiraudon G, et al. Right ventricular dysplasia: a report of 24 adult cases. *Circulation* 1982; **65**: 384–98.

26 Thiene G, Nava A, Corrado D, Rossi L, Pennelli N. Right ventricular cardiomyopathy and sudden death in young people. *N Engl J Med* 1988; **318**: 129–133.

27 Laurent M, Descaves C, Biron Y, Deplace C, Almange C, Daubert JC. Familial form of arrhythmogenic right ventricular dysplasia. *Am Heart J* 1987; **113**: 827–29.

28 Dalal D, Nasir K, Bomma C, et al. Arrhythmogenic right ventricular dysplasia: a United States experience. *Circulation* 2005; **112**: 3823–32.

29 Gatzoulis MA, Balaji S, Webber SA, et al. Risk factors for arrhythmia and sudden cardiac death late after repair of tetralogy of Fallot: a multicentre study. *Lancet* 2000; **356**: 975–81.

30 Harrison DA, Harris L, Siu SC, et al. Sustained ventricular tachycardia in adult patients late after repair of tetralogy of Fallot. *J Am Coll Cardiol* 1997; **30**: 1368–73.

31 Balaji S, Lau YR, Case CL, Gillette PC. QRS prolongation is associated with inducible ventricular tachycardia after repair of tetralogy of Fallot. *Am J Cardiol* 1997; **80**: 160–63.

32 Gatzoulis MA, Till JA, Redington AN. Depolarization–repolarization inhomogeneity after repair of tetralogy of

Fallot: the substrate for malignant ventricular tachycardia? *Circulation* 1997; **95**: 401–4.

33 Murphy JG, Gersh BJ, Mair DD, et al. Long-term outcome in patients undergoing surgical repair of tetralogy of Fallot. *N Engl J Med* 1993; **329**: 593–99.

34 Nollert GD, Dabritz SH, Schmoeckel M, Vicol C, Reichart B. Risk factors for sudden death after repair of tetralogy of Fallot. *Ann Thorac Surg* 2003; **76**: 1901–5.

35 Jonsson H, Ivert T, Brodin LA, Jonasson R. Late sudden deaths after repair of tetralogy of Fallot: electrocardiographic findings associated with survival. *Scand J Thorac Cardiovasc Surg* 1995; **29**: 131–39.

36 Hokanson JS, Moller JH. Significance of early transient complete heart block as a predictor of sudden death late after operative correction of tetralogy of Fallot. *Am J Cardiol* 2001; **87**: 1271–77.

37 Gatzoulis MA, Till JA, Somerville J, Redington AN. Mechanoelectrical interaction in tetralogy of Fallot: QRS prolongation relates to right ventricular size and predicts malignant ventricular arrhythmias and sudden death. *Circulation* 1995; **92**: 231–37.

38 Deuchar D, Lopez Bescos L, Chakorn S. Fallot's tetralogy. A 20-year surgical follow-up. *Br Heart J* 1972; **34**: 12–22.

39 Downar E, Harris L, Kimber S, et al. Ventricular tachycardia after surgical repair of tetralogy of Fallot: results of intraoperative mapping studies. *J Am Coll Cardiol* 1992; **20**: 648–55.

40 Nasir K, Bomma C, Tandri H, et al. Electrocardiographic features of arrhythmogenic right ventricular dysplasia/cardiomyopathy according to disease severity: a need to broaden diagnostic criteria. *Circulation* 2004; **110**: 1527–34.

41 Horowitz LN, Vetter VL, Harken AH, Josephson ME. Electrophysiologic characteristics of sustained ventricular tachycardia occurring after repair of tetralogy of Fallot. *Am J Cardiol* 1980; **46**: 446–52.

42 Kugler JD, Pinsky WW, Cheatham JP, Hofschire PJ, Mooring PK, Fleming WH. Sustained ventricular tachycardia after repair of tetralogy of Fallot: new electrophysiologic findings. *Am J Cardiol* 1983; **51**: 1137–43.

43 Miljoen H, State S, de Chillou C, et al. Electroanatomic mapping characteristics of ventricular tachycardia in patients with arrhythmogenic right ventricular cardiomyopathy/dysplasia. *Europace* 2005; **7**: 516–24.

44 Josephson ME. *Clinical Cardiac Electrophysiology: Techniques and Interpretations*. 3rd ed. Lippincott, Williams, & Wilkins, Philadelphia, PA, 2002.

45 Harken AH, Horowitz LN, Josephson ME. Surgical correction of recurrent sustained ventricular tachycardia following complete repair of tetralogy of Fallot. *J Thorac Cardiovasc Surg* 1980; **80**: 779–81.

46 Horton RP, Canby RC, Kessler DJ, et al. Ablation of ventricular tachycardia associated with tetralogy of Fallot: demonstration of bidirectional block. *J Cardiovasc Electrophysiol*. 1997; **8**: 432–35.

47 Burton ME, Leon AR. Radiofrequency catheter ablation of right ventricular outflow tract tachycardia late after complete repair of tetralogy of Fallot using the pace mapping technique. *Pacing Clin.Electrophysiol* 1993; **16**: 2319–25.

48 Basso C, Thiene G, Corrado D, Angelini A, Nava A, Valente M. Arrhythmogenic right ventricular cardiomyopathy: dysplasia, dystrophy, or myocarditis? *Circulation* 1996; **94**: 983–91.

26 CHAPTER 26

Role of Mapping in Arrhythmogenic Right Ventricular Cardiomyopathy

Molly Sachdev, MD, MPH, *Hugh Calkins,* MD

The Johns Hopkins University School of Medicine, Baltimore, MD, USA

Summary

Arrhythmogenic right ventricular dysplasia/cardiomyopathy (ARVD) is a genetic cardiomyopathy characterized by progressive replacement of right ventricular myocardium with fatty and fibrous tissue [1, 2]. The prevalence of ARVD has been estimated to be 1 in 5000 in the United States. Ventricular tachycardia (VT) is the most feared complication in patients with ARVD. The main objective of ARVD management is to prevent sudden cardiac death and symptomatic ventricular arrhythmias. Implantable cardioverter defibrillators remain the cornerstone of strategies to prevent sudden cardiac death in this patient population. Antiarrhythmic drugs and catheter ablation are used primarily as adjunctive procedures in patients with ARVD who are experiencing frequent symptomatic episodes of nonsustained or sustained ventricular arrhythmias

The purpose of this chapter is twofold. Firstly, we seek to provide a concise review of the approaches to diagnosis and management of patients with ARVD. Secondly, we seek to review the role of electrical and electroanatomic mapping in both diagnosis and management of patients with ARVD.

Diagnosis of ARVD

The diagnosis of ARVD is established based on the criteria set by the Task Force of the Working Group of Myocardial and Pericardial Disease of the European Society of Cardiology and of the Scientific Council on Cardiomyopathies of the International Society and Federation of Cardiology [3]. These criteria are shown in Table 26.1.

Specific cardiac tests that are recommended in all patients suspected of having ARVD include an ECG; a signal-averaged ECG (SAECG), a Holter monitor, and an echocardiogram. Exercise stress testing should also be performed. When appropriate, more detailed analysis of RV size and function can be provided by cardiac MR and/or CT. If the results of the noninvasive tests point toward a diagnosis of ARVD, invasive testing including endomyocardial biopsy, right ventricular angiography, and electrophysiology testing are recommended to establish the diagnosis and to help provide further information to guide treatment recommendations.

Cardiac Mapping, Third Edition Edited by Mohammad Shenasa, Gerhard Hindricks, Martin Borggrefe, and Günter Breithardt
 ISBN: 978-1-405-17572-2

Table 26.1 Diagnostic Criteria for ARVD/C.[a]

	Major Criteria	*Minor Criteria*
Structural or functional abnormalities	1. Severe dilation and reduction of RVEF with mild or no LV involvement 2. Localized RV aneurysm (akinetic or dyskinetic areas with diastolic bulging) 3. Severe segmental dilatation of the RV	1. Mild global RV dilation and/or EF reduction with normal LV 2. Mild segmental dilation of the RV 3. Regional RV hypokinesis
Tissue characterization	Infiltration of RV by fat with presence of surviving strands of cardiomyocytes	
ECG depolarization/ conduction abnormalities	1. Localized QRS complex duration >110 msec in V1, V2, or V3 2. Epsilon wave in V1, V2, or V3	Late potentials in SAECG
ECG repolarization abnormalities		Inverted *T*-waves in right precordial leads (V2-V3 above age 12 yr in absence of RBBB)
Arrhythmias		1. LBBB VT (sustained or nonsustained) on ECG, Holter or ETT 2. Frequent PVCs (>1000/24 hr on Holter)
Family history	Family history of ARVD confirmed by biopsy or autopsy	1. Family history of premature sudden death (<35 yr) due to suspected ARVD 2. Family history of clinical diagnosis based on present criteria

[a] The criteria state that an individual must have two major, or one major plus two minor, or four minor criteria from different categories to meet the diagnosis of ARVD/C.

Electrocardiographic Evaluation

ECG abnormalities are detected in up to 90% of ARVD patients. *T*-wave inversion (TWI) in leads V1–V3 is a well-established ECG feature of ARVD, and in the absence of a RBBB is considered as a minor diagnostic criterion, present in 87% of patients with ARVD.

Another typical ECG feature of ARVD is the "epsilon wave," which are "postexcitation" electrical potentials of small amplitude that occur at the end of the QRS complex and at the beginning of the ST segment. Epsilon waves are seen in 33% of ARVD patients and are considered a major diagnostic criterion for ARVD. Slowed electrical conduction in the right ventricle, as a result of ARVD, may also cause localized widening of QRS complex ($\geq$110 msec) in the right precordial leads, which is observed in 64% of the patients. Prolonged *S*-wave upstroke in V1 through V3 $\geq$ 55 msec is the most prevalent ECG feature and correlates with disease severity and induction of ventricular tachycardia on electrophysiological study [4]. Late potentials on signal-averaged ECG (SAECG) recordings are the counterpart of the epsilon waves and are considered a minor criterion for the diagnosis of ARVD [5].

Imaging of the Right Ventricle

Right ventricular size and function can be evaluated using a variety of imaging modalities including echocardiography, angiography, CMR, and CT. According to the Task Force criteria, a major criterion for ARVD is defined as the presence of severe dilatation and/or functional loss of the RV. A less severe abnormality of RV size and/or function is considered to be minor criteria for ARVD. It can be appreciated that the Task Force Criteria are fairly nonspecific, in that no definition of "severe" vs. "less severe" has been agreed on. Although each of the available modalities for evaluation of RV size and function can detect severe structural abnormalities of the RV, the diagnostic accuracy of these tests is less certain when used for evaluation of patients with mild disease.

Myocardial Biopsy

Performance of an endomyocardial biopsy is commonly performed in the evaluation of patients with suspected ARVD. This technique is most sensitive when performed on the free wall at a site of regional RV dysfunction or thinning. It is important to recognize that ARVD can be a patchy disease and that clear evidence for the diagnosis will only be obtained in one-third of affected individuals. However, when the biopsy shows fibrotic or fiboyfatty myocyte replacement, with less than 65% residual myocytes the diagnosis of ARVD is clearly established [3]. An endomyocardial biopsy is also useful in excluding other conditions such as sarcoidosis, which can be confused with ARVD [6].

Genetics and Pathophysiology

ARVD is a heritable condition, typically with an autosomal dominant pattern of inheritance and variable penetrance. Most studies have reported a familial pattern of disease in approximately one-third of probands [7]. ARVD is primarily a disease of desmosomes. To date, eleven different genetic variants of ARVD have been mapped [8–13].

Identification of a gene abnormality in a family member does not provide definitive information regarding risk. The presence of an abnormal gene does not determine the phenotypic expression that can be variable. Middle-aged family members with specific mutations have been identified who have no evidence of the disease. However, genetic analysis may be of clinical value in identifying those offspring that need to be followed most intensively for the development of ARVD. While absence of this mutation does not totally exclude the risk of development of ARVD, our experience suggests that it is much less likely to develop. In contrast, if the offspring does carry a specific mutation more intensive screening for identification of early ARVD (i.e., biannual noninvasive testing after puberty) and/or restriction of athletic activity may be warranted.

Differential Diagnosis

Although it is not difficult to diagnose an overt case of ARVD, differentiation of ARVD at its early stages from idiopathic ventricular tachycardia (IVT), a usually benign and nonfamilial arrhythmic condition, remains a clinical challenge [14, 15]. Most recently, as described below, it has been shown that voltage mapping may also help differentiate the two conditions.

It is extremely important to determine if the patient has IVT or ARVD for two reasons. Firstly, IVT is a benign condition that is not associated with a risk of sudden death and therefore is not an indication for placement of an ICD. In contrast, there is a clear association between ARVD and sudden cardiac death. For this reason, many patients with ARVD undergo placement of an ICD. Secondly, ARVD is hereditary, whereas IVT is not. As a result, when a diagnosis of ARVD is made, screening of all first-degree family members is recommended.

Ventricular Tachycardia in ARVD

Ventricular tachycardia in ARVD is common and is felt to be similar mechanistically to ischemic scar–mediated VT. Areas of fibrofatty infiltration in ARVD form inexcitable "islets" or anatomic barriers which, combined with areas of slow conduction, allow for reentrant circuits to form. Most patients with VT have predominately left bundle branch VT that can be from multiple right ventricular sites and demonstrate variable morphology.

There has been one report of up to twelve different types of VT in one individual with the disease [16]. RBBB VT rarely occurs and usually indicates left ventricular involvement. The ventricular arrythmias that originate in the right ventricle may be asymptomatic and detected by routine ECG or they may cause palpitations, syncope, or sudden cardiac death [17]. ICD implantation is recommended in the United States for all patients with a definitive diagnosis of ARVD. Antiarrhythmic drugs have been tried with some success at palliation. Catheter ablation has also been employed for treatment of ventricular tachycardia in ARVD since the early 1990s [18].

ICD Implantation

A decision to implant an ICD is critically important because many of these patients are young, asymptomatic, and have a long life expectancy. ICDs are not complication-free and require replacement every five years. In addition, the probability of lead

failure increases with time given the progressive nature of the disease.

Although the precise indications for ICD implantation in patients with ARVD are not well defined, we recently reported that the incidence of appropriate therapy was greater for patients with definite compared with probable ARVD, for patients with positive electrophysiologic study, for patients who received the device for secondary prevention, and in patients with PKP2 mutations [19, 20].

We recommend ICD implantation for all patients who meet the strict Task Force criteria for ARVD. Per the American Heart Association recommendations, an ICD should be implanted in all patients for secondary prevention and for primary prevention in patients with ARVD and any of the following high-risk features: extensive RV disease; LV involvement; one or more affected family members with SCD; or unexplained syncope consistent with a tachyarrhythmia (Grade 2C) [21].

Electrophysiology and Electroanatomic Mapping in ARVD

Mapping of the right ventricle either using standard electrophysiologic technique or facilitated with an electroanatomic mapping system may be of value both in the diagnosis of ARVD and with catheter ablation of ventricular tachycardia. In this section, we will review the results of studies of electroanatomic mapping of the right ventricle in differentiating ARVD from normal patients. We will then discuss the role of mapping in performance of catheter ablation of ventricular tachycardia.

Electroanatomic Mapping of the Right Ventricle and Diagnosis of ARVD

As ARVD VT can be difficult to differentiate from idiopathic VT, some have advocated using electroanatomic voltage mapping to aid in the diagnosis. Boulos and colleagues performed two studies that showed that ARVD is often characterized by multiple low-voltage areas as compared both to control patients who have no evidence of VT and patients with RVOT VT.

In their first study, completed in 2001, they performed voltage mapping of seven subjects who met Task Force criteria for ARVD as compared to six subjects who were undergoing electrophysiologic study for evaluation of supraventricular arrythmias and had no evidence of right ventricular disease. In both groups of patients, there was regional variation in voltage, with the septum characterized by the highest values and the outflow tract with the lowest values. The areas of dysfunctional RV also exhibited abnormally low-amplitude electrograms. The normal voltage values observed in the control group (unipolar: 11.9 ± 0.3 mV; bipolar: 4.6 ± 0.2 mV [mean $\pm$ SEM]) and in the unaffected zones in the ARVD group (unipolar: 10.4 ± 0.2 mV; bipolar: 4.6 ± 0.2 mV) were reduced significantly in the dysplastic areas (unipolar: 3.3 ± 0.1 mV; bipolar: 0.5 ± 0.1 mV).

These low-voltage areas mainly involved the RV anterolateral free wall, apex, and inflow and outflow tracts and ranged from small discrete areas to more extensive involvement. The pathologic electroanatomic findings were concordant with MRI and echocardiographic findings [22]. A representative color-coded CARTO voltage map of a patient with ARVD, adapted from their published work, is displayed in Figure 26.1. Pathologic areas of low voltage are displayed in red and normal myocardium is shownin purple.

In 2005, the same group further considered the value of voltage mapping in differentiating patients with ARVD compared to idiopathic ventricular tachycardia. This study consisted of three groups, twelve patients with RVOT tachycardia, nine patients who had ARVD based on Task Force criteria, and nine control patients who were undergoing electrophysiologic study for a variety of supraventricular arrhythmias. They concluded that endocardial electrographic parameters do not differ between patients who have RVOT tachycardia and control patients and is characterized by preserved voltage and short durations throughout the right ventricle. Durations were measured manually as the time between the earliest electrical activity to the onset of the decay artifact. Patients with ARVD, however, have lower amplitude, prolonged electrographic duration, and a decreased amplitude/duration ratio as compared with the unaffected zones in the same hearts and with all regions in the RVOT tachycardia and control groups [23].

Miljoen and colleagues further characterized the electroanatomic mapping characteristics of patients

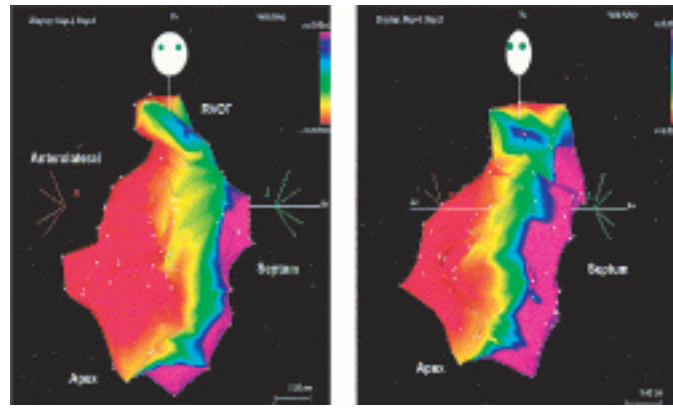

Figure 26.1 Electroanatomic map of the right ventricle (RV) in a patient with ARVD. Anteroposterior (left) and left anterior oblique (right) views of the RV unipolar voltage maps of the same patient. There is an extensive area of low voltage (red indicates <2 mV) in the apex and anterolateral free wall, with the septum being spared (purple indicates >5 mV). Intermediate colors represent border zones. KEY: LA = left atrium; RA = right atrium; RVOT = right ventricular outflow tract. Adapted and reprinted with permission from Ref. 22

with ARVD. Eight maps were obtained during sinus rhythm with low-voltage areas observed on all maps. Four patients were found to have low-voltage areas localized close to the tricuspid annulus on the lateral free wall and/or the inferior wall of the right ventricle; two other patients had a low-voltage area on the RV outflow tract (posterior wall and lateral wall); and the remaining two patients had multiple low-voltage areas. These low-voltage areas corresponded to the abnormal zones (thickening, akinesia, bulging) described on magnetic resonance imaging for whom this test was available [24].

Electroanatomic Mapping and Histologic Correlation in ARVD

The results of electroanatomic mapping have also been found to correlate well with pathologic findings on endomyocardial biopsy in addition to the other imaging modalities mentioned above.

In 2005, Corrado et al. showed that low-amplitude areas found at voltage mapping were associated with myocyte loss and fibrofatty replacement at endomyocardial biopsy. His group evaluated 31 patients who fulfilled Task Force criteria for ARVD after noninvasive evaluation, and performed both RV electroanatomic voltage mapping and endomyocardial biopsy to validate the diagnosis. Twenty of 31 patients had an abnormal RV electroanatomic voltage mapping showing more than one area with bipolar electro-grams with voltage values <0.5 mV.

Low-voltage areas were sharply demarcated and typically surrounded by a border zone with reduced signal amplitudes (0.5–1.5 mV), which merged into normal myocardium (>1.5 mV). These low-voltage areas were also significantly correlated with echocardiographic or angiographic RV wall motion abnormalities as well as pathologic findings at biopsy. Eleven of 31 patients, however, showed preserved electrogram voltage, histopathological evidence of inflammatory cardiomyopathy, and a more benign clinical course [25]. Figure 26.2 is taken from their work and shows an example of an abnormal voltage map and corresponding endomyocardial biopsy.

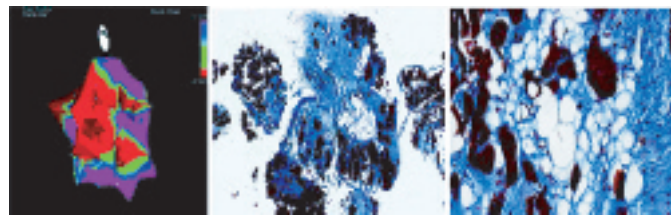

Figure 26.2 Endomyocardial biopsy in a representative patient with abnormal RV electroanatomic voltage map. (Left) Right anterior oblique view of RV bipolar voltage map showing low-voltage values (red indicates <0.5 mV) in anteroinfundibular, inferobasal, and apical regions. (Middle) EMB sample showing massive myocardial atrophy and fibrofatty replacement (trichrome; magnification 6×). (Right) Close-up showing residual myocytes entrapped within fibrous and fatty tissue (trichrome; magnification 40×). Adapted and reprinted with permission from Ref. 25.

In 2008, the same group furthered their findings and performed voltage mapping and endomyocardial biopsy in 27 patients with presumed right ventricular outflow tract tachycardia and no echocardiographic/angiographic evidence of right ventricular dysfunction. Electroanatomical voltage mapping was normal in 20 of 27 patients. The other seven patients, however, showed electroanatomical scar areas that correlated with fibrofatty myocardial replacement at biopsy. They concluded that electroanatomical mapping is able to identify a subgroup of patients with RVOT tachycardia and concealed ARVD by detecting RVOT electroanatomical scars on voltage mapping that correlates well with fibrofatty myocardial replacement at biopsy [26].

Therefore, although voltage mapping is not specifically a task force criterion for diagnosis of ARVD, in cases of clinical uncertainty, some have successfully used voltage mapping. Multiple areas of low voltage specifically surrounding the tricuspid valve are considered to be highly suggestive of the disease and correlates with biopsy findings. It is our experience, however, that low voltage does not necessarily imply diseased myocardium but commonly results from poor tissue contact. This is particularly true in regions of the RV near the tricuspid valve. We have seen a large number of patients overdiagnosed /misdiagnosed with ARVD based on low voltage observed at the time of electroanatomic mapping. Based on this experience, we urge electrophysiologists to use great caution when considering a diagnosis of ARVD when the only evidence for this disease is low voltage on an electroanatomic map.

Further research is needed to determine if electroanatomic mapping provides information that will facilitate the early diagnosis of ARVD. It is notable in this regard that most studies to date have been performed in patients with overt ARVD in which the diagnosis is not in question. Therefore, although the initial studies appear promising, we do not recommend voltage mapping as a diagnostic strategy at this time.

Role of Mapping in Catheter Ablation of VT in Patients with ARVD

Electroanatomic mapping has also been used as a tool to guide catheter ablation of VT in patients with ARVD. In 2003, Reithmann and his group were among the first to successfully use this strategy among five patients with recurrent VT. Three-dimensional electroanatomic activation maps were created with the CARTO system, which allows detailed reconstruction of chamber geometry. The maps of the ventricular tachycardias revealed a homogenous propagation of electrical activity from the site of earliest activity. These sites were found to be in an aneurysmal outflow tract in two patients, at the border of aneurysms near the tricuspid valve in two patients, and at the border of an apical aneurysm in a single patient. Radiofrequency current was applied to the site of earliest activity, which led to termination in three patients and rendered the "clinical" ventricular tachycardia noninducible in four patients. Overrall in the 7 ± 3 months of postprocedure follow-up, the amount of ventricular tachycardia was greatly reduced [27].

Marchlinski et al. performed catheter ablation in 19 patients with clinical evidence of ARVD also through the use of electroanatomic mapping. All patients underwent detailed right ventricular voltage mapping and most underwent left ventricular voltage mapping. In addition, activation and entrainment mapping were used in three patients with hemodynamically stable VT; in the remaining 16 patients with unmappable VT, substrate mapping was used.

Linear lesions were made with the site of ablation guided by pace mapping. These lesions were extended from the most abnormal myocardium with a signal amplitude of less than 0.5 mV through to the valve annulus or normal myocardium with a signal amplitude of greater than 1.5 mV. Seventeen of 19 patients had no VT after ablation during a mean follow-up of 27 ± 22 months. The other two patients had infrequent occurrences.

However, the long-term efficacy results in this study may be overstated as 68% patients underwent a second ablation procedure. The long-term single-procedure success rate in this series was $<35\%$. Their group also concluded that endocardial bipolar voltage abnormalities tend to be perivalvular and predominately involve the RV free wall, although the septum is also commonly affected, and the apex is generally spared [28].

Verma et al. reported their experience in 22 patients with ARVD/C, each of whom had

hemodynamically unstable VT. They used a similar ablation strategy as the Marchlinski group. Voltage mapping was performed to define areas of scar (<0.5 mV) and abnormal myocardium (0.5–1.5 mV). Linear lesions were created in these abnormal regions, targeting sites with pace maps similar to the patients clinical VT. The lesions either connected the abnormal region to a valve continuity or other scar, or encircled the abnormal region. Acute success with no inducible VT at the end of the procedure was achieved in 18 (82%) patients, with VT recurrence rates of 23%, 27%, and 47% at 1, 2, and 3 years, respectively. They concluded that although acute successes are high, recurrences are frequent during long-term follow-up [29].

Most recently, our group has published data on 24 patients enrolled in the Johns Hopkins ARVD registry, who underwent one or more RFA procedures for treatment of VT. A total of 48 RFA procedures across multiple centers were performed using both 3D electroanatomical and conventional mapping similar to the other groups and patients were followed up for 32 ± 36 months. Of these procedures, 22 (46%), 15 (31%), and 11 (23%) resulted in elimination of all inducible VTs, clinical VT but not all, and none of the inducible VTs, respectively. Forty (85%) procedures were followed by recurrence. The cumulative VT recurrence-free survival was 75%, 50%, and 25% after 1.5, 5, and 14 months, respectively. The cumulative VT recurrence-free survival did not differ by procedural success, mapping technique, or repetition of procedures. The high rate of recurrence in our study, and others, likely reflects the fact that ARVD/C is a diffuse cardiomyopathy with progressively evolving electrical substrate [30].

The results of these studies have several obvious and immediate clinical implications. Firstly, the very high rate of VT recurrence reported in studies of catheter ablation of VT in ARVD patients makes it clear that catheter ablation of VT in ARVD patients cannot and should not be considered curative. Although the precise indications for ICD implantation in ARVD are not well established, we recommend ICD implantation for all patients who meet the strict Task Force criteria for ARVD [31].

Secondly, the results of this and other studies of catheter ablation of VT in patients with ARVD call into question the early use of catheter ablation as an effective antiarrhythmic strategy in these patients. Although there is some anecdotal evidence to suggest that catheter ablation of VT may decrease the frequency of VT episodes and appropriate ICD shocks in this patient population, this has not been well studied.

In fact, there have been no large studies that have closely examined the frequency of ICD shocks before and after catheter ablation of VT in ARVD patients. Even if these data were available, the results may reflect the clustering of VT episodes. In this regard, it is notable that in a recent case report, the ARVD patient with "VT storm" responded to treatment with antiarrhythmic drugs [32].

It is clear that further studies will be needed to determine the clinical role of catheter ablation of VT in patients with ARVD. Until these data are available, we recommend that catheter ablation of VT in patients with ARVD only be used as a palliative procedure to reduce the frequency of VT episodes, particularly after failure of one or more antiarrhythmic drugs. Moreover, we recommend that these procedures be performed at centers highly experienced with catheter ablation of ventricular arrhythmias.

Conclusion

ARVD is a rare but important cause of ventricular arrhythmias and sudden cardiac death. Although the diagnosis of ARVD in patients with a severe form of the disease is fairly straightforward, patients with more mild disease are challenging. Electroanatomic mapping of the right ventricle has an important and established role in the facilitation of catheter ablation in patients with hemodynamically unstable VT.

In contrast, the role of electroanatomic mapping in the diagnosis of ARVD is less well established. Although some studies have presented data to support a role for electroanatomic mapping in the diagnosis of ARVD, our experience suggests that the role is limited. We feel that great caution should be used when considering the presence of "low voltage" on an electroanatomic map to be suggestive or diagnostic of ARVD. We have found that it is far more likely that the areas of low voltage result from poor catheter–tissue contact. Other limitations of using electroanatomic mapping as a diagnostic tool are the associated expense and invasive nature of this type of diagnostic test.

References

1 Marcus FI, Fontaine GH, Guiraudon G, et al. Right ventricular dysplasia: a report of 24 adult cases. *Circulation* 1982; **65**: 384–98.

2 Marcus FI, Fontaine G. Arrhythmogenic right ventricular dysplasia/cardiomyopathy: a review. *Pacing Clin Electrophysiol* 1995; **18**: 1298–314.

3 McKenna WJ, Thiene G, Nava A, et al. Diagnosis of arrhythmogenic right ventricular dysplasia/cardiomyopathy. Task Force of the Working Group Myocardial and Pericardial Disease of the European Society of Cardiology and of the Scientific Council on Cardiomyopathies of the International Society and Federation of Cardiology. *Br Heart J* 1994; **71**: 215–18.

4 Nasir K, Bomma C, Tandri H, et al. Electrocardiographic features of arrhythmogenic right ventricular dysplasia/cardiomyopathy according to disease severity: a need to broaden diagnostic criteria. *Circulation* 2004; **110**: 1527–34.

5 Breithardt G, Cain ME, el-Sherif N, et al. Standards for analysis of ventricular late potentials using high-resolution or signal-averaged electrocardiography: a statement by a Task Force Committee of the European Society of Cardiology, the American Heart Association, and the American College of Cardiology. *Circulation* 1991; **83**: 1481–88.

6 Shiraishi J, Tatsumi T, Shimoo K, et al. Cardiac sarcoidosis mimicking right ventricular dysplasia. *Circ J* 2003; **67**: 169–71.

7 Dalal D, Nasir K, Bomma C, et al. Arrhythmogenic right ventricular dysplasia: a United States experience. *Circulation* 2005; **112**: 3823–32.

8 Ahmad F. The molecular genetics of arrhythmogenic right ventricular dysplasia-cardiomyopathy. *Clin Invest Med* 2003; **26**: 167–78.

9 Gerull B, Heuser A, Wichter T, et al. Mutations in the desmosomal protein plakophilin-2 are common in arrhythmogenic right ventricular cardiomyopathy. *Nat Genet* 2004; **36**: 1162–64.

10 Heuser A, Plovie RE, Ellinor TP, et al. Mutant desmocollin-2 causes arrhythmogenic right ventricular cardiomyopathy. *Am J Hum Genet* 2006; **79**: 1081–88.

11 Syrris P, Ward D, Asimaki A, et al. Clinical expression of plakophilin-2 mutations in familial arrhythmogenic right ventricular dysplasia. *Circulation* 2006; **113**: 356–64.

12 Dalal D, Lorraine H, Calkins H, et al. Clinical features of arrhythmogenic right ventricular dysplasia/ cardiomyopathy associated with mutations in plakophilin-2. *Circulation* 2006; **113**: 1641–49.

13 Pilichou K, Nava A, Basso C, et al. Mutations in demoglein-2 gene are associated with arrhythmogenic right ventricular cardiomyopathy. *Circulation* 2006; **113**: 1171–79.

14 O'Donnell D, Cox D, Bourke J, Mitchell L, Furniss S. Clinical and electrophysiological differences between patients with arrhythmogenic right ventricular dysplasia and right ventricular outflow tract tachycardia. *Eur Heart J* 2003; **24**: 801–10.

15 Tandri H, Bluemke DA, Ferrari VA, et al. Findings on magnetic resonance imaging of idiopathic right ventricular outflow tachycardia. *Am J Cardiol* 2004; **94**: 1441–45.

16 Corrado D, Basso C, Thiene G, et al. Spectrum of clinicopathologic manifestations of arrhythmogenic right ventricular cardiomyopathy/dysplasia: a multicenter study. J Am Coll Cardiol 1997; 30:1512-20.

17 Fontaine G, Tonet J, Gallais Y, et al. Ventricular tachycardia catheter ablation in arrhythmogenic right ventricular dysplasia: a 16-year experience. *Curr Cardiol Rep* 2000; **2**: 498–506.

18 Borggrefe M, Willems S, Chen X, et al. Catheter ablation of ventricular tachycardia using radiofrequency current. *Herz* 1992; **17**: 171–78.

19 Piccini JP, Dalal D, Calkins H, et al. Predictors of inappropriate implantable defibrillator therapies in patients with arrhythmogenic right ventricular dysplasia. *Heart Rhythm* 2005; **2**: 1188–94.

20 Dalal D, Lorraine H, Calkins H, et al. Clinical features of arrhythmogenic right ventricular dysplasia/ cardiomyopathy associated with mutations in plakophilin-2. *Circulation* 2006; **113**: 1641–49.

21 Zipes DP, Camm AJ, Borggrefe M, et al. ACC/AHA/ESC 2006 guidelines for management of patients with ventricular arrhythmias and the prevention of sudden cardiac death: a report of the American College of Cardiology/ American Heart Association Task Force and the European Society of Cardiology Committee for Practice Guidelines (Writing Committee to Develop Guidelines for Management of Patients with Ventricular Arrhythmias and the Prevention of Sudden Cardiac Death). *J Am Coll Cardiol* 2006; **48**: e247.

22 Boulos M, Lashevsky I, Reisner S, et al., Electroanatomic mapping of arrhythmogenic right ventricular dysplasia. *J Am Coll Cardiol* 2001; **38**: 2020–27.

23 Boulos M, Lashevsky I, Gepstein L, Usefulness of electroanatomical mapping to differentiate between right ventricular outflow tract tachycardia and arrhythmogenic right ventricular dysplasia. *Ameri J Cardiol* 2005; **95**: 935–40.

24 Miljoen H, State S, de Chillou C, et. al. Electroanatomic mapping characteristics of ventricular tachycardia in patients with arrhythmogenic right ventricular cardiomyopathy/dysplasia. *Europace* 2005; **7**: 516–24.

25 Corrado D, Basso C, Leoni L. Three-dimensional electroanatomic voltage mapping increases accuracy of

diagnosing arrhythmogenic right ventricular cardiomyopathy/dysplasia. *Circulation* 2005; **111**: 3042–50.

26 Corrado D, Basso C, Leoni L. Three-dimensional electroanatomical voltage mapping and histologic evaluation of myocardial substrate in right ventricular outflow tract tachycardia. *J Am Coll Cardiol* 2008; **51**: 731–39.

27 Reithman, C, Hahnfield A, Remp, T, et. al. Electroanatomic mapping of endocardial right ventricular activation as a guide for catheter ablation in patients with arrhythmogenic right ventricular dysplasia. *PACE* 2003; **26**: 1308–16.

28 Marchlinski FE, Zado E, Dixit S, et al. Electroanatomical substrate and outcome of catheter ablative therapy for ventricular tachycardia in setting of right ventricular cardiomyopathy, *Circulation* 2004; **110**: 2293–98

29 Verma A, Kilicaslan F, Schweikert RA, et al. Short- and long-term success of substrate-based mapping and ablation of ventricular tachycardia in arrhythmogenic right ventricular dysplasia, *Circulation* 2005; **111**: 3209–16.

30 Dalal D, Jain R, Tandri, H, Dong, J et al. Long-term efficacy of catheter ablation of ventricular tachycardia in patients with arrhythmogenic right ventricular dysplasia/cardiomyopathy. *J Am Coll Cardiol* 2007; **50**: 432–40.

31 Piccini JP, Dalal D, Roguin A, et al. Predictors of appropriate implantable defibrillator therapies in patients with arrhythmogenic right ventricular dysplasia. *Heart Rhythm* 2005; **2**: 1188–94.

32 Strohmer B, Schernthaner C, Pichler M. Multiple appropriate and spurious defibrillator shocks in a patient with right ventricular cardiomyopathy. *Int J Cardiol* 2005; **102**: 363–66.

27

CHAPTER 27

Mapping of Idiopathic Ventricular Tachycardias: RV and LV Outflow and Septal Tachycardias

Mohammad Ali Sadr-Ameli, MD, *Majid Haghjoo,* MD, *Zahra Emkanjoo,* MD

Department of Pacemaker and Electrophysiology, Rajaie Cardiovascular Medical and Research Center, Iran University of Medical Sciences, Tehran, Iran

Summary

Ventricular tachycardia (VT) occurs most often in patients with structural heart disease. Although ischemic heart disease and cardiomyopathies are the most common cardiac disorders associated with VT, these arrhythmias may occur in patients who have no apparent structural heart disease (known as idiopathic VT). Idiopathic VT accounts for approximately 10% of all sustained monomorphic VT in the United States. Several different forms of idiopathic VT have been recognized, and they have been classified with respect to the VT origin, its response to pharmacological agents, and behavior of VT. Although idiopathic VTs can have various sites of origin and mechanisms, they can usually be cured by catheter ablation techniques.

Idiopathic Left Septal Ventricular Tachycardia

Idiopathic left septal VT (LSVT) is the most common form of idiopathic left VT [1–3]. The idiopathic left posterior fascicular tachycardia first was recognized as an electrocardiographic entity in 1979 by Zipes et al [4]. In 1981, Belhassen and colleagues reported for the first time verapamil-sensitivity of the tachycardia [5]. In 1988, Ohe et al. [6] described a second form of this VT with right bundle branch block (RBBB) and right axis configuration. The third form of this VT, known as left upper septal VT, was reported by Shimoike et al in 2000 [7]. In 2004, we described for the first time coexistence of the two patterns (RBBB-left axis and RBBB-right axis) of idiopathic LSVT in the same patient [8].

Cardiac Mapping, Third Edition Edited by Mohammad Shenasa, Gerhard Hindricks, Martin Borggrefe, and Günter Breithardt
 ISBN: 978-1-405-17572-2

Clinical Characteristics

This type of idiopathic VT is characterized by a dramatic response to the intravenous verapamil. The QRS duration is relatively narrow (120–160 msec), explaining the nomenclature of "fascicular tachycardia." Idiopathic LSVT occurs in relatively young patients, and onset is usually before 30 years of age [9]. This form of VT occurs more frequently in males than females. The electrocardiogram (ECG) during sinus rhythm shows no abnormality. Results of signal-averaged ECGs are also normal. Coronary

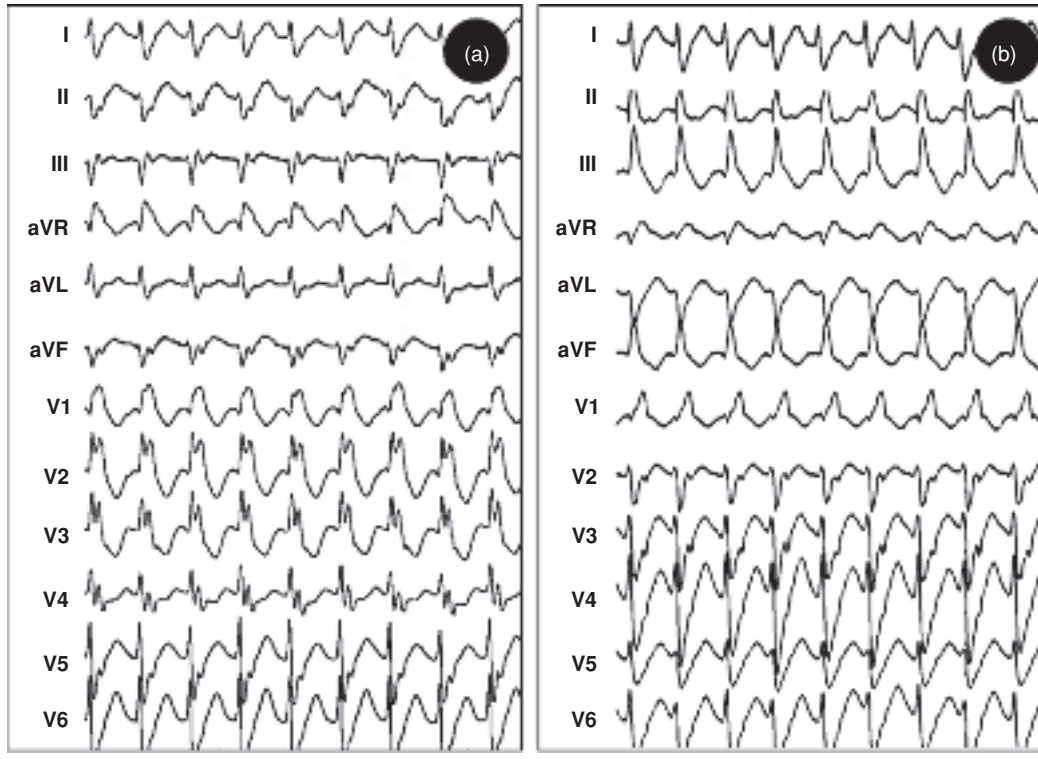

Figure 27.1 Electrocardiographic pattern of two common forms of the idiopathic left septal ventricular tachycardia. (a) Twelve-lead ECG of a patient with left posterior fascicular tachycardia. Note that this form of fascicular tachycardia is characterized by the right bundle branch block morphology with superior axis configuration. (b) Twelve-lead ECG in patient with left anterior fascicular tachycardia. There is characteristic right bundle branch block with inferior axis configuration.

angiography and left ventriculography are usually normal. Most patients experience recurrent episodes of well-tolerated sustained VT. However, this VT can be incessant and may cause a reversible tachycardia-induced cardiomyopathy [10, 11].

According to the QRS configuration during tachycardia, LSVT can be classified into three subgroups:

1 left posterior fascicular tachycardia with RBBB and left or right superior axis morphology in 90–95% of patients (Figure 27.1a);

2 left anterior fascicular tachycardia with RBBB and inferior axis in less than 10% of patients (Figure 27.1b);

3 left upper septal tachycardia with narrow QRS configuration and normal axis (very rare). There are also reports of coexistent LSVT and atrioventricular nodal reentry (AVNRT) [12–15] or atrioventricular reentry [16].

Electrophysiologic Mechanism

Although both reentry and triggered activity have been proposed as possible mechanisms for this form of VT [4, 6], the weight of evidence is in favor of reentry. The mechanism of reentry is supported by the fact that tachycardia can be induced and terminated with programmed stimulation [3, 17], an inverse relationship exists between the coupling interval of extrastimulus and the echo interval [6], criteria for manifest and concealed entrainment are demonstrated [6, 17], and diastolic potentials are recorded [18–21].

It appears that the fascicle of the left bundle branch may be not involved in the reentrant circuit of LSVT [22]. Endocardial mapping during the tachycardia localized the earliest site of activation to the Purkinje network of left posterior fascicles near the inferoposterior left ventricular septum in patients with RBBB and left superior axis

configuration, and to the inferoapical region in those with RBBB and right superior axis morphology. The remaining patients with RBBB and inferior axis have their exit near the anterosuperior left ventricular septum within the Purkinje network of left anterior fascicles.

In contrast, the entrance site to the zone of slow conduction is thought to be located near the base of the left interventricular septum and provides a possible explanation for the observation that manifest entrainment is more easily obtained when pacing from the right ventricular outflow tract (RVOT) than from the right ventricular apex.

Based on the results of prior studies [19, 21, 23], a working hypothesis has been proposed for the tachycardia circuit in LSVT. In this model, activation proceeds antegradely over a region of abnormal Purkinje tissue, which gives rise to a diastolic potential (DP). The impulse then enters the Purkinje tissue of the left posterior or anterior fascicles, giving rise to Purkinje potentials (PP). The antegrade limb appears to depend mainly on the slow inward calcium current; therefore, it is verapamil-sensitive. Adenosine and Valsalva maneuvers usually have no effect on this form of tachycardia. During sinus rhythm, antegrade conduction proceeds rapidly over the posterior or anterior fascicles (Figure 27.2). The impulse may also conduct antegradely over and partially penetrate adjacent abnormal Purkinje fibers. These fibers are also activated retrogradely from the posterior fascicle, which give rise to retro PP or late potentials.

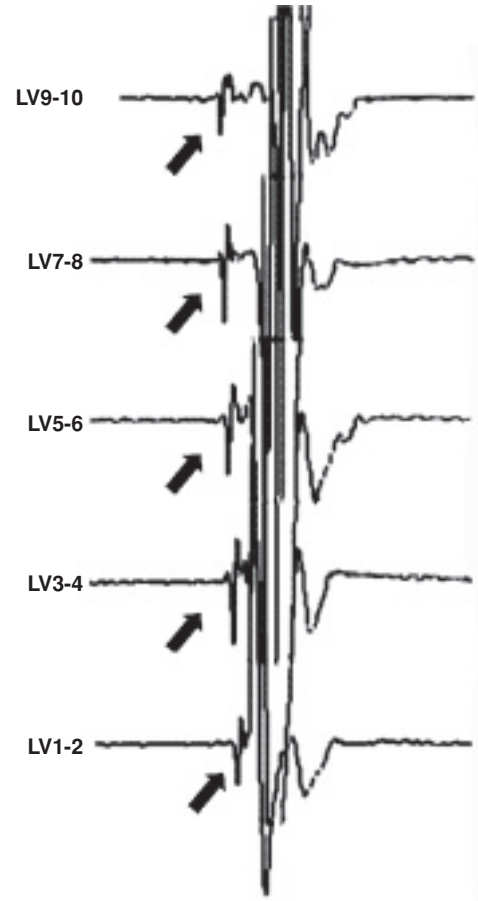

Figure 27.2 Purkinje fiber activation sequence during sinus rhythm. Note that sequential high-frequency potentials (Purkinje potential) were recorded along the left ventricular septum from proximal to distal portions (arrows).

Mapping Characteristics

Multiple strategies have been employed to identify the appropriate site for ablation in patients with idiopathic LSVT. Initially, the site of VT origin was determined either by identifying the site of the earliest ventricular activation during tachycardia (activation mapping) or by finding the pacing site that gives a QRS morphology identical to that of the VT (pace mapping).

Nakagawa et al. [18] first reported the importance of PP as a marker for successful ablation of LSVT. The earliest distinct potential precedes the QRS by 15–42 msec during tachycardia. The ablation was successful at the site of the earliest distinct potentials and unrelated to the timing of ventricular activation.

More recently, the interest has focused on the identification of late DPs during ventricular tachycardia. Wen et al. [24] for the first time demonstrated that a successful ablation site for this VT is away from the VT exit site in the mid and the inferior apical septum and is located at the superior midseptal area. Kottkamp et al. [25] demonstrated continuous or mid-diastolic electrical activity preceding PP at these sites in patients with this VT and suggested these activities as markers for successful ablation. The results of subsequent studies indicated that the DP is recorded in a small region (0.5–1.0 cm^3) slightly proximal to the earliest PP recording

site during VT and is included in the area where PP is recorded (2.0–3.0 cm^3) [19]. DP is activated from the basal to apical sites of the left ventricle toward the earliest PP recording site. In contrast, the PP is activated bidirectionally toward the basal and apical sites along the left posterior fascicle during sinus rhythm.

The results of our recent study indicated that the PP and the DP precede the onset of the QRS complex by 18 ± 4 msec and 53 ± 18 msec [26]. In contrast to the results of the study by Tsuchiya et al. [19], our study also showed that, compared to DP alone, earliest PP (with or without concomitant DP) may be superior for selection of a target site of RF ablation in patients with ILVT [26].

Entrainment study from the RVOT demonstrated a manifest entrainment and the DP is captured orthodromically. The application of low output (0.5–1.0 mA, 1–2 msec), to the site where the PP and the DP are simultaneously recorded, could capture only the PP and caused concealed entrainment. QRS morphology identical to that of VT is demonstrated during pacing at a cycle length 10–20 msec shorter than that of VT. The postpacing interval is equal to the VT cycle length, and the interval from the stimulus to QRS onset is equal to that from the PP to QRS onset during VT. The DP is activated from the basal to the apical site by pacing stimuli, and the interval between the DP before and after the last pacing stimulus is equal to the pacing cycle length. Thus, the DP is orthodromically activated by these pacing stimuli. The activation time from the PP to the DP during pacing is long, and the same as that during VT. More rapid pacing resulted in a delay in activation from the PP to the DP but not in the DP itself, indicating that a decremental property exists between the PP and the DP at the proximal site of the mapping catheter that caused the slow conduction in fascicular tachycardia.

Idiopathic Right Ventricular Outflow Tract Tachycardia

The most common form of idiopathic VT originates from the RVOT and is observed in 60–80% of patients who develop VT in the absence of structural heart disease. The clinical features and general ECG characteristics (left bundle branch block morphology and inferior axis) of RVOT-VT were described by Buxton in 1983 [27]. Jadonath et al. [28] and Gumbrielle et al. [29] determined the utility of the 12-lead ECG in localizing the origin of RVOT-VT in patients who underwent ablation of their arrhythmia [28].

Clinical Characteristics

Idiopathic RVOT-VT is often provoked by exercise, and the number of tachycardia episodes reduces at night. This form of idiopathic VT occurs more commonly in females than males, with most cases occurring in the fourth and fifth decades of life. The tachycardia usually takes the form of repetitive monomorphic nonsustained VT or paroxysmal monomorphic sustained VT. The most common form is the repetitive one typically occurring at rest or after exercise, whereas paroxysmal sustained VT typically occurs during exercise or emotional stress. However, there may be considerable overlap between these two forms of RVOT-VT.

The ECG during sinus rhythm usually reveals no abnormality. Complete or incomplete RBBB is observed in 10% of patients. The results of echocardiography are usually within normal limits; slight RV enlargement has been rarely reported. Although RVOT-VT has a benign prognosis in most patients, tachycardia-induced cardiomyopathy is reported following both incessant sustained VT [30] and frequent RVOT ectopy [31]. The AVNRT may be associated with RVOT-VT in 15% of patients [32, 33].

Electrophysiologic Mechanism

Most evidence to date supports the hypothesis that idiopathic RVOT-VT is caused by triggered activity (catecholamine-dependent delayed afterdepolarization). In support of this hypothesis is the demonstration that tachycardia can be initiated by programmed stimulation with variable success and low reproducibility; there is a direct relationship between the coupling interval and the echo interval; and manifest or concealed entrainment cannot be demonstrated during tachycardia. Given that adenyl cyclase and L-type calcium current are essential for the activity of cAMP-mediated triggered activity, triggered arrhythmia is sensitive to beta-blockade, calcium-channel blockade, vagal maneuvers, and adenosine.

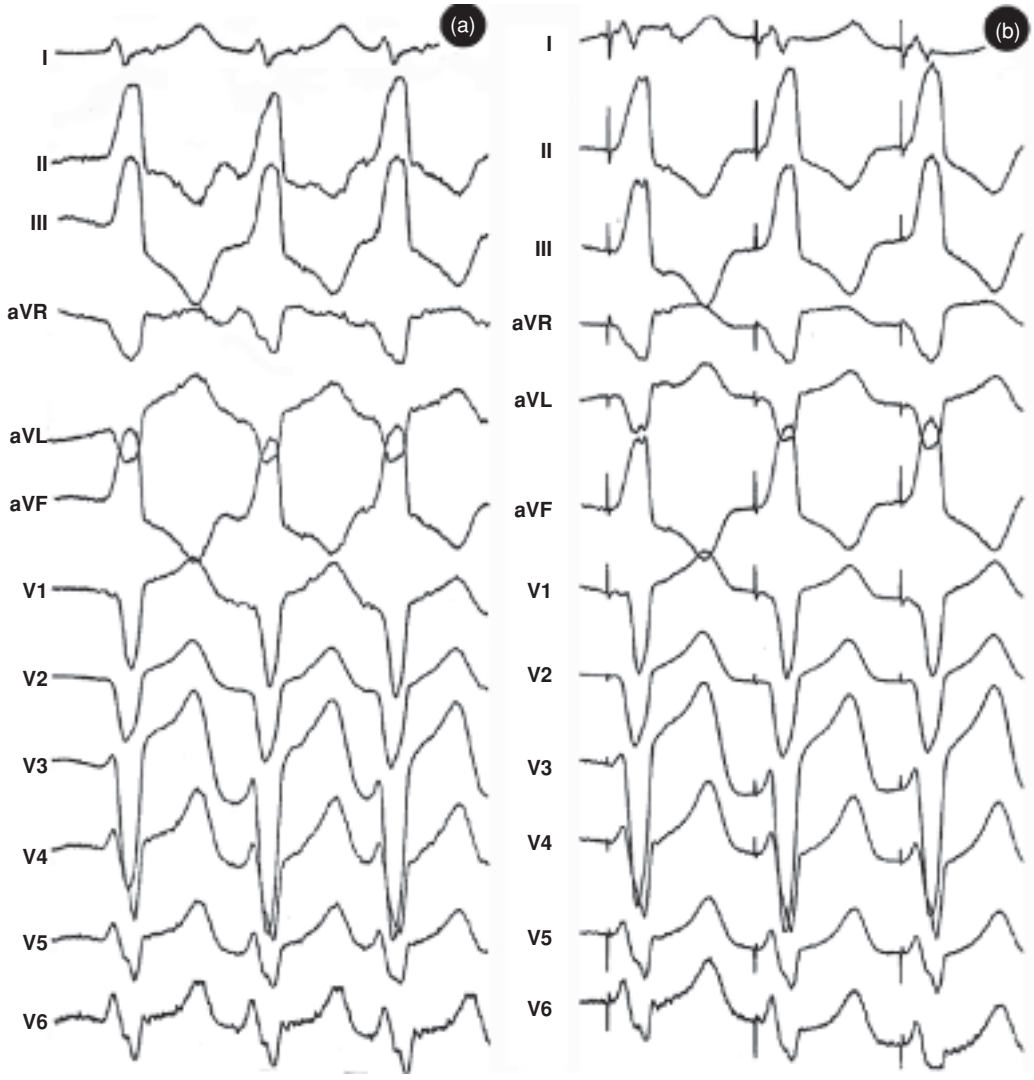

Figure 27.3 The match between the pace map and the patient's tachycardia. (a) Twelve-lead ECG of the right ventricular outflow tract tachycardia. (b) The pace-map is identical to the 12-lead ECG of VT regarding the R/S ratio and subtle notching in all of the 12 ECG leads.

Recently, it has been hypothesized that a somatic cell mutation in the cAMP-dependent signal transduction pathway occurring during myocardial development may be an etiology for some cases of RVOT-VT [34].

Mapping Characteristics

Until now, several mapping techniques have been described to detect the appropriate site for ablation in patients with RVOT-VT. In activation mapping, successful ablation sites are generally associated with activation times 10–45 msec before the onset of earliest surface QRS.

Recently, pace mapping has become the preferred method for finding the site of successful ablation in patients with RVOT-VT (Figure 27.3). However, pace mapping is difficult and time-consuming, and has certain limitations related to resolution. Identical pace map can be obtained up to 8 mm from a tachycardia focus [35]. Pace mapping is performed

Table 27.1 Differential Electrocardiographic Characteristics of Right and Left Outflow Tract Tachycardias

		LVOT-VT			
	RVOT-VT	*Basal septal VT*	*Aortomitral continuity VT*	*Epicardial VT*	*Cusp VT*
QRS morphology	LBBB, inferior axis	LBBB, inferior axis	RBBB, inferior axis	LBBB with initial slurring, inferior axis	W- or M-shaped, inferior axis
Precordial transition	V2–V4, V2 in subpulmonic VT	V1 or V2	Before V1	V2–V4	V1–V2 in LCC-VT V2–V3 in RCC-VT
Other characteristics	Left-sided: QS in aVL > aVR Right-sided: QS in aVR > aVL	An *S*-wave in I	Broad monophasic *R*-wave across precordium	RS/QRS > 55% Deep QS in I and aVL Tall R in inferior leads R in V2 < both V1 and V3	R/QRS > 50% R/S > 30% Deep S in V2 Tall R in inferior leads

KEY: RVOT-VT = right ventricular outflow tract tachycardia; LVOT-VT = left ventricular outflow tract tachycardia; LBBB = left bundle branch; RBBB = right bundle branch; LCC-VT = left coronary cusp VT; RCC-VT = right coronary cusp VT.

during sinus rhythm at a cycle length equal to that of the spontaneous or induced VT. The match between the pace map and the patient's tachycardia is evaluated in all 12 ECG leads by comparing the R/S ratio and subtle notching in the QRS complex. An identical match for at least 11 out of 12 ECG leads is necessary for ablation.

Estimation of the tachycardia origin from the findings of a 12-lead ECG during VT or premature ventricular complex may facilitate pace mapping and shorten the procedure time (Table 27.1). RVOT tachycardias have a left bundle branch (LBBB) morphology with precordial transition in leads V2–V4. An *R*-wave transition in lead V2 suggests a site of origin immediately inferior to the pulmonic valve, or. more rarely, the left ventricular outflow tract (LVOT). The QRS duration during VT is usually more than 140 msec if it originates from the free wall aspect of the RVOT, and 140 msec or less if tachycardia originates from the septal aspect of the RVOT.

Likewise, the *RR′* or *Rr′* complex in leads II and III is more suggestive of RVOT free wall origin due to sequential activation of the right and left ventricles, whereas monophasic *R*-wave in these leads is in favor of septal origin. For further localization of the VT origin, relative QS amplitude of aVL and aVR would be informative. If QS in aVR is greater than aVL, the VT origin is located in the right upper aspect of RVOT. Likewise, if QS in aVL is greater than aVR then the VT origin is likely left upper region of the RVOT.

In conclusion, successful ablation of outflow tract tachycardia begins with a careful analysis of the 12-lead ECG pattern coupled with recognition of the common sites of VT origin. Pace mapping is done in regions of interest based on analysis of the 12-lead ECG during VT with an attention to an exact match for all 12 ECG leads. Activation mapping with unipolar and bipolar recordings is used to confirm the pace-map findings. Other useful techniques include the three-dimensional electroanatomic and noncontact mapping systems.

Idiopathic Left Ventricular Outflow Tract Tachycardia

In patients with adenosine-sensitive VT only 10–15% have a LVOT origin. The LVOT-VT is suggested by a RBBB morphology in lead V1 or atypical LBBB morphology associated with an early precordial transition in lead V2. The LVOT-VT can

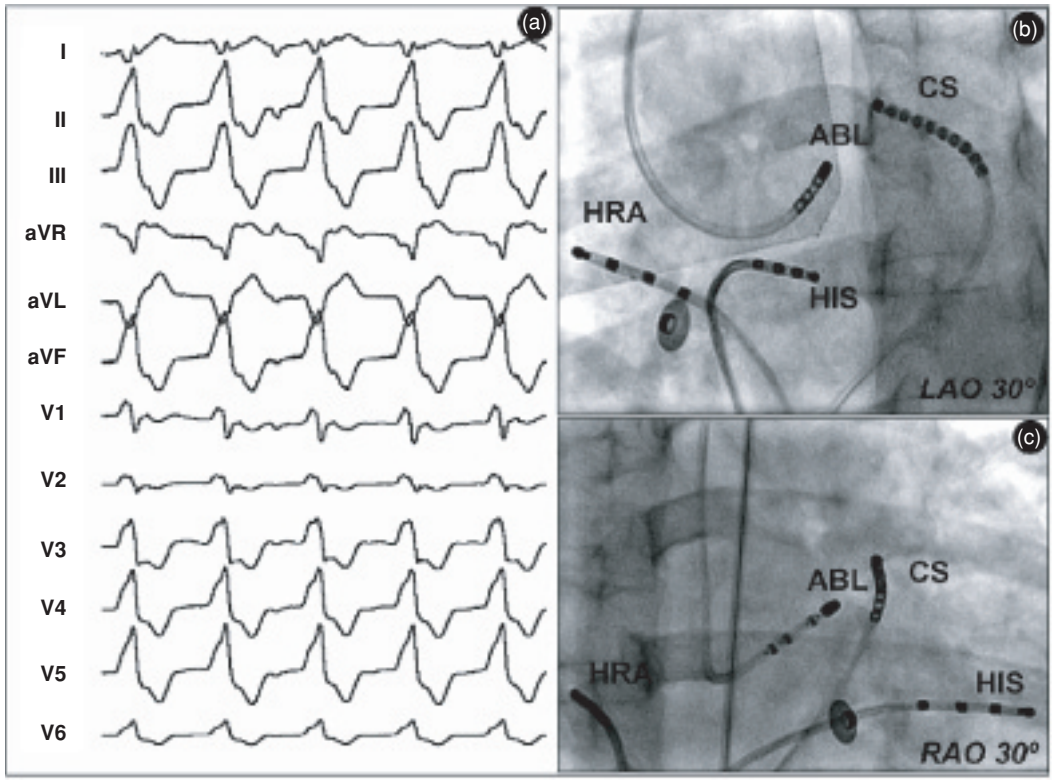

Figure 27.4 Idiopathic left ventricular outflow tract tachycardia originating from aorto-mitral continuity. (a) Characteristic 12-lead ECG in a patient with idiopathic left ventricular outflow tract tachycardia with right bundle branch morphology and inferior axis configuration. Note that there is broad *R*-wave across the precordial leads with AV dissociation. (b) (c) Successful ablation site in two fluoroscopic views (right anterior oblique and left anterior oblique, respectively).

originate from several sites, including the superior basal region of the left interventricular septum, the aorto-mitral continuity (Figure 27.4), aortic coronary cusps, and the great cardiac and anterior interventricular veins. First cases of the LVOT-VT were reported by Callans et al. [36] and Yeh et al. [37]. Shimoike et al. [38] and Sadanaga et al. [39] reported patients with repetitive monomorphic VT who underwent successful radiofrequency ablation from the left coronary cusp. Da Paola et al. [40] reported the mapping and ablation through the coronary venous system.

Clinical Characteristics

LVOT-VT is distributed almost equally between males and females, with most cases occurring in the fifth decade of life. Similar to the RVOT-VT, both monomorphic nonsustained VT or frequent ectopy and sustained monomorphic VT were described. There is also report of LVOT-VT association with AVNRT [41].

Electrophysiologic Mechanism

LVOT-VT is assumed to be caused by the same mechanism(s) as RVOT-VT. The VT cannot be entrained and demonstrates sensitivity to adenosine, verapamil, Valsalva maneuver, carotid sinus pressure, edrophonium, and beta-blockade, finding consistent with catecholamine-dependent triggered activity.

Mapping Characteristics

In view of the similarity with the arrhythmogenic mechanism, LVOT-VT can be mapped by the same techniques as those used for the mapping of RVOT-VT. Therefore, pace mapping, activation mapping, and ECG estimation of tachycardia focus

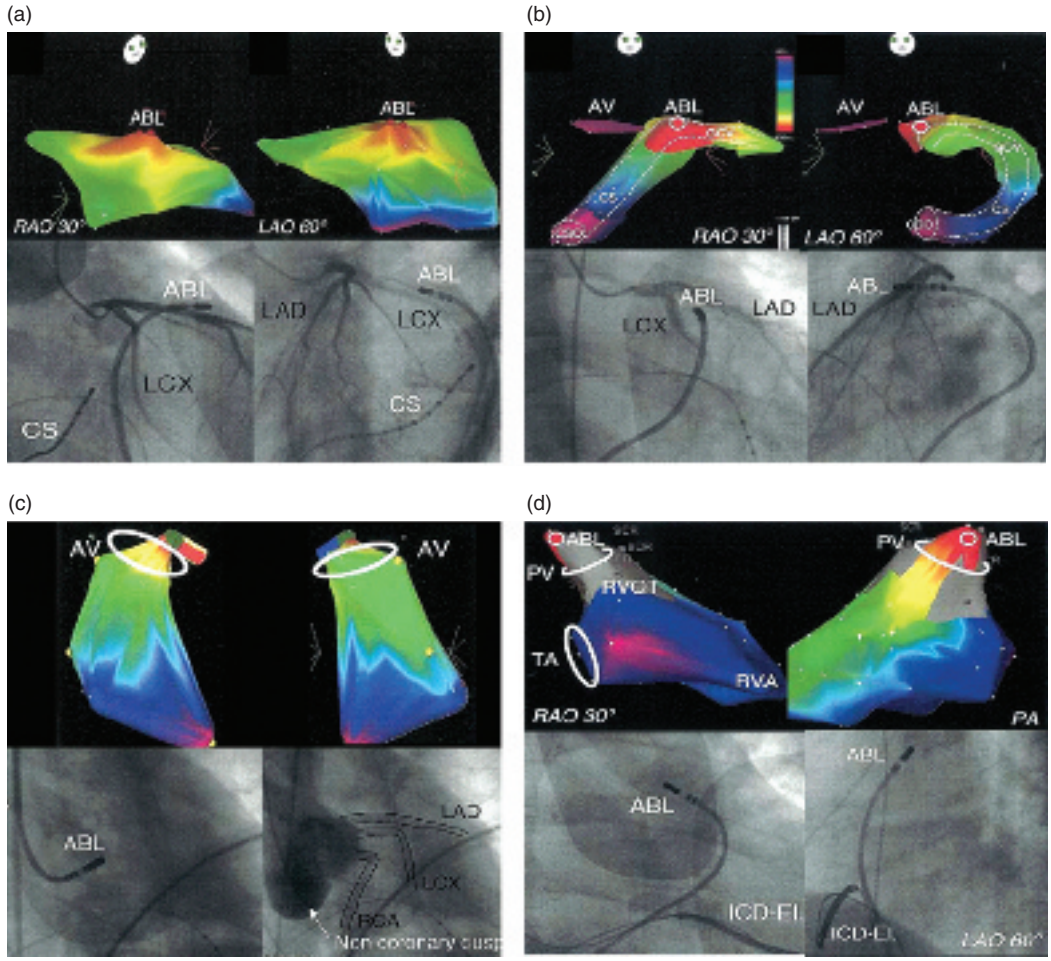

Figure 27.5 Idiopathic epicardial left ventricular outflow tract tachycardia. (a) Ablation of idiopathic VT from the epicardium through a percutaneous pericardial access. Epicardial electroanatomic activation maps during VT. Ablation (dark red dots) at the earliest activation site (red color) was successful. Radiographs show the ablation site in relation to the left coronary artery. (b) Successful ablation of idiopathic VT from the great cardiac vein (GCV) via the coronary sinus (CS). CS electroanatomic activation maps during idiopathic VT. Radiographs show the ablation site. (c) Left ventricular outflow tract electroanatomic activation maps including the aortic sinus of Valsalva during idiopathic VT. Radiographs show the ablation catheter (ABL) at the site of successful ablation in the noncoronary cusp. (d) Right ventricular electroanatomic activation maps including the proximal part of the pulmonary artery. Radiographs show the site of successful ablation. KEY: AV = aortic valve; CSO = coronary sinus ostium; ICD-El = implantable defibrillator's electrode; LAD = left anterior descending; LAO = left anterior oblique; LCX = left circumflex; PA = posteroanterior; PV = pulmonary valve; RAO = right anterior oblique; RCA = right coronary artery; VT = ventricular tachycardia. Reprinted with permission from Arya A, Piorkowski C, Sommer P, et al. Idiopathic outflow tract tachycardias: current perspectives. *Herz* 2007; 32: 218–25.

(Table 27.1) are the main techniques to identify an appropriate site for ablation. In view of the limitations related to the activation and pace mapping, ablation can be guided by electroanatomic mapping systems in difficult cases (Figure 27.5).

The VT origin from the basal left interventricular septum is suggested by a LBBB morphology associated with an early precordial transition in leads V1 or V2, whereas the LVOT-VT originating from the aorto-mitral continuity is associated with RBBB

morphology in lead V1 and broad monophasic *R*-wave across precordium.

The VT originating from the region of aortic coronary cusp has a precordial transition that is earlier than the RVOT region. The *R*-wave is positive by V2 or V3 with right coronary cusp (RCC) VT and by V1 or V2 for left coronary cusp (LCC) VT. The cusp VT has a longer *R*-wave duration and greater amplitude in leads V1 or V2 than RVOT tachycardia (R/QRS duration >50% and R/S amplitude >30%) [42]. There is also a deep *S*-wave in lead V2 and relatively large *R*-waves in the inferior leads due to their subepicardial location. The cusp VT originates most commonly from the LCC, followed by the RCC, and rarely noncoronary cusp (NCC). Of note, the NCC is notable for atrial capture during pace mapping as it abuts the interatrial septum. LCC-VT is often associated with a W- or M-shaped pattern in lead V1, and thus it is difficult to classify as a true LBBB or RBBB pattern. The LCC-VT tends to have a QS or rS complex in lead I, whereas the RCC-VT has greater amplitude in lead I.

The VT originating from LV epicardial site frequently has similar patterns to the LCC. The majority of these VT were seen to cluster at the junction of the great cardiac vein/anterior interventricular vein and proximal anterior interventricular vein [43]. The epicardial VT are characterized by a LBBB morphology in lead V1 and all had slurring (delta-wave-like) in their initial portion of the QRS (onset of *R*- or *r*-wave to nadir of *S* duration in any precordial lead/total QRS duration >55%). The epicardial VT in this region is also associated with deep QS morphology in leads I and aVL, precordial transition in V2 to V4, and tall *R*-wave in the inferior leads. These VT may also show a characteristic QRS transition pattern break with the QRS in lead V2 being less positive or having a smaller *R*-wave than both lead V1 and lead V3.

Because of the close anatomic relation to the coronary arteries, measures must be taken to avoid injuring these elements during ablation within coronary cusps. Coronary angiography should be performed before ablation to assure that there is more than 10 mm between ablation catheter and the ostium of the left main coronary artery, and the left main coronary artery should be cannulated as a marker and for prevention during radiofrequency energy delivery. Radiofrequency energy is targeted to achieve a temperature of 55°C by delivering 15–30 W. Ablation should be performed during continuous fluoroscopy to observe for catheter dislodgment. Coronary angiography is often performed immediately after the ablation to rule out spasm, dissection, or thrombus.

Before applying radiofrequency energy to an epicardial site, simultaneous coronary arteriography and coronary sinus venography should be performed to identify the spatial relationship between the target vein and the adjacent coronary artery. After ablation, coronary arteriography should be repeated and an echocardiogram should be done to rule out hemopericardium.

References

1 Lin FC, Finley CD, Rahimtoola SH, et al. Idiopathic paroxysmal ventricular tachycardia with a QRS pattern of right bundle branch block and left axis deviation: a unique clinical entity with specific properties. *Am J Cardiol* 1983; **52**: 95–100.

2 German LD, Packer DL, Bardy GH, et al. Ventricular tachycardia induced by atrial stimulation in patients without symptomatic cardiac disease. *Am J Cardiol* 1983; **52**: 1202–7.

3 Klein GJ, Millman PJ, Yee R. Recurrent ventricular tachycardia responsive to verapamil. *Pacing Clin Electrophysiol* 1984; **7**: 938–48.

4 Zipes DP, Foster PR, Troup PJ, et al. Atrial induction of ventricular tachycardia: reentry versus triggered automaticity. *Am J Cardiol* 1979; **44**: 1–8.

5 Belhassen B, Rotmensch HH, Laniado S. Response of recurrent sustained ventricular tachycardia to verapamil. *Br Heart J* 1981; **46**: 679–82.

6 Ohe T, Shimomura K, Aihara N, et al. Idiopathic sustained left ventricular tachycardia: clinical and electrophysiological characteristics. *Circulation* 1988; **77**: 560–68.

7 Shimoike E, Ueda N, Maruyama T, et al. Radiofrequency catheter ablation of upper septal idiopathic left ventricular tachycardia exhibiting left bundle branch block morphology. *J Cardiovasc Electrophysiol* 2000; **11**: 203–7.

8 Haghjoo M, Arya A, Emkanjoo Z, et al. Radiofrequency catheter ablation of idiopathic left ventricular tachycardia originating in both left posterior and anterior fascicles. *J Interv Card Electrophysiol* 2004; **11**: 217–20.

9 Ohe T, Kusano KF, Morita H, et al. Catheter ablation of idiopathic ventricular tachycardia and bundle branch reentrant ventricular tachycardia. In: Zipes DP, Haissaguerre

M, eds. *Catheter Ablation of Arrhythmia*, 2nd ed. Futura Publishing Company, New York, 2002: 345–71.

10 Arya A, Haghjoo M, Davari P, et al. Resolution of tachycardia-induced cardiomyopathy following ablation of verapamil-sensitive idiopathic left ventricular tachycardia. *Pediatr Cardiol* 2006; **27**: 146–48.

11 Benito Bartolomé F, Sánchez Fernández-Bernal C. Reversibility of cardiomyopathy after therapy of incessant left ventricular tachycardia with radiofrequency ablation in a newborn infant. *An Esp Pediatr* 2000; **53**, 156–58.

12 Arya A, Haghjoo M, Emkanjoo Z, et al. Radiofrequency catheter ablation of atrioventricular nodal reentrant tachycardia: it is not always as it is expected. *Indian Pacing Electrophysiol J* 2004; **4**: 217–20.

13 Wagshal AB, Mittleman RS, Schuger CD, et al. Coincident idiopathic left ventricular tachycardia and atrioventricular nodal reentrant tachycardia: control by radiofrequency catheter ablation of the slow atrioventricular nodal pathway. *Pacing Clin Electrophysiol* 1944; **17**: 386–96.

14 Weng KP, Chiou CW, Kung MH, et al. Radiofrequency catheter ablation of coexistent idiopathic left ventricular tachycardia and atrioventricular nodal reentrant tachycardia. *J Chin Med Assoc* 2005; **68**: 479–83.

15 Bottoni N, Donateo P, Quartieri F, et al. Two unusual cases of coincident atrioventricular nodal reentrant tachycardia and ventricular tachycardia. *Ital Heart J* 2005; **6**: 765–70.

16 Watanabe I, Kunimoto S, Kondo K, et al. Radiofrequency catheter ablation of coexistent atrioventricular reciprocating tachycardia and left ventricular tachycardia originating in the left anterior fascicle. *Jpn Circ J* 1999; **63**: 223–27.

17 Okumura K, Matsuyama K, Miyagi H, et al. Entrainment of idiopathic ventricular tachycardia of left ventricular origin with evidence for reentry with an area of slow conduction and effect of verapamil. *Am J Cardiol* 1988; **62**: 727–32.

18 Nakagawa H, Beckman KJ, McClelland JH, et al. Radiofrequency catheter ablation of idiopathic left ventricular tachycardia guided by a Purkinje potential. *Circulation* 1993; **88**: 2607–17.

19 Tsuchiya T, Okumura K, Honda T, et al. Significance of late diastolic potential preceding Purkinje potential in verapamil-sensitive idiopathic left ventricular tachycardia. *Circulation* 199; **99**: 2408–13.

20 Nogami A, Naito S, Tada H, et al. Demonstration of diastolic and presystolic potentials as critical potentials in a macroreentry circuit of verapamil-sensitive idiopathic left ventricular tachycardia. *J Am Coll Cardiol* 2000; **36**: 811–23.

21 Aiba T, Suyama K, Aihara N, et al. The role of Purkinje and pre-Purkinje potentials in the reentrant circuit of verapamil-sensitive idiopathic LV tachycardia. *Pacing Clin Electrophysiol* 2001; **24**: 333–44.

22 Kuo JY, Tai CT, Chiang CE, et al. Is the fascicle of left bundle branch involved in the reentrant circuit of verapamil-sensitive idiopathic left ventricular tachycardia? *Pacing Clin Electrophysiol* 2003; **26**: 1986–92.

23 Ouyang F, Cappato R, Ernst S, et al. Electroanatomic substrate of idiopathic left ventricular tachycardia: unidirectional block and macroreentry within the Purkinje network. *Circulation* 2002; **105**: 462–69.

24 Wen MS, Yeh SJ, Wang CC, et al. Successful radiofrequency ablation of idiopathic left ventricular tachycardia at a site away from the tachycardia exit. *J Am Coll Cardiol* 1997; **30**: 1024–31.

25 Kottkamp H, Chen X, Hindricks G, et al. Idiopathic left ventricular tachycardia: new insight into electrophysiological characteristics and radiofrequency catheter ablation. *Pacing Clin Electrophysiol* 1995; **18**: 1285–97.

26 Arya A, Haghjoo M, Emkanjoo Z, et al. Comparison of presystolic Purkinje and late diastolic potentials for selection of ablation site in idiopathic verapamil sensitive left ventricular tachycardia. *J Interv Card Electrophysiol* 2004; **11**: 135–41.

27 Buxton AE, Waxman HL, Marchlinski FE, et al. Right ventricular tachycardia: clinical and electrophysiologic characteristics. *Circulation* 1983; **68**: 917–27.

28 Jadonath RL, Schwartzman DS, Preminger MW, et al. Utility of the 12-lead electrocardiogram in localizing the origin of right ventricular outflow tract tachycardia. *Am Heart J* 1995; **130**: 1107–13.

29 Gumbrielle TP, Bourke JP, Doig JC, et al. Electrocardiographic features of septal location of right ventricular outflow tract tachycardia. *Am J Cardiol* 1997; **79**: 213–16.

30 Vigen J, Hill P, Biblo LA, et al. Tachycardia-induced cardiomyopathy secondary to right ventricular outflow tract tachycardia: improvement of left ventricular function after radiofrequency catheter ablation of the arrhythmia. *J Cardiovasc Electrophysiol* 1997; **8**: 445–50.

31 Takemoto M, Yoshimura H, Ohba Y, et al. Radiofrequency catheter ablation of premature ventricular complexes from right ventricular outflow tract improves left ventricular dilation and clinical status in patients without structural heart disease. *J Am Coll Cardiol* 2005; **45**: 1259–65.

32 Kazemi B, Arya A, Haghjoo M, et al. Coincident atrioventricular nodal reentrant and idiopathic ventricular tachycardia. *Asian Cardiovasc Thorac Ann* 2006; **14**: 284–88.

33 Kautzner J, Cihak R, Vancura V, et al. Coincidence of idiopathic outflow tract tachycardia and atrioventricular nodal reentrant tachycardia. *Europace* 2003; **5**: 215–20.

34 Lerman BB, Dong B, Stein KM, et al. Right ventricular outflow tract tachycardia due to a somatic cell mutation in G protein subunit αi2. *J Clin Invest* 1998; **101**: 2862–68.

35 Green LS, Lux RL, Ershler PR, et al. Resolution of pace mapping stimulus site separation using body surface potentials. *Circulation* 1994; **90**: 462–68.

36 Callans DJ, Menz V, Schwartzman D, et al. Repetitive monomorphic ventricular tachycardia from left ventricular outflow tract: electrocardiographic patterns consistent with a left ventricular site of origin. *J Am Coll Cardiol* 1997; **29**: 1023–27.

37 Yeh SJ, Wen MS, Wang CC, et al. Adenosine-sensitive ventricular tachycardia from the anterobasal left ventricle. *J Am Coll Cardiol* 1997; **30**: 1339–45.

38 Shimoike E, Ohnishi Y, Ueda N. et al. Radiofrequency catheter ablation of the left ventricular outflow tract tachycardia from a coronary cusp: a new approach to the tachycardia focus. *J Cardiovasc Electrophysiol* 1999; **10**: 1005–9.

39 Sadanaga T, Saeki K, Yoshimoto T, et al. Repetitive monomorphic ventricular tachycardia of the left coronary cusp origin. *Pacing Clin Electrophysiol* 1999; **22**: 1553–56.

40 Da Paola AV, Melo WDS, Tavora MZP, et al. Angiographic and electrophysiological substrates for ventricular tachycardia mapping through the coronary veins. *Heart* 1998; **79**: 59–63.

41 Haghjoo M, Arya A, Dehghani MR et al. Coexistence of atrioventricular nodal reentrant tachycardia and idiopathic left ventricular outflow-tract tachycardia. *Indian Pacing Electrophysiol J* 2005; **5**: 149–54.

42 Ouyang F, Fotuhi P, Ho SY, et al. Repetitive monomorphic ventricular tachycardia originating from the aortic sinus cusp: electrocardiographic characterization for guiding catheter ablation. *J Am Coll Cardiol* 2002; **39**, 500–8.

43 Daniels DV, Lu YY, Morton JB, et al. Idiopathic epicardial left ventricular tachycardia originating remote from the sinus of Valsalva: electrophysiological characteristics, catheter ablation, and identification from the 12-lead electrocardiogram. *Circulation* 2006; **113**: 1659–66.

28

CHAPTER 28

Role of Different Stimulation Techniques (Pace Mapping, Entrainment Mapping) in Different Subsets of Ventricular Tachycardia

Frank Bogun, MD, *Fred Morady*, MD

Division of Cardiology, Department of Internal Medicine, University of Michigan Health System, Ann Arbor, MI, USA

Summary

The presence of entrainment identifies the mechanism of a ventricular tachycardia as reentrant. Furthermore entrainment in the setting of a hemodynamically tolerated ventricular tachycardia is used to identify critical areas of the reentry circuit that are amenable to radiofrequency ablation. If a ventricular tachycardia is not hemodynamically tolerated, pace-mapping is used to localize the exit site. For focal ventricular tachycardias, pace-mapping is helpful in identifying the site of origin.

Introduction

Entrainment pacing and pace-mapping are complementary mapping techniques that provide information about mechanisms as well as the site of origin of ventricular arrhythmias. Entrainment techniques have been used to characterize the mechanism of reentrant arrhythmias, including atrial flutter, postinfarction ventricular tachycardia, AV nodal reentry tachycardia, atrial tachycardia, and orthodromic reciprocating tachycardia.

Cardiac Mapping, Third Edition Edited by Mohammad Shenasa, Gerhard Hindricks, Martin Borggrefe, and Günter Breithardt
 ISBN: 978-1-405-17572-2

Classic entrainment must be distinguished from concealed entrainment. During classic entrainment of ventricular tachycardia, the following criteria are present:

1 Constant fusion except for the last beat that is entrained but not fused when pacing is performed during tachycardia (Figure 28.1a).

2 Progressive fusion when pacing at progressively more rapid rates (Figure 28.1a,b)

3 Resumption of the original ventricular tachycardia upon the cessation of pacing.

4 Interruption of the arrhythmia due to localized conduction block.

During entrainment, the wave front from a pacing stimulus enters the excitable gap of the reentry

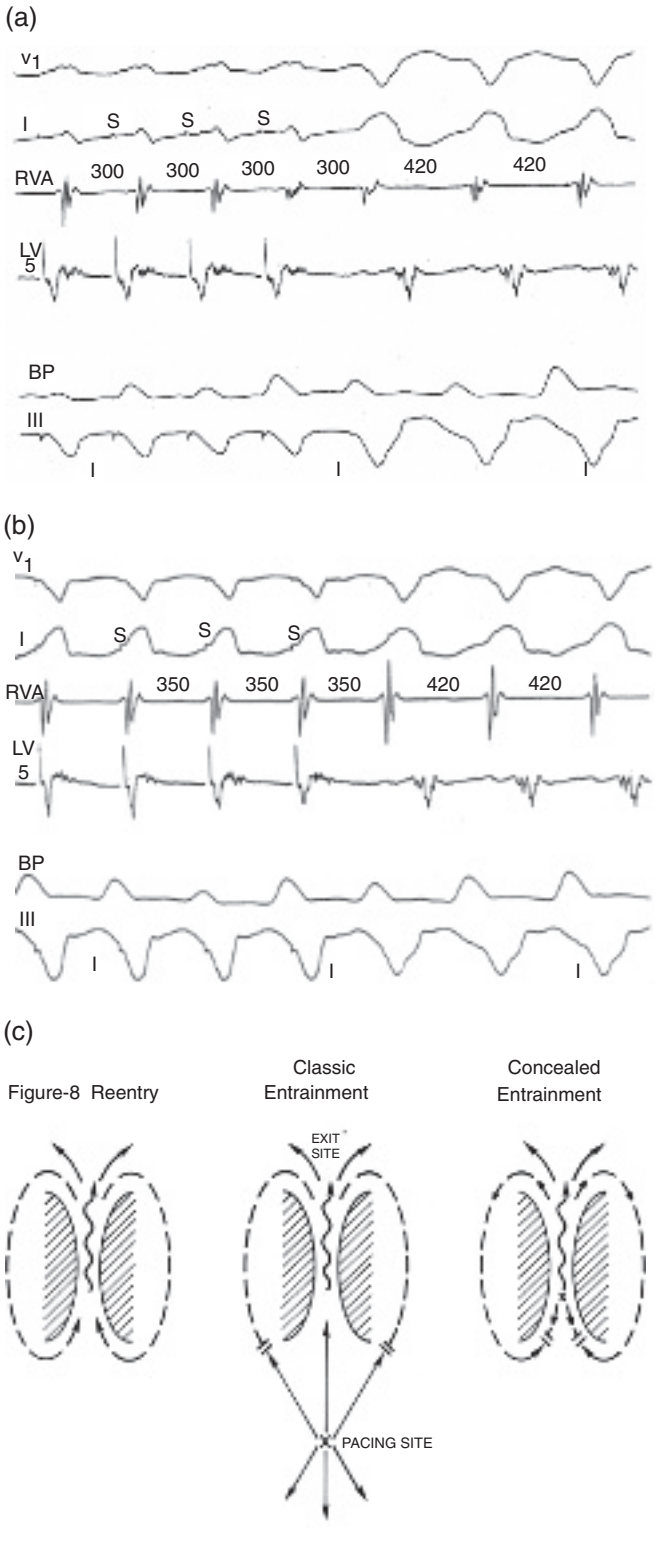

Figure 28.1 (a) Leads V1, I, and III, intracardiac tracings (RVA, LV) and pressure tracings (BP) in a postinfarction patient during VT. Pacing is performed during VT at a cycle length of 300 msec with the mapping catheter located in the left ventricle (LV). The QRS complexes during pacing are fused. The last entrained beat is not fused. This is typical of classic entrainment. (b) Shown are the same recordings as in part (a). Pacing is performed at a cycle length of 350 msec. There is less fusion compared to the tracings in part (a) where pacing was performed at a cycle length of 300 msec. This is an example of progressive fusion, which also is typical of classic entrainment. (c) A figure-of-8 model of postinfarction reentry. Pacing proximal to the area of slow conduction results in classic entrainment. Pacing within the protected zone of slow conduction results in concealed entrainment.

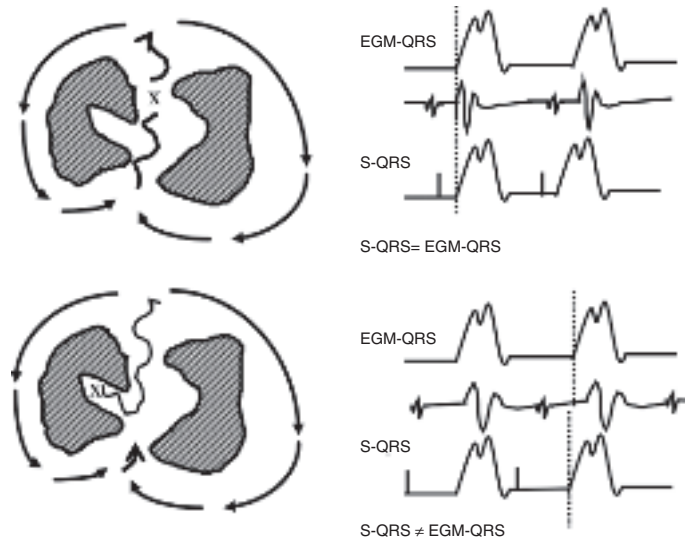

Figure 28.2 Schema of the figure-of-8 reentry circuit with the mapping catheter being located at a critical isthmus (upper panel) and at a bystander site (lower panel). For the critical isthmus site, surface ECG tracings illustrating the uninterrupted VT are shown on top followed by intracardiac tracings from the mapping catheter (middle). Note the isolated potential from which the onset of the EGM-QRS interval is measured. In the bottom tracing the QRS complex during entrainment mapping is shown. The stimulus–QRS interval is measured from the stimulus artifact to the beginning of the QRS complex (indicated by the dotted line). The EGM-QRS interval matches the stimulus–QRS interval at the critical isthmus. In the lower panel, the catheter is within a bystander pathway. The recordings to the right are analogous to the recordings in the top panel. The simulus–QRS interval is longer than the EGM–QRS interval. Ablation here is highly unlikely to be effective.

circuit. It then propagates through the zone of slow conduction in the orthodromic direction (i.e., same direction as the wave front of the spontaneous reentrant tachycardia), thereby resetting it to the paced rate. An antidromic wave front collides and fuses with the orthodromic wave front of the preceding beat (Figure 28.1c).

The demonstration of entrainment establishes the presence of reentry with an excitable gap. In classic entrainment, pacing is performed proximal to the zone of slow conduction. If pacing is performed from within the zone of slow conduction, concealed entrainment may be demonstrated. In this form of entrainment, during pacing, the antidromic wave front from the pacing impulse is blocked in the area of slow conduction (Figure 28.1c, right panel). The orthodromic wave front from the pacing impulse exits from the area of slow conduction, entraining the tachycardia to the pacing rate (Figure 28.2a). Because the antidromic wave front is blocked within the area of slow conduction, it does not collide with the orthodromic wave front of the previous beat, and therefore there is no fusion. This results in acceleration of the tachycardia to the pacing cycle length without a change in QRS morphology, even when pacing is performed at progressively faster rates. Often there is a long stimulus-QRS interval since pacing is performed within the zone of slow conduction (Figure 28.2a).

The presence of concealed entrainment has greatly enhanced the ability to identify and localize the critical components of reentrant ventricular tachycardia. This is the case predominantly for postinfarction VT [1] but also for other scar-related ventricular tachycardias in the setting of dilated cardiomyopathy [2] or prior ventriculotomy for repair of congenital heart disease [3, 4].

Use of Entrainment Mapping and Pace-Mapping for Ventricular Tachycardias

Concealed entrainment helps to identify critical components of a reentrant VT. However a significant limitation of entrainment mapping is that it can only be used in hemodynamically tolerated VTs. Pace-mapping can be used to identify the site of

origin of a focal VT or the exit site of a reentrant VT. The advantage of pace mapping is that it is feasible for hemodynamically unstable VTs.

Use of Entrainment Mapping/Pace-Mapping in Postinfarction VT

In the setting of healed myocardial infarction, reentry is the mechanism of sustained monomorphic VT and entrainment mapping can be used in the setting of hemodynamically tolerated VT. The ideal patient for a mapping and ablation procedure has VTs (the fewer the better) that are hemodynamically tolerated and that can be reproducibly induced. Unfortunately, this type of patient accounts for less than 10% of all patients referred with VT [5].

Entrainment mapping techniques are helpful to identify critical components of the reentry circuit of tolerated postinfarction VT. Depending on the location of the mapping catheter relative to the reentry circuit, different entrainment responses can be expected, as shown in Figures 28.1 and 28.2. The presence of concealed entrainment indicates that the mapping catheter is in contact with a protected zone of the reentry circuit. This zone may be critical to the reentry circuit or it may be a bystander area that feeds into a critical area.

If concealed entrainment is used as the only mapping criterion, the positive predictive value for an effective ablation site is approximately 50% [6]. Additional criteria in conjunction with concealed entrainment help to differentiate bystander from critical areas. Pacing is typically performed at a cycle length 20–50 msec shorter than the VT cycle length. Entrainment pacing is performed at sites with fragmented, low-voltage electrograms preceding the onset of the QRS complex during VT.

At a site of concealed entrainment, the ratio of the stimulus-QRS interval to the ventricular tachycardia cycle length as well as a comparison between stimulus–QRS interval and electrogram–QRS interval helps to further categorize the location of the mapping catheter within the protected zone of the circuit: Matching stimulus–QRS interval and electrogram–QRS intervals (Figures 28.2 and 28.3) indicate that the catheter is in contact with the common pathway of the reentry circuit. Because pacing is performed at a shorter cycle length than the VT

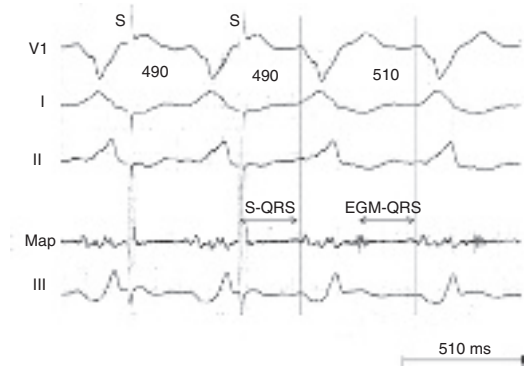

Figure 28.3 Leads V1, I, II, and III and the intracardiac recordings from the mapping catheter (map) when pacing (S) is performed during VT. The VT is entrained and there is no apparent fusion on the surface ECG leads. This is an example of concealed entrainment at a pacing site within a critical isthmus of the VT. Note the multicomponent, fragmented electrogram in diastole. The stimulus–QRS interval (S–QRS) is equal to the electrogram interval (EGM–QRS), as illustrated in Figure 28.2.

cycle length, decremental conduction may occur, resulting in a longer stimulus–QRS interval compared to the electrogram–QRS interval.

A discrepancy of up to 30 msec is acceptable evidence that the catheter is within the reentry circuit. A mismatch of >30 msec indicates that the catheter is in contact with a bystander zone and ablation at this location is unlikely to result in elimination of the VT (Figure 28.3).

A variety of techniques have been used to distinguish the critical common pathway of a reentry circuit from nonessential bystander pathways. In a study using receiver operating characteristics curves, the criterion with the best sensitivity/specificity was found to be the degree of mismatch between the stimulus–QRS and electrogram–QRS intervals [7]. A cut-off value of 30–35 msec resulted in the highest accuracy for identifying a critical component of the reentry circuit. The postpacing interval is also used to differentiate critical from bystander sites [1]. Whereas the postpacing interval encompasses an entire revolution in the reentry circuit, the stimulus–QRS interval and electrogram–QRS interval assess only a small segment of the entire circuit, namely, the segment between the pacing/recording site and the exit of the VT. In theory, this criterion (a mismatch between stimulus-QRS and electrogram-QRS interval) may

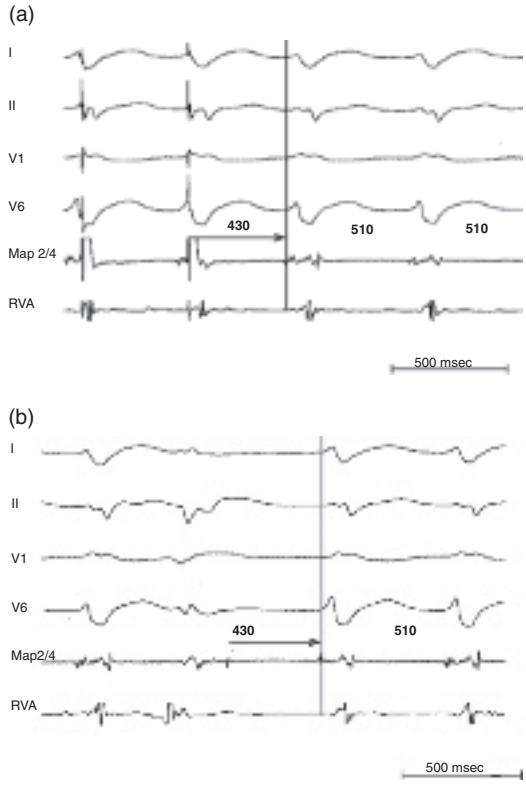

Figure 28.4 Pacing at a cycle length of 450 msec during a postinfarction VT. The third QRS complex is entrained and displays an identical QRS morphology to the spontaneous VT. The stimulus–QRS interval is 430 msec and the S–QRS/VT cycle length ratio is 0.84, suggesting that the catheter is either located in a bystander area or within the entry area of the common pathway. (b) Same format as in part (a), with the catheter located at the same site where pacing had been performed. A PVC from the right ventricle unmasks the presence of an isolated potential that cannot be dissociated from the VT. The EGM–QRS interval when measured from this potential is equal to the S–QRS interval [part (a)] indicating that the catheter is located within the critical zone (entry area) of the reentry circuit rather than a bystander site.

have the advantage of being less susceptible to factors impacting on the entire circuit.

Another criterion, the stimulus–QRS/VT cycle length ratio, also has been used to separate bystander sites from critical areas. Using computer simulations, a stimulus–QRS/VT cycle length ratio >0.7 was determined to be indicative of a pacing site within a bystander pathway. A ratio <0.6 increases the probability that the pacing site is within a critical component of the reentry circuit [7]. However, if the mapping catheter is located close to the entry site of the common pathway, ablation at this site may be effective despite a stimulus–QRS/VT cycle length ratio >0.7 (Figure 28.4a). In this situation, there often is an isolated potential present in systole or early diastole (Figure 28.4b) [8]. Furthermore when entrainment mapping is performed near the entry site of a common pathway, there should be matching stimulus–QRS and electrogram–QRS intervals.

In comparing various mapping criteria that are currently used for hemodynamically tolerated VT, the criterion with the highest positive predictive value for an effective ablation site is the termination of VT without global ventricular capture (Figure 28.5) [7, 9]. VT termination without global ventricular capture occurs only if the pacing site is within a critical component of the reentry circuit. The clinical value of this mapping criterion is limited by poor sensitivity.

Identification of isolated potentials during ventricular tachycardia is particularly helpful in identifying potential target areas for ablation. Isolated potentials are generated by activation of surviving muscle bundles within scar tissue. If the isolated potential cannot be dissociated from VT by pacing maneuvers, the accuracy of predicting an effective target site is greatly enhanced [6, 7]. Sites with isolated potentials during VT often also correspond to areas where different VT reentry circuits share

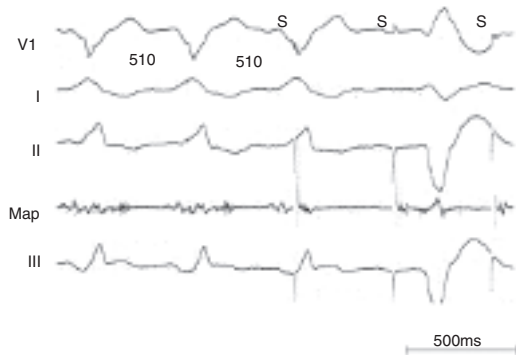

Figure 28.5 These tracings illustrate termination of VT by a subthreshold stimulus that does not result in global ventricular capture. The format is the same as in Figure 28.3. The first pacing stimulus terminates the VT without generating a QRS complex. The next QRS complex is captured and has a long stimulus–QRS interval, and occurs after termination of the VT during sinus rhythm. This was an effective ablation site.

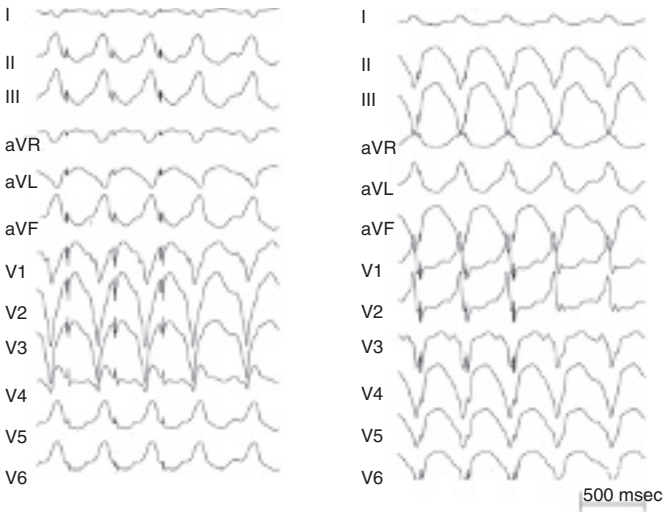

Figure 28.6 These tracings illustrate the response to pacing at a single site performed during two different VTs. In the left panel, pacing was performed during a left bundle branch block VT and there is concealed entrainment. In the right panel, pacing was performed during a different VT that had a right bundle branch block configuration. Again there is concealed entrainment. This indicates that the critical isthmus of both VT circuits shared a single common pathway with different exit sites.

critical components. Not uncommonly, concealed entrainment can be demonstrated at a particular site not just for one VT but for multiple VTs (Figure 28.6) [10].

The stimulus–QRS interval during concealed entrainment is an indicator of the distance between the mapping catheter and the VT exit site. If the stimulus–QRS interval/VT cycle length ratio is <0.3, the catheter probably is located near the exit site of the common pathway. A ratio of >0.7 with matching stimulus–QRS and electrogram–QRS intervals indicates that the catheter is located near the entry site of the circuit. A stimulus–QRS/VT cycle length ratio of 0.3–0.7 indicates a pacing site within the central component of the VT isthmus. A single application of radiofrequency energy may result in VT termination because the surviving muscle bundles form a narrow isthmus [6, 11]. However, multiple applications of radiofrequency energy may be required if the isthmus is broad.

Although these criteria are very helpful in identifying critical isthmus sites, most inducible VTs are not hemodynamically tolerated, and therefore entrainment techniques are not feasible. Pace-mapping has been found to be helpful to identify the VT exit site of nontolerated VTs along the scar border zone. [12] When combined with the presence of isolated potentials (Figure 28.7a), pace-mapping within scar tissue (Figure 28.7b) [13] may identify a component of the common pathway [14].

The spatial resolution of pace-mapping within scar tissue has not been adequately described. In a prior study, sites with perfect pace maps (i.e., a perfect QRS match in 12/12 leads), as compared to sites with a good pace map (i.e., a perfect QRS match in 10–11 of 12 leads), were located within lower voltage tissue, displayed a longer stimulus–QRS interval, and more often displayed isolated potentials during sinus rhythm. However, the probability of successful ablation was equally good at sites with perfect and good pace-maps [14]. The main draw back of pace-mapping for localizing postinfarction reentry circuits is its ability to only identify the exit site of the reentry circuit and not the entire critical isthmus.

Postventriculotomy VT

Macroreentry in the right ventricular outflow tract can occur years after corrective surgery in patients with tetralogy of Fallot. The macroreentry circuit occurs around the ventriculotomy scar in the right ventricular outflow tract and can be mapped and ablated using entrainment techniques [3]. Three-dimensional electroanatomic mapping is particularly helpful because a broad isthmus often is present and a line of block between the ventriculotomy scar and another anatomical obstacle (i.e., the tricuspid annulus) is required [4].

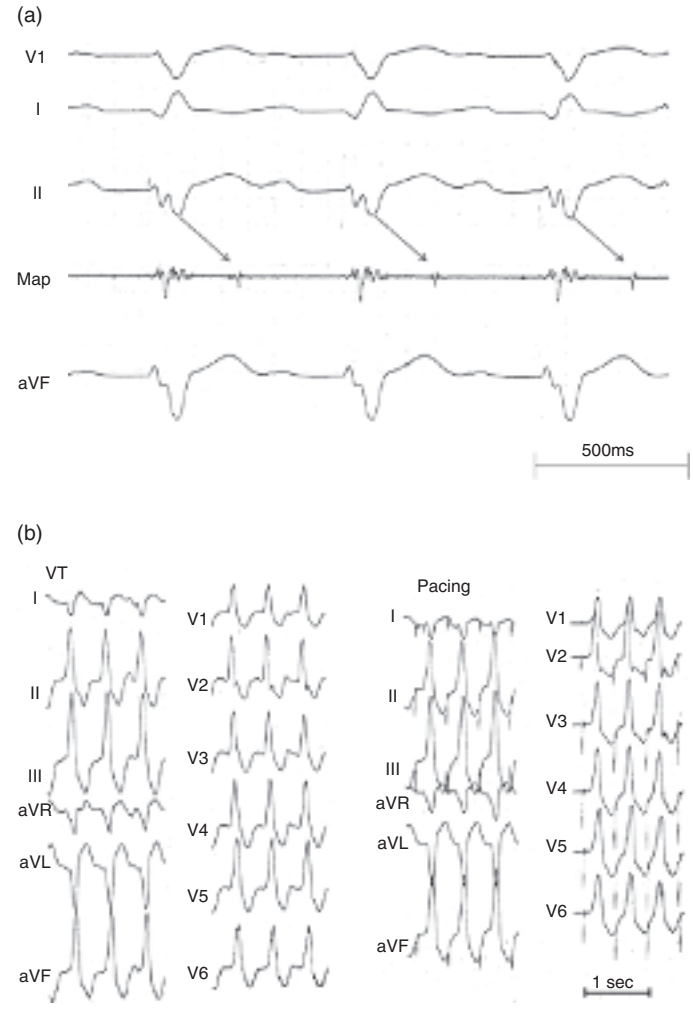

Figure 28.7 (a) Leads V1, I, II, and aVF and intracardiac electrograms from the mapping catheter (map) in a patient with postinfarction VT. An isolated potential is recorded at the basal lateral left ventricular wall (arrows). (b) This figure shows the clinical VT (left panel) compared to the pace-map (right panel) when pacing was performed at the site with the isolated potential [part (a)]. This was a critical isthmus for this VT.

Use of Entrainment Mapping/Pace-Mapping in Nonischemic Cardiomyopathy

VT in Nonischemic Cardiomyopathy

Reentry is the most common mechanism of VT in patients with nonischemic cardiomyopathy [2]. Entrainment mapping and pace-mapping can be used in a similar manner as with postinfarction VT. In contradistinction to the subendocardial location of the reentry circuit in postinfarction patients, the reentry circuit in nonischemic cardiomyopathy is more likely to be intramural or epicardial [2]. As in postinfarction VT, the use of entrainment mapping is limited to VTs that are hemodynamically tolerated. Pace-mapping can be used for VTs that are not hemodynamically tolerated [12]. Focal arrhythmias account for a minority of VTs in patients with nonischemic cardiomyopathy. Pace-mapping in conjunction with activation mapping is the mapping technique of choice to localize the site of origin of focal ventricular arrhythmias.

VT in Patients with Cardiac Sarcoidosis

VT in patients with cardiac sarcoidosis can either be caused by an acute inflammatory flare-up or after the chronic formation of scar. Granulomas set the stage for the arrhythmogenic substrate and are often located within the mid-myocardium. The endocardium or epicardium is reached by extension of myocardial lesions. Mechanisms of VT are

not completely understood. Most likely similar to postinfarction VT, scar formation results in reentry circuits. Entrainment mapping has been used successfully in patients with cardiac sarcoidosis [15].

Arrhythmogenic Right Ventricular Dysplasia

Reentry is the predominant mechanism of VT in patients with ARVD. Entrainment mapping has been used to target hemodynamically tolerated VT. The long-term results of ablation of VT in the setting of ARVD are discouraging, probably because of the progressive nature of the disease process [16, 17].

Bundle Branch Reentry

Bundle branch reentry is most likely to occur in patients with nonischemic cardiomyopathy and disease in the His–Purkinje system. The postpacing interval when pacing at the right ventricular apex is particularly helpful in establishing the diagnosis of bundle branch reentry [18]. In bundle branch reentry the postpacing interval is $\leq$30 msec, whereas a postpacing interval of $>$30 msec indicates a myocardial VT.

Use of Pace-Mapping for Idiopathic VT

Pace-mapping and activation mapping are the methods of choice for identifying the site of origin of focal arrhythmias such as right ventricular outflow tract VT. The spatial resolution of pace-mapping has been assessed in the right ventricular outflow tract and was found to be less than the spatial resolution of activation mapping [19]. The accuracy of pace-mapping is further compromised if the site of origin of a focal arrhythmia is intramural. Nevertheless, pace-mapping is the only feasible mapping technique for identifying the site of origin of a focal VT if the VT is not reproducibly inducible or hemodynamically tolerated.

Use of Entrainment Mapping and Pace-Mapping for Fascicular VT

Reentry involving the Purkinje system and possibly the Purkinje–muscle interface appears to be the underlying mechanism of fascicular VT. This type of VT can be entrained by pacing within the fascicular system, with concealed entrainment being demonstrated as in postinfarction VT. Entrainment techniques have been used in fascicular VTs to establish the reentrant mechanism of this arrhythmia. However, entrainment mapping typically is not helpful for identifying ablation sites for fascicular VT [20]. Similarly, pace-mapping has not been helpful for identifying critical ablation sites [21]. Purkinje potentials or diastolic potentials during VT identify appropriate target sites for radiofrequency ablation [20, 22].

The Purkinje system also may participate in postinfarction VT if the septum is involved, and this may result in VT with a relatively narrow QRS [23]. In this situation, the critical component is not only confined to parts of the fascicular system but also involves surviving muscle bundles within scar tissue. In the presence of hemodynamically tolerated VT, the presence of concealed entrainment is particularly helpful to identify appropriate ablation sites.

References

1 Stevenson W, Khan H, Sager P, et al. Identification of reentry circuit sites during mapping and radiofrequency ablation of ventricular tachycardia late after myocardial infarction. *Circulation* 1993; **88**: 1647–70.

2 Soejima K, Stevenson WG, Sapp JL, Selwyn AP, Couper G, Epstein LM. Endocardial and epicardial radiofrequency ablation of ventricular tachycardia associated with dilated cardiomyopathy: the importance of low-voltage scars. *J Am Coll Cardiol* 2004; **43**: 1834–42.

3 Gonska BD, Cao K, Raab J, Eigster G, Kreuzer H. Radiofrequency catheter ablation of right ventricular tachycardia late after repair of congenital heart defects. *Circulation* 1996; **94**: 1902–8.

4 Stevenson WG, Delacretaz E, Friedman PL, Ellison KE. Identification and ablation of macroreentrant ventricular tachycardia with the CARTO electroanatomical mapping system. *Pacing Clin Electrophysiol* 1998; **21**: 1448–56.

5 Kim Y, Sosa-Suarez G, Trouton T, et al. Treatment of ventricular tachycardia by transcatheter radiofrequency ablation in patients with ischemic heart disease. *Circulation* 1994; **89**: 1094–102.

6 Bogun F, Bahu M, Knight B, et al. Comparison of effective and ineffective target sites that demonstrate concealed entrainment in patients with coronary artery disease undergoing radiofrequency ablation of ventricular tachycardia. *Circulation* 1997; **95**: 183–90.

7 Bogun F, Kim HM, Han J, et al. Comparison of mapping criteria for hemodynamically tolerated, postinfarction ventricular tachycardia. *Heart Rhythm* 2006; **3**: 20–6.

8 Bogun F, Knight B, Goyal R, et al. Discrete systolic potentials during ventricular tachycardia in patients with prior myocardial infarction. *J Cardiovasc Electrophysiol* 1999; **10**: 364–69.

9 Bogun F, Krishnan SC, Marine JE, et al. Catheter ablation guided by termination of postinfarction ventricular tachycardia by pacing with nonglobal capture. *Heart Rhythm* 2004; **1**: 422–26.

10 Bogun F, Li YG, Groenefeld G, et al. Prevalence of a shared isthmus in postinfarction patients with pleiomorphic, hemodynamically tolerated ventricular tachycardias. *J Cardiovasc Electrophysiol* 2002; **13**: 237–41.

11 El-Shalakany A, Hadjis T, Papageorgiou P, Monahan K, Epstein L, Josephson ME. Entrainment/mapping criteria for the prediction of termination of ventricular tachycardia by single radiofrequency lesion in patients with coronary artery disease. *Circulation* 1999; **99**: 2283–89.

12 Marchlinski FE, Callans DJ, Gottlieb CD, Zado E. Linear ablation lesions for control of unmappable ventricular tachycardia in patients with ischemic and nonischemic cardiomyopathy. *Circulation* 2000; **101**: 1288–96.

13 Bogun F, Good E, Reich S, et al. Isolated potentials during sinus rhythm and pace-mapping within scars as guides for ablation of postinfarction ventricular tachycardia. *J Am Coll Cardiol* 2006; **47**: 2013–19.

14 Bogun F, Bahu M, Knight B, et al. Response to pacing at sites of isolated diastolic potentials during ventricular tachycardia in patients with previous myocardial infarction. *J Am Coll Cardiol* 1997; **30**: 505–13.

15 Koplan BA, Soejima K, Baughman K, Epstein LM, Stevenson WG. Refractory ventricular tachycardia secondary to cardiac sarcoid: electrophysiologic characteristics, mapping, and ablation. *Heart Rhythm* 2006; **3**: 924–29.

16 Ellison KE, Friedman PL, Ganz LI, Stevenson WG. Entrainment mapping and radiofrequency catheter ablation of ventricular tachycardia in right ventricular dysplasia. *J Am Coll Cardiol* 1998; **32**: 724–28.

17 Dalal D, Jain R, Tandri H, et al. Long-term efficacy of catheter ablation of ventricular tachycardia in patients with arrhythmogenic right ventricular dysplasia/cardiomyopathy. *J Am Coll Cardiol* 2007; **50**: 432–40.

18 Merino JL, Peinado R, Fernandez-Lozano I, et al. Bundle-branch reentry and the postpacing interval after entrainment by right ventricular apex stimulation: a new approach to elucidate the mechanism of wide-QRS-complex tachycardia with atrioventricular dissociation. *Circulation* 2001; **103**: 1102–8.

19 Taj M, Ting M, Kim H, et al. Spatial resolution of pace-mapping of idiopathic ventricular tachycardia/ectopy originating in the right ventricular outflow tract. *Heart Rhythm J* 2006; **3**: S288-P5-85.

20 Nakagawa H, Beckman K, McClelland J, et al. Radiofrequency ablation of idiopathic left ventricular tachycardia guided by a Purkinje potential. *Circulation* 1994; **88**: 2607–17.

21 Bogun F, El-Atassi R, Daoud E, Man KC, Strickberger SA, Morady F. Radiofrequency ablation of idiopathic left anterior fascicular tachycardia. *J Cardiovasc Electrophysiol* 1995; **6**: 1113–16.

22 Nogami A, Naito S, Tada H, et al. Demonstration of diastolic and presystolic Purkinje potentials as critical potentials in a macroreentry circuit of verapamil-sensitive idiopathic left ventricular tachycardia. *J Am Coll Cardiol* 2000; **36**: 811–23.

23 Bogun F, Good E, Reich S, et al. Role of Purkinje fibers in postinfarction ventricular tachycardia. *J Am Coll Cardiol* 2006; **48**: 2500–7.

29

CHAPTER 29

Endocardial Catheter Pace Mapping of Ventricular Tachycardias

Mithilesh K. Das, MD, *John C. Lopshire,* MD, *Deepak Bhakta,* MD, *Anil V. Yadav,* MD, *John M. Miller,* MD

Indiana University School of Medicine, Indianapolis, IN, USA

Summary

Several mapping techniques are used during catheter ablation of ventricular tachycardia (VT), including activation mapping, pace mapping, entrainment mapping, and substrate mapping. These mapping techniques complement one another, and all of these tools can be used to localize the critical isthmus of a hemodynamically stable sustained reentrant monomorphic VT, whereas activation mapping and pace mapping are the only useful techniques available for localizing the exit sites of a focal VT or frequent symptomatic premature ventricular complexes (PVCs).

Pace mapping is performed to replicate 12-lead ECG configuration of a spontaneous or induced VT. If the pace map from the isthmus site of a reentrant VT has a long S–QRS that is similar to the electrogram (Egm) during VT, and yields complete replication of each feature of each ECG lead, it signifies that the catheter is located on the critical isthmus, which is an expected site of successful ablation.

Activation and pace mapping of a Purkinje-like potential prior to a PVC that initiates polymorphic VT and ventricular fibrillation is helpful in determining the successful site of ablation of these arrhythmias. Pace mapping is especially useful when VT is hemodynamically unstable because both activation and entrainment mapping require that the VT should be easily inducible, sustained, and hemodynamically stable so that sampling of Egm timing from multiple sites and repeated pacing maneuvers can be performed.

Introduction

Catheter ablation of ventricular tachycardia (VT) in the electrophysiology (EP) laboratory remains a challenging procedure. Several mapping techniques are used during catheter ablation of ventricular tachycardia [1, 2] including activation mapping, pace mapping, entrainment mapping and substrate mapping (Table 29.1). These mapping techniques complement one another, and all of these tools can be used to localize the critical isthmus of a hemodynamically stable sustained reentrant monomorphic VT (MMVT), whereas activation mapping and pace mapping are the only useful techniques

Cardiac Mapping, Third Edition Edited by Mohammad Shenasa, Gerhard Hindricks, Martin Borggrefe, and Günter Breithardt
 ISBN: 978-1-405-17572-2

Table 29.1 Comparison of Mapping Techniques.

	Activation mapping	*Entrainment mapping*	*Pace mapping*	*Substrate mapping*
Hemodynamically stable VT				
Focal	+	−	+	−
Macroreentry	+	+	+/−	+
Hemodynamically Unstable VT				
Focal	−	−	+	−
Macroreentry	−	−	+/−	+
Isolated PVCs	+	−	+	−

KEY: VT = ventricular tachycardia; PVCs = premature ventricular complexes; + = useful; − = not useful; +/− = sometimes useful.

available for localizing the exit sites of a focal VT or frequent symptomatic premature ventricular complexes (PVCs) [3, 4].

Activation mapping identifies the critical isthmus of a MMVT by the presence of one or multiple mid- to late-diastolic electrograms (Egms) during the VT and a presystolic Egm during a focal VT. Entrainment mapping is also a very useful technique for mapping a sustained MMVT and is initially performed from a site remote from the presumed isthmus by pacing at a cycle length marginally faster than that of the induced VT to demonstrate QRS fusion (manifest entrainment). Pacing is then performed at progressively faster rates from a site remote to the VT circuit to demonstrate progressive fusion of the VT morphology on the 12-lead ECG, confirming its reentrant mechanism (entrainment with progressive fusion). Entrainment mapping can then be performed from additional sites, comparing the difference between the interval from the stimulus (S) artifact to the electrogram at the pacing site on the first return complex of VT (the postpacing interval) and the VT cycle length as a indicator of proximity of the pacing site to a critical isthmus.

Finally, pacing can entrain from the site of presumed critical isthmus to confirm its participation in VT. This results in a 12-lead QRS morphology identical to the VT and if the PPI at that site is equal to or minimally longer (<30 msec) than the VT cycle length, it indicates that the mapping catheter is placed in the isthmus of the reentrant circuit (entrainment with concealed fusion). Mapping techniques for hemodynamically unstable MMVTs are limited to pace mapping and substrate mapping. Mapping and ablation for polymorphic VT or ventricular fibrillation (VF) is difficult because of a changing wavefront propagation, rapid heart rate, hemodynamic instability and poorly defined endpoint of success. Only the rare forms of polymorphic VT and VF that are triggered by repetitive monomorphic PVCs can currently be ablated successfully [5].

Pace mapping is performed to replicate the 12-lead ECG configuration of a spontaneous or induced VT and complements the findings of activation and entrainment mapping [3]. Pace mapping can help to localize the critical isthmus of a reentrant VT and the site of origin of a focal VT. It is especially useful when VT is hemodynamically unstable because both activation and entrainment mapping require that the VT should be easily inducible, sustained, and hemodynamically stable so that sampling of Egm timing from multiple sites and repeated pacing maneuvers can be performed.

Additionally, pace mapping is the only potentially useful technique for mapping a VT in the absence of structural heart disease when a 12-lead ECG of VT has been recorded during the clinical arrhythmia, but the VT is not inducible in the EP laboratory. Furthermore, entrainment mapping is not helpful for a focal VT mapping [6]. The purpose of the chapter is to describe the techniques, uses, and limitations of pace mapping.

Techniques

Pace mapping for VT and PVCs is performed by pacing from sites in the ventricles to entirely replicate

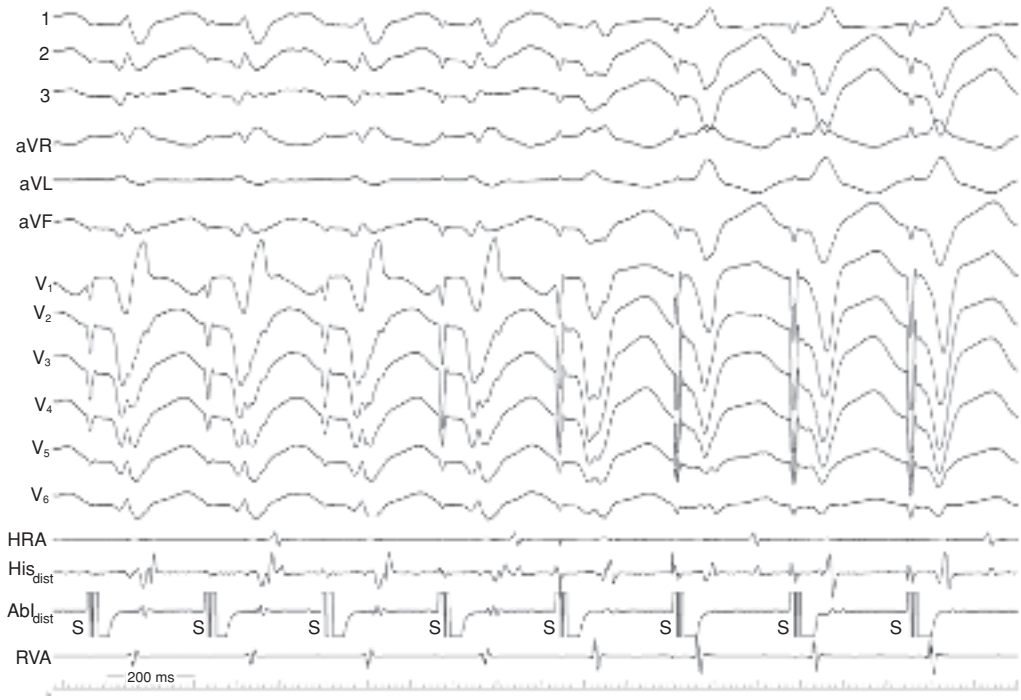

Figure 29.1 Effect of stimulus strength on pace map and S (stimulus)–QRS interval. Changing output at a fixed pacing rate at one site yields RBBB QRS when pacing at low output, whereas at a higher output (associated with shorter S–QRS), LBBB morphology is seen. Note that if pacing is done only at high output when looking for RBBB VT match, one may miss a good site because only LBBB will be seen.

the 12-lead QRS morphology of the VT induced in the EP laboratory or recorded on a standard ECG during the clinical arrhythmia, thereby to indicate the site of origin of a focal VT and critical isthmus of a reentrant VT. A careful analysis of the clinical VT ECG is prudent because it may be the only clue to target the area of interest if VT is not inducible. During a focal VT, its origin may be localized by endocardial pace mapping with precision in most cases except for the uncommon VTs originating from a deep intramural or epicardial focus.

It is important to understand that the QRS morphology obtained during pace mapping depends not only on the location of the catheter in relation to the VT circuit or exit site but also on several other factors. These include location of scar, catheter contact to the myocardial tissue, pacing output, unipolar vs. bipolar pacing, and interelectrode distance during bipolar pacing. Unipolar pacing at the same catheter tip location can result in QRS complexes that are different from those obtained with bipolar pacing, presumably due to an anodal contribution during bipolar pacing with the latter [7]. The use of bipolar pace mapping to localize sites of origin of ventricular tachycardia may result in less spatial resolution than unipolar pace-mapping.

Pace mapping should be performed at a rate similar to the target VT, using the minimum possible pacing output to ensure capture. Use of high pacing output may result in a relatively larger area of myocardial capture in the vicinity of the isthmus and may give rise to an erroneous QRS morphology, even when the pacing is performed in the true isthmus.

Figure 29.1 shows the effect of stimulus strength on both pace map and S–QRS interval with changing output at a fixed pacing rate. Pacing at the same site yields RBBB QRS when pacing at low output, whereas at a higher output (associated with shorter S–QRS), LBBB morphology is seen. If pacing is done only at high output when looking for a RBBB VT

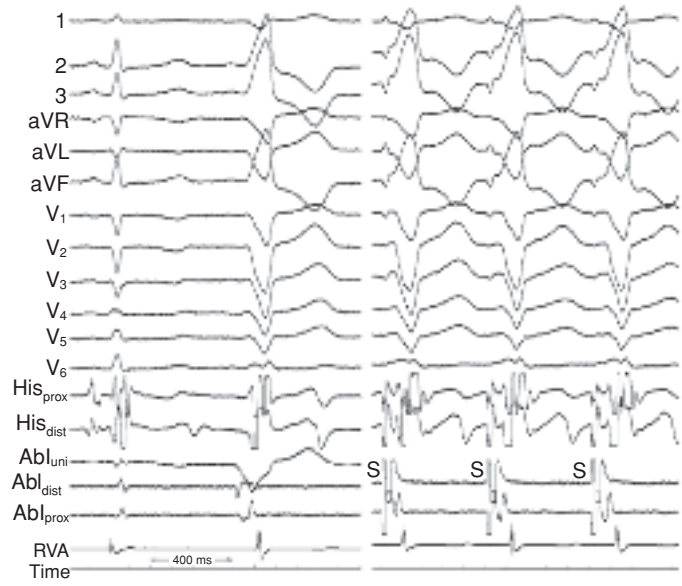

Figure 29.2 Pace mapping of a focal premature ventricular complex (PVC). Ablation distal (abl d) has an early potential site just prior to QRS onset. There is also a QS pattern in the unipolar recording (uni) from the ablation catheter. Pacing from the ablation catheter entirely replicates all 12 ECG leads including notches.

match, one may miss a potentially good ablation site because only the LBBB configuration will be seen. Therefore the pacing output should be set high enough to capture the myocardium within the scar tissue and low enough to have acceptable precision. Inability to capture the myocardium at an output of 10 mA or more despite good electrode–tissue contact denotes the presence of scar tissue that is unlikely to participate in the VT circuit.

The 12-lead ECG during pace mapping should be matched carefully with the 12-lead ECG of the clinical VT or the target PVCs. This is facilitated by displaying all 12 ECG leads of paced complexes and target VT side-by-side in adjacent windows on the monitor. Examples of good and poor pace maps are shown in Figures 29.2 and 29.3. Proper electrode positions should be checked on the thorax before the EP study to increase the reproducibility of pace mapping in patients in whom VT was recoded on a 12-lead ECG. Template matching algorithms have been developed to quantitate the degree of the 12-lead ECG match [8].

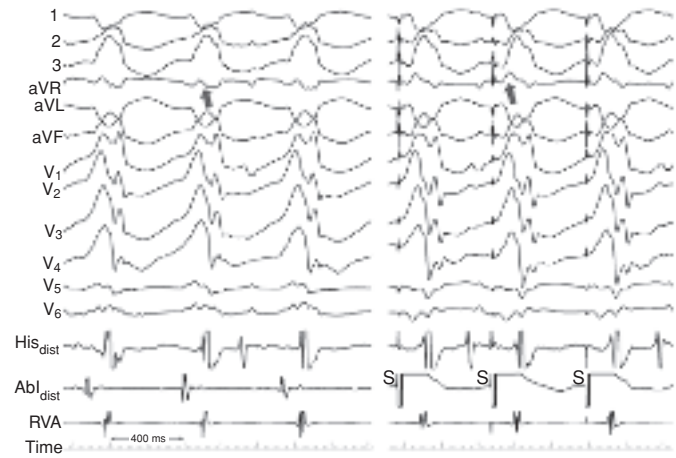

Figure 29.3 An example of a "not so good" or "poor" pace map in reentrant VT. Pace map on right, VT on left,. At first look the match appears to be close for QRS morphology in most of the leads, but is obviously different in lead aVR. Subtle differences are present in almost all leads.

Pace Mapping for VT

Most VTs in patients with myocardial scar from prior myocardial infarction, dilated cardiomyopathy, Chagas' disease, sarcoidosis, arrhythmogenic right ventricular cardiomyopathy, etc., are based on macroreentry in regions of established scar. As a general rule in postinfarct and LV cardiomyopathic scar-based VT, all left bundle branch block (LBBB) VTs arise from the left ventricular (LV) septum or paraseptal free wall, whereas right bundle branch block (RBBB) VTs can arise on the septum or free walls.

Furthermore, the QRS morphology in a reentrant VT also depends on other factors such as the amount of scar and orientation of heart in the thorax (horizontal vs. vertical) or on other pathology in the thoracic cavity (e.g., pneumonectomy) causing an alteration of the QRS vector. Sustained MMVT in patients with myocardial infarction scars is usually caused by myocardial reentry in the infarct border zone.

Most of these VT circuits have areas of surviving strands of myocardium interlaced with scar tissue, forming an anatomical barrier or an area of a functional block. These factors can provide the basis for the existence of an insolated thin strand of myocardium through which the impulse can propagate relatively slowly during diastole. Slow conduction through such a protected isthmus does not contribute to the surface ECG because of the low voltage generated by excitation of a very small mass of myocardium in the isthmus [9].

When the wave front leaves the isthmus at the exit site from which the more normal myocardium is rapidly depolarized, the QRS complex of VT results. When pace mapping is performed within such an isthmus, the stimulated wave front can only proceed along certain paths, which occur in at least two directions: the orthodromic and antidromic directions of propagation during VT. Similar to the reentrant VT, the wave front during pace mapping is only detected on the surface ECG when it leaves this protected isthmus. Pacing from the exit site should give rise to a similar QRS morphology and the S-QRS interval that is relatively short and similar to the electrogram (Egm) to QRS (Egm–QRS) interval.

Pacing proximal to the exit sites should give similar results except that the S–QRS and Egm–QRS intervals will be longer due to slow conduction of the impulse from that site to the exit site [10]. Pace mapping of a reentrant VT in Figure 29.4 shows a long Egm–QRS (arrow) and similar S–QRS with pacing, and complete replication of each feature of each ECG lead. When the isthmus is short, or the catheter is positioned more proximally (at an entrance site), the stimulated antidromic wave front leaves the protected isthmus at the entrance and propagates to the surrounding myocardium producing a different

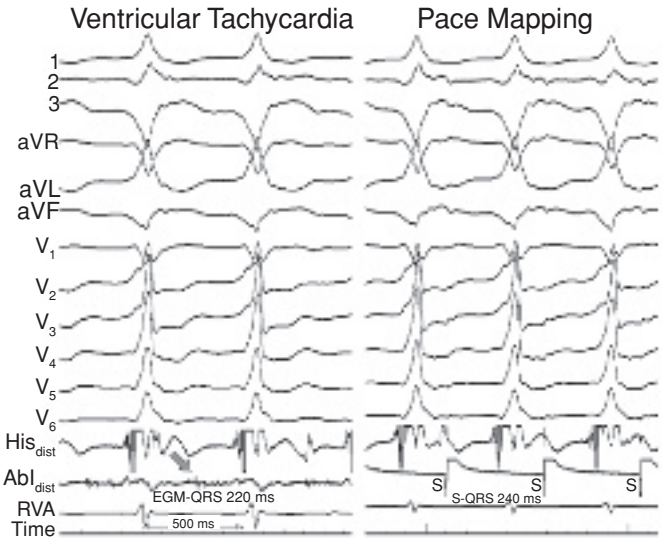

Figure 29.4 Pace mapping of a reentrant VT due to prior myocardial infarction. There is a long electrogram (Egm)–QRS interval (arrow) and similar stimulus–QRS with pacing, and complete replication of each feature of each ECG lead.

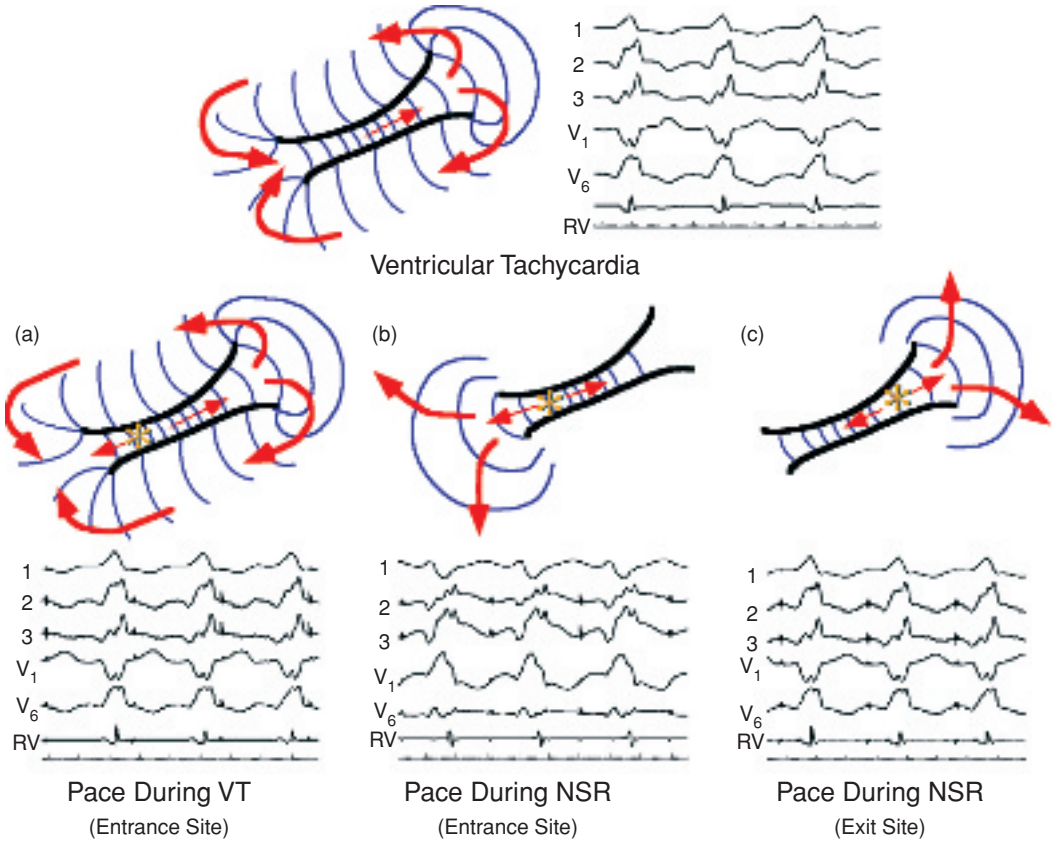

Figure 29.5 Entrainment vs. pace mapping for a reentrant VT. QRS morphology depends on the effect of pacing location in the reentrant circuit. VT is shown, as well as (a) pacing during VT near the entrance (proximal to the slow conduction zone) resulting in long S–QRS and QRS complexes identical to those of VT. In (b), pacing at the same site, but during NSR, shows a completely different QRS because the wave front can take a shorter path to normal myocardium than going through the diastolic corridor. In (c), pacing near the exit yields a QRS match with a shorter S–QRS interval.

QRS morphology. If the orthodromic wave front reaches the exit, a fused QRS complex is produced that includes depolarization from both antidromic and orthodromic wave fronts. Therefore, the resultant QRS morphology depends on the precise location of the pacing site relative to the reentrant circuit.

Figure 29.5 shows that pacing during VT near an entrance (proximal to much slow conduction) results in a long S–QRS and QRS morphology identical to VT, whereas pacing at the same site, but during sinus rhythm, shows a completely different QRS morphology because the pacing site has less slow conduction toward the exit site at which global myocardial activation begins compared to the diastolic corridor. Pacing near the exit yields a QRS match with a shorter S–QRS. On the contrary, focal VTs are associated with S–QRS and Egm–QRS that are equal and usually less than 40 msec.

Pace mapping during the baseline non-VT rhythm (sinus rhythm or atrial fibrillation, etc.) is similar to pacing during VT (entrainment) in that both aim to replicate the QRS complex recorded during VT. However, the techniques differ in that lines of block are established and maintained when pacing during VT, whereas they may not be present to constrain the spread of the paced wave front when performed during sinus rhythm. Therefore, pacing at the same site during VT may yield a QRS configuration very different from that obtained with pacing during sinus rhythm (Figure 29.5).

How to Interpret a Pace Map?

As mentioned earlier, an ideal pace map is considered to be "perfect" or "exact" if the QRS complexes in all 12 leads during pacing are identical to those of the targeted VT (i.e., superimposable). A pace map is considered to be "good" if the QRS complexes during pacing and VT are identical in 10 or 11 of the 12 leads [9, 11].

An ideal pace map in a reentrant VT has the same features and is usually derived when pacing from a site with a mid-diastolic potential and a long Egm–QRS (with an equal S–QRS during pacing). However, pace mapping should be interpreted carefully even if the Egm–QRS during pace mapping is short; this is because the reentry circuit exit is usually located at the border zone of myocardial scar and often has a short S–QRS and a perfect pace map from that site, suggesting that it may be a desirable target for ablation [12].

If pacing at sites near a presumed isthmus always produces QRS morphologies different from those of VT, then it indicates that the circuit is possibly located deep in to the myocardium, or functional block defines the circuit during VT. In one study, pace mapping did not match either of a patient's induced VTs in 15% of VTs with an identified isthmus, although a long S–QRS interval was present [9]. These findings are consistent with pace mapping at proximal isthmus sites, with propagation away from the circuit in the antidromic direction, as discussed above.

The longest S-QRS intervals of the identified isthmus with a mean of 94 ± 33 msec were much shorter than the longest S–QRS intervals of all sites in each patient, with a mean of 160 ± 70 msec ($P < 0.05$) [9]. The authors concluded that long S–QRS sites may be more proximal in isthmuses, where the antidromic wave front during pace mapping is able to propagate away from the reentry circuit, producing a QRS different from that of VT. These observations are consistent with a previous study showing that 66% of the sites at which the pace-mapping QRS complex resembled VT had an S–QRS interval <120 msec during entrainment, but in 89% of reentry circuit isthmus sites at which pace mapping did not match the VT QRS, the S–QRS during entrainment was >120 msec [13].

This is a likely explanation for the observation that the longest S–QRS sites in most patients do not match any of the induced VTs. It is also possible that some of these long S–QRS sites are located in bystander regions of abnormal conduction. A bystander channel of one VT circuit can be a critical isthmus of another circuit, so that ablation in these areas may also be appropriate if more than one VT with a relatively similar morphology is induced [9].

Pace Mapping for Focal MMVT or Isolated PVCs/Couplets/Bigeminy

Focal MMVT are generally encountered in patients with adenosine-sensitive idiopathic VT, but are rarely present in patients with myocardial infarction scar [14, 15]. There are two main methods of mapping these VTs: activation mapping and pace mapping.

Pace mapping is helpful in identifying the site of origin of a focal VT that may arise from any site in the ventricles. The majority arise in the right ventricular outflow tract (RVOT), but other common non-RVOT sites are the left ventricular outflow region, the mitral annulus, the tricuspid annulus, the interventricular septum, and the aortic sinuses of Valsalva. Therefore, careful attention should be paid to the 12-lead ECG of these VTs or PVCs because it helps to focus mapping efforts in the potential region of VT origin.

As mentioned earlier, entrainment mapping cannot be used in mapping a focal VT (no circuit), and activation and pace mapping are the mainstays for localizing the site of origin. Activation mapping is useful in the presence of frequent monomorphic PVCs or VT episodes, comparing the timing of activation of the Egm from the catheter tip electrode with the onset of the QRS complexes. The bipolar electrogram is universally used for this purpose, seeking a timing of 10–40 msec prior to the QRS onset. The unipolar recording from the catheter tip is also very helpful. At the suspected site of origin this should have a sharp "QS" deflection that times with the bipolar recording and precedes the QRS onset by a similar amount [16].

Of note, catheter-induced PVCs may also result in a sharp QS pattern, but the PVC morphology will match the clinical VT or PVC only when the catheter is located at the site of origin of VT. Pacing at the ideal site for ablation should exactly replicate the 12-lead ECG of the previously recorded target QRS complex, including any small notches, indicating

that stimulation is being performed from the site of ectopic impulse formation. Ablation at sites with a so-called "perfect" pace map is generally successful. Similar pace maps can be obtained when pacing from within 1–2 cm radius; thus, ablation at sites with only a "good" pace map is less likely to be successful in focal VTs [17].

As mentioned earlier, VTs in the setting of structural heart disease have a reentrant mechanism in the majority of patients, but a focal source of sustained MMVT has been reported in coronary artery disease (CAD) as well as in nonischemic cardiomyopathy [14, 18]. A focal mechanism of VT has been found in 5–8% of VTs in CAD [15, 18]. Similarly, a focal automatic mechanism was found to be responsible for the VT in 7/26 (27%) patients with nonischemic cardiomyopathy, who underwent radiofrequency ablation for VT in one study [19]. Thus, searching for mid-diastolic potentials and other criteria that apply to reentrant tachycardias would be fruitless, because activation times at the VT focus typically precede the QRS onset by only 10–40 ms. Pacing from the site of earliest prepotential (Egm) recorded during activation mapping should give rise to QRS morphology similar to that of the clinical VT and the VT induced during the EP study.

Utility of Pace Mapping for Macroreentrant VT

An exact pace map ("match") can be obtained in 49–81% of VTs [11]. The sensitivity and specificity of the pace map for successful radiofrequency ablation was studied with respect to the presence of isolated diastolic potentials in a study in which 81 VTs were induced in 19 patients. Pace mapping was performed at 681 distinct sites [11]. Isolated potentials were found more frequently at sites with "good" or "perfect" pace maps than at sites that were simply abnormal during VT ($p < 0.0001$). Pace maps at 65% of sites that displayed an isolated potential were either perfect or good, compared with 5% of sites with abnormal/fragmented Egms ($p < 0.0001$). At sites with isolated potentials, the mean S–QRS interval was longer than at sites with abnormal Egm (108 ± 43 msec vs. 81 ± 54 msec, $p < 0.0001$). With a cutoff isoelectric interval of ≥ 20 msc for the definition of isolated potentials, the sensitivity and specificity for identifying an isthmus area were 80% and 84%, respectively. With an isoelectric interval of $\geq$50 msec, the sensitivity and specificity for identifying an isthmus area were 54% and 90%, respectively.

Sites with a perfect pace map had a longer isoelectric segment separating the ventricular Egms from the isolated potential as compared with sites with closely matching pace maps (105 ± 79 msec vs. 70 ± 51 msec; $p < 0.001$). Pace mapping complemented the findings of entrainment mapping and by combining the two techniques, 41(50%) VT isthmus sites could be identified in 16 of 18 patients.

All but one of the isthmus sites displayed isolated potentials during sinus rhythm. Of 81 VTs for which no isthmus could be identified, 22 were no longer inducible after the ablation. None of the 16 patients in whom $\geq$1 isthmus could be identified had arrhythmic events during a follow-up of 10 months. Therefore matching pace maps at sites of isolated potentials identify critical components of postinfarction VT circuits. Pace mapping at the site of fractionated Egms (diastolic potentials) in the region of suspected isthmus resulted in progressive prolongation of the S–QRS interval as the pacing site moved along the isthmus consistent with pacing progressively further from the exit [20].

In summary, pace mapping is helpful in localizing the critical isthmus in up to 85% of VTs. The optimum site for ablation defined by activation mapping should be confirmed by entrainment mapping if the reentrant VT is readily inducible, sustained and hemodynamically stable. Pace mapping can be used to corroborate the findings of activation and entrainment mapping [21].

Pace Mapping for Polymorphic VT and VF

The majority of the polymorphic VTs are not amenable to any of the mapping techniques used for MMVT. Substrate mapping of the myocardial scar is often performed to interrupt potential circuits of reentry. However, rare forms of polymorphic VT originate from the right ventricular outflow tract (RVOT) in structurally normal hearts and in the LV in patients with history of myocardial infarction [22, 23]. These are triggered by monomorphic PVCs, which are usually preceded by a Purkinje-like potential.

In idiopathic polymorphic VT, activation and pace mapping of PVCs that initiate polymorphic VT can identify its site of origin. Radiofrequency ablation at these sites eliminates these trigger PVCs, preventing recurrence of malignant polymorphic VT or VF episodes with a high success rate. Although this variety of life-threatening VT is initiated by a repetitive monomorphic PVC, the QRS morphology changes in the subsequent beats, and rapid pace mapping from the earliest site of activation also results in a change of QRS morphology similar to the clinical polymorphic VT [24]. It is presumed that a shift in exit site during rapid pacing is responsible for the changing QRS morphology. Radiofrequency ablation of the PVC that initiates polymorphic VT or VF in patients with CAD can also be curative.

Limitations

One of the main limitations of pace mapping has always been lack of adherence to a strict definition of a pace "match"—that is, replication of the QRS morphology in each lead such that the pace map can be superimposed on the VT and show no differences. Some electrophysiologists have had failed ablation attempts after accepting "close" pace maps as indicating the source of a focal VT and have therefore discounted the value of pace mapping.

Another limitation is that it is sometimes difficult to determine whether a "perfect" pace map is an essential goal because sometimes successful radiofrequency ablation sites do not have a perfect or good pace map. A deep myocardial or subepicardial focus of circuit for VT or PVC during endocardial mapping may not produce nearly a perfect 12-lead pacing QRS match. Additionally, several other factors also influence a pace map. These include the size and polarity of the mapping/ablation electrode, degree of contact with the tissue, pacing output, area of a critical isthmus, depth of VT circuit in the myocardium and, scar or organized clot overlying the VT circuit.

A relatively larger tip catheter has a larger "antenna" for mapping and capturing relatively large amounts of myocardium during pacing and may produce a non-identical map even though ablation can be performed successfully at that site. Pacing at different regions of a protected isthmus may give rise to different pace maps, especially if the protected isthmus is relatively short and is surrounded by more healthy myocardium. Therefore, pacing at a good site in scar-based VT, but near the entrance to the isthmus, can produce a poor-appearing pace map. The sensitivity of pace mapping in locating the potential site of successful ablation in a scar-related reentrant VT is not ideal. Finally, the specificity of pace mapping is compromised if pacing is performed with a high output due to noncapture of the isthmus with nonspecific capture of surrounding myocardium.

Conclusion

Pace mapping is a useful technique during radiofrequency ablation of VT. It is typically used to confirm or corroborate the findings of other mapping techniques rather than being used as primary tool. However, sometimes it may be the only means to localize the site of origin of a focal VT or the critical isthmus of a reentrant VT, if the VT cannot be induced in the EP laboratory or the VT is hemodynamically unstable. Pace mapping can also be used to target the PVCs for radiofrequency ablation that trigger polymorphic VT or VF in these uncommon patients. However, like any tool, pace mapping must be used correctly to obtain the optimal result.

References

1 Rothman SA, Hsia HH, Cossu SF, Chmielewski IL, Buxton AE, Miller JM. Radiofrequency catheter ablation of postinfarction ventricular tachycardia: long-term success and the significance of inducible nonclinical arrhythmias. *Circulation* 1997; **96**: 3499.

2 Stevenson WG, Soejima K. Catheter ablation for ventricular tachycardia. *Circulation* 2007; **115**: 2750.

3 Josephson ME, Waxman HL, Cain ME, Gardner MJ, Buxton AE. Ventricular activation during ventricular endocardial pacing. II. Role of pace-mapping to localize origin of ventricular tachycardia. *Amer J Cardiol* 1982; **50**: 11.

4 Josephson ME, Horowitz LN, Spielman SR, Waxman HL, Greenspan AM. Role of catheter mapping in the preoperative evaluation of ventricular tachycardia. *Amer J Cardiol* 1982; **49**: 207.

5 Haissaguerre M, Shoda M, Jais P, et al. Mapping and ablation of idiopathic ventricular fibrillation. *Circulation* 2002; **106**: 962.

6 Waxman HL, Josephson ME. Ventricular activation during ventricular endocardial pacing: I. Electrocardiographic patterns related to the site of pacing. *Amer J Cardiol* 1982; **50**: 1,

7 Kadish AH, Schmaltz S, Morady F. A comparison of QRS complexes resulting from unipolar and bipolar pacing: implications for pace-mapping. *Pacing Clin Electrophysiol* 1991; **14**: 823.

8 Gerstenfeld EP, Dixit S, Callans DJ, Rajawat Y, Rho R, Marchlinski FE. Quantitative comparison of spontaneous and paced 12-lead electrocardiogram during right ventricular outflow tract ventricular tachycardia. *J Amer Coll Cardiol* 2003; **41**: 2046.

9 Brunckhorst CB, Delacretaz E, Soejima K, Maisel WH, Friedman PL, Stevenson WG. Identification of the ventricular tachycardia isthmus after infarction by pace mapping. *Circulation* 2004; **110**: 652.

10 Harada T, Tomita Y, Nakagawa T, et al. Pace-mapping conduction delay at reentry circuit sites of ventricular tachycardia after myocardial infarction. *Heart Vessels* 1997; **12**: 232.

11 Bogun F, Good E, Reich S, et al. Isolated potentials during sinus rhythm and pace-mapping within scars as guides for ablation of post-infarction ventricular tachycardia. *J Amer Coll Cardiol* 2006; **47**: 2013.

12 Stevenson WG, Sager P, Nademanee K, et al. Identifying sites for catheter ablation of ventricular tachycardia. *Herz* 1992; **17**: 158.

13 Stevenson WG, Sager PT, Natterson PD, Saxon LA, Middlekauff HR, Wiener I. Relation of pace mapping QRS configuration and conduction delay to ventricular tachycardia reentry circuits in human infarct scars. *J Amer Coll Cardiol* 1995; **26**: 481.

14 Scott LG, Gervacio-Domingo GT, Altemose MA, Zipes DP, Miller, JM. Ablation of non-infarct-related ventricular tachycardia in patients with prior myocardial infarction. *J Amer College Cardiol* 2001; **37**: 99A (Abstract).

15 Lopera G, Stevenson WG, Soejima K, et al. Identification and ablation of three types of ventricular tachycardia involving the His–Purkinje system in patients with heart disease. *J Cardiovasc Electrophysiol* 2004; **15**: 52.

16 Miller JM, Pezeshkian NG, Yadav AV. Catheter mapping and ablation of right ventricular outflow tract ventricular tachycardia. *J Cardiovasc Electrophysiol* 2006; **17**: 800.

17 Azegami K, Wilber DJ, Arruda M, Lin AC, Denman RA. Spatial resolution of pace-mapping and activation mapping in patients with idiopathic right ventricular outflow tract tachycardia. *J Cardiovasc Electrophysiol* 2005; **16**: 823.

18 Soejima K, Stevenson WG, Sapp JL, Selwyn AP, Couper G, Epstein LM. Endocardial and epicardial radiofrequency ablation of ventricular tachycardia associated with dilated cardiomyopathy: the importance of low-voltage scars. *J Amer Coll Cardiol* 2004; **43**: 1834.

19 Delacretaz E, Stevenson WG, Ellison KE, Maisel WH, Friedman PL. Mapping and radiofrequency catheter ablation of the three types of sustained monomorphic ventricular tachycardia in nonischemic heart disease. *J Cardiovasc Electrophysiol* 2000; **11**: 11.

20 Stevenson WG, Weiss JN, Wiener I, et al. Fractionated endocardial electrograms are associated with slow conduction in humans: evidence from pace-mapping. *J Amer Coll Cardiol* 1989; **13**: 369.

21 El-Shalakany A, Hadjis T, Papageorgiou P, Monahan K, Epstein L, Josephson ME. Entrainment/mapping criteria for the prediction of termination of ventricular tachycardia by single radiofrequency lesion in patients with coronary artery disease. *Circulation* 1999; **99**: 2283.

22 Okada T, Yamada T, Murakami Y, Yoshida N, Ninomiya Y, Toyama J. Mapping and ablation of trigger premature ventricular contractions in a case of electrical storm associated with ischemic cardiomyopathy. *Pacing Clin Electrophysiol* 2007; **30**: 440.

23 Marrouche NF, Verma A, Wazni O, et al. Mode of initiation and ablation of ventricular fibrillation storms in patients with ischemic cardiomyopathy. *J Amer Coll Cardiol* 2004; **43**: 1715.

24 Noda T, Shimizu W, Taguchi A, et al. Malignant entity of idiopathic ventricular fibrillation and polymorphic ventricular tachycardia initiated by premature extrasystoles originating from the right ventricular outflow tract. *J Amer Coll Cardiol* 2005; **46**: 1288.

30

CHAPTER 30

Electrical and Anatomical Mapping of Different Pathologies: Ischemic, Dilated, and Hypertrophic Cardiomyopathies

Arash Arya, MD,[1] *Hans Kottkamp,* MD, PhD,[2]
Christopher Piorkowski, MD,[1] *Gerhard Hindricks,* MD, PhD[1]

[1]University of Leipzig Heart Center, Leipzig, Germany
[2]Hirslanden Heart Center, Zurich, Switzerland

Summary

The circuits of cardiac arrhythmias, especially ventricular arrhythmias in patients with structural heart disease, comprise complex 3D structures spanning from endocardium to epicardium, which should be defined and targeted for ablation in a 3D moving environment, that is, the heart. Electroanatomical mapping of ventricular arrhythmias has facilitated the delineation and more effective ablation of the arrhythmia circuits. In this chapter, we review the application of mapping systems for ablation of ventricular tachycardias associated with various structural heart diseases.

Electroanatomical Mapping in Ischemic Cardiomyopathy

Today, catheter ablation can be used effectively for controlling recurrent ventricular tachycardia (VT) in patients with ischemic heart disease (IHD) [1–20]. Catheter ablation alone is considered by some investigators as primary therapy for patients with hemodynamically tolerated VT. However, it should be mentioned that usually more hemodynamically unstable VT are inducible in these patients; the process of coronary heart disease is a progressive and unpredictable one; and long-term mortality of these patients is comparable with those with more unstable VT. Therefore, most investigators recommend catheter ablation as an adjuvant therapy to implantable cardioverter–defibrillators regardless of hemodynamic status of the ischemic VT [7–9, 13, 14].

The anatomical substrate of monomorphic VT usually comprises of a reentry circuit at the rim of a healed dense scar after myocardial infarction, which usually persists after its formation [8A, 21, 22]. Regardless of the strategy used for ablation of VT, detailed mapping preceding ablation should be

Cardiac Mapping, Third Edition Edited by Mohammad Shenasa, Gerhard Hindricks, Martin Borggrefe, and Günter Breithardt
 ISBN: 978-1-405-17572-2

done to minimize the lesion size and side effects of catheter ablation. QRS morphology, location of myocardial infarction, and evaluation of left ventricular anatomy can direct the detailed mapping to a selected section of the left ventricle and hence shorten the procedure time in this group of usually critically ill patients.

Kottkamp et al. described the arrhythmogenic substrate in 28 postinfarction patients with VT and showed that individually tailored substrate description guiding the placement of linear lesion lines that transected potential isthmuses, rendered ventricular tachycardia in 80% of patients completely noninducible. They showed that construction of regional target area maps allowed short procedure times, with a resulting low incidence of complications in these critically ill patients [9]. The pathophysiologic basis and interventional management of ischemic VT are discussed in detail elsewhere (see Chapters 23 and 24).

Activation and Entrainment Mapping

Figure 30.1 summarizes the ablation strategies in patients with IHD. Activation and entrainment mapping are usually useful in patients with monomorphic hemodynamically tolerated VT, although limited entrainment mapping during short periods of induced VT after substrate mapping can help to verify the potential targets for ablation in patients with hemodynamically unstable VT [8A].

Volkmer et al. compared the two main strategies of VT ablation using the Carto™ system in 47 patients with IHD [23]. In the mapping group (22 patients), the circuit of the clinical VT was reconstructed. During VT, the critical area of slow conduction was identified using diastolic potentials and conventional concealed entrainment pacing. In those patients in whom mapping of VT was not possible, pathological myocardium was identified by substrate-mapping based on fragmented, late- and/or low-amplitude (<1.5 mV) bipolar potentials during sinus rhythm or pacing. The site of ablation was primarily determined by pace-mapping inside or at the border of this pathological myocardium. The long-term success rate was 75% when defined as freedom from any ventricular tachyarrhythmia (VT or VF) during a follow-up of 25 ± 13 months. On subgroup analysis, patients in the VT-mapping group were not significantly different from patients in the substrate-mapping group with respect to age, ejection fraction, VT cycle length, and the number of radiofrequency applications. The acute and long-term results of ablation were comparable between both groups [23].

In ischemic VT, the tachycardia circuit is complex. Therefore, activation mapping alone rarely results in successful focal ablation in contrast to patients with idiopathic VT. However, initial activation mapping along with QRS morphology and

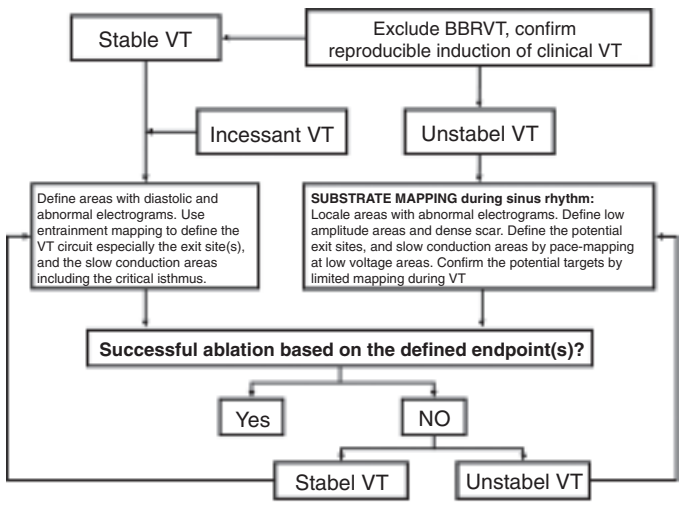

Figure 30.1 Algorithm shows the summary of the approach to ablation of ventricular tachycardia in patients with ischemic heart disease which can be applied also to other patients with structural heart disease. See the text for discussion. KEY: VT = ventricular tachycardia; BBRVT = bundle branch reentry ventricular tachycardia.

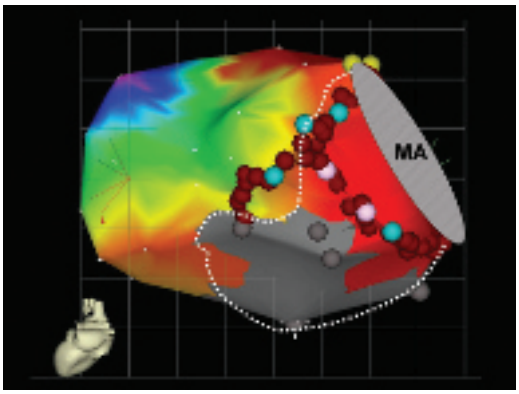

Figure 30.2 Inferoposterior view of an electroanatomic reconstruction of the inferior wall in a patient with remote inferior wall myocardial infarction. Localization of the infarct zone prior to the procedure has resulted in successful ablation with targeted reconstruction and electroanatomical mapping of the left ventricle instead of whole chamber mapping. The color code represents voltages (where red is the lowest voltage, purple is the highest voltage, and the gray area represents dense scar). Blue and purple dots represent the areas with diastolic potentials and best pace-mapping, respectively. Linear ablation as depicted by red dots terminated the VT and rendered it noninducible. KEY: MA = mitral annulus.

anatomical data from the left ventricle (i.e., echocardiography, magnetic resonance imaging, coronary angiography and left ventriculography) can help to localize the region of interest for high-density mapping, thereby reducing the procedure time (Figure 30.2).

Hsia et al. have characterized the arrhythmia circuit in 26 patients with hemodynamically stable VT using electroanatomical mapping [24]. Entrainment mapping was performed in 53 VT of which 19 entrance, 37 isthmus, 48 exit, and 32 outer loop sites were identified. The authors defined a conducting channel as a path of multiple orthodromically activated sites within the VT circuit that demonstrated an electrogram amplitude higher than that of surrounding areas as evidenced by differences in color-coded voltages. Forty-seven (84%) of 56 entrance or isthmus sites were located within dense scar (<0.5 mV). Nearly all exits (92%) were located in abnormal endocardium (<1.5 mV), with more than half (54%) located in the border zone (0.5–1.5 mV). VT-related conducting channels were identified in 18 of 32 VTs with detailed mapping (average length 32 ± 22 mm). The voltage threshold in the conducting channels ranged from 0.1 mV to 0.7 mV (mean 0.33 ± 0.15 mV) [24].

Entrainment refers to continuous resetting of a reentrant tachycardia by pacing at a cycle length 10–30 msec faster than the clinical tachycardia [25–31]. In order to be able to perform entrainment mapping, the VT should be stable, hemodynamically tolerable, and reproducibly inducible. After localizing the potential reentrant circuit of scar-related stable monomorphic VT, the entrainment mapping would help to define its different components as shown in Figures 30.3. The location of the protected isthmus is within the infarct area, and the

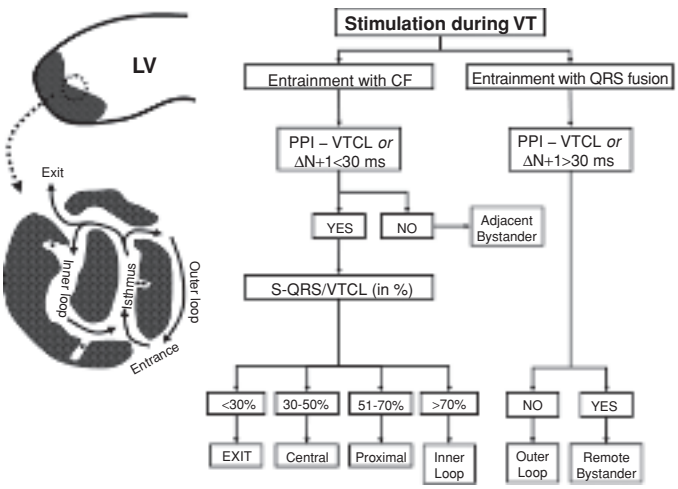

Figure 30.3 A reentry circuit with the corresponding components is illustrated in the left panel. The right panel shows the algorithm for definition of different component of the circuit. See the text for discussion. KEY: VT = ventricular tachycardia; CF = concealed fusion; PPI = postpacing interval; VTCL = VT cycle length; * = remote bystander; ** = adjacent bystander.

recorded bipolar voltage in these areas is typically ≤0.5 mV.

Radiofrequency ablation at sites that show concealed entrainment, a postpacing interval approximating the tachycardia cycle length, and an S–QRS interval greater than 60 msec (but less than 70% of the tachycardia cycle length and within 10 msec of the electrogram–QRS interval), is more likely to terminate the VT. It should be mentioned that concealed entrainment *alone* is not always an indication of a successful ablation site because pacing in the bystander pathways would also produce concealed entrainment [30]. Therefore these sites should be verified by the other entrainment criteria (Figure 30.3). Recording of isolated diastolic potentials or continuous diastolic activity at these sites will increase the possibility of successful ablation to 70–90% [30].

Substrate Mapping

Although theoretically activation and entrainment mapping are very interesting and promising, in a significant number of patients further mapping techniques are required for successful ablation [1, 2, 4, 5, 8A, 9]. In a consecutive series of patients with ischemic CMP referred for the ablation of hemodynamically tolerated VT [8A], 25% could not be ablated successfully using entrainment and activation mapping. In addition, in patients with hemodynamically unstable VT, and those with repeated nonsustained VT, which comprise a large fraction of patients who are referred for catheter ablation, only a limited entrainment mapping can be done, and detailed characterization of the reentrant circuit is often not possible.

The experiences from cardiac surgery helped to develop this new strategy for the ablation of unstable VT or for those who cannot be successfully ablated with activation and entrainment mapping. Surgical subendocardial resection or partial encircling endocardial ventriculotomy are successful in up to 90% of patients who survive the operation [8A, 8B, 9]. In this approach, extending the surgical lesions to the adjacent anatomical barriers improve the results. In order to reproduce the same success rate, a good visualization of LV anatomy with proper demarcation of the low voltage and infarct scar areas is needed.

In this case, data from electroanatomical bipolar voltage mapping combined with data from various imaging modalities can localize the scar area. The presumed VT exit sites and circuit(s) are then determined by pace mapping and abnormal potential recordings are marked. Linear lesions are created from dense scar passing through these points and the infarct border zone and connecting to the nearest anatomical obstacle or normal myocardium. Other groups connect all unexcitable regions within the infarct zone with linear lesions to ablate the abnormal fractionated electrograms in these regions. Figures 30.2 and 30.4 show examples of such an ablation technique.

Recently, a remote magnetic navigation and ablation system has been introduced and has been used for the ablation of various cardiac arrhythmias.

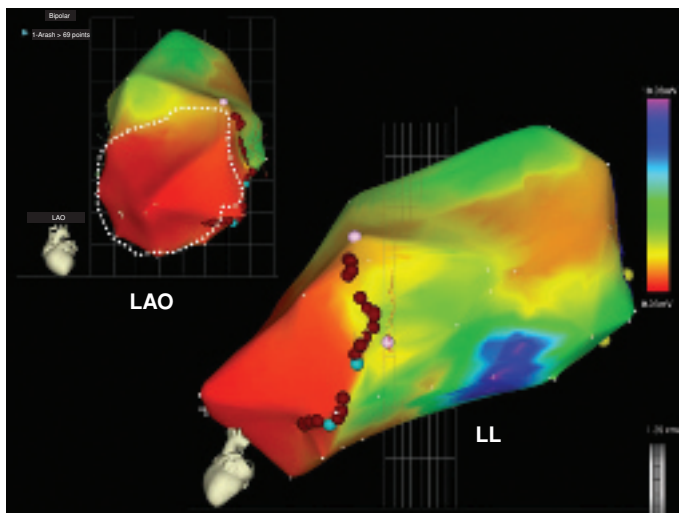

Figure 30.4 Left lateral and left anterior oblique views of an electroanatomic reconstruction of the left ventricle in a patient with remote anteroseptal myocardial infarction. The color code represents voltages (where red is the lowest voltage and purple is the highest voltage). Blue and purple dots represent the areas with recorded diastolic potentials and the best pace-mapping, respectively. Linear ablation as depicted by red dots terminated the VT and rendered it noninducible.

Aryana et al. assessed the applicability of the remote magnetic navigation system combined with Carto-RMT to perform ablation in 24 consecutive patients with a history of VT related to various structural heart diseases including IHD [32]. Twenty-one of 77 inducible VT were targeted during VT with the remotely navigated radiofrequency ablation catheter alone. With a combination of entrainment and activation mapping, 17 of 21 VT (81%) were successfully ablated using a 4-mm catheter; however, for the remainder, manual irrigated radiofrequency ablation was necessary. In concert with a manually navigated irrigated ablation catheter, 75 of 77 VTs (97%) were ultimately ablated [32].

Trigger Ablation

Occasionally, in patients with IHD frequent episodes of polymorphic VT are triggered by monomorphic premature ventricular beats. Ablation of these premature ventricular beats may control the episodes of polymorphic VT. Activation and pace mapping of these trigger beats may help to localize the site of origin, which is usually from surviving Purkinje fibers surrounding the infarct zone [33–34].

Electroanatomical Mapping in Dilated Cardiomyopathy

The potential mechanisms of VT in patients with dilated cardiomyopathy (DCM) are reentry and triggered activity. Reentry within the myocardium is the most common cause, although bundle branch reentry and focal VT due to triggered activity also occur and are responsible for up to 25% of VT in patients with DCM (Figure 30.5) [35].

Clinical experience with catheter ablation of VT in patients with DCM is very limited because sustained monomorphic VT in these patients is an infrequent clinical presentation [35–39]. Although the principles used for the ablation of ventricular tachycardia in patients with DCM are those that have already been explained for ischemic cardiomyopathy, there are several important differences.

The epicardial origin of VT is more frequent in patients with DCM, and abnormal epicardial signals are recorded frequently in these patients; abnormal endocardial electrograms are less frequent, and are less fractionated than in ischemic CMP. They tend to be localized to the basal areas of the left ventricle. The endocardial scars in these patients are usually located near the valves. Electroanatomic mapping can be used to define the areas of scar and abnormal electrograms. In addition, activation, entrainment, and pace mapping can be used to define the potential exits and arrhythmia circuits [35, 36]. The limited success rate in published series compared to ischemic VT reflects the high prevalence of intramyocardial and epicardial circuits in these patients. Therefore, in the case of unsuccessful ablation, epicardial mapping and ablation should be strongly considered in these patients [35–38].

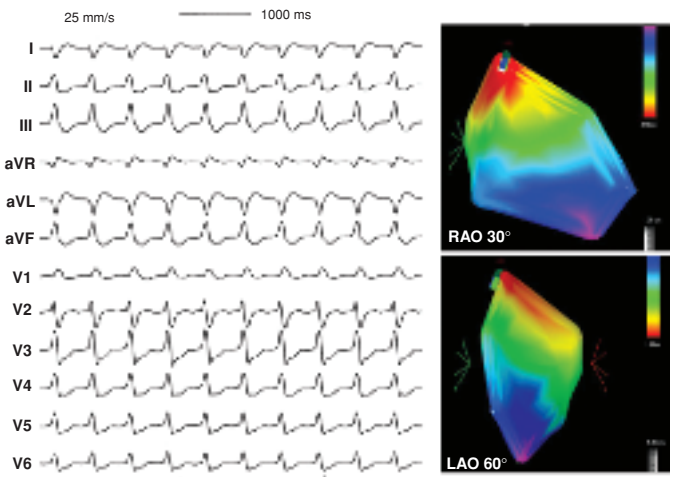

Figure 30.5 An example of focal ventricular tachycardia in a patient with dilated cardiomyopathy. The 12-lead ECG is depicted in the left panel. Right and left anterior oblique views of an electroanatomic reconstruction of the left ventricle are presented in the right panel. The color code represents activation time (where red is the earliest and purple is the latest activation). Focal ablation at the earliest activation site terminated the VT and rendered it noninducible.

Soejima et al. have studied 28 patients with dilated CMP and sustained VT. Endocardial and epicardial mapping was done in 28 and 8 patients, respectively [36]. Using pace-mapping and entrainment mapping, the authors were successful in defining the mechanism of the VT in all patients. Ventricular tachycardia was due to focal VT in 5 patients, bundle-branch reentry in 2 patients, and myocardial reentry in 22 patients (both focal and reentry VT in one patient). All patients with myocardial reentry had endocardial (20 of 20 patients) and/or epicardial (7 of 7 patients mapped) scar tissue. Of the 19 VT-isthmuses identified, 12 were associated with an endocardial and 7 with an epicardial scar. All myocardial reentrant VT were abolished in 12 of 22 patients, and inducible VT was modified in 4 patients. During follow-up of 334 ± 280 days, 54% of patients with myocardial reentry were free of VT despite frequent episodes before ablation [36].

Electroanatomical Mapping in Hypertrophic Cardiomyopathy

Hypertrophic cardiomyopathy is a genetic heart disease associated with sudden death and ventricular arrhythmias. Disordered myocardial structure, fibrosis, microvascular disease, and repeated episodes of myocardial ischemia are the substrate for electrical instability in hypertrophic cardiomyopathy [40–42]. Nonsustained ventricular tachycardia occurs in 20–25% of patients with hypertrophic cardiomyopathy during Holter monitoring [43–45]. These episodes are usually brief, infrequent, and are not associated with symptoms.

The prevalence of nonsustained VT is associated with LV mass (as a substrate for the arrhythmia) and reaches 50% or more in patients with septal thickness of 30 mm or greater [46]. The implantable cardioverter–defibrillator (ICD) offers successful prevention of sudden cardiac death in these patients. In most of these cases, the lethal arrhythmia is ventricular fibrillation or a short run of a monomorphic VT degenerating into ventricular fibrillation or rapid polymorphic VT [47].

Contrary to patients with ischemic and dilated cardiomyopathy, sustained monomorphic VT is rare in these patients. It can be speculated that in these patients, short episodes of nonsustained monomorphic ventricular tachycardia work as a trigger. They may be either self-terminating or degenerate due to frequent wave break into a polymorphic VT or ventricular fibrillation. Therefore, it is of no surprise that the data on the ablation of monomorphic VT in patients with hypertrophic CMP are limited [48–51].

Rodriguez et al. have reported ablation of monomorphic VT in a patient with hypertrophic cardiomyopathy. The authors used the following criteria to guide radiofrequency ablation: the presence of entrainment without fusion, equal intervals from the stimulus to the beginning of the QRS complex and from the electrogram to the QRS complex during VT, and the first postpacing interval identical to the tachycardia cycle length. This suggests that in rare occasions, reentrant monomorphic VT can occur in these patients and that VT can be mapped and ablated using the same criteria as in patients with ischemic heart disease. Other mechanisms for monomorphic VT in these patients, including focal VT preceded by the Purkinje potential and VT induced after percutaneous transluminal alcohol septal myocardial ablation, have already been described [48, 51].

Percutaneous transluminal alcohol septal myocardial ablation is appropriate for patients with heart failure who are refractory to medical treatment for hypertrophic obstructive cardiomyopathy. Although there is no consensus whether this procedure may occasionally be arrhythmogenic, some cases of reentrant monomorphic VT after septal ablation have been reported, suggesting that the same substrate as in patients with myocardial infarction could be responsible for ventricular arrhythmias after this procedure. However, we can clearly exclude the presence of this arrhythmogenic substrate before the septal ablation [49, 50].

Conclusion

With the advent of advanced cardiac-mapping systems, catheter ablation has emerged as a useful alternative to more conventional treatment options and ablation techniques. Now catheter ablation can be used effectively for the controlling of recurrent VT in patients with structural heart disease, especially those with IHD. Today, successful ablation of unstable and polymorphic VT and certain forms of ventricular fibrillation expanded the treatment

options in these patients. Different strategies can be used for ablation of VT in these patients; however, regardless of the strategies used for VT ablation, detailed mapping preceding ablation minimizes the lesion size and potential side effects of catheter ablation.

It should be mentioned that despite all the abovementioned advances, the catheter ablation of VT is still considered as an adjunctive therapy to implantable cardioverter–defibrillator in patients with ventricular tachyarrhythmic events. Catheter ablation in these cases is indicated especially in those who receive multiple appropriate shocks and experience electrical storms.

Reddy et al. have recently evaluated the role of empiric substrate-based catheter ablation in patients with a history of a myocardial infarction who underwent defibrillator implantation for spontaneous VT or VF [52]. Patients were randomly assigned to defibrillator implantation alone or with adjunctive catheter ablation. The 30 days mortality after ablation was zero, and there were no significant changes in ventricular function, functional class, and mortality during the mean follow-up period of 22.5 ± 5.5 months. However, 20 patients in the control group (31%) and 6 patients in the ablation group (9%) received shocks during the follow-up period ($P = 0.003$).

Based on recent advances in the field of catheter ablation further studies are needed to define the possible role of empiric catheter ablation in patients underwent ICD implantation for primary and secondary prevention of sudden cardiac death.

References

Ischemic Cardiomyopathy

1 Bogun F, Good E, Reich S, et al. Isolated potentials during sinus rhythm and pace-mapping within scars as guides for ablation of postinfarction ventricular tachycardia. *J Am Coll Cardiol* 2006; **47**: 2013–19.

2 Deneke T, Muller KM, Lemke B, et al. Human histopathology of electroanatomic mapping after cooled-tip radiofrequency ablation to treat ventricular tachycardia in remote myocardial infarction. *J Cardiovasc Electrophysiol* 2005; **16**: 1246–51.

3 Calkins H. Further insights into appropriate target sites and outcomes of catheter ablation of ventricular tachycardia in postinfarction patients. *J Cardiovasc Electrophysiol* 2005; **16**: 472–73.

4 Verma A, Marrouche NF, Schweikert RA, et al. Relationship between successful ablation sites and the scar border zone defined by substrate mapping for ventricular tachycardia postmyocardial infarction. *J Cardiovasc Electrophysiol* 2005; **16**: 465–71.

5 Szumowski L, Sanders P, Walczak F, et al. Mapping and ablation of polymorphic ventricular tachycardia after myocardial infarction. *J Am Coll Cardiol* 2004; **44**: 1700–6.

6 Pirk J, Bytesnik J, Kautzner J, et al. Surgical ablation of postinfarction ventricular tachycardia guided by mapping in sinus rhythm: long-term results. *Eur J Cardiothorac Surg* 2004; **26**: 323–29.

7 Della Bella P, Riva S, Fassini G, et al. Incidence and significance of pleomorphism in patients with postmyocardial infarction ventricular tachycardia: acute and long-term outcome of radiofrequency catheter ablation. *Eur Heart J* 2004; **25**: 1127–38.

8A Callans DJ. Ablation of ventricular tachycardia in coronary artery disease. In: Huang s, Wood M, eds. *Ablation of Cardiac Arrhythmias*. Elsevier-Saunders, Philadelphia, 2006: 511–32.

8B Borggrefe M, Podczeck A, Ostermeyer J, et al. Long-term results of electrophysiologically guided antitachycardia surgery in ventricular tachyarrhythmias: a collaborative study on 665 patients. In: Breithardt G, Borggrefe M, Zipes DP, eds. *Nonpharmacological Therapy of Tachy-Arrhythmias*. Futura, New York, 1987: 109–32.

9 Kottkamp H, Wetzel U, Schirdewahn P, et al. Catheter ablation of ventricular tachycardia in remote myocardial infarction: substrate description guiding placement of individual linear lesions targeting noninducibility. *J Cardiovasc Electrophysiol* 2003; **14**: 675–81.

10 Kautzner J, Cihak R, Peichl P, Vancura V, Bytesnik J. Catheter ablation of ventricular tachycardia following myocardial infarction using three-dimensional electroanatomical mapping. *Pacing Clin Electrophysiol* 2003; **26**: 342–47.

11 Khan HH, Maisel WH, Ho C, et al. Effect of radiofrequency catheter ablation of ventricular tachycardia on left ventricular function in patients with prior myocardial infarction. *J Interv Card Electrophysiol* 2002; **7**: 243–47.

12 O'Donnell D, Bourke JP, Anilkumar R, Simeonidou E, Furniss SS. Radiofrequency ablation for postinfarction ventricular tachycardia: report of a single centre experience of 112 cases. *Eur Heart J* 2002; **23**: 1699–705.

13 Della Bella P, De Ponti R, Uriarte JA, et al. Catheter ablation and antiarrhythmic drugs for haemodynamically tolerated postinfarction ventricular tachycardia: long-term outcome in relation to acute electrophysiological findings. *Eur Heart J* 2002; **23**: 414–24.

14 Schilling RJ. Can catheter ablation cure postinfarction ventricular tachycardia*? Eur Heart J* 2002; **23**: 352–54.

15 O'Callaghan PA, Poloniecki J, Sosa-Suarez G, Ruskin JN, McGovern BA, Garan H. Long-term clinical outcome of patients with prior myocardial infarction after palliative radiofrequency catheter ablation for frequent ventricular tachycardia. *Am J Cardiol* 2001; **87**: 975–79.

16 Sosa E, Scanavacca M, d'Avila A, Oliveira F, Ramires JA. Nonsurgical transthoracic epicardial catheter ablation to treat recurrent ventricular tachycardia occurring late after myocardial infarction. *J Am Coll Cardiol* 2000; **35**: 1442–49.

17 Callans DJ, Zado E, Sarter BH, Schwartzman D, Gottlieb CD, Marchlinski FE. Efficacy of radiofrequency catheter ablation for ventricular tachycardia in healed myocardial infarction. *Am J Cardiol* 1998; **82**: 429–32.

18 Stevenson WG, Friedman PL, Kocovic D, Sager PT, Saxon LA, Pavri B. Radiofrequency catheter ablation of ventricular tachycardia after myocardial infarction. *Circulation* 1998; **98**: 308–14.

19 Stevenson WG, Friedman PL, Ganz LI. Radiofrequency catheter ablation of ventricular tachycardia late after myocardial infarction. *J Cardiovasc Electrophysiol* 1997; **8**: 1309–19.

20 Harada T, Stevenson WG, Kocovic DZ, Friedman PL. Catheter ablation of ventricular tachycardia after myocardial infarction: relation of endocardial sinus rhythm late potentials to the reentry circuit. *J Am Coll Cardiol* 1997; **30**: 1015–23.

21 Hsia HH, Callans DJ, Marchlinski FE. Characterization of endocardial electrophysiological substrate in patients with nonischemic cardiomyopathy and monomorphic ventricular tachycardia. *Circulation* 2003; **108**: 704–10.

22 Hsia HH, Marchlinski FE. Characterization of the electroanatomic substrate for monomorphic ventricular tachycardia in patients with nonischemic cardiomyopathy. *Pacing Clin Electrophysiol* 2002; **25**: 1114–27.

23 Volkmer M, Ouyang F, Deger F, et al. Substrate mapping versus tachycardia mapping using CARTO in patients with coronary artery disease and ventricular tachycardia: impact on outcome of catheter ablation. *Europace* 2006; **8**: 968–76.

24 Hsia HH, Lin D, Sauer WH, Callans DJ, Marchlinski FE. Anatomic characterization of endocardial substrate for hemodynamically stable reentrant ventricular tachycardia: identification of endocardial conducting channels. *Heart Rhythm* 2006; **3**: 503–12.

25 Pak HN, Kim YH, Lim HE, et al. Role of the posterior papillary muscle and purkinje potentials in the mechanism of ventricular fibrillation in open chest dogs and swine: effects of catheter ablation. *J Cardiovasc Electrophysiol* 2006; **17**: 777–83.

26 Waldo AL, Henthorn RW, Plumb VJ, MacLean WA. Demonstration of the mechanism of transient entrainment and interruption of ventricular tachycardia with rapid atrial pacing. *J Am Coll Cardiol* 1984; **3**: 422–30.

27 Waldo AL, Henthorn RW. Use of transient entrainment during ventricular tachycardia to localize a critical area in the reentry circuit for ablation. *Pacing Clin Electrophysiol* 1989; **12**: 231–44.

28 Morady F, Kadish A, Rosenheck S, et al. Concealed entrainment as a guide for catheter ablation of ventricular tachycardia in patients with prior myocardial infarction. *J Am Coll Cardiol* 1991; **17**: 678–89.

29 Callans DJ, Hook BG, Josephson ME. Comparison of resetting and entrainment of uniform sustained ventricular tachycardia: further insights into the characteristics of the excitable gap. *Circulation* 1993; **87**: 1229–38.

30 Bogun F, Bahu M, Knight BP, et al. Comparison of effective and ineffective target sites that demonstrate concealed entrainment in patients with coronary artery disease undergoing radiofrequency ablation of ventricular tachycardia. *Circulation* 1997; **95**: 183–90.

31 Stevenson WG, Friedman PL, Sager PT, et al. Exploring postinfarction reentrant ventricular tachycardia with entrainment mapping. *J Am Coll Cardiol* 1997; **29**: 1180–89.

32 Aryana A, d'Avila A, Heist EK, et al. Remote magnetic navigation to guide endocardial and epicardial catheter mapping of scar-related ventricular tachycardia. *Circulation* 2007; **115**: 1191–200.

33 Kohsaka S, Razavi M, Massumi A. Idiopathic ventricular fibrillation successfully terminated by radiofrequency ablation of the distal Purkinje fibers. *Pacing Clin Electrophysiol* 2007; **30**: 701–4.

34 Nogami A, Sugiyasu A, Kubota S, Kato K. Mapping and ablation of idiopathic ventricular fibrillation from the Purkinje system. *Heart Rhythm* 2005; **2**: 646–49.

Dilated Cardiomyopathy

35 Wood MA. Ablation of ventricular tachycardia associated with nonischemic cardiomyopathies. In: Huang S, Wood M, eds. *Ablation of Cardiac Arrhythmias*, Elsevier-Saunders, Philadelphia, 2006: 535–62.

36 Soejima K, Stevenson WG, Sapp JL, Selwyn AP, Couper G, Epstein LM. Endocardial and epicardial radiofrequency ablation of ventricular tachycardia associated with dilated cardiomyopathy: the importance of low-voltage scars. *J Am Coll Cardiol* 2004; **43**: 1834–42.

37 Swarup V, Morton JB, Arruda M, Wilber DJ. Ablation of epicardial macroreentrant ventricular tachycardia associated with idiopathic nonischemic dilated cardiomyopathy by a percutaneous transthoracic approach. *J Cardiovasc Electrophysiol* 2002; **13**: 1164–68.

38 Kottkamp H, Hindricks G, Chen X, et al. Radiofrequency catheter ablation of sustained ventricular tachycardia in idiopathic dilated cardiomyopathy. *Circulation* 1995; **92**: 1159–68.

39 Breithardt G, Borggrefe M, Karbenn U, Schwarzmaier J, Rohner D. Successful catheter ablation of refractory incessant ventricular tachycardia in a case with dilated cardiomyopathy. *Eur Heart J* 1986; **7**: 817–19.

Hypertrophic Cardiomyopathy

40 Adabag AS, Maron BJ. Implications of arrhythmias and prevention of sudden death in hypertrophic cardiomyopathy. *ANE* 2007; **12**: 171–80.

41 Spirito P, Seidman CE, McKenna WJ, Maron BJ. The management of hypertrophic cardiomyopathy. *N Engl J Med* 1997; **336**: 775–85.

42 Maron BJ, McKenna WJ, Danielson GK, et al. American College of Cardiology/European Society of Cardiology Clinical Expert Consensus Document on Hypertrophic Cardiomyopathy. A report of the American College of Cardiology Task Force on Clinical Expert Consensus Documents and the European Society of Cardiology Committee for Practice Guidelines Committee to Develop an Expert Consensus Document on Hypertrophic Cardiomyopathy. *J Am Coll Cardiol* 2003; **42**: 1687–1713.

43 Monserrat L, Elliott PM, Gimeno JR, Sharma S, Penas-Lado M, McKenna WJ. Nonsustained ventricular tachycardia in hypertrophic cardiomyopathy: an independent marker of sudden death risk in young patients. *J Am Coll Cardiol* 2003; **42**: 873–79.

44 Cecchi F, Olivotto I, Montereggi A, Squillatini G, Dolara A, Maron BJ. Prognostic value of nonsustained ventricular tachycardia and the potential role of amodarone treatment in hypertrophic cardiomyopathy: assessment in an unselected non-referral-based patient population. *Heart* 1998; **79**: 331–36.

45 Adabag AS, Casey SA, Kuskowski MA, Zenovich AG, Maron BJ. Spectrum and prognostic significance of arrhythmias on ambulatory Holter electrocardiogram in hypertrophic cardiomyopathy. *J Am Coll Cardiol* 2005; **45**: 697–704.

46 Spirito P, Bellone P, Harris KM, Bernabo P, Bruzzi P, Maron BJ. Magnitude of left ventricular hypertrophy and risk of sudden death in hypertrophic cardiomyopathy. *N Engl J Med* 2000; **342**: 1778–85.

47 Jayatilleke I, Doolan A, Ingles J, et al. Long-term follow-up of implantable cardioverter–defibrillator therapy for hypertrophic cardiomyopathy. *Am J Cardiol* 2004; **93**: 1192–94.

48 Okumura Y, Watanabe I, Ohkubo K, Saito S. Successful catheter ablation for incessant ventricular tachycardia in a patient with hypertrophic cardiomyopathy. *Circ J* 2007; **1**: 1164–68.

49 Hori Y, Ueda M, Nakayama T, et al. Occurrence of de novo sustained monomorphic ventricular tachycardia induced after percutaneous transluminal alcohol septal myocardial ablation for hypertrophic obstructive cardiomyopathy. *Int J Cardiol* 2007; **19**: 403–7.

50 Simon RD, Crawford FA 3rd, Spencer WH 3rd, Gold MR. Sustained ventricular tachycardia following alcohol septal ablation for hypertrophic obstructive cardiomyopathy. *Pacing Clin Electrophysiol* 2005; **28**: 1354–56.

51 Rodriguez LM, Smeets JL, Timmermans C, et al. Radiofrequency catheter ablation of sustained monomorphic ventricular tachycardia in hypertrophic cardiomyopathy. *J Cardiovasc Electrophysiol* 1997; **8**: 803–6.

52 Reddy ZK, Reynolds MR, Neuzil P, et al. Prophylactic catheter ablation for the prevention of defibrillator therapy. *N Engl J Med* 2007; **357**: 2657–65.

31

CHAPTER 31

Mapping and Ablation of Tachyarrhythmias in Patients with Congenital Heart Disease

Edward P Walsh, MD

Children's Hospital Boston, Boston, MA, USA

Summary

As a result of remarkable advances in cardiac surgical techniques over the last several decades, most children born with complex congenital heart disease (CHD) now survive well into adulthood. However, despite effective repairs done early in life, a large percentage of these patients continue to suffer from arrhythmias and other serious long-term cardiac sequelae. There are many unique electrophysiologic features to consider in this population:

1 grossly distorted underlying anatomy,
2 potentially abnormal location and function for the atrioventricular (AV) conduction tissues,
3 the presence of incision lines and surgical patches that influence propagation wavefronts,
4 residual hemodynamic abnormalities that promote anisotropy through cardiac chamber dilation and increased wall thickness,
5 unusual vascular connections that complicate catheter navigation during interventional procedures.

Issues of this sort will have a major impact on both the genesis of arrhythmias and the performance of mapping studies. It is the purpose of this chapter to review the common forms of tachycardia encountered in the CHD population, with a focus on catheter mapping and ablation techniques.

Anatomy of the AV Conduction System in CHD

The embryologic accidents responsible for congenital heart defects can influence the development and disposition of the specialized AV conduction tissues. The original motivation for study of this issue was the pressing need for cardiac surgeons to anticipate position of the AV node and His–Purkinje system during open heart repairs and thereby avoid heart block [1], but the relevance now extends to interventional electrophysiology procedures where these tissues must be located accurately in order to understand propagation patterns and avoid inadvertent damage during ablation. Fortunately, a large body of pathologic [2, 3] and clinical mapping work [4, 5] has now accumulated to permit localization in most varieties of CHD defects with reasonable precision.

In simple forms of CHD, the AV node occupies the normal location within the apical aspect

Cardiac Mapping, Third Edition Edited by Mohammad Shenasa, Gerhard Hindricks, Martin Borggrefe, and Günter Breithardt
 ISBN: 978-1-405-17572-2

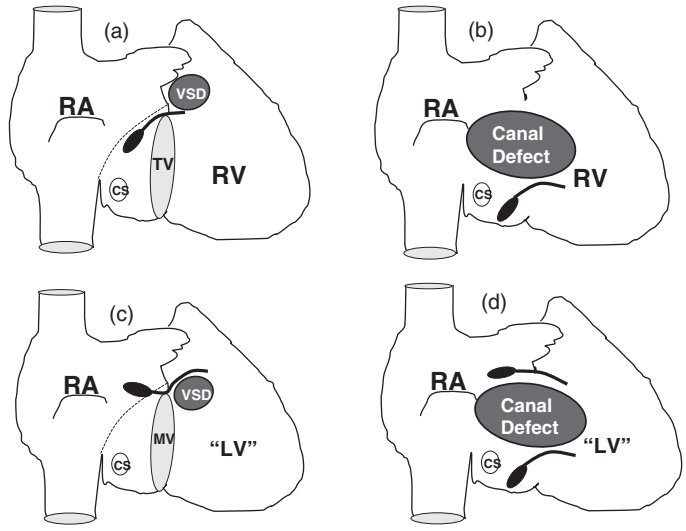

Figure 31.1 Diagrammatic view of locations for the proximal AV conducting tissue in patients with congenital heart defects: (a) Simple defect where the compact node is normally located within Koch's triangle; (b) defect of the atrioventricular canal where the compact node is displaced in a posterior location; (c) congenitally corrected transposition with inverted ventricles where the compact node is displaced in an anterior location; (d) "twin" nodes in the setting of combined canal defect and ventricular inversion. See the text for details. KEY: CS = coronary sinus; "LV" = right-sided left ventricle; MV = right-sided mitral valve; RA = right atrium; RV = right ventricle; TV = tricuspid valve; VSD = ventricular septal defect.

of Koch's triangle, and the His bundle penetrates toward the ventricles in the usual fashion. If a ventricular septal defect (VSD) happens to be present, the His bundle will simply run along the inferior rim of the defect [6] without substantial alteration in its overall course (Figure 31.1a). Thus, for relatively straightforward lesions (e.g., secundum-type atrial septal defect, simple VSD, Ebstein's anomaly, and tetralogy of Fallot), a His bundle electrogram will be recorded as expected along the superior-medial rim of the tricuspid valve. Chamber enlargement may distort the fluoroscopic silhouette to increase the challenge of catheter positioning to some degree, but registration of a high-quality His deflection and the ability to infer location of the compact AV node are usually not difficult in these particular patients.

Whenever CHD lesions involve defects in the so-called AV canal region (e.g., primum-type atrial septal defect, or complete common AV canal defect), septal tissues that normally constitute Koch's triangle are absent or deficient. The AV node and His bundle in this setting become significantly displaced to a more posterior location [7,8] relative to the customary triangle boundaries (Figure 31.1b). Accordingly, the proper catheter location for His bundle recording will be lower than expected along the right-sided AV valve, with a signal frequency and amplitude that are often attenuated when surgical patches used for repair overlie this area of interest.

Another CHD lesion involving significant displacement of the AV conduction tissues is congenitally corrected transposition of the great arteries (so-called L-TGA), where the left ventricle (LV) and right ventricle (RV) are inverted, and the LV ejects into the pulmonary circulation. Although the anatomic components of Koch's triangle are indeed present in this condition, the AV node develops in an anterior position near the base of the right atrial appendage [9], well outside the triangle borders (Figure 31.1c). The His bundle will still penetrate toward the ventricles along the superior-medial aspect of the right-sided AV valve (the mitral valve in this case). If a VSD happens to be present, this is the one situation where the His bundle travels along the upper rim of the defect [10]. The proper site for the His electrogram will not vary much from normal despite dramatic nodal displacement.

In rare instances, a complex CHD malformation can involve the combination of an AV canal defect

and congenitally corrected transposition. Some patients with this anatomy will be found to have two separate AV nodes and His bundles, the first involving the posterior location typical of a canal defect, with the second in the anterior location typical for ventricular inversion [11]. This unusual condition has been referred to as "twin AV nodes," and can result in reciprocating tachycardias [12] between the duplicated conduction systems (Figure 31.1d). Careful mapping along the AV ring will disclose two separate sites for His bundle recording, and tachycardia can usually be eliminated by ablating the weaker of the two.

Accessory AV Pathways in CHD

The incidence of accessory pathways (AP) in patients with CHD is not appreciably higher than in structurally normal hearts, except for the special situation involving Ebstein's anomaly of the tricuspid valve where as many as 20% of patients have one or more abnormal AV connections [13].

Experience with surgical and catheter mapping has shown that these APs tend to cluster along right free-wall and septal regions where the tricuspid valve deviates away from the true AV groove [14, 15], suggesting a likely developmental link between the valve abnormality and defects in electrical insulation. Pathway localization can be challenging in Ebstein's owing to exceptionally thin RV muscle that often generates fractionated and low-amplitude electrograms. The challenge is further increased by the presence of multiple APs in more than half these patients, sometimes creating a confusing assortment of tachycardia patterns. It is not surprising that success rates with catheter ablation in Ebstein's are somewhat lower (85%) and recurrence rates higher (25%) when compared to structurally normal hearts.

The key to AP mapping and ablation in Ebstein's anomaly is an accurate definition of the true AV groove at the level of the coronary artery, which is not to be confused with mobile edge of the tricuspid valve leaflet displaced toward the apex of the RV (Figure 31.2). It is insufficient to rely on relative amplitudes of atrial vs. ventricular electrograms for this purpose because of the extensive ventricular signal fractionation, but a selective right coronary angiogram will provide a reliable roadmap during

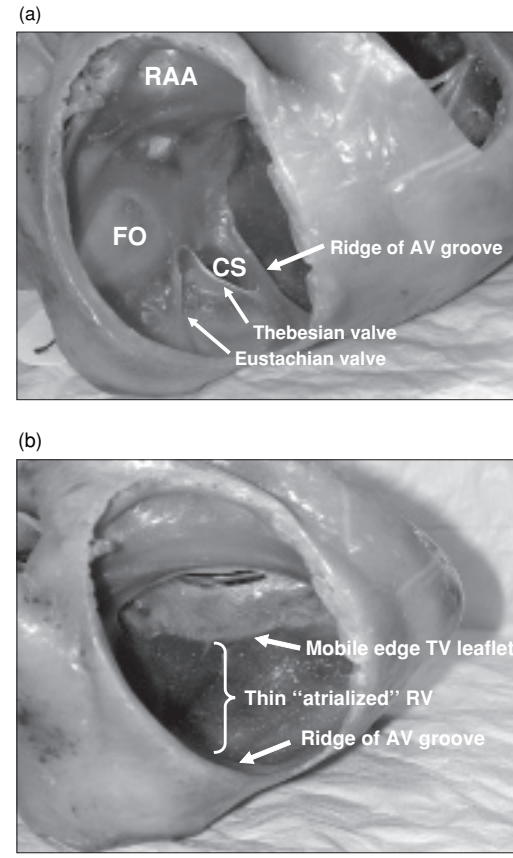

Figure 31.2 Autopsy specimen from a patient with Ebstein's malformation, with the lateral right atrial wall removed to reveal intracardiac anatomy. In panel (a), a prominent ridge is apparent at the level of the atrioventricular groove where the edge of the tricuspid valve would be found in a normal heart, but as shown in panel (b) when the heart is tilted to expose the ventricular inlet, the mobile edge of the valve leaflet is displaced far down into the body of the right ventricle. Between the ridge and the mobile leaflet edge is the so-called "atrialized" muscle of the right ventricle, which is thin and fibrotic. KEY: AV = atrioventricular; CS = coronary sinus; FO = fossa ovalis; RAA = right atrial appendage; RV = right ventricle; TV = tricuspid valve.

procedures to define the proper level for AP mapping and ablation [16]. In exceptionally difficult cases, a thin multielectrode catheter can be positioned for mapping directly within the lumen of the right coronary artery [17], but this maneuver is rarely necessary.

Accessory pathways are encountered sporadically in CHD malformations other than Ebstein's, ranging from a simple atrial septal defect to a complex

single ventricle [5, 16, 18]. Anatomic details must be well understood whenever mapping and ablation are attempted in such cases, not only as a way to facilitate AP localization, but also to predict likely location of the normal AV conduction tissues.

Atrial Tachycardias in CHD

Atrial tachycardias account for the vast majority of arrhythmias in the CHD population. The electrical pathophysiology involves a complex interplay between surgically induced conduction obstacles, natural conduction obstacles (e.g., crista terminalis, valve orifices, venous junction sites), and hypertrophy and fibrosis from chronic hemodynamic stress. Most of these arrhythmias involve organized macroreentrant circuits, though in some cases focal tachycardias and atrial fibrillation may occur. Treatment options are diverse and may include pharmacologic therapy, antibradycardia pacing, antitachycardia pacing, arrhythmia surgery, and catheter ablation [19, 20]. Comments here will be largely restricted to the underlying electrophysiologic features, mapping characteristics, and results for catheter therapy.

Intraatrial Reentrant Tachycardia (IART) in CHD

The right atrium (RA) bears the brunt of surgical intervention for CHD. During most types of repair performed on cardiopulmonary bypass, the RA suffers the insults of caval cannulation scars, a lateral atriotomy scar, and sometimes an atrial septal patch. Even when surgery is successful, the RA chamber must often contend with abnormal postoperative pressure and volume loads, best exemplified by the Fontan operation for single ventricle where the RA is exposed directly to pulmonary artery pressure. The potential for macroreentry to develop within this abnormal substrate is easy to appreciate. Atrial tachycardias can occur in nearly all types of CHD after open-heart procedures [21], even simple atrial septal defect closure, though the incidence is clearly highest among patients with extensive atrial suture lines, as occurs with the Fontan operation, and the Mustard or Senning operations for transposition of the great arteries [22–25]. In these particular subgroups, as many as 50% of patients will develop atrial macroreentry during extended follow-up.

Atrial macroreentry circuits seen in CHD patients can follow a number of potential routes within the RA that vary according to the underlying defect and method used for repair. The importance of clear anatomic knowledge and appreciation for all surgical details cannot be overemphasized. If a patient has four cardiac chambers in normal orientation, and surgery involved nothing beyond simple patching of septal defects and/or valve repairs (e.g., atrial septal defect, VSD, or tetralogy of Fallot correction), then the most commonly encountered circuit involves reentry around the tricuspid valve ring through the cavo-tricuspid isthmus (CTI), similar in many ways to conventional atrial flutter [26, 27].

Unlike common flutter, cycle lengths tend to be relatively long (250–400 msec) in CHD patients due to slow conduction velocity along the scarred lateral RA wall, so that the surface electrocardiogram does not necessarily display classic sawtooth flutter waves, but instead can have more discrete *P*-waves with long isoelectric time in between. Furthermore, it is common for these patients to have the potential for secondary reentrant loops around lateral wall atriotomy lines, sometimes functioning as a figure-of-eight in conjunction with tricuspid valve reentry [28].

If too much attention is focused on the concept of flutter through the traditional CTI region, these secondary circuits will be missed. For all these reasons, the noncommittal term intraatrial reentrant tachycardia (IART) has become the preferred descriptive nomenclature when discussing macroreentrant circuits in CHD patients. It leaves open a far broader range of possibilities for the electrocardiographic appearance, cycle length, circuit location, and approach to ablation.

The reentrant routes for IART become more complex whenever large atrial baffles are used for surgical repair. In the case of Mustard or Senning operations for transposition of the great arteries, systemic venous return is redirected toward the mitral valve with a large patch sutured from the superior and inferior vena cavae along the back of the atria. In the process, the tricuspid valve receives the pulmonary venous return and becomes sequestered on the left side of the circulation.

The most common IART circuits in these patients still involve macroreentry through the CTI around the tricuspid valve ring [26, 29, 30], but in order

to reach this tissue for mapping or ablation, the catheter tip has to be directed retrograde through the aortic and tricuspid valves, or alternatively, via trans-baffle puncture from the IVC pathway into the neo-left atrium using a modification of the Brockenbrough technique [31]. Secondary IART circuits can occasionally be found in Mustard and Senning patients along the caval suture lines.

By far the most complicated forms of IART occur in CHD patients who have undergone the Fontan operation [26, 32–34]. Circuits in these patients can involve the lateral RA wall, the atrial septum, pericaval tissue, the mouth of coronary sinus, and even parts of the left atrium (LA). Because a standard right-sided AV valve is absent in most single ventricles, reentry involving the CTI is not usually possible. The majority of Fontan patients will have multiple circuits identified during a mapping session.

Mapping and ablation of IART must begin with a clear definition of cardiac anatomy and review of past surgical records to generate a workable substrate map. Anatomic details can be collected from preprocedure echocardiograms, cardiac MRI, or CT imaging. These data can then be used during the case with any combination of angiography, intracardiac echo, and 3D electroanatomic registration to develop a shell of one or both atria.

New technology allowing MRI or CT imaging data to be merged with electroanatomic signals is particularly well suited for this purpose. Before inducing IART, it is often useful to construct a baseline RA activation map in sinus rhythm and annotate the anatomic shell with conduction features of interest, such as double potentials (suggesting suture lines) and areas of low voltage (suggesting regions of scar or patch), all of which are then viewed relative to the caval entry sites, the coronary sinus, Eustachian ridge, and the CTI (if a tricuspid valve is present) to obtain a preview of possible routes for IART circuits.

Programmed stimulation from the RA is nearly always successful in reproducing clinical IART events for CHD patients (Figure 31.3). Short 8-beat burst pacing in the RA at progressively rapid rates down to atrial refractoriness usually proves slightly

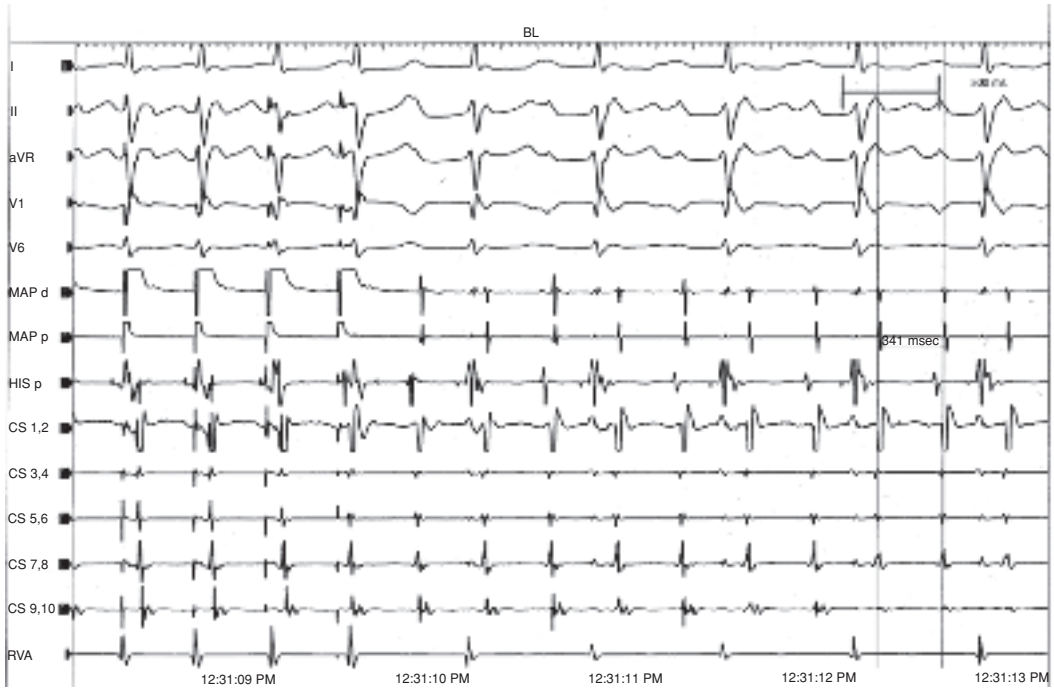

Figure 31.3 Recordings from a 28-year-old with tricuspid stenosis and pulmonary atresia after a Fontan operation undergoing ablation for intraatrial reentrant tachycardia. The tachycardia, which conducts here in a 2:1 fashion, was easily induced with eight beats of right atrial pacing. Tachycardia cycle length (341 msec) is much longer than classic flutter, and the *P*-wave appears sharp and discrete unlike classic flutter waves. A macroreentrant circuit was mapped along the lateral right atrial wall related to an atriotomy scar.

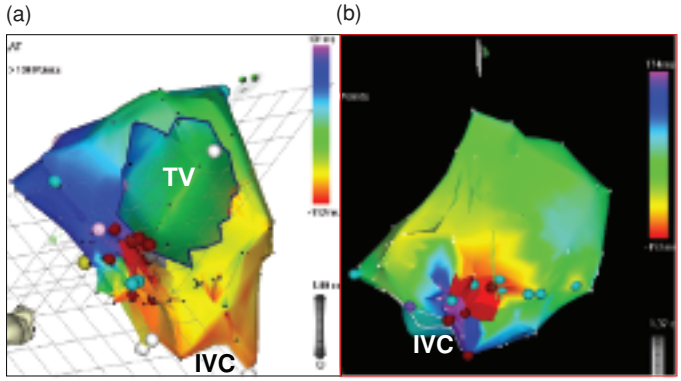

Figure 31.4 Examples of electroanatomic maps during macroreentrant IART in relatively simple forms of congenital heart disease. The activation sequence proceeds according to the color code (red > yellow > green > blue > purple). Panel (a) shows a map from a patient with repaired tetralogy of Fallot involving counterclockwise macroreentry around the tricuspid valve through the cavo-tricuspid isthmus. A series of RF applications (red dots) terminated IART and created bidirectional conduction block at the isthmus. Panel (b) shows the lateral wall of the right atrium from a patient after closure of atrial and ventricular septal defects. There was a long line of split potentials (blue dots) corresponding to an atriotomy incision line. The tachycardia pattern suggested a narrow channel of slow conduction through a gap in the line. A series of RF applications focused on this gap successfully interrupted the circuit. KEY: IVC = inferior vena cava; TV = tricuspid valve.

more effective for induction purposes than standard extrastimulus testing, and isoproterenol may be required in some cases. Because IART has generally long cycle lengths compared to classic flutter, 1:1 AV conduction is common, and the rapid ventricular response can be poorly tolerated in patients with depressed ventricular function and/or single ventricle. It is often advisable to have an arterial line in place to monitor blood pressure in CHD patients with compromised hemodynamics, and to have an AV node blocking agent such as diltiazem readily available to slow the ventricular response when necessary. With these routine precautions, CHD patients can usually be allowed to stay in sustained IART for long periods to permit careful mapping.

Since the initial reports of successful IART ablation in the mid 1990s, mapping techniques have evolved dramatically. Early methodology involved conventional linear multipolar catheters, with high reliance on entrainment pacing and postpacing interval analysis to verify when tissue was involved in the circuit [35, 36]. Though successful in most cases, these procedures were quite arduous because only small segments of the atrium could be mapped at any one time. Clinical trials with various designs for basket catheters offered some incremental improvement in map quality [37], but it was not until technology for 3D mapping became available that finer details of IART propagation could be fully appreciated [38, 39]. Both noncontact mapping systems and point-by-point electroanatomic mapping systems have now been used successfully for these studies.

Examples of electroanatomic maps for IART in several common forms of CHD are shown in Figures 31.4, 31.5, and 31.6. If the underlying anatomic substrate is well understood, and if adequate data points are sampled, then the route of propagation is usually clear enough from activation maps to permit identification of vulnerable sites for ablation attempts. Should uncertainty remain after the activation map is created, traditional entrainment maneuvers with postpacing interval analysis can be used to better clarify the circuit.

Although most IART mapping challenges have now been overcome, achieving successful and permanent conduction block with radiofrequency (RF) ablation can still be a demanding exercise whenever the target area is wide, the atrial muscle is thick, or surgical patches interfere with catheter positioning and tip contact. This has led to the widespread adoption of irrigated-tip and large-tip ablation catheters for IART procedures [40, 41], resulting in improved acute success rates up to 90% with these more

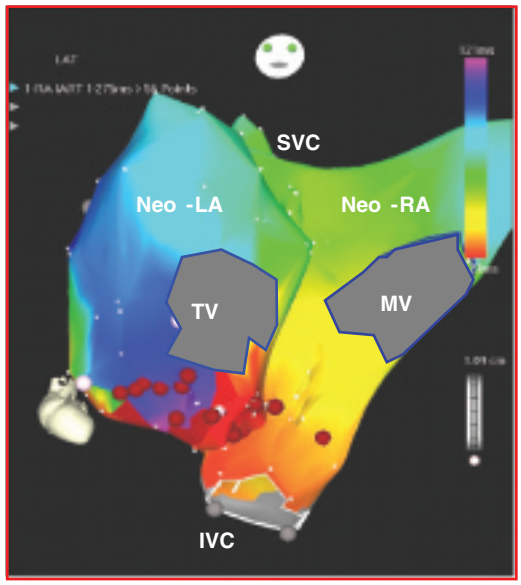

Figure 31.5 Electroanatomic map during IART in a patient after the Mustard operation. The activation sequence proceeds according to the color code (red > yellow > green > blue > purple). The circuit involved counterclockwise macroreentry around the tricuspid valve ring. The ablation catheter tip was delivered retrograde through the aortic and tricuspid valves to the isthmus area where a series of RF applications (red dots) eliminated the circuit. KEY: IVC = inferior vena cava; MV = mitral valve; Neo-LA = the functional left atrium created by the atrial baffle; Neo-RA = the functional right atrium created by the atrial baffle; SVC = superior vena cava; TV = tricuspid valve.

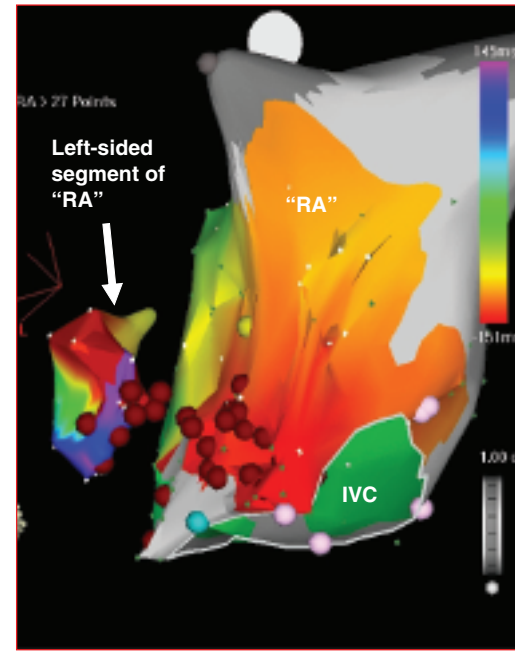

Figure 31.6 Electroanatomic map during IART in a patient after a lateral tunnel-type Fontan connection, viewed from the back wall of the atrium. The activation sequence proceeds according to the color code (red > yellow > green > blue > purple). In this case the surgical patch used to construct the lateral tunnel sequestered a small portion of the right atrium into the left side of the circulation. The timing of signals acquired from the "RA" side of the patch could not account for the entirety of the IART cycle length, and aggressive RF applications (red dots) along the "RA" side of the patch could slow IART slightly, but never terminated the circuit. Only after trans-septal puncture into the small chamber on the opposite side of the patch was the circuit mapped in its entirety, and a successful ablation site identified. KEY: IVC = inferior vena cava; "RA" = portion of the right atrium on the right side of the tunnel patch.

aggressive tools for RF power delivery. The recurrence rate after acutely successful ablation now falls within the reasonable range of 10–25% for most forms of CHD, although for certain Fontan patients with multiple IART circuits and extremely thick atrial walls, recurrence rates remain disappointingly high (over 40%), and alternate therapy such as arrhythmia surgery may be required [42, 43].

Focal Atrial Tachycardia in CHD

Not all atrial tachycardias in CHD patients involve macroreentry circuits. About 5–10% of cases can be identified with clinical presentation and an electrocardiographic appearance that may be grossly indistinguishable from IART, though the tachycardia appears to emanate from a point-source during detailed mapping [44, 45]. These focal tachycardias can be initiated and terminated with programmed stimulation, operate at fairly fixed cycle lengths, and respond promptly to direct current cardioversion.

Such characteristics would tend to implicate either localized triggered activity or microreentry as the underlying mechanism. Mapping reveals radial propagation away from a discrete epicenter that is usually located within the RA near the edge of a surgical suture line (Figure 31.7). The local electrogram can appear fractionated with long-duration electrical activity [45]. Ablation efforts can be focused either on the point of earliest activation, or around the periphery to isolate the target site. Tachycardia

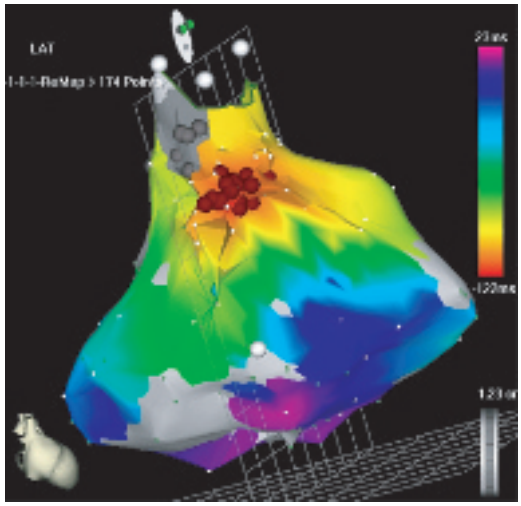

Figure 31.7 Electroanatomic map of a focal atrial tachycardia from a patient with an atriopulmonary-type Fontan operation, showing the lateral wall of a very dilated right atrium. The activation sequence proceeds according to the color code (red > yellow > green > blue > purple). A region of scar (gray area) was identified near the junction of the superior vena cava and right atrium. Earliest activation during focal tachycardia was mapped to a point along the upper lateral atrium, just below the scar region. A series of RF applications at this site eliminated tachycardia without damaging the sinus node or the phrenic nerve, both of which were in relatively close proximity.

will often terminate promptly with a single well-positioned RF application, confirming the focal nature of this disorder. Ablation success rates are on the order of 80%, and recurrences are rare.

Atrial Fibrillation in CHD

Discussion up to this point has concentrated on the common forms of atrial tachycardia arising from disordered conduction within RA tissues, but a small subset of CHD patients can be identified with hemodynamic abnormalities affecting primarily the left heart, and atrial fibrillation can develop as a consequence. Examples include congenital aortic valve disease, mitral valve disease, palliated single ventricle with biatrial enlargement, and large defects of the atrial septum [46].

Experience with mapping and ablation of atrial fibrillation in the setting of CHD is very limited, but because the efficacy of alternate treatments is so imperfect, efforts are now underway at some centers to explore catheter ablation in some difficult cases. Mapping in CHD patients reveals a pattern for fibrillation that is similar to that encountered in elderly patients with acquired heart disease. The most rapid and irregular fibrillatory activity is found within the LA in the vicinity of the pulmonary veins, with passive propagation to the RA through Bachmann's bundle and lower atrial septum. Occasionally, atrial activity recorded from the RA endocardium may look deceptively regular and organized if left-to-right conduction is limited by surgical scars (e.g., large atrial septal patch), even mimicking IART on occasion, but recordings from the coronary sinus and LA will reveal the true nature of the more rapid generator within the LA. It can sometimes seem daunting to enter the LA in CHD patients through thick atrial septal patches, but with experience and careful technique, Brockenbrough puncture through prosthetic patch material can be accomplished safely (Figure 31.8).

Several publications have described encouraging results with surgical ablation for atrial fibrillation in CHD using a modified Cox procedure [47], but the experience with catheter techniques has been only anecdotal to date. In the six cases performed at our center, the intended lesion set in the LA involved encirclement of the left and right pulmonary veins, a connecting line between the pulmonary vein circles, an extension line from the left vein circle to left atrial appendage, and an extension line to the posterior mitral valve ring (Figure 31.9). The short-term success rate has been 50% in our limited recent experience, but follow-up duration remains too short to estimate the longer-term recurrence risk.

Ventricular Tachycardia in CHD

A small but concerning incidence of sudden death from ventricular tachycardia (VT) continues to be observed in certain forms of CHD many years after surgical repair. This issue is most relevant for patients who have undergone a ventriculotomy and/or patching of a ventricular septal defect, when macroreentry develops near regions of surgical scar within the RV. Tetralogy of Fallot is the best-studied example of this phenomenon. Roughly 10% of tetralogy patients develop VT by adulthood, with an incidence of sudden death measured at 2% per decade of follow-up [48–52].

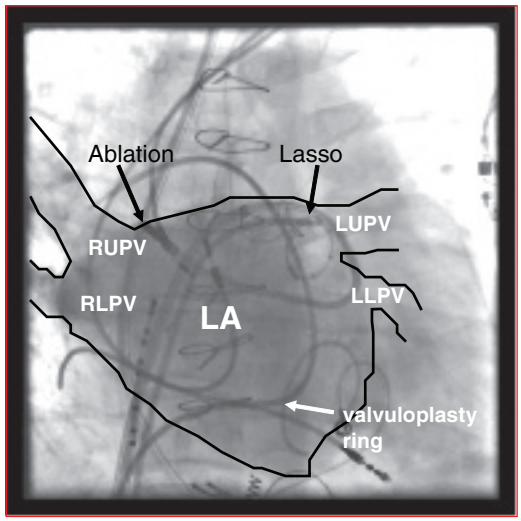

Figure 31.8 Angiogram (frontal view) done in preparation for ablation of atrial fibrillation, outlining the pulmonary veins and left atrium in a young woman with congenitally corrected transposition who had a Rastelli operation along with closure of atrial and ventricular septal defects. She required pacing for complete heart block, as well as re-operation for valvuloplasty with ring placement for a regurgitant left-sided AV valve. Refractory atrial fibrillation developed in this severely dilated left atrium. A Lasso catheter is seen positioned near the left upper pulmonary vein, and an irrigated-tip ablation catheter is near the right upper pulmonary vein. Access to the left atrium for mapping and ablation necessitated double trans-septal punctures through thick patch material. KEY: LA = left atrium; LLPV and LUPV = left lower and left upper pulmonary veins, respectively; RLPV and RUPV = right lower and right upper pulmonary veins, respectively.

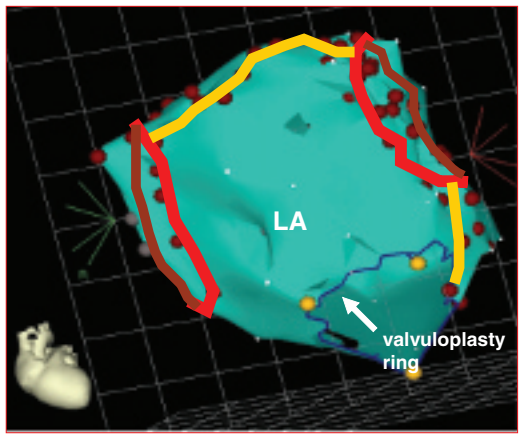

Figure 31.9 Lesion set used for atrial fibrillation ablation in same patient shown in Figure 31.8. KEY: LA = left atrium.

Multiple risk factors for VT and sudden death have now been identified in the tetralogy population [53–59] including:

1 older age at surgery;
2 older age at follow-up;
3 history of prior palliative shunts;
4 poor ventricular systolic function;
5 advanced degrees of pulmonary regurgitation with RV dilation;
6 residual pulmonary stenosis;
7 inducible VT at electrophysiologic study;
8 high-grade ventricular ectopy on Holter monitoring
9 QRS duration exceeding 180 msec on electrocardiogram.

Although the predictive accuracy of this list during clinical decision making is only moderate at best, the items do suggest a central theme of long-term hemodynamic stress on RV muscle as an important contributor to the development of VT.

The dominant mechanism for VT in tetralogy patients involves monomorphic macroreentry [60, 61]. Data from both epicardial surgical mapping and endocardial catheter mapping implicates tissue in the RV outflow tract as critical to propagation of these circuits (Figure 31.10). Almost all tetralogy patients have surgically induced conduction

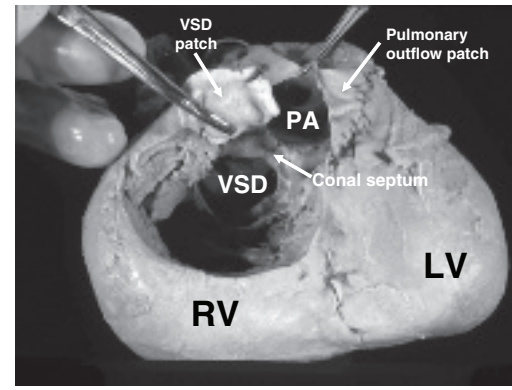

Figure 31.10 Autopsy specimen from a patient with tetralogy of Fallot who died while undergoing surgical repair. To better visualize the intracardiac anatomy in this specimen, the anterior wall of the right ventricle (RV) has been resected, and the ventricular septal defect (VSD) patch has been partially detached and deflected superiorly with forceps. The essential anatomy of tetralogy can be appreciated, including the thickened and dilated right ventricle, the VSD, and the conal septum between the VSD and the pulmonary artery (PA). KEY: LV = left ventricle.

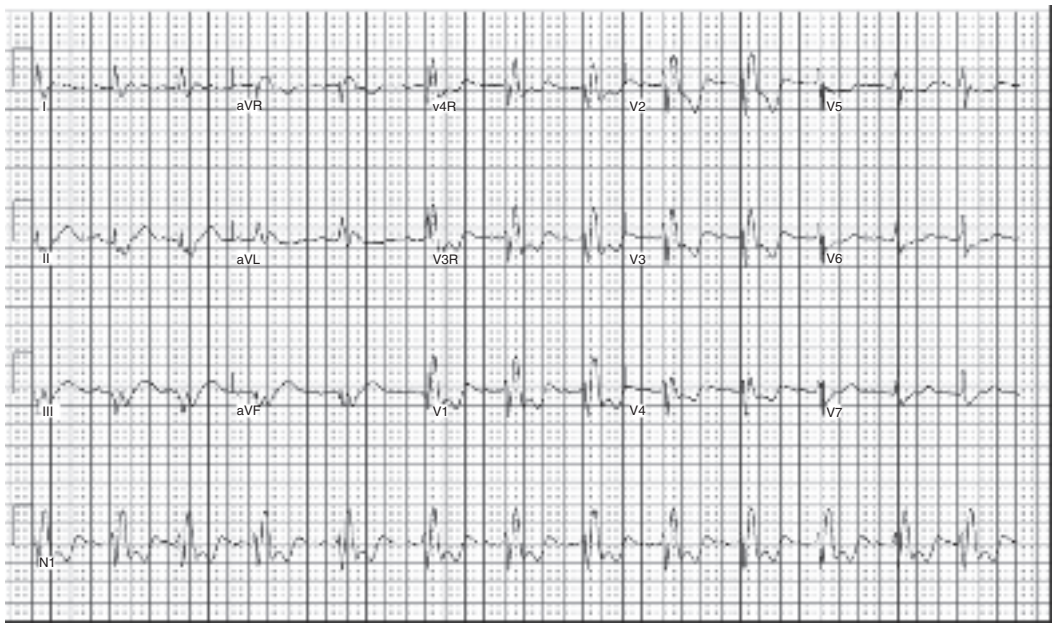

Figure 31.11 Electrocardiogram in sinus rhythm from a patient with repaired tetralogy of Fallot and a history of recurrent ventricular tachycardia. The tracing is notable for right-bundle-branch block, left-anterior hemiblock, and a very prolonged QRS duration of 210 msec. Right-bundle branch block will be present in >90% of postoperative tetralogy patients.

disturbances through this region as evidenced by the presence of right-bundle-branch block on their sinus rhythm electrocardiogram, and mapped VT circuits are typically observed to utilize this area as a slow conduction zone during macroreentry (Figure 31.11).

Quite predictably, VT propagating through this territory will feature a QRS morphology with left-bundle-branch block and an inferior-directed axis in the frontal plane (Figure 31.12). Programmed stimulation is usually effective in reproducing these circuits [57]. While some CHD patients may have slow VT capable of supporting the circulation during prolonged periods of mapping, the majority will have VT with relatively fast rates (>200 beats per minute) that can compromise cardiac output, particularly in the setting of poor ventricular function. Thus, mapping strategy will have to be adjusted according to the ability of the patient to tolerate a sustained tachycardia.

All VT mapping studies in tetralogy patients can begin with detailed substrate mapping during sinus rhythm to create an anatomic shell of the RV, annotated as appropriate with anatomical landmarks and low-voltage scar regions (Figure 31.13). This can be accomplished by performing a RV angiogram at the beginning of the case, or by importing structural data from MRI or CT into a 3D mapping system. The potential route(s) for reentry can usually be deduced with reasonable accuracy from the sinus rhythm map based on identification of a narrow conduction isthmus in the RV outflow area between surgical scars and natural conduction obstacles.

From published clinical mapping studies, the most common locations for such an isthmus (Figure 31.14) in tetralogy include the conal septum (between the VSD and pulmonary valve), the rightward aspect of the anterior RV (between the tricuspid valve and the outflow tract scar), and the cranial end of an RV outflow tract incision (if a non-transannular patch was used).

After VT is induced, detailed mapping can be performed with point-by-point electroanatomic technique if the patient is sufficiently tolerant of tachycardia to permit acquisition of necessary data from the RV endocardium (see Figure 31.13b). If the patient is poorly tolerant of VT, more limited maps can be performed that focus only on suspect areas

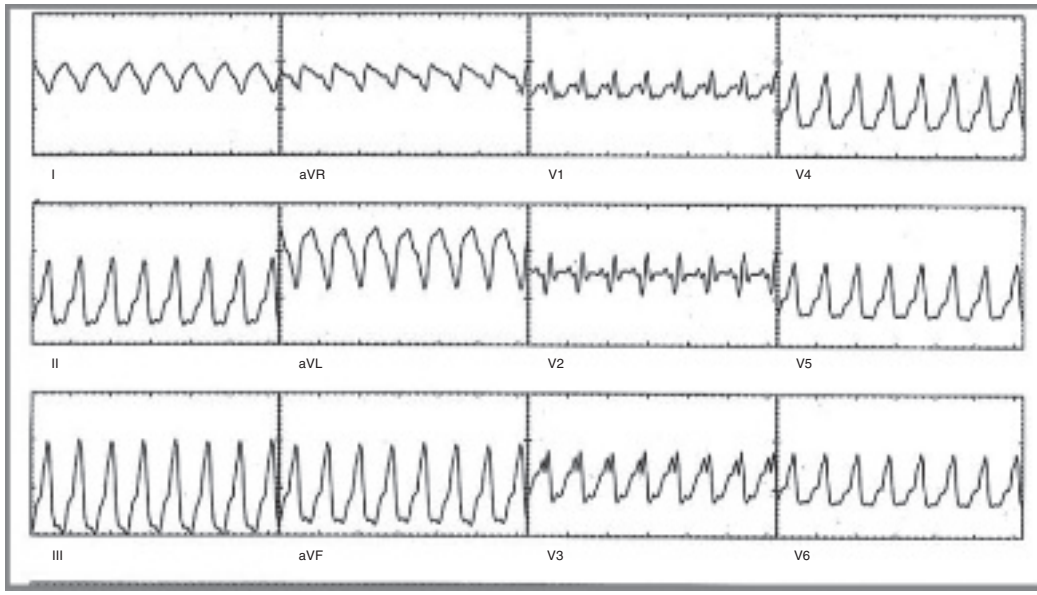

Figure 31.12 Electrocardiogram during sustained monomorphic ventricular tachycardia from a patient with repaired tetralogy of Fallot. The pattern of left-bundle-branch block with an inferior axis is typical for the macroreentry circuits involving right ventricular outflow tract tissues in these patients.

in the RV where a narrow isthmus was suspected from the baseline substrate map. Alternatively, non-contact mapping technology can be used to collect a rapid activation map from just a few beats of VT. Entrainment analysis and pace-mapping can also be employed to verify participation of specific sites. All these methodologies will have their own advantages and drawbacks in CHD patients, but as long as the underlying anatomy and conduction patterns in the RV have been meticulously ascertained in the baseline substrate map, all can be used successfully to identify a probable reentrant circuit and suggest potential sites for ablation.

The initial publications describing catheter ablation for VT in tetralogy patients consisted of isolated case reports describing acute success with various

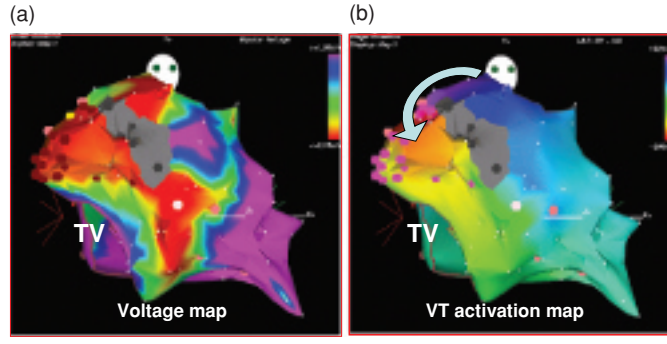

Figure 31.13 Substrate mapping and activation sequence mapping of ventricular tachycardia in a patient with repaired tetralogy of Fallot. Panel (a) shows a voltage map of the right ventricle, where the scale ranges from 0.1 mV (red) to >1.0 mV (purple), and areas with voltage <0.1 mV are marked as gray scar. The right ventricular outflow area is notable for a large scar surrounded by diffusely low voltage, corresponding to the infundibular incision and patching used for surgical repair. Panel (b) shows the activation sequence map during sustained ventricular tachycardia according to the color code (red > yellow > green > blue > purple). The area of low voltage in the outflow area was critical to propagation of this circuit. KEY: TV = tricuspid valve.

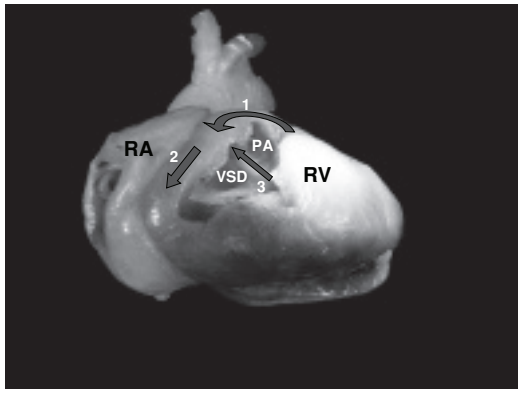

Figure 31.14 Autopsy specimen from a young patient with tetralogy of Fallot who died prior to any surgical intervention. The anterior surface of the right ventricle (RV) has been resected to display intracardiac anatomy. If one imagines this resected area being replaced with a surgical patch, three potential narrow corridors (arrows) for macroreentry can be appreciated in the outflow region: (1) between the cranial end of the patch and the pulmonary valve , (2) between the right side of the patch and tricuspid valve, and (3) through the conal septum between the ventricular septal defect (VSD) and the pulmonary artery (PA). KEY: RA = right atrium.

mapping techniques [62–70], but could offer no measure of long-term outcomes. Subsequently, more extensive data became available from two institutional series involving a combined total of 36 subjects mapped primarily with standard linear catheter techniques and ablated with 4-mm tipped RF catheters [71, 72].

The acute success rate for the combined experience averaged 72% (with inadequate map data accounting for most of the failures), and the follow-up recurrence risk averaged 25%. More recently, two elegant publications [73, 74] have described 3D mapping in a combined total of 21 cases, with an improved acute success rate of 90%, and recurrence risk reduced to about 16%. The lowest incidence of recurrence reported to date (9%) involved 11 cases in which an irrigated-tip catheter was the exclusive method for RF delivery.

Creating effective transmural conduction block with RF energy in the thick-walled RV of tetralogy patients is obviously a challenge, and it may be reasonable to suggest that irrigation and large-tip catheters with high-output generators offer the best chance of permanent success during these procedures. Until the uncertain risk of VT recurrence after ablation is lower, most centers will continue to relegate RF ablation to an ancillary role as a way of reducing the shock burden for CHD patients who already have an implantable defibrillator in place [75, 76], but it may come to assume a more primary function as techniques continue to improve.

Conclusion

The excellent results now seen with childhood surgery for CHD are creating a rapidly expanding population of adolescent and young adult survivors who are at risk for developing a complex assortment of atrial and ventricular tachycardias related to their anatomic defects and surgical scars. Catheter ablation represent an important therapeutic option for this population. Clear knowledge of the underlying anatomy and all prior surgical interventions is essential for successful mapping of such arrhythmias.

One of the important spin-off benefits of tachycardia mapping and ablation in CHD patients has been a better appreciation of the exact relationship between reentry and the pathologic substrate caused by long-standing hemodynamic abnormalities and the position of certain surgical scars. This knowledge has contributed to refinements in surgical strategy that have significantly reduced the incidence of arrhythmias for the current generation of CHD patients.

For example, transposition of the great arteries is now managed with direct arterial switch rather than large atrial baffles; Fontan connections are being constructed in a way to minimize right atrial dilation; and tetralogy of Fallot is being repaired at younger ages with smaller incisions and attempts to preserve pulmonary valve competence as a way to reduce scarring in the RV [77–81]. Prospective studies are also in progress to test whether more strategic locations can be found for atriotomy incisions to negate the potential for reentry on the lateral RA wall [82]. It is anticipated that such modifications will improve the long-term prognosis for complex CHD.

References

1 Lillehei CW, Sellers RD, Bonnabeau RC, Eliot RS. Chronic postsurgical complete heart block, with particular reference to prognosis, management, and a new *P* -wave pacemaker. *J Thorac Cardiovasc Surg* 1963; **46**: 436–56.

2 Anderson RH, Ho SY. The disposition of the conduction tissues in congenitally malformed hearts with reference to their embryological development. *J Perinat Med* 1991; **19**: 201–6.

3 Anderson RH, Ho SY, Becker AE. The surgical anatomy of the conduction tissues. *Thorax* 1983; **38**: 408–20.

4 Dick M, Norwood WI, Chipman C, Castaneda AR. Intraoperative recording of specialized atrioventricular conduction tissue electrograms in 47 patients. *Circulation* 1979; **59**: 150–60.

5 Levine J, Walsh EP, Saul JP. Catheter ablation of accessory pathways in patients with congenital heart disease including heterotaxy syndrome. *Am J Cardiol* 1993; **72**: 689–94.

6 Anderson RH, Allwork SP, Ho SY, Lenox CC, Zuberbuhler JR. Surgical anatomy of tetralogy of Fallot. *J Thorac Cardiovasc Surg* 1981; **81**: 887–96.

7 Thiene G, Wenick ACG, Frescura C, et al. Surgical anatomy and pathology of the conduction tissues in atrioventricular defects. *J Thorac Cardiovas Surg* 1981; **82**: 928–37.

8 Ih S, Fukuda K, Okada R, Saitoh S. Histopathological correlation between the QRS axis and disposition of the atrioventricular conduction system in common atrioventricular orifice and in its related anomalies. *Jpn Circ J* 1983; **47**: 1368–76.

9 Lev M, Licata RH, May RC. The conduction system in mixed levocardia with ventricular inversion (corrected transposition). *Circulation* 1963; **28**: 232–37

10 Anderson RH, Becker AE, Arnold R, Wilkinson JL. The conducting tissues in congenitally corrected transposition. *Circulation* 1974; **50**: 911–23.

11 Symons JC, Shinebourne EA, Joseph MC, Lincoln C, Ho Y, Anderson RH. Criss-cross heart with congenitally corrected transposition: report of a case with d-transposed aorta and ventricular preexcitation. *Eur J Cardiol* 1977; **5**: 493–505.

12 Epstein MR, Saul JP, Weindling SN, Triedman JK, Walsh EP. Atrioventricular reciprocating tachycardia involving twin atrioventricular nodes in patients with complex congenital heart disease. *J Cardiovasc Electrophysiol* 2001; **12**: 671–79.

13 Attenhofer Jost CH, Connolly HM, Edwards WD, Hayes D, Warnes CA, Danielson GK. Ebstein's anomaly: review of a multifaceted congenital cardiac condition. *Swiss Med Wkly* 2005; **135**: 269–81.

14 Oh JK, Holmes DR, Jr, Hayes DL, Porter CB, Danielson GK. Cardiac arrhythmias in patients with surgical repair of Ebstein's anomaly. *J Am Coll Cardiol* 1985; **6**: 1351–57.

15 Reich JD, Auld D, Hulse E, Sullivan K, Campbell R. The Pediatric Radiofrequency Ablation Registry's experience with Ebstein's anomaly. Pediatric Electrophysiology Society. *J Cardiovasc Electrophysiol* 1998; **9**: 1370–77.

16 Chetaille P, Walsh EP, Triedman JK. Outcomes of radiofrequency catheter ablation of atrioventricular reciprocating tachycardia in patients with congenital heart disease. *Heart Rhythm* 2004; **1**: 168–173.

17 Shah MJ, Jones TK, Cecchin F. Improved localization of right-sided accessory pathways with microcatheter-assisted right coronary artery mapping in children. *J Cardiovasc Electrophysiol* 2004; **15**: 1238–43.

18 Van Hare GF, Lesh MD, Stanger P. Radiofrequency catheter ablation of supraventricular arrhythmias in patients with congenital heart disease: results and technical considerations. *J Am Coll Cardiol* 1993; **22**: 883–90.

19 Garson A, Bink-Boelkens MTE, Hesslein PS, et al. Atrial flutter in the young: a collaborative study of 380 cases. *J Am Coll Cardiol* 1985; **6**: 871–78.

20 Walsh EP, Cecchin F. Arrhythmias in adult patients with congenital heart disease. *Circulation* 2007; **115**: 534–45.

21 Roos-Hesselink J, Perlroth MG, McGhie J, Spitaels S. Atrial arrhythmias in adults after repair of tetralogy of Fallot: correlations with clinical, exercise, and echocardiographic findings. *Circulation* 1995; **91**: 2214–19.

22 Fishberger SB, Wernovsky G, Gentles TL, et al. Factors that influence the development of atrial flutter after the Fontan operation. *J Thorac Cadiovas Surg* 1997; **113**: 80–6.

23 Cecchin F, Johnsrude CL, Perry JC, Friedman RA. Effect of age and surgical technique on symptomatic arrhythmias after the Fontan procedure. *Am J Cardiol* 1995; **76**: 386–91.

24 Manning PB, Mayer JE, Wernovsky G, Fishberger SB, Walsh EP. Staged operation to Fontan increases the incidence of sinoatrial node dysfunction. *J Thorac Cardiovasc Surg* 1996; **111**: 833–40.

25 Flinn CJ, Wolff GS, Dick M, et al. Cardiac rhythm after the Mustard operation for complete transposition of the great arteries. *N Engl J Med* 1984; **3310**: 1635–38.

26 Collins KK, Love BA, Walsh EP, Saul JP, Epstein MR, Triedman JK. Location of acutely successful radiofrequency catheter ablation of intraatrial reentrant tachycardia in patients with congenital heart disease. *Am J Cardiol* 2000; **86**: 969–74.

27 Van Hare GF. Electrical–anatomic correlations between typical atrial flutter and intra-atrial reentry following atrial surgery. *J Electrocardiol* 1998; **30**: 77–84.

28 Walsh EP. Ablation of postoperative atrial tachycardia in congenital heart disease patients. In: *Catheter Ablation of Arrhythmias*. Huang SK, Wood , eds., Saunders/Elsevier, Philadelphia, 2006: 237–58.

29 Kanter RJ, Papagiannis J, Carboni MP, Ungerleider RM, Sanders WE, Wharton JM. Radiofrequency catheter ablation of supraventricular tachycardia substrates after Mustard and Senning operations for d-transposition of the great arteries. *J Am Coll Cardiol* 2000; **35**: 428–41.

30 Van Hare GF, Lesh MD, Ross BA, Perry JC, Dorostkar PC. Mapping and radiofrequency ablation of intraatrial reentrant tachycardia after the Senning or Mustard procedure for transposition of the great arteries. *Am J Cardiol* 1996; **77**: 985–91.

31 Perry JC, Boramanand NK, Ing FF. Trans-septal technique through atrial baffles for 3-dimensional mapping and ablation of atrial tachycardia in patients with d-transposition of the great arteries. *J Interv Card Electrophysiol* 2003; **9**: 365–69.

32 Triedman JK, Alexander ME, Berul CI, Bevilacqua LM, Walsh EP. Electroanatomic mapping of entrained and exit zones in patients with repaired congenital heart disease and intra-atrial reentrant tachycardia. *Circulation* 2001; **103**: 2060–65.

33 Mandapati R, Walsh EP, Triedman JK. Pericaval and periannular intra-atrial reentrant tachycardias in patients with congenital heart disease. *J Cardiovasc Electrophysiol* 2003; **14**: 119–22.

34 Nakagawa H, Shah N, Matsudaira K, et al. Characterization of reentrant circuit in macroreentrant right atrial tachycardia after surgical repair of congenital heart disease: isolated channel between scars allow "focal" ablation. *Circulation* 2001; **103**: 699–709.

35 Kalman JK, Van Hare GF, Olgin JE, Saxon LA, Stark SI, Lesh MD: Ablation of incisional reentrant atrial tachycardia complicating surgery for congenital heart disease. *Circulation* 1996; **93**: 502–12

36 Triedman JK, Bergau DM, Saul JP, Epstein MR, Walsh EP. Efficacy of radiofrequency ablation for control of intraatrial reentrant tachycardia in patients with congenital heart disease. *J Am Coll Cardiol* 1997; **30**: 1032–38.

37 Triedman JK, Jenkins KJ, Colan SD, Saul JP, Walsh EP. Intra-atrial reentrant tachycardia after palliation of congenital heart disease: characterization of multiple macroreentrant circuits using fluoroscopically based three-dimensional endocardial mapping. *J Cardiovasc Electrophysiol* 1997; **8**: 259–70.

38 Delacretaz E, Ganz LI, Friedman PL, et al. Multiple atrial macroreentry circuits in adults with repaired congenital heart disease: entrainment mapping combined with three-dimensional electroanatomic mapping. *J Am Coll Cardiol* 2001; **37**: 1665–76.

39 Triedman JK. Atrial reentrant tachycardias. In: *Cardiac Arrhythmias in Children and Young Adults with Congenital Heart Disease*, Walsh EP, Saul JP, Triedman JK, eds. Lippincott. Williams & Wilkins, Philadelphia, 2001: 137–60.

40 Triedman JK, Alexander MA, Love BA, et al. Influence of patient factors and ablative technologies on outcomes of radiofrequency ablation of intra-atrial tachycardia in patients with congenital heart disease. *J Am Coll Cardiol* 2002; **39**: 1827–35.

41 Triedman JK, Delucca JM, Alexander ME, Berul CI, Cecchin F, Walsh EP. Prospective trial of electroanatomically guided, irrigated catheter ablation of atrial tachycardia in patients with congenital heart disease. *Heart Rhythm* 2005; **2**: 700–5.

42 Deal BJ, Mavroudis C, Backer CL, Johnsrude CL, Rocchini AP. Impact of arrhythmia circuit cryoablation during Fontan conversion for refractory atrial tachycardia. *Am J Cardiol* 1999; **83**: 563–68.

43 Mavroudis C, Backer CL, Deal BJ, Johnsrude C, Strasburger J. Total cavopulmonary conversion and maze procedure for patients with failure of the Fontan operation. *J Thorac Cardiovasc Surg* 2001; **122**: 863–71.

44 Seslar SP, Alexander ME, Berul CI, Cecchin F, Walsh EP, Triedman JK. Ablation of nonautomatic focal atrial tachycardia in children and adults with congenital heart disease. *J Cardiovasc Electrophysiol* 2006; **17**: 359–65.

45 de Groot NM, Zeppenfeld K, Wijffels MC, et al. Ablation of focal atrial arrhythmia in patients with congenital heart defects after surgery: role of circumscribed areas with heterogeneous conduction. *Heart Rhythm* 2006; **3**: 526–35.

46 Kirsh JA, Walsh EP, Triedman JK. Prevalence of and risk factors for atrial fibrillation and intraatrial reentrant tachycardia among patients with congenital heart disease. *Am J Cardiol* 2002; **90**: 338–40.

47 Mavroudis C, Deal BJ, Backer CL, et al. J. Maxwell Chamberlain Memorial Paper for congenital heart surgery. 111 Fontan conversions with arrhythmia surgery: surgical lessons and outcomes. *Ann Thorac Surg* 2007; **84**: 1457–65.

48 Murphy JG, Gersh BJ, Mair DD, et al. Long-term outcome in patients undergoing surgical repair of tetralogy of Fallot. *N Engl J Med* 1993; **329**: 593–99.

49 Deanfield JE, McKenna WJ, Presbitero P, England D, Graham GR, Hallidie-Smith K. Ventricular arrhythmia in unrepaired and repaired tetralogy of Fallot: relation to age, timing of repair, and haemodynamic status. *Br Heart J* 1984; **52**: 77–81.

50 Nollert G, Fischlein T, Bouterwek S, Bohmer C, Klinner W, Reichart B. Long-term survival in patients with repair of tetralogy of Fallot: 36-year follow-up of 490 survivors of the first year after surgical repair. *J Am Coll Cardiol* 1997; **30**: 1374–83.

51 Silka MJ, Hardy BG, Menashe VD, Morris CD. A population-based prospective evaluation of risk of sudden cardiac death after operation for common congenital heart defects. *J Am Coll Cardiol* 1998; **32**: 245–51.

52 Norgaard MA, Lauridsen P, Helvind M, Pettersson G. Twenty- to thirty-seven-year follow-up after repair for tetralogy of Fallot. *Eur J Cardiothorac Surg* 1999; **16**: 125–30.

53 Gatzoulis MA, Balaji S, Webber SA, et al. Risk factors for arrhythmia and sudden cardiac death late after repair of tetralogy of Fallot: a multicentre study. *Lancet*. 2000; **356**: 975–81.

54 Kavey RE, Thomas FD, Byrum CJ, Blackman MS, Sondheimer HM, Bove EL. Ventricular arrhythmias and biventricular dysfunction after repair of tetralogy of Fallot. *J Am Coll Cardiol* 1984; **4**: 126–31.

55 Burns RJ, Liu PP, Druck MN, Seawright SJ, Williams WG, McLaughlin PR. Analysis of adults with and without complex ventricular arrhythmias after repair of tetralogy of Fallot. *J Am Coll Cardiol* 1984; **4**: 226–33.

56 Cullen S, Celermajer DS, Franklin RC, Hallidie-Smith KA, Deanfield JE. Prognostic significance of ventricular arrhythmia after repair of tetralogy of Fallot: a 12-year prospective study. *J Am Coll Cardiol* 1994; **23**: 1151–55.

57 Khairy P, Landzberg MJ, Gatzoulis MA, et al. Prognostic significance of electrophysiologic testing post tetralogy of Fallot repair: a multicenter study. *Circulation* 2004; **109**: 1994–2000.

58 Harrison DA, Harris L, Siu SC, et al. Sustained ventricular tachycardia in adult patients late after repair of tetralogy of Fallot. *J Am Coll Cardiol* 1997; **30**: 1368–73.

59 Therrien J, Siu SC, Harris L, et al. Impact of pulmonary valve replacement on arrhythmia propensity late after repair of tetralogy of Fallot. *Circulation* 2001; **103**: 2489–94.

60 Horowitz LN, Vetter VL, Harken AH, Josephson ME. Electrophysiologic characteristics of sustained ventricular tachycardia occurring after repair of tetralogy of Fallot. *Am J Cardiol* 1980; **46**: 446–52.

61 Downar E, Harris L, Kimber S, et al. Ventricular tachycardia after surgical repair of tetralogy of Fallot: results of intraoperative mapping studies. *J Am Coll Cardiol* 1992; **20**: 648–55.

62 Burton ME, Leon AR. Radiofrequency catheter ablation of right ventricular outflow tract tachycardia late after complete repair of tetralogy of Fallot using the pace mapping technique. *Pacing Clin Electrophysiol* 1993; **16**: 2319–25.

63 Biblo LA, Carlson MD. Transcatheter radiofrequency ablation of ventricular tachycardia following surgical correction of tetralogy of Fallot. *Pacing Clin Electrophysiol* 1994; **17**: 1556–60.

64 Goldner BG, Cooper R, Blau W, Cohen TJ. Radiofrequency catheter ablation as a primary therapy for treatment of ventricular tachycardia in a patient after repair of tetralogy of Fallot. *Pacing Clin Electrophysiol* 1994; **17**: 1441–46.

65 Chinushi M, Aizawa Y, Kitazawa H, Kusano Y, Washizuka T, Shibata A. Successful radiofrequency catheter ablation for macroreentrant ventricular tachycardias in a patient with tetralogy of Fallot after corrective surgery. *Pacing Clin Electrophysiol* 1995; **18**: 1713–16.

66 Horton RP, Canby RC, Kessler DJ, et al. Ablation of ventricular tachycardia associated with tetralogy of Fallot: demonstration of bidirectional block. *J Cardiovasc Electrophysiol* 1997; **8**: 432–35.

67 Papagiannis J, Kanter RJ, Wharton JM. Radiofrequency catheter ablation of multiple haemodynamically unstable ventricular tachycardias in a patient with surgically repaired tetralogy of Fallot. *Cardiol Young* 1998; **8**: 379–82.

68 Saul JP, Alexander ME. Preventing sudden death after repair of tetralogy of Fallot: complex therapy for complex patients. *J Cardiovasc Electrophysiol* 1999; **10**: 1271–87.

69 Rostock T, Willems S, Ventura R, Weiss C, Risius T, Meinertz T. Radiofrequency catheter ablation of a macroreentrant ventricular tachycardia late after surgical repair of tetralogy of Fallot using the electroanatomic mapping (CARTO). *Pacing Clin Electrophysiol* 2004; **27**: 801–4.

70 Frangini P, Vergara I, Fajuri A, Gonzalez R, Baeza M. Radiofrequency ablation of ventricular tachycardia in a patient after surgery for tetralogy of Fallot: case report. *Rev Med Chil* 2005; **133**: 675–80.

71 Gonska BD, Cao K, Raab J, Eigster G, Kreuzer H. Radiofrequency catheter ablation of right ventricular tachycardia late after repair of congenital heart defects. *Circulation* 1996; **94**: 1902–8.

72 Morwood JG, Triedman JK, Berul CI, et al. Radiofrequency catheter ablation of ventricular tachycardia in children, and in young adults with congenital heart disease. *Heart Rhythm* 2004; **1**: 301–8.

73 Zeppenfeld K, Schalij MJ, Bartelings MM, et al. Catheter ablation of ventricular tachycardia after repair of congenital heart disease: electroanatomic identification of the critical right ventricular isthmus. *Circulation* 2007; **116**: 2241–52.

74 Kriebel T, Saul JP, Schneider H, Sigler M, Paul T. Noncontact mapping and radiofrequency catheter ablation of fast and hemodynamically unstable ventricular tachycardia after surgical repair of tetralogy of Fallot. *J Am Coll Cardiol* 2007; **50**: 2162–68.

75 Stephenson EA, Batra AS, Knilans TK, et al. A multicenter experience with novel implantable cardioverter–defibrillator configurations in the pediatric and congenital heart disease population. *J Cardiovasc Electrophysiol* 2006; **17**: 41–6.

76 Alexander ME, Cecchin F, Walsh EP, Triedman JK, Bevilacqua LM, Berul CI. Implications of implantable defibrillator therapy in congenital heart disease and pediatrics. *J Cardiovas Electrophysiol* 2004; **15**: 72–6.

77 Rhodes LA, Wernovsky G, Keane JF, et al. Arrhythmias and intracardiac conduction after the arterial switch operation. *J Thor Cardiovas Surg* 1995; **109**: 303–10.

78 Stamm C, Friehs I, Mayer JE Jr, et al. Long-term results of the lateral tunnel Fontan operation. *J Thorac Cardiovasc Surg* 2001; **121**: 28–41.

79 Giannico S, Hammad F, Amodeo A, et al. Clinical outcome of 193 extracardiac Fontan patients: the first 15 years. *J Am Coll Cardiol* 2006; **47**: 2065–73.

80 Walsh EP, Rockenmacher S, Keane JF, Hougen TJ, Lock JE, Castaneda AR. Late results in patients with tetralogy of Fallot repaired during infancy. *Circulation* 1988; **77**: 1062–67.

81 Hamada H, Terai M, Jibiki T, Nakamura T, Gatzoulis MA, Niwa K. Influence of early repair of tetralogy of Fallot without an outflow patch on late arrhythmias and sudden death: a 27-year follow-up study following a uniform surgical approach. *Cardiol Young* 2002; **12**: 345–51.

82 Collins KK, Rhee EK, Delucca JM, et al. Modification to the Fontan procedure for the prophylaxis of intra-atrial reentrant tachycardia: short-term results of a prospective randomized blinded trial. *J Thorac Cardiovasc Surg* 2004; **127**: 721–29.

32 CHAPTER 32

Transthoracic Epicardial Mapping and Ablation of Ventricular Tachycardia

André d'Avila, MD,[1] *Mauricio Scanavacca,* MD,[2] *Eduardo Sosa,* MD[2]

[1]Massachusetts General Hospital, Boston, MA, USA
[2]University of Sao Paulo Medical School, Sao Paulo, Brazil

Summary

Recently introduced in 1995 (1–4), transthoracic epicardial mapping and ablation has recently become an important adjunctive or even a preferable strategy to eliminate a diverse range of cardiac arrhythmias including scar-related ventricular tachycardia [5, 6], atrial fibrillation [7, 8], accessory pathways [9, 11], and idiopathic ventricular tachycardia [12]. In addition, the pericardial approach is being considered for a number of other cardiovascular applications such as localized drug delivery, epicardial pacing and myocardial injection of biological agents such as myoprogenitor cells.

Not long ago, epicardial mapping and ablation could only be undertaken during cardiac surgery and was thus restricted to the surgical theater. Attempts to map the epicardial surface with a less invasive approach, through thoracoscopy, were soon abandoned, not only because it must be performed in the operating room, but also because of the difficulty in keeping the catheter stable when opening of the pericardial space is required. Alternatively, insertion of a multipolar catheter into the epicardial veins may be used to obtain epicardial signals. However, mapping is limited by the cardiac anatomy and the technique is not helpful when the site of origin is not close enough to the epicardial vessels to be mapped. Thus, transthoracic epicardial mapping became necessary for epicardial mapping and ablation in the EP Laboratory.

Transthoracic Epicardial Access

Transthoracic epicardial puncture is therefore the most important step in the whole procedure, and it can be relatively safe and efficiently undertaken in the electrophysiology laboratory [1, 2]. Briefly, a regular Tuohy-17G needle used for epidural anesthesia is used for this procedure. The needle is introduced at a 45° angle and gently advanced under fluoroscopy until close to the cardiac silhouette. Needle angle is adjusted according to the region that the operator wishes to access. This region is most frequently the medial third of the right ventricle, where, based on the coronary angiography,

Cardiac Mapping, Third Edition Edited by Mohammad Shenasa, Gerhard Hindricks, Martin Borggrefe, and Günter Breithardt
 ISBN: 978-1-405-17572-2

no major coronary vessels can be found. This area is monitored by fluoroscopy in several projections (anteroposterior, left anterior oblique, right anterior oblique). Operator experience is crucial to visualize the heart as a 3D structure while looking at a 2D image. The presence of a catheter at the right ventricular apex and in the coronary sinus is a useful reference to guide the needle tip.

In order to demonstrate the precise site of the needle tip, 1 mL of contrast media is injected. When the needle tip is inside the pericardial space, contrast medium can be seen surrounding the cardiac silhouette. Visualization of a thin layer of contrast in the pericardial space is crucial, as this confirms that the needle is correctly placed in the pericardial space. The needle tip can occasionally perforate the right ventricle, something that can be easily recognized after injection of contrast medium. If this happens, the needle is slightly retracted and a little more contrast medium is injected until the pericardial space is reached (Figure 32.1).

Although the pericardium normally does not offer much resistance, firmer pressure is sometimes necessary, thus the importance of the visualization of contrast medium in the pericardial space. Finally, a soft floppy-tip guidewire is introduced in the pericardial space through the puncture needle. As a rule, the guidewire easily slips into the pericardial space. Guidewire position is also monitored through fluoroscopy. An 8 Fr introducer is then placed in the pericardial space and the guidewire removed. Finally, under fluoroscopy, a quadripolar deflectable catheter with a 4-mm tip is inserted into the pericardial space for mapping and ablation. When the ablation catheter is introduced in the epicardial space, extensive mapping may be performed without increasing the procedure risk, because there are no anatomical structures (except by the presence of pericardial reflections and sinuses) in the normal pericardial sac to restrict catheter movement.

Entering the Epicardial Space After Cardiac Surgery

Postoperative pericardial adhesions were thought to preclude both the puncture attempt and the ability to maneuver the ablation catheter inside the

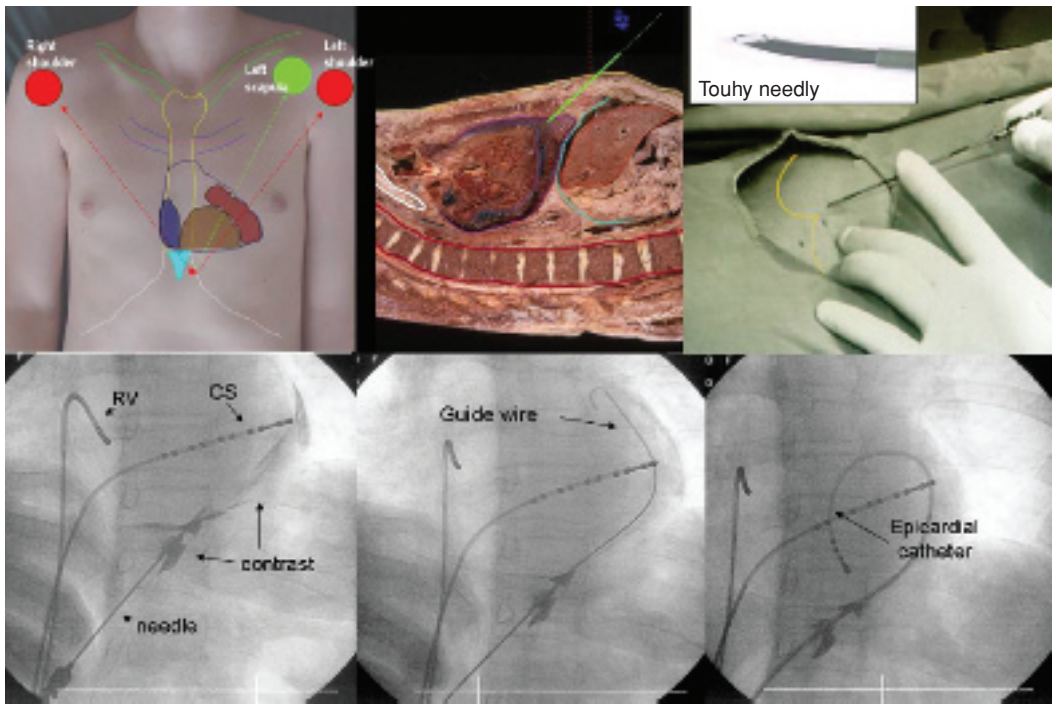

Figure 32.1 Technique used to insert the mapping catheter in the pericardial space. A regular needle used for epidural anesthesia (shown in detail in the upper left corner) is used during transthoracic puncture according to the technique described by Krikorian and Hancock to drain epicardial effusions. KEY: RV = right ventricle. See text for details.

pericardial sac. However, it is possible to undergo epicardial mapping and ablation in this cohort of patients. In this situation, the puncture should be directed toward the inferior wall of the heart because of the higher density of the adhesions on the anterior aspect of the heart where the pericardial sac is typically opened during heart surgery. As in patients without prior cardiac surgery, contrast should be used to verify the location of the needle tip as it is advanced. However, instead of the typical appearance of a "sluggish" layering of the contrast medium around the heart, the contrast will pool along the inferior aspect of the heart.

In the authors' experience, it is possible to perform an inferior puncture in up to 30–40% of the patients after cardiac surgery. However, in most of these patients adhesion will prevent a successful puncture. In this situation, the operator can feel a "cracking" sensation when the needle is advanced through the thick pericardium. In some patients with previous pericarditis, the operator may face the same challenges. Because of the intense adhesion of the pericardium to the right ventricular wall, an injection of contrast after the cracking sensation is passed will typically reveal that the needle is into the RV cavity. Multiple attempts of entering such a thick/adhered pericardium may result in multiple RV perforation, which may result in the formation of a small RV pseudoaneurysm as recently noted in our practice.

In our current approach, no more than three attempts to enter the pericardial cavity are made after cardiac surgery. Alternatevely, as proposed by Soejima [13], a surgical approach is a safe option to gain access to the epicardial sac in patients with difficult pericardial puncture. Typically, a 3-in. vertical incision is made in the midline epigastrium and the abdominal fascia was opened in the linea alba, veering to the left of the xyphoid process superiorly. This approach is well tolerated by the patients.

Epicardial Mapping

When the catheter is into the pericardial space, it can be easily manipulated to cover the entire surface of the right and left ventricles as well as the atria. The limits of this surface are marked by pericardial reflection. The lateral and posterior left ventricular wall of both ventricles and atria are easier to map than the anterior wall. Another noteworthy peculiarity found in this approach is catheter stability. When the catheter is not being manipulated, it rests stable in a selected site, following ventricular wall motion. This stable catheter position is obtained by apposition of the two layers of pericardium and the weight of both lungs lying against it [14.] Moreover, the negative pressure found in the pericardial space may also contribute to that. In this sense, the epicardial catheter is more easily manipulated and shows more stability than the endocardial catheter, which tends to be expelled every systole, especially when inside the left ventricular cavity.

Epicardial electrograms are as clear as endocardial elctrograms, and their interpretation follows the same pattern as for standard endocardial signs. The possibility of mapping an extensive epicardial surface permits the assessment of electrical activity at very close sites, thus displaying more data about electrical activity of the heart. This is not usually possible with endocardial mapping, because the presence of papillary muscles and chordae as well as repetitive ventricular systoles are obstacles for the free manipulation of the endocardial catheter.

Finding an adequate epicardial target site for sustaining the VT, just as in endocardial mapping, depends on diastolic activity analysis and, when feasible, response to programmed ventricular stimulation (Figure 32.2). However, we have observed that the epicardial bipolar stimulation thresholds are extremely high. Thus, in order to obtain regular capture, stimuli higher than 10 mA are often necessary. Because unipolar stimulation causes a great deal of interference thus limiting analysis of recordings, this technique has not been used in our laboratory. Apart from that, because Chagas' VT is usually associated with multiple morphologies, pacing techniques frequently can interrupt clinical VT or induce unstable VT. The presence of diastolic activity during induced VT, as well as the use of entrainment mapping technique, has shown that transthoracic epicardial mapping could safely and effectively identify the epicardial circuits (Figure 32.3).

Identifying Epicardial Fat During Epicardial Ablation

The presence of epicardial fat interposed between the ablation catheter and the epicardial surface of the heart can be a significant hindrance in

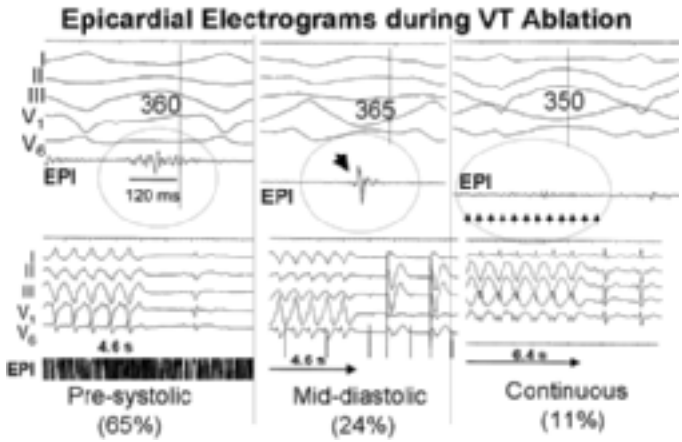

Figure 32.2 Bipolar pacing from the distal par of epicardial electrodes demonstrates epicardial electrograms recorded during VT ablation. Shown are ECG leads I, II, V_1, and V_6. KEY: PCS = proximal coronary sinus; DCS = distal coronary sinus; RVA = right ventricular apex; LV endo = left ventricular endocardial catheter; LV epic = left ventricular epicardial catheter.

procedural success because it can decrease the effectiveness of ablation.

Identifying the presence of epicardial fat tissue during electrophysiological catheter mapping is not straightforward [15]. In a previous study, we examined characteristics of bipolar epicardial electrogram and the epicardial ventricular stimulation threshold obtained with a standard 4-mm tip ablation catheter during open-chest cardiac surgery in areas covered by fat. Prior to extracorporeal circulation in 10 patients (6 women, 52 ± 6 years and LVEF $= 43 \pm 11\%$) undergoing CABG surgery, electrograms were obtained from 44 areas without and 45 areas with epicardial fat randomly distributed along the free-wall of the left ventricle and the right ventricular outflow tract. The presence of fat <5 mm in thickness did not modify the bipolar stimulation threshold between areas with and without fat (4.8 ± 1.6 versus 4.6 ± 1.8 mA, $p =$ NS). Similarly, the peak-to-peak bipolar voltage amplitude (40 ± 5 mm vs. 43 ± 4 mm) and the bipolar electrogram duration (43.6 ± 5 msec vs. 43.5 ± 6 msec) were not modified by the epicardial fat. In areas with a layer of epicardial fat >5 mm in thickness ventricular capture was not successful at even 10 mA. Thus, epicardial fat <5 mm interposed between the ablating catheter and the epicardium does not modify either the amplitude/duration of the bipolar epicardial electrogram, or the epicardial ventricular stimulation threshold.

Therefore, the presence of an epicardial fat layer <5 mm may not be enough to mimic scar. Although epicardial fat will not produce a fractionated electrogram, a thicker fat layer may decrease the bipolar amplitude of the epicardial electrogram to confound are ability to discriminate between fat and scar [14]. In this situation, the operator should revisit these areas several times to try to establish these differences precisely. It is not rare that areas of supposed epicardial scar can be "cleaned" as one investigates the same region using a different catheter curve and/or a different approach (e.g., inferior vs. anterior) to ensure better contact.

Epicardial Catheter Ablation

Experimental studies on canine hearts were designed to analyze the effects of linear and punctiform lesions caused by radiofrequency ablation on both epicardial surface of the ventricular myocardium, coronary vessels and aorta [16]. Nine mongrel dogs (24 ± 6 kg) underwent lateral thoracotomy to allow positioning and suture of the ablation catheters against the left ventricular epicardial surface.

Temperature-controlled applications were delivered through a multielectrode catheter placed perpendicularly to the proximal and distal portion of the interventricular coronary artery and a regular 4-mm tip catheter placed besides the vessel. The multielectrode catheter was also placed around the descending aorta where linear lesions were created. All animals were sacrificed 14 days after the last application. There were 117 pulses were delivered through the multipolar catheter to create 24 linear lesions in the epicardial left ventricular surface

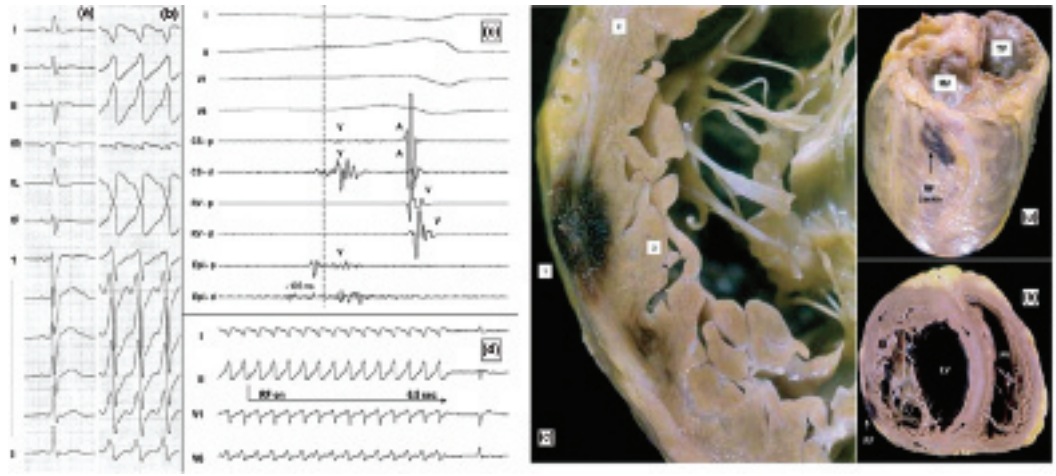

Figure 32.3 A 63-year old patient with severe idiopathic dilated cardiomyopathy, who had been on the heart transplant list for 6 months was admitted due to frequent episodes of sustained monomorphic ventricular tachycardia (VT). ECG showed a pseudo-delta wave of 45 msec, an intrinsicoid deflection time of 100 msec in V2, and an RS complex duration of 155 msec, suggesting that the VT exit site was located in the epicardial basal–lateral wall of the left ventricle (Figure 32.1a,b). A 4-mm-tip ablation catheter was used for ablation.

Epicardial mapping of well-tolerated incessant VT identified fractionated ventricular electrograms—105 msec before the onset of the QRS complex, which were used to guide RF ablation. Prior to RF delivery, a coronary angiogram showed no coronary arteries nearby the ablation catheter. VT was interrupted within 6.5 sec of the first RF application (Figure 32,1c,d). A second 60-sec RF pulse was delivered at the same site in sinus rhythm. The patient remained free of symptoms for the following 10 days when elective cardiac transplantation was carried out. Endocardial mapping/ablation was not performed. The heart was examined after transplant and epicardial RF lesions were clearly identified.

Panel (a) shows a posterior view of the left ventricle. Both atria were removed during heart transplantation to receive the donor's heart. Mitral (MV) and tricuspid valve (TV) are apparent. RF lesions can be identified as the black/purple spot located basally (close to the mitral annulus) and lateral to a marginal branch of the circumflex coronary artery. The remaining visceral pericardium seems intact and shows no evidence of pericarditis.

Panel (b) illustrates a cross-sectional view of the left and right ventricles at the level of RF epicardial lesion (white arrow and RF towards the black spot). The left ventricle was dilated and a circumferential intramural layer of scar tissue can be noted (black arrows) mainly in the interventricular septum and at the infero-lateral wall of the left ventricle.

In panel (c), RF lesion (#1) and the intramural layer of scar tissue (#2) can be better appreciated. RF lesion extends from the epicardial surface of the heart to about 1 mm beyond the intramural layer of scar but preserves the remaining "healthy" intramural and subendocardial cardiac muscle (#3).

(1007 mm). These applications produced lesions 8.5 ± 1 mm long/electrode, 7 ± 2 mm wide and 3.8 ± 1 mm deep. Mean temperature, impedance, and power were 70 ± 12°C, 10 ± 6 W, and 161 ± 29 Ω, respectively.

Twenty-six vessels were found along 606 mm of linear lesions: in all of them, RF applications induced extracellular matrix accumulation in the media without neointima formation. Severe media hyperplasia was noted in one artery and intravascular thrombosis in six other arteries. Veins related to the arteries were always patent. Multivariate regression analysis identified the internal perimeter of the vessel (0.78 ± 0.49 mm vs. 1.79 ± 0.83 mm [$p < .05$]) as the only variable associated with artery damage. Therefore, during epicardial application of RF energy, the larger the coronary artery, the safer the application will be because medial hyperplasia and intravascular thrombosis were only found in the smallest vessels. In the aorta, RF applications caused moderate destruction of the elastic lamina and lesions can be transmural. The effects of epicardial RF applications on the adjacent structures (pericardium and lungs) were also evaluated in swine hearts. As far as the lungs are concerned, injury is restricted, allowing us to assume that no functional

hazards could emerge. In these animals no pericardial perforation was observed [16].

Although acute lesions are not typically seen during epicardial catheter ablation, a recent work by Miranda (doctoral thesis, published in Portuguese, 2002) demonstrated the presence of intense neointima formation 3 months after epicardial RF pulses had been intentionally delivered on the top of the circumflex coronary artery. Therefore, the decision on whether or not to deliver a RF pulse during epicardial ablation should take into account the distance between the tip of the ablation catheter and a coronary artery (obtained by coronary angiography immediately before the application is delivered) and the clinical scenario.

Cooled RF Ablation

As pointed out earlier, standard RF ablation can be used during epicardial catheter ablation with an acute success rate between 60% and 70%. However, the lack of convective cooling of the ablation electrode by the blood would be expected to limit power delivery in the pericardial space. This suggests that standard RFA may not be as effective when delivered to the epicardium compared with lesions delivered to the endocardium.

Using experimental goat and porcine model systems, we recently studied the dimensions and characteristics of standard and cooled-tip (internal saline irrigation) RFA lesions delivered to normal or infarcted myocardium [17]. In this study, a total of 80 RF energy applications were delivered to 10 normal animals, of which 33 were standard temperature-controlled applications. Eleven of 33 pulses were delivered to the epicardial tissue covered by fat, whereas the remaining 22 pulses were delivered to epicardium without overlying epicardial fat. Three lesions were not found during gross pathological inspection of the heart. Standard RFA lesions were 3.7 ± 1.3 mm in depth in areas without epicardial fat. However, in areas covered by 3.1 ± 1.2 mm epicardial fat, standard RF did not create any appreciable lesions in the myocardial tissue [14].

The cooled-tip RFA catheter was used to deliver 44 lesions to normal ventricular epicardial tissue, of which 7 and 37 lesions were located at areas with or without overlying fat tissue, respectively (mean thickness of the fat layer was 2.6 ± 1.2 mm. In the absence of epicardial fat, these cooled-tip RF lesions (6.7 ± 1.7 mm) were significantly deeper than those seen during standard. Cooled-tip RF applications were also delivered in a total of 22 epicardial locations in 7 chronically infarcted animals. These lesions measured 14.6 ± 2.7 mm in length, 11.8 ± 2.9 mm in width, and 5.6 ± 1.2 mm in depth. Therefore, cooled-tip RFA produces larger and deeper epicardial lesions than standard RFA. The presence of epicardial fat interposed between the catheter tip and the myocardial tissue prevents lesion formation with standard RFA, but only moderately attenuates the efficacy of cooled-tip ablation. Over infarcted epicardial tissue targets, cooled-tip RFA was able to generate lesions of substantial depth [15].

Epicardial Cryoablation

The lack of convective cooling of the ablation electrode by the blood suggests that cryoablation may be the ideal energy source for epicardial ablation because the absence of blood flow within the pericardial space should result in significantly (i) faster cooling rates, (ii) colder achieved temperatures, and (iii) a greater thawing time during epicardial cryoablation because these variables, along with the number of thawing cycles, determine the size of the cryolesion.

We were surprised, however, that a significant difference was not found in the size and depth of endocardial and epicardial focal cryolesions in a recent study performed in our animal facility with a 7 Fr 6-mm-tip cryoablation catheter. Focal cryoapplications were delivered to 80 endocardial targets and 28 epicardial targets. The length, width, and depth of endocardial cryolesions was 9.7 ± 0.4 mm, 7.3 ± 1.4 mm, and 4.8 ± 0.2 mm, respectively, and for epicardial cryolesions it was 10.2 ± 1.4 mm, 7.7 ± 2 mm, and 4.6 ± 0.9 mm, respectively ($P > .05$).

Endocardial cryolesions created by the focal cryoablation catheter delivered to the right ($n = 13$) and left ($n = 4$) ventricular outflow tract created smaller cryolesions (8 ± 1 mm in length, 5.3 ± 1.1 mm in width, and 3.3 ± 1.6 mm in depth) than observed at other sites. Thus, although cryoablation can create deep lesions when deployed on the ventricular epicardium, endocardial and epicardial cryolesions created with a focal cryoablation catheter are very similar in size and depth.

How to Avoid Damage to the Coronary Arteries

There are three theoretical ways to damage the coronary arteries during transthoracic epicardial mapping and/or ablation. First, it has been postulated that the needle can perforate a coronary artery, but this is exceedingly unlikely to occur during transthoracic puncture because there are no major epicardial vessels close to right apical ventricular wall (the area where the needle tip is inserted).

It has also been suggested that after it is in the pericardial space, the ablation catheter could tear an epicardial vessel. However, contrary to most people's beliefs, these vessels are not so superficially located; they are covered by the visceral pericardium and lay in a deep groove of adipose tissue in the epicardial ventricular muscle.

Finally, a major concern involves the effect of RF pulse application on the coronary arteries. Taking into account experimental data suggesting that coronary artery occlusion depends more on the vessel caliber than on the type of application, we established that the minimal distance between catheter tip and the artery was 12 mm (three times the catheter tip). So, in some patients in whom the site of application is located close to the coronary sinus (where a major coronary artery may be found), a coronary angiogram is obtained before applying RF pulses to determine the distance between the catheter tip and the coronary artery.

Continuous electrocardiographic monitoring of the ST segment was undertaken in the first 10 patients during the entire procedure and in the first 24 hr after it, but no ST changes were detected in any of them. Serial analysis of MB fraction of creatine phosphokinase was determined every 4 hr during the first 24 hr.

Is There an Electrogram Pattern Predictive of Successful Application During Transthoracic RF Epicardial Catheter Ablation to Treat VT?

When patients with chronic Chagasic cardiomyopathy are subjected to RF pulses for VT interruption, results of epicardial mapping show a variety of electrograms. These electrograms have multiple characteristics, certainly because of the heterogeneous ventricular involvement in this cardiopathy. Unfortunately, the epicardial stimulation threshold in the area of slow conduction is high enough to prevent ventricular capture in most patients. Thus, entrainment maneuvers cannot be performed to define whether a site is part of the circuit. A study was therefore carried out in order to define whether there are epicardial electrogram patterns predictive of ablation success and whether thermo mapping can be safely and effectively used to guide RF epicardial ablation.

A regular ablation catheter was introduced into the pericardial space by transthoracic puncture during 21 procedures in 19 consecutive patients with Chagasic VT. A total of 239 sites were analyzed and the electrograms defined as mid-diastolic potentials, continuous activity, and early signal. A 60°C pulse was delivered for 10 sec at each site. Electrogram duration and precocity were determined for each application and a 12-lead ECG for ST segment analysis was obtained after VT interruption.

VT was interrupted at 47 of 239 sites (19%). At 57 sites, electrograms were defined as mid-diastolic signals (24%). VT interruption occurred in five sites (9%) whereas 52 applications did not interrupt VT. Duration and precocity did not differ between successful and unsuccessful applications. Electrograms were defined as continuous electrical activity at 27 sites (11%) and interruption occurred in eight of them (30%). In 19 sites where continuous electrical activity was found, RF application did not change VT. An early electrogram was found in 155 sites (65%). RF interrupted VT in 34 sites (22%), but electrogram duration (181 $\pm$ 72 ms vs. 177 $\pm$ 68 ms) and precocity (107 $\pm$ 47 ms vs. 94 $\pm$ 44 ms) did not differ among these sites. No early or late complications occurred during follow-up.

Electrogram pattern was therefore not helpful in defining a site for a successful epicardial RF application. Although safe, epicardial catheter ablation based on empirical thermo mapping is not ideal. VT interruption based on this technique was achieved in 20% of the attempted sites, making necessary a large number of applications to successfully treat these patients. These results mimic those found for endocardial ablation [24].

Complications

Although epicardial ablation has been performed worldwide for more than 10 years, data on the procedural safety of this procedure are as yet scant. At this point, we had neither a quality control system for data collection, nor an independent system of monitoring. At this point, we can offer a limited observational view in approximately 600 procedures performed in three centers with large experience in epicardial catheter ablation (Heart Institute in Sao Paulo, Brazil; Brigham and Women's and Massachusetts General Hospital in Boston, MA).

Postprocedure Pericarditis

After epicardial ablation, pericarditis occurs in virtually all patients to some extent as the result of a local inflammatory response [18]. The clinical manifestation varies from mild pericarditis to large hemorrhagic pericardial effusion and, rarely, cardiac tamponade. Standard oral antiinflammatory nonsteroidal and corticosteroid agents are typically employed to treat clinically significant episodes. However, these are typically employed "after-the-fact" in individuals who are already experiencing symptoms. We have recently evaluated the efficacy and safety of intrapericardial instillation of 2 mg of triamcinolone after pericardial mapping and ablation in a porcine model of catheter-related pericarditis. Surprisingly, the instillation of 2 mg/kg of intrapericardial triamcinolone at the end of the procedure effectively prevents postprocedure inflammatory adhesion formation in all five animals.

We have used intrapericardial instillation of corticosteroids in 60 consecutive patients over the last 3 years (unpublished data). For patients undergoing pericardial mapping alone, 1 mg/kg was used, whereas 2 mg/kg of methilprednisolone (equivalent to triamcinolone) were used for patients undergoing both pericardial mapping and ablation. In all patients, the instillation of pericardial corticosteroids at the end of the procedure was associated with no instances of (i) infection, (ii) clinically significant pericarditis as manifest by hemodynamic compromise/tamponade, or (iii) rehospitalization after a mean follow-up of 464 ± 303 days.

We felt compelled to consider intrapericardial instillation of corticosteroids after epicardial ablation when one of our patients, successfully ablated for recurrent VT, was readmitted to the hospital two weeks after the procedure with intense pericardial pain complicated by a hemorrhagic effusion requiring pericardiocentesis. Based on our clinical experience and the promising experimental results, we felt that we needed to implement some strategy that allowed us to continue to use medications such as coumadin after a pericardial procedure, and yet avoid the hemorrhagic effusion complication. While intravenous steroid instillation was an option, we were concerned about the systemic antiinflammatory effects, and thus incorporated the instillation of pericardial steroids as a standard clinical practice after epicardial catheter ablation; since that point, we have not seen this complication again.

RV Puncture and Hemopericardium

RV puncture can occur in up to 10% of patients. Approximately 50% of these perforations will result in intrapericardial bleeding, but a fair portion of these patients will not have any bleeding into the pericardial cavity. When pericardial bleeding occurs, it typically ceases after up to 350 cc of blood is drained. However, when drainage is larger than 400 cc, the operator should be cautious and the procedure should be held until a better understanding of the situation can be obtained.

Large pericardial effusions may suggest that the needle and/or the epicardial sheath created an important laceration of the right ventricle. It is difficult to define when a patient who experience this complication should be taken to surgery. However, the operator should be prepared for that when blood drainage from the epicardial cavity does not decrease after 350 cc. In our experience, three patients underwent cardiac surgery for persistent intrapericardial bleeding. In all of then RV perforation was created when the sheath was introduced into the right ventricle and the decision to take them to the OR was made after 500 cc of blood had been drained.

In two patients, surgery was necessary because the epidural needle perforated, respectively, an epicardial vein and a distal branch of a right ventricular marginal coronary artery. In this last patient, the presence of a arterial blood (light red) was noted when blood was being drained from the epicardial cavity.

Damage to Infradiaphragmatic Vessels

In three patients, an infra-diaphragmatic vessel was perforated when the needle was advanced toward the heart. Interestingly, all patients tolerated the ablation procedure without experience hemodynamic collapse. After the procedure, the presence of abdominal pain followed by a drop in the hematocrit was promptly investigated by CT and/or abdominal ultrasound, which revealed the presence of blood into the abdominal cavity. Two of these patients were clinically managed but required blood transfusion. In one patient, surgical intervention was needed to control the bleeding. The presence of abdominal pain after an epicardial procedure should be considered an important warning sigh of this rare complication.

Ventricular Pseudo-Aneurysm

We have recently experienced two unexpected but severe complications of epicardial catheter ablation. In one of the cases, the presence of persistent chest pain was investigated by CT after the procedure and revealed a small right ventricular pseudo-aneurysm. A second CT obtained one week after showed that the pseudo-aneurysm was diminishing and open heart surgery was not indicated. Of note, epicardial puncture in this patient was not successful due to the presence of intense adhesion after CAGB performed 12 years prior to the ablation procedure. However, several attempts of entering the epicardial space resulted in RV perforation. After this index case, we have limited the number of attempts after open-heart surgery to a maximum of three after which a surgical subxyphoid window should be indicated.

Severe Coronary Vasospasm

During catheter manipulation along the anterior of the left ventricle in a patient without previous cardiac surgery, a severe ST elevation in all precordial leads followed by abrupt hemodynamic collapse was noted. The patient had experienced an episode of severe vasospasm when a stent was implanted in his LAD 3 weeks prior to the ablation procedure. Of note, this complication was noted prior to any RF application had been delivered. An intra-aortic balloon pump was inserted and an intracoronary injection of nitrates reversed the vasospasm of the left main territory. The patient recovered without sequelae despite 30 min of CPR.

Conclusion

Epicardial catheter ablation is a new and essential approach for the treatment of cardiac arrhythmias. It can be performed safely in most patients, but important complication such as damage to epicardial coronary arteries and RV perforation may occur. This technique allows identification of epicardial circuits, the prevalence of which seems to depend on the underlying heart disease being more frequent in Chagasic than in post-MI VT. Therefore, the usefulness of this technique will depend on the prevalence of epicardial circuits in a given population. This approach is limited by concern regarding the potential adverse effects of RF ablation on the epicardial coronary arteries. Hemopericardium, a predictable complication that can be easily controlled in the electrophysiology laboratory, occurs in 10% of patients undergoing this procedure, but coronary artery injury, possibly preventable by a coronary angiogram prior to ablation, is uncommon (<1%). Thus, we believe that the procedure should be incorporated into the electrophysiological routine of mapping and ablation of VT associated with structural heart disease.

References

1 Sosa E, Scanavacca M, d'Avila A, et al. A new technique to perform epicardial mapping in the electrophysiology laboratory. *J Cardiovasc Electrophysiol* 1996; **7**: 531–36.

2 Sosa E, Scanavacca M, d'Avila A, et al. Endocardial and epicardial ablation guided by nonsurgical transthoracic epicardial mapping to treat recurrent ventricular tachycardia. *J Cardiovasc Electrophysiol* 1998; **9**: 229–39.

3 Sosa E, Scanavacca M, d'Avila A, et al. Nonsurgical transthoracic epicardial catheter ablation to treat recurrent ventricular tachycardia occurring late after myocardial infarction. *J Am Coll Cardiol* 2000; **35**: 1442–49.

4 Sosa E, Scanavacca M, d'Avila A. Transthoracic epicardial catheter ablation to treat recurrent ventricular tachycardia. *Curr Cardiol Rep* 2001; **3**: 451–58.

5 d'Avila A, Scanavacca M, Sosa E.Transthoracic epicardial catheter ablation of ventricular tachycardia. *Heart Rhythm* 2006; **3**: 1110–11.

6 Soejima K, Stevenson WG, Sapp JL, et al. Endocardial and epicardial radiofrequency ablation of ventricular tachycardia associated with dilated cardiomyopathy: the importance of low-voltage scars. *J Am Coll Cardiol* 2004; **43**: 1834–42.

7 Reddy VY, Neuzil P, Ruskin JN. Extra-ostial pulmonary venous isolation: use of epicardial ablation to eliminate a point of conduction breakthrough. *J Cardiovasc Electrophysiol* 2003; **14**: 663–66.

8 Pak HN, Hwang C, Lim HE, et al. Hybrid epicardial and endocardial ablation of persistent or permanent atrial fibrillation: a new approach for difficult cases. *J Cardiovasc Electrophysiol* 2007; **18**: 917–23.

9 Valderrabano M, Cesario DA, Ji S, et al. Percutaneous epicardial mapping during ablation of difficult accessory pathways as an alternative to cardiac surgery. *Heart Rhythm* 2004; **1**: 311–16

10 Schweikert RA, Saliba WI, Tomassoni G, et al. Percutaneous pericardial instrumentation for endo-epicardial mapping of previously failed ablations. *Circulation* 2003; **108**: 1329–35.

11 Ho I, d'Avila A, Ruskin J, et al. Images in cardiovascular medicine: percutaneous epicardial mapping and ablation of a posteroseptal accessory pathway. *Circulation*. 2007; **115**: e418–21.

12 Daniels DV, Lu YY, Morton JB, et al. Idiopathic epicardial left ventricular tachycardia originating remote from the sinus of Valsalva. *Circulation* 2006.; **113**: 1659–66.

13 Soejima K, Couper G, Cooper JM, Sapp JL, Epstein LM, Stevenson G. Subxiphoid surgical approach for epicardial catheter-based mapping and ablation in patients with prior cardiac surgery or difficult pericardial access. *Circulation* 2004; **110**: 1197–201.

14 d'Avila A, Scanavacca M, Sosa E, et al. Pericardial anatomy for the interventional electrophysiologist. *J Cardiovasc Electrophysiol* 2003; **14**: 422–30.

15 Abbara S, Desai JC, Cury RC, Butler J, Nieman K, Reddy VY. Mapping epicardial fat with multidetector computed tomography to facilitate percutaneous transepicardial arrhythmia ablation. *Eur J Radiol* 2006; **57**: 417–22.

16 d'Avila A, Gutierrez P, Scanavacca M, et al. Effects of radiofrequency pulses delivered in the vicinity of the coronary arteries. *Pacing Clin Electrophysiol* 2002; **25**: 1488–95.

17 d'Avila A, Houghtaling C, Gutierrez P, et al. Catheter ablation of ventricular epicardial tissue: a comparison of standard and cooled-tip radiofrequency energy. *Circulation* 2004; **109**: 2363–69.

18 d'Avila A, Neuzil P, Thiagalingam A, et al. Experimental efficacy of pericardial instillation of antiinflammatory agents during percutaneous epicardial catheter ablation to prevent postprocedure pericarditis. *J Cardiovasc Electrophysiol* 2007; **18**: 1178–83.

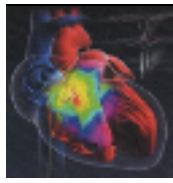

PART VI
New Frontiers

Cardiac Mapping, Third Edition Edited by Mohammad Shenasa, Gerhard Hindricks, Martin Borggrefe, and Günter Breithardt
 ISBN: 978-1-405-17572-2

33

CHAPTER 33

Mapping of Ventricular Tachycardia and Fibrillation: Role of the Purkinje System

Paul B. Tabereaux, MD, MPH, *Derek J. Dosdall,* PhD, *Raymond E. Ideker,* MD, PhD

Department of Medicine, Division of Cardiovascular Disease, Department of Physiology, and Department of Biomedical Engineering, University of Alabama at Birmingham, Birmingham, AL, USA

Summary

The Purkinje system may play an important role in the initiation and maintenance of ventricular cardiac arrhythmias. In both ventricular tachycardia and ventricular fibrillation, the Purkinje system has been implicated via multiple mechanisms in sustaining these life-threatening rhythms. The need to be able to map the source of these rhythms to the Purkinje system remains an important strategy as a target for catheter ablation. This chapter reviews the current clinical and basic science findings of the complex mapping studies that have recorded from the Purkinje system during arrhythmia.

Anatomy of the Purkinje Network

The description of Purkinje fibers was first made in 1845 by Jan Evangelista Purkyne who was studying sheep hearts and provided the following observations: "On the inner wall of the ventricle of the sheep heart, I noticed with the unaided eye . . . a net of gray, flat, gelatin-like fibers. Those gray fibers formed by these bodies are found 5–6 together in a transverse direction, arranged in longitudinal rows along the bundle."

In the intervening century and a half since this initial observation has been followed by a number of studies that have supplied a much more complete understanding of the mechanisms and role that Purkinje fibers play in conducting electrical signals from the bundle branches to the working myocardium of the ventricles.

For example, in 1986, a more complex description of the Purkinje system was given by Viragh and Porte for which three types of fibers were characterized: "Purkinje I fiber reserved for the proximal bundle branch fibers located between the bifurcation and the arborization of the bundle. The Purkinje II are located in the bundle branch arborizations and are larger and connected by intercalated discs. The terminal or Purkinje III fibers establish continuity between the conducting and contracting myocardial cells. These seem to correspond with the transitional fibers described in bovine and canine heart" [1, 2].

Cardiac Mapping, Third Edition Edited by Mohammad Shenasa, Gerhard Hindricks, Martin Borggrefe, and Günter Breithardt
 ISBN: 978-1-405-17572-2

The Purkinje system has several physiological and electrophysiological properties different from myocardial tissue. In animal studies performed in the 1970s examining the ventricular response to ischemic injury, the Purkinje fibers remained intact and without loss of function [3–5]. Therefore, despite severe ischemia, hyperkalemia, or acidosis, this specialized conducting tissue remained sufficiently healthy to function, despite injury to the working ventricular muscle [5].

There are probably at least three reasons for this decreased sensitivity of Purkinje fibers to ischemia. One is that they have a lower oxygen demand because they have little actin and myosin so they perform much less work during contraction than do the ventricular muscle fibers. A second reason is that they have much greater glycogen stores than the working ventricular myocardium, so they are better able to survive by anaerobic glycolysis. A third reason is that in humans the Purkinje fibers are near the endocardium so they receive oxygen by diffusion from the ventricular cavities. However, although they survive and function, Purkinje fibers are usually not normal electrophysiologically in ischemic regions. These findings may partially explain why the Purkinje system appears to be a source for the initiation of ventricular arrhythmias in patients, particularly those with ischemic injury.

Recording Purkinje Activation in Humans

Dangman et al. studied the Purkinje system of explanted human hearts at the time of cardiac transplantation [6]. In five patients the electrophysiologic characteristics of ventricular muscle and Purkinje fibers were evaluated. Compared to noninfarcted hearts, hearts with infarcted regions exhibited longer APDs in ventricular muscle and a much greater dispersion of APDs in the surrounding tissue. Epinephrine and ouabain injected into the hearts caused delayed afterdepolarizations (DADs) arising from the Purkinje fibers, suggesting that triggered activity is possible in the human ventricle [6].

Bogun and Morady assessed the role of Purkinje fibers in monomorphic VT in patients with myocardial infarction (MI) [7]. In their study, 81 consecutive patients with post-MI monomorphic VT were taken to the clinical electrophysiology laboratory and mapped to determine the source of the VT and ablation therapy. Eleven VTs were inducible and mapped in nine of the patients. Entrainment mapping was used to confirm the reentry circuit involving the MI scar [7].

Purkinje potentials were recorded in the VT reentry circuit at the exit site in all nine patients with VTs. Ablation lesions delivered over the site of these Purkinje potentials resulted in immediate termination of VT in all of these patients. Haissaguerre and colleagues investigated polymorphic ventricular tachycardia (PMVT) following MI [8]. In a series of five patients with recurrent PMVT with anterior MIs, pace mapping and activation mapping were used to identify the earliest activation site of premature ventricular contractions that initiated the PMVT. In all cases these potentials were located in the Purkinje network at the MI border zone. Ablation of the Purkinje system at these localized areas led to complete suppression of further episodes of PMVT [8].

Ventricular fibrillation (VF) was also mapped by Haissaguerre et al. in patients with structurally normal hearts [9, 10]. Twenty-seven patients with primary idiopathic VF were taken to the clinical electrophysiology laboratory and found to have premature beats that were similar to those during resuscitation. In 23 of the patients, mapping showed premature beats arising from the Purkinje system. Mapping localized ten of these to the ventricular septum, nine to the anterior right ventricle, and in four patients from both sites. Following localized ablation of these sites, no further episodes of VF occurred [9, 10]. Studies by other investigators have also shown that selective radio-frequency ablation of the Purkinje system can effectively terminate and prevent idiopathic VT and VF in some patients [11, 12].

Mechanisms of Purkinje Fiber Activation During VT

Early observations in animals suggested that Purkinje fibers were likely to be involved in both reentry and focal sources of VT following myocardial ischemia. Martins showed that in dogs in which the LAD was occluded and plunge needles were placed in the left ventricle (LV), Purkinje fiber recordings demonstrated a focal source in 60% of the VTs that

occurred in the first 30 min following ischemic occlusion [13]. Similar studies in dogs have suggested that Purkinje activity precedes both ectopy and late VT (>24 hr following MI). Multiple mechanisms for VT arising from the subendocardium have been considered in past research. Some evidence exists for almost all mechanisms of arrhythmia including: triggered activity from DADs [14–16], abnormal automaticity [17], reentry, microreentry [18, 19], and other nonreentrant mechanisms [20].

Macroreentry has been identified in humans in whom both diastolic and presystolic Purkinje potentials may occur in idiopathic LV tachycardia [21]. These VTs have a right bundle branch appearance on ECG with a left axis deviation and are verapamil-sensitive. Mapping of these VTs have localized them to the distal portions of the specialized Purkinje tissue in the LV, the left posterior fascicle, or the papillary muscles. Although activation of the Purkinje fibers and ventricular myocardium is almost inseparable in most of the LV, as pointed out by Chen et al, there exists an increased heterogeneity of conduction over the regions of the papillary muscles [22]. This was initially shown by Joyner et al. who paced the papillary ventricular muscle near the cordae tendineae, yet activated the Purkinje system initially at the opposite end of the papillary muscle as a result of the location of the Purkinje–ventricular myocardial junctions at the insertion of the papillary muscle into the ventricular free wall [23].

The source to sink safety factor of propagation from Purkinje fibers to ventricular muscle is lower than that from ventricular muscle to Purkinje fibers, leading to unidirectional block and reentry [24–26]. Also, the anatomical sudden change in fiber direction formed by the insertion of the papillary muscle into the ventriclar free wall may perpetuate any arrhythmia that arises and lead to sustained VT [24–26]. Radiofrequency ablation of both the diastolic and presystolic potentials near papillary muscles terminates the reentrant arrhythmias and suggests that their close proximity to the papillary muscle make it an important structural boundary that causes sustained arrhythmias.

Purkinje Fiber Involvement in VF

Canine studies by Worley et al. revealed that as VF progressed, a transmural gradient of activation rates developed such that the endocardium activated more rapidly than the epicardium [27–29]. Although the activation rate was approximately the same transmurally during early VF, as VF continued over 20 min, the rate of VF slowed, primarily toward the epicardium, so that the endocardial activation rate increasingly outpaced that near the epicardium. Possible causes for this phenomenon are (i) oxygen in the ventricular cavities prevents the endocardium from becoming ischemic as VF continues so that it activates more rapidly than the ischemic remainder of the ventricular walls, and (ii) the rapid activations come from Purkinje fibers on the endocardium, which have been shown to be more resistant than the working myocardium to the effects of ischemia [3, 5, 28–30].

While the refractory period of Purkinje fibers is longer than that of working myocardium at slow activation rates, at the rapid activation rates of VF, the refractory period of Purkinje fibers is as short as or shorter than that of working myocardium [31]. Therefore, it is physiologically possible for Purkinje fibers to activate sufficiently rapidly to be partially or entirely responsible for maintaining VF.

Further evidence to support the role of Purkinje fibers in VF comes from canine heart studies in which the subendocardium was ablated by painting the endocardium with either Lugol's solution or phenol [27, 32]. Chemical ablation of the Purkinje fiber–rich subendocardial layer in canine hearts has been reported to dramatically elevate the VF threshold, making inducibility difficult if not impossible [27]. Conversely, another study reported that Lugol's ablation did not significantly alter the VF threshold [33]. However, some Purkinje fibers may have not been ablated by this procedure because Purkinje potentials can be recorded at a depth of 2 mm in the left ventricular free wall [34], while application of Lugol's solution produces necrosis to a depth of only about 0.5 mm [27, 32].

Chen's group substituted air for cavitary blood and showed that the transmural gradient of activation rate was still present but that it disappeared after the Purkinje fibers were ablated by applying Lugol's solution to the endocardium [35]. These findings suggest that Purkinje tissue, and not subendocardial myocardium protected from ischemia by oxygenated cavitary blood, is responsible for the transmural gradient of LDVF activation rate.

If Purkinje fibers are driving the rapid activation rate in LDVF in canines, activation fronts should arise from endocardial Purkinje fibers and propagate toward the slower activating epicardium. As is the case with humans, the Purkinje fiber system in dogs is limited primarily to the endocardial surface [34, 36–38], while in pigs it arborizes almost transmurally so that Purkinje–muscle junctions are present from the endocardium through the myocardium nearly to the epicardium [39–42].

Thus, if Purkinje fibers play a role in VF maintenance, the intramural location of the fastest activating regions should differ in dogs and pigs. To test this hypothesis, Newton et al. recorded 75–100 plunge needles in the right ventricular (RV) and LV freewalls and septum of six pigs and five dogs during extended VF. A previously developed and tested method was used to estimate the VF activation rate from the dominant frequency and to estimate conduction block from double peaks in the FFT power spectrum of the electrode recordings [43]. For the first 70 sec of VF in both pigs and dogs, the dominant frequency was slightly higher at the epicardium than at the endocardium, whereas the incidence of double peaks was highest at the endocardium and lowest at the epicardium for the entire LV and RV base. The distribution changed little for the first 3 min of VF in pigs, but reversed by 2 min in dogs so that the dominant frequency was highest at the endocardium and lowest at the epicardium as was mentioned earlier. Thus, estimated activation rates and conduction block incidence are not uniformly distributed transmurally during long duration VF (LDVF) in dogs.

During the first 1–2 min of VF, the faster-activating epicardium at the LV base exhibited less conduction block than the slower endocardium, raising the possibility that, at least in dogs, VF is not being driven during this period by activation fronts arising from the Purkinje fibers. This pattern in pigs was consistent, but its reversal by 2 min of VF in dogs supports the hypothesis that activation during LDVF is driven by Purkinje fibers in both species [43].

The study by Newton et al. analyzed only the first 3 min of VF because the FFT method to estimate activation rate and conduction block was developed only for short-duration VF. Allison and coworkers have since analyzed the first 10 min of LDVF by identifying activation times to determine the activation rate [44].

VF activation remains rapid transmurally in the pig, consistent with activation wavefronts during LDVF arising from the almost transmural Purkinje fibers in this species. In the dog, however, after the first few minutes of VF, rapid activation is only present near the endocardium where Purkinje spikes can sometimes be observed. The activation sequences along the plunge needles in dogs suggest that LDVF wavefronts pass from the endocardium toward the epicardium and that many of them block en route. These findings are consistent with an epicardial mapping study which demonstrated that after 5–10 min of LDVF, most wavefronts break through to the epicardium and terminate by conduction block [45].

Tabereaux and coworkers mapped the Purkinje network directly on the subendocardium in isolated canine hearts [46]. Six hearts were isolated, perfused with crystalloid solution, and the LV cavity opened via an incision in the RV free wall and distal septum between the areas supplied by the perforators of the posterior descending and the left anterior descending coronary arteries to expose the endocardial surface and papillary muscles of the LV.

Unipolar recordings were made using a 504-electrode (24 columns × 21 rows) array with 1 mm spacing seated over the endocardial insertion of the left anterior papillary muscle. VF was then induced using a DC shock applied to the RV, perfusion was terminated, and mapping was performed for 10 min consecutively. Six epochs of data, each 5 sec long, during this time period were examined, one epoch at the beginning of VF and at 1, 3, 5, 7, and 10 min after the start of VF.

Purkinje fiber (PF) activations were quantified and distinguished from the ventricular working myocardium activations (V) by evaluating the recorded potentials and their temporal derivatives. PF activations were shorter and sharper than V activations and arose in four types of patterns in relation to V activations: (i) depolarization propagating from V to PF presumably through a retrograde conduction at a PF–V junction site (Figure 33.1); (ii) PF arising from the leading edge of a V activation presumably through retrograde conduction at a PF–V junction site (Figure 33.2); (iii) propagation of PF from the border of the mapped region

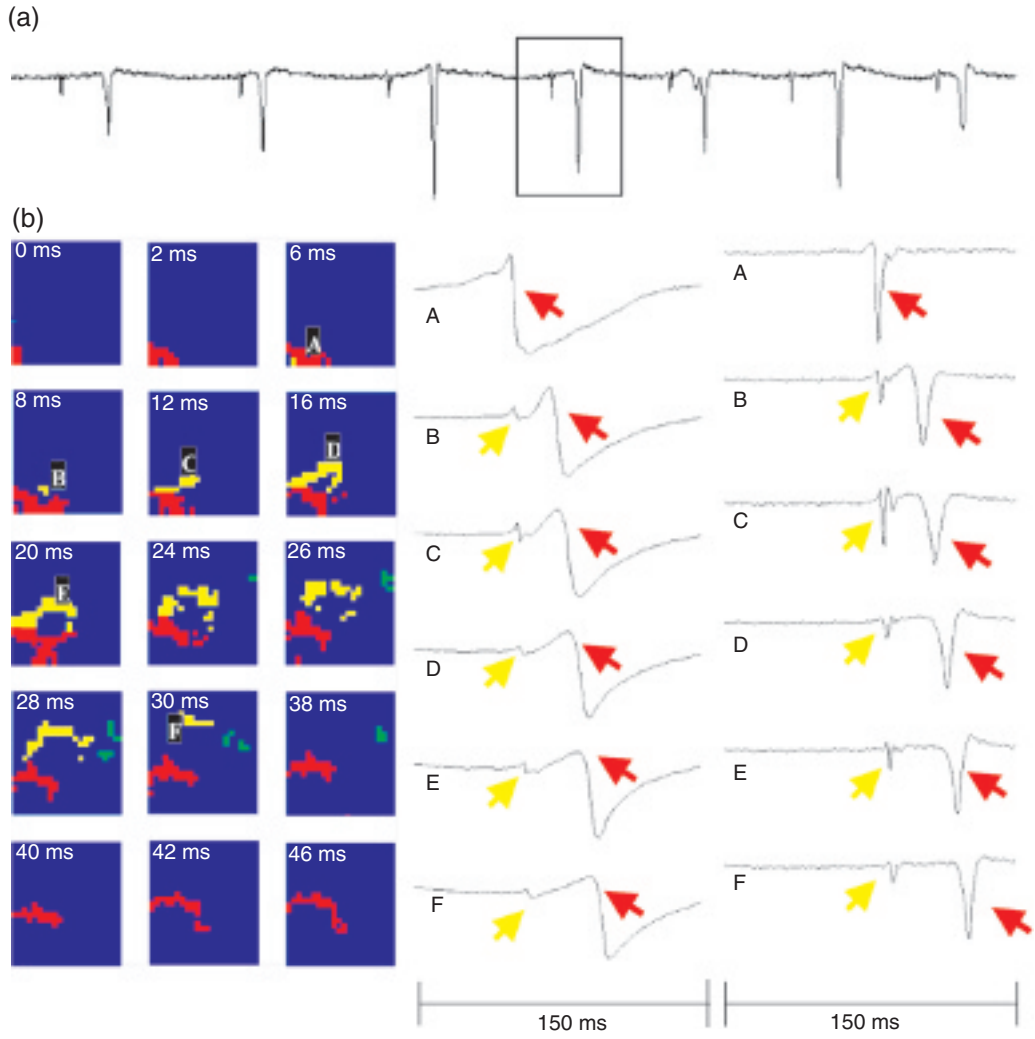

Figure 33.1 A 1.5-sec example of the *dV/dt* of the recording from one electrode in the array is provided in panel (a) with a box highlighting the individual beat displayed in panel (b). In panel (b), a V-to-PF activation pattern is shown in which the PF activation (yellow) appears to arise from the leading edge of the V wavefront (red) as it propagates across the array. The selected panels represent frames from a dynamic display of the activation patterns. The frames are separated at variable time intervals with the time for each frame in white. Green represents a nonrelated wavefront. Letters A–F indicate the locations of electrodes whose potentials (left) and temporal derivative of the potentials (right) are shown during the wavefront propagation.

activating V in the mapped region (Figure 33.3); and (iv) PF or V arising de novo in the mapped region (Figure 33.4).

These findings were the first description of the mapping of PF activation patterns on the endocardium in an ex vivo isolated heart preparation during LDVF. The importance of the findings are to show that the Purkinje fiber network is highly active during all stages of VF and to raise the possibility that focal activation may be arising from the subendocardium to maintain VF. This possibility is startling because it has been assumed that VF is exclusively maintained by reentry within the working myocardium. Other studies have also suggested the involvement of Purkinje fibers during VF, but the mechanisms remained unresolved [3, 4, 47–49].

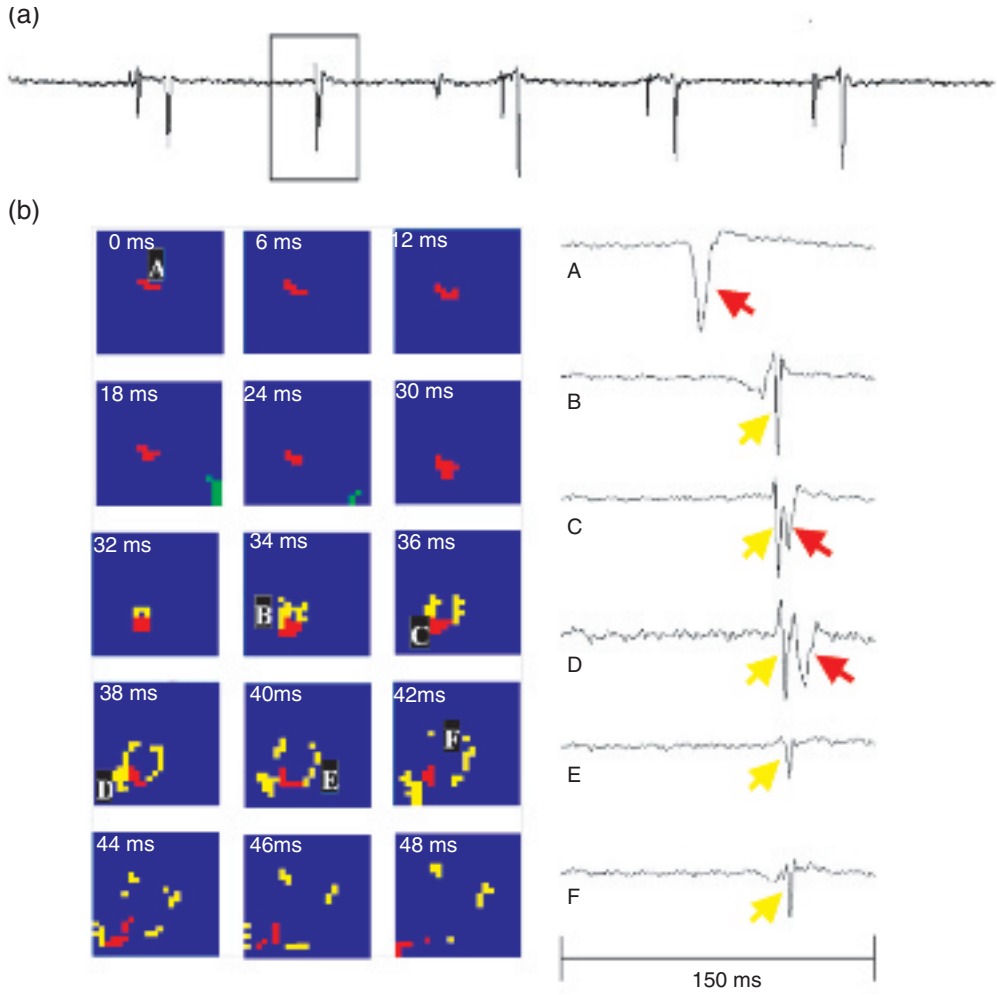

Figure 33.2 A 1.5-sec example of the *dV/dt* at one electrode is provided in panel (a) with a box highlighting the individual beat displayed in panel (b). In panel (b), a V-to-PF activation pattern is shown in which the V (red) activation propagates downward on the array until reaching a PF–V junction site and in a retrograde fashion activating the PF (yellow). The box in panel (a) represents the selected beat displayed in panel (b). The temporal derivative of the labeled electrode recording is shown. Green represents a nonrelated wavefront.

The finding that activation is propagating within the PF system throughout the first 10 min of VF does not necessarily mean that Purkinje fibers are responsible for the maintenance of VF; Purkinje activation could merely be activated retrogradely from the working myocardium. Indeed, activations were demonstrated to be conducting from the ventricular working myocardium to the Purkinje network in a retrograde fashion (Figures 33.1 and 33.2).

However, the findings also showed antegrade activation of ventricular myocardium arising from Purkinje activation in VF (Figure 33.3). This finding suggests that the Purkinje fibers are an integral part of activation circuits during LDVF, which raises the possibility that the Purkinje fibers are partially or entirely responsible for maintaining LDVF. The finding of frequent focal activations arising from the Purkinje fibers preceding ventricular activation during VF is intriguing (Figure 33.4). This activation pattern could be caused by intramural wavefronts traveling from the epicardium toward the endocardium with breakthrough on the

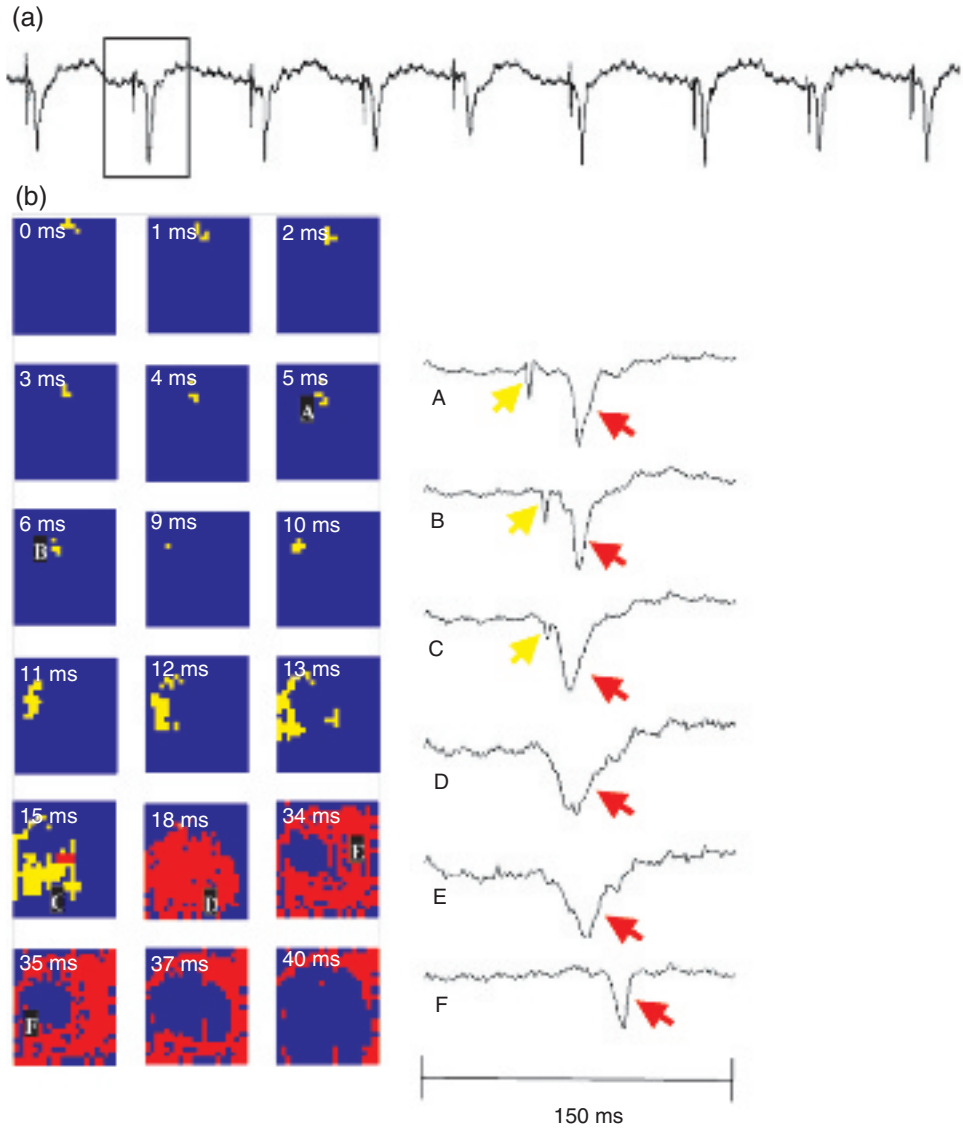

Figure 33.3 A 1.5-sec example of the *dV/dt* is provided in panel (a) with a box highlighting the individual beat displayed in panel (b). In panel (b), a PF (yellow)-to-V (red) activation pattern is shown. A rapidly propagating Purkinje wavefront enters the top aspect of the array and propagates to the bottom left, stimulating a PF–V junction after which an expanding Purkinje ring of activation appears followed by a more slowly activating ring of ventricular myocardium. The box in panel (a) represents the selected beat displayed in panel (b). The temporal derivatives of the labeled electrodes recordings are shown.

endocardial surface. However, the studies of Newton and Allison and coworkers demonstrated that after the first 2 min of VF, activation wavefronts in dogs primarily proceed from the endocardium to the epicardium [43, 44]. Therefore, it is unlikely that all of these apparent foci on the endocardium are actually breakthrough of intramural wavefronts.

This conclusion is bolstered by a recent 3D mapping study in pigs that demonstrated true foci arising in LDVF [50]. It was not possible to record from the Purkinje fibers in this 3D mapping

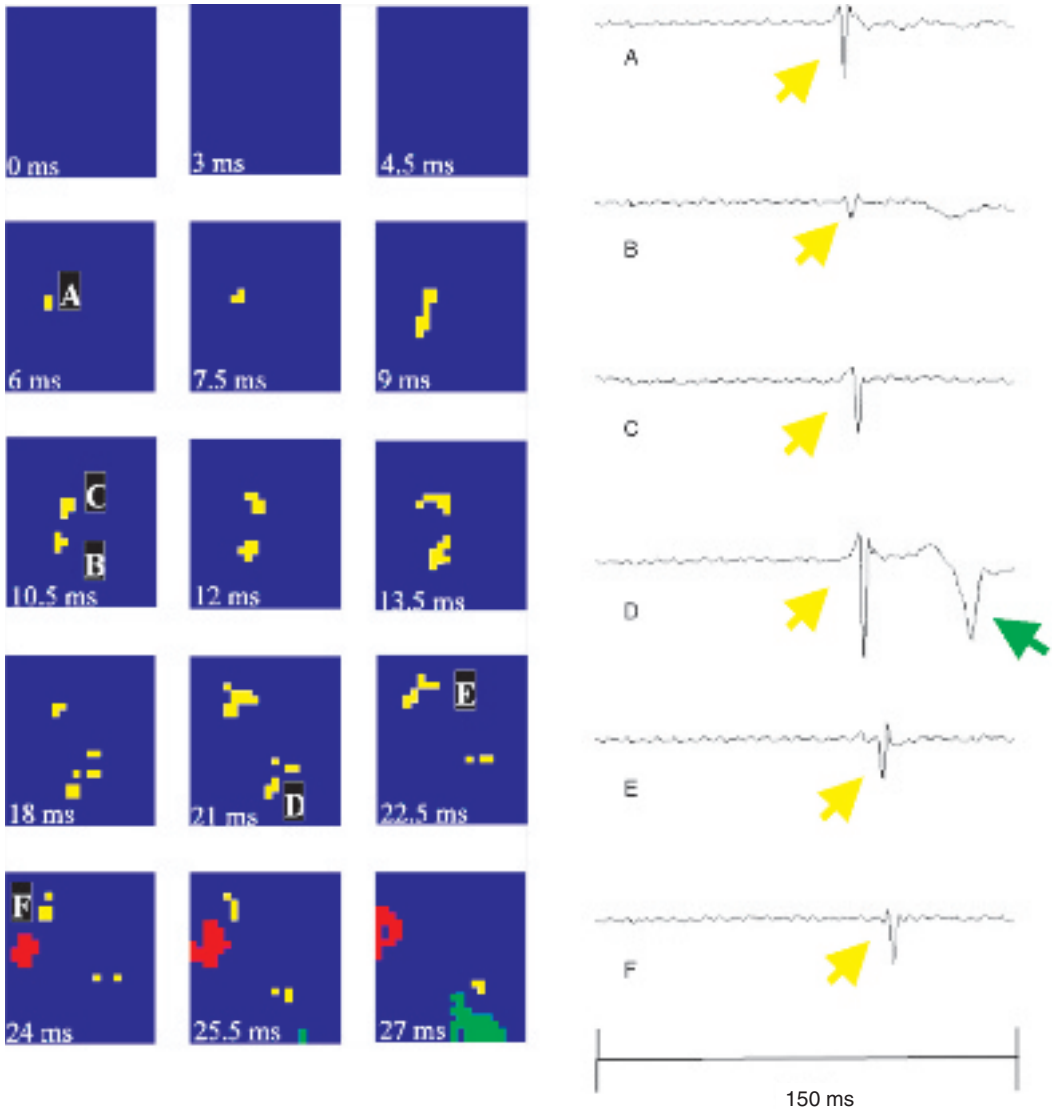

Figure 33.4 A focal activation arising from the center of the array. The focal appearing PF activation (yellow) is followed by a V (red) activation wavefront. The temporal derivative of individual electrode recordings shows the wavefront initiating at electrode (a) and spreading outward toward electrodes (d) and (e). The green arrow represents a nonrelated wavefront.

study so it is not known if these foci arose in the working myocardium or were caused by Purkinje activations entering the working myocardium at Purkinje–myocardial junctions to form a focal activation pattern in the working myocardium. Thus, it remains to be determined if these foci are caused by reentry circuits partially or entirely within the Purkinje system, or if they are caused by triggered activity or abnormal automaticity in the Purkinje fibers or in the working myocardium.

Acknowledgements

This work has been supported in part by National Institutes of Health grants HL-28429, HL-66256, and HL-85370. We would also like to thank Kate Sreenan for her editorial assistance in preparing the manuscript.

References

1 Kugler JH, Parkin JB. Continuity of Purkinje fibers with cardiac muscle. *Anat Rec* 1956; **126**: 335–41.

2 Martinez-Palomo A, Alanis J, Benitez D. Transitional cardiac cells of the conductive system of the dog heart: distinguishing morphological and electrophysiological features. *J Cell Biol* 1970; **47**: 1-17.

3 Friedman PL, Stewart JR, Fenoglio JJ, Jr., Wit AL. Survival of subendocardial Purkinje fibers after extensive myocardial infarction in dogs. *Circ Res* 1973; **33**: 597–611.

4 Friedman PL, Stewart JR, Wit AL. Spontaneous and induced cardiac arrhythmias in subendocardial Purkinje fibers surviving extensive myocardial infarction in dogs. *Circ Res* 1973; **33**: 612–26.

5 Gilmour RF, Jr., Zipes DP. Different electrophysiological responses of canine endocardium and epicardium to combined hyperkalemia, hypoxia, and acidosis. *Circ Res* 1980; **46**: 814–25.

6 Dangman KH, Danilo P, Jr., Hordof AJ, Mary-Rabine L, Reder RF, Rosen MR. Electrophysiologic characteristics of human ventricular and Purkinje fibers. *Circulation* 1982; **65**: 362–68.

7 Bogun F, Good E, Reich S, et al. Role of Purkinje fibers in postinfarction ventricular tachycardia. *J Am Coll Cardiol* 2006; **48**: 2500–7.

8 Szumowski L, Sanders P, Walczak F, et al. Mapping and ablation of polymorphic ventricular tachycardia after myocardial infarction. *J Am Coll Cardiol* 2004; **44**: 1700–6.

9 Haissaguerre M, Shah DC, Jais P, et al. Role of Purkinje conducting system in triggering of idiopathic ventricular fibrillation. *Lancet* 2002; **359**: 677–78.

10 Haissaguerre M, Shoda M, Jais P, Nogami A, Shah DC, Kautzner J, et al. Mapping and ablation of idiopathic ventricular fibrillation. *Circulation* 2002; **106**: 962–67.

11 Nogami A, Sugiyasu A, Kubota S, Kato K. Mapping and ablation of idiopathic ventricular fibrillation from the Purkinje system. *Heart Rhythm* 2005; **2**: 646–69.

12 Hayashi M, Kobayashi Y, Iwasaki YK, et al. Novel mechanism of postinfarction ventricular tachycardia originating in surviving left posterior Purkinje fibers. *Heart Rhythm* 2006; **3**: 908–18.

13 Arnar DO, Bullinga JR, Martins JB. Role of the Purkinje system in spontaneous ventricular tachycardia during acute ischemia in a canine model. *Circulation* 1997; **96**: 2421–29.

14 le Marec H, Dangman KH, Danilo P, Jr., Rosen MR. An evaluation of automaticity and triggered activity in the canine heart one to four days after myocardial infarction. *Circulation* 1985; **71**: 1224–36.

15 Coetzee WA, Opie LH. Effects of components of ischemia and metabolic inhibition on delayed afterdepolarizations in guinea pig papillary muscle. *Circ Res* 1987; **61**: 157–65.

16 Xing D, Martins JB. Triggered activity due to delayed afterdepolarizations in sites of focal origin of ischemic ventricular tachycardia. *Am J Physiol Heart Circ Physiol* 2004; **287**: H2078–84.

17 Hoffman BF, Rosen MR. Cellular mechanisms for cardiac arrhythmias. *Circ Res* 1981; **49**: 1–15.

18 Pogwizd SM, Corr PB. Reentrant and nonreentrant mechanisms contribute to arrhythmogenesis during early myocardial ischemia: results using three-dimensional mapping. *Circ Res* 1987; **61**: 352–71.

19 Pogwizd SM, Corr PB. Mechanisms underlying the development of ventricular fibrillation during early myocardial ischemia. *Circ Res* 1990; **66**: 672–95.

20 Janse MJ, van Capelle FJ, Morsink H, et al. Flow of "injury" current and patterns of excitation during early ventricular arrhythmias in acute regional myocardial ischemia in isolated porcine and canine hearts: evidence for two different arrhythmogenic mechanisms. *Circ Res* 1980; **47**: 151–65.

21 Nogami A, Naito S, Tada H, et al. Demonstration of diastolic and presystolic Purkinje potentials as critical potentials in a macroreentry circuit of verapamil-sensitive idiopathic left ventricular tachycardia. *J Am Coll Cardiol* 2000; **36**: 811–23.

22 Chen PS, Karagueuzian HS, Kim YH. Papillary muscle hypothesis of idiopathic left ventricular tachycardia. *J Am Coll Cardiol* 2001; **37**: 1475–76.

23 Joyner RW, Ramza BM, Tan RC. Effects of stimulation frequency on Purkinje–ventricular conduction. *Ann N Y Acad Sci* 1990; **591**: 38–50.

24 Kim YH, Xie F, Yashima M, et al. Role of papillary muscle in the generation and maintenance of reentry during ventricular tachycardia and fibrillation in isolated swine right ventricle. *Circulation* 1999; **100**: 1450–59.

25 Thakur RK, Klein GJ, Sivaram CA, et al. Anatomic substrate for idiopathic left ventricular tachycardia. *Circulation* 1996; **93**: 497–501.

26 Berenfeld O, Jalife J. Purkinje–muscle reentry as a mechanism of polymorphic ventricular arrhythmias in a 3-dimensional model of the ventricles. *Circ Res* 1998; **82**: 1063–77.

27 Damiano RJ, Jr., Smith PK, Tripp HF, Jr., et al. The effect of chemical ablation of the endocardium on ventricular fibrillation threshold. *Circulation* 1986; **74**: 645–52.

28 Lazzara R, el-Sherif N, Scherlag BJ. Electrophysiological properties of canine Purkinje cells in one-day-old myocardial infarction. *Circ Res* 1973; **33**: 722–34.

29 . Fixler DE, Saunders KW, Sugg WL. Subendocardial underperfusion during acute aorticopulmonary shunting in anesthetized dogs. *Am Heart J* 1974; **87**: 483–90.

30 Bagdonas AA, Stuckey JH, Piera J, Amer NS, Hoffman BF. Effects of ischemia and hypoxia on the specialized

conducting system of the canine heart. *Am Heart J* 1961; **61**: 206–18.

31 Carmeliet E, Vereecke J. *Electrogenesis of the Action Potential and Automaticity*. Williams and Wilkins Co., Balitmore, 1979.

32 Janse MJ, Kleber AG, Capucci A, Coronel R, Wilms-Schopman F. Electrophysiological basis for arrhythmias caused by acute ischemia: role of the subendocardium. *J Mol Cell Cardiol* 1986; **18**: 339–55.

33 Chen PS, Wolf PL, Cha YM, Peters BB, Topham SL. Effects of subendocardial ablation on anodal supernormal excitation and ventricular vulnerability in open-chest dogs. *Circulation* 1993; **87**: 216–29.

34 Spach MS, Huang SN, Ayers CR. Electrical and anatomic study of the Purkinje system of the canine heart. *Am Heart J* 1963; **65**: 664–73.

35 Cha YM, Uchida T, Wolf PL, et al. Effects of chemical subendocardial ablation on activation rate gradient during ventricular fibrillation. *Am J Physiol* 1995; **269**: H1998–2009.

36 Antzelevitch C, Sicouri S, Litovsky SH, et al. Heterogeneity within the ventricular wall: electrophysiology and pharmacology of epicardial, endocardial, and M cells. *Circ Res* 1991; **69**: 1427–49.

37 Forsgren S, Carlsson E, Strehler E, Thornell LE. Ultrastructural identification of human fetal Purkinje fibres: a comparative immunocytochemical and electron microscopic study of composition and structure of myofibrillar M-regions. *J Mol Cell Cardiol* 1982; **14**: 437–49.

38 Schnabel PA, Richter J, Schmiedl A, et al. The ultrastructural effects of global ischaemia on Purkinje fibres compared with working myocardium: a qualitative and morphometric investigation on the canine heart. *Virchows Arch A Pathol Anat Histopathol* 1991; **418**: 17–25.

39 Tranum-Jensen J, Wilde AA, Vermeulen JT, Janse MJ. Morphology of electrophysiologically identified junctions between Purkinje fibers and ventricular muscle in rabbit and pig hearts. *Circ Res* 1991; **69**: 429–37.

40 Holland RP, Brooks H. The QRS complex during myocardial ischemia: an experimental analysis in the porcine heart. *J Clin Invest* 1976; **57**: 541–50.

41 Hamlin RL, Burton RR, Leverett SD, Burns JW. Ventricular activation process in minipigs.*J Electrocardiol* 1975; **8**: 113–16.

42 Tribulova N, Manoach M. Is the antiarrhythmic effects of PA related to wavelength? *Circulation* 1999; **99**: 2220–21 (Comment).

43 Newton JC, Smith WM, Ideker RE. Estimated global transmural distribution of activation rate and conduction block during porcine and canine ventricular fibrillation. *Circ Res* 2004; **94**: 836–42.

44 Allison JS, Qin H, Dosdall DJ, et al. The transmural activation sequence in porcine and canine left ventricle is markedly different during long-duration ventricular fibrillation. *J Cardiovasc Electrophysiol* 2007; **18**: 1306–12.

45 Huang J, Rogers JM, Killingsworth CR, Singh KP, Smith WM, Ideker RE. Evolution of activation patterns during long-duration ventricular fibrillation in dogs. *Amer J Physiol Heart Circ Physiol* 2004; **286**: H1193–200.

46 Tabereaux PB, Walcott GP, Rogers JM, et al. Activation patterns of Purkinje fibers during long-duration ventricular fibrillation in an isolated canine heart model. *Circulation* 2007; **116**: 1113–19.

47 Scherlag BJ, el-Sherif N, Hope R, Lazzara R. Characterization and localization of ventricular arrhythmias resulting from myocardial ischemia and infarction. *Circ Res* 1974; **35**: 372–83.

48 Moak JP, Rosen MR. Induction and termination of triggered activity by pacing in isolated canine Purkinje fibers. *Circulation* 1984; **69**: 149–62.

49 Elharrar V, Zipes DP. Cardiac electrophysiologic alterations during myocardial ischemia. *Am J Physiol* 1977; **233**: H329–45.

50 Li L, Jin Q, Huang J, Smith WM, Ideker RE. Reentry within the working myocardium is not the sole mechanism by which ventricular fibrillation is maintained. *Circulation* 2007; **116**: II–278.

51 Worley SJ, Swain JL, Colavita PG, Smith WM, Ideker RE. Development of an endocardial–epicardial gradient of activation rate during electrically induced, sustained ventricular fibrillation in dogs. *Am J Cardiol* 1985; **55**: 813–20.

34 CHAPTER 34

Mapping Rotors in Animals and Humans During Atrial Fibrillation

Omer Berenfeld, PhD, *Jérôme Kalifa*, MD, PhD

Center for Arrhythmia Research, University of Michigan, Ann Arbor, MI, USA

Summary

Atrial fibrillation (AF) is the most common sustained arrhythmia, and despite more than a century of research its underlying mechanisms are not fully understood. Experimental studies using high-resolution optical mapping of impulse propagation during AF in the isolated sheep heart demonstrate that acetylcholine (ACh) dose-dependent reentrant sources in the left atrium can drive the fibrillatory activity throughout both atria. Using phase representation of the local impulse kinetics we establish that rotors can arise from unidirectional blocks of propagation at functional obstacles in that model. Further spatiotemporal tracking of the wavebreak sites identifies a functional isthmus in the wake of such an obstacle whose minimal width supporting a figure-of-eight reentry sustenance is of about 4 mm.

In the absence of ACh, increasing the intra-atrial pressure revealed a consistent increase in the frequency and dominance of activation in an area between the atrium and a pulmonary vein with the appearance of intermittent reentrant activity there. Finally, in some patients, the dependency of the activation rate on adenosine, which acts on the same membrane channels that are regulated by ACh, is compatible with reentrant activity being the underlying mechanism of AF maintenance.

Introduction

Atrial fibrillation (AF) is the most common sustained arrhythmia [1] and, despite more than a century of intensive research, it continues to challenge scientists [2, 3]. Mapping and analysis of the spatiotemporal organization of wave propagation during fibrillation can provide important clues about its underlying mechanisms. Mapping data recently published by our group support the hypothesis that acute AF in the structurally normal sheep heart [4–9] and in some patients [10] is not a totally random phenomenon. These data are consistent with the widely accepted notion that paroxysmal AF in patients is initiated by focal triggers localized in one or more pulmonary veins (PVs) [11] and is accessible by catheter-based ablation procedures [12]. On the other hand, in persistent AF the prevailing theory is that multiple random wavelets of activation coexist to create a chaotic cardiac rhythm [13], and that AF ablative therapy is more challenging [14–17].

Reentrant activity, which is also known as rotors, vortices, or spiral waves [18], has been shown to underlie various types of ventricular and atrial

Cardiac Mapping, Third Edition Edited by Mohammad Shenasa, Gerhard Hindricks, Martin Borggrefe, and Günter Breithardt
 ISBN: 978-1-405-17572-2

arrhythmias [3, 19, 20]. Yet, there is an ongoing debate on the precise nature, location, and mode of initiation of these reentrant sources. While AF may be the result of the breakup of multiple, randomly propagating wavelets that rotate briefly [21, 22], it may also relate to a discrete and steady rotor generating wave fronts that break at fixed heterogeneities [3]. These two different mechanisms are hypothesized to have different signatures on fibrillation dynamics; the latter showing more organization and stability in its patterns of wave propagation.

The purpose of this chapter is to discuss evidence that suggests that maintenance of acute AF in animals and patients depends on a localized reentrant source(s) in the left atrium (LA) and fibrillatory propagation in the right atrium (RA). To characterize the activation patterns on the surface of the atria we have used a combination of high-resolution video imaging techniques and bipolar electrograms recordings [23]. The chapter focuses on describing the electrical activation of the atria in space and time and makes extensive use of spectral and phase analyses to provide a solid and impartial quantification of the complex patterns of propagation as observed during AF in both animals [5, 24] and patients [10, 25].

Reentrant Activity During Acute AF in the Isolated Sheep Heart

The general working hypothesis that acute AF results from activity of a small number of high-frequency reentrant sources localized in one atrium, with fibrillatory conduction to the other atrium, is based primarily on results obtained in our isolated, Langendorff-perfused, sheep heart experimental model. It enabled studying the mechanisms of acute AF induced by burst pacing in the presence of acetylcholine (ACh). Overall, our results strongly indicate that AF in the sheep heart is the result of high-frequency periodic sources located in the LA, with fibrillatory conduction toward the RA [4, 7, 8]. As dominant frequencies (DFs) were found to be organized during AF, and local activity rate corresponded to the dominant frequency spectra of global recordings [4], we localized the source that maintains AF by a combined use of optical mapping and frequency analysis. (see also Videoclip 24 )

Not only did we find a clear difference between mean LA and RA dominant frequencies (5.7 $\pm$ 1.4 Hz), but we also found that a left-to-right impulse propagation was present in about 80% of cases along the Bachmann's bundle and the inferoposterior pathway [8]. As suggested by more recent studies, repetitive activation may also originate from the septum [26] or the pulmonary veins [11, 26, 27]. Altogether, it is possible to submit that AF, as seen on the ECG, results from rapidly successive wave fronts emanating from fast sources localized in the LA and propagating through both atria while interacting with anatomic and/or functional obstacles, leading to fragmentation and wavelet formation [4, 7–9].

Figure 34.1 shows data from an AF episode in which the site of the high-frequency periodic activity was localized [7]. In Figure 34.1a, an isochrone map of optical activity from the LA shows one cycle of a vortex that rotated clockwise at a period of 68.6 $\pm$ 8.9 msec ($\sim$14.7 Hz) and persisted for the entire length of the episode (25 min). The fact that the frequency of this source was equal to the highest and narrowest DF (most regular signal) recorded from all sites (optical and electrical recordings; see Mandapati et al. [7] for details) provides evidence that a rotor was the mechanism underlying the maintenance of this AF episode [28].

The summation of the activity throughout the field of view (LA pseudo-ECG in Figure 34.1b) demonstrates that the entire LA was being activated at 14.7 Hz. To assess the exact role of a given reentrant activity in determining the global dominant frequency of an episode we collected 14 identified LA vortices with completed rotations. Figure 34.1c shows the relation between the rotation period of those vortices and the inverse of the global dominant frequency obtained from the power spectrum of the corresponding LA pseudo-ECG. As the slope of the linear fitted curve is 0.93 ($R = 0.91$), it is strongly suggested that the periodicity of rotating spiral waves is a main contributor to the dominant frequency in the optically mapped region. Measurements of the dimensions of the core of these rotating waves revealed minuscule cores; the mean core perimeter and area were 10.4 $\pm$ 2.8 mm and 3.8 $\pm$ 2.8 mm^2, respectively.

However, several other studies have described also incomplete reentry and multiple unstable

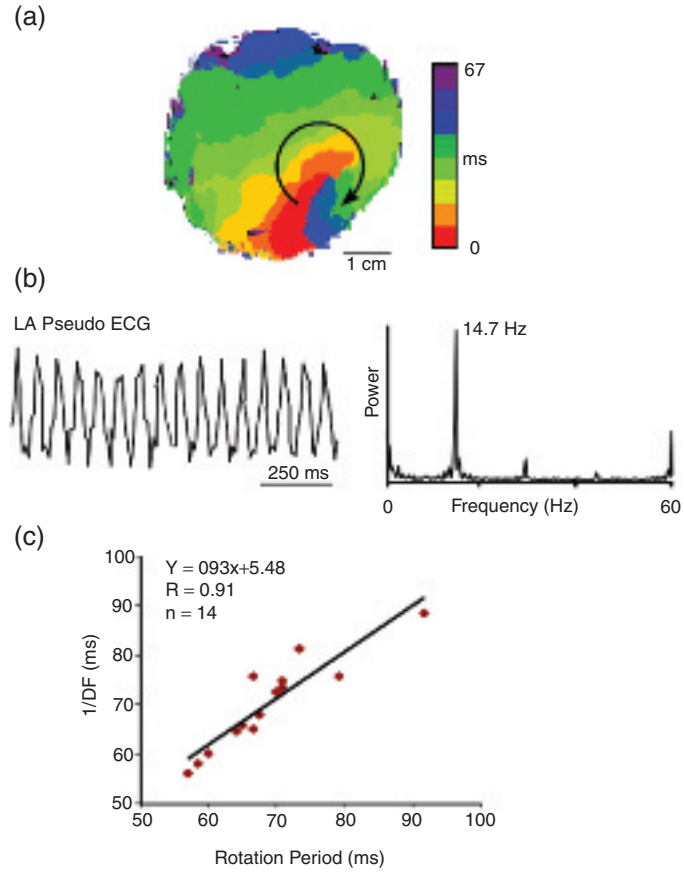

Figure 34.1 Reentrant sources of AF (a) Isochrone map of optical activity from the free wall of the LA during sustained AF showing a clockwise reentry (b) Optical pseudo-ECG of the LA during the same episode of AF with its corresponding power spectrum (c) Correlation between inverse DF from pseudo-ECGs of entire movies (~3 sec long) and rotation period of rotors found within an episode of AF. KEY: DF = dominant frequency. Reproduced with permission from Ref. [7].

reentrant circuits in various AF settings [4, 22, 23, 26, 29, 30]. As these results seem to be consistent with the multiple wavelet hypothesis [13, 22], only a few studies have revisited an older idea, originally put forth by Lewis [31] and later by Scherf [32], that a single high-frequency source of stable reentry may be an underlying mechanism for the maintenance of AF. According to this concept, despite the presence of a unique and periodic source at any given time, the electrical activity elsewhere could still present as incomplete or as short-lived and unstable reentrant circuits because of fibrillatory conduction [9].

For instance, Schuessler et al. [33] found that in an isolated canine right atrial preparation, increasing concentrations of ACh converted multiple reentrant circuits into a single, relatively stable high-frequency reentry that generated fibrillatory conduction. Thus, it seems that the results of the ACh-induced AF presented in Figure 34.1 are in agreement with those of Schuessler et al. [33] and both support the hypothesis that a single or a small number of sources of ongoing reentrant activity is the mechanism underlying AF in this setting.

Generation of Reentrant Activity

To map and quantify the dynamics of reentrant activity we utilized the phase mapping technique, a method effective in highlighting the formation of wavebreaks and the resulting phase singularity points, around which the reentrant waves pivot [24]. Briefly, the method consists of transforming the transmembrane signal from each pixel in the movie into the representation of its action potential stage and assigning it a time-variable phase value between $-\pi$ and π radians [6]. This phase value is then color-coded and phase maps for each instant are constructed for all pixels. Under this transformation, colors represent the different action potential phases (e.g., blue is the plateau phase and red the

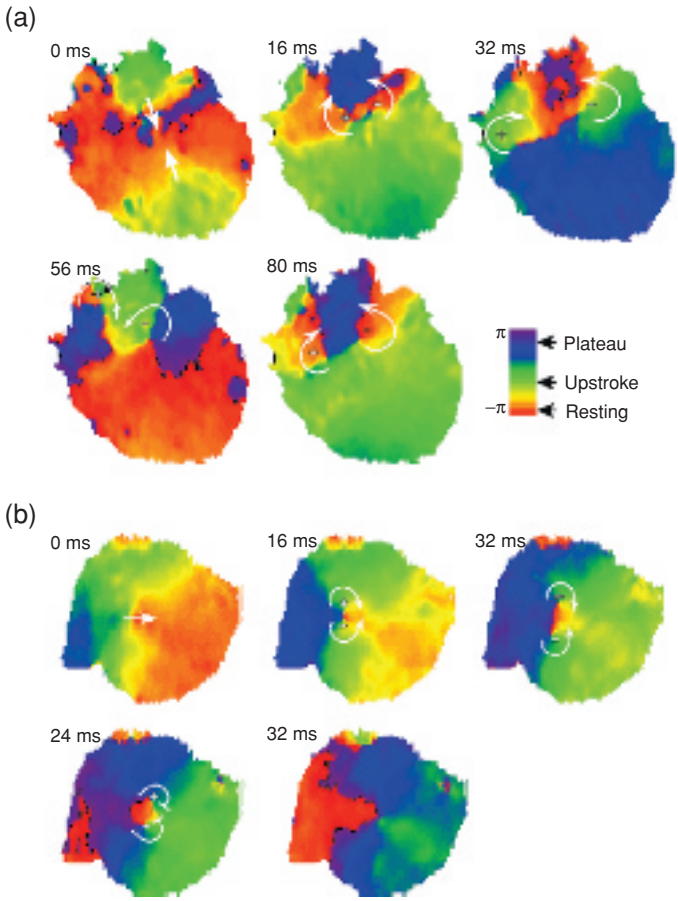

Figure 34.2 Phase representation of wave breakup and reentry formation (a) A sequence of phase maps at the indicated times demonstrating generation of figure-of-eight reentry (b) A sequence of phase maps demonstrating a failure in generating reentry. The color bar scale indicates phase values between $-\pi$ and π radians with approximated action potential stages (in part a). See text for details. Reproduced with permission from Ref. [6].

refractory phase; see Figure 34.2). Thus, the pivoting location of a reentrant activity is represented by sites where all colors converge and where the phase is not defined [i.e., phase singularity (PS)].

Wavebreaks, as indicated by the presence of phase singularity points, occurred frequently during the analyzed episodes of AF. On average, we counted a total of 70 ± 40 (range 23–154) phase singularity points formed per 400 msec of recording (50 frames) [6]. When tracking the trajectory of the phase singularity points, it was found that they meander and drift, but tend to cluster in a limited region of the mapped area in a nonrandom fashion. In the vast majority of the cases the lifespan of the phase singularity points was found to be exceedingly short. The mean lifespan was 19.5 ± 18.3 msec with a range that varied from 8.33 msec (1 frame) to 200 msec. Approximately 98% of phase singularity points existed less than the average rotation period of a rotor, which was ∼85 ms in our experiments; only 10 out 556 phase singularity points (∼2%) were found to have a duration greater than or equal to one rotation during sustained AF [6].

In Figure 34.2 we present an in-depth experimental verification of theoretical predictions for the initiation of a wavebreak, secondary to the interaction of a wave front with a functional obstacle during AF (i.e., vortex shedding) [34, 35]. In panel (a) we demonstrate how a pair of phase singularity points is produced at a broken ends of the wavelets [6] on the epicardial surface of the LA, and leads to a relative long-lasting episode of figure-of-eight reentry (∼3 rotations). At 0 msec, there are two depolarizing wave fronts present (depicted by the color green/yellow). The wave seen at the upper edge of the field of view propagates downward and

extinguishes upon refractory tissue (red) in the center of the field of view. As shown in the frame at 16 msec, the wave on the lower edge of our mapping fields propagates upward and breaks upon a functional obstacle (red) resulting in two phase singularity points ("+" and "−") of opposite chirality. At 32 msec, the two counter-rotating wavelets begin to propagate around the two phase singularity points. At 56 msec, the two free ends of the wavelets merge and begin to propagate between the phase singularities. At this time, the inter-PS distance is 6.8 mm. The panel at 80 msec shows the wave front after successfully propagating through the functional isthmus and completing a full cycle of figure-of-eight reentry. In our study we also found cases where the functional isthmus between the phase singularity points was not wide enough to allow propagation establishing a sustained reentry.

In panel (b) of Figure 34.2 we present phase maps of AF where two counter-rotating wavelets, formed after a wavebreak, were unable to complete a full rotation. At 0 msec, the activation wave front (green/yellow) is seen propagating into a heterogeneously recovered region, resulting in two wavebreaks, one of each side of the small obstacle of refractoriness in the center of the field (red). At 8 msec, the chirality of each of the newly formed phase singularity points is indicated by "+" and "−". At 16 msec, the fronts of two counter-rotating wavelets appear midway through the rotation wrapping around the two phase singularity points. At 24 msec the wavelets have fused and are attempting to propagate between the phase singularity points; the inter-PS distance is 3.3 mm. The two counter-rotating wavelets mutually annihilate and the reentry is not completed (i.e., the wavelets initially rotate around their corresponding phase singularity points, but do not complete a full rotation before disappearing) as shown in the map at 32 msec.

In our experiments, we measured inter-PS distance in 15 cases of completed and 25 cases of incomplete figure-of-eight reentry. We found that the inter-PS distance for the two groups is uniformly distributed but in ranges that do not overlap; all inter-PS distances for incomplete reentry were found to be less than about 4 mm while all inter-PS distances for complete reentry were above that value ($p < 0.001$). Thus, we have established that the minimal distance between two phase singularity points that allow for the sustenance of a figure-of-eight reentry in the LA of our model is about 4 mm.

This observation is in good agreement with those of Cabo et al. [35] who in ventricular tissue estimated a critical isthmus of 2.5–3.5 mm for propagation failure depending on stimulation frequency and fiber orientation. It is therefore demonstrated that the mechanism for the generation of reentrant sources during AF could be the collisions of wavefronts with functional obstacles. The fact that the phase singularity points tend to cluster in certain areas [6] indicate that the underlying structure, or other fixed properties of the tissue, are also involved in the generation of those obstacles.

The reentrant activity seen in Figure 34.1 did not have a counter-rotating activity visible in the mapped field, to complete a figure-of-eight as analyzed in Figure 34.2a. We nevertheless cannot exclude its existence elsewhere, or consider the fact that a single reentry can be produced by a similar mechanism [18]. Based on this finding we can speculate that the absence of complete reentrant activity observed in the RA is probably due to a higher critical inter-PS distance there. In fact, Schuessler et al. [33] found that in the canine isolated right atrium sustained arrhythmia resulted from stable single reentry only at very high concentrations of acetylcholine.

Increased Intra-Atrial Pressure and Rotor Dynamics

Because AF is commonly associated with atrial dilation [36–38], we employed yet another experimental model of sustained AF under conditions of acutely increased intra-atrial pressure to explore AF dynamics. We tested the hypothesis that dilation induces arrhythmogenic sources at the superior PVs during AF. This experimental model was adapted from a well-characterized model of stretch-related AF [39–41]. A pressure of 10 cm H_2O was found to be the lower limit to obtain very sustained AF episodes. In comparison, below 10 cm H_2O, AF usually terminates after 10–20 min [41].

As in the studies presented above, frequency analysis was used to characterize the organization of activity during AF [5, 9] and to establish the likelihood of localizing sources maintaining the AF from which propagation is originating [8]. In Figure 34.3, panels

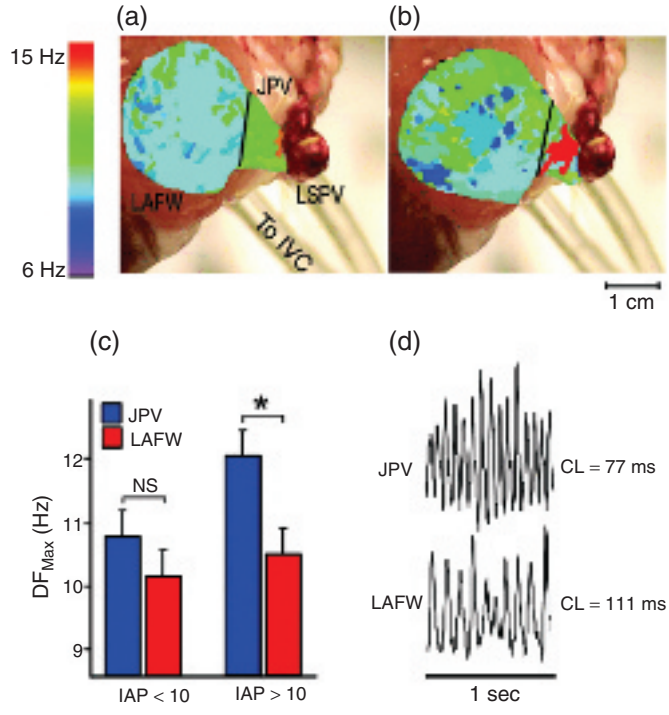

Figure 34.3 (a) (b) DF maps from one heart at intra-atrial pressures of 5 and 18 cm H_2O, respectively. DF maps are superimposed on color picture of a heart for illustrative purposes (c) Bar graph showing DF_{max} (mean ± SEM) in the PV junction (blue) and LA free wall (red) at intra-atrial pressures of <10 and >10 cm H_2O (* $P < 0.001$) (d) Single-pixel recordings from PV junction and LA free wall at 30 cm H_2O. KEY: DF = dominant frequency; IAP = intra-atrial pressure; LAFW = left atrium free wall; LSPV = left superior pulmonary vein; JPV = LSPV junction; IVC = inferior vena cava; CL = cycle length. Reproduced with permission from Ref. (41).

(a) and (b) are representative dominany frequency maps obtained simultaneously from the LA free wall (LAFW) and the LA superior PV junction (JPV) in one heart at intra-atrial pressures (IAPs) of 5 and 18 cm H_2O, respectively. These maps clearly illustrate the strong dependence of frequency on intra-atrial pressure. Below 10 cm H_2O, the difference between the maximum dominant frequency (DF_{max}) in the PV junction and LA free wall was not significant (10.8 ± 0.3 vs. 10.2 ± 0.3 Hz; $P = 0.6$; Figure 34.3c). However, at pressures >10 cm H_2O, DF_{max} in the PV junction was significantly higher than that in the LA free wall (12.0 ± 0.2 and 10.5 ± 0.2 Hz, respectively; mean ± SEM; $n = 9$; $P < 0.001$; see also representative single-pixel recordings in panel (d). At all pressures, DF_{max} in both the PV junction and LA free wall was significantly higher than the largest frequency recorded in the right atrial free wall (7.8 ± 0.3 Hz; $P < 0.001$).

As described previously, propagation of waves in AF may be highly periodic, both spatially and temporally [4]. Such spatio-temporal periodicities (STPs) may take various forms, including periodic waves emerging from the edge of the recording field, breakthroughs occurring at constant frequencies, and in some cases, stable rotors [4]. We found similar STP waves in high IAP–associated AF. In Figure 34.4 we show quantification of directionality and STP of electrical activation as a function of the intra-atrial pressure during AF. Clearly, the direction of propagation from left superior PV to LA free wall (blue symbols) was very consistent. In all experiments the directionality of local excitation in the PV junction area that corresponded to the highest frequencies correlated strongly with intra-atrial pressure ($r = 0.79$, $P = 0.02$; Figure 34.4b).

In contrast, the directionality of the LA free wall to the left superior PV had a negative and statistically nonsignificant correlation with pressure ($r = 0.54$, $P = 0.09$). In Figure 34.4c, the number of STP wavefronts (normalized to the maximum number of STP wavefronts) in the PV junction correlated strongly with intra-atrial pressure ($r = 0.92$, $P = 0.002$). Figure 34.4d shows an example of a rotor in the PV junction, the cycle length of which

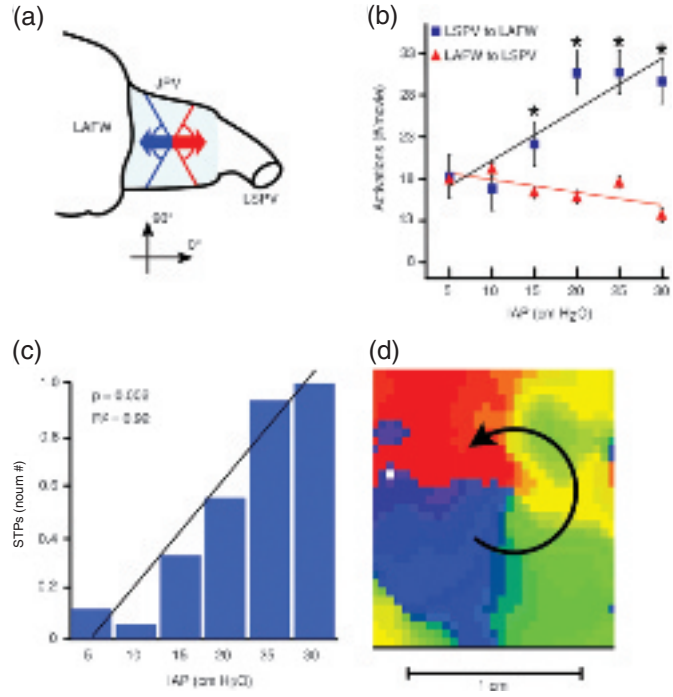

Figure 34.4 (a) Schematic directionality of activity from the PVs to LA free wall (blue arrow) and from the LA free wall to left superior PV (red arrow) assessed at the PV junction region (shaded area) (b) Number of activations (mean ± SEM) moving from left superior PV to LA free wall and from LA free wall to left superior PV (*$P < 0.01$ compared with LA free wall to left superior PV). Colors are the same as in part (a). (c) Relation between the normalized number of STP wavefronts by episode and the level of pressure (d) Phase map of a rotor recorded in the PV junction at 15 cm H_2O. *Key*: STP = spatiotemporal periodicity; rest of abbreviations are as in Figure 34.3. Reproduced with permission from Ref. [41].

(70 msec) was equal to $1/DF_{max}$ calculated from the same movie. Similar rotors were observed in three out of nine experiments. It was found that below 10 cm H_2O, AF terminates because its reentrant sources become slow and unstable.

These data are particularly valuable when one considers that there is evidence that in patients with paroxysmal AF, the diameters of the superior PV ostia are markedly dilated compared with the inferior PV ostia [42], particularly when considered as arrhythmogenic PVs [43]. However, the electrophysiological mechanisms linking PV and LA dilatation to maintenance of AF have not been established. Our data demonstrate that the sources of rapid atrial activation during stretch-related AF are located in the PV region and that their level of spatio-temporal organization correlates with pressure. The extent to which STP excitation waves observed in the PV junction are generated by microreentrant activity in the endocardial PV sleeves requires further investigation, and those data only provide a partial mechanistic explanation for the precise role of the PVs in AF maintenance in the setting of atrial dilatation.

Activation Frequency and Rotor Drivers in Humans

Identifying rotors as drivers of AF directly in patients is very difficult with the existing mapping techniques [44, 45]. Yet, the acetylcholine dose–dependent acceleration of rotor frequency [46] offered an idea that enabled translating animal experiments to human patients and gave us the opportunity to obtain evidence, albeit indirect, for the presence of rotors as drivers through pharmacologic means. Translation was made possible also by the fact that adenosine, which is widely used in the clinic, is known to activate the same Kir3.x subfamily of inward rectifier potassium channels as acetylcholine [47–49].

By increasing K^+ conductance in the atrium, both acetylcholine and adenosine hyperpolarize the cell membrane, abbreviate the action potential duration and the refractory period, and inhibit spontaneous pacemaker discharge as well as early and delayed depolarizations [47, 48]. On the other hand, they both accelerate reentrant activity [46]. Thus, in a recent study [25], we used adenosine to test the

hypothesis that localized reentry maintains AF also in humans. We determined the effects of adenosine infusion on dominant frequency at varying locations of both atria with the idea that adenosine-induced acceleration reveals reentry as the mechanism of AF maintenance and rules out an automatic or triggered mechanism.

We generated baseline DF maps of the LA using novel real-time spectral analysis software that allowed determination of the specific high-DF sites likely to harbor the AF drivers [10] in paroxysmal AF patients. Then the adenosine effect was measured at the primary and secondary high DF sites in the LA. Figure 34.5 shows a representative example where the AF frequency at the baseline was relatively slow (<5 Hz) and 3 high-DF sites were identified with the primary high-DF site being located near the right interior PV (red arrow). Panels (b) and (c) show that while the adenosine infusion practically abolished the ventricular activity as detected by V5, the dominant frequency at the primary high-DF site accelerated from 4.64 Hz at the baseline to 6.35 Hz at the peak of the adenosine effect. An additional adenosine infusion performed while measuring activity at a secondary high-DF site also showed an increase in dominant frequency, but to a lesser extent. Interestingly, in this patient the arrhythmia terminated during postmapping ablation at the primary high-DF site, supporting again the critical role of such sites as AF drivers [10]. Compared to the baseline, adenosine significantly accelerated the primary and secondary high-DF sites in these patients from

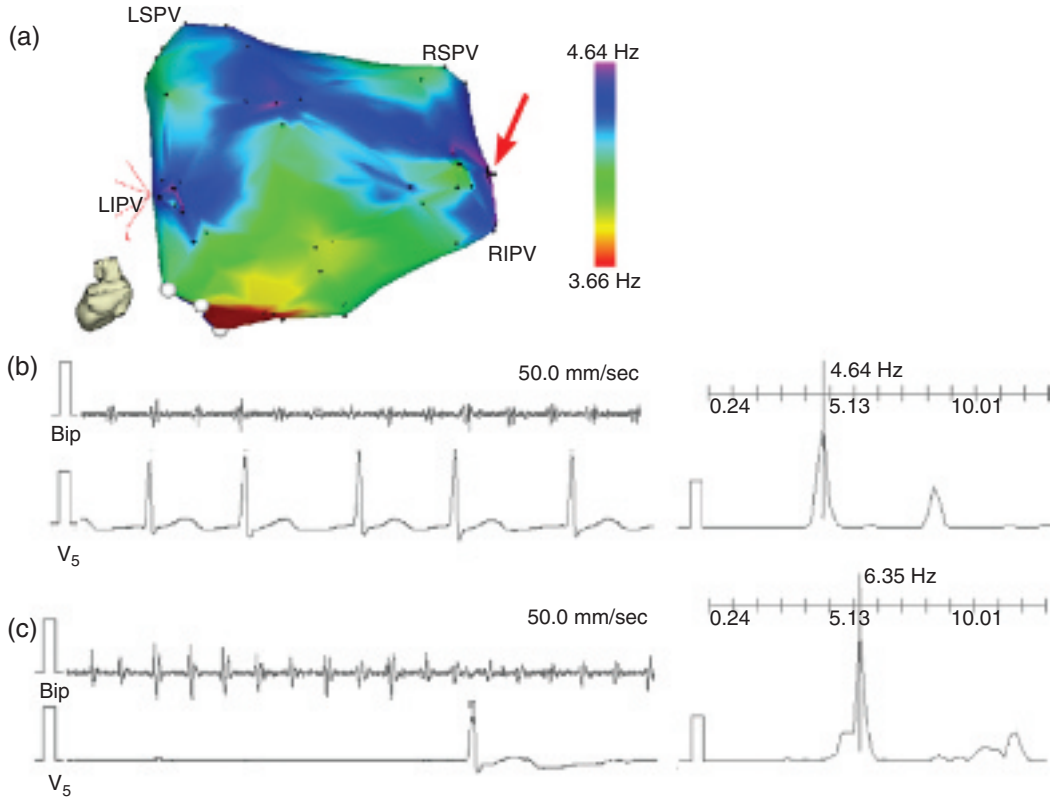

Figure 34.5 Accelerating effect of adenosine on a high-DF site (a) LA posterior view of a DF map from a paroxysmal AF patient. The DF map was produced by the real-time frequency-mapping CARTO system before infusion of adenosine. Red arrow indicates primary high-DF site near the right inferior PV. (b) Baseline recording at the primary high-DF site with its power spectrum and simultaneous V_5 reference. (c) Recording at the primary high-DF site with power spectrum and simultaneous V_5 reference during peak adenosine effect showing increase of DF. KEY: LSPV, RSPV, LIPV, RIPV = Left/right superior/inferior pulmonary veins (PVs); Bip = bipolar catheter. Reproduced with permission from Ref. [25].

about 5 Hz to 6.7 Hz [25], demonstrating that the sites involved in the maintenance of AF are clearly affected by adenosine.

In a larger cohort of paroxysmal and persistent AF patients, Atienza et al. [25] analyzed the effect of adenosine on the activation rate at specific regions at the junction of the PVs and the LA (PV-LAJ), the high right atrium (HRA) and the coronary sinus. In general, patients with persistent AF demonstrated significantly higher maximal baseline dominant frequencies than paroxysmal AF patients ($p < 0.001$). However, adenosine infusion in persistent AF patients increased local dominant frequencies only in the HRA. The increase in the PV-LAJ was not statistically significant and there was no change in the dominant frequency of the coronary sinus. In sum, adenosine infusion increased frequency primarily at sites that activated at the highest rate at the baseline. In paroxysmal AF patients, adenosine increased activation frequency in the PV–LAJ. In persistent AF patients, the highest-frequency sources accelerated by adenosine were located in either atria but not at PV sites. Thus, the response to adenosine is consistent with reentrant drivers maintaining AF that have different locations in paroxysmal compared with persistent AF patients [25].

Conclusion

Experimental studies of acute AF in an isolated sheep heart in the presence of acetylcholine [3] or increased intra-atrial pressure [41] demonstrate that high-frequency reentrant sources in the free and posterior wall of the left atrium drive the fibrillatory activity throughout both atria. Following a growing body of work investigating how measurements of the cycle length of activity in patients during AF can contribute to its treatment [10, 25, 50, 51], we have focused our analysis in humans on the distribution of dominant frequencies during AF. Using electro-anatomic mapping and Fourier spectral methods we generated 3D, whole-atrial dominant frequency maps on which high-DF sites were ablated and resulted in significant slowing of the arrhythmia and termination of sustained AF in 87% of patients with paroxysmal AF [10]. The response of the arrhythmia to adenosine was consistent with the mechanistic hypothesis that reentry in those high-DF sites maintains AF in humans, and that reentrant drivers have different locations in paroxysmal compared with persistent AF patients [25].

Clearly, the ability to localize drivers that maintain AF and to characterize their mechanism should enable novel therapies, whether ablative, electrical, pharmacological, or hybrid [10, 25]. To our knowledge, however, the detailed molecular, cellular, and pathophysiological mechanisms that determine the predilection of the highest-frequency reentrant sources to the LA and the PVs region remains a mystery. Integrated studies describing phenomena ranging from the molecular and cellular to the tissue levels will probably be needed to address this important clinical question. The combination of improved mapping techniques [44, 45, 52, 53], together with time and frequency domain measures such as dominant frequency [10, 25] and fractionation [54], should help clinicians gain insight into AF mechanisms and therapeutics.

Acknowledgement

The research contributing to this chapter was supported in part by grants PO1HL039707, RO1HL060843, and RO1HL087055 from the National Institutes of Health, and from Postdoctoral Fellowship and Scientist Development Grant 0230311N from the American Heart Association.

References

1 Feinberg WM, Blackshear JL, Laupacis A, et al. Prevalence, age distribution, and gender of patients with atrial fibrillation. *Arch Intern Med* 1995; **155**: 469–73.

2 Nattel S. New ideas about atrial fibrillation 50 years on. *Nature* 2002;**415**: 219–26.

3 Jalife J, Berenfeld O, Mansour M. Mother rotors and fibrillatory conduction: a mechanism of atrial fibrillation. *Cardiovasc Res.* 2002; **54**:204–16.

4 Skanes AC, Mandapati R, Berenfeld O, et al. Spatiotemporal periodicity during atrial fibrillation in the isolated sheep heart. *Circulation* 1998; **98**: 1236–48.

5 Berenfeld O, Mandapati R, Dixit S, et al. Spatially distributed dominant excitation frequencies reveal hidden organization in atrial fibrillation in the Langendorff-perfused sheep heart. *J Cardiovasc Electrophysiol* 2000; **11**: 869–79.

6 Chen J, Mandapati R, Berenfeld O, et al. Dynamics of wavelets and their role in atrial fibrillation in the isolated sheep heart. *Cardiovasc Res* 2000; **48:** 220–32.

7 Mandapati R, Skanes A, Chen J, et al. Stable microreentrant sources as a mechanism of atrial fibrillation in the isolated sheep heart. *Circulation* 2000; **101**: 194–99.

8 Mansour M, Mandapati R, Berenfeld O, et al. Left-to-right gradient of atrial frequencies during acute atrial fibrillation in the isolated sheep heart. *Circulation* 2001; **103**: 2631–36.

9 Berenfeld O, Zaitsev AV, Mironov SF, et al. Frequency-dependent breakdown of wave propagation into fibrillatory conduction across the pectinate muscle network in the isolated sheep right atrium. *Circ Res* 2002; **90**: 1173–80.

10 Sanders P, Berenfeld O, Hocini M, et al. Spectral analysis identifies sites of high-frequency activity maintaining atrial fibrillation in humans. *Circulation* 2005; **112**: 789–97.

11 Haissaguerre M, Jais P, Shah DC, et al. Spontaneous initiation of atrial fibrillation by ectopic beats originating in the pulmonary veins. *N Engl J Med* 1998; **339**: 659–66.

12 Haissaguerre M, Shah DC, Jais P, et al. Mapping-guided ablation of pulmonary veins to cure atrial fibrillation. *American Journal of Cardiology* 2000; **86**, 9K-19K.

13 Moe GK, Abildskov JA. Atrial fibrillation as a self-sustaining arrhythmia independent of focal discharges. *Amer Heart J* 1959; **58**: 59–70.

14 Haissaguerre M, Jais P, Shah DC et al. Catheter ablation of chronic atrial fibrillation targeting the reinitiating triggers. *J Cardiovasc Electrophysiol* 2000; **11**: 2–10.

15 Benussi S, Pappone C, Nascimbene S et al. A simple way to treat chronic atrial fibrillation during mitral valve surgery: the epicardial radiofrequency approach. *Eur J Cardio-Thoracic Surg* 2000; **17**: 524–29.

16 Knight BP, Weiss R, Bahu M, et al. Cost comparison of radiofrequency modification and ablation of the atrioventricular junction in patients with chronic atrial fibrillation. *Circulation* 1997; **96**: 1532–36.

17 Oral H, Pappone C, Chugh A, et al. Circumferential pulmonary-vein ablation for chronic atrial fibrillation. *N Engl J Med* 2006; **354**: 934–41.

18 Wellner M, Berenfeld O. Theory of reentry. In: Zipes DP, Jalife J, eds. *Cardiac Electrophysiology: From Cell to Bedside*. W.B. Saunders, Philadelphia, 2004: 317–26.

19 Jalife J, Berenfeld O. Molecular mechanisms and global dynamics of fibrillation: an integrative approach to the underlying basis of vortex-like reentry. *J Theor Biol* 2004; **230**: 475–87.

20 Nattel S, Shiroshita-Takeshita A, Cardin S, et al. Mechanisms of atrial remodeling and clinical relevance. *Curr Opin Cardiol* 2005; **20**: 21–5.

21 Moe GK, Rheinboldt WC, Abildskov JA. A computer model of atrial fibrillation. *Amer Heart J* 1964; **67**: 200–20.

22 Allessie MA, Lammers WJEP, Bonke FIM, et al. Experimental evaluation of Moe's wavelet hypothesis of atrial fibrillation. In: Zipes DP, Jalife J, eds. *Cardiac Electrophysiology and Arrhythmias*. Grune & Stratton, Orlando, 1985: 265–75.

23 Gray RA, Pertsov AM, Jalife J. Incomplete reentry and epicardial breakthrough patterns during atrial fibrillation in the sheep heart. *Circulation* 1996; **94**: 2649–61.

24 Gray RA, Pertsov AM, Jalife J. Spatial and temporal organization during cardiac fibrillation. *Nature* 1998; **392**: 75–8.

25 Atienza F, Almendral J, Moreno J et al. Activation of inward rectifier potassium channels accelerates atrial fibrillation in humans: evidence for a reentrant mechanism. *Circulation* 2006; **114**: 2434–42.

26 Kumagai K, Khrestian C, Waldo AL. Simultaneous multisite mapping studies during induced atrial fibrillation in the sterile pericarditis model: insights into the mechanisms of its maintenance. *Circulation* 1997; **95**: 511–21.

27 Haissaguerre M, Jais P, Shah DC, et al. Spontaneous initiation of atrial fibrillation by ectopic beats originating in the pulmonary veins. *N Engl J Med* 1998; **339**: 659–66.

28 Jalife J, Berenfeld O, Skanes A et al. Mechanisms of atrial fibrillation: mother rotors or multiple daughter wavelets, or both? *J Cardiovasc Electrophysiol* 1998; **9**: S2–S12.

29 Ortiz J, Niwano S, Abe H, et al. Mapping the conversion of atrial flutter to atrial fibrillation and atrial fibrillation to atrial flutter: insights into mechanisms. *Circ Res* 1994; **74**: 882–94.

30 Ikeda T, Wu TJ, Uchida T, et al. Meandering and unstable reentrant wave fronts induced by acetylcholine in isolated canine right atrium. *Am J Physiol* 1997; **273**: H356–H370.

31 Lewis T. *The Mechanism and Graphic Registration of the Heart Beat*. 3rd ed. Shaw & Sons, London, 1925.

32 Scherf D. Studies on auricular tachycardia caused by aconitine administration. *Proc Soc Exp Biol Med* 1947; **64**: 233–39.

33 Schuessler RB, Grayson TM, Bromberg BI, et al. Cholinergically mediated tachyarrhythmias induced by a single extrastimulus in the isolated canine right atrium. *Circ Res* 1992; **71**: 1254–67.

34 Starobin JM, Zilberter YI, Rusnak EM, et al. Wavelet formation in excitable cardiac tissue: the role of wavefront–obstacle interactions in initiating high-frequency fibrillatory-like arrhythmias. *Biophys J* 1996; **70**: 581–94.

35 Cabo C, Pertsov AM, Davidenko JM, et al. Vortex shedding as a precursor of turbulent electrical activity in cardiac muscle. *Biophys J* 1996; **70**: 1105–11.

36 Manyari DE, Patterson C, Johnson D, et al. Atrial and ventricular arrhythmias in asymptomatic active elderly subjects: correlation with left atrial size and left ventricular mass. *Am Heart J* 1990; **119**: 1069–76.

37 Cristal N, Peterburg I, Szwarcberg J. Atrial fibrillation developing in the acute phase of myocardial infarction: prognostic implications. *Chest* 1976; **70**: 8–11.
38 Murgatroyd FD, Camm AJ. Atrial arrhythmias. *Lancet* 1993; **341**: 1317–22.
39 Ravelli F, Allessie M. Effects of atrial dilatation on refractory period and vulnerability to atrial fibrillation in the isolated Langendorff-perfused rabbit heart. *Circulation* 1997; **96**: 1686–95.
40 Bode F, Katchman A, Woosley RL, et al. Gadolinium decreases stretch-induced vulnerability to atrial fibrillation. *Circulation* 2000; **101**: 2200–05.
41 Kalifa J, Jalife J, Zaitsev AV, et al. Intra-atrial pressure increases rate and organization of waves emanating from the superior pulmonary veins during atrial fibrillation. *Circulation* 2003; **108**: 668–71.
42 Lin WS, Prakash VS, Tai CT, et al. Pulmonary vein morphology in patients with paroxysmal atrial fibrillation initiated by ectopic beats originating from the pulmonary veins: implications for catheter ablation. *Circulation* 2000; **101**: 1274–81.
43 Yamane T, Shah DC, Jais P, et al. Dilatation as a marker of pulmonary veins initiating atrial fibrillation. *J Intervent Card Electrophysiol* 2002; **6**: 245–49.
44 Sanders P, Hocini M, Jais P, et al. Characterization of focal atrial tachycardia using high-density mapping. *J Am Coll Cardiol* 2005; **46**: 2088–99.
45 Hsu LF, Jais P, Hocini M, et al. High-density circumferential pulmonary vein mapping with a 20-pole expandable circular mapping catheter. *Pacing Clin Electrophysiol* 2005; **28**: S94–S98.
46 Sarmast F, Kolli A, Zaitsev A, et al. Cholinergic atrial fibrillation: I-K, I-ACh gradients determine unequal left/right atrial frequencies and rotor dynamics. *Cardiovasc Res* 2003; **59**: 863–73.
47 Kabell G, Buchanan LV, Gibson JK, et al. Effects of adenosine on atrial refractoriness and arrhythmias. *Cardiovasc Res* 1994; **28**: 1385–89.
48 Belardinelli L, Shryock JC, Song Y, et al. Ionic basis of the electrophysiological actions of adenosine on cardiomyocytes. *FASEB J* 1995; **9**: 359–65.
49 Khositseth A, Clapham DE, Ackerman MJ. Intracellular signaling and regulation of cardiac ion channels. In: Zipes DP, Jalife J, eds. *Cardiac Electrophysiology: From Cell to Bedside*. W.B. Saunders, Philadelphia, 2004: 33–41.
50 Pappone C, Rosanio S. (2004) Pulmonary vein isolation for atrial fibrillation. In: Zipes DP, Jalife J, eds. *Cardiac Electrophysiology: From Cell to Bedside*. W.B. Saunders, Philadelphia: 1039–52.
51 Haissaguerre M, Sanders P, Hocini M, et al. Changes in atrial fibrillation cycle length and inducibility during catheter ablation and their relation to outcome. *Circulation* 2004; **109**: 3007–13.
52 Kalifa J, Klos M, Zlochiver S, et al. Endoscopic fluorescence mapping of the left atrium: a novel experimental approach for high-resolution endocardial mapping in the intact heart. *Heart Rhythm* 2007; **4**: 916–24.
53 Rostock T, Rotter M, Sanders P, et al. High-density activation mapping of fractionated electrograms in the atria of patients with paroxysmal atrial fibrillation. *Heart Rhythm* 2006; **3**: 27–34.
54 Nademanee K, McKenzie J, Kosar E, et al. A new approach for catheter ablation of atrial fibrillation: mapping of the electrophysiologic substrate. *J Amer Coll Cardiol* 2004; **43**: 2044–53.

35

CHAPTER 35

Role of Mapping in Channelopathies: Brugada Syndrome, Long-QT Syndrome, and Idiopathic VF

Sergio Richter, MD, *Pedro Brugada,* MD, PhD

Free University of Brussels (UZ Brussel) VUB, Brussels, Belgium

Summary

Recent advances in genetics and molecular biology have made it possible to define a series of new diseases leading to cardiac arrhythmias: the channelopathies. These diseases affect the structure and function of cardiac ion channels and result in atrial and ventricular tachyarrhythmias, disorders of impulse formation and conduction defects. These arrhythmogenic disorders are hereditary and in general occur in individuals with a structurally normal heart. Because there is no discrete lesion (like in myocardial infarction) as substrate for the arrhythmias, mapping in channelopathies is confronted with very specific problems. The mechanisms of these arrhythmias and the challenges encountered while trying to map them are discussed in this chapter.

Introduction

With an estimated overall incidence of 0.1–0.2% per year, sudden cardiac death (SCD) is a leading cause of mortality in the developed world [1, 2]. Ventricular fibrillation (VF) is the most common underlying mechanism of SCD. Whereas the majority of SCD victims have known or previously unrecognized structural heart disease, in approximately 5–10% of out-of-hospital SCD survivors, no cardiac or extracardiac abnormalities can be identified [3]. Survivors of electrocardiographically documented VF with an apparently normal heart have therefore long been classified as having idiopathic VF [3, 4].

However, with advanced progress in molecular biology, a substrate of so-called idiopathic VF has been defined. The characterization of inherited disorders has provided important insights into the molecular pathogenesis of cardiac arrhythmias. Four inherited arrhythmogenic disorders caused by ion channelopathies due to mutations in 14 different genes have been identified and linked to SCD in individuals without structural heart disease [5, 6]. Once diagnosed, a channelopathy should therefore be considered a different entity from a primary electrical disease and not a subgroup of idiopathic

Cardiac Mapping, Third Edition Edited by Mohammad Shenasa, Gerhard Hindricks, Martin Borggrefe, and Günter Breithardt
 ISBN: 978-1-405-17572-2

VF. The most common and best-studied ion channelopathies are the congenital long-QT syndromes (LQTS) and Brugada syndrome. At present, cardiac mapping in channelopathies is chiefly directed at experimentally investigating the underlying arrhythmogenic substrate and arrhythmia mechanism, and clinically targeting focal trigger sources to guide catheter ablation.

Mapping of the Arrhythmogenic Substrate

Clinical observations based on the electrocardiogram indicate that human VF is almost always preceded by a mono- or polymorphic ventricular tachycardia (VT) lasting several beats before degenerating to VF [7]. What had originally been described as the "early tachysystolic stage of VF" [8] was later demonstrated to correspond to a single spiral or figure-of-eight reentrant wavefront [9, 10].

The onset of human VF can generally be characterized by a triggering event initiating VT and subsequent degeneration of VT to VF [11]. A critical prerequisite for a triggering beat to initiate reentry is that an electrical wave propagating through cardiac tissue breaks locally. Fibrillation occurs when a localized wavebreak induces reentry and triggers a cascade of new wavebreaks [12, 13]. However, in structurally normal ventricles, physiological triggers such as spontaneous premature ventricular contractions (PVCs) are usually not able to generate localized wavebreak with sufficient adjacent excitable tissue to initiate functional (scroll wave) reentry [9].

Preexisting electrophysiological tissue heterogeneity plays a key role in inducing localized wavebreak and reentry in the structurally intact heart, and can be due to electrical remodeling, heterogeneous autonomic innervation, cardiotropic drug effects, or genetic abnormalities [13]. In a variety of inherited ion channelopathies including long-QT syndromes and Brugada syndrome, spatial dispersion of refractoriness within the ventricular wall is thought to underlie the substrate of electrophysiological tissue heterogeneity which predisposes to the development of potentially life-threatening reentrant ventricular arrhythmias when critically amplified [5]. In addition, localized anatomical tissue heterogeneity seems to be operative in at least some patients with Brugada syndrome [14, 15].

Brugada Syndrome

Experimental and clinical studies have provided mounting evidence that heterogeneity of ventricular repolarization and slow conduction contribute to the pathophysiology underlying Brugada syndrome [14–16]. Both of the proposed pathophysiological mechanisms strongly consider the right ventricular outflow tract (RVOT) as the utmost region of tissue heterogeneity providing the electrophysiological substrate of right precordial ST-segment elevation and ventricular arrhythmias [14, 15]. A new hypothesis on the pathophysiology of Brugada syndrome has recently been introduced and is based on abnormal expression of cardiac neural crest cells in heart development, particularly in the morphogenesis of the RVOT [17]. Cardiac mapping in Brugada syndrome aims therefore at this anatomo-functional region of the right ventricle (RV) to enhance understanding of the underlying mechanisms.

Heterogeneity of Ventricular Repolarization

The linkage of the Brugada phenotype to mutations in a gene encoding the cardiac sodium (Na) channel α-subunit (SCN5A) has paved the way to understanding the cellular basis and arrhythmia mechanisms of Brugada syndrome [18]. Most recently, more than 100 mutations in SCN5A have been linked to the syndrome; however, no more than 30% of phenotypically affected individuals harbor SCN5A mutations [19, 20]. Those SCN5A mutations studied in expression systems have shown to result in functional reduction in peak Na current (INA).

Based on their seminal experimental work involving arterially perfused RV wedge preparations, Yan and Antzelevitch [21] proposed that reduction in INA superimposed on intrinsic transmural differences in the transient outward potassium current Ito creates a steep voltage gradient across the ventricular wall by heterogeneous loss of action potential (AP) dome and shortening of the AP in the RV epicardium.

Both transmural and epicardial dispersion of repolarization develops as a consequence. The marked

imbalance of currents allows for local reexcitation of RVOT epicardial loss-of-dome sites by neighboring areas with prolonged AP duration (APD) producing functional, so-called phase 2 reentry [22]. Phase 2 reentry may lead to the development of a closely coupled extrasystole triggering polymorphic ventricular arrhythmia [21, 23]. Support for this hypothesis relies predominantly on animal models of Brugada syndrome involving arterially perfused RV wedge preparations [16, 21, 24, 25].

Advanced high-resolution optical mapping techniques provide an important tool for detailed study of electrical heterogeneity of APs and activation sequences on the endocardial and epicardial surface in RV wedge preparations [25, 26]. Briefly, perfused wedges of RV myocardium are placed in an imaging chamber, and after staining with a voltage-sensitive dye the imaged surface of the wedges is stabilized against a flat optical window. Fluorescent light from the excited wedges is filtered and focused onto a photodiode array with image intensifiers. The voltage of the optical signal recorded at each site is automatically displayed in color and plotted as an isopotential map. Transmembrane optical APs can be recorded, AP duration measured, depolarization and repolarization contour maps constructed, and dispersion of repolarization calculated.

Using this optical mapping technique, Aiba and colleagues [25] have most recently studied cellular mechanisms for trigger and maintenance of polymorphic VT and VF in an experimental model of Brugada syndrome. Repolarization contour maps demonstrated that in Brugada-simulated conditions, spontaneous phase 2 reentry-induced extrasystoles preferentially originate from small RV epicardial sites having a maximal gradient of repolarization (Figure 35.1).

Optical isopotential maps displaying the epicardial distribution of loss-of-dome and restore-of-dome AP areas during impulse propagation showed that phase 2 reentry resulted from reexcitation of a loss-of-dome (early repolarization) site by a sufficiently large adjacent restore-of-dome area with activation propagating around a refractory region of the epicardium (Figure 35.2). Importantly, depolarization disturbance was not associated with the occurrence of phase 2 reentry-induced extrasystoles

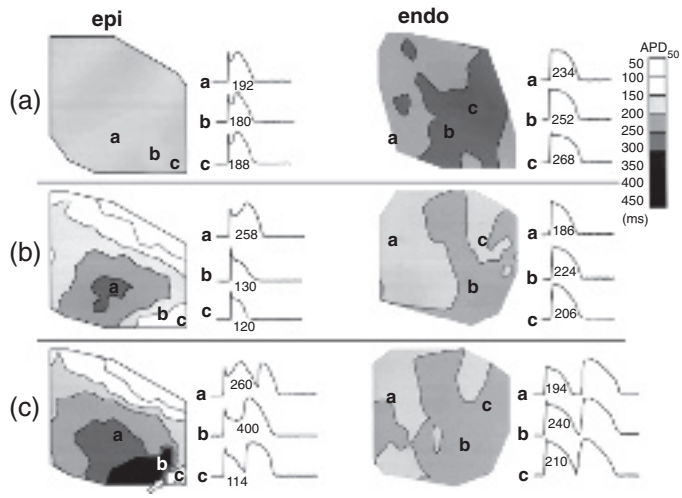

Figure 35.1 Action potential duration (APD) measured from optical APs at 50% repolarization (APD_{50}) contour map on the right ventricular (RV) epicardium (epi) and endocardium (endo) in a RV wedge preparation model of Brugada syndrome. (a) Control conditions show almost homogeneous endo- and epicardial APs. (b) Brugada-simulated conditions create marked AP heterogeneity in the epicardium but not endocardium. (c) Phase 2 reentry originates from a small RV epicardial area with maximal gradient of repolarization (arrow). Endocardial APs are less heterogeneous under conditions leading to epicardial phase 2 reentry. Reprinted with permission from Ref. 25.

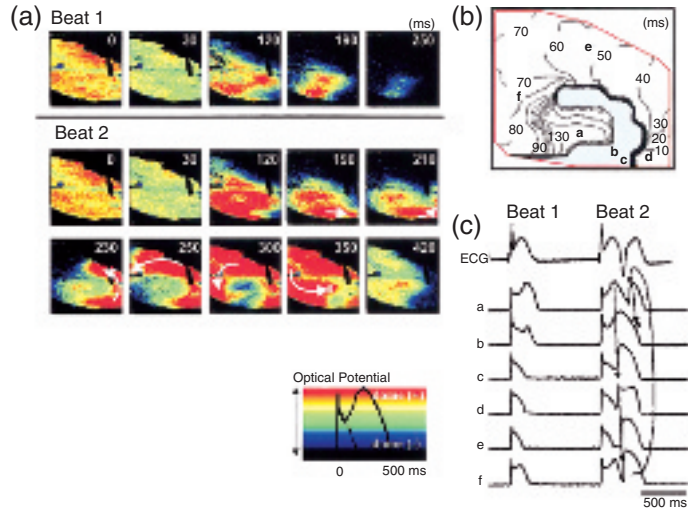

Figure 35.2 Optical isopotential maps representing the epicardial distribution of loss-of-dome and restore-of-dome action potential (AP) areas during propagation of beats with (#2) and without (#1) phase 2 reentry in a RV wedge preparation model of Brugada syndrome (a). Depolarization map (b) and optical APs (c) at each epicardial site (a)–(f) demonstrate that phase 2 reentry results from reexcitation of a loss-of-dome site (d) with activation propagating around a refractory region of the epicardium. Reprinted with permission from Ref. 25.

but with its susceptibility to ventricular fibrillation. Epicardial depolarization maps obtained during endocardial pacing showed remarkable conduction delay in wedges with episodes of VF.

Unlike in nonsustained polymorphic VT, spatial phase analysis of VF episodes revealed that the initial phase 2 reentry wave broke up into multiple wavelets at epicardial sites of delayed conduction (Figure 35.3). Simultaneous activation mapping of the endo- and epicardial surface in another Brugada syndrome RV wedge preparation model similarly demonstrated a close correlation between epicardial origin of the initiating spontaneous reentry beat and a localized area with a short recovery time [24] (Figure 35.4). However, the epicardium was not always actively involved in subsequent reentrant arrhythmias, which were localized to either the epi- or endocardial region with passive activation of the other, suggesting the presence of conduction delay or block within or between epi- and/or endocardial tissue.

These experimental findings not only support the hypothesis that a steep repolarization gradient in the RV epicardium but not the endocardium plays a key role in initiating phase 2 reentry, but also provide important insights into the role of slow conduction in the maintenance of ventricular reentry in Brugada syndrome. However, validation of spatial dispersion of ventricular repolarization and phase 2 reentry in human myocardium is challenging, because it requires simultaneous endocardial and epicardial electrogram recording.

Support for this hypothesis is chiefly limited to a small study of monophasic AP (MAP) recordings in three Brugada patients undergoing open chest surgery [27]. Simultaneous endo- and epicardial MAP recordings from the RVOT revealed prolonged and abnormal spike-and-dome APs at epicardial but not endocardial sites (Figure 35.5). Although the resulting transmural dispersion of repolarization related to the clinically observed ST-segment elevation, abbreviated loss-of-dome epicardial APs, however, were not present. Thus, direct evidence of an electrophysiological substrate for phase 2 reentry in humans is still lacking

Slow Conduction

Considering that Brugada syndrome is an inherited channelopathy causing sodium channel dysfunction, sufficient functional reduction in INA is not only expected to impact on AP shape and duration but also on conduction velocity, amplifying both dispersion of ventricular repolarization and conduction slowing within the heart [28, 29]. In

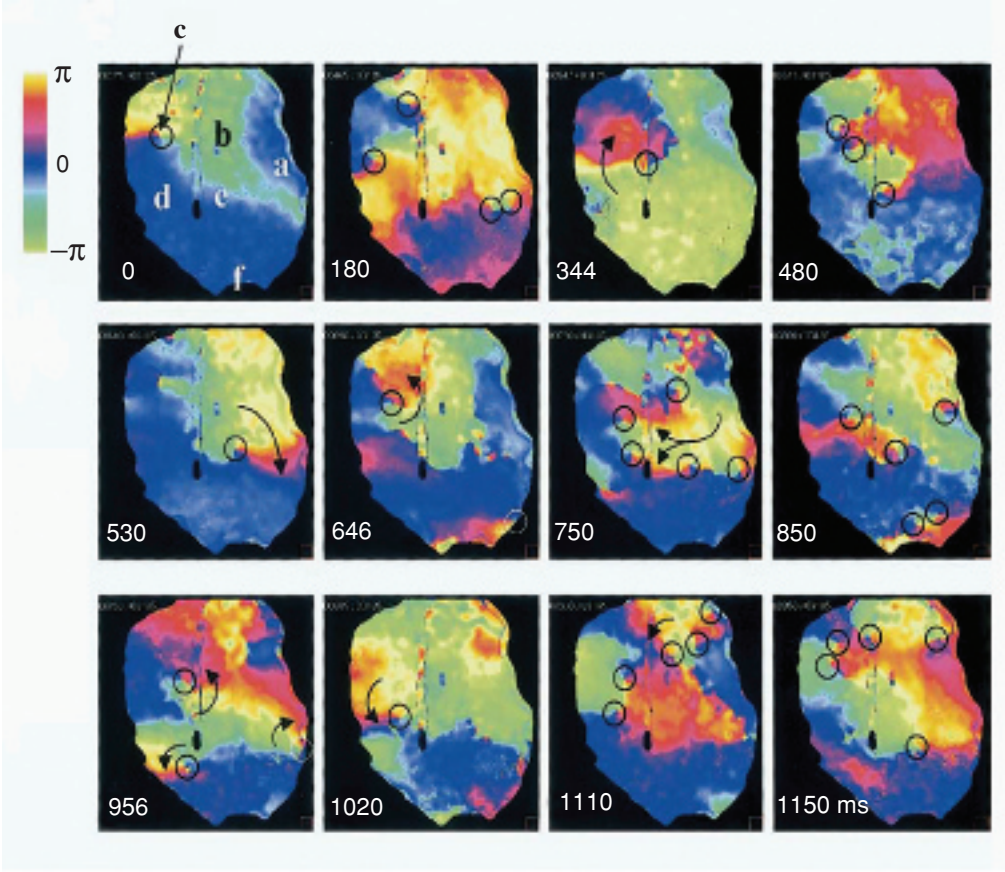

Figure 35.3 Spatial phase analysis of ventricular fibrillation triggered by epicardial phase 2 reentry in a RV wedge preparation model of Brugada syndrome. Optical APs are selected from epicardial sites (a)–(f) indicated on the first phase movie image. Initial phase 2 reentry (site c) breaks up into multiple wavelets at epicardial sites of delayed conduction (open circles), detected by crowding of isochrones on the depolarization map (not shown). Modified and reprinted with permission from Ref. 25.

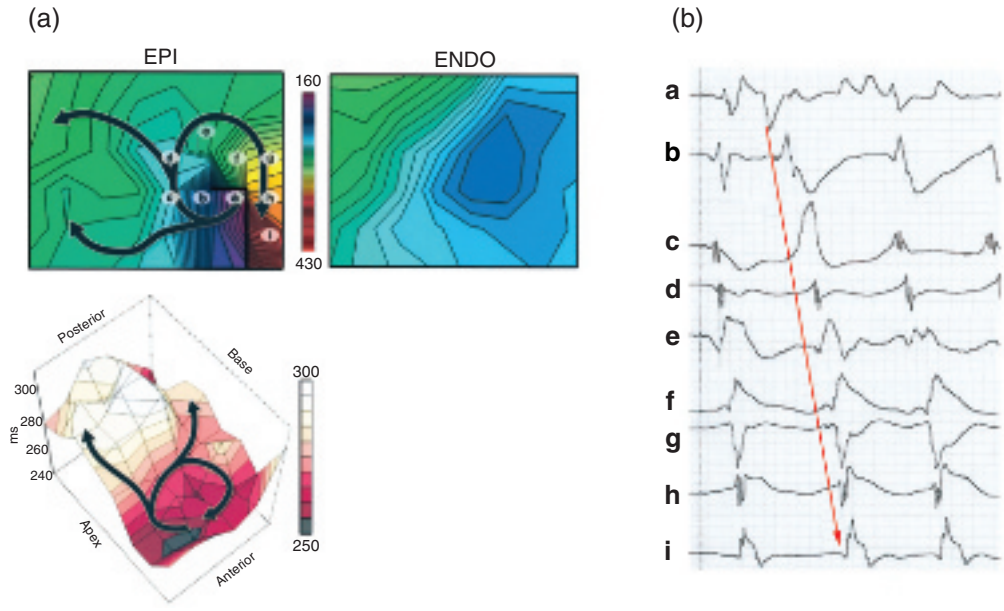

Figure 35.4 Relation of epicardial origin of a spontaneous VT triggering beat to local recovery time in a RV wedge preparation model of Brugada syndrome. (a) Epicardial (EPI) and endocardial (ENDO) activation maps show that the initiating reentrant beat originates from the epicardial site *a* in the nadir of local recovery time. (b) Bipolar electrograms recorded at sites (a)–(i) indicated on the epicardial activation map. Modified and reprinted with permission from Ref. 24.

fact, some SCN5A mutations have been shown to cause familial cardiac conduction disease [30–33]. It is therefore not surprising that conduction defects are frequently observed in patients with Brugada syndrome, particularly in those linked to SCN5A mutations [34]. Electrocardiographic signs of general conduction slowing include PR prolongation, QRS widening, fascicular or right bundle-branch block, and sinus node dysfunction [14, 15, 35, 36].

The close correlationship between PR prolongation and HV conduction delay in genotyped individuals further supports the impact of the

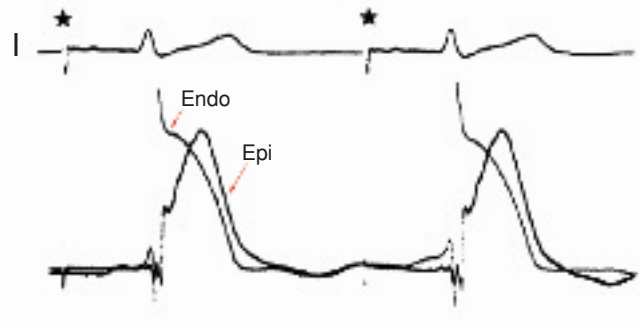

Figure 35.5 Simultaneous endocardial (endo) and epicardial (epi) monophasic action potential (MAP) recordings from the right ventricular outflow tract and surface electrocardiographic lead I during open chest surgery in a patient with Brugada syndrome. The epicardial MAP recording reveals prolonged and abnormal spike-and-dome APs compared with the endocardial MAP. Note the absence of abbreviated loss-of-dome epicardial APs, lacking direct evidence of an electrophysiological substrate for phase 2 reentry in humans. KEY: * = pacing spikes. Modified and reprinted with permission from Ref. 27.

sodium channel on conduction [34, 36, 37]. Moreover, INA reduction has been linked to cellular structural abnormalities and degenerative changes including interstitial fibrosis [38, 39], which may contribute to intra- and interventricular conduction delay. However, only a minority of patients with Brugada syndrome harbor a known SCN5A mutation [19, 20].

Although involvement of other genes still awaiting discovery are expected, sodium channel dysfunction is probably not the only key player in many phenotypically affected individuals. It has been appreciated that critical degrees of conduction slowing predispose to reentrant arrhythmias and represent a final common pathway to VF susceptibility [40]. There is now strong evidence that slow conduction in the RVOT is critically involved in the electrophysiological mechanisms of ST-segment elevation and arrhythmogenesis in Brugada syndrome, regardless of the presence of a sodium channel mutation [41–44].

Clinical observations that typical ST-segment elevation is invariably confined to the right precordial leads at the fourth and higher intercostal spaces [14, 15], and that triggering premature beats frequently have left bundle-branch block, inferior axis deviation [45] support the RVOT region as the substrate of tissue heterogeneity. Based on the concept of localized conduction delay in the RVOT, the group of Wilde proposed that membrane potential gradients between RVOT (delayed) and surrounding RV myocardium (early) contribute to right precordial ST-segment elevation and ventricular reentry [15].

This qualitative model derives from the mechanism thought to cause ST-segment elevation and reentrant arrhythmias in regional ischemia where greatly different membrane potentials exist between ischemic and nonischemic zones [46, 47]. Evidence supporting this hypothesis comes from several clinical studies on mapping of delayed activation and conduction slowing to the RVOT [41–43, 48, 49].

Body surface potential mapping (BSPM) is a noninvasive tool that allows detailed analysis of potential distributions on the thorax as to activation and recovery independently [50]. BSPM measures of the spatial distribution and amplitude of ST-segment elevation in Brugada syndrome mapped the location of maximum amplitude to chest areas reflecting the RVOT [48, 49, 51]. Ventricular activation time maps based on BSPM localized conduction delay to the upper right anterior chest overlying the RVOT [49].

It is noteworthy that delayed repolarization detected by prolonged activation recovery intervals (ARIs) appeared secondary to conduction delay in the same area. Similarly, *R*-wave isochrone maps obtained from BSPM revealed conduction delay in the RV anterior wall and the outflow tract in patients with late *r′* waves and ST-segment elevation in V1 and V2, but repolarization detected by QRST integral maps was similar in conditions with and without ST-segment elevation [41].

In addition to BSPM, signal-averaged electrocardiogram (SAE) recording enables detection of delayed ventricular activation by late potentials (LPs), which are frequently prevalent in Brugada syndrome, particularly in patients with spontaneous or inducible VF [41, 52–55]. Hisamatsu et al. [48] integrated 48 unipolar signal-averaged electrocardiograms into a 87-lead body surface map and showed that the site of remarkable delayed potentials coincided with the area of maximum ST-segment elevation mapped to the RVOT. However, direct mapping of the RVOT epicardial surface is demanding in in situ human hearts.

Nagase et al. [42] elegantly mapped delayed epicardial activation to the RVOT using an electrical guidewire introduced into the right coronary conus branch (Figure 35.6a). Delayed ventricular potentials recorded epicardially were not seen during simultaneous mapping at endocardial RVOT sites, but corresponded well to late potentials on signal-averaged electrocardiogram recordings (Figure 35.6b). Additional clinical evidence for conduction slowing derives indirectly from tissue Doppler imaging findings of delayed RV contraction correlating with the magnitude of ST-segment elevation [43].

Although late ventricular potentials and contractile dysfunction commonly represent delayed myocardial activation secondary to structural defects, both may alternatively be explained by a delayed second upstroke of the epicardial AP or phase 2 reentry [56]. Because of the lack of clinically detectable structural abnormalities, linkage to SCN5A mutations and known effects of sodium channel blockers, Brugada syndrome has long been accepted to

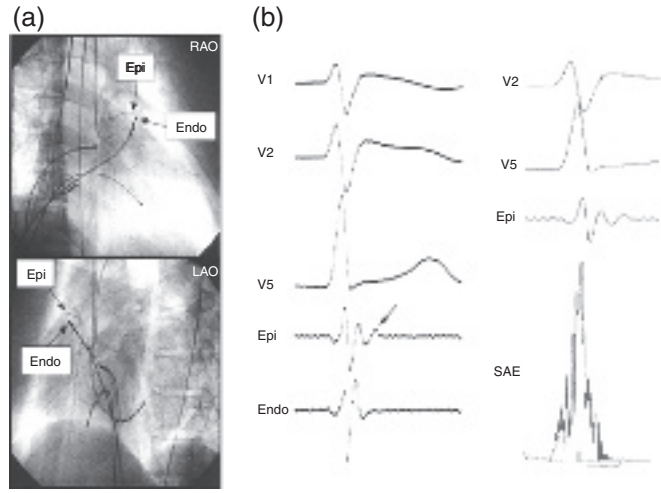

Figure 35.6 Epicardial mapping of the right ventricular outflow tract (RVOT) using a electrical guidewire introduced into the conus branch of the right coronary artery. (a) Fluoroscopic right anterior oblique (RAO) and left anterior oblique (LAO) views show the position of the epicardial guidewire (Epi) and quadripolar mapping catheter at the corresponding endocardial site (Endo). (b) Surface electrocardiogram leads V1, V2, and V5, intracardiac electrograms from the RVOT epicardium (Epi) and endocardium (Endo), and signal-averaged electrocardiogram (SAE). A delayed ventricular potential (arrow) is present at the epicardial but not endocardial recording site that corresponds well to the late potentials recorded on signal-averaged electrocardiograms. Filtered QRS = 128 msec; root mean square voltage of terminal 40 msec = 4.5 μV; duration of low-amplitude signals <40 μV = 61 msec). Modified and reprinted with permission from Ref. 42.

constitute a functional rather than structural defect [16, 56]. However, the delayed activation restricted to the RVOT strongly denotes the presence of a preexisting regional different substrate in the RV.

In this context, electrical uncoupling may play an important role in both conduction slowing and transmural heterogeneity. Potential subclinical anatomic substrates leading to electrical uncoupling in the Brugada syndrome are interstitial fibrosis, primarily or secondary to INA reduction [38, 39], and/or gap junction defects secondary to inhomogenous connexin distribution or ectopic excitable tissue in the RVOT [17, 57, 58].

Most recently, elegant cardiac mapping of an explanted heart from a genotyped Brugada patient has been performed in in-situ-like conditions, providing intriguing evidence in favor of the delayed-activation concept [44].

High-density activation mapping using multielectrode recordings positioned at endo- and epicardial right and left ventricular sites revealed crowding of isochrones in the RVOT indicative of slow conduction (Figure 35.7a). Interestingly, VF-initiating beats arose from RV endo- and not epicardium as it would be expected with phase 2 reentry, and displayed fractionated endocardial electrograms. In addition, abnormal (broad) restitution of propagation was found in the RVOT, with incremental conduction slowing occurring over a wide range of coupling intervals (Figure 35.7b).

Moreover, ECG computer simulation based on 3D activation maps [59] related conduction delay in the RVOT to lifetime recorded ECG abnormalities in leads V1–V3. Arguing further against heterogeneity of action potential duration as the principal underlying mechanism, RVOT cross-recordings of MAP duration did not show a significant transmural repolarization gradient at any paced cycle length.

Genetic (SCN5AmtG1935S → enhanced slow inactivation) and histological findings (RV fibrosis) obtained in this study support the proposed link between INA reduction and degenerative changes in RV myocardial architecture [38, 39]. However, it is tempting to speculate if INA reduction comes first—the chicken or the egg. Enhanced INA reduction may promote development of interstitial fibrosis and/or superimpose on primary subclinical

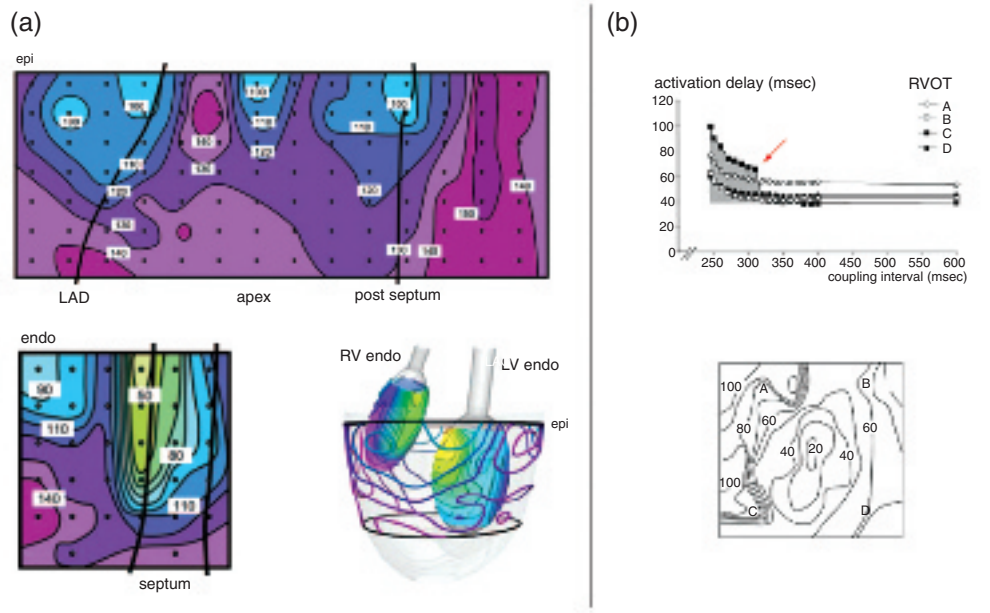

Figure 35.7 Activation mapping in an explanted heart from a genotyped patient with Brugada syndrome. (a) High-density activation mapping using multielectrode recordings positioned at endocardial (endo) and epicardial (epi) right ventricular (RV) and left ventricular (LV) sites reveals crowding of isochrones at the endocardial RV outflow tract (RVOT) indicative of slow conduction. (b) Restitution of propagation is abnormal in the RVOT with incremental conduction slowing occuring over a wide range of coupling intervals (upper panel). At the RVOT site (c), where crowding of isochrones is present (lower panel), a sudden increase in conduction time occurs at a coupling interval of 320 msec (arrow). Modified and reprinted with permission from Ref. 44.

structural abnormalities in the RVOT unmasking the Brugada syndrome phenotype.

Considering the disease to be a progressive process, both assumptions may explain why the spontaneous phenotype is rarely observed in children and adolescents and why the first arrhythmic event typically manifests at middle age. Potential underlying mechanisms for primary structural (micro-) derangements are not (yet) known. Abnormal expression of cardiac neural crest cells in myocardial development of the RVOT has most recently been brought to attention [17]. Developmental remnants of node-like cells in the RVOT [60, 61] or genetically determined nonphysiological regression of RVOT myocardium are further candidates.

Long-QT Syndrome

Congenital long-QT syndrome is an inherited disorder caused by several mutations in at least 10 genes encoding ion channel, anchoring, or caveolin proteins involved in cellular repolarization [5]. Despite genotype-related differences in phenotype, the final common pathway is AP prolongation and impaired repolarization reserve due to reduction in net repolarization current by either enhancing depolarization (sodium, calcium) or reducing repolarization (potassium) currents. There is convincing evidence that both early afterdepolarizations (EADs) and spatial dispersion of ventricular repolarization play a causative role in LQTS-associated arrhythmogenesis [62–65].

While prolongation of ventricular repolarization predisposes to the generation of secondary calcium (Ca^{2+}) -triggered depolarizations during the plateau or early repolarization phase of the AP [66, 67], an underlying substrate of inhomogeneous ventricular repolarization seems essential for a focal (EAD-triggered) premature beat to initiate and maintain functional reentry [68–70]. Intrinsic electrical heterogeneity can critically be amplified by ion channel mutations (congenital forms), pharmacological agents, or clinical conditions (aquired

forms) that reduce net repolarizing current leading to action potential duration prolongation in preferential areas within the ventricular wall (M and Purkinje cells) [65]. The resulting marked spatial dispersion of action potential duration creates pockets of inexcitable myocardium secondary to extended refractory periods that form regions of functional block and promote torsades de pointes (TdP) polymorphic VT [68–71].

Insights into the complex mechanisms of long-QT–related arrhythmia predominantly derive from several experimental models of long-QT syndromes [72] involving different mapping strategies [68, 73–75], of which optical AP mapping and 3D mapping of activation recovery interval distribution are of particular importance. In addition to providing information detailing myocardial activation during torsades de pointes, these mapping techniques have the advantage of capturing the recovery process occurring over the course of a single reentrant cycle and elucidating its spatial and temporal relationship to activation [68, 76, 77].

MAP recording has been appreciated to explore localized myocardial activation and repolarization in intact hearts and used to evaluate the mechanism of torsades de pointes by identification of afterdepolarizations and increased dispersion of action potential duration [63, 74, 78–83]. Although the accompanying low spatial resolution limits detailed mapping of activation and recovery, MAP recording holds the great feature of direct visualization of EADs in human hearts or in vivo animal models of long-QT syndromes [83–85].

It has become clear that EAD-induced triggered activity plays a key role in torsades de pointes initiation [63, 64, 66, 86–88]. MAP studies have identified EADs occuring at spontaneous or stimulation-dependent initiation of torsades de pointes [63, 74, 81, 82]. However, it remains difficult to verify a causal relationship between the presence of EADs, EAD-triggered beats, and torsades de pointes. Moreover, MAP recording is hampered by a continuous shift in the site of origin of EADs and triggering beats and technical challenges to electrode stability and artefact registration [83].

Although some degree of controversy has been introduced as to whether EAD-triggered activity is crucial only for the TdP-initiating premature beat or also for maintenance of the arrhythmia by repetitive rapid firing from several foci [67, 68, 75], experimental studies using 3D activation mapping [71, 89–91] or optical mapping [69, 70] have demonstrated the reentrant nature of torsades de pointes based on increased spatial dispersion of ventricular repolarization.

In a landmark study using 3D mapping in a canine surrogate model for LQT3, El-Sherif and colleagues [71] have elegantly shown that the TdP-initiating beat arose from a subendocardial focal site and resulted in functional conduction block at sites with significant spatial dispersion of activation recovery interval, commonly between epicardial and mid-myocardial zones (Figure 35.8a).

The subsequent beats of torsades de pointes were due to reentrant excitation in the form of continuously varying scroll waves (Figure 35.8b). High-resolution 3D isochronal mapping of ventricular activation was performed using multiple extracellular unipolar electrograms obtained from 64 plunge needle electrodes placed throughout the ventricles (Figure 35.8a). Repolarization maps were constructed by electrogram analysis of 3D ARI distribution [68]. With use of optical AP mapping in a guinea pig model of LQT3, the group of El-Sherif [70] further investigated the contribution of spatial distribution of action potential duration and subendocardial focal activity to arrhythmogenesis in response to heart rate and endocardial cryoablation.

LQTS-simulated conditions in perfused intact hearts resulted in rate-dependent marked epicardial action potential duration dispersion and zones of nonuniform action potential duration gradients. These zones provided a substrate for functional conduction block and reentrant excitation when challenged by a spontaneous (EAD-triggered) premature beat arising from a subendocardial focus.

Importantly, endocardial cryoablation abolished spontaneous focal activity and reentrant arrhythmias, but the increased spatial dispersion of action potential duration persisted and could be challenged by a premature stimulus to induce ventricular reentry. Similarly, an experimental model of LQT1 in the canine perfused wedge preparation strongly supported the concept of EAD-induced extrasystole as trigger and dispersion of repolarization as substrate for torsades de pointes [65].

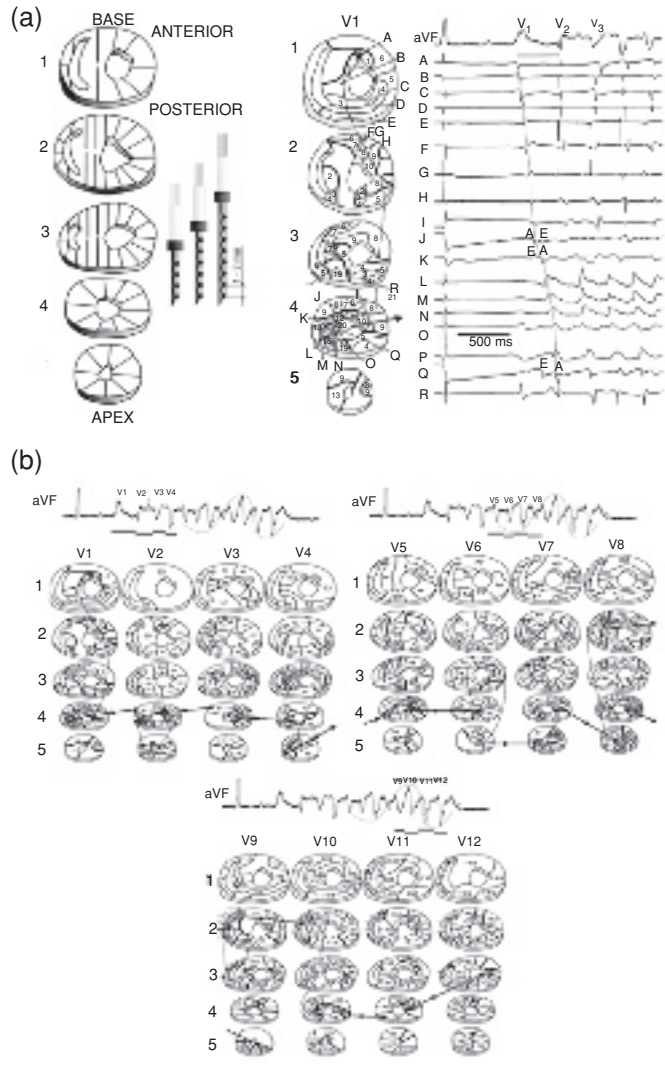

Figure 35.8 Tridimensional activation mapping in a canine surrogate model for long-QT syndrome. (a) Schematic 3D representation of a canine heart cut transversely into five sections labeled 1–5 from base to apex. Plunge needles with 4–8 unipolar electrodes spaced 1–2 mm apart are placed throughout both ventricles (left panel). Tridimensional activation pattern of initiation of a 12-beat nonsustained polymorphic ventricular tachycardia. V1–V3 refer to the first three tachycardia beats. Activation is represented as closed isochrone contours of 20 msec labeled as a tenth of the value to facilitate analysis of the activation pattern. Heavy solid lines represent arcs of functional conduction block. The triggering beat (V1) arises as a focal subendocardial activity (asterisk). From the site of earliest activation, the wavefront spreads in a circuitious route (dashed arrow). Local electrograms selected along the reentrant pathway (A to R, as denoted on the activation map) illustrate continuous diastolic bridging during the first reentrant cycle of 400 msec. Multicomponent or fractionated electrograms are recorded from areas of crowding isochrones (right panel). (b) Continuous 3D activation pattern of the arrhythmia demonstrates that all subsequent beats (V2–V12) are due to reentrant excitation with varying configuration of the reentrant circuit. Note the twisting QRS morphology on the simulated surface lead aVF. Modified and reprinted with permission from Ref. 71.

Cooling the perfusate eliminated spontaneous EAD-triggered activity and torsades de pointes, while the presence of an underlying substrate for reentry in form of transmural dispersion of repolarization was demonstrated by the ability to easily induce torsades de pointes with a single extrastimulus from the epicardium. Three-dimensional activation and optical mapping localized the zones of steep spatial action potential duration gradients resulting in functional conduction block and reentrant excitation to epicardial and/or intramyocardial layers [68, 70, 71, 89]. These observations suggest a role of mid-myocardial (M) cells in development and facilitation of functional block and torsades de pointes in intact hearts.

Different electrophysiological and pharmacological properties of distinct cell types across the ventricular wall, particularly those of M cells, are well recognized in experimental conditions [92–94]. However, cell-to-cell electrotonic coupling in intact hearts is expected to attenuate the functional expression of electrical heterogeneity [95, 96]. Using optical AP mapping in a wedge preparation model of LQT2 with intact transmural cell coupling, the functional topography of M cells and their role in torsades de pointes have recently been investigated [69].

In response to bradycardia and/or d-sotalol, bands of M cells exhibited markedly prolonged repolarization that were mapped to mid-myocardial layers with extentions to either deep subepicardial or subendocardial sites. The complex distribution of M cells created zones of steep spatial gradients of repolarization and refractory borders leading to functional block and intramural reentry in response to a premature epicardial stimulus. Unfortunately, in this surrogate model of LQT2, spontaneous triggered activity was suppressed by cooling and could therefore not be mapped to a specific site.

Although in vitro experiments have demonstrated EAD-triggered activity in isolated M cells and Purkinje fibers but other cell types as well [88], detailed mapping of intact hearts in different long-QT syndrome models almost consistently revealed a subendocardial (Purkinje) focal origin of the spontaneous TdP-triggering beat [68, 70, 71, 89]. However, using optical mapping of APs and intracellular Ca^{2+} in a rabbit surrogate model of LQT2, Ca^{2+}-triggered EAD activity has not only been mapped to the Purkinje network but also to non-endocardial sites [67]. Notwithstanding, evidence is convincing that both EAD-mediated triggered activity and functional reentry contribute to the genesis of torsades de pointes, but the exact arrhythmia mechanism may vary depending on the experimental or animal model used and the type of underlying ionic abnormality.

Catheter Mapping of Focal Trigger Sources

In clinical practice, the role of mapping in channelopathies and idiopathic VF consists in conventionally targeting and guiding ablation of focal sources of PVCs that trigger polymorphic VT or VF, irrespective of the underlying arrhythmogenic substrate.

Optical mapping studies have shown that activation in VF can occur as a localized, quasi-focal, dominant frequency [97–100].

As with atrial fibrillation [101, 102], this so-called focal source (mother rotor) hypothesis posits that VF can be driven by a single focal source of repetitively activating dominant frequencies with fibrillatory conduction generating secondary multiple wavelet reentry in a critical mass of ventricular myocardium. Although optical mapping studies cannot be applied to in situ human myocardium to identify similar mechanisms in human VF, conventional clinical mapping and successful ablation have recently provided support for a crucial role of focal PVC triggers in a subgroup of patients with idiopathic VF [103–110] and ion channelopathies [111–113].

Common to all the reported patients with VF amenable to catheter ablation is the clinical presence of frequent isolated PVCs of similar or identical morphology and coupling interval to the first initiating beat of documented VF ("focal VF") (Figure 35.9). Catheter mapping revealed that focal PVC triggers preferentially originate from the RVOT in the Brugada syndrome, the distal Purkinje system in long-QT syndromes, and from both in idiopathic VF. Mapping techniques used to accurately localize the trigger source are the conventional ones established for mapping and ablation of focal nonsustained arrhythmias: (i) activation mapping using unipolar and/or bipolar recordings;

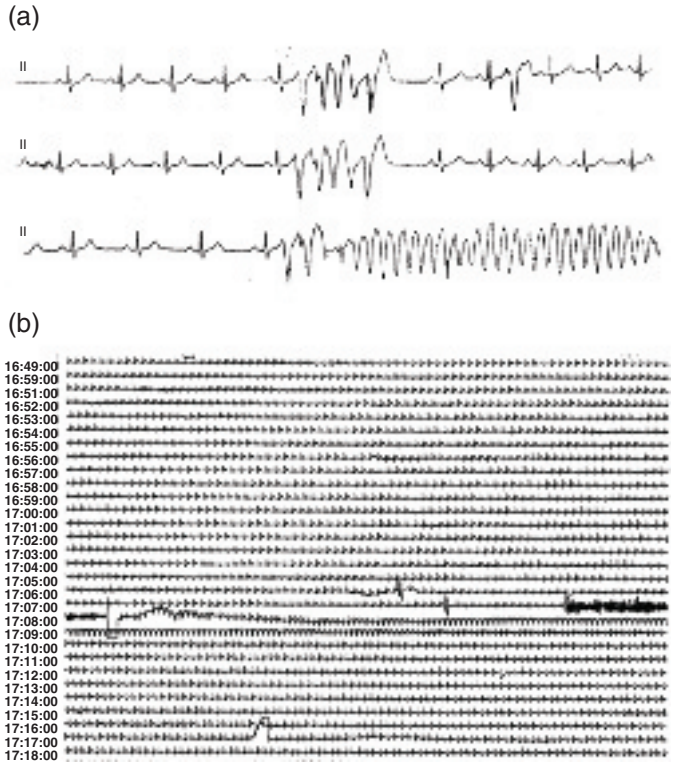

Figure 35.9 Premature ventricular beats (PVCs) of similar morphology and coupling interval to the first initiating beat of documented ventricular fibrillation (VF). (a) monitor registrations in a patient with idiopathic VF shows runs of nonsustained polymorphic ventricular tachycardia and an episode of VF initiated by PVCs of almost identical morphology. (b) Holter monitoring in a Brugada patient with implantable cardioverter defibrillator (ICD) reveals absence of PVCs except immediately prior to VF. The preceding isolated PVC couplets have the same features as the one initiating VF, subsequently treated by ICD shock therapy.

(ii) pace mapping; (iii) noncontact 3D mapping using a 64-electrode array balloon; and (iv) endocardial mapping using MAP recordings.

Mapping of RVOT-PVCs

Focal PVC triggers arising from the RVOT have successfully been localized and ablated by targeting the earliest endocardial electrogram relative to the onset of the ectopic QRS complex and/or the site of identical pace mapping [103, 104, 106, 109, 111], or by noncontact mapping of the earliest intracardiac activation [108, 112]. At successful ablation sites, the earliest electrogram preceded the QRS onset by 10–40 msec, and no specific discrete or slow potential was recorded [106, 109].

Less commonly, endocardial mapping of extracellular MAP recordings has been used to identify and ablate the site of early or delayed afterdepolarizations in arrhythmias due to triggered activity [83, 85, 114]. In patients with no structural heart disease and normal electrocardiogram, isolated PVCs and monomorphic VT arising from the RVOT are common and usually considered benign [115]. These arrhythmias typically have a left bundle-branch block, inferior axis deviation, and can safely be ablated with high success rates [116].

However, because the reported idiopathic VF patients with monofocal triggers mapped to the RVOT represent a highly selected cohort of VF survivors, the incidence of malignant idiopathic RVOT arrhythmias remains unknown. To discriminate malignant from benign idiopathic RVOT extrasystoles remains challenging and conflicting data exist about the role of the coupling interval in predicting malignant arrhythmias [106, 109, 117–119].

Short-coupled (<320 msec) premature beats in patients with structurally normal heart have been associated with spontaneous occurrence of non-pause-dependent polymorphic VT, syncope, and cardiac arrest, whereas long coupling intervals (>400 msec) have been typically seen in patients with benign RVOT arrhythmias [118–120]. In contrast, Noda et al. [109] observed long coupling intervals (409 ± 62 msec) in patients with idiopathic VF, which were not different from those with benign monomorphic RVOT-VTs. Moreover, Haïssaguerre

[106] and Viskin [119] reported a couple of patients with malignant polymorphic arrhythmias induced by relatively long-coupled (mean 350–355 msec) RVOT extrasystoles.

Similarly, inconclusive clinical observations on extrasystoles triggering polymorphic VT have been made in Brugada syndrome [41, 45, 111, 121–123]. PVCs are rarely recorded in patients with Brugada syndrome [41, 45] except immediately prior to onset of polymorphic VT/VF (Figure 35.9b) [121]. VF-preceding and initiating PVCs are almost identical and predominantly originate from the RVOT [45, 111, 112, 121, 122], the region hypothesized to provide maximal dispersion of refractoriness and/or slow conduction in Brugada syndrome.

Kakishita et al. [121] reported that 67% of documented VF episodes were preceded and triggered by similar isolated PVCs, and multiple episodes in same patients have shown to be initiated by similarly configurated and coupled PVCs [121, 122]. These findings suggest a site-specificity of focal triggers, the presence of which may reflect an acutely increased vulnerability of the RVOT myocardium. However, the absence of frequent (if any) spontaneous PVCs in Brugada syndrome is a major limitation to clinical mapping, rendering catheter ablation a rarity [111, 112].

Antzelevitch and colleagues [16, 21] proposed that subepicardial phase 2 reentry is the mechanism of triggering beats arising from the RVOT, but direct evidence of phase 2 reentry has not been obtained clinically. If phase 2 reentry is operative, one would expect short-coupled PVCs triggering polymorphic VT [21, 23]. However, in the vast majority of clinical studies, the mean coupling interval of initiating ectopies was rather long, usually exceeding 380 msec with QRS onset close to the end of the *T*-wave [45, 121, 122]. Only few reports demonstrated truly short-coupled (<320 msec) malignant PVCs in patients with Brugada syndrome supporting phase 2 reentry as a possible mechanism [123].

Mapping of Purkinje-Triggered PVCs

Another specific source of VF-triggering extrasystoles in patients with no demonstrable structural heart disease and normal electrocardiogram originates from the specialized intraventricular conduction system [105, 106, 110, 113]. Haïssaguerre et al. [106] reported their multicenter experience on clinical mapping and ablation of Purkinje-triggered PVCs in 23 patients with recurrent episodes of non-pause-dependent VF. The trigger source was localized by endocardial mapping of the earliest Purkinje activation during ectopy, and exceptionally by pace mapping if frequent spontaneous PVCs were absent.

An initial sharp potential of <10 msec duration that preceded the local myocardial electrogram by <15 msec during sinus rhythm was defined as a peripheral Purkinje potential. A Purkinje origin was identified if such a Purkinje potential preceded the local myocardial electrogram also during the target ectopy. The focal PVC triggers were equally found to originate from the right and left ventricular (LV) Purkinje system and had characteristically a short QRS duration (126 ± 18 msec). At successful ablation sites, the earliest peripheral Purkinje activation preceded the local myocardial electrogram by 38 ± 28 msec.

Importantly, at the same Purkinje site of the triggering PVC, conduction block or different conduction times and electrogram morphologies have been observed, particularly at LV Purkinje target sites (Figure 35.10a). In addition, repetitive beats of nonsustained polymorphic VT arising from a single mapping site were preceded by Purkinje potentials with variable conduction (15–120 msec) to the local myocardium (Figure 35.10b). The mechanism underlying these observations is speculation, multiple firing foci, limited foci with distinct wave propagation, or Purkinje–muscular reentry [124] may be operative.

Unlike results reported for triggering PVCs arising from the RVOT in Brugada syndrome and idiopathic VF, the coupling interval of Purkinje-triggered PVCs was pretty short (280 ± 26 msec), frequently resulting in the *R*-on-*T* phenomenon. The Purkinje network plays also an important role in the generation of malignant ventricular arrhythmias associated with long-QT syndromes. There is strong evidence that torsades de pointes is initiated by EADs [63, 64, 66, 86–88]. EADs can generate extrasystoles by reaching threshold potential. These EAD-induced triggered beats arise predominantly from the subendocardial Purkinje network [68, 71]. Its importance in initiating torsades de pointes has further been demonstrated by chemical or cryoablation of the endocardium eliminating spontaneous EAD-triggered extrasystolic

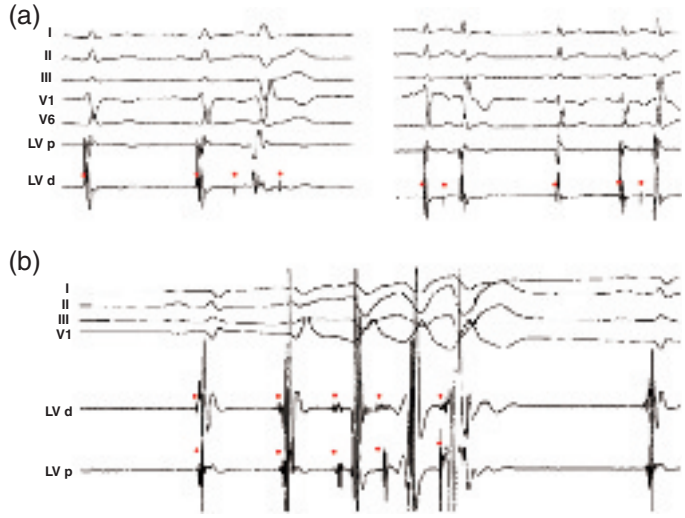

Figure 35.10 Endocardial catheter mapping of frequent Purkinje triggers in idiopathic ventricular fibrillation. Surface electrocardiogram leads I, II, III, V1, and V6 and intracardiac electrograms from the endocardial mapping electrode at successful ablation sites. (a) Morphologically different premature beats originating from the left ventricular (LV) Purkinje system are preceded by a sharp potential (asterisks) with varying conduction times or block to local myocardium. Note that the Purkinje potentials also precede sinus beats. (b) Repetitive beats of nonsustained polymorphic VT arising from a single mapping site are preceded by Purkinje potentials with variable conduction time. Modified and reprinted with permission from Ref. 106.

activity [70, 125]. Therefore, catheter mapping and focal endocardial ablation seems promising in patients with frequent isolated PVCs with similar morphology and coupling as the TdP-initiating beats.

However, as in patients with Brugada syndrome, PVCs are uncommon in long-QT syndromes remote from arrhythmic episodes, and the high efficacy of beta-blockers makes documentation of frequent isolated PVCs even more unlikely. This important practical limitation to mapping focal Purkinje triggers in long-QT syndromes is reflected by the very limited numbers of reported cases.

For instance, Haïssaguerre et al. [111] successfully mapped and ablated frequent Purkinje triggers of multiple morphology in three patients with a clinical diagnosis of long-QT syndromes. The mapping technique was identical to that described for Purkinje-triggered idiopathic VF. The earliest endocardial Purkinje potential during target PVC preceded the local myocardial activation by a mean of 34 ± 17 msec. Mapping during nonsustained polymorphic VT revealed Purkinje activity preceding each beat with varying Purkinje-to-muscle conduction times. These clinical observations support the notion that repetitive electrical discharges originating from unifocal sources in the distal Purkinje network may contribute to the genesis of VF in at least some patients with idiopathic VF and long-QT syndromes.

Conclusion

The major role of cardiac mapping in channelopathies lies in experimental and clinical investigation of the underlying electrophysiological substrate and arrhythmia mechanism. Mapping of focal trigger sources of VF has recently brought to practice with the important clinical implication of guiding catheter ablation to reduce the burden of VF episodes and device shocks or possibly cure focal idiopathic VF. However, the extent to which malignant focal triggers can be identified in patients with channelopathies and idiopathic VF is unknown, and long-term clinical experience is required to establish efficacy, safety, and clinical applicability of catheter-based mapping and ablation of focal VF.

Acknowledgement

We are greatly indebted to Carlo de Asmundis for his skilled technical assistance.

References

1 Myerburg RJ, Kessler KM, Castellanos A. Sudden cardiac death: epidemiology, transient risk, and intervention assessment. *Ann Intern Med* 1993; **119**: 1187–97.

2 Zipes DP, Wellens HJ. Sudden cardiac death. *Circulation* 1998; **98**: 2334–51.

3 Survivors of out-of-hospital cardiac arrest with apparently normal heart: need for definition and standardized clinical evaluation. Consensus Statement of the Joint Steering Committees of the Unexplained Cardiac Arrest Registry of Europe and of the Idiopathic Ventricular Fibrillation Registry of the United States. *Circulation* 1997; **95**: 265–72.

4 Viskin S, Belhassen B. Idiopathic ventricular fibrillation. *Am Heart J* 1990; **120**: 661–71.

5 Antzelevitch C. Heterogeneity and cardiac arrhythmias: an overview. *Heart Rhythm* 2007; **4**: 964–72.

6 Schulze-Bahr E. Arrhythmia predisposition: between rare disease paradigms and common ion channel gene variants. *J Am Coll Cardiol* 2006; **48**: A67–A78.

7 Kempf FC, Jr., Josephson ME. Cardiac arrest recorded on ambulatory electrocardiograms. *Am J Cardiol* 1984; **53**: 1577–82.

8 Wiggers CJ. Studies of ventricular fibrillation caused by electric shock: II. Cinematographic and electrocardiographic observations of the natural process in the dog's heart: its inhibition by potassium and the revival of coordinated beats by calcium. *Am Heart J* 1930; **5**: 351–365.

9 Chen PS, Wolf PD, Dixon EG, et al. Mechanism of ventricular vulnerability to single premature stimuli in open-chest dogs. *Circ Res* 1988; **62**: 1191–209.

10 Bonometti C, Hwang C, Hough D, et al. Interaction between strong electrical stimulation and reentrant wavefronts in canine ventricular fibrillation. *Circ Res* 1995; **77**: 407–16.

11 Weiss JN, Garfinkel A, Karagueuzian HS, Qu Z, Chen PS. Chaos and the transition to ventricular fibrillation: a new approach to antiarrhythmic drug evaluation. *Circulation* 1999; **99**: 2819–26.

12 Davidenko JM, Pertsov AV, Salomonsz R, Baxter W, Jalife J. Stationary and drifting spiral waves of excitation in isolated cardiac muscle. *Nature* 1992; **355**: 349–51.

13 Weiss JN, Qu Z, Chen PS, et al. The dynamics of cardiac fibrillation. *Circulation* 2005; **112**: 1232–40.

14 Antzelevitch C, Brugada P, Borggrefe M, et al. Brugada syndrome: report of the second consensus conference: endorsed by the Heart Rhythm Society and the European Heart Rhythm Association. *Circulation* 2005; **111**: 659–70.

15 Meregalli PG, Wilde AA, Tan HL. Pathophysiological mechanisms of Brugada syndrome: depolarization disorder, repolarization disorder, or more? *Cardiovasc Res* 2005; **67**: 367–78.

16 Antzelevitch C. The Brugada syndrome: ionic basis and arrhythmia mechanisms. *J Cardiovasc Electrophysiol* 2001; **12**: 268–72.

17 Elizari MV, Levi R, Acunzo RS, et al. Abnormal expression of cardiac neural crest cells in heart development: a different hypothesis for the etiopathogenesis of Brugada syndrome. *Heart Rhythm* 2007; **4**: 359–65.

18 Chen Q, Kirsch GE, Zhang D, et al. Genetic basis and molecular mechanism for idiopathic ventricular fibrillation. *Nature* 1998; **392**: 293–96.

19 Priori SG, Napolitano C, Gasparini M, et al. Natural history of Brugada syndrome: insights for risk stratification and management. *Circulation* 2002; **105**: 1342–47.

20 Schulze-Bahr E, Eckardt L, Breithardt G, et al. Sodium channel gene (SCN5A) mutations in 44 index patients with Brugada syndrome: different incidences in familial and sporadic disease. *Hum Mutat* 2003; **21**: 651–52.

21 Yan GX, Antzelevitch C. Cellular basis for the Brugada syndrome and other mechanisms of arrhythmogenesis associated with ST-segment elevation. *Circulation* 1999; **100**: 1660–66.

22 Krishnan SC, Antzelevitch C. Flecainide-induced arrhythmia in canine ventricular epicardium: phase 2 reentry? *Circulation* 1993; **87**: 562–72.

23 Lukas A, Antzelevitch C. Phase 2 reentry as a mechanism of initiation of circus movement reentry in canine epicardium exposed to simulated ischemia. *Cardiovasc Res* 1996; **32**: 593–603.

24 Kimura M, Kobayashi T, Owada S, et al. Mechanism of ST elevation and ventricular arrhythmias in an experimental Brugada syndrome model. *Circulation* 2004; **109**: 125–31.

25 Aiba T, Shimizu W, Hidaka I, et al. Cellular basis for trigger and maintenance of ventricular fibrillation in the Brugada syndrome model: high-resolution optical mapping study. *J Am Coll Cardiol* 2006; **47**: 2074–85.

26 Akar FG, Spragg DD, Tunin RS, Kass DA, Tomaselli GF. Mechanisms underlying conduction slowing and arrhythmogenesis in nonischemic dilated cardiomyopathy. *Circ Res* 2004; **95**: 717–25.

27 Kurita T, Shimizu W, Inagaki M, et al. The electrophysiologic mechanism of ST-segment elevation in Brugada syndrome. *J Am Coll Cardiol* 2002; **40**: 330–34.

28 Tan HL, Bezzina CR, Smits JP, Verkerk AO, Wilde AA. Genetic control of sodium channel function. *Cardiovasc Res* 2003; **57**: 961–73.

29 Bezzina CR, Shimizu W, Yang P, et al. Common sodium channel promoter haplotype in asian subjects underlies variability in cardiac conduction. *Circulation* 2006; **113**: 338–44.

30 Schott JJ, Alshinawi C, Kyndt F, et al. Cardiac conduction defects associate with mutations in SCN5A. *Nat Genet* 1999; **23**: 20–1.

31 Tan HL, Bink–Boelkens MT, Bezzina CR, et al. A sodium-channel mutation causes isolated cardiac conduction disease. *Nature* 2001; **409**: 1043–47.

32 Kyndt F, Probst V, Potet F, et al. Novel SCN5A mutation leading either to isolated cardiac conduction defect or Brugada syndrome in a large French family. *Circulation* 2001; **104**: 3081–86.

33 Herfst LJ, Potet F, Bezzina CR, et al. Na^+ channel mutation leading to loss of function and nonprogressive cardiac conduction defects. *J Mol Cell Cardiol* 2003; **35**: 549–57.

34 Smits JP, Eckardt L, Probst V, et al. Genotype–phenotype relationship in Brugada syndrome: electrocardiographic features differentiate SCN5A-related patients from non-SCN5A-related patients. *J Am Coll Cardiol* 2002; **40**: 350–56.

35 Brugada P, Brugada J. Right bundle branch block, persistent ST segment elevation, and sudden cardiac death: a distinct clinical and electrocardiographic syndrome: a multicenter report. *J Am Coll Cardiol* 1992; **20**: 1391–96.

36 Alings M, Wilde A. "Brugada syndrome" clinical data and suggested pathophysiological mechanism. *Circulation* 1999; **99**: 666–73.

37 Wang DW, Viswanathan PC, Balser JR, George AL, Jr., Benson DW. Clinical, genetic, and biophysical characterization of SCN5A mutations associated with atrioventricular conduction block. *Circulation* 2002; **105**: 341–46.

38 Bezzina CR, Rook MB, Groenewegen WA, et al. Compound heterozygosity for mutations (W156X and R225W) in SCN5A associated with severe cardiac conduction disturbances and degenerative changes in the conduction system. *Circ Res* 2003; **92**: 159–68.

39 Royer A, van Veen TA, Le Bouter S, et al. Mouse model of SCN5A-linked hereditary Lenegre's disease: age-related conduction slowing and myocardial fibrosis. *Circulation* 2005; **111**: 1738–46.

40 Tomaselli GF, Zipes DP. What causes sudden death in heart failure? *Circ Res* 2004; **95**: 754–63.

41 Kasanuki H, Ohnishi S, Ohtuka M, et al. Idiopathic ventricular fibrillation induced with vagal activity in patients without obvious heart disease. *Circulation* 1997; **95**: 2277–85.

42 Nagase S, Kusano KF, Morita H, et al. Epicardial electrogram of the right ventricular outflow tract in patients with the Brugada syndrome: using the epicardial lead. *J Am Coll Cardiol* 2002; **39**: 1992–95.

43 Tukkie R, Sogaard P, Vleugels J, de Groot IK, Wilde AA, Tan HL. Delay in right ventricular activation contributes to Brugada syndrome. *Circulation* 2004; **109**: 1272–77.

44 Coronel R, Casini S, Koopmann TT, et al. Right ventricular fibrosis and conduction delay in a patient with clinical signs of Brugada syndrome: a combined electrophysiological, genetic, histopathologic, and computational study. *Circulation* 2005; **112**: 2769–77.

45 Morita H, Fukushima-Kusano K, Nagase S, et al. Site-specific arrhythmogenesis in patients with Brugada syndrome. *J Cardiovasc Electrophysiol* 2003; **14**: 373–79.

46 Janse MJ, Kleber AG. Electrophysiological changes and ventricular arrhythmias in the early phase of regional myocardial ischemia. *Circ Res* 1981; **49**: 1069–81.

47 Pogwizd SM, Corr PB. Reentrant and nonreentrant mechanisms contribute to arrhythmogenesis during early myocardial ischemia: results using three-dimensional mapping. *Circ Res* 1987; **61**: 352–71.

48 Hisamatsu K, Kusano KF, Morita H, et al. Relationships between depolarization abnormality and repolarization abnormality in patients with Brugada syndrome: using body surface signal-averaged electrocardiography and body surface maps. *J Cardiovasc Electrophysiol* 2004; **15**: 870–76.

49 Izumida N, Asano Y, Doi S, et al. Changes in body surface potential distributions induced by isoproterenol and Na channel blockers in patients with the Brugada syndrome. *Int J Cardiol* 2004; **95**: 261–68.

50 Yamada K. Body surface isopotential map: past, present and future. *Jpn Circ J* 1981; **45**: 1–14.

51 Shimizu W, Matsuo K, Takagi M, et al. Body surface distribution and response to drugs of ST segment elevation in Brugada syndrome: clinical implication of eighty-seven-lead body surface potential mapping and its application to twelve-lead electrocardiograms. *J Cardiovasc Electrophysiol* 2000; **11**: 396–404.

52 Ikeda T, Sakurada H, Sakabe K, et al. Assessment of noninvasive markers in identifying patients at risk in the Brugada syndrome insight into risk stratification. *J Am Coll Cardiol* 2001; **37**: 1628–34.

53 Kanda M, Shimizu W, Matsuo K, et al. Electrophysiologic characteristics and implications of induced ventricular fibrillation in symptomatic patients with Brugada syndrome. *J Am Coll Cardiol* 2002; **39**: 1799–805.

54 Eckardt L, Bruns HJ, Paul M, et al. Body surface area of ST elevation and the presence of late potentials correlate to the inducibility of ventricular tachyarrhythmias in Brugada syndrome. *J Cardiovasc Electrophysiol* 2002; **13**: 742–49.

55 Ajiro Y, Hagiwara N, Kasanuki H. Assessment of markers for identifying patients at risk for life-threatening arrhythmic events in Brugada syndrome. *J Cardiovasc Electrophysiol* 2005; **16**: 45–51.

56 Antzelevitch C. Late potentials and the Brugada syndrome. *J Am Coll Cardiol* 2002; **39**: 1996–99.

57 Vaidya D, Tamaddon HS, Lo CW, et al. Null mutation of connexin43 causes slow propagation of ventricular activation in the late stages of mouse embryonic development. *Circ Res* 2001; **88**: 1196–202.

58 Poelzing S, Akar FG, Baron E, Rosenbaum DS. Heterogeneous connexin43 expression produces electrophysiological heterogeneities across ventricular wall. *Am J Physiol Heart Circ Physiol* 2004; **286**: H2001–9.

59 van Oosterom A, Oostendorp TF. ECGSIM: an interactive tool for studying the genesis of QRST waveforms. *Heart* 2004; **90**: 165–68.

60 de Jong F, Opthof T, Wilde AA, et al. Persisting zones of slow impulse conduction in developing chicken hearts. *Circ Res* 1992; **71**: 240–50.

61 Moorman AF, Christoffels VM. Cardiac chamber formation: development, genes, and evolution. *Physiol Rev* 2003; **83**: 1223–67.

62 Surawicz B. Electrophysiologic substrate of torsade de pointes: dispersion of repolarization or early afterdepolarizations? *J Am Coll Cardiol* 1989; **14**: 172–84.

63 el-Sherif N, Zeiler RH, Craelius W, Gough WB, Henkin R. QTU prolongation and polymorphic ventricular tachyarrhythmias due to bradycardia-dependent early afterdepolarizations: afterdepolarizations and ventricular arrhythmias. *Circ Res* 1988; **63**: 286–305.

64 el-Sherif N, Turitto G. The long-QT syndrome and torsade de pointes. *Pacing Clin Electrophysiol* 1999; **22**: 91–110.

65 Antzelevitch C, Shimizu W. Cellular mechanisms underlying the long-QT syndrome. *Curr Opin Cardiol* 2002; **17**: 43–51.

66 Antzelevitch C, Sicouri S. Clinical relevance of cardiac arrhythmias generated by afterdepolarizations: role of M cells in the generation of U waves, triggered activity and torsade de pointes. *J Am Coll Cardiol* 1994; **23**: 259–77.

67 Choi BR, Burton F, Salama G. Cytosolic Ca^{2+} triggers early afterdepolarizations and torsade de pointes in rabbit hearts with type 2 long-QT syndrome. *J Physiol* 2002; **543**: 615–31.

68 el-Sherif N, Caref EB, Yin H, Restivo M. The electrophysiological mechanism of ventricular arrhythmias in the long-QT syndrome: tridimensional mapping of activation and recovery patterns. *Circ Res* 1996; **79**: 474–92.

69 Akar FG, Yan GX, Antzelevitch C, Rosenbaum DS. Unique topographical distribution of M cells underlies reentrant mechanism of torsade de pointes in the long-QT syndrome. *Circulation* 2002; **105**: 1247–53.

70 Restivo M, Caref EB, Kozhevnikov DO, El–Sherif N. Spatial dispersion of repolarization is a key factor in the arrhythmogenicity of long-QT syndrome. *J Cardiovasc Electrophysiol* 2004; **15**: 323–31.

71 El-Sherif N, Chinushi M, Caref EB, Restivo M. Electrophysiological mechanism of the characteristic electrocardiographic morphology of torsade de pointes tachyarrhythmias in the long-QT syndrome: detailed analysis of ventricular tridimensional activation patterns. *Circulation* 1997; **96**: 4392–99.

72 Eckardt L, Haverkamp W, Borggrefe M, Breithardt G. Experimental models of torsade de pointes. *Cardiovasc Res* 1998; **39**: 178–93.

73 Hoffman BF, Rosen MR. Cellular mechanisms for cardiac arrhythmias. *Circ Res* 1981; **49**: 1–15.

74 Vos MA, Verduyn SC, Gorgels AP, Lipcsei GC, Wellens HJ. Reproducible induction of early afterdepolarizations and torsade de pointes arrhythmias by d-sotalol and pacing in dogs with chronic atrioventricular block. *Circulation* 1995; **91**: 864–72.

75 Asano Y, Davidenko JM, Baxter WT, Gray RA, Jalife J. Optical mapping of drug-induced polymorphic arrhythmias and torsade de pointes in the isolated rabbit heart. *J Am Coll Cardiol* 1997; **29**: 831–42.

76 Efimov IR, Huang DT, Rendt JM, Salama G. Optical mapping of repolarization and refractoriness from intact hearts. *Circulation* 1994; **90**: 1469–80.

77 Kanai A, Salama G. Optical mapping reveals that repolarization spreads anisotropically and is guided by fiber orientation in guinea pig hearts. *Circ Res* 1995; **77**: 784–802.

78 Ben-David J, Zipes DP. Differential response to right and left ansae subclaviae stimulation of early afterdepolarizations and ventricular tachycardia induced by cesium in dogs. *Circulation* 1988; **78**: 1241–50.

79 Ben-David J, Zipes DP. Alpha-adrenoceptor stimulation and blockade modulates cesium-induced early afterdepolarizations and ventricular tachyarrhythmias in dogs. *Circulation* 1990; **82**: 225–33.

80 Bailie DS, Inoue H, Kaseda S, Ben-David J, Zipes DP. Magnesium suppression of early afterdepolarizations and ventricular tachyarrhythmias induced by cesium in dogs. *Circulation* 1988; **77**: 1395–402.

81 Sato T, Hirao K, Hiejima K. The relationship between early afterdepolarization and the occurrence of torsades de pointes: an in vivo canine model study. *Jpn Circ J* 1993; **57**: 543–52.

82 Zabel M, Hohnloser SH, Behrens S, Li YG, Woosley RL, Franz MR. Electrophysiologic features of torsades de pointes: insights from a new isolated rabbit heart model. *J Cardiovasc Electrophysiol* 1997; **8**: 1148–58.

83 Franz MR. Current status of monophasic action potential recording: theories, measurements and interpretations. *Cardiovasc Res* 1999; **41**: 25–40.

84 Kurita T, Ohe T, Shimizu W, et al. Early afterdepolarization-like activity in patients with class IA induced long-QT syndrome and torsades

de pointes. *Pacing Clin Electrophysiol* 1997; **20**: 695–705.

85 Moore HJ, Franz MR. Monophasic action potential recordings in humans. *J Cardiovasc Electrophysiol* 2007; **18**: 787–90.

86 Shimizu W, Ohe T, Kurita T, et al. Early afterdepolarizations induced by isoproterenol in patients with congenital long-QT syndrome. *Circulation* 1991; **84**: 1915–23.

87 Roden DM. Early afterdepolarizations and torsade de pointes: implications for the control of cardiac arrhythmias by prolonging repolarization. *Eur Heart J* 1993; **14**: 56–61.

88 Yan GX, Wu Y, Liu T, Wang J, Marinchak RA, Kowey PR. Phase 2 early afterdepolarization as a trigger of polymorphic ventricular tachycardia in acquired long-QT syndrome: direct evidence from intracellular recordings in the intact left ventricular wall. *Circulation* 2001; **103**: 2851–56.

89 El-Sherif N, Caref EB, Chinushi M, Restivo M. Mechanism of arrhythmogenicity of the short-long cardiac sequence that precedes ventricular tachyarrhythmias in the long-QT syndrome. *J Am Coll Cardiol* 1999; **33**: 1415–23.

90 Kozhevnikov DO, Yamamoto K, Robotis D, Restivo M, El–Sherif N. Electrophysiological mechanism of enhanced susceptibility of hypertrophied heart to acquired torsade de pointes arrhythmias: tridimensional mapping of activation and recovery patterns. *Circulation* 2002; **105**: 1128–34.

91 Chinushi M, Caref EB, Restivo M, Noll G, Aizawa Y, El-Sherif N. Cycle length–associated modulation of the regional dispersion of ventricular repolarization in a canine model of long-QT syndrome. *Pacing Clin Electrophysiol* 2001; **24**: 1247–57.

92 Antzelevitch C, Sicouri S, Litovsky SH, et al. Heterogeneity within the ventricular wall: electrophysiology and pharmacology of epicardial, endocardial, and M cells. *Circ Res* 1991; **69**: 1427–49.

93 Sicouri S, Antzelevitch C. A subpopulation of cells with unique electrophysiological properties in the deep subepicardium of the canine ventricle: the M cell. *Circ Res* 1991; **68**: 1729–41.

94 Sicouri S, Antzelevitch C. Electrophysiologic characteristics of M cells in the canine left ventricular free wall. *J Cardiovasc Electrophysiol* 1995; **6**: 591–603.

95 Lesh MD, Pring M, Spear JF. Cellular uncoupling can unmask dispersion of action potential duration in ventricular myocardium: a computer modeling study. *Circ Res* 1989; **65**: 1426–40.

96 Yan GX, Shimizu W, Antzelevitch C. Characteristics and distribution of M cells in arterially perfused canine left ventricular wedge preparations. *Circulation* 1998; **98**: 1921–27.

97 Gray RA, Jalife J, Panfilov AV, et al. Mechanisms of cardiac fibrillation. *Science* 1995; **270**: 1222–23; author reply 1224–25.

98 Zaitsev AV, Berenfeld O, Mironov SF, Jalife J, Pertsov AM. Distribution of excitation frequencies on the epicardial and endocardial surfaces of fibrillating ventricular wall of the sheep heart. *Circ Res* 2000; **86**: 408–17.

99 Samie FH, Berenfeld O, Anumonwo J, et al. Rectification of the background potassium current: a determinant of rotor dynamics in ventricular fibrillation. *Circ Res* 2001; **89**: 1216–23.

100 Pak HN, Oh YS, Liu YB, et al. Catheter ablation of ventricular fibrillation in rabbit ventricles treated with beta-blockers. *Circulation* 2003; **108**: 3149–56.

101 Jais P, Haissaguerre M, Shah DC, et al. A focal source of atrial fibrillation treated by discrete radiofrequency ablation. *Circulation* 1997; **95**: 572–76.

102 Chen PS, Wu TJ, Hwang C, et al. Thoracic veins and the mechanisms of nonparoxysmal atrial fibrillation. *Cardiovasc Res* 2002; **54**: 295–301.

103 Kusano KF, Yamamoto M, Emori T, Morita H, Ohe T. Successful catheter ablation in a patient with polymorphic ventricular tachycardia. *J Cardiovasc Electrophysiol* 2000; **11**: 682–85.

104 Takatsuki S, Mitamura H, Ogawa S. Catheter ablation of a monofocal premature ventricular complex triggering idiopathic ventricular fibrillation. *Heart* 2001; **86**: E3.

105 Haissaguerre M, Shah DC, Jais P, et al. Role of Purkinje conducting system in triggering of idiopathic ventricular fibrillation. *Lancet* 2002; **359**: 677–78.

106 Haissaguerre M, Shoda M, Jais P, et al. Mapping and ablation of idiopathic ventricular fibrillation. *Circulation* 2002; **106**: 962–67.

107 Saliba W, Abul Karim A, Tchou P, Natale A. Ventricular fibrillation: ablation of a trigger? *J Cardiovasc Electrophysiol* 2002; **13**: 1296–99.

108 Betts TR, Yue A, Roberts PR, Morgan JM. Radiofrequency ablation of idiopathic ventricular fibrillation guided by noncontact mapping. *J Cardiovasc Electrophysiol* 2004; **15**: 957–59.

109 Noda T, Shimizu W, Taguchi A, et al. Malignant entity of idiopathic ventricular fibrillation and polymorphic ventricular tachycardia initiated by premature extrasystoles originating from the right ventricular outflow tract. *J Am Coll Cardiol* 2005; **46**: 1288–94.

110 Nogami A, Sugiyasu A, Kubota S, Kato K. Mapping and ablation of idiopathic ventricular fibrillation from the Purkinje system. *Heart Rhythm* 2005; **2**: 646–49.

111 Haissaguerre M, Extramiana F, Hocini M, et al. Mapping and ablation of ventricular fibrillation associated with long-QT and Brugada syndromes. *Circulation* 2003; **108**: 925–28.

112 Darmon JP, Bettouche S, Deswardt P, et al. Radiofrequency ablation of ventricular fibrillation and multiple right and left atrial tachycardia in a patient with Brugada syndrome. *J Interv Card Electrophysiol* 2004; **11**: 205–9.

113 Srivathsan K, Gami AS, Ackerman MJ, Asirvatham SJ. Treatment of ventricular fibrillation in a patient with prior diagnosis of long-QT syndrome: importance of precise electrophysiologic diagnosis to successfully ablate the trigger. *Heart Rhythm* 2007; **4**: 1090–93.

114 Lerman BB. Mechanism of outflow tract tachycardia. *Heart Rhythm* 2007; **4**: 973–76.

115 Lerman BB, Stein KM, Markowitz SM, Mittal S, Slotwiner DJ. Ventricular arrhythmias in normal hearts. *Cardiol Clin* 2000; **18**: 265–91, vii.

116 Joshi S, Wilber DJ. Ablation of idiopathic right ventricular outflow tract tachycardia: current perspectives. *J Cardiovasc Electrophysiol* 2005; **16**: S52–S58.

117 Belhassen B, Viskin S. What is the drug of choice for the acute termination of paroxysmal supraventricular tachycardia: verapamil, adenosine triphosphate, or adenosine? *Pacing Clin Electrophysiol* 1993; **16**: 1735–41.

118 Leenhardt A, Glaser E, Burguera M, Nurnberg M, Maison-Blanche P, Coumel P. Short-coupled variant of torsade de pointes: a new electrocardiographic entity in the spectrum of idiopathic ventricular tachyarrhythmias. *Circulation* 1994; **89**: 206–15.

119 Viskin S, Rosso R, Rogowski O, Belhassen B. The "short–coupled" variant of right ventricular outflow ventricular tachycardia: a not-so-benign form of benign ventricular tachycardia? *J Cardiovasc Electrophysiol* 2005; **16**: 912–16.

120 Viskin S, Lesh MD, Eldar M, et al. Mode of onset of malignant ventricular arrhythmias in idiopathic ventricular fibrillation. *J Cardiovasc Electrophysiol* 1997; **8**: 1115–20.

121 Kakishita M, Kurita T, Matsuo K, et al. Mode of onset of ventricular fibrillation in patients with Brugada syndrome detected by implantable cardioverter defibrillator therapy. *J Am Coll Cardiol* 2000; **36**: 1646–53.

122 Chinushi M, Washizuka T, Chinushi Y, Higuchi K, Toida T, Aizawa Y. Induction of ventricular fibrillation in Brugada syndrome by site-specific right ventricular premature depolarization. *Pacing Clin Electrophysiol* 2002; **25**: 1649–51.

123 Gang ES, Priori SS, Chen PS. Short coupled premature ventricular contraction initiating ventricular fibrillation in a patient with Brugada syndrome. *J Cardiovasc Electrophysiol* 2004; **15**: 837.

124 Berenfeld O, Jalife J. Purkinje–muscle reentry as a mechanism of polymorphic ventricular arrhythmias in a 3-dimensional model of the ventricles. *Circ Res* 1998; **82**: 1063–77.

125 Caref EB, Restivo, M., Chinushi, M., El-Sherif, N. Primary role of subendocardial activity in the initiation of torsades de pointes (TdP) in the long-QT syndrome. *Pacing Clin Electrophysiol* 1997; **20**: 1080.

36

CHAPTER 36

Molecular Cardiovascular Imaging with SPECT and PET

Michael Schäfers, MD, *Günter Breithardt,* MD, FESC, FACC, FHRS, *Otmar Schober,* MD, PhD, FESC

University of Münster, Münster, Germany

Summary

Although both, preventive measures on the population level and curative medicine have contributed to the continuing decline in age-adjusted cardiovascular mortality in recent years, early identification of the individual subject at risk for cardiovascular complications remains a great challenge. Prevention of cardiovascular events, which are responsible for approximately one-third of all deaths in industrialized societies, primarily needs diagnostic tools, which can predict these events before they occur.

Current imaging technologies, which are predominantly based on morphological and functional imaging approaches of vessels and the myocardium, seem to fail in this respect, because these do not "see" (visualize) the underlying and most important molecular pathways activated in cardiovascular pathophysiology. One example is the atherosclerotic lesion, where state-of-the-art high-resolution multislice computer tomography (MSCT) can three-dimensionally depict coronary artery stenoses and calcium deposition in the vessel wall. However, even these high-tech approaches cannot visualize the inflammatory cellular and molecular processes finally resulting in instability of an atherosclerotic lesion, plaque rupture, and the clinical sequelae—myocardial infarction or stroke.

New imaging technologies noninvasively looking at molecular targets and their dynamic regulation in cardiovascular diseases in vivo are urgently needed. Although having identified challenging cardiovascular diseases and being aware of the unique potential of novel molecular imaging might seem to be sufficient to develop new diagnostic molecular imaging tools, the approach toward these technologies remains a huge challenge.

Spectrum and Applications of Currently Available Cardiovascular Imaging Technologies

Morphological and functional imaging approaches such as coronary angiography and echocardiography have been established algorithms in clinical cardiology for many years and represent state-of-the-art equipment for cardiovascular diagnostics. These methods assess the morphology of the coronary arteries, valve function as well as cardiac motion.

Recent developments have provided fast MSCT techniques to noninvasively study coronary arteries. Due to the diagnostic analogy with the classical angiographical approach, noninvasive

Cardiac Mapping, Third Edition Edited by Mohammad Shenasa, Gerhard Hindricks, Martin Borggrefe, and Günter Breithardt
 ISBN: 978-1-405-17572-2

MSCT-based coronary angiography has a great potential to replace invasive diagnostic angiography in certain conditions. In addition, MSCT can quantify calcium deposits in the coronary vessel wall ("calcium scoring"), which are a sign of atherosclerosis; the value of calcium score with respect to the prediction of future cardiac events is currently under debate [1].

Besides MSCT, cardiac magnetic resonance imaging (MRI) for the 3D assessment of cardiac function, structural analysis of the myocardium, and visualization of coronary arteries has been greatly improved. Competing with the classical scintigraphic approach for viability assessment—i.e., ^{18}F-fluorodesoxyglucose-PET—contrast-enhanced MRI is increasingly being used to detect myocardial scar following myocardial infarction ("late enhancement") [2]. Although most of these techniques have been clinically available, have been used for many decades, and have been further developed, they are limited in their predictive power for future events such as acute coronary syndromes.

In the cardiovascular field, significant improvement of both diagnostic and therapeutic algorithms is expected from the use of "molecular medicine" approaches. Molecular medicine spans from new molecular–analytical methods in vitro, through the identification of key molecular pathways and targets, toward therapeutic compounds that specifically interact with the identified targets in vivo.

This new trend in medicine may be facilitated by innovative ways of imaging, that is, molecular imaging, which directly and noninvasively visualize molecular pathways in normal and diseased conditions in vivo. Applying new molecular imaging technologies in cardiovascular medicine promises new and exciting insight into molecular aspects of various cardiovascular pathologies. The image-derived molecular "map" of the heart and the vessels will hopefully provide unique individual molecular information that can be used in improved patient management.

Future molecular imaging of cardiovascular diseases will need interdisciplinary development and validation of new imaging approaches. In general, these methods should offer:

- High molecular sensitivity (to detect small amounts of molecular targets);
- High temporal and spatial resolution (to precisely localize and follow a pathway over time);
- Noninvasivity (to allow for individual serial assessment);
- Three dimensions (to resemble anatomy);
- Availability (to guarantee wide clinical applications);
- No side effects (to reduce risk and improve patients comfort);
- Low radiation exposure (ALARA principle).

On the basis of these prerequisites, scintigraphic approaches such as single photon emission tomography (SPECT) and positron emission tomography (PET) seem well suited, because they are clinically available, possess a very high molecular sensitivity (detection of nano-/picomolar concentrations in vivo) while having a fair spatial but good temporal resolution, are three-dimensional, and have been in use for several decades for the study of cardiovascular function without showing relevant side effects (e.g., quantification of myocardial perfusion using ^{99m}Tc-labelled compounds).

Consistently, SPECT and PET currently provide the only clinically available molecular imaging approaches in cardiovascular imaging, for example, the study of myocardial presynaptic sympathetic innervation using ^{123}I-meta-iodobenzylguanidine (^{123}I-MIBG) or the assessment of myocardial glucose utilization using ^{18}F-fluorodesoxyglucose (FDG-PET).

FDG-PET is a prime example of an ideal molecular imaging approach: FDG, labelled by the positron emitter ^{18}F, is a chemical analogue of glucose and is specifically transported into myocytes and other cells by insulin-dependent GLUT-1 transporters. The chemical modification of FDG as compared to the "original" glucose is biologically inert (no side effects), allows for intracellular phosphorylation of FDG by hexokinase while further metabolism in the citric acid cycle is blocked. Therefore, FDG is trapped by viable myocytes reflecting (visualizing) glucose uptake and hexokinase-dependent phosphorylation, and accumulates over time, further amplifying the imaging signal (radioactivity).

One challenge toward innovative molecular imaging is the development of specific tracers/radiopharmaceuticals. These should specifically bind to the molecular target in vivo by their specific biological binding capacities (receptor antagonists

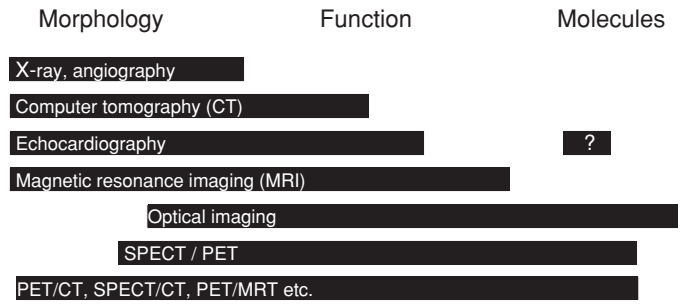

Figure 36.1 Current and potential future spectrum of cardiovascular imaging in vivo. Graph shows the individual spectrum of various imaging modalities with respect to imaging of morphology, function, and molecules. Note that a single modality cannot cover the whole spectrum; therefore, combined imaging approaches such as PET/CT or PET/MRI are expected to present powerful tools for future clinical cardiovascular diagnostics.

and agonists, enzyme inhibitors, etc.) and enable imaging by reporting the molecular signal to outside the body by their attached label (e.g., radioactive isotopes for SPECT or PET).

A specific and unique challenge in *cardiac* molecular imaging is the movement of the heart in combination with the size of the structures of interest, e.g., coronary arteries, which results in low sensitivity and spatial resolution and drastically diminished signal-to-noise ratios. Motion detection by ECG- and respiratory triggering of the acquisitions with retrospective motion compensation are now under development to overcome these drawbacks. Finally, molecular imaging approaches should be combined with high-resolution morphological imaging (the multimodality approach, e.g., PET/CT) and new tracers to finally provide optimized, comprehensive, and clinically available imaging protocols for cardiovascular molecular imaging [3].

Apart from scintigraphic approaches, optical technologies using innovative fluorescence-labelled tracers can be used. These technologies are at least as sensitive as scintigraphic approaches. However, a clear drawback is the relatively poor penetrance and its huge portion of light scattering when travelling through tissue. Both issues currently prevent the design of a noninvasive imaging device to image deep structures such as the heart in the human thorax. Structures close to the surface (e.g., carotid arteries) may be accessible for planar imaging. An alternative invasive approach can be the use of fluorescent light-sensitive catheter tips to image molecular signals from the vascular wall. This is further hampered by the huge absorption of light by blood [4].

Because relevant molecular targets are typically expressed in nano-/picomolar concentrations in tissues (receptors, enzymes, etc.), MSCT and current MRI are not sensitive enough to detect these signals. However, MRI in combination with innovative contrast-enhancement strategies can improve its sensitivity in the future. Ultrasound has also shown its potential for molecular imaging when combined with targeted micro-/nanobubbles [5] (Figure 36.1).

Current and Potential Future Applications of Cardiovascular Molecular Imaging

An overwhelming number of theoretically attractive molecular targets exists for cardiovascular molecular imaging. The accessibility of the targets in the different compartments of the heart and the vessels is illustrated in Figure 36.2. Research should be focused on a clear clinical challenge/area and, within this area, on a well-defined number of molecular targets that have a reasonable level of feasibility. In the following sections, the principal strategy from target identification toward clinical application of a newly developed molecular imaging approach is shown for the molecular imaging of autonomic nerve function and atherosclerotic plaques.

Molecular Imaging of the Autonomic Nervous System

Although less established in clinical practice than perfusion imaging, examination of the cardiac autonomous nervous system is of potential value. This may apply especially to arrhythmogenic diseases not

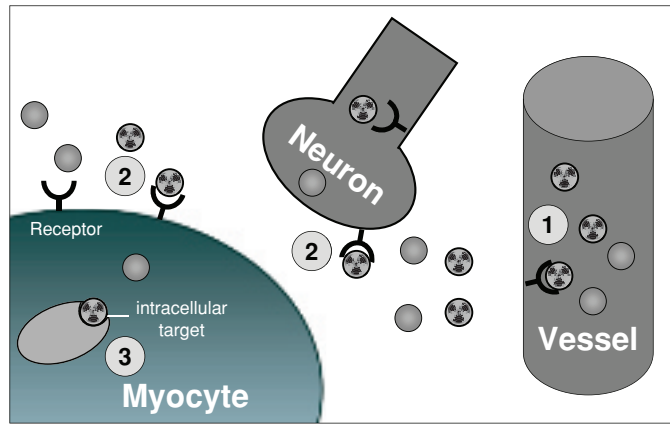

Figure 36.2 In the heart, three major compartments are relevant for molecular imaging: the myocardium, vessels, and nerves. Because radioactive tracers are typically injected intravenously, they will primarily distribute with the blood flow within the vessels. Intravascular targets are therefore theoretically easy to reach [1]. All other molecular targets need a transport of the tracer through the endothelium into the interstitial space, where tracers can bind to membrane-bound targets on neurons, myocytes, and other cells [2]. Intracellular targeting is hampered by the cell membrane as a natural barrier. This approach therefore often needs consideration of a transmembrane transport strategy to finally bind the tracers to the targets [3].

associated with functional and anatomic changes detectable by conventional imaging, and may also be useful in ischemic heart disease where aberrations in autonomous nervous function may be a relevant parameter.

Both pre- and postsynaptic function of the sympathetic and parasympathetic nervous system are accessible by radiopharmaceutical techniques. At present, the sympathetic arm has received most attention. Presynaptic function of sympathetic innervation has been examined with the SPECT radiotracer (^{123}I)-meta-iodobenzylguanidin [(^{123}I)MIBG] and the PET radiotracer (^{11}C)-meta-hydroxyephedrine [(^{11}C)HED] in various cardiovascular disorders.

Both tracers behave similarly to norepinephrine, the physiological neurotransmitter. Whereas both SPECT and PET can depict regional inhomogeneities, PET allows for absolute quantitation of presynaptic function. Many reports have shown evidence for involvement of the sympathetic nervous system in various cardiovascular diseases as studied by scintigraphic molecular imaging. For instance, it has been shown that after non-*Q*-wave myocardial infarction sympathetic denervation occurs at the site of the infracted myocardium, which extends also "downstream" after *Q*-wave myocardial infarction [6].

Clinically relevant arrhythmias after MI often arise in denervated but viable tissue. Sympathetic function is impaired for a prolonged time after an ischemic event in patients with coronary spastic angina as shown by (^{123}I)MIBG [7]. Shortly after cardiac transplantation, complete denervation exists, whereas reinnervation may occur in the transplanted organ later on [8]. Additionally, it has been shown with (^{123}I)MIBG that sympathetic function has a prognostic value. For example, in patients with congestive heart failure prognosis is worse for patients with impaired presynaptic function [9]. Recently, it was shown that in patients with idiopathic right ventricular outflow tract tachycardia, (^{123}I)MIBG was able to predict future arrhythmic events [10]. (^{123}I)MIBG can also be used to predict improvement of left ventricular function after initiation of β-blocker and angiotensin converting enzyme (ACE) inhibitor therapy [11].

The density of β-adrenoceptors is an important parameter of postsynaptic function. It has been quantified by using radiolabelled β-adrenoceptors antagonists and PET. (^{11}C)CGP 12177 is a nonselective β-adrenoceptor antagonist that has seen the most widespread application in clinical research [12].

Cardiomyopathies that give rise to potentially lethal arrhythmias are associated with typical

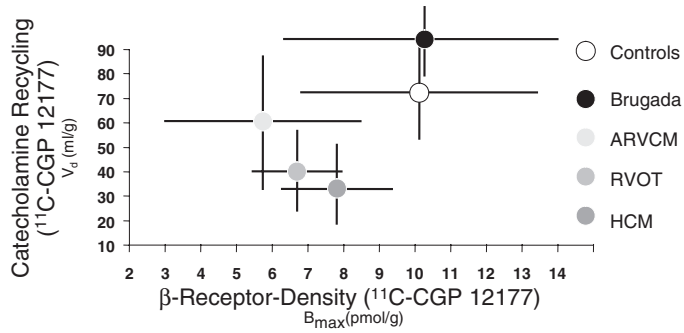

Figure 36.3 Quantitation of presynaptic and postsynaptic sympathetic function in arrhythmogenic diseases and cardiomyopathies measured with PET and the radiotracers (^{11}C)HED and (^{11}C)CGP 12177 (see text for details). The graph shows postsynaptic beta receptor density on the abscissa and presynaptic catecholamine recycling on the ordinate for several conditions being associated with ventricular tachyarrhythmias (arrhythmogenic right ventricular cardiomyopathy, right ventricular outflow tract tachycardia, hypertrophic cardiomyopathy, and Brugada syndrome). Given are the mean and the standard deviation for each type.

aberrations in sympathetic function. It has been shown with PET using the radiotracers (^{11}C)HED and (^{11}C)CGP 12177 for pre- and postsynaptic imaging that in patients with hypertrophic cardiomyopathy (HCM), arrhythmogenic right ventricular dysplasia (ARVD) and right-ventricular outflow tract tachycardia (RVOT), presynaptic neurotransmitter recycling and postsynaptic receptor density are downregulated (Figure 36.3).

In contrast, in patients with the Brugada syndrome the presynaptic neurotransmitter recycling is upregulated while postsynaptic receptor densities were within normal range [13–16]. These changes in innervation mirror differences in clinical appearance: whereas the former cardiomyopathies typically lead to arrhythmias under stress conditions, the Brugada syndrome is associated with potentially lethal arrhythmias occurring at rest. Labelled β-adrenoceptor antagonists selective for the β_1-adrenoceptor subtype are under development and await application in imaging research [17, 18].

Another objective of innervation imaging is to assess the parasympathetic arm of the autonomous nervous system. The parasympathetic nervous system uses acetylcholine as a neurotransmitter with muscarinic receptors. ^{11}C-methylquinuclidinylbenzilat ((^{11}C)MQNB) is a radiotracer that allows quantitation of muscarinic receptor densities [19].

Le Guludec et al. studied heart transplant patients and found no differences in receptor density and affinity constants of the myocardial muscarinic receptors [20]. The same group found upregulation of muscarinic receptor density in patients with idiopathic dilated cardiomyopathy [21].

Molecular Imaging of Atherosclerotic Plaques

The imaging of the lumen of arteries by angiography is not sufficient to assess the risk for individual atherosclerotic plaques to rupture. Many myocardial infarctions are caused by plaques that rupture before they cause critical stenoses. These "soft" plaques may escape detection by imaging modalities that visualize the vessel lumen instead of the atherosclerotic plaque developing in the vessel wall itself [22]. The assessment of calcifications within the arterial wall by means of electron beam tomography or MSCT may yield an independent risk factor for coronary heart disease, but the location of the calcium deposits are not equivalent to the location of vulnerable plaques [23]. However, like angiography, it also fails to identify unstable plaques that are likely to rupture and require interventions. Patient management can be improved by targeted interventions if unstable atherosclerotic plaques prone to rupture can be identified in time.

The molecular and cellular processes in plaque formation and plaque rupture are increasingly understood, providing a basis for the development of targeted molecular imaging techniques using

radiotracers. Thorough assessment of plaques by means of molecular imaging may be accompanied by assessment of plaque morphology using intravascular ultrasound (IVUS), CT, and MRI.

Several different radiotracers for imaging plaque instability have begun to emerge in recent years and show great promise.

(^{18}F)FDG

(^{18}F)-FDG is accumulated in areas with high concentrations of activated macrophages and leucocytes and therefore serves as a surrogate marker of inflammation. It is not surprising that (^{18}F)-FDG has been successfully used as a marker for atherosclerotic plaques with persisting inflammation. Studies in the carotid artery have shown that symptomatic plaques (associated with microembolization) show higher (^{18}F)-FDG uptake than nonsymptomatic plaques [24]. Studies in the carotid and great arteries of the body with combined PET/CT have shown that (^{18}F)-FDG uptake and calcification are discordant in many cases, underscoring the assumption that measurement of calcification cannot be used to identify unstable plaques.

Application of (^{18}F)-FDG uptake as a surrogate marker for inflammation in coronary artery plaques is hampered by the significant background uptake in the left ventricular myocardium and by cardiac movement during image acquisition. Although controlled metabolic conditions may limit myocardial glucose utilization, (^{18}F)-FDG is still largely unsuitable for effective coronary plaque imaging.

Matrix Metalloproteinase Inhibitors

The thrombogenic core of a plaque is separated from the vessel lumen by a fibrous cap. The integrity of this cap is an important determinant of plaque stability. Proteolysis of the extracellular matrix by activated matrix metalloproteinases (MMPs) can serve as a potent indicator for plaque instability (i.e., propensity of the plaque to rupture).

Radiotracers based on MMP inhibitors that only bind to activated MMPs have been developed and successfully tested in animal experiments [25, 26]. Radiotracer development can take advantage of the fact that MMPs are well characterised and that a number of synthetic MMP inhibitors have been developed for cancer treatment. PET imaging is possible when using ^{124}I or ^{18}F as the radiolabel. Figure 36.4 shows a feasibility study for MMP imaging in apoE$^{-/-}$ mouse models of MMP-rich vascular lesions following carotid ligation. Several other MMP inhibitors have been successfully labelled with ^{11}C and ^{18}F for PET imaging [27]. Recently, precursors for SPECT- and PET-imaging based on barbiturate derivatives with high MMP binding potential have been developed that promise improved MMP selectivity [28].

Annexin V and Caspase Inhibitors

The presence of apoptosis can also serve as a marker for the unstable plaque because apoptosis of macrophages and other cells is generally driving the atherosclerotic plaque toward instability. Annexin V is known to bind to phosphatidylserine, a negatively charged membrane phospholipid externalized to

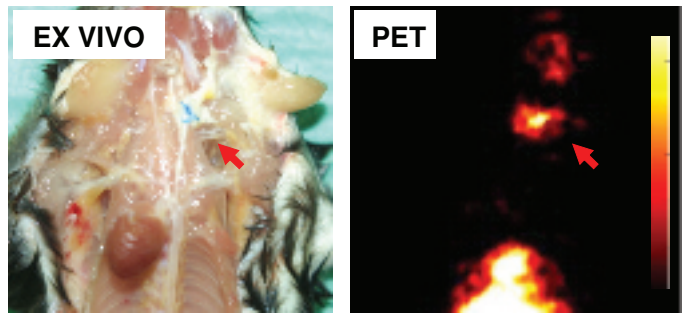

Figure 36.4 Ex vivo photography of the surgical site (left panel) and corresponding whole body coronal slice (0.4 mm thick) through a left carotid lesion (right panel) developing 4 weeks after ligation of the left common carotid artery and hypercholesterolemic diet in a apoE$^{-/-}$ mouse. An intense uptake of the radiolabelled broad spectrum MMP inhibitor ^{124}I-HO-CGS 27023A into the left carotid lesion (arrow) 30 min after intravenous injection is visible using high resolution small animal PET (quadHIDAC, Oxford Positrons Ltd., Oxford, UK).

the cell surface during the early apoptotic signalling cascade. Annexin V labelled with ^{99m}Tc can be used to visualise vulnerable plaques in animals and in humans using SPECT. Kolodgie et al. have observed in rabbits and Johnson et al. in swine that plaques have a high uptake of this radiotracer and that this uptake reflects the amount of apoptosis [29, 30]. Kietselaer et al. have successfully applied ^{99m}Tc-Annexin V in humans [31]. Hartung et al. have shown in rabbits that cholesterol-lowering therapy by dietary modification and statin intake leads to a decrease in ^{99m}Tc-annexin V accumulation in atherosclerotic lesions, implying plaque stabilization [32]. However, phosphatidylserine is a molecular target not exclusively regulated by apoptosis in vivo. It is also elevated by other forms of cell stress not necessarily leading to apoptosis. In contrast, activation of caspases inside the cells signals the initiation of the irreversible cascade towards apoptosis. Caspases, therefore, are likely to be better and specific molecular targets for molecular imaging of apoptosis. Targeting an intracellular enzyme with a radiotracer (e.g., a radiolabelled caspase inhibitor) is conceptually more challenging than targeting a cell-surface receptor such as phosphatidylserine. First approaches aim for this type of molecular imaging of apoptosis [33, 34].

Apoptosis also plays an important role in diseases affecting cardiomyocytes such as myocardial infarction, myocarditis and nonischemic cardiomyopathies. As examples, it has been shown that imaging of annexin V accumulation depicts tissue at risk after myocardial infarction with reversible damage [35]. Elevated annexin V uptake can be found after heart transplantation in case of acute transplant rejection [36] that correlates with caspase-3 staining in histology.

Endothelin

Endothelin (ET) is a strong vasoconstrictor and has three isoforms, ET-1, ET-2, and ET-3 that mainly bind to the two ET receptors ET_AR and ET_BR. ET_AR can be found in smooth muscle cells whereas ET_BR are located primarily in vascular endothelial cells. ET-1 is generated from its precursor big ET-1 by help of the endothelin-converting enzyme (ECE)-1 and plays an important role in the regulation of the vascular tone. Elevated levels of ET-1 lead to endothelial dysfunction. Additionally, ET-1 is implicated in angiogenesis, restenosis after balloon angioplasty and atherosclerosis. ET-1, ECE-1 and ET-receptor upregulation can be found in atherosclerotic lesions especially in the inflammatory stages [37]. ET-1, ECE-1 and ET receptors may therefore be suitable targets for the imaging of unstable atherosclerotic plaques.

Johnström et al. [38] have successfully labelled ET-1 with the positron emitter ^{18}F. Biodistribution and organ uptake was visualised in rats with a dedicated small animal PET scanner. Although myocardial binding of ^{18}F-ET-1 with good ET-receptor affinity was observed in vitro, myocardial uptake was minimal. Additional experiments showed that rapid clearance of the radiotracer from the blood in the lung and in the kidneys, where the density of ET_BR is high, is responsible for the faint myocardial uptake. Significant myocardial uptake with PET was only observed when injection occurred after blockage of the ET_BR receptors with the antagonist BQ788 [38], effectively allowing the ^{18}F-ET-1 to reach the myocardium. Dinkelborg et al. have shown an uptake of a ^{99m}Tc-labelled endothelin derivative in atherosclerotic plaques in a rabbit model both in vivo and ex vivo [39]. The uptake was proportional to smooth muscle cell count but not to the densities of macrophages.

The authors hypothesised that this radiotracer may be feasible for the early detection of atherosclerosis. Many different radiotracers based on antagonists of ET-receptors, either selective or unselective for ET_AR or ET_BR, have been developed and successfully tested in animal studies, most of them for use with PET [40–43]. At this stage it is still unclear whether these ET-related radiotracer developments are suitable for the imaging of atherosclerotic plaques in humans; however, these tracers may also find widespread use in the cardiovascular field outside of plaque imaging, for example, for investigations on endothelial dysfunction, angiogenesis and restenoses.

Conclusions and Perspectives

Molecular cardiovascular imaging with scintigraphic techniques has received a new impetus with advances in genetic diagnostics and molecular therapies. While the assessment of myocardial perfusion and metabolism with radiotracer techniques has been long established in cardiovascular routine diagnosis, newer methodologies, especially in the field of gene and cell imaging, have only started to

emerge. Initial studies have confirmed the feasibility and applicability of these methods and promise an exciting future for both basic research and clinical applications. The nature of the radiotracer technique, together with the development of dedicated small-animal SPECT and PET scanners, allow for a unique translational application from animals to humans. Imaging characteristics of devices for small animals and humans are very similar in relation to body size. Radiotracer techniques are very sensitive so that molecular targets with a low molar density can still be assessed without disturbing the biochemical system if the specific activity of the radiotracer is high enough. Numerous inorganic and organic molecules can be radiolabelled with no or little changes of their biochemical behavior.

Radiotracer imaging techniques do not give high-resolution anatomical information so that combinations of SPECT and PET with CT and MRI are becoming increasingly valuable. Sensitivity and true molecular information is provided by SPECT and PET, whereas anatomic, morphological, and functional assessment is possible with CT and MRI. Imaging of the constantly moving structures such as coronary arteries represents a special challenge for SPECT and PET imaging. A truly interdisciplinary approach with specialists from the fields of engineering, physics, mathematics, computer science, biology, chemistry, and medicine working together will be necessary to overcome these obstacles.

The role of molecular imaging in arrhythmia research and management will need further extensive and innovative research. The methodology for imaging the autonomic nervous system and arteriosclerotic plaques is promising.

Acknowledgements

This work was supported by the Deutsche Forschungsgemeinschaft (DFG), Sonderforschungsbereich SFB 656 MoBil, Münster, Germany.

References

1 Berman DS, Hachamovitch R, Shaw LJ, et al. Roles of nuclear cardiology, cardiac computed tomography, and cardiac magnetic resonance: noninvasive risk stratification and a conceptual framework for the selection of noninvasive imaging tests in patients with known or suspected coronary artery disease. *J Nucl Med* 2006; **47**: 1107–18.

2 Isbell DC, Kramer CM. Magnetic resonance for the assessment of myocardial viability. *Curr Opin Cardiol* 2006; **21**: 469–72.

3 Schwaiger M, Ziegler S, Nekolla SG. PET/CT: challenge for nuclear cardiology. *J Nucl Med* 2005; **46**: 1664–78.

4 Jaffer FA, Weissleder R. Seeing within: molecular imaging of the cardiovascular system. *Circ Res* 2004; **94**: 433–45.

5 Behm CZ, Lindner JR. Cellular and molecular imaging with targeted contrast ultrasound. *Ultrasound Q* 2006; **22**: 67–72.

6 Inoue H, Zipes DP. Results of sympathetic denervation in the canine heart: supersensitivity that may be arrhythmogenic. *Circulation* 1987; **75**: 877–87.

7 Inobe Y, Kugiyama K, Miyagi H, et al. Long-lasting abnormalities in cardiac sympathetic nervous system in patients with coronary spastic angina: quantitative analysis with iodine 123 metaiodobenzylguanidine myocardial scintigraphy. *Am Heart J* 1997; **134**: 112–18.

8 Wilson RF, Laxson DD, Christensen BV, McGinn AL, Kubo SH. Regional differences in sympathetic reinnervation after human orthotopic cardiac transplantation. *Circulation* 1993; **88**: 165–71.

9 Yamada T, Shimonagata T, Fukunami M, et al. Comparison of the prognostic value of cardiac iodine-123 metaiodobenzylguanidine imaging and heart rate variability in patients with chronic heart failure: a prospective study. *J Am Coll Cardiol* 2003; **41**: 231–38.

10 Paul M, Schäfers M, Kies P, et al. Impact of sympathetic innervation on recurrent life-threatening arrhythmias in the follow-up of patients with idiopathic ventricular fibrillation. *Eur J Nucl Med Mol Imaging* 2006; **33**: 866–70.

11 Nakata T, Wakabayashi T, Kyuma M, Takahashi T, Tsuchihashi K, Shimamoto K. Cardiac metaiodobenzylguanidine activity can predict the long-term efficacy of angiotensin-converting enzyme inhibitors and/or beta-adrenoceptor blockers in patients with heart failure. *Eur J Nucl Med Mol Imaging* 2005; **32**: 186–94.

12 Kopka K, Law MP, Breyholz HJ, et al. Noninvasive molecular imaging of beta-adrenoceptors in vivo: perspectives for PET-radioligands. *Curr Med Chem* 2005; **12**: 2057–74.

13 Kies P, Wichter T, Schäfers M, et al. Abnormal myocardial presynaptic norepinephrine recycling in patients with Brugada syndrome. *Circulation* 2004; **110**: 3017–22.

14 Schäfers M, Dutka D, Rhodes CG, et al. Myocardial presynaptic and postsynaptic autonomic dysfunction in hypertrophic cardiomyopathy. *Circ Res* 1998; **82**: 57–62.

15 Schäfers M, Lerch H, Wichter T, et al. Cardiac sympathetic innervation in patients with idiopathic right ventricular outflow tract tachycardia. *J Am Coll Cardiol* 1998; **32**: 181–86.

16 Wichter T, Schäfers M, Rhodes CG, et al. Abnormalities of cardiac sympathetic innervation in arrhythmogenic right ventricular cardiomyopathy: quantitative assessment of presynaptic norepinephrine reuptake and postsynaptic

beta-adrenergic receptor density with positron emission tomography. *Circulation* 2000; **101**: 1552–58.

17 Kopka K, Wagner S, Riemann B, et al. Design of new beta1-selective adrenoceptor ligands as potential radioligands for in vivo imaging. *Bioorg Med Chem* 2003; **11**: 3513–27.

18 Wagner S, Kopka K, Law MP, et al. Synthesis and first in vivo evaluation of new selective high affinity beta1-adrenoceptor radioligands for SPECT based on ICI 89,406. *Bioorg Med Chem* 2004; **12**: 4117–32.

19 Delforge J, Janier M, Syrota A, et al. Noninvasive quantification of muscarinic receptors in vivo with positron emission tomography in the dog heart. *Circulation* 1990; **82**: 1494–504.

20 Le Guludec D, Delforge J, Syrota A, et al. In vivo quantification of myocardial muscarinic receptors in heart transplant patients. *Circulation* 1994; **90**: 172–78.

21 Le Guludec D, Cohen-Solal A, Delforge J, et al. Increased myocardial muscarinic receptor density in idiopathic dilated cardiomyopathy: an in vivo PET study. *Circulation* 1997; **96**: 3416–22.

22 Falk E, Shah PK, Fuster V. Coronary plaque disruption. *Circulation* 1995; **92**: 657–71.

23 Greenland P, LaBree L, Azen SP, Doherty TM, Detrano RC. Coronary artery calcium score combined with Framingham score for risk prediction in asymptomatic individuals. *JAMA* 2004; **291**: 210–15.

24 Rudd JH, Warburton EA, Fryer TD, et al. Imaging atherosclerotic plaque inflammation with (^{18}F)–fluorodeoxyglucose positron emission tomography. *Circulation* 2002; **105**: 2708–11.

25 Kopka K, Breyholz HJ, Wagner S, et al. Synthesis and preliminary biological evaluation of new radioiodinated MMP inhibitors for imaging MMP activity in vivo. *Nucl Med Biol* 2004; **31**: 257–67.

26 Schäfers M, Riemann B, Kopka K, et al. Scintigraphic imaging of matrix metalloproteinase activity in the arterial wall in vivo. *Circulation* 2004; **109**: 2554–59.

27 Breyholz HJ, Wagner S, Levkau B, Schober O, Schäfers M, Kopka K. A ^{18}F-radiolabeled analogue of CGS 27023A as a potential agent for assessment of matrix metalloproteinase activity in vivo. *Q J Nucl Med Mol Imaging* 2007; **51**: 24–32.

28 Breyholz HJ, Schäfers M, Wagner S, et al. C-5-disubstituted barbiturates as potential molecular probes for noninvasive matrix metalloproteinase imaging. *J Med Chem* 2005; **48**: 3400–9.

29 Johnson LL, Schofield L, Donahay T, Narula N, Narula J. ^{99m}Tc-annexin V imaging for in vivo detection of atherosclerotic lesions in porcine coronary arteries. *J Nucl Med* 2005; **46**: 1186–93.

30 Kolodgie FD, Petrov A, Virmani R, et al. Targeting of apoptotic macrophages and experimental atheroma with radiolabeled annexin V: a technique with potential for noninvasive imaging of vulnerable plaque. *Circulation* 2003; **108**: 3134–39.

31 Kietselaer BL, Reutelingsperger CP, Heidendal GA, et al. Noninvasive detection of plaque instability with use of radiolabeled annexin A5 in patients with carotid artery atherosclerosis. *N Engl J Med* 2004; **350**: 1472–73.

32 Hartung D, Sarai M, Petrov A, et al. Resolution of apoptosis in atherosclerotic plaque by dietary modification and statin therapy. *J Nucl Med* 2005; **46**: 2051–56.

33 Faust A, Wagner S, Law MP, et al. The nonpeptidyl caspase binding radioligand (S)-1-(4-(2-(^{18}F)Fluoroethoxy)-benzyl)-5-(1-(2-methoxymethylpyrrolidinyl)s ulfonyl)isatin ((^{18}F)CbR) as potential positron emission tomography-compatible apoptosis imaging agent. *Q J Nucl Med Mol Imaging* 2007; **51**: 67–73.

34 Kopka K, Faust A, Keul P, et al. 5-Pyrrolidinylsulfonyl isatins as a potential tool for the molecular imaging of caspases in apoptosis. *J Med Chem* 2006; **49**: 6704–15.

35 Hofstra L, Liem IH, Dumont EA, et al. Visualization of cell death in vivo in patients with acute myocardial infarction. *Lancet* 2000; **356**: 209–12.

36 Narula J, Acio ER, Narula N, et al. Annexin-V imaging for noninvasive detection of cardiac allograft rejection. *Nat Med* 2001; **7**: 1347–52.

37 Ihling C, Szombathy T, Bohrmann B, Brockhaus M, Schaefer HE, Loeffler BM. Coexpression of endothelin-converting enzyme-1 and endothelin-1 in different stages of human atherosclerosis. *Circulation* 2001; **104**: 864–69.

38 Johnström P, Fryer TD, Richards HK, et al. Positron emission tomography using 18F-labelled endothelin-1 reveals prevention of binding to cardiac receptors owing to tissue-specific clearance by ET B receptors in vivo. *Br J Pharmacol* 2005; **144**: 115–22.

39 Dinkelborg LM, Duda SH, Hanke H, Tepe G, Hilger CS, Semmler W. Molecular imaging of atherosclerosis using a technetium-99m-labeled endothelin derivative. *J Nucl Med* 1998; **39**: 1819–22.

40 Holtke C, Law MP, Wagner S, et al. Synthesis, in vitro pharmacology and biodistribution studies of new PD 156707-derived ET(A) receptor radioligands. *Bioorg Med Chem* 2006; **14**: 1910–17.

41 Holtke C, von Wallbrunn A, Kopka K, et al. A fluorescent photoprobe for the imaging of endothelin receptors. *Bioconjug Chem* 2007; **18**: 685–94.

42 Johnstrom P, Fryer TD, Richards HK, et al. In vivo imaging of cardiovascular endothelin receptors using the novel radiolabelled antagonist (^{18}F)-SB209670 and positron emission tomography (microPET). *J Cardiovasc Pharmacol* 2004; **44**: S34–S38.

43 Johnström P, Rudd JH, Richards HK, et al. Imaging endothelin ET(B) receptors using (^{18}F)-BQ3020: in vitro characterization and positron emission tomography (microPET). *Exp Biol Med (Maywood)* 2006; **231**: 736–40.

37

CHAPTER 37

Optical Mapping: Its Impact on Understanding Arrhythmia Mechanisms

Guy Salama, PhD,[1] *Bum-Rak Choi,* PhD[2]

[1]University of Pittsburgh, Pittsburgh, PA, USA
[2]Rhode Island Hospital and Brown Medical School, Providence, RI, USA

Summary

Mapping cardiac electrical activity using fluorescence imaging techniques (optical mapping) has made significant contributions to our understanding of cardiac arrhythmia mechanisms. The advantages brought on by optical mapping include: unprecedented details of cardiac electrical activity at high spatial and temporal resolution and optical recordings of action potentials with signals similar to the shape and time course of action potentials recorded with intracellular microelectrodes. Moreover, optical mapping can image electrical activity at sampling rates sufficiently fast to map rapid activation of cardiac tissue under sinus rhythm, during reentry, as well as provide detailed maps of repolarization sequences. Studies using optical mapping of isolated heart preparations have thus provided new insights in various fields where conventional methods proved to be unsuitable; namely studies of: dispersion of repolarization, restitution kinetics of action potential durations, rate-dependent changes of repolarization, phase singularities, mechanisms underlying wave breaks in ventricular fibrillation (VF), activation of the ventricles via the specialized conduction system, and defibrillation mechanisms. Optical mapping techniques have been extended to new research areas that until recently were not practical. For instance, optical mapping can be used to elucidate the effects of spatial distributions of ion channel expression and other regulatory proteins and to characterize the arrhythmia phenotype of genetically engineered animals designed as models of human congenital diseases. Optics makes it possible to combine voltage and other fluorescent probes to simultaneously map several parameters (i.e. Voltage and intracellular Calcium) and to map spatial heterogeneities of intracellular calcium handling, and determine the role of intracellular Ca^{2+} as mechanisms that precipitate cardiac arrhythmias.

Cardiac Mapping, Third Edition Edited by Mohammad Shenasa, Gerhard Hindricks, Martin Borggrefe, and Günter Breithardt
 ISBN: 978-1-405-17572-2

Introduction

It is generally thought that cardiac arrhythmias are mostly due to reentrant electrical waves that continuously reexcite cardiac tissue [1–3]. Initiation and maintenance of these reentrant waves have been a major focus of research, to better understand the mechanisms underlying cardiac arrhythmias and also search for better treatment to stop and prevent reentry.

The development of vortex-like reentry or spiral waves and their trajectory may, in principle, vary due to spatial heterogeneities of cellular properties such as refractoriness, restitution kinetics of action potential durations, and fiber anisotropy. Therefore, the location and circuits of reentry, and the relationship between anatomical and functional characteristics of tissue, have frequently been the subjects of research and debate.

The fundamental goal is to map reentry circuits to gain a greater understanding of the mechanisms that initiate and maintain reentry as well as the possible factors that precipitate cardiac arrhythmias. However, due to the complexity of wave propagation and their abrupt changes in direction during fibrillation, it has been difficult to track propagation patterns quantitatively to analyze the structure and dynamics of arrhythmias with conventional electrode techniques.

Fluorescence imaging with voltage-sensitive dyes [4] can provide high spatial and temporal maps of activation, but like electrode techniques the recordings are limited to the surface of heart. However, optical mapping offers several advantages:

(a) The fluorescence changes emanating from voltage-sensitive dyes vary linearly with changes in the transmembrane potential measured with intracellular microelectrodes. As a result, the shape and time course of the optical action potential (AP), and the local activation and repolarization time-points, detect membrane potential changes with high accuracy that cannot be obtained using extracellular electrodes. Moreover, ionic and pharmacological interventions did not distort the fidelity of the optical action potential; its sh action potentiale and repolarization time course continue to correctly track changes in action potential due to rate, hypoxia, ischemia, adrenergic activity, ionic concentrations, species differences, and different cell types found in different regions of the heart.

(b) Mapping can be easily done in a large area of the heart at high spatial and temporal resolution with high-speed imaging devices such as photodiode arrays, or CCD or CMOS cameras. In contrast to surface electrograms, anatomical landmarks can be easily identified from the raw image of the heart taken from most cameras, and optical recordings are impervious to electrical distortion and saturation of operational amplifiers caused by electrical stimulation even during strong defibrillation shocks.

(c) Along with mapping electrical activity, optical probes of other parameters can be simultaneously recorded from multiple sites (i.e., intracellular Ca^{2+} concentration) that have greatly enhanced the power of these techniques. This chapter introduces the general principle of optical mapping apparatus and detectors and how they have been applied to investigate cardiac arrhythmia mechanisms.

Fluorescence Probes and Imaging Instruments

The principle of optical mapping of electrical activity is to label cardiac membranes with a dye that exhibits large changes in fluorescence and/or absorption during changes in transmembrane potential that can be detected with high-speed imaging instruments. Probes that detect transmembrane potential (Vm) changes are known as fast voltage-sensitive dyes and can be delivered to the cell membrane (known as staining procedure) by adding the dye directly to the aqueous solution used to perfuse the heart or dissolving the dye in a stock solution containing a vehicle to help deliver the dye to the cell membranes.

Merocyanine 540 was the first dye used to measure a cardiac action potential optically, with a fractional fluorescence change ($\Delta F/F$) of merely 1–2% per action potential [5]. Despite the small fluorescent change, the finding was most encouraging compared to measurements of Vm from squid giant axons where the fluorescence changes were ten times smaller often requiring signal averaging, and there were additional concerns due to phototoxic effects [6, 7]. Since then, numerous voltage-sensitive dyes have been discovered with improved characteristics that benefit mapping of electrical activity.

The most popular voltage-sensitive dye among cardiac researchers has been di-4-ANEPPS [8, 9] due to its fast response to Vm, ease of staining, negligible phototoxicity in perfused hearts, and bright

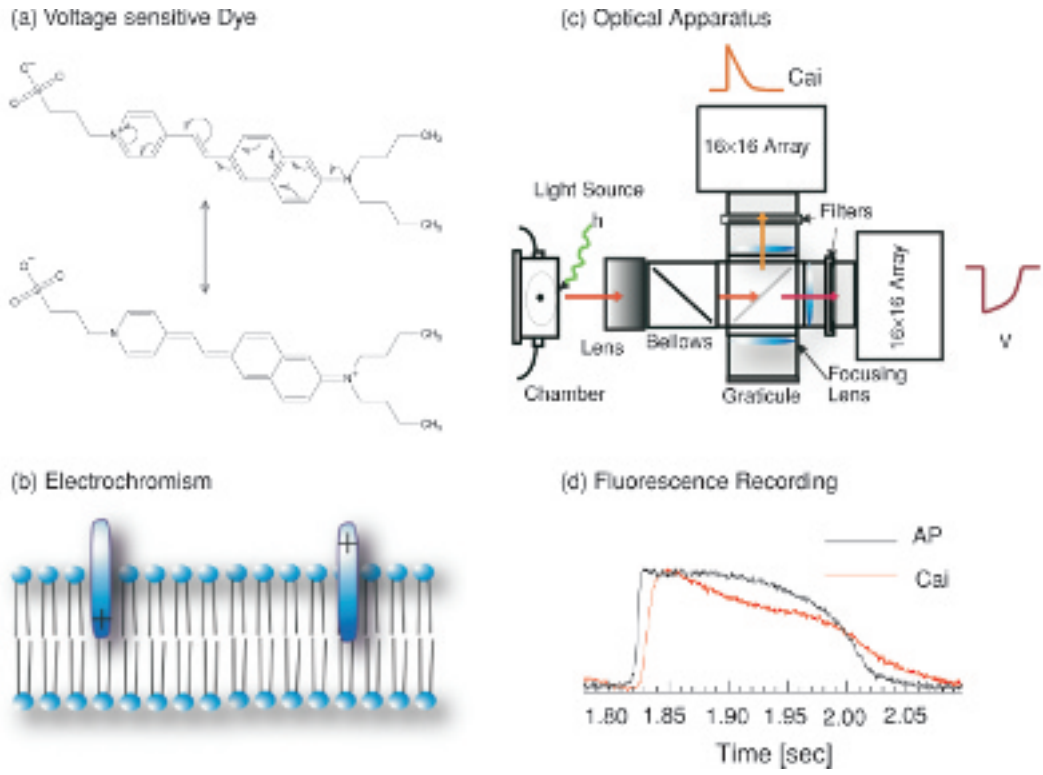

Figure 37.1 Fluorescence probes and schematics of optical mapping apparatus. (a) Electrochromic mechanisms for voltage-sensitive dye, di-4-ANEPPS. The chemical structure includes polar groups (—SO3—) and lipophilic hydrocarbon changes (butyl groups) to orient voltage-sensitive dye parallel to the electric field across the cell membrane. (b) The molecule can shift a charge in different resonance states, depending on the electrical field, resulting in fluorescence changes corresponding to Vm changes. (c) Optical mapping apparatus (taken from Ref. 41, Figure 1A). Typical apparatus includes heart chamber, excitation light source, lenses and filters to collect emission from fluorescence probes, and detectors such as photodiode arrays or CCD cameras to simultaneously map Vm and intracellular free Ca^{2+} concentration, Cai. (d) Typical recordings from one Vm and one Cai pixel viewing the same site on the heart (taken from Ref. 41, Figure 2B).

fluorescence signals, with relatively less intense excitation light. Figure 37.1 shows the chemical structure of di-4-ANEPPS and its electrochromic characteristics. An important feature of the dye is its bifunctional structure with a hydrophilic negative charge in one side and hydrophobic carbon chains in the other. The bipolar nature of dye promotes the delivery of the dye to the membrane such that it is preferentially inserted perpendicular to the cell membrane (Figure 37.1b) [9].

As a result, transmembrane potential changes can shift fluorescence from VSD rapidly by a reorganization of its outer shell of electrons. The response time to Vm is instantaneous (within microseconds), which allows for the detection of action potential upstrokes from isolated myocytes. It is important to point out that the dye senses the orientation of Vm. When stained from the extracellular side of the membrane, a dye may exhibit an increase in fluorescence during an action potential, but when stained from the cytosolic of the membrane, the same dye will exhibit a decrease in fluorescence during an action potential.

The reversal of the fluorescence change implies that if the dye is internalized during the course of the measurement, the fluorescence changes tend to cancel out from dye molecules bound from the outside vs. inside. In addition, at high concentrations, most dyes tend to form dimmers that quench their fluorescence emission, and as a result an excessive amount of dye staining becomes counterproductive.

The dye-staining process can be as simple as perfusion of the heart with a dye containing Tyrode's

solution for a few minutes. Typically, the voltage-sensitive dye is dissolved in dimethyl sulfoxide (1 mg/mL) and an aliquot or bolus of stock solution is added to the perfusate or injected directly in the cannula used to perfuse the heart. As little as 25 μL of stock solution (∼ 1 mM) is typically sufficient to yield optical action potentials with an excellent signal-to-noise (S/N) ratio from rabbit hearts, and the concentrations of dye should be adjusted to the size of the heart.

Longer wavelength dyes were developed in attempts to record action potentials from deeper layers within ventricular tissue. These dyes, such as PGH1, tend to be more hydrophobic and difficult to dissolve at physiological pH. Such dyes can be delivered by making a stock solution containing a surfactant such as Pluronic L44 to improve dye delivery [10]. In the case of isolated tissue preparation that requires superfusion of tissue, reasonable signals can be obtained after longer perfusion of dye solution (∼45 min) [11]. More recently, dye delivery of long-wavelength dyes was shown to be effective by increasing dye solubility either by preparing a dye stock solution in Tyrode's with low pH (∼6.0–6.4) or by covalently linking a polyethylene glycol to the dye structure [12].

Fluorescence changes can be simultaneously measured from multiple sites using imaging devices such as CCD (charge-coupled devices) cameras. Camera lenses are a popular choice to focus the entire heart on the small sensor chips such as Nikon F-mount or Navitar C-mount lenses. With such a configuration [panel (c)], the working distance is typically large, in the range 5–10 cm, making light collection rather inefficient.

In contrast, photodiode arrays and CMOS (complementary metal-oxide semiconductor) cameras have considerably larger sensor areas (1.8 × 1.8 or 1.0 × 1.0 cm^2) requiring less demagnification of the image and considerably shorter working distance and light collection. Uniform illumination of the heart can be achieved with one or two tungsten halogen lamps or several light guides from multiple light sources, ring-like arrangement around the collection lens, Hg-Xe arc lamps, or more recently with high-intensity light-emitting diodes (LED) and can be obtained for large fields of view (>1 cm). In contrast, a high magnification is needed for a smaller heart such as mice (∼ 5 mm field of view), which are obtained by reducing the working distance and epi-illumination arrangement with a dichroic box is recommended [13].

The fluorescence signal from a single pixel represents the sum of optical action potentials from many cells in a volume primarily determined by pixel size, magnification, numerical aperture of camera lens, and the wavelength of the fluorescence light. The depth resolution can be estimated with following equation,

$$d = \frac{\lambda \cdot n}{NA^2} + \frac{n \cdot e}{M \cdot NA},$$

where d is depth of focus, NA is a numerical aperture of the camera lens, M is magnification, e is the dimension of single pixel, n is a refractive index (water ∼1.3), and λ is the emission wavelength.

In addition, light scattering by cardiac tissue also influences depth resolution. Depth resolution of a typical setup with a CCD camera is in the range of 100 μm ∼ 2 mm depending on magnification. Therefore, signals should be interpreted appropriately when highly complex, inhomogeneous tissue will be mapped such as SA or AV node and endocardial surface with Purkinje fibers attached.

Applications of Optical Mapping Technique

Mapping Activation, Repolarization, Action Potential Duration, and Its Restitution Kinetics

A major advantage of optical mapping is the ability to record action potentials simultaneously from multiple locations. Figure 37.2 shows a typical example of fluorescence signals recorded with photodiode arrays at 2000 f/sec. The signal-to-noise ratio can be over 100:1 and the shape of action potentials is similar to transmembrane potential recordings with microelectrodes. Activation, repolarization, and action potential duration (APD) are automatically detected from first and second derivatives of fluorescence recording (F). Panel (b) shows an example of first (dF/dt) and second derivatives (d^2F/dt^2) [14]. The peak of dF/dt and d^2F/dt^2 corresponds to the rapid rise of action potential upstroke and downstroke of repolarization (red circles) which can be automatically detected using peak detection algorithm [14]. Panel (c)–(e) are maps of activation, repolarization, and APD [15].

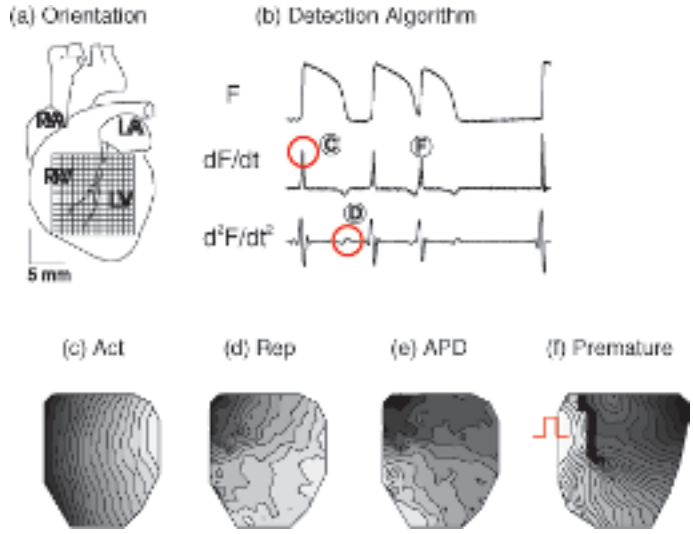

Figure 37.2 Mapping activation, repolarization, and dispersion of APD. (a) Orientation of the heart and the region viewed by the array. (b) Examples of fluorescence signals from guinea pig heart and automated detection of activation and repolarization. *dF/dt*: first derivative of fluorescence signal ($F(t)$). *d2F/dt2:* second derivative of $F(t)$. Both (*dF/dt*) max and (*d2F/dt2*) max can be used to detect activation and repolarization, respectively. (c)–(e) Activation, repolarization, and APD maps (taken from Ref. 41, Figure 5). The brighter the color the earlier the activation time. Note that the repolarization map is different from the activation map, indicating intrinsic spatial heterogeneities in ion channel expression in different regions of the heart. (f) Activation map of the premature beat.

The APD map indicates that APDs are shorter at the apex than the base in guinea pig hearts [15, 16], as well as all the hearts that have been studied thus far: mice [13], rabbits [17], and dogs (unpublished experiments). As a result, premature beat encounters refractoriness at the base and propagates toward the apex region first where the action potentials have already recovered from refractoriness, leading to unidirectional conduction block and rotating waves (panel f) [15].

Patterns in Ventricular Fibrillation

The hallmark of ventricular fibrillation is the shift from regular rhythmic contractions to a "can of worms" appearance of random local contractions and complex irregular ECG patterns. Mapping activation waves during ventricular fibrillation using an array of surface electrode recordings often encounter difficulties in analyzing the precise propagation pathway during rapid Vm oscillations because of the far-field integration of voltage by electrograms. In contrast, Vm measured from optical mapping show oscillations similar to what would be measured by an array of intracellular microelectrodes (Figure 37.3c).

With the high sampling rate of a CMOS camera (up to 10,000 f/sec), activation patterns during VF can be traced with great accuracy. For example, panel (b) represents a series of activation maps obtained from a CMOS camera with a spatial resolution of 100 × 100 μm^2 and a temporal resolution 0.5-msec intervals [18]. The activation patterns were recorded with unparalleled accuracy, making it possible to discern wave collisions, conduction blocks, and wave fractionations.

With such detail, further analysis made it possible to correlate activation patterns with anatomical obstacles such as major vessels [18, .19], fiber orientations [20], and the location of scars. Similarly, wave fractionation or wave break sites could be correlated with functional lines of block that occurred dynamically due to dispersion of repolarization and APD restitution kinetics [21]. In addition, the high signal-to-noise ratio and spatial resolution of optical mapping using a CMOS camera made it possible to examine the shape and time course of action potentials at and near wavebreak sites in VF (within 300 μm), and was shown to coincide with nodes of spatially discordant electrical alternans [18].

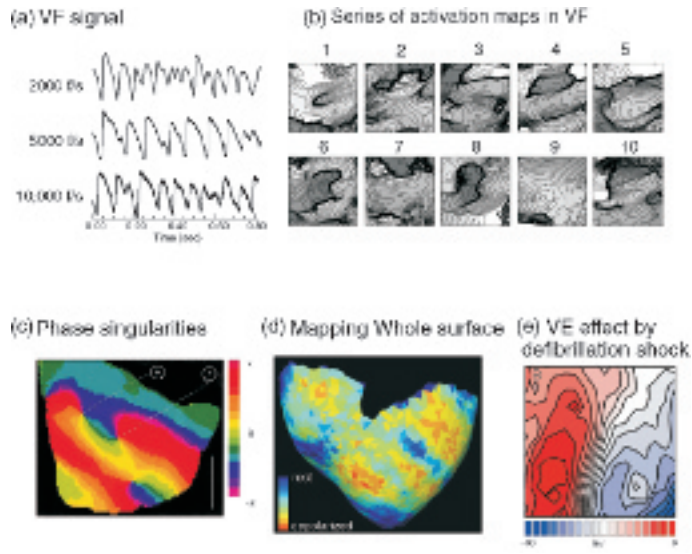

Figure 37.3 Mapping electrical activity in fibrillation and during defibrillation shocks. (a) Typical fluorescence recordings of VF in guinea pig hearts (taken from Ref. 18, Figure 1B). (b) Series of activation maps in VF (1×1 cm^2 field of view, 2 msec isochronal lines). (c) Phase maps and identification of phase singularities (taken from Ref. 23, Figure 2A). (d) Activation maps from the entire epicardial surface using panoramic optical mapping (taken from Ref. 25, Figure 3). (e) Transmembrane potential distribution during a defibrillation shock produced a virtual electrode (VE) effect on the epicardium (taken from Ref. 42, Figure 5B).

The study suggests that spatially discordant alternans may be an important mechanism underlying VF maintenance through the creation of new daughter waves at wavebreak sites [18]. The nature and organization of VF dynamics has been shown to depend on the osmolarity and tonicity of the perfusate. In Langendorff-perfused guinea pig hearts, switching the perfusate from an iso-osmotic to a hypo-osmotic solution produced a gradual time-dependent shift of VF frequencies from complex FFT to a single high-frequency rotor. The changes in VF dynamics occurred over several minutes and were reversed by switching back to iso-osmotic conditions or by adding an inhibitor of chloride channels [22]. Moreover, the channel most likely responsible for volume regulation in heart cell, ClC-3, has been found to be heterogeneously distributed between the right and left ventricles. As a result, the dominant high frequencies (28–30 Hz) during VF were observed only under hypo-osmotic conditions and on the left but not the right ventricle, which is consistent with the distribution of ClC-3 [22].

The complex wave propagations can be further analyzed by localizing the center of rotation and then tracing their behavior. Gray et al. [23] applied a time-embedding approach to convert fluorescence signals into an angular variable. With this algorithm, the state of cardiac myocytes can be represented as a periodic phase value ($-\pi$ to π) that corresponds from the activation to the repolarization/refractoriness. The center of rotors can be defined as phaseless point (phase singularity; see Figure 37.3c). Therefore, complex patterns of wave propagation can be analyzed by tracking creation and annihilation of phase singularities and their distribution [19, 23].

In principle, phase singularities are valid surrogates for wavebreak sites, except when baseline drift and a low signal-to-noise ratio compromise the analysis, resulting in false positives. The improved characteristics of CMOS cameras make it possible to identify wavebreak sites directly using image analysis algorithms [18]. The method has shown that for VF elicited by burst pacing, wavebreaks do not preferentially occur at anatomical obstacles such as large coronary vessels, but are coincident with the nodes of spatially discordant voltage alternans [18].

One of the limitations of a single camera system is that only one part of the surface of the heart was mapped, with little information around the

perimeter of the heart. As a result, waves often disappear from the field of view, and it is difficult to track wave fronts and to investigate mechanisms of phase singularity formation. Rogers et. al. [24, 25] recently used a set of cameras to image the entire surface of the heart, including the anterior, posterior, and both sides, and then reconstructed wave propagation from the whole surface of the heart [panel (d)]. The panoramic optical mapping method can trace all the wave fronts from the complete epicardial surface. With panoramic mapping, Rogers et. al. (provided new insights regarding the maintenance of VF; most wave fronts from the epicardium can be tracked in time as well as their creation and annihilation. which suggests that the essential events in VF have been observed on the surface of the heart and nonepicardial ectopic source(s) such as the "mother rotor" have not been required to maintain VF [25].

Distribution of Transmembrane Potential During Defibrillation Shocks

One of the great advantages of optical mapping is that the fluorescence recording is impervious to electrical stimulation artifacts. Microelectrode and surface electrode recordings exhibit sharp spikes during electrical stimuli, which may saturate the operations amplifiers, especially during strong shock. These shock artifacts hamper electrogram recordings and subsequent analysis of the potential distribution across the tissue elicited by the electric shock as well as wave propagations.

Efimov et. al. [26, 27] investigated Vm distributions during and after strong shocks (Figure 37.3e) and presented compelling evidence for the generation of virtual electrode phenomena in cardiac tissue. Due to nonuniform resistance along the muscle fiber in intra/extracellular space (as predicted from the bidomain theory), strong shocks caused one region of the tissue to depolarize while other becomes hyperpolarized, resulting in nonuniform Vm distribution. This nonuniform Vm distribution elicited by the shock is called the "virtual electrode" (VE) effect because hyperpolarization of tissue can be seen near the cathode without the position of the real anode during strong shock.

Mapping the VE effect using optical the mapping technique has extended our understanding of mechanisms of defibrillation and provided clues as to why in some cases the shock fails to stop fibrillation. Defibrillation failure occurs because a new wave front is formed at the boundary between depolarized and hyperpolarized region of tissue and the wave spreads unidirectionally across the hyperpolarized region, resulting in a new reentrant wave (scroll wave) [26].

Mapping Genetically Engineered Animal Models

Progress in molecular biology has led the way to the development of transgenic animal models of human cardiac pathology, and the contribution of these models to our understanding of mechanisms underlying these pathologies has been enormous [28]. Except for a few rabbit models of long QT, transgenic models have been routinely generated in mice.

For cardiac electrophysiology, the small dimensions of mouse heart (<5 mm) make it particularly challenging to map mouse hearts using multiple extracellular surface or monophasic action potential (MAP) electrodes and track wave propagation. Optical mapping with a high magnification lens has been a practical approach for mouse cardiac electrophysiology [29–31]. In addition, action potentials can be recorded with excellent signal-to-noise ratio, sufficient to map activation, repolarization, and restitution kinetics, even in embryonic mouse heart [32] and zebra fish heart [33].

The heterogeneous distribution of ion channels can increase vulnerability to arrhythmias by increasing the dispersion of repolarization. In the long-QT animal model, slowly inactivating K+ current was repressed by the dominant negative transgenic approach, and these transgenic mice exhibit prolonged QT intervals and VT induction by programmed stimulation [13].

Mechanisms of VT in this model were investigated by mapping conduction blocks and reentry formation with a photodiode array and high magnification lenses. Figure 37.4a is an example of an APD map from transgenic heart [13]. The dispersion of APD was accentuated in this transgenic long-QT model, exhibiting shorter at the apex than at the base. A premature impulse applied at the apex produced a sustained VT that did not occur with stimulation at the base. Mapping of premature beat revealed a line of conduction block in the middle caused by increased dispersion of repolarization.

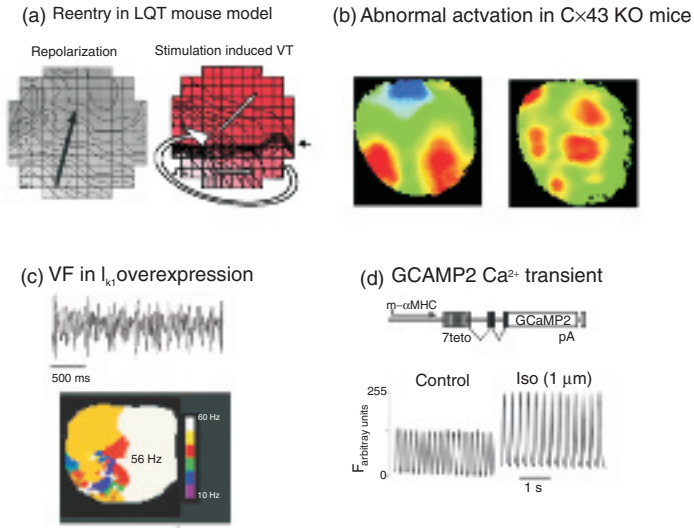

Figure 37.4 Mapping genetically engineered animal models. (a) Increase of repolarization dispersion in long-QT mouse model increases reentry formation during premature stimulation (taken from Ref. 29, Figures 4D and 6D). (Left panel) APD maps showing longer APD at the base. (Right panel) Premature stimulation encounters conduction block toward the base and forms reentry due to longer APD at the base. (b) Activation pattern under sinus rhythm in control (left panel) and Cx43 knockout mice (right panel) (taken from Ref. 30, Figure 2D,E). (c) High-frequency rotors under IK1 overexpression condition. APD shortening by IK1 overexpression increased rotation speed of spiral waves at higher frequency (taken from Ref. 31, Figure 2). (d) Ca^{2+}-sensitive GFP was expressed selectively in the heart of transgenic mice using the α-myosin heavy chain promoter resulting in mice with green hearts. The genetically encoded GCaMP2 Ca^{2+} sensor yielded Ca^{2+} transients beat-to-beat that increased in amplitude after an addition of isoproterenol (Iso) (taken from Ref. 38, Figures 1D,E).

This finding suggests that potassium channels are not uniformly distributed and an increase of APD dispersion increases vulnerability to conduction block and reentry formations [13].

Panel (b) illustrates another example of the transgenic mouse model. Connexin 43 is a major gap junction in the ventricle, and its potential roles in various pathologies have been well documented, including heart failure, development, diabetics, and myocardial infarction. Because the homozygous Cx43 knockout is lethal, a conditional knockout model was developed to delay the embryonic mortality [34]. These mice displayed a progressive reduction in the amplitude of the QRS complex without changes in the action potential amplitudes measured from single myocytes.

The cause of QRS anomalies was investigated by mapping the activation pattern under sinus rhythm with optical mapping [30]. Panel (b) shows activation maps from control (left) and transgenic hearts (right). The sinus activation in Cx43 knockout heart revealed multiple sites of epicardial breakthrough and subsequent wave front collisions, which account for the highly arrhythmogenic behavior of the Cx43 deficient heart.

In addition to knockout animal models, the overexpression of specific proteins can be used to evaluate their role in modifying arrhythmia dynamics. Theoretical and experimental studies suggest a tight link between wavelength of the action potential (wavelength = conduction velocity * APD) and the dimension of reentry circuits, which is limited by head–tail interaction around the center of rotation.

In mammalian hearts, a major determinant of repolarization reserve is the inwardly rectifying K+ current, IK1, which has been found to be critical to rotor stability. Jalife and his colleagues investigated the effects of IK1 by generating a mouse model that overexpresses the channel protein (Figure 37.4c). In this model, APD shortened significantly as expected due to an increase of IK1. The rotation speed of spiral waves increased markedly (26 Hz in control vs. 44 Hz in transgenic hearts), confirming the

relationship between wavelength and spiral wave dynamics. These studies suggested that heterogeneities of IK1 levels between right and left ventricles might account for the higher VF frequencies found in the left compared to the right ventricles of guinea pig hearts [35].

An alternative explanation is that the guinea pig hearts used in these studies were perfused under hypo-osmotic conditions, which would result in the activation of chloride currents (preferentially on the left compared to the right ventricles). Several types of Cl^- channels are found in cardiac cells; Ca^{2+} activated, PKA, or PKC-dependent and volume-regulated Cl^- channel [36]. Among these, the activation of volume-regulated (or swelling-activated) chloride current (ICl, vol) by perfusion with a solution made hypo-osmotic by 45 mOsM was shown to transform VF from complex to a highly organized dominant high frequency [22].

Recent advances in molecular engineering allowed the design of proteins that serve as optical indicators of cellular behavior. These genetically encoded sensors can target key lineages and tissues or even specific subcellular locations, allowing us to investigate physiological and pathological processes at the molecular level.

Genetically encoded sensors such as voltage, Ca^{2+}, and small molecules have been used effectively but limited to lower organisms or cell cultures. Modification and improvement of genetically encoded sensors have resulted in stable expression and high signal characteristics in mammalian system, allowing in vivo mapping of specific physiological events [37, 38].

Figure 37.4c shows an example of a genetically encoded Ca^{2+} sensor, GCaMP2 [38]. The construct is composed of green fluorescence protein and calmodulin, increasing fluorescence upon Ca^{2+} binding to this construct. As a result, Ca^{2+} transient can be measured from GCaMP2 hearts and their kinetics can be investigated in great detail without addition of dyes [panel (d)] [38].

Limitations of Optical Mapping

The most significant limitation of the optical mapping technique is the distortion of fluorescence signals due to muscle contractions. These motion artifacts can be abated by specially designed chambers or by pharmacological agents that block contractions (i.e., electrochemical uncouplers) that presumably do not alter intracellular Ca^{2+} handling or electrical properties of the heart.

Of the compounds that interrupt excitation-contraction coupling, 2,3-butanedione monoxime (BDM) and cytocholasin D have been extensively used despite known pharmacological alterations that may modify what is being measured. These chemicals produce side effects such as APD prolongation or shortening, a slowing down of conduction velocity, etc., and these effects are highly species dependent [39]; as a result, experimental results should be interpreted with caution.

More recently, the myosin II-ATPase inhibitor, blebbistatin, was found to block contractions with negligible effects on action potential and intracellular Ca^{2+} transients in rabbit hearts [40]. However, while blebbistatin appears to be effective in rabbit hearts, it is not effective in other species such as mouse hearts (unpublished results).

Conclusion and Future Directions

Exciting new efforts are being made to improve signal quality and to record electrical activity from deeper layers inside the ventricular wall. With the development of 3D mapping system in combination with new long-wavelength probes and genetically encoded sensors, one can expect that in the next decade, optical mapping will make great strides by providing images of physiological events in ever greater detail and will flourish with new advances in basic science regarding cardiac arrhythmia mechanisms and by offering new treatment modalities in the clinical setting.

Acknowledgements

This work was supported by grant awards from a Beginning Grant-in-Aid from the Western Pennsylvania Affiliate of the American Heart Association to B.R. Choi and NIH HL057929, HL70722, and HL69097 to G. Salama.

References

1 Mines GR. On circulating excitation in heart muscle and their possible relation to tachycardia and fibrillation. *Trans Royal Soc Can* 1914; **8**: 43–53.

2 Jalife J. Ventricular fibrillation: mechanisms of initiation and maintenance. *Annu Rev Physiol* 2000; **62**: 25–50.

3 Schmitt FO, Erlanger J. Directional differences in the conduction of impulse through heart muscle and their possible relation to extrasystolic and fibrillatory contractions *Am J Physiol* 1928; **87**: 326–47.

4 Salama G, Lombardi R, Elson J. Maps of optical action potentials and NADH fluorescence in intact working hearts. *Am J Physiol* 1987; **252**: H384–94.

5 Salama G, Morad M. Merocyanine 540 as an optical probe of transmembrane electrical activity in the heart. *Science* 1976; **191**: 485–87.

6 Davila HV, Salzberg BM, Cohen LB, Waggoner AS. A large change in axon fluorescence that provides a promising method for measuring membrane potential. *Nat New Biol* 1973; **241**: 159–60.

7 Ross WN, Salzberg BM, Cohen LB, et al. Changes in absorption, fluorescence, dichroism, and Birefringence in stained giant axons: optical measurement of membrane potential. *J Membr Biol* 1977; **33**: 141–83.

8 Loew LM, Cohen LB, Dix J, et al. A naphthyl analog of the aminostyryl pyridinium class of potentiometric membrane dyes shows consistent sensitivity in a variety of tissue, cell, and model membrane preparations. *J Membr Biol* 1992; **130**: 1–10.

9 Fluhler E, Burnham VG, Loew LM. Spectra, membrane binding, and potentiometric responses of new charge shift probes. *Biochemistry* 1985; **24**: 5749–55.

10 Salama G, Choi BR, Azour G, et al. Properties of new, long-wavelength, voltage-sensitive dyes in the heart. *J Membr Biol* 2005; **208**: 125–40.

11 Nikolski V, Efimov I. Fluorescent imaging of a dual-pathway atrioventricular–nodal conduction system. *Circ Res* 2001; **88**: E23–30.

12 Patrick MJ, Ernst LA, Waggoner AS, Tai CS, Salama G. Enhanced aqueous solubility of long-wavelength voltage-sensitive dyes by covalent linkage of polyethylene glycol chain. *Org Biomol Chem* 2007; **5**: 3347–53.

13 Baker LC, London B, Choi BR, Koren G, Salama G. Enhanced dispersion of repolarization and refractoriness in transgenic mouse hearts promotes reentrant ventricular tachycardia. *Circ Res* 2000; **86**: 396–407.

14 Efimov IR, Huang DT, Rendt JM, Salama G. Optical mapping of repolarization and refractoriness from intact hearts. *Circulation* 1994; **90**: 1469–80.

15 Choi BR, Salama G. Simultaneous maps of optical action potentials and calcium transients in guinea pig hearts: mechanisms underlying concordant alternans. *J Physiol* 2000; **529**: 171–88.

16 Kanai A, Salama G. Optical mapping reveals that repolarization spreads anisotropically and is guided by fiber orientation in guinea pig hearts. *Circ Res* 1995; **77**: 784–802.

17 Choi BR, Burton F, Salama G. Cytosolic Ca^{2+} triggers early afterdepolarizations and torsade de pointes in rabbit hearts with type 2 long-QT syndrome. *J Physiol* 2002; **543**: 615–31.

18 Choi BR, Jang W, Salama G. Spatially discordant voltage alternans cause wavebreaks in ventricular fibrillation. *Heart Rhythm* 2007; **4**: 1057–68.

19 Valderrabano M, Chen PS, Lin SF. Spatial distribution of phase singularities in ventricular fibrillation. *Circulation* 2003; **108**: 354–59.

20 Choi BR, Liu T, Lavasani M, Salama G. Fiber orientation and cell–cell coupling influence ventricular fibrillation dynamics. *J Cardiovasc Electrophysiol* 2003; **14**: 851–60.

21 Laurita KR, Girouard SD, Rosenbaum DS. Modulation of ventricular repolarization by a premature stimulus: role of epicardial dispersion of repolarization kinetics demonstrated by optical mapping of the intact guinea pig heart. *Circ Res* 1996; **79**: 493–503.

22 Choi BR, Hatton WJ, Hume JR, Liu T, Salama G. Low osmolarity transforms ventricular fibrillation from complex to highly organized, with a dominant high-frequency source. *Heart Rhythm* 2006; **3**: 1210–20.

23 Gray RA, Pertsov AM, Jalife J. Spatial and temporal organization during cardiac fibrillation [see comments] [published erratum appears in *Nature* 1998 May 14; **393**: 191]. *Nature* 1998; **392**: 75–78.

24 Kay MW, Walcott GP, Gladden JD, Melnick SB, Rogers JM. Lifetimes of epicardial rotors in panoramic optical maps of fibrillating swine ventricles. *Am J Physiol Heart Circ Physiol* 2006; **291**: H1935–41.

25 Rogers JM, Walcott GP, Gladden JD, Melnick SB, Kay MW. Panoramic optical mapping reveals continuous epicardial reentry during ventricular fibrillation in the isolated swine heart. *Biophys J* 2007; **92**: 1090–95.

26 Efimov IR, Cheng Y, Van Wagoner DR, Mazgalev T, Tchou PJ. Virtual electrode-induced phase singularity: a basic mechanism of defibrillation failure. *Circ Res* 1998; **82**: 918–25.

27 Efimov IR, Cheng YN, Biermann M, Van Wagoner DR, Mazgalev TN, Tchou PJ. Transmembrane voltage changes produced by real and virtual electrodes during monophasic defibrillation shock delivered by an implantable electrode. *J Cardiovasc Electrophysiol* 1997; **8**: 1031–45.

28 Nerbonne JM. Studying cardiac arrhythmias in the mouse: a reasonable model for probing mechanisms? *Trends Cardiovasc Med* 2004; **14**: 83–93.

29 Baker LC, London B, Choi BR, Koren G, Salama G. Enhanced dispersion of repolarization and refractoriness in transgenic mouse hearts promotes reentrant ventricular tachycardia. *Circ Res* 2000; **86**: 396–407.

30 Morley GE, Danik SB, Bernstein S, et al. Reduced intercellular coupling leads to paradoxical propagation across the Purkinje–ventricular junction and aberrant myocardial

activation. *Proc Natl Acad Sci U S A* 2005; **102**: 4126–29.

31 Noujaim SF, Pandit SV, Berenfeld O, et al. Up-regulation of the inward rectifier K+ current (I K1) in the mouse heart accelerates and stabilizes rotors. *J Physio.* 2007; **578**: 315–26.

32 Rothenberg F, Nikolski VP, Watanabe M, Efimov IR. Electrophysiology and anatomy of embryonic rabbit hearts before and after septation. *Am J Physiol Heart Circ Physiol* 2005; **288**: H344–51.

33 Sedmera D, Reckova M, deAlmeida A, et al. Functional and morphological evidence for a ventricular conduction system in zebrafish and Xenopus hearts. *Am J Physiol Heart Circ Physiol* 2003; **284**: H1152–60.

34 Gutstein DE, Morley GE, Fishman GI. Conditional gene targeting of connexin 43: exploring the consequences of gap junction remodeling in the heart. *Cell Commun Adhes* 2001; **8**: 345–48.

35 Samie FH, Berenfeld O, Anumonwo J, et al. Rectification of the background potassium current: a determinant of rotor dynamics in ventricular fibrillation. *Circ Res* 2001; **89**: 1216–23.

36 Hume JR, Duan D, Collier ML, Yamazaki J, Horowitz B. Anion transport in heart. *Physiol Rev* 2000; **80**: 31–81.

37 Kotlikoff MI. Genetically encoded Ca^{2+} indicators: using genetics and molecular design to understand complex physiology. *J Physiol* 2007; **578**: 55–67.

38 Tallini YN, Ohkura M, Choi BR, et al. Imaging cellular signals in the heart in vivo: Cardiac expression of the high-signal Ca^{2+} indicator GCaMP2. *Proc Natl Acad Sci U S A* 2006; **103**: 4753–58.

39 Baker LC, Wolk R, Choi BR, et al. Effects of mechanical uncouplers, diacetyl monoxime, and cytochalasin D on the electrophysiology of perfused mouse hearts. *Am J Physiol Heart Circ Physiol* 2004; **287**: H1771–79.

40 Fedorov VV, Lozinsky IT, Sosunov EA, et al. Application of blebbistatin as an excitation–contraction uncoupler for electrophysiologic study of rat and rabbit hearts. *Heart Rhythm* 2007; **4**: 619–26.

41 Choi BR, Salama G. Simultaneous maps of optical action potentials and calcium transients in guinea pig hearts: mechanisms underlying concordant alternans. *J Physiol* 2000; **529**: 171–88.

42 Efimov IR, Aguel F, Cheng Y, Wollenzier B, Trayanova N. Virtual electrode polarization in the far field: implications for external defibrillation. *Am J Physiol Heart Circ Physiol* 2000; **279**: H1055–70.

38

CHAPTER 38

The Kinetics of Intracellular Calcium and Arrhythmogenesis in Ischemia/Reperfusion: A Calcium-Centric Mechanism of Arrhythmia

Nabil El-Sherif, MD, *Gil Bub,* PhD, *Vikram Lakireddy,* MD

SUNY Downstate Medical Center, Brooklyn, NY, USA

Summary

Ischemia/reperfusion is associated with elevated intracellular calcium and alteration in calcium kinetics. There are several lines of evidence to suggest that alteration of sarcoplasmic reticulum function and calcium kinetics will alter membrane voltage and play a significant role in the genesis of cardiac arrhythmias in the setting of ischemia/reperfusion. The correlation between altered calcium kinetics and arrhythmogenesis has been investigated in a Langendorff-perfused guinea pig heart preparation utilizing simultaneous recordings of membrane voltage and intracellular calcium transient.

At least three possible electrophysiological mechanisms by which altered calcium kinetics can result in arrhythmias can be cited: (i) Calcium alternans resulting in membrane voltage alternans, that is, action potential duration alternans and increased dispersion of repolarization; (ii) focal arrhythmias triggered by early afterdepolarizations, or delayed afterdepolarizations; (ii) uncoupling of calcium/membrane voltage which may play a crucial role in wave break and the initiation and maintenance of ventricular tachyarrhythmias.

Introduction

Calcium (Ca^{2+}) plays two pivotal roles in cardiac excitation–contraction coupling. Ca^{2+} drives myofilament activation and carries or regulates ionic currents that are responsible for normal electrical rhythms, as well as for life-threatening arrhythmias. Ca^{2+} entry via Ca^{2+} current triggers sarcoplasmic reticulum (SR) Ca^{2+} release via ryanodine receptors (RyRs), and relaxation is driven by Ca^{2+} transport by the SR Ca^{2+}–ATPase and Na^{+}–Ca^{2+} exchange [1].

Ischemia/reperfusion is associated with elevated intracellular Ca^{2+} (Cai) and alteration in Cai

Cardiac Mapping, Third Edition Edited by Mohammad Shenasa, Gerhard Hindricks, Martin Borggrefe, and Günter Breithardt
 ISBN: 978-1-405-17572-2

kinetics [2–4]. There are several lines of evidence to suggest that alteration of SR function and Cai kinetics will alter membrane voltage (Vm) and play a significant role in the genesis of cardiac arrhythmias in the setting of ischemia/reperfusion. At least three possible electrophysiologic mechanisms can be cited:

1 Cai alternans (Alt) resulting in Vm alternans, that is, action potential duration (APD) Alt and increased dispersion of repolarization (DR);

2 focal arrhythmias triggered by early afterdepolarizations (EAD), or delayed afterdepolarizations (DAD);

3 uncoupling of Cai/Vm, which may play a crucial role in wavebreak and the initiation and maintenance of ventricular tachyarrhythmia (VT).

The correlation between altered Cai, and arrhythmogenesis has been investigated in theoretical models [5], and at the subcellular [6], cellular [7–9] and myocyte culture levels [10]. However, there is obvious lack of studies that directly correlate alterations of Cai/APs, and arrhythmias in an intact heart preparation. The recent availability of techniques capable of simultaneous analysis of Cai and action potentials in perfused whole-heart preparations [11, 12] provides a unique opportunity to investigate in detail the spatiotemporal alterations of these parameters during ischemia/reperfusion.

Technical Considerations

For the experiments described in this chapter, Cai and voltage transients were captured using a protocol and equipment that have been previously described [11]. Briefly, hearts were collected from guinea pigs (female, 350–450 g). Hearts were Langendorff-perfused with a modified Tyrode solution (130 NaCl, 25 $NaHCO_3$, 1.20 $MgSO_4$, 4.0 KCl, 20 dextrose, 1.25 $CaCl_2$, at pH 7.4, bubbled with 95% O_2–5% CO_2) with a flow rate of 12–16 mL min-L, at 70 mmHg pressure. Hearts were placed in a custom-made chamber to reduce movement artifact, and stained with a voltage-sensitive dye (RH237, Invitrogen, 10–20 μL of a 1 mg mL-1 solution in dimethyl sulfoxide, DMSO) and calcium indicator (Rhod-2 AM Invitrogen, 0.2 mg in 0.2 mL DMSO).

Excitation light from a tungsten–halogen source was filtered (520 ± 20 nm), and focused on the surface of the heart (Figure 38.1). Emitted fluorescent light was collected with a camera lens (85 mm, f1:1.4, Nikon) and passed through a dichroic mirror (630 nm, Omega Optical, Brattleboro, VT). Fluorescence images of the heart were then focused on two 16 × 16 element photodiode arrays (C675-103; Hamamatsu Corporation, Bridgewater, NJ). Cai was imaged using fluorescent light collected below 630 nm after having been passed through a 585 ± 20 nm interference filter, and Vm was imaged using fluorescence above 630 nm after being passed through a 715-nm cut-off filter. The optical apparatus was adjusted so that Cai and Vm transients were imaged from a 16 mm^2 area of the left ventricle. Outputs from the photodiode arrays were amplified up to 1000 times depending on experimental conditions and digitized at 12-bit resolution prior to offline analysis.

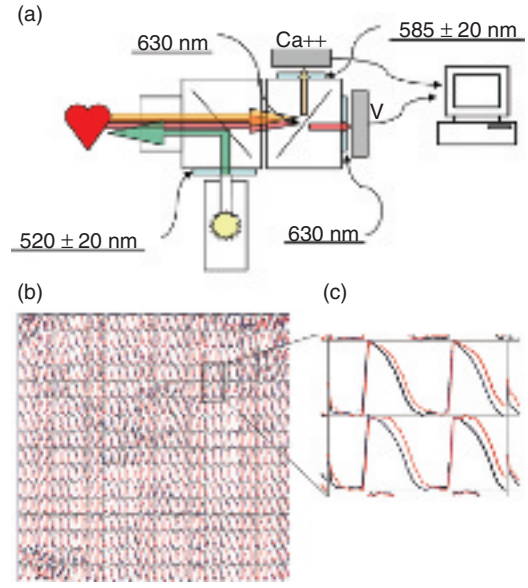

Figure 38.1 (a) Diagramatic illustration of the dual optical mapping system first described by Choi BR, Salama G. *J Physiol (London)* 2000; 529: 171–88. (b) An example of the 16 × 16 pixel simultaneous recordings of the action potential (AP) and intracellular calcium transient (CaiT). (c) An expanded view from two pixels. In this and subsequent figures, the action potential is colored blue and the CaiT is colored red.

Figure 38.1b illustrates the 256-pixel epicardial window of simultaneous recording of Vm (in blue) and Cai (in red). Figure 38.1c shows an expanded view from two pixels. Global no-flow ischemia was

applied to the preparation after acquiring initial measurements of Vm and Cai during sinus rhythm. The perfusion pump was turned off for 10–15 min to induce ischemia and then restarted for reperfusion for 10–15 min. Cai and Vm traces were continuously recorded during both ischemia and reperfusion.

Contrasting Effects of Ischemia on the Kinetics of Cai Transient (CaiT) and Vm Underlie Electrical Alternans

In recent years, repolarization alternans has been considered a strong marker of electrical instability and VT in the clinical setting [13]. Alternans of Cai and action potential have been investigated in both theoretical [5] and experimental models [11] utilizing a variety of techniques. In spite of extensive literature on the mechanisms of electrical alternans in normal preparations and in response to marked shortening of cycle length (CL), the pathophysiology of electrical alternans during ischemia is not well investigated.

Ischemia is known to be associated with alterations of the action potential and Cai kinetics, as well as electrical alternans and VT. Previous studies of electrical alternans in experimental models of ischemia utilized analysis of extracellular electrograms [14, 15], monophasic action potentials [16], or a floating microelectrode technique [17]. More recently, recordings of optical signals showing ischemia-induced alternans of either the CaiT [18] or action potential [19] have been reported. However, the correlation between alternans of CaiT and the action potential during ischemia has not been investigated.

In a recent study [20], we investigated ischemia-induced alterations in action potentials and CaiT leading to alternans utilizing simultaneous recordings of optical signals of membrane voltage and CaiT. Our study demonstrated that ischemia-induced contrasting changes on the kinetics of Vm and CaiT can explain both the vulnerability of ischemic heart to alternans and the marked spatial heterogeneity of repolarization during alternans.

Ischemia resulted in a varying degree of shortening of APD. On the other hand, ischemia resulted in delay of the upstroke of CaiT in relation to the upstroke of the action potential, broadening of the peak deflection, and slowing of the decay of CaiT with an overall increase of the duration of CaiT. The ischemia-induced contrasting changes in the action potential duration (D) and CaiT-D could result in a situation in which full repolarization of the action potential could occur at a time when the decay of CaiT has just started. The introduction of a pacing stimulus at a relatively short CL could succeed in generating a full action potential at a time before the decay of the preceding CaiT and would thus result in a markedly reduced CaiT. This would perturb the classic negative feedback system of normal Cai autoregulation [21] and result in alternans of subsequent CaiT amplitude. This process could follow a gradual or abrupt increase of the heart rate (Figure 38.2).

Spatial Heterogeneity of APD and Electrical Alternans

Ischemia results in marked heterogeneity of the shortening of APD. On the other hand, ischemia was associated with less spatial variation in the degree of prolongation of CaiT-D. This is illustrated in Figures 38.3 and 38.4.

Figure 38.3 shows recordings from two separate pixels from the same experiment. Ischemia resulted in a similar degree of lengthening of CaiT-D, but in markedly different degrees of shortening of APD. A critical short CL resulted in the same degree of CaiT alternans at the two sites. However, APD alternans did not develop at the site with the short APD while significant APD alternans occurred at the site with the long APD.

Figure 38.4 shows repolarization maps of two consecutive beats at a pacing CL of 300 msec from the same experiment shown in Figure 38.3. The figure illustrates the marked increase in spatial dispersion of repolarization of alternate beats. The spatially heterogeneous shortening of APD during ischemia coupled with a relatively more spatially homogeneous lengthening of CaiT duration was identified as playing a major role in the development of APD-Alt and the greater degree of dispersion of APD during ischemia.

The mechanism of the spatially heterogeneous shortening of APD during ischemia is related, among other factors, to the degree of local increase of Ko which is a net outcome of Ki efflux and washout from the extracellular space. On the other

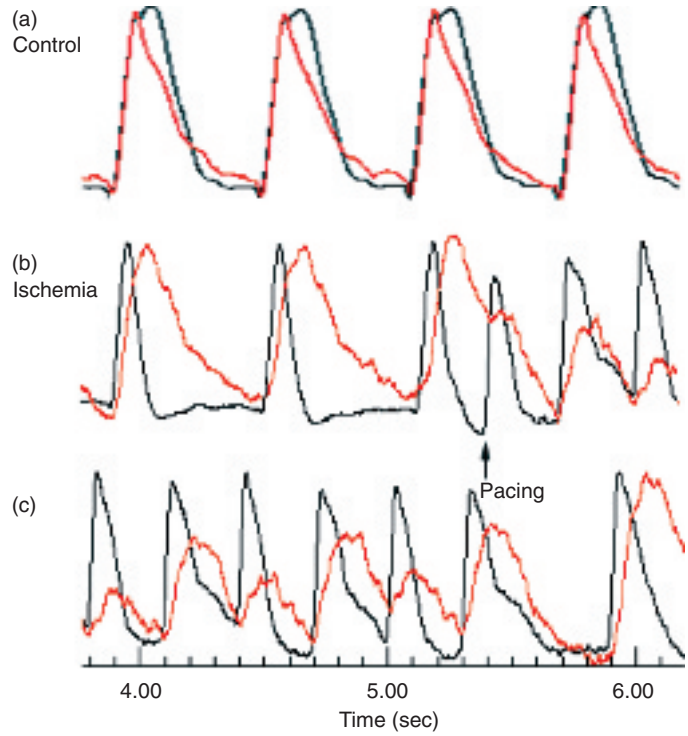

Figure 38.2 Typical ischemia-induced alterations of AP and CaiT and their relationship to electrical alternans. Panel (a) shows control recordings from a representative pixel. The heart was paced at a cycle length (CL) of 600 msec. Panel (b) was obtained after 10 min of no-flow ischemia. The first three beats were at a cycle length of 600 msec. Ischemia resulted in significant shortening of APD from 330 msec during control to 160 msec with no significant change in action potential amplitude. On the other hand, ischemia resulted in a delay of the upstroke of CaiT in relation to the upstroke of the action potential from 8 msec during control to 36 msec. Further, ischemia resulted in broadening of the peak deflection and slowing of the decay of CaiT with an overall increase of the duration of the CaiT from 345 msec during control to 436 msec following ischemia. Faster pacing was abruptly introduced at cycle length of 300 msec (marked by arrow). The introduction of a pacing stimulus at the shorter cycle length of 300 msec succeeded in capturing the heart and generating an action potential. However, the AP upstroke coincided with a time before the decay of the preceding CaiT and generated a markedly reduced CaiT and the onset of Alt of subsequent CaiT amplitude (alternans ratio of 50%). The CaiT alternans was associated with concordant alternans of APD whereby the larger CaiT was associated with the longer APD (280 msec), while the smaller CaiT was associated with the shorter APD (150 msec). When the slower pacing cycle was resumed at the end of panel (c), the CaiT immediately returned to the baseline amplitude and duration. Time scale is the same for the three panels. Reprinted with permission from Lakireddy V, Baweja P, Syed A, Bub G, Boutjdir M, El-Sherif N. *Am J Physiol* 2005; 288: H400–7.

hand, ischemia-induced lengthening of the duration of CaiT is related primarily to depressed kinetics of Cai cycling, which seems to be more spatially homogeneous. It has been suggested that CaiT controls the duration of the action potential through effects on one or several Ca-regulated ionic currents [19]. Our findings de-emphasize, but do not exclude, the role of alternation of the magnitude of CaiT in modulating ADP and ADP alternans in the setting of acute ischemia.

The Kinetics of Spontaneous Calcium Oscillations and Arrhythmogenesis in the in Vivo Heart During Ischemia/Reperfusion

Ischemia/reperfusion is associated with elevated Cai and alteration in Cai kinetics [1–4]. When the myocardial cell and SR Ca^{2+} loading become sufficiently high, the SR Ca^{2+} can also generate spontaneous, that is, not triggered by sarcolemmal depolarization, Ca^{2+} oscillations (S-CaOs). The

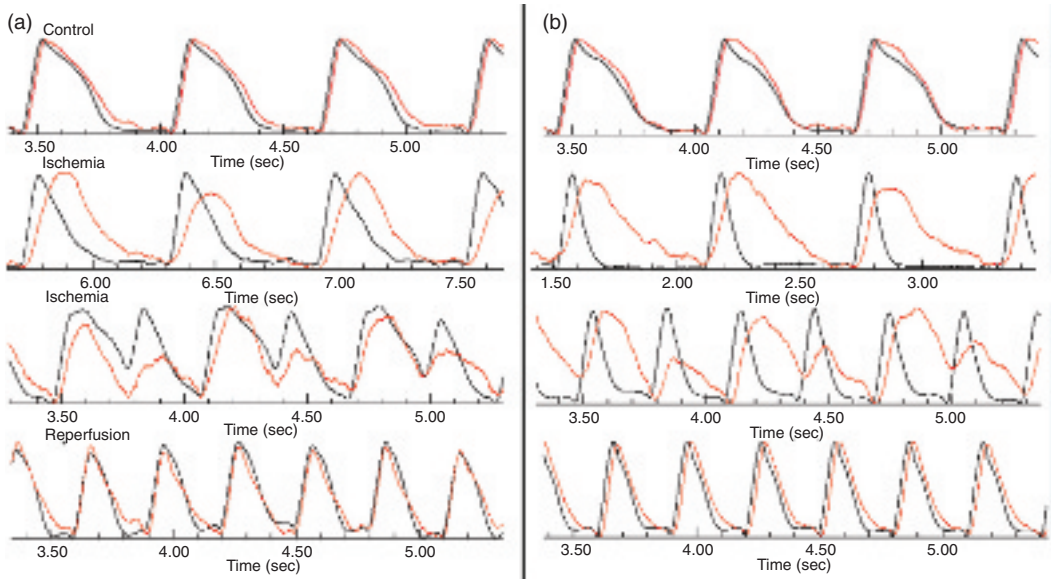

Figure 38.3 Recording from a different experiment to illustrate the effects of spatial heterogeneity of ischemia-induced shortening of APD on the development of electrical alternans and dispersion of repolarization. Panels (a) and (b) show sequential recordings from two separate pixels in the epicardial optical field. Control recordings during pacing at cycle length of 600 msec are shown on top and demonstrate that the AP and CaiT at both sites have largely similar configuration and duration. The second panel was obtained following 10 min of no-flow ischemia while pacing was maintained at a cycle length of 600 msec. Pixel (a) showed shortening of APD from 305 msec during control to 230–250 msec in alternate beats during ischemia. On the other hand, pixel (b) showed marked shortening of APD from 310 msec during control to 150 msec during ischemia. The increase in CaiT-D at both sites was comparable. CaiT alternans developed at both sites with Alt ratio of 25% at site (a) and 16% at site (b). CaiT alternans was associated with 20 msec alternans of APD at site (a), but no discernible alternans at site (b). The overall dispersion of APD in the optical field was 80 msec and 100 msec in alternate beats. The third panel was obtained 45 sec later when the pacing cycle length was decreased from 600 to 300 msec. Marked CaiT alternans of approximately equal degree developed at both pixels [alternans ratio of 55% at (a) and 58% at (b)]. However, the CaiT alternans was associated with marked concordant APD alternans at site (a) but no discernible alternans at site (b). The overall dispersion of APD in the optical field was 68 and 176 ms in alternate beats. The bottom panel was obtained following 2 min of reperfusion while pacing was maintained at a cycle length of 300 msec and shows complete resolution of CaiT and APD alternans. Reprinted with permission from Lakireddy V, Baweja P, Syed A, Bub G, Boutjdir M, El-Sherif N. *Am J Physiol* 2005; 288: H400–7.

increase in Cai caused by S-CaOs can cause a depolarizing inward current secondary to the Ca^{2+} activation of nonspecific ionic channels and/or the Na^{+}–Ca^{2+} exchanger [22]. When the depolarizing current reaches threshold it can generate a spontaneous action potential.

The correlation between S-CaOs and arrhythmogenesis has been investigated in theoretical models [5], and at the subcellular [6], cellular [7–9], and myocyte culture levels [10, 23]. However, there is an obvious lack of studies that directly investigate how the kinetics of S-CaOs correlate with a specific arrhythmia in the in vivo heart. The recent availability of techniques capable of simultaneous analysis of CaiT and action potential in perfused whole-heart preparations [11, 12] provides a unique opportunity to investigate, in detail, this relationship in the setting of ischemia/reperfusion. It is expected that, because of the limitation of the mapped epicardial optical field, a minority of arrhythmias can be linked to S-CaOs. However, the kinetic behavior of S-CaOs vis-à-vis a specific ventricular arrhythmia in the in vivo heart can be directly analyzed and can provide valuable insight into arrhythmogenesis.

In a recent study from our laboratory, 23 of 135 episodes of ventricular arrhythmias were linked to S-CaOs that were considered to arise from or close to the mapped epicardial window [24]. Self-limited

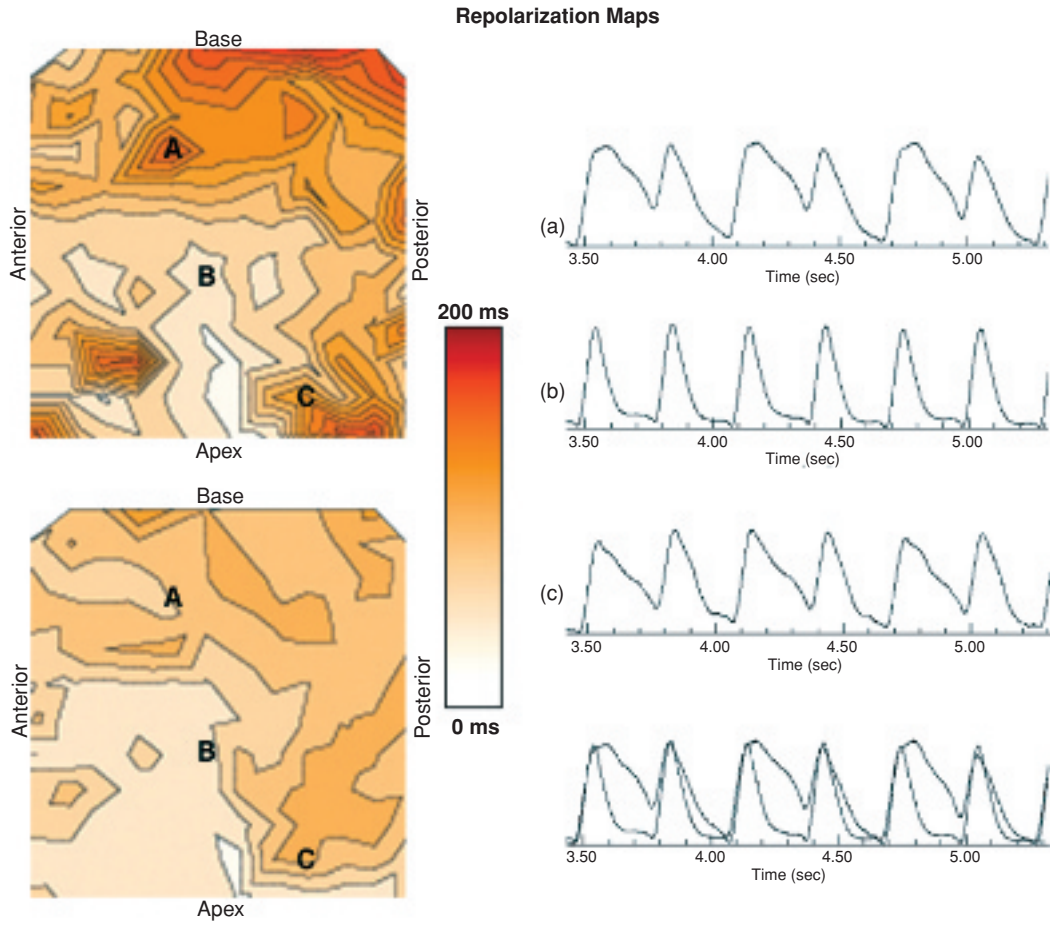

Figure 38.4 Repolarization maps of two consecutive beats at a pacing cycle length of 300 msec from the same experiment shown in Figure 38.3. Action potential recordings from pixels (a) and (b), as well as from a third pixel (c), are shown on the right panel. The three pixels represent recordings from the base, center, and apex of the LV. The action potential recordings from pixels (a) and (b) are superimposed in the bottom panel and show that the dispersion of APD in alternate beats varied from 45 msec to 162 msec. The repolarization maps of two subsequent beats drawn at 20 msec isochrones are shown in the left panel. The top map shows marked spatial dispersion of APD as reflected in the crowded isochrones. The APD was relatively short at the center of the lower half of the optical field and was much longer at the basal sections and both the right and left apical sections, resulting in at least three separate zones of marked gradient of repolarization. The bottom map of the subsequent beat shows a more organized repolarization pattern and much less of a degree of spatial dispersion of repolarization. Reprinted with permission from Lakireddy V, Baweja P, Syed A, Bub G, Boutjdir M, El-Sherif N. *Am J Physiol* 2005; 288: H400–7.

or sustained S-CaOs had a cycle length of 130–430 msec and could trigger propagated ventricular depolarizations. Self-limited S-CaOs that followed the basic beat action potential (AP)/CaiT closely resembled phase 3 early afterdepolarizations. Fast S-CaOs can remain confined to a localized site (concealed; Figure 38.5) or exhibit varying conduction patterns. This can manifest as: (i) an isolated premature beat, bigeminal, or trigeminal rhythm; (ii) ventricular tachycardia when a regular 2:1 conduction from the focal site develops; (iii) ventricular fibrillation when a complex conduction pattern results in wavebreak and reentrant excitation.

Figures 38.5–38.7 illustrate examples where ischemia/reperfusion resulted in a bigeminal rhythm as well as runs of monomorphic VT secondary to S-CaOs. During control recordings in Figure 38.5, the upstroke of the CaiT followed the upstroke of

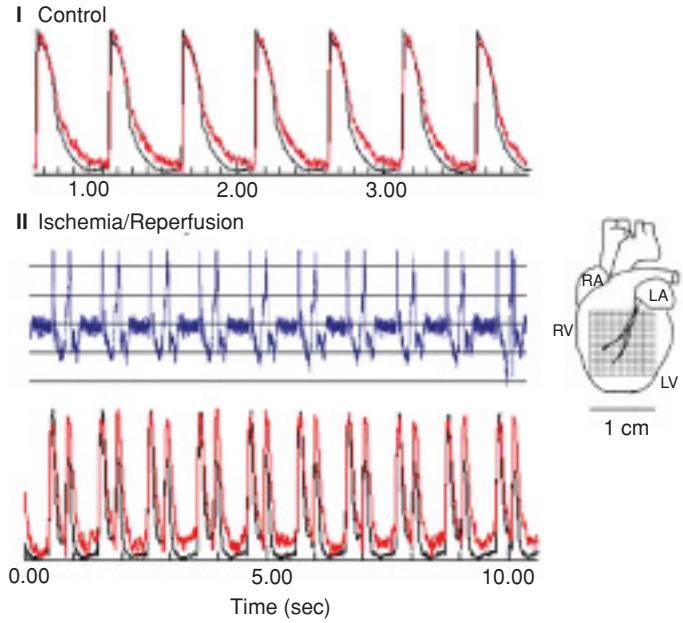

Figure 38.5 Ischemia/reperfusion resulting in a bigeminal rhythm: Recordings obtained from one of the experiments following 15 min of ischemia and 30 sec of reperfusion. The diagram illustrates the position of the epicardial optical field (lower right corner). Panel I illustrates control recording from one of the pixels during pacing at 500 msec. An expanded view at the right of panel I shows that the upstroke of the CaiT followed the upstroke of the AP by 8 msec as calculated from the *dF/dt* max shown below. The recording in panel II was obtained following 15 min of ischemia and 30 sec of reperfusion. The top tracing is an electrogram (in blue) that shows the development of a single spontaneous premature beat that followed each paced beat in a bigeminal pattern. The bottom tracing represent the same pixel shown in control during the bigeminal rhythm. Reprinted with permission from Lakireddy V, Bub G, Baweja P, Syed A, Boutjdir M, El-Sherif N. The kinetics of spontaneous calcium oscillations and arrhythmogenesis in the in vivo heart during ischemia/reperfusion. *Heart Rhythm* 2006; 3: 58–66.

the action potential by 8 msec. This interval is calculated from the *dF/dt* max shown in the figure. Figure 38.6 was obtained from the same experiment during the bigeminal rhythm and illustrates simultaneous recordings from three pixels in the optical field labeled A, B, and C The spatial distribution in the optical field of pixels showing similar recordings is shown in color in the diagram.

A recording similar to A was seen in four neighboring pixels (2×2 mm^2) and illustrates a basic paced beat with full AP/CaiT followed by three oscillatory subthreshold potentials at a CL of 170–180 msec. During the basic beat the upstroke of the CaiT followed the upstroke of the action potential by 5 msec. On the other hand, during the three subthreshold oscillatory responses, the upstroke of the CaiT preceded the upstroke of the subthreshold depolarization by 5–12 msec. The recording in B represents the recordings from a larger zone surrounding the A zone.

Whereas the first and third oscillatory responses of both CaiT and membrane depolarization gradually decreased in amplitude and failed to conduct outside the localized site of origin, the second oscillatory response gradually increased in amplitude. The majority of the mapped field, represented by the recording in C, only revealed a single premature full AP/CaiT coupled to the basic beat AP/CaiT in a bigeminal rhythm. The figure illustrates that while at the localized site of origin the second S-CaOs preceded the associated membrane depolarization by 12 msec, a few millimeters outside the site of origin the CaiT followed the associated membrane depolarization by 2–10 msec.

Figure 38.7 illustrates recordings during VT at a CL of 340–360 msec that alternated with periods of bigeminal rhythm. Recordings from the site of origin of S-CaOs (zone A in Figure 38.6) as well as from outside the site of origin of S-CaOs (zone C in Figure 38.6) are shown in the middle panel. The

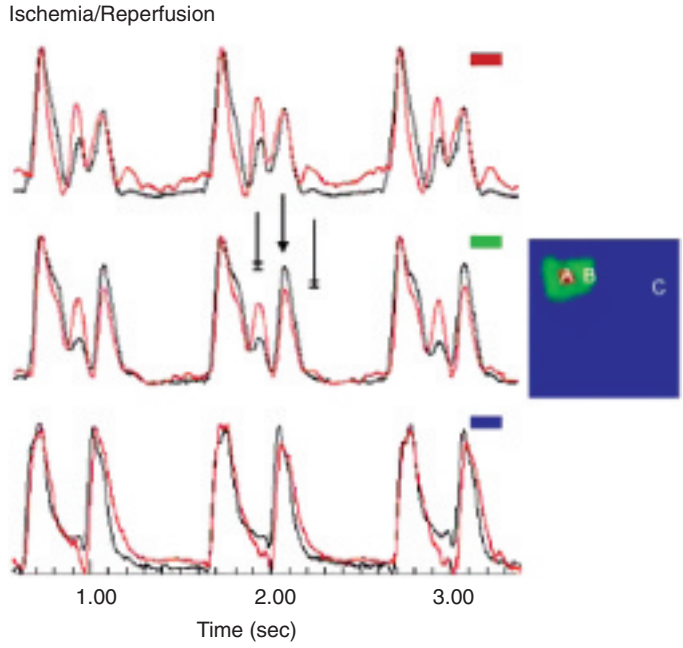

Figure 38.6 S-CaOs resulting in a bigeminal rhythm: Recording obtained from the same experiment shown in Figure 38.5 during the bigeminal rhythm that illustrates simultaneous tracings from three pixels, labeled (a), (b), and (c). The spatial distribution in the optical field of pixels showing similar recordings is shown in color in the diagram. A recording similar to (a) was seen in four neighboring pixels (2×2 mm^2) and illustrates a basic beat with full AP/CaiT followed by three subthreshold S-CaOs and associated membrane depolarizations at a cycle length of 170–180 msec. The first and third S-CaOs failed to conduct outside the localized site of origin. Only the second S-CaO resulted in a fully developed propagating AP/CaiT outside the localized site of origin. Published with permission from Lakireddy V, Bub G, Baweja P, Syed A, Boutjdir M, El-Sherif N. The kinetics of spontaneous calcium oscillations and arrhythmogenesis in the in vivo heart during ischemia/reperfusion. *Heart Rhythm* 2006; 3: 58–66.

recordings show that the VT was the result of repetitive S-CaOs at CL of 170–180 msec with every other S-CaO triggering a propagated fully developed action potential. Thus, the CL of the VT (340–360 msec) was double the CL of the S-CaOs. The bottom panel of Figure 38.7 illustrates the voltage maps of the first three beats of the VT (labeled A–C) and shows that activation consistently originated at or close to the site of origin of S-CaOs and propagated in a centrifugal pattern to the rest of the optical field consistent with focal activation.

The Dynamics of intracellular Ca Transients/Membrane Voltage (CaiT/Vm) Uncoupling and Arrhythmogenesis

The dynamics of CaiT/Vm uncoupling during ischemia/reperfusion and its contribution to arrhythmogenesis remains largely unexplained. Wavebreak can occur at sites of CaiT/Vm uncoupling. It is reasonable to suspect that a higher degree of CaiT/Vm uncoupling may be associated with prolonged episodes of VT, while better CaiT/Vm coupling may be associated with short self-terminating VT. Any quantitative measure of Cai dynamics during ischemia ideally should be able to measure differences in Vm and Cai signals for both short and long runs of paroxysmal VT. However, the two established statistical measures (dominant frequency analysis and mutual information) have shortcomings in this regard.

The dominant frequency (DF) defined as the frequency with the maximal power in a time series can be evaluated for single-peak spectra and also for more complex, multiple-peak spectra [25]. In principle, it is possible to measure CaiT/Vm synchrony by comparing the dominant frequency for Cai and Vm transients on a pixel-by-pixel basis, but

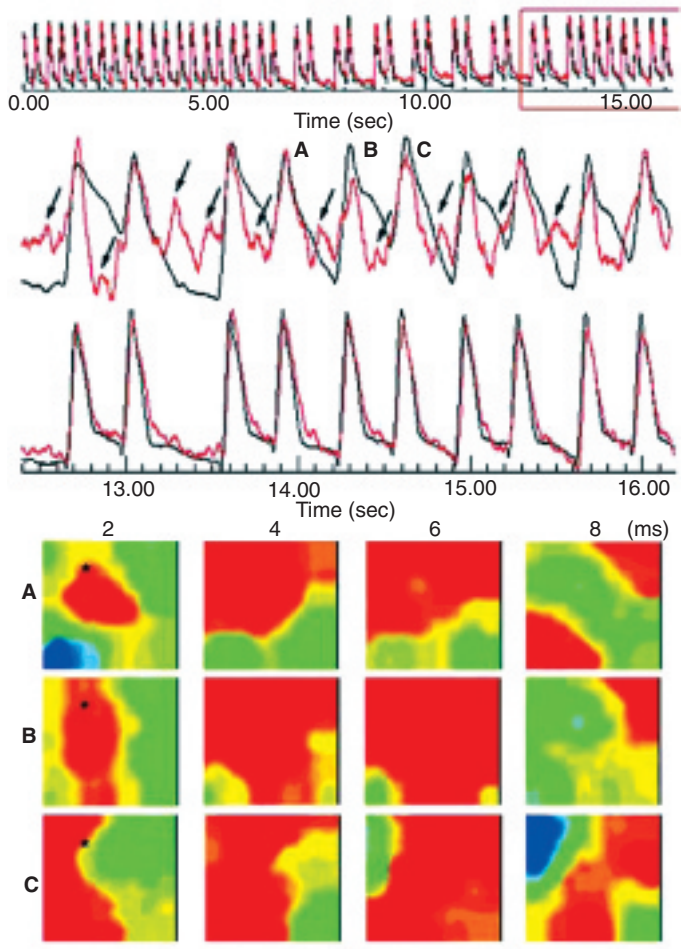

Figure 38.7 Monomorphic VT secondary to 2:1 propagation of sustained fast S-CaOs: Recordings obtained from the same experiment shown in Figures 38.1 and 38.2 following 90 sec of reperfusion when runs of VT at a cycle length of 340–360 msec alternated with periods of bigeminal rhythm [top 15 sec recording from pixel (c)]. An expanded recording of the last bigeminal pair and the second run of VT (marked by the box) from pixels (a) and (c) are shown in the middle panel. The recording in pixel (a) shows that the VT represented a 2:1 response to a fast S-CaOs (a cycle length of approximately 170–180 msec). The S-CaOs not associated with full action potentials are marked by arrows. The bottom panel illustrates consecutive frames (at 2 msec) of the voltage maps of the first three beats of the VT [labeled (a), (b), and (c)]. Activation consistently originated at or close to pixel (a) and conducted in a centrifugal pattern to the rest of the optical field consistent with focal activation. The conduction velocity was relatively fast and the entire optical field was activated within 8 msec. Published with permission from Lakireddy V, Bub G, Baweja P, Syed A, Boutjdir M, El-Sherif N. The kinetics of spontaneous calcium oscillations and arrhythmogenesis in the in vivo heart during ischemia/reperfusion. *Heart Rhythm* 2006; 3: 58–66.

problems with this approach exist. Firstly, spectral analysis does not well characterize aperiodic waveforms that are expected to exist during fibrillation. Secondly, the value of the dominant frequency is arbitrary and potentially ambiguous when spectral peaks of similar amplitude exist [26]. Further, the dominant frequency measure in effect discards information: by assigning a single frequency value to a complex waveform, it is likely that small oscillations due to abnormal Cai dynamics would be missed. An additional problem is that a relatively long segment (~2 sec) [25] is required to determine the frequency

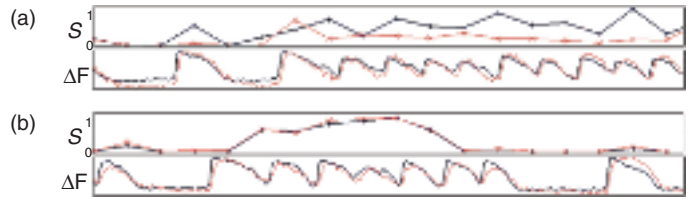

Figure 38.8 Graphs of entropy vs. time calculated from Vm and CaiT records for two VT episodes of different duration captured during *I*/*R*. Entropy values for both CaiT and Vm for the short-duration VT episode closely track each other. In contrast, entropy values for the longer-duration episode are not similar for the longer-duration VT episode, suggesting a higher degree of CaiT/Vm uncoupling.

content of a signal with any accuracy; this duration exceeds the shorter VT episodes observed during ischemia/reperfusion.

Mutual information is a statistic that quantifies the interdependence of two variables by comparing individual and joint probability densities of the variables. In the case of Cai/Vm measurements, mutual information represents the amount of information that one can acquire about Cai, given that Vm is known. Mutual information was found to decrease during sustained VF for optically measured Vm and Cai traces [27], indicating that Cai and Vm dynamics become uncoupled. Although mutual information has been shown to be a powerful statistic for measuring Cai/Vm uncoupling, its statistical power depends on the duration of the traces. Vm and Cai need to be continuously measured for many tens of seconds during fibrillation for mutual information to be accurately measured. Mutual information is therefore not a reliable statistic for the short paroxysmal VT episodes observed during ischemia reperfusion.

Towards Quantification of Asynchrony in VT

Spatio-temporal entropy is a measure that has been applied to quantify wavefront fractionation in excitable tissues [28, 29]. As opposed to dominant frequency and mutual information measurements, entropy characterizes wavefront shape over a spatio-temporal volume, as opposed to comparing time series on a trace-by-trace basis. Entropy is assessed by determining the volume occupied by individual wavefronts in a space–time cube constructed from the data. High entropy values indicate that there is a wide range of different-sized wavefronts, while low entropy indicate that all wavefronts are roughly the same size. When applied to quantifying Cai and Vm dynamics, entropy differences between Vm and Cai records would indicate that there are differences in patterns of wave propagation, which can be used as a measure of Cai uncoupling.

Figure 38.8 shows graphs of entropy vs. time calculated from Vm and CaiT records for two VT episodes of different duration captured during ischemia/reperfusion. Entropy values for both CaiT and Vm for the short-duration VT episode closely track each other. In contrast, entropy values for the longer-duration episode are not similar for the longer duration VT episode, suggesting a higher degree of CaiT/Vm uncoupling. Although entropy measurement allows for measuring uncoupling for both short and long records, additional validation of its statistical power is required.

References

1 Bers DM. Calcium and cardiac rhythms: physiological and pathological. *Circ Res* 2002; **90**: 16–17.

2 Sharma AA, Saffitz JH, Lee BI, Sobel BE, Corr P. Alpha-adrenergic-mediated accumulation of calcium in reperfused myocardium. *J Clin Invest* 1983; **72**: 802–7.

3 Marban E, Kitakaze M, Koretsune Y, Yue DT, Chacko VP, Pike MM. (1990). Quantification of Ca^{2+} in perfused hearts: critical evaluation of the 5F-BAPTA and nuclear magnetic resonance method as applied to the study of ischemia and reperfusion. *Circ Res* 1990; **66**: 1255–67.

4 Steenbergen C, Fralix TA, Murphy E. Role of increased cytosolic free calcium concentration in myocardial ischemic injury. *Basic Res Cardiol* 1993; **88**: 456–70.

5 Chudin E, Goldhaber J, Garfinkel A, Weiss J, Kogan B. Intracellular Ca^{2+} dynamics and the stability of ventricular tachycardia. *Biophys J* 1999; **77**: 2930–41.

6 Kockskamper J, Blatter A. Subcellular Ca^{2+} alternans represents a novel mechanism for the generation of

arrhythmogenic Ca^{2+} waves in cat atrial myocytes. *J Physiol* 2002; **545**: 65–79.

7 Thandroyen FT, Morris AC, Hagler HK, et al. Intracellular calcium transients and arrhythmia in isolated heart cells. *Circ Res* 1991; **69**: 810–19.

8 Miura M, Ishide N, Oda H, Sakurai M, Shinozaki T, Takishima T. Spatial features of calcium transients during early and delayed afterdepolarizations. *Am J Physiol* 1993; **256**: H439–44.

9 De Ferrari GM, Viola MC, D'Amato E, Antolini R, Forti S. Distinct patterns of calcium transient during early and delayed afterdepolarizations induced by isoproterenol in ventricular myocytes. *Circulation* 1995; **91**: 2510–15.

10 Arutunyan A, Swift LM, Sarvazyan N. Initiation and propagation of ectopic waves: insights from an in vitro model of ischemia-reperfusion injury. *Am J Physiol* 2002; **283**: H741–49.

11 Choi BR, Salama G. Simultaneous maps of optical action potentials and calcium transients in guinea pig hearts: mechanisms underlying concordant *Alt J Physiol (London)* 2000; **529**: 171–88.

12 Laurita KR, Singal A. Mapping action potentials and calcium transients simultaneously form the intact heart. *Am J Physiol* 2001; **280**, H2053–60.

13 Rosenbaum DS, Jackson LE, Smith JM, Garan H, Ruskin J, Cohen RJ. Electrical alternans and vulnerability to ventricular arrhythmias. *N Engl J Med* 1994; **330**: 235–41.

14 Tachibana H, Kubota I, Yamaki M, Watanabe T, Tomoike H. Discordant S-T alternans contributes to formation of reentry: a possible mechanism of reperfusion arrhythmia. *Am J Physiol* 1995; **275**: H116–21.

15 Nearing BD, Verrier RL. Progressive increases in complexity of *T*-wave oscillations herald ischemia-induced ventricular fibrillation. *Circ Res* 2002; **91**: 727–32.

16 Kurz RW, Mohabir R, Ren X-L, Franz MR. Ischemia-induced alternans of action potential duration in the intact heart: dependence on coronary flow, preload, and cycle length. *Eur Heart J* 1993; **14**: 1410–20.

17 Downer E, Janse MJ, Durrer D. The effect of acute coronary artery occlusion on subepicardial transmembrane potential in the intact porcine heart. *Circulation* 1977; **56**: 217–24.

18 Qian YW, Clusin WT, Lin SF, Hon J, Sung RS. Spatial heterogeneity of calcium transient alternans during the early phase of myocardial ischemia in the blood-perfused rabbit heart. *Circulation* 2001; **104**: 2082–87.

19 Qian YW, Sung RJ, Lin SF, Province R, Clusin WT. Spatial heterogeneity of action potential alternans during global ischemia in the rabbit heart. *Am J Physiol* 2003; **285**: H2722–33.

20 Lakireddy V, Baweja P, Syed A, Bub G, Boutjdir M, El-Sherif N. Contrasting effects of ischemia on the kinetics of membrane voltage and intracellular calcium transient underlie electrical alternans. *Am J Physiol Heart Circ Physiol* 2005; **288**: H400–7.

21 Eisner DA, Choi HS, Diaz ME, O'Neill SC, Trafford AW. Integrative analysis of calcium cycling in cardiac muscle. *Circ Res* 2000; **87**: 1087–94.

22 Lakatta EG, Guarnieri T. Spontaneous myocardium calcium oscillation: are they linked to ventricular fibrillation? *J Cardiovasc Electrophysiol* 1993; **4**: 473–89.

23 Bub G, Talento K, Shrier A, Glass I.(2003). Spontaneous initiation and termination of complex cardiac rhythms. *J Cardiovasc Electrophysiol* 2003; **14**: S229–39.

24 Lakireddy V, Bub G, Baweja P, Syed A, Boutjdir M, El-Sherif N. The kinetics of spontaneous calcium oscillations and arrhythmogenesis in the in vivo heart during ischemia/reperfusion. *Heart Rhythm* 2006; **3**: 58–66

25 Zaitsev AV, Berenfeld O, Mironov SF, Jalife J, Pertsov AM. Distribution of excitation frequencies on the epicardial and endocardial surfaces of fibrillating ventricular wall of the sheep heart. *Circ Res* 2000; **86**: 408–17.

26 Choi BR, Lui T, Salama G. Letter to the Editor: Ventricular fibrillation: mother rotor or multiple wavelets? *Circ Res* 2001; **89**: e30.

27 Omichi C, Lamp ST, Lin SF, et al. Intracellular Ca dynamics in ventricular fibrillation. *Am J Physiol Heart Circ Physiol* 2004; **286**: H1836–44.

28 Jung P, Wang J, Wackerbauer R, Showalter K. Coherent structure analysis of spatiotemporal chaos, *Phys Rev E* 2000; **61**: 2095–98.

29 Bub G, Shrier A, Glass L. Global organization of dynamics in oscillatory heterogeneous excitable media. *Phys Rev Lett* 2005; **94**: 028105.

39 CHAPTER 39

Role of Body Surface Mapping

Christian Vahlhaus, MD, *Günter Breithardt,* MD, FESC, FACC, FHRS, *Lars Eckardt,* MD

University Hospital Münster, Münster, Germany

Summary

Since its introduction into clinic more than 100 years ago standard electrocardiography (ECG) with its 6 bipolar Einthoven and its 6 unipolar Wilson leads has never become less important. In the 1960s the term body surface mapping was coined to describe the use of multiple unipolar or bipolar leads to discover new fields of application. Body surface mapping helps to detect ischemia and to identify the stenotic vessel. It may also be helpful in locating accessory pathways, sites of origin of idiopathic ventricular tachycardias and exit sites of reentrant ventricular tachycardias. With body surface mapping the effect of biventricular pacing on both inter- and intraventricular delay was demonstrated. The circumscribed and localised nature of activation changes observed in Brugada syndrome was characterised by body surface mapping. In patients with long QT syndrome body surface mapping emerged as a useful method to predict the effectiveness of beta blocking drugs in preventing torsade-de-pointes tachycardia. Electrocardiographic imaging will open up new options for characterising and non-invasively diagnosing focal left ventricular tachycardias and ventricular asynchrony in heart failure patients.

Introduction

In many areas of medicine today, the electrocardiogram (ECG) remains the cornerstone of diagnosis. Eugene Braunwald has called the introduction of the ECG by Willem Einthoven more than 100 years ago one of the greatest achievements of the twentieth century, and considers its development to be the birth of modern cardiology [1]. Shlomo Stern has called the ECG the cardiologist's best friend [2].

The diagnostic potential of conventional (12-lead) ECG has been greatly expanded and fortified by the results of basic and clinical electrophysiology. Analysis of rhythm, electric axis, activation sequence, and repolarization pattern allows more or less pathognomonic insights. In disorders such as the long- or short-QT syndromes (LQTS or SQTS), Brugada syndrome, catecholaminergic polymorphic ventricular tachycardia, and others, the ECG is the modality with the highest diagnostic yield. Once the mechanisms of arrhythmias, or the changes associated with cardiomyopathy or induced by acute ischemia or ion-channel-abnormalities are detected, the ECG has a great impact on therapy, often with prognostic importance: For example, the immediate need of monitoring and therapy in patients with ST-elevation or QT-prolongation with torsade de pointes tachycardia.

Cardiac Mapping, Third Edition Edited by Mohammad Shenasa, Gerhard Hindricks, Martin Borggrefe, and Günter Breithardt
 ISBN: 978-1-405-17572-2

Cardiac electrical events occur in a complex 3D organ, but are depicted by a limited number of leads. Although their number has been greatly increased since the initial recording by Einthoven with a single bipolar lead to the present standards that include the extremity leads as well as the precordial (Wilson) leads, there may still be more information in the electrical sources emerging from heart than generally used. The very first attempts were made at the end of the nineteenth century. Waller was the first who used rudimentary body surface maps even if he only attributed the potential pattern of his 10–20 recorded electrocardiograms from the human chest to the presence of an electrical dipole [3].

The heart, however, generates a potential field that is more complex than that produced by a dipole. Therefore, as early as in the 1960s, the term "body surface mapping" was coined by Taccardi and coworkers. Multiple unipolar or bipolar leads were recorded from the body surface in dogs [4] and in humans [5] to display and analyze the complexity of potential distribution on maps. Departure maps were generated to analyze the difference between an average map related to a normal population and an individual map under examination for detection of posterior myocardial infarction [6], estimation of infarct size [7], and diagnosis of left ventricular hypertrophy [8].

Successful application of inverse calculations in the 1970s [9] were followed by body surface mapping studies to detect coronary artery disease [10], to identify sites of VT origin [11], and to measure the efficacy of antiarrhythmic drug therapy in patients with ventricular tachycardia [12]. Multichannel measurement at sampling rates as high as 2000 samples/sec, as well as processing of such data, enabled innovative research. Importantly, findings gleaned from mapping point not only to improved assessment by mapping, but also to improved analysis by conventional ECG means using strategies derived from mapping research. For example, with body surface potential mapping, lead positions in addition to the precordial (Wilson) leads V1–V3 were found that were important for detection of Brugada-type ST-changes [13].

Coronary Artery Disease

Localized cardiac electrophysiological abnormalities produce characteristic body surface ECG signatures. The conventional (12-lead) ECG does not adequately sample potential distribution information. Therefore, there is the likelihood of missing or underestimating the information that is most important for detecting and classifying abnormal activity.

Body surface ST potential distributions obtained from patients with documented myocardial infarction were compared with those from normal subjects [6–8]. Most significant differences occurred in regions not usually sampled by the conventional ECG in post infarction [14] as well as in stress-induced ischemic patients [15].

The limited diagnostic accuracy of the conventional (12-lead) ECG in discriminating anterior from inferior ischemia by analyzing stress induced ST-segment depression has been affirmed [16]. In contrast, body surface isochrone maps during stress testing can reflect the site of myocardial ischemia. In patients having a stenosis in the left anterior descending artery, changes were located mainly on the left anterior chest, whereas in stenoses in the right coronary artery, they were located mainly on the right lower thoracic surface [17].

Ischemic repolarization changes are detectable and quantifiable by body surface mapping even at low levels of cardiac stress and they persist up to 5 min following stress testing [18]. ST-T integral and *T*-wave amplitude are sensitive and specific markers of transient myocardial ischemia. The ST-T area contains information additional to ST depression and thus has independent discriminative value in detecting ischemia [19].

Mapping of Tachycardias

In the era of antitachycardia surgery for Wolff–Parkinson–White (WPW) syndrome, the location of minima in the early delta wave detected by body surface mapping was a simple and accurate index of the site of accessory pathway. Body surface mapping was useful for the diagnosis of the presence of bilateral accessory pathways [20, 21] and allowed discrimination among 38 different LV and RV segments of ectopic endocardial impulse formation in patients with normal cardiac anatomy [22].

Today, however, body surface mapping has lost its importance because antitachycardiac surgery has been replaced by radiofrequency catheter ablation. This latter technique requires meticulous mapping

and identification of the location of the accessory pathway within a few millimeters. This has not been possible with the relatively crude resolution of body surface recordings. Today, standard ECG criteria are sufficient to guide the electrophysiologist to the area of interest for ablation of ventricular tachycardia [23–25] and accessory pathways [26, 27].

With body surface mapping, the site of origin of idiopathic ventricular tachycardia is localized to successfully guide catheter ablation [28]. Also, for catheter ablation of scar-related ventricular tachycardia, body surface mapping identifies VT exit sites [29]. Body surface mapping allows reconstruction of the ECG by subtracting overlapping *T*-waves from the QRS complexes during VT [30]. The high spatial resolution of body surface mapping improves the diagnostic accuracy of QT-dispersion in patients with dilated cardiomyopathy [31]. Abnormal body surface mapping is associated with inducible ventricular tachycardia [32].

There are excellent correlations between virtual electrograms calculated from body surface mapping data and direct epicardial mapping. Such reconstruction has led to a new imaging modality, called electrocardiographic imaging, which was developed by Rudy and coworkers [33]. It captures important features of cardiac electrical excitation in humans noninvasively [34]. With electrocardiographic imaging based on body surface mapping, the epicardial activation sequence of focal left ventricular tachycardia is reconstructed. This correlates with subsequent maps obtained using standard techniques. Therefore, body surface mapping has the potential to guide diagnosis and therapy in patients presenting with focal left ventricular tachycardia [35].

Electrical Dysynchrony

In damaged myocardium, the electrical activation may be changed from a uniform high-velocity wave front invading the working myocardium through the Purkinje network to areas of decreased velocity and altered direction of electrical propagation. This abnormal ventricular activation may lead to QRS prolongation and to asynchronous contraction with impaired left ventricular mechanical performance. As a consequence, delayed ventricular contraction occurs in the region of the lateral (posterior) wall.

There is an inverse relationship between ejection fraction and the extent of delayed LV activation manifesting as a bundle branch block–like pattern [36–38], which is a powerful predictor of mortality [39]. All major trials on cardiac resynchronization therapy (biventricular pacing) have used QRS-duration as the principal inclusion criterion. Because the QRS-duration at the baseline is not predictive of the response to cardiac resynchronization therapy, body surface mapping has been used to further investigate electrical dysynchrony [40].

With body surface mapping, the effect of biventricular pacing on both inter- and intraventricular delay as been demonstrated [40]. Electrocardiographic imaging derived from body surface mapping has shown that LV (but not RV) pacing alone can be as effective as biventricular pacing for electrical resynchronization. Efficacy of cardiac resynchronization therapy depends strongly on the patient-specific electrophysiologic substrate [41]. Because electrocardiographic imaging is a relatively new modality, its diagnostic yield and clinical significance of electrocardiographic imaging in cardiac resynchronization therapy candidates has not yet been validated.

Ion Channel Diseases

Brugada and Brugada identified a rare entity in patients with a right bundle branch block–like ECG pattern with characteristic ST-segment elevation in right precordial leads who suffer from polymorphic ventricular tachycardia and/or ventricular fibrillation [42]. Genotyping identified mutations in the cardiac sodium channel SCN5A in a subset of patients [43–45].

Phenotyping revealed different types of ECG changes having different diagnostic yield [46–49]. Because the position of the right precordial electrode seemed crucial, body surface mapping was applied. It showed that such ECG changes were more prominent in the second and third intercostal spaces, that is, considerably above the standard leads V1 and V2 (Figure 39.1) [13].

Body surface mapping reproducibly confirmed the circumscribed and localized nature of these changes in activation [50]. This led to the suggestion to add recordings at these sites to the conventional 12-lead ECG in patients suspected of having Brugada syndrome [51]. The size of the body surface

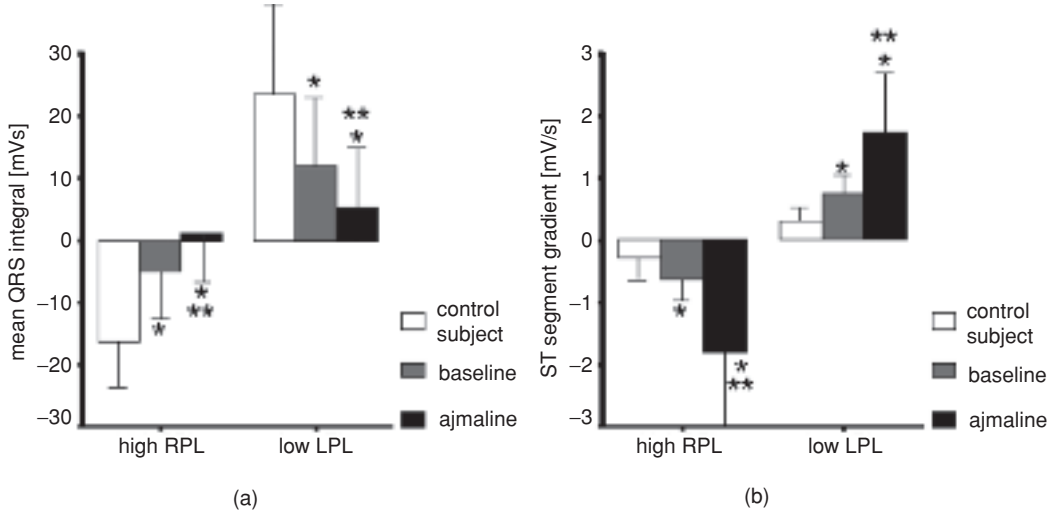

Figure 39.1 ECG characteristics identified by (a) mean QRS integral and (b) ST gradient for control subjects and patients with Brugada syndrome for areas outside the standard leads V1–V6; high right precordial leads (high RPL) were placed on the second and third intercostals space; low left precordial leads (low LPL) were recorded between the fifth and seventh intercostal space. Under resting conditions, the high RPL area showed increased QRS integrals (-5 ± 8 vs. -16 ± 8 mV/msec) and more negative ST slopes (-0.62 ± 0.41 vs. -0.29 ± 0.40 mV/sec) compared to control. In contrast, the QRS integrals and ST segment gradients measured in the standard ECG leads V1–V3 were not statistically different between Brugada and control patients. Significant changes compared to * = control and ** = measurement at baseline (nonparametric Mann–Whitney U-test, *P*, 0.001) [13].

area, in which ST elevation was found, correlated with the inducibility of VT during programmed ventricular stimulation [52]. The role of these parameters, however, is still unsettled with regard to the present controversy about risk stratification between Brugada et al. [53] and others [54, 55].

Body surface mapping has also been applied in patients with long-QT syndrome [44, 45, 56, 57]. With body surface mapping, the effect of atrial pacing and beta-blocking drugs on spatial dispersion of repolarization has been investigated [58].

Different subtypes of long-QT syndrome have been characterized: Sympathetic stimulation causes a greater increase in spatial dispersion of repolarization in LQT1 than in LQT2; the exercise-induced prolongation of the QT interval in LQT1 has been reproduced [59–62]. Measurement of body surface recovery time using body surface mapping is useful for diagnosing borderline long-QT syndrome [63]. QRS-isointegral mapping based on body surface mapping has emerged as a useful method to predict the effectiveness of beta-blocking drugs in preventing torsade de pointes tachycardia in patients with long-QT syndrome [64, 65].

References

1 Braunwald E. The Simon Dack lecture. Cardiology: the past, the present, and the future. *J Am Coll Cardiol* 2003; **42**: 2031–41.

2 Stern S. Electrocardiogram: still the cardiologist's best friend. *Circulation* 2006; **113**: 753–56.

3 Waller AD. On the electromotive changes connected with the beat of the mammalian heart and of the human heart in particular. *Philos Trans R Sot* 1889; **B180**: 169–70.

4 Taccardi B. Distribution of heart potentials on dog's thoracic surface. *Circ Res* 1962; **11**: 862–69.

5 Taccardi B. Distribution of heart potentials on the thoracic surface of normal human subjects. *Circ Res* 1963; **12**: 341–52.

6 Flowers NC, Horan LG, Sohi GS, Hand RC, Johnson JC. New evidence for inferoposterior myocardial infarction on surface potential maps. *Am J Cardiol* 1976; **38**: 576–81.

7 Tonooka I, Kubota I, Watanabe Y, Tsuiki K, Yasui S. Isointegral analysis of body surface maps for the assessment of location and size of myocardial infarction. *Am J Cardiol* 1983; **52**: 1174–80.

8 Kornreich F, Montague TJ, Rautaharju PM, Kavadias M, Horacek MB, Taccardi B. Diagnostic body surface potential map patterns in left ventricular hypertrophy during PQRST. *Am J Cardiol* 1989; **63**: 610–17.

9 Barr RC, Spach MS. Inverse calculation of QRS-T epicardial potentials from body surface potential distributions for normal and ectopic beats in the intact dog. *Circ Res* 1978; **42**: 661–75.

10 Green LS, Lux RL, Haws CW. Detection and localization of coronary artery disease with body surface mapping in patients with normal electrocardiograms. *Circulation* 1987; **76**: 1290–97.

11 Faugere G, Savard P, Nadeau RA, et al. Characterization of the spatial distribution of late ventricular potentials by body surface mapping in patients with ventricular tachycardia. *Circulation* 1986; **74**: 1323–33.

12 Mitchell LB, Hubley-Kozey CL, Smith ER, et al. Electrocardiographic body surface mapping in patients with ventricular tachycardia: assessment of utility in the identification of effective pharmacological therapy. *Circulation* 1992; **86**: 383–93.

13 Bruns HJ, Eckardt L, Vahlhaus C, et al. Body surface potential mapping in patients with Brugada syndrome: right precordial ST segment variations and reverse changes in left precordial leads. *Cardiovasc Res* 2002; **54**: 58–66.

14 Kornreich F, Montague TJ, Rautaharju PM. Body surface potential mapping of ST segment changes in acute myocardial infarction: implications for ECG enrollment criteria for thrombolytic therapy. *Circulation* 1993; **87**: 773–82.

15 Hanninen H, Takala P, Makijarvi M, et al. Recording locations in multichannel magnetocardiography and body surface potential mapping sensitive for regional exercise-induced myocardial ischemia. *Basic Res Cardiol* 2001; **96**: 405–14.

16 Fuchs RM, Achuff SC, Grunwald LF, Yin FC, Griffith LS. Electrocardiographic localization of coronary artery narrowings: studies during myocardial ischemia and infarction in patients with one-vessel disease. *Circulation* 1982; **66**: 1168–76.

17 Igarashi H, Yamaki M, Kubota I, et al. Relation between localization of coronary artery disease and local abnormalities in ventricular activation during exercise tests. *Circulation* 1990; **81**: 461–69.

18 Montague TJ, Johnstone DE, Spencer CA, et al. Body surface potential maps with low-level exercise in isolated left anterior descending coronary artery disease. *Am J Cardiol* 1988; **61**: 273–82.

19 Hanninen H, Takala P, Rantonen J, et al. ST-T integral and *T*-wave amplitude in detection of exercise-induced myocardial ischemia evaluated with body surface potential mapping. *J Electrocardiol* 2003; **36**: 89–98.

20 Misaki T, Watanabe G, Fujiki A. [Usefulness of body surface potential maps to determine ablation site in patients with WPW syndrome]. *Nippon Rinsho* 1995; **53**: 119–26.

21 Giorgi C, Ackaoui A, Nadeau R, Savard P, Primeau R, Page P. Wolff–Parkinson–White VCG patterns that mimic other cardiac pathologies: a correlative study with the preexcitation pathway localization. *Am Heart J* 1986; **111**: 891–902.

22 SippensGroenewegen A, Spekhorst H, van Hemel NM, et al. Body surface mapping of ectopic left and right ventricular activation: QRS spectrum in patients without structural heart disease. *Circulation* 1990; **82**: 879–96.

23 Miller JM, Marchlinski FE, Buxton AE, Josephson ME. Relationship between the 12-lead electrocardiogram during ventricular tachycardia and endocardial site of origin in patients with coronary artery disease. *Circulation* 1988; **77**: 759–66.

24 Ito S, Tada H, Naito S, Kurosaki K, et al. Development and validation of an ECG algorithm for identifying the optimal ablation site for idiopathic ventricular outflow tract tachycardia. *J Cardiovasc Electrophysiol* 2003; **14**: 1280–86.

25 Yang Y, Saenz LC, Varosy PD, et al. Using the initial vector from surface electrocardiogram to distinguish the site of outflow tract tachycardia. *Pacing Clin Electrophysiol* 2007; **30**: 891–98.

26 Arruda MS, McClelland JH, Wang X, et al. Development and validation of an ECG algorithm for identifying accessory pathway ablation site in Wolff–Parkinson–White syndrome. *J Cardiovasc Electrophysiol* 1998; **9**: 2–12.

27 McGavigan AD, Clark E, Quinn FR, Rankin AC, Macfarlane PW. Localization of accessory pathways in the Wolff–Parkinson–White pattern: physician versus computer interpretation of the same algorithm. *Pacing Clin Electrophysiol* 2007; **30**: 998–1002.

28 Peeters HA, SippensGroenewegen A, Wever EF, et al. Clinical application of an integrated 3-phase mapping technique for localization of the site of origin of idiopathic ventricular tachycardia. *Circulation* 1999; **99**: 1300–11.

29 Sapp JL, Gardner MJ, Parkash R, Basta M, Warren JW, Horacek BM. Body surface potential mapping to aid ablation of scar-related ventricular tachycardia. *J Electrocardiol* 2006; **39**: S87–S95.

30 Jokiniemi T, Simelius K, Nenonen J, Tierala I, Toivonen L, Katilal T. Baseline reconstruction for localization of rapid ventricular tachycardia from body surface potential maps. *Physiol Meas* 2003; **24**: 641–51.

31 Aiba T, Inagaki M, Shimizu W, et al. Recovery time dispersion measured from 87-lead body surface potential mapping as a predictor of sustained ventricular tachycardia in patients with idiopathic dilated cardiomyopathy. *J Cardiovasc Electrophysiol* 2000; **11**: 968–74.

32 Lacroix D, Dubuc M, Kus T, Savard P, Shenasa M, Nadeau R. Evaluation of arrhythmic causes of syncope: correlation between Holter monitoring, electrophysiologic testing, and body surface potential mapping. *Am Heart J* 1991; **122**: 1346–54.

33 Oster HS, Taccardi B, Lux RL, Ershler PR, Rudy Y. Electrocardiographic imaging: noninvasive characterization of intramural myocardial activation from inverse-reconstructed epicardial potentials and electrograms. *Circulation* 1998; **97**: 1496–1507.

34 Ghanem RN, Jia P, Ramanathan C, Ryu K, Markowitz A, Rudy Y. Noninvasive electrocardiographic imaging (ECGI): comparison to intraoperative mapping in patients. *Heart Rhythm* 2005; **2**: 339–54.

35 Intini A, Goldstein RN, Jia P, et al. Electrocardiographic imaging (ECGI): a novel diagnostic modality used for mapping of focal left ventricular tachycardia in a young athlete. *Heart Rhythm* 2005; **2**: 1250–52.

36 Shenkman HJ, Pampati V, Khandelwal AK, et al. Congestive heart failure and QRS duration: establishing prognosis study. *Chest* 2002; **122**: 528–34.

37 McCullough PA, Hassan SA, Pallekonda V, et al. Bundle branch block patterns, age, renal dysfunction, and heart failure mortality. *Int J Cardiol* 2005; **102**: 303–8.

38 Silvet H, Amin J, Padmanabhan S, Pai RG. Prognostic implications of increased QRS duration in patients with moderate and severe left ventricular systolic dysfunction. *Am J Cardiology* 2001; **88**: 182–85.

39 Baldasseroni S, Opasich C, Gorini M, et al. Left bundle-branch block is associated with increased 1-year sudden and total mortality rate in 5517 outpatients with congestive heart failure: a report from the Italian network on congestive heart failure. *Am Heart J* 2002; **143**: 398–405.

40 Pastore CA, Tobias N, Samesima N, et al. Body surface potential mapping investigating the ventricular activation patterns in the cardiac resynchronization of patients with left bundle-branch block and heart failure. *J Electrocardiol* 2006; **39**: 93–102.

41 Jia P, Ramanathan C, Ghanem RN, Ryu K, Varma N, Rudy Y. Electrocardiographic imaging of cardiac resynchronization therapy in heart failure: observation of variable electrophysiologic responses. *Heart Rhythm* 2006; **3**: 296–310.

42 Brugada P, Brugada J. Right bundle branch block, persistent ST segment elevation and sudden cardiac death: a distinct clinical and electrocardiographic syndrome. A multicenter report. *J Am Coll Cardiol* 1992; **20**: 1391–96.

43 Chen Q, Kirsch GE, Zhang D, et al. Genetic basis and molecular mechanism for idiopathic ventricular fibrillation. *Nature* 1998; **392**: 293–96.

44 Priori SG, Napolitano C, Schwartz PJ, Bloise R, Crotti L, Ronchetti E. The elusive link between LQT3 and Brugada syndrome: the role of flecainide challenge. *Circulation* 2000; **102**: 945–47.

45 Priori SG. Long-QT and Brugada syndromes: from genetics to clinical management. *J Cardiovasc Electrophysiol* 2000; **11**: 1174–78.

46 Shimizu W, Matsuo K, Takagi M, et al. Body surface distribution and response to drugs of ST segment elevation in Brugada syndrome: clinical implication of eighty-seven-lead body surface potential mapping and its application to twelve-lead electrocardiograms. *J Cardiovasc Electrophysiol* 2000; **11**: 396–404.

47 Hisamatsu K, Kusano KF, Morita H, et al. Usefulness of body surface mapping to differentiate patients with Brugada syndrome from patients with asymptomatic Brugada syndrome. *Acta Med Okayama* 2004; **58**: 29–35.

48 Izumida N, Asano Y, Doi S, et al. Changes in body surface potential distributions induced by isoproterenol and Na channel blockers in patients with the Brugada syndrome. *Int J Cardiol* 2004; **95**: 261–68.

49 Hisamatsu K, Kusano KF, Morita H, et al. Relationships between depolarization abnormality and repolarization abnormality in patients with Brugada syndrome: using body surface signal-averaged electrocardiography and body surface maps. *J Cardiovasc Electrophysiol* 2004; **15**: 870–76.

50 Yokokawa M, Takaki H, Noda T, et al. Spatial distribution of repolarization and depolarization abnormalities evaluated by body surface potential mapping in patients with Brugada syndrome. *Pacing Clin Electrophysiol* 2006; **29**: 1112–21.

51 Hisamatsu K, Morita H, Fukushima KK, et al. Evaluation of the usefulness of recording the ECG in the 3rd intercostal space and prevalence of Brugada-type ECG in accordance with recently established electrocardiographic criteria. *Circ J* 2004; **68**: 135–38.

52 Eckardt L, Bruns HJ, Paul M, et al. Body surface area of ST elevation and the presence of late potentials correlate to the inducibility of ventricular tachyarrhythmias in Brugada syndrome. *J Cardiovasc Electrophysiol* 2002; **13**: 742–49.

53 Brugada JF, Brugada RF, Brugada P. Determinants of sudden cardiac death in individuals with the electrocardiographic pattern of Brugada syndrome and no previous cardiac arrest. *Circulation* 2003; **108**: 3092–96.

54 Paul M, Gerss J, Schulze-Bahr E, et al. Role of programmed ventricular stimulation in patients with Brugada syndrome: a meta-analysis of worldwide published data. *Eur Heart J* 2007; **28**: 2126–33.

55 Ohkubo KF, Watanabe IF, Takagi YF, et al. Electrocardiographic and electrophysiologic characteristics in patients with Brugada-type electrocardiogram and inducible ventricular fibrillation: single-center experience. *Circ J* 2007; **71**: 1437–41.

56 Compton SJ, Lux RL, Ramsey MR, et al. Genetically defined therapy of inherited long-QT syndrome: correction of abnormal repolarization by potassium. *Circulation* 1996; **94**: 1018–22.

57 De Ambroggi L. [Heterogeneities of ventricular repolarization and vulnerability to arrhythmia: how to detect them with noninvasive methods?]. *Cardiologia* 1999; **44**: 355–60.

58 Shimizu W, Kamakura S, Kurita T, Suyama K, Aihara N, Shimomura K. Influence of epinephrine, propranolol, and atrial pacing on spatial distribution of recovery time measured by body surface mapping in congenital long-QT syndrome. *J Cardiovasc Electrophysiol* 1997; **8**: 1102–14.

59 Tanabe Y, Inagaki M, Kurita T, et al. Sympathetic stimulation produces a greater increase in both transmural and spatial dispersion of repolarization in LQT1 than LQT2 forms of congenital long-QT syndrome. *J Am Coll Cardiol* 2001; **37**: 911–19.

60 Shimizu W, Tanabe Y, Aiba T, et al. Differential effects of beta-blockade on dispersion of repolarization in the absence and presence of sympathetic stimulation between the LQT1 and LQT2 forms of congenital long-QT syndrome. *J Am Coll Cardiol* 2002; **39**: 1984–91.

61 Hekkala AM, Vaananen H, Swan H, Oikarinen L, Viitasalo M, Toivonen L. Reproducibility of computerized measurements of QT interval from multiple leads at rest and during exercise. *Ann Noninvasive Electrocardiol* 2006; **11**: 318–26.

62 Perhonen MA, Haapalahti P, Kivisto S, et al. Effect of physical training on ventricular repolarization in type 1 long-QT syndrome: a pilot study in asymptomatic carriers of the G589D KCNQ1 mutation. *Europace* 2006; **8**: 894–98.

63 Shimizu W, Kamakura S, Ohe T, et al. Diagnostic value of recovery time measured by body surface mapping in patients with congenital long-QT syndrome. *Am J Cardiol* 1994; **74**: 780–85.

64 Nirei T. [Variation of body surface QRST isointegral map in patients with idiopathic long-QT syndrome]. *Nippon Rinsho* 1995; **53**: 139–44.

65 Katsuki T, Takata S, Usuda K, Kobayashi K. [QRST isointegral maps on exercise in patients with congenital long-QT syndrome]. *Nippon Rinsho* 1995; **53**: 145–50.

40

CHAPTER 40

Electrocardiographic Imaging of Heart Failure Patients with Left Bundle Branch Block: Effects of Right Ventricular Pacing and Cardiac Resynchronization Therapy

Niraj Varma, MD, FRCP,[1] *Ping Jia,* PhD,[1] *Yoram Rudy,* PhD[2]

[1]Case Western Reserve University, Cleveland, OH, USA
[2]Washington University in St. Louis, St. Louis, MO, USA

Summary

Understanding of the electrical activation of the heart during pathological conditions and in response to pacing is limited. We used electrocardiographic imaging (ECGI), which maps epicardial ventricular excitation noninvasively, to evaluate intrinsic conduction during left bundle branch block (LBBB) in eight patients with left ventricular (LV) dysfunction and their responses to right ventricular (RV) pacing and cardiac resynchronization therapy (CRT).

During intrinsic conduction with LBBB, LV activation was heterogeneous and unpredictable, with regions of delayed and/or absent conduction. Sites of terminal LV activation varied. The anterior LV was susceptible to block and slow conduction. RV pacing or CRT sometimes created regions of slow LV conduction, indicating functional electrical characteristics of local tissue. RV pacing prolonged RV activation. Interventricular electrical synchrony usually improved with CRT, especially with lateral LV lead positions, but this did not correlate with changes in QRS duration.

We conclude that ECGI provided unique insight into ventricular activation during LV dysfunction. Complex electrophysiologic barriers, sometimes dependent on paced wavefront geometry and its direction of propagation, may determine the outcome of pacing therapies.

Introduction

Left bundle branch block (LBBB) activation pattern or right ventricular (RV) pacing increase mortality in patients with heart failure [1, 2]. In contrast,

Cardiac Mapping, Third Edition Edited by Mohammad Shenasa, Gerhard Hindricks, Martin Borggrefe, and Günter Breithardt
 ISBN: 978-1-405-17572-2

preexcitation of the inferolateral left ventricle (LV) by cardiac resynchronization therapy (CRT) in patients with wide baseline QRS improves overall survival [3]. Hence, the electrical activation sequence in LV dysfunction has important effects on survival.

However, descriptions of cardiac electrical activation under normal conditions or in the presence of LV pathology, or during pacing, are remarkably scarce [4–7]. This information is necessary in order to understand diverse responses to pacing that occur clinically. For example, RV pacing may benefit some patients but cause deterioration in others, and 30% of patients may not respond to CRT [8, 9]. Investigation requires high-resolution electrical mapping of ventricular excitation, which until recently could not be obtained noninvasively.

Electrocardiographic imaging (ECGI) is a novel noninvasive imaging modality for cardiac electrophysiology (EP) and arrhythmias [10, 11]. ECGI images epicardial potentials, electrograms, isochrones (activation sequences), and repolarization patterns from body surface electrocardiographic measurements. The methodology has been detailed previously [10].

Briefly, ECGI acquires body surface potentials at 1-msec intervals during the cardiac cycle using a 224-electrode vest. Epicardial geometry and body surface electrode positions are registered simultaneously by CT scan. The body surface potential data and the geometry data are processed with algorithms developed to compute epicardial potentials over the entire epicardium, from which epicardial electrograms (typically 600 over the heart surface), activation isochrones, and repolarization patterns are constructed.

All images are obtained during a single beat, thus facilitating imaging of nonsustained and polymorphic arrhythmias. The system has been validated extensively in animal models [12–17], and in humans by comparison to direct epicardial mapping during open-heart surgery [18] and to catheter mapping [19, 20]. Reconstruction accuracy superior to 10 mm has been consistently obtained in human subjects. This chapter is based on our previously published study [21] where we tested the hypothesis that during LV dysfunction, disease process may alter electrical substrate and modulate effects of LBBB and pacing. We also tested whether interventricular electrical resynchronization was accurately described by QRS width, and assessed the influence of LV lead position.

ECGI was applied to eight typical patients undergoing CRT (72 ± 11 years, 6 male) (Table 40.1). Patients were categorized as responders if there was evidence of reverse modeling defined by more than 10% improvement in echocardiographic measures of left ventricular ejection fraction (LVEF) (increase) and LV internal dimension (decrease). The earliest postimplant echocardiogram was obtained 6 months after implantation to permit time for remodeling following CRT. Intrinsic conduction (six patients had AV conduction with LBBB) was compared to RV pacing (RVP) and to biventricular pacing with optimal atrioventricular intervals [defined echocardiographically by the Ritter method [22]]. Ventricular activation times and sequences during intrinsic and paced rhythms were examined. Time zero was set at the beginning of QRS for all native rhythm episodes and at ventricular pacing stimuli for all paced episodes.

Intrinsic LBBB Activation

Following the onset of body surface QRS, epicardial activation started with RV breakthrough in all six patients (Figure 40.1). Epicardial activation spread radially from the RV breakthrough site, with the latest activation of the RV at the basal RV or anterior/inferior paraseptal region. The duration of the entire RV activation was 36 ± 8 msec after QRS onset.

Mean LV activation time during intrinsic conduction was longer (76 ± 23 msec) relative to that of RV epicardium, compared to only 40 msec in normal adults [10], which is consistent with LBBB. LV activation sequences were diverse. For example, in patient #1 multiple wavefronts contributed to overall LV activation which ended posterolaterally. In patient #3 [not illustrated here; see [21]], activation could not spread directly to the inferior LV but slowly propagated transseptally from the RV to reach the LV lateral and posterior walls by spreading inferoposteriorly from the anterior LV.

In three patients—#4, #7, and #8 [not illustrated here; see [21]]—LV epicardial activation started from the septoapical region, spreading laterally and ending at the lateral or posterolateral base. In patient #5, the activation wavefront spread superiorly

Table 40.1 Patient Characteristics.

Patient	1	2	3	4	5	6	7	8
Disease	*CAD*	*CAD*	*CAD*	*DCM*	*CAD*	*CAD*	*CAD*	*DCM*
LVEF (%)	20	10	25	15	25	30	15	15
Response	R	NR	R	NR	R	NR	NR	NR
Native rhythm: intrinsic conduction (msec)								
QRS	160		180	140	180		140	130
RV activation	40		51	30	29		38	32
LV activation	90		144	101	141		111	88
Esyn	−50		−93	−71	−113		−73	−56
RV pacing (msec)								
QRS	200		150	190	190	160	170	
RV activation	70		36	90	88	63	64	
LV activation	130		124	133	149	139	135	
Esyn	−60		−88	−43	−61	−76	−71	
CRT (msec)								
QRS	120	150	120	200	150	160	120	140
RV activation	68	75	42	69	88	61	60	52
LV activation	79	148	87	130	68	134	59	78
Esyn	−11	−73	−45	−61	20	−73	1	−26

KEY: CAD = coronary artery disease; DCM = dilated cardiomyopathy; LVEF = left ventricular (LV) ejection fraction; R = responder to CRT (cardiac resynchronization therapy); NR = nonresponder; RV = right ventricular; activation = mean ventricular activation time from the beginning of QRS (for intrinsic beats) or pacing artifact (for paced beats); Esyn = electrical interventricular synchronization index. Compiled with permission from Ref. [21].

from the inferior LV rather than from the apical region, ending at the midanterolateral wall.

In patients #4, #5, #7, and #8, activation that crossed the septum from the RV was prevented from spreading directly to the LV by an anterior line(s)/region(s) of block. It reached the lateral wall by way of either apical or inferior LV. Latest activation was at the inferoposterior base. This "U-shaped" activation was also reported by endocardial mapping [5]. Frequently, these lines of block and areas of slow conduction were functional. Thus, some line(s)/region(s) of block shifted to other locations, disappeared, or emerged later during pacing.

Lines of block were sometimes multiple, generating complex conduction barriers. For example, in patient #6 (Figure 40.2), two lateral lines of block forced electrical activation to propagate in a counterclockwise direction regardless of the pacing mode. Some lines remained unchanged with a change of pacing mode, suggesting fixed boundaries of anatomical origin. Previous reports with endocardial mapping also revealed heterogenous LV activation patterns with differing location and extents of specific ventricular delays [5, 7, 23]. Therefore, LV activation as recorded both epicardially and endocardially is heterogenous in the presence of heart disease, possibly due to lesions of the specialized conduction tissue, presence of scar regions, and slow cell-to-cell conduction [24].

Right Ventricular (RV) Pacing

RV pacing has been postulated to simulate LBBB, though few direct comparisons have been made. In this study, RV pacing was performed from the RV midseptal position in patients #1 and #6, and from the apex in the others. Overall, QRS duration (177 ± 20 msec vs. LBBB: 155 ± 22 msec, p = NS), and LV activation (135 ± 9 msec vs. LBBB: 113 ± 24 ms, p = NS) did not change significantly compared to intrinsic conduction during LBBB. However, RV pacing slowed RV activation (RVP 64 ± 19 vs. intrinsic conduction 37 ± 8 msec, $p < 0.03$). Areas of LV (functional) conduction delays changed

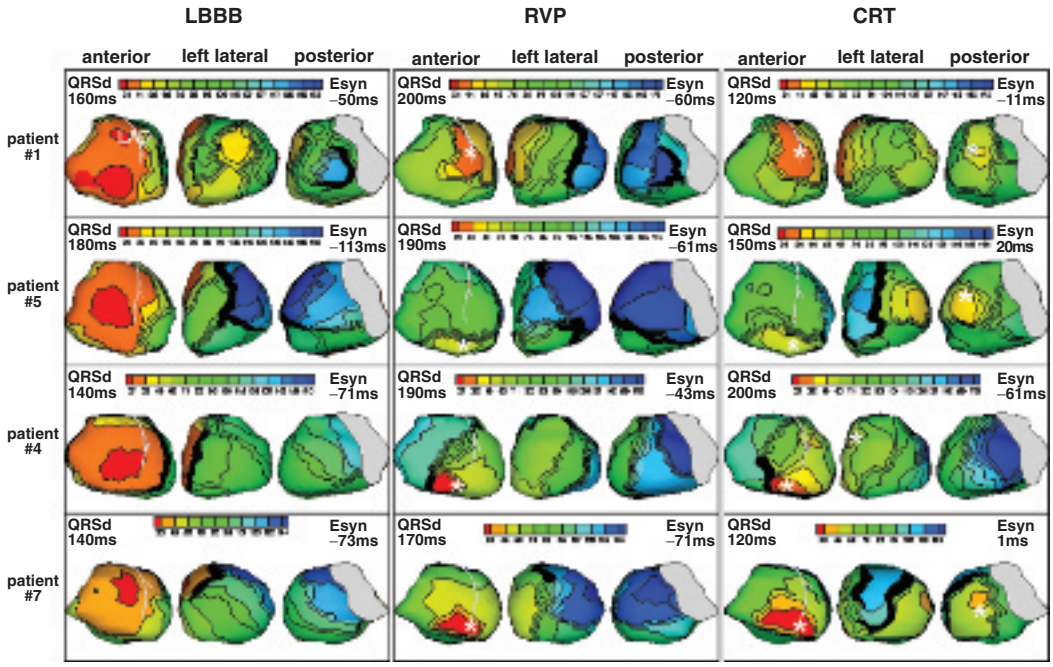

Figure 40.1 Epicardial isochrone maps for four representative patients. Patients #1 and #5 were CRT responders, and patients #4 and #7 were nonresponders. Intrinsic conduction with LBBB (left panels), right ventricular pacing (RVP, middle panels) and biventricular pacing during cardiac resynchronization therapy (CRT, right panels) are depicted. Epicardial surfaces of both ventricles are displayed in three views: anterior, left lateral, and posterior. There is overlap between adjacent views. The left anterior descending (LAD) coronary artery is shown. Thick black markings indicate line/region of conduction block. Pacing sites are marked by asterisks. KEY: Esyn = electrical synchrony index (smaller absolute value corresponds to greater synchrony, see text and Ref. [21] for definition); QRSd = QRS duration.

Left panels (intrinsic conduction during LBBB: Ventricular activation of right ventricle (RV) was followed by a much delayed left ventricular (LV) activation, indicating left bundle branch block (LBBB). Several different LV activation patterns are depicted. Patient #1 had LV breakthrough at 49 msec (left lateral view). Combined wavefronts advancing from apical, inferior, and superior LV all contributed to overall LV activation, which ended at the posterolateral wall. In patient #5, the LV activation wavefront spread superiorly from the inferior LV to end anterolaterally. Patients #4 and #7 demonstrated apical-to-basal epicardial conduction. Wavefronts emerged from a septoapical origin, then spread laterally to end at the lateral or posterolateral base.

Middle panels (response to right ventricular pacing (RVP): Note RVP changed areas of slow conduction/lines of block compared to intrinsic activation, indicating that this pacing mode is not simply equivalent to LBBB. For example, in patient #1, a line of block appears anteriorly, but in patient #5 a preexisting line of block is shortened. These data point to the functional nature of conduction block in these regions.

Right panels (responses to biventricular pacing; CRT): Patients #1 and #5 were responders with lateral LV lead positions. In patient #1, CRT dissolved the anterior line of block evident during RVP, activating the anterior and anterolateral LV relatively evenly compared to intrinsic conduction. Interventricular synchrony improved (Esyn less negative). In patient #5, Esyn became positive (from −113 to 20 msec) indicating LV preexcitation, though an anterior line of block persisted.

In contrast, patients #4 and #7 were nonresponders. In patient #4, LV pacing resulted in marked slowing of the paced wavefront in the lateral LV wall, in contrast to intrinsic conduction when conduction was relatively rapid in the same area. Esyn changed marginally from −71 to −61 msec, indicating ineffective resynchronization in this nonresponder. QRS duration prolonged. In patient #7, CRT induced a line of functional block in the anterolateral LV (not apparent with RVP). Despite this, Esyn improved because the LV lead was sited laterally. Compiled with permission from Ref. [21].

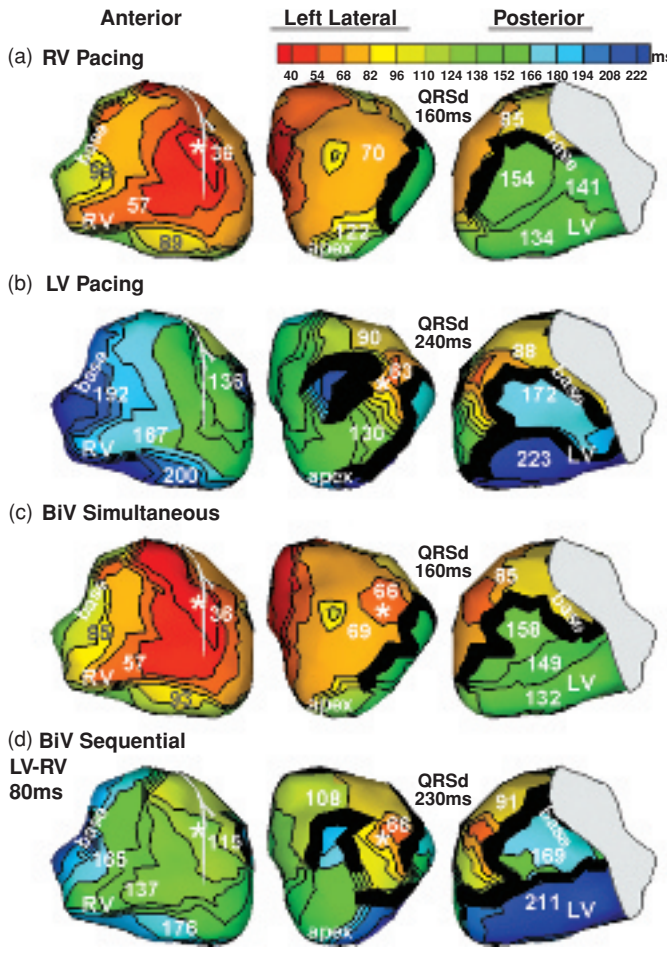

Figure 40.2 Imaging (anterior, left lateral, and posterior views) in patient #6, during different pacing modes. (a) Right ventricular (RV) pacing. (b) Left ventricular (LV) pacing. (c) Cardiac resynchronization therapy with simultaneous biventricular (BiV) pacing. (d) Cardiac resynchronization therapy with LV pacing preset of 80 msec relative to RV pacing (sequential pacing mode). Activation times (in msec) of selected regions are indicated on the map.

In this patient, 12-lead ECGs recorded after implant were similar during simultaneous biventricular pacing and during RV pacing. Imaging revealed the underlying mechanism. During simultaneous biventricular pacing (c), RV pacing breakthrough occurred 30 msec earlier than LV breakthrough. The RV-paced wavefront had arrived at the LV lead location just when LV pacing breakthrough was commencing. Consequently, LV pacing did not influence overall ventricular activation. Thus, ventricular activation was similar in RV pacing and simultaneous biventricular pacing (parts a and c). In contrast, when LV pacing occurred 80 msec prior to RV pacing, LV activation resembled that during LV pacing alone (parts d and b, respectively), except for RV activation advanced slightly (30 msec) due to RV electrode effect.

The modulating effect of complex conduction barriers on paced wavefront propagation was illustrated. A line of block across the LV lateral free wall was present consistently over all pacing modes. It prevented any anterior activation from propagating inferiorly to the midlateral region. This area was activated by a wavefront propagating from the inferior LV (for RV or biventricular simultaneous pacing, parts a and c), or possibly by an intramural wavefront (for LV or biventricular sequential pacing, parts b and d). In addition, during LV or biventricular sequential pacing, a line of block between lateral and inferior LV prevented lateral activation from propagating inferiorly. This was a functionally determined line of unidirectional block, because wavefront propagation in the reverse direction was permitted in the other two pacing modes. Because of these complex barriers, global activation could propagate around the heart only in a counterclockwise fashion. The inferior LV could be activated only by wavefront spreading from the RV. In terms of electrical synchrony, biventricular sequential pacing was better than biventricular simultaneous pacing in this patient. Compiled with permission from Ref. [21].

with RV pacing compared to corresponding intrinsic rhythm. In patient #5, pacing dissolved the anterior line of block present during intrinsic conduction. In contrast, a similar line was induced by RV pacing in patient #1, when it had not been present before (Figure 40.1). Hence, RV pacing was not simply equivalent to LBBB. This may explain prolonged LV activation times observed with RV pacing in patients with LBBB and LV dysfunction and associated increase in mortality [2, 25, 26].

Biventricular Pacing

The movie file (Videoclip 25 👁) provides an animation of epicardial potential progression during biventricular pacing in patient #1. With biventricular pacing, LV activation patterns were different among patients. Variations are illustrated in Figure 40.1. Patient #5 was a responder to CRT. LVEF increased from 25% to 40% and LV internal dimension decreased by 10%. Activation spread from the lateral wall LV pacing site and ended locally at basal LV after 110 msec.

On the anterior LV, the latest activation occurred at 138 msec immediately adjacent to a line of block (which was also present during LBBB). Note that the existence of this line of block did not preclude response to CRT in this case. RV and LV electrical synchrony improved compared to intrinsic conduction. In contrast, patient #4 did not respond to CRT. LV pacing from an anterior position slowed LV lateral wall activation relative to native rhythm. Activation time to the basal LV doubled. The region of slow conduction only appeared during pacing, indicating dependence of propagation of the paced wavefront on the electrical substrate adjacent to the pacing lead.

In patient #6 (Figure 40.2), ECGs recorded during CRT and RV pacing were similar. ECGI provided an explanation for this effect. Propagation of LV-paced wavefronts was severely limited. Thus, during simultaneous biventricular pacing (Figure 40.2c), RV-paced wavefronts had already reached the LV as LV pacing breakthrough was just initiating, that is, the LV-paced wavefront was delayed (presumably by an encircling area of slow conduction) and had a negligible effect on overall activation. However, sequential pacing with LV preactivation (Figure 40.2d) permitted LV pacing contribution to biventricular activation.

Patient #2 improved two functional classes (NYHA IV to II) within four weeks of CRT. However, ECGI demonstrated that he had fixed anterior anatomic block from extensive anterior and anterolateral LV infarction. Excitation generated by the anteriorly located LV lead activated the RV but not the LV, that is, LV pacing had a negligible effect in the presence of heavy scar burden.

Postimplant echocardiography demonstrated progressive deterioration with LV dilatation and diminishing ejection fraction. The patient deceased from heart failure nine months later. This apparent paradox illustrates a placebo clinical response (well recognized in device trials) with subjective benefit occurring despite lack of electrical or echocardiographic evidence.

Left Ventricular (LV) Pacing

Three patients with intact atrioventricular conduction in whom the device was programmed for LV pacing alone showed fusion between intrinsic excitation and the LV paced beat. Depending on the relative length of the PR interval and optimal atrioventricular delay, the degree of fusion varied (Figure 40.3).

Resynchronization with Biventricular Pacing

To assess interventricular resynchronization with CRT, we derived the index Esyn, the mean activation time difference between lateral RV and LV free walls, that is, directly from measurements on the heart. Interventricular synchrony was indicated when Esyn equaled zero. RV preexcitation corresponded to negative Esyn and LV preexcitation to positive Esyn. At baseline during intrinsic conduction with LBBB, Esyn was -76 ± 23 msec representing delayed LV activation. RVP did not change Esyn significantly (-67 ± 15, $p =$ NS). In one case (patient #5) Esyn (which reports relative RV to LV activation) improved because RV activation slowed while LV activation was minimally altered.

With biventricular pacing, overall, Esyn changed significantly from -76 ± 24 during intrinsic conduction to -31 ± -32 msec ($p < 0.01$) in response to CRT, indicating improved interventricular synchronization (Figure 40.4). This was not matched

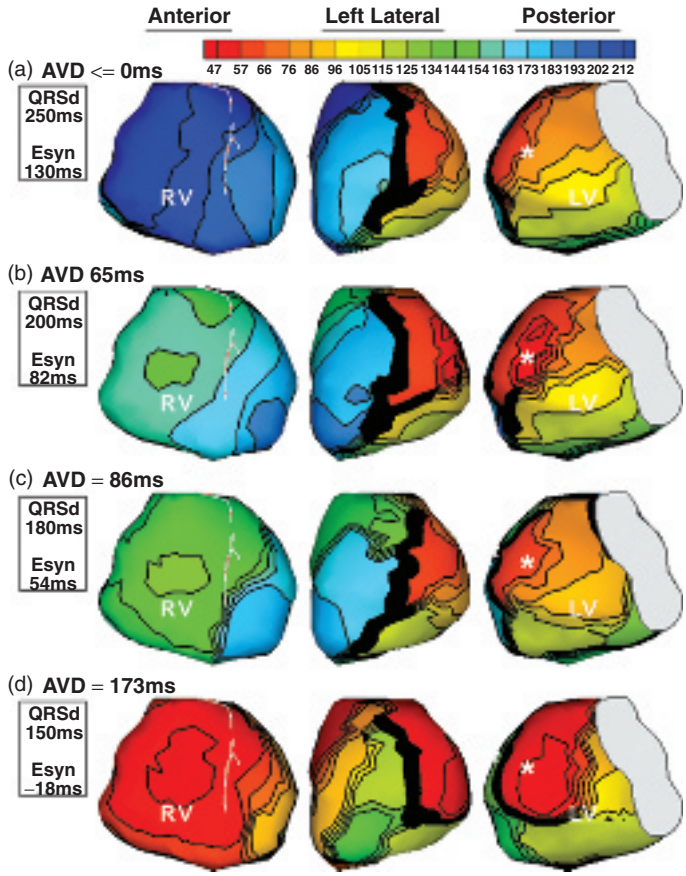

Figure 40.3 Imaging (anterior, left lateral, and posterior views) during atrially synchronized LV pacing in patient #5 who had underlying LBBB. This series of LV-paced beats with progressively increased atrioventricular (AV) delays demonstrates increasing degree of fusion of LV-paced activation with RV activation via intrinsic right bundle branch conduction. Thus, (a) shows pure LV paced activation without fusion, and (b)–(d) demonstrate progressively greater fusion. Esyn improved as fusion increased (d). (a) LV-paced activation sequence without fusion. (b)–(d) Fusion beats with progressively earlier intrinsic right ventricular (RV) activation (time of RV breakthrough) relative to LV pacing. (b) Right ventricular breakthrough at 153 msec after LV pacing. (c) RV breakthrough at 132 msec after LV pacing. (d) RV breakthrough at 45 msec after LV pacing. Compiled with permission from Ref. [21].

by changes in QRS width (native rhythm 155 ± 22 vs. CRT 146 ± 28 msec, p = NS). In some individuals, Esyn and QRS changes were driven in opposite directions, for example, in patient #8 Esyn improved from −56 to −26 msec with CRT, but QRS duration (QRSd) increased slightly from 130 msec to 140 msec. The lack of correlation between QRS and Esyn demonstrates that the widely used QRSd measure is only a reflection on the body surface of the total duration of ventricular activation and not a specific index of interventricular synchronization. This may underlie the weakness of QRS in predicting response to CRT.

However, improved Esyn did not predict clinical response consistently; for example, patients #6–#8 remained nonresponders despite improved interventricular electrical synchronization. Recent data indicate that intra-LV rather than RV-LV dysynchrony is more important for predicting response [27]. Lack of correlation can also be due to inconsistent mechanical response to electrical resynchronization in different patients.

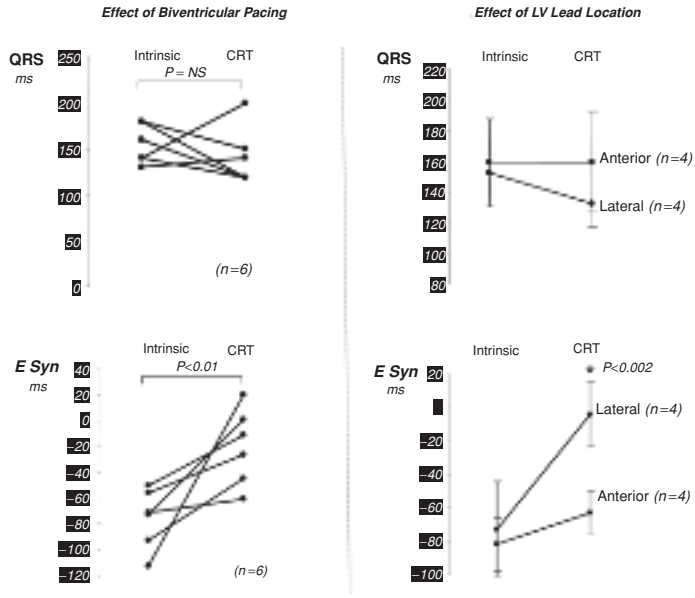

Figure 40.4 Effects on QRS duration (QRS, top panels) and electrical interventricular synchronization (Esyn, bottom panels) of biventricular pacing (left panels) and either anterior or lateral LV lead locations (right panels). (Left) Biventricular pacing produced no overall difference in QRS duration (top), but improved Esyn (bottom); that is, QRS did not accurately report interventricular resynchronization. (Right) Influence of LV lead position. Anterior lead positions did not abbreviate the QRS (top), and resulted in less resynchronization (increased Esyn, bottom).

Lead position affected resynchronization (Figure 40.4). Patients (#1, #5, #7, and #8) with lateral leads were better electrically resynchronized than those with an anteriorly located LV leads (patients #2, #3, #4, and #6). This is probably due to the high likelihood of encountering regions of conduction block and slow conduction (anatomic and functional) in the anterolateral aspects that interfere with propagation from the anterior to the lateral wall. Under these conditions, RV activation was more influenced than LV activation which did not differ substantially from intrinsic conduction in LBBB. This ECGI finding may explain superior clinical benefit with lateral lead placement compared to anterior placement [28].

Implications

The study provided unique insights into propagation of intrinsic and paced wavefronts in the presence of LV disease. During intrinsic conduction with LBBB, wide inter-individual variability of LV activation has been observed. This may affect CRT efficacy. LV lead placement in current practice is directed to the inferolateral LV wall, assumed to be consistently the latest region to be activated and responsible for mechanical dyssynchrony [29]. However, preexcitation of this area with epicardial LV stimulation empirically without electrical mapping did not always yield maximum contractility improvement [30]. In contrast, LV lead placement directed to endocardial sites of latest conduction delay yielded greater increases in contractility, especially when this late activated area was large [31].

The results presented here extend this understanding by demonstrating that areas of terminal epicardial LV depolarization may be variably located, and vulnerable to development of complex functional conduction barriers with pacing. This observation suggests that efficacy of LV pacing should consider not only the sequence of activation (i.e., pacing from the region of most delayed activation to maximize synchrony), but also electrical properties of local substrate adjacent to lead position.

This is illustrated by the complex conduction barriers limiting the LV-paced wavefront propagation in patient #6 (Figure 40.2). Anteriorly directed LV

lead positions frequently encountered anterior LV lines of block, rendering them less effective in resynchronization. This study demonstrated significant RV (as well as LV) activation delays with RV pacing, either alone or in conjunction with simultaneous biventricular pacing. This may be avoided by LV pacing with critically timed atrioventricular (AV) delays resulting in fusion of the propagated paced wavefront with intrinsic conduction via an intact right bundle (Figure 40.3). This CRT mode may avoid RV hemodynamic deficit associated with simultaneous biventricular pacing [32].

Future

Clinical morbidity of disordered electrical activation in LBBB and RVP may be mediated by mechanical effects. Successful treatment by CRT requires improved hemodynamic function but, as a pacing therapy, its effects will be governed by electrical properties. This study, using ECGI's unique ability to provide high-resolution mapping of cardiac electrical activity, confirmed that patients with heart failure demonstrate wide and unpredictable variations in baseline ventricular activation and in responses to pacing.

LV disease alters local electrical properties resulting in areas of inexcitability and slow/blocked conduction which may be anatomically or functionally determined. These complexities may affect mechanical responses to RV pacing or CRT. Integration of data from electrical and mechanical mapping may be required to direct optimal lead placement and improve clinical outcome with CRT. This demands prospective evaluation in clinical trials.

Acknowledgements

In addition to the authors, Charulatha Ramanathan, PhD, Raja N. Ghanem, PhD, and Kyungmoo Ryu, PhD, also participated in the ECGI study on which this chapter is based. The study was supported by NIH-NHLBI Merit Award R37-HL-033343 and Grant RO1- HL-49054 to Y.R.

Disclosures

Y.R. chairs the scientific advisory board and holds equity in CardioInsight Technologies (CIT). CIT does not support any research conducted by Y.R., including the results presented here. P.J. is an equity holder and a paid employee of CIT.

References

1 Baldasseroni S, Opasich C, Gorini M, et al. Left bundle-branch block is associated with increased 1-year sudden and total mortality rate in 5517 outpatients with congestive heart failure: a report from the Italian network on congestive heart failure. *Am Heart J* 2002; **143**: 398–405.

2 Wilkoff BL, Cook JR, Epstein et al. Dual-chamber pacing or ventricular backup pacing in patients with an implantable defibrillator: the Dual Chamber and VVI Implantable Defibrillator (DAVID) Trial. *JAMA* 2002; **288**: 3115–23.

3 Cleland JG, Daubert JC, Erdmann E, et al. The effect of cardiac resynchronization on morbidity and mortality in heart failure. *N Engl J Med* 2005; **352**: 1539–49.

4 Durrer D, van Dam RT, Freud GE, Janse MJ, Meijler FL, Arzbaecher RC. Total excitation of the isolated human heart. *Circulation* 1970; **41**: 899–912.

5 Auricchio A, Fantoni C, Regoli F, et al. Characterization of left ventricular activation in patients with heart failure and left bundle-branch block. *Circulation* 2004; **109**: 1133–39.

6 Vassallo JA, Cassidy DM, Marchlinski FE, et al. Endocardial activation of left bundle branch block. *Circulation* 1984; **69**: 914–23.

7 Vassallo JA, Cassidy DM, Miller JM, Buxton AE, Marchlinski FE, Josephson ME. Left ventricular endocardial activation during right ventricular pacing: effect of underlying heart disease. *J Am Coll Cardiol* 1986; **7**: 1228–33.

8 Goldberger JJ. Right ventricular pacing: has DAVID slain this Goliath? *Heart Rhythm* 2005; **2**: 835–36.

9 Abraham WT, Fisher WG, Smith AL, et al. Cardiac resynchronization in chronic heart failure. *N Engl J Med* 2002; **346**: 1845–53.

10 Ramanathan C, Ghanem RN, Jia P, Ryu K, Rudy Y. Noninvasive electrocardiographic imaging for cardiac electrophysiology and arrhythmia. *Nat Med* 2004; **10**: 422–28.

11 Ramanathan C, Jia P, Ghanem R, Ryu K, Rudy Y. Activation and repolarization of the normal human heart under complete physiological conditions. *Proc Natl Acad Sci U S A* 2006; **103**: 6309–14.

12 Burnes JE, Taccardi B, Rudy Y. A noninvasive imaging modality for cardiac arrhythmias. *Circulation* 2000; **102**: 2152–58.

13 Burnes JE, Taccardi B, Ershler PR, Rudy Y. Noninvasive electrocardiographic imaging of substrate and intramural ventricular tachycardia in infarcted hearts. *J Am Coll Cardiol* 2001; **38**: 2071–78.

14 Burnes JE, Taccardi B, MacLeod RS, Rudy Y. Noninvasive ECG imaging of electrophysiologically abnormal substrates in infarcted hearts: a model study. *Circulation* 2000; **101**: 533–40.

15 Ghanem RN, Burnes JE, Waldo AL, Rudy Y. Imaging dispersion of myocardial repolarization, II: noninvasive reconstruction of epicardial measures. *Circulation* 2001; **104**: 1306–12.

16 Oster HS, Taccardi B, Lux RL, Ershler PR, Rudy Y. Electrocardiographic imaging: noninvasive characterization of intramural myocardial activation from inverse-reconstructed epicardial potentials and electrograms. *Circulation* 1998; **97**: 1496–507.

17 Oster HS, Taccardi B, Lux RL, Ershler PR, Rudy Y. Noninvasive electrocardiographic imaging: reconstruction of epicardial potentials, electrograms, and isochrones and localization of single and multiple electrocardiac events. *Circulation* 1997; **96**: 1012–24.

18 Ghanem RN, Jia P, Ramanathan C, Ryu K, Markowitz A, Rudy Y. Noninvasive electrocardiographic imaging (ECGI): comparison to intraoperative mapping in patients. *Heart Rhythm* 2005; **2**: 339–54.

19 Wang Y, Cuculich PS, Woodard PK, Lindsay BD, Rudy Y. Focal atrial tachycardia after pulmonary vein isolation: noninvasive mapping with electrocardiographic imaging (ECGI). *Heart Rhythm* 2007; **4**: 1081–84.

20 Intini A, Goldstein RN, Jia P, et al. Electrocardiographic imaging (ECGI): a novel diagnostic modality used for mapping of focal left ventricular tachycardia in a young athlete. *Heart Rhythm* 2005; **2**: 1250–52.

21 Jia P, Ramanathan C, Ghanem RN, Ryu K, Varma N, Rudy Y. Electrocardiographic imaging of cardiac resynchronization therapy in heart failure: observation of variable electrophysiologic responses. *Heart Rhythm* 2006; **3**: 296–310.

22 Ritter P, Padeletti L, Gillio-Meina L, Gaggini G. Determination of the optimal atrioventricular delay in DDD pacing: comparison between echo and peak endocardial acceleration measurements. *Europace* 1999; **1**: 126–30.

23 Rodriguez LM, Timmermans C, Nabar A, Beatty G, Wellens HJ. Variable patterns of septal activation in patients with left bundle branch block and heart failure. *J Cardiovasc Electrophysiol* 2003; **14**: 135–41.

24 Akar FG, Spragg DD, Tunin RS, Kass DA, Tomaselli GF. Mechanisms underlying conduction slowing and arrhythmogenesis in nonischemic dilated cardiomyopathy. *Circ Res* 2004; **95**: 717–25.

25 Hayes JJ, Sharma AD, Love JC, Herre JM, Leonen AO, Kudenchuk PJ. Abnormal conduction increases risk of adverse outcomes from right ventricular pacing. *J Am Coll Cardiol* 2006; **48**: 1628–33.

26 Varma N. Left ventricular conduction delays in response to right ventricular apical pacing: influence of LV dysfunction and bundle branch block. *J Cardiovasc Electrophsyiol* 2007; **19**: 114–22.

27 Bordachar P, Lafitte S, Reuter S, et al. Echocardiographic parameters of ventricular dyssynchrony validation in patients with heart failure using sequential biventricular pacing. *J Am Coll Cardiol* 2004; **44**: 2157–65.

28 Butter C, Auricchio A, Stellbrink C, et al. Effect of resynchronization therapy stimulation site on the systolic function of heart failure patients. *Circulation* 2001; **104**: 3026–29.

29 Leclerq C KD. Retiming the failing heart: principles and current clinical status of cardiac resynchronization. *J Am Coll Cardiol* 1999; **39**: 194–201.

30 Dekker AL, Phelps B, Dijkman B, et al. Epicardial left ventricular lead placement for cardiac resynchronization therapy: optimal pace site selection with pressure–volume loops. *J Thorac Cardiovasc Surg* 2004; **127**: 1641–47.

31 Tse HF, Lee KL, Wan SH, et al. Area of left ventricular regional conduction delay and preserved myocardium predict responses to cardiac resynchronization therapy. *J Cardiovasc Electrophysiol* 2005; **16**: 690–95.

32 Lee KL, Burnes JE, Mullen TJ, et al. Avoidance of right ventricular pacing in cardiac resynchronization therapy improves right ventricular hemodynamics in heart failure patients. *J Cardiovasc Electrophysiol* 2007; **18**: 497–504.

41

CHAPTER 41

How to Better Map and Future Directions in Cardiac Mapping

Mohammad Shenasa, MD, FACC, FAHA, FESC, FHRS,[1]
Jafar Shenasa, MSc,[1] *Javad Rahimian,* PhD[2]

[1]Department of Cardiovascular Services, O'Connor Hospital, San Jose, CA, USA
[2]Department of Radiation Oncology, University of California-Los Angeles, Los Angeles, CA, USA

Summary

Cardiac Mapping is at its crossroads. With landmark of atrial fibrillation ablation and other complex atrial and ventricular arrhythmias, multimodality imaging has found its place in basic and clinical electrophysiology laboratory. Image fusion and integration has significantly improved our understanding of arrhythmia substrate, mechanism and success rate of ablative procedures.

Novel mapping and imaging technologies such as cardiac MRI, MR spectroscopy, diffused optical spectroscopy, optical imaging, cardiac coherence tomography is under evaluation for clinical use. These techniques with high resolution capabilities and future perspectives are discussed. The crucial role of mapping/imaging in early phenotyping of disease, risk definition, management guidance, ablative procedures, and outcome assessment is expanding rapidy in ways previously thought unrealistic.

Cardiac Mapping: Past, Present and Future

The history of cardiac mapping dates to the late nineteenth- and early twentieth-century pioneers such as Sir Thomas Lewis, J.A. MacWilliam, G.B. Mines and many others who reported on the investigation of activation sequences of cardiac normal and abnormal rhythms that were investigated in open chest animals [1–6]. This is well described by Wellens in Chapter 1 of the current edition and by Janse in the previous editions. Cardiac mapping has evolved from sequential analog maps to its most complex three- to four-dimensional multimodality real-time (virtual) mapping and imaging.

With the use of computers in the 1950s and 1960s, many technical obstacles were removed. The previous limitations on the number of recording channels, sample frequencies, etc., are now resolved. The field of cardiac imaging and mapping has recently experienced major growth and technological advances, and is under rapid evolution, particularly in the areas of molecular imaging, cardiac CT, MRI, and image integration, producing multimodality and hybrid systems that are already in clinical practice.

These new systems provide a rapid acquisition of cardiac potentials, anatomical reconstruction of

Cardiac Mapping, Third Edition Edited by Mohammad Shenasa, Gerhard Hindricks, Martin Borggrefe, and Günter Breithardt
 ISBN: 978-1-405-17572-2

entire heart or specific chambers, and provide a virtual map. The ultimate goal of such systems is to provide accurate anatomical and physiological (functional) characteristics of the target organ and tissue, and deliver the appropriate therapies and or interventions such as stem cell implant or ablative procedures.

Currently, several advanced mapping systems are commercially available such as electroanatomical mapping (Carto™, Biosense-Webster, Diamond Bar, CA), the noncontact mapping/NavX™ mapping system (St. Jude Medical, St. Paul, MN), basket catheter mapping, Loca-Lisa™ (Medtronic, Minneapolis, MN) mapping, and the real-time navigation mapping system [7] The advantages and disadvantages are discussed in this book and elsewhere [8]. The principle of cardiac mapping using different methods, that is, noncontact and electroanatomical, are also discussed elsewhere. Each system should provide the ability for registration activation (isochronal mapping) and repolarization (isopotential mapping) simultaneously with unipolar and bipolar modes.

Because significant differences exist between unipolar and bipolar recordings, they should provide complementary information. In this chapter we will briefly discuss some specific topics on the future of cardiac mapping. Finally, there is already a trend toward noninvasive imaging and mapping and hopefully noninvasive ablation (interventional procedures), which will also be discussed.

Future of Cardiac Electrophysiological Mapping

Introduction

Radiofrequency (RF) catheter ablation has been proven to be a safe and effective procedure to treat significant number of cardiac arrhythmias. Success can be as high as 95% in patients with supraventricular tachycardia involving accessory pathways or atrioventricular nodal tachycardia, and accordingly, catheter ablation is considered the treatment of choice for these pathologies [9–11].

A noninvasive imaging technique to identify and depict the areas responsible for cardiac arrhythmias is desirable. Current mapping techniques are invasive or semi-invasive in nature, and require catheterization under long fluoroscopy procedures that expose the patient, as well as the interventional cardiologist and the personnel in the angiography suites, to significant ionizing radiation. We outline here the new approaches underway that have the potential to lead us to our ultimate objective of noninvasive image-guided electrophysiological mapping of the heart.

Optical Imaging

Bioluminescence

A new molecular imaging technique based on bioluminescence and fluorescence imaging is currently under development for in vitro and ex vivo applications [12]. Bioluminescence is the process of light emission in living organisms. Bioluminescence imaging utilizes native light emission from one or several organs by administering targeted bioluminescence probes. The light photons emitted from the body are detected using a charged-coupled device (CCD) detector from these targeted bioluminescence probes, near infrared (NIR) fluorochromes, activatable NIR fluorochromes, and red-shifted fluorescents proteins [13].

A notable theoretical advantage of this technique is the fact that multiple probes with different spectral characteristics can be potentially imaged using a multichannel analyzer. In addition, the technique is noninvasive and inexpensive. The applications are similar to karyotyping [14], and the study technique is limited photon transmission through an opaque tissue, yielding a reduced bioluminescence signal. The depth you may currently study in animal model is about 2 cm [12].

Optical mapping of heart electrical activity is done with the use of optical imaging techniques based on voltage-sensitive dyes or probes. Optical recordings of transmembrane potentials can be performed in a wide range of spatial resolutions from the subcellular level to the whole heart [15]. The technique is currently being investigated, and involves injection of voltage-sensitive dyes such as RH421, di-4-ANEPPS, and di-8-ANEPPS that have spectroscopic properties that change linearly with membrane potential changes in the normal physiological range of transmembrane voltages in heart [16]. The exact mechanisms underlying the voltage-dependent spectroscopic properties of voltage-sensitive dyes are not fully understood;

however, the theories of electrochromic [17] and solvatochromic mechanism [18] have been mostly used to explain the properties of the fluorescence dyes.

Arora et al, used high-resolution optical mapping in isolated whole-atrial preparations from 33 normal dogs and found that the normal pulmonary veins have the necessary electrophysiological substrate to support both the reentry and focal activity [19]. Similarly, Mandapati et al. used optical mapping and frequency analysis of the sheep atrium to investigate the microreentrant mechanisms of atrial fibrillation in sheep heart [20].

Kalifa et al. [21] has used an endoscopic fluorescence, or so-called "biophotonic," technique to map electrical activity in the posterior left atrium in an intact heart with high-resolution imaging. They used an endoscope coupled to a 532-nm excitation laser for illumination and a CCD camera for imaging of potentiometric dye fluorescence (di-4-ANEPPS, 80 × 80 pixels, 200–800 frames/sec). Detailed description of the bioluminescence optical technique is explained elsewhere [15, 21–24].

Del Nido et al. [25] developed a method for in vivo quantization of cytosolic RHOD2 concentration that in conjunction with calcium-dependent fluorescence measurements permits estimation of cytosolic calcium levels in perfused rabbit hearts. Reflective absorbance of excitation light by RHOD2 loaded into myocardium was used as an index of dye concentration, and the ratio of fluorescence intensity to absorbance as a measure of cytosolic calcium concentration.

There are still many obstacles to overcome for applying this technique in a clinical setting, notably the absence of a voltage-sensitive dye that is not phototoxic and satisfies the optical requirements. In addition, this technique is invasive in nature, and requires catheterization to detect the photons. Further refinement of the technique as it applies to optical detection technologies, catheter design, and more sensitive CCD cameras to detect faint optical photons from deeper tissue is warranted. Hopefully in the near future we will see the use of optical mapping in clinical settings using a single-electrode catheter, and biophotonic imaging modalities will provide 3D cardiovascular tissues structural imaging. Other techniques such as near infrared are currently being investigated.

Fluorescent cardiac imaging has been used experimentally in animals to evaluate myocardial perfusion during coronary stenosis and has proven to be a reliable quantification of myocardial ischemia [26]. Multiple infrared-sensitive devices with different dyes are currently being investigated for clinical use.

Diffused Optical Spectroscopy (DOS)

DOS quantifies concentration of water, fat, and certain chromophores (e.g., hemoglobin) by measuring the absorption and scattering spectra of four near-infrared (NIR) wavelengths. Optical methods are advantageous, because they are noninvasive, quantitative, and relatively inexpensive; and they also pose no risk from ionizing radiation. These techniques are based on highly sensitive, quantitative measurements of optical and functional contrast between healthy and diseased tissues. The technique was developed by Tromberg et al. [27] at the University of California Irvine, and used to detect breast lesions [28].

This system uses frequency domain photon migration (FDPM). FDPM employs intensity-modulated NIR light to characterize tissue quantitatively in terms of its optical parameters, that is, the reduced-scattering coefficient (μ_s') and the absorption coefficient (μ_a). The concentration of significant NIR absorbers [deoxyhemoglobin (Hb), oxyhemoglobin (HbO_2), water, and fat] can be calculated by using measured μ_a values [20, 30]. Scattering of transmitted light in tissue occurs in multiple directions as a consequence of spatial variations in the refractive index, which are influenced by cellular and extracellular matrix density [31, 32]. Both μ_a and μ_s' provide an understanding of changes in tissue cellularity, metabolic activity, physiology, and host response to cancer. Detection of lesions is based on the functional contrast between normal and diseased tissue in the same patient.

The technique uses a photodiode and a photomultiplier tube to measure the absorption and scatter spectra of four different NIR wavelengths (at 674, 803, 849, and 956 nm), and subsequently determine tissue concentration of hemoglobin (total, oxy, and deoxy- forms), oxygen saturation (S_tO_2), blood volume fraction, water, and fat contents, and cellular structures. DOS makes spectroscopic measurements in the frequency rather than time domain and, therefore, can continuously monitor the total

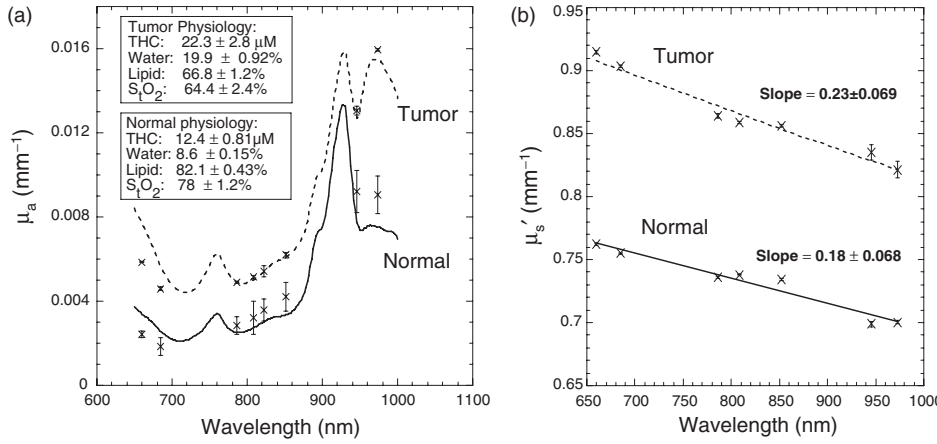

Figure 41.1 (a) (b) DOS absorption (u_a) and scattering (u_s') spectra of normal tissue and breast tumor.

path that the NIR light has traveled in the tissue of interest.

A continuous laser source is modulated at all frequencies, and the phase shift between the light entering and exiting the tissue can be recorded. The resultant spectra demonstrate distinct peaks for water, fat, total hemoglobin concentration, and oxy and deoxy hemoglobin. Using appropriate modifications of the Beer–Lambert law and calibration phantoms, minimal changes in concentration of these molecules can be measured in vivo [33]. Figure 41.1a,b depicts the contrast between the absorption coefficient (μ_a) and the reduced-scattering coefficient (μ_s') of normal tissue and a breast tumor, respectively.

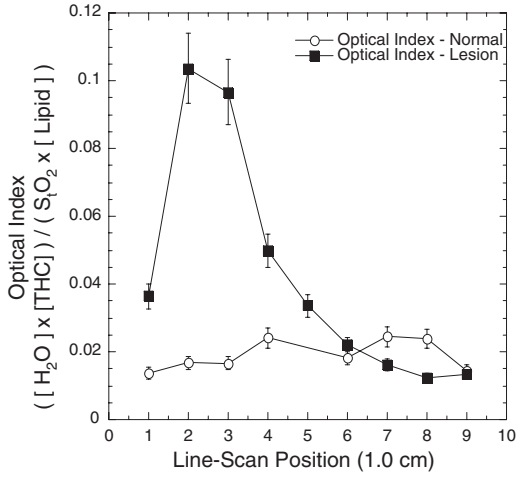

Figure 41.2 Tissue optical index (TOI) for normal tissue and breast tumor.

A tissue optical index (TOI) has been developed that incorporates the various optical parameters into a single number to make interpretation of data easier.

$$\text{TOI} = ([\text{water}][\text{THC}]/[S_tO_2][\text{Lipid}])$$

Elevated TOI values are suggestive of high metabolic activity that is usually seen in malignancy. The tumor tissue usually demonstrates increased absorption in the 650–850 nm spectral range, which corresponds to higher total THC. The lipid peak at 920 nm is present in normal breast tissue and breast tumors, and the 960 nm water peak is prominent in the tumor. The differences in spectra between the two tissue types are manifestations of multiple physiological changes associated with increased vascularization (angiogenesis), cellularity, oxygen consumption, and edema in the tumor. Figure 41.2 compares the TOI of a breast malignant tumor and normal tissue.

The technique can be modified and adapted to match the requirements in a cardiac study. However, the physiology of healthy heart tissue is complex, influenced by contraction, blood flow, and calcifications. Consequently, to establish a better basis for optical detection and diagnosis based on differential functional contrast, the optical properties of normal heart tissue have to be carefully examined and characterized. The technique requires a fiber optic catheter to transmit and detect short pulses of NIR light at four different frequencies between 650 and 1000 nm.

The source modulation frequencies are in the range 50–1000 MHz. These are amplitude-modulated using a network analyzer. In addition, a steady-state (SS) spectroscopic system with a white light source is used to measure μ_a values where FDPM wavelengths do not exist. The scattered photons are transmitted through the fiber optic catheter, and are detected by an avalanche photodiode detector that records the diffuse light signals after propagation through the tissue, attached via a fiber optic cable to a signal-processing computer. The laser lights are intensity modulated, and information is detected at each point. The theory, and instrumentation used in FDPM are described in details elsewhere [34]. Furthermore, the technique can be adapted to measure the absolute concentrations of voltage-sensitive nonphototoxic optical beacons to map the electrophysiology of the heart. Similar principles are theoretically applicable to the myocardium under different conditions, that is, ischemia infarction, fibrosis, and hypertrophic.

DOS measurements have underlying physiological meaning: high total hemoglobin concentration (THC) corresponds to elevated tissue blood volume fraction; high water content suggests edema and increased cellularity; decreased lipid content reflects displacement of parenchymal adipose tissue; and decreased S_tO_2 indicates increased tissue oxygen metabolism. DOS is safe, portable, relatively inexpensive, and does not use ionizing radiation. DOS, unfortunately, does not provide precise anatomical localization or size of the lesion. The primary limitation of DOS is related to the fact that light propagates diffusely in tissue. DOS is also dependent on the depth and the size of the lesion. In addition, DOS does not have the resolution of an MRI image, and is not suitable for screening or detection of lesions <0.5 cm. There are no known risks associated with NIR exposure at the power levels used for cardiac study.

Magnetic Resonance Imaging (MRI) and Magnetic Resonance Spectroscopy (MRS)

MRI and MRS are based on the detection of the oscillating magnetic field induced from a special set of nuclides that possess a net spin in the presence of a strong external magnetic field. MRI generally refers to the determination of the distribution of one molecule, such as water or fat, within a tissue at high spatial resolution. The detection of the naturally occurring nuclide ^{1}H found in water and fats is usually used for MRI studies providing an adequate signal-to-noise ratio to create images with submillimeter resolution in vivo.

Magnetic resonance spectroscopy (MRS) is the name given to the technique that exploits the magnetic properties of certain nuclei. In principle, MRS is applicable to any nucleus possessing spin. MRS provides information on the number and type of chemical entities in a molecule, as well as measures the organ chemistry. The most common nuclei that are used are ^{1}H (proton), ^{23}Na (sodium), ^{31}P (phosphorus). Due to much higher molar tissue concentration, proton spectroscopy is easier to perform and provides a much higher signal-to-noise ratio than sodium, phosphorus, or the metabolites with low concentration. These combined effects cause the MRS images to have very poor spatial and temporal resolution. Proton MRS can be performed within 10–15 min and can be added on to conventional MR imaging protocols. It can be used to serially monitor biochemical changes in the organ.

The impact of MRS is an invaluable tool in understanding protein and nucleic acid structure and function. When placed in a magnetic field, MRS active nuclei (such as ^{1}H or ^{13}C or ^{31}P) absorb at a frequency characteristic of the isotope. The resonant frequency, the energy of the absorption, and the intensity of the signal are proportional to the strength of the magnetic field. A detailed review of the basic physical principles of MRI and MRS, as well as their potential clinical applications, are described elsewhere [35].

MR spectroscopy is the only method for noninvasive detection of various aspects of cardiac metabolism in humans. While the ^{1}H nucleus of water and fat molecules is the signal source for MR imaging, the MR spectroscopic technique allows for the study of a number of other nuclei, such as ^{13}C, ^{19}F, ^{23}Na, ^{31}P, ^{39}K, and ^{87}Rb. Clinical applications presently are confined to the ^{31}P nucleus. ^{31}P-MR spectroscopy allows the noninvasive study of cardiac high-energy phosphate metabolites, ATP, and phosphocreatine. The phosphocreatine/ATP ratio is considered an index of the energetic state of the heart. Possible clinical indications include heart failure, valve disease, and coronary artery disease. In heart failure, the phosphocreatine/ATP ratio is

reduced and correlates with clinical severity, ejection fraction, and prognosis [36]. Absolute quantification of high-energy phosphates may allow diagnosis of myocardial viability. Major technical developments, leading to improved spatial and temporal resolution, will be necessary to establish MR spectroscopy as a routine clinical tool.

MRS Clinical Applications

There are numerous MRS studies of the brain. MRS is used to determine the degrees of malignancy of gliomas [37] and the efficacy of radiation therapy treatment of the tumors in the brain [38]. In addition, the MRS can be used to determine cerebral ischemia and infarction due to markedly elevated lactate, which are the key spectroscopic features of cerebral hypoxia and ischemia. Choline is elevated, and both NAA (a neuronal marker) and creatine are reduced. If cerebral infarction ensues, lipids increase. Furthermore, MRS has proven to be useful in assessing the degree of neuronal injury and predicting patient outcomes after head injury and trauma. Clinical outcome correlates inversely to the NAA/creatine ratio. The presence of any lactate or lipid indicates a worse prognosis [35].

Cardiac MRS is a noninvasive technique that provides unique information regarding cardiac metabolism through the observation of proton and phosphorous metabolites. Grist et al. have described a technique to acquire gated cardiac MR imaging, as well as ^{1}H and ^{31}P MR spectroscopy using a doubly tuned surface coils [39]. Bottomley has shown changes in cardiac ^{31}P spectra after acute myocardial infarction of the anterior wall [40]. In a review article about the MRS of the human heart, Bottomley P.A. has concluded that the ^{31}P MRS of phosphocreatine (PCr) and adenosine triphosphate (ATP) concentrations of about 11 and 6 umol per gram wet weight, respectively with a PCr/ATP ratio of around 1.8 in normal heart. The PCR/ATP ratio and the metabolite concentrations calculated using ^{31}P MRS were found to be abnormal in patients with hypertrophic and dilated cardiomyopathy, left ventricular hypertrophy, valve disease, transplanted hearts, myocardial infarction, and reversible ischemia. Therefore, the PCR/ATP ratio is considered to be an index of the energetic state of the heart, and reduced ratio has a link with heart failure [41]. There are currently no direct studies of cardiac electrophysiology mapping using either MRI or MRS.

Diffusion Tensor Imaging (DTI) and Fiber Tracking (FT)

Conventional diffusion MRI studies the displacement distribution of the water molecules present within an image voxel. This noninvasive in vivo technique provides unique clues to the structure and geometric organization of tissues. The diffusion MRI probes random diffusion–driven displacements of molecules in the tissue structure at a microscopic scale well beyond the image resolution. Necause diffusion is truly a 3D physical process that is totally independent of MR effect or magnetic field, the molecular mobility in tissue may be anisotropic, as in brain white matter [42]. With diffusion tensor imaging, diffusion anisotropy effects can be fully extracted, characterized, and exploited, providing even more exquisite details on tissue microstructure.

An advanced application of diffusion tensor imaging (DTI) is fiber tracking of the myocardium, which in combination with functional MRI may open a window on the important issues of electrical conductivity, propagation, tissue connectivity, and orientation in space of fibers. This approach opens a complete new way to gain direct and in vivo information on the organization in space of oriented tissues such as in the myocardium. Technical descriptions of diffusion tensor imaging are described elsewhere [42, 43]. Knowledge of the myocardial fiber orientations plays an important role in the realistic modeling of the electrical and mechanical activity of the heart, and changes in this configuration may be of significant importance to understand the remodeling after myocardial infarction. Indeed, the conductivity is typically four times larger along the fibers than in the transverse direction; the orientation of the fibers creates a strong anisotropy in the constitutive law of the material, and also constrains the direction of the contraction stress [44].

Hsu et al. has correlated quantitatively the magnetic resonance myocardial fiber-orientation mapping directly with standard histological techniques [45]. Their data showed that the eigenvector of the largest diffusion tensor eigenvalue corresponds to the local fiber orientation. Their results highlight the utility and validity of the MR diffusion tensor imaging methodology as a 3D noninvasive means

to elucidate tissue architecture, particularly in evaluating myocardial structural changes that are linked to electrical or mechanical dysfunction.

Hocini et al. used an isolated heart with incised PVs to show that fiber orientation changes at the PV-LA junction play a key role in the occurrence of conduction disturbances [46]. Furthermore, Choi et al. studied fiber orientation and cell–cell coupling influencing ventricular fibrillation dynamics [47]. Rohmer et al. reconstructed and visualized the heart fiber structures in three dimensions using diffusion tensor magnetic resonance imaging data of the excised human heart. Fibers were reconstructed using the first eigenvectors of the diffusion tensors. The sheets were reconstructed using the second and third eigenvectors and visualized as surfaces. Their results showed the fibers lie in sheets that have transmural structure. Their quantitative measurements showed that the sheets as opposed to the fibers are organized into laminar orientations without dominant populations. Figure 41.3 shows the visualization of the fiber structure of the left ventricle [48]; (see Videoclip 26.) Tissue classification and characterization using multispectral image processing of MRI data may provide further insight to the different cardiac pathologies. Figure 41.4 shows and example of DTI of the left ventricle in a mouse model at healthy ischemia and infarction [49]. The principles of this technique have been reported by Zhukov and Barr [50].

Multimodality Electrophysiological Mapping

Drummond et al. [51] developed a system for simultaneous ^{31}P MRS and optical transmembrane potential measurement in rabbit hearts. ^{31}P nuclear magnetic resonance (NMR) is used to evaluate five metabolic markers (pH, sugar phosphates, phosphocreatine, phospholipid intermediates, and ATP). The action potential duration is measured with a transmembrane potential-sensitive fluorescent dye, di-4-ANEPPS. The system was intended to correlate the action potentials with the metabolic markers and their changes during the time course of cardiac ischemia. Their results showed the ability to use the new probe to acquire a spectrum in the presence of the optical elements within the magnet, suggesting the possibility that ^{31}P NMR spectroscopy and optical transmembrane potential measurements can be performed in hearts simultaneously.

The future of cardiac mapping lies in a noninvasive image-guided multimodality technique utilizing image fusion. The imaging will show the anatomy and physiology superimposed on the heart electrical mapping, using either optical mapping or conventional ECG. CT or MRI provide the anatomical information; SPECT and PET scans provide the information about the physiology and viability of the myocardium; and MRS provides chemistry and ionic diffusion across cell membrane. Gated DTI of the heart can potentially be a noninvasive image-guided technique to map the regions with fiber orientation changes due to infarction or other anomalies that may be responsible for arrhythmias. This can be validated by applying optical fluorescence mapping fused with the gated DTI images.

Ideally for a noninvasive technique the principles of diffuse optical tomography (DOT) [52] should be used with nonphototoxic voltage-sensitive dyes to map the electrophysiology of the heart in three dimensions fused to MRI or the fiber tracking image of the heart. This image should give one the electrical mapping as well as the physiology and construction of the fiber of the heart muscle.

Electrophysiology of the heart depends on the Na+, K+, and Ca++ ionic movement across the cell membrane. Disruption of ionic movements due to infarction or other physiological disturbances can be the cause of arrhythmias. Future mapping should utilize diffusion tensor imaging of ^{23}Na, ^{39}K, ^{31}P, and fiber tracking based on these ions. Even though the concentration of these ions is very small compared to ^{1}H, using clinically available 3T or 7T magnet MRIs with specifically designed gradient coils for cardiac studies, a higher signal-to-noise ratio of these ions can be acquired for imaging. The absolute concentration of these ions superimposed on the gated MRI images of the heart, and DTI of the ions one can have the anatomical information with chemistry, and orientation of the ionic diffusion. This information is invaluable to the interventional cardiologist/electrophysiologists.

Therefore, cardiovascular MRI and spectroscopy carries the following applications [53, 54]:

- coronary artery imaging,
- quantification of blood flow,
- coronary artery flow quantification,

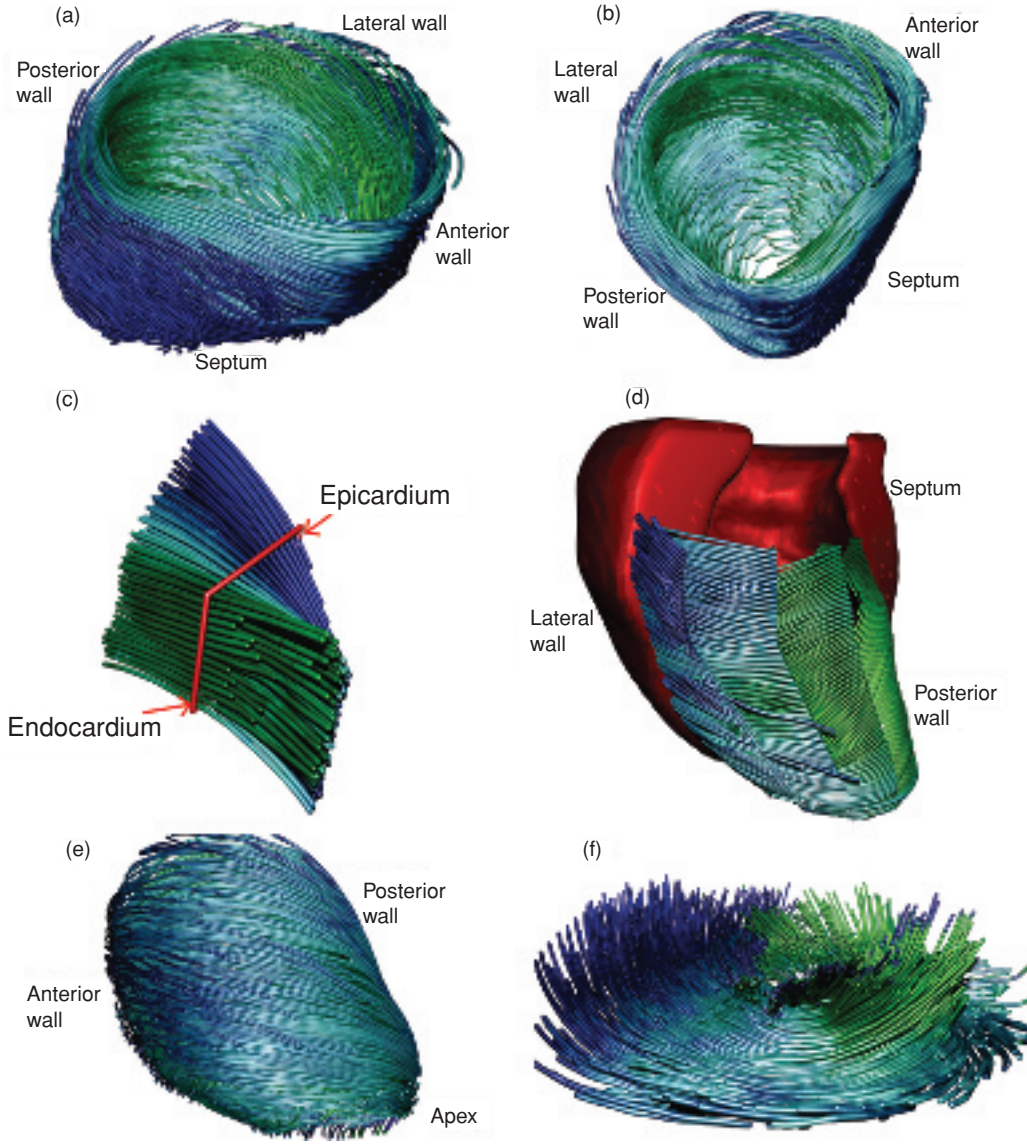

Figure 41.3 Visualization of the fiber structure of the left ventricle. (a) The visualization was created by using a cylindrical mesh of 1000 seed points throughout the entire volume. Left-handed to right-handed rotation of the fibers going from the epicardium to endocardium can be seen. The nearest wall is the septum. (b) The heart is displayed with the posterior wall on the bottom. (c) Short section of the left ventricle that illustrates the smooth variation of the fiber angle and its sign inversion across the wall from epicardium to endocardium. (d) Orientation of the fibers by sections in the anterior wall from the septal to the lateral wall. For each section, the fibers are plotted closer to the endocardium. The smooth change of direction can be seen while the fiber bundle wraps around the endocardium. (e) Helical visualization of the fibers from the apex to the base. (f) Fiber tracks close to the apex. The twist around the apex can be appreciated. It is worth noticing the smooth continuity of some bundles of fibers going down from the endocardium (green), passing the midwall (in light blue), and going up again (dark blue). The large variations between green and blue in the middle of the apex are due to the fast change from left-handed to right-handed rotation. In the center, the comparison between left-handed and right-handed rotation is not accurate as the fibers become more aligned with the central axis of the left ventricle. Reprinted with permission from Rohmer D, Sitek A, Gullberg GT. Reconstruction and visualization of fiber and laminar structure in the normal human heart from ex vivo diffusion tensor magnetic resonance imaging (DTMRI) data (technical note). *Invest. Radiol* 2007; 42: 777–89.

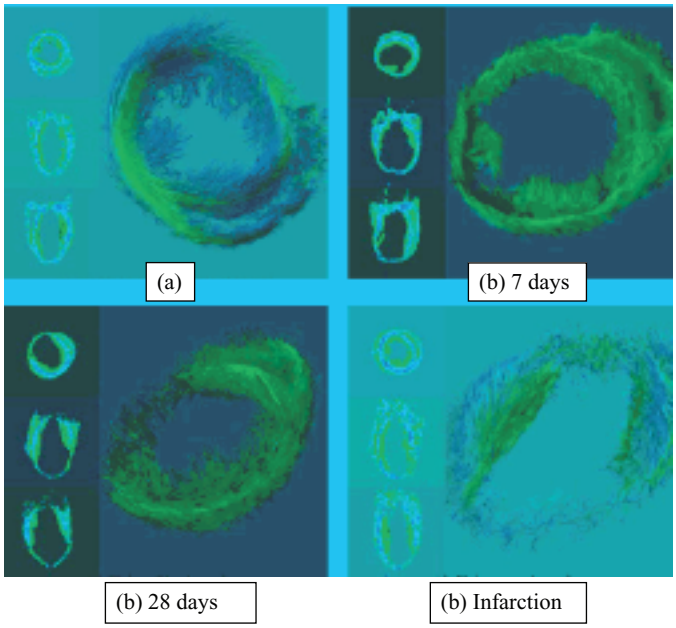

Figure 41.4 The diffusion tensor imaging (DTI) visualization of (a) healthy heart and (b) at 7 days and 28 days of ischemia and infarction in mouse. Reprinted with permission from Ref. (49).

- heart failure,
- cardiomyopathies,
- functional and diffusion tensor imaging,
- cardiac spectroscopy,
- image-based guidance for stem cell therapies,
- cardiac-based guidance mapping and ablation therapy.

Specific Issues

Image Integration and Fusion

In the Introduction to the first edition of *Cardiac Mapping,* we wrote, "Cardiac mapping has always been an integral part of experimental and clinical electrophysiology." The current and future of cardiac mapping and interventional electrophysiology will depend on integration of cardiac imaging to cardiac mapping or cardiac image–based mapping.

Image integration has provided a new look at cardiac anatomy and mapping as well as at interventional electrophysiology. Klemm et al. have used a contact and noncontact mapping system together to simultaneously create the geometry and voltage maps in patients with ischemic multiple ventricular tachyarrhythmia's [55]. The study provided rapid identification of critical border zones for ablation procedures (Figure 41.5). (See Videoclips 27–29. 👁).

Almost all imaging technologies can be fused to one another and provide accurate road maps. Examples include the following:

1. CT integration with electroanatomical mapping. The combination is currently widely used, particularly for atrial fibrillation ablation to construct the atrial geometry and its relation to adjacent structures [56]. See Figure 41.6. CT angio of the left atrium with its corresponding electroanatomical mapping of a patient with paroxysmal atrial fibrillation. (See Videoclip 30. 👁) Figure 41.7 illustrates CT angiography of the left atrium in two different patients demonstrating variants of pulmonary vein anatomy, panels (a) and (b) fly through (virtual) of the left atrium and pulmonary veins of the same patient. Martinek et al. studied the impact of CT image integration on electroanatomical mapping, and compared the results with the use of electroanatomical mapping alone. They found that integration into the current mapping system has significantly improved success rate of radiofrequency ablation of atrial fibrillation [57]. Both CT and MRI provide better landmarks for anatomical mapping. The relationship of chamber anatomy to the arrhythmia substrate, either focal or reentry, is critical in certain cases such as atrial fibrillation, right atrial tachycardia, and right or left ventricular outflow tract tachycardias. Combination of these image technologies with information obtained during ablation

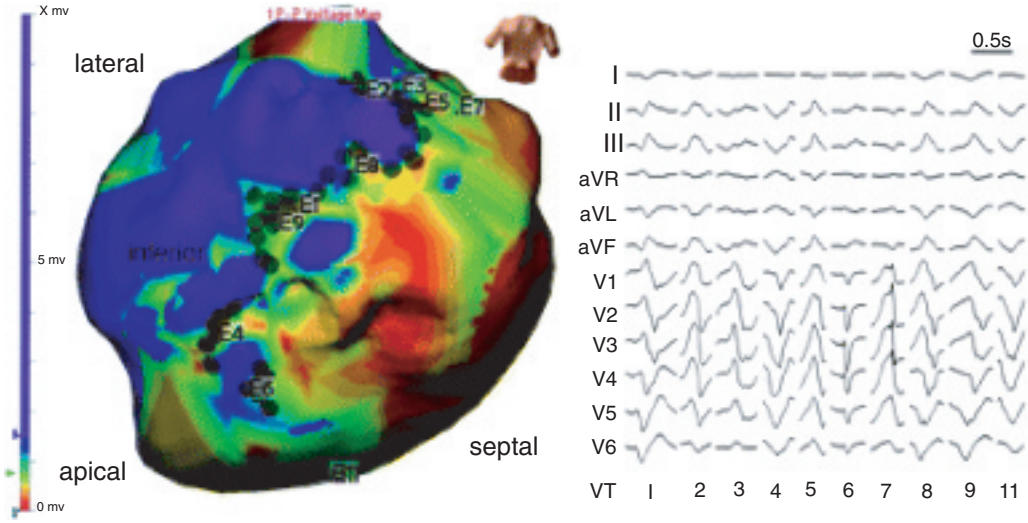

Figure 41.5 Contact voltage map of patient #5 that shows superimposed VT exits (E) defined by noncontact mapping and applied ablation lesions. (Left) Exit sites were defined by the onset of the reconstructed unipolar QS deflection that preceded the VT QRS complex. The color range represents bipolar voltage amplitudes (peak-to-peak) with control sliders set from 0 (red) to 1.5 mV (purple). The modified posterior view shows exits of distinct VT entities as defined by QRS morphology; exits are numbered in the order of induction. A critical border was identified with exits 1–9 (excluding E4 and E6) located on the same aspect of an extended septal-to-inferior myocardial scar area. The median voltage of the critical border was 0.8 mV. The ablation lesions followed the contour of the contact map to approach VT1–VT9 (excluding VT4 and VT6). The exit of VT10 was located on the anteroseptal aspect and was therefore not visible. (Right) One cycle of each VT is displayed centered on the QRS complex. The numbers below correspond to the VT exit sites in the left panel. Please note the left bundle branch block pattern for the septal and apicoseptal VT exits (E4, E6, and E11). Reprinted with permission from Ref. [53]. See Videoclips 27–29.

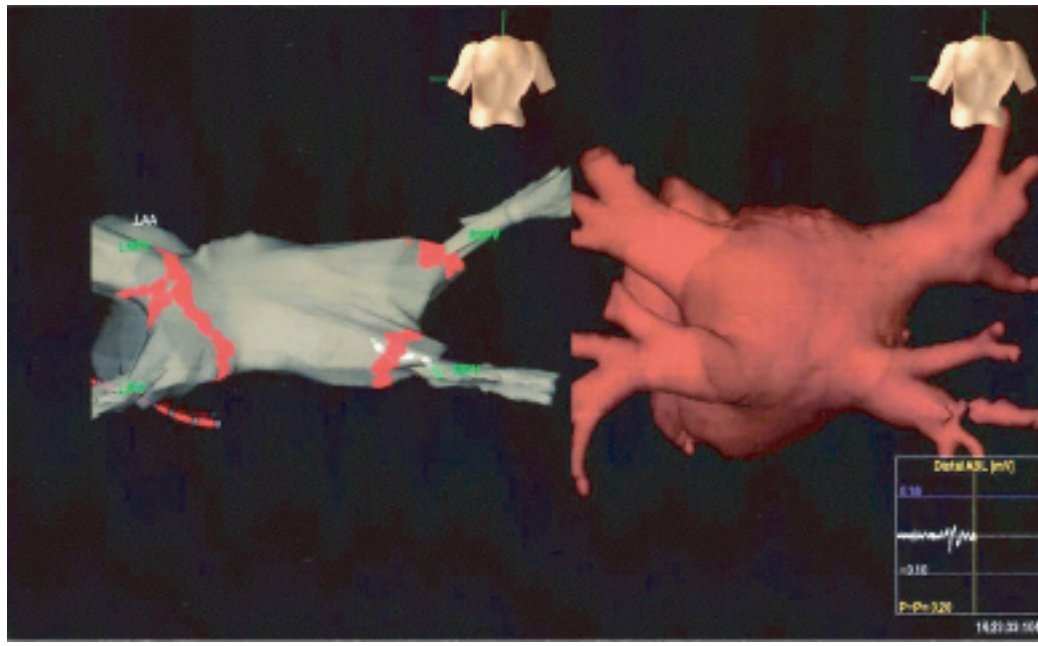

Figure 41.6 Electroanatomical mapping of the left atrium (left panel) and CT angiography of the left atrium and pulmonary veins. CT angiography of the left atrium and pulmonary veins on the right. Images were integrated during the ablation procedure. See the Videoclip 41.X. Courtesy of Jeffrey Olgin, UCSF.

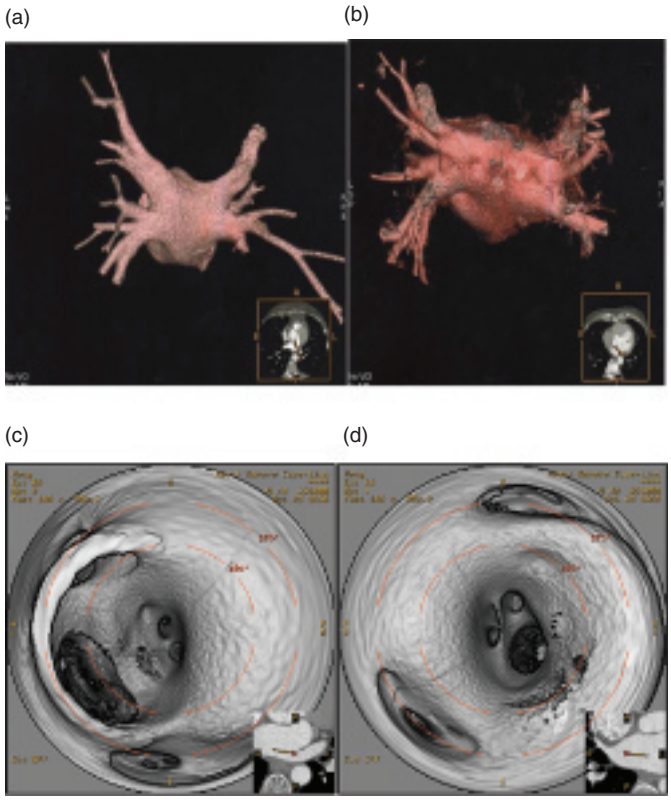

Figure 41.7 (Top panel) CT angio of the left atrium of two different patients showing variance of pulmonary vein anatomy. Panels (c) and (d) show a fly-through of the left atrium and pulmonary vein of first patient.

procedures has improved our understanding of arrhythmia mechanisms and the arrhythmogenic substrate, and has been called learning while burning [58–60].

2. PET/CT integration with electroanatomical mapping. The development of hybrid PET/CT will allow simultaneous comprehensive imaging of cardiac function and anatomy [61]. Dickfeld et al. investigated the role of PET/CT in identification of scar substrate and border zone for mapping and ablation of ventricular tachycardia [62].

3. Cardiac 3D MRI [63] and CT [64] fluoroscopy have also been used to provide detailed anatomical geometry and excellent navigation and localization for the ablation procedure. Fluoroscopy provides a direct and unmodified view of the cardiac and anatomy silhouette.

4. High-resolution electrocardiographic mapping and cardiac MRI has been used by Berger et al. This technology is similar to cyber knife radiotherapy, which uses MRI to define a patient's specific cardiac anatomy, and integrates the high-resolution EKG to provide an accurate localization of cardiac activation—in this particular case, ventricular preexcitation [65].

5. Integration of intracardiac echocardiogram with CT/electroanatomical maps [66].

6. Robotic magnetic navigation systems such as Stereotaxis is also used for mapping and ablation of a variety of cardiac arrhythmias [67, 68].

7. High-intensity ultrasound imaging is being investigated to provide 3D catheter positioning [69] and also as an ablation tool for cardiac arrhythmias.

8. Finally, integration of all imaging modalities?the one-stop shop.

As discussed, cardiac MR spectroscopy and fiber orientation together with optical mapping and in vivo molecular and channel mapping is the road to the future.

Left Ventricular Dyssynchrony and Cardiac Mapping in Resynchronization Therapy (CRT)

CRT is novel electrical therapy for patient with left ventricular (LV) systolic dysfunction and LV dyssynchrony. Several issues remain regarding

patient selection and markers of responders and nonresponders. Although some ECG and tissue Doppler echocardiographic measurement such as tissue synchronization imaging, speckle tracking, and strain rate imaging are used, almost one-third of the patients who undergo CRT are non-responders. Therefore, more reliable methods are desirable.

Methods such as tissue Doppler imaging, and 3D and 4D echocardiography, are recently suggestive, which provides a simultaneous evaluation of dyssynchrony in all segments of the heat both in cross-sectional and longitudinal views.

Electroanatomical mapping as well as noninvasive body surface mapping before or at the time of implant may help to differentiate responders from nonresponders. In the future, MR fiber tracking may be very intriguing to investigate. Helm et al. recently reported 3D mapping as well as harmonic phase images of MRI in dogs in which LV mechanical dyssynchorny had been induced [70–71]. Functional maps were analyzed which identified areas where mechanical synchrony and optimal systolic and diastolic performance was. This method may prove useful in the near future for patient selection for CRT.

Repolarization Mapping

Until recently, mapping of arrhythmias mostly focused on depolarization, but with increasing interest and better insights into repolarization and its underlying channelopathies, global mapping of repolarization has been gaining attention. Optical mapping in experimental models and noncontact mapping in humans both provide new insights into the role of repolarization in arrhythmogenesis and its management applications [72].

Role of Cardiac Mapping in Channelopathies: Cell Therapy in Electrophysiological Substrates and Genetic Engineering

Techniques such as optical mapping, MR spectroscopy, and electroanatomical mapping have been used to evaluate the feasibility and effectiveness of interventions in the above conditions [73, 74]. However, the role of cardiac mapping and potential interventions are still in the early stages of investigation.

Electrocardiogram

Despite numerous technological advances, the "old friend" electrocardiogram remains viable and useful. Innovative work done by Yorum Rudy and his colleagues on electrocardiographic imaging provides a new use of electrocardiographic measurements [75–77,]. Similarly, Brown et al. used electrographic activation time and diastolic intervals to separate focal from macroreentrant atrial tachycardias [78].

Other investigators have used different new electrocardiographic analysis to elucidate the mechanisms and locations of arrhythmias [79–81]. Spatiotemporal phase analysis of the electrocardiogram is another novel use of the simple EKG. Zhang et al. recently reported a noninvasive 3D electrocardiographic imaging of ventricular activation sequence using body surface potential recordings. The results were validated by 3D in vivo mapping in rabbits [82].

Towards a Unified Protocol

The need for a standardized protocol is warranted. It is the expected natural history of any new innovation that longitudinal studies are needed to set appropriate guidelines on criteria, definitions, and so on. Cardiac electrophysiology experienced this process in the 1970s and 1980s with programmed electrical stimulation in ventricular tachyarrhythmias.

Similarly, atrial fibrillation mapping ablation is going through the same process. Different imaging/mapping technologies with different resolutions on the one hand, and diverse mechanisms, roles of underlying disease and pathology, and ablation techniques on the other hand, have led to different results and endpoints. For example, some groups use inducibility as the endpoint, while others use isoprotererol. Some groups use fractionated electrograms as markers for ablation sites, and other investigators use vagal nerve plexi mapping. Figures 41.8 and 41.9 illustrate integrative cardiac mapping and imaging approach for catheter ablation of arrhythmias. Obviously, differences in mapping technology and ablation methods have resulted in expected differences in the outcomes [83]. Therefore, a unified approach to this problem is warranted and the first step has already been taken with expert consensus on catheter and surgical ablation of atrial fibrillation [84].

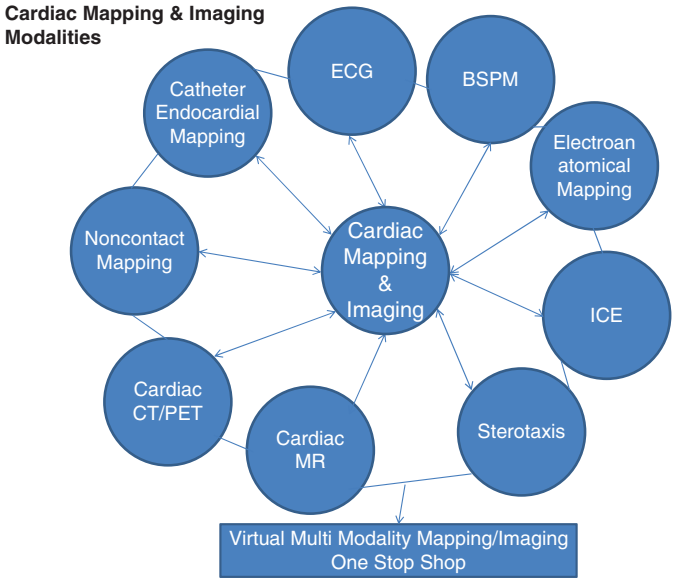

Figure 41.8 Integrative approach to cardiac mapping and imaging.

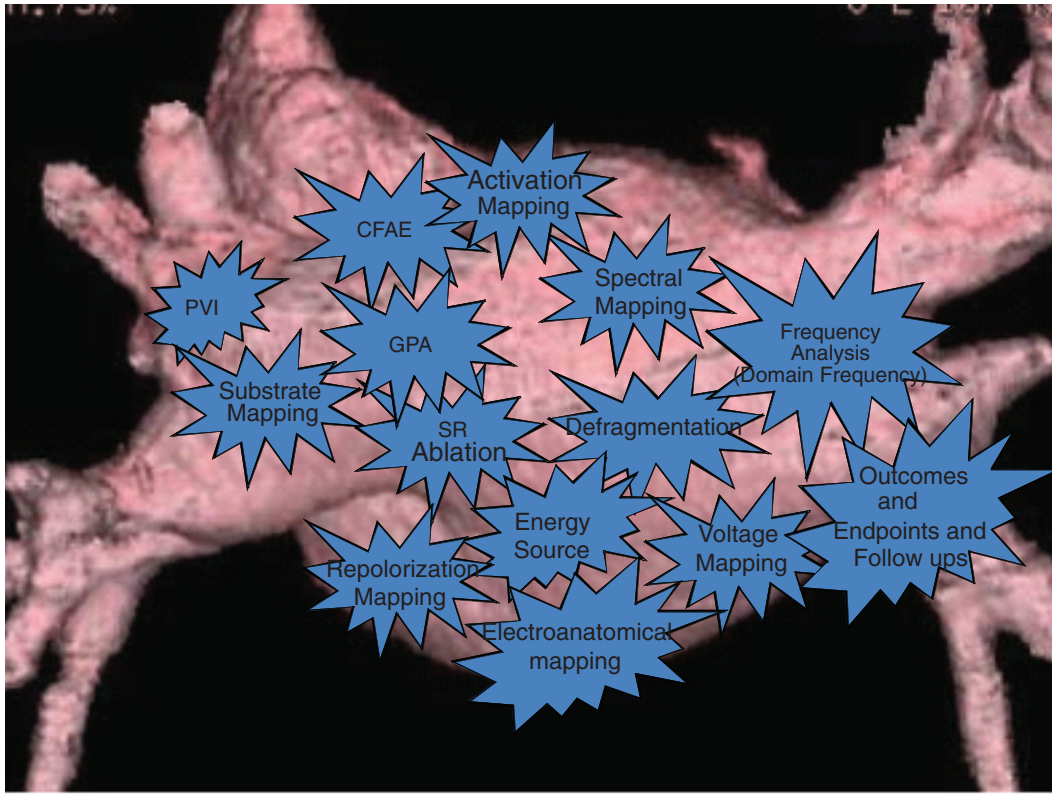

Figure 41.9 Approaches to atrial fibrillation mapping and ablation. KEY: PVI = pulmonary vein isolation; CFAE = complex fractionated atrial electrograms; GPA = ganglionic plexi ablation; SR = sinus rhythm.

Nuclear perfusion and functional imaging: (Left) Rest thallium-exercise MIBI shows inferior, anterior, and anterolateral ischemia (Right) FDG SPECT showing viability in myocardial territories.

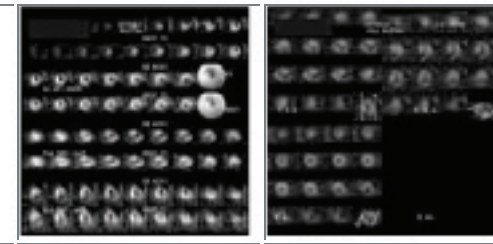

PET scanning with angiography and Biosense NOGA map overlay. Complex image processing and image overlay allows researchers to accurately and reproducibly evaluate various novel treatment options and target therapeutic agents to where they are needed.

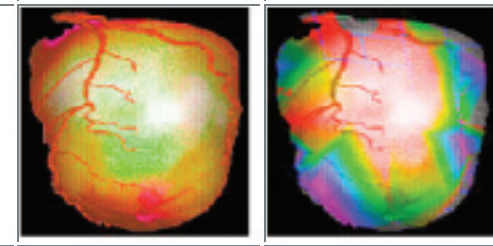

Transthoracic echocardiography (left) **and transesophageal echocardiography** (right). The availability of echocardiography and on- and offline analysis allows longitudinal assessment of various treatment strategies in addition to accurate diagnosis in several clinical situations.

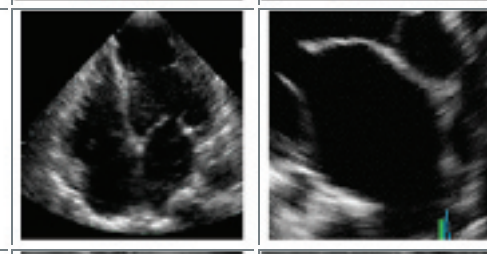

Coronary angiography and digital substraction angiography. Coronary angiography in its preclinical and clinical studies is used to assess angiogenesis and restenosis. Shown is the RCA filling by collaterals from the bypassed LAD in the heparin alginate FGF-2 study.

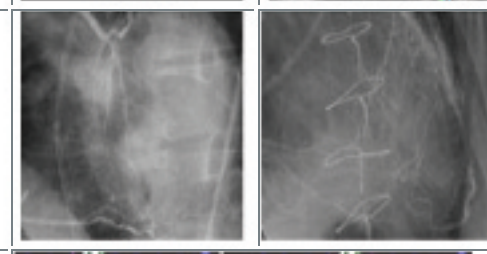

Biosense NOGA electromechanical mapping. The cardiac imaging center has extensive experience with Biosense mapping to diagnose ischemia and viability, and to direct therapeutic intervention on the heart. An electromechanical map showing anterior dysfunction (red) with preserved voltage.

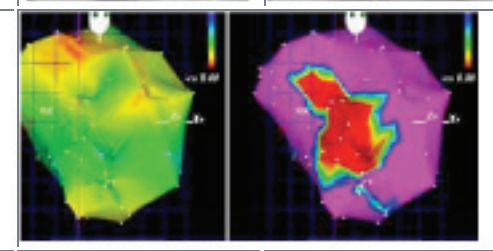

Magnetic resonance imaging. The imaging center carries out MR imaging of the coronary arteries, ventricular structures,regional wall motion, perfusion, and collateralization both for clinical and preclinical use. Shown are 4D cardiac imaging and cine functional imaging.

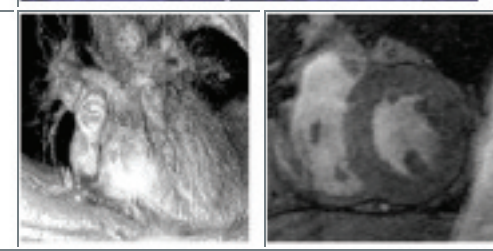

Figure 41.10 The concept of one-stop-shop multimodality image integration. Reprinted with permission from Cardiac Imaging Center, Angiogenesis Research Center, Interventional Cardiology, BIDMC/Harvard Medical School.

Intravascular imaging. This is performed using intravascular ultrasound (left), optical coherence tomography (right), and intravascular MRI. Functional imaging is done with pressure wires and Doppler flow wires to assess coronary blood flown.

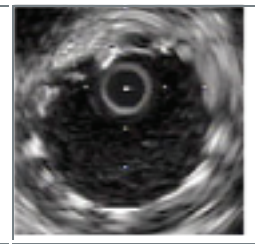

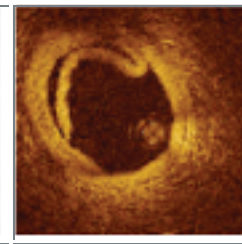

Electron beam tomography. EBCT is done to assess the coronary circulation and to assess coronary calcifications (left). All these imaging modalities are analyzed using advanced image processing techniques (motion vs. time; right) for core lab evaluation.

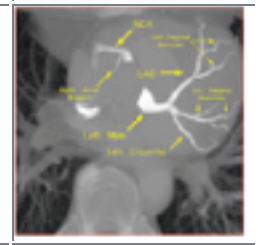

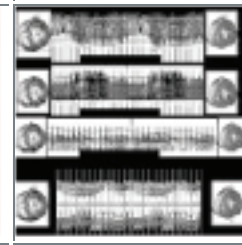

Several other imaging modalities are available: including local trajectory assessment (left) and intracoronary angioscopy (right). All these modalities are available for clinical and preclinical use.

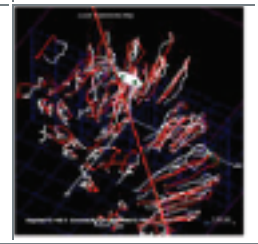

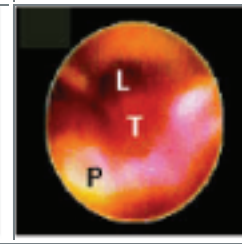

Figure 41.10 (*Continued*)

Furthermore, the need for appropriate use of image technologies and cost effectiveness must be addressed. Similarly, new energy sources and ideally noninvasive ablation of cardiac arrhythmias such as stereotaxis radio surgery is being investigated, and we may witness its clinical application soon [85, 86]. The impact of these new technologies on patient outcomes, that is, safety and efficacy, remains undefined and needs further studies [87].

Conclusion

We have outlined several new modalities that provide new insight into arrhythmogenesis. Cardiac mapping/imaging may soon advance to clinical practice and provide combined anatomical and functional (physiological) information. The future ideal mapping system will be image-guided, affordable, user-friendly, noninvasive, safe, and effective. Real-time multimodality, the so-called "one-stop-shop" as summarized in Figure 41.10, should improve the patient's outcome and shorten procedure time and avoid radiation. In the future, data representation and graphics will be easily presented on soliton resonance that will particularly be applicable to frequency analysis, spectral analysis, and voltage mapping; (see Videoclip 31) (courtesy of Hassan Shenasa). Needless to say, such procedures and technologies should undergo critical examination by the appropriate respective societies.

Acknowledgment

We wish to thank Mona Soleimanieh for her excellent preparation of this manuscript.

References

1 Lewis T. The excitatory process in the dog's heart. *Phil Trans Roy Soc, London* 1914; **205**: 375–420.
2 Lewis T, Feil HS, Stroud WD. Observations upon flutter and fibrillation. Part II. The nature of auricular flutter. *Heart* 1920; **7**: 191–245.
3 Mines GR. On dynamic equilibrium in the heart. *J Physiol* 1913; **4**: 349–83.
4 Mines GR. On circulating excitations in the heart muscles and their possibilities relation to tachycardia and fibrillation. *Trans R Soc Can* 1914; **14**: 43–52.

5 Garrey WE. The nature of fibrillary contraction of the heart: its relation to tissue mass and form. *Am J Physiol* 1914; **3**: 397–414.

6 Wiggers CJ, Wegris R. Ventricular fibrillation due to single, localized induction and condenser shocks applied during the vulnerable phase of ventricular systole. *Am J Physiol* 1940; **128**: 500–5.

7 Wittkampf FH, Weaver EF, Derksen R, et al. LocaLisa: New technique for real-time three-dimensional localization of regular intracardiac electrodes. *Circulation* 1999; **99**: 1312–17.

8 Pappone C, Santinelli V. Nonfluoroscopic mapping as a guide for atrial ablation: current status and expectations for the future. *Euro Heart J Suppl* 2007; **9**: l136–47.

9 Haissaguerre M, Gaita F, Fisher B, et. al. Elimination of arterioventricular nodal reentrant tachycardia using discrete slow potentials to guide application of radiofrequency energy. *Circulation* 1992; **85**: 2162–75.

10 Jackman WM, Beckman KJ, McClelland JH, et. al. Treatment of supraventricular tachycardia due to arterioventricular nodal reentry, by radiofrequency catheter ablation of slow pathway conduction. *N Engl J Med* 1992; **327**: 313–18.

11 Calkins H, Sousa J, el-Atassi R, et.al. Diagnosis and cure of the Wolff–Parkinson–White syndrome or paroxysmal supraventricular tachycardias during a single electrophysiological test. *N Engl J Med* 1991; **324**: 1612–18.

12 Massoud, TF, Gambhir, SS. Molecular imaging in living subjects: seeing fundamental biological processes in a new light. *Genes & Development* 2003; **17**: 545–80.

13 Weissleder, R. A clearer vision for in vivo imaging. *Nat Biotechnol* 2001; **19**: 316–17.

14 Weissleder, R. Molecular imaging: exploring the next frontier. *Radiology* 1999; **212**: 609–14.

15 Efimov IR, Biermann M, Zipes D. Fast fluorescent mapping of electrical activity in the heart: practical guide to experimental design and applications. In: *Cardiac Mapping*, 2nd ed., Shenasa M, Borggrefe M, Breithardt G (eds.). New York: Springer; 2003: 131–57.

16 Salama G. Optical measurements of transmembrane potential in heart. In Loew LM (ed.) *Spectroscopic Membrane Probes*. Boca Raton, FL: CRC Press; 1988: 137–99.

17 Loew LM. *Spectroscopic Membrane Probes*. Boca Raton, FL: CRC Press; 1988: 139–151.

18 Clarke RJ, Zouni A, Holzwarth JF. Voltage sensitivity of the fluorescent probe RH421 in a model membrane system. *Biophys J* 1995; **68**: 1406–15.

19 Arora R, Verheule S, Scott L, et al. Arrhythmogenic substrate of the pulmonary veins assessed by high-resolution optical mapping. *Circulation* 2003; **107**:1816–21.

20 Mandapati R, Skanes A, Chen J, et al. Stable microreentrant sources as a mechanism of atrial fibrillation in the isolated sheep heart. *Circulation* 2000; **101**:194–99

21 Kalifa, J, Klos M, Zlochiver S, et al. Endoscopic fluorescence mapping of the left atrium: a novel experimental approach for high-resolution endocardial mapping in the intact heart. *Heart Rhythm* 2007; **44**: 916–24.

22 Salama G, Choi BR. Optical mapping: its impact on understanding arrhythmia mechanisms. In: *Cardiac Mapping*, 3rd ed., Shenasa M, Hendricks G, Borggrefe M, Breithardt G (eds). New York: Wiley-Blackwell; 2008: 479–490.

23 Fast VG, Kleber AG. Optical mapping of the effects of defibrillation shocks in cell monolayers. In: *Cardiac Mapping*, 2nd ed., Shenasa, M., Borggrefe M, Breithardt, G (eds.). New York: Blackwell; 2003: 291–310.

24 Laurita KR, Rosenbaum DS. Optical mapping of cellular repolarization in the intact heart. In: *Cardiac Mapping*, 2nd ed., Shenasa, M., Borggrefe M, Breithardt, G (eds.), New York: Springer; 2003: 709–28.

25 Del Nido, P, Glynn, P, Buenaventura P, Salama G, Koretsky, AP. Fluorescence measurement of calcium transients in perfused rabbit heart using rhod 2. *Am J Physiol Heart Circ Physiol* 1998;**274**: 728–41.

26 Detter C, Wipper S, Russ D, et al. Fluorescent cardiac imaging: a novel intraoperative method for quantitative assessment of myocardial perfusion during graded coronary artery stenosis. *Circulation* 2007; **116**:1007–14.

27 Tromberg BJ, Shah N, Lanning R, et al. Noninvasive in vivo characterization of breast tumors using photon migration spectroscopy. *Neoplasia*, 2000; **2**: 1–15.

28 Rahimian J, Shah N, Rahbar G, et al. Optical characteristics of normal breast and breast masses with a clinical laser breast scanner (LBS). 92nd Annual Meeting, RSNA 2006. Abstract No. SSC05-07, p. 257.

29 Cope, M. Thesis, University of London, Department of Medical Physics and Bioengineering, University College, London, 1991.

30 Sevick, EM, Chance B, Leigh, J, Nioka S. Quantitation of time-resolved and frequency-resolved optical spectra for the determination of tissue oxygenation. *Anal Biochem* 1991; **195**: 330–51.

31 Beauvoit, B, Kitai, T, Chance, B. Contribution of the mitochondrial compartment to the optical properties of the rat liver: a theoretical and practical approach. *Biophys J* 1994; **67**: 2501–10.

32 Thomsen, S, Tatman, D. Physiological and pathological factors of human breast disease that can influence optical diagnosis, *Ann N Y Acad Sci* 1998; **838**: 171–93.

33 Duncan A, Meek JH, Clemence M, et al. Measurement of cranial optical path length as a function of age using phase resolved near infrared spectroscopy. *Pediatr Res* 1996; **39**: 889–94.

34 Pham TH, Coquoz O, Fishkin JB, et al. A broadbandwidth frequency domain instrument for quantitative

tissue optical spectroscopy. *Rev Sci Instruments* 2000; **716**: 1–14.

35 Hesselink, JR. Fundamentals of MR spectroscopy. http://spinwarp.ucsd.edu/neuroweb/text/mrs-txt.htm

36 Neubauer, S. Magnetic Resonance Spectroscopy of the Heart. In: Cardiovascular Magnetic Resonance, edited by Nagel, E. and Van Rossum, A. and Fleck, E. Steinkopf Verlag, Darmstadt; 2004: 257–265.

37 Nelson SJ, McKnight TR, Henry RG. Characterization of untreated gliomas by magnetic resonance spectroscopic imaging. *Neuroimag Clin* 2002; **12**: 599–613.

38 Graves EE, Nelson SJ, Vigneron DB, et al. Serial proton MR spectroscopic imaging of recurrent malignant gliomas after gamma knife radiosurgery. *AJNR* 2001; **22**: 613–24.

39 Grist TM, Kneeland JB, Rilling WR, Jesmanowicz A, Froncisz W, Hyde JS. Gated cardiac MR imaging and ^{31}P MR spectroscopy in humans at 1.5 T. *Radiology* 1989; **170**: 357–61.

40 Bottomely PA. Noninvasive study of high-energy phosphate metabolism in human heart by depth-resolved ^{31}P NMR spectroscopy. *Science* 1985; **229**: 760–72.

41 Bottomley, PA. MR spectroscopy of the human heart: the status and the challenges. *Radiology* 1994; **191**: 593–612.

42 LeBihan D, Mangin JF, Poupon C, et al. Diffusion tensor imaging: concepts and applications. *J Magn Res Imag* 2001; **13**: 534–46.

43 Rohmer D, Sitek A, Gullberg GT. Reconstruction and visualization of fiber and laminar structure in the normal human heart from ex vivo diffusion tensor magnetic resonance imaging (DTMRI) data (technical note). *Invest. Radiol* 2007; **42**: 777–89.

44 Sermesant M, Delingette H, Ayache N. An electromechanical model of the heart for image analysis and simulation. *IEEE Trans Med Imag* 2006; **25**: 612–25.

45 Hsu EW, Muzikant AL, Matulevicius SA, Penland RC, Henriquez CS. Magnetic resonance myocardial fiber-orientation mapping with direct histological correlation. *Am J Physiol Heart Circ Physiol* 1998; **274**:1627–34.

46 Hocini M, Ho SY, Kawara T, et al. Electrical conduction in canine pulmonary veins: electrophysiological and anatomic correlation. *Circulation* 2002; **105**: 2442–48

47 Choi BR, Liu T, Lavasani M, Salama G. Fiber orientation and cell–cell coupling influence ventricular fibrillation dynamics. *J Cardiovasc Electrophysiol* 2003; **14**: 851–60.

48 Scollan DF, Holmes A, Winslow R, et al. Histological validation of myocardial microstructure obtained from diffusion tensor magnetic resonance imaging. *Am J Physiol* 1998; **2756**: H2308–18.

49 Peeters THJM, Vilanova A, Strijkers GJ, ter Haar Romeny BM. Visualization of the fibrous structure of the heart. In: 11th *International Workshop Vision, Modeling, and Visualization Proceedings, November 22–24, 2006, Aachen, Germany*, Kobbelt L, Kuhlen T, Aach T, Westermann R. (eds.), pp. 309–16.

50 Zhukov L, Barr A. Heart–muscle fiber reconstruction from diffusion tensor MRI. *IEEE Visualization 2003, Proceedings of Vis 2003*, pp. 597–602.

51 Drummond A, MacDonald JM, Dumas, JH, Johnson, TA, Knisley, SB. Development of a system for simultaneous ^{31}P NMR and optical transmembrane potential measurement in rabbit hearts. Engineering in Medicine and Biology Society, 2004. IEMBS 2004. 26th Annual International Conference of the IEEE, Volume 1, pp. 2102–4.

52 Pogue BW, Davis SC, Song X, Brooksby BA, Dehghani H, Paulsen KD. Image analysis methods for diffuse optical tomography. *J Biomed Optics* 2006; **11**: 033001–16.

53 Klemm HU, Ventura R, Steven D, et al. Catheter ablation of multiple ventricular tachycardias after myocardial infarction guided by combined contact and noncontact mapping. *Circulation* 2007; **115**: 2697–2704.

54 Shenasa H, Soleimanieh M, Shenasa M. Variant of pulmonary veins using a 64-multislice computed tomography (MSCT): implications for atrial fibrillation ablation. *J Cardiovasc Comp Tomogr* 2007; **1**: S36.

55 Kim JR, Cardiovascular magnetic resonance imaging. *Cardiol Clin* 2007; **25**:1.

56 Mirowitz SA, Cardiac MR, *Magn Res Imag Clin N Am* 2003; **11**: 1

57 Martinek M, Nesser HJ, Aichinger J, et al. Impact of integration of multislice computed tomography imaging into three-dimensional electroanatomic mapping on clinical outcomes, safety, and efficacy using radiofrequency ablation for atrial fibrillation. *PACE* 2007; **30**: 1215–23.

58 Dong J, Calkins H, Solomon SB, et al. Integrated electroanatomic mapping with three-dimensional computed tomographic images for real-time guided ablations. *Circulation* 2006; **113**: 186–194.

59 Callans DJ, Schwartzman D, Gottlieb CD, et al. Insights into the electrophysiological of atrial arrhythmias gained by the catheter ablation experience: Learning while burning. Part II. *J Cardiovasc Electrophysiol* 1995; **6**: 229–43.

60 Callans DJ, Schwartzman D, Gottlieb CD, et al. Insights into the electrophysiological of atrial arrhythmias gained by the catheter ablation experience: Learning while burning. Part III. *J Cardiovasc Electrophysiol* 1996; **9**: 877–904.

61 Knuuti J, Bengek FM. Positron emission tomography and molecular imaging. *Heart* 2008; **94**: 360–67.

62 Dickfield T, Lei P, Dilsizian V, et al. Integration of three-dimensional scar maps for ventricular tachycardia ablation with positron emission tomography-computed tomography. *J Am Coll Cardiol Imag* 2008; **1**: 73–82.

63 Ector J, De Buck S, Adams J, et al. Cardiac three-dimensional magnetic resonance imaging and fluoroscopy merging: a new approach for electroanatomic

mapping to assist catheter ablation. *Circulation* 2005; **112**: 3769–76.

64 Sra J, Krum D, Malloy A, et al. Registration of three-dimensional left atrial computed tomographic images with projection images obtained using fluoroscopy. *Circulation* 2005; **112**: 3763–68.

65 Berger T, Fischer G, Pfeifer B, et al. Single-beat noninvasive imaging of cardiac electrophysiology of ventricular preexcitation. *J Am Coll Cardiol* 2006; **48**: 2045–52.

66 Jongbloed MRM, Schalij MJ, Zeppenfeld K, et al. Clinical applications of intracardiac echocardiography in interventional procedures. *Heart* 2005; **91**: 981–90.

67 Reddy VY, Malchano ZJ, Homlvang G, et al. Integration of cardiac magnetic resonance imaging with three-dimensional electroanatomic mapping to guide left ventricular catheter manipulation: feasibility in a porcine model of healed myocardial infarction. *J Am Coll Cardiol* 2004; **44**: 2202–13.

68 Aryana A, d'Avila A, Heist EK, et al. Remote magnetic navigation to guide endocardial and epicardial catheter mapping of scar-related ventricular tachycardia. *Circulation* 2007; **115**: 1191–1200.

69 de Groot N, Bootsma M, van der Velde ET, et al. Three-dimensional catheter positioning during radiofrequency ablation in patients: first application of a real-time position management system. *J Cardiovasc Electrophysiol* 2000; **11**: 1183–92

70 Helm RH, Leclercq C, Faris OP, et al. Cardiac dyssynchrony analysis using circumferential versus longitudinal strain implications for assessing cardiac resynchronization. *Circulation* 2005; **111**: 2760–67.

71 Helm RH, Byrne M, Helm AP, et al. Three-dimensional mapping of optical left ventricular pacing site for cardiac resynchronization. *Circulation* 2007; **115**: 953–61

72 Yue AM, Paisey JR, Robinson S, et al. Determination of human ventricular repolarization by noncontact mapping; validation with monophasic action potential recordings. *Circulation* 2004; **110**: 1343–50.

73 Yankelson L, Feld Y, Bressler-Stramer T, et al. Cell therapy for modification of the myocardial electrophysiological substrate. *Circulation* 2008; **117**: 720–31.

74 Haissaguerre M, Extramiana F, Hocini M, et al. Mapping and ablation of ventricular fibrillation associated with long-QT and Brugada syndromes. *Circulation* 2003; **108**: 925–28.

75 Jia P, Ramanathan C, Ghanem RN, et al. Electrocardiographic imaging of cardiac resynchronization therapy in heart failure: observations of variable electrophysiologic responses. *Heart Rhythm* 2006; **3**: 296–310.

76 Ramanatham C, Jia P, Ghanem R, et al. Activation and repolorization of the normal human heart under complete physiological conditions. *PNAS 2006*; **103**; 6309–14.

77 Intini A, Goldstein RN, Jia P, et al. Electrocardiographic imaging (ECGI), a novel diagnostic modality used for mapping of focal left ventricular tachycardia in a young athlete. *Heart Rhythm* 2005; **2**: 1250–52

78 Brown JP, Krummen DE, Feld GK, et al. Using electrocardiographic activation time and diastolic intervals to separate focal from macroreentrant atrial tachycardias. *J Am Coll Cardiol* 2007; **49**: 1965–73.

79 Narayan SM, Feld GK, Hassankhani A, et al. Quantifying intracardiac organization of atrial arrhythmias using temporospatial phase of the electrogradiogram. *J Cardiovasc Electrophysiol* 2003; **14**: 971–81.

80 Narayan SM, Hassankhani A, Feld GK, et al. Separating nonisthmus- from isthmus-dependent atrial flutter using wave front variability. *J Am Coll Cardiol* 2005; **45**: 1269–79.

81 Gerstenfeld EP, Dixit S, Bala R, et al. Surface electrocardiogram characteristics of atrial tachycardias occurring after pulmonary vein isolation. *Heart Rhythm* 2007; **4**: 1136–43.

82 Zhang X, Ramachandra I, Liu Z, et al. Noninvasive three-dimensional electrocardiographic imaging of ventricular activation sequenc. *Am J Physiol Heart Circ Physiol* 2005; **289**: H2724–32.

83 Cappato R, Calkins H, Chen S, et al. A worldwide survey on the methods, efficacy and safety of catheter ablation human atrial fibrillation. *Circulation* 2005; **111**: 1100–5.

84 Calkins H, Brugada J, Packer DL, et al. HRS/EHRA/ECAS expert consensus statement on catheter and surgical ablation of atrial fibrillation: recommendations for personnel, policy, procedures and follow-up. *Heart Rhythm J* 2007; **4**: 816–61.

85 Beller GA. A proposal for an advanced cardiovascular imaging training track. *J Am Coll Cardiol* 2006; **48**: 1299–303

86 Guerra P, Talajic M, Thibault B, et al. β-Radiation for the creation of lesions in the canine atrium. *Circulation* 2004; **110**: 911–14.

87 Wong D, Weidlich G, Sharma A, et al. Myocardial ablation by stereotactic radiosurgery: clinical, physiologic, and histologic correlation. *Proceedings of the 8th International Stereotactic Radiosurgery Society Congress, San Francisco, 2007*.

Index

Note: *Italicized page numbers refer to figures and tables*

Cardiac Mapping, Third Edition Edited by Mohammad Shenasa, Gerhard Hindricks, Martin Borggrefe, and Günter Breithardt
 ISBN: 978-1-405-17572-2